



Tesis Doctoral

La eminencia intercondílea normal y patológica

Carlos Quiles Casas

**Departamento de Anatomía, Biología Celular y
Zoología**

Conformidad de los directores:

Fdo. Dra. Yolanda Gañán Presmanes

Fdo. Dr. Domingo Macías Rodríguez

2017



Ph.D. Thesis

**Intercondylar area
in normal and pathological
tibias**

by **Carlos Quiles**

Department of Anatomy, Cell Biology and Zoology

A thesis submitted in partial fulfillment of the requirements for the
Doctor of Philosophy Degree in Medicine

2017

Copyright © 2017, Carlos Quiles

This document is copyrighted material. Under copyright law, no parts of this document may be reproduced without the expressed permission of the author.

To my parents

Acknowledgments

I owe special and personal gratitude to my father, Dr. Manuel Quiles Galindo, M.D., Ph.D., former chair (1989-2014) of the Orthopaedic Surgery and Traumatology Service at the University Hospital Infanta Cristina of Badajoz, senior professor (1985-2014) and professor emeritus (current) of Orthopaedic Surgery and Traumatology at the University of Extremadura, for his help in study design, data collection, specimen preparation, slicing, imaging, measurement, and multiple contributions and corrections to this dissertation. This special and personal gratitude is extended to my mother, Mercedes Casas Llera, R.N., operating room supervisor of the Orthopaedic Surgery and Traumatology Service at the University Hospital Infanta Cristina of Badajoz, for her help in specimen collection and fluoroscopic imaging.

I have been extremely fortunate to benefit from the contributions of my good friend Dr. Juan Antonio Constantino Cabrera, M.D., Ph.D., most specially regarding statistical analyses, graphical representations of data, formal conventions, and text structure. His constant encouragement to keep on working on this study has turned out to be invaluable.

I am very grateful to my best friend and wife María Teresa Batalla Calvín, B.Lib.Sc., who helped me with areal and slope calculations, three-dimensional point-to-plane distances, statistical analyses, and bibliography. Her many lovely qualities do not include knowledge of or an interest in Medicine, but without her this never would have been written.

I would like to express my deep gratitude to my doctoral supervisors, Dr. Yolanda Gañán Presmanes, M.D., Ph.D., senior professor (1990-present), chair (2011-present) and director of the Department of Anatomy, Cell Biology, and Zoology at the University of Extremadura; and Dr. Domingo Macías Rodríguez, M.D., Ph.D., senior professor (1994-present) of the Department of Anatomy, Cell Biology, and Zoology, and former dean (2000-2004) of the Faculty of Medicine at the University of Extremadura. Their guidance, assistance and encouragement,

as well as their contributions, especially in the fields of anatomy and histology, have been essential for the completion of this work.

I am also very grateful to Dr. Antonio Ramírez de Verger Jaén, Ph.D., senior professor of Latin Philology at the University of Seville (1982-1992), chair of Department at the University of Cádiz (1992-1995) and at the University of Huelva (1995-present), former rector of the University of Huelva (1997-2005), member of the Academy of Sciences, Arts, and Letters of Huelva. His contributions and corrections to Latin terms according to the standard *Terminologia Anatomica* – and to newly coined terms and expressions – used for this study offers a more reliable translation of anatomical terms to be used for international reference.

I am also indebted to José Luis Pereira Soria, M.D., former chair (2014-2015) of the Orthopaedic Surgery and Traumatology Service at the University Hospital Infanta Cristina of Badajoz, and to Lorenzo Castrejón Araya, M.D., for their enthusiastic contributions of arthroscopic videos of the proximal tibia to the study of the three-dimensional osseous attachment of the anterior cruciate ligament.

This PhD study is partly founded on the results of a clinical study, and I would like to acknowledge those surgeons who supported this work with their careful history taking and physical examination, in particular Francisco Parra Rodríguez, M.D., former section head (2013-2015) of the Traumatology Service at the University Hospital Infanta Cristina of Badajoz; Nefalí Muñoz Cortegana, M.D., current section head of the Traumatology Service at the University Hospital Infanta Cristina of Badajoz; and Miguel Domínguez Meléndez, M.D. It was also dependent on all the patients who were so kind to give up their time, participation, and support.

I would also like to thank the surgeons, nurses, and hospital attendants of the Orthopaedic Surgery and Traumatology Service at the University Hospital Infanta Cristina of Badajoz, for their collaboration during the collection and imaging of specimens.

Table of contents

Acknowledgments	9
Table of contents	11
List of tables	25
List of figures	29
List of abbreviations	63
Guide to the reader	67
Conventions used in this study	67
Alphanumeric references	69
Terminologia anatomica	73
I. Introduction	79
I.1. Anatomy	79
I.2. Osteophytes	85
I.2.1. Capsular osteophytes	85
I.2.2. Marginal osteophytes	86
I.2.3. Central osteophytes	88
I.2.4. Periosteal and synovial osteophytes	89
I.3. Height of the tibial spine	91
I.4. Ahlbäck classification of knee osteoarthritis	93
II. Aim	95
Study I	95
Study II	95
Study III	95
Study IV	95

Study V.....	96
Study VI	96
Study VII.....	96
Study VIII	96
Study IX.....	96
Study X.....	96
Study XI	96
Study XII.....	96
Study XIII	96
III. Materials and Methods	97
Study I. Qualitative and quantitative anatomic investigation of bony and soft tissue landmarks of the proximal tibia, and applications to radiography and arthroscopy	97
Specimen collection	97
Specimen preparation.....	97
Anterior attachments	98
ACL detachment	101
Posterior attachments.....	105
Digital processing and 3D surface	110
Selection of areas and nomenclature.....	116
Anatomic measurements	116
Scan system and fluoroscopic image scale validation.....	120
Measurement system validation.....	121
Fluoroscopic study.....	122
Statistical analyses	126
Study II. Investigation of osseous surface structure changes in pathological <i>area intercondylaris tibiae</i> compared to normal tibias, and applications to radiography.....	127
Specimen collection	127

Specimen Preparation.....	127
Fluoroscopic study	128
Notes and measurements	131
Digital processing and 3D surface	132
Normal tibias	133
Scan System Validation	134
Radiographic classification.....	136
Surface analysis.....	137
Quality	137
General	137
Intercondylar Tubercles.....	138
Condyles	138
Anterior area	140
Area 10.....	140
Area 13	141
Slope	141
Statistical analyses	142
Axial, sagittal and coronal cuts of specimens for anatomic, radiographic, and MRI investigation of normal and pathological tibias.....	143
Histologic study of the Parsons' tubercle	145
Study III. Qualitative study of the three-dimensional osseous attachment of the anterior cruciate ligament, assessed with arthroscopy.....	147
Patient selection.....	147
Method	147
Study IV. Qualitative study of the anatomic limits of avulsed bone in tibial spine fractures	149
Patient selection.....	149
Method	149
Studies V – XIII.....	151

Method	151
Measurement on MRI studies (Studies V – XII)	151
Measurements in standing AP radiographs (Studies V – XIII)	152
Study V. Qualitative and quantitative investigation of tibial tubercles in the adult population in radiography and MRI	153
Patient selection	153
Study VI. Qualitative and quantitative investigation of the tibial tubercles in children in radiography and MRI	153
Patient selection	153
Study VII. Qualitative and quantitative investigation of the tibial tubercles in adults with osteochondritis	153
Patient selection	153
Study VIII. Qualitative and quantitative investigation of the tibial tubercles in children with osteochondritis	154
Patient selection	154
Study IX. Qualitative and quantitative investigation of the tibial tubercles in patients with osteonecrosis	154
Patient selection	154
Study X. Qualitative and quantitative investigation of the Parsons' knob in the general population	154
Patient selection	154
Method	155
Study XI. Qualitative and quantitative investigation of osteoarthritic changes in tibias with a previous valgus osteotomy	155
Patient selection	155
Method	155
Study XII. Qualitative and quantitative investigation of tibias in knees with osteochondral fractures	156
Patient selection	156
Method	156

Study XIII. Qualitative and quantitative investigation of tibias in osteoarthritic knees with absence of ACL	157
Patient selection.....	157
Method	157
IV. Results	159
IV.1. Basic anatomy	159
IV.1.1. Normal tibias	159
IV.1.1.1. Demographic values	159
IV.1.1.2. Area measurements.....	159
IV.1.1.3. Soft tissue attachments	161
IV.1.2. Pathological tibias	166
IV.1.2.1. Demographic values and osteoarthritis.....	166
IV.1.2.2. Measurements and pathology	168
IV.2. Intercondylar area and tubercles	171
IV.2.1. Intercondylar area defined by the tubercles and their processes....	171
IV.2.2. Medial intercondylar tubercle, and its processes.....	173
IV.2.3. Lateral intercondylar tubercle, and its processes.....	178
IV.2.4. Tubercle size in knee radiographs and MRI.....	183
IV.2.4.1. Tubercle size in adults	183
IV.2.4.2. Tubercle size in children	187
IV.2.4.3. Tubercle size in adults with osteochondritis	189
IV.2.4.4. Tubercle size in children with osteochondritis.....	190
IV.2.4.5. Tubercle size in osteonecrosis.....	191
IV.2.4.6. Tubercle size in osteochondral fracture.....	192
IV.2.5. Degenerative changes of the intercondylar tubercles	193
IV.2.5.1. Qualitative assessment of degenerative changes	193
IV.2.5.2. Tubercle osteophytes and radiographic density	198
IV.2.5.3. Tubercle width and attrition	205
IV.2.5.4. Tubercle slope	211

IV.2.5.5. Tubercle processes	215
IV.3. Condyles.....	223
IV.3.1. Tibial condyles and intercondylar margins	223
IV.3.2. Degenerative changes of the condyles.....	228
IV.3.2.1. Condylar margin osteophytes.....	228
IV.3.2.1.1. Qualitative assessment of degenerative changes	228
IV.3.2.1.1. Quantitative assessment of osteophytes in condylar rims and corners	232
IV.3.2.2. Condyle wear	241
IV.3.2.2.1. Condyle wear patterns and grades	241
IV.3.2.2.2. Condyle wear and ACL pathology	248
IV.4. Anterior intercondylar area.....	253
IV.4.1. Common structures of the anterior intercondylar area.....	253
IV.4.2. Degenerative changes of the anterior intercondylar area.....	257
IV.4.2.1. Qualitative assessment of degenerative changes	257
IV.4.2.2. Anterior intercondylar ridge and antero-central intercondylar knob.....	264
IV.4.2.3. Parsons' knob	267
IV.4.2.3.1. Parsons' knob size, shape, forming structures, and attrition	267
IV.4.2.3.2. Anteromedial and posterior condylar corner osteophytes in X-ray studies.....	276
IV.4.3. Parsons' knob in imaging studies of the knee	280
IV.4.3.1. Parson's knob: comparison of MRI and X-ray studies	280
IV.4.3.2. Parsons' knob in valgus osteotomy.....	287
IV.5. Anteromedial part of the anterior intercondylar area	293
IV.5.1. Fingerprint, anterior sagittal ridge, and anterior knob	293
IV.5.2. Attachment of the anterior root of the medial meniscus	296
IV.5.3. Degenerative changes of the anteromedial intercondylar area.....	299

IV.6. Lateral part of the anterior intercondylar area	303
IV.6.1. Anterolateral recess, fossa, and vallecule	303
IV.6.2. Attachment of the anterior root of the lateral meniscus.....	306
IV.6.3. Degenerative changes of the anterolateral intercondylar area	308
IV.6.3.1. Qualitative assessment	308
IV.6.3.2. Quantitative assessment	310
IV.7. Posteromedial part of the anterior intercondylar area	317
IV.7.1. Anterior intercondylar staircase.....	317
IV.7.1.1. Lines and indentations of the anterior intercondylar staircase	319
IV.7.1.2. Stairs and landings of the anterior intercondylar staircase	329
IV.7.2. Attachment of the anterior cruciate ligament	332
IV.7.2.1. Shape of the ACL footprint	332
IV.7.2.2. Area of the ACL footprint	343
IV.7.2.3. Distances from ACL footprint center to anatomic landmarks	343
IV.7.2.3.1. Anterior intercondylar staircase X.....	346
IV.7.2.4. ACL bundles	347
IV.7.2.2.1. Qualitative and quantitative description.....	347
IV.7.2.2.3. Distances from ACL anteromedial and posterolateral bundles	349
.....	
IV.7.2.2.4. Distances from ACL anteromedial bundle, medial and lateral	353
parts	
IV.7.2.3. Anterior intercondylar staircase in 3D model from arthroscopic	357
video	
IV.7.2.4. Anterior intercondylar staircase in tibial spine fractures.....	360
IV.7.3. Degenerative changes of the anterior intercondylar staircase	363
IV.7.3.1. Qualitative assessment	363
IV.7.3.2. Quantitative assessment.....	366
IV.8. Intertubercular ridge	373
IV.8.1. Intertubercular area, and its anterior and posterior walls.....	373

IV.8.2. Attachment of the posterior root of the lateral meniscus	376
IV.8.3. Degenerative changes affecting the intertubercular ridge	378
IV.9. Posterior intercondylar area.....	385
IV.9.1. Posterior intercondylar area and posterior wall.....	385
IV.9.2. Attachment of the posterior root of the medial meniscus	387
IV.9.3. Degenerative changes affecting the posterior wall.....	390
IV.10. Posterior facet	395
IV.10.1. Intercondylar triangle and posterior rim.....	395
IV.10.1.1. Lines and indentations of the posterior facet	395
IV.10.1.2. Common areas of the posterior facet.....	403
IV.10.2. Attachment of the posterior cruciate ligament.....	405
IV.10.2.1. Shape and area of the PCL footprint	405
IV.10.2.2. Distances from PCL footprint center to anatomic landmarks	412
IV.10.2.3. PCL bundles.....	413
IV.10.2.3.1. Qualitative and quantitative description.....	413
IV.10.2.3.2. Distances from PCL anterolateral and posteromedial bundles.....	413
IV.10.3. Degenerative changes of the posterior facet.....	416
IV.11. General anatomic overview: imaging and histology studies	419
IV.11.1. Identification of structures in plain radiography	419
IV.11.1.1. Inferosuperior (axial) fluoroscopic images	419
IV.11.1.2. Anteroposterior fluoroscopic images	426
IV.11.1.3. Lateral fluoroscopic images.....	430
IV.11.2. Sectional anatomy and histology of normal specimens.....	434
IV.11.2.1. Anteroposterior (sagittal) cuts and radiographs	434
IV.11.2.2. Mediolateral (coronal) cuts and radiographs.....	436
IV.11.3. Sectional anatomy and histology of pathological specimens.....	441
IV.11.3.1. Anteroposterior (sagittal) cuts and radiographs.....	441

IV.11.3.2. Mediolateral (coronal) cuts and radiographs.....	447
IV.11.3.3. Horizontal (axial) cut of the tubercles.....	450
IV.11.4. Histology of the Parsons' knob.....	452
IV.12. Osteophytes and diagnosis of osteoarthritis.....	461
IV.12.1. Osteophyte grade and maximum attrition zone of the condyles..	461
IV.12.2. Osteophyte grade and condyle attrition.....	482
IV.12.3. American Knee Society Clinical Rating System.....	492
V. Discussion.....	505
V.0. Method (Study I & Study II).....	505
V.0.1. Specimen preparation.....	505
V.0.2. Scan and fluoroscopic image system validation.....	505
V.0.3. Measurement system validation.....	505
V.0.5. Anatomical measurements.....	506
V.0.6. Osteophyte grades.....	507
V.0.7. Correlation between paired specimens.....	507
V.1. General anatomy.....	509
V.1.1. Normal anatomy.....	509
V.1.1.1. Qualitative assessment of areas.....	509
V.1.1.1.1. Osseous areas.....	509
V.1.1.1.2. Attachment areas.....	509
V.1.1.2. Quantitative assessment of areas.....	510
V.1.2. Pathologic anatomy.....	511
V.2. Tubercles.....	513
V.2.1. Intercondylar area and tubercles.....	513
V.2.2. Processes.....	515
V.2.3. Tubercle size in knee radiographs.....	518
V.2.3.1. Tubercle size in adults.....	518
V.2.3.2. Tubercle size in children.....	518
V.2.3.3. Tubercle size in adults with osteochondritis.....	519

V.2.3.4. Tubercle size in children with osteochondritis	519
V.2.3.5. Tubercle size in osteonecrosis	520
V.2.3.6. Tubercle size in osteochondral fracture	520
V.2.4. Degenerative changes.....	521
V.2.4.1. General discussion	521
V.2.4.2. Tubercle size	523
V.2.4.3. Tubercle width and attrition	523
V.2.4.4. Tubercle slope.....	524
V.2.4.4. Tubercle processes.....	525
V.3. Condyles	527
V.3.1. Condyles and condylar rims	527
V.3.2. Degenerative changes.....	528
V.3.2.1. Condylar margins.....	528
V.3.2.1.1. Rims	528
V.3.2.1.2. Corners	529
V.3.2.1. Condyle wear	530
V.3.2.1.2. General discussion	530
V.3.2.2.2. Condylar wear patterns and grades.....	533
V.3.2.2.3. Condyle wear and ACL absence.....	534
V.3.2.2.3.1. Study II.....	534
V.3.2.2.3.2. Study XIII.....	536
V.4. Anterior intercondylar area	539
V.4.1. Anterior intercondylar area's ridge	539
V.4.2. Parsons' knob	539
V.4.3. Degenerative changes to the AIA	541
V.4.3.1. Anterior intercondylar ridge and anterior knob.....	541
V.4.3.2. Parsons' knob.....	542
V.4.3.2.1. General discussion	542
V.4.3.2.2. Parsons' osteophyte size, shape, forming structures	544

V.4.3.2.3. Anteromedial and posterior condylar corner osteophytes in X-ray studies.....	546
V.4.4. Parsons' knob in imaging studies of the knee.....	547
V.4.4.1. Parson's osteophyte: comparison of MRI and X-ray studies....	547
A case of congenital ACL absence	548
V.4.4.2. Parson's osteophyte in valgus osteotomy.....	549
V.5. Anteromedial part of the anterior intercondylar area.....	551
V.5.1. Fingerprint, anterior sagittal ridge, and anterior knob.....	551
V.5.2. Attachment of the anterior root of the medial meniscus.....	552
V.5.3. Degenerative changes of the anteromedial AIA.....	554
V.6. Lateral part of the anterior intercondylar area.....	555
V.6.1. Anterolateral intercondylar recess, fossa, and vallecule.....	555
V.6.2. Attachment of the anterior root of the lateral meniscus	557
V.6.3. Degenerative changes of the lateral AIA.....	559
V.7. Posteromedial part of the anterior intercondylar area.....	561
V.7.1. Anterior intercondylar staircase	561
V.7.2. Attachment of the anterior cruciate ligament.....	562
V.7.2.1. Quantitative and qualitative determination of attachment.....	562
V.7.2.1.1. ACL footprint shape	562
V.7.2.1.2. Anteromedial and anterior border of the ACL footprint	563
V.7.2.1.3. The C-shaped ACL and its lateral overlap with the ARLM attachment.....	565
V.7.2.1.4. Posterior Arch.....	567
V.7.2.1.5. Quantitative assessment of the ACL footprint area	568
V.7.2.1.6. Distances from ACL footprint center to anatomic landmarks	570
V.7.2.1.7. Anterior intercondylar staircase X	572
V.7.2.2. ACL fiber bundles	573
V.7.2.2.1. ACL division into bundles	573

V.7.2.2.2. Qualitative assessment of AM and PL footprints	575
V.7.2.2.3. Quantitative assessment of AM and PL footprint areas.....	579
V.7.2.2.4. Distances from AM and PL footprint centers to anatomic landmarks	580
V.7.2.2.5. Quantitative assessment of AMM and AML footprints, and distances to anatomic landmarks.....	581
V.7.2.3. Anterior intercondylar staircase in 3D model from arthroscopic video	582
V.7.2.4. Anterior intercondylar staircase in tibial spine fractures	583
V.7.3. Degenerative changes of the anterior intercondylar staircase	584
V.8. Intertubercular ridge	585
V.8.1. Intertubercular area.....	585
V.8.2. Attachment of the posterior root of the lateral meniscus.....	586
V.8. Degenerative changes of the intertubercular ridge	588
V.9. Posterior intercondylar area	589
V.9.1. Posterior intercondylar area and posterior wall	589
V.9.2. Attachment of the posterior root of the medial meniscus.....	590
V.9.3. Degenerative changes of the posterior intercondylar area.....	591
V.10. Posterior facet.....	593
V.10.1. Posterior intercondylar triangle and posterior rim.....	593
V.10.2. Attachment of the posterior cruciate ligament	594
V.10.2.1. Qualitative assessment and borders	594
V.10.2.2. PCL footprint area and distances from its center to anatomic landmarks.....	595
V.10.2.3. PCL bundles	596
V.10.2.3.1. Bundle division and qualitative assessment	596
V.10.2.3.2. Area of AL and PM footprints and distances to anatomic landmarks.....	598
V.10.3. Degenerative changes of the posterior facet	600
V.11. Imaging and histology studies	601

V.11.1. Identification of structures in plain radiography.....	601
V.11.2. Sectional anatomy and histology	602
V.11.3. Histology.....	603
V.12. Osteophytes and diagnosis of osteoarthritis.....	605
V.12.1. Osteophyte grade and maximum attrition zone of the condyle	605
V.12.2. Osteophyte grade and condyle attrition	606
V.12.2.1. Ahlbäck classification system of osteoarthritis.....	606
V.12.2.2. Classifications including osteophytes.....	607
V.12.3. American Knee Society Clinical Rating System	610
VI. Conclusion	613
VI.1. Anatomy	613
VI.1.1. Osseous surface.....	613
VI.1.2. Attachment areas and osseous elevations.....	613
VI.1.3. Cruciate ligament detachment: bundle distinction and references.	613
VI.2. Tubercle height and pathology	614
VI.3. Degenerative changes	614
VI.3.1. Corner osteophytes.....	614
VI.3.2. Parsons' knob and histology	614
VI.3.3. Degenerative changes	615
VI.4. Surface anatomy	615
References	617
Appendix I. German literature.....	645
Mechanik der menschlichen Gehwerkzeuge: Eine anatomisch-physiologische Untersuchung (1836).....	645
Untersuchungen über die Anatomie und Mechanik des Kniegelenkes (1855)	648
Handatlas der Anatomie des Menschen (1896) by Spalteholz.....	652

Handbuch der Anatomie und Mechanik der Gelenke unter Berücksichtigung der bewegenden Muskeln (1904)	653
Atlas der deskriptiven Anatomie des Menschen (1904) by Sobotta.....	658
Appendix II. Russian and Eastern literature.....	659
Anatome Topographica Sectionibus per Corpus Humanum Congelatum Triplici Directione Ductis Illustrata (1855).....	659
Az ember anatómiájának atlasza (1962) by Kiss and Szentágothai.....	663
Appendix III. English literature.....	665
Observations of the Head of the Tibia (1904)	665
Anatomy of the Human Body (1918) by Gray	667
Appendix IV. French and Romance literature.....	669
Traité d'Anatomie Humaine (1892) by Poirier & Charpy.....	669
Traité d'Anatomie Humaine (1899) by Testut.....	670
Traité d'anatomie humaine (1951) by Paturet.....	671
Anatomía Humana (1959) by Orts Llorca.....	673

List of tables

Table 1. Tests of normality of osseous areas.....	160
Table 2. Mean areas in mm ² and in percentage of total area of the tibia, with 95% CI.....	161
Table 3. Tests of normality of footprint areas.....	163
Table 4. Mean attachment areas in mm ² and in percentage of total area of the tibia, with 95% CI.	163
Table 5. Regression model to predict AP and ML size from ARLM attachment area, including dummy variable (Left).	164
Table 6. Regression model to predict AP and ML size from ARMM attachment area, including dummy variable (Left).	164
Table 7. Regression model to predict AP and ML size from PRLM attachment area, including dummy variable (Left).	165
Table 8. Regression model to predict AP and ML size from PRMM attachment area, including dummy variable (Left).	165
Table 9. Regression model to predict AP and ML size from ACL attachment area, including dummy variable (Left).	165
Table 10. Regression model to predict AP and ML size from PCL attachment area, including dummy variable (Left).	166
Table 11. Results for normality distribution testing of numeric data of the sample (of the 68 specimens for which all data was collected).....	170
Table 12. Distances in mm, 95% CI, Coefficient of variation (CV), Pearson correlation values for AP and ML, with their corresponding p-values.	297
Table 13. Distances in mm, 95% CI, Coefficient of variation (CV), Pearson correlation values for AP and ML, with their corresponding p-values.	307
Table 14. Distances from the ACL center to the selected points, in mm, on the surface, with 95% confidence interval (CI) and coefficient of variation (CV). Pearson correlation with AP depth (AP), and significance (AP p), and ML width (ML) and significance (ML p).....	344
Table 15. Distances from the ACL center to the selected points, on the surface: range, percentage of the AP depth (AP%) and ML width (ML%), and their 95% confidence interval (CI).	345
Table 16. Spearman's rank-order correlation between distances: ACL center to reference points and AISX to the same reference points; with p-values, and number of specimens for each distance.	347
Table 17. Distances from the center of the AM bundle of the ACL to the selected points, in mm, on the surface, with 95% confidence interval (CI) and coefficient of variation (CV). Pearson	

correlation with AP depth (AP), and significance (AP p), and ML width (ML) and significance (ML p).....	349
Table 18. Distances from the center of the AM bundle of the ACL to the selected points, on the surface: range, percentage of the AP depth (AP%) and ML width (ML%), and their 95% confidence interval (CI).....	350
Table 19. Distances from the center of the PL bundle of the ACL to the selected points, in mm, on the surface, with 95% confidence interval (CI) and coefficient of variation (CV). Pearson correlation with AP depth (AP), and significance (AP p), and ML width (ML) and significance (ML p).....	351
Table 20. Distances from the center of the PL bundle of the ACL to the selected points, on the surface: range, percentage of the AP depth (AP%) and ML width (ML%), and their 95% confidence interval (CI).....	352
Table 21. Distances from the center of the AMM bundle of the ACL to the selected points, in mm, on the surface, with 95% confidence interval (CI) and coefficient of variation (CV). Pearson correlation with AP depth (AP), and significance (AP p), and ML width (ML) and significance (ML p).....	353
Table 22. Distances from the center of the AMM bundle of the ACL to the selected points, on the surface: range, percentage of the AP depth (AP%) and ML width (ML%), and their 95% confidence interval (CI).....	354
Table 23. Distances from the center of the AML bundle of the ACL to the selected points, in mm, on the surface, with 95% confidence interval (CI) and coefficient of variation (CV). Pearson correlation with AP depth (AP), and significance (AP p), and ML width (ML) and significance (ML p).....	355
Table 24. Distances from the center of the AML bundle of the ACL to the selected points, on the surface: range, percentage of the AP depth (AP%) and ML width (ML%), and their 95% confidence interval (CI).....	356
Table 25. Distances in mm, 95% CI, Coefficient of variation (CV), Pearson correlation values for AP and ML, with their corresponding p-values.....	377
Table 26. Distances in mm, 95% CI, Coefficient of variation (CV), Pearson correlation values for AP and ML, with their corresponding p-values.....	388
Table 27. Distances from the center of the PCL footprint to the selected points, in mm, on the surface, with 95% confidence interval (CI) and coefficient of variation (CV). Pearson correlation with AP depth (AP), and significance (AP p), and ML width (ML) and significance (ML p). * Correlation is significant at the 0.05 level (2-tailed). ** Correlation is significant at the 0.01 level (2-tailed). P: posterior geniculum.....	412
Table 28. Distances from the PCL center to the selected points, on the surface: range, percentage of the AP depth (AP%) and ML width (ML%), and their 95% confidence interval (CI).....	413
Table 29. Distances from the center of the AL bundle of the PCL to the selected points, in mm, on the surface, with 95% confidence interval (CI) and coefficient of variation (CV). Pearson correlation with AP depth (AP), and significance (AP p), and ML width (ML) and significance (ML p).....	414

Table 30. Distances from the center of the AL bundle of the PCL to the selected points, on the surface: range, percentage of the AP depth (AP%) and ML width (ML%), and their 95% confidence interval (CI).	414
Table 31. Distances from the center of the PM bundle of the PCL to the selected points, in mm, on the surface, with 95% confidence interval (CI) and coefficient of variation (CV). Pearson correlation with AP depth (AP), and significance (AP p), and ML width (ML) and significance (ML p).	415
Table 32. Distances from the center of the PM bundle of the PCL to the selected points, on the surface: range, percentage of the AP depth (AP%) and ML width (ML%), and their 95% confidence interval (CI).	415
Table 33. Coefficients table for best model predicting medial condyle attrition.	483
Table 34. Coefficients table for best model predicting medial condyle attrition, without AM corner.	483
Table 35. Coefficients table for best model predicting medial condyle attrition, including Ahlbäck OA grade.....	483
Table 36. Coefficients table for best model predicting lateral condyle attrition.....	484
Table 37. Coefficients table for best model predicting lateral condyle attrition, excluding variables not commonly seen in radiographs.	484
Table 38. Study II. KS items and knee OA: Item scores (mean and 95% confidence intervals) by Ahlbäck OA grade group.	494

List of figures

- Fig. 1. Drawing of right proximal tibia (anterior is up), with soft tissues attached. Modified from Fick (1904). 79
- Fig. 2. Photograph of left proximal tibia (anterior is up), with cruciate ligaments and menisci in situ. Modified from Parsons (1906). α =anterior cornu of internal semi-lunar cartilage. β =anterior crucial ligament. ϵ =anterior cornu of external semi-lunar cartilage. γ =posterior cornu of external semi-lunar cartilage. δ =posterior crucial ligament. ξ =ligament of Wrisberg. θ =little knob on the outer margin of the internal articular facet, indicating the attachment of the anterior crucial ligament.80
- Fig. 3. Image modified from Jacobsen (1974)²¹. Left proximal tibia. (a) The most common arrangements of the areas described. (b) Another possibility for the anterior intercondylar area. Location of foramina nutricia indicated by \circ 83
- Fig. 4. Profile of the proximal tibia. Modified from Jacobsen (1976)²². Unbroken lines (on the right): Lateral tibial condyle and lateral intercondylar tubercle. Broken lines: Medial tibial condyle and medial tubercle. Dotted lines: Anterior tibial margin, tibial tuberosity, crest of anterior intercondylar area, a, and digital impression, b. Parsons' knob, A. Posterior aspect of medial condyle, B. Small circles: Head of fibula. 84
- Fig. 5. Tibia L. Dissection of specimens was performed over a millimeter paper. The medial meniscus (MM) has been cut with a scalpel in its central portion to allow for anterior and posterior horn manipulation. The lateral meniscus (ML) has been already cut. 98
- Fig. 6. Tibia L. Attachment of the anterior horn of the medial meniscus (MM). The anterior part of the medial meniscus has been reflected and traction is applied with a forceps. The central root attachment is pointed to by the scalpel. A dotted red line indicates the transition to the supplemental fibers, to the left of the image. The attachment of the (cut) anterior intermeniscal ligament to the anterior horn of the medial meniscus is depicted with an arrowhead. 99
- Fig. 7. Tibia M. Detachment of anterior horn of medial meniscus. Observe the pyrography marks in the detached area. 100
- Fig. 8. Tibia L. Overlap between the anterior root of the lateral meniscus and the ACL. A plane is developed between them with the help of a blade. ARMM (white): attachment area of anterior root of the medial meniscus. ARLM: anterior root of lateral the meniscus. 100
- Fig. 9. Tibia L. Traction is applied with the forceps to the anterior horn of the lateral meniscus (AHLM). 101
- Fig. 10. Tibia L. AM and PL bundle fibers adapt to different traction and rotation applied to the ACL, allowing for a gross determination of their division, the main mediolateral inter-space

(dotted blue line). ARLM: Anterior root of lateral meniscus. ARMM: attachment area of anterior root of medial meniscus.102

Fig. 11. Tibia L. Observe the color change in the division of anterior fibers of the ACL, pointed by the scalpel. The line depicted in red dots was deemed to represent the anterior end of the septum that divides the AM-M and AM-L bundles, and blunt dissection was started proximally. ARLM: attachment area of anterior root of lateral meniscus102

Fig. 12. Tibia L. Anteroposterior dissection of the ACL completed sharply with a scalpel in approximately the distal 5mm of the insertion. The proximal cut was made through the observed change in fibers anteriorly. Notice from the position of the anteroposterior fat inter-space and the cut fibers anteriorly, that anterior dissection was completed slightly lateral to their true division. Observe also the triangular shape of the fat in the center of the cut ACL, representing the intersection of both inter-spaces, the mediolateral and the anteroposterior ones. Notice also the other, lesser mediolateral fat inter-spaces. Burn marks from insertion of anterior horn of medial meniscus and anterior horn of lateral meniscus (lateral to ACL), already detached, can also be seen.....103

Fig. 13. Tibia L. Image corresponding to Fig. 12, augmented and modified, with borders of the triangular fat in the center of the ACL attachment (crossing of anteroposterior and mediolateral fat inter-spaces) drawn with blue dashed lines. Green dashed lines are drawn over lesser fat inter-spaces (mediolateral), corresponding to incisures in the footprint (see Fig. 15 below). Red dots mark the actual position of the mediolateral inter-space anteriorly, which in this case was not recognized at a glance (the cut was made lateral to it).....104

Fig. 14. Tibia L. The AM-M and PL bundles have been detached from the rest of the ACL, and their attachment area marked with pyrography. The remaining ACL stump is marked as the AM-L bundle.104

Fig. 15. Tibia L. Division of ACL footprint in PL, AM-M and AM-L bundle attachment areas. Notice the pyrography marks at the periphery of the ACL and in the inner divisions (anteroposterior septum digitally retouched with red dots, mediolateral septum retouched with blue dashes). Inner pyrography marks were made more lightly than outer marks: the mediolateral inter-space more lightly marked than the anteroposterior interspace. Nevertheless, damage to the ACL footprint relief can be appreciated at first sight. Two of the documented lesser fat inter-spaces, seen in Fig. 12, are drawn as green dash-dot lines.105

Fig. 16. Tibia L. Detachment of popliteus muscle (MP) from the lateral meniscus (LM). Observe the cut accessory popliteus muscle (MP) attachment on lateral meniscus (arrow).....106

Fig. 17. Tibia K. Traction and rotation applied to posterior cruciate ligament stump with the help of a forceps. Observe the twisting of the fibers near the attachment. See Fig. 18.....106

Fig. 18. Tibia K. Image corresponding to Fig. 17, augmented and modified, with dashed line drawn over the main anteroposterior inter-space found..... 107

Fig. 19. Tibia G. The PCL had been marked with pyrography over the specimen, and the AM and PL bundle separation has been drawn over the photograph with a blue dashed line. Remaining shiny white fibers (swf). PRLM: Posterior root of the lateral meniscus. PRMM: posterior root of the medial meniscus. 107

Fig. 20. The insertion of the posterior cruciate ligament (PCL) has been detached and its area marked. The posterior roots of the medial (PRMM) and lateral meniscus (PRLM) can be seen. 108

Fig. 21. Tibia L. Traction is applied to the posterior horn of the lateral meniscus to identify its central fibers. 108

Fig. 22. Tibia L. Transverse shiny white fibers (sf) were distinguished from the posterior root of the medial meniscus (PRMM) before detachment and marking. The insertion of the posterior root of the lateral meniscus (PRLM) has been detached and its area marked. 109

Fig. 23. Tibia L. Gross soft tissue remains were cleaned off after marking the attachment area of the posterior root of the medial meniscus (PRMM). 109

Fig. 24. Example of cut sanding sponge used for this study. Cut borders show the inner material (in yellow). A. Superoinferior view. B. Lateral view. 113

Fig. 25. Tibia L over the swivel stand. Photograph taken from posterolateral view at height 14cm over the table. Observe the shadows on the white cardboard and the reflective surface of the specimen. 113

Fig. 26. 3D model of tibia L. Setting of scale by applying width measurement to the machine-made cut side of the sanding sponge (notice the digital thumbtacks marking lateral and medial border points). 114

Fig. 27. 3D model of tibia L. Secondary files from mesh processing software: A. Original 3D model. B. Contour lines. C. Per-cell statistics cloud D. Mesh with height ramp. 114

Fig. 28. Raster data of 3D model of tibia L. Terrain analysis from raster: A. Relief at 0.5 Z index, light from anteromedial. B. Slope. C. Hillshade. D. Ruggedness Index. 115

Fig. 29. 3D model of Tibia L and contour lines. A standard texture (“Leather”) is used to avoid bias in selecting the purely osseous areas. 115

Fig. 30. 3D model of tibia L. Observe that a sagittal plane parallel to the posterior axis (PA) has been used instead of a line, to facilitate measurement. However, the horizontal plane (with green borders) is positioned horizontally during measurements. PAperp: plane perpendicular to PA, used to obtain the (deepest) anteroposterior measure. AA: anterior axis. 118

Fig. 31. 3D model of tibia L, seen from below (distal to proximal), hollow. ACL area selected in green, ACL area best fit plane in red, and the centroid is the centered green dot. Due to the three-dimensional shape of the ACL in this specimen, its centroid lies below the surface. 118

Fig. 32. 3D model of Tibia L: Osseous surface of the ACL attachment, isolated from the rest of the 3D model. A line (ACLPlanePerp, in orange) perpendicular to the ACL plane (ACLPlane, in red) is projected from the ACL centroid (ACLCentroid, in green). Observe how the perpendicular line crosses the selected mesh triangle (ACLCenter, in blue) when passing from below the surface (to the right) to the upper surface (to the left of the image). 119

Fig. 33. 3D model of tibia L. Magnification of anterior intercondylar aspect. Selected triangles in faded specimen’s mesh: soft tissue attachment centers active (in red with green surrounding lines), osseous landmarks in gray. Names have been placed to the left of certain osseous landmarks (see 119

Fig. 34. 3D model of tibia L. Anterior to posterior vision of the anterior intercondylar area. Distance measurement from ACL center (1) to the geniculum (2). Measurement is done on

surface projection: observe how the dashed line connecting 1 and 2 is not straight (over the surface), but follows the area's relief.....	120
Fig. 35. 3D model of tibia L. A central point is selected from ACL center triangle, defined by the coordinates shown in the upper left corner (under "First Point"). This is repeated ten times, and the difference between each selected point and the real center is collected.	121
Fig. 36. C-Arm in place for specimen imaging (A). Computer and display of the C-Arm for adjustments (B)	122
Fig. 37. (A to D). A. The tube of the C-Arm is placed 32 cm under the hand table. B and C. Over the hand table a small area is delimited by two scalpels. D. The camera of the C-Arm is centered over that area.....	122
Fig. 38. Tibia L. Inferosuperior (IS), anteroposterior (AP), and lateral (L) fluoroscopic views. Lateral fluoroscopy after metal wires were glued to the intercondylar tubercles (L2). Posterior (post), lateral (lat) and anterior (ant) sides of the specimen have been labelled for clarity....	124
Fig. 39. Tibia L. Soft tissue attachment areas painted with barium sulfate (A) and inferosuperior fluoroscopic view (B).	125
Fig. 40. Tibia L. Lateral (A) and anteroposterior (B) fluoroscopic view after barium sulfate painting.	126
Fig. 41. Tibia 15. Fresh specimen. Photograph with ruler (in cm) for scale, taken before processing.	128
Fig. 42. Tibia 15. Metal wires were glued to the specimens' intercondylar tubercles after taking the initial fluoroscopic images. A screw was inserted on the posteromedial aspect of the sanding sponge for stability in AP and lateral projections.	129
Fig. 43. Tibia 15. Inferosuperior (IS), anteroposterior (AP), and lateral (L) fluoroscopic images. After metal wires had been glued, a new projection (L2) was taken. Posterior (post), lateral (lat) and anterior (ant) sides of the specimen have been labelled for clarity.....	130
Fig. 44. Tibia 15. Outline of the specimen's features using the standard drawing.....	132
Fig. 45. 3D model of Tibia 15. Original 3D model obtained (A), with sanding sponge used for scaling. Scaled and sliced 3D model used for analysis (B).	133
Fig. 46. 176- and 48-photograph 3D models of tibia M. Cloud/cloud distance computed.....	135
Fig. 47. Different 48-photograph 3D models of tibia 10. Cloud/cloud distance computed.....	135
Fig. 48. Tibia 15. Non-weight bearing lateral (left image) and standing AP (right image) knee radiographs taken before surgery.	136
Fig. 49. Tibia 15. Close-up of standing AP (A) and non-weight-bearing lateral (B) knee radiographs.....	137
Fig. 50. 3D model of Tibia I (left-mirrored). Superoinferior view (S) with contour lines superimposed. Anterior (A) and posterior (P) views. Condyles divided in 4 similar parts, numbered 1-4 (M: Medial; L: Lateral). In yellow, main attrition areas (solid line) and complementary attrition areas (dashed line). Medial tubercle processes in red, lateral tubercle processes in blue. Other ridges in green. Common osteophytes selected in red (note how G and H are connected, as are I and AL). AM: anteromedial corner; AL: anterolateral corner; PM: posteromedial corner; PL: posterolateral corner; MA: medial rim, anterior part; MP: medial rim, posterior part; LA: lateral rim, anterior part; LP: lateral rim, posterior part.	139
Fig. 51. 3D model of tibia L. Medial and lateral tubercle slopes selected, with best-fit planes....	142

Fig. 52. 3D model of tibia 15. Medial and lateral tubercle slopes selected, with best-fit planes obtained.....	142
Fig. 53. High precision low speed saw, lateral (A) and frontal (B) views.	144
Fig. 54. Clamp for low speed saw (A), and specimen holder with sliced specimen (B).....	144
Fig. 55. Tibia C. Photograph with schematic drawing of plan for sagittal and coronal cuts.	145
Fig. 56. MRI sagittal cut through the lateral tubercle (1). Filter gallery photocopy applied over cut image Adobe Photoshop (2). LT height to the inferior aspect of the MRI slice (3). A parallel line is drawn to the visible inferior tibial cut (4). That line is ascended to the widest aspect of the visible plateau, and AP depth is measured (5). A perpendicular is drawn from this line to the tubercle peak, and a measurement is made from the point where both lines cross each other to the posterior aspect of the plateau (6).....	151
Fig. 57. Snapshot of measurements taken over the image with a DICOM viewer: tibial plateau line, with two perpendiculars drawn to the peak of the medial and lateral tubercles. ML width (W), MT height (MTh) and LT height (LTh) appear in pixels (pix).....	152
Fig. 58. Tibiofemoral angle measured in an AP standing radiograph of a normal tibia.	156
Fig. 59. Intraoperative photographs of an ACL-deficient knee included in this study.....	157
Fig. 60. 3D model of tibia L. All areas selected have been highlighted and labelled.....	160
Fig. 61. 3D model of tibia L. Insertion areas highlighted and labelled. In white, approximate areas of attachment of accessory fibers of the four meniscal roots. The approximate course of the anterior intermeniscal ligament (AIML) is also drawn.	162
Fig. 62. Histogram of Ahlbäck OA grade distribution in the sample studied, in percentage.....	167
Fig. 63. Histogram of sex distribution in each Ahlbäck OA grade, in absolute numbers.....	167
Fig. 64. Histogram of diagnosis distribution in the sample studied, in percentage.	168
Fig. 65. Box-and-whisker plot of age distribution in each Ahlbäck OA grade.	169
Fig. 66. Box-and-whisker plot of tibiofemoral angle distribution in each Ahlbäck OA grade. ..	169
Fig. 67. 3D model of tibia A. Intercondylar tubercles' ridges, with main processes and peaks drawn and labelled over the image with help of contour lines.....	172
Fig. 68. 3D model of tibia E. Intercondylar tubercles' ridges, with main processes and peaks drawn and labelled over the image with help of contour lines.....	172
Fig. 69. 3D model of tibia A. Anterior axis (AA) and a perpendicular line (AAperp), both in orange, lateral to the LT, in line with it. Posterior axis (PA) and perpendicular line (PAperp), both in red, medial to the MT, in line with it. The PL-AM axis, in red, forms a ca. 70° angle with the posterior axis, and 60° angle with the anterior axis. The PM-AL axis, in orange, forms a ca. 60° angle with the anterior axis.	173
Fig. 70. 3D model of tibia A, medial side visible. Medial tubercle peaks labelled (in white color, with number 3 omitted for clarity) and medial processes drawn and labelled (in red). A= Anteroposterior view, P=Posteroanterior view.....	175
Fig. 71. 3D model of tibia A, medial side visible. Medial tubercle peaks labelled (in white color, with number 3 omitted for clarity) and medial processes drawn and labelled (in red). M=Mediolateral view, L=Lateromedial view.	176
Fig. 72. 3D model of tibia E, medial side visible. Medial tubercle peaks labelled (in white color, with number 3 omitted for clarity) and medial processes drawn and labelled (in red). A=Anteroposterior view, P=Posteroanterior view.	177

Fig. 73. 3D model of tibia E, medial side visible. Medial tubercle peaks labelled (in white color, with number 3 omitted for clarity) and medial processes drawn and labelled (in red). M=Mediolateral view, L=Lateromedial view.....	177
Fig. 74. 3D model of tibia A, lateral side visible. Lateral tubercle peaks labelled (in white color, with number 4 omitted for clarity) and lateral processes drawn and labelled (in blue). A=Anteroposterior view, P=Posteroanterior view.....	180
Fig. 75. 3D model of tibia A, lateral side visible. Lateral tubercle peaks labelled (in white color, with number 4 omitted for clarity) and lateral processes drawn and labelled (in blue). L=Lateromedial view, M=Mediolateral view.....	181
Fig. 76. 3D model of tibia E, lateral side visible. Lateral tubercle peaks labelled (in white color, with number 4 omitted for clarity) and lateral processes drawn and labelled (in blue). A=Anteroposterior view, P=Posteroanterior view.....	182
Fig. 77. 3D model of tibia E, lateral side visible. Lateral tubercle peaks labelled (in white color, with number 4 omitted for clarity) and processes drawn and labelled (in blue). L=Lateromedial view M=Mediolateral view.	182
Fig. 78. Study V. Histogram of number of tibias in each group of relative tubercle size in radiography (Rx_TM_TL), where 1=MT, 2=LT.	184
Fig. 79. Study V. Histogram of tibias classified into Giorgi's groups (TMTL_Type), in percentage.	185
Fig. 80. Study V. Histogram of number of tibias classified into each diagnostic group: ACL, lateral meniscus (LM), medial collateral ligament (MCL), medial meniscus (MM), femoropatellar, and posterior aspect (Post) - including PCL – pathology.....	185
Fig. 81. A case of hypoplasia of the lateral tubercle in the sample for Study V.	186
Fig. 82. Study VI. Histogram of number of tibias in each group of relative tubercle size in radiography (Rx_TM_TL), where 1=MT, 2=LT.	188
Fig. 83. Study VI. 10-year-old male with longer right knee of ca. 20mm, discoid lateral meniscus, showing MT=LT in radiography (A) and MRI (B).....	188
Fig. 84. Study VI. Histogram of percentages of tibias classified into each diagnostic group: ACL, fracture (Fx), lateral meniscus (LM), medial meniscus (MM), bone edema, other pathologies, and femoropatellar pathology.	189
Fig. 85. Study VI. 3-year-old female with limp and proximal fibular epiphyseal lesion, showing a hypoplastic tibial eminence and no distinguishable tubercles.....	189
Fig. 86. Study IX. Histogram of percentage of tibias by Ahlbäck OA grade distribution.	192
Fig. 87. 3D model of tibia 32, with contour lines superimposed. Varus. MAC: 2M. MT osteophyte: grade 5; LT osteophyte: grade 2.	194
Fig. 88. 3D model of tibia 79 with contour lines superimposed. Varus. MAC: 1M. MT osteophyte: grade 2; LT osteophyte: grade 5.	195
Fig. 89. 3D model of tibia 21 with contour lines. Varus. MAC: 3M. MT width: grade 3; MT attrition: grade 2, direction AL (notice similar attrition direction of the Parsons' osteophyte). LT width: grade 3; LT attrition: grade 3, direction AL-PL.	195
Fig. 90. 3D model of tibia 89 with contour lines. Varus. MAC: 4M. MT width: grade 3; MT attrition: grade 2, direction AM-PL. LT width: grade 3; LT attrition: grade 1, direction AL...	196

Fig. 91. 3D model of tibia 65, with contour lines superimposed (image left-mirrored). Varus. MAC: 4M. B1: grade 2; B2: grade 3 (connecting with hook-shaped Parsons' osteophyte grade 5); C1: grade 4 (connecting with PM corner osteophyte grade 5); C2: grade 1; D1-D2: grade 2; D3: grade 1; E1, E2 grade 1 (notice high attrition grade in TL, PLIR and posterior TL slope). Also labelled are the Parson's knob (G), anterior sagittal ridge (J), AM, AL, and PM corner elevations. ... 196

Fig. 92. 3D model of tibia 81, with contour lines superimposed. Varus. MAC 4M. B1: grade 3; B2: grade 3 (connecting with little hook-shaped Parsons' osteophyte grade 5); C1: grade 3 (connecting with PM corner osteophyte grade 3); C2: grade 3; D1-D2: grade 3; D3: grade 4 (dependent on D3_a; observe a different D3_b ridge, both obliterating the AL recess space); E1: grade 4 (connecting with PL corner osteophyte grade 5); E2: grade 1. Also labelled are the Parson's knob (G), AM, AL, PM, and PL corner elevations.197

Fig. 93. 3D model of pathological tibia B, with contour lines superimposed. Varus. MAC: 3M. B1 osteophyte: grade 2. B2 osteophyte: grade 4 (mixing into star-shaped Parsons' osteophyte). Notice B1-B2 incisura grade -2. A marked D3_b-predominant osteophytic growth (grade 3) is seen obliterating the AL recess space, instead of the most common D3_a. Also labelled are the Parson's knob (G), AM, AL corners.197

Fig. 94. Tibia 32. A: Photograph of fresh specimen; measurements were made directly over it. B: Axial (i.e. inferosuperior) fluoroscopic image. MT and LT radiographic density: grade 3; Parsons' knob (G): grade 2. 199

Fig. 95. Study II. Histogram of relative tubercle size (TM_TL): number of tibias in each category, grouped by Ahlbäck OA grade. 1=MT, 2=LT.....200

Fig. 96. Study II. Histogram of medial tubercle (TM) osteophyte grade: number of tibias in each osteophyte grade, grouped by Ahlbäck OA grade.200

Fig. 97. Study II. Histogram of lateral tubercle (TL) osteophyte grade: number of tibias in each osteophyte grade, grouped by Ahlbäck OA grade. 201

Fig. 98. Study II. Histogram of radiographic density of the medial tubercle in inferosuperior radiographs (Rx_TM): number of tibias in each category, grouped by Ahlbäck OA grade. 201

Fig. 99. Study II. Histogram of radiographic density of the lateral tubercle in inferosuperior radiographs (Rx_TL): number of tibias in each category, grouped by Ahlbäck OA grade.202

Fig. 100. Study II. Box-and-whisker plot of MT AP size (TM_AP) distribution in each Ahlbäck OA grade..... 202

Fig. 101. Study II. Box-and-whisker plot of MT mediolateral size (TM_LAT) distribution in each Ahlbäck OA grade.203

Fig. 102. Study II. Box-and-whisker plot of LT AP size (TL_AP) distribution in each Ahlbäck OA grade..... 203

Fig. 103. Study II. Box-and-whisker plot of LT mediolateral size (TL_LAT) distribution in each Ahlbäck OA grade. 204

Fig. 104. Study II. Histogram of relative medial tubercle peak height (TMabc).204

Fig. 105. Study II. Histogram of relative lateral tubercle peak (TLabc) height.205

Fig. 106. Anteroposterior fluoroscopic image of Tibia 24. Varus. MT and LT internal attrition direction (pointed to by arrowheads).206

Fig. 107. Anteroposterior fluoroscopic image of pathological tibia E. Valgus. MT external attrition direction, LT internal attrition direction (pointed to by arrowheads).206

Fig. 108. Study II. Histogram of medial tubercle width grade (TM_Wide): number of tibias in each width grade, grouped by Ahlbäck OA grade.	207
Fig. 109. Study II. Histogram of lateral tubercle width grade (TL_Wide): number of tibias in each width grade, grouped by Ahlbäck OA grade.	207
Fig. 110. Study II. Histogram of medial tubercle attrition grade (TM_Attr): number of tibias in each attrition grade, grouped by Ahlbäck OA grade.	208
Fig. 111. Study II. Histogram of lateral tubercle attrition grade (TL_Attr): number of tibias in each attrition grade, grouped by Ahlbäck OA grade.	208
Fig. 112. Study II. Histogram of medial tubercle attrition direction (TM_Attr_Dir): number of tibias in each category, grouped by Ahlbäck OA grade.	209
Fig. 113. Study II. Histogram of lateral tubercle attrition direction (TL_Attr_Dir): number of tibias in each category, grouped by Ahlbäck OA grade.	209
Fig. 114. Study II. Histogram of medial tubercle direction in radiograph (Rx_TM_Dir): number of tibias in each category, grouped by Ahlbäck OA grade.	210
Fig. 115. Study II. Histogram of lateral tubercle direction in radiograph (Rx_TL_Dir): number of tibias in each category, grouped by Ahlbäck OA grade.	210
Fig. 116. Study II. Box-and-whisker plot of MT slope (TMAxis) distribution in each Ahlbäck OA grade.	211
Fig. 117. Study II. Box-and-whisker plot of LT slope (TLAxis) distribution in each Ahlbäck OA grade.	212
Fig. 118. Study II. Box-and-whisker plot of MT – LT slope (TMTLAxis) distribution in each Ahlbäck OA grade.	212
Fig. 119. Study II. Regression estimation for MT slope (TMAxis) vs. varus degree.	213
Fig. 120. Study II. Regression estimation for MT slope (TMAxis) vs. attrition grade of the medial condyle (Attr_M).	213
Fig. 121. Study II. Regression estimation for MT slope (TMAxis) vs. attrition grade of the lateral condyle (Attr_L).	214
Fig. 122. Study II. Histogram of external AMIR (B1) osteophyte grade: number of tibias in each osteophyte grade, grouped by Ahlbäck OA grade.	216
Fig. 123. Study II. Histogram of central AMIR (B2) osteophyte grade: number of tibias in each osteophyte grade, grouped by Ahlbäck OA grade.	216
Fig. 124. Study II. Histogram of joint central and external AMIR processes (B_B): number of tibias in each category, grouped by Ahlbäck OA grade.	217
Fig. 125. Study II. Histogram of B1–B2 incisura (B1-B2) degenerative grade: number of tibias in each osteophyte grade, grouped by Ahlbäck OA grade.	217
Fig. 126. Study II. Histogram of central PMIR (C1) osteophyte grade: number of tibias in each osteophyte grade, grouped by Ahlbäck OA grade.	218
Fig. 127. Study II. Histogram of external PMIR (C2) osteophyte grade: number of tibias in each osteophyte grade, grouped by Ahlbäck OA grade.	218
Fig. 128. Study II. Histogram of external and central ALIR (D1-D2) osteophyte grade: number of tibias in each osteophyte grade, grouped by Ahlbäck OA grade.	219
Fig. 129. Study II. Histogram of internal ALIR (D3) osteophyte grade: number of tibias in each osteophyte grade, grouped by Ahlbäck OA grade.	219

Fig. 130. Study II. Histogram of central PLIR (E1) osteophyte grade: number of tibias in each osteophyte grade, grouped by Ahlbäck OA grade.	220
Fig. 131. Study II. Histogram of external PLIR (E2) osteophyte grade: number of tibias in each osteophyte grade, grouped by Ahlbäck OA grade.	220
Fig. 132. Study II. Histogram of radiographic density of the AMIR in inferosuperior radiographs (Rx_B): number of tibias in each category, grouped by Ahlbäck OA grade.	221
Fig. 133. Study II. Histogram of radiographic density of the PMIR in inferosuperior radiographs (Rx_C): number of tibias in each category, grouped by Ahlbäck OA grade.	221
Fig. 134. Study II. Histogram of radiographic density of the ALIR in inferosuperior radiographs (Rx_D): number of tibias in each category, grouped by Ahlbäck OA grade.	222
Fig. 135. Study II. Histogram of radiographic density of the PLIR in inferosuperior radiographs (Rx_E): number of tibias in each category, grouped by Ahlbäck OA grade.	222
Fig. 136. Tibia D. Cleaning of soft tissues with enzymatic detergent during the processing of a specimen (A) makes it difficult to delineate previously evident cartilage-covered zones in the fully processed specimen (B).	225
Fig. 137. 3D model of tibia D. Superoinferior (SI) view with contour lines superimposed, anteroposterior (AP) and Posteroanterior (PA) views. Condylar areas selected, highlighted in red, and labelled. Compare with corresponding photographs of fresh and processed specimen in Fig. 136.	226
Fig. 138. 3D model of tibia C. Superoinferior (SI) view with contour lines superimposed, anteroposterior (AP) and Posteroanterior (PA) views. Condylar areas selected, highlighted in red, and labelled.	227
Fig. 139. 3D model of tibia 56. Red line drawn over medial curvature, AMIR and PMIR. Observe the elevation of the medial condylar curvature and rim posteriorly, together with the external (C2) and central PMIR processes, connecting with the anterior curvature and central AMIR process (B1).	228
Fig. 140. 3D model of tibia E. Contour lines highlighted. Red line drawn over medial curvature, AMIR and PMIR, blue line over lateral curvature, ALIR, and PLIR. External AMIR and PMIR processes are connected medially by the elevated curvature. External ALIR and PLIR processes are not clearly connected in the lateral aspect of the lateral condyle, though.	229
Fig. 141. 3D model of tibia H. Superoinferior view (SI) with contour lines superimposed. Medial view (M) with condylar plane (green line) as the horizontal plane of the specimen. AMIR and PMIR processes in red, ALIR and PLIR processes in blue. Observe the relative size of posteromedial (PM) and posterolateral (PL) corner and Parsons' (G) tubercles. Notice the elevation of the PMIR, and the connection of the ACIK elevation (H) with areas 9 and AL corner.	229
Fig. 142. Tibia 67. 3D model AP and lateral (L) views, with corresponding knee AP standing radiograph (APx) and lateral radiograph (Lx). Observe the posterior osteophyte (white arrowhead) apparently behind the lateral tubercle in the knee AP radiograph, while on the 3D model it is the posteromedial corner osteophyte the bigger one.	230
Fig. 143. Standing AP and lateral (L) knee radiographs corresponding to tibia 31. Knee radiographs were used to complement data on condylar rims and corners, when not available from the cut specimen.	230

Fig. 144. 3D model of tibia 31, with contour lines superimposed. Superoinferior (SI), anterior (A), posterior (P), lateral (L), and medial (M) views. Varus. MAC 3M. PM corner: grade 5; PL corner: grade 4. AM corner: grade 2; AL corner: grade 2; AM rim: grade 2; PM rim: grade 3; AL rim: grade 4; PL rim: grade 3. Observe marked elevation of D1-D2, and E1, as well as marked B3 (connecting with D3) and C4 processes. Notice also anterior osteophyte (N).....	231
Fig. 145. Study II. Box-and-whisker plot of AL corner AP size (Bd_AL_AP) distribution in each Ahlbäck OA grade.....	233
Fig. 146. Study II. Box-and-whisker plot of PM corner AP size (Bd_PM_AP) distribution in each Ahlbäck OA grade.....	234
Fig. 147. Study II. Box-and-whisker plot of PL corner AP size (Bd_PL_AP) distribution in each Ahlbäck OA grade.....	234
Fig. 148. Study II. Histogram of AM corner osteophyte (Bd_AM): number of tibias in each osteophyte grade, grouped by Ahlbäck OA grade.....	235
Fig. 149. Study II. Histogram of AL corner osteophyte (Bd_AL): number of tibias in each osteophyte grade, grouped by Ahlbäck OA grade.....	235
Fig. 150. Study II. Histogram of medial rim elevation, anterior aspect (Bd_MA): number of tibias in each osteophyte grade, grouped by Ahlbäck OA grade.....	236
Fig. 151. Study II. Histogram of medial rim elevation, posterior aspect (Bd_MP): number of tibias in each osteophyte grade, grouped by Ahlbäck OA grade.....	236
Fig. 152. Study II. Histogram of lateral rim elevation, anterior aspect (Bd_LA): number of tibias in each osteophyte grade, grouped by Ahlbäck OA grade.....	237
Fig. 153. Study II. Histogram of lateral rim elevation, posterior aspect (Bd_LP): number of tibias in each osteophyte grade, grouped by Ahlbäck OA grade.....	237
Fig. 154. Study II. Histogram of PM corner osteophyte (Bd_PM): number of tibias in each osteophyte grade, grouped by Ahlbäck OA grade.....	238
Fig. 155. Study II. Histogram of PL corner osteophyte (Bd_PL): number of tibias in each osteophyte grade, grouped by Ahlbäck OA grade.....	238
Fig. 156. Study II. Histogram of radiographic density of the AM corner in inferosuperior radiographs (Rx_AM): number of tibias in each category, grouped by Ahlbäck OA grade. ..	239
Fig. 157. Study II. Histogram of radiographic density of the AL corner in inferosuperior radiographs (Rx_AL): number of tibias in each category, grouped by Ahlbäck OA grade.....	239
Fig. 158. Study II. Histogram of radiographic density of the PM corner in inferosuperior radiographs (Rx_PM): number of tibias in each category, grouped by Ahlbäck OA grade....	240
Fig. 159. Study II. Histogram of radiographic density of the PL corner in inferosuperior radiographs (Rx_PL): number of tibias in each category, grouped by Ahlbäck OA grade.....	240
Fig. 160. 3D model of tibia 83, with contour lines superimposed. Varus. Medial condyle attrition grade -2 (MAC 2M, MACCo 3M). Lateral condyle attrition grade -2 (MACOp 1L).	242
Fig. 161. 3D model of tibia 82, with contour lines superimposed. Varus. Medial condyle attrition grade -3 (MAC 2M, MACCo 3M). Lateral condyle attrition grade -3 (MACOp 4L-1L).....	242
Fig. 162. 3D model of tibia 53, with contour lines superimposed. Varus. Medial condyle attrition grade -4 (MAC 4M, MACCo 3M). Lateral condyle attrition grade -4 (MACOp 1L-2L).	243
Fig. 163. Study II. Histogram of percentage of tibias in each MAC category.	243

Fig. 164. Study II. Histogram of MAC zones: number of tibias in each MAC category, grouped by Ahlbäck OA grade.	244
Fig. 165. Study II. Histogram of MAC + MACCo: number of tibias in each MAC + MACCo category, grouped by Ahlbäck OA grade. Deep: attrition follows anteroposterior direction. Wide: follows mediolateral direction. Obl: follows oblique direction.	244
Fig. 166. Study II. Histogram of percentage of tibias in each MACOp category.....	245
Fig. 167. Study II. Histogram of MACOp: number of tibias in each MACOp category, grouped by Ahlbäck OA grade.	245
Fig. 168. Study II. Histogram of MAC: number of tibias in each MAC category, grouped by MACOp category.	246
Fig. 169. Study II. Histogram of attrition of the medial condyle (Attr_M): number of tibias in each attrition grade, grouped by Ahlbäck OA grade.....	246
Fig. 170. Study II. Histogram of attrition of the lateral condyle (Attr_L): number of tibias in each attrition grade, grouped by Ahlbäck OA grade.....	247
Fig. 171. Study II. Histogram of MAC combined with its complementary areas: number of varus knees in each MAC + MACCo grade, grouped by attrition of the medial condyle. Deep: attrition follows anteroposterior direction. Wide: follows mediolateral direction. Obl: follows oblique direction.	247
Fig. 172. Study II. Histogram of the ACL instability grade (LCA): number of tibias in each category, grouped by MAC.	249
Fig. 173. Box-and-whisker plot of MT slope (TMAxis) distribution in each ACL instability grade (LCA).	249
Fig. 174. Box-and-whisker plot of LT slope (TLAxis) distribution in each ACL instability grade (LCA).	250
Fig. 175. Box-and-whisker plot of MT–LT slope (TMTLAxis) distribution in each ACL instability grade (LCA).	250
Fig. 176. Study II. Regression estimation for ACL instability grade (LCA) from MT slope (TMAxis).	251
Fig. 177. Study II. Regression estimation for ACL instability grade (LCA) from MT slope (TLAxis).	251
Fig. 178. 3D model of Tibia A, with contour lines superimposed. Superoinferior (SI) and anteroposterior (AP) views with selected areas of the anterior intercondylar area in red. Superoinferior view of anterior area (SIA) with painted lines over the main processes: AMIR (B1, B2) in red, ALIR (D3) in blue, AFIR (F1, F2) in green, AIAR (A1, A2) in white. The geniculum (G), ACIK (H), and AFIR recess (S) are also labelled.	255
Fig. 179. 3D model of Tibia D, with contour lines superimposed. Superoinferior (SI) and anteroposterior (AP) views with selected areas of the anterior intercondylar area in red. Superoinferior view of anterior area (SIA) with painted lines over the main processes: AMIR (B1) in red, ALIR (D3) in blue, AFIR (F1, F2) in green, AIAR (A1, A2) in white. The geniculum (G), ACIK (H), and AFIR recess (S) are also labelled.	256
Fig. 180. 3D model of tibia 18, with contour lines superimposed. Little hook-shaped Parsons' knob (G) formed mainly by anterior AFIR (F2) process with the AMIR and AM corner. The posterior	

AFIR process (F1) is connected directly with the elevated B2 process, with a gentler curve than is usually seen between B1 and F1. Notice the original location of the geniculum (g)..... 258

Fig. 181. 3D model of tibia 11, with contour lines superimposed. A tubercle (G) is found in the central aspect of the AIA, formed by elevated AFIR processes, ASIR (J), and anterior AIAR (A2), with a star-shaped ACIK (H) seen connected to the anterior saddle elevation, in turn connected with the anterior saddle and anterolateral knob (anterolateral corner, also elevated, is cut in the 3D model). Notice that this “Parsons’ tubercle” cannot be defined as an anteromedial intercondylar tubercle proper – since F1 and B1 are not involved (see original geniculum site, g), but rather as a generic central AFIR tubercle..... 259

Fig. 182. 3D model of tibia 52 with contour lines superimposed. The anteromedial knob (G) is mainly formed by B1, with F1 process being noticeably lower, while 1c and F2 do not contribute to the elevation. Notice the AFIR recess (S), ACIK (H), and the anterior saddle elevation (T), connected with the anterolateral knob (I) and anterolateral corner (AL). 259

Fig. 183. 3D model of tibia 40, with contour lines superimposed. Posterior process of the AFIR (F2) elevated, with star-shaped antero-central knob (H), more medial than usual, connected with the anterolateral knob (I) through the anterior saddle (T). Cone-shaped Parsons’ knob (G) medially. The anterior process (J) and anterior aspect of the AIAR (A2) are only slightly elevated. 260

Fig. 184. 3D model of tibia 19, with contour lines superimposed (left-mirrored). MAC 4M (MACCo 3M-1M-2M), condyle attrition grade 4. Parsons’ tubercle formed by AMIR (B1) and AFIR (F2, F1) and AM corner elevation, showing anterolateral attrition direction. Notice marked B2 process mixing with B3 into area 10, and marked AL corner, as well as attrition of the LT (anterior summit’s peak lower than D3 process)..... 260

Fig. 185. 3D model of tibia 75, with contour lines superimposed. Huge Parsons’ tubercle (osteophyte grade 5) formed by over posterior AFIR (F1), and connected with the ACIK (H), anterior saddle (T), anterolateral knob (I), and anterolateral corner (AL) elevation. Also elevated are the AMIR (B1, B2) and the anteromedial corner (AM), connected with the medial aspect of the Parson’s tubercle. Notice attrition on medial tubercle (AMIR and PMIR are elevated to roughly the same size as the MT summit) and posterior aspect of lateral tubercle. 261

Fig. 186. 3D model of tibia 62, with contour lines superimposed. Star-shaped Parsons’ knob (G), formed by elevations in anterior (F1) and posterior AFIR processes (F2), AMIR (B1, B2) and anteromedial corner (AM). Antero-central knob has a ridge-like appearance, connecting through the saddle (T) with the anterolateral knob (I) and the anterolateral corner (AL) elevations. Notice widening and attrition of both tubercles. 261

Fig. 187. 3D model of tibia 50, with contour lines superimposed. Hook-shaped, deep Parsons’ tubercle (G), osteophyte grade 5, formed by elevations of the AMIR (B1 and especially B2), and anteromedial corner (AM). AFIR processes are beneath the tubercle. Also elevated is the anterolateral corner (AL). 262

Fig. 188. 3D model of tibia 61 with contour lines. Tongue-shaped Parsons’ tubercle (G) formed mainly by the AMIR, the AFIR, and the anteromedial corner elevation. Cone-shaped antero-central knob (H), in contact with anterolateral knob (I) and anterolateral corner (AL). 262

Fig. 189. Histogram of number of tibias in each anterocentral knob's shape (H_Shape) category, in percentage.....	263
Fig. 190. Histogram of number of tibias in each anteromedial knob's shape (G_Shape) category, in percentage.....	263
Fig. 191. Study II. Histogram of posterior AFIR osteophyte grade: number of tibias in each osteophyte grade, grouped by Ahlbäck OA grade.	264
Fig. 192. Study II. Histogram of anterior AFIR osteophyte grade: number of tibias in each osteophyte grade, grouped by Ahlbäck OA grade.	265
Fig. 193. Study II. Histogram of joint anterior and posterior AFIR (F1-F2): number of tibias with joint AFIR, grouped by Ahlbäck OA grade.	265
Fig. 194. Study II. Histogram of AFIR recess grade (F1F2): number of tibias in each depression grade, grouped by Ahlbäck OA grade.	266
Fig. 195. Study II. Histogram of anterocentral intercondylar knob (H) osteophyte grade: number of tibias in each osteophyte grade, grouped by Ahlbäck OA grade.....	266
Fig. 196. Study II. Histogram of ACIK shape (H_Shape): number of tibias with each knob shape, grouped by Ahlbäck OA grade.	267
Fig. 197. Study II. Box-and-whisker plot of Parsons' knob AP size (G_AP) distribution in each Ahlbäck OA grade.	269
Fig. 198. Study II. Box-and-whisker plot of Parsons' knob mediolateral size (G_LAT) distribution in each Ahlbäck OA grade.....	270
Fig. 199. Study II. Histogram of tibias classified into Parsons' knob (G) size groups, in percentage.	270
Fig. 200. Study II. Histogram of Parsons' knob (G) osteophyte grade: number of tibias in each osteophyte grade, grouped by Ahlbäck OA grade.	271
Fig. 201. Study II. Histogram of Parsons' knob shape (G_Shape): number of tibias in each category, grouped by Ahlbäck OA grade.	271
Fig. 202. Study II. Histogram of percentage of tibias classified according to the forming structures of their Parsons' osteophyte (G_Form).....	272
Fig. 203. Study II. Histogram of the two main forming structures of the Parsons' knob (G_Form): number of tibias in each category, grouped by Ahlbäck OA grade.	272
Fig. 204. Study II. Histogram of the main forming structure of the Parsons' knob (G_Form_Main): number of tibias in each category, grouped by MAC.	273
Fig. 205. Study II. Histogram of the main forming structure of the Parsons' knob (G_Form_Main): number of tibias in each category, grouped by MACOp.....	273
Fig. 206. Study II. Histogram of the attrition direction of the Parsons' knob (G_Dir): number of tibias in each category, grouped by Ahlbäck OA grade.	274
Fig. 207. Study II. Histogram of the simplified attrition direction of the Parsons' knob (G_Dir_Simple): number of tibias in each category, grouped by Ahlbäck OA grade. A=anterior, P=posterior, M=medial, L=lateral.....	274
Fig. 208. Study II. Histogram of the simplified attrition direction of the Parsons' knob (G_Dir_Simple): number of tibias in each category, grouped by MAC. A=anterior, P=posterior, M=medial, L=lateral.	275

Fig. 209. Study II. Histogram of the simplified attrition direction of the Parsons' knob (G_Dir_Simple): number of tibias in each category, grouped by MACOp. MACOp values not labelled represent medial MACOps (1M, 2M, 3M, or 4M)	275
Fig. 210. AP and lateral (L) fluoroscopic views of tibia 31 (see corresponding knee radiographs in Fig. 143, and 3D model in Fig. 144). PM: posteromedial corner osteophyte. G: Parson's knob.	276
Fig. 211. Tibia 70. 3D model with contour lines (SI), AP and lateral (L) fluoroscopic views, standing AP radiograph (APx) and lateral knee radiograph (Lx). Observe Parsons' tubercle (G), located between MT and LT in the AP views (white line surrounding it in the AP fluoroscopic view), deeper than MT and LT in the lateral views. It seems to have been formed over the AFIR. In the lateral fluoroscopic view, metal wires are attached to both tubercles, with the thicker one over the MT.....	277
Fig. 212. AP and lateral (L) fluoroscopic views of tibia H (see corresponding 3D model in Fig. 141). Because of the posteriorly oriented cut, the AP view shows a more elevated medial rim and posteromedial corner (PM). The lateral view has been corrected by taking the condylar axis as the approximate horizontal axis of the image. G: Parsons' tubercle.....	278
Fig. 213. Study II. Histogram of the radiographic density of the Parsons' knob in inferosuperior radiograph (Rx_G): number of tibias in each category, grouped by Ahlbäck OA.	278
Fig. 214. Study II. Histogram of the relative height of the Parsons' tubercle with respect to MT, LT, AM, and AL corner osteophytes in the lateral radiograph (Rx_Height): number of tibias in each category, grouped by Ahlbäck OA. TM	279
Fig. 215. Study II. Histogram of the position of the Parsons' tubercle in AP radiograph, with respect to the anterior intercondylar staircase (Rx_IS_G): number of tibias in in center vs. medial categories, grouped by Ahlbäck OA.	279
Fig. 216. Study X. Histogram of tibias classified into simple diagnostic groups, in percentage. ACL pathology, fracture (fx), medial collateral ligament pathology (MCL), meniscal pathology, normal knees, osteoarthritis, bone edema, other pathologies, femoropatellar pathologies, and PCL pathology.....	282
Fig. 217. Study X. Histogram of simple diagnostic classes: number of tibias in each category, grouped by relative tubercle size (Rx_TM_TL). 1=MT, 2=LT. See Fig. 216. Diagnoses include ACL pathology, fracture (fx), medial collateral ligament pathology (MCL), meniscal pathology, normal knees, osteoarthritis, bone edema, other pathologies, femoropatellar pathologies, and PCL pathology.....	283
Fig. 218. Study X. Box-and-whisker plot of distribution of Parsons' osteophyte area in MRI (MRI_G_a), grouped into Ahlbäck OA grade.....	283
Fig. 219. Study X. Box-and-whisker plot of distribution of tubercle height difference in radiograph (Rx_dif_TMTL), grouped into Ahlbäck OA grade.....	284
Fig. 220. Study X. Histogram of Parsons' osteophyte presence (G_bool): number of tibias in each category, grouped by Ahlbäck OA grade	284
Fig. 221. Study X. Histogram of Parsons' osteophyte presence (G_bool): number of tibias in each diagnostic category, grouped by the presence or absence of a Parsons' osteophyte. G_bool 0: no osteophyte, G_bool 1: osteophyte present. See Fig. 216.....	285

Fig. 222. Study X. Histogram of Parsons' osteophyte type (G_type): number of tibias in each category, grouped by Ahlbäck OA grade. A=cone-shaped, B= dome-shaped, C= plateau-shaped.	285
Fig. 223. Study X. Histogram of Parsons' osteophyte overall type (G_combined): number of tibias in each category, grouped by Ahlbäck OA grade.	286
Fig. 224. Study X. Case of ACL congenital absence. Sagittal MRI slices through medial (M) and lateral (L) tubercles. Observe the posterior aspects of the tubercles reaching deeper back than usual, and the anterior peak of the lateral tubercle with a small height difference relative to the posterior peak. Lateral (L) and standing AP (AP) knee radiographs. The medial tubercle is clearly seen in both views higher than the lateral tubercle. Observe the lateral tibial osteophyte in the AP view.	286
Fig. 225. Study XI. Tibia 13, AP standing and lateral (L) knee radiographs. Classified as Ahlbäck OA grade 3, Moon grade 3 for both tubercles, Pećina type 3C for Parsons' tubercle.	288
Fig. 226. Study XI. Box-and-whisker plot of tibiofemoral angle (TF_angle) distribution grouped in Ahlbäck OA grades.	288
Fig. 227. Study XI. Histogram of Woo classification of MT (TM_class): number of tibias in each category, grouped by Ahlbäck OA grade.	289
Fig. 228. Study XI. Histogram of Woo classification of LT (TL_class): number of tibias in each category, grouped by Ahlbäck OA grade.	289
Fig. 229. Study XI. Histogram of Parsons' osteophyte shape (G_Rx_shape): number of tibias in each category, grouped by Ahlbäck OA grade. A=cone-shaped, B= dome-shaped, C= plateau-shaped.	290
Fig. 230. Study XI. Histogram of Parsons' osteophyte type (G_Rx_type): number of tibias in each category, grouped by Ahlbäck OA grade.	290
Fig. 231. Study XI. Histogram of Parsons' osteophyte combined shape and type (G_Rx_combined): number of tibias in each category, grouped by Ahlbäck OA grade.	291
Fig. 232. Study XI. Histogram of Parsons' osteophyte shape (G_Rx_shape): number of tibias in each category, grouped by alignment into valgus or varus.	291
Fig. 233. Study XI. Histogram of Parsons' osteophyte combined shape and type (G_Rx_combined): number of tibias in each category, grouped by alignment into valgus or varus.	292
Fig. 234. 3D model of Tibia L with contour lines superimposed. Superoinferior (SI), anteromedial (M) and anterolateral (L) views with selected areas of the anterior intercondylar area surrounding area 5, in red.	294
Fig. 235. 3D model of Tibia L. Anteroposterior (AP), anterosuperior (AS) and posterosuperior (PS) view of anterior intercondylar area with painted lines over the main processes (AMIR in red, ALIR in blue, AFIR in green, AIAR and ASIR in white). The geniculum (G), lateral-most border of F1 (H), and areas 5a and 5b (gray shading) are also labelled.	295
Fig. 236. Tibia M. During dissection (A), ARMM dense fibers are detached and marked with pyrography. 3D model (B) shows ARMM footprint highlighted in red, within area 5 (outlined with light green lines).	298

Fig. 237. 3D model of tibia 65, with contour lines superimposed (left-mirrored). ASIR (J) elevated, osteophyte grade 3. Also labelled are the Parsons' tubercle (G), AMIR (B), and elevations in the AM, AL and PM corners. 300

Fig. 238. 3D model of tibia 28, with contour lines superimposed. ASIR (J) elevated, osteophyte grade 3, connected with anterocentral intercondylar tubercle (H), in turn connected medially to a tongue-shaped Parsons' tubercle (G) – formed by the connection of B2 with the AFIR (i.e. more posterolateral than the usual position of the Parsons' tubercle) and laterally to the elevated anterior intercondylar saddle, anterolateral knob (I), and anterolateral corner (AL). 300

Fig. 239. Lateral knee radiograph corresponding to tibia 25 showing an anterior intercondylar tubercle (N), osteophyte grade 5. Also labelled is the Parsons' knob (G). Cut specimens usually lacked information on the AIK, and radiographs were used to complement that information.301

Fig. 240. Study II. Histogram of ASIR (J) osteophyte grade: number of tibias in each category, grouped by Ahlbäck OA grade.....301

Fig. 241. Study II. Histogram of anterior intercondylar knob (N) osteophyte grade: number of tibias in each category, grouped by Ahlbäck OA grade..... 302

Fig. 242. 3D model of Tibia A. Superoinferior view with contour lines superimposed and anterolateral groove areas selected and highlighted in red. Lateral border of F1 (H) and AL knob (I) labelled..... 304

Fig. 243. 3D model of Tibia G. Anteroposterior view with contour lines superimposed and anterolateral groove areas selected. Anterocentral knob (H), anterior saddle (T), and anterolateral knob (I) labelled. Notice the absence of an elevated ASIR..... 304

Fig. 244. 3D model of Tibia A. Superoinferior (SI) and anteroposterior (AP) views of anterior intercondylar area with painted lines over the main processes (ALIR in blue, AFIR in green, anterior saddle in light green, AIAR and ASIR in white, anterolateral fossa's medial and posterior wall in red). The lateral-most border of F1 (H), and the anterolateral knob (I) are also labelled..... 305

Fig. 245. 3D model of tibia N, with contour lines superimposed (left-mirrored). The internal ALIR process (D3, drawn in blue, with dotted line marking D3_b) is the osseous limit of a distinct ARLM footprint (delimited by a green line). The specimen shows degenerative changes: elevations of AMIR, AFIR, ASIR. Notice the horseshoe-like shape of area 10. 307

Fig. 246. 3D model of tibia G, with contour lines superimposed. Attachments of the ARLM and PRLM are highlighted in red and labelled. The anterolateral fossa is selected (fluorescent green line). 308

Fig. 247. 3D model of tibia E with contour lines superimposed. Areas of the anterolateral groove are selected and labelled (in white). Some degenerative changes can be observed: notice how the slight elevations of the anterocentral knob (H), saddle (T), and anterolateral knob (I) close the space of areas 7 and 9. Parsons' knob (G) has also been labelled. 309

Fig. 248. 3D model of tibia 85 with contour lines superimposed. Observe the elevations of D1-D2, Parsons' tubercle (G), ACIK (H), ASIR (J), anterior saddle (T), ALIK (I), and AL corner (continuous with the lateral rim). Elevations cover area 9, leaving just a narrow non-elevated

aspect lateral to the ASIR. Notice the marked osseous attrition in the medial condyle (absent in the 3D model) and in the posterior aspect of the lateral condyle.	309
Fig. 249. Study II. Histogram of AL fossa osteophyte grade: number of tibias in each category, grouped by Ahlbäck OA grade.	311
Fig. 250. Study II. Histogram of anterior saddle (T) osteophyte grade: number of tibias in each category, grouped by Ahlbäck OA grade.	311
Fig. 251. Study II. Histogram of anterolateral vallecule (valle_AL) osteophyte grade: number of tibias in each category, grouped by Ahlbäck OA grade.	312
Fig. 252. Study II. Histogram of relationship of anterior vallecule elevation with neighboring structures (valle_with): number of tibias in each category, grouped by Ahlbäck OA grade. U: ASIR. "with-" means "area 9 elevated together with".	312
Fig. 253. Study II. Histogram of anterolateral recess (AL_rec) depression grade: number of tibias in each category, grouped by Ahlbäck OA grade.	313
Fig. 254. Study II. Histogram of anterolateral intercondylar knob (I) osteophyte grade: number of tibias in each category, grouped by Ahlbäck OA grade.	313
Fig. 255. Study II. Histogram of anterolateral intercondylar osteophyte shape (I_Shape): number of tibias in each category, grouped by Ahlbäck OA grade. with-H: elevated together with ACIK.	314
Fig. 256. Study II. Histogram of anterolateral intercondylar osteophyte union with the AL corner (Bd_AL_withI): number of tibias showing a connected osteophyte.	314
Fig. 257. Study II. Histogram of anterolateral intercondylar osteophyte shape (I_Shape): number of tibias in each category, grouped by anterolateral vallecule osteophyte grade. with-H: elevated together with ACIK.	315
Fig. 258. Superoinferior view of the anterior intercondylar area of 3D models of tibias M (S-A) and J (S-B), with contour lines superimposed, with painted lines over the main processes (AMIR in red, ALIR in blue, AFIR in green, posterior wall of area 10 (area 15) and anteromedial fovea in white. Observe in tibia J, with slight degenerative changes, the more rectangular shape of area 10, the elevated central AMIR process (B2), elevated Parsons' knob, and how D3 processes form macroscopically a single D3 line (see below).	318
Fig. 259. 3D model of Tibia A with contour lines superimposed and area 10 surface highlighted. Superoinferior (S) and anterolateral (AL) views. Common incisures highlighted in red and labelled in white. Also labelled are the ALIR in blue, the AMIR in red, the AFIR in green, and the geniculum (G), the anteromedial fovea (10b), the ACIK (H), and the AIAR (A1b) in black (with the concavity in transparent white). Selected but not labelled are the sagittal line (between 10i, 10h, and 10g), and the posterior line (between 10g, 10j).	320
Fig. 260. 3D model of Tibia A with contour lines superimposed and area 10 surface highlighted. Posterosuperior (PS) and anteroposterior (A) views. Common incisures highlighted in red and labelled in white. Also labelled are the ALIR in blue, the AMIR in red, the AFIR in green, and the geniculum (G), the anteromedial fovea (10b), the ACIK (H), and the AIAR (A1b) in black (with the concavity in transparent white). Selected but not labelled are the sagittal line (between 10i, 10h, and 10g), and the posterior line (between 10g, 10j).	321
Fig. 261. 3D model of tibia A with contour lines. Area 10 highlighted. Incisures selected in red.	322

Fig. 262. 3D model of tibia B with contour lines. Area 10 highlighted. Incisures selected in red.	322
Fig. 263. 3D model of tibia C with contour lines. Area 10 highlighted. Incisures selected in red.	323
Fig. 264. 3D model of tibia D with contour lines. Area 10 highlighted. Incisures selected in red.	323
Fig. 265. 3D model of tibia E with contour lines. Area 10 highlighted. Incisures selected in red.	324
Fig. 266. 3D model of tibia F with contour lines. Area 10 highlighted. Incisures selected in red.	324
Fig. 267. 3D model of tibia G with contour lines. Area 10 highlighted. Incisures selected in red.	325
Fig. 268. 3D model of tibia H with contour lines. Area 10 highlighted. Incisures selected in red.	325
Fig. 269. 3D model of tibia I with contour lines. Area 10 highlighted. Incisures selected in red.	326
Fig. 270. 3D model of tibia J with contour lines. Area 10 highlighted. Incisures selected in red.	326
Fig. 271. 3D model of tibia K with contour lines. Area 10 highlighted. Incisures selected in red.	327
Fig. 272. 3D model of tibia L with contour lines. Area 10 highlighted. Incisures selected in red.	327
Fig. 273. 3D model of tibia M with contour lines. Area 10 highlighted. Incisures selected in red.	328
Fig. 274. 3D model of tibia N with contour lines. Area 10 highlighted. Incisures selected in red.	328
Fig. 275. 3D model of tibia A, superior (S) and anterolateral (AL) views of the intercondylar staircase with contour lines superimposed. The directions of the stairs are painted and labelled in black; the landings labelled in white. Also labelled are the ALIR in blue, the AMIR in red, the AFIR in green. Areas 10b, 15, and 7 are also labelled. Lateral view (L) with a quarter-turn staircase and ladder superimposed.....	330
Fig. 276. 3D model of tibia C, superior (S) and anterolateral (AL) views of the intercondylar staircase with contour lines superimposed. The directions of the stairs are painted and labelled in black; the landings labelled in white. Also labelled are the ALIR in blue, the AMIR in red, the AFIR in green. Areas 10b, 15, and 7 are also labelled.	331
Fig. 277. 3D model of Tibia D with ACL footprint highlighted. Superoinferior view. Main C-shaped layers selected (borders in black lines); notice the horseshoe-like shape of the layers, and the degenerative elevations surrounding area 10. ACL bundles selected (borders in light fluorescent green lines). Main zones labelled in black: outer C (1), central C (2), inner C (3), fan-like facet (4), and posterior arch (5). Also painted and labelled are the AMIR in red, the ALIR in blue, and the AFIR in green.	333
Fig. 278. 3D model of Tibia A with ACL footprint highlighted. Superoinferior (S) and anterolateral (AL) views. Main C-shaped layers selected (borders in black lines); notice the Δ-like shape. ACL	

bundles selected (borders in light fluorescent green lines). Main zones labelled in black: outer C (1), central C (2), inner C (3), fan-like facet (4), and posterior arch (5). Also painted and labelled are the ALIR in blue, the AMIR in red, the AFIR in green.....	334
Fig. 279. 3D model of Tibia A with ACL footprint highlighted. Posterosuperior (PS) and anteroposterior (A) views. Main C-shaped layers selected (borders in black lines); ACL bundles selected (borders in light fluorescent green lines). Main zones labelled in black: outer C (1), central C (2), inner C (3), fan-like facet (4), and posterior arch (5). Also painted and labelled are the ALIR in blue, the AMIR in red, the AFIR in green.	335
Fig. 280. 3D model of Tibia A. ACL bundle footprint selected and highlighted, C-layers selected.	336
Fig. 281. 3D model of Tibia B. ACL bundle footprint selected and highlighted, C-layers selected.	336
Fig. 282. 3D model of Tibia C. ACL bundle footprint selected and highlighted, C-layers selected.	337
Fig. 283. 3D model of Tibia D. ACL bundle footprint selected and highlighted, C-layers selected.	337
Fig. 284. 3D model of Tibia E. ACL bundle footprint selected and highlighted, C-layers selected.	338
Fig. 285. 3D model of Tibia F. ACL bundle footprint selected and highlighted, C-layers selected.	338
Fig. 286. 3D model of Tibia G. ACL bundle footprint selected and highlighted, C-layers selected.	339
Fig. 287. 3D model of Tibia H. ACL bundle footprint selected and highlighted, C-layers selected.	339
Fig. 288. 3D model of Tibia I. ACL bundle footprint selected and highlighted, C-layers selected.	340
Fig. 289. 3D model of Tibia J. ACL bundle footprint selected and highlighted, C-layers selected.	340
Fig. 290. 3D model of Tibia K. ACL bundle footprint selected and highlighted, C-layers selected.	341
Fig. 291. 3D model of Tibia L. ACL bundle footprint selected and highlighted, C-layers selected.	341
Fig. 292. 3D model of Tibia M. ACL bundle footprint selected and highlighted, C-layers selected.	342
Fig. 293. 3D model of Tibia N. ACL bundle footprint selected and highlighted, C-layers selected.	342
Fig. 294. 3D model of tibia C, with contour lines superimposed. Anteroposterior view of the anterior intercondylar staircase. Main incisures in black lines. * AISX: intersection between the main sagittal incisure, and the medial border of the AIAR (notice the mediolateral change in slope). G: geniculum. H: antero-central intercondylar knob. MT: medial tubercle. LT: lateral tubercle.....	346
Fig. 295. 3D model of tibia B, with contour lines superimposed (left-mirrored). ACL AM and PL bundle footprints highlighted in red. Areas 10 _{AM} and 10 _{PL} highlighted over the rest of the	

specimen (surrounding their respective bundle areas). The four areas are surrounded by light fluorescent green lines.....	348
Fig. 296. Study III. Patient 1. 3D model of ACL footprint, based on 18 arthroscopic images taken after cleaning of soft tissues, with contour lines superimposed. Notice from the situation of the contour lines that, because of the superolateral position of the arthroscope (through an anterolateral portal), the horizontal plane (as interpreted by the software) has been placed more inferiorly in its anterior aspect than the actual horizontal plane, hence the apparent upward slope from posterior to anterior. ARLM: lateral soft tissue remains (including ARLM attachment and ARLM – ACL intermingled fibers). B: medial wall of the AMIR. F1: elevation corresponding to a medial or central aspect of the posterior AFIR process. *: AISX.....	358
Fig. 297. Study III. Patient 1. Intraoperative arthroscopic image of ACL footprint, used for 3D model creation. Observe ACL soft tissue remains over area recognized as part of the AMIR in the 3D model (see Fig. 296), and ARLM attachment.	358
Fig. 298. Study III. Patient 7. 3D model of ACL footprint, based on 93 still images of arthroscopic video made from anterolateral and anteromedial portals, after cleaning of soft tissues and passing of suture loop through the ACL femoral tunnel. Contour lines superimposed. Notice remains of soft tissues on area 10, and correct 3D obtained from suture loop posteriorly (over the area), but merged with medial wall anteriorly. ARLM: lateral soft tissue remains (including ARLM attachment and ARLM – ACL intermingled fibers). MT: medial tubercle. F1: elevation corresponding to a medial or central aspect of the posterior AFIR process. *: AISX.....	359
Fig. 299. Study III. Patient 18. 3D model of ACL footprint, based on 68 still images of arthroscopic video made from the anterolateral portal, after cleaning of soft tissues. A measuring probe (+) is inserted between B1 and the medial condyle, but no 3D model was obtained of it, its image being merged with the condylar area. Medial (MC) and lateral (LC) femoral condyles also merged into the ACL footprint (notice how part of the medial femoral condyle has a more reddish color, because of the notchplasty performed). ARLM: lateral soft tissue remains (including ARLM attachment and ARLM – ACL intermingled fibers). MT: medial tubercle. B1: central AMIR process. *: AISX.....	359
Fig. 300. Study IV. 3D volume rendering of the CT of one patient. Left column, sagittal rotation of the 3D model of the tibia. Middle column, axial rotation from medial (top) to lateral (bottom) view of the 3D model of the tibia. Right column, axial rotation of the 3D model of the knee.	361
Fig. 301. Study IV. Left column, medial view of the 3D model. Middle column, superior view. Right column, lateral view. Each row corresponds to one patient, identified with a letter (A, B, and C).	362
Fig. 302. 3D model of tibia 64 with contour lines superimposed. Main AIS incisures (10g, 10h, 10i, 10j) markedly depressed, with elevated horseshoe-shaped C-layers (painted over in white). Also labelled are the external AMIR process (B1), posterior AFIR process (F1), Parson’s knob (G), internal ALIR process (D3).....	364
Fig. 303. 3D model of tibia 45 with contour lines superimposed. Observe the stepped elevations (white lines) roughly corresponding to the intercondylar C-shaped layers. Notice the intertubercular fossa (10b) in the posterior arch. Also labelled are the Parsons’ knob (G), the main incisures (10g, 10h, 10i, 10j), external AMIR process (B1), AFIR processes (F1, F2), and internal ALIR processes (D3).....	364

Fig. 304. 3D model of tibia 14 with contour lines superimposed. Observe the homogeneous elevation of the fornix and internal C (painted over with white lines), which respects a minor concavity (including the fan-like facet), where 10g and 10h begin together laterally. Also labelled are the geniculum (G), main incisures (10i, 10j), the intertubercular fossa (10b), the AMIR processes (B1, B2, B3), posterior AFIR process (F1), and internal ALIR process (D3).	365
Fig. 305. Study II. Histogram of the AIS superior stair (Xa) height grade: number of tibias in each category (0-4), grouped by Ahlbäck OA grade.....	367
Fig. 306. Study II. Histogram of the AIS inferior stair (Xd) height grade: number of tibias in each category (0-4), grouped by Ahlbäck OA grade.....	367
Fig. 307. Study II. Histogram of AIS superior landing (Xc) horizontality: number of tibias in each category, grouped by Ahlbäck OA grade. 0=more lamina-shaped; 1=more crest-shaped.....	368
Fig. 308. Study II. Histogram of the AIS inferior landing (Xf) horizontality: number of tibias in each category, grouped by Ahlbäck OA grade. 0=more lamina-shaped; 1=more crest-shaped.	368
Fig. 309. Study II. Histogram of AIS superior landing horizontality as proportion of area 10a (Xc_Xa): number of tibias in each category, grouped by Ahlbäck OA grade.....	369
Fig. 310. Study II. Histogram of AIS inferior landing horizontality as proportion of area 10d (Xf_Xd): number of tibias in each category, grouped by Ahlbäck OA grade.	369
Fig. 311. Study II. Histogram of the AIS middle landing (Xe) slope type: number of tibias in each category, grouped by Ahlbäck OA grade. Where 2=crest-type (higher slope), 0=lamina-type, -1=incisure-like (i.e. more horizontal).....	370
Fig. 312. Study II. Histogram of the AIS anteromedial fovea / fossa (Xb) depression grade: number of tibias in each category, grouped by Ahlbäck OA grade.....	370
Fig. 313. Study II. Histogram of the AIS sagittal incisure (Xg) depression: number of tibias in each category, grouped by Ahlbäck OA grade.	371
Fig. 314. Study II. Histogram of the AIS coronal incisure (Xh) depression: number of tibias in each category, grouped by Ahlbäck OA grade.	371
Fig. 315. 3D models of tibias B and J, with contour lines superimposed. Areas 12, 15, and 14a selected (fluorescent green borders), highlighted in red, and labelled. The AIS posterior arch has been painted in white. Notice how tibia J, with degenerative changes, shows steeper anterior and posterior walls of the ITR; a sharper transition between areas 15 and 10, and between 14a and the posterior intercondylar wall; a wider posterolateral recess and a flattened posterolateral fossa (with a wide and flattened LT vallecule and posterior summit); and an elevated (ridge-like) C4 process near 14a.	374
Fig. 316. 3D model of tibia B (left-mirrored), with contour lines superimposed. Superior (S), anterior (A) and posterior (P) views, with areas of the intertubercular ridge selected (borders in fluorescent green), posterior arch in white, and painted lines over the main processes (AMIR in red, ALIR in blue). Notice the secondary processes (dashed lines) in the AL, PL, and PM recesses, bordering the more excavated areas.	375
Fig. 317. Tibia D. Photograph of its posterior aspect during dissection (forceps is grasping the lateral condyle). The PCL has already been detached (its footprint, surrounding by pyrography marks, is labelled). MT: medial tubercle. PRLM: posterior root of the lateral meniscus.	377

Fig. 318. 3D model of tibia K, with contour lines superimposed. Superoinferior view. Intertubercular areas selected (light fluorescent green), with PRLM footprint highlighted in red and labelled.....377

Fig. 319. 3D model of tibia 95 with contour lines superimposed. More internal PMIR process (C4) elevated (osteophyte grade 3), with flat-like LT vallecule (*). Also labelled are processes of the AMIR (B1), PMIR (C1, C2, C3), ALIR (D1, D2, D3) and PLIR (E1, E2, E3), AFIR (F1), and elevations of Parson's knob (G), ALIK (I), AM and AL corners.379

Fig. 320. 3D model of tibia 86, with contour lines superimposed. More internal PMIR process (C4) elevated (osteophyte grade 2) and widened, and flattened LT vallecule (*). Also labelled are processes of the AMIR (B1, B2), PMIR (C1, C2, C3), ALIR (D1, D2, D3) and PLIR (E1, E2, E3), and elevations of Parson's knob (G) and PM corner.....379

Fig. 321. Anteroposterior fluoroscopic images. Tibia 63 (A) shows a widened intertubercular area (*). Tibia 84 (B) shows a narrower and higher intertubercular area (*). 380

Fig. 322. Inferosuperior fluoroscopic image of tibia 95. Red arrowhead over area 10, pointing at osteolyses in the anterior aspect of the intertubercular area, most likely corresponding to foramina nutricia in the posterior arch of area 10. Also labelled are the intercondylar medial (MT) and lateral (LT) tubercles..... 380

Fig. 323. Study II. Histogram of the PL recess (PL_rec) osteophyte grade: number of tibias in each category, grouped by Ahlbäck OA grade.381

Fig. 324. Study II. Histogram of the more internal PMIR process (C4) elevation in area 14a: number of tibias in each category, grouped by Ahlbäck OA grade.....381

Fig. 325. Study II. Histogram of the ITR / AIS height position in AP radiograph (Rx_IS): number of tibias with a normal, high, or low position, grouped by Ahlbäck OA grade..... 382

Fig. 326. Study II. Histogram of the intertubercular space width in AP radiograph (Rx_IS_Width): number of tibias with a normal, wide, or narrow space, grouped by Ahlbäck OA grade. 382

Fig. 327. Study II. Histogram of the number of osteolytic circles found in the ITR in radiographs (Rx_Osteolisis): number of tibias with the same number, grouped by Ahlbäck OA grade. One tibia showed radiographic density in this area (+3). 383

Fig. 328. 3D model of tibia L, with contour lines superimposed. Superior (S), and posterior (P) views, with areas of the posterior wall selected (borders in fluorescent green) and labelled in black; tent-shaped ridge in white; painted lines over the main processes (AMIR in red, ALIR in blue); and secondary processes with dashed lines. 386

Fig. 329. 3D model of tibia L, superior view with contour lines superimposed. Areas of the posterior wall selected (fluorescent green border) and highlighted in red. Tent-shaped ridge painted over in white color..... 387

Fig. 330. Tibia G. Photograph during dissection (posterior view). Soft tissue has been removed, only the PRMM remains attached, with shiny white fibers (pointed to with a scalpel) almost intact. 389

Fig. 331. 3D model of tibia M, with contour lines superimposed (let mirrored). Posterior view. Areas of the posterior intercondylar wall selected (light fluorescent green lines) and labelled. PRMM attachment highlighted in red. 389

Fig. 332. 3D model of tibia 98, with contour lines superimposed (left-mirrored). Elevated processes C3 (osteophyte grade 2) and E3 (grade 3), both delimiting the posteromedial fossa and posterolateral fossa, respectively. Notice also elevated D3 _b processes delimiting a narrow anterolateral fossa. Also labelled are processes of the AMIR (B1, B2, B3), PMIR (C1, C2), ALIR (D1, D2, D3 _a) and PLIR (E1, E2), and elevations of Parson's knob (G), ALIK (I), AM, AL, PM, and PL corners in white.	390
Fig. 333. 3D model of tibia 30, with contour lines superimposed (left-mirrored). Elevated processes C3 (osteophyte grade 2) and E3 (grade 3). Also labelled are processes of the AMIR (B1, B2), PMIR (C1, C2, C4), ALIR (D1, D2, D3 _a , D3 _b) and PLIR (E1, E2), and elevations of Parson's knob (G), anterior saddle (T) together with AL corner, as well as AM, PM, and PL corners in white.....	391
Fig. 334. Tibia 15. Inferosuperior fluoroscopic image (IS) and superoinferior view (SI) of the 3D model, with contour lines superimposed. Observe higher radiographic density of the posterior wall, similar to the intercondylar tubercles (TM and TL) and Parsons' knob (G), higher in the area corresponding to the tent-shaped ridge and lateral wall of the posterior facet (in white lines over 3D model). Notice also the big round central osteolysis (*) corresponding to the intertubercular fossa.....	391
Fig. 335. Study II. Histogram of the PM recess depression grade (PM_rec): number of tibias in each category, grouped by Ahlbäck OA grade.	392
Fig. 336. Study II. Histogram of the internal PMIR process (C3) elevation: number of tibias in each category, grouped by Ahlbäck OA grade.	392
Fig. 337. Study II. Histogram of the internal PLIR process (E3) elevation: number of tibias in each category, grouped by Ahlbäck OA grade.	393
Fig. 338. Study II. Histogram of radiographic density of the posterior intercondylar area in inferosuperior radiographs (Rx_AIP): number of tibias in each category, grouped by Ahlbäck OA grade.....	393
Fig. 339. 3D model of Tibia C with contour lines superimposed and area 13 selected (fluorescent green borders). Superior (S) and anterosuperior (AS) views. Main incisures highlighted in red and labelled in white. Main lines and ridges labelled in yellow, with geniculate ridge painted in white. Also painted and labelled are the secondary central PLIR in blue, secondary central PMIR in red.	396
Fig. 340. 3D model of Tibia C with area 13 selected (fluorescent green borders). Posterior (P) and posteroinferior (PI) views. Main incisures highlighted in red and labelled in white. Main lines and ridges labelled in yellow, with geniculate ridge painted in white. Also painted and labelled are the secondary central PLIR in blue, secondary central PMIR in red.	397
Fig. 341. 3D model of Tibia A with area 13 selected, incisures selected and highlighted in red.	398
Fig. 342. 3D model of Tibia B with area 13 selected, incisures selected and highlighted in red.	398
Fig. 343. 3D model of Tibia C with area 13 selected, incisures selected and highlighted in red.	399
Fig. 344. 3D model of Tibia D with area 13 selected, incisures selected and highlighted in red.	399
Fig. 345. 3D model of Tibia E with area 13 selected, incisures selected and highlighted in red.	400

Fig. 346. 3D model of Tibia G with area 13 selected, incisures selected and highlighted in red.	400
Fig. 347. 3D model of Tibia H with area 13 selected, incisures selected and highlighted in red.	401
Fig. 348. 3D model of Tibia I with area 13 selected, incisures selected and highlighted in red.	401
Fig. 349. 3D model of Tibia L with area 13 selected, incisures selected and highlighted in red.	402
Fig. 350. 3D model of Tibia M with area 13 selected, incisures selected and highlighted in red.	402
Fig. 351. 3D model of tibia C, superior view (S). Posterior facet areas selected, highlighted in red, and labelled.....	404
Fig. 352. 3D model of Tibia C, posterior view (P). Posterior facet areas selected (fluorescent green borders) and labelled in white, with a curved stair superimposed to area 13a, and a canal superimposed to area 13b. Main lines and ridges in yellow, with tent-shaped ridge painted in white. Also painted and labelled are the PLIR processes in blue, PMIR processes in red.	404
Fig. 353. 3D model of Tibia C, superior (S) and posterior (P) views. Posterior facet areas selected (fluorescent green borders) and labelled in white. Main lines and ridges in yellow, with tent- shaped ridge painted over in white. The posterior intercondylar staircase main direction (upwards) is painted in light brown. Also painted and labelled are the PLIR processes in blue, PMIR processes in red.....	405
Fig. 354. 3D model of tibia C. Superior (S), anterosuperior (AS), posterior (P) and posteroinferior (PI) views. Footprint of PCL bundles selected (fluorescent green lines). AL: anterolateral bundle of the PCL. PM: posteromedial bundle of the PCL.	406
Fig. 355. 3D model of tibia A. Footprint of PCL bundles selected and highlighted.	407
Fig. 356. 3D model of tibia B. Footprint of PCL bundles selected and highlighted.	407
Fig. 357. 3D model of tibia D. Footprint of PCL bundles selected and highlighted.	408
Fig. 358. 3D model of tibia E. Footprint of PCL bundles selected and highlighted.	408
Fig. 359. 3D model of tibia F. Footprint of PCL bundles selected and highlighted.	409
Fig. 360. 3D model of tibia G. Footprint of PCL bundles selected and highlighted.....	409
Fig. 361. 3D model of tibia H. Footprint of PCL bundles selected and highlighted.....	410
Fig. 362. 3D model of tibia I. Footprint of PCL bundles selected and highlighted.	410
Fig. 363. 3D model of tibia L. Footprint of PCL bundles selected and highlighted.	411
Fig. 364. 3D model of tibia M. Footprint of PCL bundles selected and highlighted.	411
Fig. 365. 3D model of tibia 77, with contour lines superimposed. Elevated processes C3 (grade 2) and E3 (grade 3), and elevations of the medial (C1 _b) and lateral (E1 _b) walls enclosing a more horizontal posterior facet (*), with no elevation of the ICT sagittal line. Also labelled are processes of the AMIR (B1, B2), PMIR (C1, C2), ALIR (D1, D2, D3 _a) and PLIR (E1, E2), and elevations of Parson's knob (G), AM, AL, and PM, corners in white. Observe how AL and the saddle elevation (T) form together a common osteophyte covering area 9.	416
Fig. 366. 3D model of tibia H, with contour lines superimposed; posterior view (posterior is at the bottom, medial is on the right side). Observe the more vertical (ridge-like) slope of the facet, and its enclosing by PM (grade 4) and PL (grade 3) corner osteophytes. The ICT line (13g) is not found particularly elevated (grade 1) over the surrounding areas. Notice also the ridge formed by C3 and E3 (grade 3) dividing the posterior wall in its two main faces (14b, 11), instead of the common incisure where both faces converge in normal tibias. Also labelled are the Parsons'	

knob (G), ACIK (H), and processes of the PMIR (C1, C1b, C2) and PLIR (E1, E1b, E2), as well as the ICT coronal line (10h).....	417
Fig. 367. 3D model of tibia 42, with contour lines superimposed (left-mirrored); posterior view (posterior is at the bottom, medial is on the right side). Elevated ICT sagittal line (13g, osteophyte grade 2) and vertical (i.e. ridge-like) area 13. Notice also elevated ICT coronal line (13h), lateral growth of PM corner osteophyte (enclosing area 13 from the medial wall, C1b), medial growth of PL corner osteophyte (enclosing area 13 from the lateral wall, E1b), and elevated E3 process (grade 3). Also labelled are the Parsons' knob (G), processes of the PMIR (C1, C2, C3, C4) and PLIR (E1, E2), as well as AL corner elevation.	417
Fig. 368. Study II. Histogram of area 13 (XIII) classification: number of tibias in each category, grouped by Ahlbäck OA grade. 0=facet-like (more horizontal); 1=ridge-like (more vertical)	418
Fig. 369. Study II. Histogram of ICT sagittal line (XIIIg) osteophyte grade: number of tibias in each category, grouped by Ahlbäck OA grade.	418
Fig. 370. Pathological Tibia E. Superoinferior photograph of specimen (A) and inferosuperior fluoroscopic view (B). Observe the long-type attrition of areas 3-4 (*). Note the higher density on the long LT osteophyte, with a lesser density on the MT, Parsons' (G), and PL corner osteophytes.	420
Fig. 371. Donor Tibia C. Superoinferior photograph of specimen (A). Inferosuperior fluoroscopic view (B). Observe a higher density on the MT, posterior facet (*), and LT tubercle and its external slope.	421
Fig. 372. Donor Tibia I. Superoinferior photograph of specimen (A). Inferosuperior radiograph (B). Observe a higher density on posterior corner osteophytes (PM, PL), LT (and its external slope), MT, Parsons' knob (G), ACIK (H), and AM corner.	422
Fig. 373. Donor Tibia A. Superoinferior photograph of specimen with ACL and PCL painted with barium sulfate (A). Inferosuperior radiograph (B).	423
Fig. 374. Donor Tibia A. Superoinferior photograph of specimen with attachments of ligaments and menisci painted with barium sulfate (A). Inferosuperior fluoroscopic view (B).	424
Fig. 375. Donor Tibia I with ligamentous and meniscal attachment areas painted with barium sulfate. Superoinferior photograph of specimen (A). Inferosuperior fluoroscopic view (B). .	425
Fig. 376. Tibia A. Superoinferior radiograph (A). 3D model, superoinferior view, with attachments selected.	426
Fig. 377. 3D model of tibia A: AP and PA views. Marked are AMIR (B1), PMIR (C1), ALIR (D3), AFIR (F1, F2) processes, anterior saddle (T), tent-shaped ridge (M), and ICT coronal line (13h). Medial aspect of the posterior corner (PM) and inferior aspect of lateral wall of PIA (PL) are also marked. The anterior intercondylar staircase is painted over in white, and visible recesses (with less dense radiographic areas) are labelled in white (al: anterolateral recess; pl: posterolateral recess; pm: posteromedial recess). AP fluoroscopic view with (Rx1) and without (Rx2) corresponding marks over the same recognizable structures. Notice that the processes marked as F1 and T includes the ACIK (H) in the middle, not recognizable in the fluoroscopic view. The more radiographic dense area between F2 and M corresponds probably to the MAIA (fingerprint and anterior AIAR).	427
Fig. 378. 3D model of tibia A. Anterior (A), posterior (P) and posterior view with posterior aspect transparent (PA). AP fluoroscopic view with ACL and PCL painted with barium sulfate (Rx1).	

AP fluoroscopic view with all attachments painted (Rx2). Attachment areas labelled and marked (in white, anterior attachments; in yellow, posterior attachments).....	428
Fig. 379. 3D model of pathological tibia E. Superoinferior view (SI). AP view (AP). PA view (PA). PA radiograph of specimen (Rx1). AP standing knee radiograph before TKA surgery (Rx2), with contour of intercondylar tubercles (MT, LT) and Parsons' knob (G) in white. Also labelled are AM, AL, PM, and PL corner elevations	429
Fig. 380. 3D model of tibia A. Medial view with medial side transparent (M), lateral view with lateral side transparent (L). Lateral fluoroscopic view with (Rx1) and without (Rx2) corresponding marks over recognizable structures. White line over MT (AMIR, PMIR), yellow line over LT (ALIR, PLIR). Dashed lines over condyle surfaces (white over medial, yellow over lateral one). Green line over highest (and densest) intercondylar area, including the fingerprint (5), anterior AFIR process (F2), AIS (10, following border between outer and central C-layers), posterior wall (PW) and facet (13), with changes of slope at 13h, POE, PRE. Red line over posterior AFIR process (F1).	431
Fig. 381. 3D model of tibia A. Medial view with medial side transparent (M). Lateral view with lateral side transparent (L). Lateral fluoroscopic view with ACL and PCL painted with barium sulfate (Rx1). Lateral fluoroscopic view with all attachments painted (Rx2). Attachment areas labelled and marked.	432
Fig. 382. 3D model of pathological tibia E. Lateral view (M). Medial view (L). Lateral fluoroscopic view (1). Lateral fluoroscopic view with metal bands glued to the intercondylar tubercles (2). MT has a thicker metal band attached to it. Lateral knee radiograph prior to TKA surgery (X). Anterior is to the right of the image. Contour of MT (in white) and LT (in yellow), including their anterior and posterior processes, have been drawn over images. Also labelled is the Parsons' tubercle (G).	433
Fig. 383. Tibia D. Sagittal cuts (upper left side) with corresponding radiographs (upper right side). 1=cut through lateral tubercle. 2=cut through intertubercular area. 3= cut through medial tubercle. Drawing of trabeculae of cut through medial tubercle at the bottom.	434
Fig. 384. Tibia E. 3D model with drawing of approximate location of cuts over it, with cuts numbered (in the top right corner). Photographs of sagittal cuts (left side) with corresponding radiographs (middle right side), and drawing of trabeculae of cut through lateral tubercle (at the bottom).	435
Fig. 385. 3D model of tibia G with drawing of approximate location of cuts over it, with cuts numbered corresponding to the numbers in Fig. 387, Fig. 388.....	437
Fig. 386. 3D model of tibia L with drawing of approximate location of cuts over it, with cuts numbered corresponding to the numbers in Fig. 389.....	437
Fig. 387. Tibia G. Photographs of coronal cuts (left side) with corresponding radiographs (right side), numbered according to Fig. 385.	438
Fig. 388. Tibia G. Coronal cut (top left image) with corresponding radiograph (top right image), and drawing of trabeculae (bottom image). Numbered according to Fig. 385.	439
Fig. 389 Tibia L. Photographs of coronal cuts (left side and lower right side), with corresponding radiographs (upper right side), numbered according to Fig. 386.	440

Fig. 390. Pathological tibia Ro. Fresh, unfixed specimen. Sagittal cut (top left) through ACL insertion (*). Radiograph (top right), with soft tissue surrounded by white dashed line. T1W MRI cuts through the same area (bottom images), with marked ACL attachment (*). 442

Fig. 391. Pathological tibia 21. Sagittal cuts (left side) numbered sequentially from medial condyle (2) to medial tubercle (5), with corresponding radiographs (right side). Observe the Parsons' tubercle (G) anteriorly, and a subchondral cyst (*) beneath the AMIR. 442

Fig. 392. Pathological tibia F. Fixed specimen sagittal cuts (top left) through the Parsons' tubercle. Corresponding radiographs (top right). Drawing of trabeculae (bottom image)..... 443

Fig. 393. Pathological tibia Mu. Sagittal cut through LT (top left). Corresponding radiographs (top right). Drawing of trabeculae (bottom image). Osteophyte affecting the anterior (*) and posterior peak (+). 444

Fig. 394. Pathological tibia 64. Radiograph of sagittal cut, through B2 (anterior, to the left) and C1 (posterior, with osteophyte) 444

Fig. 395. 3D model of pathological tibia 95 with drawing of approximate location of cuts over it, with cuts numbered from medial to lateral. Sagittal cuts (top left images), corresponding radiographs (top middle images), and approximate corresponding knee MRI slices before TKA surgery (top right images). 445

Fig. 396. Pathological tibia Ri. MRI sagittal slice through Parsons (MRI), fresh cut (S); radiographs of cuts (SRx); lateral knee radiograph, previous to surgery (Rx). Parsons' knob (G), ACL attachment (*), and lateral aspect of MT labelled..... 446

Fig. 397. Pathological tibia 79. Coronal cuts through eminence (left side images), numbered from anterior aspect to posterior ITR (upper to lower images). Corresponding radiographs (middle images) and approximate knee MRI slices (right side images). Labelled are osteophytes of MT (*) and LT (+)..... 447

Fig. 398. Pathological tibia 22. Coronal cuts through anterior aspect. Photograph with drawing of approximate location of cuts over it, with cuts numbered from anterior to posterior (inferior image), coronal cuts fixed (top left), and corresponding radiographs (top right). Labelled are the medial osteophyte (*), corresponding to the Parsons' knob and AMIR, and the lateral osteophyte (*), corresponding to the elevation of the AL corner and of D1-D2. 448

Fig. 399. Pathological tibia 14. Coronal cuts through the eminence (top left images). Corresponding radiographs (top right). Drawing of trabeculae (bottom image) with cyst (*). 449

Fig. 400. Pathological tibia 64. Coronal cuts through eminence (left side images), anterior to posterior (upper to lower images). Corresponding radiographs (right side images). Knee MRI slices through similar areas (bottom images, left to right). MT osteophyte (*). 450

Fig. 401. 3D model of pathological tibia 80 with approximate planes of axial cuts over it (bottom image). Axial cuts (top left images), corresponding radiographs (top right images). Observe the presence of foramina nutricia in the anterior aspect of the ITR, corresponding to the posterior arch of the AIS..... 451

Fig. 402. Coronal cut of Parsons' tubercle (lateral aspect to the left, medial to the right of the image). Prico-Sirius red stain, with myocyte nuclei in brown, collagen fibers in bright red, and elastic and muscle fibers with yellowish tones (I-1). Masson's trichrome stain, with muscle fibers

in red/pink, collagen in blue/green, and nuclei in brown (I-2). F: fibrocartilage; T: bone trabeculae; C: connective tissue.	453
Fig. 403. Scanning electron microscopy of Parsons' tubercle (coronal cut), corresponding to Fig. 402. Lateral aspect to the left, medial to the right of the image. F: fibrocartilage; T: bone trabeculae; C: connective tissue.	454
Fig. 404. Detail of Fig. 402. Prico-Sirius red stain (I-4) and polarized light microscopy (I-5). Fibers of the ACL attachment (*).	455
Fig. 405. Scanning electron microscopy corresponding to Fig. 404. Fibers of the ACL attachment (*).	456
Fig. 406. Sagittal cut of Parsons' tubercle (posterior aspect to the left, anterior to the right of the image). Prico-Sirius red stain, with myocyte nuclei in brown, collagen fibers in bright red, and elastic and muscle fibers with yellowish tones (II-1). Hematoxylin and eosin stain, with muscle fibers in dark red, collagen in pale pink, and nuclei in blue/purple (II-2). Image shows fibrocartilage surrounded by connective tissue and resting on bone trabeculae.	457
Fig. 407. Base of Parsons' tubercle (detail of Fig. 406), hematoxylin and eosin stain (II-3) and corresponding polarized light microscopy (II-4).	458
Fig. 408. Sagittal cut of Parsons' tubercle (posterior aspect to the left, anterior to the right of the image). Masson's trichrome stain, with muscle fibers in red/pink, collagen in blue/green, and nuclei in brown (II-5). Detail of its anterior base (II-6). F: fibrocartilage; C: connective tissue.	459
Fig. 409. Study II. Histogram of MT osteophyte grade (TM): number of varus knees in each category, grouped by maximum attrition area of the medial condyle of the tibia.	463
Fig. 410. Study II. Histogram of MT width (TM_Wide): number of varus knees in each category, grouped by maximum attrition area of the medial condyle of the tibia.	464
Fig. 411. Study II. Histogram of LT osteophyte grade (TL): number of varus knees in each category, grouped by maximum attrition area of the medial condyle of the tibia.	464
Fig. 412. Study II. Histogram of LT width (TL_Wide): number of varus knees in each category, grouped by maximum attrition area of the medial condyle of the tibia.	465
Fig. 413. Study II. Histogram of external AMIR process (B1) osteophyte grade: number of varus knees in each category, grouped by maximum attrition area of the medial condyle of the tibia.	465
Fig. 414. Study II. Histogram of central AMIR process (B2) osteophyte grade: number of varus knees in each category, grouped by maximum attrition area of the medial condyle of the tibia.	466
Fig. 415. Study II. Histogram of central PMIR process (C1) osteophyte grade: number of varus knees in each category, grouped by maximum attrition area of the medial condyle of the tibia.	466
Fig. 416. Study II. Histogram of external PMIR process (C2) osteophyte grade: number of varus knees in each category, grouped by maximum attrition area of the medial condyle of the tibia.	467
Fig. 417. Study II. Histogram of central and external ALIR process (D1-D2) osteophyte grade: number of varus knees in each category, grouped by maximum attrition area of the medial condyle of the tibia.	467

Fig. 418. Study II. Histogram of internal ALIR process (D3) osteophyte grade: number of varus knees in each category, grouped by maximum attrition area of the medial condyle of the tibia.	468
Fig. 419. Study II. Histogram of central PLIR process (E1) osteophyte grade: number of varus knees in each category, grouped by maximum attrition area of the medial condyle of the tibia.	468
Fig. 420. Study II. Histogram of external PLIR process (E2) osteophyte grade: number of varus knees in each category, grouped by maximum attrition area of the medial condyle of the tibia.	469
Fig. 421. Study II. Histogram of posterior AFIR process (F1) osteophyte grade: number of varus knees in each category, grouped by maximum attrition area of the medial condyle of the tibia.	469
Fig. 422. Study II. Histogram of anterior AFIR process (F2) osteophyte grade: number of varus knees in each category, grouped by maximum attrition area of the medial condyle of the tibia.	470
Fig. 423. Study II. Histogram of Parsons' knob (G) osteophyte grade: number of varus knees in each category, grouped by maximum attrition area of the medial condyle of the tibia.	470
Fig. 424. Study II. Histogram of ACIK (H) osteophyte grade: number of varus knees in each category, grouped by maximum attrition area of the medial condyle of the tibia.	471
Fig. 425. Study II. Histogram of ASIR (J) osteophyte grade: number of varus knees in each category, grouped by maximum attrition area of the medial condyle of the tibia.	471
Fig. 426. Study II. Histogram of AIK (N) osteophyte grade: number of varus knees in each category, grouped by maximum attrition area of the medial condyle of the tibia.	472
Fig. 427. Study II. Histogram of ALIK (I) osteophyte grade: number of varus knees in each category, grouped by maximum attrition area of the medial condyle of the tibia.	472
Fig. 428. Study II. Histogram of AM corner (Bd_AM) osteophyte grade: number of varus knees in each category, grouped by maximum attrition area of the medial condyle of the tibia.	473
Fig. 429. Study II. Histogram of AL corner (Bd_AL) osteophyte grade: number of varus knees in each category, grouped by maximum attrition area of the medial condyle of the tibia.	473
Fig. 430. Study II. Histogram of medial rim, anterior part (Bd_MA), osteophyte grade: number of varus knees in each category, grouped by maximum attrition area of the medial condyle of the tibia.	474
Fig. 431. Study II. Histogram of medial rim, posterior part (Bd_MP), osteophyte grade: number of varus knees in each category, grouped by maximum attrition area of the medial condyle of the tibia.	474
Fig. 432. Study II. Histogram of lateral rim, anterior part (Bd_LA), osteophyte grade: number of varus knees in each category, grouped by maximum attrition area of the medial condyle of the tibia.	475
Fig. 433. Study II. Histogram of lateral rim, posterior part (Bd_LP), osteophyte grade: number of varus knees in each category, grouped by maximum attrition area of the medial condyle of the tibia.	475
Fig. 434. Study II. Histogram of PM corner (Bd_PM) osteophyte grade: number of varus knees in each category, grouped by maximum attrition area of the medial condyle of the tibia.	476

Fig. 435. Study II. Histogram of PL corner (Bd_PL) osteophyte grade: number of varus knees in each category, grouped by maximum attrition area of the medial condyle of the tibia.....	476
Fig. 436. Study II. Histogram of AL fossa osteophyte grade: number of varus knees in each category, grouped by maximum attrition area of the medial condyle of the tibia.	477
Fig. 437. Study II. Histogram of anterior saddle (T) osteophyte grade: number of varus knees in each category, grouped by maximum attrition area of the medial condyle of the tibia.....	477
Fig. 438. Study II. Histogram of AL vallecule (valle_AL) elevation grade: number of varus knees in each category, grouped by maximum attrition area of the medial condyle of the tibia.	478
Fig. 439. Study II. Histogram of AL recess (AL_rec) osteophyte grade: number of varus knees in each category, grouped by maximum attrition area of the medial condyle of the tibia.....	478
Fig. 440. Study II. Histogram of PM recess (PM_rec) osteophyte grade: number of varus knees in each category, grouped by maximum attrition area of the medial condyle of the tibia.....	479
Fig. 441. Study II. Histogram of PL recess (PL_rec) osteophyte grade: number of varus knees in each category, grouped by maximum attrition area of the medial condyle of the tibia.....	479
Fig. 442. Study II. Histogram of more internal PMIR process (C4) osteophyte grade: number of varus knees in each category, grouped by maximum attrition area of the medial condyle of the tibia.	480
Fig. 443. Study II. Histogram of internal PMIR process (C3) osteophyte grade: number of varus knees in each category, grouped by maximum attrition area of the medial condyle of the tibia.	480
Fig. 444. Study II. Histogram of internal PLIR process (E3) osteophyte grade: number of varus knees in each category, grouped by maximum attrition area of the medial condyle of the tibia.	481
Fig. 445. Study II. Histogram of area 13 (XIII) horizontality: number of varus knees, grouped by maximum attrition area of the medial condyle of the tibia. 0=facet-like (more horizontal); 1=ridge-like (more vertical).....	481
Fig. 446. Study II. Best fit regression models obtained to predict attrition of the medial condyle (Attr_M) from total osteophyte growth.....	482
Fig. 447. Study II. Best fit regression models obtained to predict attrition of the medial condyle from central AMIR process (B2) osteophyte grade.	485
Fig. 448. Study II. Best fit regression models obtained to predict attrition of the medial condyle (Attr_M) from MT osteophyte grade (TM).....	485
Fig. 449. Study II. Best fit regression models obtained to predict attrition of the medial condyle (Attr_M) from the AL corner (Bd_AL) osteophyte grade.	486
Fig. 450. Study II. Best fit regression models obtained to predict attrition of the medial condyle (Attr_M) from Parson's knob (G) osteophyte grade.	486
Fig. 451. Study II. Best fit regression models obtained to predict attrition of the medial condyle (Attr_M) from AM corner (Bd_AM) osteophyte grade.....	487
Fig. 452. Study II. Best fit regression models obtained to predict attrition of the medial condyle (Attr_M) from Ahlbäck OA grade.	487
Fig. 453. Study II. Best fit regression models obtained to predict attrition of the lateral condyle (Attr_L) from MT osteophyte grade (TM).....	488

Fig. 454. Study II. Best fit regression models obtained to predict attrition of the lateral condyle (Attr_L) from the medial rim, anterior part (Bd_MA), osteophyte grade.	488
Fig. 455. Study II. Best fit regression models obtained to predict attrition of the lateral condyle (Attr_L) from AL corner (Bd_AL) osteophyte grade.	489
Fig. 456. Study II. Best fit regression models obtained to predict attrition of the lateral condyle (Attr_L) from central and external ALIR processes (D1-D2) osteophyte grade.	489
Fig. 457. Study II. Best fit regression models obtained to predict attrition of the lateral condyle (Attr_L) from the more internal PMIR process (C4) osteophyte grade.	490
Fig. 458. Study II. Best fit regression models obtained to predict attrition of the lateral condyle (Attr_L) from PL corner (Bd_PL) osteophyte grade.	490
Fig. 459. Study II. Best fit regression models obtained to predict attrition of the lateral condyle (Attr_L) from the internal PMIR process (C3) osteophyte grade.	491
Fig. 460. Study II. Box-and-whisker plot of distribution of points obtained for the Knee Score part of KS Knee Score (EF_SCORE), grouped into Ahlbäck OA grade.	495
Fig. 461. Study II. Box-and-whisker plot of distribution of points for the Pain (Movement) item in KS Knee Score (EF_Pain_Move), grouped into Ahlbäck OA grade.	495
Fig. 462. Study II. Box-and-whisker plot of distribution of points for the Pain (Rest) item in KS Knee Score (EF_Pain_Rest), grouped into Ahlbäck OA grade.	496
Fig. 463. Study II. Box-and-whisker plot of distribution of points for the Pain (Stairs) item in KS Knee Score (EF_Pain_Stair), grouped into Ahlbäck OA grade.	496
Fig. 464. Study II. Box-and-whisker plot of distribution of points for the Extension Lag item in KS Knee Score (EF_Ext), grouped into Ahlbäck OA grade.	497
Fig. 465. Study II. Box-and-whisker plot of distribution of points for the Flexum item in KS Knee Score (EF_Flexum), grouped into Ahlbäck OA grade.	497
Fig. 466. Study II. Box-and-whisker plot of distribution of points for the Range of Motion item in KS Knee Score (EF_ROM), grouped into Ahlbäck OA grade.	498
Fig. 467. Study II. Box-and-whisker plot of distribution of points for the Alignment item in KS Knee Score (EF_Varus), grouped into Ahlbäck OA grade.	498
Fig. 468. Study II. Box-and-whisker plot of distribution of points for the Mediolateral Instability item in KS Knee Score (EF_Inest_ML), grouped into Ahlbäck OA grade.	499
Fig. 469. Study II. Box-and-whisker plot of distribution of points for the Anteroposterior Instability item in KS Knee Score (EF_Inest_AP), grouped into Ahlbäck OA grade.	499
Fig. 470. Study II. Box-and-whisker plot of distribution of points obtained for the Function Score part of KS Knee Score (EF_FUNCT), grouped into Ahlbäck OA grade.	500
Fig. 471. Study II. Box-and-whisker plot of distribution of points for the Walking Distance item in KS Knee Score (EF_Pt_Walk), grouped into Ahlbäck OA grade.	500
Fig. 472. Study II. Box-and-whisker plot of distribution of points for the Help item in KS Knee Score (EF_Pt_Help), grouped into Ahlbäck OA grade.	501
Fig. 473. Study II. Box-and-whisker plot of distribution of points for the Climb item in KS Knee Score (EF_Pt_Climb), grouped into Ahlbäck OA grade.	501
Fig. 474. Study II. Best fit regression models obtained to predict KS Knee Score (EF_SCORE) from the combined attrition of the medial and lateral condyles (Attr_M_L).	502

Fig. 475. Study II. Best fit regression models obtained to predict KS Knee Score (EF_SCORE) from total osteophyte growth.....	502
Fig. 476. Study II. Best fit regression models obtained to predict KS Knee Score (EF_SCORE) from Ahlbäck OA grades.....	503
Fig. 477. Study II. Best fit regression models obtained to predict KS Function Score (EF_FUNCT) from the combined attrition of the medial and lateral condyles (Attr_M_L)	503
Fig. 478. Study II. Best fit regression models obtained to predict KS Function Score (EF_FUNCT) from total osteophyte growth.....	504
Fig. 479. Study II. Best fit regression models obtained to predict KS Function Score (EF_FUNCT) from Ahlbäck OA grades.....	504
Fig. 480. Maximal possible internal rotation of the femur with removal of capsular and collateral ligaments and of the menisci, but with intact cruciate ligaments. Modified from Fuss (1991) ¹¹⁷	517
Fig. 481. 3D model of tibia A, with contour lines superimposed. Main processes of the medial tubercle (in red) and lateral tubercle (in blue), labelled. In white, curves loosely following each condyle's radius of curvature, representing potential internal rotation of the femoral condyles over their respective tibial condyles. The AMIR and PLIR processes appear as potential osseous limits to translation in the different degrees of rotation. Osteophytic elevations of these processes could therefore constrain tibiofemoral movements in more unstable knees.	517
Fig. 482. 3D model of tibia A. Superoinferior view of anterior intercondylar staircase. A (with contour lines superimposed): hypothetical location of the three bundles over the marked ACL footprint, following incisures 10g and 10h for their division. B: The real footprint of the three bundles as obtained in this study. PL bundle (in cyan), AMM bundle (in magenta), and AML bundle (in bright green). Labelled are the ALIR in blue, the AMIR in red, the AFIR in green, the geniculum (G), and the ACIK (H). See also Fig. 259 and Fig. 278 for the corresponding images.	578
Fig. 483. ACL bundles. Image modified from Weber & Weber (1836) ⁹ , originally labelled Taf. V. (from digitalized copy at Europeana collections; condition: out of copyright – noncommercial re-use).....	646
Fig. 484. PCL bundles. Image modified from Weber & Weber (1836) ⁹ , originally labelled Taf. VI. (from digitalized copy at Europeana collections; condition: out of copyright – noncommercial re-use).....	647
Fig. 485. Superoinferior view of a right tibia (anterior is above). Modified from Spalteholz (1896) ¹⁴	653
Fig. 486. Schematic coronal cut of a right knee, viewed from behind. Modified from Fick (1904) ¹¹	654
Fig. 487. Depiction of a sagittal cut of a right, slightly flexed knee showing the lateral meniscus. Modified from Fick (1904) ¹¹	655
Fig. 488. Anterior view of right knee, bent, with ACL detached. Modified from Fick (1904) ¹¹	656
Fig. 489. Right knee, extended, with capsule detached (posterior view). Modified from Fick (1904) ¹¹	657
Fig. 490. Superoinferior view of a right knee (anterior is above). Modified from Sobotta (1906) ¹⁶	658

Fig. 491. Axial cuts of the knee, modified from “ice anatomy” by Pirogón (1855) ¹³	659
Fig. 492. Axial oblique cuts of the knee, modified from “ice anatomy” by Pirogón (1855) ¹³	659
Fig. 493. Sagittal cuts of the knee in extension, modified from “ice anatomy” by Pirogón (1855) ¹³	660
Fig. 494. Sagittal cuts of the knee in approximately 90° of flexion, modified from “ice anatomy” by Pirogón ¹³	661
Fig. 495. Sagittal cuts of the knee in high flexion degrees, modified from “ice anatomy” by Pirogón (1855) ¹³	661
Fig. 496. Coronal cuts of the left knee in extension, modified from “ice anatomy” by Pirogón (1855) ¹³	662
Fig. 497. Depiction of sagittal cut of the knee through lateral tubercle, with ACL attachment shown. Modified from Kiss & Szentágothai (1973) ¹⁸	663
Fig. 498. Proximal tibia with cruciate ligaments turned back (anterior is up). Image modified from Parsons (1906) ¹² . β: ACL reflected; ε: ARLM attachment; θ: AMIK (Parsons’ knob). White dashed lines (added to the original image) separate the AIAR from the main C-shaped attachment of the ACL, and also delineate the thinner central aspect of the reflected ACL stump – as the hypothesized mirror image of the AIAR. Notice the delta-like appearance of the area drawn in the ACL stump (and also of the surrounding detached fibers) corresponding to a more closed C-shaped attachment.....	666
Fig. 499. Proximal tibia. Image modified from Parsons (1906) ¹² . β: Intertubercular ridge.....	666
Fig. 500. Upper surface of right tibia. Modified from Gray (1918) ¹	667
Fig. 501. Depiction of osseous surface (left image) and attachment areas (right image). Ligamentous attachments in black, meniscal attachments in grey. Modified from Poirier (1892) ²	670
Fig. 502. Architecture of the proximal extremity of the tibia. Modified from Poirier (1892) ² ...	670
Fig. 503. Image modified from Paturet (1951) ¹⁹ (anterior is up, medial is left) Observe the ACL attachment – dotted surface – in the inferior image (B) corresponding to the comma-like elevation depicted in the osseous surface (A).	672

List of abbreviations

ABBREVIATION	ENGLISH TERM
1L	anterointernal quadrant (lateral condyle)
1M	posterointernal quadrant (medial condyle)
2L	posterointernal quadrant (lateral condyle)
2M	anterointernal quadrant (medial condyle)
3L	anteroexternal quadrant (lateral condyle)
3M	anteroexternal quadrant (medial condyle)
4L	posteroexternal quadrant (lateral condyle)
4M	posteroexternal quadrant (medial condyle)
A	anterior
ACIK	anterocentral intercondylar knob
ACL	anterior cruciate ligament
ACL-AM	anteromedial bundle of the ACL
ACL-AML	anteromedial bundle of the ACL, lateral part
ACL-AMM	anteromedial bundle of the ACL, medial part
ACL-PL	posterolateral bundle of the ACL
AFIR	anterior frontal intercondylar ridge
AFIR RECESS	recess of the anterior frontal intercondylar ridge
AHLM	anterior horn of the lateral meniscus
AHMM	anterior horn of the medial meniscus
AI	anteroinferior
AIA	anterior intercondylar area
AIAR	anterior intercondylar area's ridge
AIS	anterior intercondylar staircase
AISX	anterior intercondylar staircase's X
AL	anterolateral
AL BUNDLE	anterolateral bundle of the PCL
AL CORNER	anterolateral corner of the intercondylar area
ALF	anterolateral fossa
ALIK	anterolateral intercondylar knob
AM	anteromedial
AM BUNDLE	anteromedial bundle of the ACL
AM CORNER	anteromedial corner of the intercondylar area
AMAIA	anterior part of the MAIA
AMIK	anteromedial intercondylar tubercle
AMIR	anteromedial intercondylar ridge
AML BUNDLE	anteromedial bundle of the ACL, lateral part

AMM BUNDLE	anteromedial bundle of the ACL, medial part
ANOVA	analysis of variance (statistical test)
ANT	anterior
AP	anteroposterior
ARLM	anterior root of the lateral meniscus
ARMM	anterior root of the medial meniscus
AS	anterosuperior
ASIR	anterior intercondylar sagittal ridge
Bd	border (corner / rim)
CGD	champagne-glass drop-off
CI	confidence interval
CIAIS	coronal incisure of the AIS
CV	coefficient of variation
EF	physical examination
G	geniculum
ICT	intercondylar circular triangle
IE	intercondylar eminence of the tibia
IS	inferosuperior
IS	(anterior) intercondylar staircase
ITA	intertubercular area
ITR	intertubercular ridge
L	lateral
LAIA	lateral aspect of the AIA (anterolateral groove)
LAT	lateral
LM	lateral meniscus
LM	lateromedial
LT	lateral intercondylar tubercle
M	medial
MAC	maximum attrition zone of the condyle (articular erosion)
MACCO	complementary zones of the MAC
MACMACCO	MAC + MACCo
MACOP	opposite condyle attrition zones (relative to MAC)
MAIA	medial aspect of the AIA
MAIA	medial part of the anterior intercondylar area
ML	mediolateral
MM	medial meniscus
MT	medial intercondylar tubercle
OA	osteoarthritis
P	posterior
PA	posteroanterior
PCL	posterior cruciate ligament
PCL-AL	anterolateral bundle of the PCL
PCL-PM	posteromedial bundle of the PCL
PI	posteroinferior
PIA	posterior intercondylar area
PIR	posterior intercondylar ridge

PIS	posterior intercondylar stair
PL	posterolateral
PL BUNDLE	posterolateral bundle of the ACL
PL CORNER	posterolateral corner of the intercondylar area
PLIR	posterolateral intercondylar ridge
PM BUNDLE	posteromedial bundle of the PCL
PM CORNER	posteromedial corner of the intercondylar area
PMIR	posteromedial intercondylar ridge
POE	posteminence
POST	posterior
PRE	preeminence
PRLM	posterior root of the lateral meniscus
PRMM	posterior root of the medial meniscus
PS	posterosuperior
ROM	range of motion
Rx	radiograph / fluoroscopic view
SI	superoinferior
SIAIS	sagittal incisure of the AIS
TIL	transverse intermeniscal ligament
TS	tibial spine
TL	tuberculum laterale
TM	tuberculum mediale
TT	tibial tuberosity

Guide to the reader

Confusion exists within the common orthopaedic vernacular and in the scientific literature regarding the terminology to describe the bony surface anatomy of the tibial plateau, also head of the tibia. This work uses terminology described in prominent anatomy texts³⁻⁶ and those of recent publications.

There is a medial and lateral condyle comprising the articular surfaces of the tibial plateau. Between these articular surfaces there is an intercondylar or intercondyloid eminence, also called spine of the tibia, “which is surmounted on either side by a prominent tubercle on to the sides of which the facets are prolonged named the medial and lateral intercondylar tubercles”⁷.

Both tubercles are connected by a concave ridge, the intertubercular ridge. The intercondylar eminence is defined as the main tubercles plus the intertubercular ridge. The region anterior to the eminence is called the anterior intercondylar area (AIA), and the area behind it is the posterior intercondylar area (PIA).

Conventions used in this study

External and *internal* are used following their most common modern usage, i.e. respective to the surface. Hence, while medial and lateral are used unequivocally, external and internal are used in reference to a medial line, at the center of the intercondylar area.

Tibial height refers to inferosuperior length; tibial width refers to mediolateral length; tibial depth refers to anteroposterior length.

All specimens (in photographs, radiographs, and 3D models), unless otherwise stated, are shown in anteroposterior views with their anterior aspect anteriorly and/or at the bottom of the image, their posterior aspect posteriorly and/or at the top of the image, their medial aspect on the left side, and their lateral aspect on the right side; in lateral views they are shown with their anterior aspect on the right side, posterior aspect on the left side.

Right knees have been reversed (i.e. left-mirrored) in all images shown from an anteroposterior or posteroanterior views, to represent the structures in the same place relative to the observer.

Mediolateral and anteroposterior views that are shown in the same – or consecutive – images with the specimen reversed (i.e. lateromedial and posteroanterior views, respectively) have been flipped horizontally to show the same structures (medial or lateral, anterior or posterior) at the same place (left or right) relative to the viewer.

Ridges (including “lines”, “curves”, “processes”, “walls”, etc.) are painted over the images of the specimens with a narrow, partially transparent line following the highest points in the contour lines over the surface; therefore, elevations are not fully covered by color.

In tables of distances to attachment centers, the background of relevant numbers have been colored in gray, with lighter to darker colors showing lesser to greater relevance. The most relevant distances have been emphasized in bold.

Alphanumeric references

The following is a list of English names, with the same position relative to the *Terminologia Anatomica* of the next section. They are loosely ordered by alphanumeric reference.

Alphanumeric	Name	Abbrev.
	tibial plateau	
	head of the tibia	
12, 14a, 15	intertubercular ridge	ITR
3, 4, 12, 14a, 15	intercondylar / intercondyloid eminence of the tibia	IE
3, 4, 12, 14a, 15	tibial spine	TS
1c, 2c, 5, 7, 8, 9, 10	anterior intercondylar area	AIA
10, 5	medial aspect of the AIA	MAIA
7, 8, 9	anterolateral groove (lateral aspect of the AIA)	AL groove
11, 13, 14b	posterior intercondylar area	PIA
	posterior coronal axis	
	anterior coronal axis	
1	medial tibial condyle	
1a+1b	articular facet of the medial tibial condyle	
1a	medial meniscal footprint	
1b	nude area of the medial condyle	
	curvature of the medial condyle	
	button of the medial condyle	
1c	anteromedial corner	AM corner
1d	posteromedial corner	PM corner
	medial condylar rim	
2	lateral tibial condyle	
2a+2b	articular facet of the lateral tibial condyle	
2a	lateral meniscal footprint	
2b	nude area of the lateral condyle	
	curvature of the lateral condyle	
2c	anterolateral corner	
2d	posterolateral corner	
	lateral condylar rim	
3	medial intercondylar tubercle	MT
	summit of the MT	SMT
3a₁	anterior peak of the SMT	
3a₂	posterior peak of the SMT	
3a	(single) peak of the SMT	
	medial intercollicular vallecula	
	external slope of the MT	
3b	posterior peak of the MT	
3c	anterior peak of the MT	
3d	minor posterior peak of the MT	
4	lateral intercondylar tubercle	LT
	anterior summit of the LT	

4a	peak of the anterior summit of the LT	
	external slope of the LT	
4c	anterior peak of the LT	
4b	vallecula of the LT	
	posterior summit of the LT	
4d	peak of the LT posterior summit of the LT	
	external slope of the posterior summit of the LT	
5	anterior part of the MAIA	AMAIA
	anterior fingerprint	
	anterior coronal line of the proximal tibia	
	accessory imprint	
	<i>anterior margin of the proximal tibia</i>	
	<i>anterior wall of the proximal tibia</i>	
	<i>tibial tuberosity</i>	TT
6	See A	
7	anterolateral fossa	AL fossa
	anterolateral fovea	AL fovea
8	Anterolateral recess	
9	anterolateral vallecula	
7, 9	anterolateral groove	
	Hoffa's infrapatellar fat pad	
10	anterior intercondylar staircase	AIS, IS
10a	superior intercondylar stair	
10b	anteromedial fovea	AM fovea
	intertubercular fossa	
10c	upper landing	
10d	inferior intercondylar stair	
10e	middle landing	
10f	lower landing	
10g	sagittal incisure of the AIS	SIAIS
10g₁	sagittal branch of the SIAIS	
10g₂	oblique branch of the SIAIS	
10g₃	coronal branch of the SIAIS	
10h	coronal incisure of the AIS	CIAIS
10i	anterior incisure of the AIS	
10j	posterior incisure of the AIS	
10k	sagittal line of the AIS	
11, 14b	posterior wall of the intercondylar area	PWPIA
11	medial facet of the PWIA	
11a	lateral part of the MFPWIA	
11b	posteromedial recess	
11c	posteromedial fossa	
	posteromedial fovea	
12	intertubercular area	ITA
12a	intertubercular saddle	
12b	posterolateral recess	
12c	posterolateral fossa	
13	posterior facet of the PIA	PFPIA

13a	posterior intercondylar stair	PIS
13b	posteromedial groove	
13a+13b	intercondylar circular triangle	ICT
13c	posterior rim	
13g	ICT medial sagittal line	
13h	ICT coronal line	
13i	ICT lateral sagittal line	
13g, 13h	posterior geniculate ridge	
13j	curved incisure	
14	anterolateral aspect of the PIA	
14a	posterior wall of the ITR	
14b	lateral facet of the PWIA	
15	anterior wall of the ITR	
16	champagne-glass drop-off	CGD
A	anterior intercondylar area's ridge	AIAR
A1	posterior AIAR	
A1_a	posterior curve of the AIAR	
A1_b	concavity of the AIAR	
A2	anterior AIAR	
B	anteromedial intercondylar ridge	AMIR
B1	external AMIR process	
B2	central AMIR process	
B3	internal AMIR process	
B4	more internal AMIR process	
C	posteromedial intercondylar ridge	PMIR
C1 (C1_a)	central PMIR process	
C1_b	secondary central PMIR process (internal)	
C2	external PMIR process	
C3	internal PMIR process	
C4	more internal PMIR process	
D	anterolateral intercondylar ridge	ALIR
D1	external ALIR process	
D2	central ALIR process	
D3	internal ALIR process	
D3_a	anterior line of D3	
D3_b	posterior line of D3	
E	posterolateral intercondylar ridge	PLIR
E1 (E1_a)	central PMIR process	
E1_b	secondary central PMIR process (internal aspect)	
E2	external PMIR process	
E3	internal PMIR process	
F	anterior frontal intercondylar ridge	AFIR
F1	posterior AFIR process	
F2	anterior AFIR process	
B1, F1	geniculate ridge	
B, F, A, 15	deltoid ridge	
G	anterior intercondylar geniculum	

	anteromedial intercondylar knob	AMIK
H	anterocentral intercondylar knob	ACIK
I	anterolateral intercondylar knob	ALIK
J	anterior intercondylar sagittal ridge	ASIR
M	tent-shaped ridge	
	posterior tent-shaped incisure	
	anterior tent-shaped incisure	
N	anterior knob	
P	posterior geniculum	
Q	posterior intercondylar ridge	PIR
S	AFIR recess	
T	anterior intercondylar saddle	
V	preeminence	PRE
W	posteminence	POE

Terminologia anatomica

This work followed the latest international standard, *Terminologia Anatomica* (1998, reprinted 2011)⁸ by the Federative International Programme on Anatomical Terminologies, approved by the International Federation of Associations of Anatomists. New terms had to be adapted to the newly described areas or structures.

Alphanumeric	Nomina	Abbrev.
	extrēmitās proximālis tībiæ	
	caput tībiæ	
12, 14a, 15	crista intertūberculāris	c.i.t.
3, 4, 12, 14a, 15	ēminētia intercondylāris tībiæ	e.i.t.
3, 4, 12, 14a, 15	spīna tībiālis	
1c, 2c, 5, 7, 8, 9, 10	ārea intercondylāris anterior tībiæ	a.i.a.
10, 5	ārea mediālis āree intercondylāris anteriōris tībiæ	a.m.a.i.a.
7, 8, 9	sulcus anterior laterālis (ārea laterālis āree intercondylāris anteriōris tībiæ)	a.l.a.i.a.
11, 13, 14b	ārea intercondylāris posterior tībiæ	a.i.p.
	axis frontālis posterior tībiæ	
	axis frontālis anterior tībiæ	
1	condylus mediālis tībiæ	
1a+1b	faciēs articulāris superior condylī mediālis tībiæ	
1a	impressiō mēniscī mediālis	
1b	ārea nūda condylī mediālis	
	curvātūra condylī mediālis	
	nōdus condylī mediālis	
1c	margō anterior mediālis	
1d	margō posterior mediālis	
	margō condylī mediālis	
2	condylus laterālis tībiæ	
2a+2b	faciēs articulāris superior condylī laterālis tībiæ	
2a	impressiō mēniscī laterālis	
2b	ārea nūda condylī laterālis	
	curvātūra condylī laterālis	
2c	margō anterior laterālis	
2d	margō posterior laterālis	
	margō condylī laterālis	
3	tūberculum intercondylāre mediāle tībiæ	t.i.m.
	colliculus tūberculī intercondylāris mediālis	
3a₁	apex anterior colliculī t.i.m.	
3a₂	apex posterior colliculī t.i.m.	
3a	apex colliculī t.i.m.	
	vallēcula intercolliculāris t.i.m.	
	clīvus tūberculī mediālis	
3b	apex posterior t.i.m.	
3c	apex anterior t.i.m.	

3d	apex posterior minor t.i.m.	
4	tūberculum intercondylāre laterāle tībiæ	t.i.l.
	colliculus anterior tūberculī intercondylāris laterālis	
4a	apex colliculī anteriōris t.i.l.	
	clīvus tūberculī laterālis	
4c	apex anterior t.i.l.	
4b	vallēcula intercolliculāris laterālis	
	colliculus posterior tūberculī intercondylāris laterālis	
4d	apex colliculī posteriōris t.i.l.	
	clīvus posterior (clīvulus) tūberculī laterālis	
5	pars anterior a.m.a.i.a.	
	impressiō digitālis anterior	
	līnea anterior frontālis tībiæ	
	impressiō accessōria anterior	
	margō anterior capitis tībiæ	
	pariēs anterior capitis tībiæ	
	tūberositās anterior tībiæ	t.a.t.
6	See A	
7	fossa intercondylāris anterior laterālis	
	fovea anterior laterālis	
8	recessus anterior laterālis	
9	vallēcula anterior laterālis	
7, 9	sulcus intercondylāris anterior laterālis	
	corpus adiposum infrapatellāre	
10	scālæ intercondylārēs anteriōrēs	
10a	scāla intercondylāris superior	
10b	fovea anterior mediālis	
	fossa intertūberculāris	
10c	pars horīzontālis superior scālārum	
10d	scāla intercondylāris īnferior	
10e	pars horīzontālis media scālārum	
10f	pars horīzontālis īnferior scālārum	
10g	incīsūra sagittālis scālārum intercondylāriūm anteriōrum	i.s.s.i.a.
10g₁	rāmus sagittālis i.s.s.i.a.	
10g₂	rāmus oblīqvus i.s.s.i.a.	
10g₃	rāmus frontālis i.s.s.i.a.	
10h	incīsūra frontālis s.i.a.	
10i	incīsūra anterior s.i.a.	
10j	incīsūra posterior s.i.a.	
10k	līnea sagittālis s.i.a.	
11, 14b	pariēs posterior a.i.p.	p.p.a.i.p
11	faciēs mediālis p.p.a.i.p.	
11a	pars laterālis faciēi mediālis p.p.a.i.p.	
11b	recessus posterior mediālis	
11c	fossa posterior mediālis	
	fovea posterior mediālis	
12	area intertūberculāris	a.i.t.
12a	sella intertūberculāris	

12b	recessus posterior laterālis	
12c	fossa posterior laterālis	
13	faciēs posterior a.i.p.	
13a	scāla intercondylāris posterior	s.i.p.
13b	sulcus posterior mediālis	
13a+13b	trigōnum rotundum intercondylāre	t.r.i.
13c	līnes posterior	
13g	līnea sagittālis mediālis	t.r.i.
13h	līnea frontālis	t.r.i.
13i	līnea sagittālis laterālis	t.r.i.
13g, 13h	crista geniculāta posterior	
13j	incīsūra curva	s.i.p.
14	pars anterior laterālis	a.i.p.
14a	pariēs posterior	c.i.t.
14b	faciēs laterālis	p.p.a.i.p.
15	pariēs anterior	c.i.t.
16	dēclīve calicis tībiæ	d.c.t.
	pariēs posterior capitis tībiæ	
A	crista āreæ intercondylāris anteriōris	c.a.i.a.
A1	pars posterior	c.a.i.a.
A1_a	curvātūra posterior	c.a.i.a.
A1_b	concovitās	c.a.i.a.
A2	pars anterior	c.a.i.a.
B	crista intercondylāris mediālis anterior	c.i.m.a.
B1	rāmus externus	c.i.m.a.
B2	rāmus centrālis	c.i.m.a.
B3	rāmus internus	c.i.m.a.
B4	rāmus interior	c.i.m.a.
C	crista intercondylāris mediālis posterior	c.i.m.p.
C1 (C1_a)	rāmus centrālis	c.i.m.p.
C1_b	rāmus centrālis secundārius	c.i.m.p. (pars interna)
C2	rāmus externus	c.i.m.p.
C3	rāmus internus	c.i.m.p.
C4	rāmus interior	c.i.m.p.
D	crista intercondylāris laterālis anterior	c.i.l.a.
D1	rāmus externus	c.i.l.a.
D2	rāmus centrālis	c.i.l.a.
D3	rāmus internus	c.i.l.a.
D3_a	līnea anterior	r.i.c.i.l.a.
D3_b	līnea posterior	r.i.c.i.l.a.
E	crista intercondylāris laterālis posterior	c.i.l.p.
E1 (E1_a)	rāmus centrālis	c.i.l.p.
E1_b	rāmus centrālis secundārius	c.i.l.p. (pars interna)
E2	rāmus externus	c.i.l.p.
E3	rāmus internus	c.i.l.p.
F	crista intercondylāris frontālis anterior	c.i.f.a.
F1	rāmus posterior	c.i.f.a.
F2	rāmus anterior	c.i.f.a.

B1, F1	crista geniculāta anterior	
B, F, A, 15	crista deltoidea	
G	geniculum intercondylāre anterior	
G	nōdus intercondylāris anterior mediālis	n.i.a.m.
H	nōdus intercondylāris anterior centrālis	n.i.a.c.
I	nōdus intercondylāris anterior laterālis	n.i.a.l.
J	crista anterior sagittālis intercondylāris	c.a.s.i.
K	incīsūra sagittālis parietis posteriōris c.i.t	
M	tentōrium	
	incīsūra tentōriō similis posterior	
	incīsūra tentōriō similis anterior	
N	nōdus anterior	
P	geniculum intercondylāre posterius	
Q	crista intercondylāris posterior	
S	recessus c.i.a.	
T	sella intercondylāris anterior	
V	præēminentia intercondylāris	
W	postēminentia intercondylāris	

Nomina anatomica	Abbr.	English
ligāmentum cruciātum anterius	l.c.a.	anterior cruciate ligament
pēs anatinus		ACL duck's foot
tænioideum l.c.a.		ribbon-like ACL
sæptum frontāle l.c.a		ACL coronal septum
sæptum sagittāle l.c.a.		ACL sagittal septum
incīsūra fasciculōrum l.c.a.	(See 10g3)	ACL bundle incisure
arcus strātīfōrmis intercondylāris		C-layered ACL footprint
arcus posterior		posterior arch
arcus intercondylāris externus		outer C
arcus intercondylāris centrālis		central C
arcus intercondylāris internus		inner C
fornix l.c.a.		ACL fornix (outer C + central C)
flābellum		fan-like facet
clīmax	(See D3)	ladder
fasciculus anterior mediālis l.c.a.		ACL anteromedial bundle
pars mediālis fasciculī anteriōris mediālis l.c.a.		ACL anteromedial bundle, lateral part
pars laterālis fasciculī anteriōris mediālis l.c.a.		ACL anteromedial bundle, medial part
fasciculus posterior laterālis l.c.a.		ACL posterolateral bundle
īnseritiō coniuncta intercondylāris		ACL - ARLM common attachment
rādīx anterior mēniscī mediālis	r.a.m.m.	anterior horn of lateral meniscus
cornū anterius mēniscī mediālis	c.a.m.m.	anterior horn of medial meniscus
rādīx anterior mēniscī laterālis	r.a.m.l.	anterior root of the lateral meniscus
fibræ inmixtæ rādīcis anteriōris mēniscī laterālis		intermingled fibers of the ARLM
impressiō anterior mēniscī laterālis		ARLM footprint
		anterior root of the medial meniscus
		lateral meniscus
		medial meniscus
rādīx posterior mēniscī mediālis	r.p.m.m.	posterior root of the medial meniscus
fibræ candidæ frontāles		transverse shiny white fibers
rādīx posterior mēniscī laterālis	r.p.m.l.	posterior root of the lateral meniscus
fibræ accessōriæ rādīcis posteriōris mēniscī laterālis		supplementary fibers of the PRLM
ligāmentum cruciātum posterius		posterior cruciate ligament
fasciculus anterior laterālis l.c.p.		PCL anterolateral bundle
fasciculus posterior mediālis l.c.p.		PCL posteromedial bundle
crista fasciculōrum ligāmenti cruciātī posteriōris	(see 13g, 13h)	PCL bundle ridge
ligāmentum trānsversum genūs	l.t.g.	transverse intermeniscal ligament

Shapes and sizes of elevations and depressions

Nomina anatomica	(grade)	English
cōnus		cone
cōnus bicephalus		bicephalous cone
crista	+2	ridge
ēminentia	+5	eminence
fovea	-3	pit
fossa	-4	fossa
hāmulus		little hook
hāmus		hook
incisura	-1	notch
lāmina		lamina
līnea	+1	line
lingula		tongue
nōdus	+3	knob
plānum	0	flat area
recessus	-2	recess
sulcus	-5	groove
stella		star
tūberculum	+4	tubercle

I. Introduction

I.1. Anatomy

The tibial intercondylar area has been traditionally described in anatomy books in a simplified manner.

The first detailed descriptions of the area and soft tissue insertions (Fig. 1) were done by German researchers in their description of the knee anatomy and function: the seminal studies by brothers Wilhelm Weber & Eduard Weber (1836)⁹ and Heinrich Ludwig Ferdinand Robert (1855)¹⁰ were later complemented by the study of Rudolf Fick (1904)¹¹. See Appendix I for more information on the German contribution to the study of the proximal tibial anatomy.

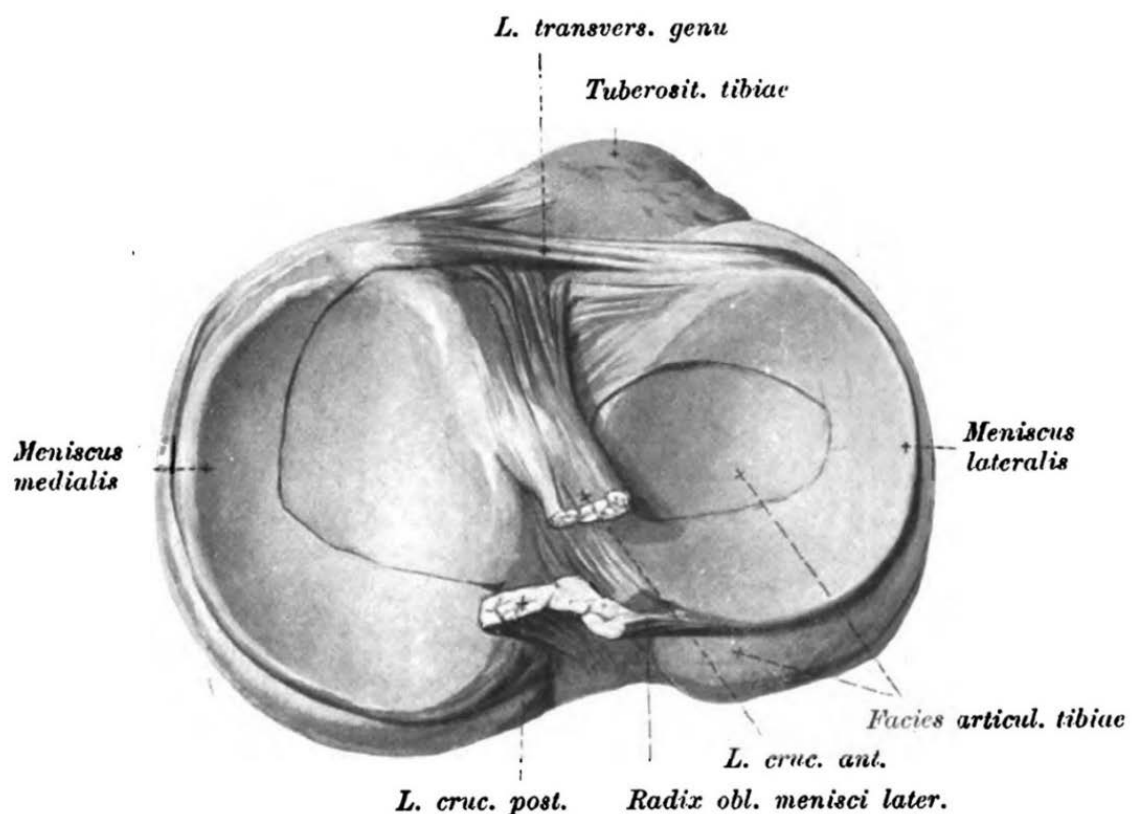


Figure 1. Drawing of right proximal tibia (anterior is up), with soft tissues attached. Modified from Fick (1904).

These works have been largely overlooked outside the German literature, where this area has not received much attention until recently, the most notable exception being Frederick Gymer Parsons' report (1906)¹² on the anatomy of the proximal tibia, which has become well known for offering the first description of his eponymous knob near the anteromedial attachment of the anterior cruciate ligament (Fig. 2).

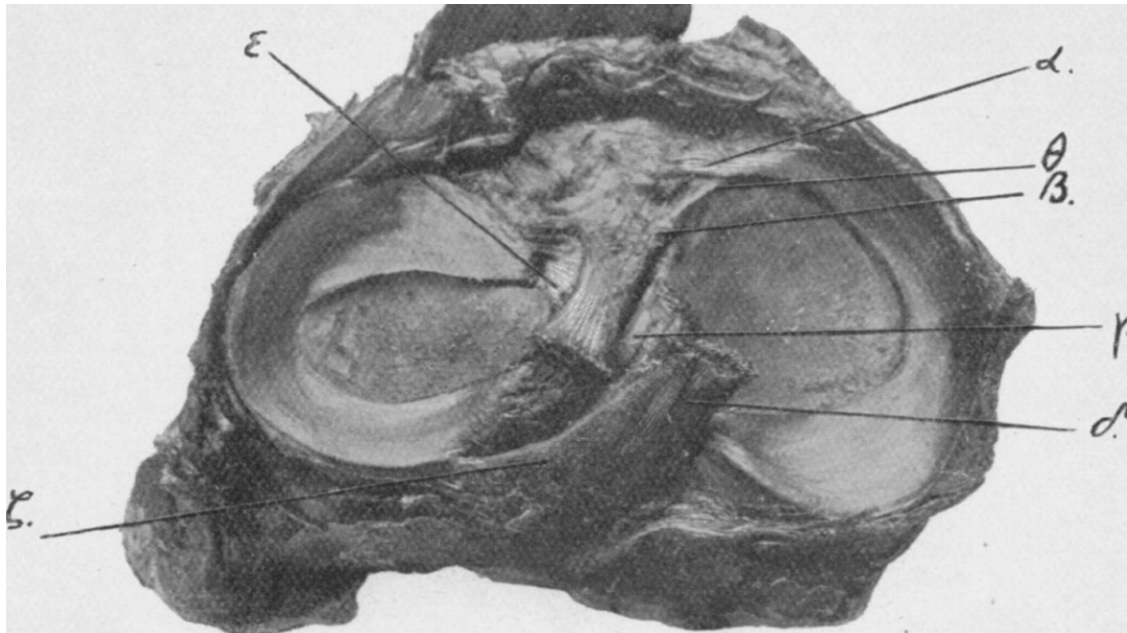


Figure 2. Photograph of left proximal tibia (anterior is up), with cruciate ligaments and menisci in situ. Modified from Parsons (1906). α=anterior cornu of internal semi-lunar cartilage. β=anterior cruciate ligament. ε=anterior cornu of external semi-lunar cartilage. γ=posterior cornu of external semi-lunar cartilage. δ=posterior cruciate ligament. ξ=ligament of Wrisberg. θ=little knob on the outer margin of the internal articular facet, indicating the attachment of the anterior cruciate ligament.

The most popular anatomy texts used during the past centuries only shortly mention – or depict – some aspects of the intercondylar area; these include among others the works (see Appendices I-IV), with multiple reprints and editions, by Nikoláj Ivánovich Pirogóv (1852)¹³, Henry Gray (1858)¹, Paul-Julien Poirier & Adrien Charpy (1892)², Werner Spalteholz (1896)¹⁴, Léo Testut (1899)¹⁵, Robert Heinrich Johannes Sobotta (1904)¹⁶, Francisco Orts Llorca (1944)¹⁷, Szentágothai János & Kiss Ferenc (1946)¹⁸, or George Paturet (1951)¹⁹.

Remarkable during this time was the work by Ian Scott Smillie (1946)²⁰, the first book published dealing exclusively with knee injuries, which might have given an impulse to a more thorough investigation of knee anatomy.

International reports with detailed anatomic descriptions of the intercondylar area began in the 1970s, when surgical treatment of torn cruciate ligaments was

more frequently performed, due to the increased sport activity in the general population, and the wish of older people to keep an active life.

Because the more popular surgical techniques involve reconstructing the ligaments by replacing them with a graft, the need exists to know the exact position, area, and shape of ligamentous footprints, as well as their relationship with neighboring structures.

Meniscal pathology involving their attachment is rare, but sometimes grafts are used for reconstruction, and a precise knowledge of their footprints is also necessary as anatomic reference (and to avoid damaging them) during ligament reconstruction.

The anatomic study by Jacobsen (1974)²¹ deserves a special mention among all such recent works for creating an ordered anatomic scheme, by delimiting and numbering the zones of the proximal tibia, and more specifically of the intercondylar area (Fig. 3).

Jacobsen defined the *area intercondylaris tibiae* as the area between the hyaline cartilage-covered medial and lateral tibial condyles together with the *tuberculum mediale & laterale* which are partly covered with hyaline cartilage. It comprises the *area intercondylaris anterior*, the *area intercondylaris posterior* and the *eminentia intercondylaris* in between. He described and measured the following areas:

- Area 1a is the part of the cartilage which normally ‘articulates’ with the medial meniscus.
- Area 1b is the part articulating directly with the cartilage on the medial femoral condyle.
- Area 1c does not belong to the actual articular socket: it is a plane facet extending obliquely down from the articular surface towards the area intercondylaris anterior.
- Area 1d is a corresponding area, sloping down towards the area intercondylaris posterior tibiae
- Area 2a is the ‘imprint’ of the meniscus lateralis.
- Area 2b is the area of contact with the cartilage on the lateral femoral condyle.
- Area 2c is covered with thin cartilage: it is in contact with the anterior horn of the lateral meniscus.

- Area 3 indicates the tuberculum mediale covered with articular cartilage.
- Area 4 is the tuberculum laterale covered with articular cartilage.
- The tuberculum laterale and tuberculum mediale are connected by a concave ridge which passes from the central side of the tuberculum mediale obliquely backwards and laterally to meet the tuberculum laterale. This ridge crista intertubercularis (c.i.t) comprises large areas (11 and 12) and smaller areas (14 and 15). Anteriorly the ridge first slopes rather steeply down (cf. the small area 15) but thereafter the inclination continues evenly into area 10. Posteriorly, it drops rather abruptly down towards area 13.
- Area 6 is a longitudinal ridge crista areae intercondylaris anterior. The ridge runs approximately in an anteroposterior direction, but bends in a faint curve posteriorly between areas 8 and 10 towards the lateral side.
- Area 5 is the anterior part of the medial plateau of the area intercondylaris anterior. It serves as the site of insertion for the cornu anterius menisci medialis.
- Area 7 is the term for the oblique wall dropping more or less abruptly from the anterior part of the crista areae intercondylaris anterior towards the deep lateral valley, area 9. Together with area 9 it forms a bowl in which the corpus adiposum infrapatellare settles and has its attachment.
- Area 8 is that part which is occupied by the insertion of the cornu anterius menisci lateralis.
- Area 9 is the deep valley laterally which extends posteriorly to the site where the medial wall of the tuberculum laterale meets the crista areae intercondylaris anterior.
- Area 10 is the insertion facet of the tibia for the ligamentum cruciatum anterius.
- Area 11 is an almost vertically oriented facet on the posterior, sloping side of the tuberculum mediale, giving insertion to the cornu posterius menisci medialis.
- Area 12 is the insertion facet for the cornu posterius menisci lateralis
- Area 13 is situated posterior to and at the foot of the eminence massif, deeply depressed between the two condylar joint surfaces. It gives insertion to the *ligamentum cruciatum posterius*.

- Area 14 is the inferior part of the posterior wall of the *crista intertubecularis*.
- Area 15 is behind area 10, along the anterior wall of the *crista intertubecularis*.

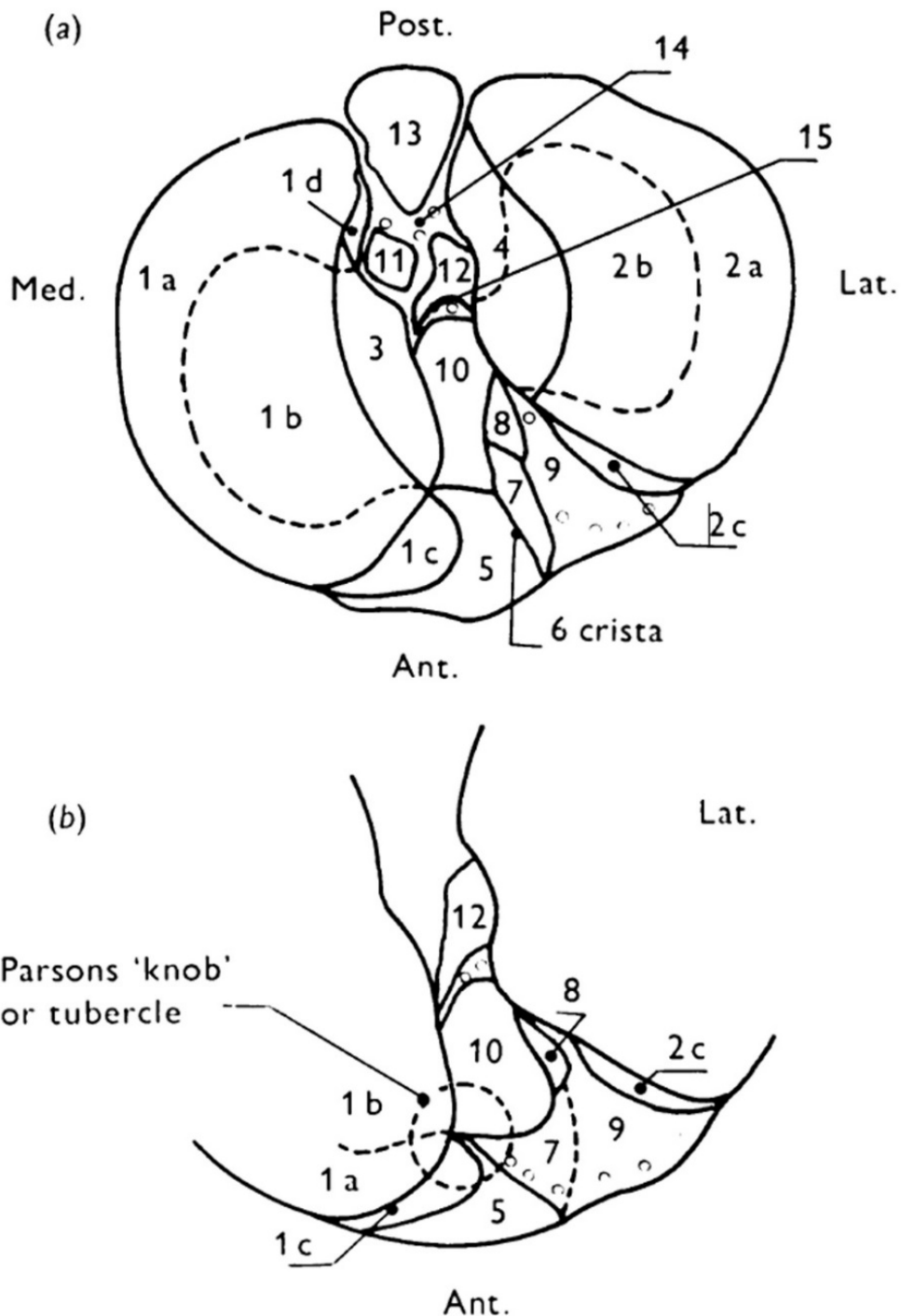


Figure 3. Image modified from Jacobsen (1974)²¹. Left proximal tibia. (a) The most common arrangements of the areas described. (b) Another possibility for the anterior intercondylar area. Location of foramina nutricia indicated by o.

Jacobsen's outline of the main areas has been used in this work to develop a more systematic description of the osseous surface.

He used this detailed description of the proximal tibial anatomy in a later work²² on its lateral radiographic profile (Fig. 4).

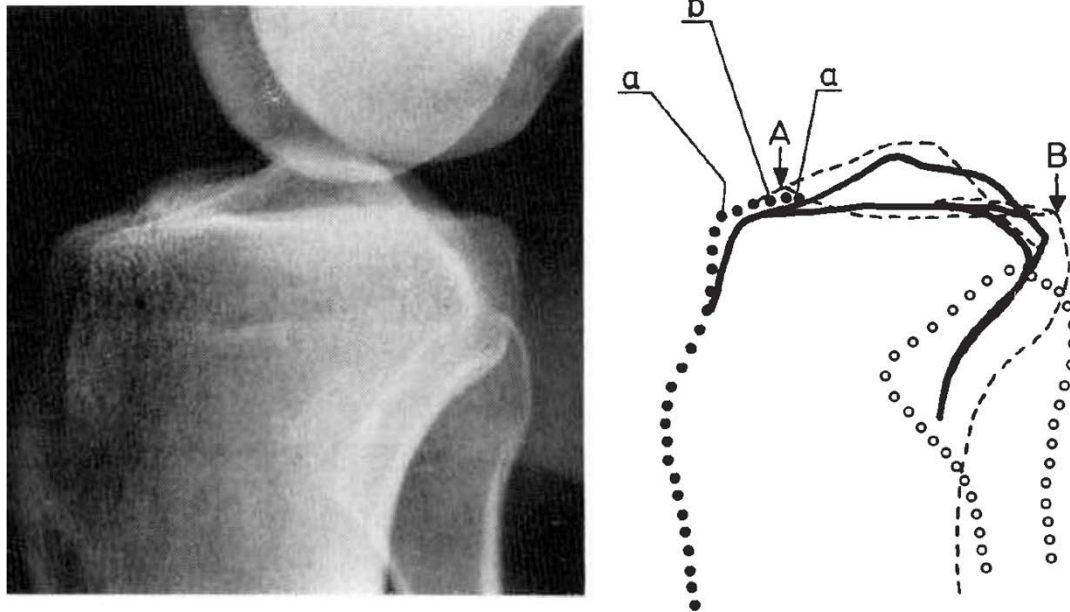


Figure 4. Profile of the proximal tibia. Modified from Jacobsen (1976)²². Unbroken lines (on the right): Lateral tibial condyle and lateral intercondylar tubercle. Broken lines: Medial tibial condyle and medial tubercle. Dotted lines: Anterior tibial margin, tibial tuberosity, crest of anterior intercondylar area, a, and digital impression, b. Parsons' knob, A. Posterior aspect of medial condyle, B. Small circles: Head of fibula.

I.2. Osteophytes

Osteophytes are usually considered to be the most characteristic abnormality of degenerative joint disease^{293, 294}. According to Resnick²³, “most typically, osteophytes arise as a revitalization or reparative response by remaining cartilage, although they may also develop from periosteal or synovial tissue. The features of conversion of cartilage to bone in osteoarthritis resemble those accompanying normal endochondral ossification (at an epiphyseal plate in a growing skeleton) with vascular invasion and erosion of the subchondral bone plate and calcified cartilage, and with deposition or accumulation of osseous tissue on the eroded surface”. This process of bony production has been reproduced experimentally by Thompson & Basset²⁴ by relieving a segment of a joint from all compressive stress.

Osteoarthritic osteophyte formation has been shown by Gilbertson²⁵ to accompany cartilage loss in dogs, and to start soon after disease introduction. In a murine model of osteoarthritis, a good correlation was reported between osteophyte size and cartilage damage²⁶.

Heine²⁷ considered osteophytes not a specific feature of osteoarthritis, since they are seen occasionally at the head of the humerus or at the condyles of the femur in the absence of other manifestations of osteoarthritis. Danielsson & Hernborg²⁸ found that only about one-third of the individuals with radiographically obvious osteophytes in the knee joint later in life developed structural changes. Hernborg & Nilsson²⁹ considered that osteophytes in the knee joint were probably related to age, and were not necessarily an early sign of osteoarthritis. However, they were found to be associated with a more frequent subsequent development of osteoarthritis (defined as structural changes in the form of subchondral sclerosis and cysts), and to grow at a faster rate in such cases.

Thomas et al.³⁰ found that osteophytosis was the most prevalent radiographic abnormality occurring in OA of the knee. The osteophyte formation appeared as “marginal bony outgrowths” or “intra-articular surface irregularities”.

I.2.1. Capsular osteophytes

Soft tissue traction may lead to tensile stresses through the capsule (anterior and posterior margins), ligaments and menisci, leading in turn to enthesophyte formation at the site of bony attachment. These are called “capsular osteophytes” by Resnick²³.

This was the preferred explanation for bone spurs in Parsons¹² and Politzer & Prick³¹ and the experimental work of Noyes et al.³² demonstrated that such a bony response would be seen with repeated, slow strain-rate tensile loading.

I.2.2. Marginal osteophytes

The so-called “marginal osteophytes” by Resnick²³ are thought to represent compression osteophytes, appearing usually at the site where articular cartilage is continuous with synovial membrane and periosteum, and where the developing outgrowth extends into the “free” articular space along the path of least resistance.

The most favored conception historically is that they represent outgrowths from the subchondral bone, and so is found early in Pommer³³, Heine²⁷, Lang³⁴.

Ahlbäck³⁵ found a close correlation between the location of osteophytes and the location of capsular recesses, studied with arthrography. Thus, “osteophytes were located where the synovial membrane of the recess had direct contact with the periosteum. They displaced the recesses away from the bone”. The tibial osteophytes were found to be “often largest in obliquely forward and backward directions.” In medial arthrosis osteophytes were found to be oriented horizontally on the medial condyle but longitudinally on the lateral condyle, and similar patterns were observed in lateral arthrosis.

Ahlbäck thought that the shapes of osteophytes demonstrated that at the compression side of an arthritic knee joint they grew horizontally, and at the traction side longitudinally, and that this could be explained as a result of the capsule bulging out into a fold at a narrowed articulation: it would present no obstacle to osteophyte growth on the affected articular surface, but tautness of the capsule on the traction site would correlate to the longitudinal growth of osteophytes. Also, osteophytes were found to be generalized, found on the three articulations in knees with a single articulation was affected. He gave the description “generalized osteophytosis”. He found, however, that in some knees there were local accentuations of the generalized osteophytosis; in some cases with osteoarthritis osteophytes were absent or minimal; and in some cases the most voluminous osteophytes were found at certain sites, regardless of the localization of the cartilage destruction.

Jaffe³⁶ called them “marginal exostoses” that overhang the periphery of the articulating surfaces more or less like lips, or ledges. They are continuous with

the adjacent bone area, and are generally “composed of spongy trabeculae and fatty intertrabecular marrow”. Usually, marginal osteophytes are delimited by a layer of bone continuous with the bony end plate, and this is often covered partly by fibrocartilage or periosteum, or both. When this fibrocartilaginous covering has been partially or wholly worn away, the bony surface is exposed and becomes more and more eburnated.

Marginal osteophytes would represent according to Jaffe outgrowths from the subchondral bone, i.e. they start in an area at the periphery of the articular cartilage that “has become vascularized from the direction of the subchondral marrow. The cartilage around the vascularized region becomes calcified. In this way the formation of new endochondral bone at the margin of the cartilage is stimulated. The direction of growth of the osseous tissue is determined by molding pressure upon the articular surface. In the course of the growth of this new bone, a marginal exostosis develops, for the bone pushes outward along the line of least resistance. That is, it grows outward from the undermined cartilage toward the margin of the articulating surface. Finally, the spongy exostosis becomes entirely continuous with the adjacent subchondral spongy trabeculae.”

On the other hand, Keefer et al.³⁷ maintained that sometimes such osteophytes seem to be the result of a mechanical mushrooming outward of tissue in this region, due to forcible flattening of the articular surface. Jaffe³⁶ believed that if this were the case, “one would expect to find fiber marrow, splintered trabeculae, and signs of previous hemorrhage”.

Also, Nichols and Richardson³⁸ thought that osteophytes originate as new bone appositions formed from periosteal, perichondrial or capsular tissue at the margin of the articular surface, and Auxhausen³⁹ that they begin with synovial hyperplasia at the margins of the articular cartilage, and osteophyte are therefore reactive-regenerative sequelae of cartilage damage.

Eburnation and increased bone density typically occur in regions where the articular cartilage is lost. Chondrogenesis and enchondral ossification in response to abnormal stresses on the articular surface are responsible for osteophyte formation, as found by Moskowitz and Goldberg⁴⁰, van der Kraan and van den Berg⁴¹. Therefore, osteophytes are assumed to develop in areas of the joint that still possess some articular cartilage.

Cartilage loss and subsequent sclerosis and eburnation in certain regions of the tibial plateaus may indicate – at least in part – a shift in the areas of femoral compression on the tibial cartilage, leading to a more frequent osteophyte formation in adjacent or opposite areas (possibly with more preserved cartilage) of the tibial plateaus⁴².

Alexander⁴³ found evidence that osteophytes at a joint margin were unvectorized developments of chondrogenesis occurring in the direction of least resistance. He suggested that peaking of the tibial tubercle as a feature of OA is indistinguishable from an osteophyte arising at any other articular margin – subjected to less resistance than the area of the weight-bearing tibial plateau which articulates directly with the femoral condyles –, and should therefore carry the same significance.

Radiographically, Resnick²³ describes marginal osteophytes as “lips of new bone around the edges of the articulation. They may be smooth, pitted, or undulating in appearance and are of variable size. The excrescences frequently predominate in one side of the joint. Marginal osteophytes develop initially in areas of relatively normal joint space, and are usually unassociated with significant adjacent sclerosis or cyst formation; articular space loss, eburnation, and subchondral cysts are findings that are characteristic of pressure segments of the joint.”

I.2.3. Central osteophytes

“Central” or “intra-articular” osteophytes have a similar pathogenesis to marginal osteophytosis. According to Jaffe³⁶, in central areas in which articular cartilage still exist, hypervascularity of subchondral bone stimulates endochondral ossification, a phenomenon he called “reduplication” of cartilage and bone. The resulting excrescences are button-like or “flat exostoses”, which show newly formed cartilage “deposited on eroded remnants of the original articular cartilage”. They are often demarcated at their base by remnants of the original calcified cartilage.

Microscopic examination showed: “(1) a layer of regenerated articular cartilage, and then, successively, (2) a new zone of calcified cartilage, (3) spongy bone, (4) some original articular cartilage, often showing a considerable degree of regeneration, (5) the original calcified cartilage zone and bony end plate, and finally (6) the subchondral bone. The bone formed between the more superficially

located cartilage and the original calcified cartilage zone may eventually communicate and coalesce with the subchondral bone. Where this happens over an extensive area, the appearance of such an area will ultimately resemble that of the bumpy irregularities.”

Jaffe distinguished this process from the “shifting” of the bone-cartilage border, where this border migrates toward the joint as a bumpy irregularity in the contour of the articular surface, without leaving behind any portion of the original zone of calcified cartilage: “As a result of endochondral ossification within the articular cartilage, the frontier between the cartilage and subchondral bone tends to shift.”

According to Resnick²³, central osteophytes lead to a “bumpy articular contour on radiographic examination. The small excrescences can be misinterpreted as evidence of intra-articular osseous (“loose”) bodies or cartilage calcification (chondrocalcinosis). The presence of continuity between the osteophyte and the underlying bone and of ossification rather than calcification should lead to correct analysis of the radiographs”.

I.2.4. Periosteal and synovial osteophytes

They may develop in certain articulations “through irritative stimulation of periosteum to new bone formation or, on the neck of the femur, from synovial membrane, which in this site is the counterpart of the periosteum” ³⁶ by the periosteum or synovial membrane. This phenomenon is most characteristic in the femoral neck, where it is termed buttressing^{44, 45}.

I.3. Height of the tibial spine

Mouchet & Nouredine⁴⁶, from measurements made on radiographs, found the medial tubercle to be taller than the lateral tubercle in 73% of the cases, the same height in 13% and shorter in 10%: in 4% they found an undivided, rounded intercondylar eminence. A classification of the spine according to the relative height of tubercles was proposed by Bauer⁴⁷, where 62% were type I (MT > LT), 30% type II (MT=LT), 8% were type III (LT > MT). Similar findings were confirmed by Schlüter & Becker⁴⁸, with MT>ML in 75.3%, MT=ML in 15.5%, ML>MT in 9.1% of cases, and three special cases of a plateau-like shape of the spine, with five other cases of a compact block developed between the tubercles; and in Jonasch⁴⁹, with MT>ML in 78.5%, MT=ML in 13.9%, ML>MT in 7.6%.

This classification was later expanded by Giorgi⁵⁰ based on the examination of 2500 radiographs, supporting the existence of these three anatomic variations, adding a fourth type with hypoplasia of the whole spine (already noted by Bauer), and a fifth, rarer case of complete aplasia of the tibial spine, where the patient complained of pain and instability, and physical examination demonstrated an abnormal anteroposterior stability, which was hypothesized to represent changes to both cruciate ligaments. This classification was later included in Smillie's reference book on knee injuries²⁰.

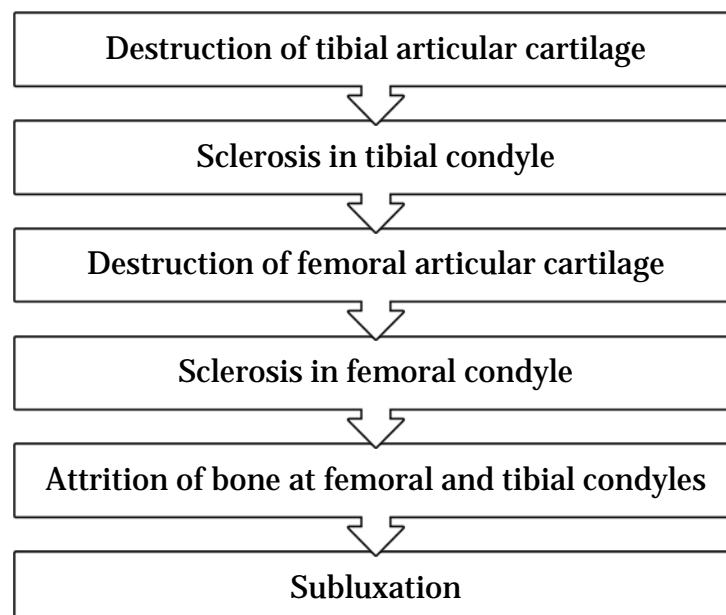
A relationship was suggested in Smillie in the first edition of his book²⁰ between repeated microtrauma and osteochondritis dissecans, due to impingement between the tibial spine and the femoral condyle, in both the juvenile and adult varieties. According to him, debate had long existed as to the importance of tibial spine size in development of osteochondral lesions. Fairbank⁵¹ was the first to record the observation of excessive medial tubercle size in cases of osteochondritis dissecans with lesions located at the classical site, while Freiberg⁵² had already asserted before him that excessive height in the medial eminence of the spine is unnecessary for contact to occur. Smillie, comparing the function of joints to the assembling of parts in the engineering industry, relates the disease to abnormal contact between its component parts. He cites radiological evidence of injury in the tibial spine in cases of osteochondritis – namely sclerosis, flattening, and fracture –, and proposes other etiologic factors, such as instability, genu recurvatum, or decrease of joint space.

I.4. Ahlbäck classification of knee osteoarthritis

The Ahlbäck classification is probably the most commonly used system for classification of knee osteoarthritis. The staging used today was described by Ahlbäck and Rydberg⁵³ in a study for 359 patients with medial OA, with a distribution between the 5 stages varying between 3% and 38%. Also, there were no cases with lateral OA, and the authors pointed out that this scoring system had not been evaluated on cases with lateral OA. Ahlbäck grading of this subgroup has not been studied in the subsequent literature⁵⁴.

Given its emphasis on bone loss, it seems to be more applicable to a patient population with late stages of osteoarthritis, where a classification is relevant for treatment decision. However, according to radiographs presented by Ahlbäck in his thesis³⁵, he was aware of cases with obvious bone attrition despite the presence of a visible joint opening, and this inconsistency has not been addressed in posterior publications. When the joint space has not been obliterated, the tibial or femoral edge facing the joint line is comparatively smooth and it is often unclear whether there is bone destruction or not, potentially confounding grades 1 and 3⁵⁴.

Ahlbäck described the arthrosis at the medial tibiofemoral articulation as developing usually in the following sequence:



Ahlbäck recorded four types of bone changes (sclerosis, cysts, attrition, and osteophytes), and used three alternatives to evaluate narrowing of the articular space, evaluating the smallest width of the knee joint on weight-bearing

radiographs. The joint space was classified as narrowed when it was: (1) “narrower than half the width of the articular space in the other articulation of the same knee or the same articulation of the other knee”, (2) when “it decreased between non-weight-bearing and weight-bearing positions”, or 3) when “it was narrower than 3 mm”, or a combination of them. Other studies have also focused on visualizing the smallest width on weight-bearing radiographs⁵⁵⁻⁵⁹.

II. Aim

The general aim of this work is to describe with detail the normal anatomy of the intercondylar area, comparing it with degenerative changes found in pathological specimens – especially in those with advanced osteoarthritic disease –, including imaging and histological studies. The relationship of these changes with changes in the condyles and the articular joint space is also evaluated in this study.

Study I

To describe the qualitative and quantitative anatomy of the attachments of the cruciate ligaments and menisci with reference to pertinent surgically identifiable osseous landmarks.

It was hypothesized that definable and consistent identification of the soft tissue attachments in relation to these osseous landmarks was possible to help guide future surgical repair and reconstruction protocols.

Study II

To analyze the wear of the tibial plateaus, and to describe the qualitative anatomy of the osseous surface in tibias with degenerative changes, related to normal anatomic landmarks.

It was hypothesized that a simple, consistent classification of osteophytic elevations could be obtained to help refine future classifications of osteoarthritis.

Study III

To identify the three-dimensional osseous surface structures that serve as reference for reconstruction of the ACL, with the help of a traditional arthroscopic video system.

Study IV

To assess the limits of bone avulsed in tibial spine fractures.

Study V

To assess differences in medial and lateral tubercle height in MRI and radiographic studies, in adults without osseous lesions around the knee joint.

Study VI

To assess differences in medial and lateral tubercle height in MRI and radiographic studies, in patients without epiphyseal fusion.

Study VII

To assess the hypothesis of the size of the medial and lateral tubercles influencing the appearance of osteochondritis dissecans in adults.

Study VIII

To assess the hypothesis of the size of the medial and lateral tubercles influencing the appearance of osteochondritis dissecans in children.

Study IX

To assess the hypothesis of the size of the medial and lateral tubercles influencing the appearance of osteonecrosis.

Study X

To assess the hypothesis of the Parsons' knob representing an osteophyte related to osteoarthritic changes of the knee.

Study XI

To assess the hypothesis of the Parsons' knob representing an osteophyte related to osteoarthritic changes of the knee, in relation to proximal tibial valgus osteotomy.

Study XII

To assess the hypothesis of the size of the medial and lateral tubercles influencing the appearance of osteochondral fractures.

Study XIII

To assess the hypothesis of the medial and lateral tubercle osteophytes influencing the degenerative tear of ACL in osteoarthritis.

III. Materials and Methods

Study I. Qualitative and quantitative anatomic investigation of bony and soft tissue landmarks of the proximal tibia, and applications to radiography and arthroscopy

Specimen collection

Fourteen formaldehyde-preserved cadaveric specimens from donors with no history of injury or knee complaints were used in the study. The integrity of all ligamentous and meniscal structures were verified during dissection.

Exclusion criteria included history of injury (2 specimens, fracture around the knee), history of knee complaints (4 specimens, painful osteoarthritis), injury to ligamentous structures (1 specimen, torn anterior cruciate ligament).

Specimens were obtained under a protocol approved by the research ethics committee of the University Hospital Infanta Cristina of Badajoz, and the study was performed according to the ethical standards of the World Medical Association Declaration of Helsinki, Ethical Principles for Medical Research Involving Human Subjects.

Specimen preparation

During extraction, the capsule, anterior cruciate ligament, and posterior cruciate ligament were cut near the femoral attachment to allow macroscopic and microscopic examination of the soft tissue attachments. All other soft tissues were left intact if possible on the specimen.

Electronic medical records of donors were reviewed, looking for exclusion criteria. Specimens were cut with a bone saw below the articular surface, parallel to the joint line and aiming posteriorly below the insertion of the PCL.

After extraction, all specimens were placed in containers filled with a 4% formaldehyde solution, and stored at room temperature until processing. High-

resolution images with defined settings were obtained of each specimen during the preparation process using a digital camera (FE-370, Olympus Corporation, Shinjuku, Tokyo, Japan) mounted on a fixed solid support, perpendicular to the surgical table, viewing from superior to inferior. The specimens were placed over millimeter papers for scale (Fig. 5).

Preparation began with gross macroscopic evaluation, with special attention for soft tissue attachments. A fixed temperature solid-point burner with a number 1 universal tip was used to delineate soft tissue insertions with round marks.

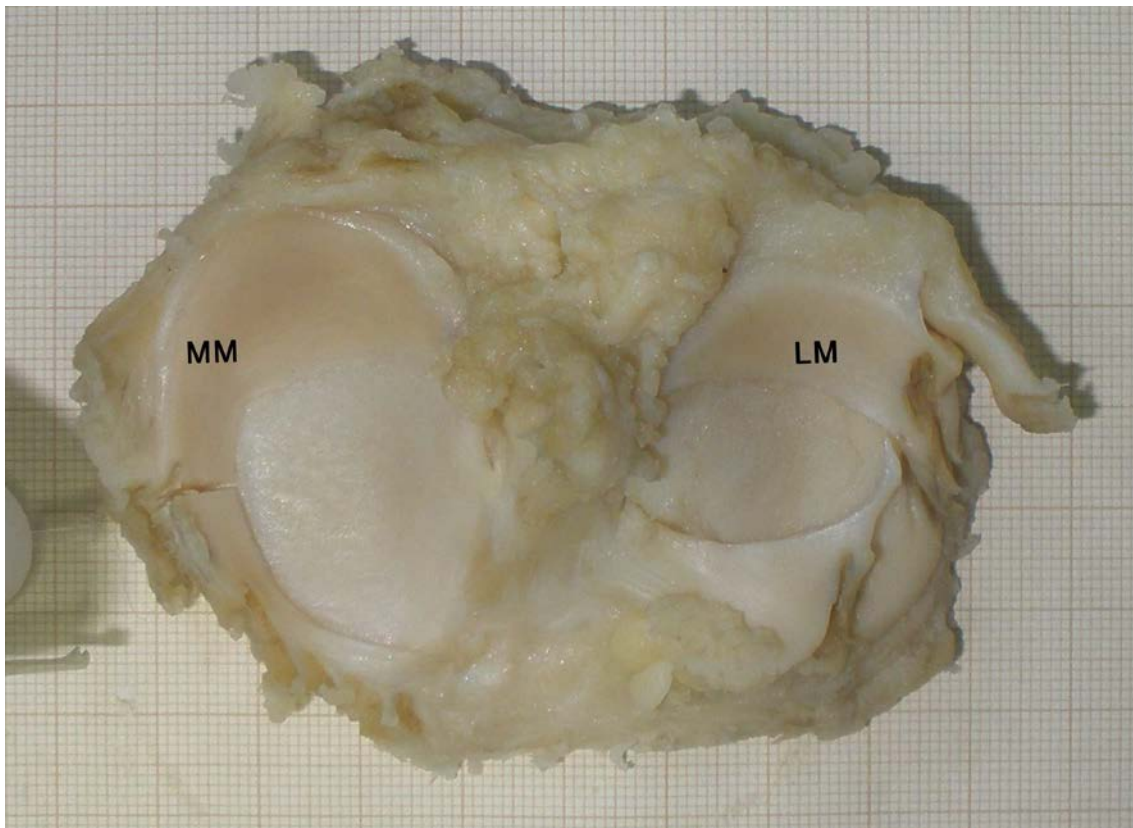


Figure 5. Tibia L. Dissection of specimens was performed over a millimeter paper. The medial meniscus (MM) has been cut with a scalpel in its central portion to allow for anterior and posterior horn manipulation. The lateral meniscus (ML) has been already cut.

Anterior attachments

Anterior attachments were marked and detached first. The central, most prominent portions of the native attachment of the meniscal roots were identified, by varying the tension on each root to define the area of the attachment site with the densest tissue concentration. Any portions of the meniscal roots not deemed a part of the central, densest attachment were considered superficial fibers.

In all specimens the attachment of the central portion of the anterior root of the medial meniscus (ARMM) was first identified (Fig. 6), marked with the solid-point burner, and detached (Fig. 7).

The anterior cruciate ligament (ACL) was then reflected to reveal the native insertion of the anterior root of the lateral meniscus, which runs deeply beneath and overlaps with the ACL when seen in a proximal to distal direction. The lateral meniscal attachments to the posterior aspect of the anterior cruciate ligament were excised from the lateral meniscus (Fig. 8). The anterior horn of the lateral meniscus was then identified (Fig. 9), marked, and detached before ACL preparation, to reveal the anterolateral limit of the ACL.

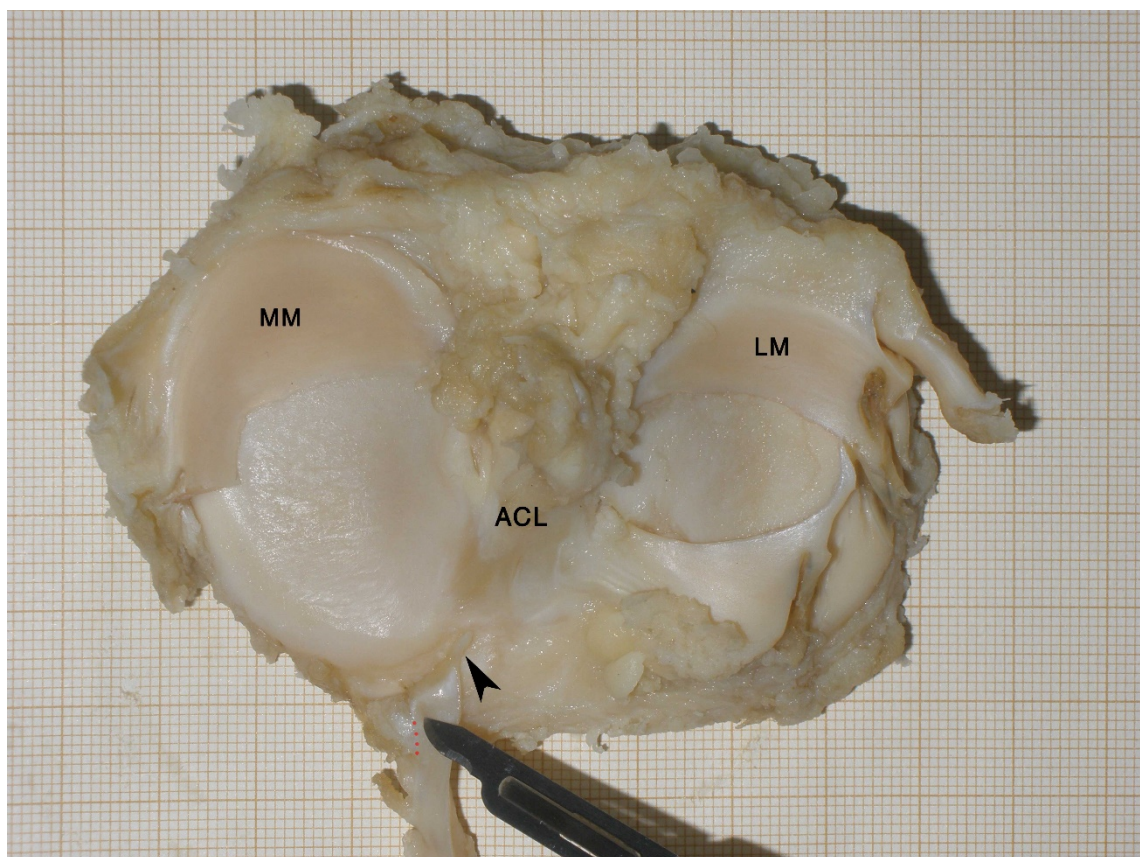


Figure 6. Tibia L. Attachment of the anterior horn of the medial meniscus (MM). The anterior part of the medial meniscus has been reflected and traction is applied with a forceps. The central root attachment is pointed to by the scalpel. A dotted red line indicates the transition to the supplemental fibers, to the left of the image. The attachment of the (cut) anterior intermeniscal ligament to the anterior horn of the medial meniscus is depicted with an arrowhead.



Figure 7. Tibia M. Detachment of anterior horn of medial meniscus. Observe the pyrography marks in the detached area.

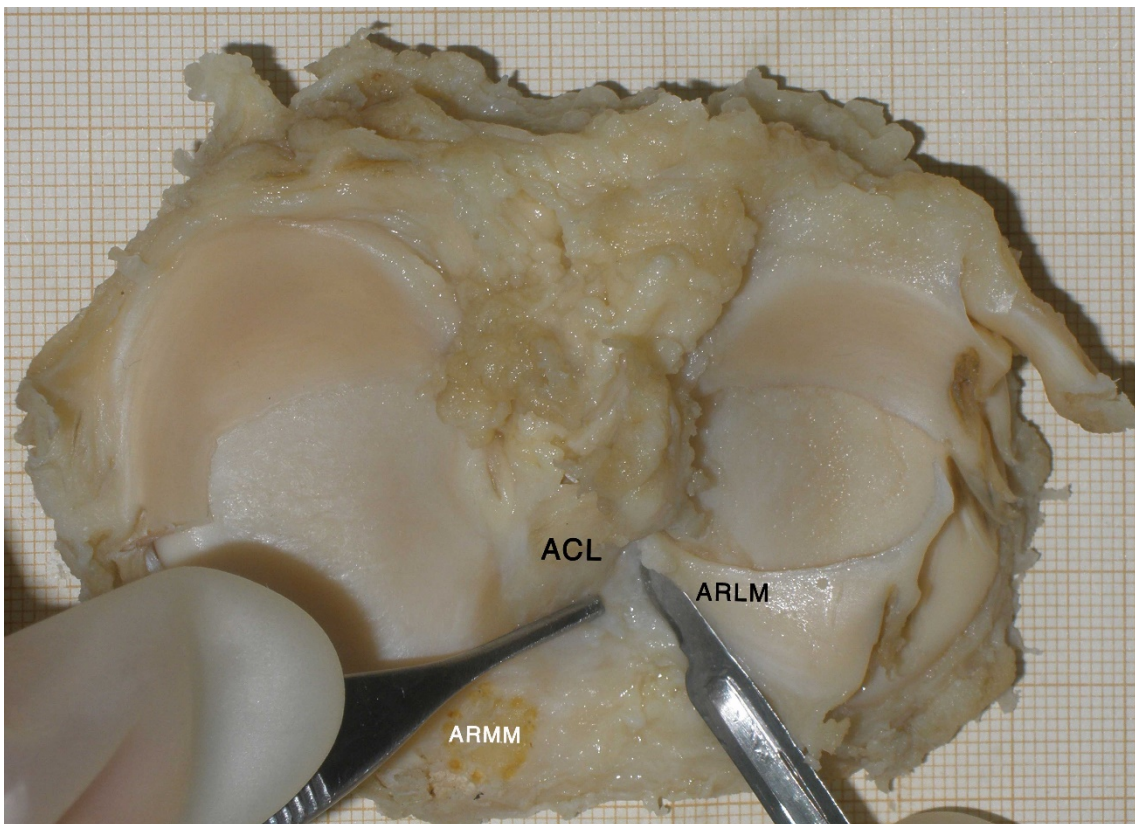


Figure 8. Tibia L. Overlap between the anterior root of the lateral meniscus and the ACL. A plane is developed between them with the help of a blade. ARMM (white): attachment area of anterior root of the medial meniscus. ARLM: anterior root of lateral the meniscus.

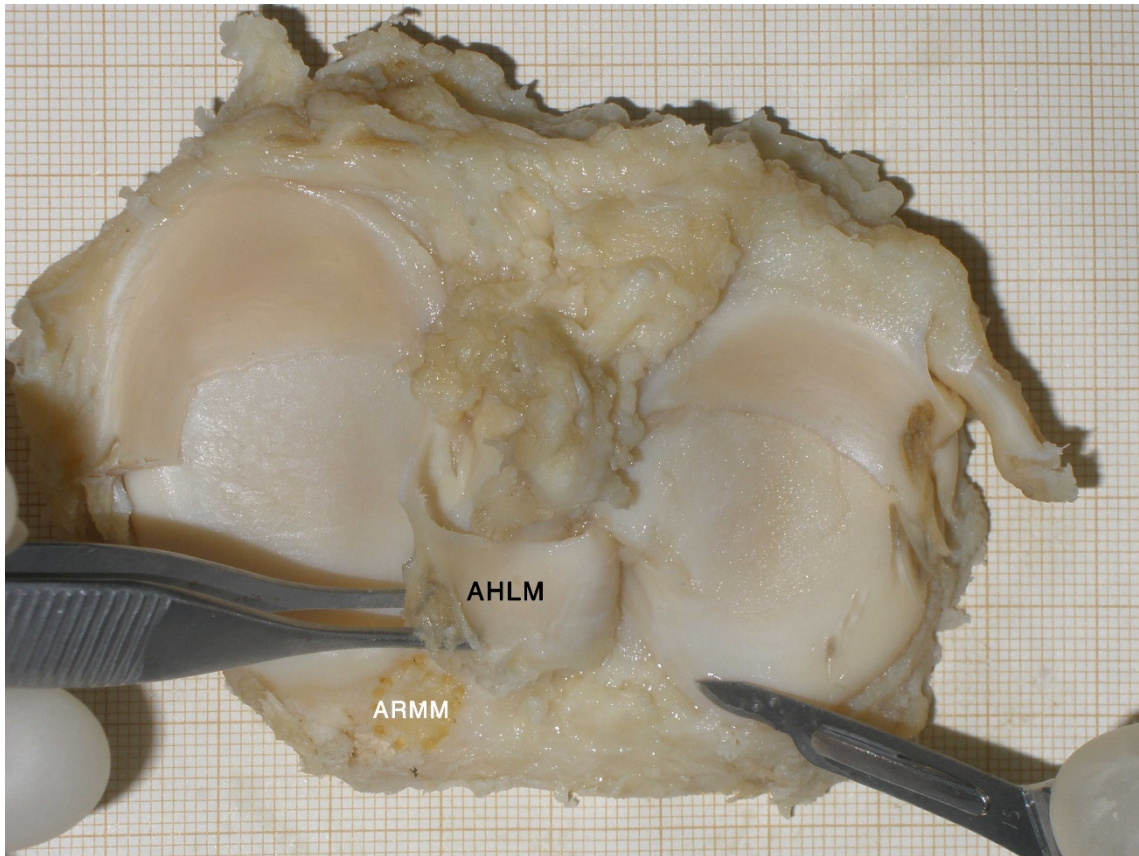


Figure 9. Tibia L. Traction is applied with the forceps to the anterior horn of the lateral meniscus (AHLM).

ACL detachment

In all specimens the ACL was excised at its attachment, marking its periphery with pyrography during the process. In one tibia (tibia L), pyrography marks were also made of each identified fiber bundle. In the other specimens, dissection of individual bundles was documented qualitatively and drawn schematically but not marked, to avoid damaging the topographic relief of the ACL footprint.

As a potential division of fiber bundles, fat-filled proximal inter-spaces were identified and documented during dissection. The ACL stump was held with forceps and tension was applied proximally, perpendicular to the tibial plateau, and applying rotational and translational movements (Fig. 10).

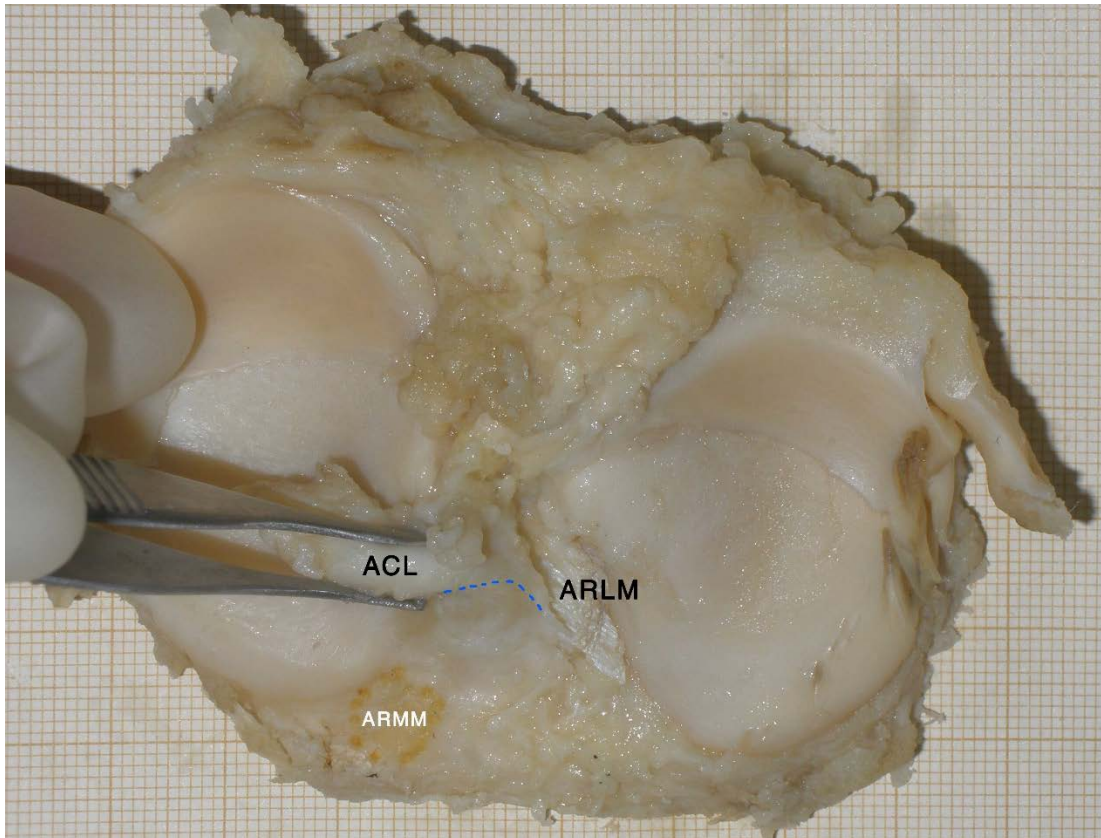


Figure 10. Tibia L. AM and PL bundle fibers adapt to different traction and rotation applied to the ACL, allowing for a gross determination of their division, the main mediolateral inter-space (dotted blue line). ARLM: Anterior root of lateral meniscus. ARMM: attachment area of anterior root of medial meniscus.

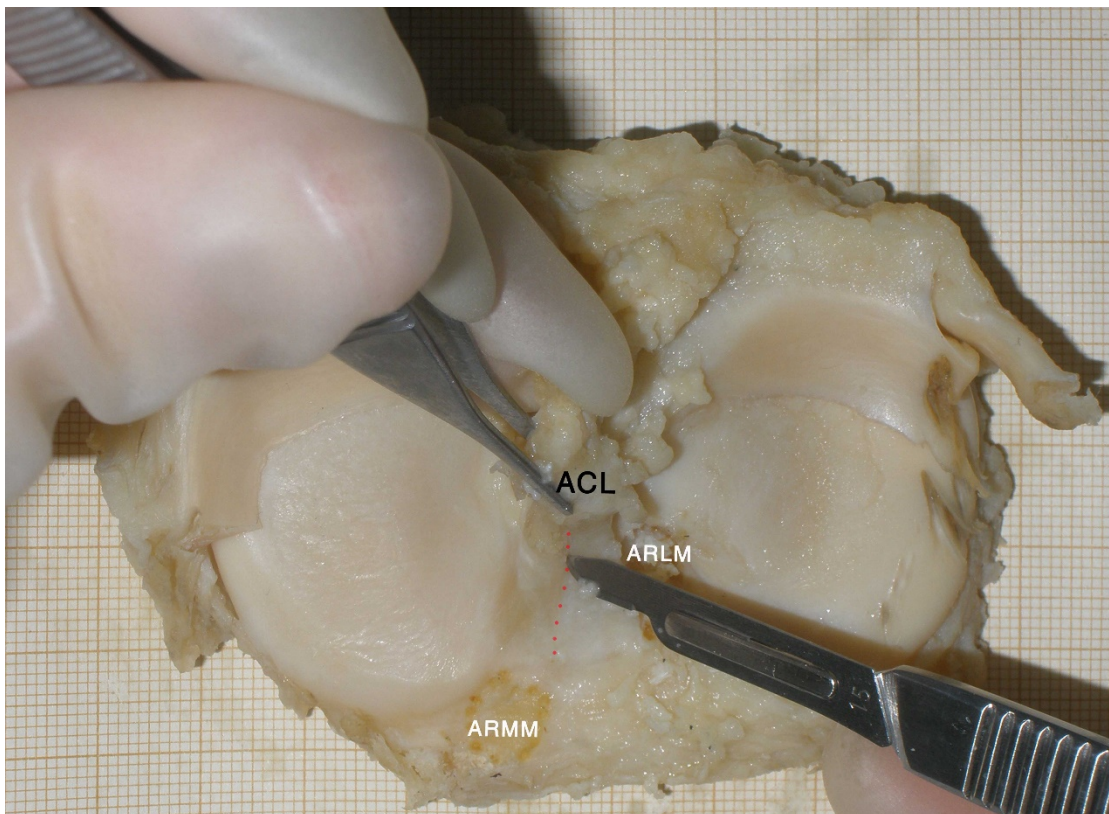


Figure 11. Tibia L. Observe the color change in the division of anterior fibers of the ACL, pointed by the scalpel. The line depicted in red dots was deemed to represent the anterior end of the septum that divides the AM-M and AM-L bundles, and blunt dissection was started proximally. ARLM: attachment area of anterior root of lateral meniscus

Different fat-filled zones (Fig. 12, Fig. 13) were seen and documented.

The ACL was separated first proximally, and the plane of separation developed bluntly distally, through the observed anteroposterior inter-space (Fig. 11), dividing the anterior aspect in a lateral and a medial part, which was detached (Fig. 14).

Detachment of the ACL was completed by separating the stump through the identified mediolateral inter-space, detaching the posterolateral bundle, and marking the periphery of the ACL (Fig. 15).

Blunt division of the ACL stumps could not be carried out to their tibial origin, and the blade had to be used in all cases to finish dissection to bone.

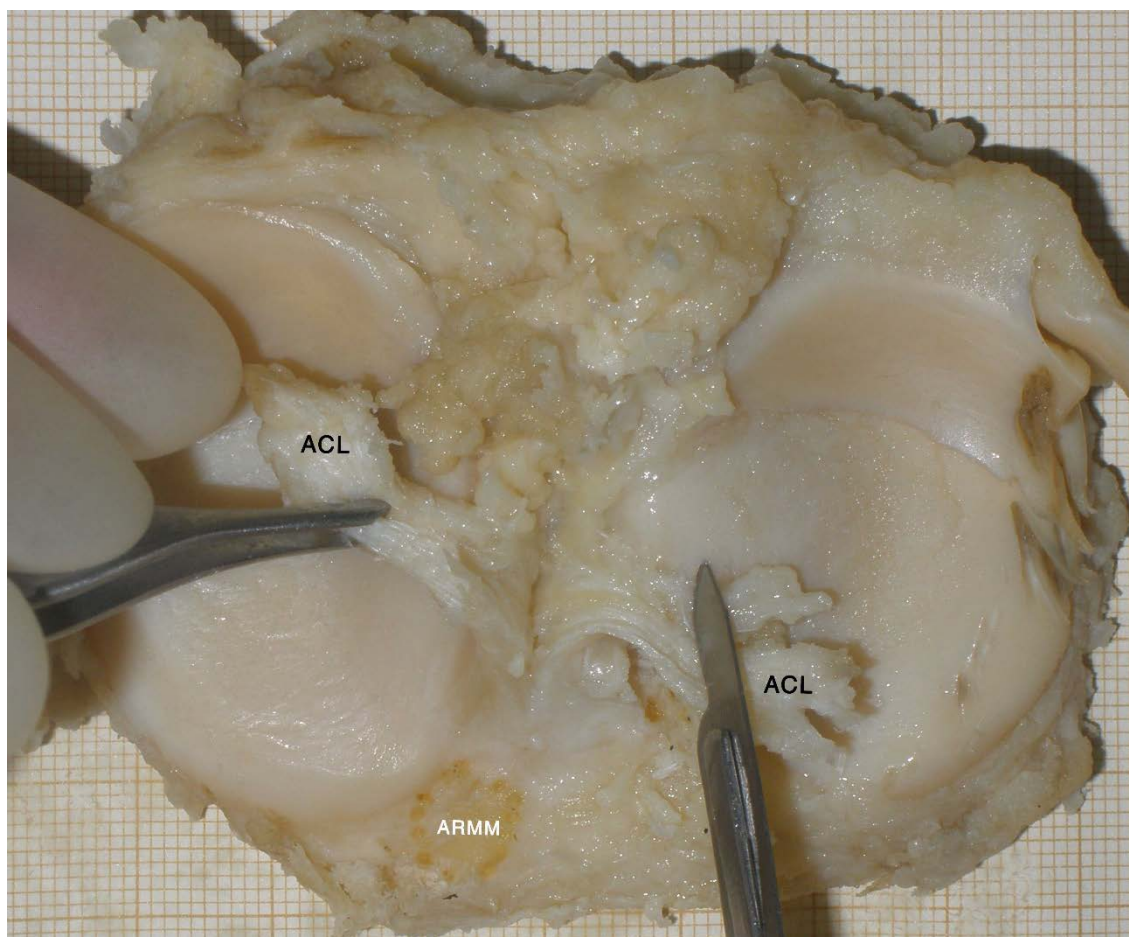


Figure 12. Tibia L. Anteroposterior dissection of the ACL completed sharply with a scalpel in approximately the distal 5mm of the insertion. The proximal cut was made through the observed change in fibers anteriorly. Notice from the position of the anteroposterior fat inter-space and the cut fibers anteriorly, that anterior dissection was completed slightly lateral to their true division. Observe also the triangular shape of the fat in the center of the cut ACL, representing the intersection of both inter-spaces, the mediolateral and the anteroposterior ones. Notice also the other, lesser mediolateral fat inter-spaces. Burn marks from insertion of anterior horn of medial meniscus and anterior horn of lateral meniscus (lateral to ACL), already detached, can also be seen.

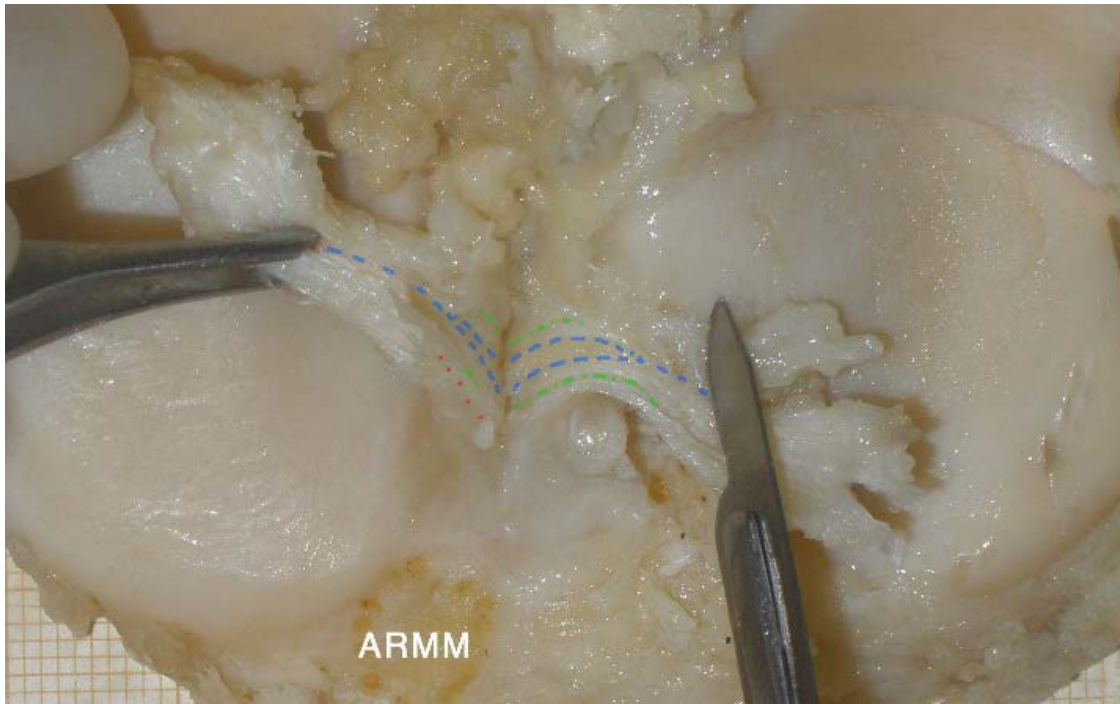


Figure 13. Tibia L. Image corresponding to Figure 12, augmented and modified, with borders of the triangular fat in the center of the ACL attachment (crossing of anteroposterior and mediolateral fat inter-spaces) drawn with blue dashed lines. Green dashed lines are drawn over lesser fat inter-spaces (mediolateral), corresponding to incisures in the footprint (see Figure 15 below). Red dots mark the actual position of the mediolateral inter-space anteriorly, which in this case was not recognized at a glance (the cut was made lateral to it).

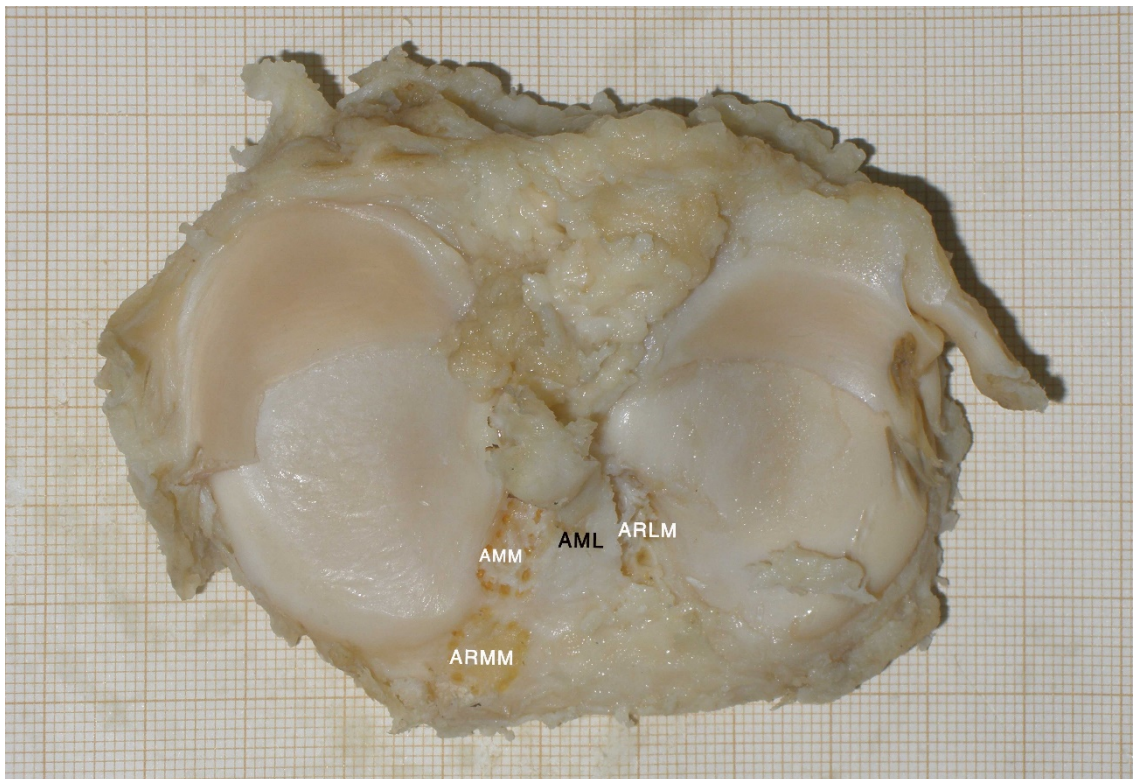


Figure 14. Tibia L. The AM-M and PL bundles have been detached from the rest of the ACL, and their attachment area marked with pyrography. The remaining ACL stump is marked as the AM-L bundle.

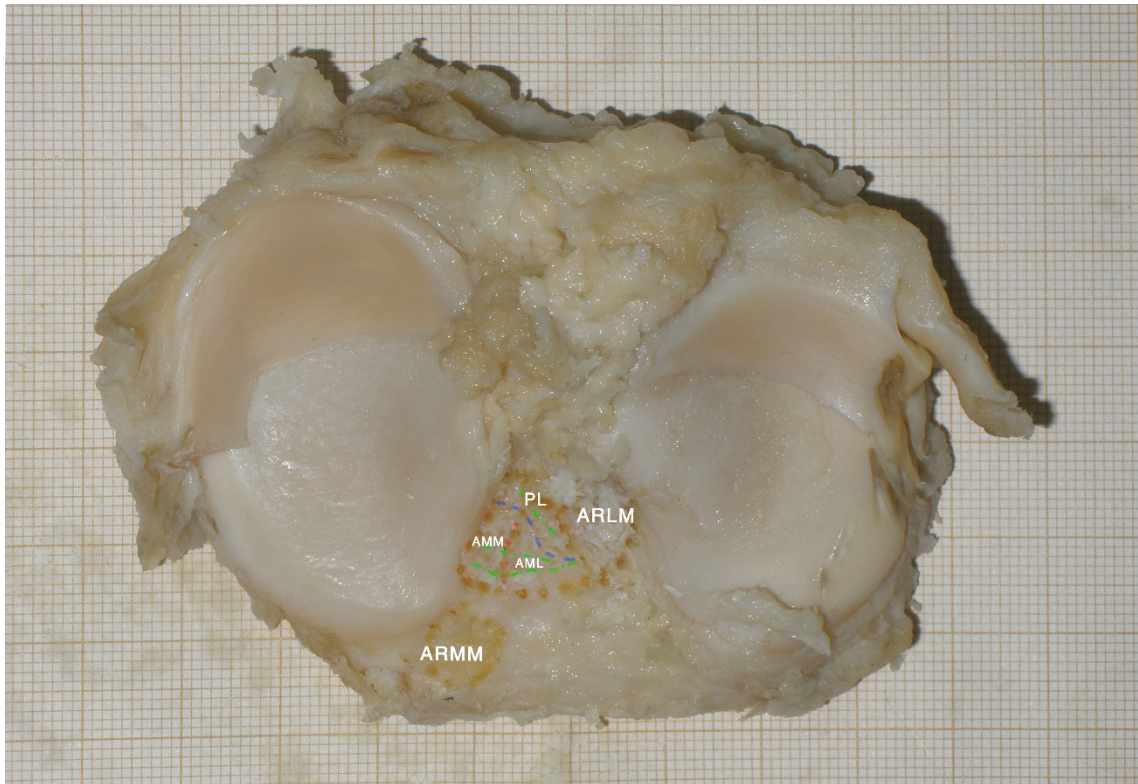


Figure 15. Tibia L. Division of ACL footprint in PL, AM-M and AM-L bundle attachment areas. Notice the pyrography marks at the periphery of the ACL and in the inner divisions (anteroposterior septum digitally retouched with red dots, mediolateral septum retouched with blue dashes). Inner pyrography marks were made more lightly than outer marks: the mediolateral inter-space more lightly marked than the anteroposterior interspace. Nevertheless, damage to the ACL footprint relief can be appreciated at first sight. Two of the documented lesser fat inter-spaces, seen in Figure 12, are drawn as green dash-dot lines.

Posterior attachments

Synovium, fat tissue and attachments of the posterior meniscomfemoral ligaments of Humphrey and Wrisberg, as well as the popliteus muscle, were excised (Fig. 16).

The posterior cruciate ligament (PCL) stump was held with forceps and tension was applied proximally, perpendicular to the tibial plateau, and applying rotational and translational movements (Fig. 17, Fig. 18). The PCL was separated in two bundles first proximally, and the plane of separation developed distally, through the observed anteroposterior and mediolateral inter-spaces.

Bundle limits were documented qualitatively and drawn schematically (Fig. 19). Then the PCL insertion was detached, and its periphery marked with the solid-point burner (Fig. 20).

The posterior root attachment centers were identified, as described above for the anterior attachments, by varying tension and positioning on the posterior horns of the menisci (Fig. 21), and marking the peripheries only of the densest areas of the individual fiber bundles (Fig. 22).

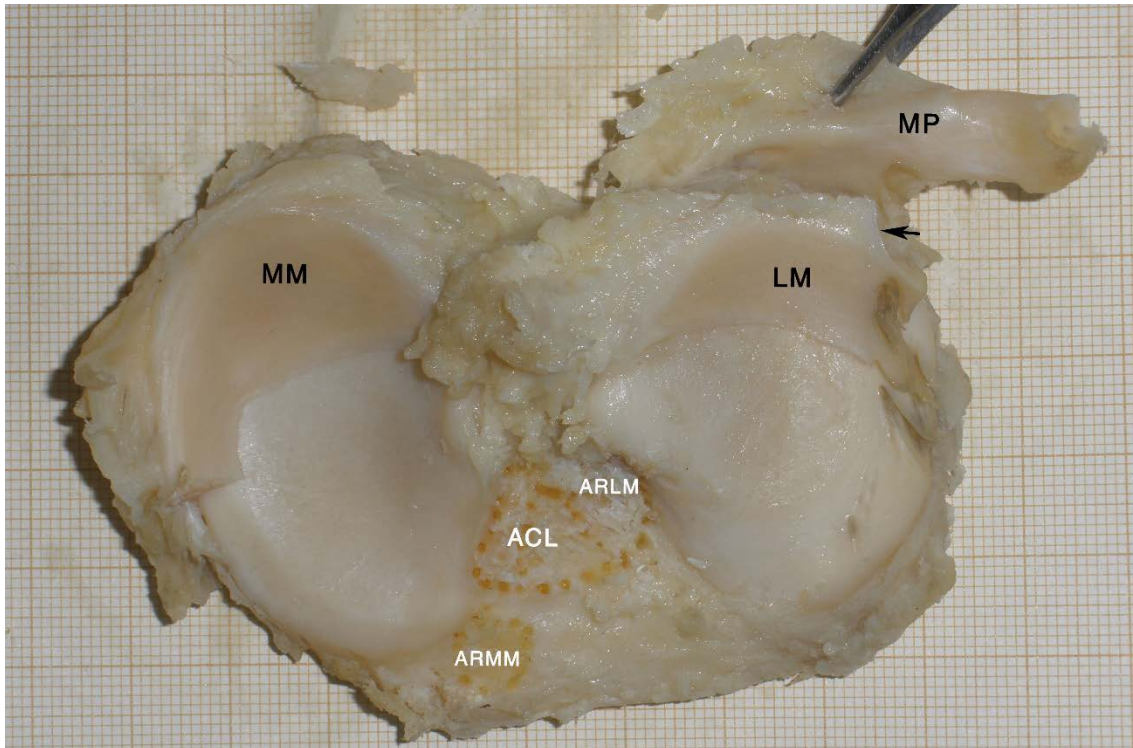


Figure 16. Tibia L. Detachment of popliteus muscle (MP) from the lateral meniscus (LM). Observe the cut accessory popliteus muscle (MP) attachment on lateral meniscus (arrow).

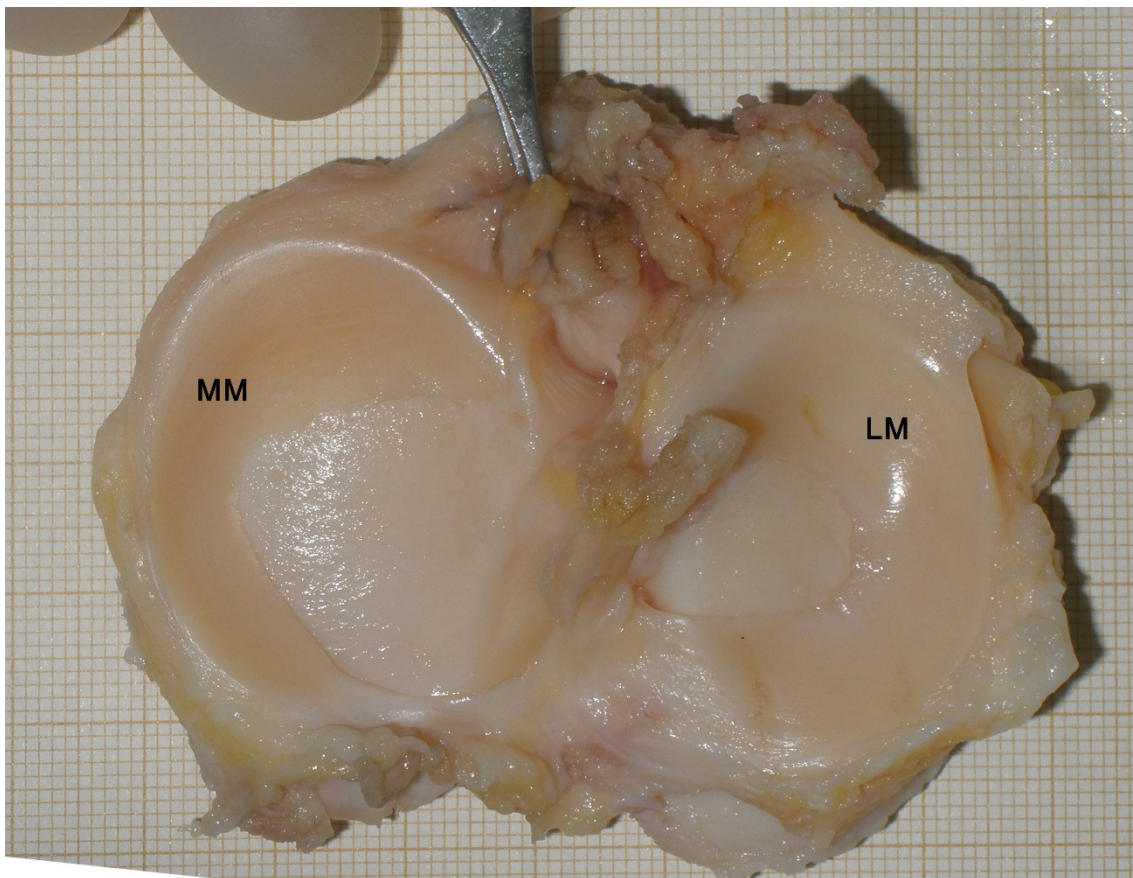


Figure 17. Tibia K. Traction and rotation applied to posterior cruciate ligament stump with the help of a forceps. Observe the twisting of the fibers near the attachment. See Figure 18.



Figure 18. Tibia K. Image corresponding to Figure 17, augmented and modified, with dashed line drawn over the main anteroposterior inter-space found.

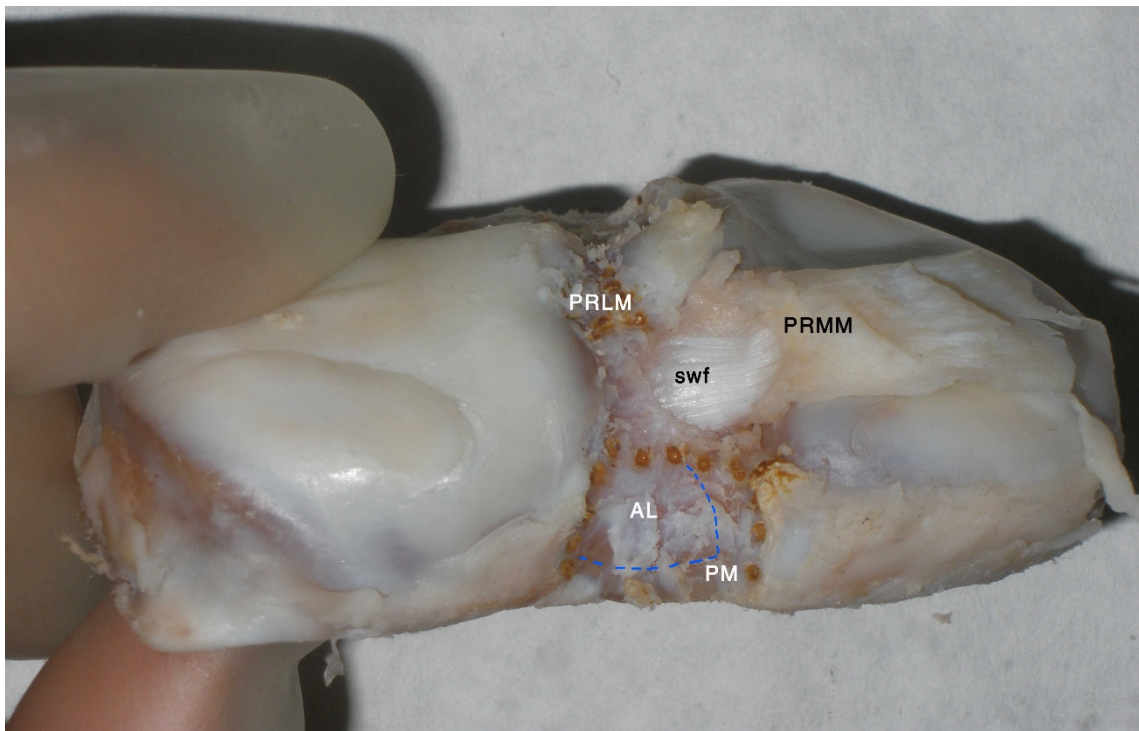


Figure 19. Tibia G. The PCL had been marked with pyrography over the specimen, and the AM and PL bundle separation has been drawn over the photograph with a blue dashed line. Remaining shiny white fibers (swf). PRLM: Posterior root of the lateral meniscus. PRMM: posterior root of the medial meniscus.

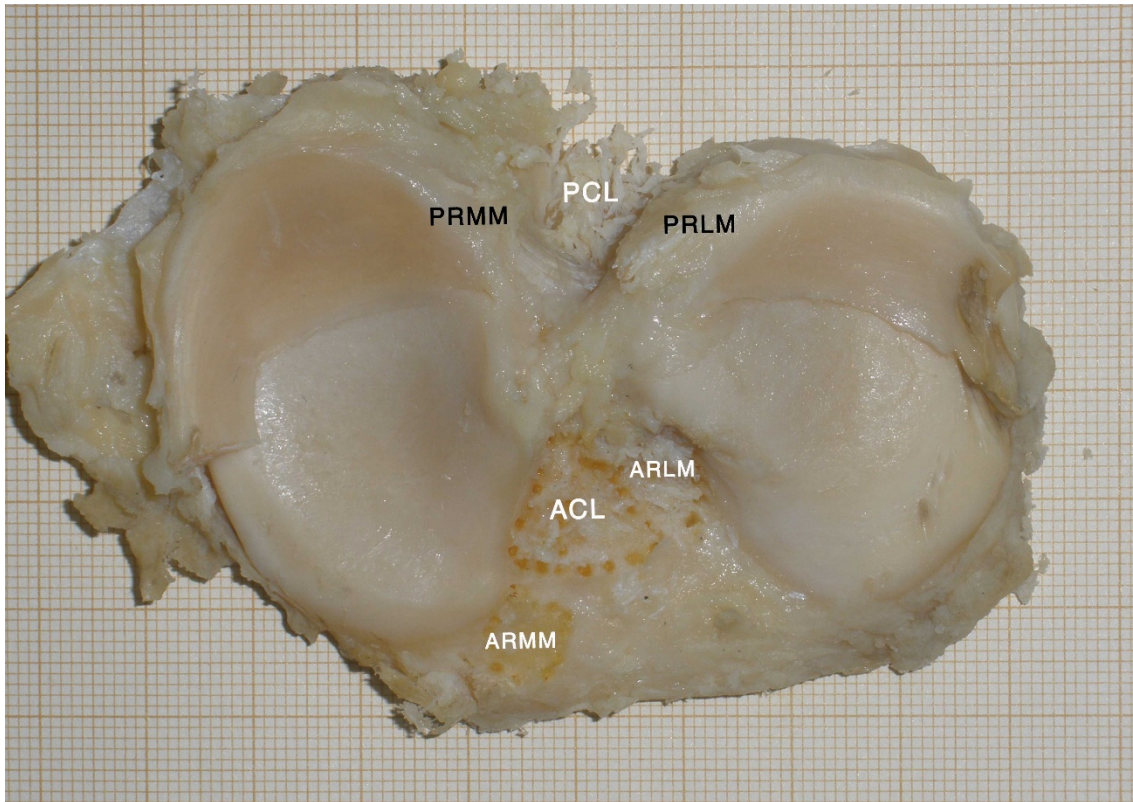


Figure 20. The insertion of the posterior cruciate ligament (PCL) has been detached and its area marked. The posterior roots of the medial (PRMM) and lateral meniscus (PRLM) can be seen.

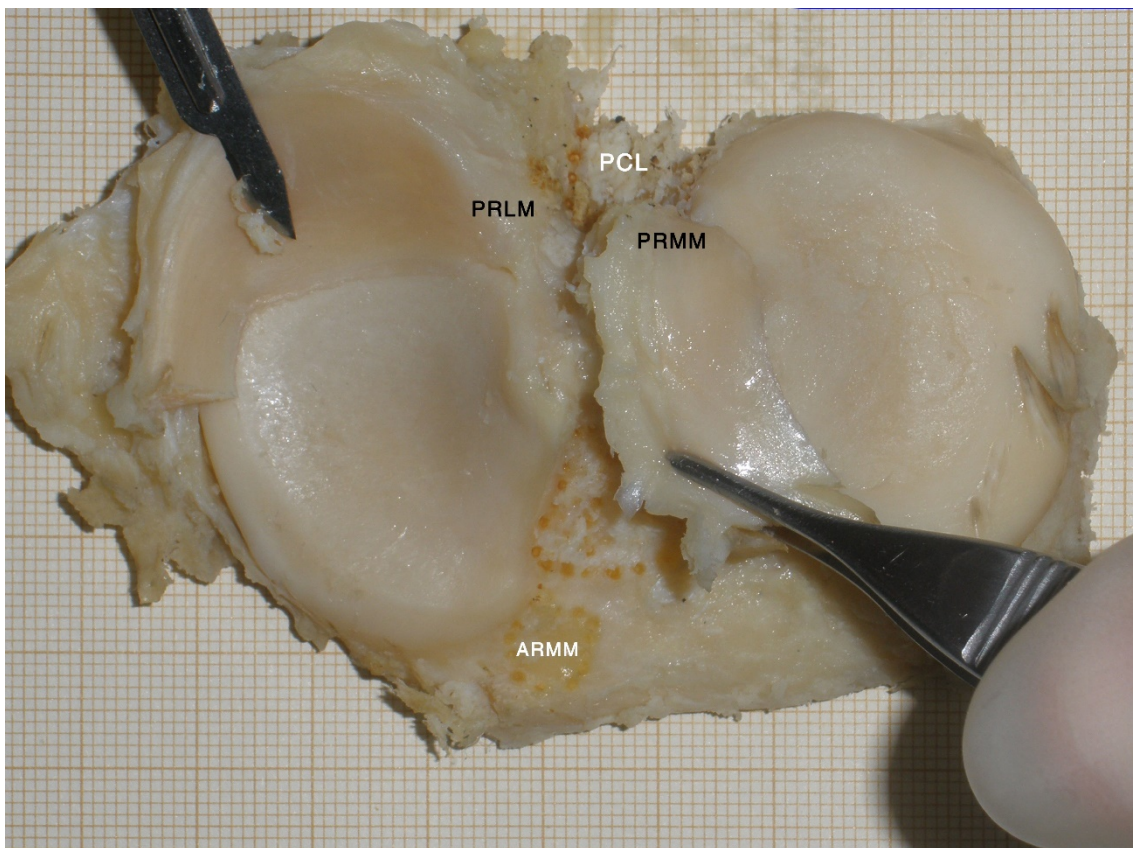


Figure 21. Tibia L. Traction is applied to the posterior horn of the lateral meniscus to identify its central fibers.

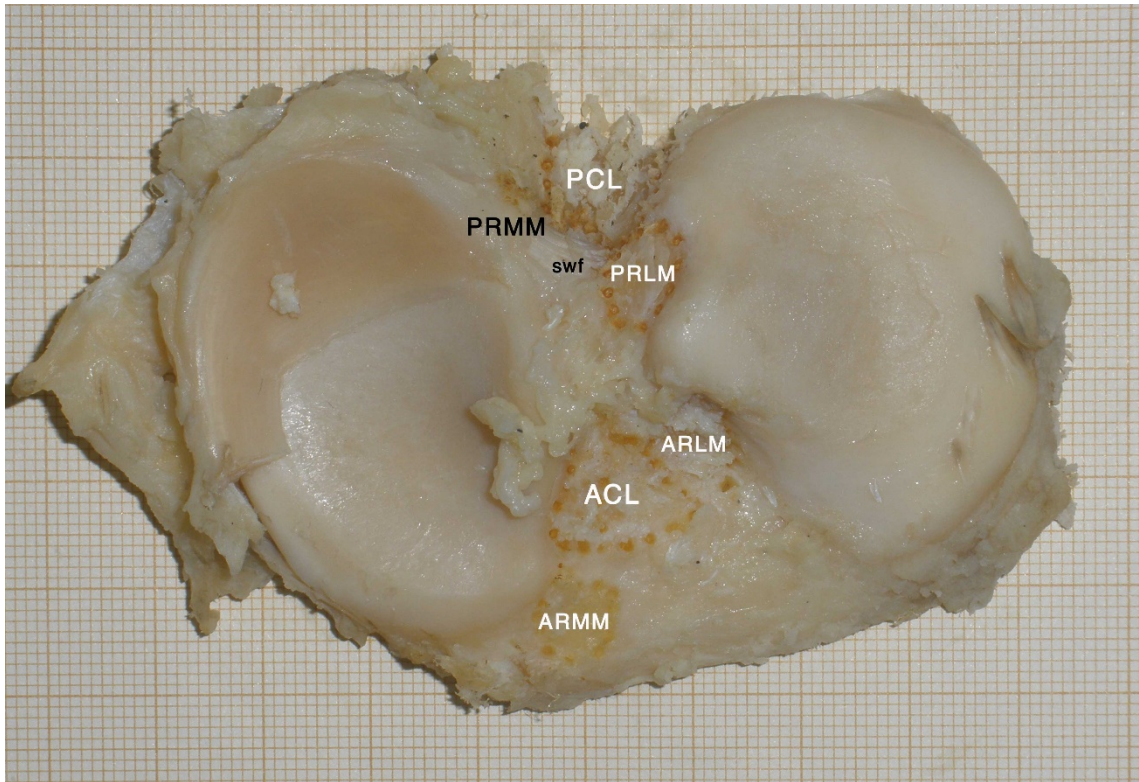


Figure 22. Tibia L. Transverse shiny white fibers (sf) were distinguished from the posterior root of the medial meniscus (PRMM) before detachment and marking. The insertion of the posterior root of the lateral meniscus (PRLM) has been detached and its area marked.

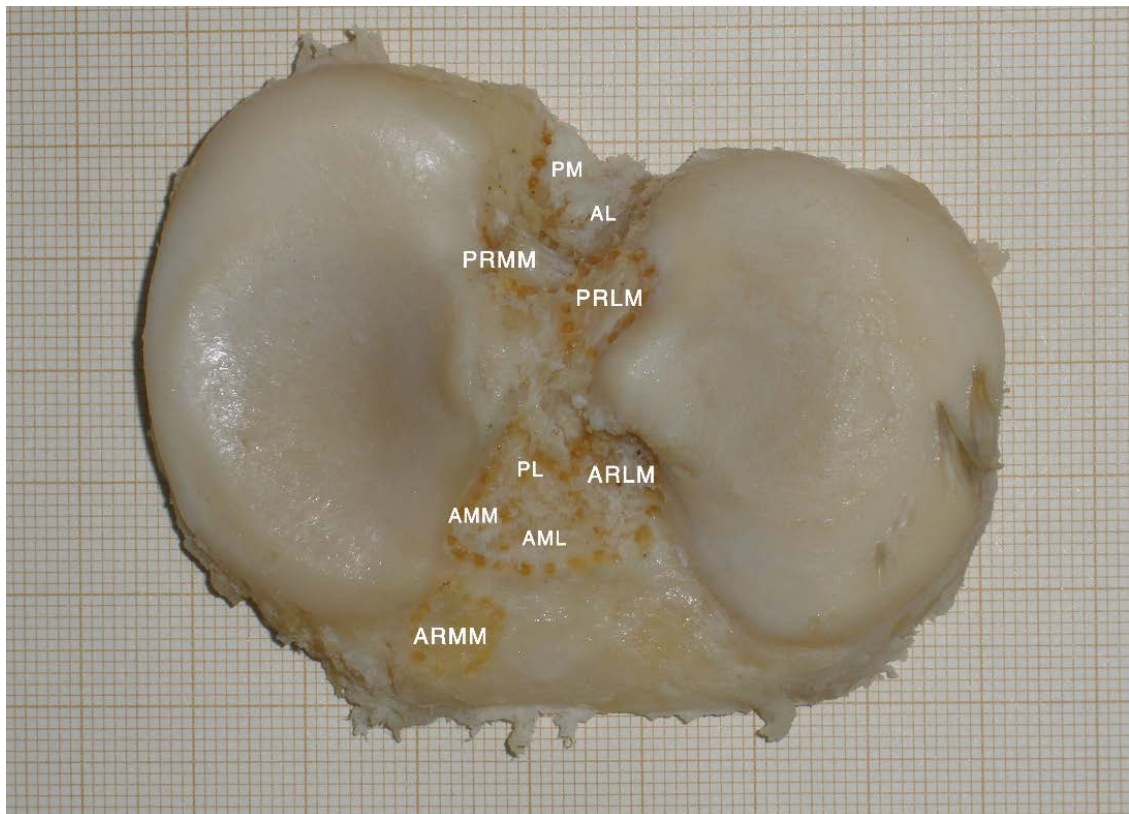


Figure 23. Tibia L. Gross soft tissue remains were cleaned off after marking the attachment area of the posterior root of the medial meniscus (PRMM).

After careful cleaning of the remaining soft tissues (see Fig. 23), all specimens were placed for twenty-four hours in a container filled with enzymatic liquid detergent (Instrunet 4EZ+T ®, Inibsa, Lliçà de Vall, Spain), made of nonionic surfactant (<10%), triethanolamine (>5%), and a protease enzyme (>1%). The remaining soft tissues were stripped off the plateaux with a number 15 scalpel and a 4.5mm wide curved-blade periosteal elevator. They were then dried in an oven at 90° for ten to twelve hours.

Digital processing and 3D surface

Pyrography marks of all soft tissue insertions were retouched with a marker pen. ACL bundle division marks were not retouched. Then high-resolution scaled digital photographs were taken of each specimen with a high image quality camera (EOS 6D, Canon Inc., Ōta, Tokyo, Japan), with a precise configuration: aperture priority f 1/16, ISO speed 100, a 4:3 aspect ratio, a resolution of 4864 x 3648 pixels (image saved in RAW and JPG formats), minimum focus distance (at 45.11 cm), and automatic focus (with 11-point autofocus system, close-up mode and the rest of options left at default configuration). Photographs were shot from a computer using live preview, with automatic focus, and shutter speed was dependent on the precise amount of light at the moment.

Natural light (but no direct sunlight) illuminated the specimens mainly from one side (photograph hours 10:00 AM to 19:00 PM, Central European Time at 38°52'44"N 6°58'1"W, October 2015), and was compensated with artificial light from above (4000-6000 lumens), left (1000 lumens), and around it (4 x 200 lumens) by multiple lamps in the best configuration possible to avoid shadows and reflections or bright spots on or below the specimens.

All specimens were put over the same cubic sanding sponge (Fig. 24), and centered on a round swivel stand (diameter 30.5 cm, Aleratec Inc., Chatsworth, California, U.S.), in front of a black wall as background (Fig. 25). A colored cardboard was attached to the surface of the round swivel stand and divided in 32 marks equidistant to each other, obtaining $\pi/16$ radians (i.e. a difference between photographs of 11.25 degrees). A plastic ruler was attached to the cardboard for scale. The table where the swivel was located had a static mark in front of it; each photograph at the same height was taken with the mark of the swivel located in line with the table mark. After each photograph, the swivel was rotated until the next swivel mark was in line with the table mark.

The camera was placed on a tripod, initially separated 45 cm from the specimen in a straight line, horizontal with the table. Automatic focus was improved by selecting the object area for each shot in the computer's live preview, and image sharpness was judged on the computer's high definition monitor (Dell Ultrasharp U2713H, 2560 x 1440 pixels, Dell Inc., Round Rock, Texas, U.S.). After the first 32 photographs of each specimen were taken, the height was increased 7 cm and the camera was moved closer and leaned towards the specimen as necessary for a correct focus. Then another 32 photographs were taken. That operation was repeated thrice more until reaching 28 cm over the swivel and 160 photographs. 16 photographs more (a total of 176 photographs per specimen) were taken after adding 20 cm to the posterior legs of the tripod, rotating the swivel $\pi/8$ radians after each photograph.

In one specimen (tibia C), to compensate for its extra height, the tripod was elevated 7 cm over the 28 cm mark, to take 32 photographs more, and one final, fully vertical photograph was also taken to guarantee a vertical overview of the tibial plateau (209 photographs in total).

Then all JPG images were cropped using image processing software (Adobe Photoshop C6, Adobe Systems Inc., San Jose, California, U.S.) to avoid objects that could distort the three-dimensional (3D) model creation: static objects (not moving with the swivel), out-of-focus objects, and shadows were cut from the scene, and the images saved as new JPG files.

All cropped images of each specimen were processed by photogrammetry software (Autodesk Memento Beta version 1.13, Autodesk Inc., San Rafael, California, U.S.) to create 3D models, selecting the options of *Best Quality* and *Smart Crop* for all of them.

The sanding sponge was measured in height (mean 26.58 mm \pm 0.07) and length (68.57 \pm 0.12) ten times at a center point, with an electronic digital caliper (resolution 0.01 mm, repeatability 0.01 mm, accuracy 0.00254 mm, by Mannesmann AG, Düsseldorf, Germany), setting both measures to all 3D models to scale them. The measurement of the cube length was applied to the standard border of the superior face of the cube in the 3D model, by selecting the lateral and medial corner points (Fig. 26). Then the cube's height was measured in the 3D model, and if deemed within an error range conventionally selected by the author (length \pm 0.25 mm, height \pm 0.1 mm of the real measurement), the scale

was set for the model (maximum expected error inferior to 10 μm per specimen). Else the length was applied again to a different line connecting a lateral and medial point, parallel to the anterior border of the superior face, until an acceptable measure range in length and height was obtained.

The 3D models were then cropped with the same software, cutting off the cube and other objects, and leaving only a hollow mesh of the tibial plateau. They were exported as Wavefront OBJ files with the options set for *Maximum Face Count* and *Rebake Textures*.

The exported OBJ files were processed in 3D point cloud and mesh processing software (CloudCompare, version 2.6.1 64 bit, GNU GPL software). Points sampling on each 3D model (approximately 1,000,000), generating normals. All sampled models were rasterized, and the grid edited to obtain a size of approximately 1200 x 900 (definite size depending on the model exact sizes). Files were exported from the created raster (standard parameters projection direction z, average cell height, and fill with interpolate 0.0000): cloud (per-cell statistics cloud exported as scalar field) for height analysis, raster (GEOTIFF file) and matrix (TXT file) for GIS software processing, mesh (OBJ, PLY files) and image (JPG) for further observation. Contour plots were generated for all 3D models starting at tibial plateau base height (variable depending on the cropped model), at step 0.30 with minimum vertex 8 and exported as Sinusx SX files (Fig. 27).

Raster files were imported in geographic information system software (QGIS 2.12.0-Lyon, QGIS development Team, GNU GPL software) and terrain analysis performed for slope, aspect, hillshade, relief, and ruggedness index (Fig. 28).

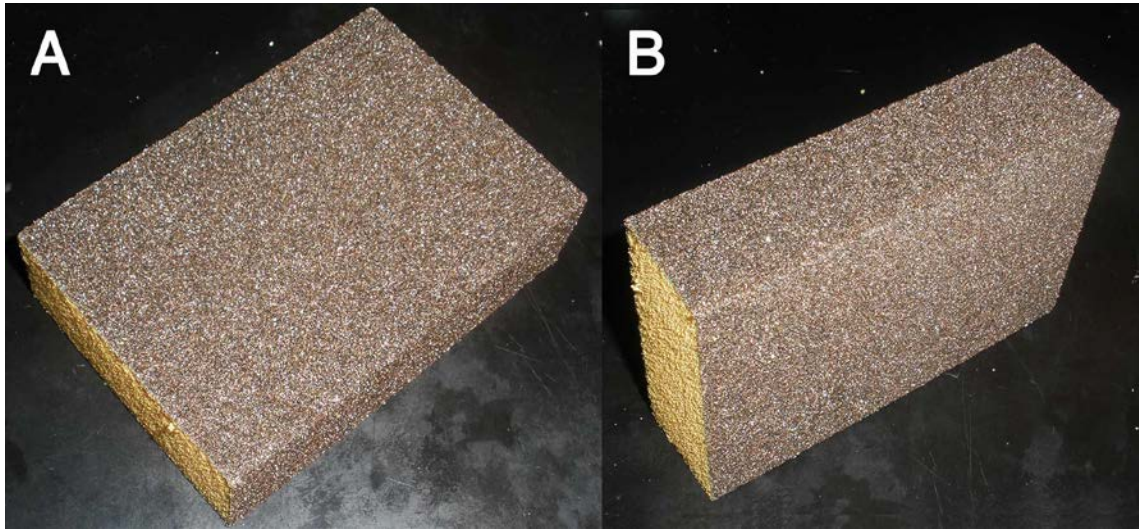


Figure 24. Example of cut sanding sponge used for this study. Cut borders show the inner material (in yellow). A. Superoinferior view. B. Lateral view.

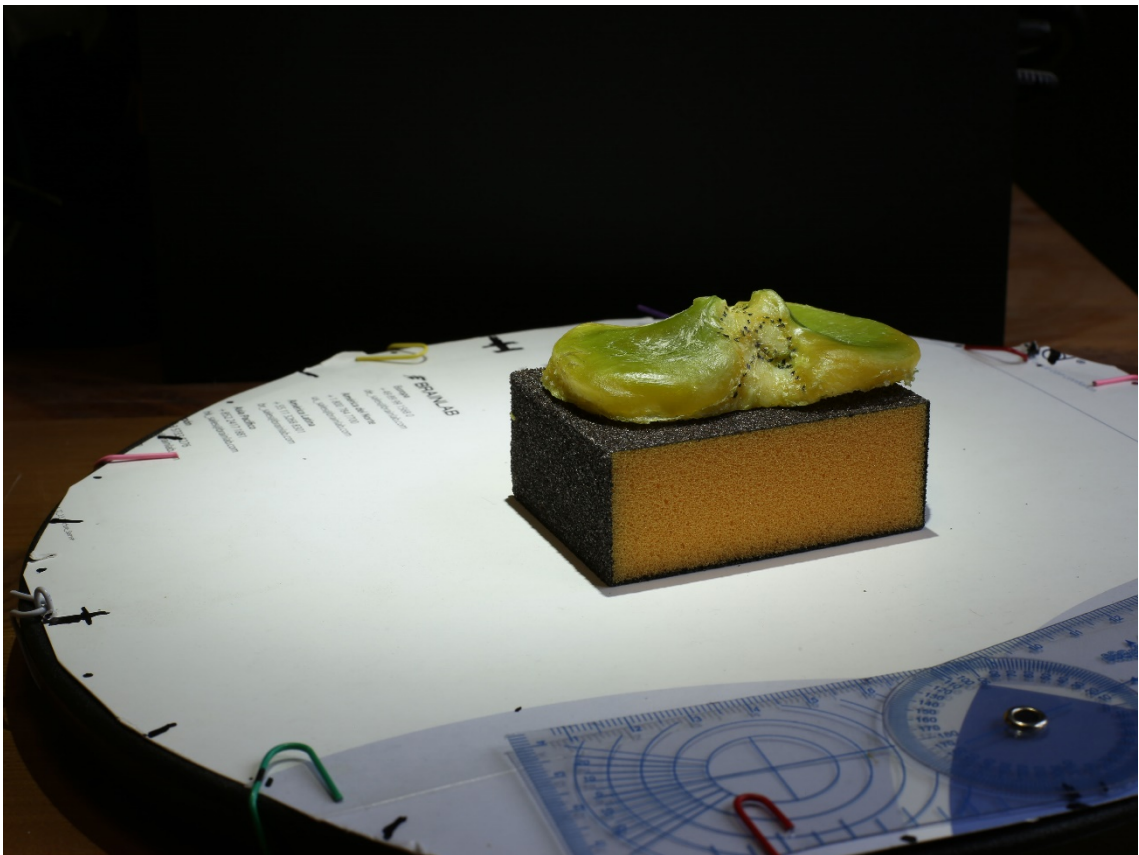


Figure 25. Tibia L over the swivel stand. Photograph taken from posterolateral view at height 14cm over the table. Observe the shadows on the white cardboard and the reflective surface of the specimen.

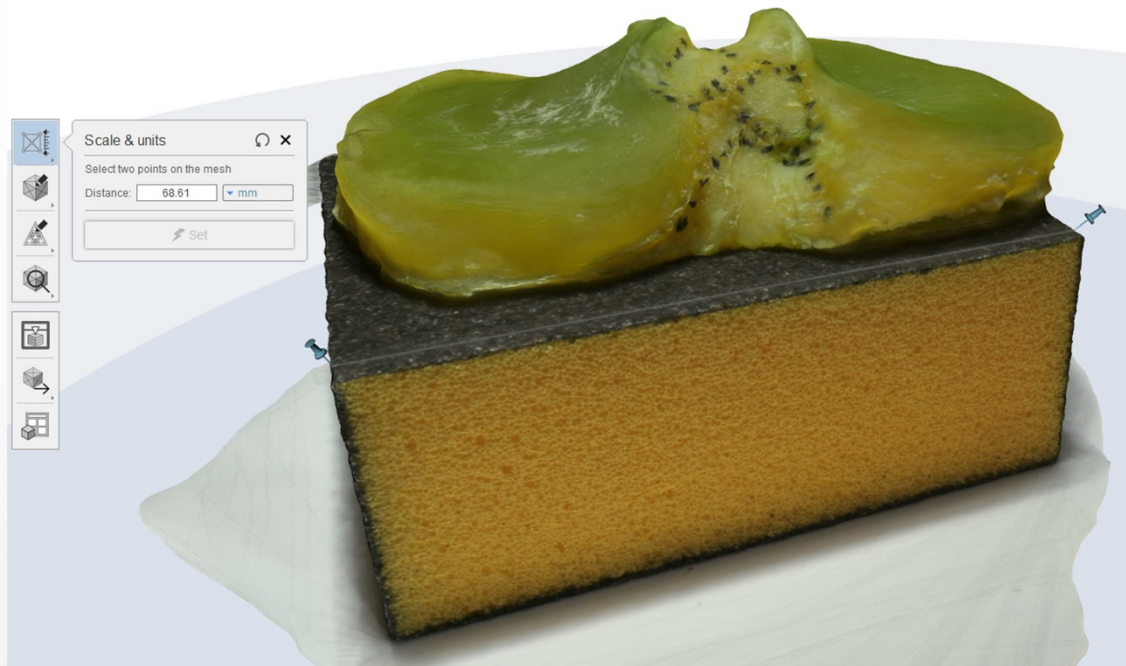


Figure 26. 3D model of tibia L. Setting of scale by applying width measurement to the machine-made cut side of the sanding sponge (notice the digital thumbtacks marking lateral and medial border points).

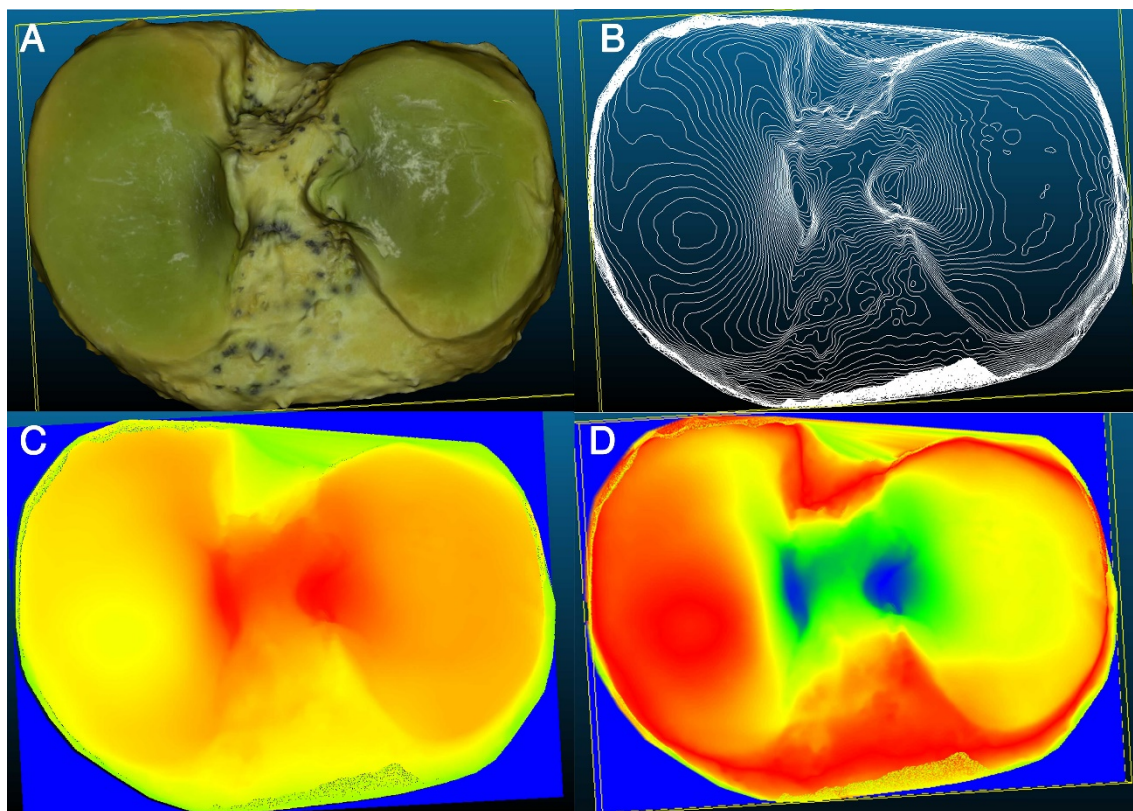


Figure 27. 3D model of tibia L. Secondary files from mesh processing software: A. Original 3D model. B. Contour lines. C. Per-cell statistics cloud D. Mesh with height ramp.

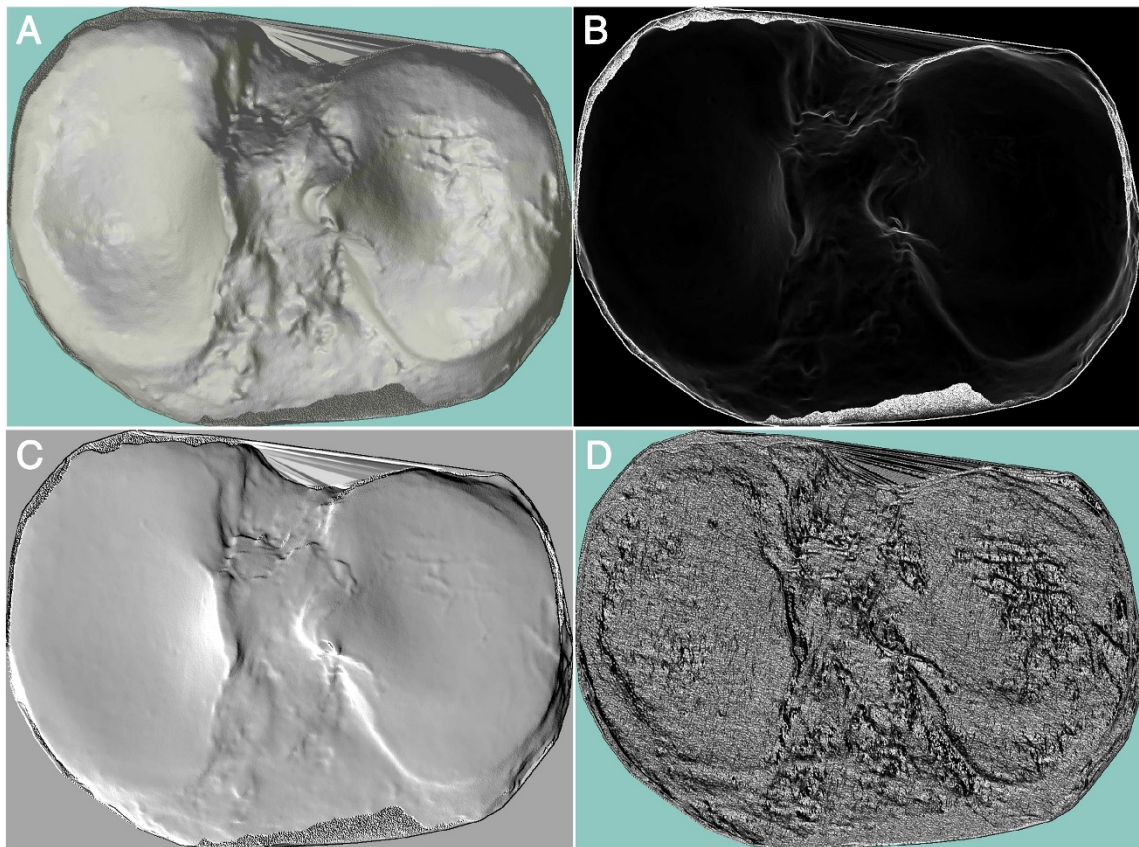


Figure 28. Raster data of 3D model of tibia L. Terrain analysis from raster: A. Relief at 0.5 Z index, light from anteromedial. B. Slope. C. Hillshade. D. Ruggedness Index.

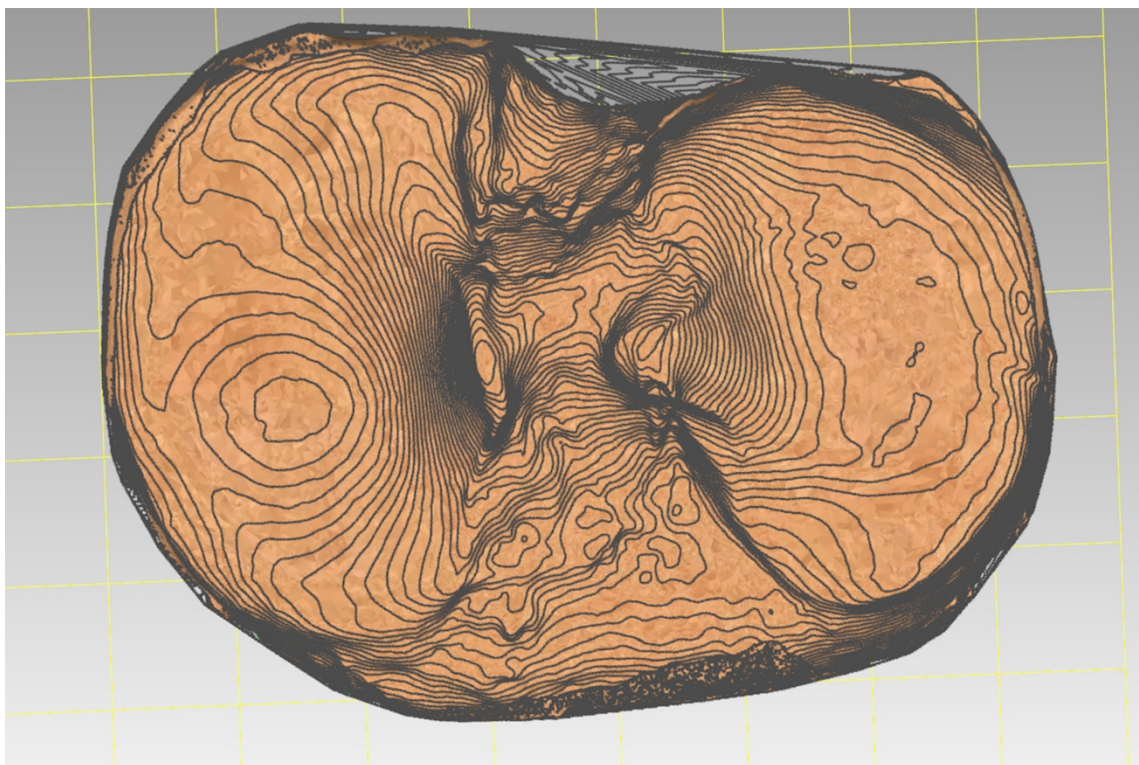


Figure 29. 3D model of Tibia L and contour lines. A standard texture (“Leather”) is used to avoid bias in selecting the purely osseous areas.

Selection of areas and nomenclature

The 3D model (OBJ file) and the contour plot (SX file) of each specimen were imported together for analysis into 3D design software (Geomagic Studio 2014 64 bit, 3D Systems, Rock Hill, South Carolina, U.S.). Meniscal root attachments, ligament attachments, and osseous surfaces were selected in the 3D model and exported as individual files.

Areas were selected departing from Jacobsen's²¹ systematic anatomic description (see above Fig. 3), adapting their original description to findings in other, posterior studies, including this one. Therefore, referenced areas are not necessarily coincident with the areas described in his work. Speculative terms given to osseous structures, referencing them by their soft tissue attachments – as found in Jacobsen and in many other previous studies – were not used in this study: terms such as *ACL tubercle*, *ACL ridge*, etc. were avoided in this work when describing osseous surfaces.

- Areas were given an alphanumeric reference.
- Subareas were given a number and a lowercase letter. Subzones of subareas were given a number – lowercase letter – number sequence.
- Specific structures (elevations or depressions), dividing or crossing those areas, were given a capital letter.
- Substructures were given a capital letter – number name.

For a summary of references, names, abbreviations, etc. see Conventions used in this study above.

When selecting osseous areas, the 3D model was processed with a standard texture (Fig. 29), to avoid the bias of mixing soft tissue attachment areas (pyrography marks, or pen marks surrounding them) with areas described based only on their osseous relief.

Additional files were used for further examination of the anatomic features of specimens, such as the scalar fields for height analysis, and graphical visualization of slope, aspect, hillshade, relief, and ruggedness index.

Anatomic measurements

Landmarks were selected for anatomic horizontal and sagittal plane creation, to define the two- and three-dimensional coordinate system of each specimen's model. The posterior tibial axis was drawn connecting the posterior limits of the

medial and lateral condyles, and the anterior tibial axis connecting the anterior limits (Fig. 30).

A three-dimensional horizontal plane was created by selecting the condyles without the main intercondylar tubercles, and obtaining its best fit plane. A sagittal axis was created perpendicular to the posterior tibial axis through a middle point in the anteromedial intercondylar ridge.

Mediolateral size (or width) was measured with the specimen fixed in the three-dimensional horizontal plane, following the two-dimensional vector of the posterior tibial axis to its widest measure. Anteroposterior size (or depth) was similarly measured following the perpendicular vector of the posterior tibial axis. Inferosuperior size (or height) was measured by obtaining a perpendicular vector from the horizontal plane that crossed the selected point.

Pertinent three-dimensional areas were calculated, and best fit planes and centroids of the areas were obtained.

To approximate area centers from centroids, a line perpendicular to the area's best fit plane was defined through the area centroid. Because the 3D design software works with polygon mesh triangles but not vertices, the surface triangle that the perpendicular line crossed was selected (Fig. 31, Fig. 32). When the perpendicular line crossed near the middle of two triangles, both were selected. Area centers of all soft tissue attachments were selected in this manner.

Other triangles were also collected from all 3D models as osseous reference points (Fig. 33), as described below in each section. For knobs and tubercles, the highest point was selected; for ridges, the highest point in its approximate middle aspect was selected; for walls of certain enclosed areas, a point perpendicular in a mediolateral direction was selected.

Distances between each pair of selected triangles were measured by selecting the central points of each triangle. The triangle centers were selected by hand each time, due to limitations of the design software in measurement analysis.

Measures were taken with the option *On Surface Projection* (Fig. 34), i.e. by fitting the shortest path over the surface of the 3D model (and not in a straight line from point to point), to imitate probe measurements that can be obtained during arthroscopy. Only in those measurements in which the lateral fossa or the tubercles had to be circumvented by the software (with curves to get the minimal distance) was a straight point-to-point line measurement taken. All reported measurements were performed by the author, to avoid interobserver variability.

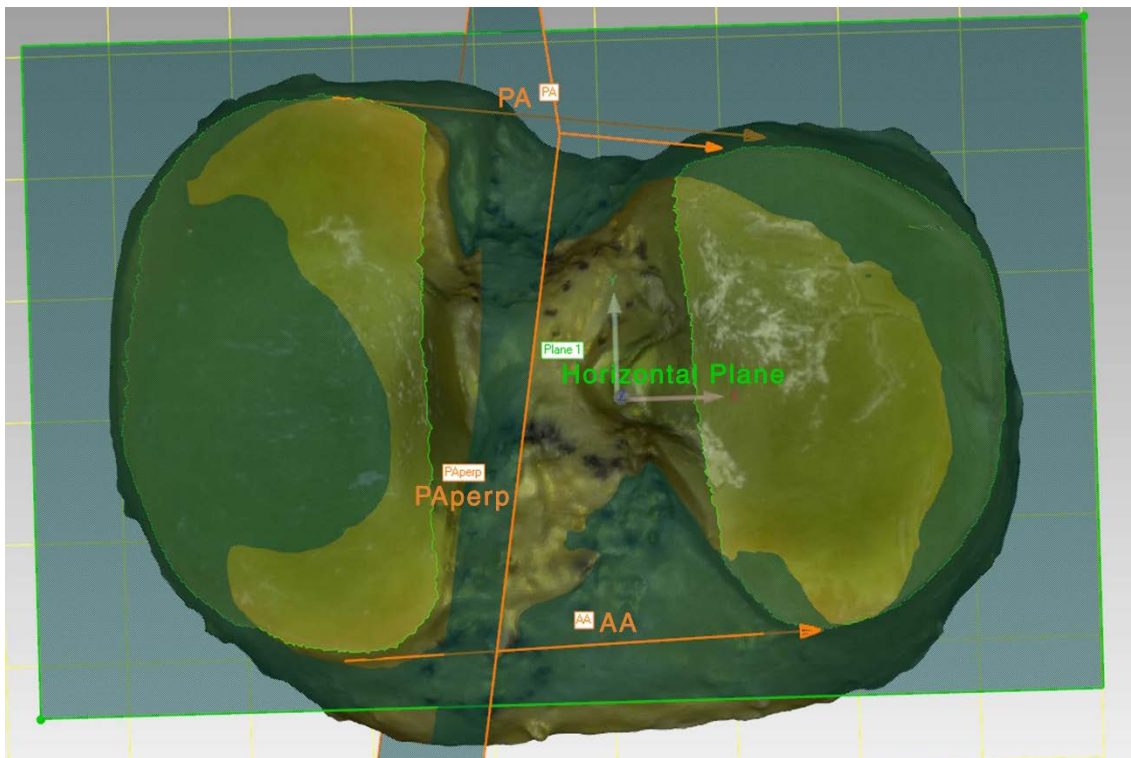


Figure 30. 3D model of tibia L. Observe that a sagittal plane parallel to the posterior axis (PA) has been used instead of a line, to facilitate measurement. However, the horizontal plane (with green borders) is positioned horizontally during measurements. PAperp: plane perpendicular to PA, used to obtain the (deepest) anteroposterior measure. AA: anterior axis.

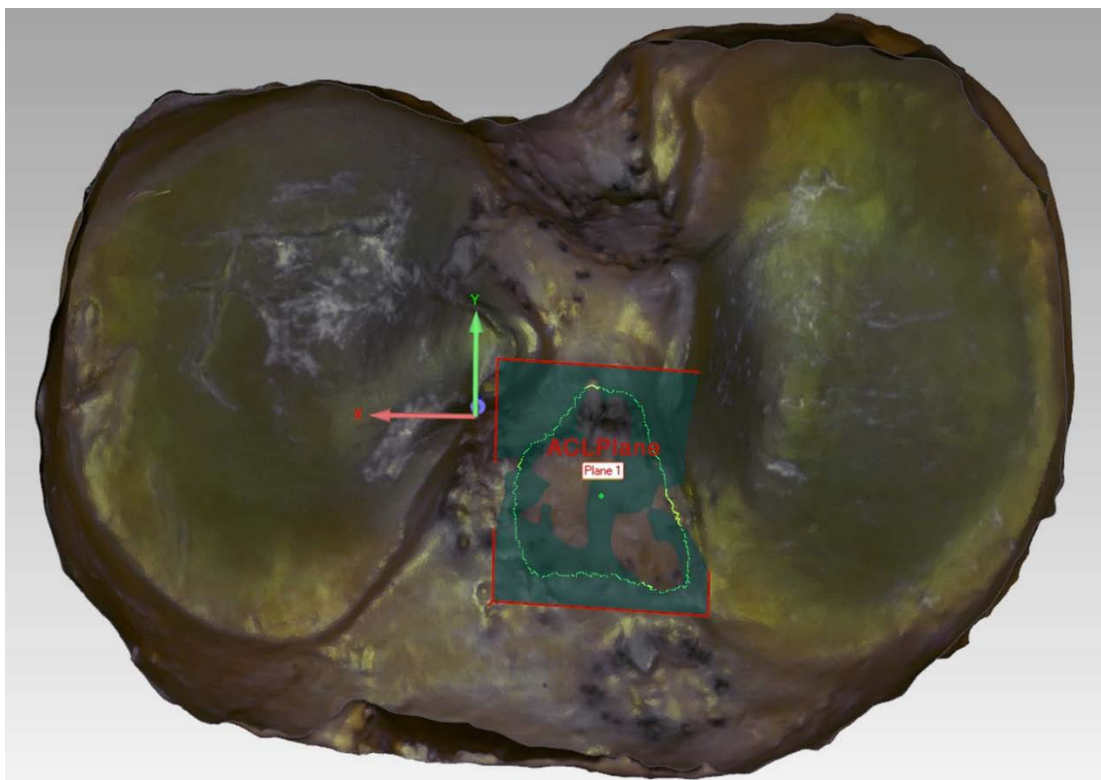


Figure 31. 3D model of tibia L, seen from below (distal to proximal), hollow. ACL area selected in green, ACL area best fit plane in red, and the centroid is the centered green dot. Due to the three-dimensional shape of the ACL in this specimen, its centroid lies below the surface.

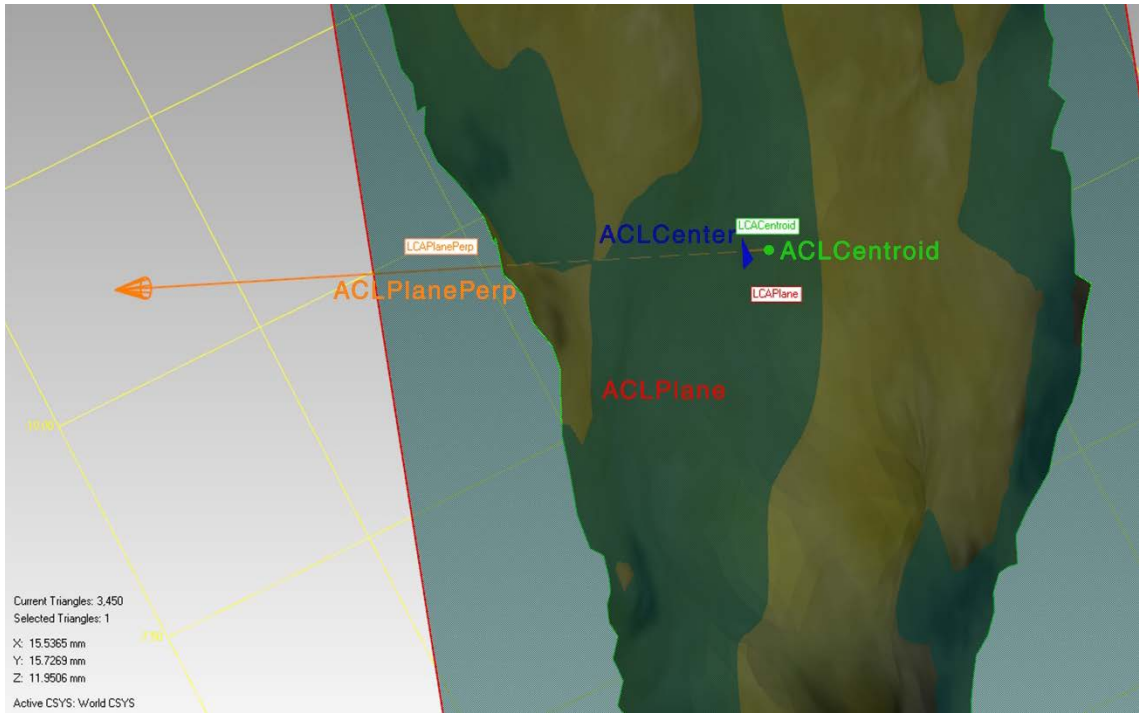


Figure 32. 3D model of Tibia L: Osseous surface of the ACL attachment, isolated from the rest of the 3D model. A line (ACLPlanePerp, in orange) perpendicular to the ACL plane (ACLPlane, in red) is projected from the ACL centroid (ACLCentroid, in green). Observe how the perpendicular line crosses the selected mesh triangle (ACLCenter, in blue) when passing from below the surface (to the right) to the upper surface (to the left of the image).

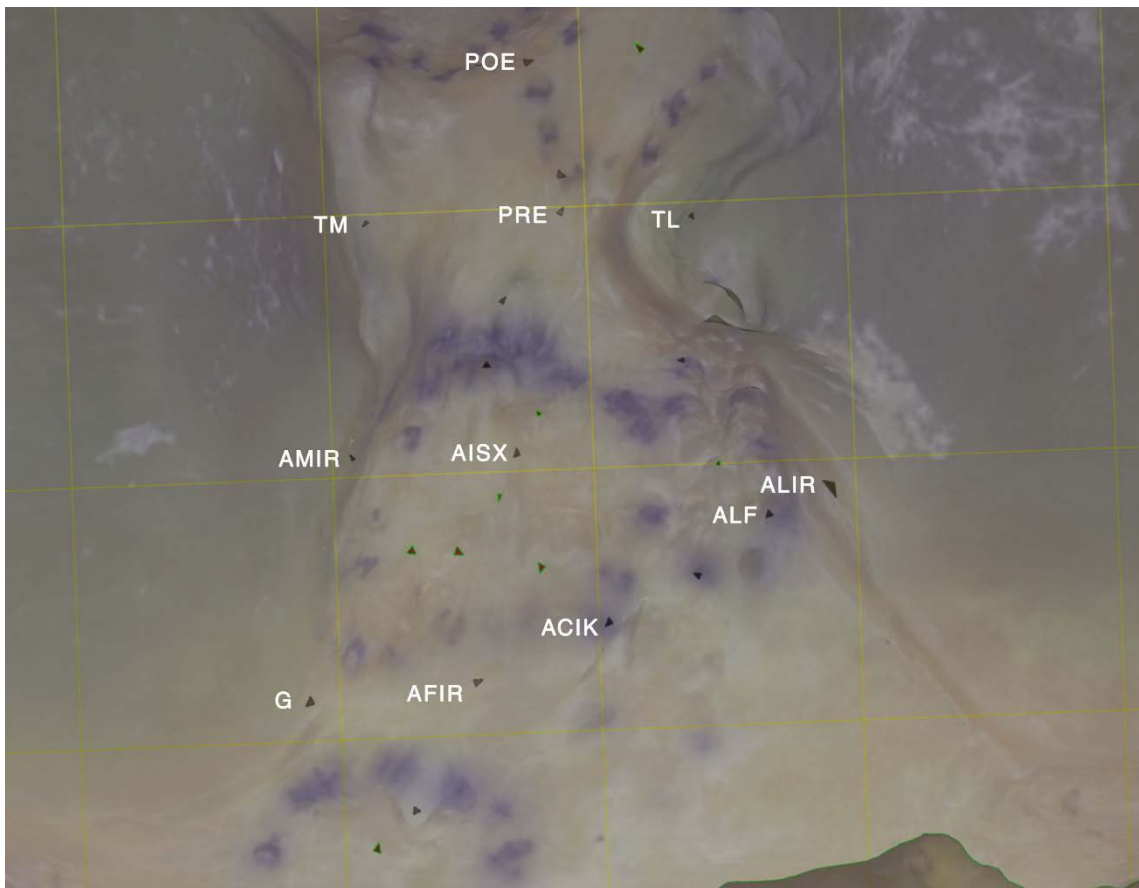


Figure 33. 3D model of tibia L. Magnification of anterior intercondylar aspect. Selected triangles in faded specimen's mesh: soft tissue attachment centers active (in red with green surrounding lines), osseous landmarks in gray. Names have been placed to the left of certain osseous landmarks (see List of Abbreviations above).

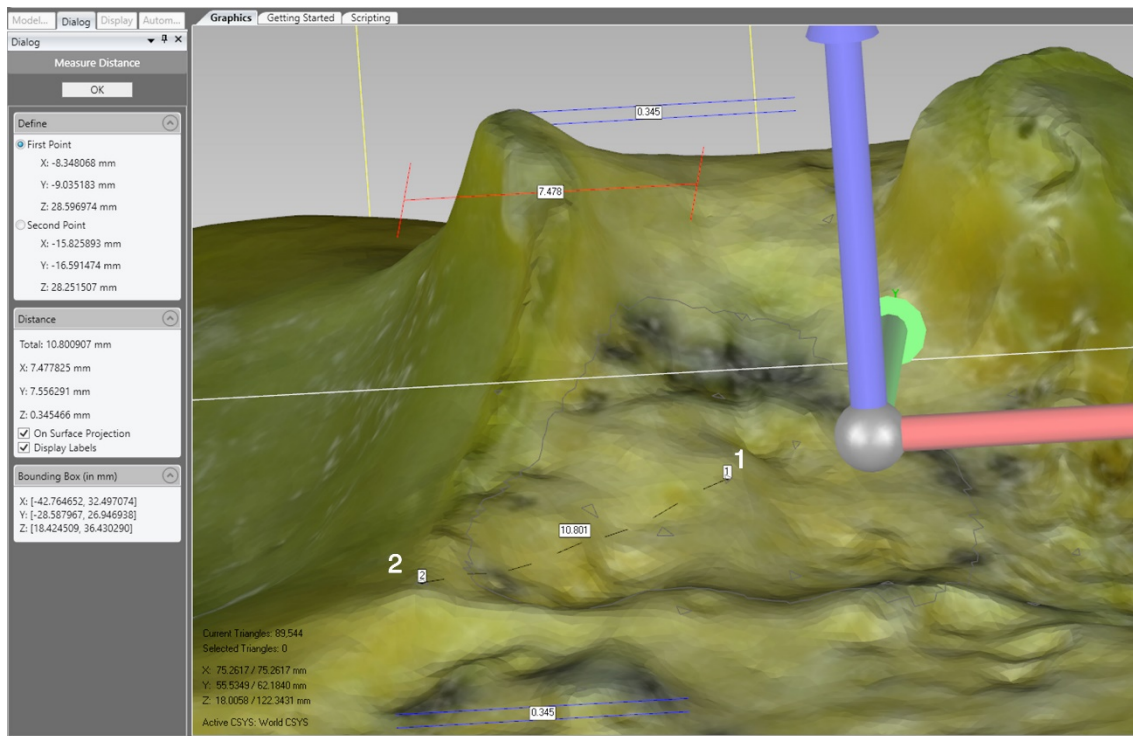


Figure 34. 3D model of tibia L. Anterior to posterior vision of the anterior intercondylar area. Distance measurement from ACL center (1) to the geniculum (2). Measurement is done on surface projection: observe how the dashed line connecting 1 and 2 is not straight (over the surface), but follows the area's relief.

Scan system and fluoroscopic image scale validation

The 3D design software was used to measure ML width, AP depth, and to select the maximum height at the medial tubercle's apex (related vertically to the inferior aspect of the sanding sponge). The same measurements were taken from fluoroscopic images of the specimens with a DICOM viewer (Weasis 2.0.5, dcm4che, GNU GPL software), and with a digital caliper from the specimens. A Pearson product-moment correlation was run between the measurements of the specimens and their 3D models, and the specimens and their fluoroscopic images.

The difference in means between the specimens and their 3D models was $+0.02146\% \pm 0.176\%$ overall, or 0.0913 ± 0.1271 mm, range -0.1039 to $+0.2413$ mm, showing a strong, positive correlation between paired measurements for ML width ($r = 0.9526$), AP depth ($r = 0.9651$), and height ($r=0.9212$).

The difference in means between the specimens and their fluoroscopic images was $-0.1078\% \pm 0.2592\%$ overall, or -0.1283 ± 0.3146 mm, range -0.6923 to $+0.5569$ mm, showing a strong, positive correlation between paired measures for ML width ($r = 0.929$), AP depth ($r = 0.9493$), and height ($r=0.8962$).

Measurement system validation

The error of triangle center to triangle center measurements was estimated by collecting 10 values from all soft tissue insertion centers (including bundle centers), i.e. by selecting the estimated center of each triangle 10 times (Fig. 35), and calculating its difference with the true center of the triangle with a spreadsheet (Microsoft Excel 2013, Microsoft, Redmond, WA, US). This process was repeated for each specimen. The average test value of all tibias (including one- and two-triangle areas) was 0.0721 mm. This gives a maximum average error for triangle center to triangle center measurement of less than 0.13 mm. Therefore, values less than 0.13 mm can be attributed to human error with the measuring software, while values greater than 0.13 mm can be attributed to true differences in distance.

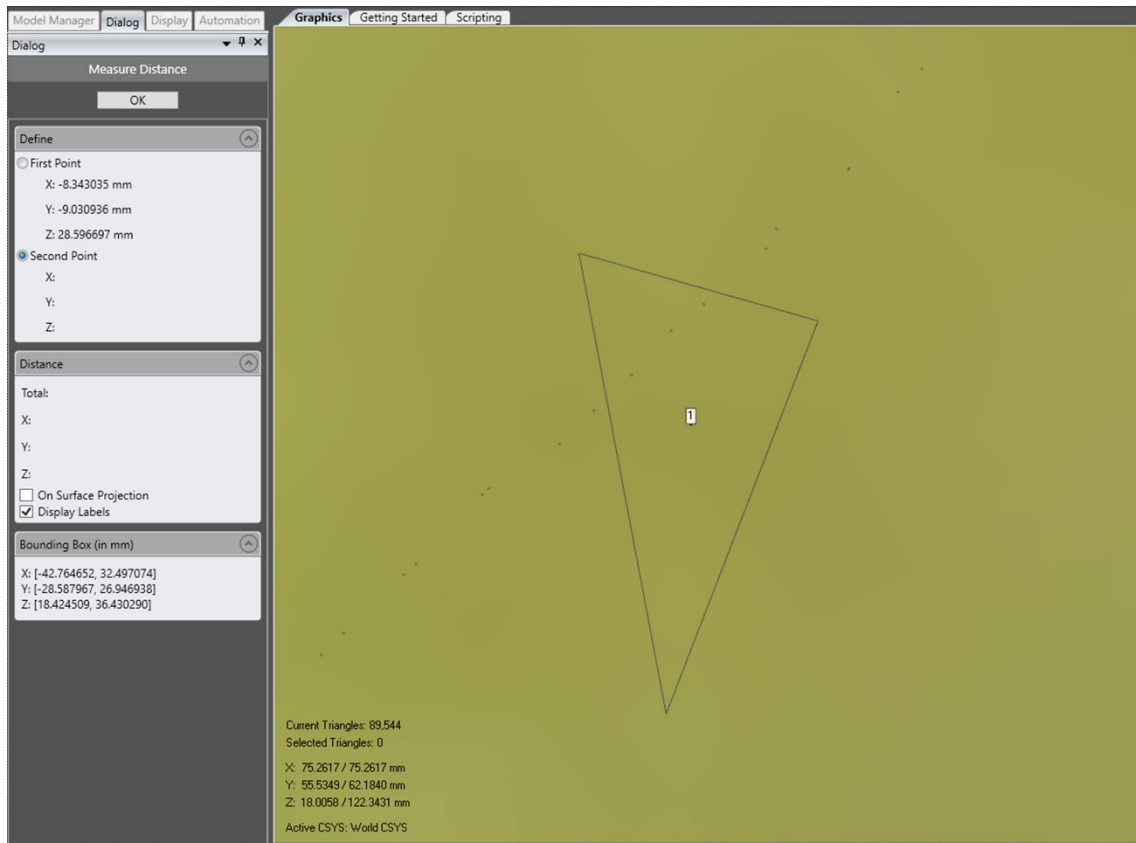


Figure 35. 3D model of tibia L. A central point is selected from ACL center triangle, defined by the coordinates shown in the upper left corner (under "First Point"). This is repeated ten times, and the difference between each selected point and the real center is collected.

Fluoroscopic study

Digital fluoroscopic images were taken of all specimens in the three planes with a C-Arm fluoroscopy unit (Arcadis® Orbic 3D, Siemens AG, Erlangen, Germany; see Fig. 36). Specimens were positioned on a radiotransparent hand table attached to an operating table, at a constant, base height (Fig. 37). The C-Arm was placed at an inclination of 0° to the vertical, with the tube 32 cm under the hand table, and centering the camera over the specimen.

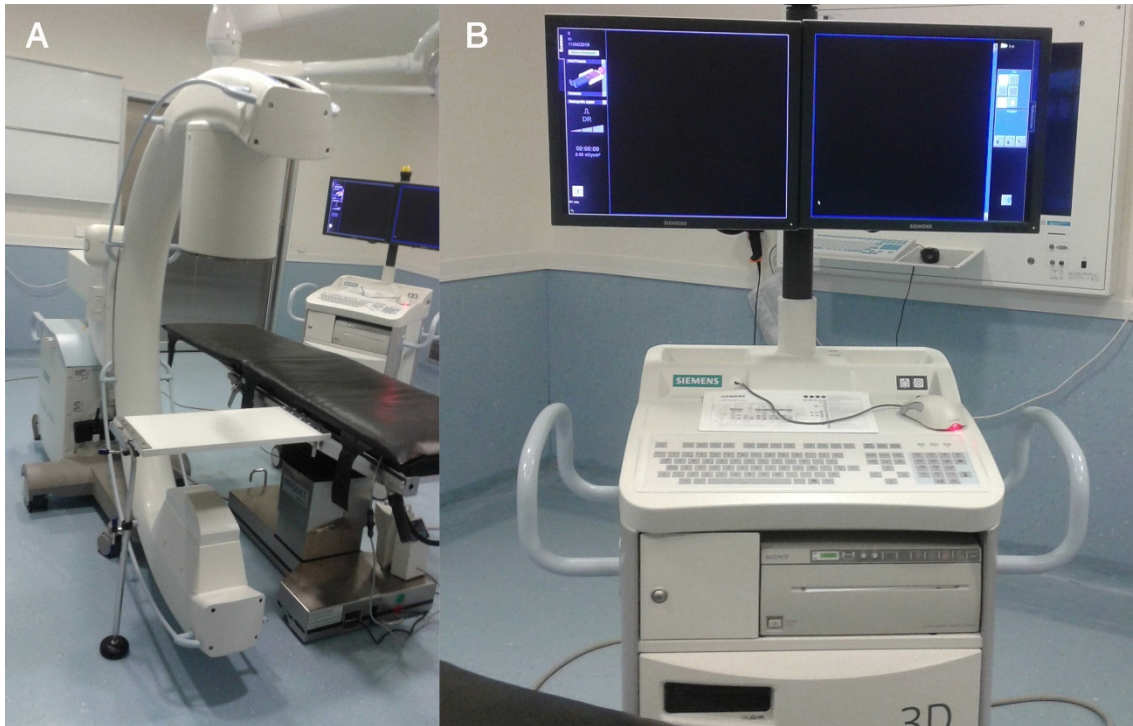


Figure 36. C-Arm in place for specimen imaging (A). Computer and display of the C-Arm for adjustments (B)

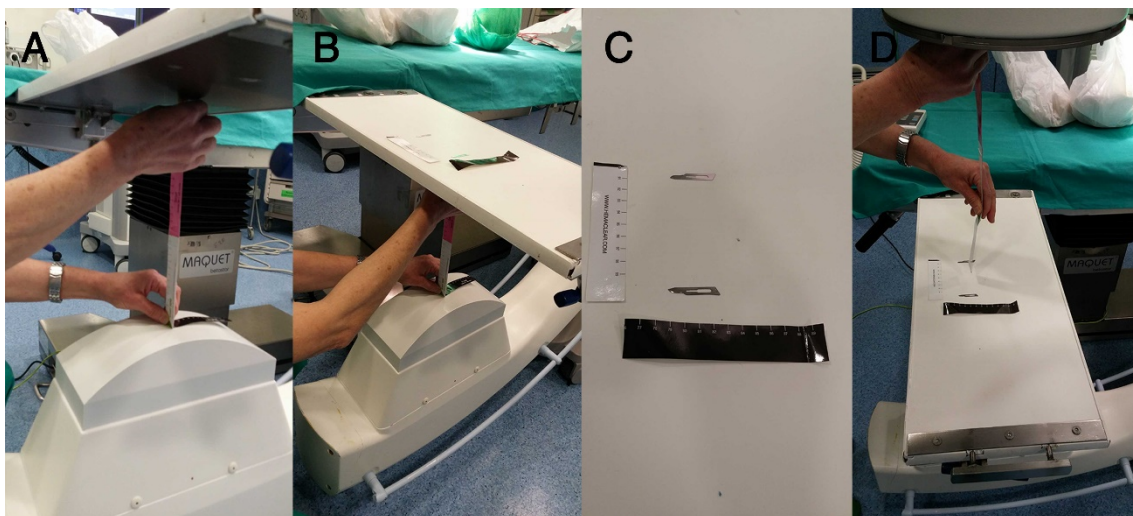


Figure 37. (A to D). A. The tube of the C-Arm is placed 32 cm under the hand table. B and C. Over the hand table a small area is delimited by two scalpels. D. The camera of the C-Arm is centered over that area

All specimens were placed between two number 15 scalpel blades for reference, and each digital image obtained contained at least a measurable part of one of the blades.

For the inferosuperior (i.e. axial) view, specimens were positioned on the hand table (Fig. 38). After that view was obtained, each specimen was glued with instant adhesive – cyanoacrylate glue – proximally to a cubic sanding sponge. This allowed for the placement of specimens on the table at exactly 90° for perpendicular anteroposterior and lateral views, by changing the side on which it stood. Images were taken with the automatic technique for radiographic examination of the hand.

Then a single metal wire was glued to the lateral tubercle, and a double metal wire to the medial tubercle, and new radiographs were taken of all specimens in the lateral plane in order to better identify each one.

Then the metal wires were removed by hand, the glue cleaned with acetone, and the insertion areas surrounded by pyrography marks were painted with a thick radiopaque liquid, made of barium sulfate in suspension mixed with water (Barilux, Iberoinvesa Pharma, Madrid, Spain), and new inferosuperior (Fig. 39), anteroposterior, and lateral radiographs (Fig. 40) were taken.

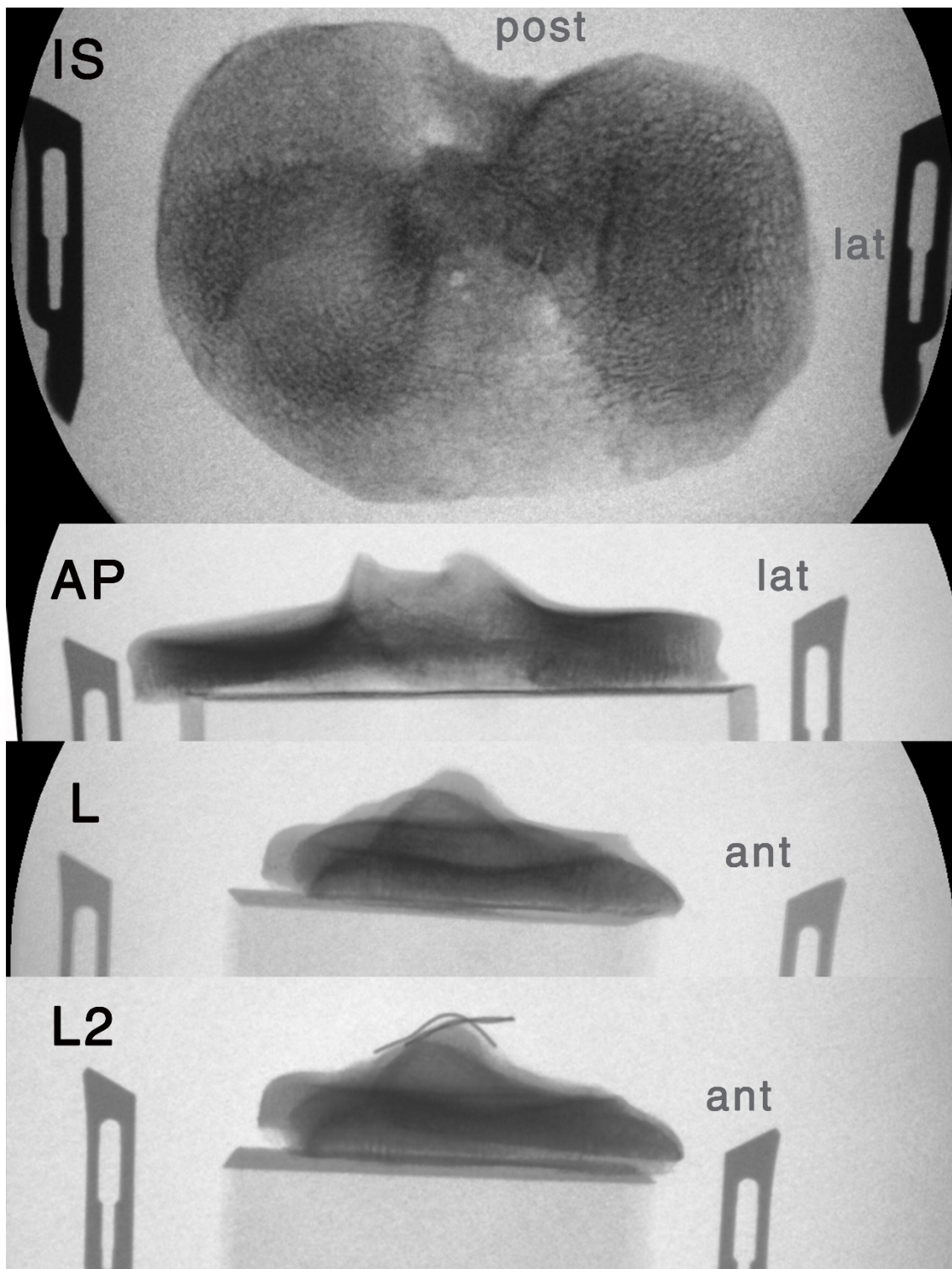


Figure 38. Tibia L. Inferosuperior (IS), anteroposterior (AP), and lateral (L) fluoroscopic views. Lateral fluoroscopy after metal wires were glued to the intercondylar tubercles (L2). Posterior (post), lateral (lat) and anterior (ant) sides of the specimen have been labelled for clarity.

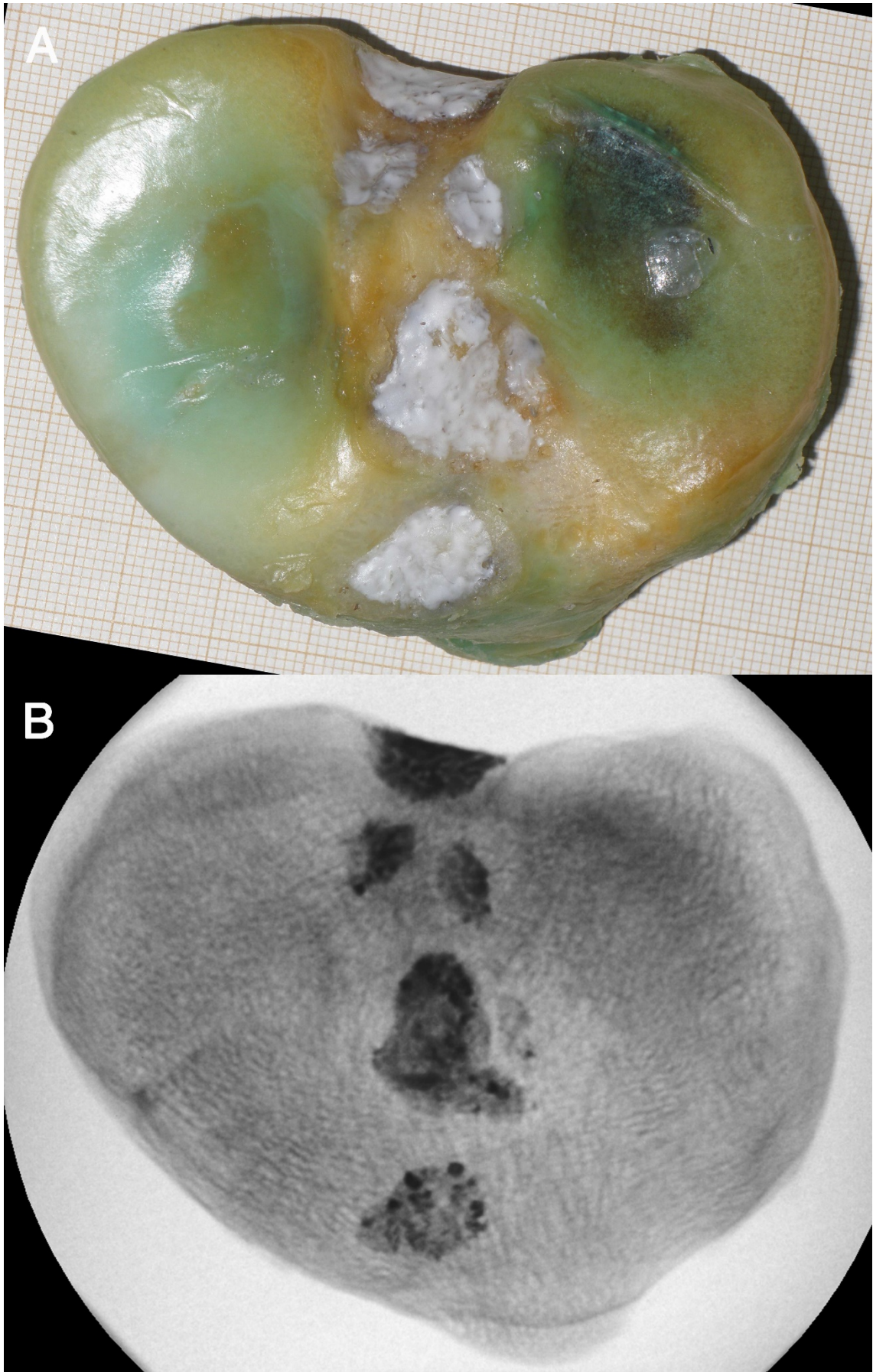


Figure 39. Tibia L. Soft tissue attachment areas painted with barium sulfate (A) and inferosuperior fluoroscopic view (B).

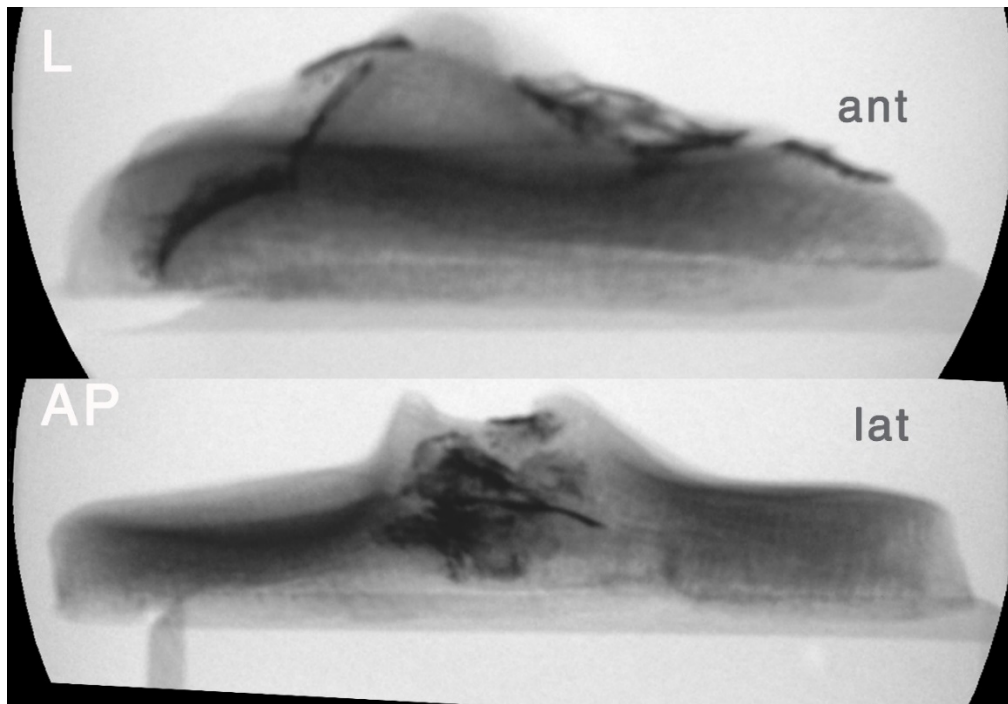


Figure 40. Tibia L. Lateral (A) and anteroposterior (B) fluoroscopic view after barium sulfate painting.

Statistical analyses

As the information on the smallest and largest anatomical measurements is very important for individual planning of anatomical ACL reconstructions, morphometric measurements were tested for deviation from the normal distribution using Shapiro-Wilk tests and Box-and-Whisker plots. For the Shapiro-Wilk tests, a p value of 0.05 was considered significant. Due to the normal distribution of all morphometric variables – $p[0.05]$ – in this study, mean, average, 95% confidence interval, and range were calculated for continuous data, with results presented rounded to one decimal (0.1 mm).

Specimen characteristics were presented as number of specimens and associated percentages for categorical parameters.

Data were collected into Microsoft Excel 2013, Microsoft, Redmond, WA, US) for sorting, and analyses were conducted with IBM SPSS Statistics 23.0 (IBM Corporation, Armonk, NY, US)

Study II. Investigation of osseous surface structure changes in pathological *area intercondylaris tibiae* compared to normal tibias, and applications to radiography

Specimen collection

A hundred consecutive patients undergoing knee replacement for osteoarthritis, from May 2014 to July 2015, were asked to consent and donate their removed tibial surface, obtained under a protocol approved by the research ethics committee of the University Hospital Infanta Cristina, Badajoz. All but one accepted to participate in this study, performed according to the ethical standards of the World Medical Association Declaration of Helsinki, Ethical Principles for Medical Research Involving Human Subjects.

Exclusion criterion was major damage to the anterior intercondylar area (three specimens). Ninety-six specimens were collected and preserved in formaldehyde.

The electronic medical records of all patients included in the study was checked prior to surgery. Past medical and surgical history, medications, history of the knee complaints and physical examination, as well as results of the American Knee Society Clinical Rating System applied to them, was recorded and analyzed.

The integrity of the anterior cruciate ligament was checked during knee dissection, and those specimens with chronically torn or absent ligaments were noted for further analysis.

Specimen Preparation

After extraction in the operating room, all specimens were placed in small containers filled with a 4% formaldehyde solution, and stored at room temperature until processing.

High-resolution images were obtained of each specimen before the preparation process using a digital camera (FE-370, Olympus Corporation, Shinjuku, Tokyo, Japan) mounted on a fixed solid support, viewing the specimen from superior to inferior. All specimens were placed near a small ruler for scale (Fig. 41).

Then specimens were washed with tap water, soft-tissue was removed with a scalpel, periosteal elevator, rongeur, and cutting forceps, washed again, and then put in an oven at 90° C for ten to twelve hours.



Figure 41. Tibia 15. Fresh specimen. Photograph with ruler (in cm) for scale, taken before processing.

Fluoroscopic study

Radiographic images were taken of all specimens in the three planes, as explained for Study I above (Fig. 43). Lateral views were also taken after metal wires were glued to the intercondylar tubercles (Fig. 42).

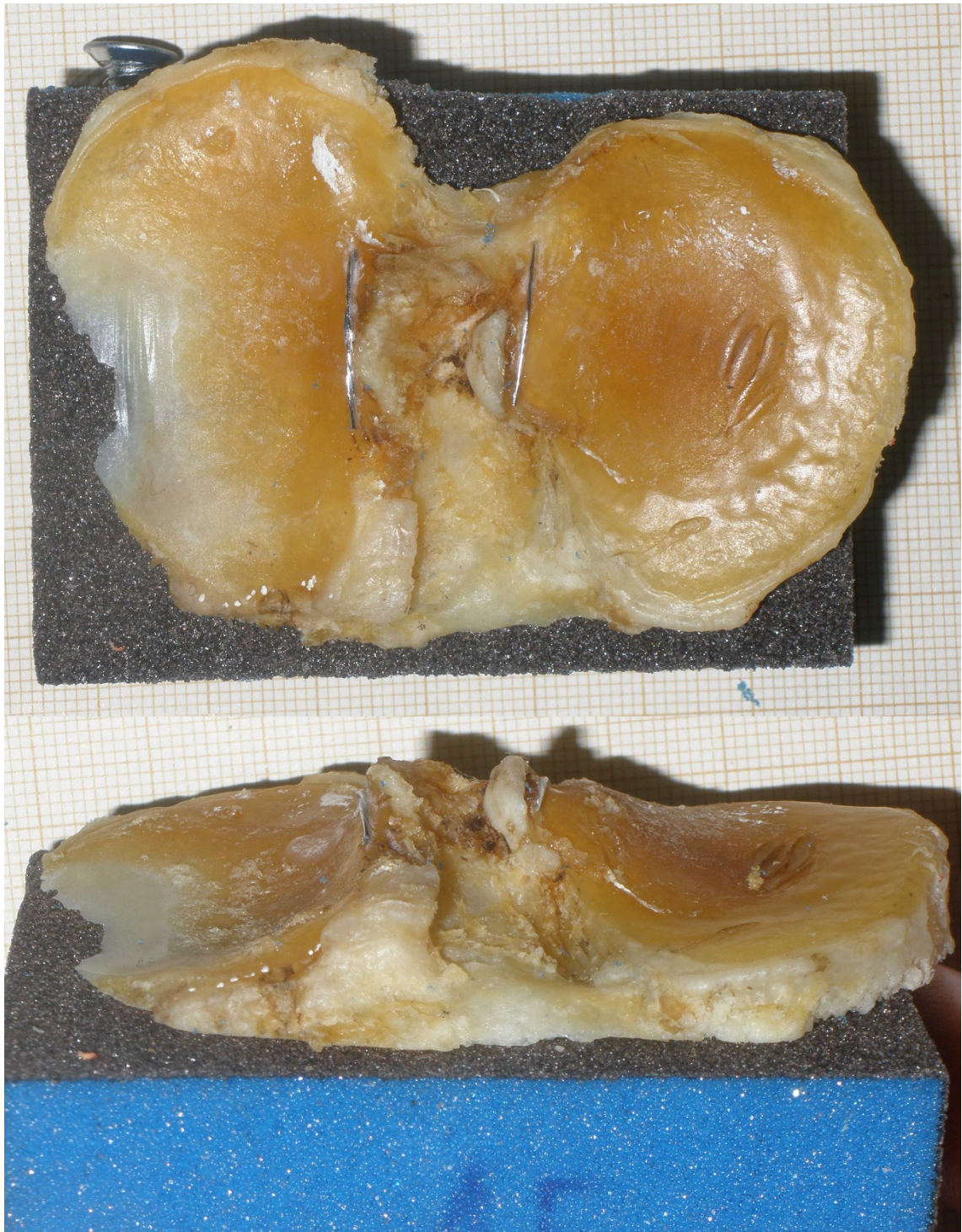


Figure 42. Tibia 15. Metal wires were glued to the specimens' intercondylar tubercles after taking the initial fluoroscopic images. A screw was inserted on the posteromedial aspect of the sanding sponge for stability in AP and lateral projections.

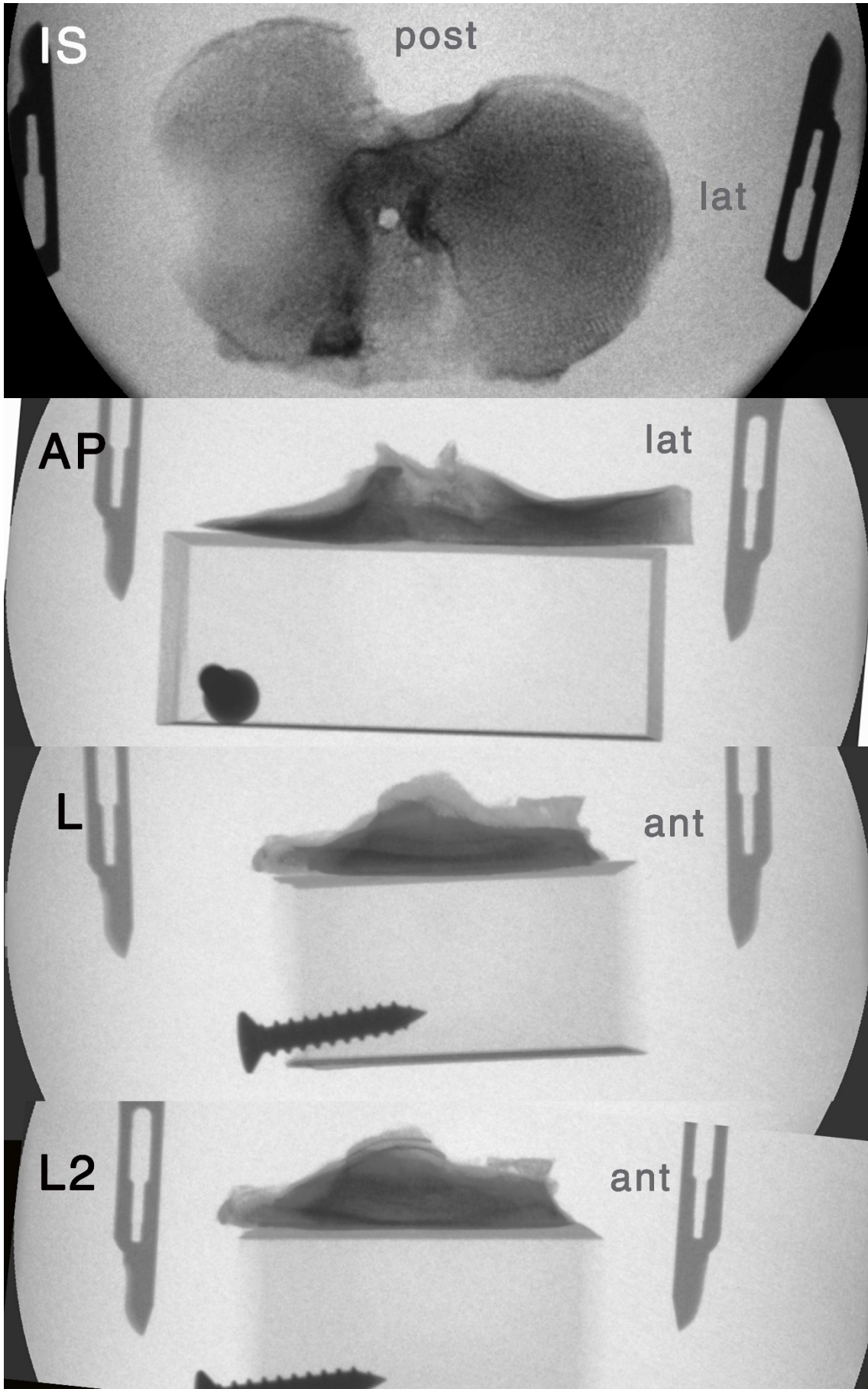


Figure 43. Tibia 15. Inferosuperior (IS), anteroposterior (AP), and lateral (L) fluoroscopic images. After metal wires had been glued, a new projection (L2) was taken. Posterior (post), lateral (lat) and anterior (ant) sides of the specimen have been labelled for clarity.

Notes and measurements

All dried specimens were carefully observed, and obvious pathological changes were recorded with help from a standardized drawing (Fig. 44).

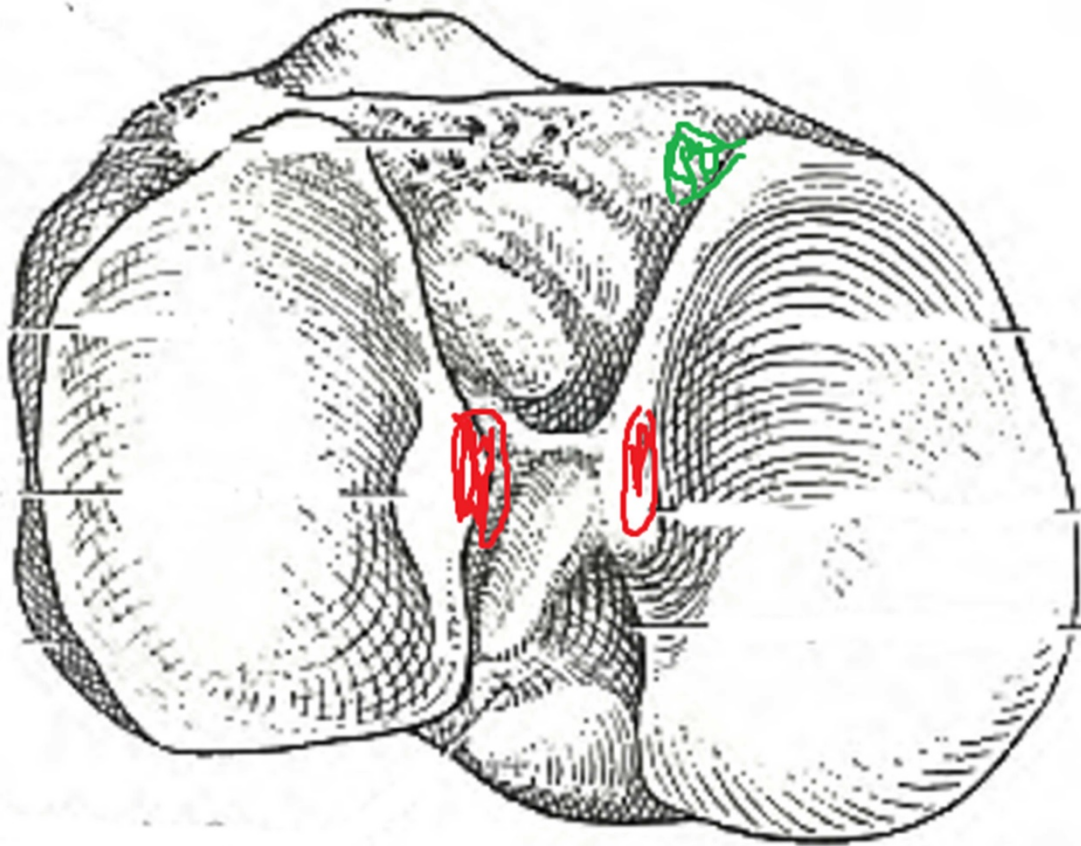
The following structures were measured in anteroposterior depth and mediolateral width over the dry specimen: the Parsons' knob; the lateral and medial tubercles' osteophytes (including their anterior and posterior aspect); the anterolateral, posteromedial, and posterolateral corner osteophytes.

Manual measurements were taken with an electronic digital caliper (resolution 0.01 mm, repeatability 0.01 mm, accuracy 0.00254 mm, by Mannesmann AG, Düsseldorf, Germany). The scaled digital photograph – or a semi-flexible ruler placed over the precise structure – were only used in certain structures with a limited access for the digital caliper's jaws.

In the inferosuperior radiographic view, the density of certain structures was given a value, from 0 (lowest density, mostly undifferentiated from surrounding tissues) to 3 (highest density): the medial tubercle, its anterior and posterior processes; the lateral tubercle, its anterior and posterior processes; the geniculum; the anteromedial corner, the anterolateral corner, the posteromedial corner, and the posterolateral corner; and posterior intercondylar area, or more precisely the posterior wall and its union with the posterior facet. Osteolytic zones were also recorded.

In the anteroposterior radiographic view, the relative height of the intercondylar tubercles, the Parsons' knob, and the condylar margins were noted. The bending direction of the peak of each tubercle was also noted, and their perceived attrition level was assessed as high, medium, or low. The intertubercular area was judged as high, medium, or low with respect to the tubercles' peaks, and the tightness of the intertubercular area as narrow, normal, or wide.

In the lateral radiographic view, the relative depth of the intercondylar tubercles, the Parsons' knob, and the condylar corners were noted.



Parsons de forma triangular
 10 x 5
 Osteofitos en ambas
 espinas que estrechan el
 espacio

Figure 44. Tibia 15. Outline of the specimen's features using the standard drawing.

Digital processing and 3D surface

Metal wires were removed as in Study I above.

Eighty-four specimens were used for 3D surface analysis. Nine were used for histology of the Parsons' knob, and three for investigation radiologic trabecular architecture.

Digital processing was similar to that used for Study I. Differences with donor tibias were as follows:

- Photograph hours were 9:00 AM to 21:00 PM, Central European Time at 38°52'44"N 6°58'1"W, August 2015.
- The round swivel stand was divided in 16 equidistant marks, obtaining $\pi/8$ radians (i.e. a difference between photographs of 22.5 degrees).

- Photographs were taken at a height slightly above the horizontal plane from the specimen's base, at 14 cm, and at 28 cm above the horizontal.
- The height and length measured for the sanding sponge used in donor tibias (26.58 x 68.57 mm) was used for setting both measures to scale sanding sponges in all 3D models of pathological specimens (Fig. 45).

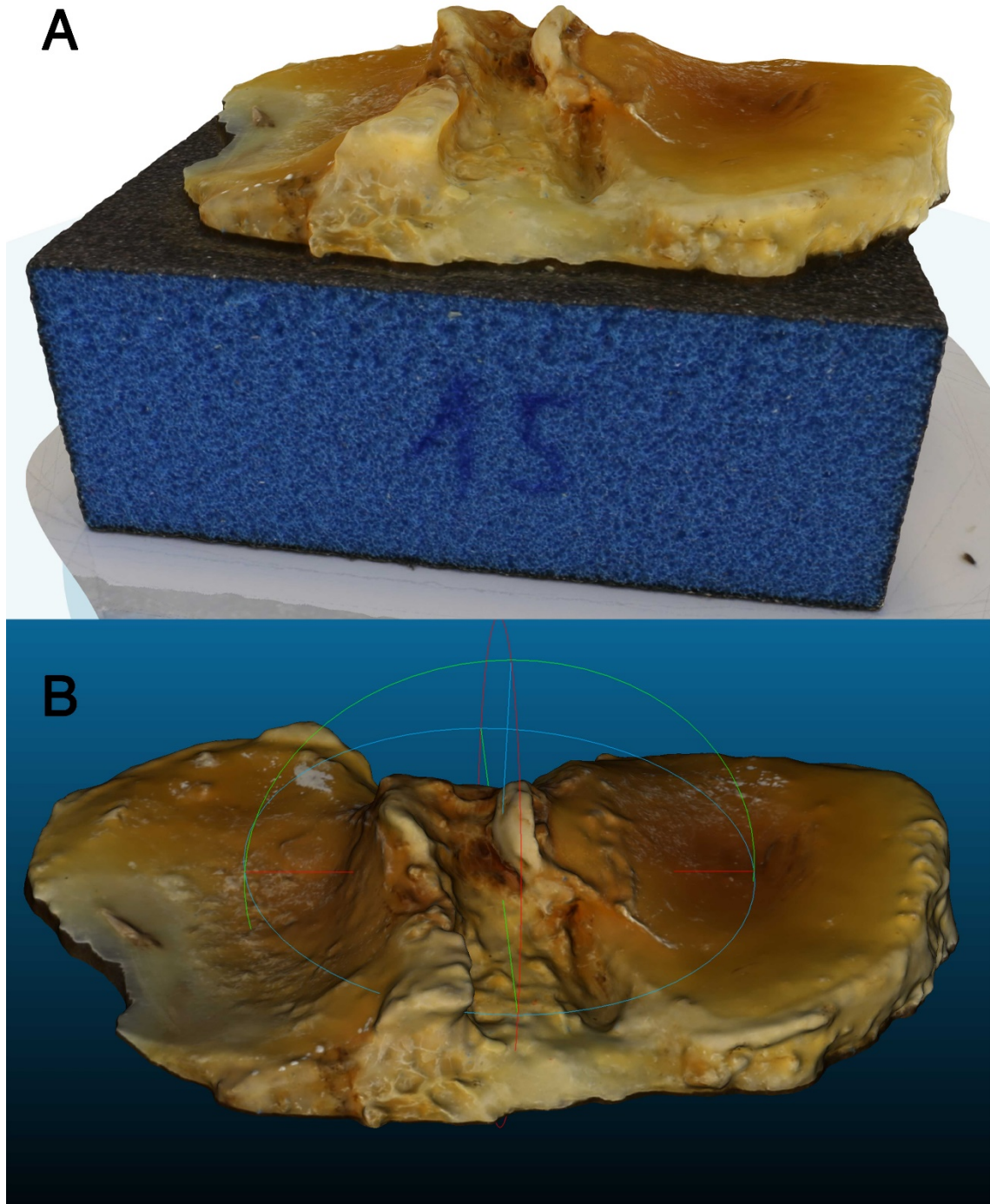


Figure 45. 3D model of Tibia 15. Original 3D model obtained (A), with sanding sponge used for scaling. Scaled and sliced 3D model used for analysis (B).

Normal tibias

Tibias collected and prepared for Study I were also included in this study.

Scan System Validation

Quantitatively, accuracy and precision of the 3D models of pathological tibias used in this study – made with 48 photographs, instead of the 176 used for donor tibias – was tested by obtaining a new 3D model of four of the donor specimens used for Study I (tibias A, E, I, and M). These new models were made each with 48 photographs, 16 taken from the horizontal, 16 from 14 cm above it, and 16 from 27 cm above it.

For each of the four validated specimens, the original 176-photograph model and the corresponding 48-photograph model were imported as a pair into the 3D point cloud and mesh processing software (CloudCompare, version 2.7 64 bit, GPL Software) for further analysis. The average mean difference of faces (mesh triangles) between the 176- and the 48-photograph models was found to be $+6.045 \pm 3.16\%$. *Points sampling* was made on both 3D models (approximately 1,000,000), generating normals. Both sampled models were aligned manually first, and then with automatic registration (*fine registration, ICP*). Once aligned, a cloud/cloud distance was computed (Fig. 46). The mean average distance of the four model pairs was 0.123 ± 0.292 mm.

The 3D model pairs were qualitatively found to be quite similar, with no gross differences noted. Models with less photographs were wider, with less defined external borders. Apart from the external borders of the specimen, the inner aspects of the intercondylar area were the most affected among this study's areas of interest. In arthritic tibias the differences were more marked.

Another set of 48 photographs were made of three pathological specimens (tibias 10, 53, 61), their 3D models obtained, and the differences with their corresponding previous 3D models compared (Fig. 47). Quantitatively, the mean difference of faces (mesh triangles) between each pair was found to be $0.91\% \pm 0.177\%$. The mean cloud/cloud average distance of the three model pairs was 0.036 ± 0.218 mm, with the more arthritic one (tibia 61) having more average distance and markedly more variability than the less arthritic one (tibia 53).

Because of the variable presence of osteophytes in arthritic tibias, it was qualitatively found that structures behind and between them were less accurately represented with 48-photograph models, and the model variability increased with arthritic changes. Therefore, the more degenerative changes a tibia had, the

less reliable a precise measurement was with a 48-photograph model. The overall proximal tibial and intercondylar shape were usually conserved, though.

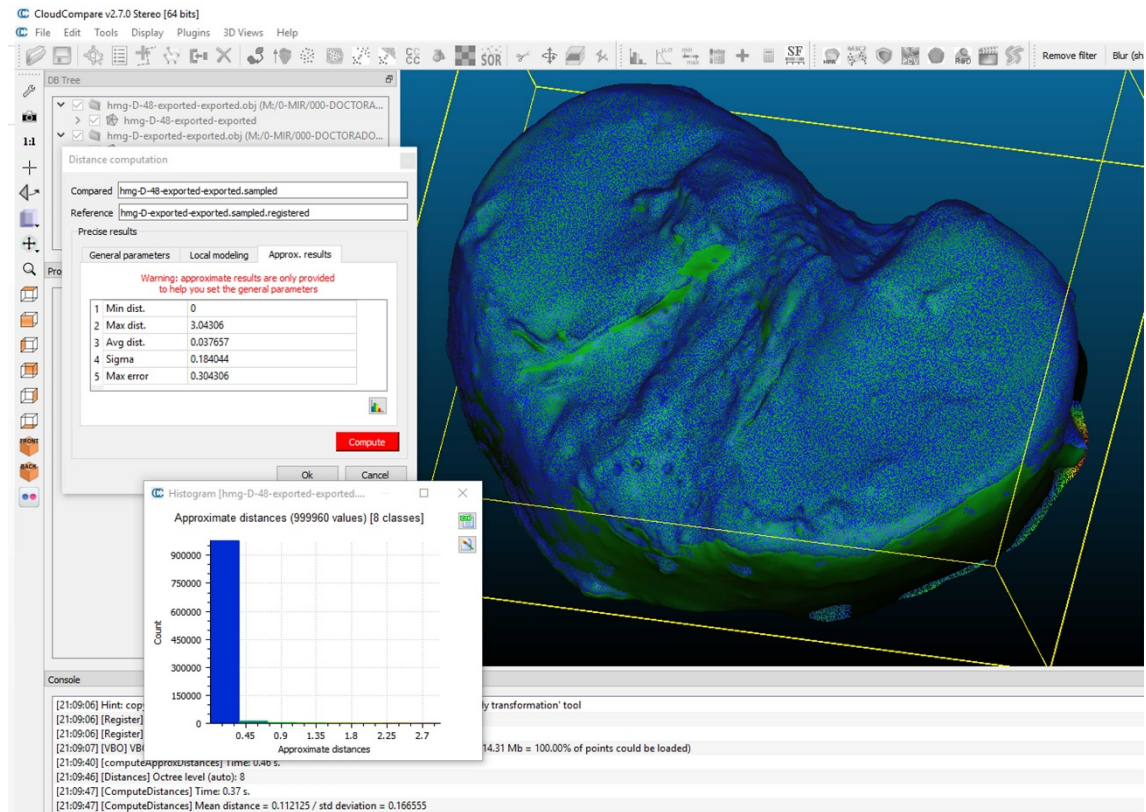


Figure 46. 176- and 48-photograph 3D models of tibia M. Cloud/cloud distance computed.

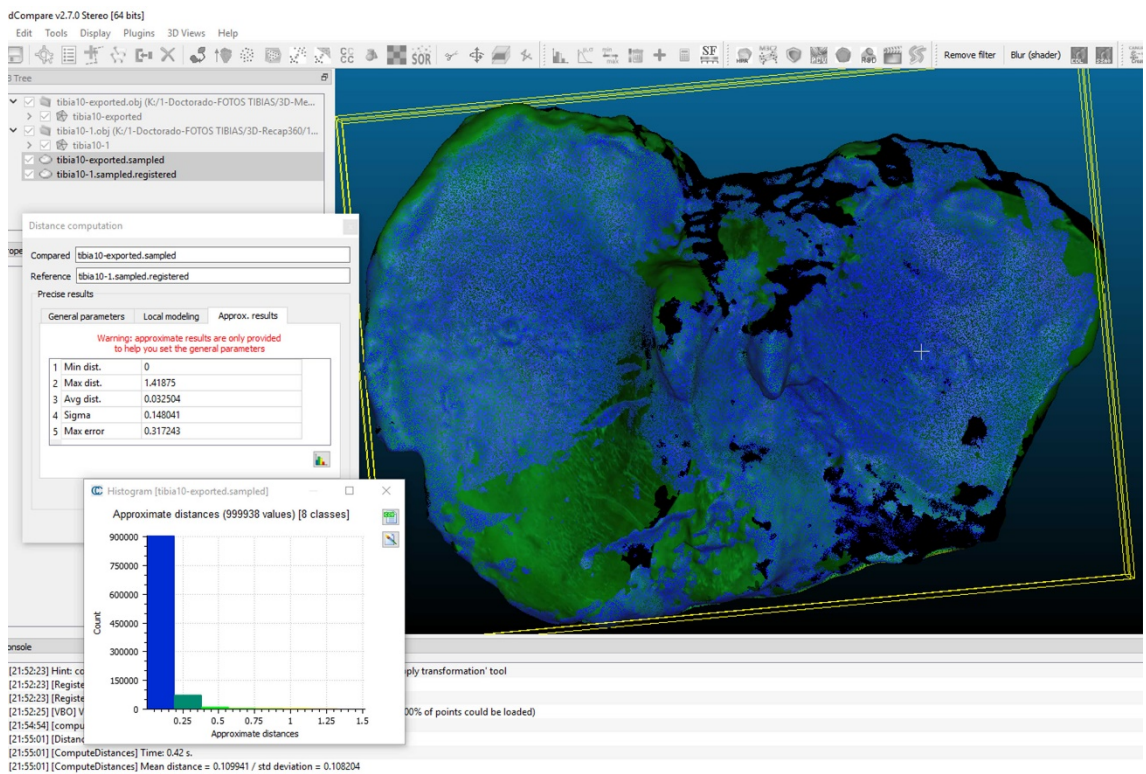


Figure 47. Different 48-photograph 3D models of tibia 10. Cloud/cloud distance computed.

Radiographic classification

Previous digital radiographs of each patient's knee were also collected from the regional Extremadura Health Service imaging database system (Centricity, GE Healthcare, Little Chalfont, UK). These included a standing AP and non-weight-bearing lateral projections (Fig. 48, Fig. 49).

All tibias were graded according to the Ahlbäck classification of osteoarthritis: grade 1, narrowing of the articular space; grade 2, obliteration or almost obliteration of the articular space; grade 3, bone attrition less than 5 mm; grade 4, bone attrition between 5 and 15 mm; and grade 5, bone attrition greater than 15 mm. Grade 5 is usually identified by marked tibiofemoral subluxation in the anteroposterior and lateral views.

Tibiofemoral angle was measured according to McDaniel's best reported method⁶⁰, by utilizing the center of the base of the tibial tubercles.

All radiographs were reviewed and measured by a single, experienced rater (a senior orthopaedic surgeon).

Specimens from Study I, for which no previous X-rays were available, were classified according to the knee joint condition after arthrotomy, allowing for full joint inspection and range of motion (including loading simulation).



Figure 48. Tibia 15. Non-weight bearing lateral (left image) and standing AP (right image) knee radiographs taken before surgery.



Figure 49. Tibia 15. Close-up of standing AP (A) and non-weight-bearing lateral (B) knee radiographs.

Surface analysis

All 3D models were observed meticulously in 3D point cloud and mesh processing software, and with help from geographic information software files.

Quality

Tibias cut during surgery for TKA showed a wide variation. The condition of all 3D models investigated in Study II was judged subjectively, based on the available surface for analysis of the intercondylar area (in AP depth and ML width), with condyle integrity assessed as of secondary interest, giving a grade as follows: A, excellent quality; B, good quality; C, fair quality; and D, poor quality.

General

All variables were classified by the author. They were first assessed in all 3D models, without classifying them. In a second assessment, all variables were classified again in all specimens, graded, and noted. All classified variables were then compared in a third round with the corresponding 3D model, and the value given was corrected when needed.

Osteophytic changes were classified into five grades, from +1 to +5, a higher grade representing a higher elevation than the inferior one. Depressions and attritions

were also classified into five grades, from -1 to -5, a lower degree representing a lower depression or deeper attrition than the higher one. A simple naming of grades was given as follows: -5, groove (*sulcus*); -4, fossa; -3, fovea; -2, recess (*recessus*); -1, incisura; 0, lamina; +1, line (*linea*); +2, ridge (*crista*); +3, cone (*conus*); +4, tuberculum; +5, eminence (*eminentia*). The terms cone and fovea are suited for round structures, but in long structures the terms high ridge and deep recess would be more appropriate.

In all structures studied, a 0 was not given in absolute numbers (as a “base” grade for each structure): their perceived base elevation or depression over surrounding areas in non-pathological tibias was taken into account instead. Therefore, the anteromedial intercondylar ridge (central process) had a base grade +2, ridge; the anterolateral aspect of the anterior intercondylar area had a base grade -5, groove; the anterolateral recess had a base grade of -4, fossa; and so on.

Osteophytes found in specimens from Study I were selected for area and volume analysis (Fig. 50).

Intercondylar Tubercles

Medial and lateral tubercles were also classified according to widening (grades 0-4), erosion (grades 0-4), and direction of erosion in the horizontal plane (which was later classified into simpler groups for further analysis). Tubercle peaks were ranked by height with respect to each other, and these classified into simpler groups. Main tubercle processes (see below IV.2. Intercondylar area and tubercles) were also included in this study.

Condyles

The medial tibial condyle of each specimen was divided in four parts or quadrants: an imaginary anteroposterior line, approximately parallel to the medial tubercle and its anterior and posterior processes, divided the condyle in approximately equal medial and lateral halves. An imaginary mediolateral line perpendicular to it in the middle of the area divided the condyle in an approximately equal anterior and posterior half. The same method was applied to divide the lateral condyle in four parts (Fig. 50).

The area of maximum attrition of the condyle (MAC) was defined for each tibia as the quadrant where the main zone of articular erosion lied. Neighboring affected zones were defined as complementary MAC (MACCO). Together, MAC and MACCO formed the overall attrition areas (MACMACCO). MACMACCO was

classified into simpler groups for further analysis. Main affected quadrants on the opposite condyle (MACOp) were also selected. As an example in the case of specimen I (Fig. 50), MAC is 3M, MACCo is 4M, and MACOp is 1L.

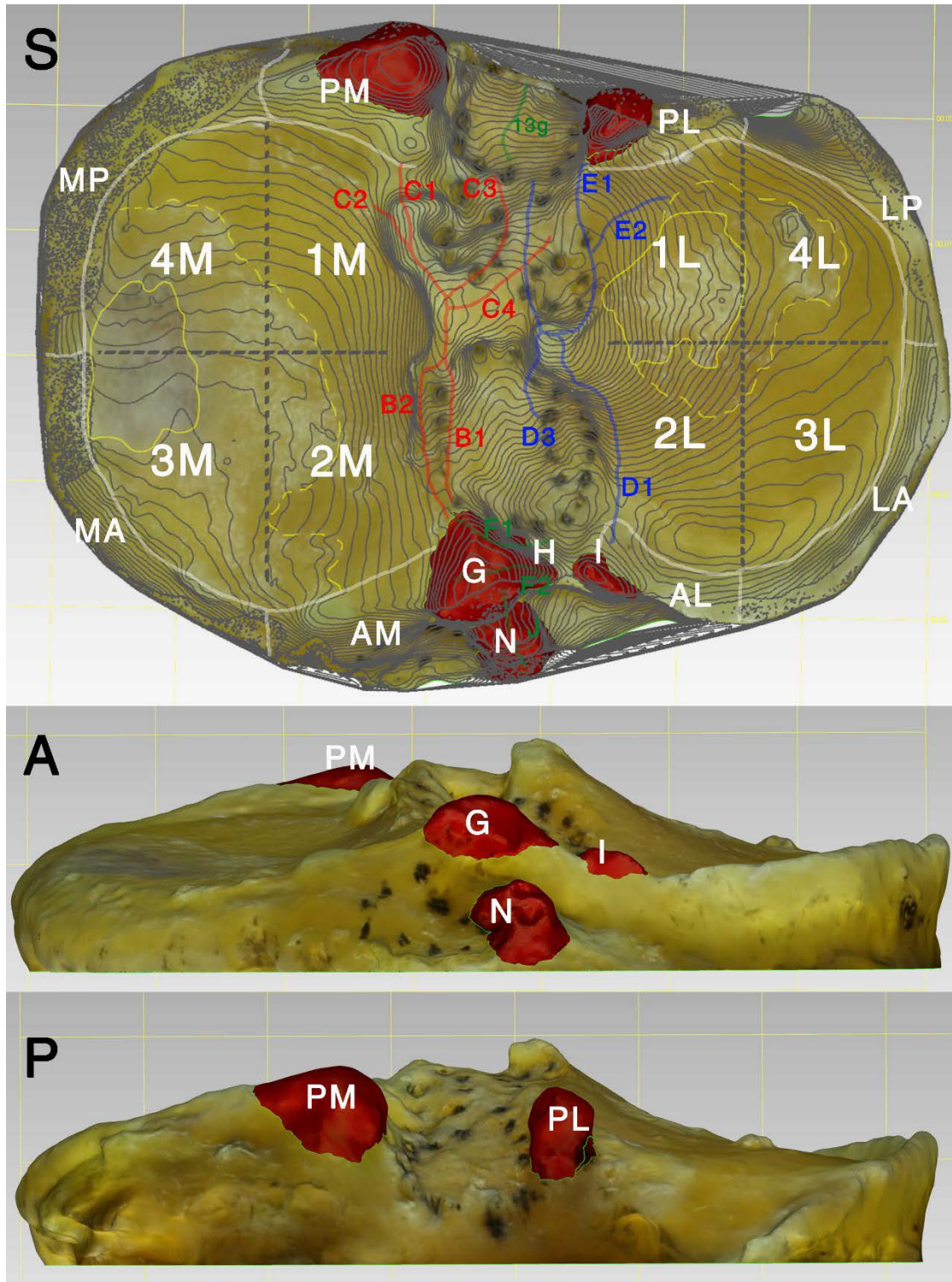


Figure 50. 3D model of Tibia I (left-mirrored). Superoinferior view (S) with contour lines superimposed. Anterior (A) and posterior (P) views. Condyles divided in 4 similar parts, numbered 1-4 (M: Medial; L: Lateral). In yellow, main attrition areas (solid line) and complementary attrition areas (dashed line). Medial tubercle processes in red, lateral tubercle processes in blue. Other ridges in green. Common osteophytes selected in red (note how G and H are connected, as are I and AL). AM: anteromedial corner; AL: anterolateral corner; PM: posteromedial corner; PL: posterolateral corner; MA: medial rim, anterior part; MP: medial rim, posterior part; LA: lateral rim, anterior part; LP: lateral rim, posterior part.

Damage to the chondral surface was graded using the 5-level scoring system by Weidow⁶¹: 0, no visible change; -1, cartilage fibrillation; -2, cartilage destruction without exposure of subchondral bone; -3, exposed subchondral bone without cartilage and no or minor attrition of bone; and -4, obvious attrition of bone. The attrition of both the medial and lateral condyles were classified this way.

The margins of the condyles were divided into their interior intercondylar corners (anterior and posterior), corresponding to areas 1c, 1d medially, and 2c, 2d laterally (see IV.3. Condyles below); and the external rims, which were divided in an anterior and posterior parts (Fig. 50).

Anterior area

The anteromedial intercondylar (or Parsons') knob was classified into a general shape in each specimen; its forming structures were defined; and its erosion direction determined. Erosion directions and forming structures were then classified into simpler groups for further analysis.

The same general shape classification was also given to the anteroventral intercondylar knob, and to the anterolateral intercondylar knob. Both were also given a special binary classification, in case they formed a common elevation with each other or surrounding structures.

The anterior frontal intercondylar ridge processes were classified in a binary manner as forming a common ridge or not, and their separation (anterior frontal intercondylar ridge recess) was classified using depression grades.

The anterolateral fossa, 7, and the anterior vallecule, 9, were also classified as a common structure binarily, as either forming a groove or fossa, or not.

Area 10

Area 10 was analyzed as a ridge with two main slopes. See below (§IV.7.1. Anterior intercondylar staircase) for a more precise description of the ridge as a staircase, and the slopes as the stairs that form it.

The height of each slope was classified into five degrees, with the highest reference point (+4) being the intertubercular ridge, and the lowest reference point (0) being the anterolateral fossa.

Each slope presented a more horizontal area, whose size was compared to the whole slope, to classify slopes into one of three categories: 0-33% (less horizontal

area than vertical ridge), 34-66%, and 67-99% (more horizontal area than vertical ridge).

An inconstant, intermediate horizontal area between both slopes was classified into a binary vertical ridge vs. horizontal area.

The main constant indentations found in area 10, the sagittal incisure and the coronal incisure, were classified using the general depression grades.

Area 13

Area 13 was usually cut during extraction, and only part of the facet was available for study. When present, it was classified as a steep or as a gentle slope.

Slope

Observation of tibias and analysis with GIS software suggested changes in intercondylar tubercles' external slopes. The hypothesis was then developed that slope changes were associated with degenerative changes.

Therefore, the external slope of the medial and lateral tubercles were selected in 3D design software (Geomagic Studio 2014 64 bit, 3D Systems, Rock Hill, South Carolina, U.S.), and a three-dimensional best-fit plane was obtained for each one in models of donor (Fig. 51) and pathological specimens (Fig. 52). Three two-dimensional angles in the coronal plane were obtained using software (Microsoft Excel 2013, Microsoft, Redmond, WA, US):

- the supplementary of the angle formed by both slopes;
- the angle formed by the medial slope plane with the horizontal plane;
- the angle formed by the lateral slope plane with the horizontal plane.

They were calculated as the acute angle determined by the normal vectors of these planes:

$$\vec{n}_1 = (A_1, B_1, C_1), \vec{n}_2 = (A_2, B_2, C_2)$$

The angle was obtained as the absolute value of the arccosine of the scalar product of both vectors, divided by the product of their modulus:

$$\alpha(\pi_1, \pi_2) = \alpha(\vec{n}_1, \vec{n}_2) = \arccos \frac{|A_1 * A_2 + B_1 * B_2 + C_1 * C_2|}{\sqrt{(A_1^2 + B_1^2 + C_1^2)} * \sqrt{(A_2^2 + B_2^2 + C_2^2)}}$$

In pathological tibias, cut with a surgical guide, the horizontal plane was assumed to be the X axis (1, 0, 0), while in normal tibias the horizontal plane was defined by selecting the condyles, (as explained above).

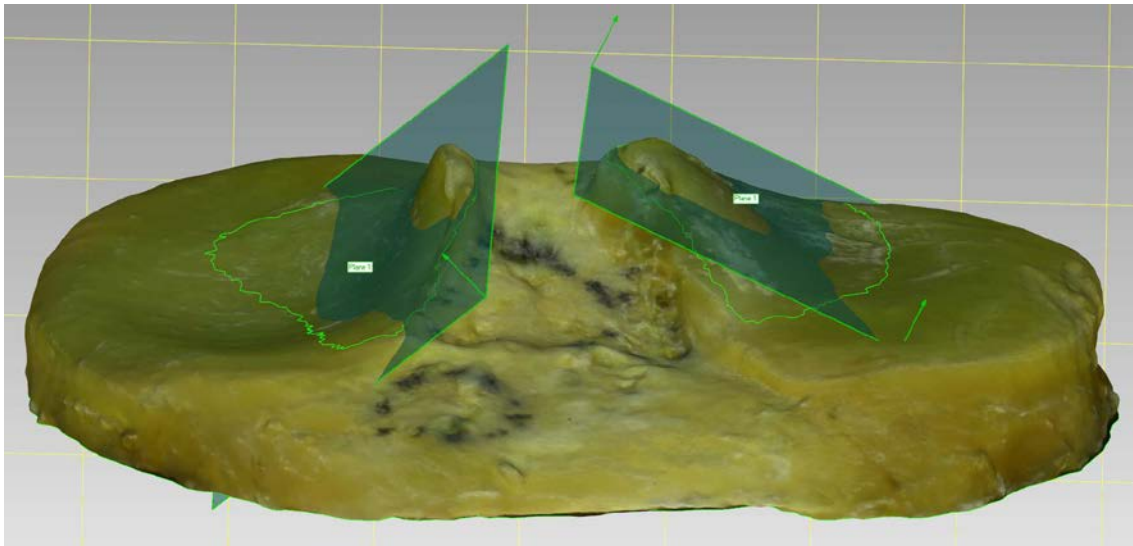


Figure 51. 3D model of tibia L. Medial and lateral tubercle slopes selected, with best-fit planes.

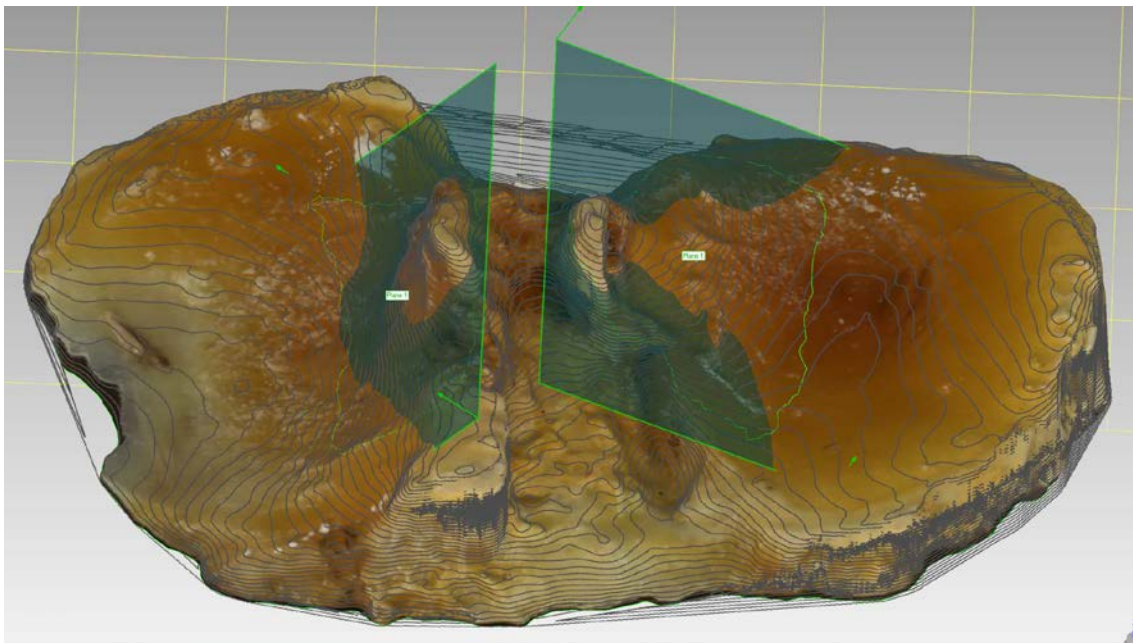


Figure 52. 3D model of tibia 15. Medial and lateral tubercle slopes selected, with best-fit planes obtained.

Statistical analyses

Morphometric measurements and continuous data (age, American Knee Society Rating System scores) were tested for deviation from the normal distribution using Kolmogorov-Smirnov tests and Box-and-Whisker plots. For the Kolmogorov-Smirnov tests, a p value of 0.05 was considered significant.

Mean, average, 95% confidence interval, and range were presented for continuous data, with results presented rounded to one decimal (0.1 mm). Specimen characteristics were presented as number of specimens and associated percentages for categorical parameters.

Tests were two-sided, with a type-I error set at $\alpha=0.05$. Comparisons between independent groups were performed using χ^2 or Fisher's exact tests for categorical variables, and using ANOVA or Kruskal-Wallis tests as appropriate (homoscedasticity verified using Bartlett's test) for quantitative parameters. Spearman rank-order correlations were obtained for comparisons between ordinal variables.

Data were collected into Microsoft Excel 2013, Microsoft, Redmond, WA, US) for sorting, and analyses were conducted with IBM SPSS Statistics 23.0 (IBM Corporation, Armonk, NY, US)

Axial, sagittal and coronal cuts of specimens for anatomic, radiographic, and MRI investigation of normal and pathological tibias.

To study the profile and inner osseous structure of the intercondylar eminence, specimens were cut in anteroposterior, mediolateral and axial planes. Radiographs of the cuts were taken to observe their trabecular structure, and assess the distribution of forces to which the different zones were subjected.

Four specimens from Study I without degenerative signs, and thirteen pathological specimens (five of which had knee MRI previous to extraction) were selected. The intercondylar eminence was separated from the rest of the proximal tibia with an electric diamond circular saw blade, and after that a high precision low speed saw (Isomet 2000, Buehler, Lake Bluff, IL, US) was used to obtain bone slices 2mm thick (Fig. 53, Fig. 54).

Specimens were cut according to a previous plan (Fig. 55): In two donor specimens, cuts were done in an anteroposterior plane, perpendicular to the posterior intercondylar axis of the tibial plateaus. In two donor specimens, cuts were done in a mediolateral plane, parallel to the intertubercular ridge through the attachment of the ARMM, through the anterior border of the ACL attachment area, through the middle aspect of the ACL and ARLM attachment area, through the peaks of both intercondylar tubercles, and through the attachments of the PRLM, the PRMM, and the PCL.

In twelve of the pathological specimens, cuts were made in an anteroposterior plane in seven specimens, and in mediolateral plane in five. Five of these twelve pathological specimens (three of the anteroposterior group, and two of the mediolateral group) had a previous MRI, and cuts were made in a plane as similar

as possible to MRI cuts, so that they supplied more information about the internal trabecular structure of bone associated to the information on soft tissue from MRI.

Photographs were taken of all cuts, and radiographs were made of them in a specimen and small animal X-ray system (Faxitron MX-20 radiography system, Faxitron Bioptics, Tucson, AZ, US). Osseous cuts were glued with cyanoacrylate to the envelop of the X-ray film used (Insight, Carestream Health, Rochester, NY, US), so there was almost no distortion of the X-ray images, and all specimen sizes were comparable with each other. The X-ray technique used was 30 Kv, 3 mA, for 3 seconds.

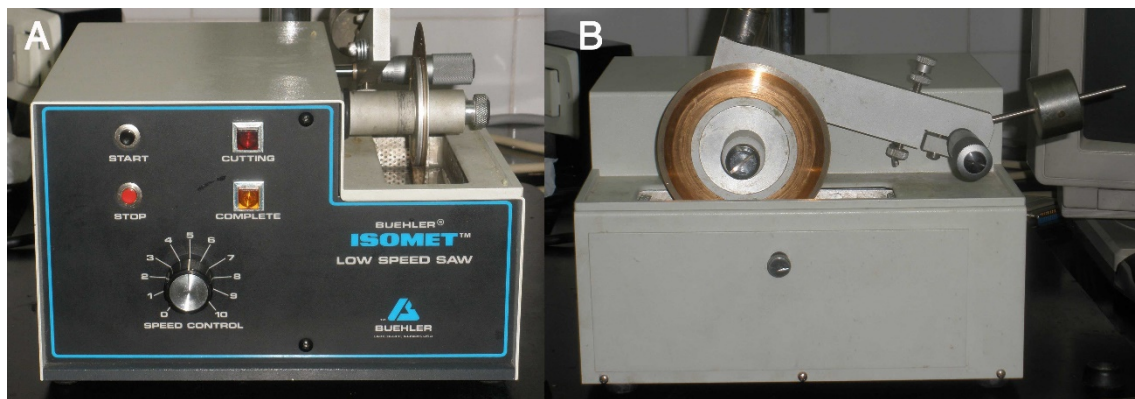


Figure 53. High precision low speed saw, lateral (A) and frontal (B) views.

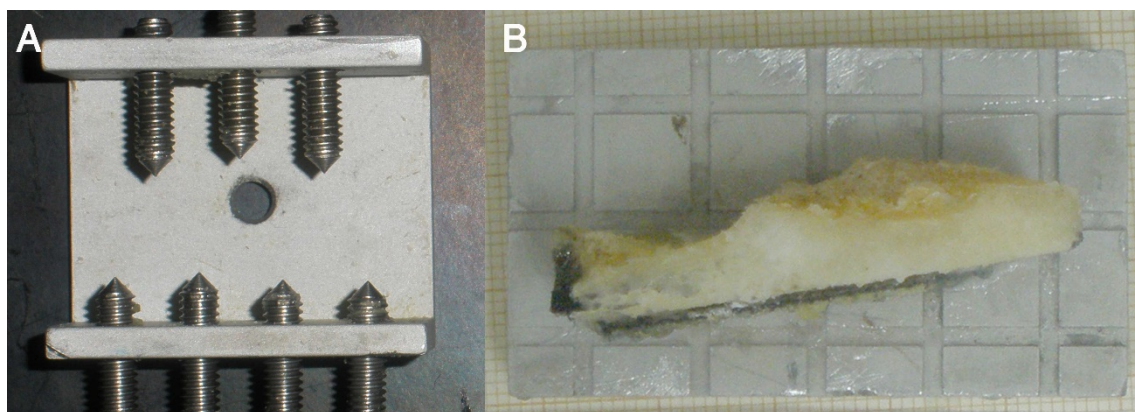


Figure 54. Clamp for low speed saw (A), and specimen holder with sliced specimen (B).

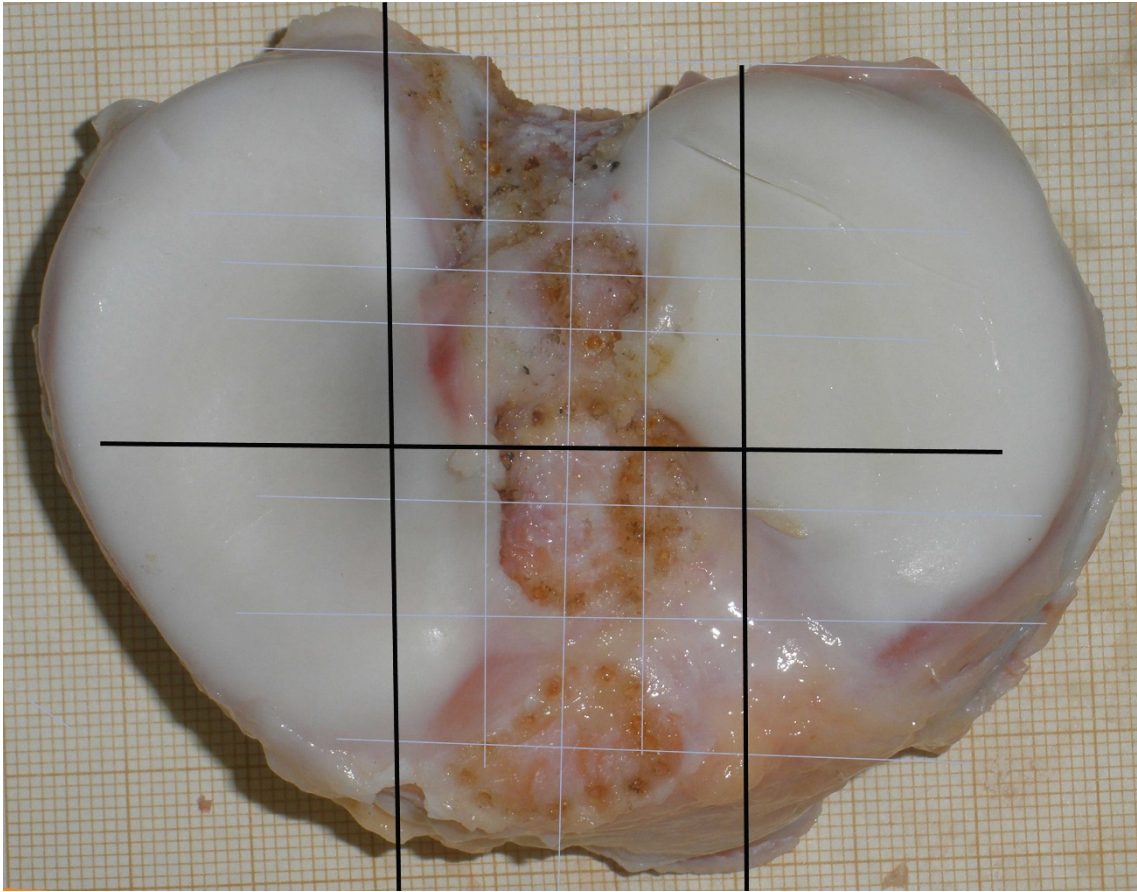


Figure 55. Tibia C. Photograph with schematic drawing of plan for sagittal and coronal cuts.

Histologic study of the Parsons' tubercle

In order to study the structure and relationship with surrounding soft tissues, nine specimens were processed by decalcification performed in nitric acid solution.

Dehydration was performed in a series of graded methyl alcohol (30% 1-2h, 50% 1-2h, 70% 1-2h or more if necessary, 90% 1-2h, 100% twice, 2-4h). Xylene was used for clearance.

Specimens were embedded in liquid paraffin twice (for 12h each) in an oven at 60° C. The anterior ridge and Parsons' tubercle were both sampled from the center of the bony landmark. Solid paraffin blocks were cut into 100 µm slices at room temperature with a rotating microtome (Microm HM 310, GMI, Ramsey, MN, US), and stored in a low temperature heater until they were stained.

Specimens were stained with the Masson's trichrome, Prico-Sirius red, and hematoxylin and eosin stain methods. To evaluate the relationship between the bony landmark and ACL ligament border, each specimen was carefully inspected

with a stereomicroscope (Nikon SMZ1500, Nikon, Tokyo, Japan), and with help from image analysis software (SigmaScanPro 5.0, Systat Software, Chicago, IL, US) for visual inspection and measurements. Visual and histological evaluations were assessed through their comparison to previous photographs and radiographs of the specimen.

Polarized light and scanning electronic microscopy was performed on some slices.

Study III. Qualitative study of the three-dimensional osseous attachment of the anterior cruciate ligament, assessed with arthroscopy

Patient selection

The study group included patients with a confirmed diagnosis of full ACL tear undergoing arthroscopic surgical repair in the Orthopaedic Surgery Service of the University Hospital Infanta Cristina of Badajoz, from December 2015 to August 2016. All patients included had a diagnostic MRI study previous to the surgery, stored in the regional Extremadura Health Service imaging database system (Centricity, GE Healthcare, Little Chalfont, UK). Nineteen nonpaired knees were included in the study. Twenty-two arthroscopically repaired ACL were excluded, because of technical problems with the video image (twelve patients) or its recording (ten patients).

Method

The ACL attachment area was inspected during surgery with an arthroscopy system (1188 HD Video Arthroscopy Tower System, Stryker, Kalamazoo, MI, US), and the ACL stump was debrided with a shaver or radiofrequency wand, or both. After exposing the ACL osseous footprint, a video was recorded from the anterolateral portal with an endoscopy video recorder (SDC Ultra, Stryker, Kalamazoo, MI, US), using a 30° wide-angle lens arthroscope optic and sheath (Karl Storz, Tuttlingen, DE). It was recorded slowly, with circular movements around the ACL footprint (and rotating the arthroscope at the same time), to complete a 360° view just above the bone. This was repeated at least twice more, bringing the arthroscope some mm higher with each turn. When available, a 70° optic was also used and the operation repeated. In three cases, both the anterolateral and anteromedial portals were used. In the last two cases recorded, a calibrated probe was placed in the anterolateral groove, to allow for measurements of the 3D model.

The video recorded was then visualized in video editing software (Vegas Pro 13.0, Sony, Minato, Tokyo, JP), and as many good quality still images as possible were exported.

In five cases images were cropped to obtain squared, central images. In the other fourteen cases, the original images (with a round image surrounded by black background) were used. All valid images of each patient were processed by

photogrammetry software (Autodesk Memento Beta version 1.13, Autodesk Inc., San Rafael, California, U.S.) to create 3D models, selecting the options of *Best Quality* and *Smart Crop* for all of them.

Qualitative investigation of the 3D model obtained also included observing contour lines, obtained in 3D point cloud and mesh processing software (CloudCompare, version 2.6.1 64 bit, GNU GPL software), as explained in Study I, Digital processing.

Study IV. Qualitative study of the anatomic limits of avulsed bone in tibial spine fractures

Patient selection

The study group included all patients with a confirmed diagnosis of tibial spine fracture and a CT imaging study, diagnosed and treated in the University Hospital Infanta Cristina of Badajoz, according to the database system (FileMaker Pro 5.5, FileMaker, Santa Clara, CA, US). Clinical history and operative reports from arthroscopic surgery was collected, when available. Images (including MRI cuts when available) were collected from the regional Extremadura Health Service imaging database system (Centricity, GE Healthcare, Little Chalfont, UK), from January 2006 to August 2015. Seven patients included in the database system, but without digital CT images, were excluded. Twenty-two nonpaired knees were included in the study.

Method

The bone avulsion was observed in all MRI and CT cuts available, and known anatomic osseous reference zones surrounding the attachment area of the ACL were recorded as damaged or intact.

Studies V – XIII

Method

Measurement on MRI studies (Studies V – XII)

Two sagittal cuts were selected from each MRI study: one through the MT, and one through the LT, both where their peak was highest. The measuring process was done with a raster graphics editor (Adobe Photoshop CS2, Adobe Systems, San Jose, CA, US). Images were converted to grayscale, then a filter *Gallery Photocopy* was used to leave an almost lineal drawing of the MRI image.

A perpendicular line was drawn from the tubercle peak to the inferior aspect of the cut image of the tibia over each selected and processed MRI slice, and with both measures the relative height of the tubercles was obtained in millimeters.

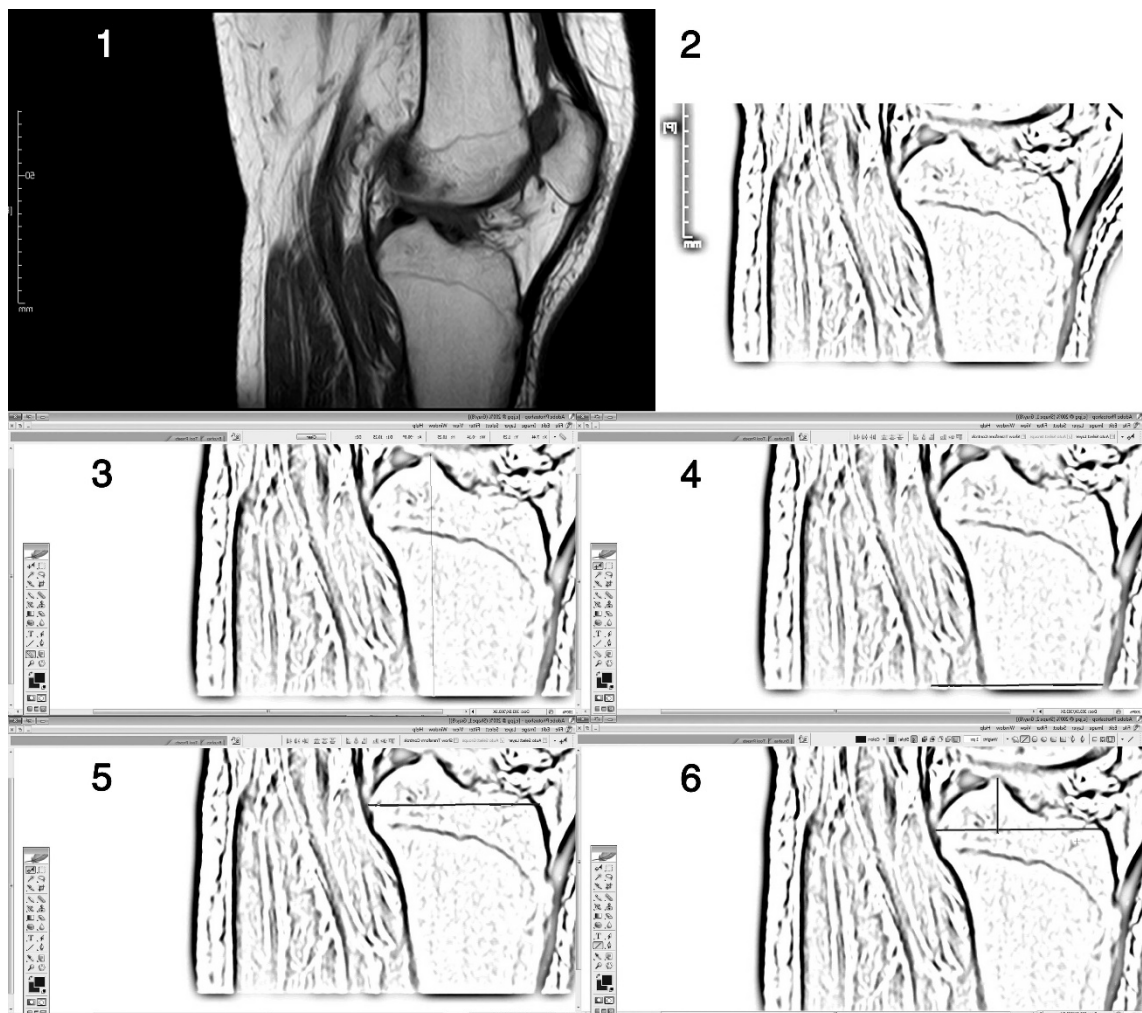


Figure 56. MRI sagittal cut through the lateral tubercle (1). Filter gallery photocopy applied over cut image Adobe Photoshop (2). LT height to the inferior aspect of the MRI slice (3). A parallel line is drawn to the visible inferior tibial cut (4). That line is ascended to the widest aspect of the visible plateau, and AP depth is measured (5). A perpendicular is drawn from this line to the tubercle peak, and a measurement is made from the point where both lines cross each other to the posterior aspect of the plateau (6).

A line parallel to the inferior “cut” of the tibia was drawn in the longest anteroposterior dimension, and a perpendicular from the tip of each tubercle cut that line: the distance from this intersection to the posterior tibial aspect was recorded, thus obtaining the distance of each tubercle relative to the posterior tibia (Fig. 56).

Measurements in standing AP radiographs (Studies V – XIII)

Radiographs collected included a close-up of a standing AP and a non-weight-bearing lateral projection. Because calibration of radiographs was not a standard practice in all Radiology services in the region, a ratio had to be used.

Measurement of the tibial tubercles in radiographs was therefore done following Donnelly⁶², by selecting the tibial plateau line, the densest aspect of the plateau – usually the anterior condylar margin, from the most medial to the most lateral point. A perpendicular to each tubercle was drawn, and the distances of the plateau line and both perpendiculars were recorded.

The ratio of the height of each tubercle above the tibial plateau to the overall ML width of the tibial plateau was calculated (see Fig. 57, lateral tubercle height ratio = LTh/W , medial tubercle height ratio = MTh/W).

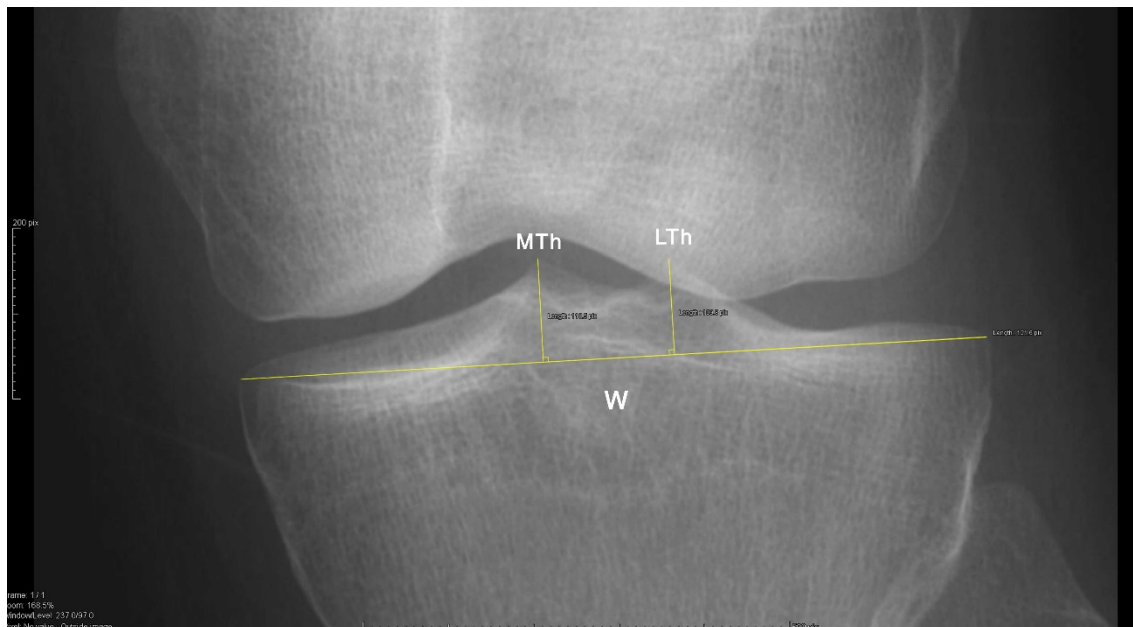


Figure 57. Snapshot of measurements taken over the image with a DICOM viewer: tibial plateau line, with two perpendiculars drawn to the peak of the medial and lateral tubercles. ML width (W), MT height (MTh) and LT height (LTh) appear in pixels (pix).

Study V. Qualitative and quantitative investigation of tibial tubercles in the adult population in radiography and MRI

Patient selection

The study group included patients with MRI and radiographs of the same knee in the period from June 2013 to May 2014, available in the regional Extremadura Health Service imaging database system (Centricity, GE Healthcare, Little Chalfont, UK). To randomize the selection, a function was used in Microsoft Excel (Microsoft, Redmond, WA, US) to generate pseudo-random numbers among the 365-day span of the study, and one patient with MRI study of each consecutive generated day (who also had an X-ray study of the same knee in a previous or later date, not earlier or later than one year) was selected.

Patients who had MR and radiographic imaging studies but had osseous lesions were excluded from this study: those excluded had osteoarthritic changes (37%), or fractures (11%). Patient selection was stopped when one hundred nonpaired knees were included in the study.

Study VI. Qualitative and quantitative investigation of the tibial tubercles in children in radiography and MRI

Patient selection

The study group included all patients without epiphyseal fusion, which had MRI and radiographic studies of the same knee in the period from January 2009 to September 2014. Images were collected from the regional Extremadura Health Service imaging database system (Centricity, GE Healthcare, Little Chalfont, UK). Patients with osseous or osteochondral lesions were also included. Seventy-nine nonpaired knees were included in the study. Patients with knee dysplasia (two cases) were excluded.

Study VII. Qualitative and quantitative investigation of the tibial tubercles in adults with osteochondritis

Patient selection

The study group included all adult patients with a confirmed diagnosis of osteochondritis dissecans, diagnosed and treated in the University Hospital Infanta Cristina of Badajoz from January 2009 to December 2014, according to the database system (FileMaker Pro 5.5, FileMaker, Santa Clara, CA, US). All patients with MRI and radiographic studies of the same knee were included in the study, and their images collected from the regional Extremadura Health

Service imaging database system (Centricity, GE Healthcare, Little Chalfont, UK). Twenty-five nonpaired knees were included in the study.

Study VIII. Qualitative and quantitative investigation of the tibial tubercles in children with osteochondritis

Patient selection

The study group included all patients without epiphyseal fusion with a confirmed diagnosis of osteochondritis dissecans, and with digital radiographic and MRI studies, from January 2009 to December 2014. Patients had been studied in the University Hospital Infanta Cristina of Badajoz. Clinical history was obtained from the hospital's database system (FileMaker Pro 5.5, FileMaker, Santa Clara, CA, US). Images were collected from the regional Extremadura Health Service imaging database system (Centricity, GE Healthcare, Little Chalfont, UK).

Seventeen nonpaired knees were included in the study.

Study IX. Qualitative and quantitative investigation of the tibial tubercles in patients with osteonecrosis

Patient selection

The study group included all patients with a diagnosis of osteonecrosis, who had MRI and radiographic studies of the same knee in the period from January 2009 to December 2014. All patients were diagnosed and treated in the University Hospital Infanta Cristina of Badajoz, according to the database system (FileMaker Pro 5.5, FileMaker, Santa Clara, CA, US). Their images were collected from the regional Extremadura Health Service imaging database system (Centricity, GE Healthcare, Little Chalfont, UK). Fifty-one knees of forty-nine patients were included in the study.

Study X. Qualitative and quantitative investigation of the Parsons' knob in the general population

Patient selection

The study group included patients with MRI and radiography studies of the same knee in the period from June 2009 to December 2013, available the regional Extremadura Health Service imaging database system (Centricity, GE Healthcare, Little Chalfont, UK). To randomize the selection, a function was used in Microsoft Excel (Microsoft, Redmond, WA, US) to generate pseudo-random numbers among the 1643 days of the study's time span, and one patient with MRI

or radiographic study of each consecutive generated day (who also had a radiographic or MRI study, respectively, of the same knee in a previous or later date, not earlier or later than one year) was selected. Patient selection was stopped when one hundred and fifty-eight nonpaired knees had been included in the study.

Method

In all selected knees the presence of a Parsons' knob in either image was recorded: when present, it was given a number for radiographic size and a letter for radiographic type according to Pećina et al.⁶³. The absolute measurement of base and height of the Parsons' knob in MRI was recorded in millimeters, by selecting the sagittal cut where the knob seemed higher. The diagnosis and Ahlbäck OA grade of each imaged knee was also recorded for further analysis.

Study XI. Qualitative and quantitative investigation of osteoarthritic changes in tibias with a previous valgus osteotomy

Patient selection

The study group included all patients who had undergone proximal tibial valgus osteotomy surgery at least 5 years before the last imaging study, and who had radiographic studies of the same knee available, in the period from June 2009 to December 2013. All patients had been treated in the Orthopaedic Surgery Service at the University Hospital Infanta Cristina of Badajoz, according to the database system (FileMaker Pro 5.5, FileMaker, Santa Clara, CA, US). Their images were collected from the regional Extremadura Health Service imaging database system (Centricity, GE Healthcare, Little Chalfont, UK). Sixty knees (of fifty-one patients) were included in the study.

Method

In all selected knees the Parsons' knob, if present, was given a number and letter for radiographic size and type according to the Pećina classification⁶³. Tibiofemoral angle was measured according to McDaniel's best reported method⁶⁰, by utilizing the center of the base of the tibial tubercles (Fig. 58). Alignment into varus, valgus or normal, and OA grade according to Ahlbäck were also recorded. Medial and lateral tubercle osteophytes were classified according to Moon⁶⁴.

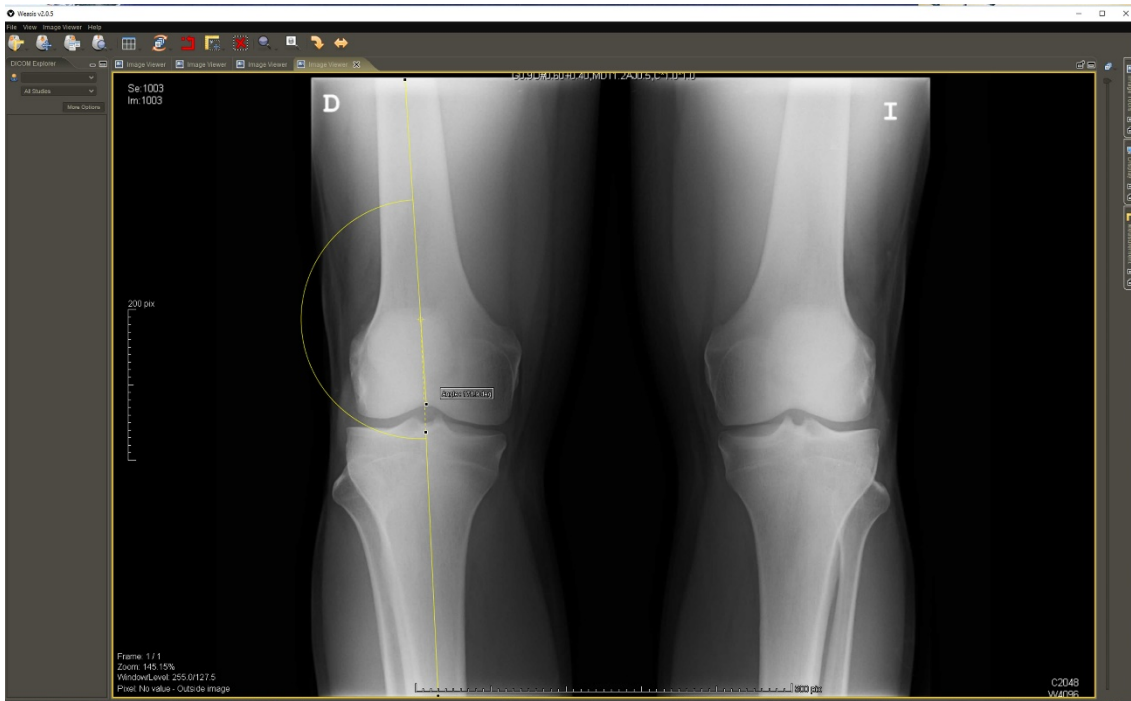


Figure 58. Tibiofemoral angle measured in an AP standing radiograph of a normal tibia.

Study XII. Qualitative and quantitative investigation of tibias in knees with osteochondral fractures

Patient selection

The study group included all patients with a confirmed diagnosis of osteochondral fracture, who had MRI and radiography studies of the same knee in the period from January 2009 to December 2014. All patients had been treated in the Orthopaedic Surgery Service at the University Hospital Infanta Cristina of Badajoz, according to the database system (FileMaker Pro 5.5, FileMaker, Santa Clara, CA, US). Their images were collected from the regional Extremadura Health Service imaging database system (Centricity, GE Healthcare, Little Chalfont, UK). Nine nonpaired knees were included in the study.

Method

The affected femoral condyle, and the presence of patellar tracking problems, were also recorded for further analysis.

Study XIII. Qualitative and quantitative investigation of tibias in osteoarthritic knees with absence of ACL

Patient selection

The study group included all patients with a visually confirmed diagnosis of ACL chronic tear or absence during arthrotomy (Fig. 59), of those undergoing TKA surgery from May 2014 to June 2015 in the Orthopaedic Surgery Service of the University Hospital Infanta Cristina of Badajoz. Twelve nonpaired knees were identified as ACL absent and included in the study.

Previous radiographs were obtained from the regional Extremadura Health Service imaging database system (Centricity, GE Healthcare, Little Chalfont, UK), including at least a standing AP and a non-weight-bearing lateral projection.

Method

Knees were classified into Ahlbäck OA grades, and the tibiofemoral angle was also measured.

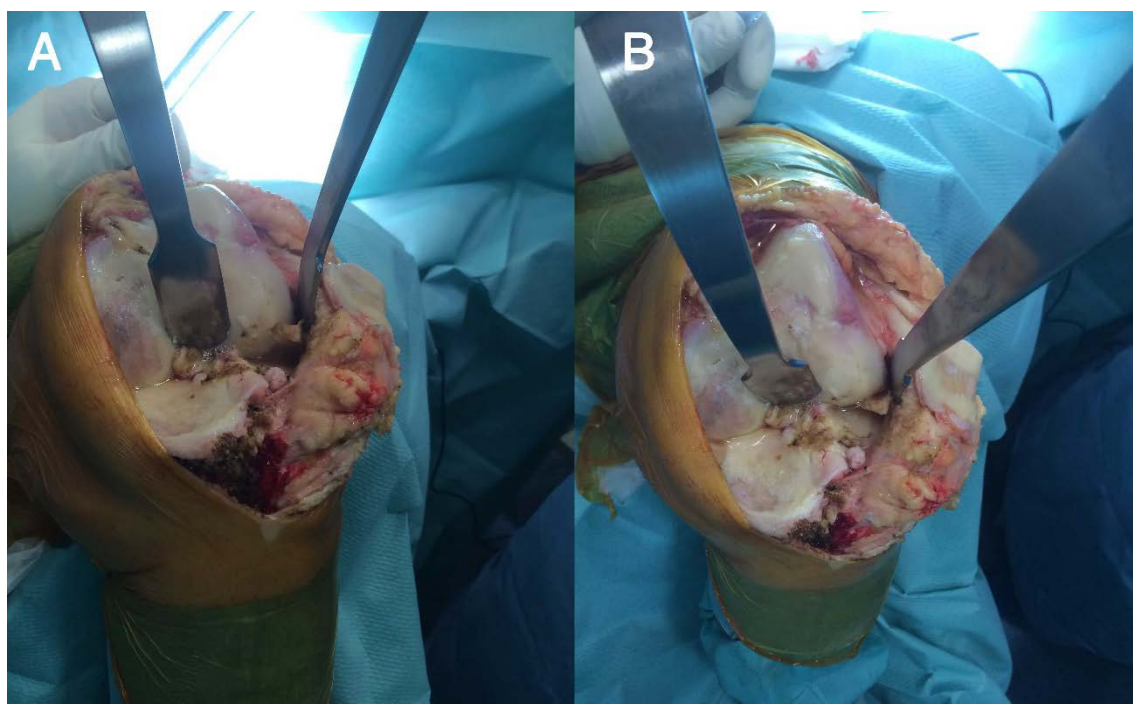


Figure 59. Intraoperative photographs of an ACL-deficient knee included in this study

IV. Results

IV.1. Basic anatomy

IV.1.1. Normal tibias

IV.1.1.1. Demographic values

There were 6 right and 8 left tibial plateaus, with a mean age of 49 years (range, 16 to 76 years) at the time of death. Specimens had an average tibial mediolateral width (and standard deviation) of 50.4 ± 2.8 mm, and anteroposterior depth of 72.4 ± 4.4 mm.

Four specimens showed osteoarthritic changes: two grade IV (male, paired), and two grade II (male, paired) according to the Outerbridge classification.

IV.1.1.2. Area measurements

2 specimens were damaged in the posterior facet fully, 4 partially, and 2 marginally, 3 showed partial damage anteriorly (affecting areas 5, 9).

An independent *t*-test found a statistically significant difference in proximal tibial width and depth depending on sex: AP depth, $t(12)=2.512$, $p=0.039$ (mean male, 52.6 mm, female, 46.8 mm; mean difference, 5.8 ± 5.4 mm); ML width, $t(12)=3.107$, $p=0.010$ (mean male, 75.4 mm, female, 67.9 mm; mean difference, 7.5 ± 5.3 mm).

No statistically significant difference was found between right and left knees: AP depth, $t(12)=0.614$, $p=0.538$ (mean left, 50.8 mm, right, 49.2 mm); $t(12)=0.419$, $p=0.685$ (mean left, 72.8 mm, right, 71.4 mm).

Selected areas (Fig. 60) were measured in all specimens. These measurements were tested for normality (Table 1), and mean size was obtained in square millimeters and in percentage of total area (Table 2).

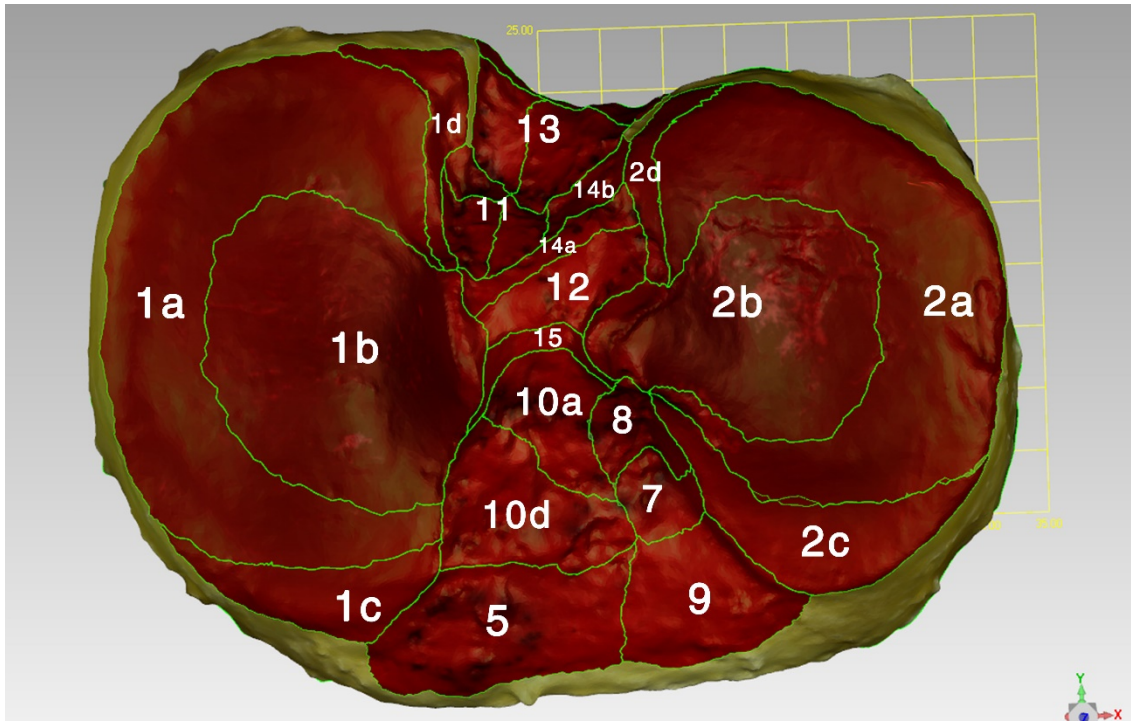


Figure 60. 3D model of tibia L. All areas selected have been highlighted and labelled

Table 1. Tests of normality of osseous areas.

	KOLMOGOROV-SMIRNOV			SHAPIRO-WILK		
	Statistic	df	Sig.	Statistic	df	Sig.
1A	.177	6	.200*	.923	6	.525
1B	.182	6	.200*	.938	6	.646
1C	.261	6	.200*	.896	6	.351
1D	.145	6	.200*	.980	6	.951
2A	.239	6	.200*	.906	6	.411
2B	.277	6	.169	.836	6	.120
2C	.157	6	.200*	.944	6	.689
2D	.261	6	.200*	.895	6	.344
5	.247	6	.200*	.857	6	.180
7	.195	6	.200*	.922	6	.517
8	.258	6	.200*	.879	6	.263
9	.359	6	.015	.793	6	.051
10	.200	6	.200*	.977	6	.937
11	.247	6	.200*	.876	6	.253
12	.267	6	.200*	.885	6	.293
13	.165	6	.200*	.947	6	.717
14	.318	6	.058	.801	6	.060
15	.269	6	.198	.817	6	.083
AP	.164	6	.200*	.947	6	.712
ML	.300	6	.099	.780	6	.039

*. This is a lower bound of the true significance.

Table 2. Mean areas in mm² and in percentage of total area of the tibia, with 95% CI.

AREA	Mean (mm²)	95% CI (mm²)	Mean (%)	95% CI (%)
1a	620.95	529.63 – 712.27	18.66	16.55–20.77
1b	487.09	425.00 – 549.17	14.94	13.93 –15.95
1c	79.51	58.87 – 100.14	2.36	1.84 –2.89
1d	52.96	34.17 – 71.74	1.51	1.04 –1.99
2a	532.24	446.42 – 618.06	16.08	14.54 –17.64
2b	409.28	372.23 – 446.32	12.05	10.37 –13.72
2c	67.10	41.98 – 92.23	1.96	1.36 –2.56
2d	30.28	19.06 – 41.51	0.85	0.63 –1.07
5	226.50	180.20 – 272.80	6.90	5.56 –8.24
7	48.08	34.47 – 61.69	1.47	1.04–1.90
8	55.14	43.23 – 67.04	1.67	1.35 –2.00
9	155.20	121.45 – 188.94	4.46	3.63 –5.29
10	196.67	162.85 – 230.48	5.96	5.25 –6.66
11	105.97	94.51 – 117.42	3.32	2.91 –3.72
12	64.99	56.07 – 73.92	2.02	1.74 –2.30
13	208.65	159.47 – 257.83	5.31999	4.4389 –6.2011
14	51.22	41.14 – 61.30	1.55286	1.3519 –1.7538
15	21.40	15.24 – 27.56	0.6402	0.4901 –0.7903

IV.1.1.3. Soft tissue attachments

Selected attachment areas (Fig. 61) were measured in all specimens. These measurements were tested for normality (Table 3), and mean size was obtained in square millimeters and in percentage of total area (Table 4).

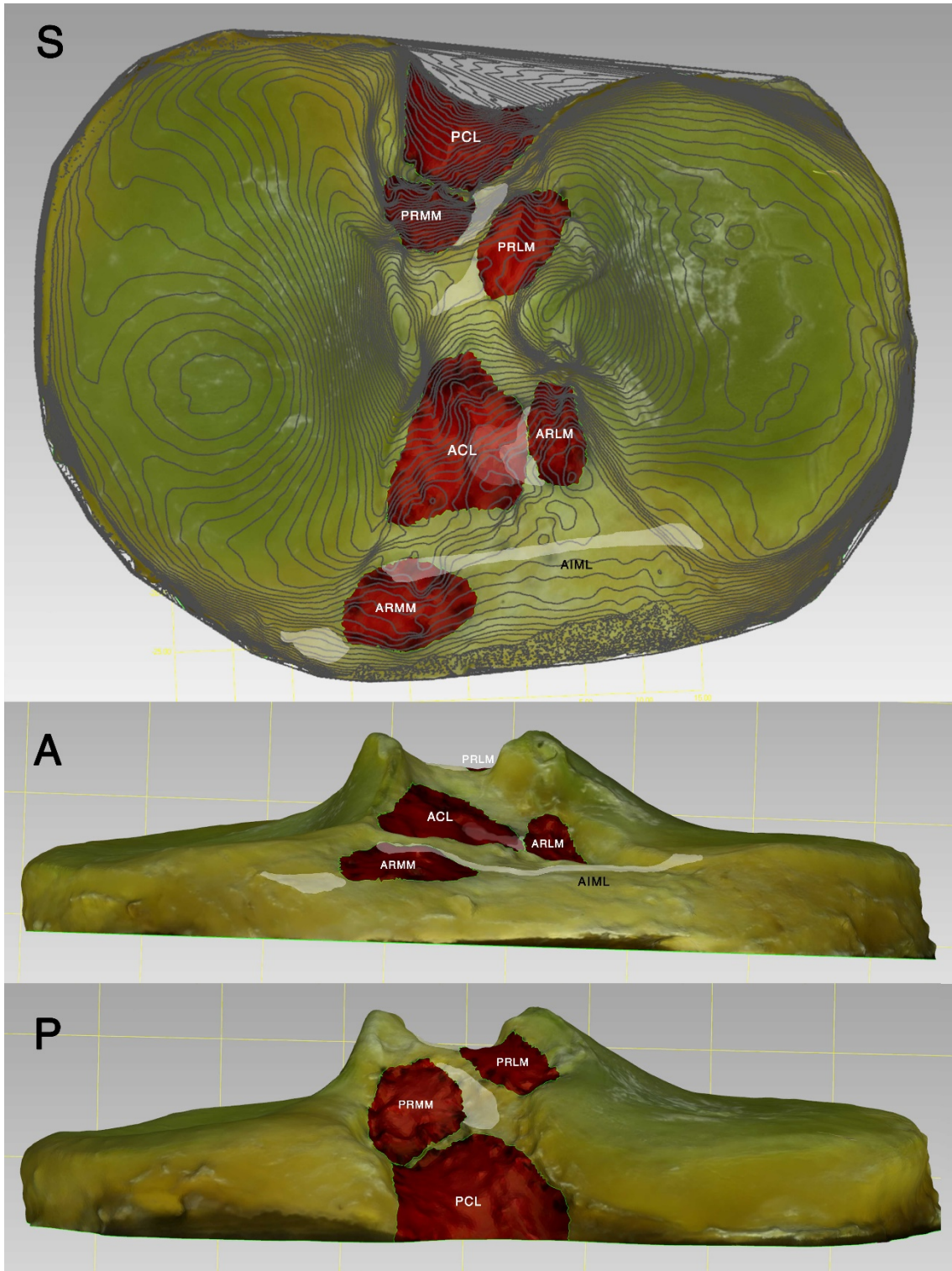


Figure 61. 3D model of tibia L. Insertion areas highlighted and labelled. In white, approximate areas of attachment of accessory fibers of the four meniscal roots. The approximate course of the anterior intermeniscal ligament (AIML) is also drawn.

Table 3. Tests of normality of footprint areas.

	KOLMOGOROV-SMIRNOV			SHAPIRO-WILK		
	Statistic	df	Sig.	Statistic	df	Sig.
ARMM	.246	8	.168	.919	8	.420
ARLM	.160	8	.200*	.980	8	.963
PRLM	.187	8	.200*	.917	8	.408
PRMM	.219	8	.200*	.909	8	.348
ACL	.195	8	.200*	.874	8	.164
ACL-AM	.172	8	.200*	.943	8	.641
ACL-AMM	.228	8	.200*	.893	8	.251
ACL-AML	.199	8	.200*	.853	8	.102
ACL-PL	.216	8	.200*	.867	8	.142
PCL	.175	8	.200*	.939	8	.604
PCL-AL	.247	8	.166	.892	8	.247
PCL-PM	.139	8	.200*	.981	8	.969
AGE	.176	8	.200*	.949	8	.702

*. This is a lower bound of the true significance.

Table 4. Mean attachment areas in mm² and in percentage of total area of the tibia, with 95% CI.

	Mean (mm ²)	95% CI (mm ²)	Mean (%)	95% CI (%)
ARMM	38.78	33.30 – 44.26	1.19	1.09 – 1.29
ARLM	78.51	64.92 – 92.11	2.42	1.99 – 2.85
PRLM	36.10	30.52 – 41.69	1.14	0.93 – 1.36
PRMM	51.33	41.68 – 60.99	1.56	1.36 – 1.76
ACL	145.18	120.45 – 169.91	4.40	3.88 – 4.92
ACL-AM	84.27	66.80 – 101.74	2.53	2.18 – 2.87
ACL-AMM	46.60	36.71 – 56.49	1.40	1.20 – 1.60
ACL-AML	37.69	29.62 – 45.75	1.13	0.97 – 1.29
ACL-PL	60.87	51.59 – 70.15	1.87	1.62 – 2.13
PCL	144.56	115.21 – 173.90	3.71	3.13 – 4.30
PCL-AL	64.88	51.30 – 78.47	1.78	1.49 – 2.07
PCL-PM	74.83	59.16 – 90.51	1.92	1.59 – 2.25

A multiple regression was run to predict AP and ML size of the proximal tibia from all selected attachment areas, and a dummy variable was included for left vs. right knees.

It was found that the regression model changed when the dummy variable was included, with the left knees having B=2.239 for ML width, and B=1.773 for AP depth, when the dummy variable was included. The regression model also changed if only left or right knees were selected. In all cases, the regression models obtained had an $R^2=1$.

A regression model was also run for each attachment area separately, to predict its size from its specimen's AP and ML size, and the dummy variable. The dummy variable was included in all cases in the regression models, although it was not statistically significant in any case (Table 5 – Table 10).

Table 5. Regression model to predict AP and ML size from ARLM attachment area, including dummy variable (Left).

ARLM	Sum of Squares	df	Mean Square	F	Sig.
Regression	544.606	3	181.535	4.129	.048
Residual	351.732	8	43.966		
Total	896.338	11			
R	R Square	Adjusted R Square		Std. Error of the Estimate	
.779	.608	.460		6.63072	
	Unstandardized Coefficients		Standardized Coefficients	t	Sig.
	B	Std. Error	Beta		
(Constant)	-52.789	26.254		-2.011	.079
Left	2.938	3.841	.170	.765	.466
AP	-.250	1.102	-.130	-.227	.826
ML	1.410	.920	.881	1.533	.164

Table 6. Regression model to predict AP and ML size from ARMM attachment area, including dummy variable (Left).

ARMM	Sum of Squares	df	Mean Square	F	Sig.
Regression	1710.915	3	570.305	2.460	.147
Residual	1622.647	7	231.807		
Total	3333.562	10			
R	R Square	Adjusted R Square		Std. Error of the Estimate	
.716	.513	.305		15.22520	
	Unstandardized Coefficients		Standardized Coefficients	t	Sig.
	B	Std. Error	Beta		
(Constant)	-37.047	62.476		-.593	.572
Left	-11.650	9.278	-.333	-1.256	.250
AP	-4.097	2.531	-1.087	-1.619	.150
ML	4.469	2.124	1.416	2.105	.073

Table 7. Regression model to predict AP and ML size from PRLM attachment area, including dummy variable (Left).

PRLM	Sum Squares	of	df	Mean Square	F	Sig.
Regression	209.324		3	69.775	1.224	.362
Residual	456.114		8	57.014		
Total	665.438		11			
R	R Square		Adjusted R Square	Std. Error of the Estimate		
.561	.315		.058	7.55078		
	Unstandardized Coefficients		Standardized Coefficients	t	Sig.	
	B	Std. Error	Beta			
(Constant)	-7.186	29.897		-.240	.816	
Left	2.225	4.374	.149	.509	.625	
AP	-2.005	1.255	-1.214	-1.597	.149	
ML	1.944	1.048	1.410	1.856	.101	

Table 8. Regression model to predict AP and ML size from PRMM attachment area, including dummy variable (Left).

PRMM	Sum Squares	of	df	Mean Square	F	Sig.
Regression	555.566		3	185.189	.815	.521
Residual	1818.416		8	227.302		
Total	2373.982		11			
R	R Square		Adjusted R Square	Std. Error of the Estimate		
.484	.234		-.053	15.07654		
	Unstandardized Coefficients		Standardized Coefficients	t	Sig.	
	B	Std. Error	Beta			
(Constant)	-37.009	59.695		-.620	.553	
Left	-3.016	8.734	-.107	-.345	.739	
AP	.239	2.506	.077	.095	.926	
ML	1.041	2.092	.400	.498	.632	

Table 9. Regression model to predict AP and ML size from ACL attachment area, including dummy variable (Left).

ACL	Sum Squares	of	df	Mean Square	F	Sig.
Regression	17024.355		3	5674.785	17.094	.001
Residual	2655.809		8	331.976		
Total	19680.164		11			
R	R Square		Adjusted R Square	Std. Error of the Estimate		
.930	.865		.814	18.22021		
	Unstandardized Coefficients		Standardized Coefficients	t	Sig.	
	B	Std. Error	Beta			
(Constant)	-331.129	72.142		-4.590	.002	
Left	-10.909	10.555	-.135	-1.033	.332	
AP	2.325	3.029	.259	.768	.465	
ML	5.068	2.528	.676	2.005	.080	

Table 10. Regression model to predict AP and ML size from PCL attachment area, including dummy variable (Left).

PCL	Sum of Squares	df	Mean Square	F	Sig.
Regression	3076.335	3	1025.445	6.433	.138
Residual	318.831	2	159.416		
Total	3395.166	5			
R	R Square	Adjusted R Square	Std. Error of the Estimate		
.952	.906	.765	12.62599		
	Unstandardized Coefficients		Standardized Coefficients	t	Sig.
	B	Std. Error	Beta		
(Constant)	375.650	400.208		.939	.447
Left	-8.383	16.875	-.176	-.497	.669
AP	-16.312	11.335	-.808	-1.439	.287
ML	8.344	3.110	1.312	2.683	.115
ML	8.344	3.110	1.312	2.683	.115

IV.1.2. Pathological tibias

IV.1.2.1. Demographic values and osteoarthritis

Almost half of the studied specimens were classified as Ahlbäck OA grade 3. Only 10 tibias were classified as grade 0 (all of them from Study I), and 9 were classified as grade 4 (Fig. 62).

Most specimens from Study I were classified during arthrotomy as Ahlbäck grade 0, but for a pair (male, 63 years) classified as grade 3, and another pair (male, age 76), classified as grade 1. These corresponded to specimen pairs classified as Outerbridge grades IV and II in Study I, respectively.

Approximately 65% of those included were female (Fig. 63), and the most common diagnosis was osteoarthritis (Fig. 64).

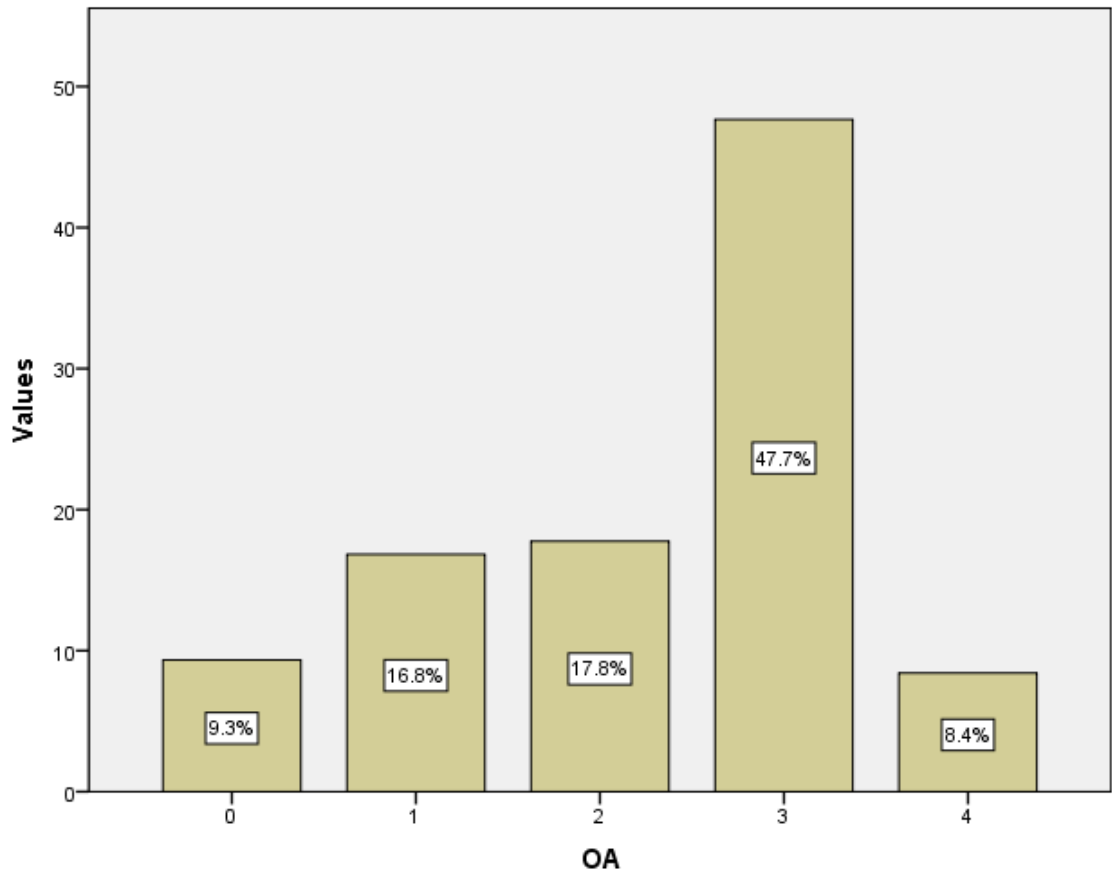


Figure 62. Histogram of Ahlbäck OA grade distribution in the sample studied, in percentage.

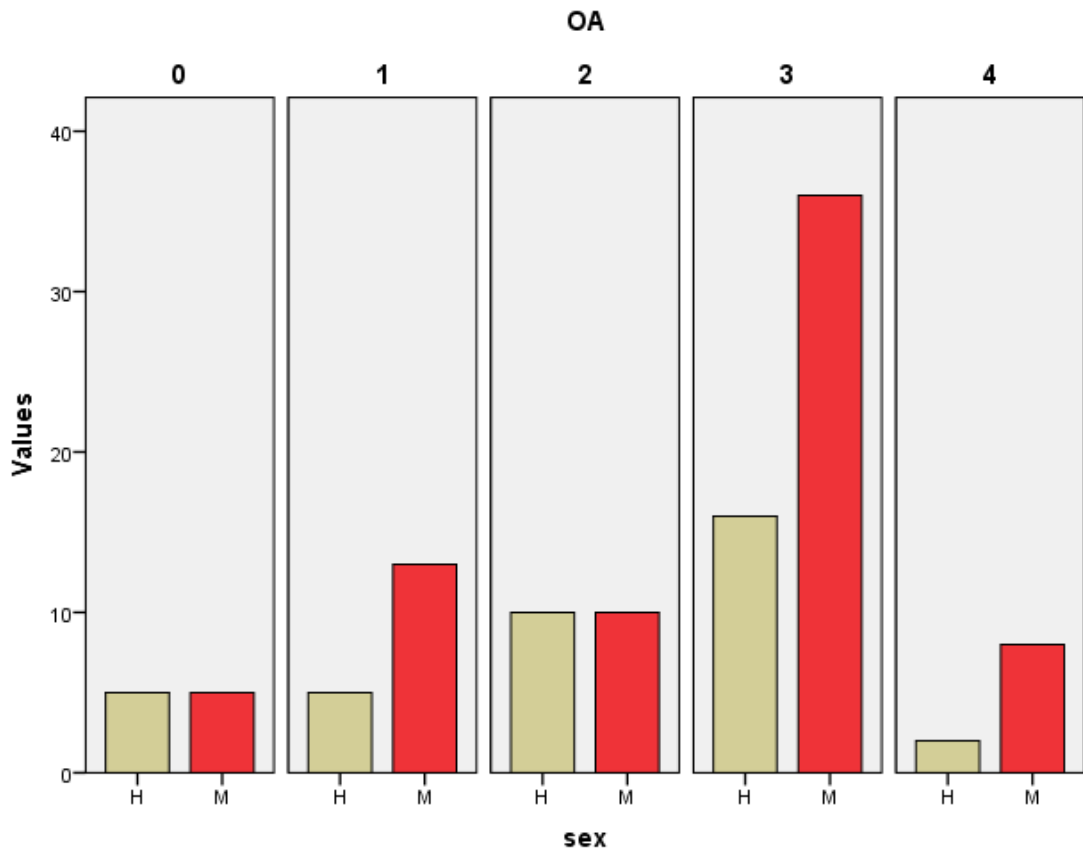


Figure 63. Histogram of sex distribution in each Ahlbäck OA grade, in absolute numbers.

IV.1.2.2. Measurements and pathology

The quality of the surface was excellent (grade A) in 45% of specimens studied, good (grade B) in 34%, fair (grade C) in 17%, and poor (grade D) in 2%.

The quality of the available 3D models showed no correlation with knee OA: $r_s(85)=0.078$, $p=0.475$.

Testing for normality distribution of numeric data (Table 11) showed that age, tubercle slope (MTAxis, LTAxis, MTLTAxis) and the AP depth of the Parsons' knob (G_LAT) had a normal distribution. The rest of numeric data significantly deviated from a normal distribution, although 28 tibias that did not have all variables recorded were excluded from the analysis.

No significant association was found between age and knee OA (Fig. 65).

A Kruskal-Wallis H test showed that there was a statistically significant difference in varus degree between the different Ahlbäck OA grade groups: $\chi^2(3)=33.644$, $p<0.001$, with a mean varus degree of 3.5° (95% CI, $1.2^\circ - 5.8^\circ$) for OA grade 1; 7.1° (95% CI, $5.5^\circ - 8.8^\circ$) for OA grade 2; 8.9° (95% CI, $8.2^\circ - 9.6^\circ$) for OA grade 3; and 13.3° (95% CI, $10.3^\circ - 16.3^\circ$) for OA grade 4 (Fig. 66).

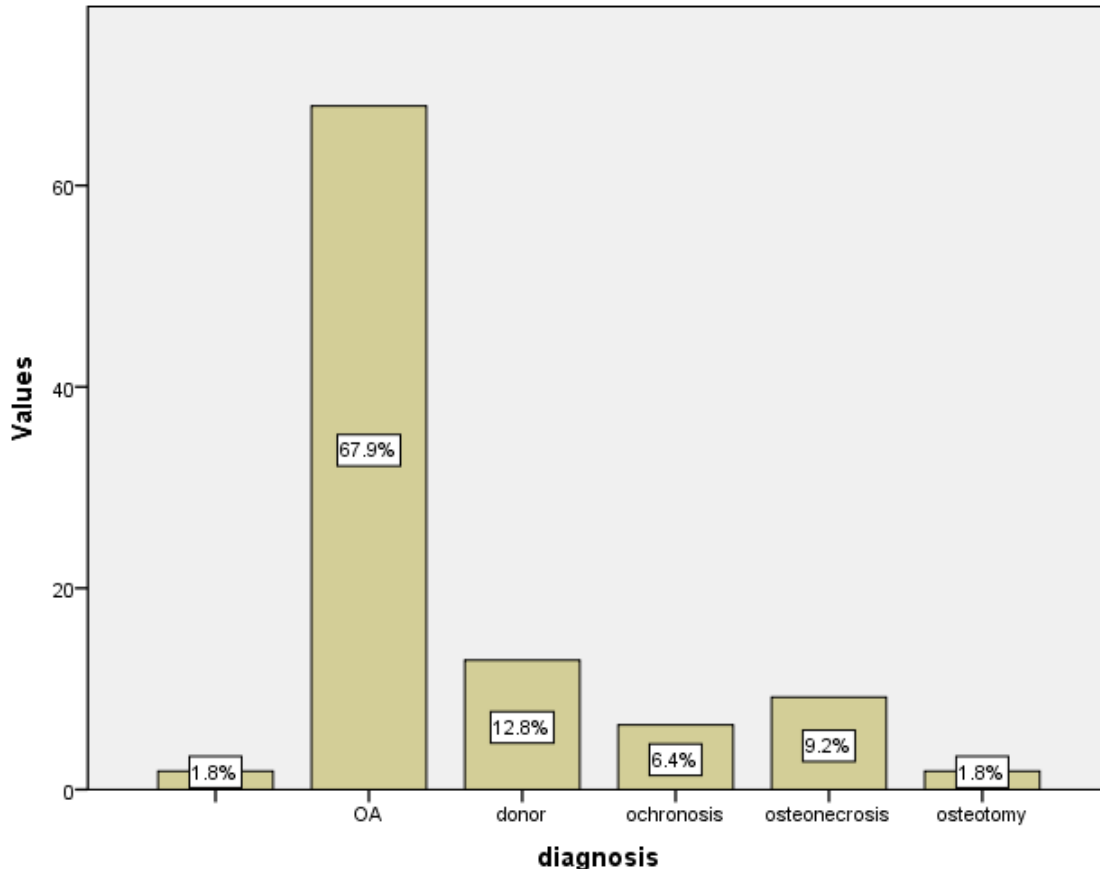


Figure 64. Histogram of diagnosis distribution in the sample studied, in percentage.

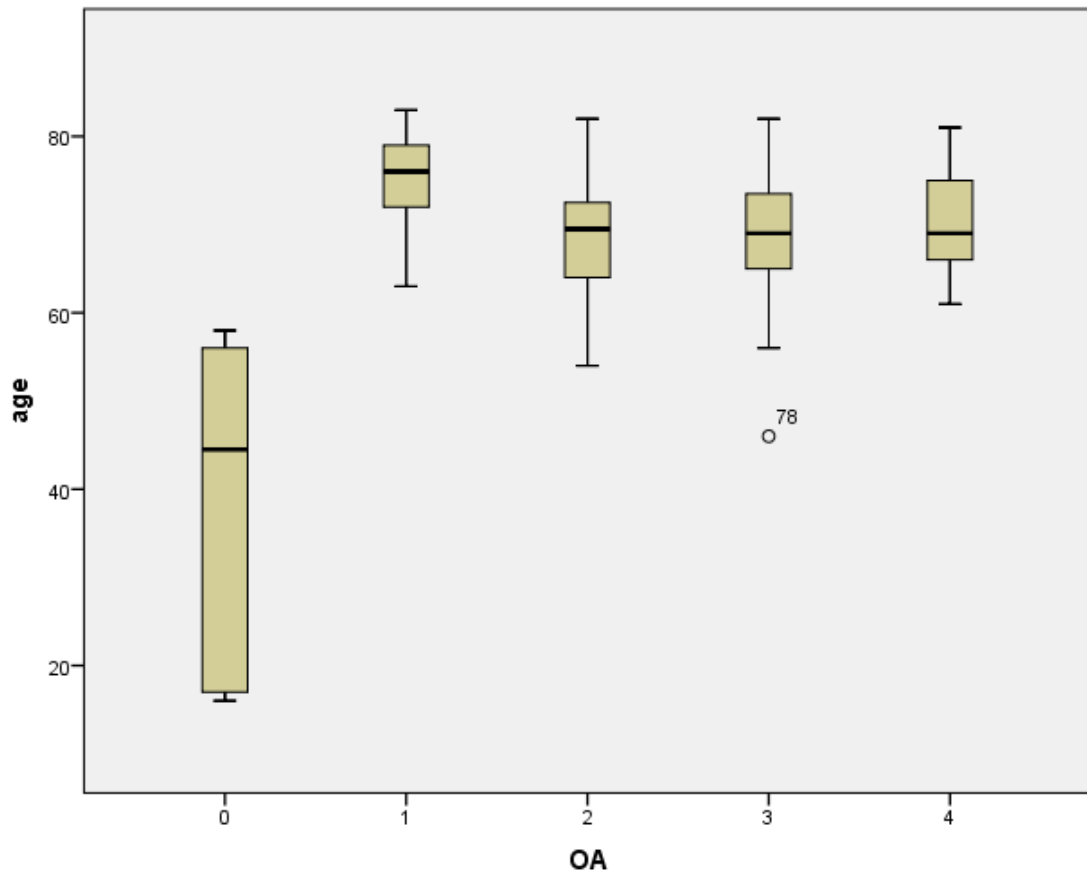


Figure 65. Box-and-whisker plot of age distribution in each Ahlbäck OA grade.

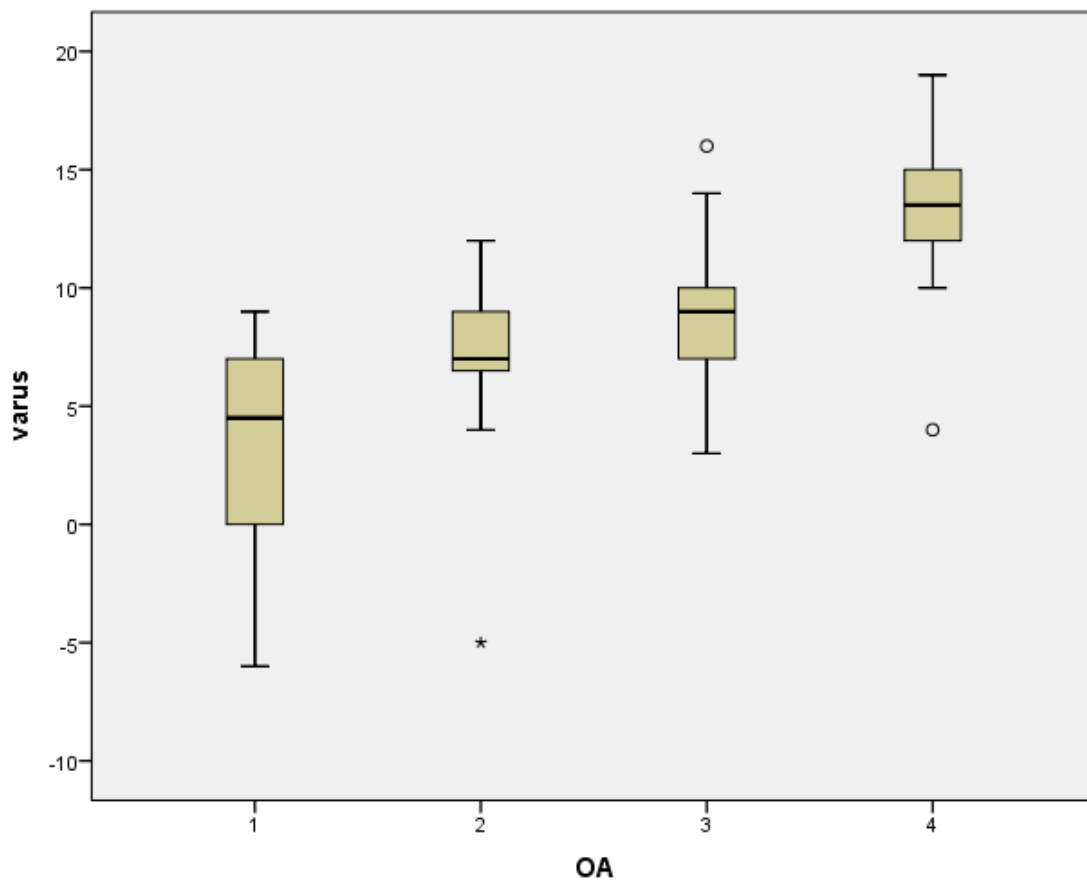


Figure 66. Box-and-whisker plot of tibiofemoral angle distribution in each Ahlbäck OA grade.

Table 11. Results for normality distribution testing of numeric data of the sample (of the 68 specimens for which all data was collected).

	Kolmogorov Smirnov	SIG.	Shapiro-Wilk	SIG.
AGE	0.086	0.200*	0.966	0.058
VARUS	0.146	0.001	0.952	0.011
MT Depth	0.152	0.000	0.866	0.000
MT Width	0.110	0.040	0.944	0.004
LT Depth	0.126	0.009	0.905	0.000
LT Width	0.136	0.003	0.915	0.000
MTAXIS	0.069	0.200*	0.988	0.775
LTAXIS	0.085	0.200*	0.978	0.259
MTLTAXIS	0.081	0.200*	0.976	0.216
G Depth	0.133	0.004	0.942	0.003
G Width	0.104	0.063	0.960	0.030
Bd AL Depth	0.261	0.000	0.853	0.000
Bd AL Width	0.441	0.000	0.443	0.000
Bd PM Depth	0.297	0.000	0.779	0.000
Bd PM Width	0.441	0.000	0.545	0.000
Bd PL Depth	0.329	0.000	0.782	0.000
Bd PL Width	0.389	0.000	0.704	0.000
EF_Pain_Move	0.331	0.000	0.711	0.000
EF_Pain_Rest	0.489	0.000	0.446	0.000
EF_Pain_Stair	0.312	0.000	0.734	0.000
EF_Ext	0.266	0.000	0.765	0.000
EF_Flexum	0.502	0.000	0.395	0.000
EF_ROM	0.112	0.034	0.950	0.009
EF_Varus	0.433	0.000	0.578	0.000
EF_Inest_ML	0.445	0.000	0.588	0.000
EF_Inest_AP	0.526	0.000	0.274	0.000
EF_SCORE	0.136	0.003	0.912	0.000
EF_Pt_Walk	0.286	0.000	0.776	0.000
EF_Pt_Help	0.310	0.000	0.725	0.000
EF_Pt_Climb	0.271	0.000	0.785	0.000
EF_FUNCT	0.200	0.000	0.870	0.000

*. This is a lower bound of the true significance.

NOTE. G = Parsons' knob. Bd = corner. EF_ = Physical examination items (from the American Knee Society Clinical Rating System). Knee Score (SCORE) includes pain with movements (Pain_Move), pain while resting (Pain_Rest), pain with stair climbing (Pain_Stair), extension lag (Ext), flexum, range of motion (ROM), varus, and instability (Inest) in AP and ML planes. Knee function (FUNCT) includes walking distance (Pt_Walk), use of help (Pt_Help), and stair climbing (Pt_Climb).

IV.2. Intercondylar area and tubercles

IV.2.1. Intercondylar area defined by the tubercles and their processes

The intercondylar area is defined in this study as the central area of the proximal tibia, between the highest medial and lateral elevations. Hyaline cartilage covers the area external to these limits, as well as the peaks of both tubercles.

Both tubercles consistently showed anterior and posterior downward slopes. Each slope could in turn be divided into different constituent lines or ridges, hereupon called processes. In the following alphanumeric names given to the processes (capital letter + number), a number 1 is given to each ridge's main process, defined as the process delimiting the condyle from the intercondylar area (i.e. the ones most frequently found as relatively highest in normal specimens). At or near the separation of each process from their ridges, a peak could be identified, especially in medial or lateral views (Fig. 67, Fig. 68).

In normal specimens, the lateral tubercle axis followed a line perpendicular to the anterior tibial axis, and the medial tubercle axis followed a line similar to a perpendicular to the posterior axis.

The lateral border of the posterior intercondylar area and the medial border of the anterior intercondylar area formed a posterolateral- anteromedial line, while the medial border of the posterior intercondylar area and the lateral border of the anterior intercondylar area formed a posteromedial- anterolateral line (Fig. 69).

In normal specimens, both lines were found to be approximately at 60° from each other, and crossed at a point central to the anterior aspect of the intertubercular ridge, forming an hourglass-like intercondylar area.

Both lines were approximately 60° from the anterior axis. The posterior axis showed a slightly greater angle (ca. 70°) with the posterolateral- anteromedial line, and a slightly smaller angle (ca. 50°) with the posteromedial- anterolateral line.

The medial tubercle showed an almost constant high anterior aspect and low posterior aspect, the lateral tubercle a high posterior aspect and low anterior aspect.

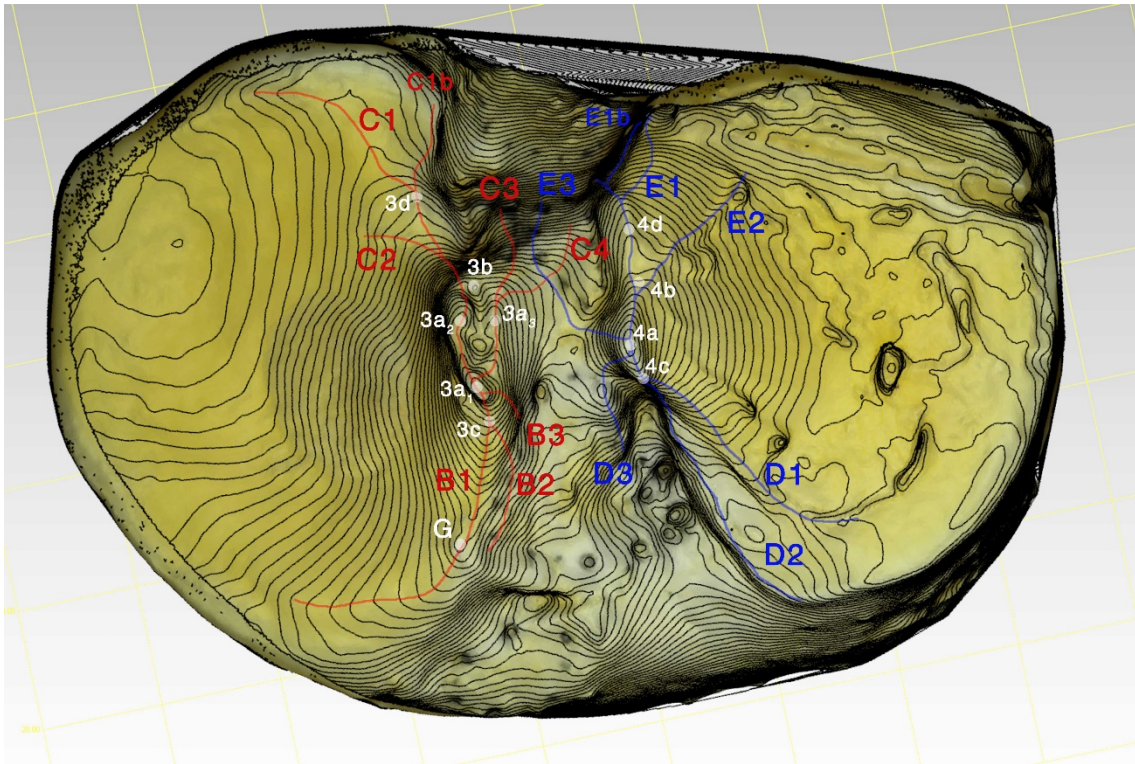


Figure 67. 3D model of tibia A. Intercondylar tubercles' ridges, with main processes and peaks drawn and labelled over the image with help of contour lines.

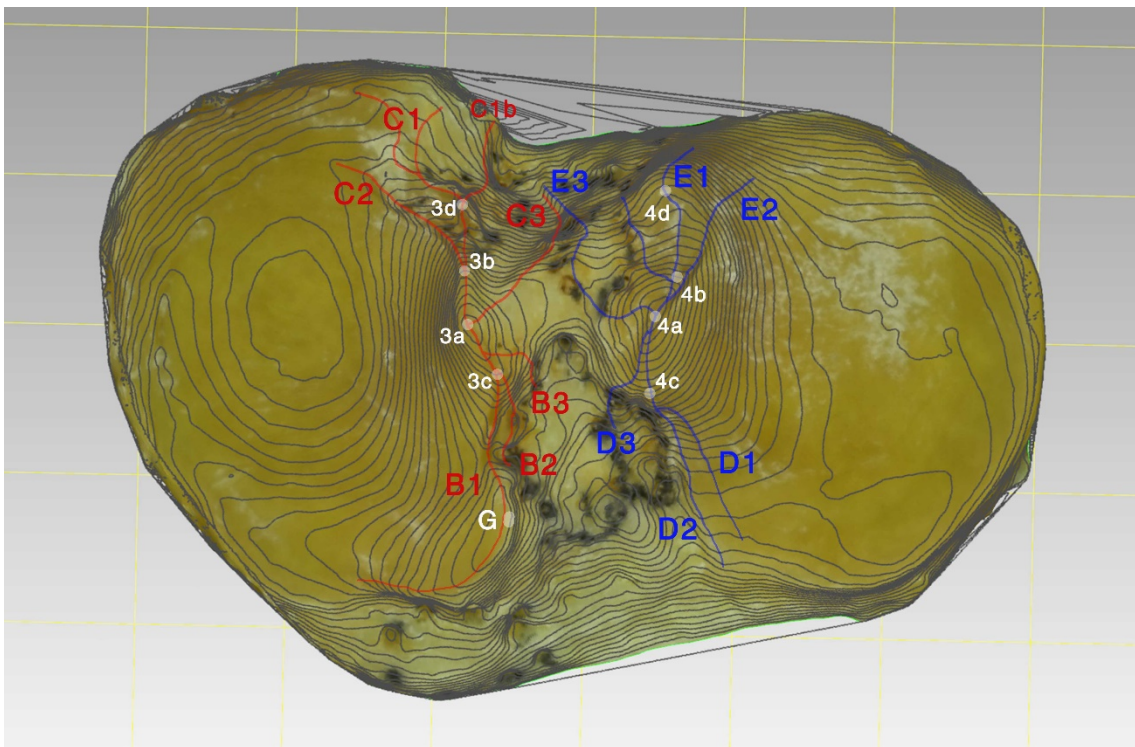


Figure 68. 3D model of tibia E. Intercondylar tubercles' ridges, with main processes and peaks drawn and labelled over the image with help of contour lines.

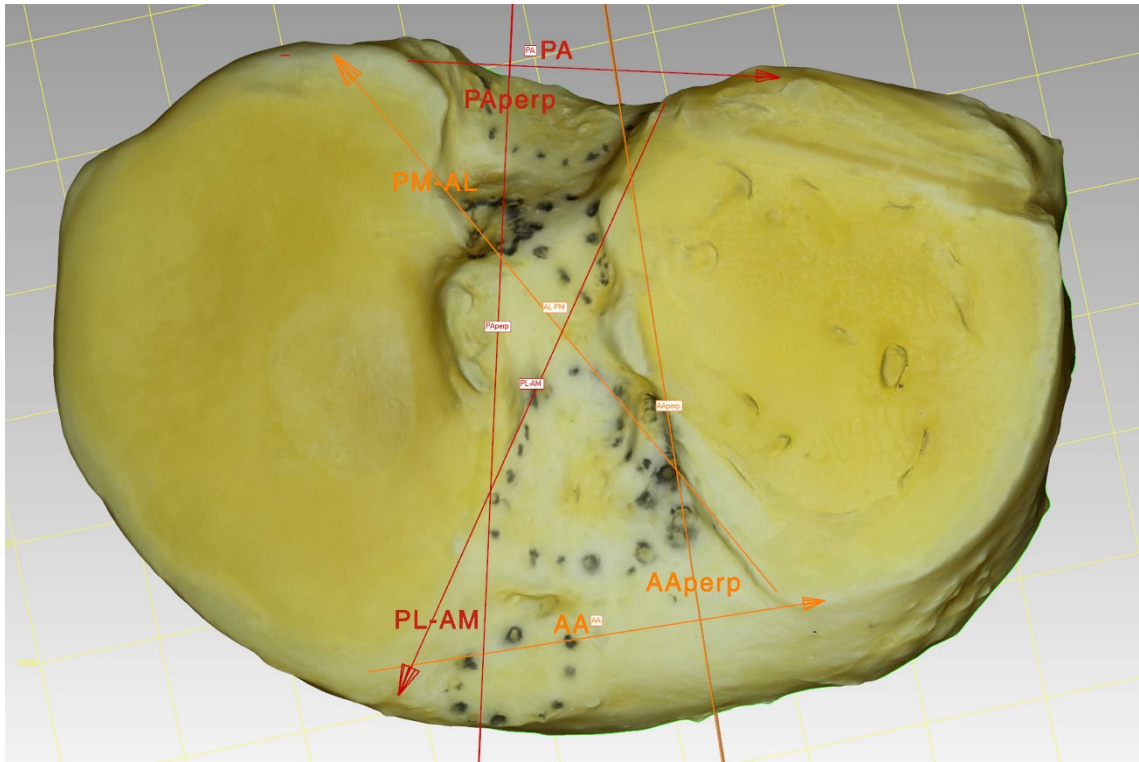


Figure 69. 3D model of tibia A. Anterior axis (AA) and a perpendicular line (AAperp), both in orange, lateral to the LT, in line with it. Posterior axis (PA) and perpendicular line (PAperp), both in red, medial to the MT, in line with it. The PL-AM axis, in red, forms a ca. 70° angle with the posterior axis, and 60° angle with the anterior axis. The PM-AL axis, in orange, forms a ca. 60° angle with the anterior axis.

IV.2.2. Medial intercondylar tubercle, and its processes

The medial tubercle (MT), **3**, was found in nine specimens to have two distinct small peaks in its summit: one anterior, higher peak, **3a₁**, and one posterior, smaller one, **3a₂**, both linked by an intermediate valley, or (in tibias A, E, nonpaired) a small depression. In five tibias, a single peak, **3a**, was found (see Fig. 70 and Fig. 71 for an example of a normal tibia, and Fig. 72 and Fig. 73 for an example of tibia with degenerative changes).

A steep external slope was observed downwards in a medial direction from the peak or peaks, becoming gentler when approaching the medial condyle. A similar internal MT slope was observed in its anterior aspect, while it was smoother downward and posteriorly, into areas 12, 14a.

The anteromedial intercondylar ridge (AMIR), **B**, is the smoothly downward anterior sloping ridge from the summit of the medial tubercle. Its main constituent processes were as follows:

- The external AMIR process, **B1**, followed a straight posteroanterior line, forming a medially concave curve in its anterior aspect.
- The central AMIR process, **B2**, followed a straight anterior line and curves laterally following the anterior frontal intercondylar ridge. At or near the separation of both processes, a subpeak was found, **3c**.
- An internal AMIR process, **B3**, could be seen as a curved elevation into the posterior aspect of area 10 from the medial tubercle, in a lateral direction.

The posteromedial intercondylar ridge (PMIR), **C**, is the steep downward sloping structure from the medial tubercle summit, forming the posterolateral border of the medial condyle, until the posteromedial margin. It was formed by four main processes:

- The central PMIR process, **C1**, formed the posterolateral border of the medial condyle, curving medially at its posterior aspect. A secondary central PMIR process, **C1b**, followed C1 internally downwards, dividing the medial wall of the posterior intercondylar area in a superior and an inferior half.
- The external PMIR process, **C2**, was a constant anteriorly concave curved elevation that followed the medial meniscal footprint posteriorly. At or near its separation from the MT, a subpeak, **3d**, could be identified.
- The internal PMIR process, **C3**, was a medially concave curved ridge. At or near its separation from the MT, a subpeak, **3b**, could be differentiated.
- The more internal PMIR process, **C4**, crossed the posterior intercondylar area in a posterolateral direction.

In donors, the most common order of MT peak height was $3a_1 > 3a_2 > 3b > 3c > 3d$, although $3b > 3c$ and $3c > 3b$ were equally distributed, with the latter more likely in younger donors.

In nine specimens, two peaks were found: the mean height of $3a_1$ was 8.4 mm (95% CI 7.1 – 9.7 mm; range, 6.4 mm to 11.1 mm); the mean height of $3a_2$ was 8.4 mm (95% CI 7.0 – 8.3 mm; range, 6.2 mm to 9.1 mm). The mean height of the highest point (in three cases $3b$ was the highest, and in five specimens only one peak was found) was 8.3 mm (95% CI 7.3 – 9.3 mm; range, 6.0 mm to 11.4 mm).

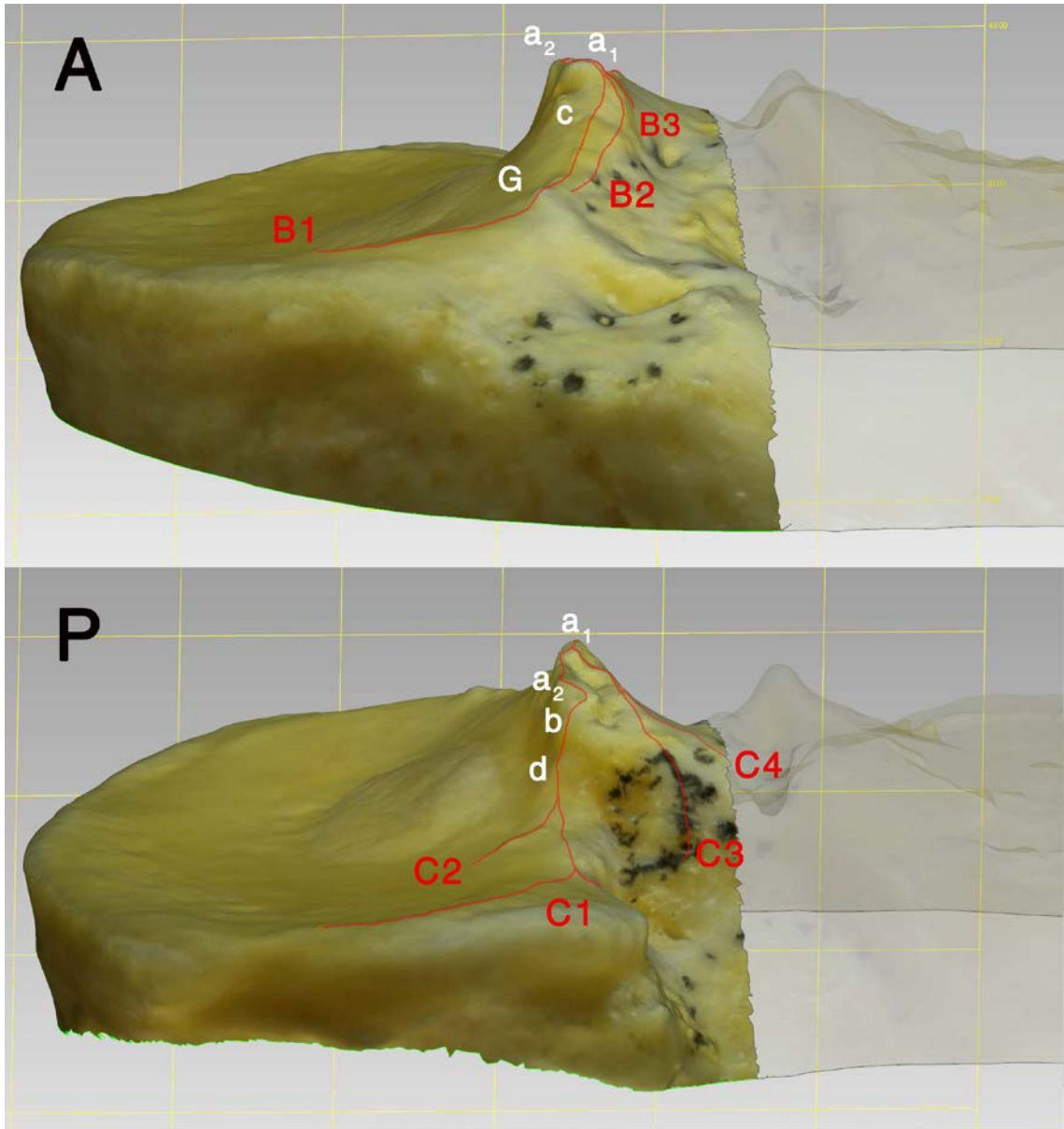


Figure 70. 3D model of tibia A, medial side visible. Medial tubercle peaks labelled (in white color, with number 3 omitted for clarity) and medial processes drawn and labelled (in red). A= Anteroposterior view, P=Posteroanterior view.

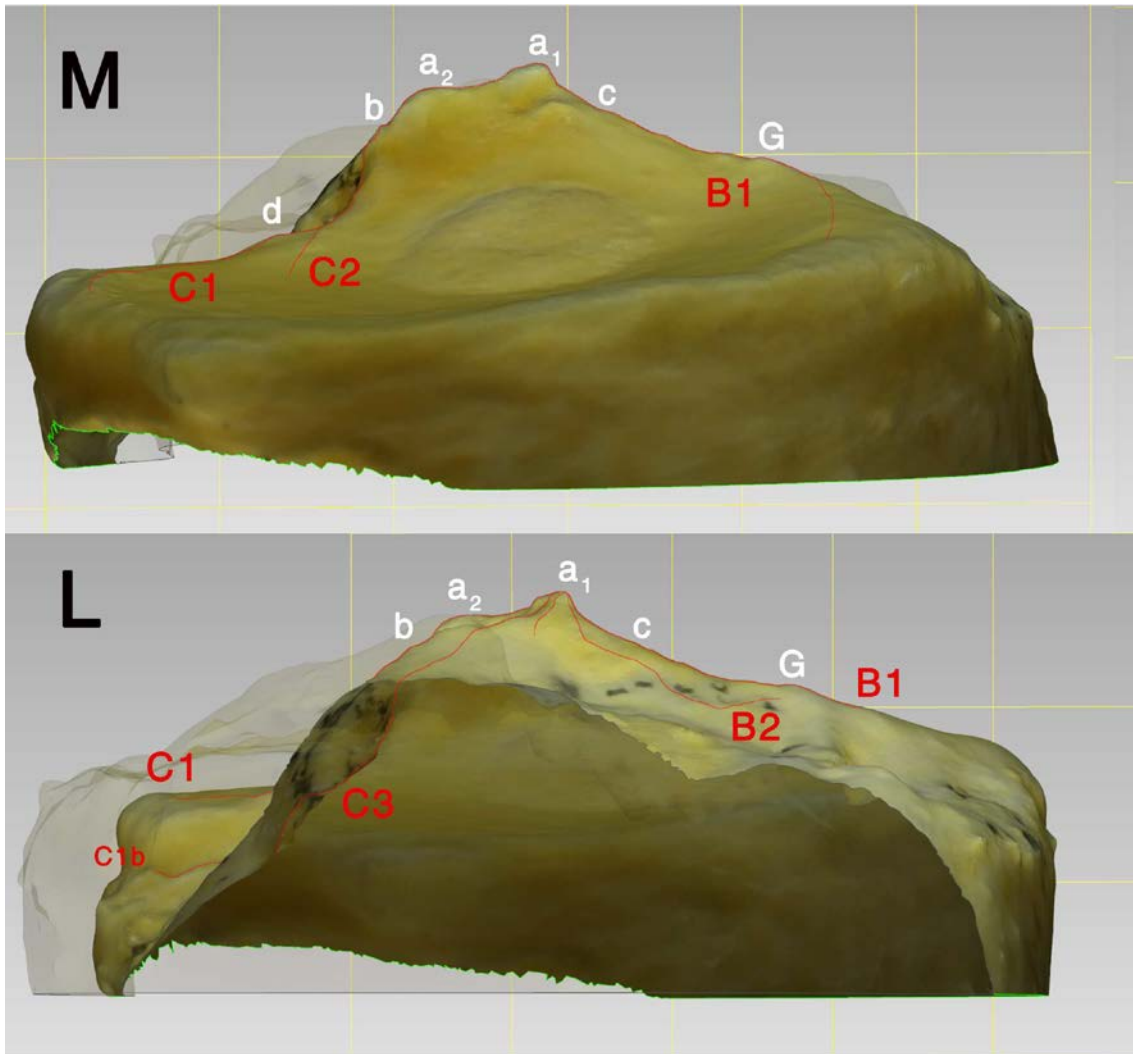


Figure 71. 3D model of tibia A, medial side visible. Medial tubercle peaks labelled (in white color, with number 3 omitted for clarity) and medial processes drawn and labelled (in red). M=Mediolateral view, L=Lateromedial view.

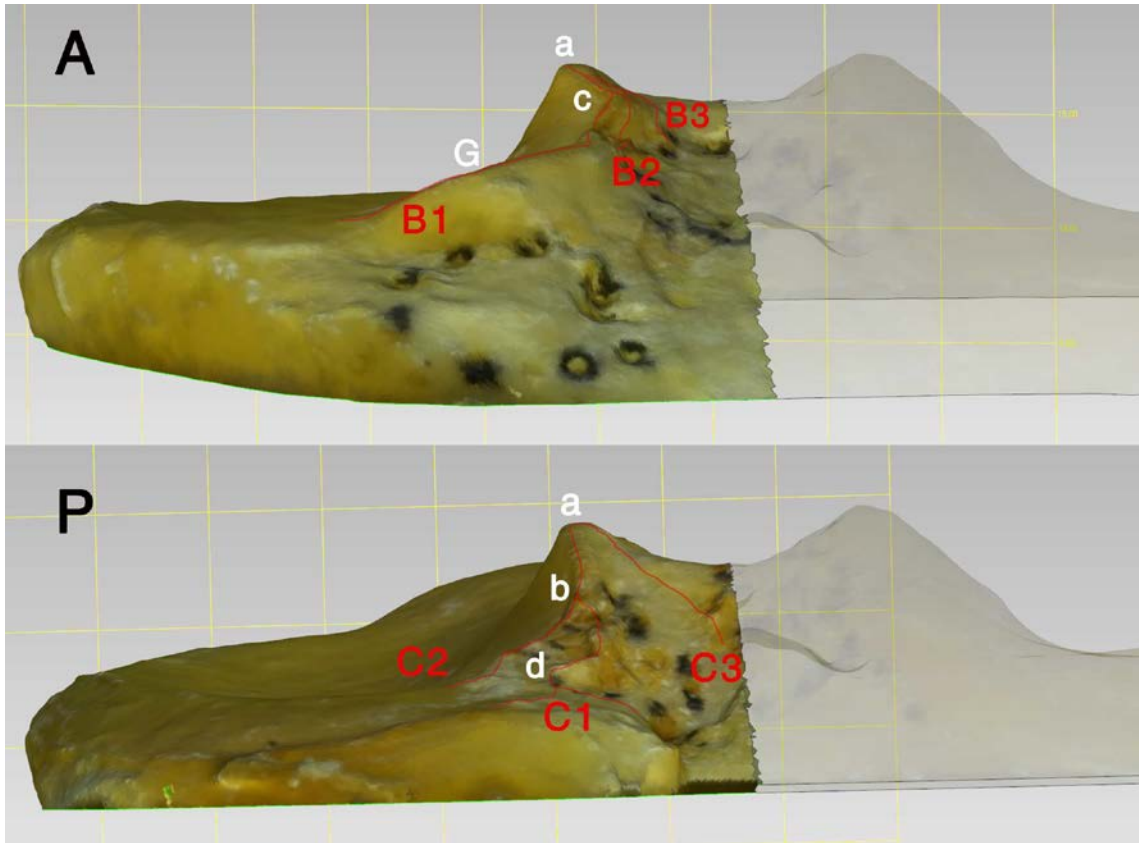


Figure 72. 3D model of tibia E, medial side visible. Medial tubercle peaks labelled (in white color, with number 3 omitted for clarity) and medial processes drawn and labelled (in red). A=Anteroposterior view, P=Posteroanterior view.

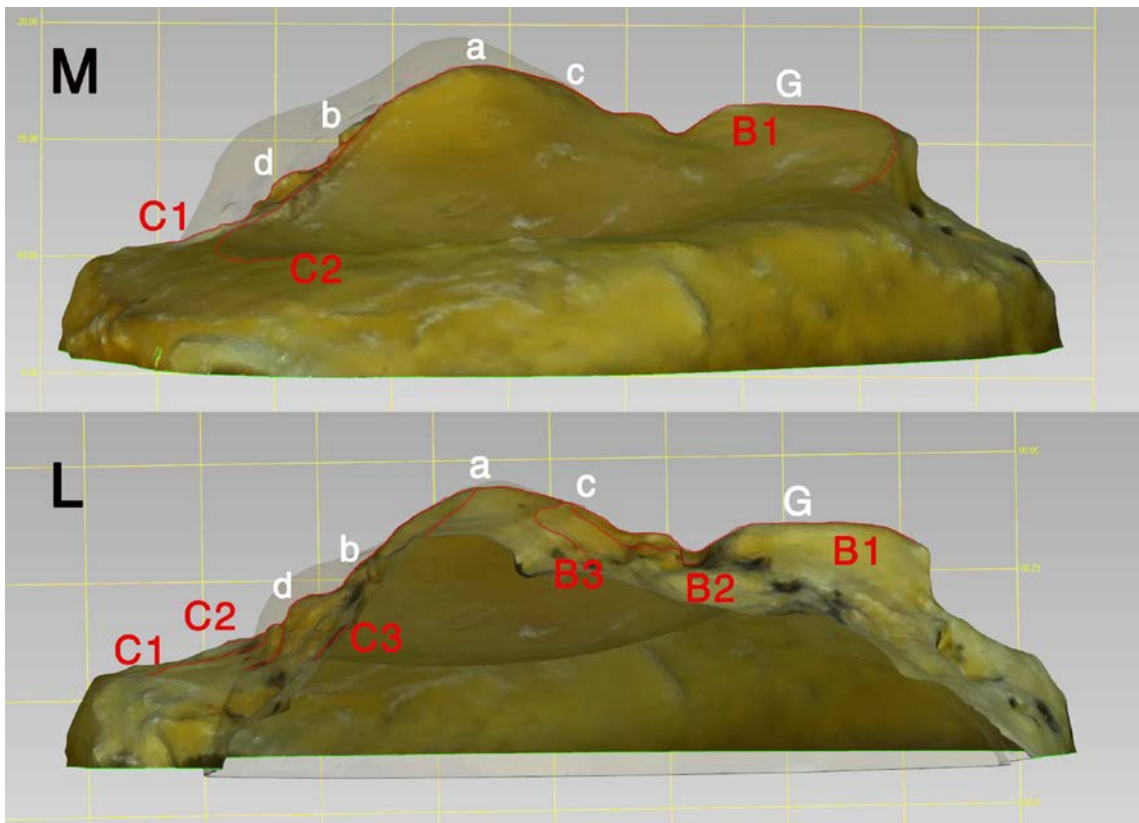


Figure 73. 3D model of tibia E, medial side visible. Medial tubercle peaks labelled (in white color, with number 3 omitted for clarity) and medial processes drawn and labelled (in red). M=Mediolateral view, L=Lateromedial view.

IV.2.3. Lateral intercondylar tubercle, and its processes

The lateral tubercle (LT), **4**, showed two constant summits, an anterior and a posterior one, reaching together deeper than the medial tubercle summit, each one appearing to form its own independent aspect of the tubercle (see Fig. 74 and Fig. 75 for an example of a normal tibia, and Fig. 76 and Fig. 77 for an example of a tibia with degenerative changes).

The peak of the anterior summit, **4a**, was generally lower than the MT summit's peak. Its external slope descends smoothly, unlike that of the medial tubercle. Medially, it had an internal slope steeper than the lateral one, and also steeper than the internal slope of the medial tubercle. Because of that, both slopes converged nearer to the lateral tubercle within the intertubercular ridge.

The anterior summit followed anteriorly a sharp, concave slope, the anterolateral intercondylar ridge (ALIR), **D**. This was formed by three main processes:

- An external ALIR process, **D1**, followed an anterolateral direction, curving laterally in its anterior aspect to follow the lateral meniscal footprint.
- The central ALIR process, **D2**, with a more straight anterior direction than **D1**, is proposed as the true medial osseous border of the lateral condyle. Medial to it was a steep wall downwards to the anterior intercondylar area. At or near the separation of both processes, a subpeak was encountered, **4c**.
- The internal ALIR process, **D3**, was a slight elevation that enters area 10, starting at the anterior peak of the lateral tubercle, and following a curve concave laterally.
 - In some cases, two different elevated curves were observed: a main curve, **D3a**, and a more posterior and lateral one, **D3b**.

The anterior summit sloped gently posteriorly from its peak into a constant, more smoothly sloped area, the lateral tubercle vallecule, **4b**. This vallecule formed the posterior aspect of the posterior summit, until encountering a sharp posterior slope, the tip anterior to it being proposed as the posterior subpeak (the peak of the posterior summit), **4d**.

After that short steep slope posteriorly, a smoother, longer slope could be observed again in a posterior direction, leading to the posteromedial border of the lateral condyle, which curved smoothly in a lateral direction.

The posterior summit was found to have its own short external slope in a posterolateral direction, narrower and more curved (i.e. with a smaller radius of curvature) than the main lateral slope.

The posterolateral intercondylar ridge (PLIR), **E**. It was formed by three main processes:

- The central PLIR process, **E1**, followed the highest contour line of the vallecule and the posterior slope, forming the internal border of the lateral condyle until it reached the smooth posterolateral margin of the condyle. At or near the posterior subpeak, 4d, a secondary central PLIR process, **E1b**, followed E1 internally downwards. In seven specimens, it followed posteriorly, dividing the lateral wall of the posterior intercondylar area in a superior and an inferior half.
- The external PLIR process, **E2**, was a curve branching off at or near the vallecule subpeak, 4b, coursing laterally into the lateral condyle. It follows the lateral meniscal footprint, and marks the border between the main LT slope (anteriorly) and the slope of the posterior summit (posteriorly).
- The internal PLIR process, **E3**, was a curve concave laterally that crossed the intertubercular ridge into the posterior facet.

In donors, the most common order of LT peak height was $4a > 4c > 4b > 4d$, although $4b > 4c$ and $4c > 4b$ were equally distributed (no difference was found between both categories when compared with tibias with degenerative changes).

The mean height of 4a was 7.8 mm (95% CI 6.9 – 8.6 mm; range, 5.7 mm to 9.4 mm); the mean height of 4b was 4.6 mm (95% CI 3.8 – 5.4 mm; range, 2.1 mm to 6.2 mm). The mean height of the highest point (in two cases 4b was the highest point, but less than 1 mm higher than 4a), was 7.8 mm (95% CI 7.0 – 8.6 mm; range, 5.9 mm to 9.5 mm).

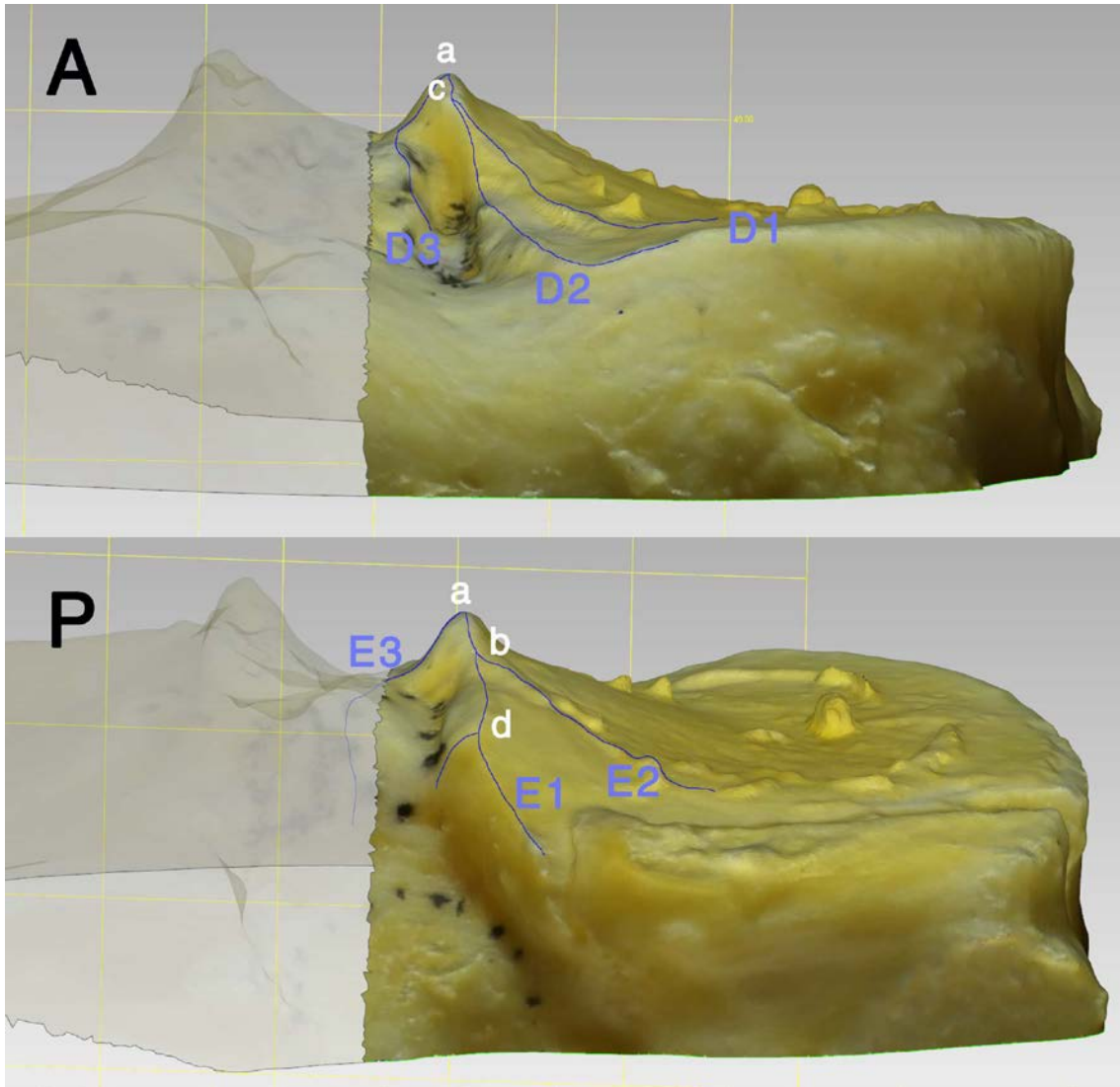


Figure 74. 3D model of tibia A, lateral side visible. Lateral tubercle peaks labelled (in white color, with number 4 omitted for clarity) and lateral processes drawn and labelled (in blue). A=Anteroposterior view, P=Posteroanterior view.

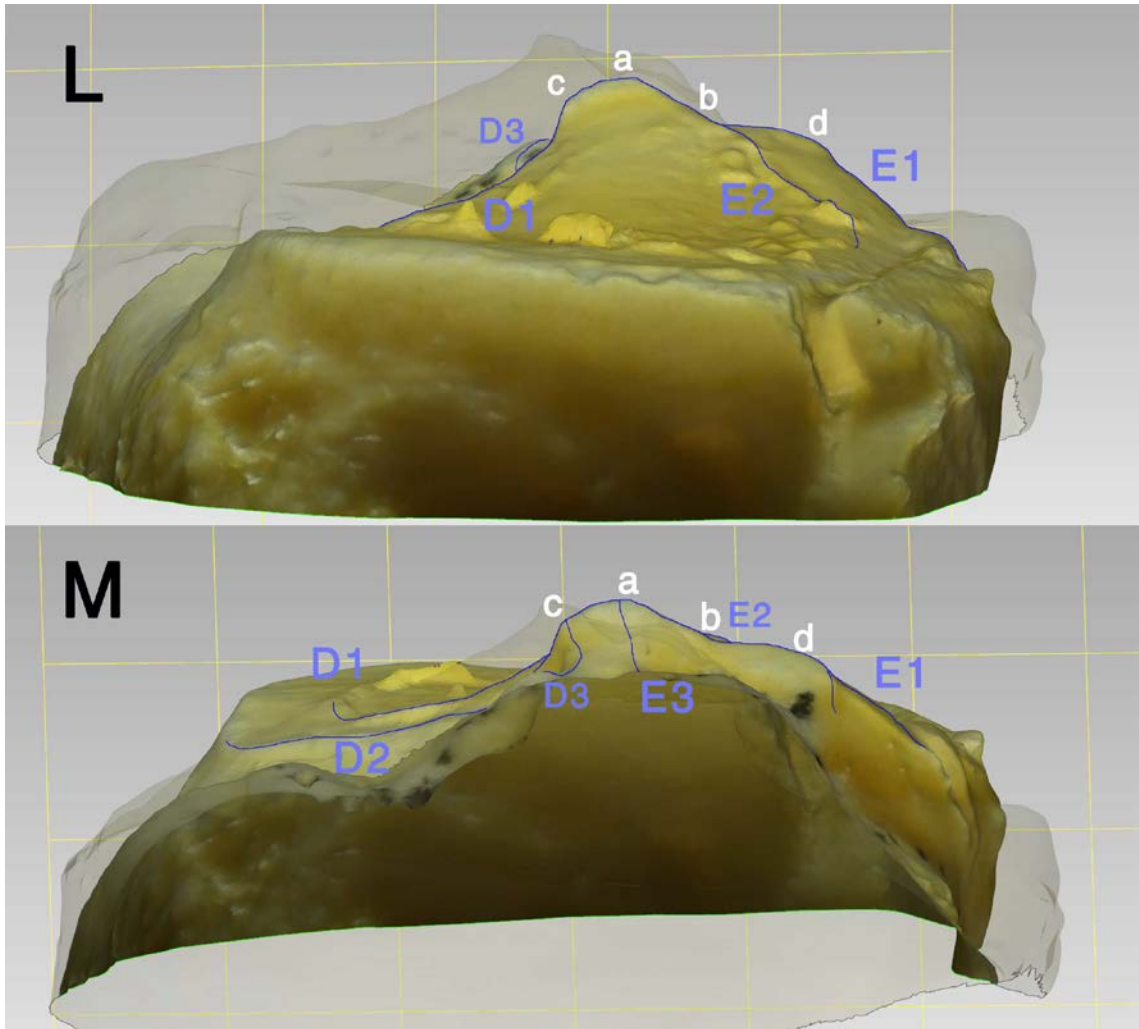


Figure 75. 3D model of tibia A, lateral side visible. Lateral tubercle peaks labelled (in white color, with number 4 omitted for clarity) and lateral processes drawn and labelled (in blue). L=Lateromedial view, M=Mediolateral view.

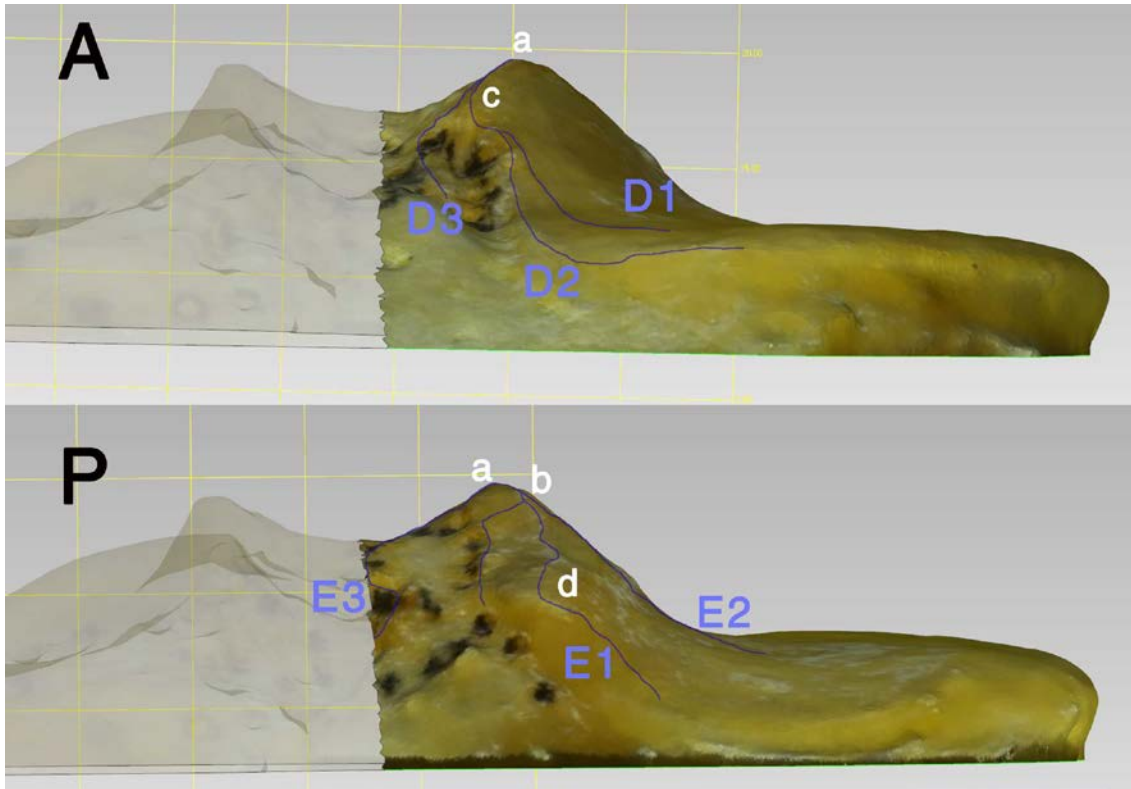


Figure 76. 3D model of tibia E, lateral side visible. Lateral tubercle peaks labelled (in white color, with number 4 omitted for clarity) and lateral processes drawn and labelled (in blue). A=Anteroposterior view, P=Posteroanterior view.

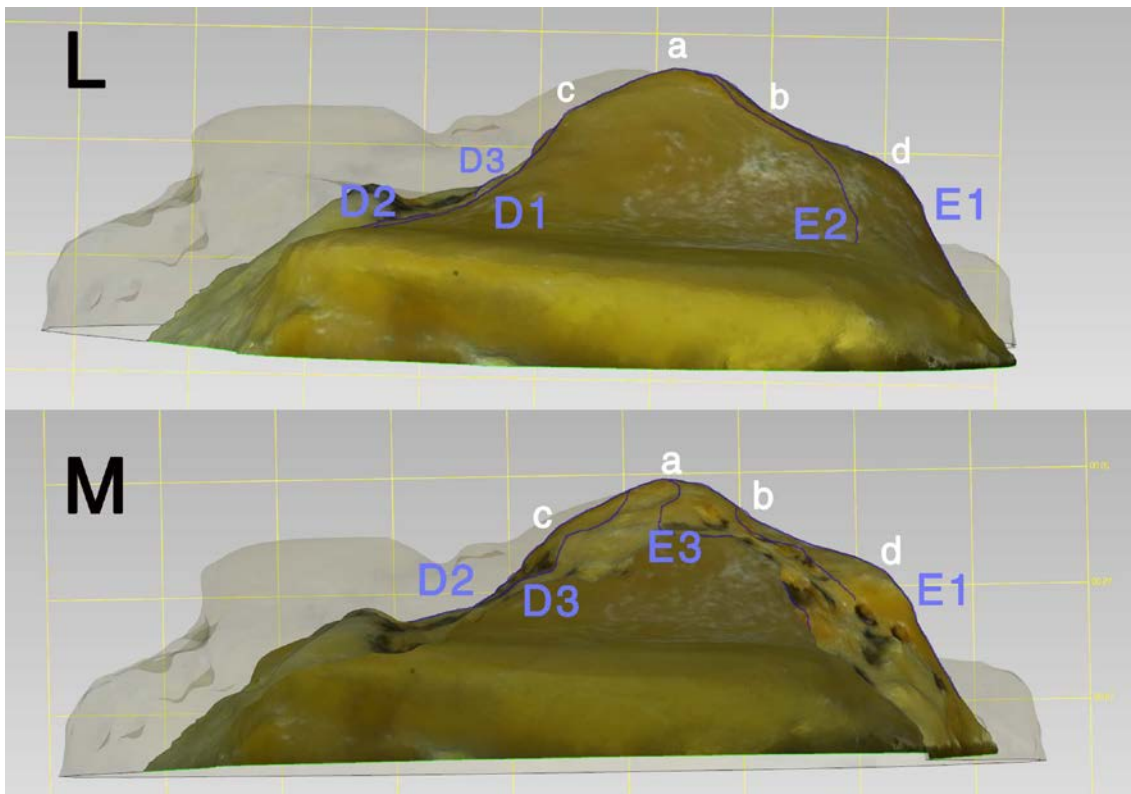


Figure 77. 3D model of tibia E, lateral side visible. Lateral tubercle peaks labelled (in white color, with number 4 omitted for clarity) and processes drawn and labelled (in blue). L=Lateromedial view M=Mediolateral view.

IV.2.4. Tubercle size in knee radiographs and MRI

These are the results of studies VIII-XI

IV.2.4.1. Tubercle size in adults

Results for Study V, for 100 normal tibias, showed that the mean age of selected patients was 28.4 years (range, 17 to 39 years) at the time of the last imaging study. Of them, 67% were male, and 51 % were left knees.

78% had MT>LT, 18% had LT>MT (Fig. 78). No clear difference in height between tubercles, MT=LT, was found in 4%. Classification of radiography according to Giorgi⁵⁰ was possible in 93 tibias, obtaining 75% of type 2 (hyperplasia of the medial tubercle), 16% of type 3 (hyperplasia of the lateral tubercle), one case or 1% of hypoplasia of the lateral tubercle (Fig. 81), here classified as type 4 (hypoplasia of the tibial spine), and one clear case, or 1%, of type 1 (hyperplasia of the spine, with both tubercles equal). No case of type 5 (agenesis of the tibial spine) was found in this sample (Fig. 79).

The main difference found in MRI was $1.5 \pm 0.3\text{mm}$ (range, -2.2 mm to 5.2 mm), where positive value indicates MT>LT. Percentage of the ML proximal tibial width (measured in the AP radiograph) showed a mean height for the MT of $12.1 \pm 0.4\%$ of the ML width (range, 1% to 16.7%), and a LT mean height of $10.4 \pm 0.4\%$ of the ML width (range, 0% to 14.2%). Their difference had an average of $1.7 \pm 0.5\%$ (range -8.7% to 14.4%, where positive value indicates MT>LT) of the radiographic ML width.

No significant association was found between pathology groups (Fig. 80) and the relative MT-LT size: $\chi^2(12)=4.883$, $p=0.962$.

The highest peak of the MT was at $3.8 \pm 0.1\text{ mm}$, or $41.8 \pm 1.1\%$ from the posterior aspect of the proximal tibia, while the highest peak of the LT was at $3.5 \pm 0.2\text{ mm}$, or $38.9 \pm 0.9\%$ from that point.

The tibial AP depth was measured in the MRI slices selected to measure the height and position of each tubercle, and a dependent *t*-test was run between both measurements, resulting in $t(99)=0.469$, $p=0.640$. Due to the correlation ($r=0.83$, $p<0.001$) and *t*-value, the two measurements (tibial depth at MT slice 51.6 mm; tibial depth at LT slice 51.4 mm) had no statistically significant difference, even though the sagittal cut through the medial tubercle showed a trend toward a deeper measure.

Proximal tibia AP depth in MRI showed a bigger size in men (mean AP depth, 54.4 mm in the MT slice, 54.5 mm in the LT slice) than in women (mean AP depth, 45.9 mm in the MT slice, 45.1 mm in the LT slice): $t(98)= 8.27, p<0.001$ for the MT slice; $t(98)= 8.904, p<0.001$ for the LT slice.

Radiographic MT height showed a significant difference between men (mean MT height, 12.4%) and women (mean MT height, 11.3%); $t(98)=2.452, p=0.033$. That difference was not observed in LT proportional height in men (mean LT height, 10.4%) and women (mean LT height, 10.4%): $t(98)=0.063, p=0.944$.

A difference was also apparent in distance from the posterior tibial aspect (P) to the MT and LT in men (P–MT, 4 mm; P–LT, 3.8 mm) compared to women (P–MT, 3.2 mm; P–LT, 2.9 mm): $t(98)= 6.203, p<0.001$ for P–MT; $t(98)=5.496, p<0.001$ for P–LT. However, that difference did not reach significance in the proportion that this distance represented with the ML width of the proximal tibia in men (P–MT, 42.3%; P–LT, 39.5%) compared to women (P–MT, 40.9%; P–LT, 37.9%): $t(98)=1.424, p=0.158$ for P–MT; $t(98)=1.66, p=0.100$ for P–LT.

No significant differences in MT–LT height difference was noted in MRI in men (mean difference, 1.7 mm) compared to women (mean difference, 1.1 mm), $t(98)=1.57, p=0.120$. This difference almost reached significance in proportion of ML width in AP radiography between men (mean difference, 2%) and women (mean difference, 0.9%), $t(98)=2.049, p=0.051$.

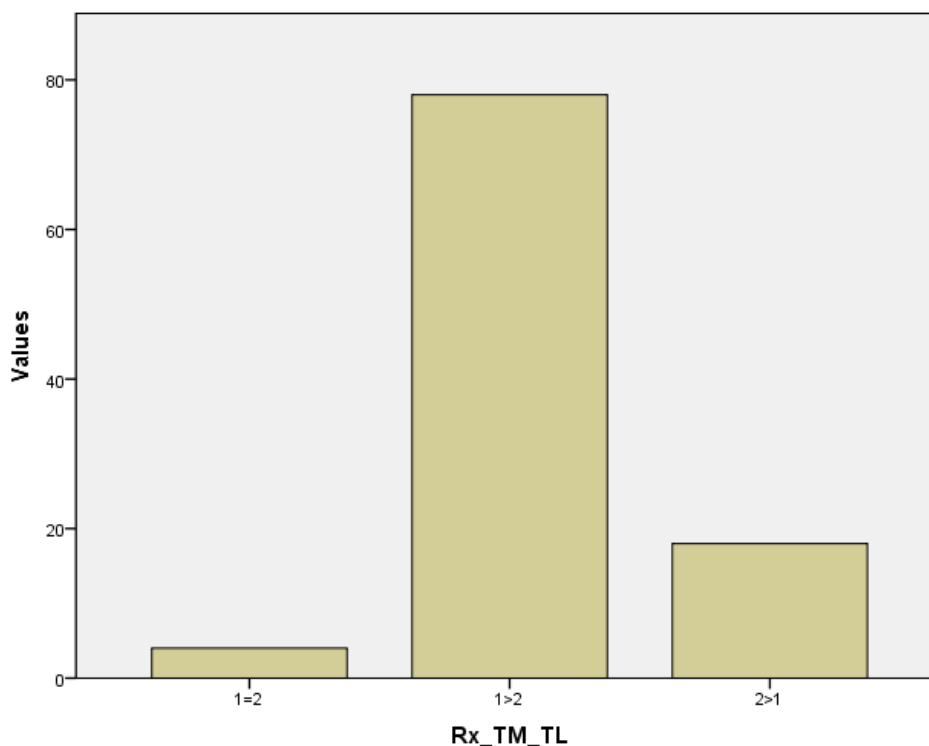


Figure 78. Study V. Histogram of number of tibias in each group of relative tubercle size in radiography (Rx_TM_TL), where 1=MT, 2=LT.

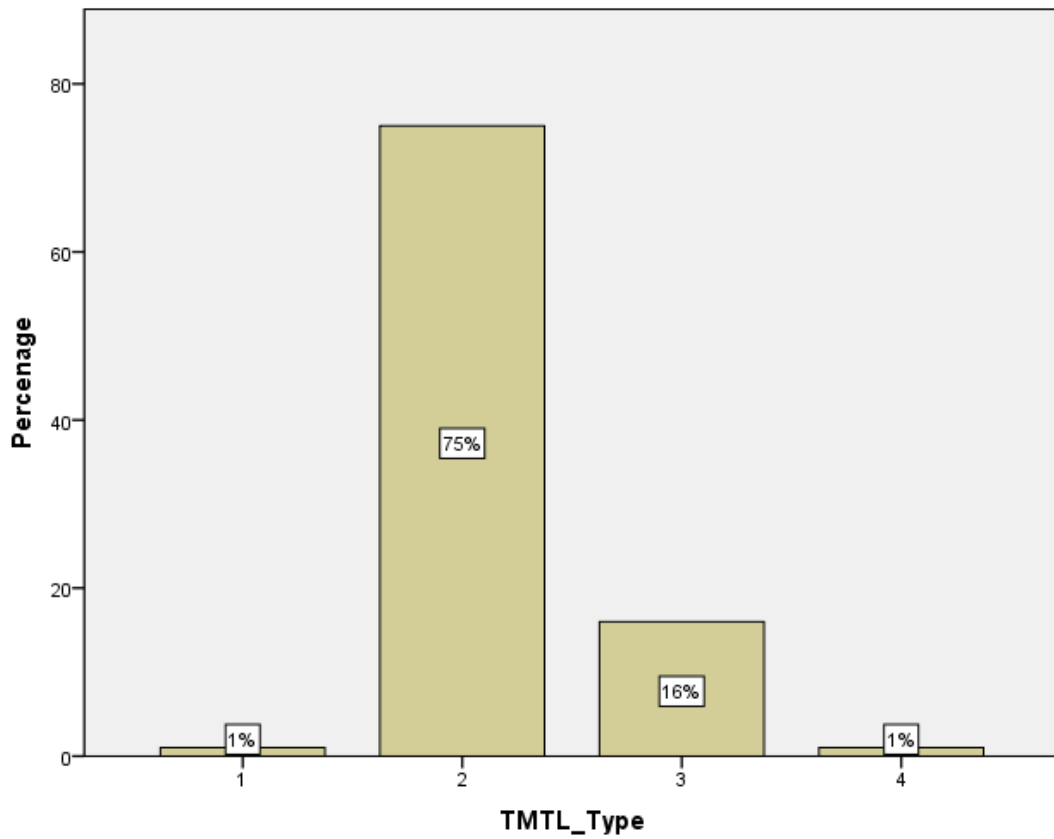


Figure 79. Study V. Histogram of tibias classified into Giorgi's groups (TMTL_Type), in percentage.

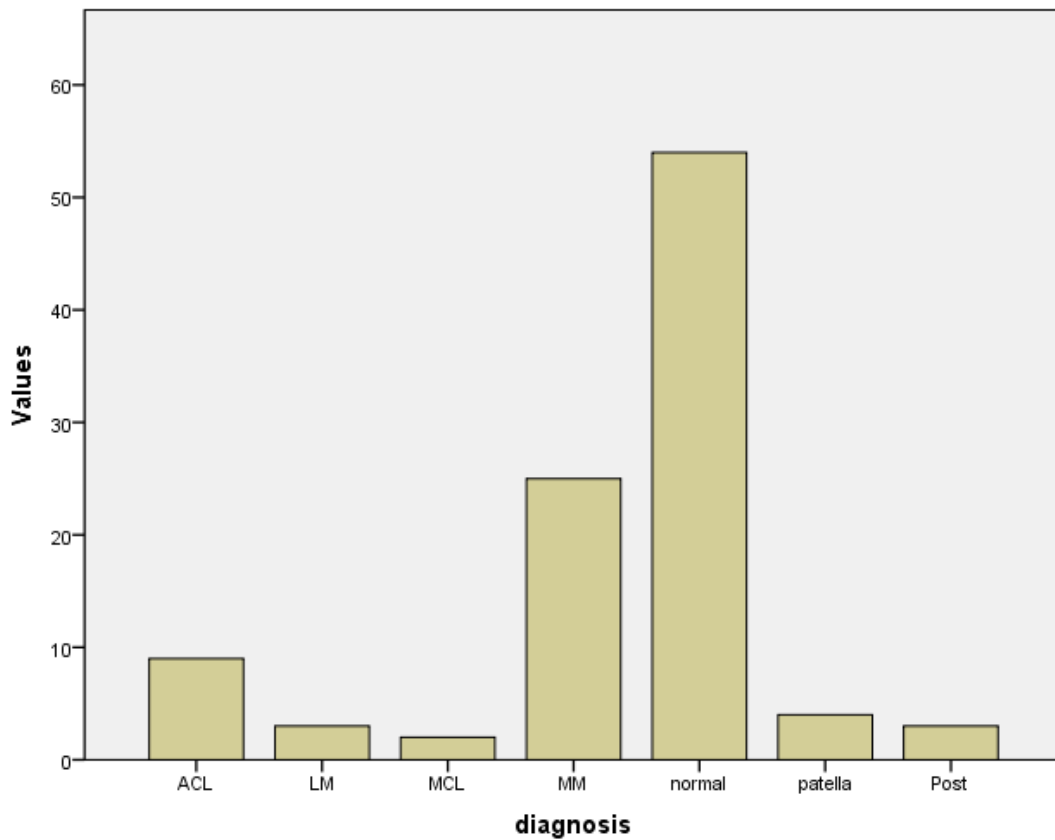


Figure 80. Study V. Histogram of number of tibias classified into each diagnostic group: ACL, lateral meniscus (LM), medial collateral ligament (MCL), medial meniscus (MM), femoropatellar, and posterior aspect (Post) - including PCL – pathology.



Figure 81. A case of hypoplasia of the lateral tubercle in the sample for Study V.

IV.2.4.2. Tubercle size in children

Results for Study VI, for 79 nonpaired tibias, showed a mean age of 12 years (range, 3 to 16 years): 52% were males, and there was an almost equal distribution of left (50.6%) and right knees.

86% had a MT>LT, 9% LT>MT, and 1% MT=LT, while in 4% individual tubercles could not be distinguished (Fig. 82, Fig. 83). A case of hypoplastic tibial eminence was also found (Fig. 84).

A significant association was found between simple diagnostic groups (see Fig. 85) and the relative MT–LT size: $\chi^2(21)=45.272$, $p=0.002$. Frequency distribution analysis showed that lateral meniscal pathology had LT>MT in 29% (2 cases of lateral meniscal tears), and LT=MT in 14% (1 case of discoid lateral meniscus). Also, LT>MT was found in 20% in the groups of patella (a case of patellar subluxation), bone edema (one case with apparent depression of the lateral condyle, hence higher LT compared to the articular line), and one in the “other” group (a case of osteomyelitis). The group of normal tibias showed only 5.3 % of LT>MT.

The main difference found in MRI was 1.2 ± 0.3 mm (range, -2.2 mm to 4 mm), where positive value indicates MT>LT. Percentage of the ML proximal tibial width (measured in the AP radiograph) showed a mean height for the MT of $14.2 \pm 0.5\%$ of the ML width (range, 8.6% to 22%), and a LT mean height of $12.5 \pm 0.6\%$ of the ML width (range, 6.8% to 20.5%). Their difference had an average of $1.7 \pm 0.3\%$ (range, -2.1% to 5.9%, where positive value indicates MT>LT) of the radiographic ML width.

Age did not show a significant association with the differences between MT and LT: in MRI, $r=-0.156$, $p=0.177$; in radiography, $r=0.034$, $p=0.771$. Age did have a significant, although low, correlation with MT size ($r=-0.567$, $p<0.001$), and LT size ($r=-0.542$, $p<0.001$).

No statistically significant difference was found in the distribution of age in males (mean age, 12.3 years) compared to females (mean age, 11.8 years), $t(77)=0.657$, $p=0.514$. Because of that, further differences in tubercle height were looked for between male and female groups.

As in adult normal tibias, radiographic MT height showed a significant difference between men (MTh, 14.7%) and women (MTh, 13.6%); $t(73)=2.135$, $p=0.036$. LT proportional height in men (LTh, 13%) and women (LTh, 12%) showed no

statistical significance, although the p -value was much nearer to the significance threshold than in adults: $t(73)=1.852, p=0.068$.

Also similar to normal adult tibias, no significant differences in MT–LT height difference was noted in MRI or radiography in men (mean difference in MRI, 1.3 mm; in radiography, 17.2%) than in women (mean difference in MRI, 1.1 mm; in radiography, 16.5%): $t(74)=0.584, p=0.561$ for MRI; $t(73)=0.170, p=0.865$ for radiography.

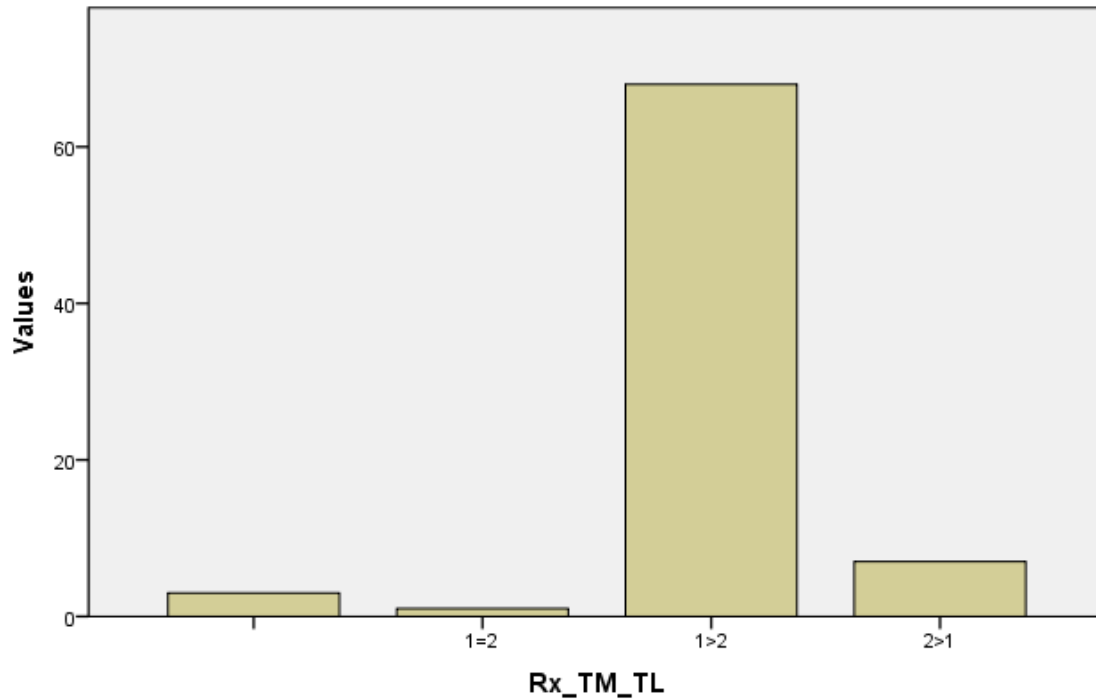


Figure 82. Study VI. Histogram of number of tibias in each group of relative tubercle size in radiography (Rx_TM_TL), where 1=MT, 2=LT.

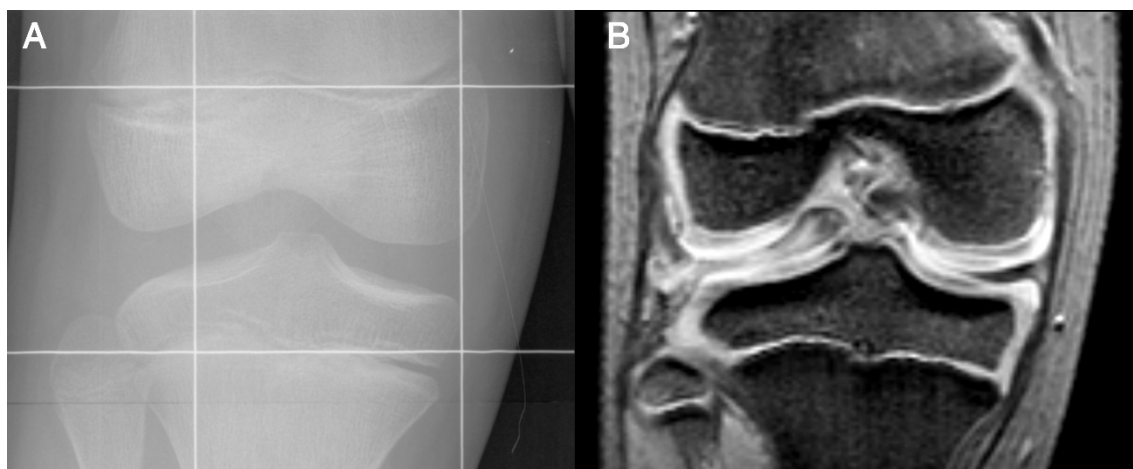


Figure 83. Study VI. 10-year-old male with longer right knee of ca. 20mm, discoid lateral meniscus, showing $MT=LT$ in radiography (A) and MRI (B).

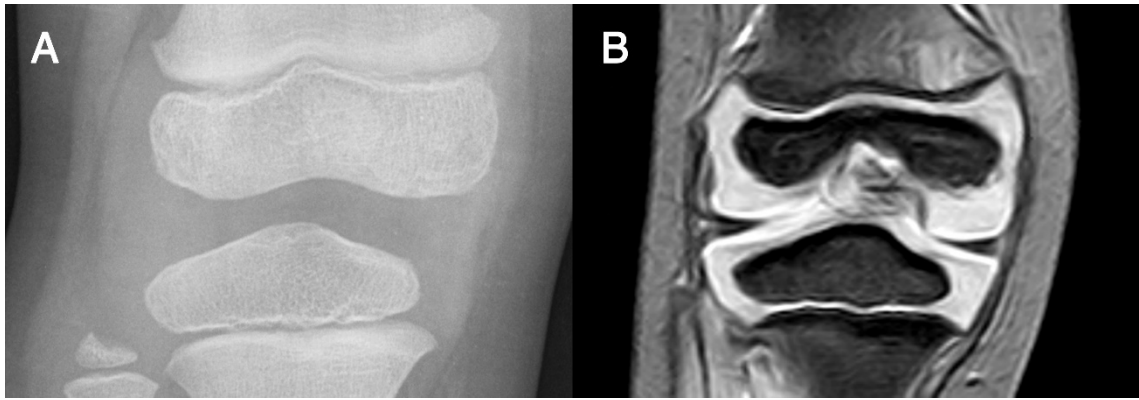


Figure 84. Study VI. 3-year-old female with limp and proximal fibular epiphyseal lesion, showing a hypoplastic tibial eminence and no distinguishable tubercles.

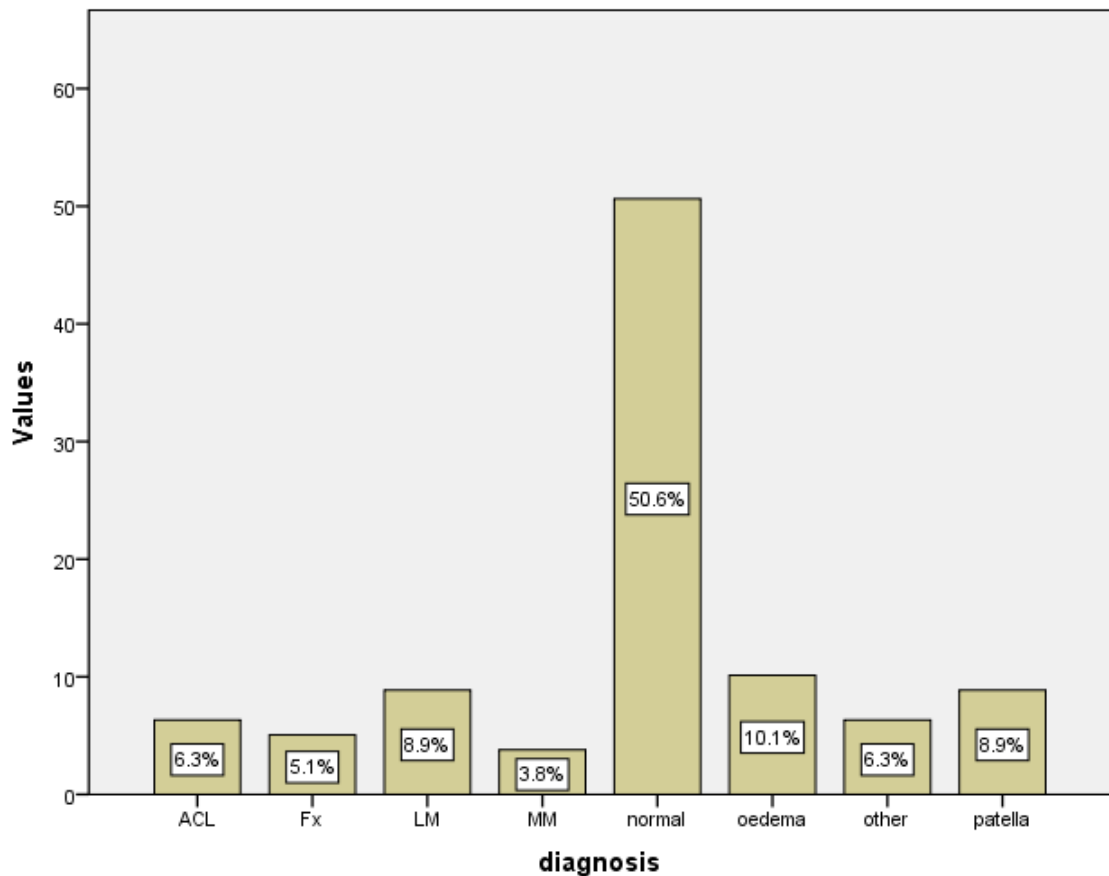


Figure 85. Study VI. Histogram of percentages of tibias classified into each diagnostic group: ACL, fracture (Fx), lateral meniscus (LM), medial meniscus (MM), bone edema, other pathologies, and femoropatellar pathology.

IV.2.4.3. Tubercle size in adults with osteochondritis

Results for Study VII, for 25 knees, showed a mean age of 34.6 years (range, 17 to 65 years), 76% were males, 52% were left knees. 80% had MT>LT, 12% had LT>MT, and 8% had MT=LT. Ahlbäck OA classification yielded 56% grade 0, and 44% grade 1.

The main difference found in MRI was 1.2 ± 0.7 mm (range, -1.4 mm to 3.9 mm), where positive value indicates MT>LT. Percentage of the ML proximal tibial width (measured in the AP radiograph) showed a mean height for the MT of 12.4 ± 1.1 % of the AP width (range, 8.5% to 17.9%), and an LT mean height of 10.8 ± 0.9 % of the ML width (range, 7.1% to 16.6%). Their difference had an average of 1.6 ± 0.8 % (range -2.2% to 4.5%, where positive value indicates MT>LT) of the radiographic ML width.

A Kruskal-Wallis H test showed no statistically significant differences between Ahlbäck OA grade groups in terms of tubercle height difference in MRI, $\chi^2(1)=0.004$, $p=0.951$; height difference in radiography, $\chi^2(1)=0.001$, $p=0.978$; MT height, $\chi^2(1)=0.494$, $p=0.482$; or LT height, $\chi^2(1)=1.111$, $p=0.292$.

No significant differences were found between men and women: MT height in radiograph (men, 12.7%; women, 11.6%), $t(22)=1.110$, $p=0.292$; LT height in radiograph (men, 10.6%; women, 11.2%), $t(22)=-0.762$, $p=0.456$; difference in MT–LT height in MRI (men, 1.3 mm; women, 1.1 mm), $t(21)=0.205$, $p=0.842$; difference in MT–LT height in radiography (men, 2%; women, 0.4%), $t(23)=1.975$, $p=0.082$.

IV.2.4.4. Tubercle size in children with osteochondritis

Results for Study VIII, for 17 knees with open epiphyses, showed a mean age of 12.2 years (range, 8 to 16 years), 71% were males, 53% were left knees. All tibias had MT>LT. The medial condyle was affected in 76.5% of cases, and the lateral condyle in 23.5%.

The main difference found in MRI was 1.4 ± 0.4 mm (range, 0.6 mm to 2.7 mm), where positive value indicates MT>LT. Percentage of the ML proximal tibial width (measured in the AP radiograph) showed a mean height for the MT of 13.4 ± 1.2 % of the ML width (range, 11% to 20.2%), and a LT mean height of 11.4 ± 1 % of the ML width (range, 8.8% to 17%). Their difference had an average of 2 ± 0.6 % (range -0.7% to 4.1%, where positive value indicates MT>LT) of the radiographic ML width.

No differences were found between affected condyle and age in a dependent t -test (mean medial condyle, 12.4 years; mean lateral condyle, 11.5 years), $t(15)=0.698$, $p=0.885$; nor between affected condyle and sex, $\chi^2(1)=2.179$, $p=0.140$.

A significant association was found between affected condyle and the MT–LT height difference (mean for medial condyle, 2.4%; mean for lateral condyle,

0.8%), $t(15)=5.656$, $p<0.001$. That difference was not found in terms of absolute distances in mm, as measured in MRI (mean for medial condyle, 1.4 mm; mean for lateral condyle, 1.2 mm), $t(11)=0.893$, $p=0.408$.

An association was also found in dependent t -test between condyle location of the osteochondritis and MT height (mean for medial condyle, 13.8%; mean for lateral condyle, 12%), $t(15)=2.222$, $p=0.044$. No statistically significant difference was found with LT height (mean for medial condyle, 11.4%; mean for lateral condyle, 11.2%), $t(15)=0.260$, $p=0.799$.

No differences were significant between men and women: MT height in radiograph (men, 13.7%; women, 12.7%), $t(15)=0.985$, $p=0.343$; LT height in radiograph (men, 11.8%; women, 10.5%), $t(15)=1.489$, $p=0.162$; difference in MT–LT height in MRI (men, 1.3mm; women, 1.6mm), $t(11)=-0.716$, $p=0.493$; difference in MT–LT height in radiography (men, 1.9%; women, 2.2%), $t(15)=-0.566$, $p=0.586$.

IV.2.4.5. Tubercle size in osteonecrosis

Results for Study IX, for 47 nonpaired knees, and 4 paired knees, showed a mean age of 51 years (range, 33 to 83 years), 31% were males, and 53% left knees. 88% had MT>LT, 10% had LT>MT, and 2% had MT=LT. Their classification in knee OA grades according to the Ahlbäck classification can be seen in Fig. 86.

The main difference found in MRI was 1.5 ± 0.7 mm (range, -2.6 to 5 mm), where positive value indicates MT>LT. Percentage of the ML proximal tibial width (measured in the AP radiograph) showed a mean height for the MT of 13.5 ± 0.5 % of the ML width (range, 9.3% to 18.2%), and a LT mean height of 11.5 ± 0.5 % of the ML width (range, 7.4% to 14.6%). Their difference had an average of 2 ± 0.5 % (range -2.3% to 5.6 %, where positive value indicates MT>LT) of the radiographic ML width.

A Kruskal-Wallis H test showed that no statistically significant differences exist between the different Ahlbäck OA grade groups in terms of height difference in MRI, $\chi^2(3)=1.216$, $p=0.749$; height difference in radiography, $\chi^2(3)=4.018$, $p=0.404$; MT height, $\chi^2(4)=1.933$, $p=0.748$; or LT height, $\chi^2(4)=2.336$, $p=0.674$.

Different to normal tibias, MT height (as proportion of the ML width in AP radiograph) showed no significant differences between men (mean, 13.6%) and women (mean, 13.4%); $t(49)=0.274$, $p=0.786$. LT proportional height in men

(mean, 11.4%) and women (mean, 11.5%) showed, as in normal tibias, no statistical significance: $t(49)=-0.150, p=0.882$.

No significant differences in MT–LT height difference was noted in MRI or radiography in men (mean difference in MRI, 1.6 mm; in radiography, 2.1%) compared to women (mean difference in MRI, 1.5 mm; in radiography, 1.9%): $t(28)=0.147, p=0.884$ for MRI; $t(49)=0.413, p=0.683$ for radiography.

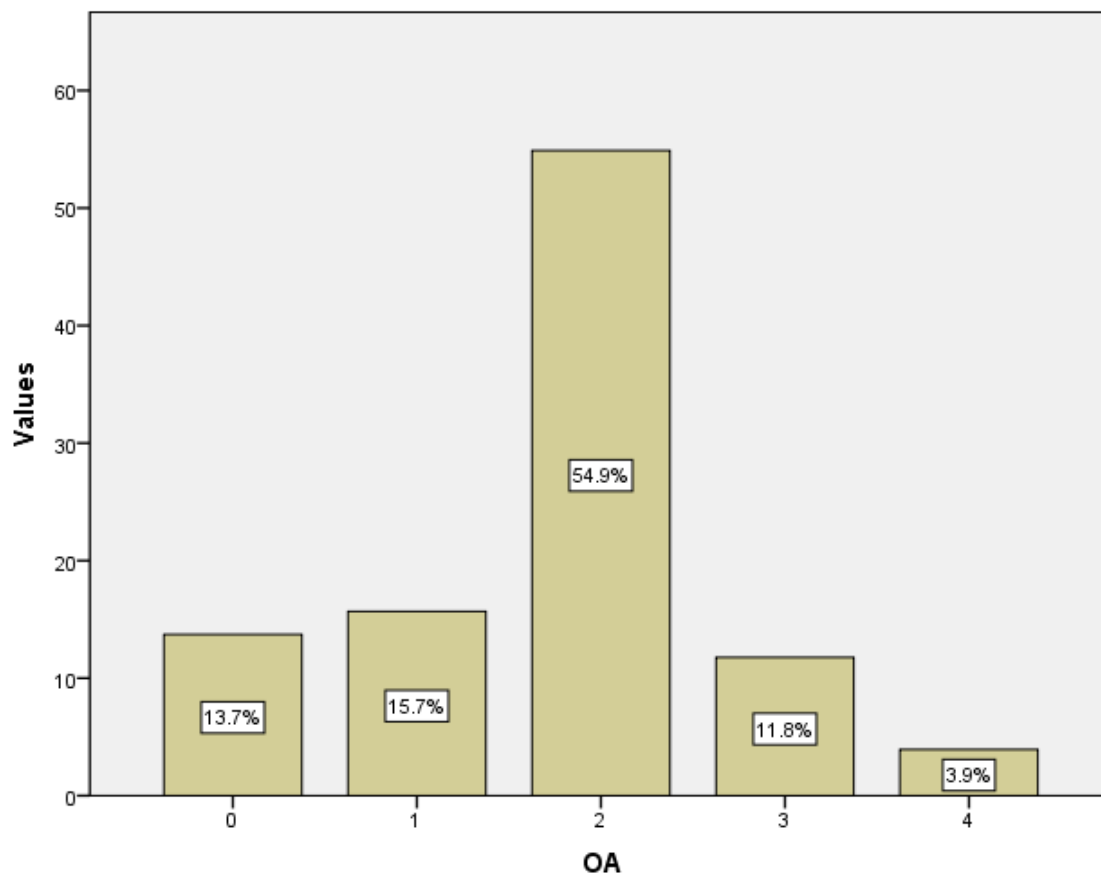


Figure 86. Study IX. Histogram of percentage of tibias by Ahlbäck OA grade distribution.

IV.2.4.6. Tubercle size in osteochondral fracture

Results for Study X, for 9 tibias, showed a mean age of 21.1 years (range, 12 to 42 years), 56% were males, 56% were left knees; 89% had MT>LT, and 11% LT>MT.

The main difference found in MRI was 1 ± 1.5 mm (range, -1.3 mm to 3.7 mm), where positive value indicates MT>LT. Percentage of the ML proximal tibial width (measured in the AP radiograph) showed a mean height for the MT of $12.9 \pm 2.1\%$ of the ML width (range, 8.3% to 15.2%), and a LT mean height of $11.2 \pm 2.5\%$ of the ML width (range, 6.6% to 13.7%). Their difference had an average of $1.7 \pm 1.1\%$ (range -3.9% to 3.5%, where positive value indicates MT>LT) of the radiographic ML width.

Similar to normal adult tibias, no significant differences in MT–LT height difference was noted in MRI or radiographs in men (mean difference in MRI, 0.2 mm; in radiographs, 1.4%) than in women (mean difference in MRI, 1.9 mm; in radiographs, 1.5%): $t(6)=-1.803$, $p=0.122$ for MRI; $t(6)=-0.971$, $p=0.344$ for radiographs.

A difference was found in MT–LT height between knees with an affected medial condyle (mean difference in MRI, 3.7 mm; in radiographs, 2.8%) and those affected in its lateral condyle (in MRI, 0.7 mm; in radiographs, 1.7%); but that difference was significant only in MRI: $t(6)=2.546$, $p=0.044$ for MRI; $t(6)=0.740$, $p=0.487$ for radiographs. No difference was found in terms of tubercle height difference between those who had a patellar tracking pathology (three cases) and those who did not.

IV.2.5. Degenerative changes of the intercondylar tubercles

IV.2.5.1. Qualitative assessment of degenerative changes

The main intercondylar tubercles showed osteophytic growths (Fig. 87, Fig. 88), their external slopes showed a wide range of anatomic variation (Fig. 89, Fig. 90), and tubercles and processes (and their osteophytes) showed erosion in their highest aspects. In some tibias with degenerative changes, the main LT slope was gentler in the upper part and steeper in the lower one, forming together a convex lateral slope.

In specimens with degenerative changes affecting the anterior and posterior processes, the lateral tubercle axis approached in some cases a line perpendicular to the posterior axis, while the medial tubercle followed a line similar to a perpendicular to the anterior axis.

Some tibias showed an elevated posteromedial intercondylar ridge, reaching in some cases a height similar to the posterolateral intercondylar ridge, sometimes even greater (Fig. 91). That change was not observed in the ALIR, which did not reach the elevation of the AMIR in any of the specimens studied (Fig. 92).

B1 was often found higher than B2 in normal specimens. When the AMIR was found elevated, B2 and B1 could show different relative elevations: $B1 > B2$, $B1 = B2$, or $B2 > B1$. In many specimens B1 and B2 could not be differentiated from each other, and generally a mixed B1-B2 process was observed, with a posteriorly higher B2 blending with an anterior, medially curving B1; or, more often, a higher B1 that curved medially followed by B2, usually with a medium to big, more

medially located Parsons' knob or tubercle as the only hint for the previous presence of B1 (Fig. 93).

At the origin of B1 and B2, in front of the medial tubercle, a small anteromedial incisure could often be seen.

In many tibias with degenerative changes, the area between D1 and D2 – i.e. the posterior part of the anterolateral corner – became elevated, forming in some cases a common D1-D2 area.

In some tibias the vallecule and posterior summit were found as a much wider area than was found in normal tibias, with their superior aspect more flattened. Part of the posterior summit's external slope appeared embedded in this wider posterior summit, and a simpler, laterally-oriented external slope (i.e. with less radius of curvature) remained. With higher degenerative changes, the vallecule was found to be shorter, and its slope steeper, more clearly separated from the posterior subpeak anteriorly by a small, smoother slope.

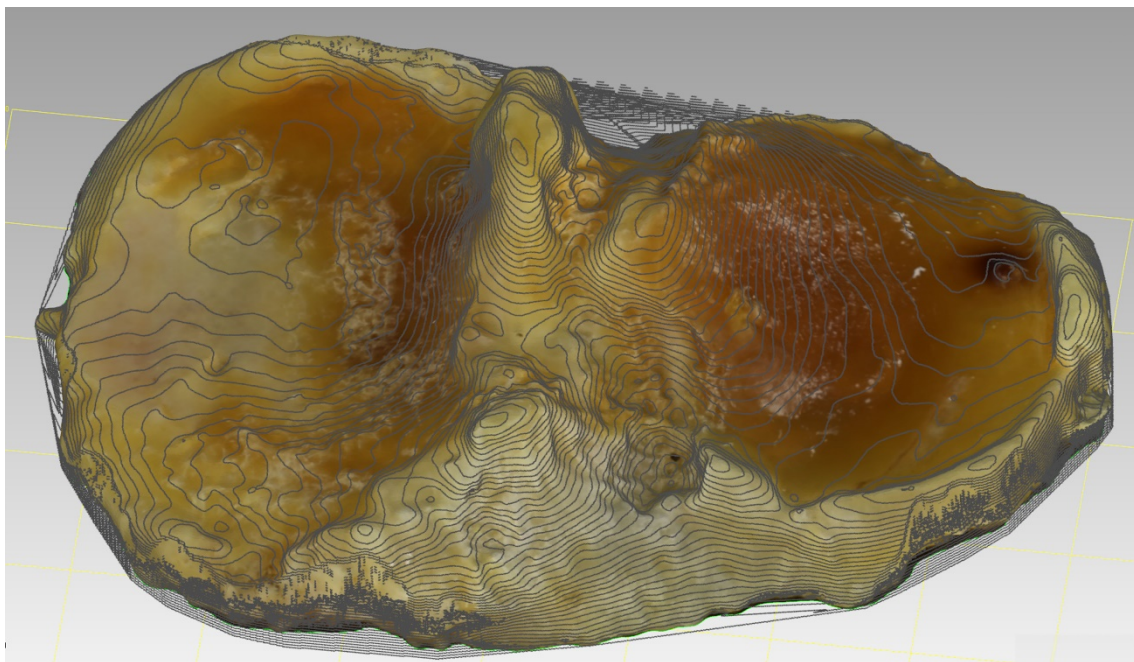


Figure 87. 3D model of tibia 32, with contour lines superimposed. Varus. MAC: 2M. MT osteophyte: grade 5; LT osteophyte: grade 2.

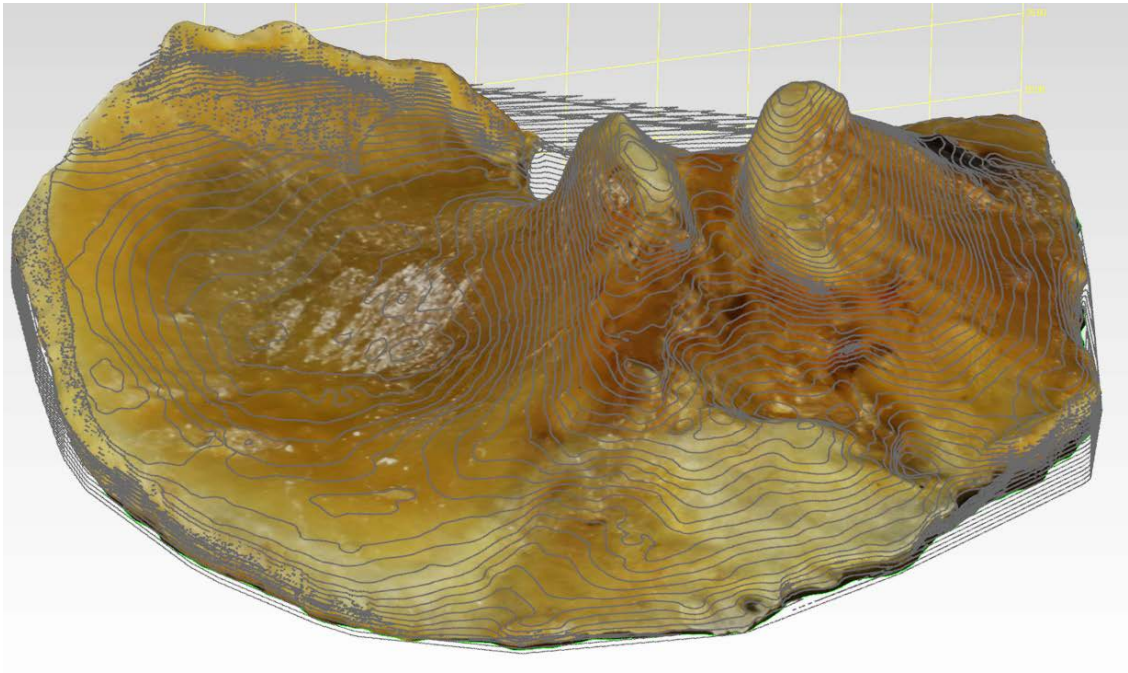


Figure 88. 3D model of tibia 79 with contour lines superimposed. Varus. MAC: 1M. MT osteophyte: grade 2; LT osteophyte: grade 5.

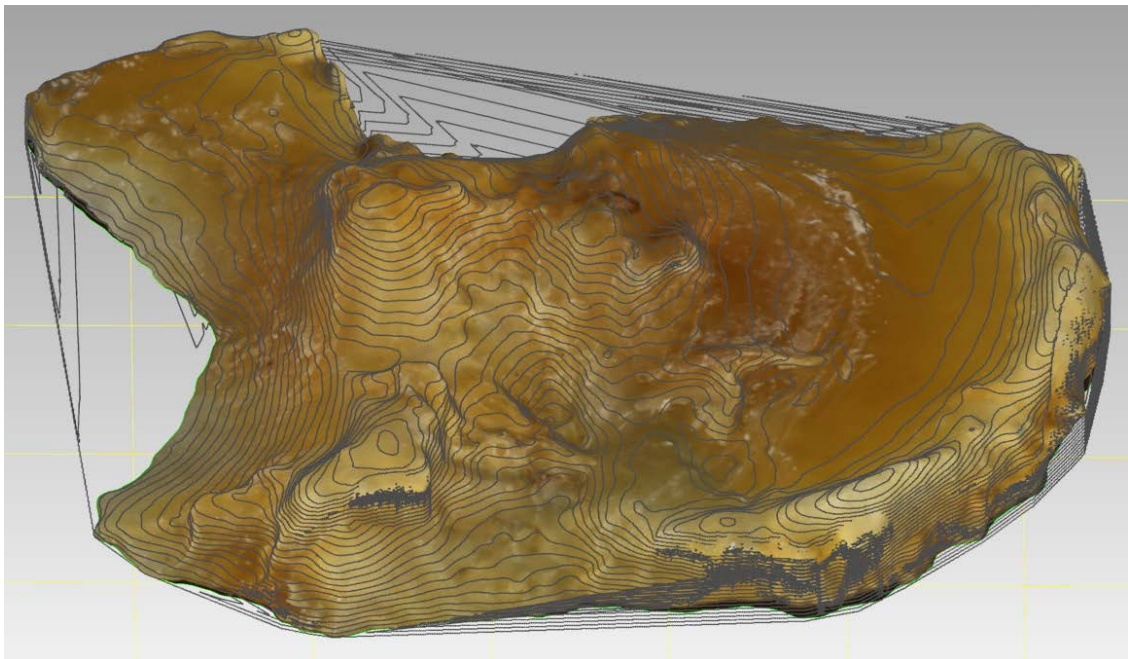


Figure 89. 3D model of tibia 21 with contour lines. Varus. MAC: 3M. MT width: grade 3; MT attrition: grade 2, direction AL (notice similar attrition direction of the Parsons' osteophyte). LT width: grade 3; LT attrition: grade 3, direction AL-PL.

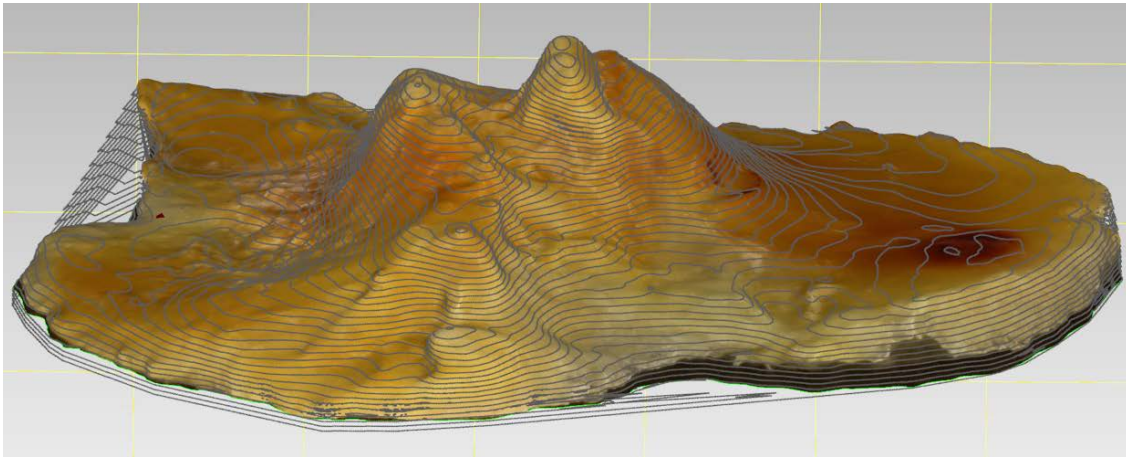


Figure 90. 3D model of tibia 89 with contour lines. Varus. MAC: 4M. MT width: grade 3; MT attrition: grade 2, direction AM-PL. LT width: grade 3; LT attrition: grade 1, direction AL.

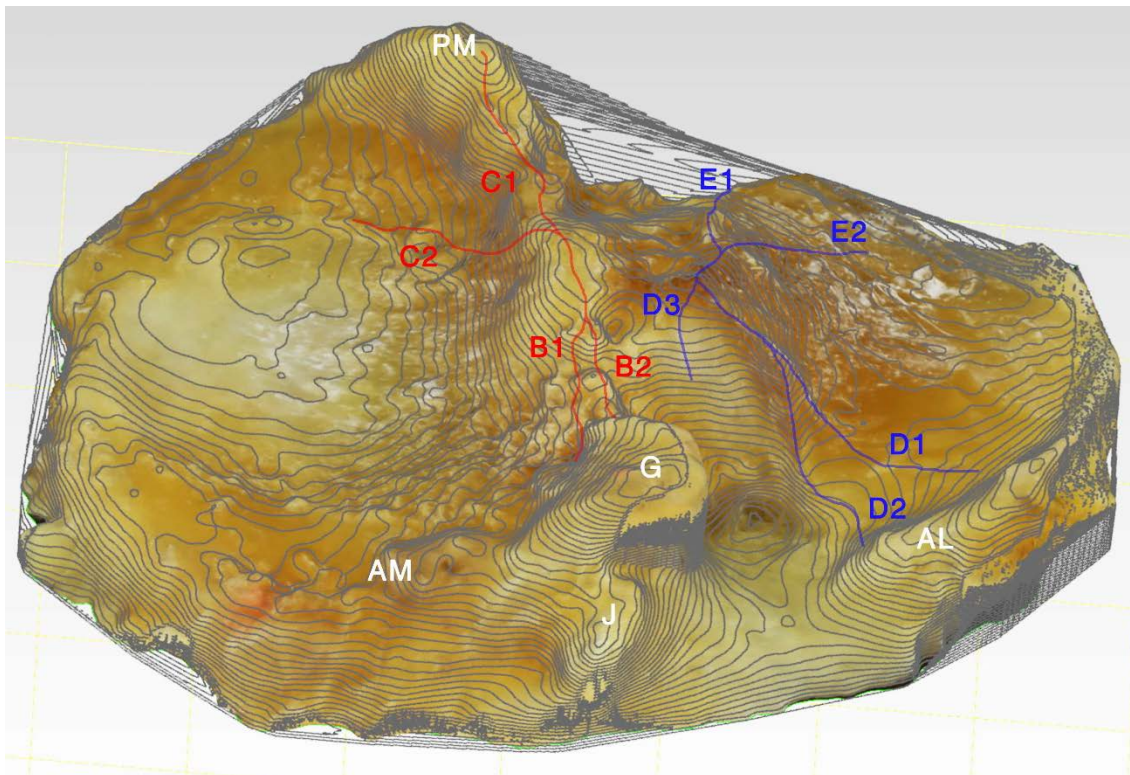


Figure 91. 3D model of tibia 65, with contour lines superimposed (image left-mirrored). Varus. MAC: 4M. B1: grade 2; B2: grade 3 (connecting with hook-shaped Parsons' osteophyte grade 5); C1: grade 4 (connecting with PM corner osteophyte grade 5); C2: grade 1; D1-D2: grade 2; D3: grade 1; E1, E2 grade 1 (notice high attrition grade in TL, PLIR and posterior TL slope). Also labelled are the Parson's knob (G), anterior sagittal ridge (J), AM, AL, and PM corner elevations.

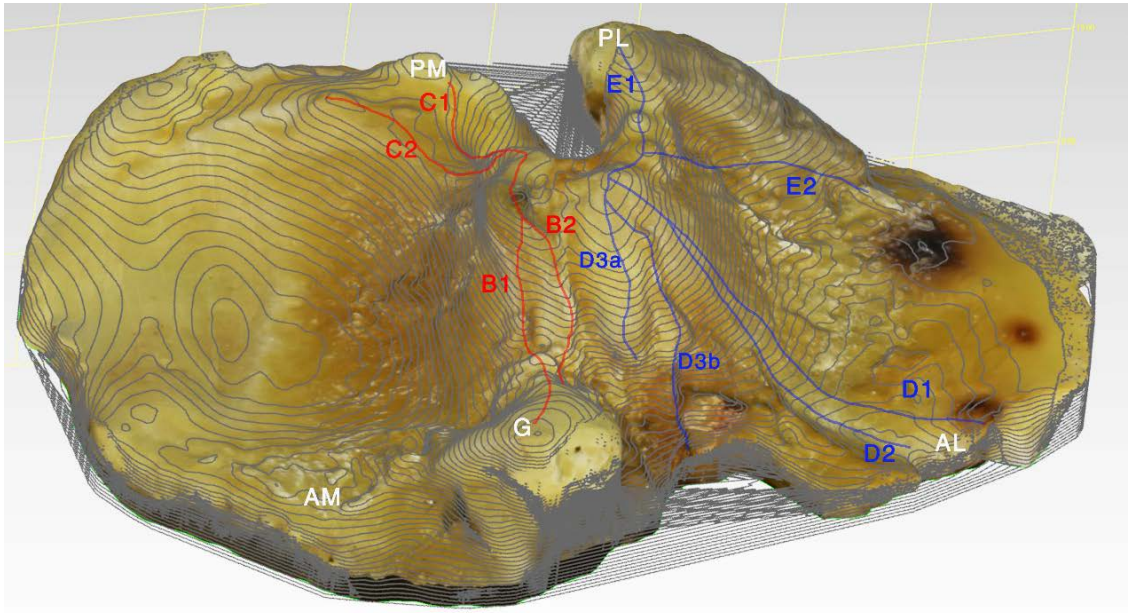


Figure 92. 3D model of tibia 81, with contour lines superimposed. Varus. MAC 4M. B1: grade 3; B2: grade 3 (connecting with little hook-shaped Parsons' osteophyte grade 5); C1: grade 3 (connecting with PM corner osteophyte grade 3); C2: grade 3; D1-D2: grade 3; D3: grade 4 (dependent on D3_a; observe a different D3_b ridge, both obliterating the AL recess space); E1: grade 4 (connecting with PL corner osteophyte grade 5); E2: grade 1. Also labelled are the Parson's knob (G), AM, AL, PM, and PL corner elevations.

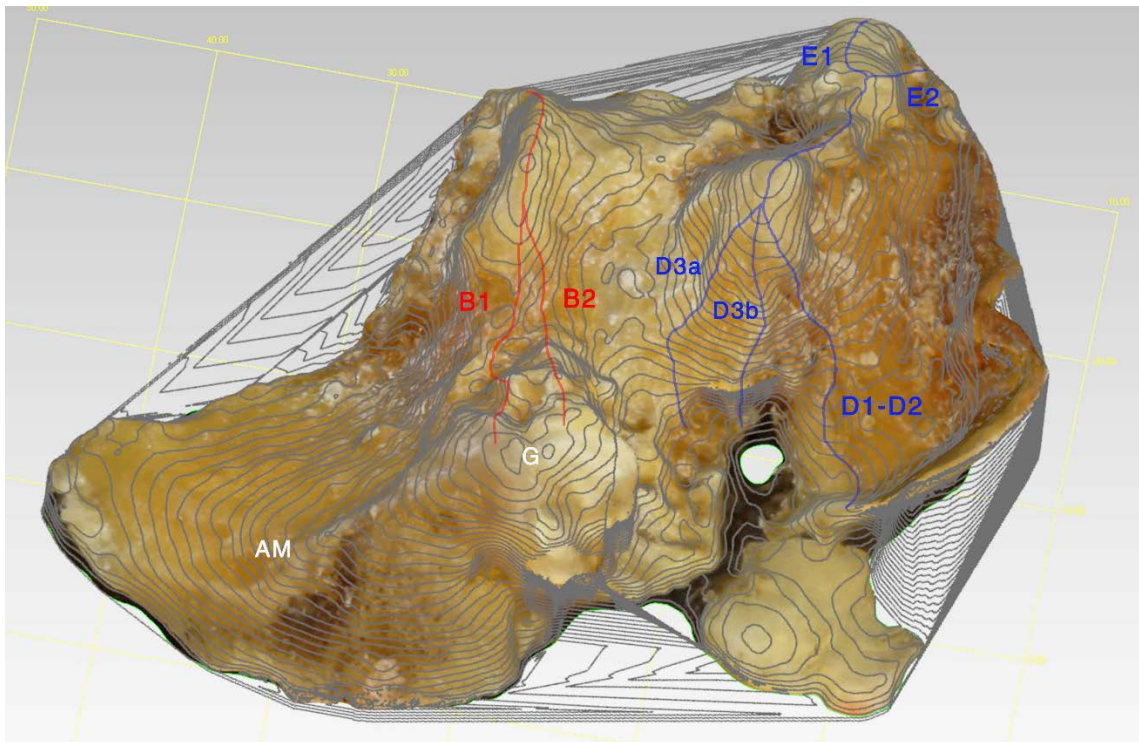


Figure 93. 3D model of pathological tibia B, with contour lines superimposed. Varus. MAC: 3M. B1 osteophyte: grade 2. B2 osteophyte: grade 4 (mixing into star-shaped Parsons' osteophyte). Notice B1-B2 incisura grade -2. A marked D3_b-predominant osteophytic growth (grade 3) is seen obliterating the AL recess space, instead of the most common D3_a. Also labelled are the Parson's knob (G), AM, AL corners.

IV.2.5.2. Tubercle osteophytes and radiographic density

The relative size of the main intercondylar tubercles in pathological tibias showed the following distribution: 62% MT>LT, 33% LT>MT, 4% MT=LT.

The relative size of both tubercles was assessed to observe their association with the Ahlbäck classification, and with alignment. No statistically significant association was found between relative size and knee OA (Fig. 95): $\chi^2(8)=7.321$, $p=0.502$.

Pathological tibias with LT>MT (mean tibiofemoral angle, 7.2°) showed a diminished tibiofemoral angle than MT>LT (mean tibiofemoral angle, 8.5°), without achieving statistical significance, $t(91)=-1.444$, $p=0.152$.

A Spearman's rank-order correlation was run to determine the relationship between tubercle osteophyte grade and knee OA grade. There was a weak to moderate positive correlation between both classifications, which was statistically significant: medial tubercle (Fig. 96), $r_s(98)=0.451$, $p<0.001$; lateral tubercle (Fig. 97), $r_s(98)=0.331$, $p=0.001$.

Density in axial radiography (Fig. 94) was found to be weakly correlated with knee OA in the medial tubercle (Fig. 98), $r_s(98)=0.226$, $p=0.034$; but not in the lateral tubercle (Fig. 99), $r_s(98)=0.162$, $p=0.116$.

Regarding tubercle osteophyte size measured directly over the specimens, a Kruskal-Wallis H test did not show a statistically significant difference between knee OA grade groups: MT AP depth (Fig. 100), $\chi^2(3)=3.641$, $p=0.303$; MT ML width (Fig. 101), $\chi^2(3)=4.549$, $p=0.208$; LT AP depth (Fig. 102), $\chi^2(3)=1.232$, $p=0.745$; LT ML width (Fig. 103): $\chi^2(3)=3.302$, $p=0.347$.

Measures did not show a statistically significant difference between the different osteophyte grade groups, either: MT AP depth, $\chi^2(3)=2.768$, $p=0.429$; MT ML width, $\chi^2(3)=4.659$, $p=0.199$; LT AP depth, $\chi^2(3)=2.341$, $p=0.505$; LT ML width, $\chi^2(3)=3.166$, $p=0.367$.

The relative height of peaks observed along the MT (Fig. 104) and LT (Fig. 105) processes was not found to be significantly associated with knee OA, nor with tibiofemoral alignment or MAC. A simplified relative peak height (including only the first two peaks) was not associated with any of those variables, either.

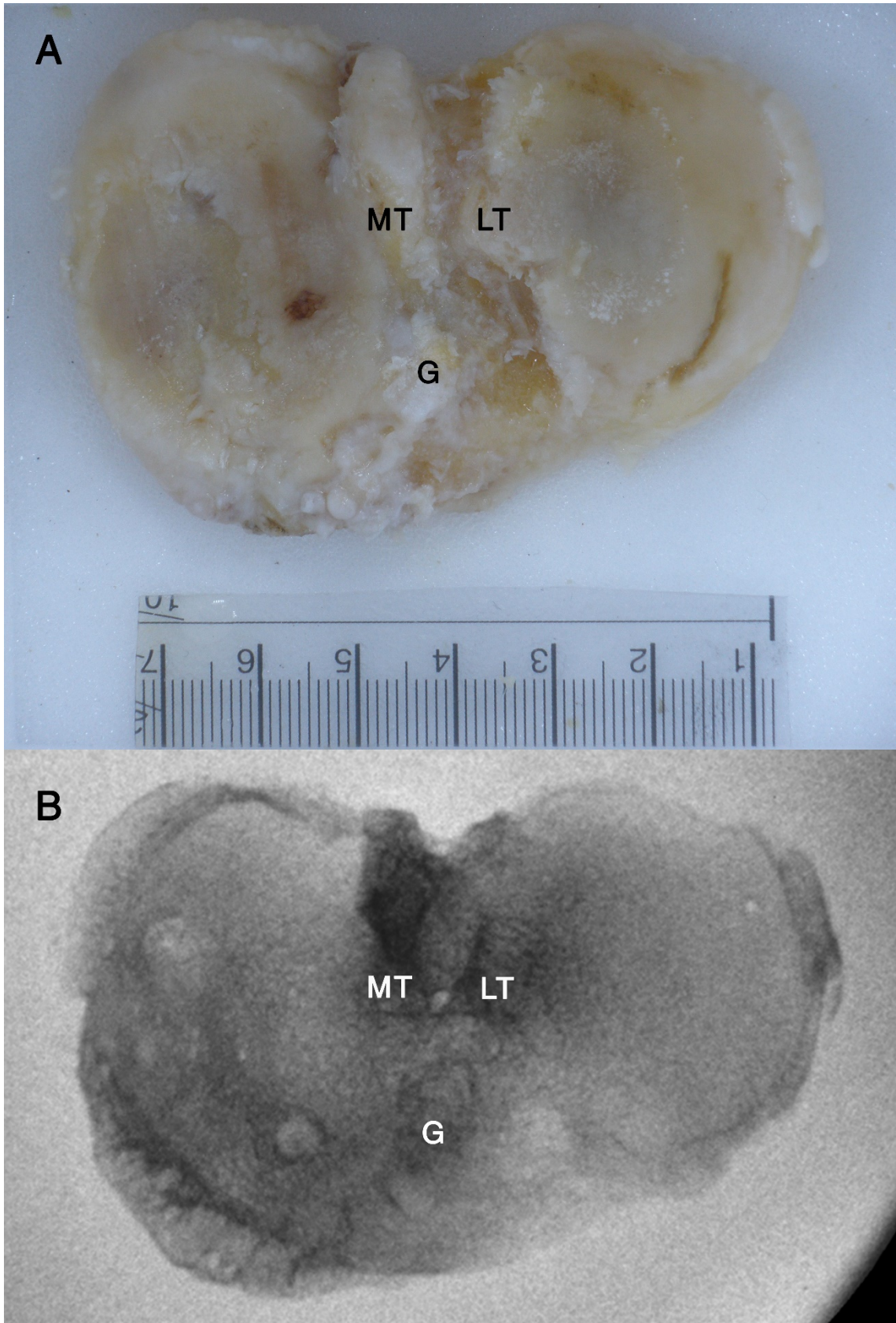


Figure 94. Tibia 32. A: Photograph of fresh specimen; measurements were made directly over it. B: Axial (i.e. inferosuperior) fluoroscopic image. MT and LT radiographic density: grade 3; Parsons' knob (G): grade 2.

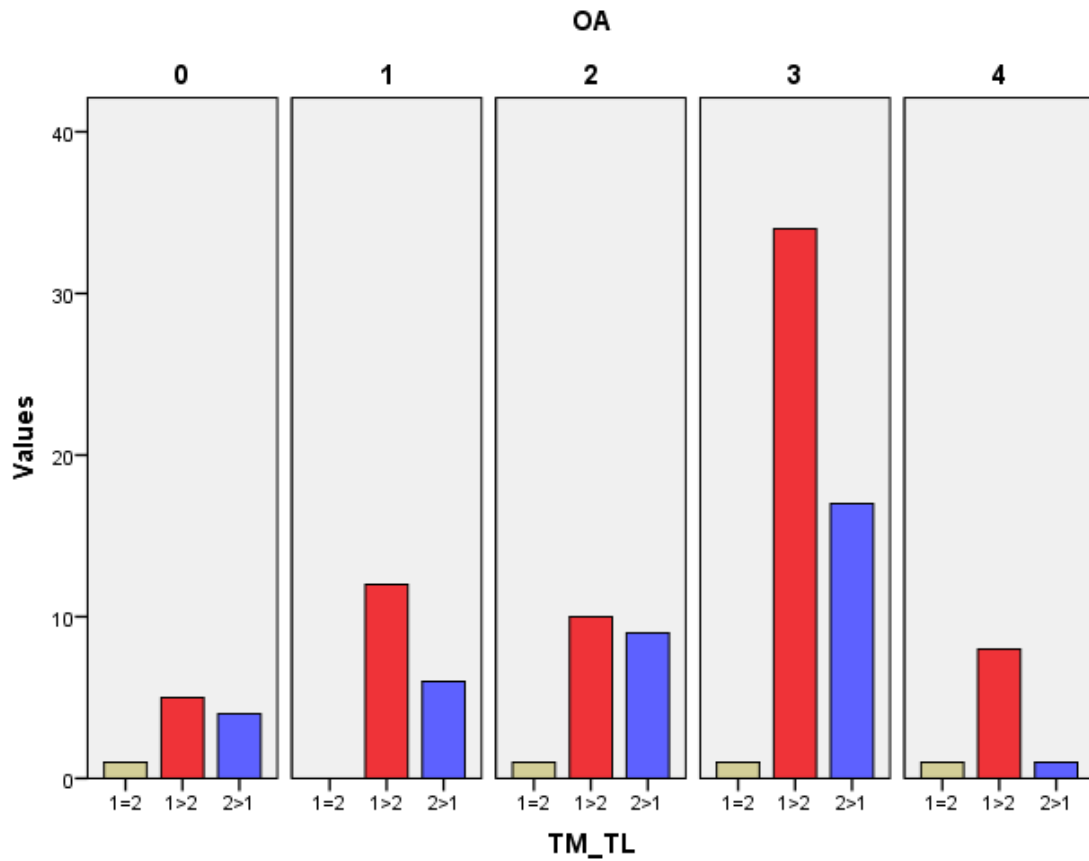


Figure 95. Study II. Histogram of relative tubercle size (TM_TL): number of tibias in each category, grouped by Ahlbäck OA grade. 1=MT, 2=LT.

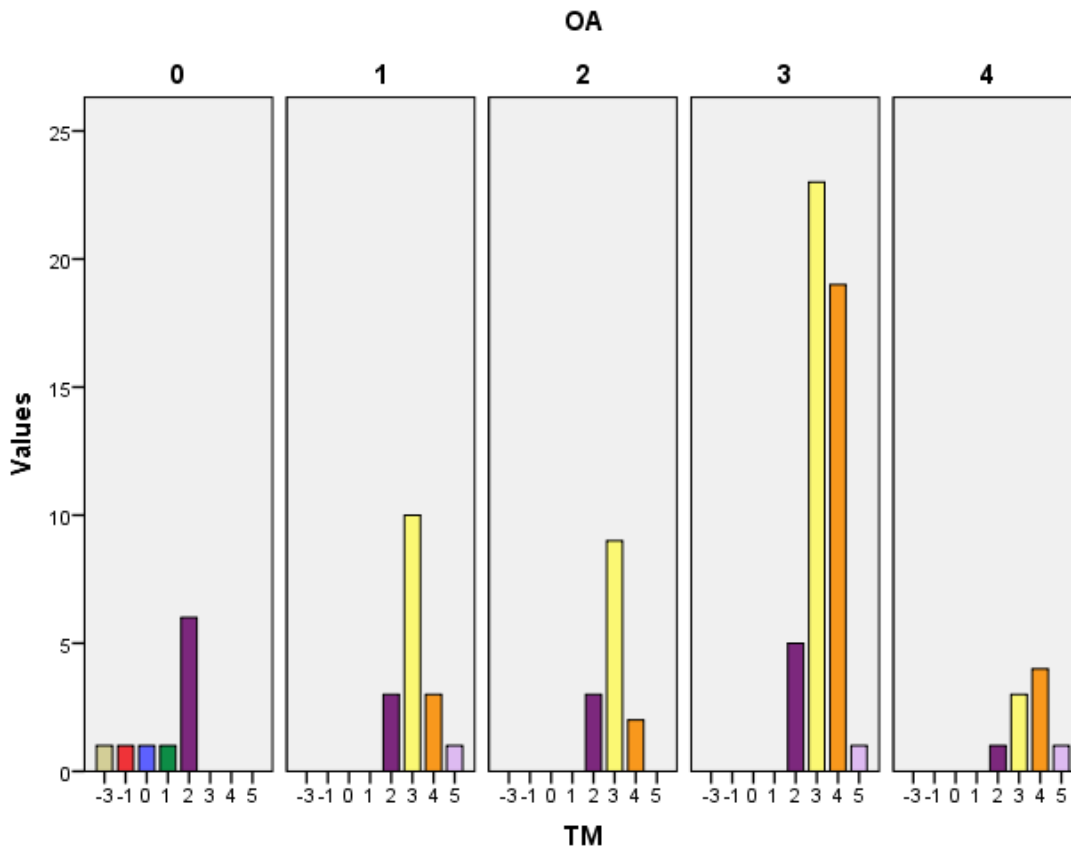


Figure 96. Study II. Histogram of medial tubercle (TM) osteophyte grade: number of tibias in each osteophyte grade, grouped by Ahlbäck OA grade.

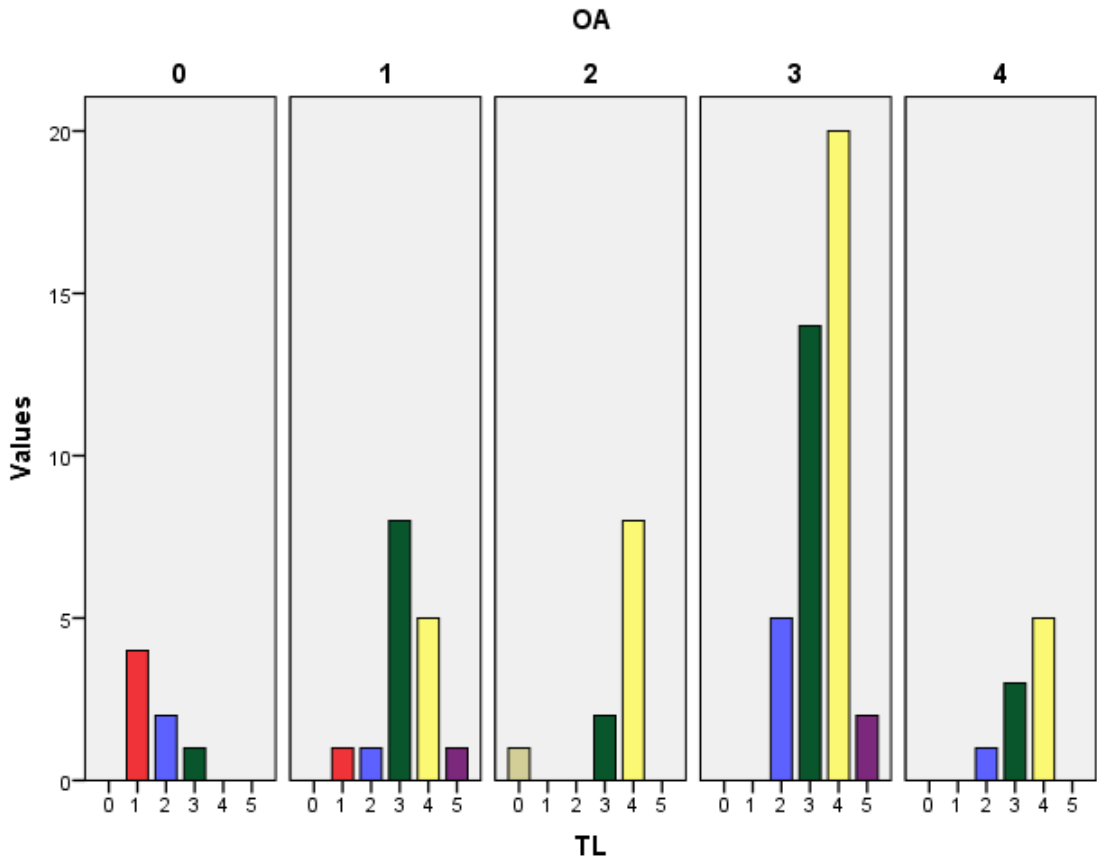


Figure 97. Study II. Histogram of lateral tubercle (TL) osteophyte grade: number of tibias in each osteophyte grade, grouped by Ahlbäck OA grade.

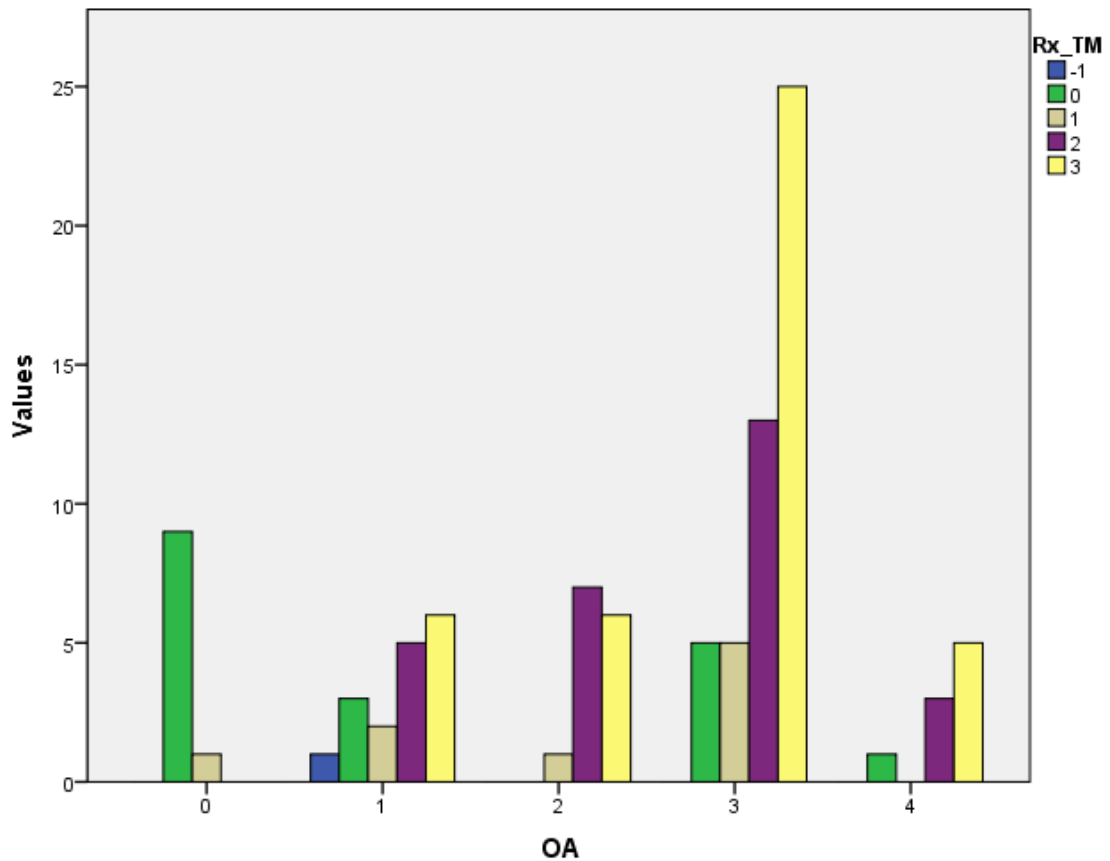


Figure 98. Study II. Histogram of radiographic density of the medial tubercle in inferosuperior radiographs (Rx_TM): number of tibias in each category, grouped by Ahlbäck OA grade.

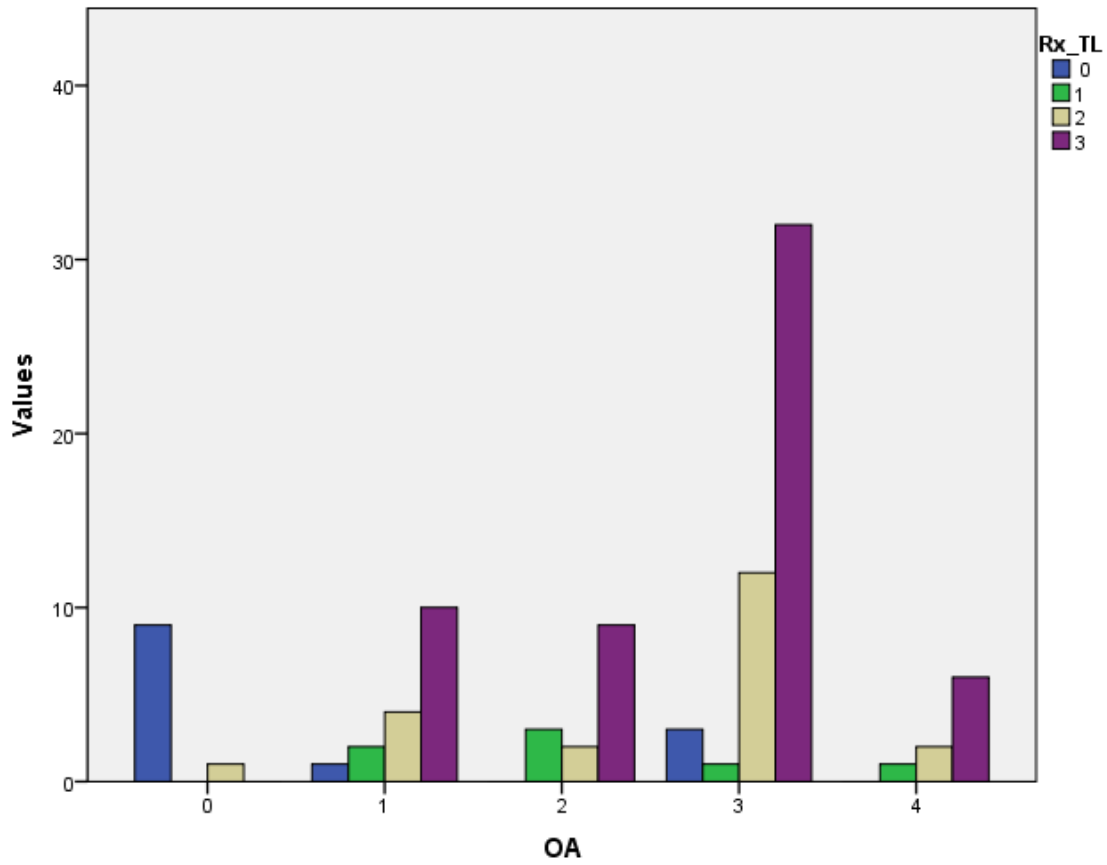


Figure 99. Study II. Histogram of radiographic density of the lateral tubercle in inferosuperior radiographs (Rx_TL): number of tibias in each category, grouped by Ahlbäck OA grade.

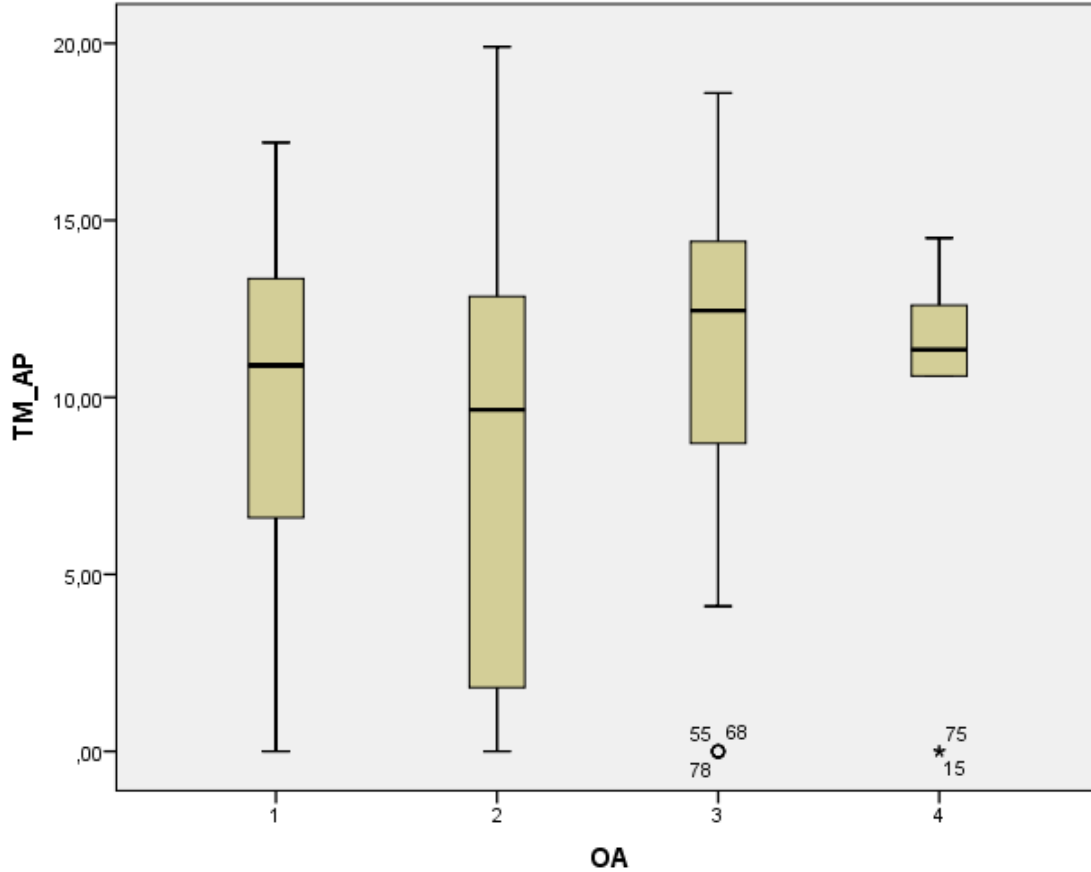


Figure 100. Study II. Box-and-whisker plot of MT AP size (TM_AP) distribution in each Ahlbäck OA grade.

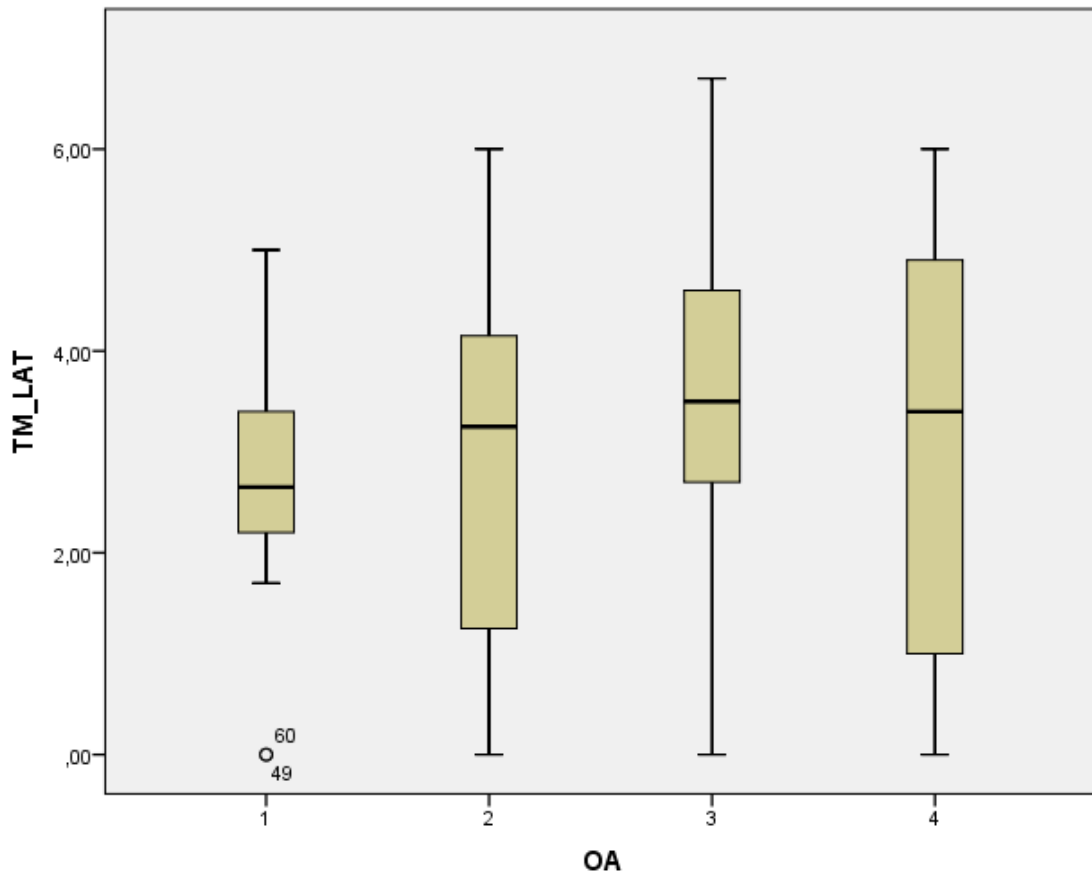


Figure 101. Study II. Box-and-whisker plot of MT mediolateral size (TM_LAT) distribution in each Ahlbäck OA grade.

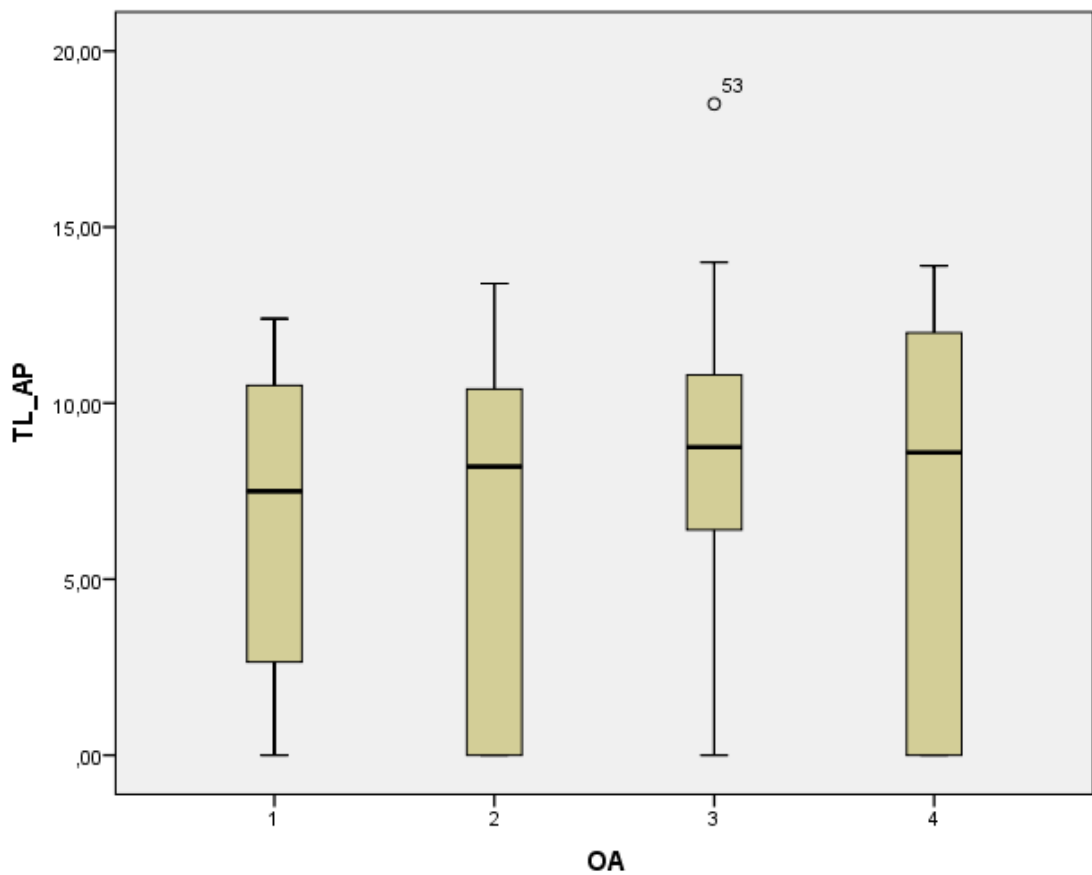


Figure 102. Study II. Box-and-whisker plot of LT AP size (TL_AP) distribution in each Ahlbäck OA grade.

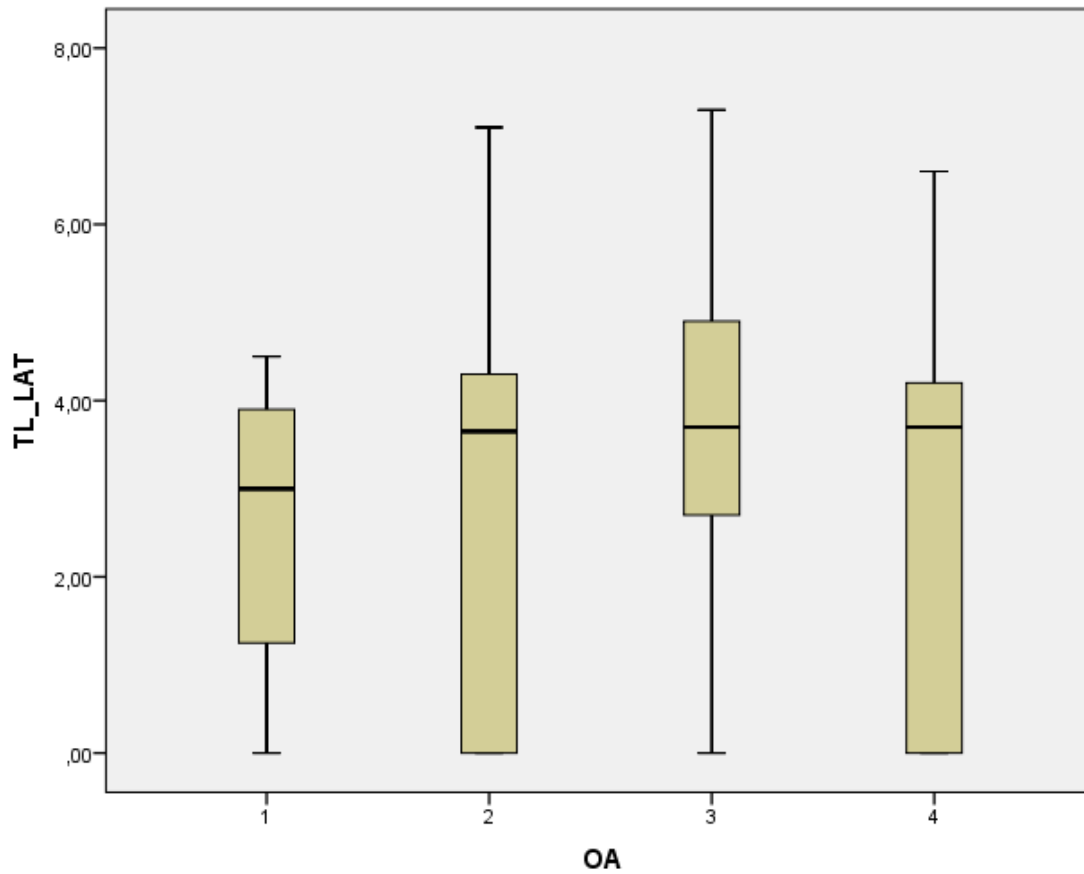


Figure 103. Study II. Box-and-whisker plot of LT mediolateral size (TL_LAT) distribution in each Ahlbäck OA grade.

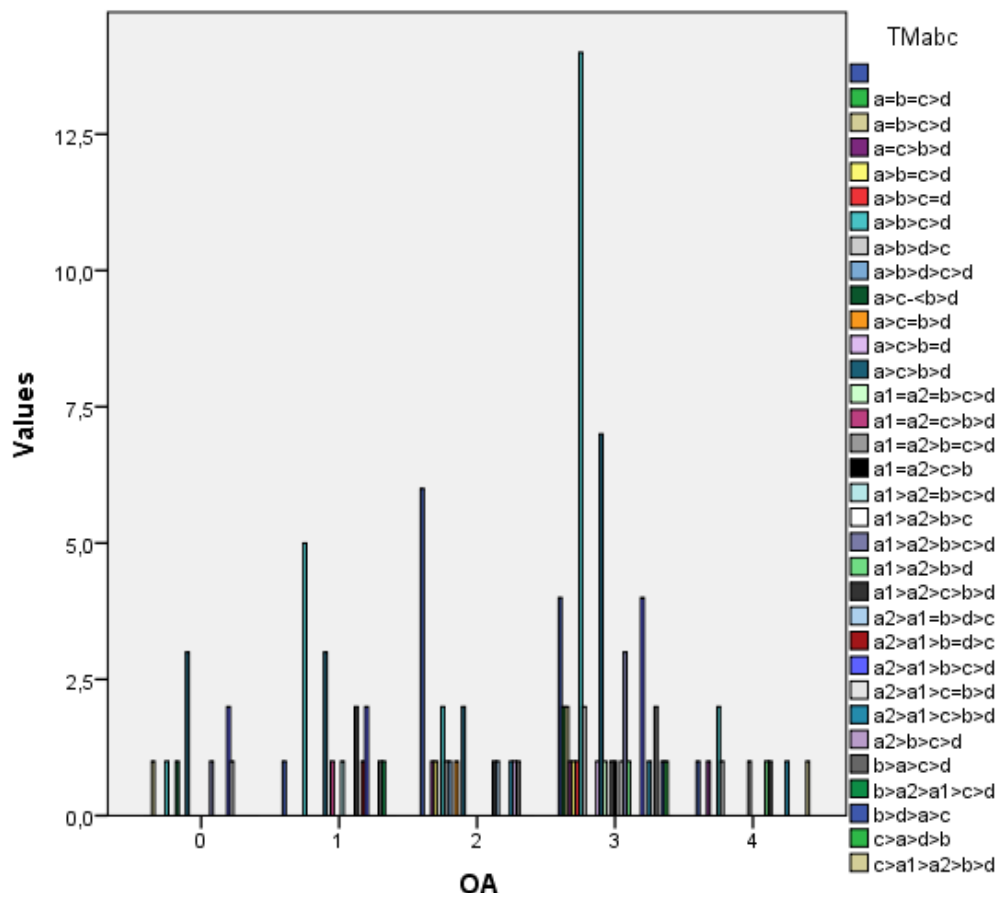


Figure 104. Study II. Histogram of relative medial tubercle peak height (TMabc).

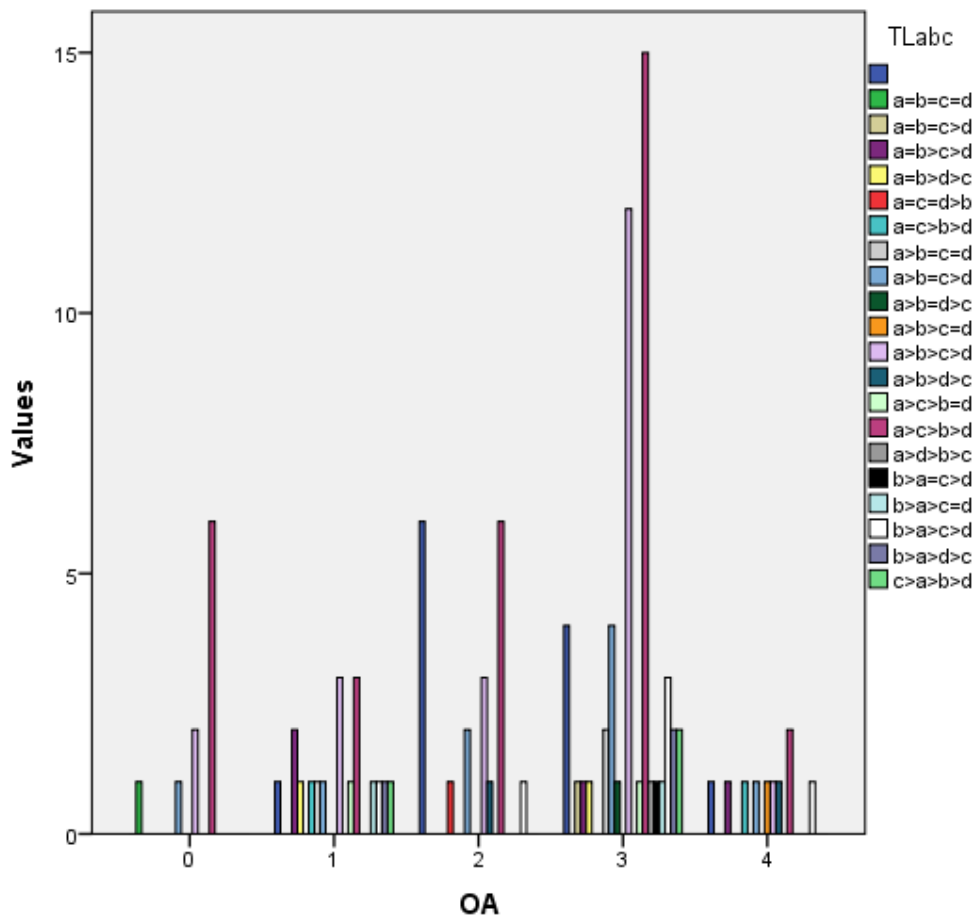


Figure 105. Study II. Histogram of relative lateral tubercle peak (TLabc) height.

IV.2.5.3. Tubercle width and attrition

There was a significant but weak correlation between tubercle width knee OA: medial tubercle (Fig. 108), $r_s(98)=0.395$, $p<0.001$; lateral tubercle (Fig. 109), $r_s(98)=0.272$, $p=0.007$;

The association between MT attrition and knee OA did not reach significance (Fig. 110), $r_s(98)=0.197$, $p=0.051$; while LT attrition was significantly but weakly correlated with knee OA (Fig. 111), $r_s(98)=0.383$, $p<0.001$.

The association of MT attrition direction and knee OA did not achieve significance (Fig. 112): $\chi^2(40)=51.967$, $p=0.097$ (Phi=0.672, Cramer's V=0.336). However, the simplified MT attrition direction (AM vs. AL) was significantly associated with tibiofemoral alignment, $\chi^2(6)=16.613$, $p=0.011$, with frequency distribution showing more valgus and neuter knees (5 of 7 valid knees) associated with AL direction, and more varus knees associated with AM direction (51 of 85 valid knees).

LT attrition direction also showed a strong, significant association with OA (Fig. 113), $\chi^2(48)=76.885$, $p=0.005$ (Phi=0.834, Cramer's V=0.417), with frequency distribution analysis showing more AL (as well as AM-PL, and L) involvement with higher OA grades, while AM (and also AL-PM) was associated with lower OA grades. Simplified LT attrition direction (AL vs. AM) also showed a significant association with tibiofemoral alignment, $\chi^2(6)=13.110$, $p=0.041$, with frequency distribution showing more varus knees associated with the AL group, while neuter and valgus knees showed an equal distribution between AM and AL attrition direction.

Tubercle direction as seen on X-ray (Fig. 106, Fig. 107) showed a non-significant association with knee OA in the medial tubercle (Fig. 114), $\chi^2(12)=17.964$, $p=0.117$ (Phi=0.428, Cramer's V=0.247); and a significant association with knee OA in the lateral tubercle (Fig. 115), $\chi^2(12)=22.311$, $p=0.034$ (Phi=0.477, Cramer's V=0.275).

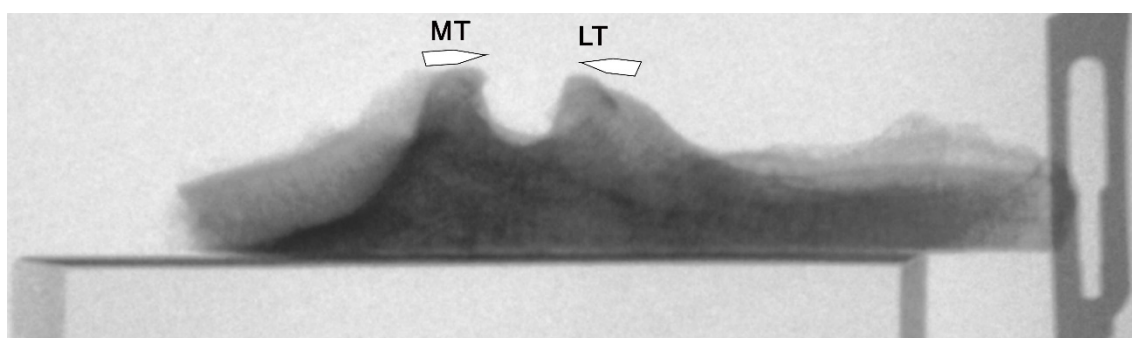


Figure 106. Anteroposterior fluoroscopic image of Tibia 24. Varus. MT and LT internal attrition direction (pointed to by arrowheads).

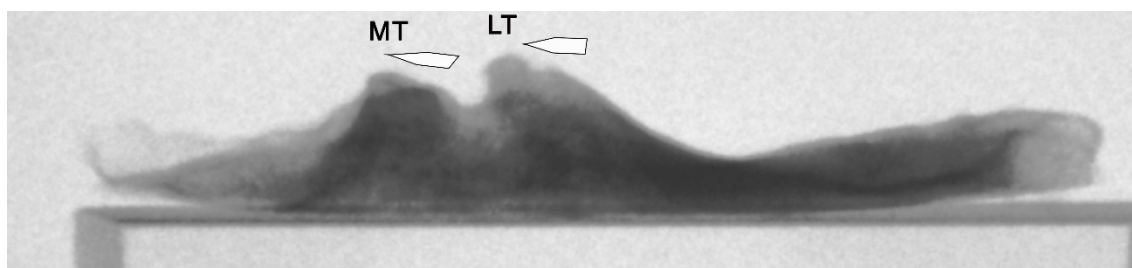


Figure 107. Anteroposterior fluoroscopic image of pathological tibia E. Valgus. MT external attrition direction, LT internal attrition direction (pointed to by arrowheads).

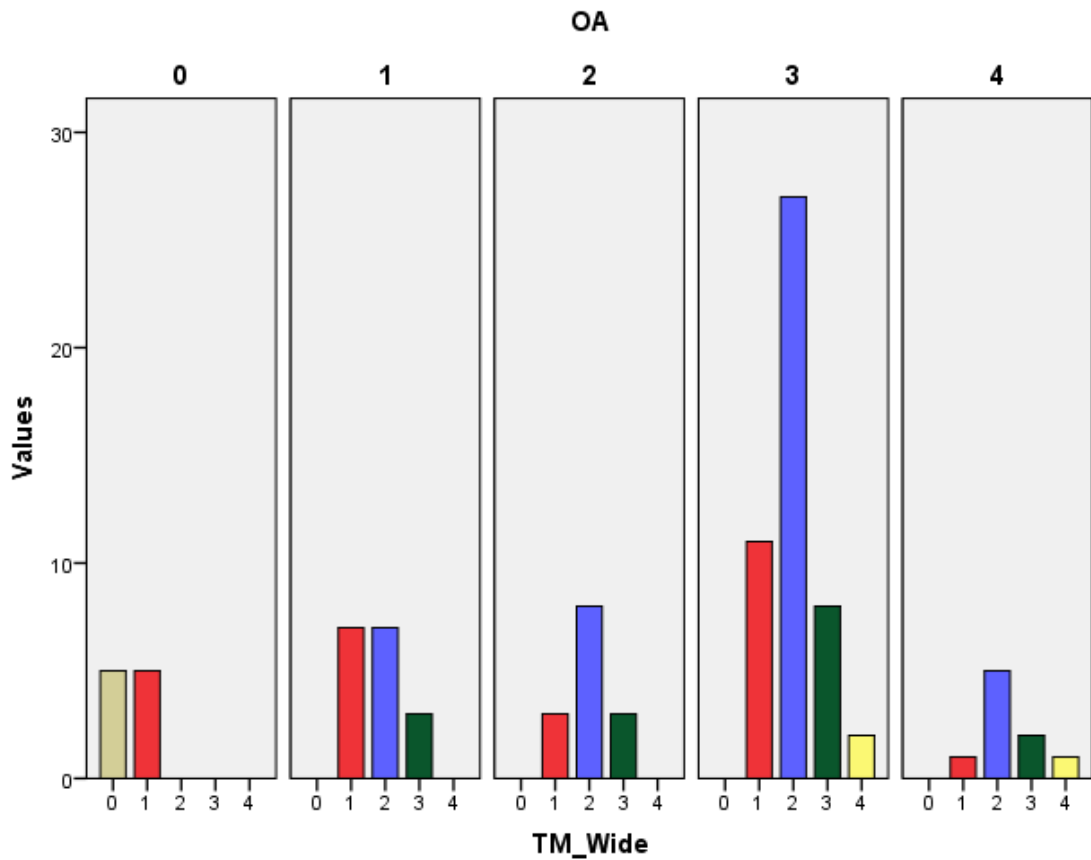


Figure 108. Study II. Histogram of medial tubercle width grade (TM_Wide): number of tibias in each width grade, grouped by Ahlbäck OA grade.

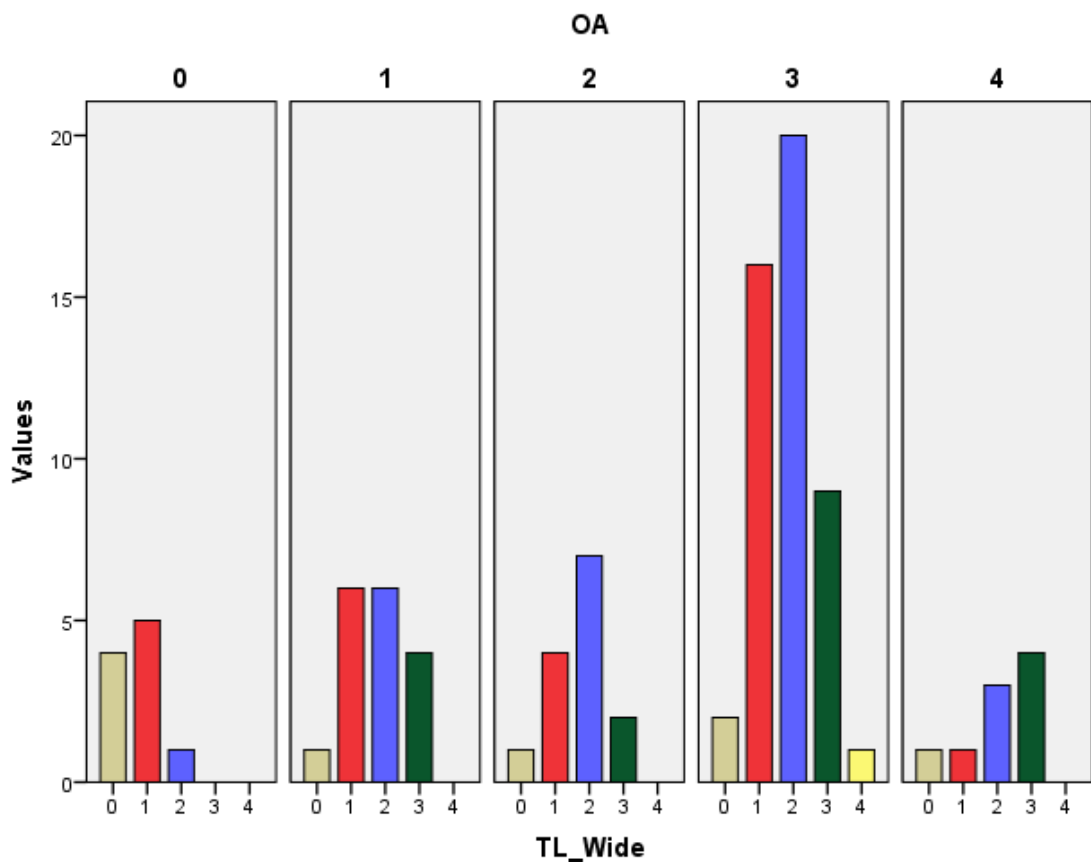


Figure 109. Study II. Histogram of lateral tubercle width grade (TL_Wide): number of tibias in each width grade, grouped by Ahlbäck OA grade.

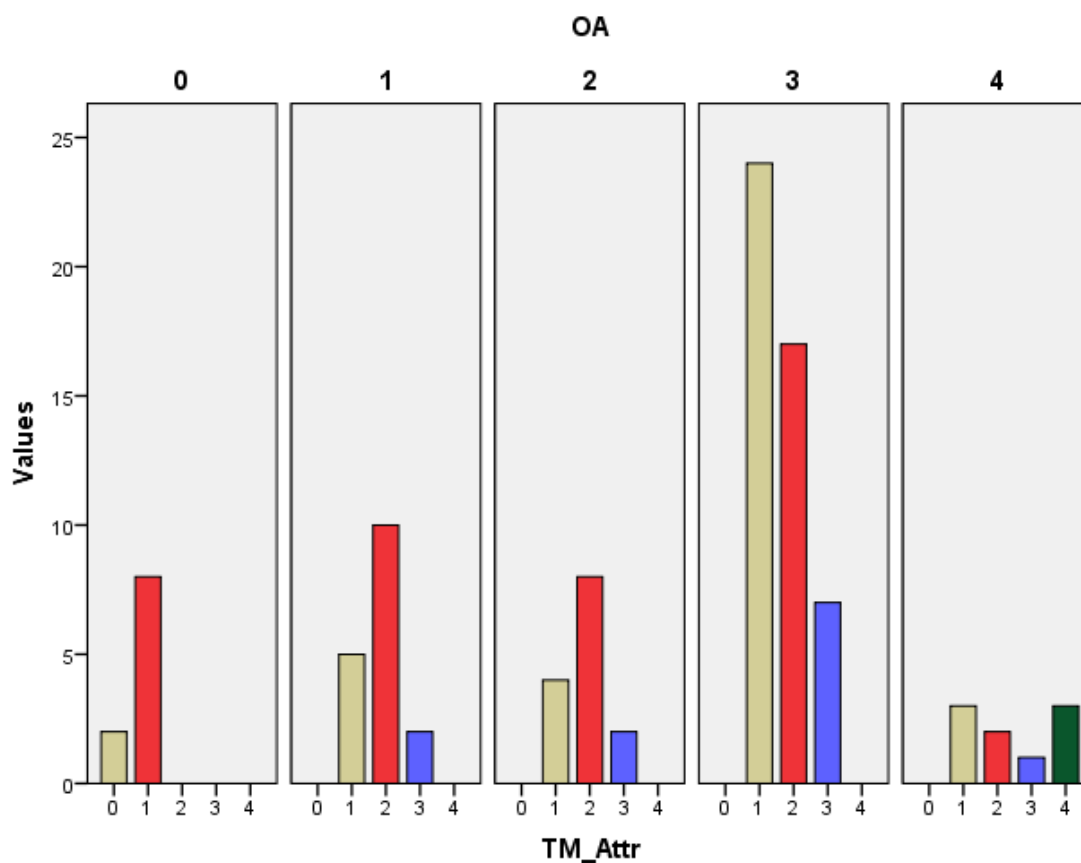


Figure 110. Study II. Histogram of medial tubercle attrition grade (TM_Attr): number of tibias in each attrition grade, grouped by Ahlbäck OA grade.

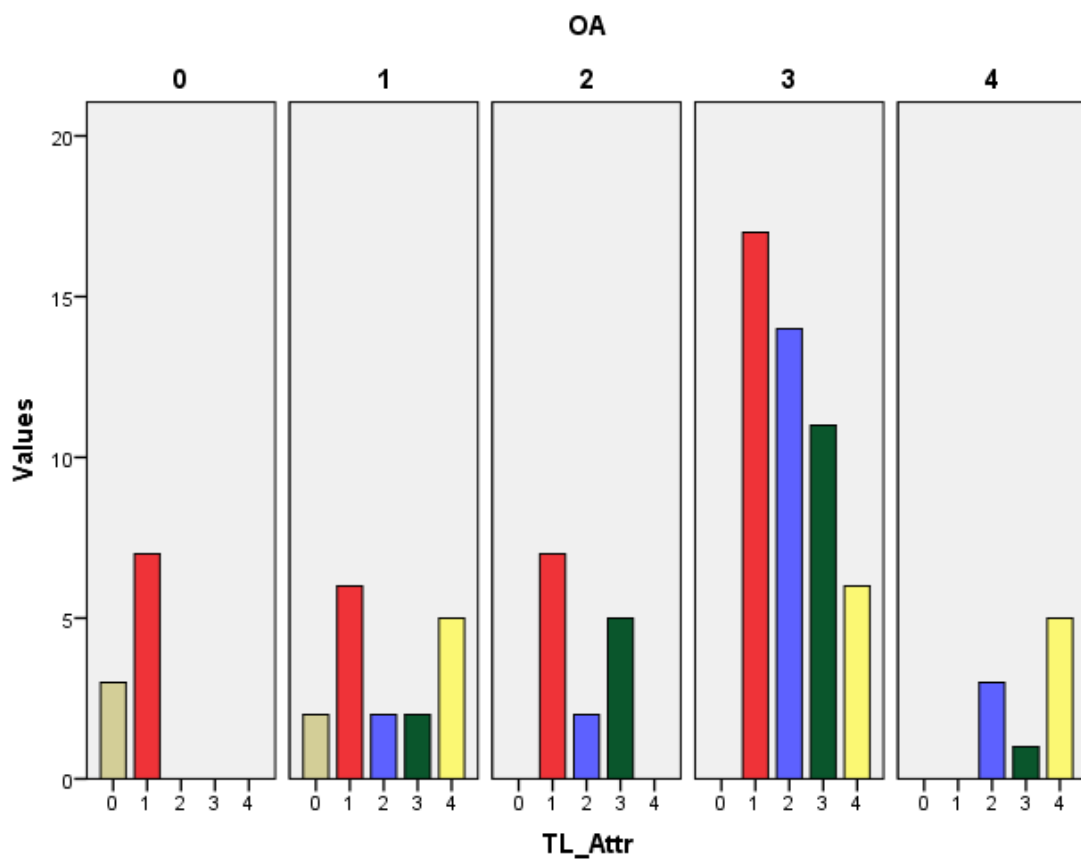


Figure 111. Study II. Histogram of lateral tubercle attrition grade (TL_Attr): number of tibias in each attrition grade, grouped by Ahlbäck OA grade.

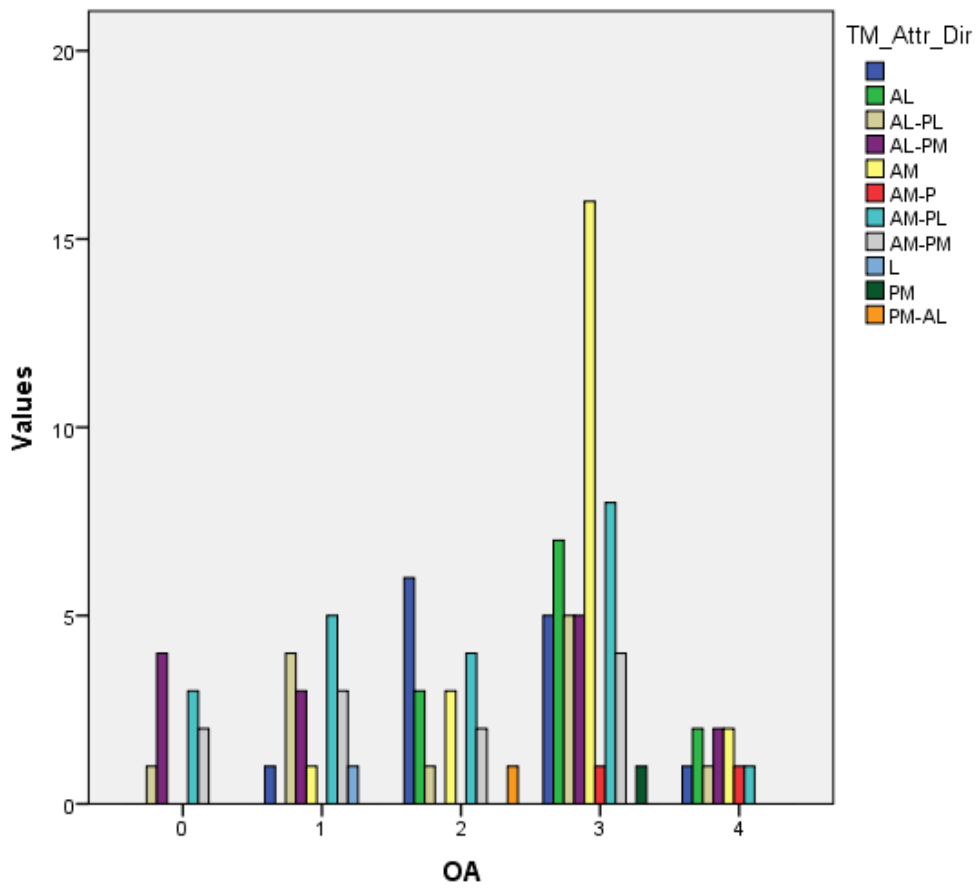


Figure 112. Study II. Histogram of medial tubercle attrition direction (TM_Attr_Dir): number of tibias in each category, grouped by Ahlbäck OA grade.

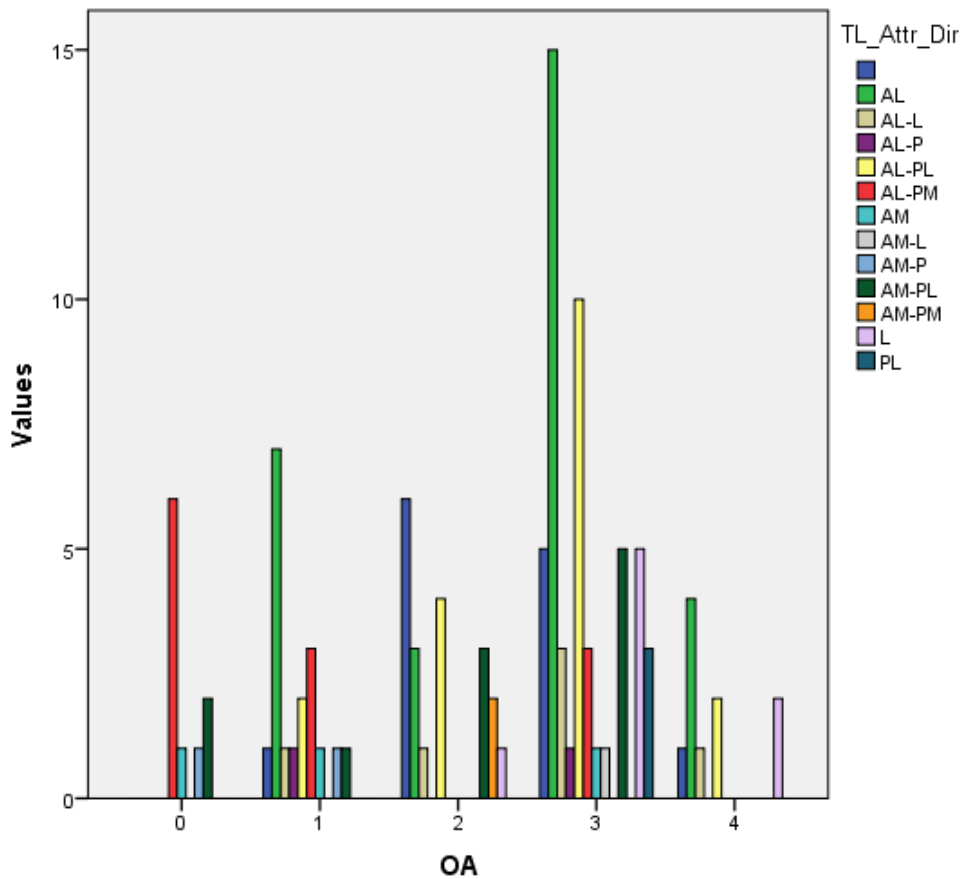


Figure 113. Study II. Histogram of lateral tubercle attrition direction (TL_Attr_Dir): number of tibias in each category, grouped by Ahlbäck OA grade.

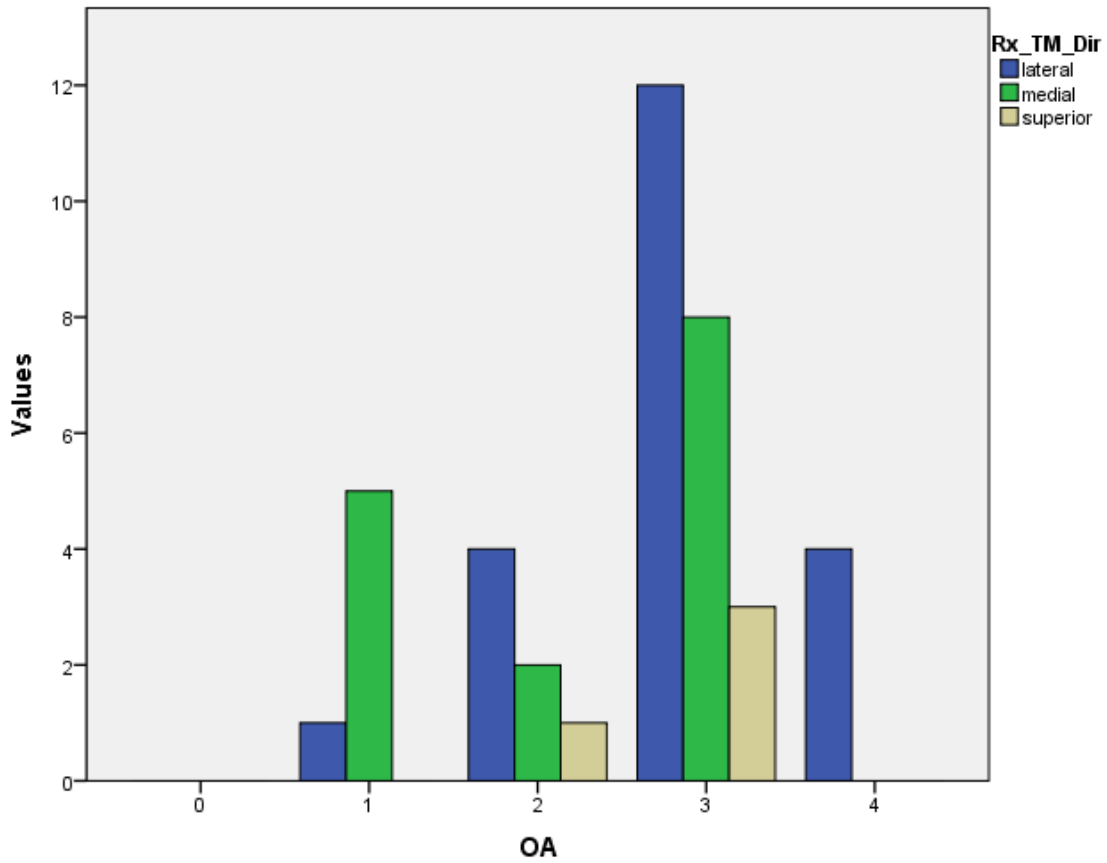


Figure 114. Study II. Histogram of medial tubercle direction in radiograph (Rx_TM_Dir): number of tibias in each category, grouped by Ahlbäck OA grade.

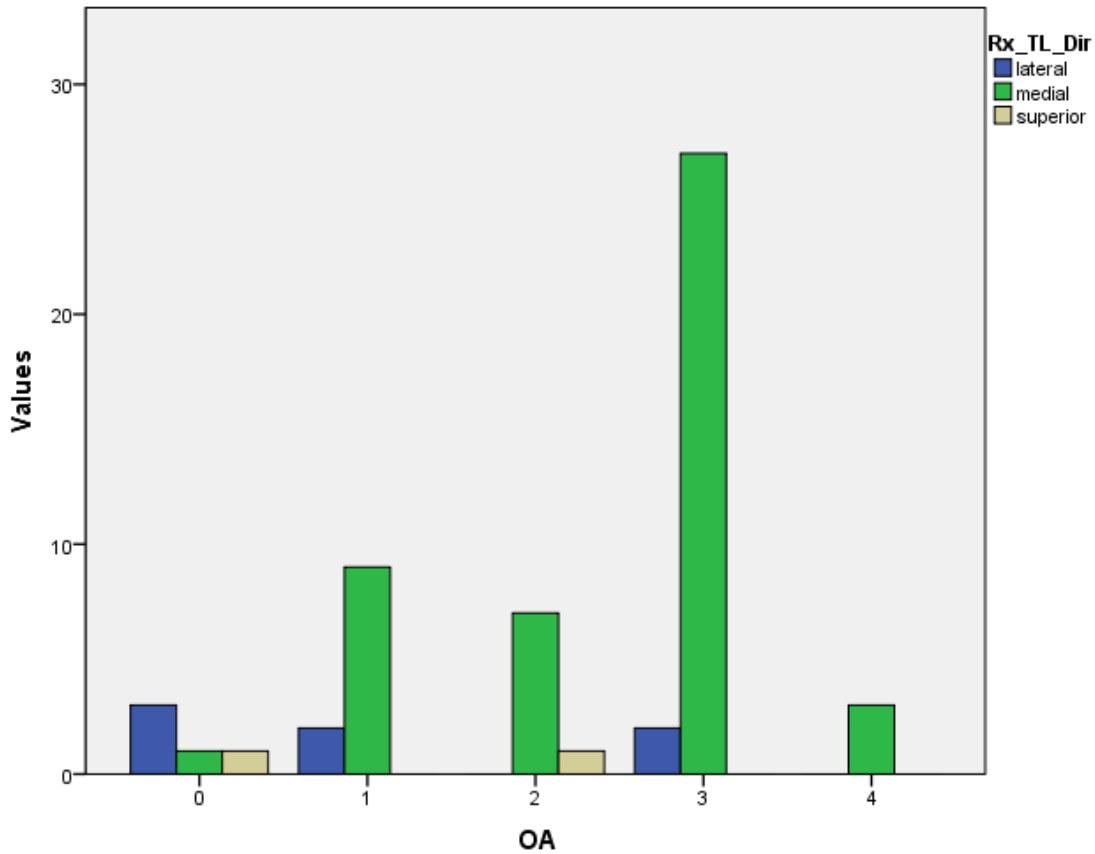


Figure 115. Study II. Histogram of lateral tubercle direction in radiograph (Rx_TL_Dir): number of tibias in each category, grouped by Ahlbäck OA grade.

IV.2.5.4. Tubercle slope

MT and LT slopes, as well as the MT–LT common slope, showed a weak correlation with the Ahlbäck OA classification, and ANOVA analysis showed no statistically significant differences among group means:

- MT (Figure 116): $F(4,93)=0.302$, $p=0.876$.
- LT (Figure 117): $F(4,93)=1.355$, $p=0.256$.
- MT–LT (Figure 118): $F(4,93)=0.859$, $p=0.492$.

They also showed a weak correlation with tibiofemoral angle, with ANOVA analysis showing a significant but very weak positive correlation ($R=0.311$, $p=0.42$) for MT (Fig. 119).

When compared to medial condyle attrition, MT and LT slopes showed a best fit for a cubic regression model, not achieving statistical significance in ANOVA analysis: MT (Fig. 120), $p=0.063$; LT (Fig. 121), $p=0.311$.

When compared to MAC and MACOp, ANOVA analysis showed no statistically significant differences for the 4 affected zones in terms of MT and LT slopes.

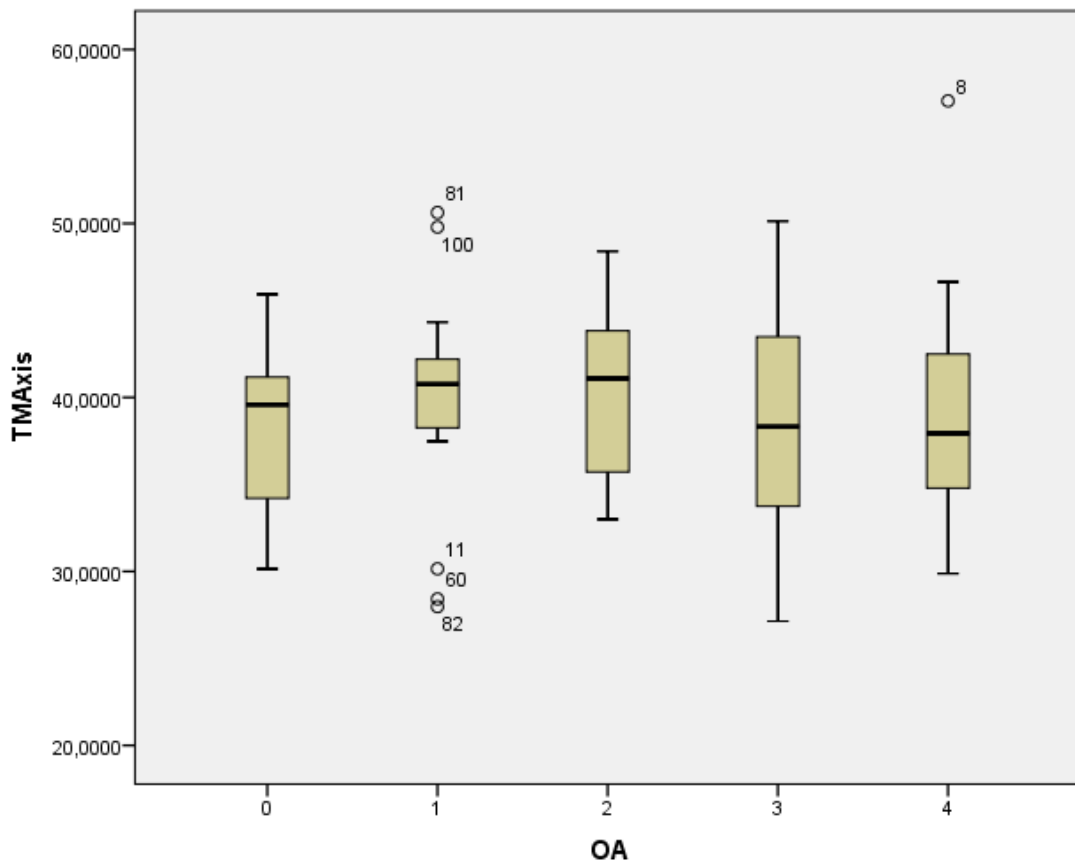


Figure 116. Study II. Box-and-whisker plot of MT slope (TMAxis) distribution in each Ahlbäck OA grade.

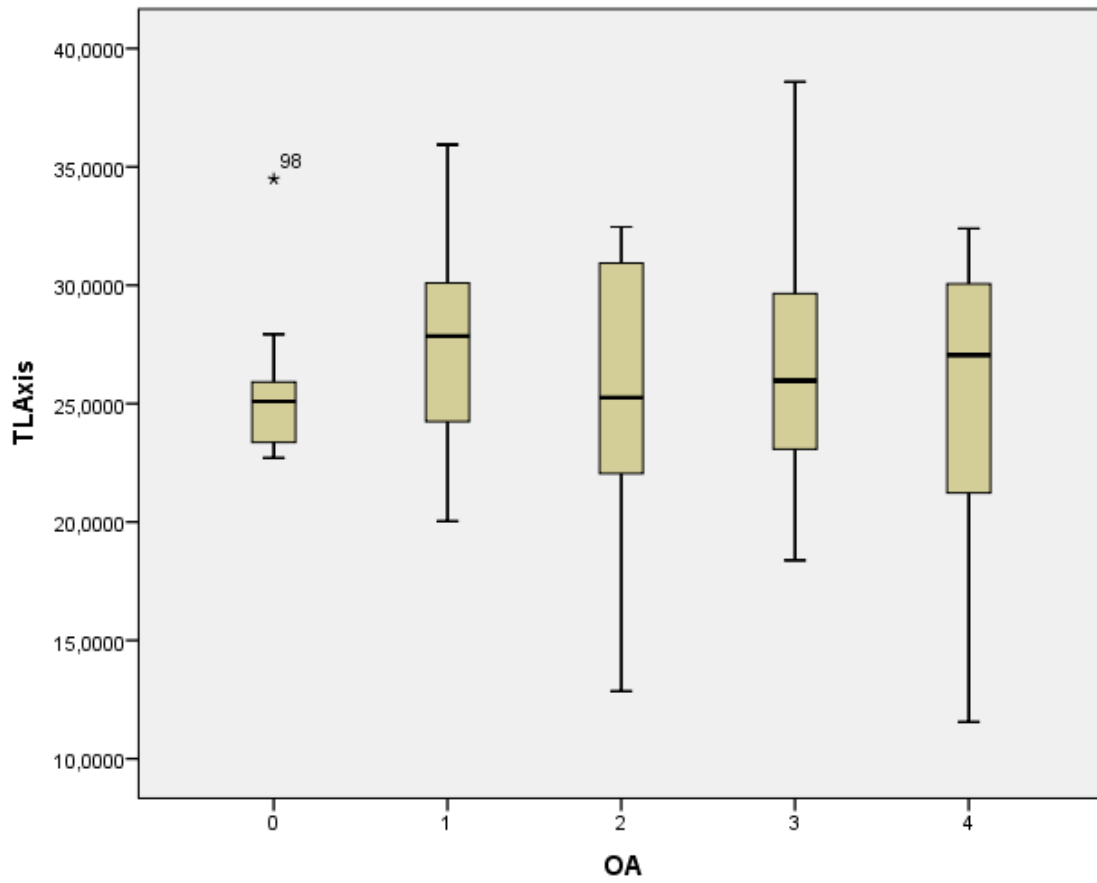


Figure 117. Study II. Box-and-whisker plot of LT slope (TLAxis) distribution in each Ahlbäck OA grade.

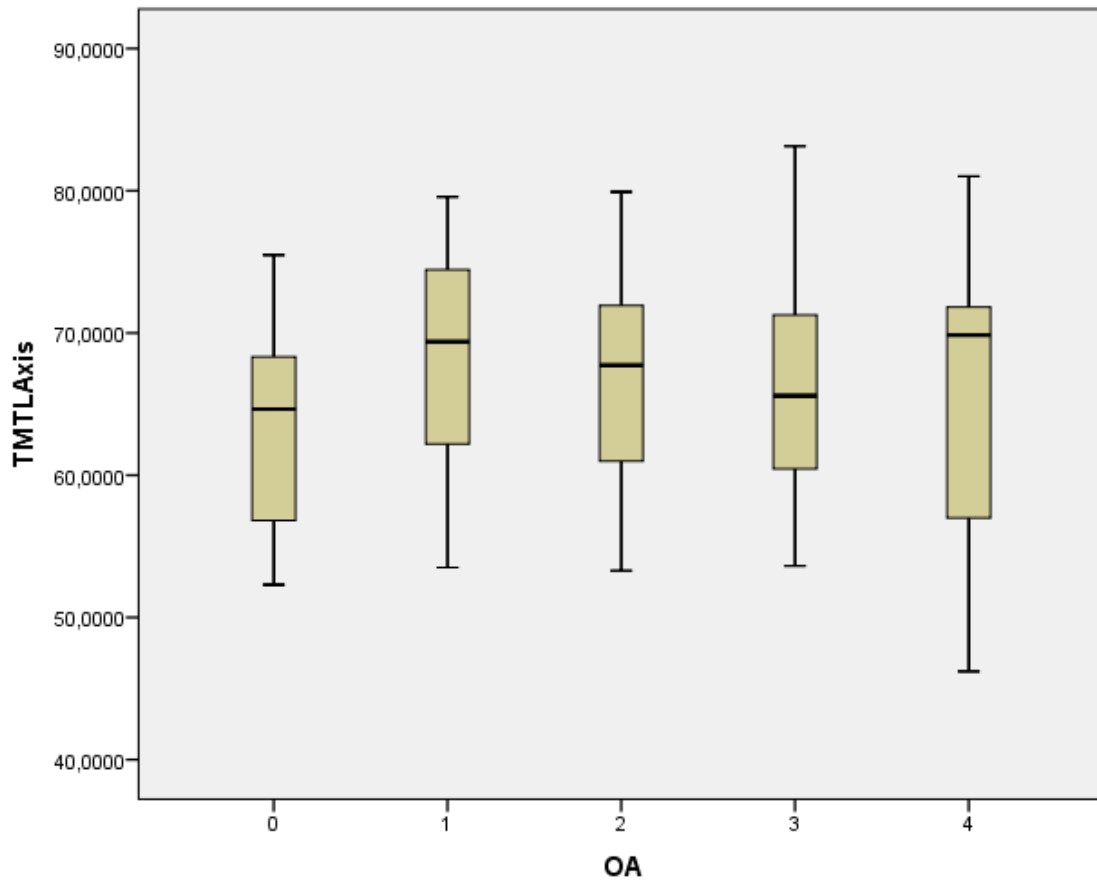


Figure 118. Study II. Box-and-whisker plot of MT - LT slope (TMTLAxis) distribution in each Ahlbäck OA grade.

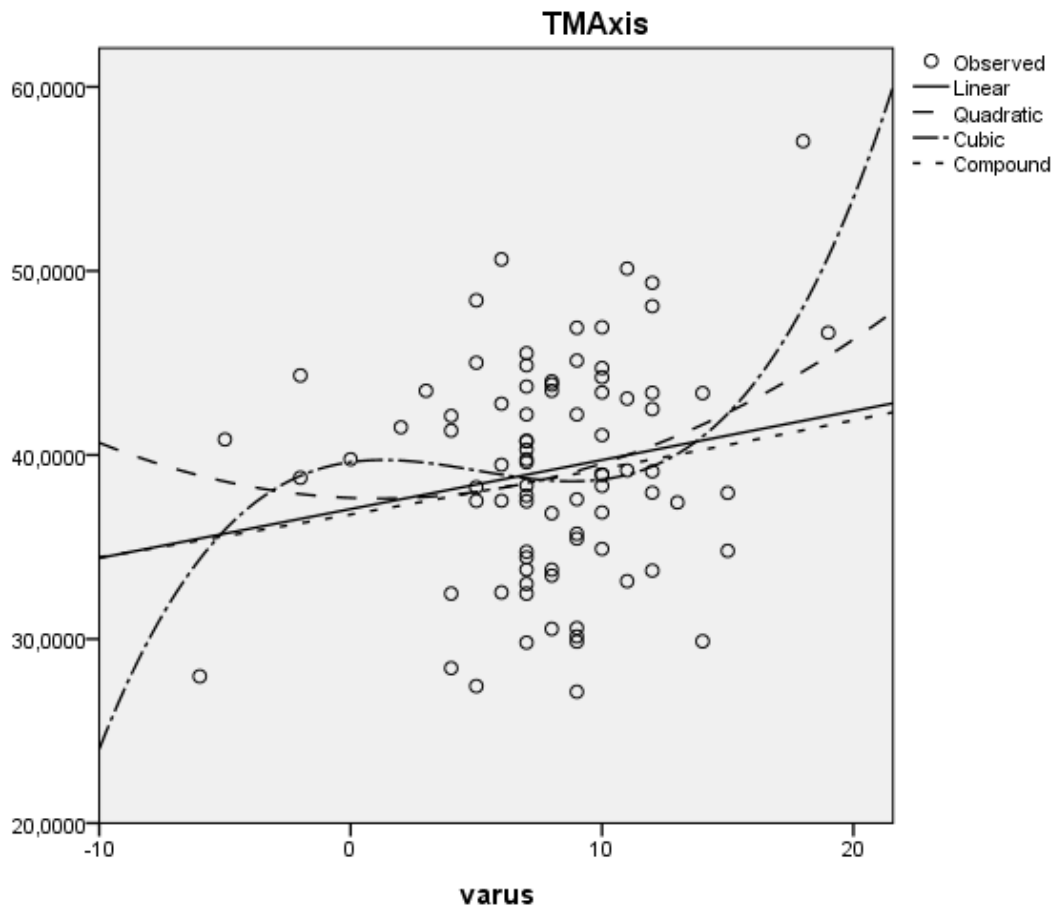


Figure 119. Study II. Regression estimation for MT slope (TMAxis) vs. varus degree.

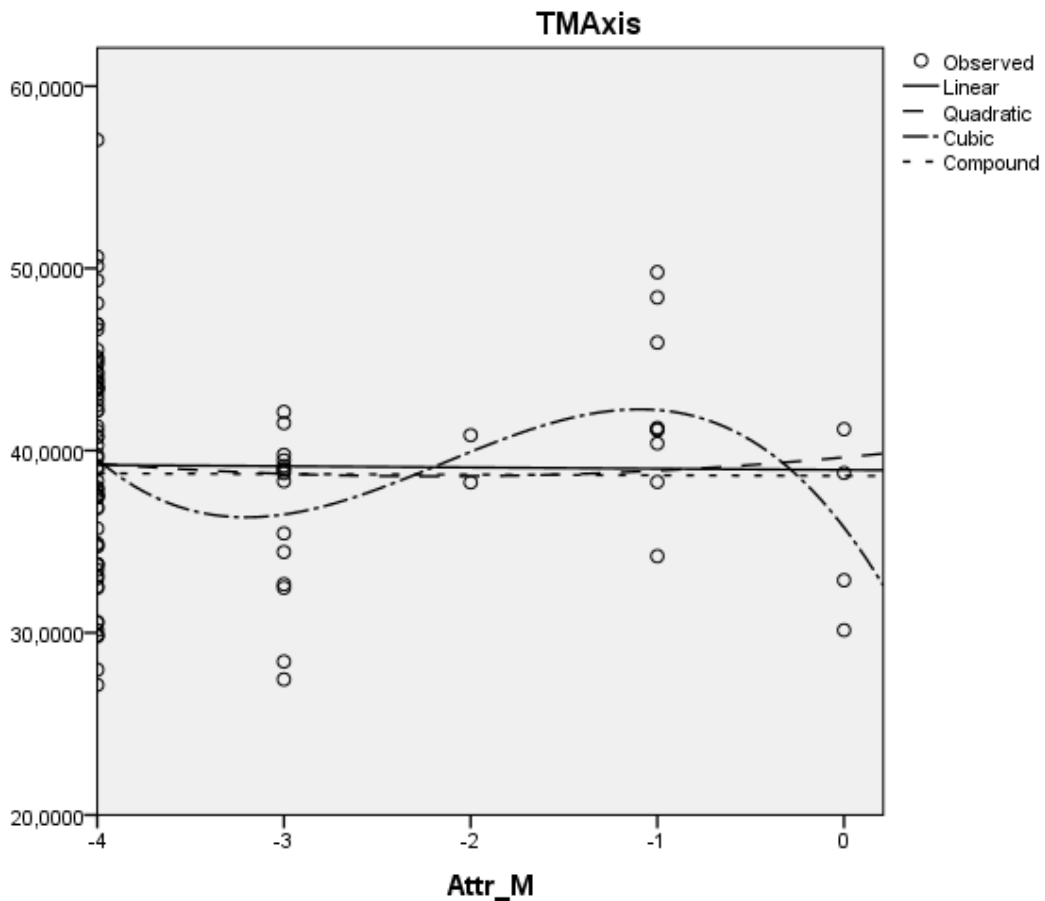


Figure 120. Study II. Regression estimation for MT slope (TMAxis) vs. attrition grade of the medial condyle (Attr_M).

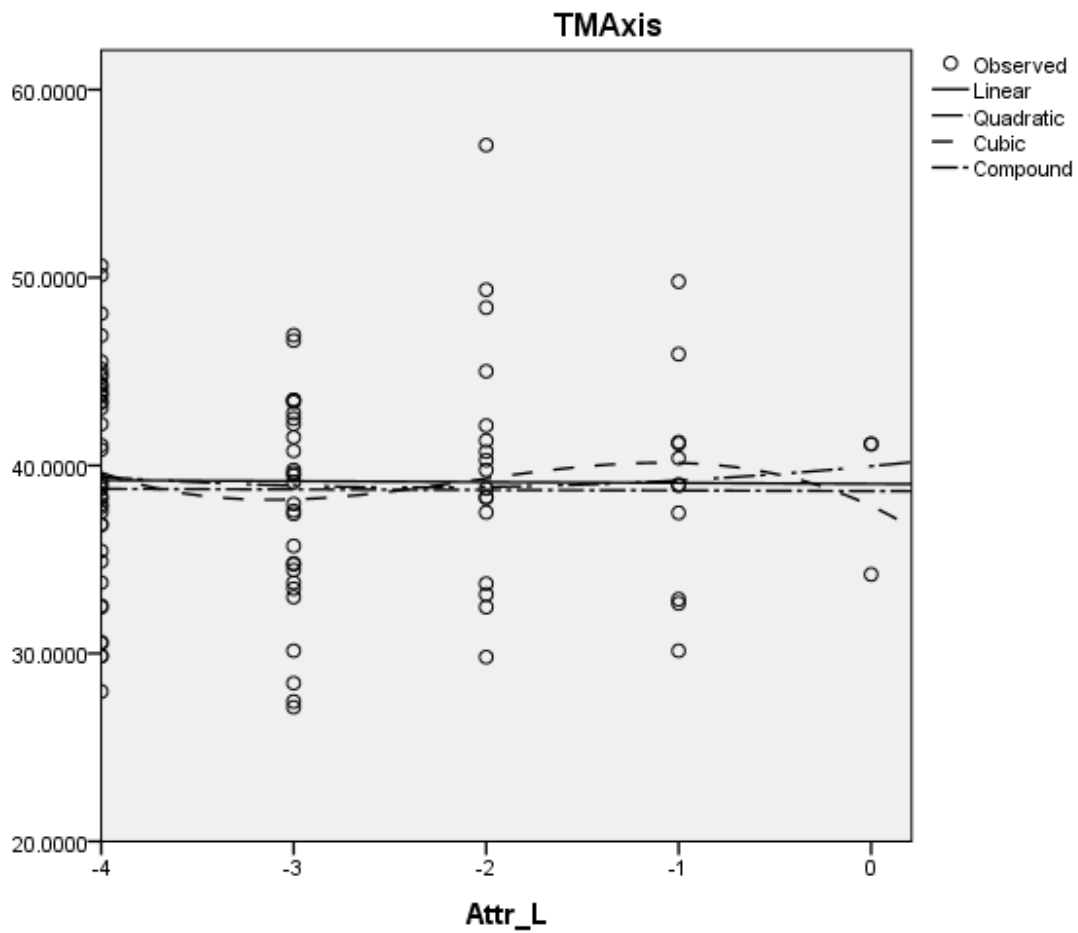


Figure 121. Study II. Regression estimation for MT slope (TMAxis) vs. attrition grade of the lateral condyle (Attr_L).

IV.2.5.5. Tubercle processes

Osteophyte grade of most tubercle processes was significantly but weakly correlated with knee OA:

- B1 (Figure 122): $r_s(98)=0.257$, $p=0.011$.
- B2 (Figure 123): $r_s(98)=0.254$, $p=0.012$.
- C2 (Figure 127): $r_s(96)=0.263$, $p=0.010$.
- D1D2 (Figure 128): $r_s(98)=0.274$, $p=0.006$.
- D3 (Figure 129): $r_s(98)=0.278$, $p=0.006$.
- E1 (Figure 130): $r_s(98)=0.346$, $p=0.001$.

No significant association was found between knee OA and osteophyte grade for C1 (Fig. 126), $r_s(97)=0.139$, $p=0.175$; and for E2 (Fig. 131), $r_s(98)=0.084$, $p=0.422$;

The union of B1 and B2 (Fig. 124) was not significantly associated with knee OA, $\chi^2(8)=13.702$, $p=0.090$. However, frequency distribution analysis showed a trend of higher OA grades showing a clearer differentiation between the two.

The inconstant incisura between B1 and B2 showed a significant, negative weak correlation with knee OA (Fig. 125), $r_s(98)=-0.235$, $p=0.020$.

Axial radiographic density showed no significant correlation with knee OA:

- B (Figure 132): $r_s(98)=0.077$, $p=0.448$.
- C (Figure 133): $r_s(98)=0.107$, $p=0.292$.
- D (Figure 134): $r_s(98)=-0.058$, $p=0.573$.
- E (Figure 135): $r_s(98)=0.143$, $p=0.160$.

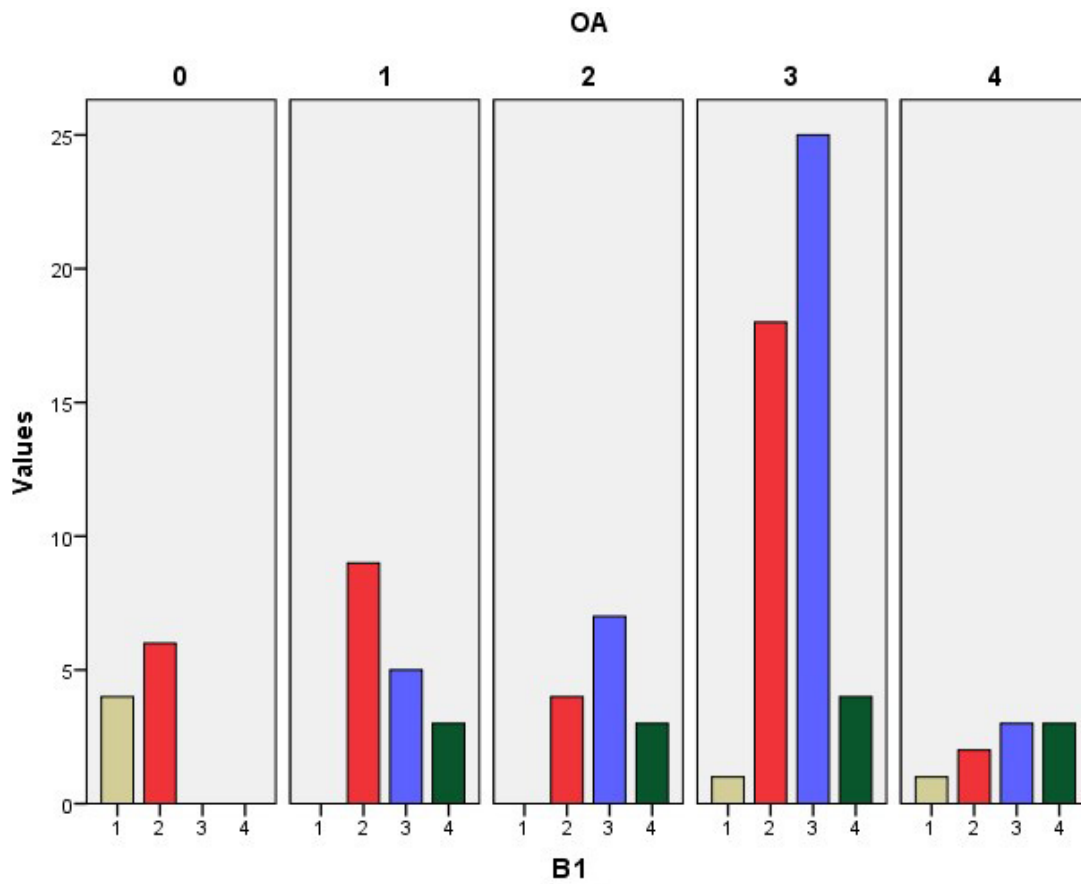


Figure 122. Study II. Histogram of external AMIR (B1) osteophyte grade: number of tibias in each osteophyte grade, grouped by Ahlbäck OA grade.

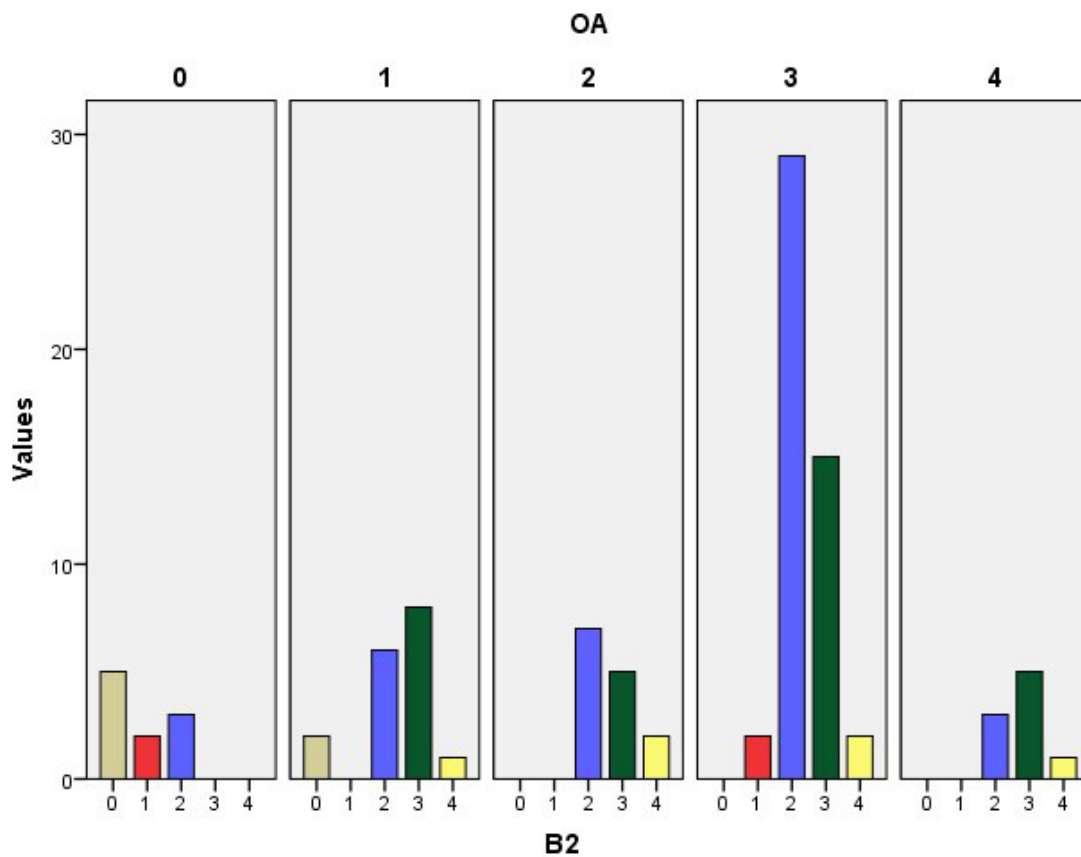


Figure 123. Study II. Histogram of central AMIR (B2) osteophyte grade: number of tibias in each osteophyte grade, grouped by Ahlbäck OA grade.

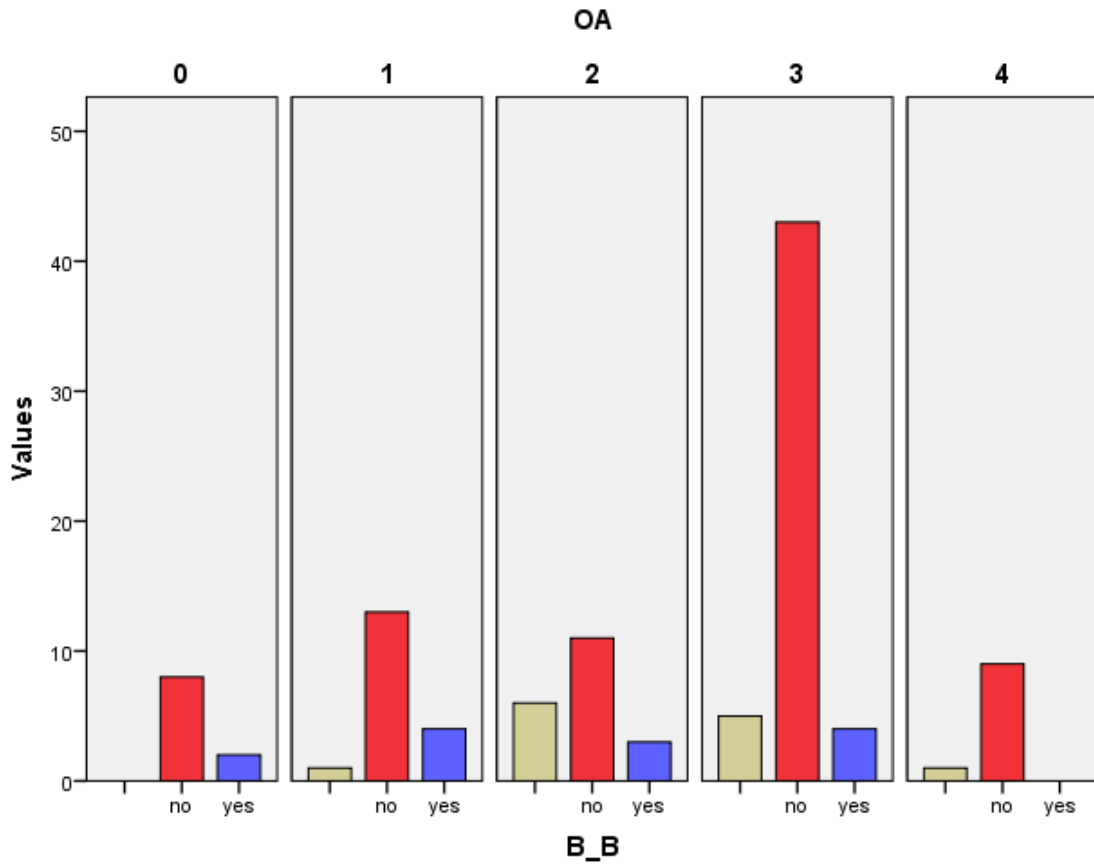


Figure 124. Study II. Histogram of joint central and external AMIR processes (B_B): number of tibias in each category, grouped by Ahlbäck OA grade.

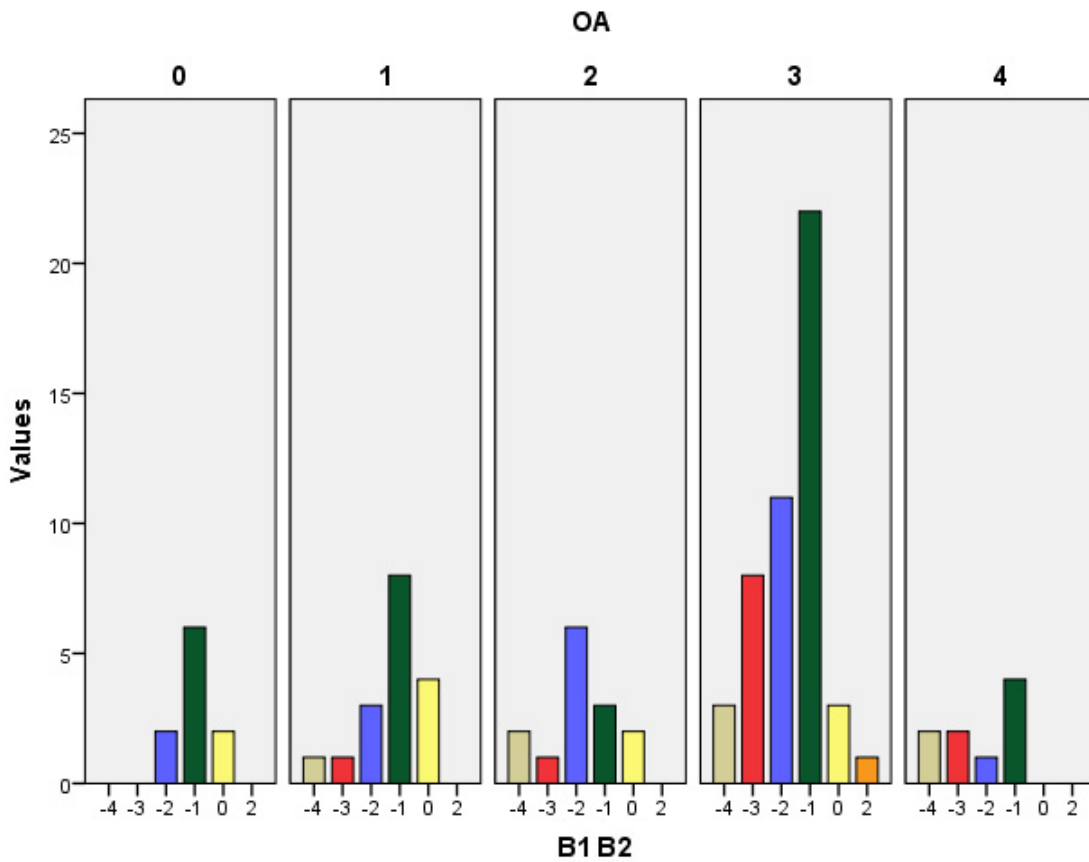


Figure 125. Study II. Histogram of B1-B2 incisura (B1-B2) degenerative grade: number of tibias in each osteophyte grade, grouped by Ahlbäck OA grade.

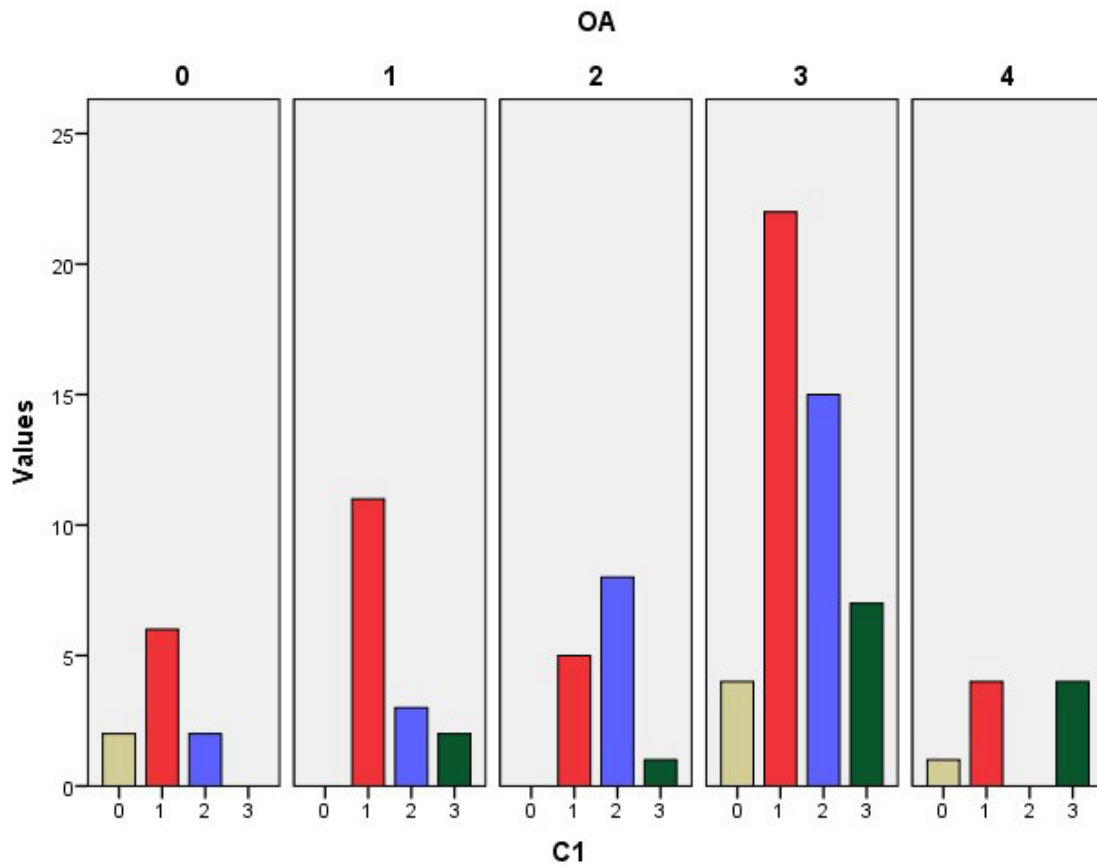


Figure 126. Study II. Histogram of central PMIR (C1) osteophyte grade: number of tibias in each osteophyte grade, grouped by Ahlbäck OA grade.

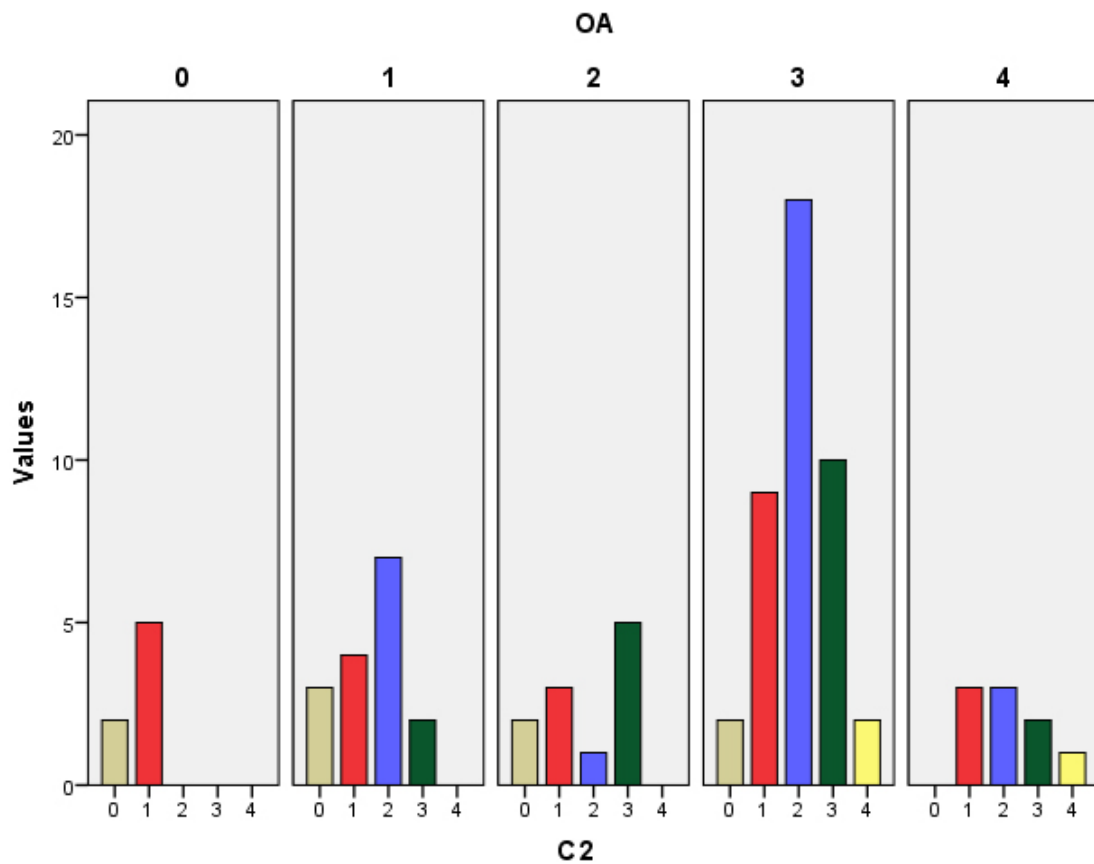


Figure 127. Study II. Histogram of external PMIR (C2) osteophyte grade: number of tibias in each osteophyte grade, grouped by Ahlbäck OA grade.

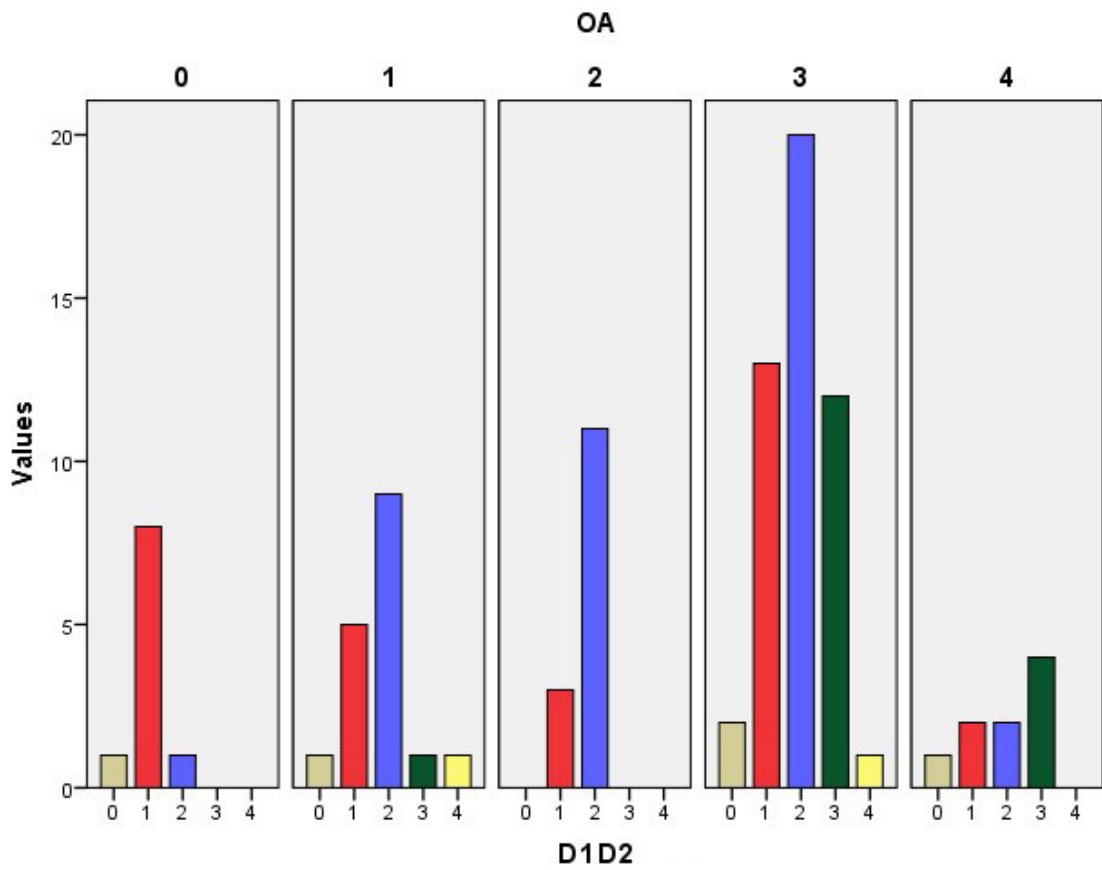


Figure 128. Study II. Histogram of external and central ALIR (D1-D2) osteophyte grade: number of tibias in each osteophyte grade, grouped by Ahlbäck OA grade.

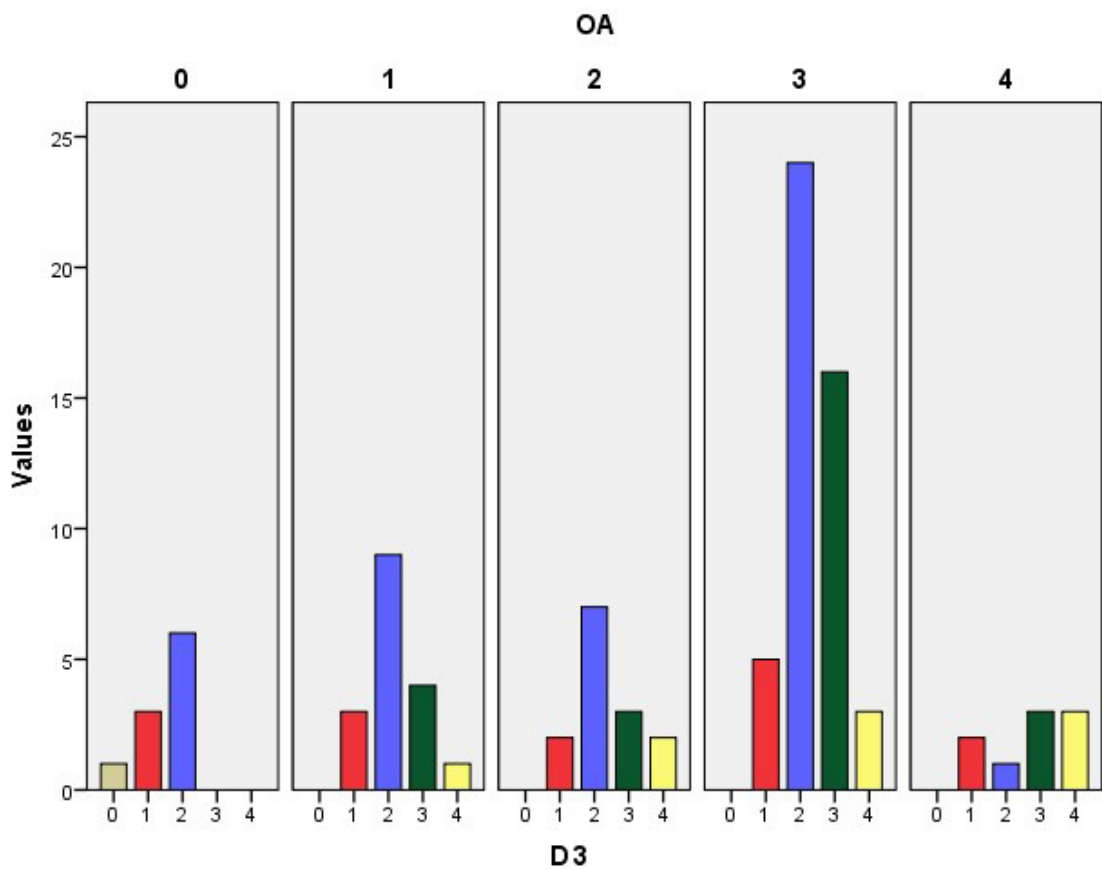


Figure 129. Study II. Histogram of internal ALIR (D3) osteophyte grade: number of tibias in each osteophyte grade, grouped by Ahlbäck OA grade.

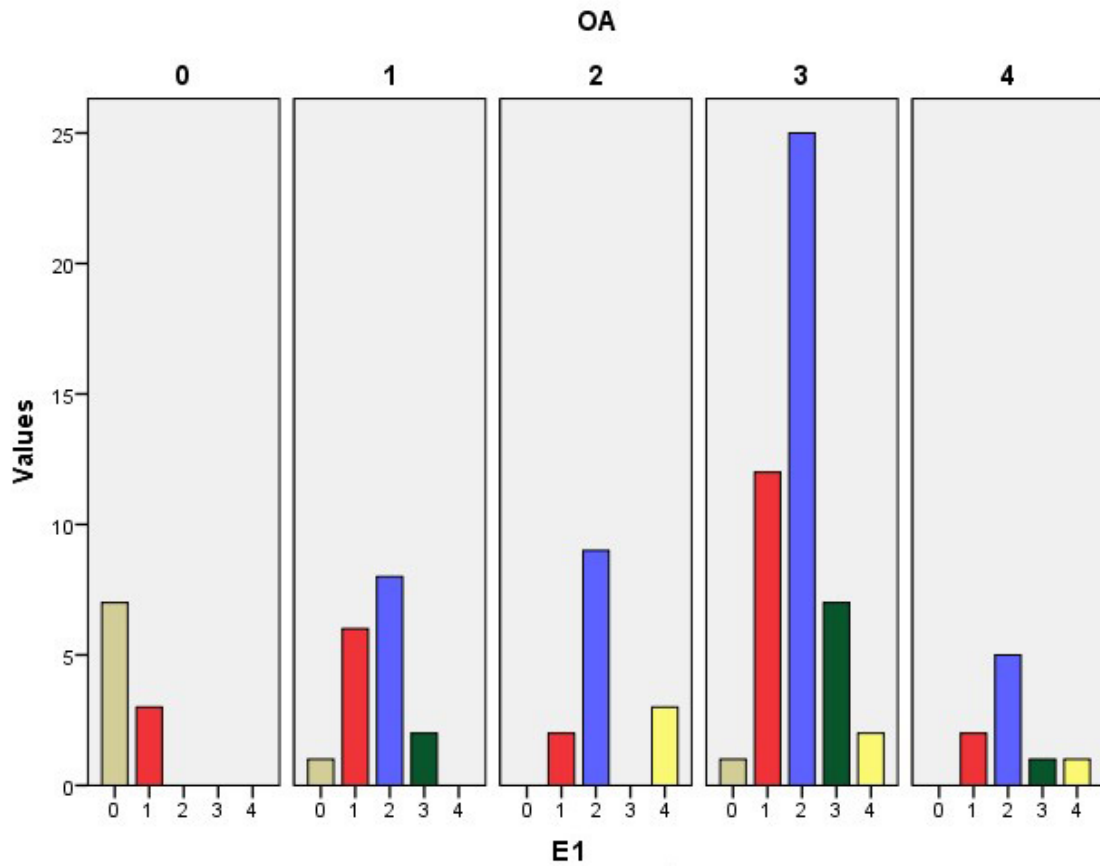


Figure 130. Study II. Histogram of central PLIR (E1) osteophyte grade: number of tibias in each osteophyte grade, grouped by Ahlbäck OA grade.

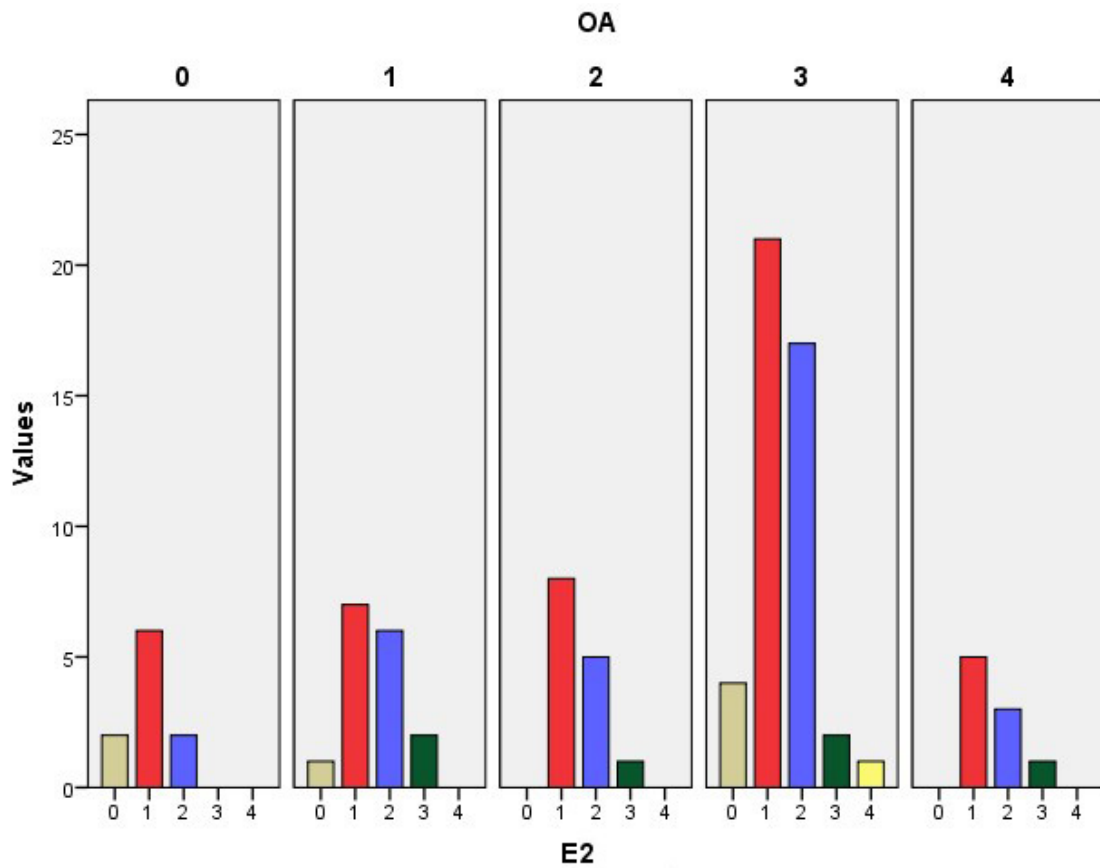


Figure 131. Study II. Histogram of external PLIR (E2) osteophyte grade: number of tibias in each osteophyte grade, grouped by Ahlbäck OA grade.

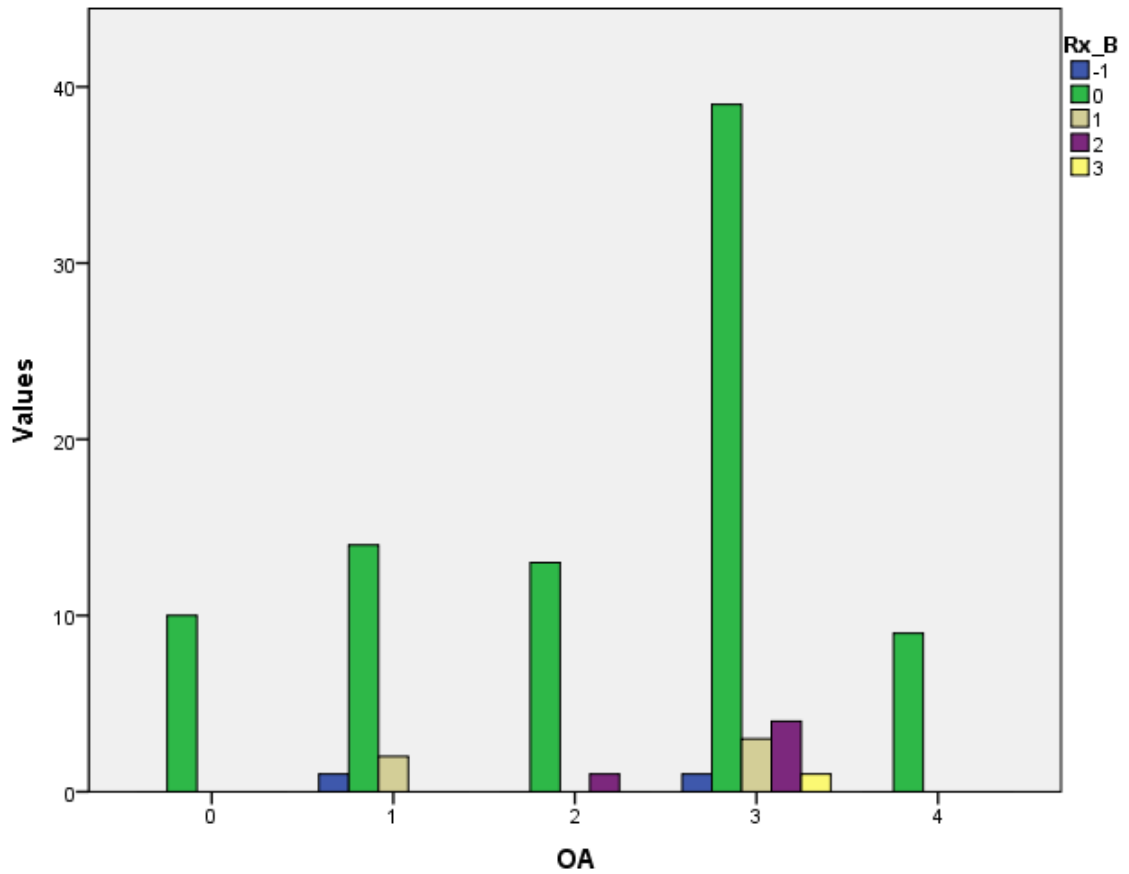


Figure 132. Study II. Histogram of radiographic density of the AMIR in inferosuperior radiographs (Rx_B): number of tibias in each category, grouped by Ahlbäck OA grade.

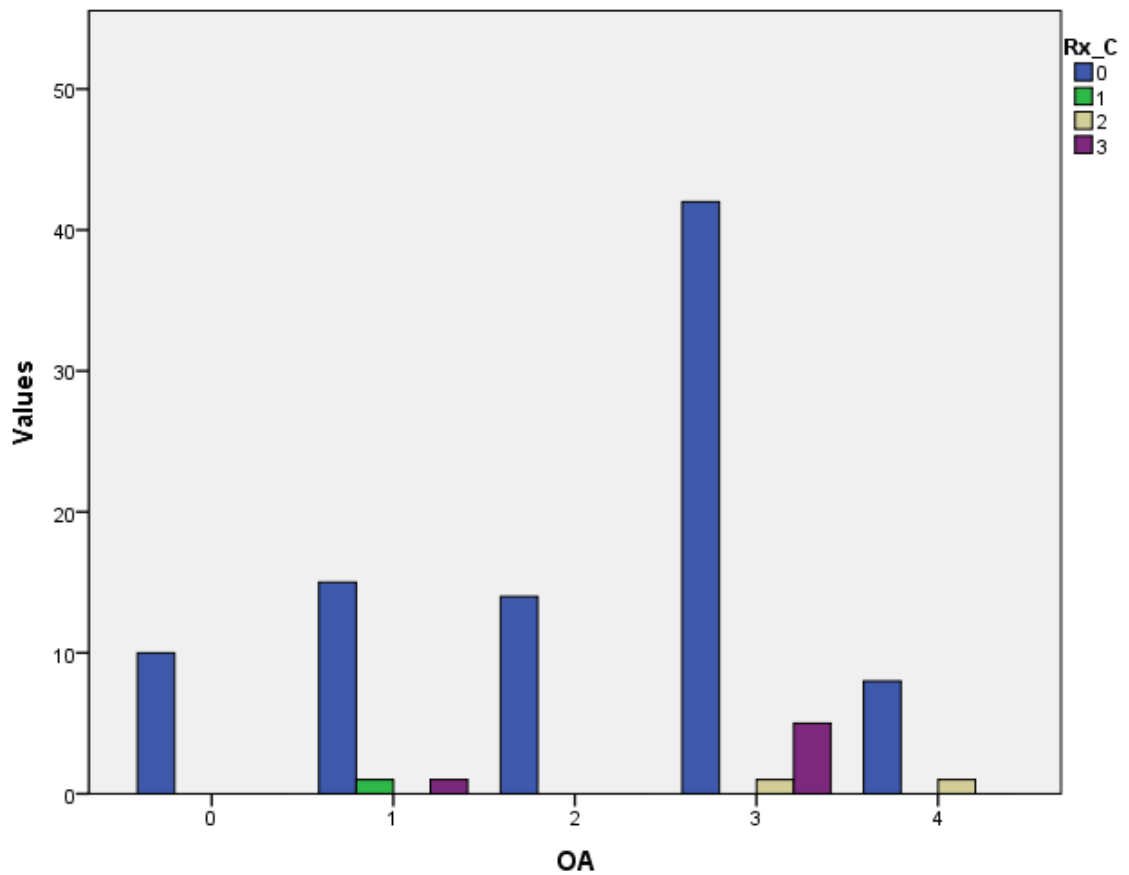


Figure 133. Study II. Histogram of radiographic density of the PMIR in inferosuperior radiographs (Rx_C): number of tibias in each category, grouped by Ahlbäck OA grade.

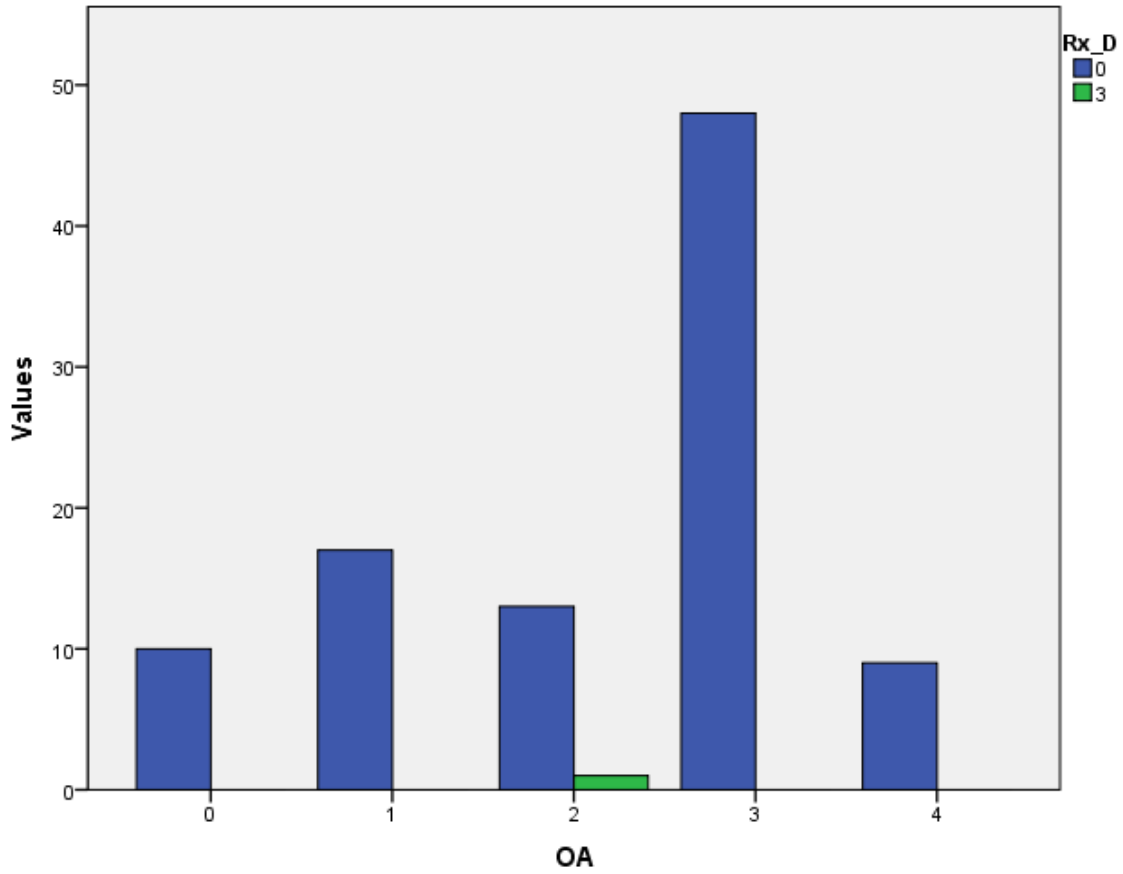


Figure 134. Study II. Histogram of radiographic density of the ALIR in inferosuperior radiographs (Rx_D): number of tibias in each category, grouped by Ahlbäck OA grade.

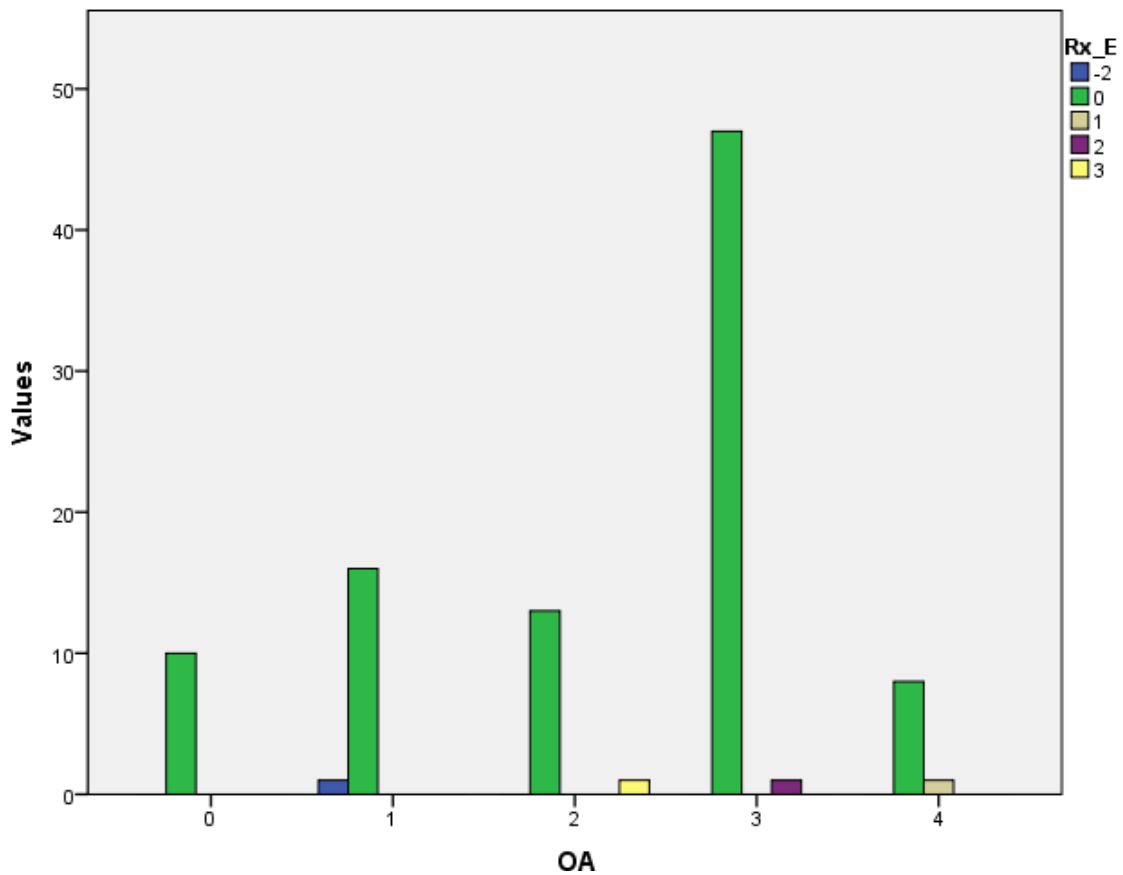


Figure 135. Study II. Histogram of radiographic density of the PLIR in inferosuperior radiographs (Rx_E): number of tibias in each category, grouped by Ahlbäck OA grade.

IV.3. Condyles

IV.3.1. Tibial condyles and intercondylar margins

Cartilage-covered areas of the medial tibial condyle were marked **1a**, **1b**, **1c**, **1d**, and cartilage-covered lateral tibial condyle, **2a**, **2b**, **2c**, **2d** (Fig. 137, Fig. 138).

Photographs of the specimens before or during processing (Fig. 136) were used in all specimens for an approximate delimitation of cartilage-intense medial meniscal footprint, **1a**, and lateral meniscal footprint, **2a**.

A constant internally concave curved elevation was observed on the osseous surface near the border between 1a and 1b, connecting the external AMIR process, B1, with the external PMIR process, C2. The narrow intermediate zone of thinner cartilage dividing both areas lied internal to this dividing osseous line.

A slight round elevation or *button* was seen within 1b in two, paired normal tibias medial to the medial tubercle.

The external ALIR process, D1, and the external PLIR process, E2, were followed laterally by an internally concave curved elevation in all tibias, but in normal specimens it ceased to be visible in the external aspect of the lateral plateau.

The medial and lateral condylar rims were slightly elevated over areas 1a and 2a respectively, surrounding them externally. Their interior aspects were the anterior and posterior intercondylar corners.

The anteromedial (AM) corner, **1c**, extended obliquely anteriorly and laterally down from the articular surface towards the anterior intercondylar area. It was delimited posteriorly by the external PMIR process, B1, and followed the medial meniscal footprint laterally to area 5. Its main feature was the presence of a very thin layer of cartilage, which disappeared along the anteromedial wall of the anterior intercondylar area, delimiting it from area 5.

The anterolateral (AL) corner, **2c**, was a transition zone with thinner cartilage found between areas 2b and areas 8, 7, and 9. The margin lied in an intermediate step formed between the (higher) external ALIR process, D1, and the (lower) external ALIR processes, D2, the true anteromedial osseous limit of the lateral condyle. The corner sloped smoothly downward from 4c, and medially into the anterior intercondylar area.

The posteromedial (PM) corner, **1d**, posterolateral to the external PMIR process, was covered by thin cartilage, and sloped gently down laterally into the posterior

intercondylar area. The posteriormost aspect of the PM corner was slightly elevated over area 1d, sloping downward laterally into the posterior intercondylar area, and medially following the posterior rim. The inferior border of the PM corner was formed by the secondary central PMIR process, C1_b.

The posterolateral (PL) corner, **2d**, was the medially convex curved facet sloping downward towards posterior aspect of the lateral condyle, delimited externally by the central PLIR process, E1. The inferior and medial border of the PL corner was formed by the secondary central PLIR process, E1_b.

The posteriormost medial aspect of the lateral condyle sloped very smoothly downward with a convex curve in a posterolateral direction. Thus, while the posteromedial corner, 1d, sloped inwards, toward the posterior intercondylar area, the posterolateral corner, 2d, curved smoothly in an outward direction.

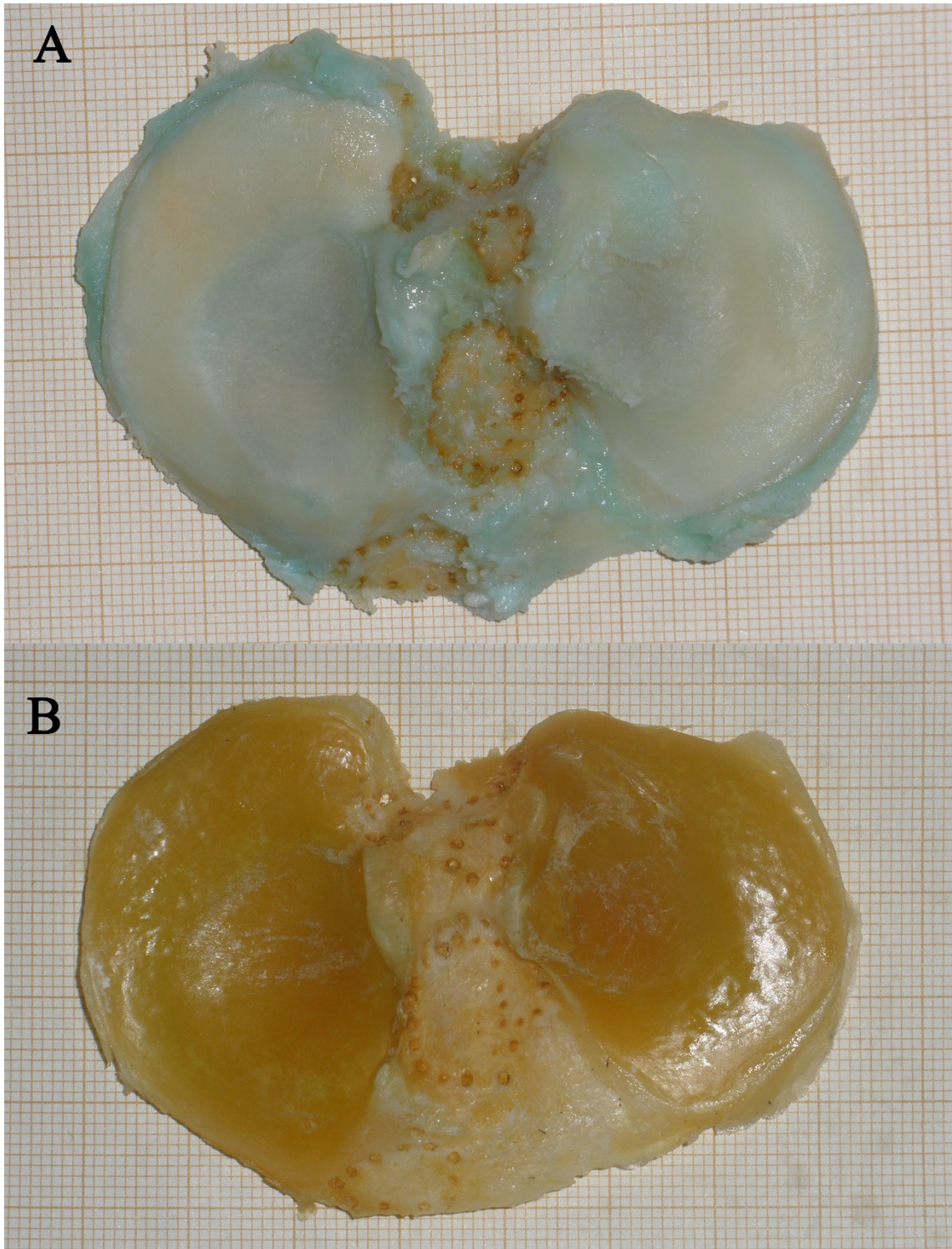


Figure 136. Tibia D. Cleaning of soft tissues with enzymatic detergent during the processing of a specimen (A) makes it difficult to delineate previously evident cartilage-covered zones in the fully processed specimen (B).

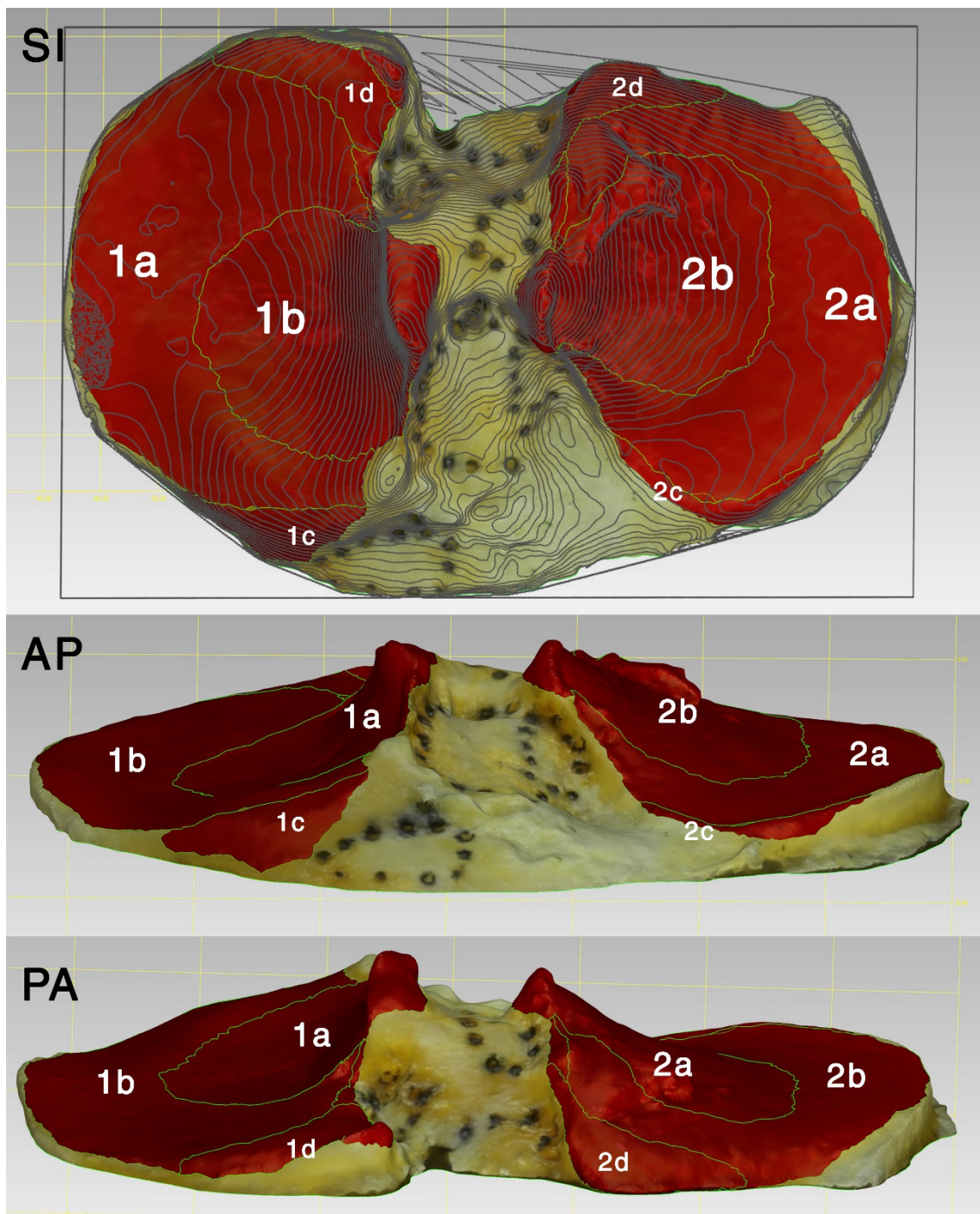


Figure 137. 3D model of tibia D. Superoinferior (SI) view with contour lines superimposed, anteroposterior (AP) and Posteroanterior (PA) views. Condylar areas selected, highlighted in red, and labelled. Compare with corresponding photographs of fresh and processed specimen in Figure 136.

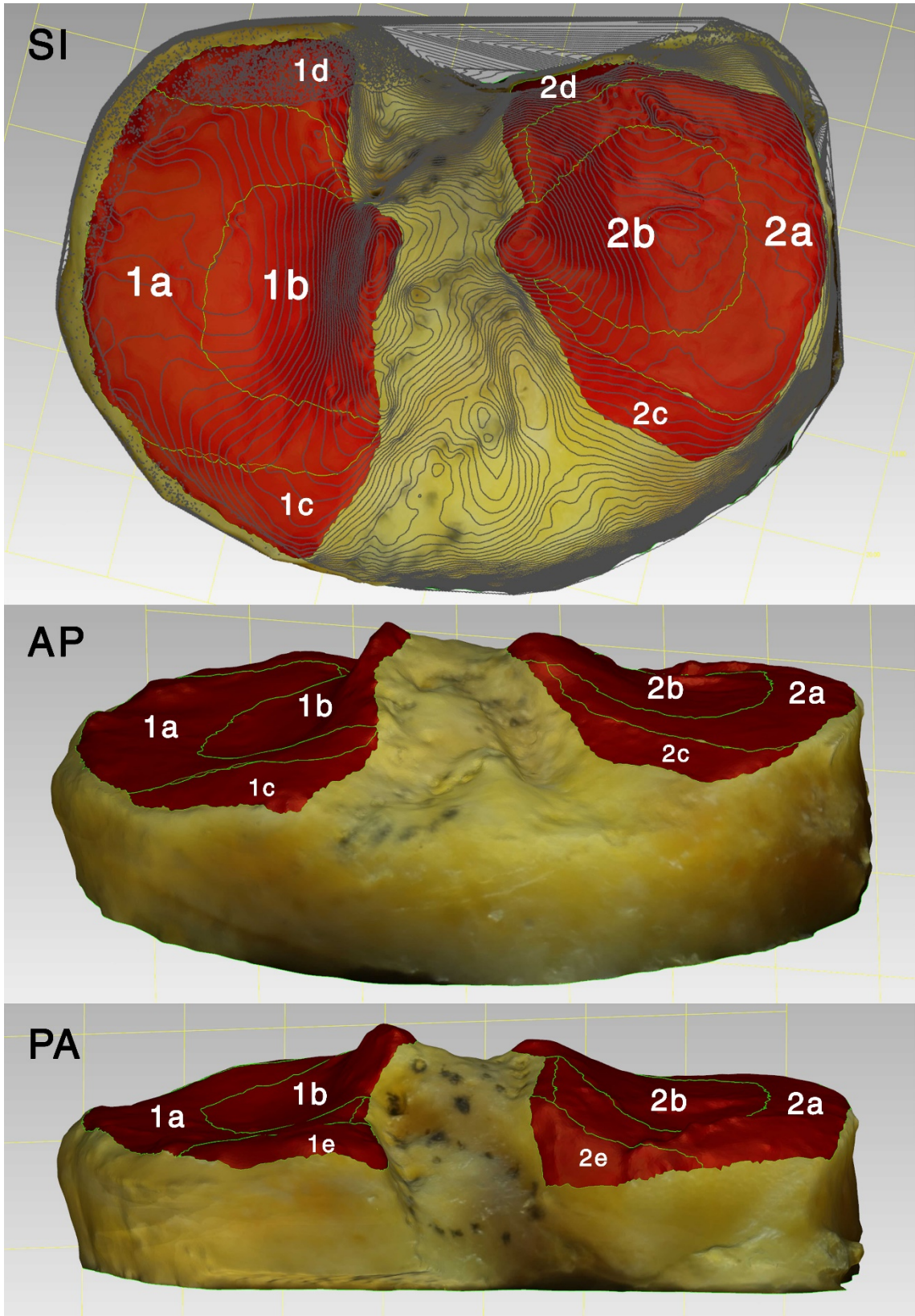


Figure 138. 3D model of tibia C. Superoinferior (SI) view with contour lines superimposed, anteroposterior (AP) and Posteroanterior (PA) views. Condylar areas selected, highlighted in red, and labelled.

IV.3.2. Degenerative changes of the condyles

IV.3.2.1. Condylar margin osteophytes

IV.3.2.1.1. Qualitative assessment of degenerative changes

It was qualitatively found that the curvature of the medial condyle became often elevated into a ridge (Fig. 139), even though the anterior and posterior processes forming it could follow different lines or ridges in an external direction. The curvature of the lateral condyle was also found elevated, but the anterior and posterior lateral processes (which formed it) were often found not to be connected, and followed usually a more straight external direction (Fig. 140).

Osteophytes were found in the four corners described for normal tibias. From more to less frequently encountered, elevations were found in the posteromedial corner, the posterolateral corner, the anteromedial corner, and the anterolateral corner (Fig. 141). The anteromedial corner osteophyte could be found connected to the Parsons' knob, and the anterolateral corner osteophyte could be found connected to osteophytes of the anterolateral knob, D1-D2 process, antero-central knob, and area 9.

In order of elevation – without taking into account the Parsons' tubercle –, the posteromedial corner osteophyte was potentially the widest and highest (Fig. 142), followed at a distance by the posterolateral corner osteophyte (Fig. 143, Fig. 144), and then the anterior corner elevations, both lower than the posterior ones relative to surrounding areas (i.e. not taking into account the posterior sagittal tibial slope).

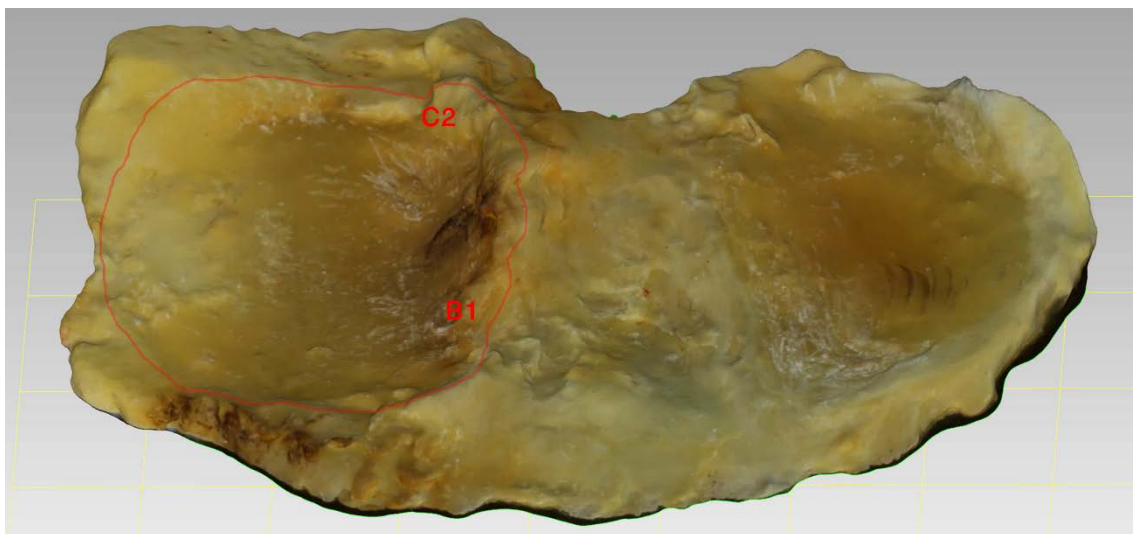


Figure 139. 3D model of tibia 56. Red line drawn over medial curvature, AMIR and PMIR. Observe the elevation of the medial condylar curvature and rim posteriorly, together with the external (C2) and central PMIR processes, connecting with the anterior curvature and central AMIR process (B1).

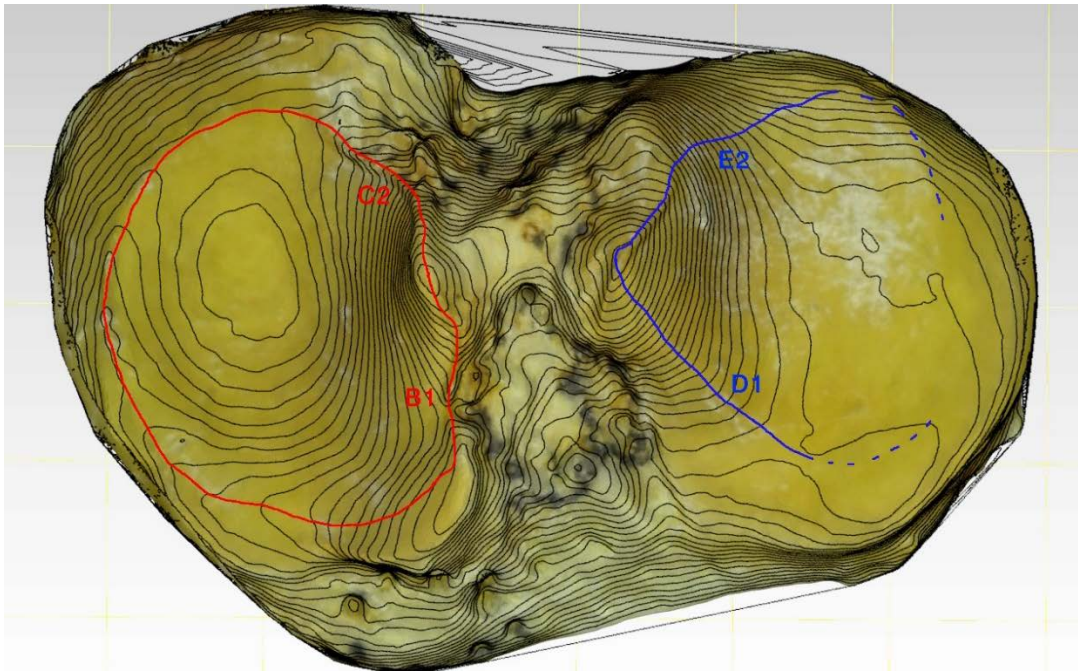


Figure 140. 3D model of tibia E. Contour lines highlighted. Red line drawn over medial curvature, AMIR and PMIR, blue line over lateral curvature, ALIR, and PLIR. External AMIR and PMIR processes are connected medially by the elevated curvature. External ALIR and PLIR processes are not clearly connected in the lateral aspect of the lateral condyle, though.

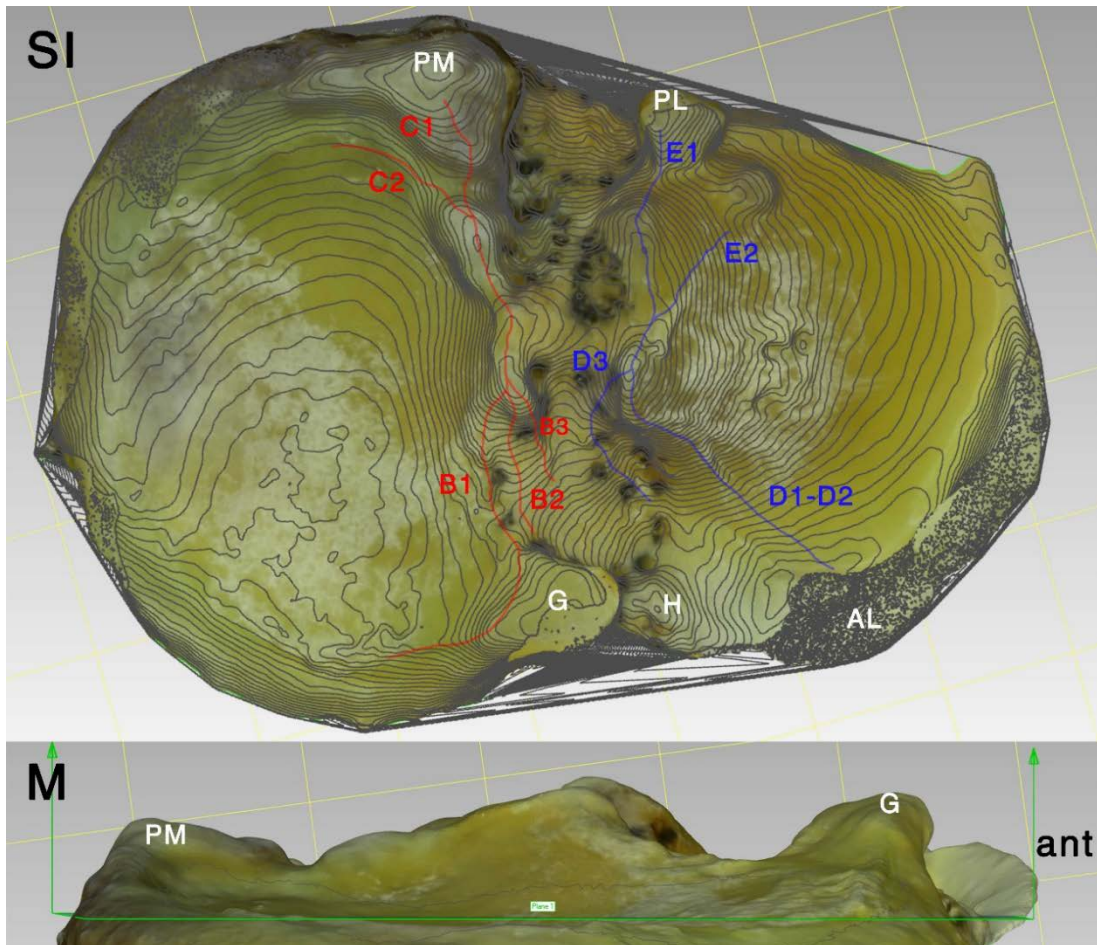


Figure 141. 3D model of tibia H. Superoinferior view (SI) with contour lines superimposed. Medial view (M) with condylar plane (green line) as the horizontal plane of the specimen. AMIR and PMIR processes in red, ALIR and PLIR processes in blue. Observe the relative size of posteromedial (PM) and posterolateral (PL) corner and Parsons' (G) tubercles. Notice the elevation of the PMIR, and the connection of the ACIK elevation (H) with areas 9 and AL corner.

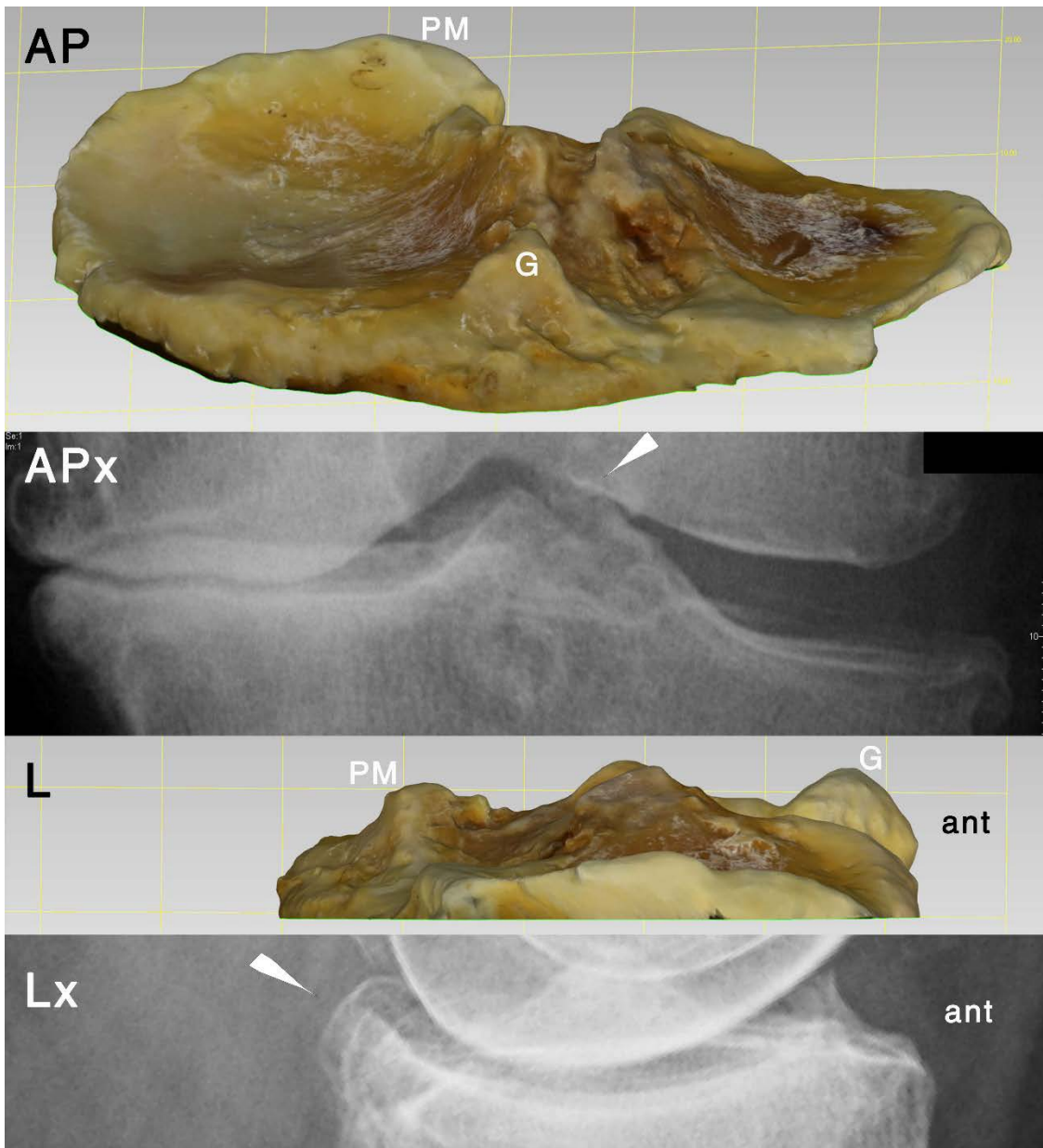


Figure 142. Tibia 67. 3D model AP and lateral (L) views, with corresponding knee AP standing radiograph (APx) and lateral radiograph (Lx). Observe the posterior osteophyte (white arrowhead) apparently behind the lateral tubercle in the knee AP radiograph, while on the 3D model it is the posteromedial corner osteophyte the bigger one.



Figure 143. Standing AP and lateral (L) knee radiographs corresponding to tibia 31. Knee radiographs were used to complement data on condylar rims and corners, when not available from the cut specimen.

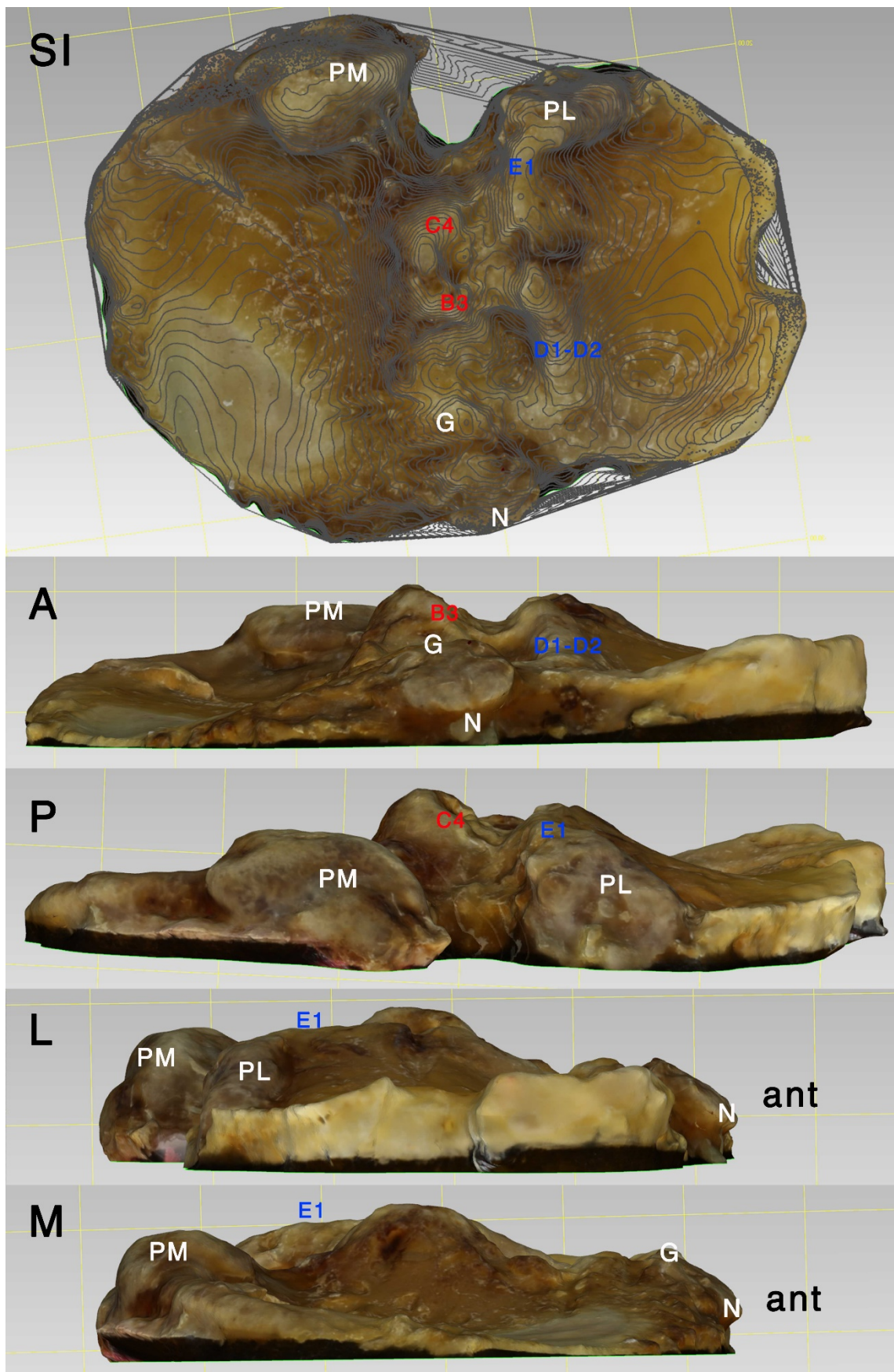


Figure 144. 3D model of tibia 31, with contour lines superimposed. Superoinferior (SI), anterior (A), posterior (P), lateral (L), and medial (M) views. Varus. MAC 3M. PM corner: grade 5; PL corner: grade 4. AM corner: grade 2; AL corner: grade 2; AM rim: grade 2; PM rim: grade 3; AL rim: grade 4; PL rim: grade 3. Observe marked elevation of D1-D2, and E1, as well as marked B3 (connecting with D3) and C4 processes. Notice also anterior osteophyte (N).

IV.3.2.1.1. Quantitative assessment of osteophytes in condylar rims and corners

The posteromedial corner elevation in donor specimens (n=3, knee OA grades 1-3) showed a mean height of 4.8 mm (range, 1.6 mm to 8.6 mm) over the condylar plane, a mean area of 111.5 mm² (range, 18.9 mm² to 189.1 mm²), mean volume of 121.8 mm³ (range, 5.1 mm³ to 232.3 mm³).

The posterolateral corner (n=2, knee OA grades 1 and 3) showed a mean relative height of 5 mm (range, 4.5 mm to 5.4 mm), a mean area of 126.8 mm² (range, 92.5 mm² to 151.1 mm²), and a mean volume of 108.1 mm³ (range, 90.3 mm³ to 125.8 mm³).

A Kruskal-Wallis test was performed that showed no statistically significant differences between Ahlbäck OA grade groups in AP measurements of corner osteophytes:

- AL corner (Figure 145): $\chi^2(3)=3.106$, $p=0.376$.
- PM corner (Figure 146): $\chi^2(3)=3.548$, $p=0.315$.
- PL corner (Figure 147): $\chi^2(3)=2.603$, $p=0.457$.

A Spearman's rank-order correlation was run to determine the relationship between osteophyte grade of condylar margins and knee OA. There was generally a moderate positive correlation between both grades, which was statistically significant in all cases:

- AM corner (Figure 148): $r_s(98)=0.538$, $p<0.001$;
- AL corner (Figure 149): $r_s(98)=0.445$, $p<0.001$;
- Medial rim, anterior aspect (Figure 150): $r_s(97)=0.433$, $p<0.001$;
- Medial rim, posterior aspect (Figure 151): $r_s(97)=0.378$, $p<0.001$;
- Lateral rim, anterior aspect (Figure 152) : $r_s(97)=0.411$, $p<0.001$;
- Lateral rim, posterior aspect (Figure 153): $r_s(94)=0.378$, $p=0.002$;
- PM corner (Figure 154): $r_s(97)=0.412$, $p<0.001$;
- PL corner (Figure 155): $r_s(92)=0.345$, $p=0.001$.

Radiographic density of the four main corners showed no significant correlation with knee OA:

- AM corner (Figure 156): $r_s(98)=-0.024$, $p=0.811$.
- AL corner (Figure 157), $r_s(98)=0.161$, $p=0.114$.
- PM corner (Figure 158), $r_s(98)=0.084$, $p=0.410$.
- PL corner (Figure 159), $r_s(98)=0.113$, $p=0.269$.

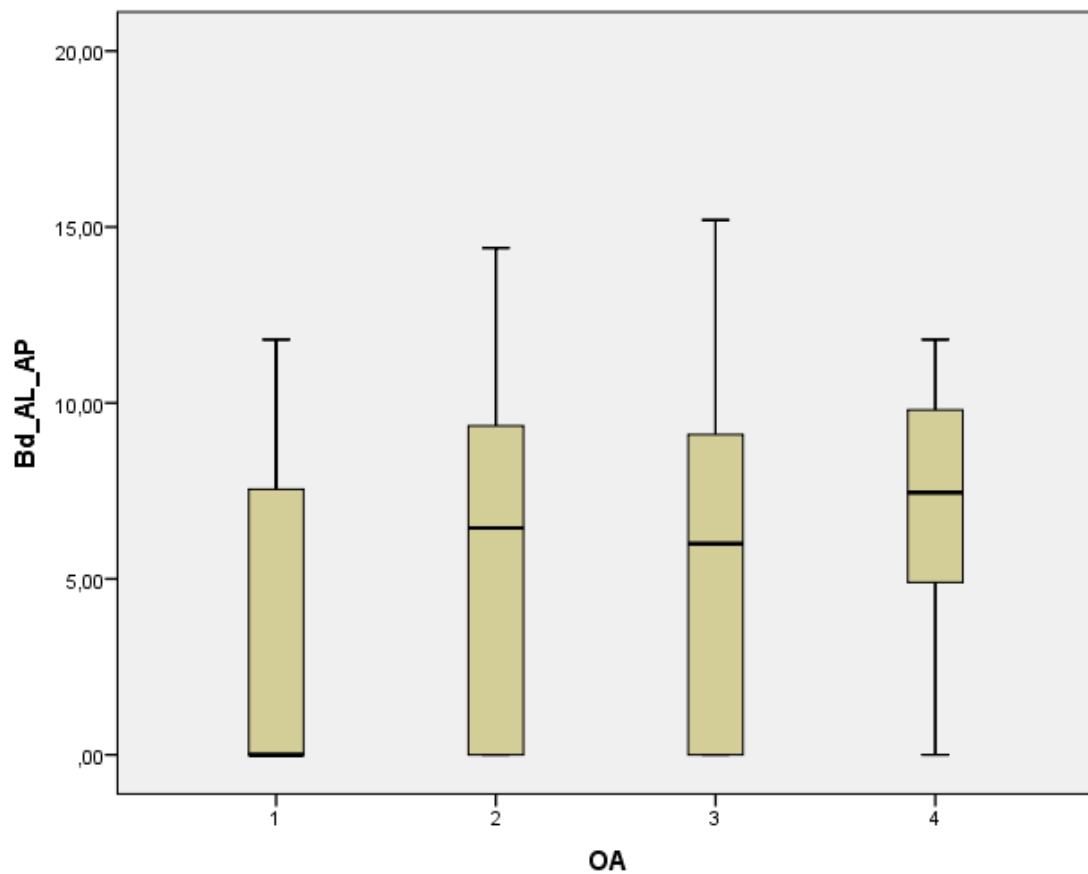


Figure 145. Study II. Box-and-whisker plot of AL corner AP size (Bd_AL_AP) distribution in each Ahlbäck OA grade.

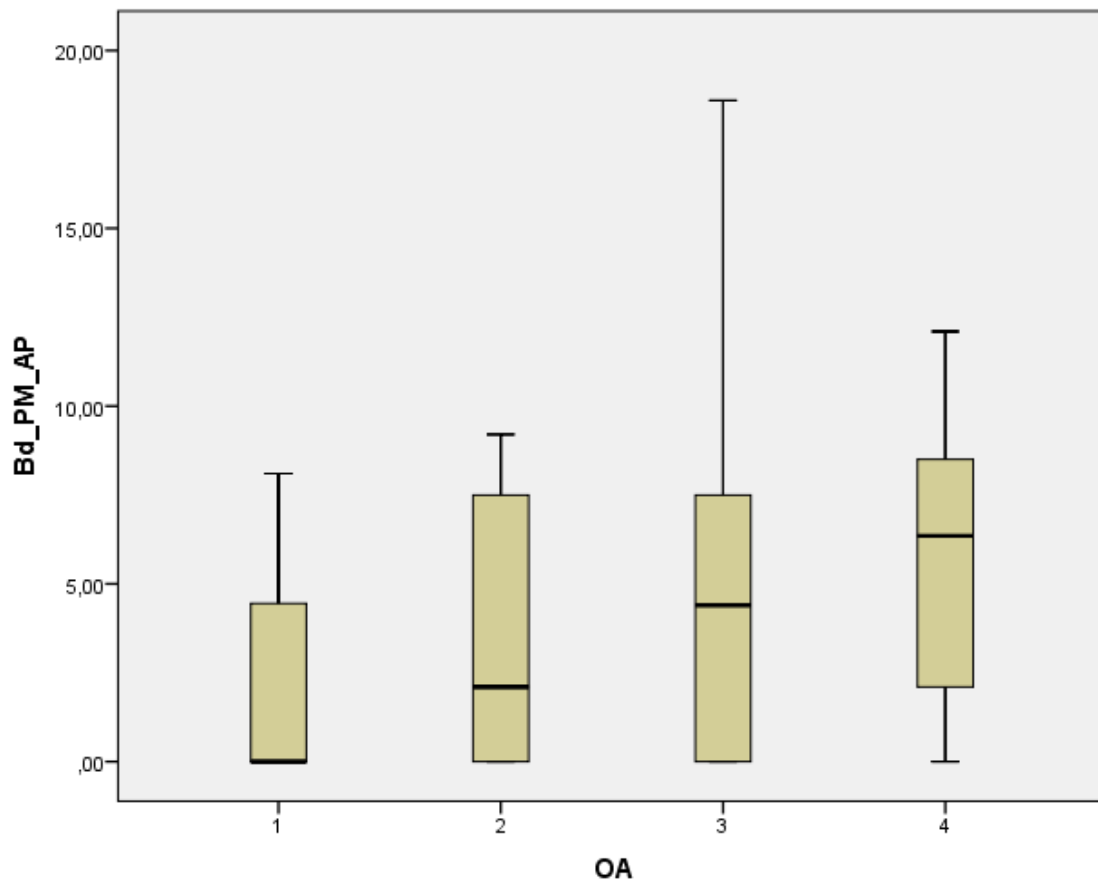


Figure 146. Study II. Box-and-whisker plot of PM corner AP size (Bd_PM_AP) distribution in each Ahlbäck OA grade.

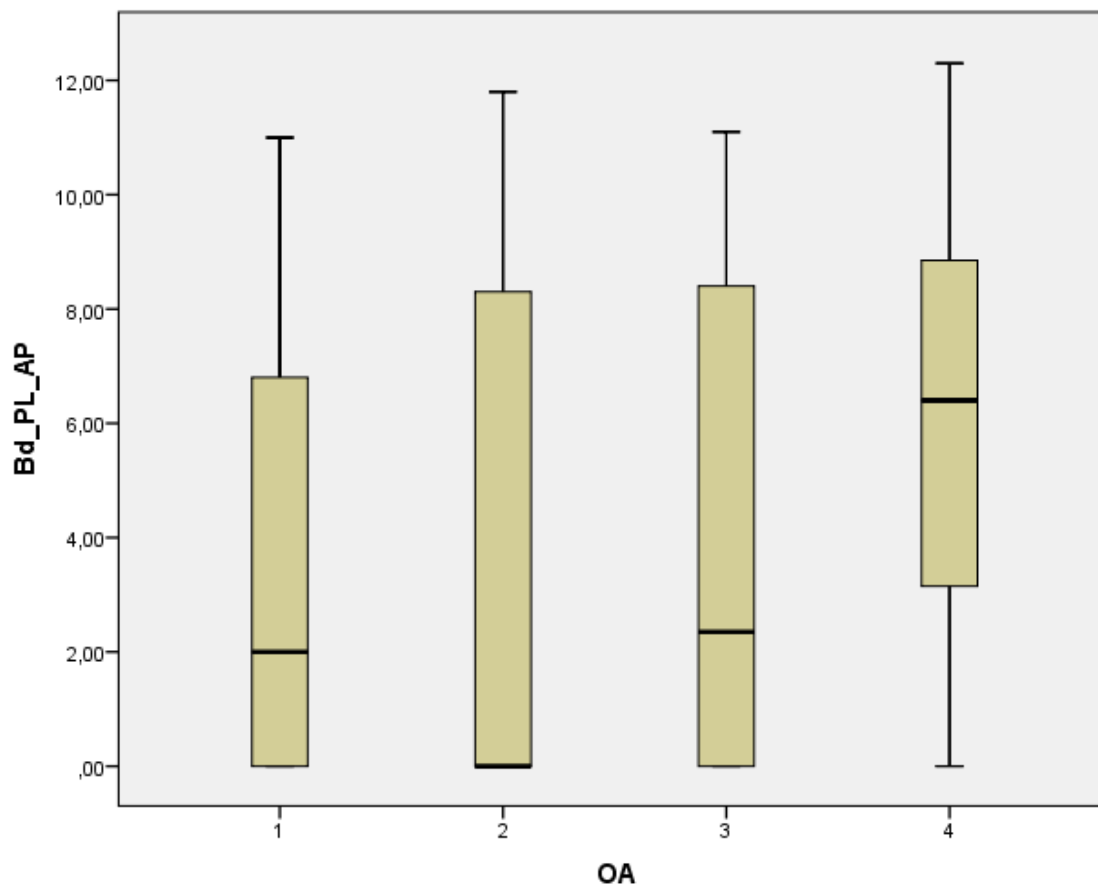


Figure 147. Study II. Box-and-whisker plot of PL corner AP size (Bd_PL_AP) distribution in each Ahlbäck OA grade.

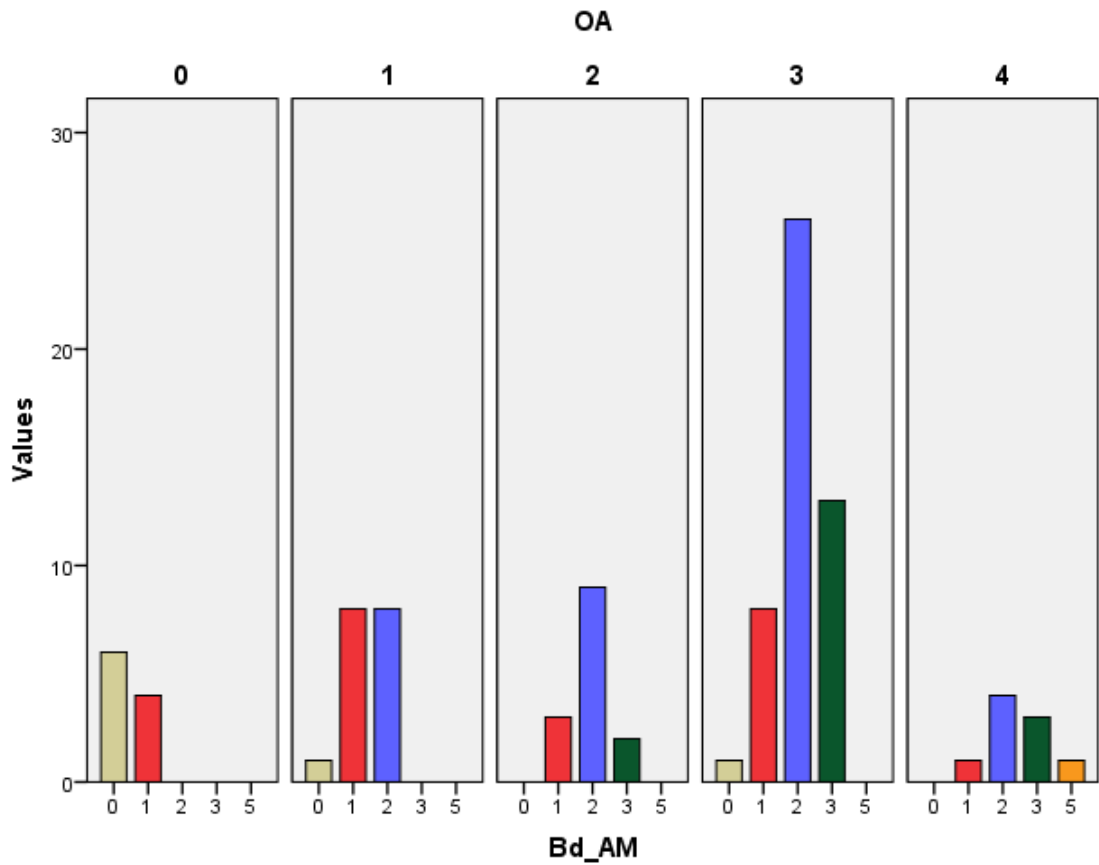


Figure 148. Study II. Histogram of AM corner osteophyte (Bd_AM): number of tibias in each osteophyte grade, grouped by Ahlbäck OA grade.

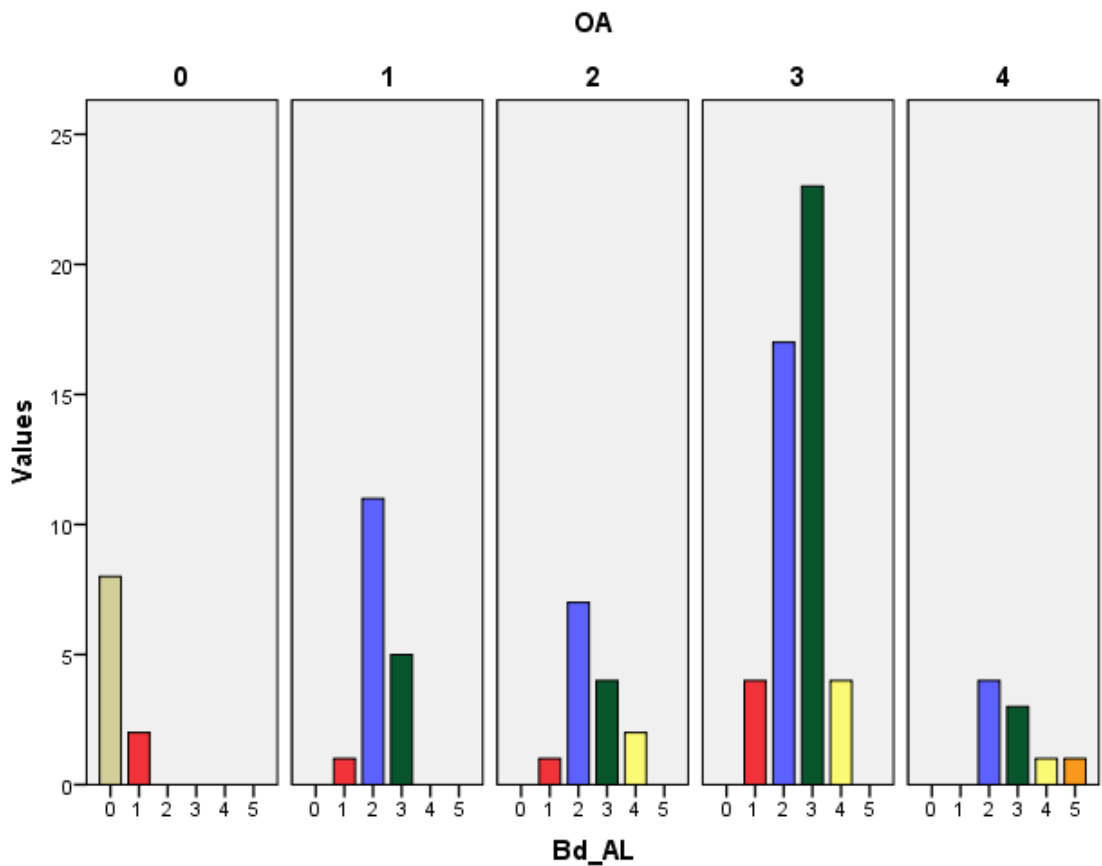


Figure 149. Study II. Histogram of AL corner osteophyte (Bd_AL): number of tibias in each osteophyte grade, grouped by Ahlbäck OA grade.

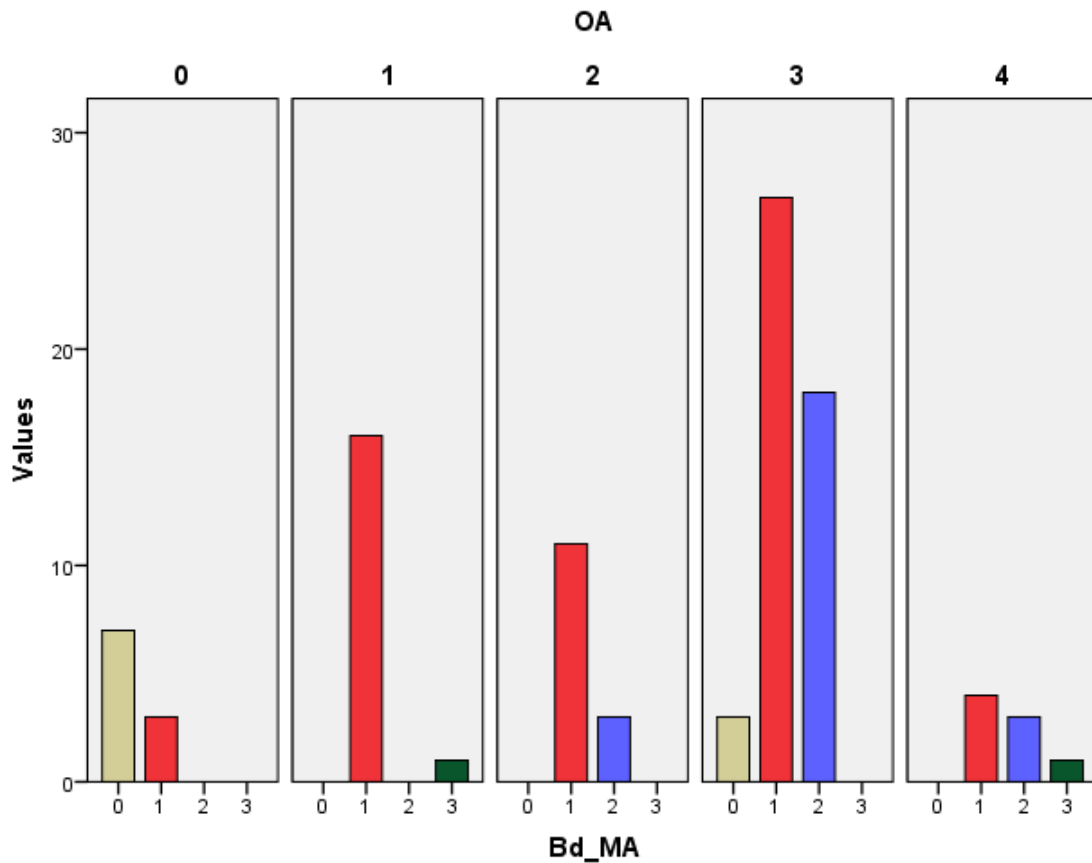


Figure 150. Study II. Histogram of medial rim elevation, anterior aspect (Bd_MA): number of tibias in each osteophyte grade, grouped by Ahlbäck OA grade.

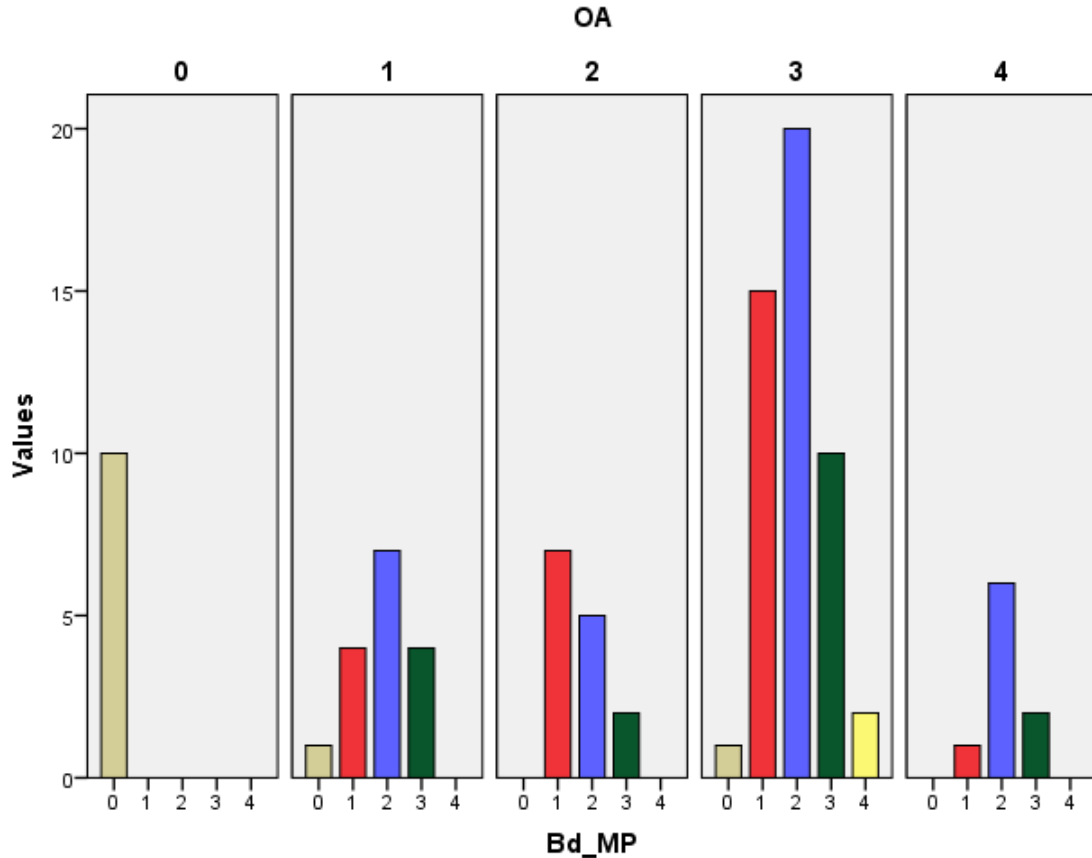


Figure 151. Study II. Histogram of medial rim elevation, posterior aspect (Bd_MP): number of tibias in each osteophyte grade, grouped by Ahlbäck OA grade.

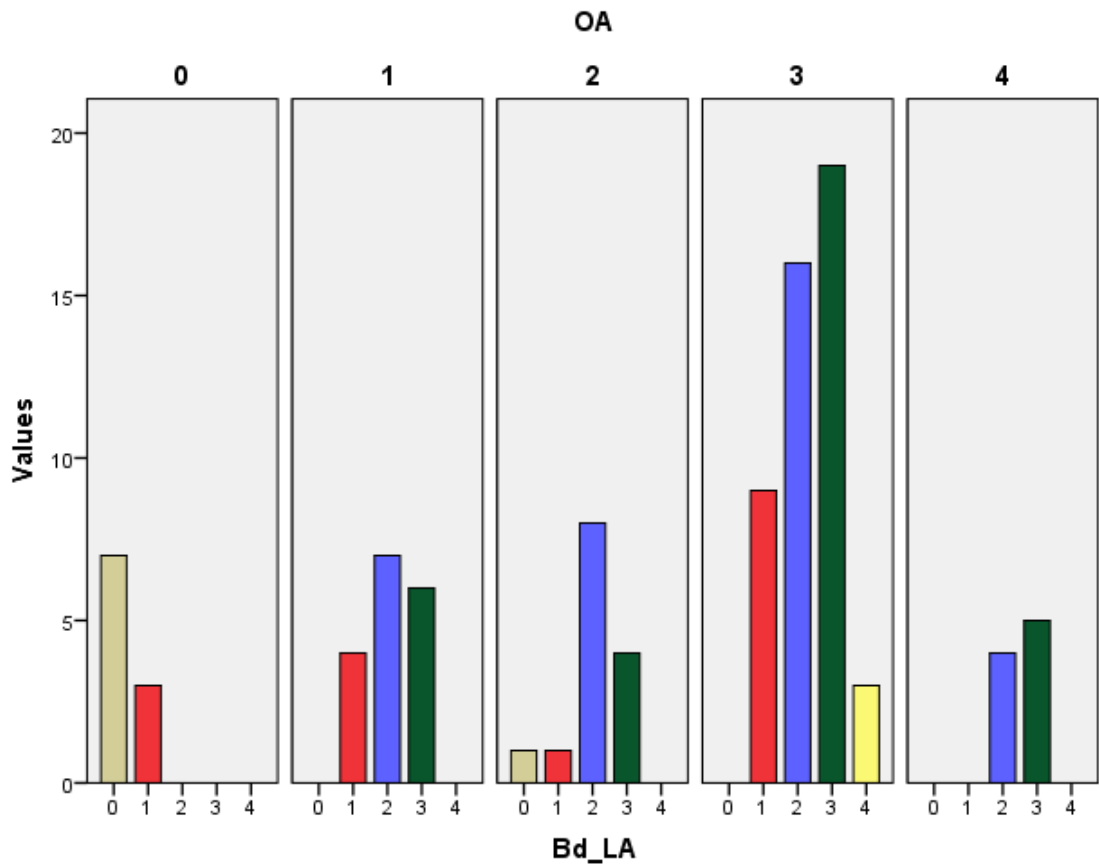


Figure 152. Study II. Histogram of lateral rim elevation, anterior aspect (Bd_LA): number of tibias in each osteophyte grade, grouped by Ahlbäck OA grade.

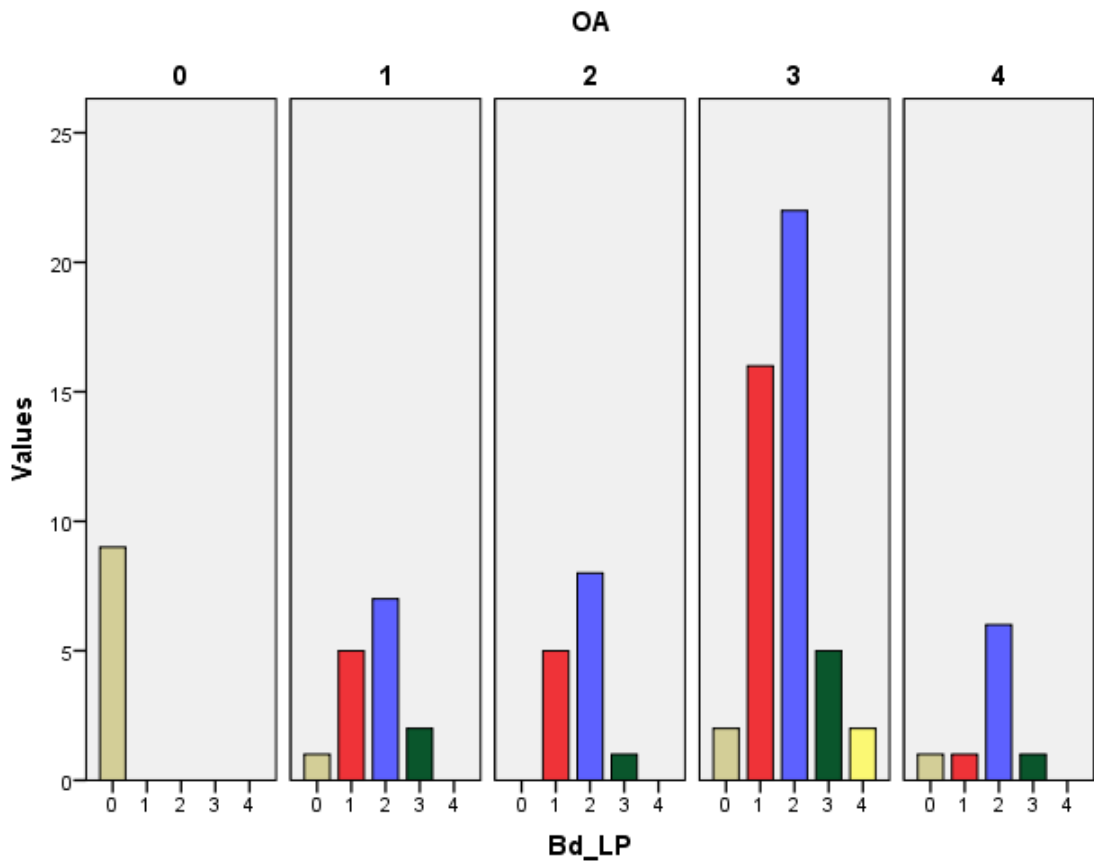


Figure 153. Study II. Histogram of lateral rim elevation, posterior aspect (Bd_LP): number of tibias in each osteophyte grade, grouped by Ahlbäck OA grade.

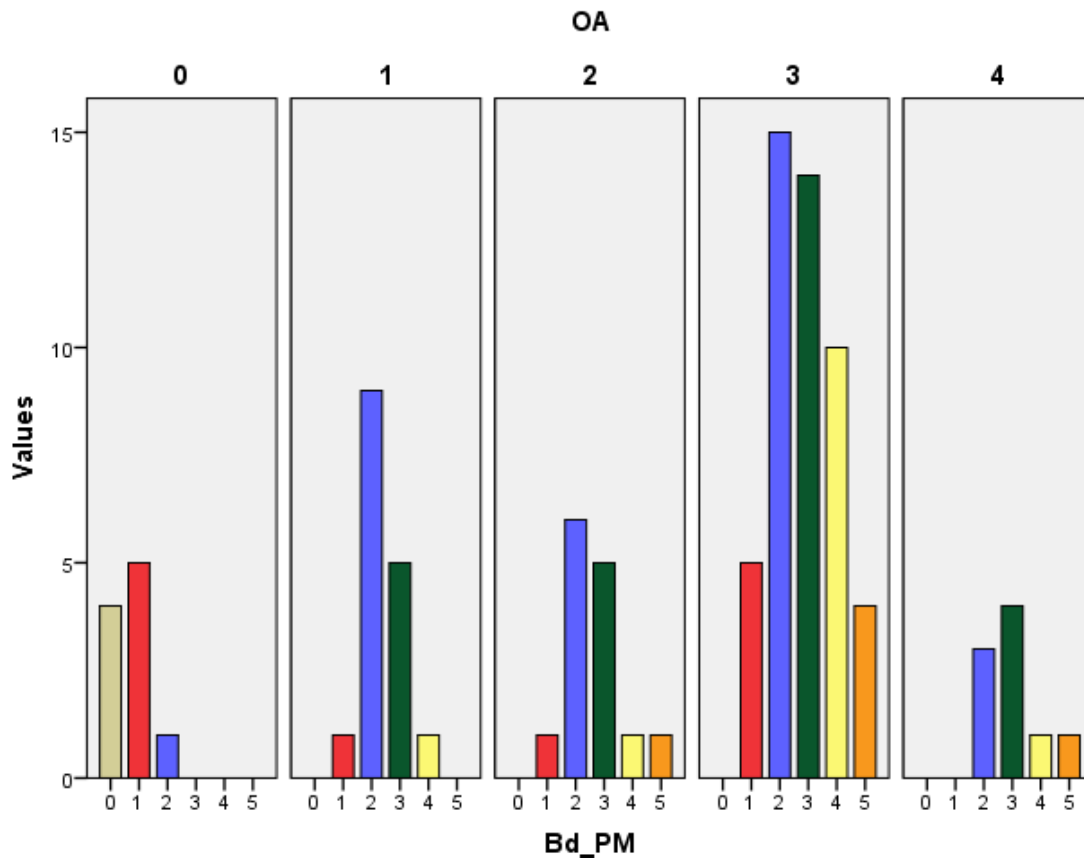


Figure 154. Study II. Histogram of PM corner osteophyte (Bd_PM): number of tibias in each osteophyte grade, grouped by Ahlbäck OA grade.

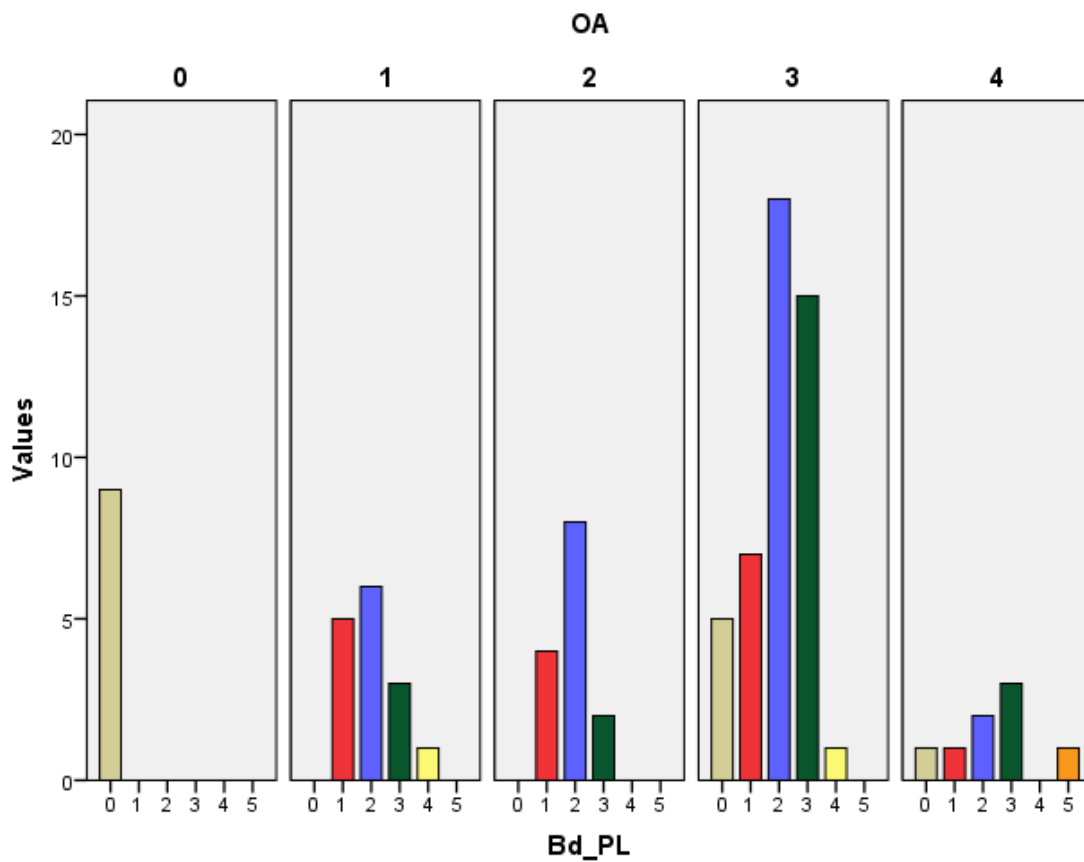


Figure 155. Study II. Histogram of PL corner osteophyte (Bd_PL): number of tibias in each osteophyte grade, grouped by Ahlbäck OA grade.

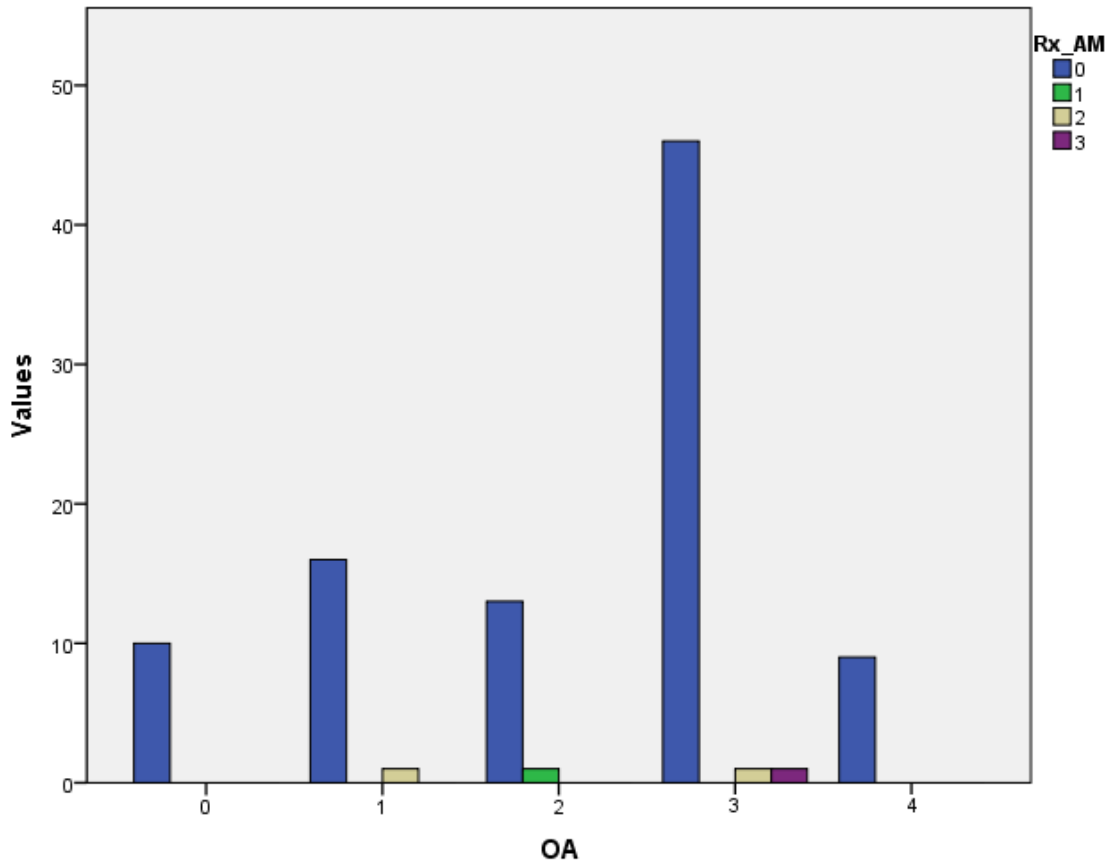


Figure 156. Study II. Histogram of radiographic density of the AM corner in inferosuperior radiographs (Rx_AM): number of tibias in each category, grouped by Ahlbäck OA grade.

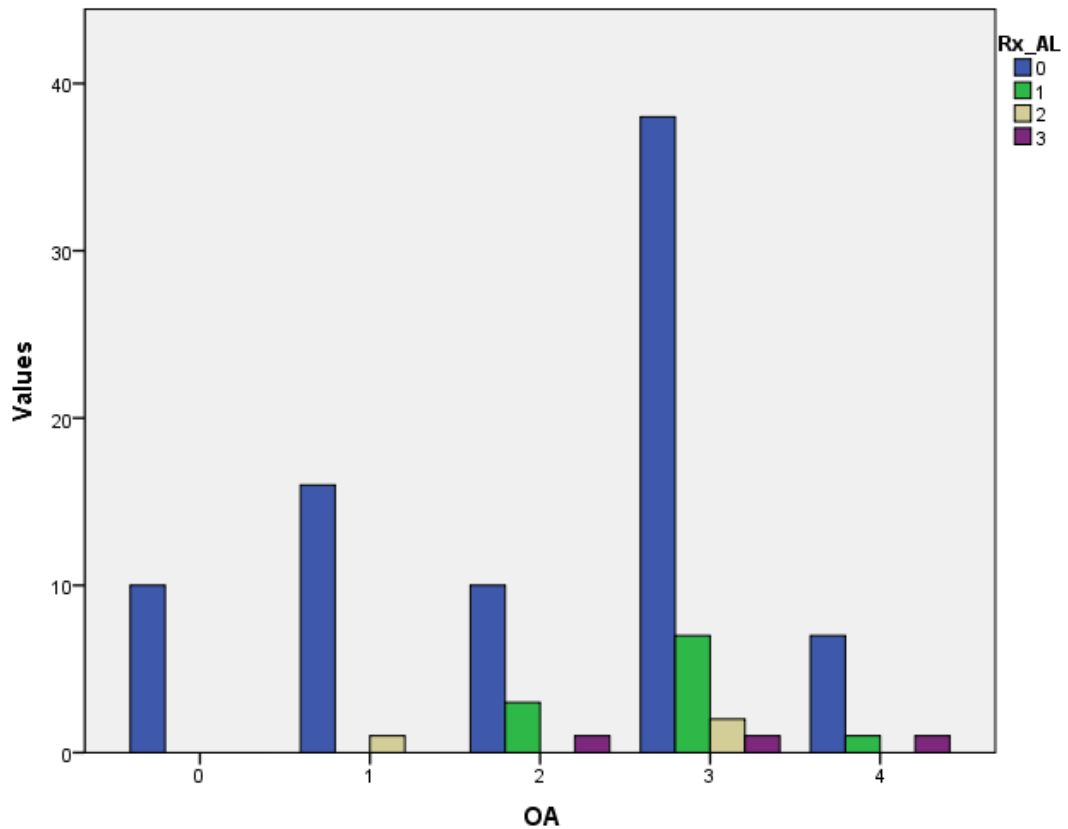


Figure 157. Study II. Histogram of radiographic density of the AL corner in inferosuperior radiographs (Rx_AL): number of tibias in each category, grouped by Ahlbäck OA grade.

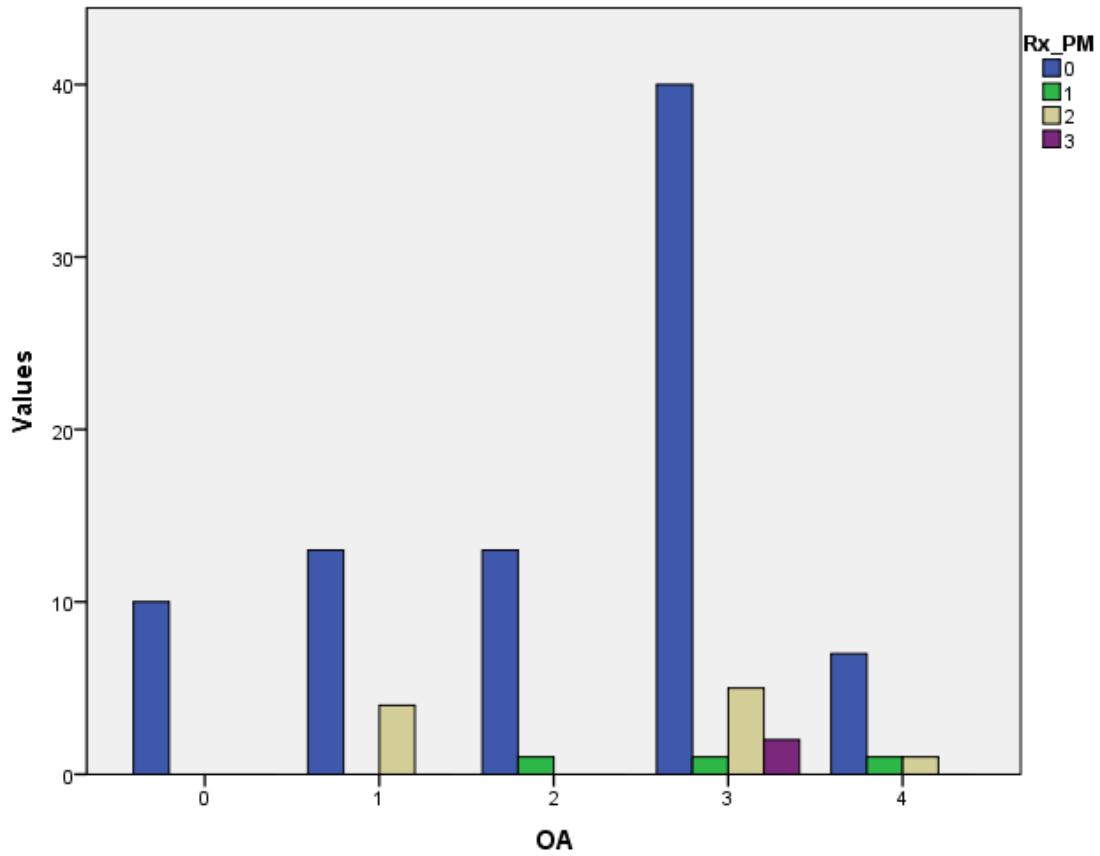


Figure 158. Study II. Histogram of radiographic density of the PM corner in inferosuperior radiographs (Rx_PM): number of tibias in each category, grouped by Ahlbäck OA grade.

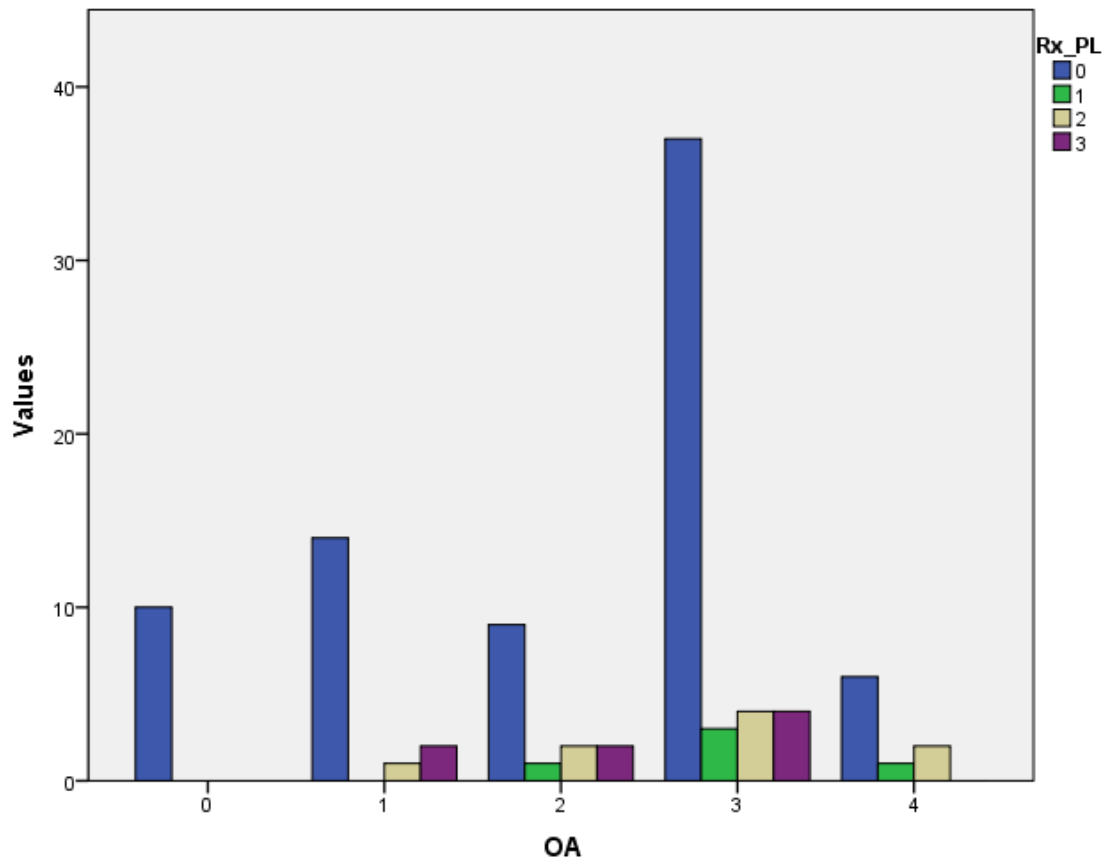


Figure 159. Study II. Histogram of radiographic density of the PL corner in inferosuperior radiographs (Rx_PL): number of tibias in each category, grouped by Ahlbäck OA grade.

IV.3.2.2. Condyle wear

IV.3.2.2.1. Condyle wear patterns and grades

Different patterns of medial and lateral condylar wear were observed (see Fig. 160, Fig. 161, and Fig. 162). The proportion of specimens classified according to areas of maximum attrition of the condyle (MAC) is shown in Fig. 163. In medial OA (N=92) MAC was found mainly in the anteromedial part of the condyle, 3M (47%), followed by the posteromedial part, 4M (26%), and anterolateral part, 2M (18%). The most pronounced bone attrition in lateral OA (N=5) was found in the posterolateral part, 4L (60%).

MAC was found to be strongly associated with Ahlbäck OA classification (Fig. 164): $\chi^2(32)=70.382$, $p<0.001$ (Phi=0.800, Cramer's V=0.400). Qualitatively, 3M and 4M were associated with higher OA grades, while 1M and 2M zones were more commonly affected in lower OA grades.

MAC plus its complementary areas of attrition (MACCo) was also strongly associated with Ahlbäck OA classification (Fig. 165): $\chi^2(88)=140.733$, $p<0.001$ (Phi=1.198, Cramer's V=0.599). The main affected zones in medial OA were 3M-wide-deep (16%) followed by 3M-wide (11%), 3M-deep (11%), 4M-wide-deep (9%), 2M-wide (9%), and 4M-deep (6%).

The proportion of specimens classified according to opposite MAC areas (MACOp) is shown in Fig. 166. In medial OA (Fig. 167) the most common MACOp were 1L (24%) and 1L-2L (23%), 2L-1L (19%), 1L-4L (13%), 2L (11%). No statistical differences were found between OA groups and MACOp.

MAC showed a strong association with MACOp (Fig. 168), $\chi^2(120)=529.066$, $p<0.001$ (Phi=2.173, Cramer's V=0.768), as did MACCo with MACOp, $\chi^2(360)=894.755$, $p<0.001$ (Phi=2.826, Cramer's V=0.730). Examination of the frequency distribution revealed that the most common MACOp for 3M was 1L (94.3%), and the most commonly associated MACOp for 4M was 2L (88%). MACOp for 2M was most frequently 1L (76.4%), and for 1M it was 2L (57.2%).

The attrition grade was found to be significantly correlated with Ahlbäck OA classification, with higher knee OA grades associated with more attrition: in the medial condyle (Fig. 169), $r_s(98)=-0.554$, $p<0.001$; and in the lateral condyle (Fig. 170), $r_s(98)=-0.395$, $p<0.001$. Bone attrition of the medial condyle was strongly associated with attrition of the lateral condyle: $r_s(98)=0.701$, $p<0.001$.

MAC in medial OA was also strongly associated with attrition grades (Fig. 171), $\chi^2(88)=193.847$, $p<0.001$ (Phi=1.406, Cramer's $V=0.703$). Frequency distribution analysis showed that 3M and 4M were associated with higher attrition grades, while 1M and 2M zones were associated with lower attrition grades.

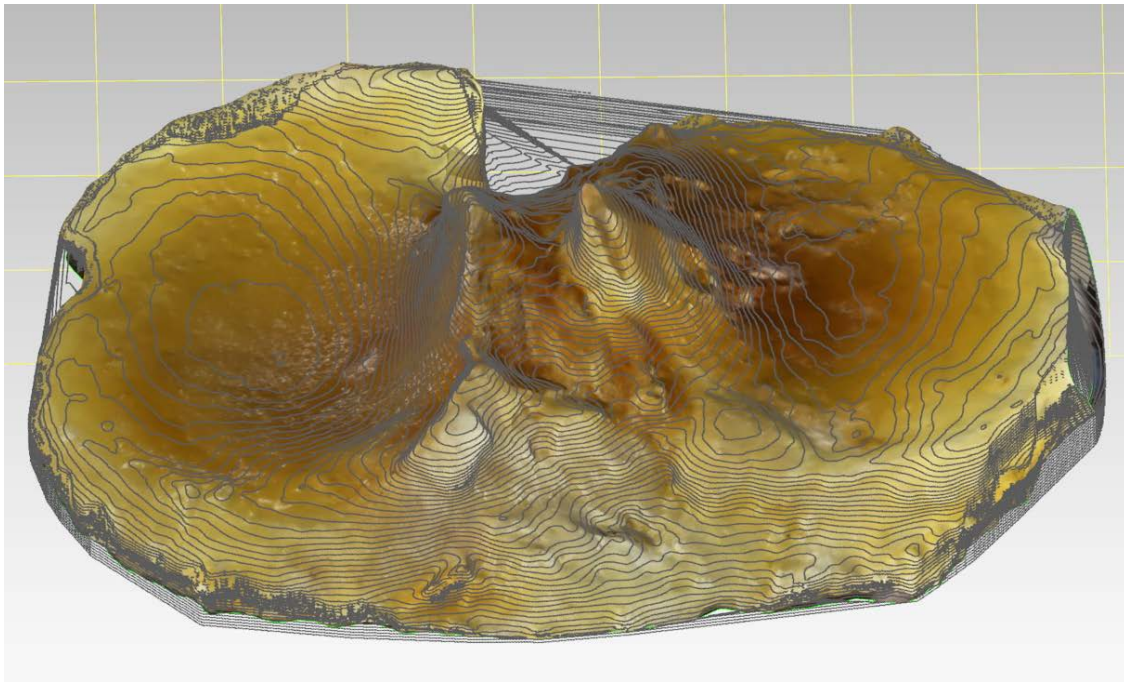


Figure 160. 3D model of tibia 83, with contour lines superimposed. Varus. Medial condyle attrition grade -2 (MAC 2M, MACCo 3M). Lateral condyle attrition grade -2 (MACOp 1L).

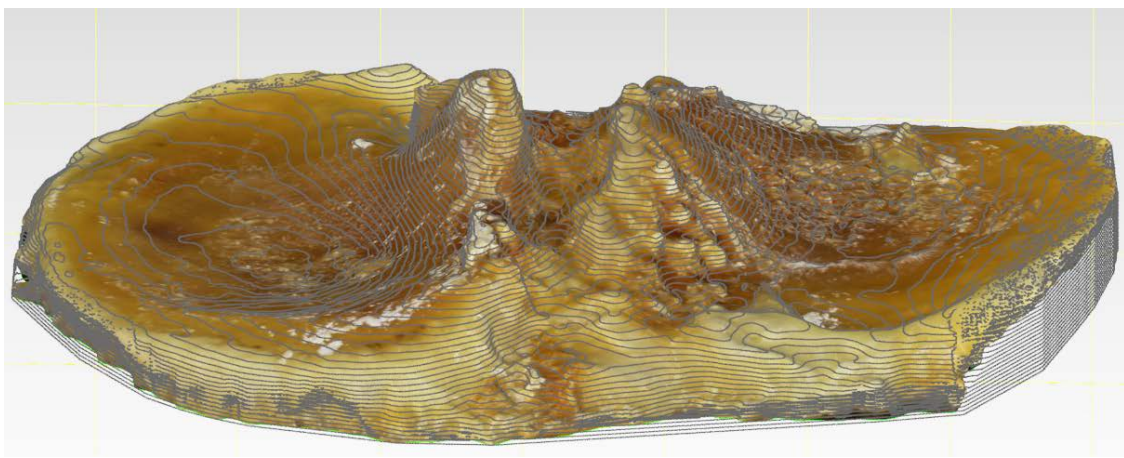


Figure 161. 3D model of tibia 82, with contour lines superimposed. Varus. Medial condyle attrition grade -3 (MAC 2M, MACCo 3M). Lateral condyle attrition grade -3 (MACOp 4L-1L).

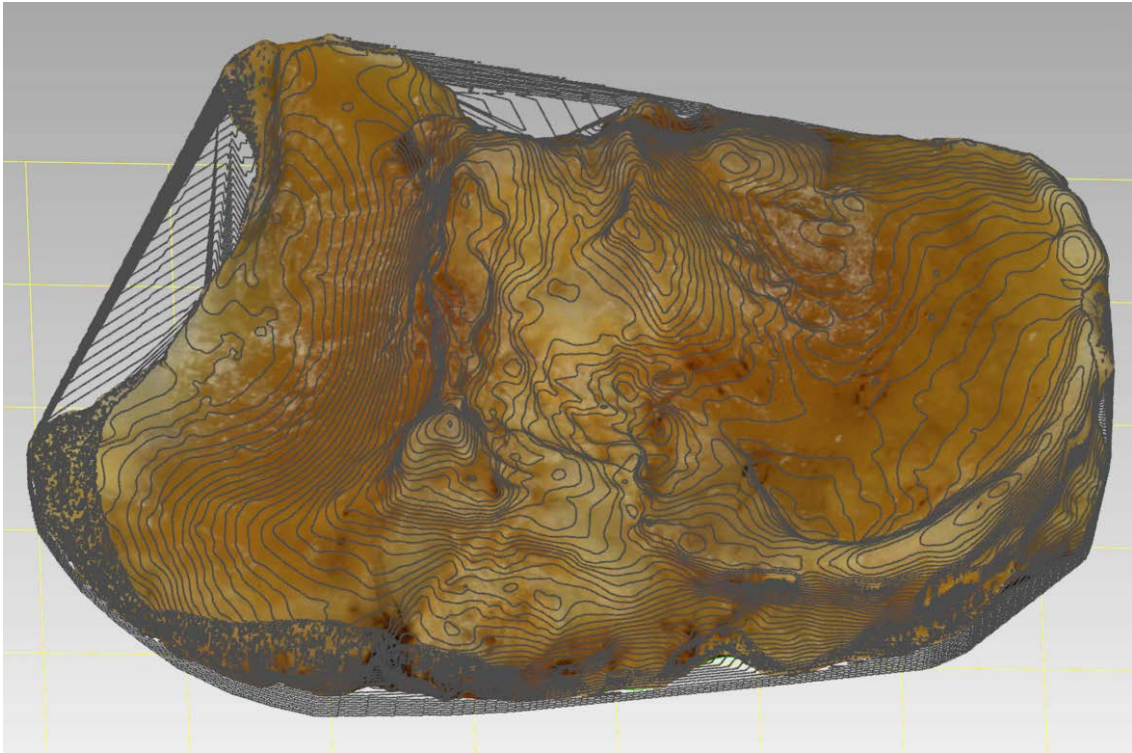


Figure 162. 3D model of tibia 53, with contour lines superimposed. Varus. Medial condyle attrition grade -4 (MAC 4M, MACCo 3M). Lateral condyle attrition grade -4 (MACOp 1L-2L).

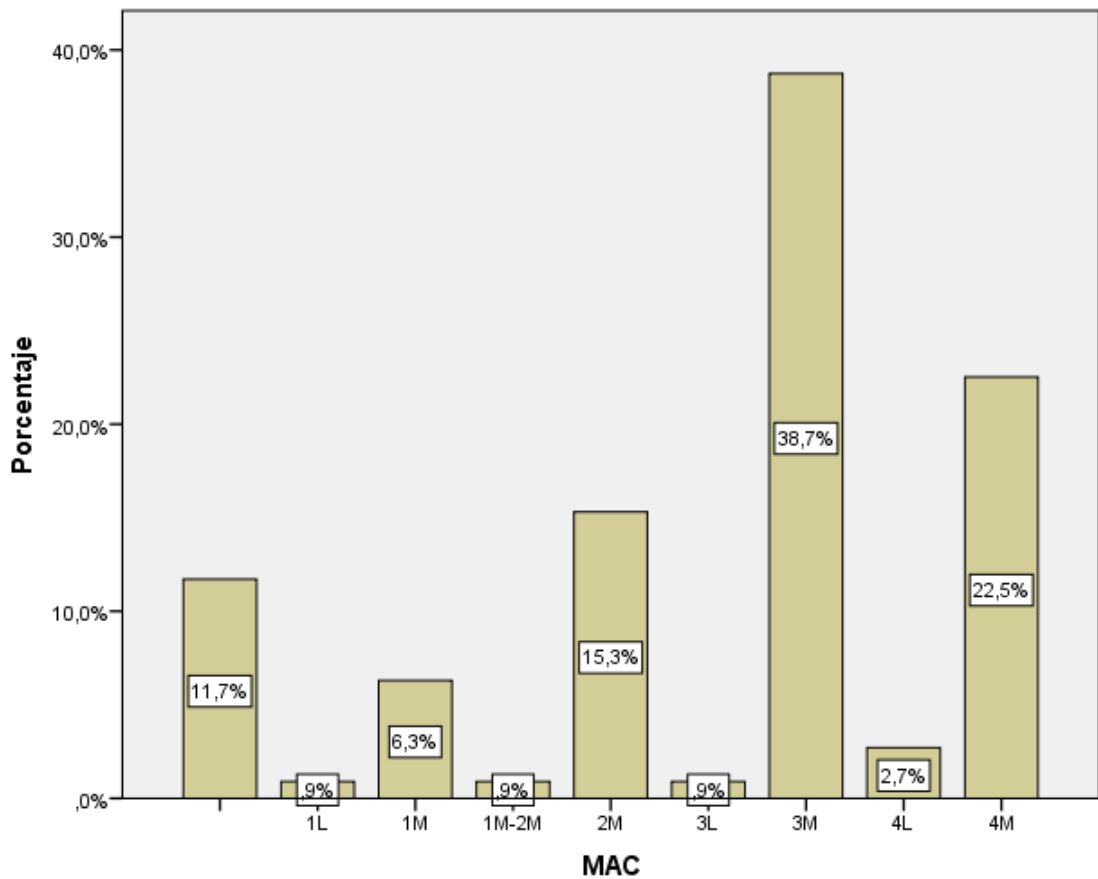


Figure 163. Study II. Histogram of percentage of tibias in each MAC category.

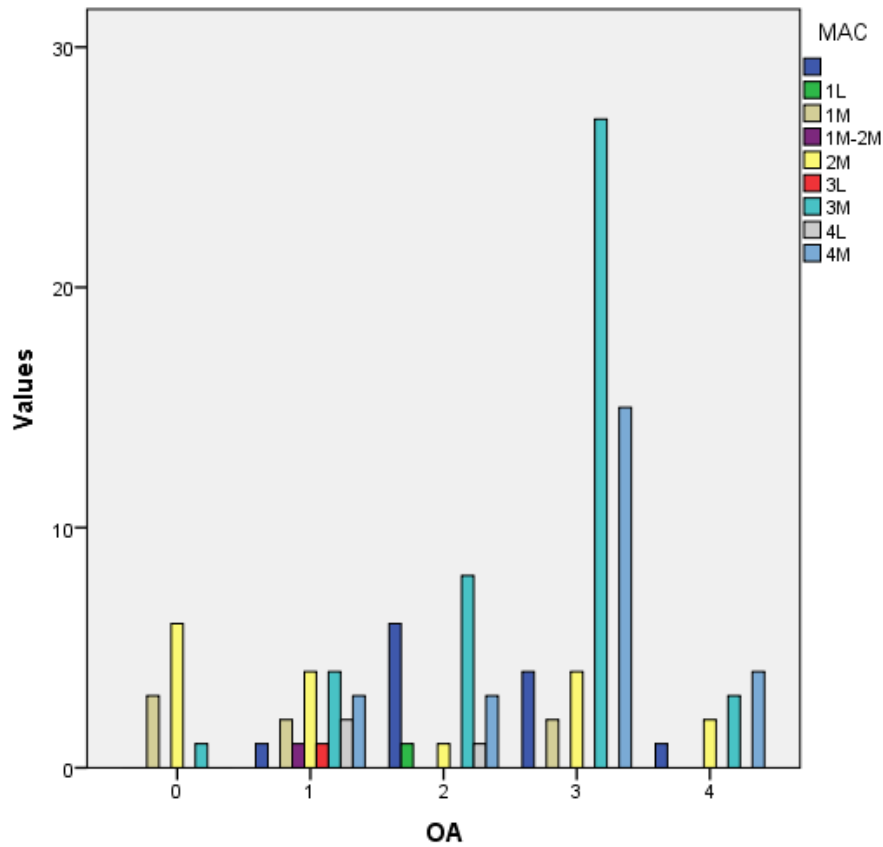


Figure 164. Study II. Histogram of MAC zones: number of tibias in each MAC category, grouped by Ahlbäck OA grade.

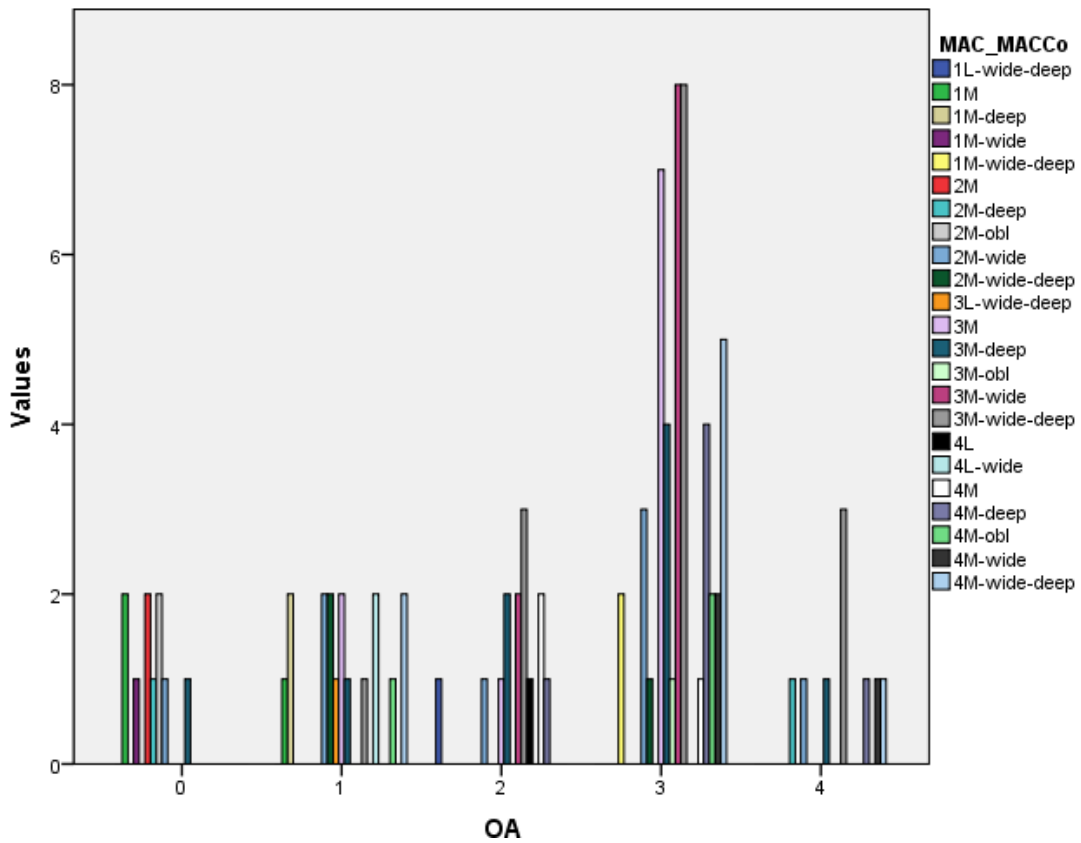


Figure 165. Study II. Histogram of MAC + MACCo: number of tibias in each MAC + MACCo category, grouped by Ahlbäck OA grade. Deep: attrition follows anteroposterior direction. Wide: follows mediolateral direction. Obl: follows oblique direction.

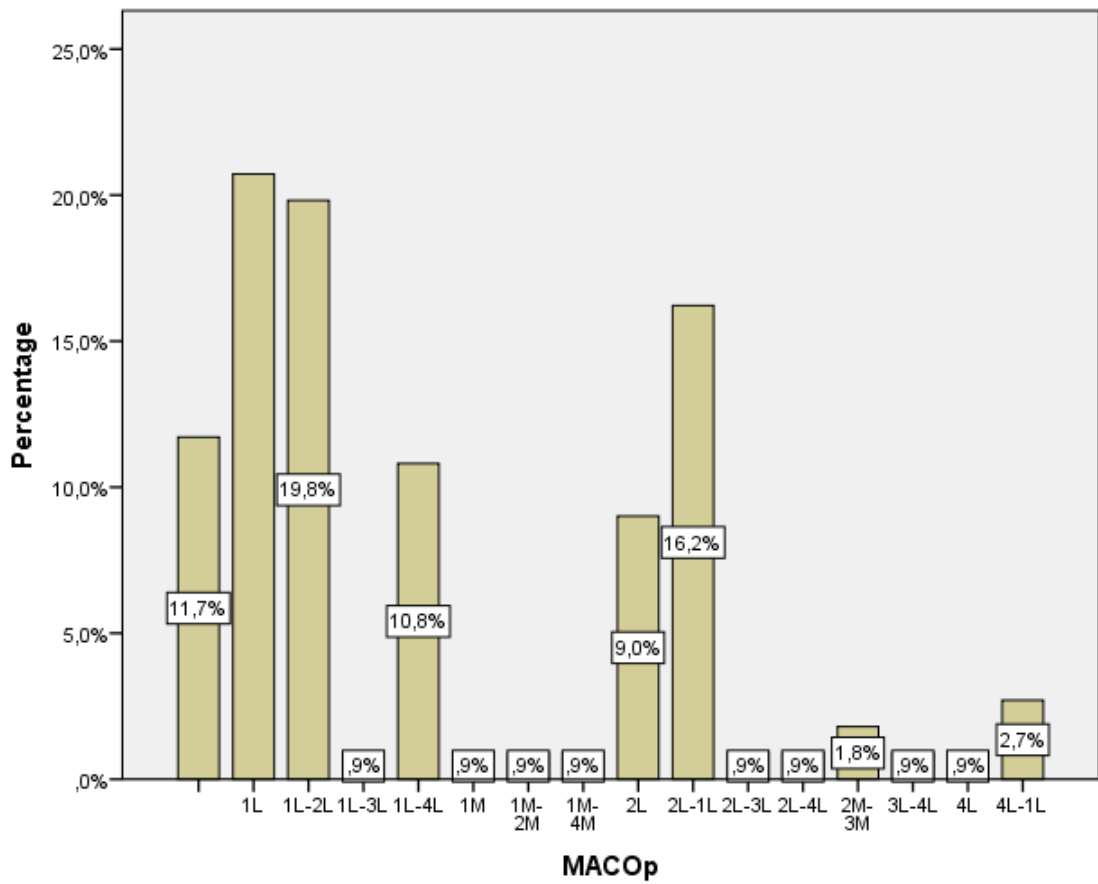


Figure 166. Study II. Histogram of percentage of tibias in each MACOp category.

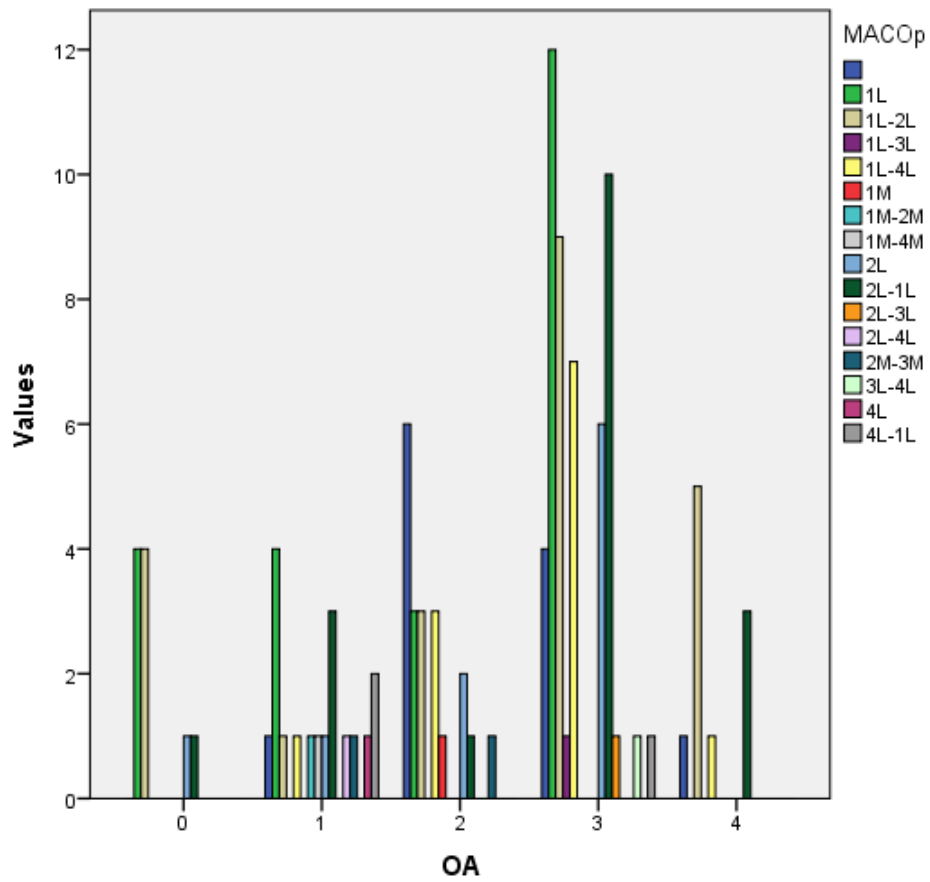


Figure 167. Study II. Histogram of MACOp: number of tibias in each MACOp category, grouped by Ahlbäck OA grade.

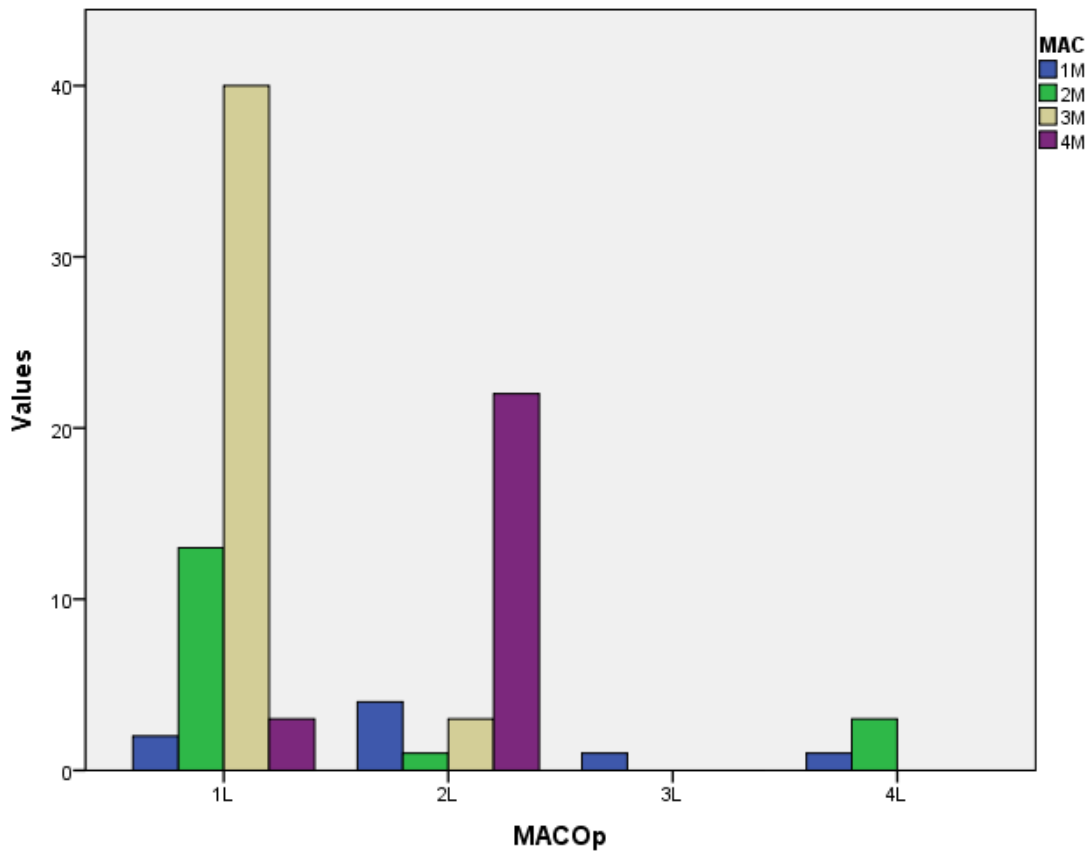


Figure 168. Study II. Histogram of MAC: number of tibias in each MAC category, grouped by MACOp category.

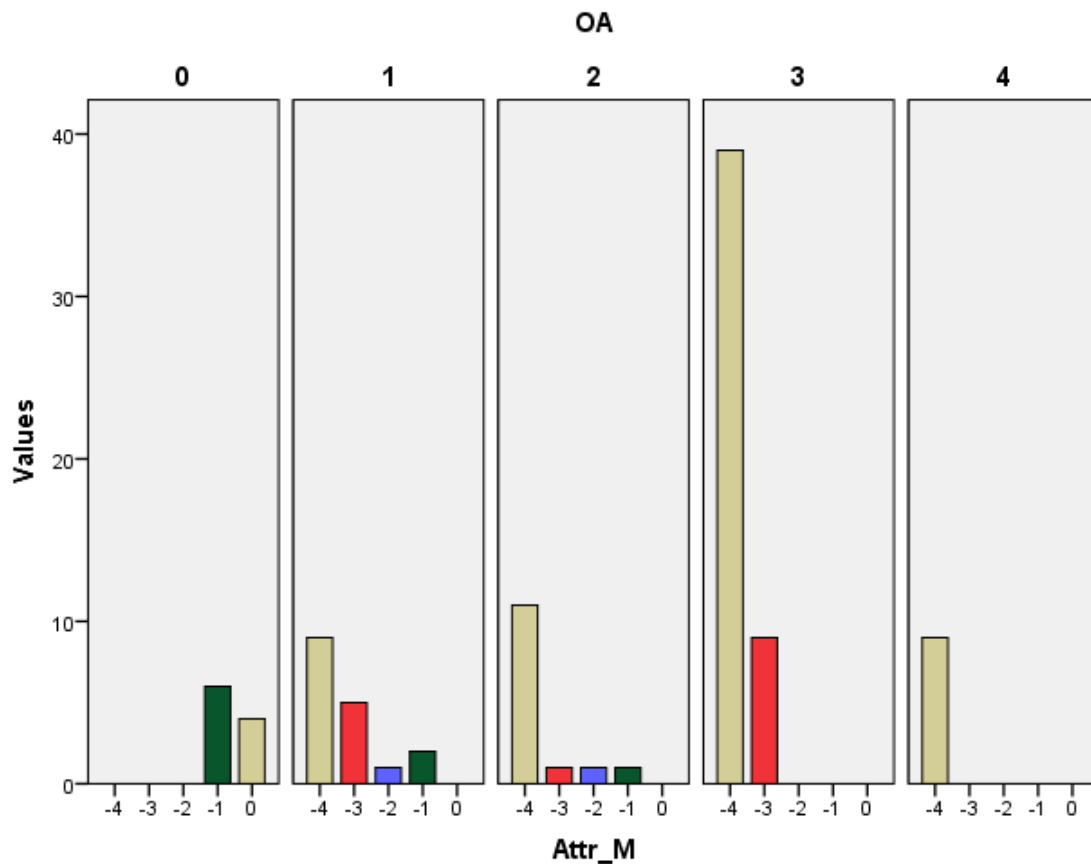


Figure 169. Study II. Histogram of attrition of the medial condyle (Attr_M): number of tibias in each attrition grade, grouped by Ahlbäck OA grade.

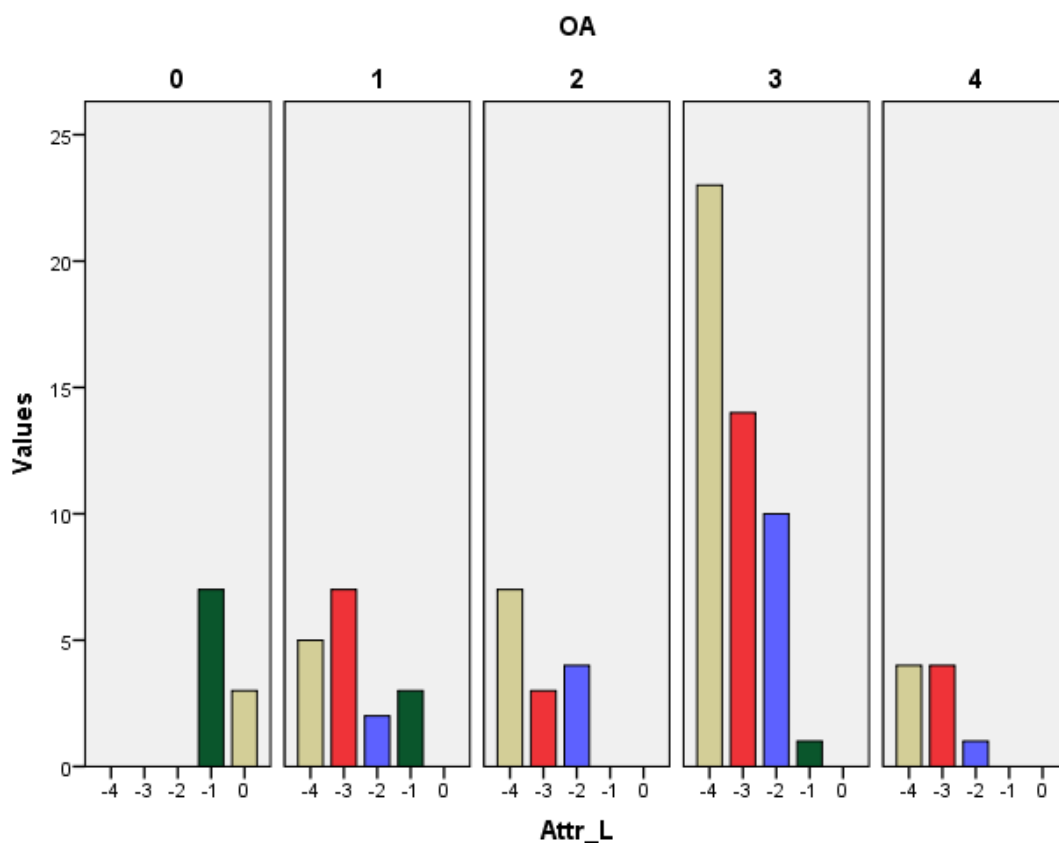


Figure 170. Study II. Histogram of attrition of the lateral condyle (Attr_L): number of tibias in each attrition grade, grouped by Ahlbäck OA grade.

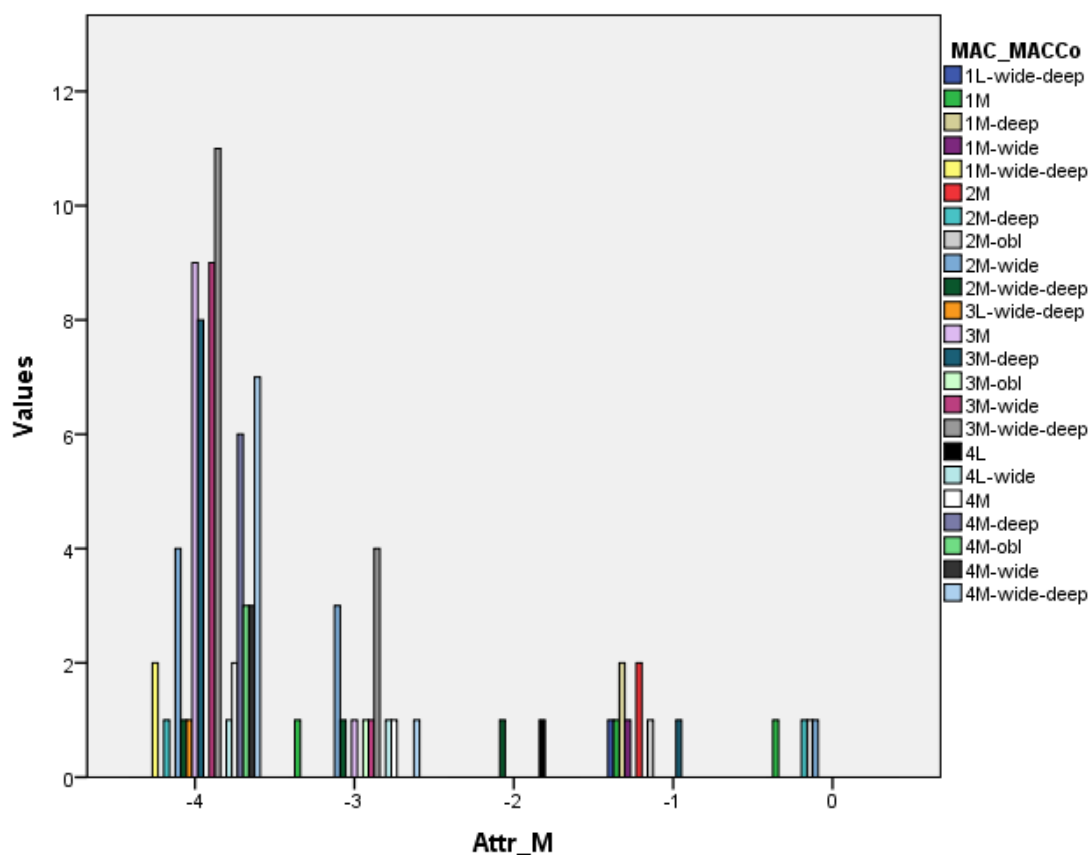


Figure 171. Study II. Histogram of MAC combined with its complementary areas: number of varus knees in each MAC + MACCo grade, grouped by attrition of the medial condyle. Deep: attrition follows anteroposterior direction. Wide: follows mediolateral direction. Obl: follows oblique direction.

IV.3.2.2.2. Condyle wear and ACL pathology

From Study II, all affected knees were in varus, in 3% the ACL was absent, instability was found during physical examination in 2%, and in 7% the patient reported “giving way” of the knee during history taking.

A strong, statistically significant association was found between ACL pathology and MAC (Fig. 172), $\chi^2(9)=17.369$, $p=0.043$ (Phi=0.432, Cramer’s V=0.250). Frequency distribution analysis showed that clear AP instability or ACL absence was associated with posterior MAC areas (1M and 4M), while instability in history taking (“giving way”) was associated with medial MAC areas (3M and 4M).

A positive but weak correlation was found between alignment and ACL pathology, $r_s(84)=0.275$, $p=0.011$; and a negative and weak correlation between attrition of the medial condyle and ACL pathology, $r_s(98)=-0.129$, $p=0.207$. No association was found between MT-LT relative height and ACL pathology: $\chi^2(6)=2.051$, $p=0.915$ (Phi=0.145, Cramer’s V=0.102).

Because of the small size of ACL pathology groups, a Kruskal-Wallis H test was performed to compare their mean medial and lateral tubercle slopes: MT (Fig. 173), $\chi^2(3)=3.105$, $p=0.376$; LT (Fig. 174), $\chi^2(3)=2.860$, $p=0.414$; MT–LT (Fig. 175), $\chi^2(3)=0.658$, $p=0.883$. It showed an MT slope of 39.2° for ACL instability grade 0 (N=86), 40.4° for grade 1 (N=7), 32° for grade 2 (N=2), and 39° for grade 3 (N=3).

The best-fit regression models obtained to predict ACL pathology from tubercle slope were cubic, although they were not found to be significantly correlated: MT (Fig. 176), $F(3, 94)=1.113$, $p=0.348$, $R^2=0.034$; LT (Fig. 177), $F(3, 94)=0.836$, $p=0.477$, $R^2=0.026$.

In Study XIII, 12 patients were found with an absent ACL during TKA, with a mean age of 71.3 years (range, 62 to 79 years), 58% were female, and in 83% the pathology was found on their left knee (their non-dominant side).

The mean tibiofemoral angle of the knees with absent ACL was 178.3° (95% CI 172.4 – 184.2°), with 50% having MT>LT, 33% LT>MT, and 17% MT=LT. 67% were in varus, 25% in valgus, and 8% in neuter alignment. Classification into OA by Ahlbäck yielded 8% grade 1, 33% grade 2, 41% grade 3, and 17% grade 4.

Percentage of the ML proximal tibial width (measured in the AP radiograph) showed a mean height for the MT of 13.3 ± 1.4% of the AP width (range, 10.3% to

16.8%), and an LT mean height of $12.2 \pm 1.3\%$ of the ML width (range, 7.9% to 15.0%). Their difference had an average of $1.1 \pm 1.7\%$ (range -3.0% to 7.4%, where positive value indicates $MT > LT$) of the radiographic ML width.

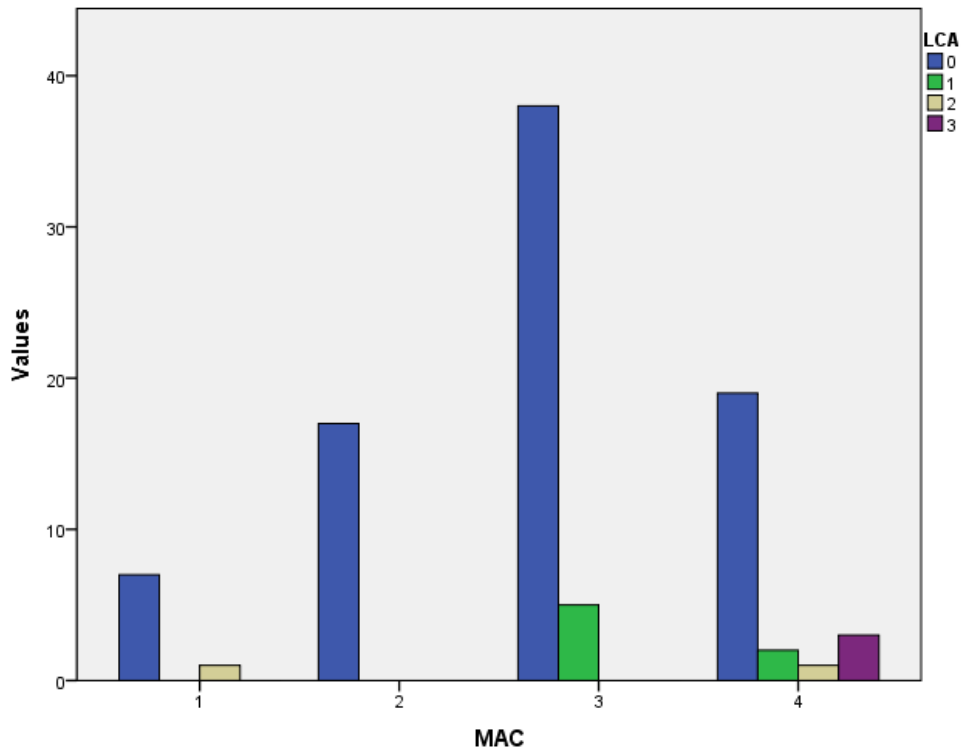


Figure 172. Study II. Histogram of the ACL instability grade (LCA): number of tibias in each category, grouped by MAC.

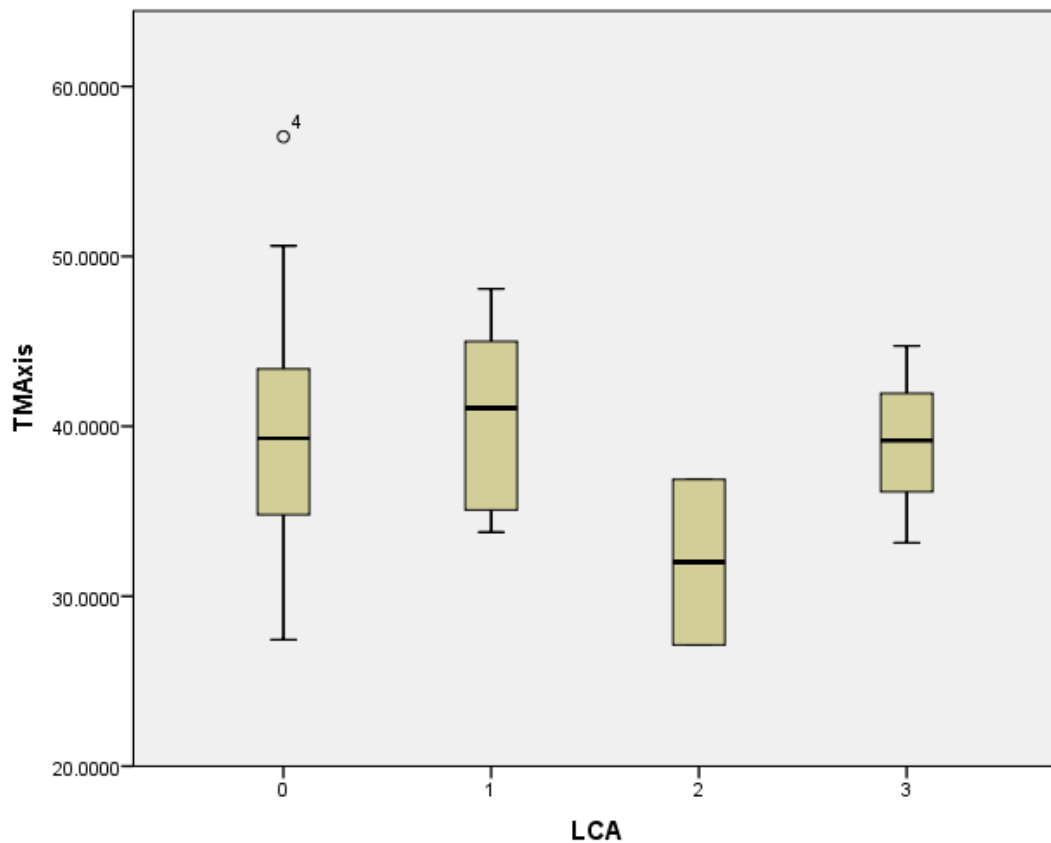


Figure 173. Box-and-whisker plot of MT slope (TMAxis) distribution in each ACL instability grade (LCA).

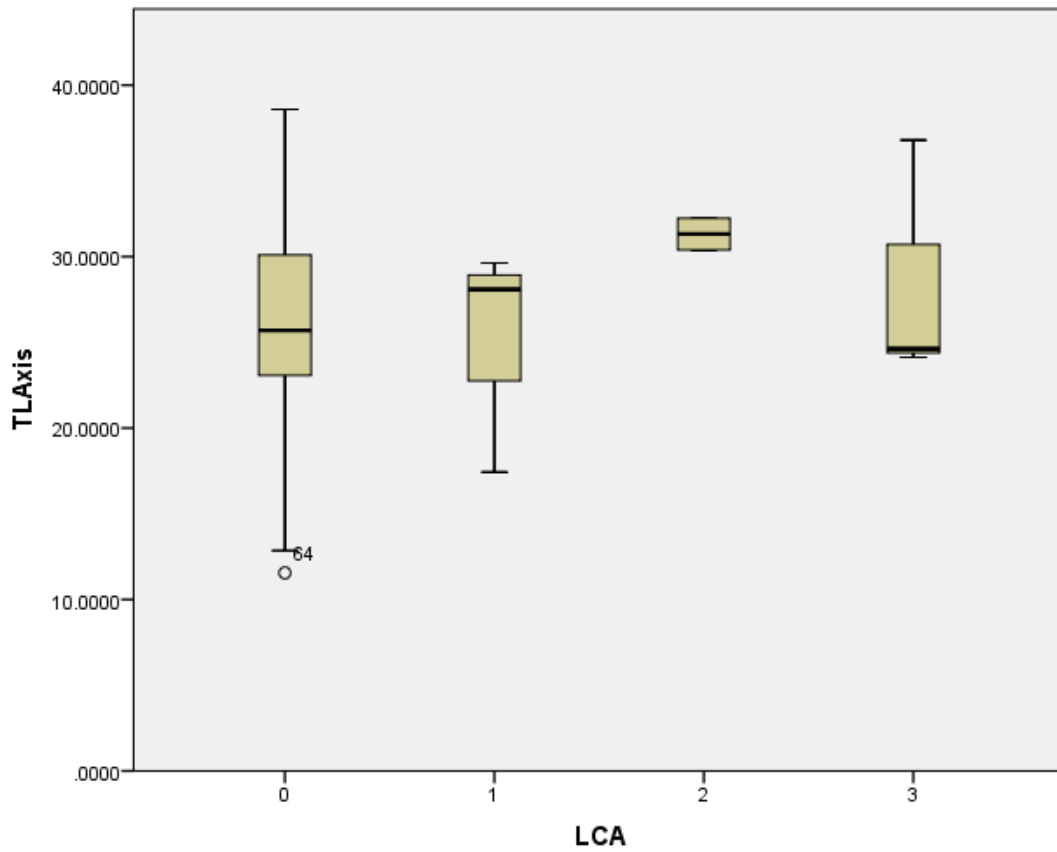


Figure 174. Box-and-whisker plot of LT slope (TLAxis) distribution in each ACL instability grade (LCA).

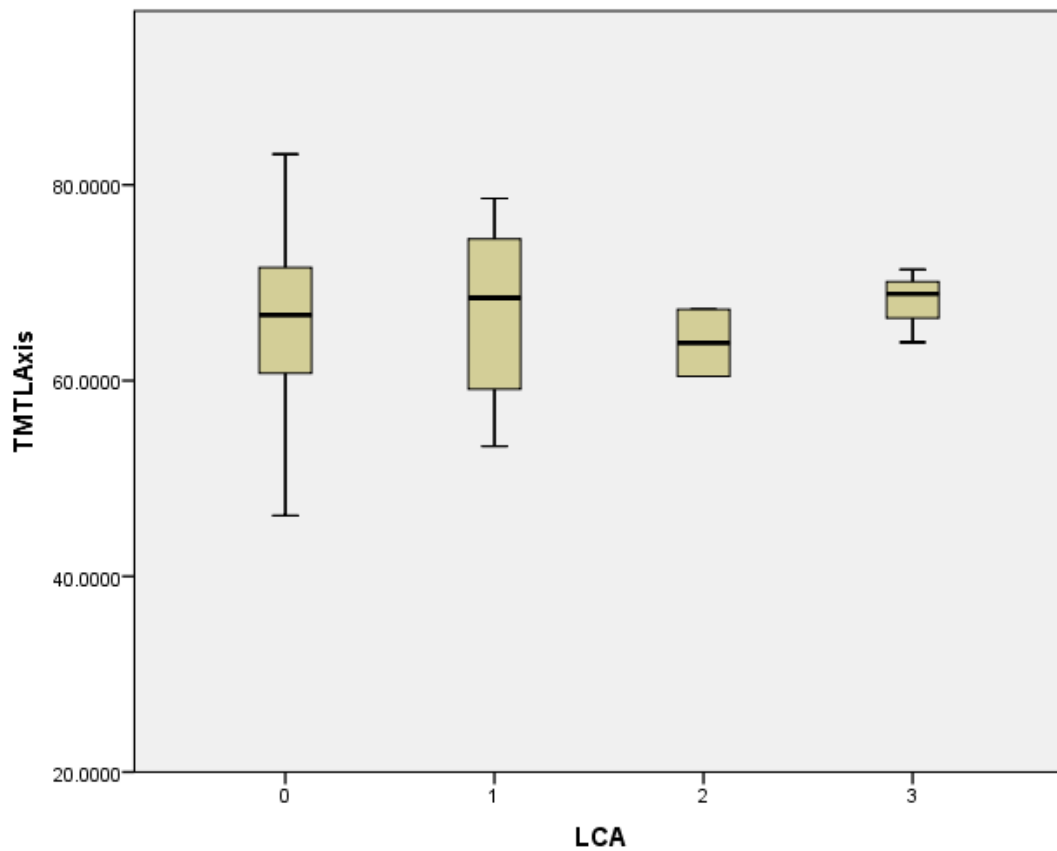


Figure 175. Box-and-whisker plot of MT-LT slope (TMTLAxis) distribution in each ACL instability grade (LCA).

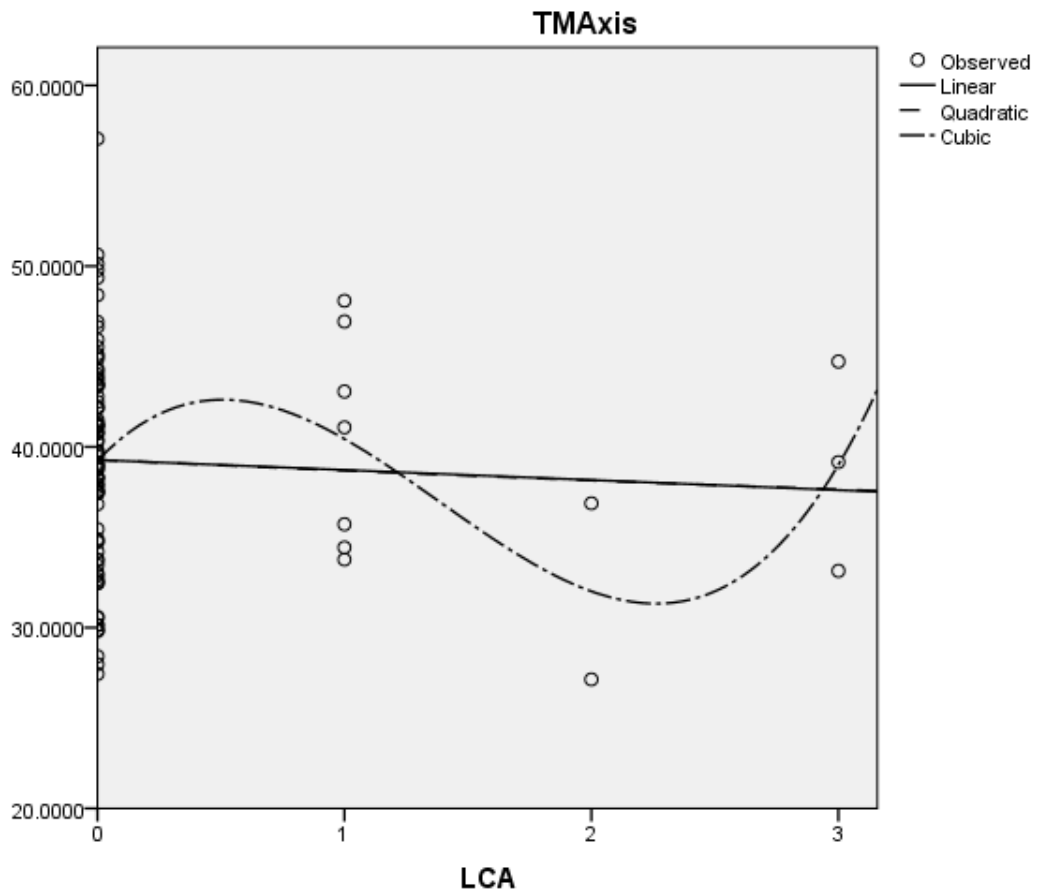


Figure 176. Study II. Regression estimation for ACL instability grade (LCA) from MT slope (TMAxis).

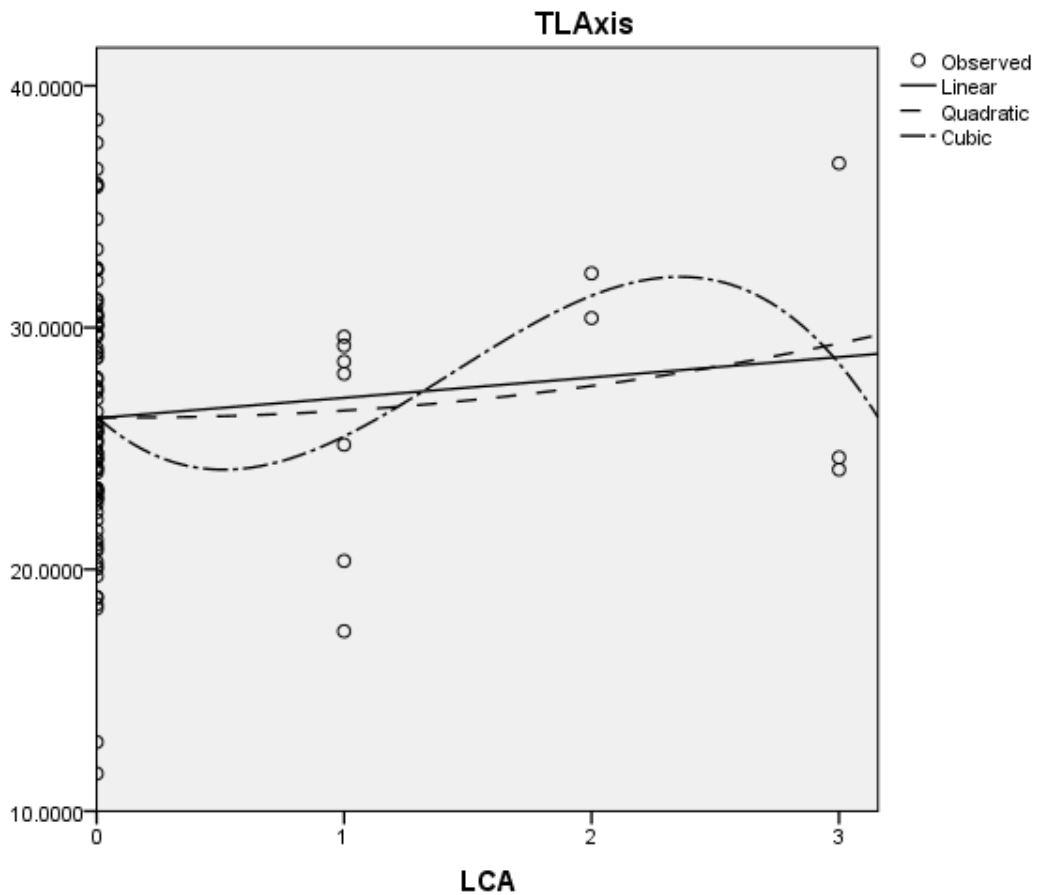


Figure 177. Study II. Regression estimation for ACL instability grade (LCA) from MT slope (TLAxis).

IV.4. Anterior intercondylar area

IV.4.1. Common structures of the anterior intercondylar area

The anterior intercondylar area (AIA) was defined as the central anterior area of the tibial plateau, located between condyles. It showed a triangular or general irregular quadrilateral shape – with a smaller posterior side, the anterior wall of the intertubercular ridge –, and comprised areas 1c, 2c, 5, 7, 8, 9 and 10 (Fig. 178, Fig. 179).

A constant sagittal ridge, the anterior intercondylar area's ridge (AIAR), **A**, was found dividing the AIA in two parts: a medial, taller part (MAIA), including area 10 posteriorly, and area 5 anteriorly; and a lateral, lower part (LAIA), including area 8 posteriorly, and the groove formed by areas 7 and 9.

The AIAR was found in turn formed by two different aspects, their division being marked by the posterior process of the anterior frontal intercondylar ridge:

- The posterior aspect of the AIAR, **A1**, forming the oblique lateral wall of area 10, dividing it from areas 8 and 7.
- The anterior aspect of the AIAR, **A2**, separating areas 5 and 9.

The anterior frontal intercondylar ridge (AFIR), **F** was formed by two main structures:

- The posterior AFIR process, **F1**, coincident with the anterior limit of area 10: it formed an approximately right angle with the AMIR, following a mediolateral direction with a slight posteriorly concave curve. The lateral aspect of this process marked the division of the AIAR.
- The anterior AFIR process, **F2**, was the inconstant posterior limit of area 5. It followed a straight mediolateral line (or slight anteriorly concave curve) connecting area 1c with A2.
- An incisure often appeared between both ridges, the AFIR recess, **S**, which accommodated the transverse intermeniscal ligament, served for the attachment of synovial membrane, and had lesser foramina nutricia.

The external AMIR process (B1) and the posterior AFIR process (F1) were joined at an approximately right angle, forming together an elevated structure, the anterior geniculate ridge. A constant, slightly curved corner, the intercondylar geniculum, **G**, was found at the angle formed by both processes. An inconstant protuberance, the anteromedial intercondylar knob (AMIK), also Parsons' knob,

was found in certain specimens with degenerative changes near to or instead of the elevated curved angle G.

An inconstant protuberance, the anterocentral intercondylar knob (ACIK), **H**, was found along the lateral aspect of the F1 process, usually at its lateral-most point (at the intersection with the AIAR).

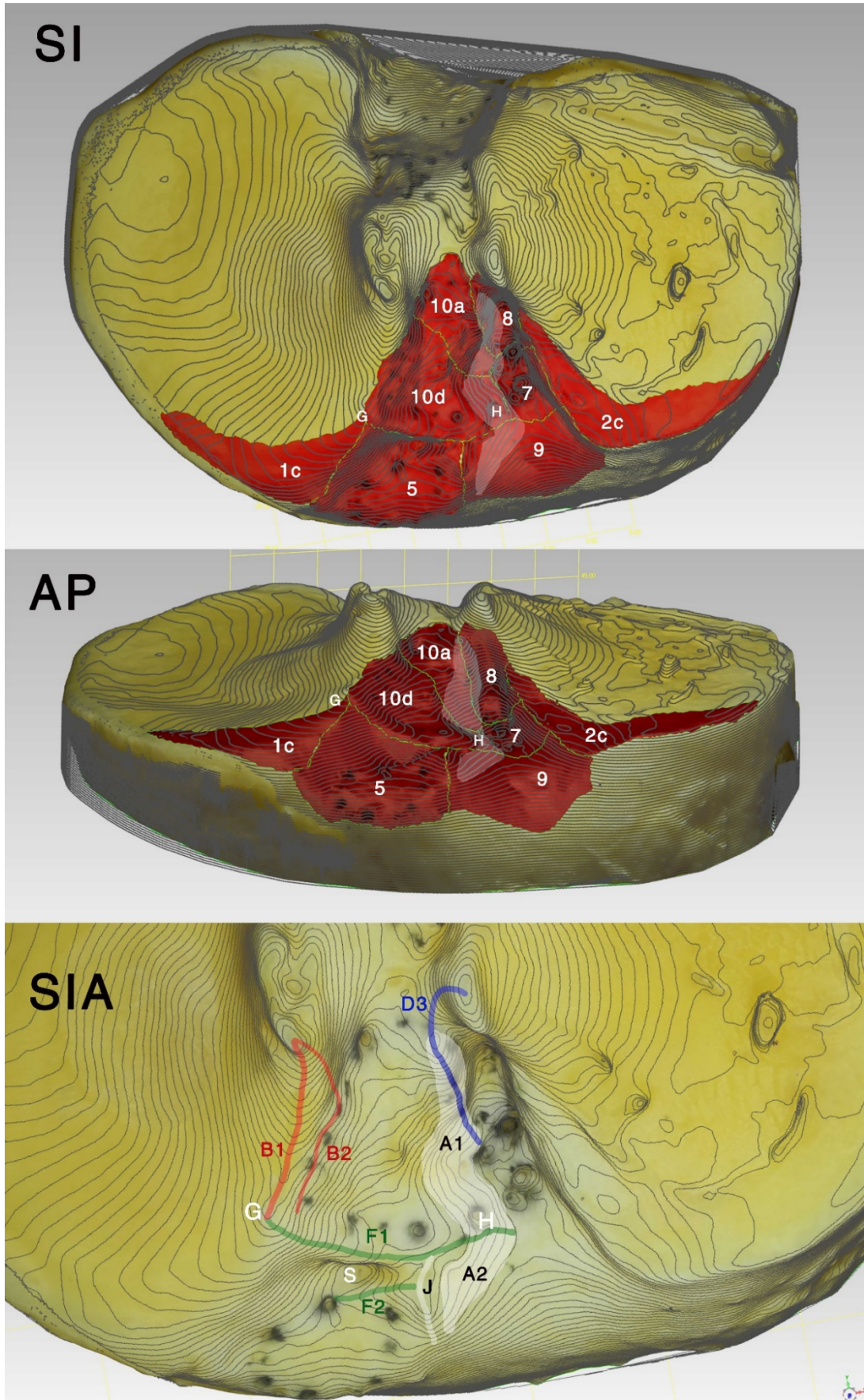


Figure 178. 3D model of Tibia A, with contour lines superimposed. Superoinferior (SI) and anteroposterior (AP) views with selected areas of the anterior intercondylar area in red. Superoinferior view of anterior area (SIA) with painted lines over the main processes: AMIR (B1, B2) in red, ALIR (D3) in blue, AFIR (F1, F2) in green, AIAR (A1, A2) in white. The geniculum (G), ACIK (H), and AFIR recess (S) are also labelled.

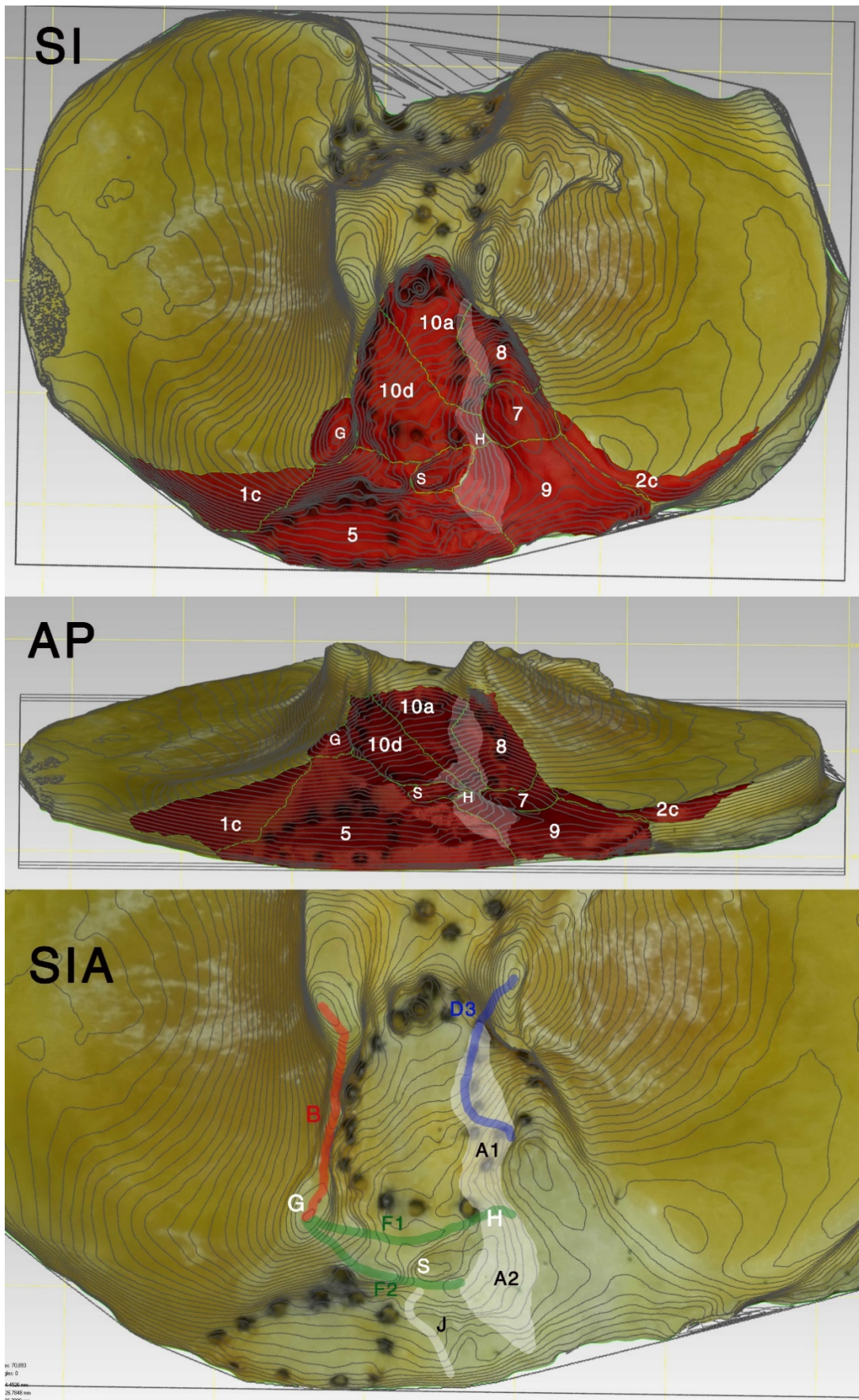


Figure 179. 3D model of Tibia D, with contour lines superimposed. Superoinferior (SI) and anteroposterior (AP) views with selected areas of the anterior intercondylar area in red. Superoinferior view of anterior area (SIA) with painted lines over the main processes: AMIR (B1) in red, ALIR (D3) in blue, AFIR (F1, F2) in green, AIAR (A1, A2) in white. The geniculum (G), ACIK (H), and AFIR recess (S) are also labelled.

IV.4.2. Degenerative changes of the anterior intercondylar area

IV.4.2.1. Qualitative assessment of degenerative changes

It was qualitatively observed in tibias with degenerative changes that both AFIR processes could be found elevated (Fig. 180). The AFIR recess was less frequently encountered, and when present it could appear deeply depressed between both constituent processes of the AFIR.

An antero-central intercondylar elevation (H) was found at the anterolateral limit of area 10 – at the crossroads between areas 10, 5 medially, and areas 7, 9 laterally: as a slight elevation over F1 in five donor tibias, as an elevated protuberance in four donor tibias with degenerative changes. The protuberance was found developed at the anterolateral limit of area 10 (Fig. 181), but also more medial to it, always along the F1 process (Fig. 183). In many pathological specimens it was also found integrated into a common elevation with nearby structures, such as the AFIR, the Parsons' knob, the anterolateral intercondylar knob, and the anterolateral corner.

In donors, the intercondylar geniculum (G) was formed by B1 and F1 in all specimens that did not show an elevation into a knob (nine tibias). In these normal tibias, G was a curved ridge, located at an approximately right angle formed between the prominent sagittal external AMIR process – which continued then externally in a slightly anteromedially curved direction, dividing the medial condyle from the anteromedial corner –, and the posterior AFIR, F1. In the rest of donors, an elevation appeared that blurred this right angle, the anteromedial intercondylar knob (AMIK), or Parsons' knob.

In some pathological tibias, the elevated internal AMIR process, B2, connected directly – and more smoothly – with F1, and the intercondylar geniculum – when not obscured by an anteromedial knob – formed an obtuse, curved angle.

In many pathological tibias, an anteromedial protuberance – the Parsons' knob or tubercle – was found near the angle formed by the geniculate ridge, but it was also found slightly distant to it, appearing as a continuation of certain elevated processes (that could be distinguished as formants of the protuberance): external or central AMIR processes (Fig. 182), anteromedial corner (Fig. 184), anterior or posterior processes of the AFIR (Fig. 185), or a combination of any of them.

The antero-central and anteromedial intercondylar elevations showed certain common shapes, classified as follows: lamina (horizontal), ridge, cone,

bicephalous cone (two conjoined cones), star (with different processes interlaced, see Fig. 186), horn, lip, little hook (two processes, a vertical one connecting with a smaller horizontal one, forming approximately a right angle), hook (with the horizontal process greater than the vertical one, see Fig. 187), and tongue (a more horizontal process projecting directly over the border, see Fig. 188),

The antero-central intercondylar knob was more commonly found as a ridge-like or cone-like elevation (Fig. 189), while the anteromedial intercondylar knob appeared more usually as a cone-like, star-like, or little hook-like elevation (Fig. 190).

Similar to the main intercondylar tubercles, erosion was found on the Parsons' elevation, and a marked direction of the erosion could be seen in many cases.

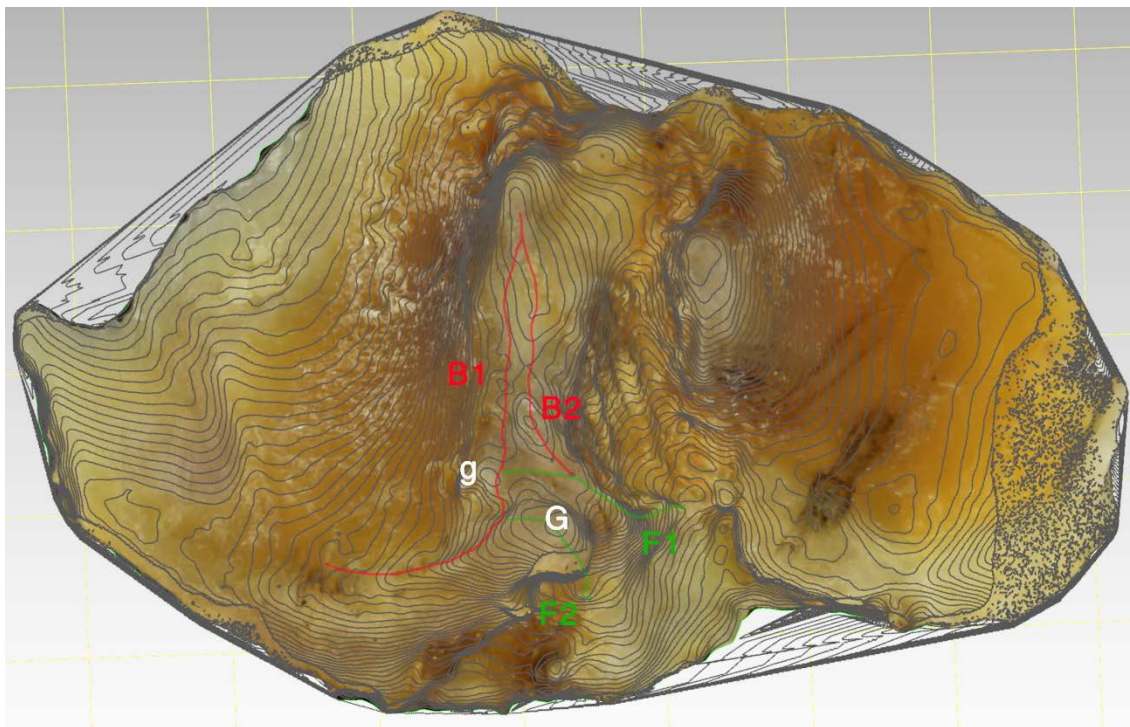


Figure 180. 3D model of tibia 18, with contour lines superimposed. Little hook-shaped Parsons' knob (G) formed mainly by anterior AFIR (F2) process with the AMIR and AM corner. The posterior AFIR process (F1) is connected directly with the elevated B2 process, with a gentler curve than is usually seen between B1 and F1. Notice the original location of the geniculum (g).

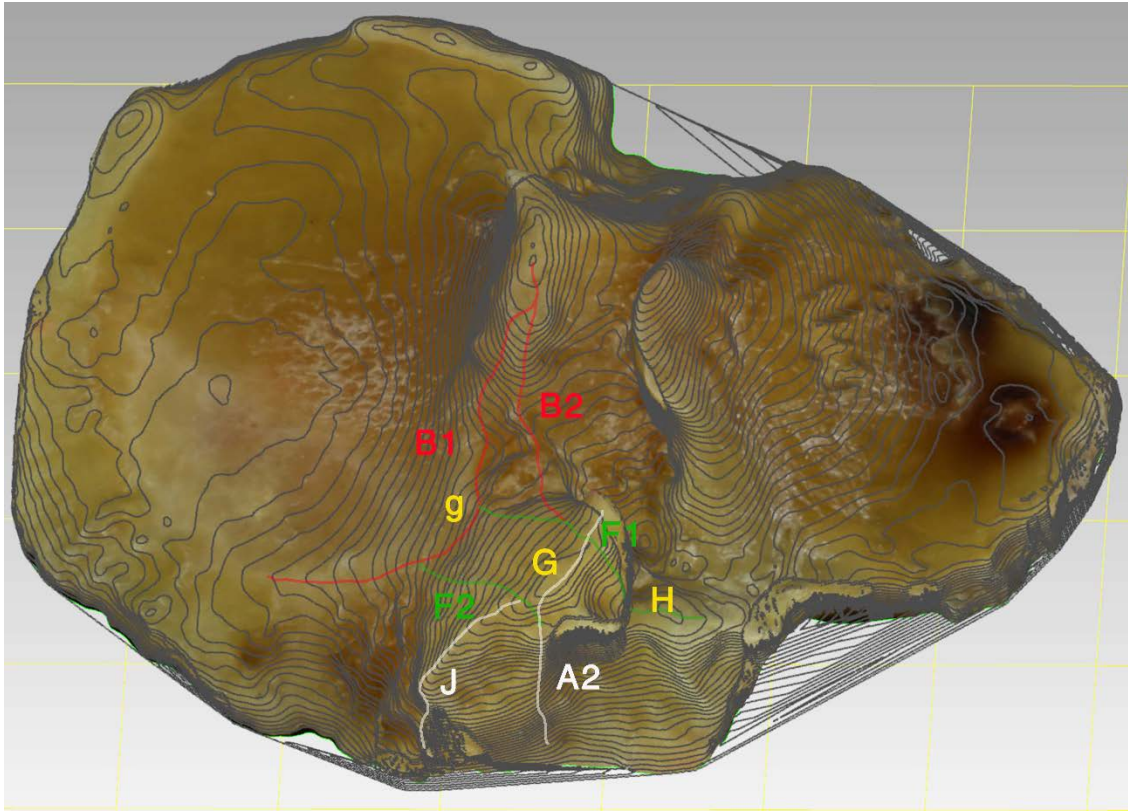


Figure 181. 3D model of tibia 11, with contour lines superimposed. A tubercle (G) is found in the central aspect of the AIA, formed by elevated AFIR processes, ASIR (J), and anterior AIAR (A2), with a star-shaped ACIK (H) seen connected to the anterior saddle elevation, in turn connected with the anterior saddle and anterolateral knob (anterolateral corner, also elevated, is cut in the 3D model). Notice that this “Parsons’ tubercle” cannot be defined as an anteromedial intercondylar tubercle proper – since F1 and B1 are not involved (see original geniculum site, g), but rather as a generic central AFIR tubercle.

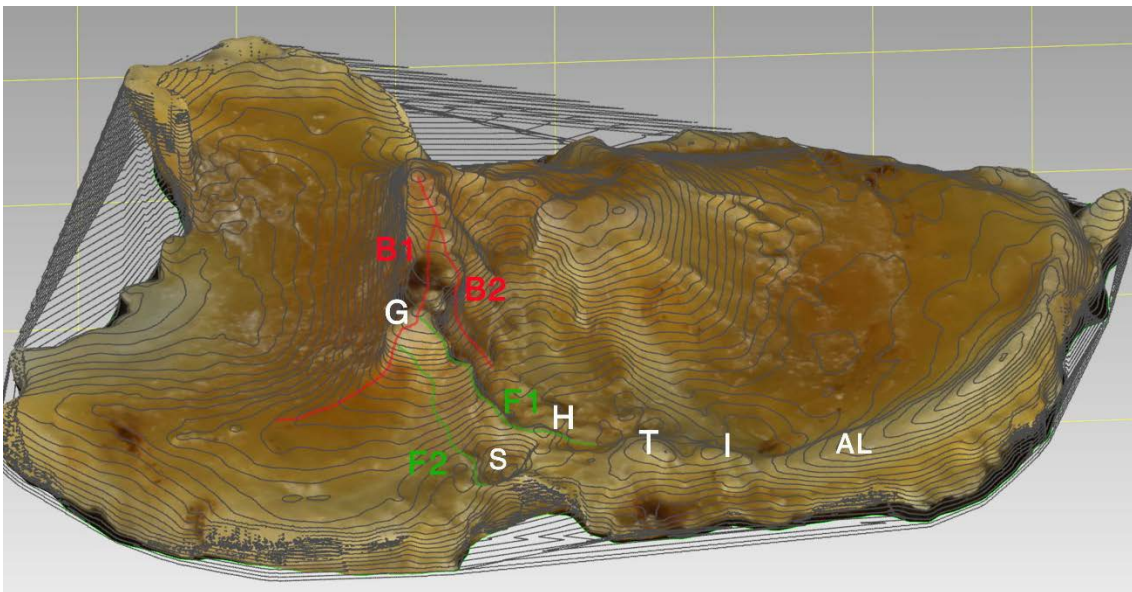


Figure 182. 3D model of tibia 52 with contour lines superimposed. The anteromedial knob (G) is mainly formed by B1, with F1 process being noticeably lower, while 1c and F2 do not contribute to the elevation. Notice the AFIR recess (S), ACIK (H), and the anterior saddle elevation (T), connected with the anterolateral knob (I) and anterolateral corner (AL).

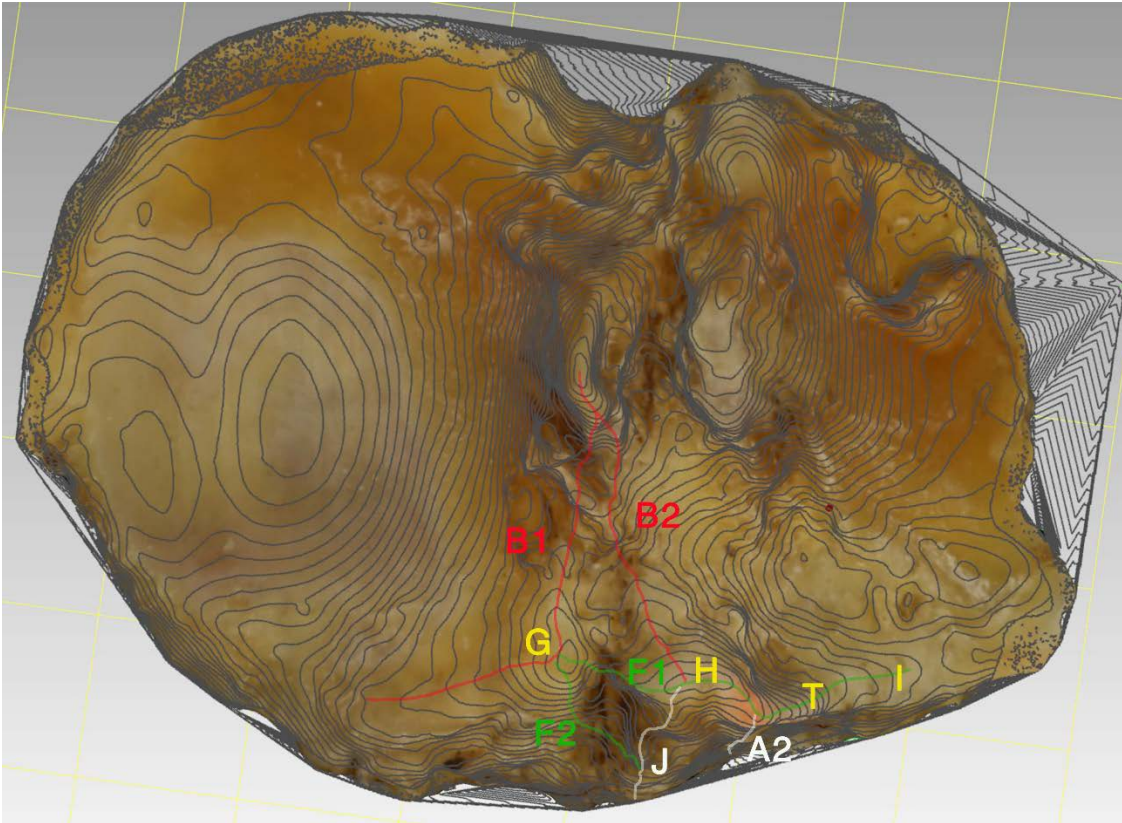


Figure 183. 3D model of tibia 40, with contour lines superimposed. Posterior process of the AFIR (F2) elevated, with star-shaped antero-central knob (H), more medial than usual, connected with the anterolateral knob (I) through the anterior saddle (T). Cone-shaped Parsons' knob (G) medially. The anterior process (J) and anterior aspect of the AIAR (A2) are only slightly elevated.

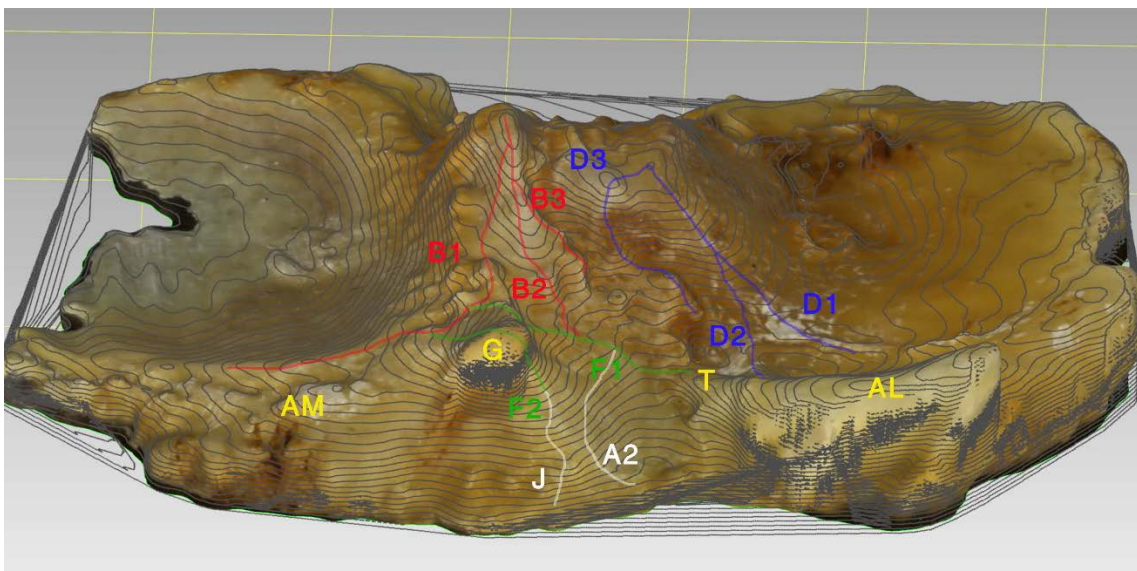


Figure 184. 3D model of tibia 19, with contour lines superimposed (left-mirrored). MAC 4M (MACCo 3M-1M-2M), condyle attrition grade 4. Parsons' tubercle formed by AMIR (B1) and AFIR (F2, F1) and AM corner elevation, showing anterolateral attrition direction. Notice marked B2 process mixing with B3 into area 10, and marked AL corner, as well as attrition of the LT (anterior summit's peak lower than D3 process).

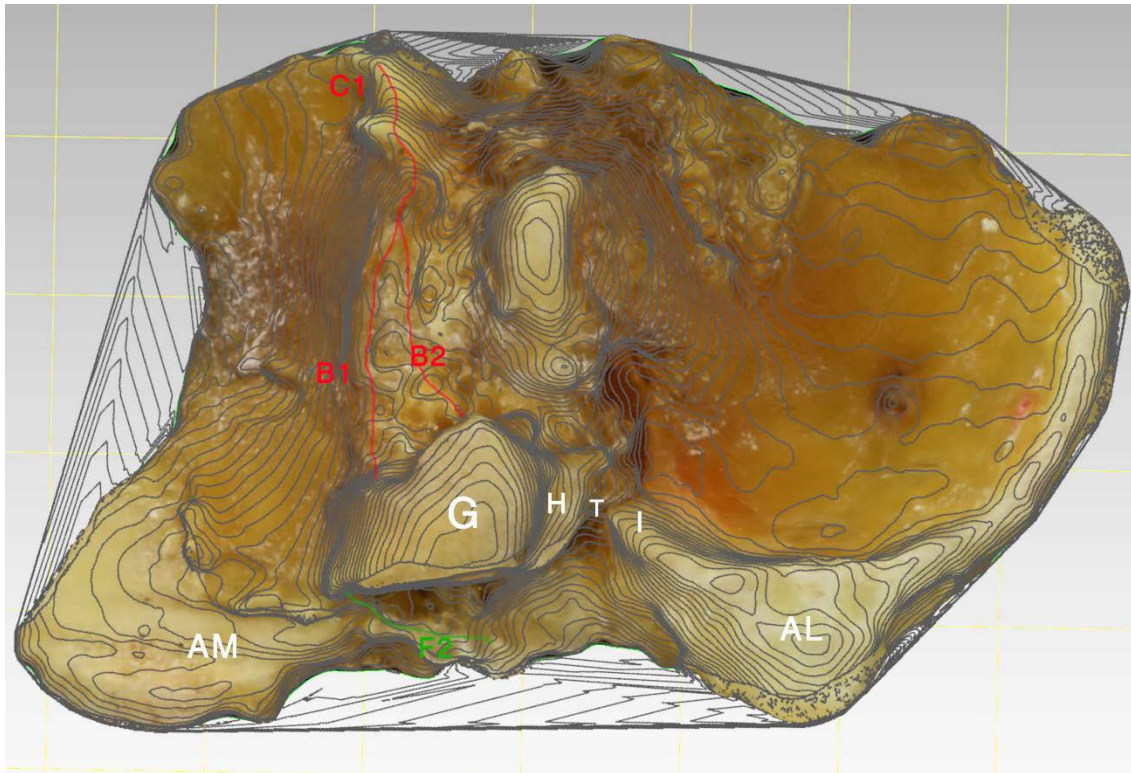


Figure 185. 3D model of tibia 75, with contour lines superimposed. Huge Parsons' tubercle (osteophyte grade 5) formed by over posterior AFIR (F1), and connected with the ACIK (H), anterior saddle (T), anterolateral knob (I), and anterolateral corner (AL) elevation. Also elevated are the AMIR (B1, B2) and the anteromedial corner (AM), connected with the medial aspect of the Parson's tubercle. Notice attrition on medial tubercle (AMIR and PMIR are elevated to roughly the same size as the MT summit) and posterior aspect of lateral tubercle.

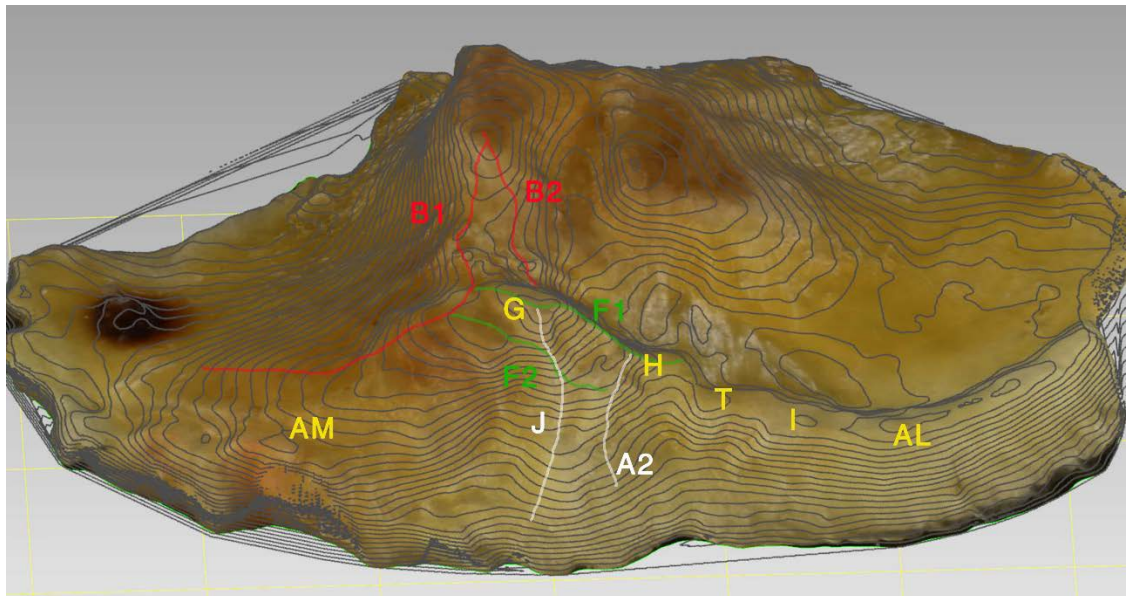


Figure 186. 3D model of tibia 62, with contour lines superimposed. Star-shaped Parsons' knob (G), formed by elevations in anterior (F1) and posterior AFIR processes (F2), AMIR (B1, B2) and anteromedial corner (AM). Anterocentral knob has a ridge-like appearance, connecting through the saddle (T) with the anterolateral knob (I) and the anterolateral corner (AL) elevations. Notice widening and attrition of both tubercles.

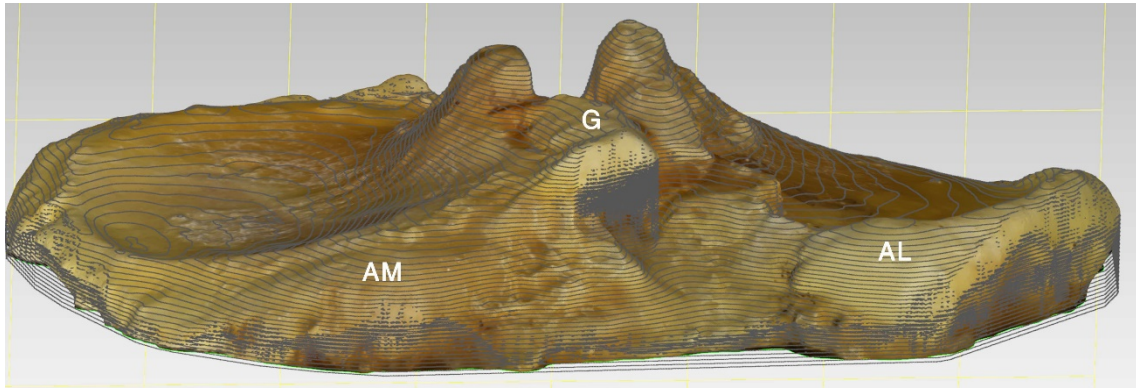


Figure 187. 3D model of tibia 50, with contour lines superimposed. Hook-shaped, deep Parsons' tubercle (G), osteophyte grade 5, formed by elevations of the AMIR (B1 and especially B2), and anteromedial corner (AM). AFIR processes are beneath the tubercle. Also elevated is the anterolateral corner (AL).

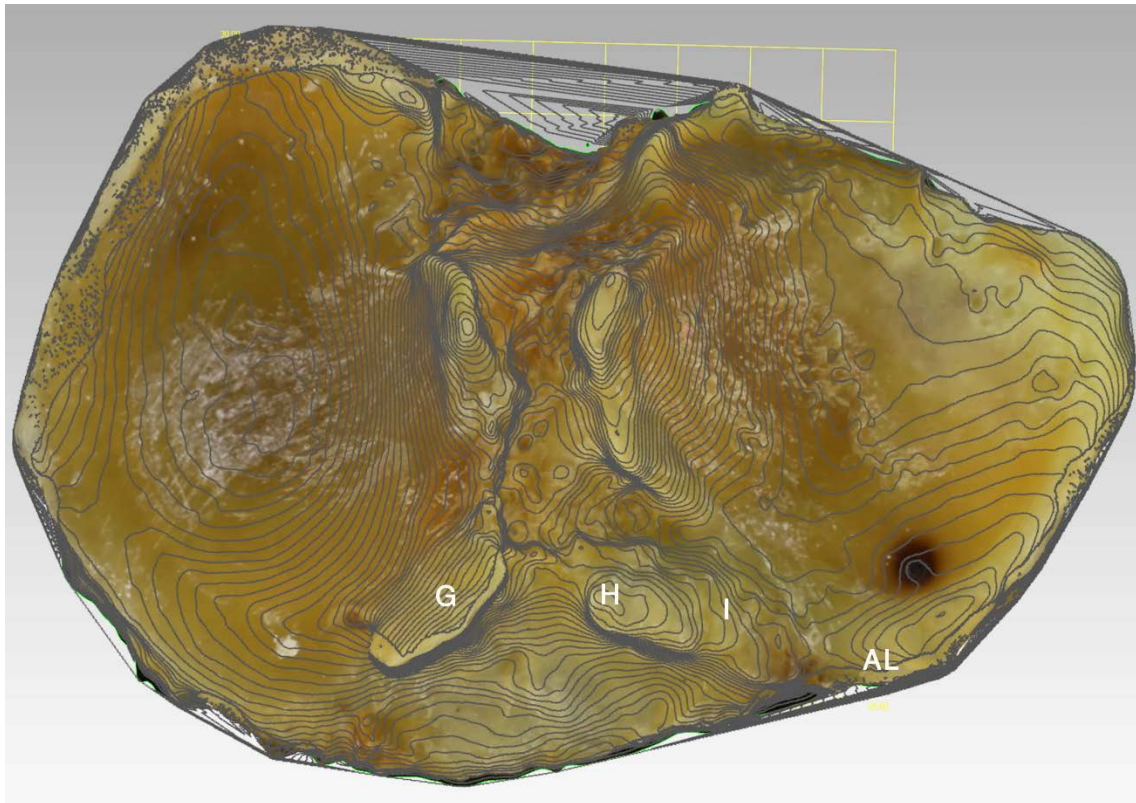


Figure 188. 3D model of tibia 61 with contour lines. Tongue-shaped Parsons' tubercle (G) formed mainly by the AMIR, the AFIR, and the anteromedial corner elevation. Cone-shaped anterocentral knob (H), in contact with anterolateral knob (I) and anterolateral corner (AL).

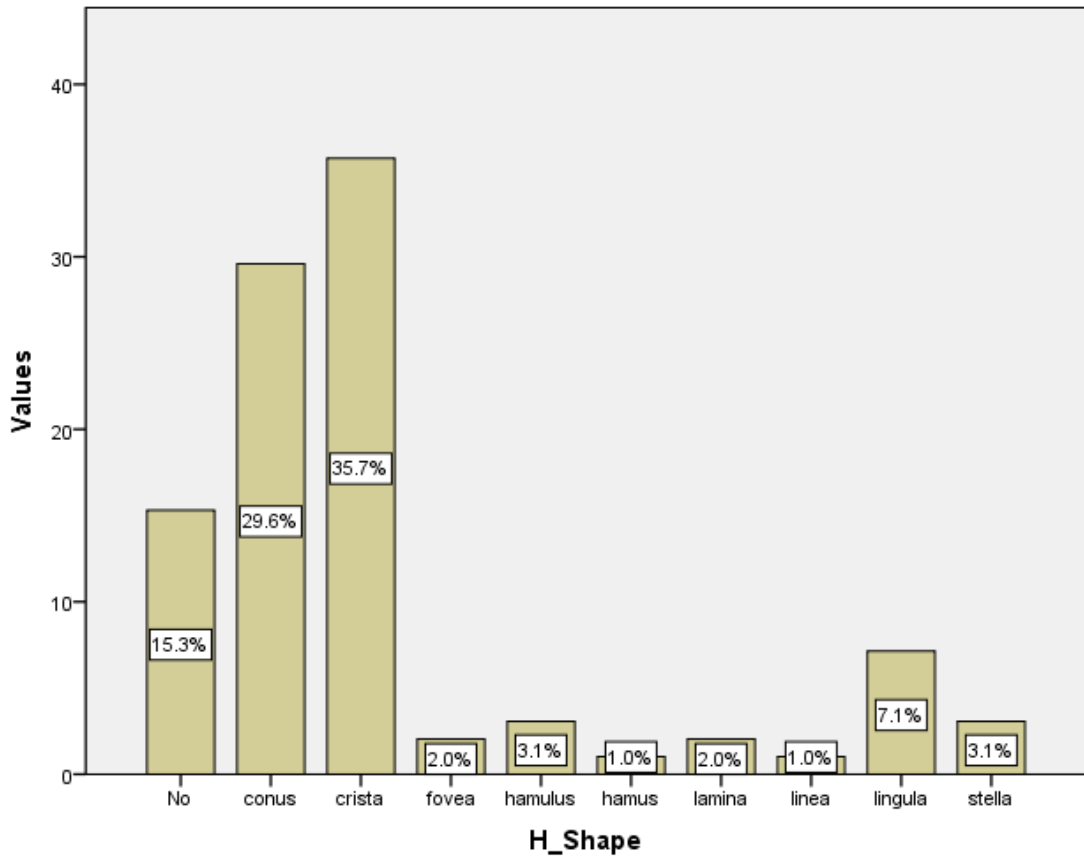


Figure 189. Histogram of number of tibias in each anterocentral knob's shape (*H_Shape*) category, in percentage.

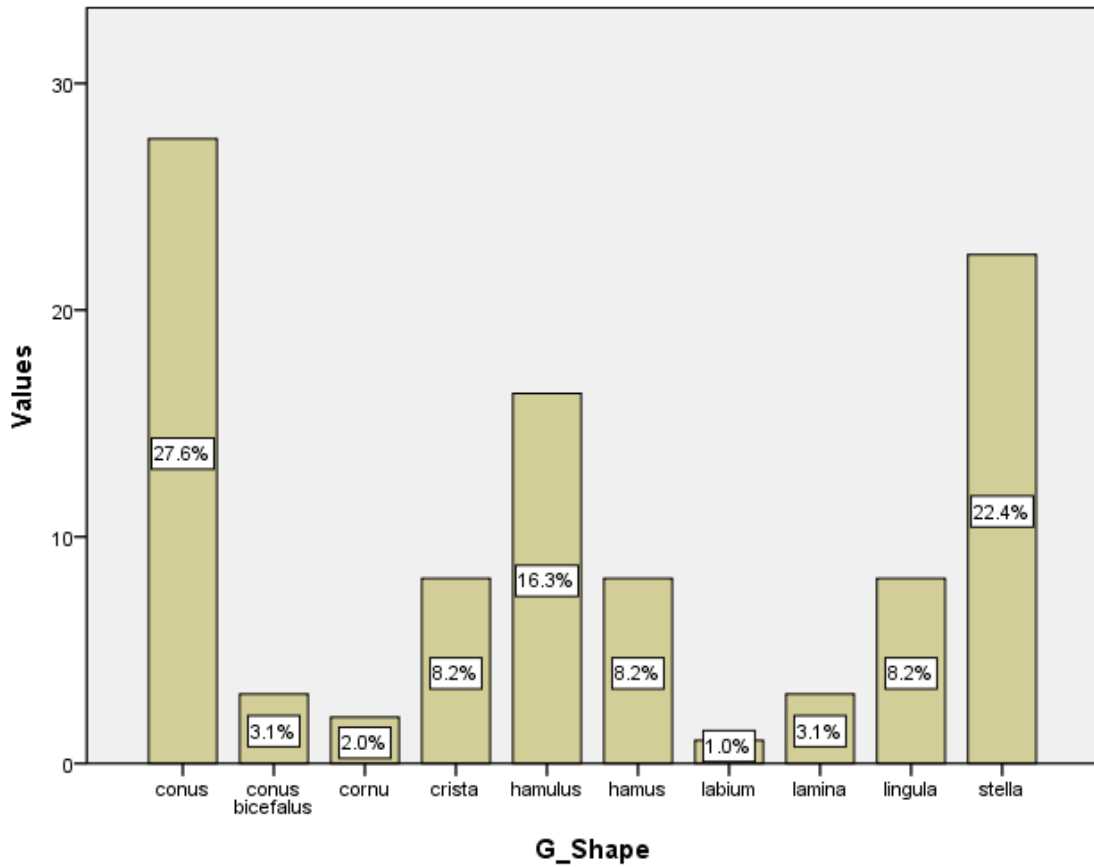


Figure 190. Histogram of number of tibias in each anteromedial knob's shape (*G_Shape*) category, in percentage.

IV.4.2.2. Anterior intercondylar ridge and anterocentral intercondylar knob

The posterior AFIR process showed a weak correlation with knee OA that did not reach statistical significance: F1 (Fig. 191), $r_s(98)=0.195$, $p=0.054$. The anterior AFIR process showed a significant positive correlation with knee OA, though: F2 (Fig. 192), $r_s(98)=0.334$, $p=0.001$. Their union into a single AFIR ridge, F, showed a non-significant association with knee OA (Fig. 193), $\chi^2(4)=9.058$, $p=0.060$.

The AFIR recess depression grade showed no significant correlation with knee OA (Fig. 194), $r_s(95)=0.089$, $p=0.391$.

The anterocentral intercondylar knob in donor specimens ($n=4$, Ahlbäck OA grades 0-3) showed a mean height of -0.1 mm (range, -1 mm to 0.8 mm) over the condylar plane, a mean area of 24.7 mm² (range, 19.6 mm² to 38.5 mm²), and a mean volume of 5.4 mm³ (range, -2 mm³ to 12.8 mm³).

Neither the ACIK osteophyte grade nor its shape showed a significant correlation with knee OA: H osteophyte grade, (Fig. 195), $r_s(95)=0.068$, $p=0.514$; H shape, (Fig. 196), $\chi^2(36)=24.291$, $p=0.931$.

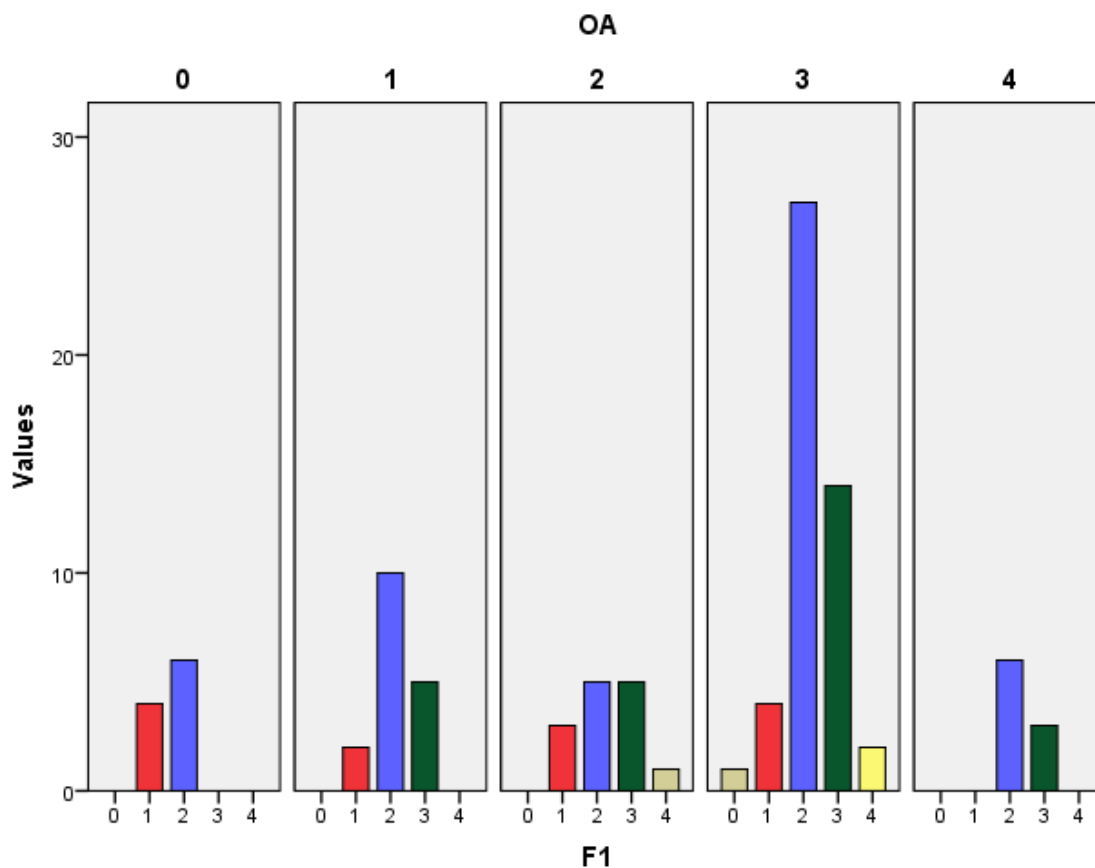


Figure 191. Study II. Histogram of posterior AFIR osteophyte grade: number of tibias in each osteophyte grade, grouped by Ahlbäck OA grade.

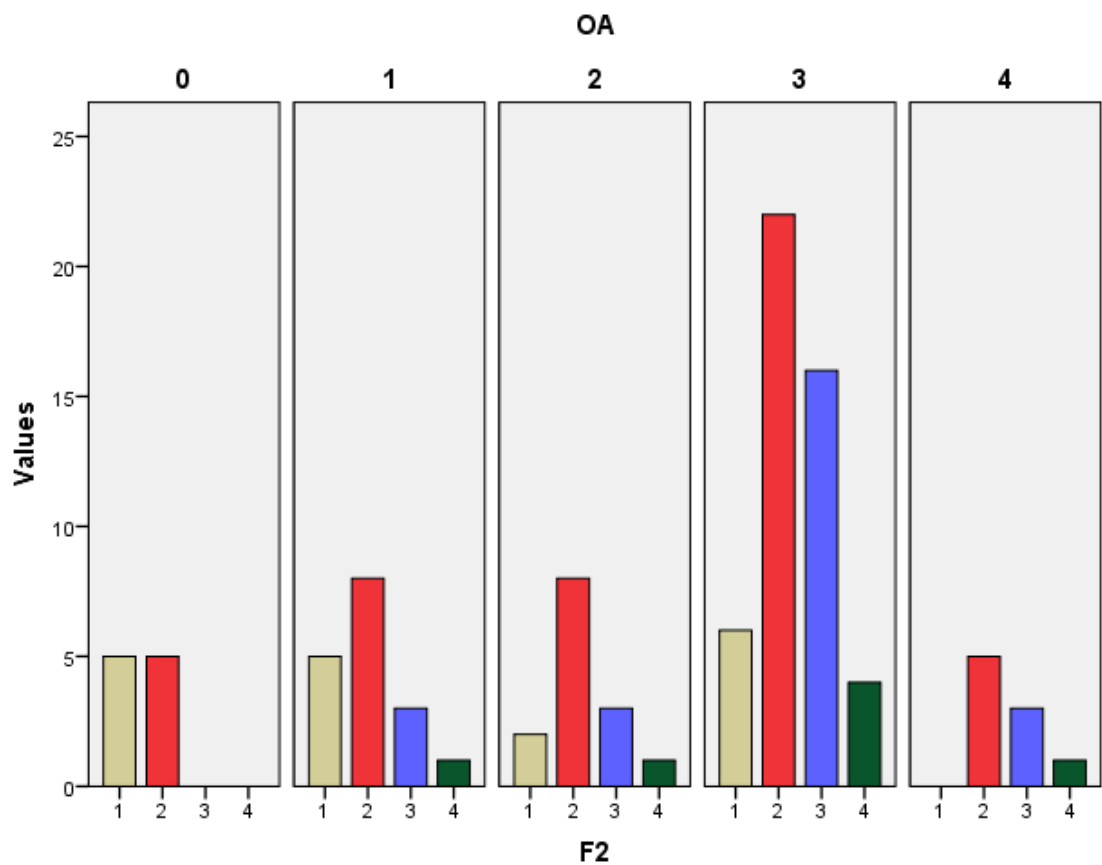


Figure 192. Study II. Histogram of anterior AFIR osteophyte grade: number of tibias in each osteophyte grade, grouped by Ahlbäck OA grade.

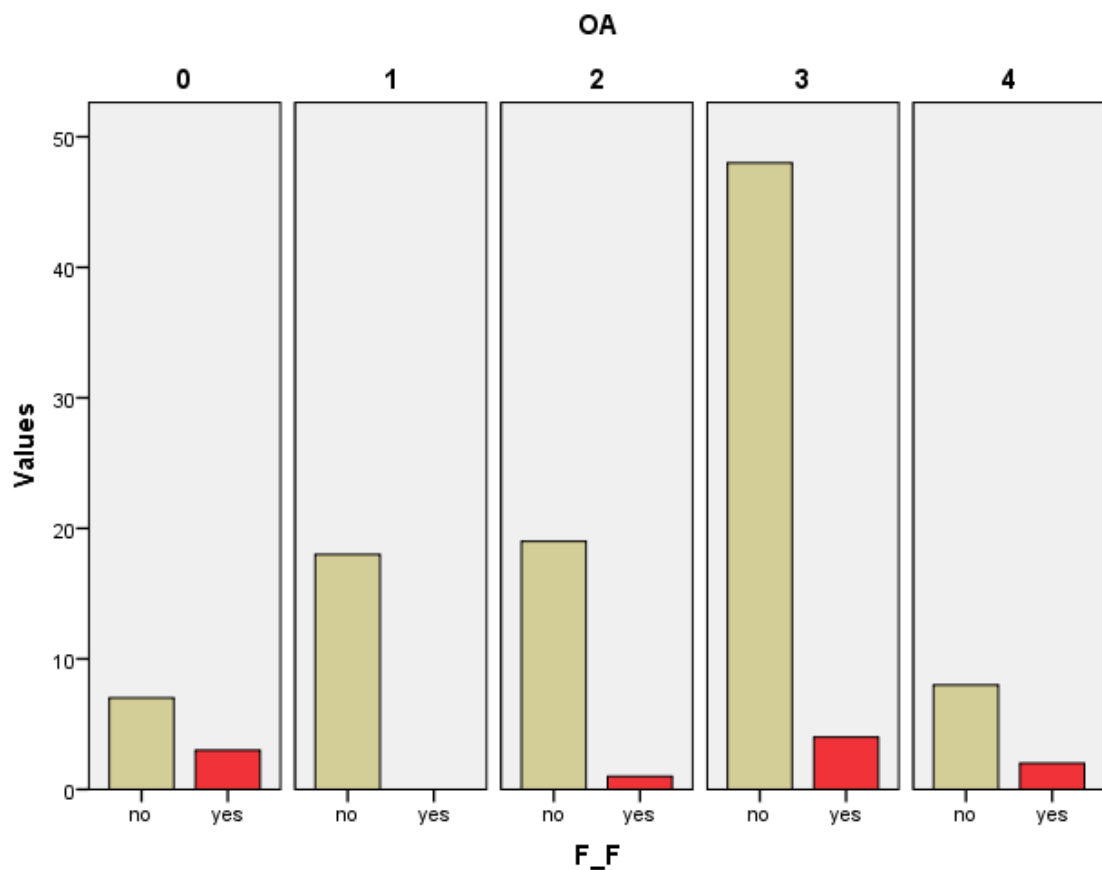


Figure 193. Study II. Histogram of joint anterior and posterior AFIR (F1-F2): number of tibias with joint AFIR, grouped by Ahlbäck OA grade.

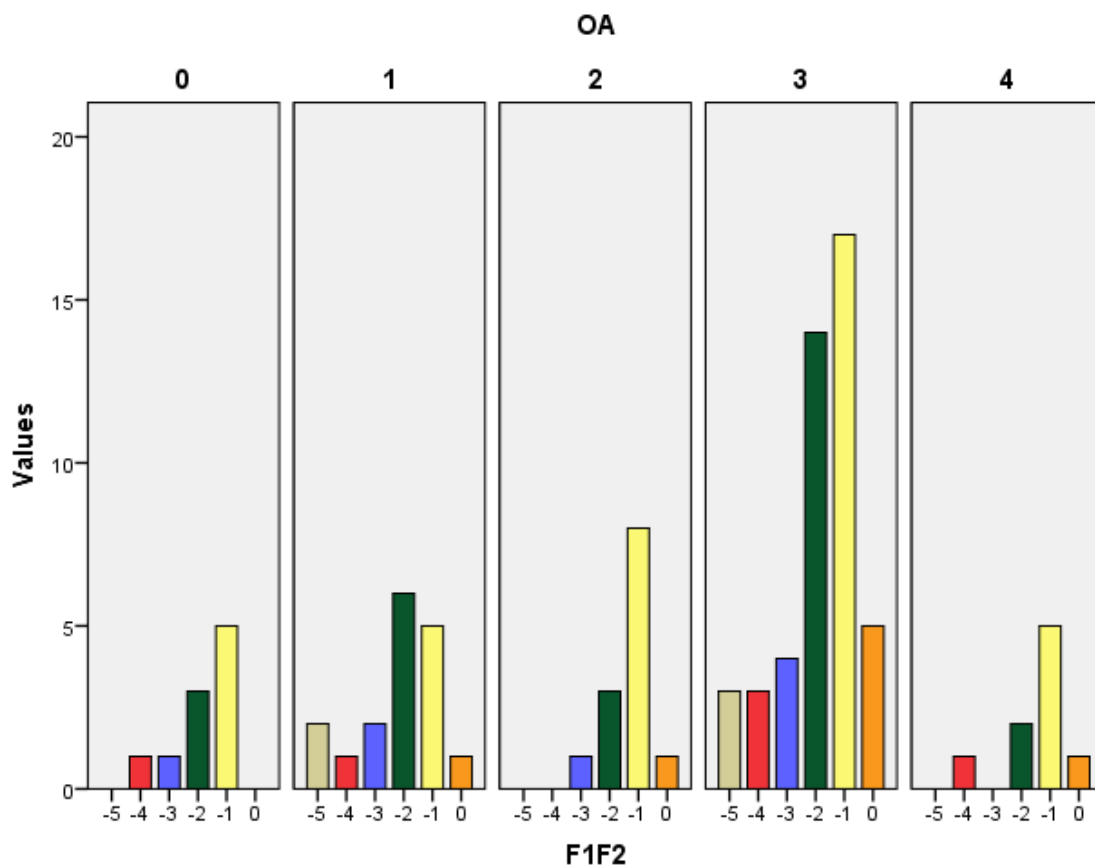


Figure 194. Study II. Histogram of AFIR recess grade (F1F2): number of tibias in each depression grade, grouped by Ahlbäck OA grade.

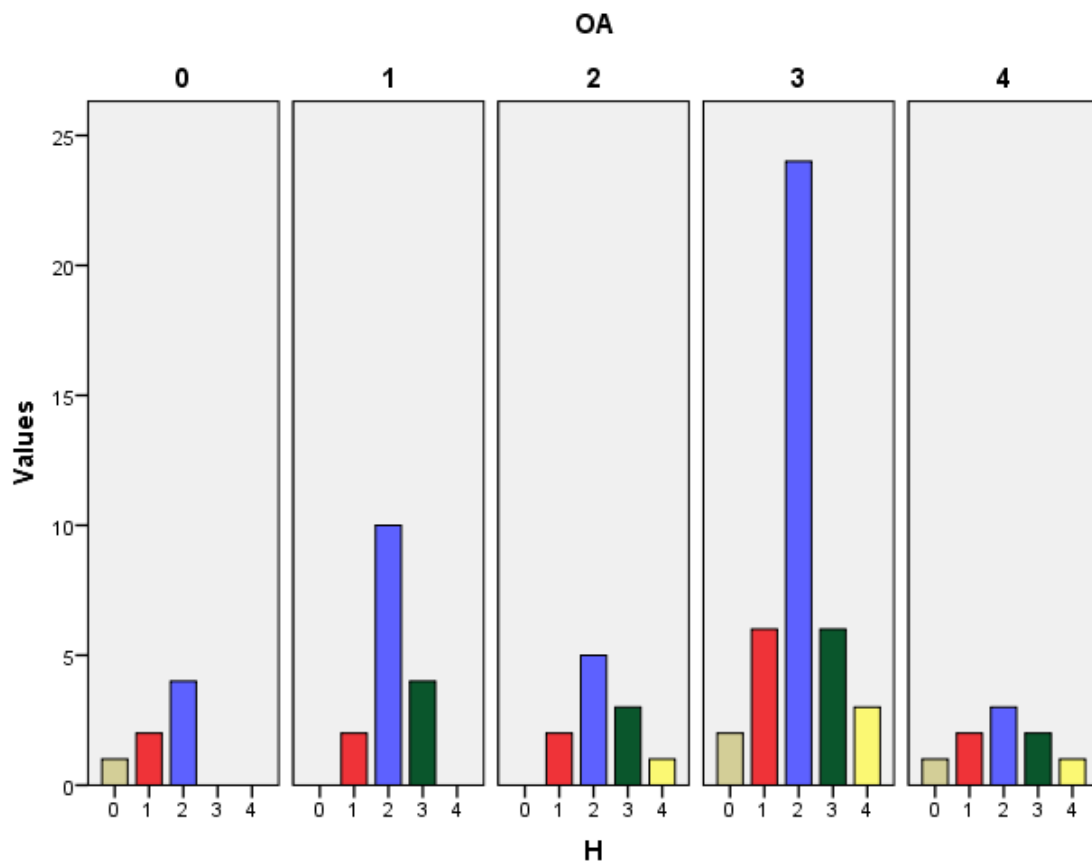


Figure 195. Study II. Histogram of anterocentral intercondylar knob (H) osteophyte grade: number of tibias in each osteophyte grade, grouped by Ahlbäck OA grade.

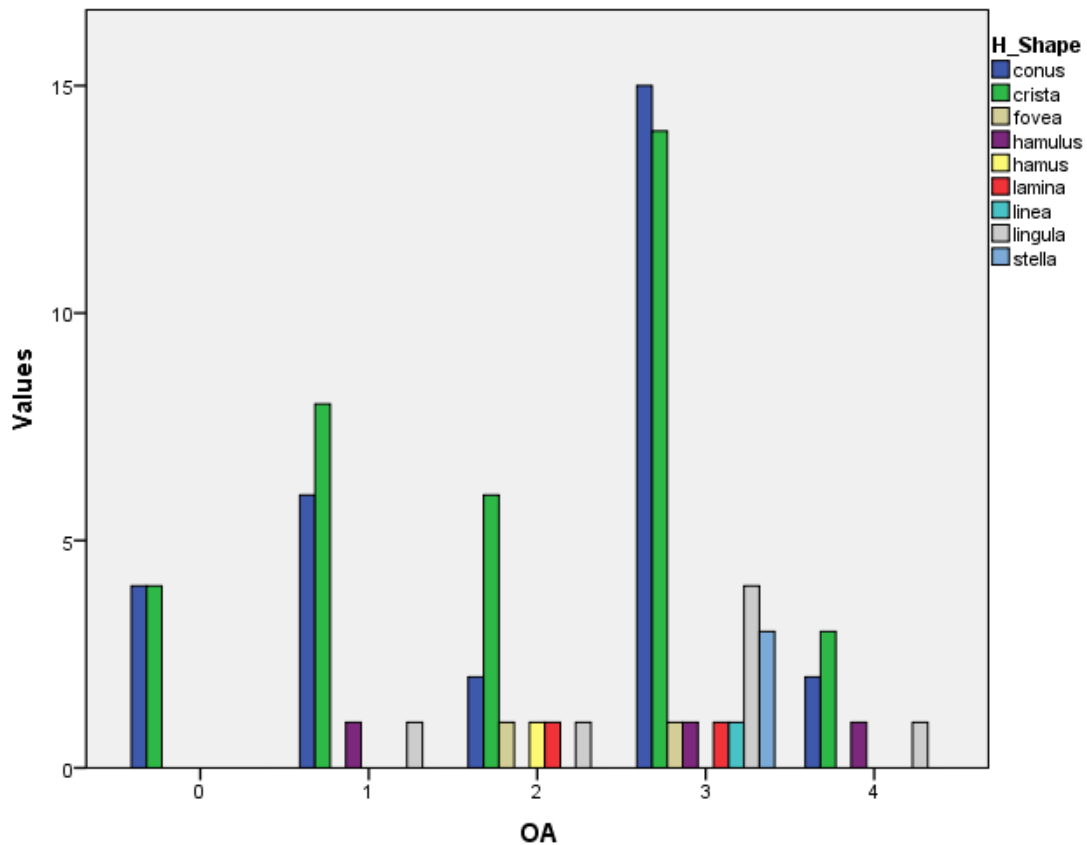


Figure 196. Study II. Histogram of ACIK shape (H_Shape): number of tibias with each knob shape, grouped by Ahlbäck OA grade.

IV.4.2.3. Parsons' knob

IV.4.2.3.1. Parsons' knob size, shape, forming structures, and attrition

The anteromedial knob in donor specimens (n=6, Ahlbäck OA grades 0-3) showed a mean height of 5 mm (range, 3.8 mm to 6.4 mm) over the condylar plane, a mean area of 78.6 mm² (range, 26.9 mm² to 132.5 mm²), and a mean volume of 64.4 mm³ (range, 9.1 mm³ to 130.3 mm³).

A Kruskal-Wallis H test showed that there was a statistically significant difference between knee OA and Parsons' knob size: AP depth (Fig. 197), $\chi^2(3)=8.311$, $p=0.040$; and ML width (Fig. 198), $\chi^2(3)=10.780$, $p=0.013$. The mean knob sizes obtained for the different Ahlbäck OA grade groups were as follows:

- 5 x 5.1 mm (95% CI, AP 2.9 – 8.1 mm, LAT 2.7–7.7 mm) for OA grade 1;
- 6.1 x 5.3 mm (95% CI, AP 3.9 – 8.4 mm, LAT 3.2–7.4 mm) for OA grade 2;
- 8.3 x 8.3 mm (95% CI, AP 7.2 – 9.3 mm, LAT 7.1–9.4 mm) for OA grade 3;
- 8.5 x 8.6 mm (95% CI, AP 5.8 – 11 mm, LAT 5.6–11.6 mm) for OA grade 4.

They were not found to be associated with age, though: AP depth, $r_s(96)=-0.006$, $p=0.952$; ML width, $r_s(96)=0.094$, $p=0.362$. A weak, positive correlation was found with tibiofemoral alignment, statistically significant with ML width: AP depth, $r_s(96)=0.186$, $p=0.069$; ML width, $r_s(96)=0.225$, $p=0.028$ (where positive value means varus alignment). Both measures were moderately associated with each other: $r_s(96)=0.696$, $p<0.001$.

The Parsons' knob osteophyte grade (Fig. 199) showed a statistically significant moderate positive correlation with knee OA (Fig. 200), $r_s(98)=0.442$, $p<0.001$; a weak correlation with age, $r_s(98)=0.333$, $p=0.001$; but not with varus, $r_s(84)=0.112$, $p=0.312$. Osteophyte grade showed a moderate association with measures of the knob taken over the specimen: AP depth, $r_s(84)=0.532$, $p<0.001$, ML width, $r_s(84)=0.538$, $p<0.001$.

The shape of the Parsons' knob was also strongly associated with knee OA (Fig. 201), $\chi^2(40)=67.440$, $p=0.004$ (Phi=0.783, Cramer's V=0.392). Analysis of the frequency distribution showed relatively more star-shaped knobs, and especially little hook- and hook-shaped knobs in higher OA grades, while ridge- and tongue-shaped knobs were more commonly seen in lower OA grades. The cone-type was the more evenly distributed shape among the 5 OA grades.

A wide variety of structures formed the Parsons' knob (Fig. 202), which also defined its exact position in the boundary of areas 10, 1c, and 5. Simplified to its two main forming structures, a significant strong association was found with knee OA (Fig. 203), $\chi^2(64)=92.704$, $p=0.011$ (Phi=0.973, Cramer's V=0.486). Frequency distribution analysis showed that Parsons' knob formed by 1c (as the main or secondary formant) was more frequent in higher OA grades, while B as main formant, and especially F as secondary, were more common with lower OA grades.

The Parsons' knob main forming structure also showed a significant association with MAC (Fig. 204), $\chi^2(12)=21.511$, $p=0.043$ (Phi=0.481, Cramer's V=0.278); and with MACOp (Fig. 205), $\chi^2(16)=34.679$, $p=0.004$ (Phi=0.595, Cramer's V=0.297).

Parsons' knob attrition direction (Fig. 206) showed no statistically significant association with OA type, $\chi^2(40)=98.420$, $p=0.210$, and neither did simplified attrition direction with OA type (Fig. 207), $\chi^2(40)=25.942$, $p=0.766$.

Simplified attrition direction did not show a significant association with condyle attrition areas: with MAC (Fig. 208), $\chi^2(24)=26.626$, $p=0.322$ (Phi=0.535, Cramer's V=0.309); but it showed a significant, strong association with MACOp (Fig. 209), $\chi^2(120)=304.965$, $p<0.001$ (Phi=1.650, Cramer's V=0.583). Frequency distribution analysis for MAC showed that 1M was associated mainly with A and AL attrition direction; 2M was associated mainly with AM direction; 3M mainly with AL, A, L, and PL directions; and 4M mainly with A and AM attrition directions.

No association was found between ACL pathology and osteophyte grade, $\chi^2(15)=7.012$, $p=0.957$; nor with simplified attrition direction, $\chi^2(24)=16.536$, $p=0.868$ (Phi=0.411, Cramer's V=0.237).

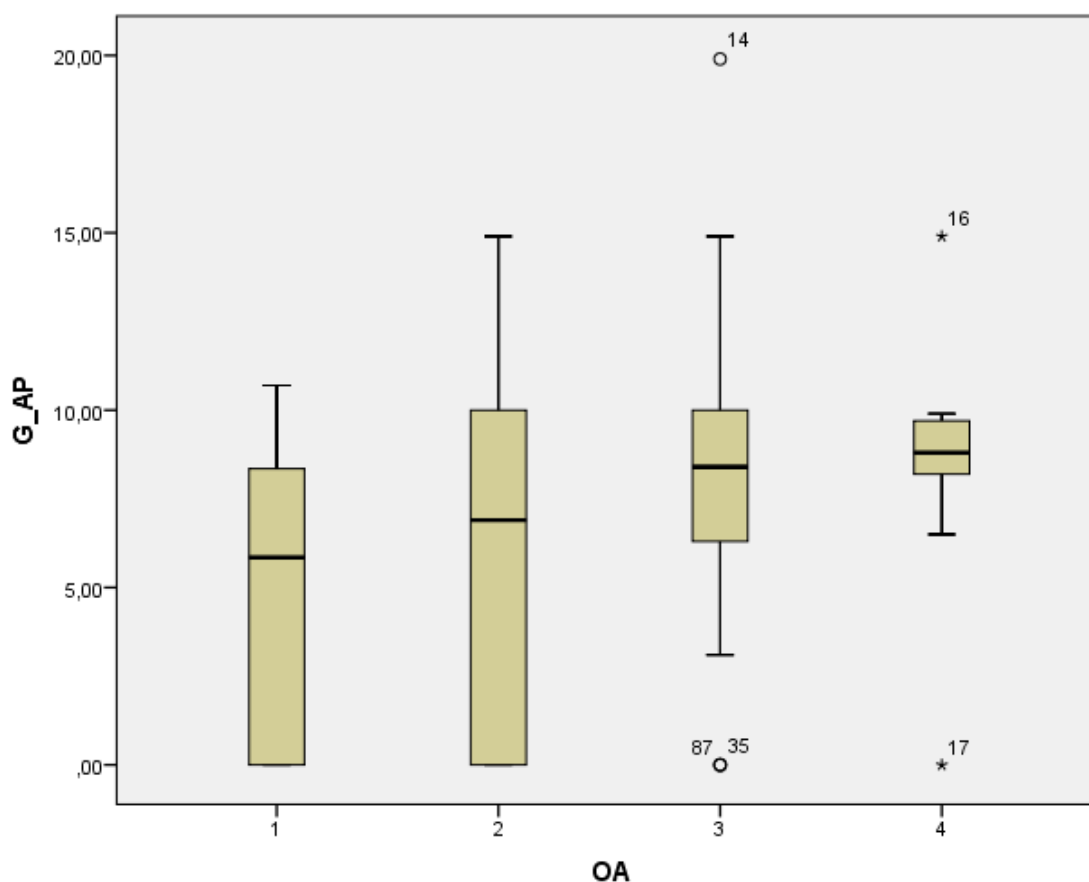


Figure 197. Study II. Box-and-whisker plot of Parsons' knob AP size (G_AP) distribution in each Ahlbäck OA grade.

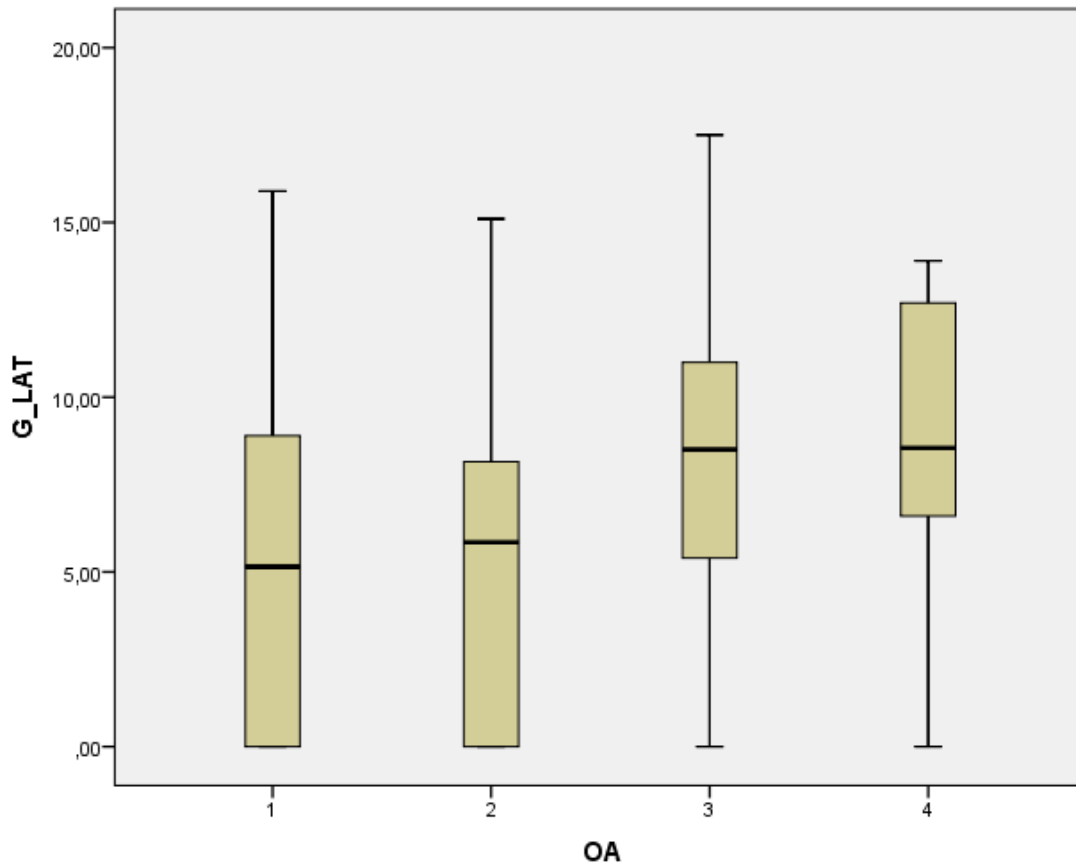


Figure 198. Study II. Box-and-whisker plot of Parsons' knob mediolateral size (G_LAT) distribution in each Ahlbäck OA grade.

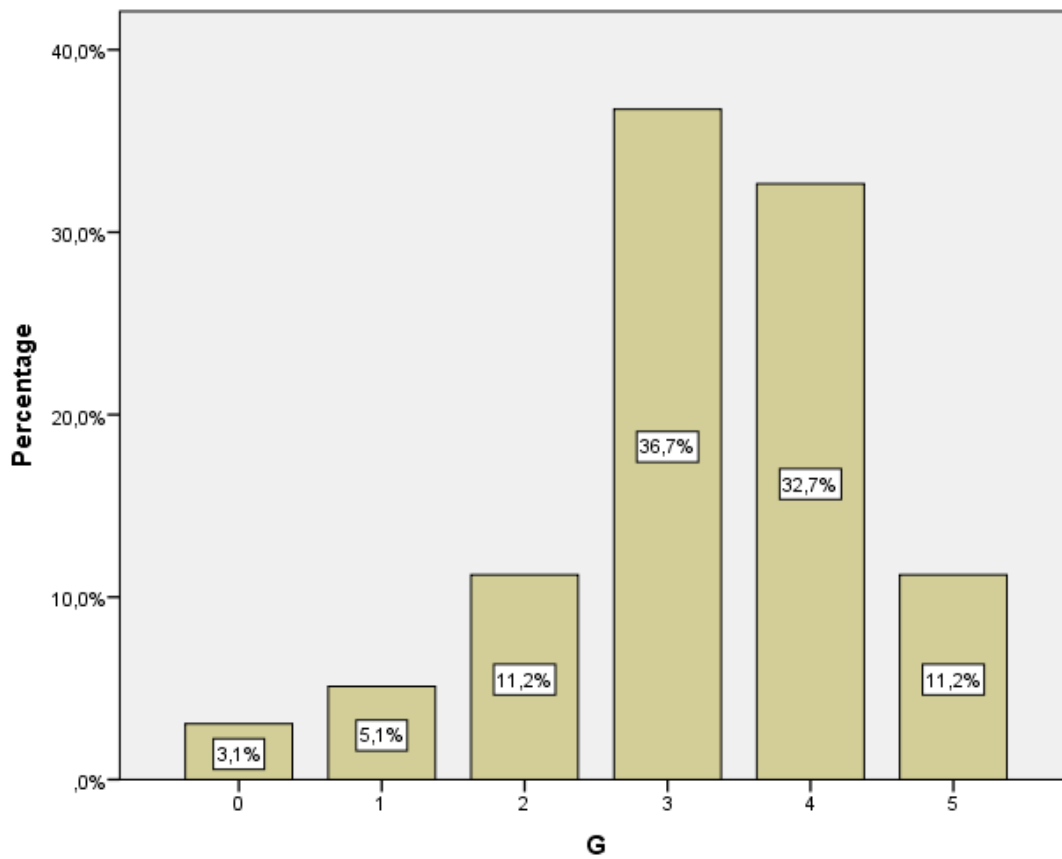


Figure 199. Study II. Histogram of tibias classified into Parsons' knob (G) size groups, in percentage.

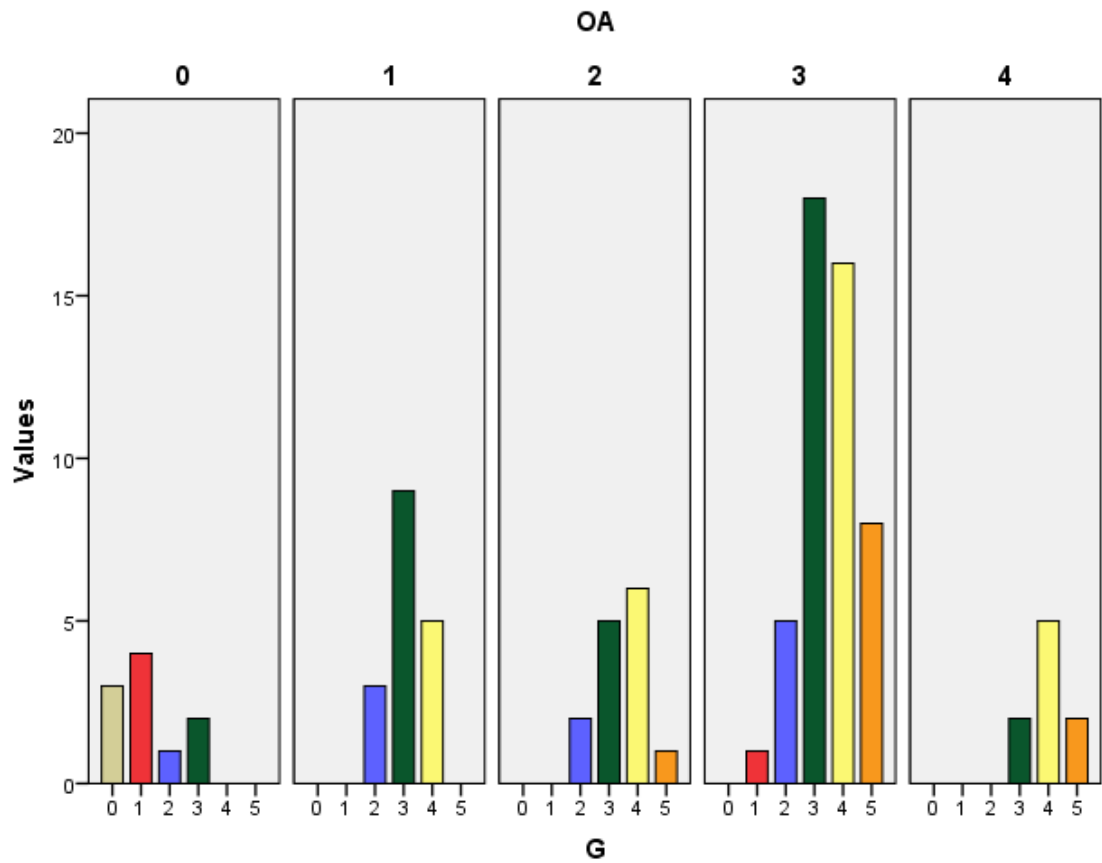


Figure 200. Study II. Histogram of Parsons' knob (G) osteophyte grade: number of tibias in each osteophyte grade, grouped by Ahlbäck OA grade.

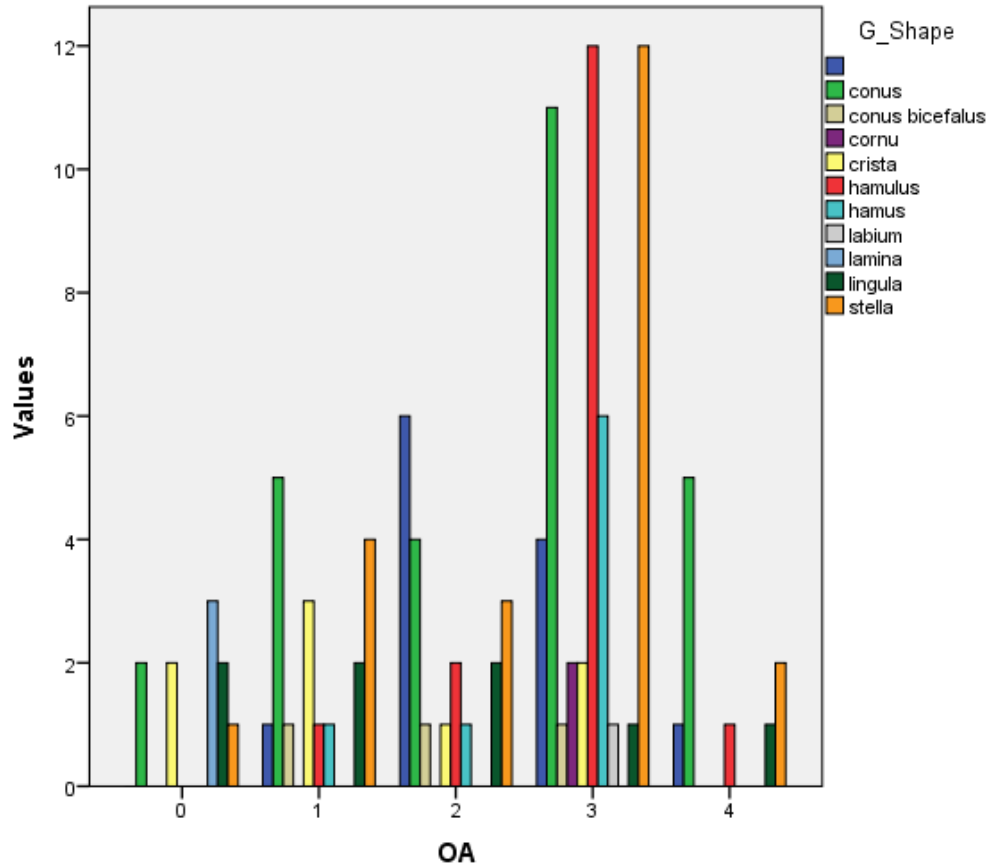


Figure 201. Study II. Histogram of Parsons' knob shape (G_Shape): number of tibias in each category, grouped by Ahlbäck OA grade.

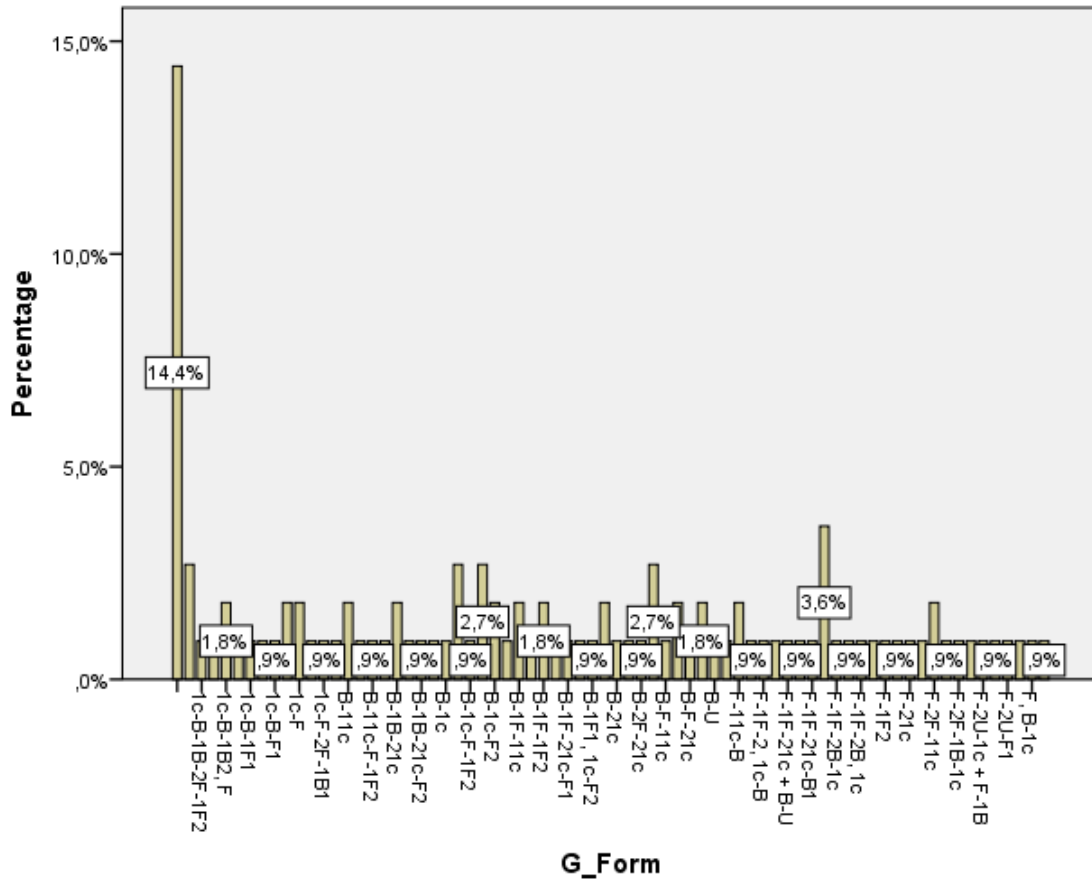


Figure 202. Study II. Histogram of percentage of tibias classified according to the forming structures of their Parsons' osteophyte (G_Form).

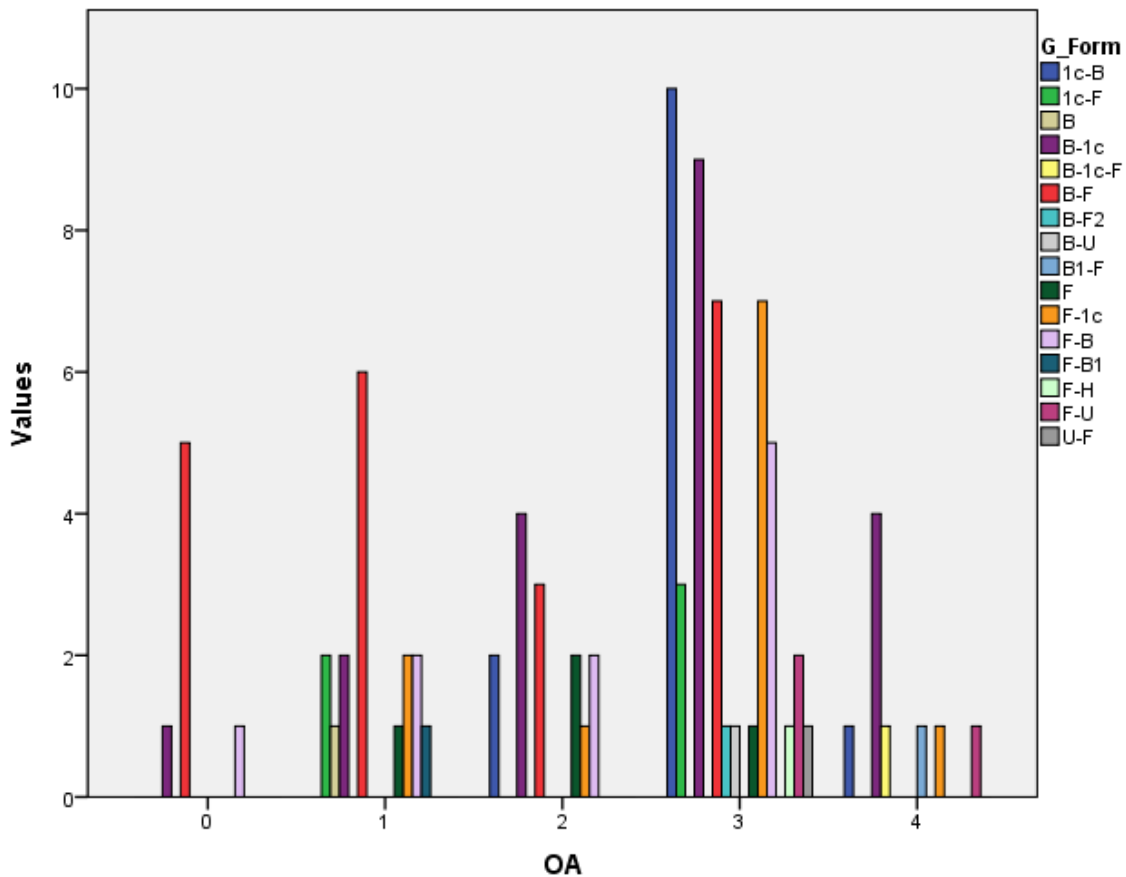


Figure 203. Study II. Histogram of the two main forming structures of the Parsons' knob (G_Form): number of tibias in each category, grouped by Ahlbäck OA grade.

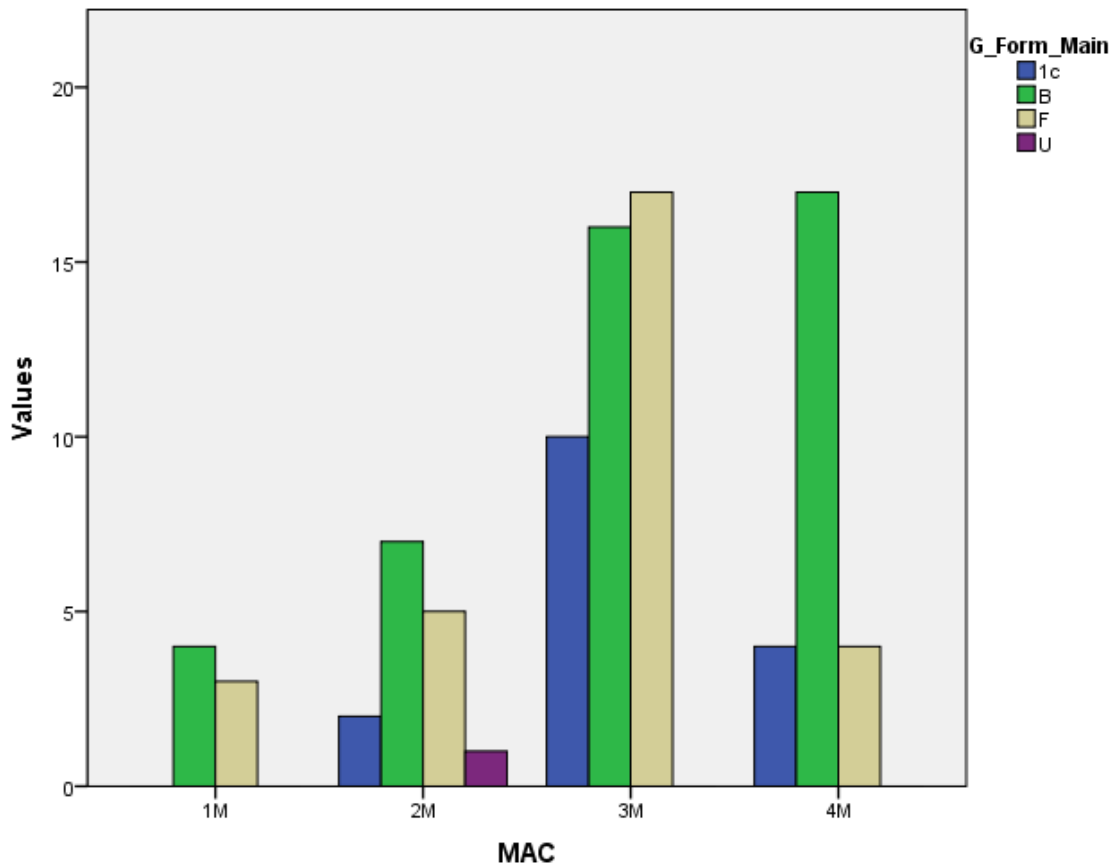


Figure 204. Study II. Histogram of the main forming structure of the Parsons' knob (*G_Form_Main*): number of tibias in each category, grouped by MAC.

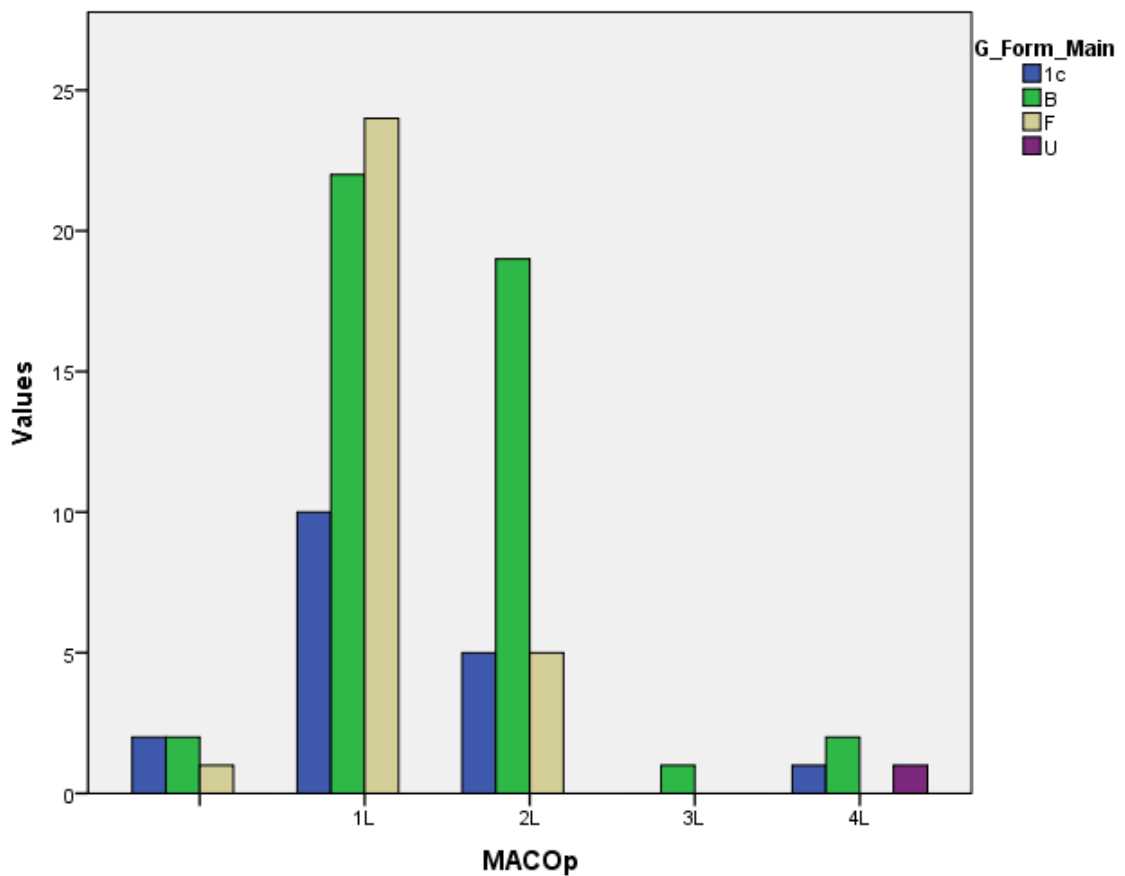


Figure 205. Study II. Histogram of the main forming structure of the Parsons' knob (*G_Form_Main*): number of tibias in each category, grouped by MACOp.

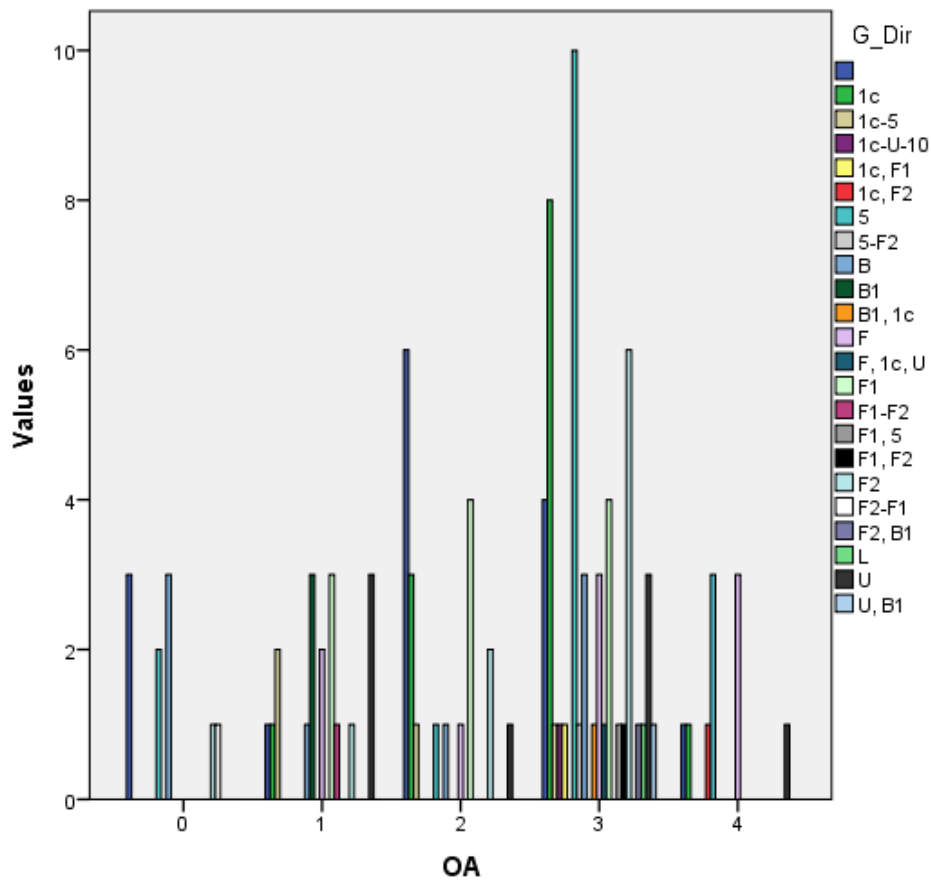


Figure 206. Study II. Histogram of the attrition direction of the Parsons' knob (G_Dir): number of tibias in each category, grouped by Ahlbäck OA grade.

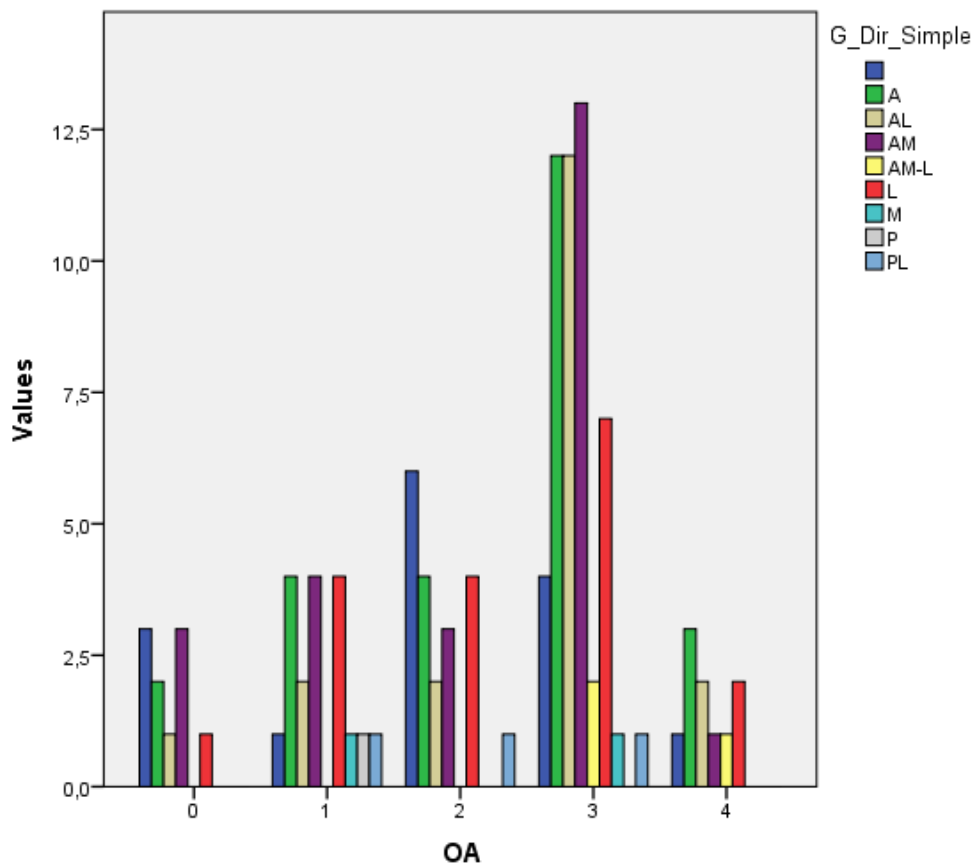


Figure 207. Study II. Histogram of the simplified attrition direction of the Parsons' knob (G_Dir_Simple): number of tibias in each category, grouped by Ahlbäck OA grade. A=anterior, P=posterior, M=medial, L=lateral.

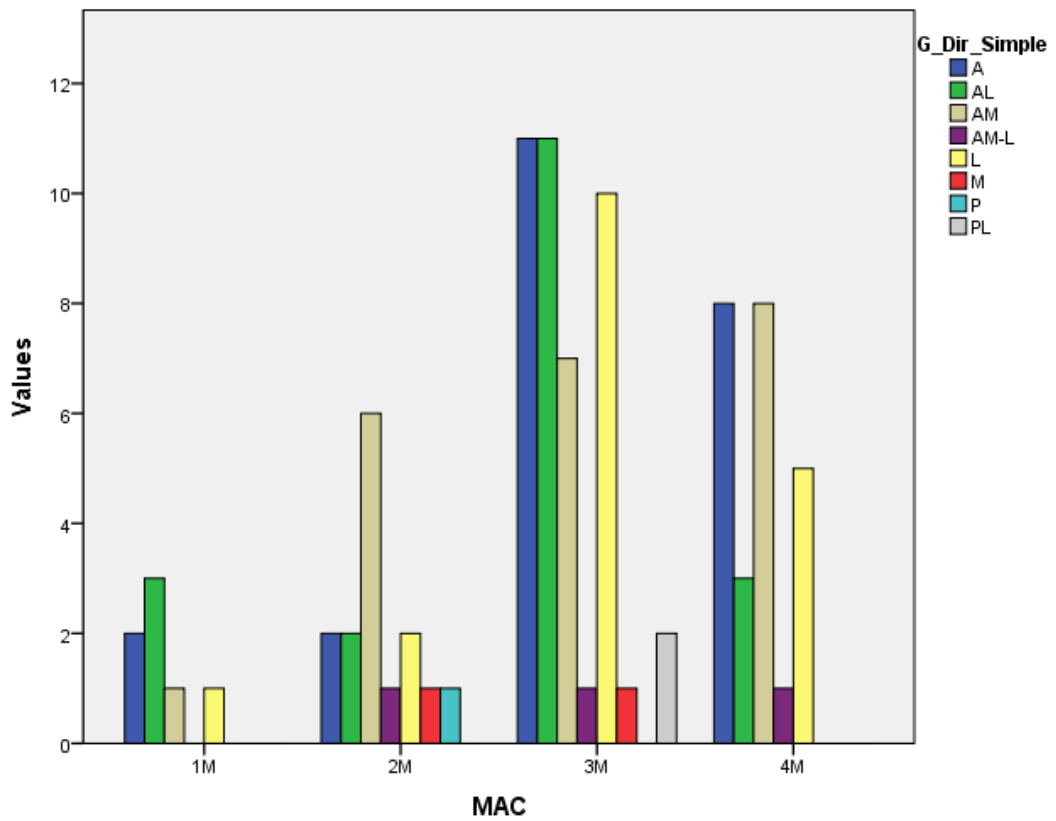


Figure 208. Study II. Histogram of the simplified attrition direction of the Parsons' knob (*G_Dir_Simple*): number of tibias in each category, grouped by MAC. A=anterior, P=posterior, M=medial, L=lateral.

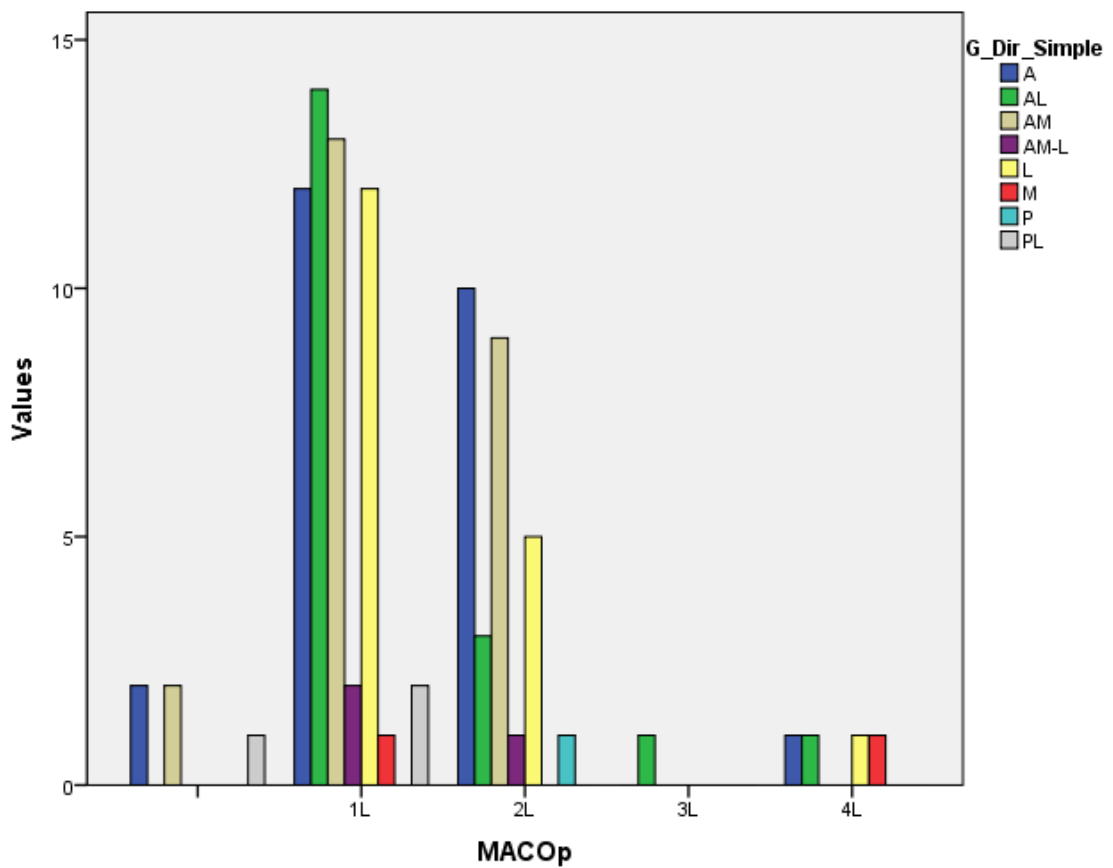


Figure 209. Study II. Histogram of the simplified attrition direction of the Parsons' knob (*G_Dir_Simple*): number of tibias in each category, grouped by MACOp. MACOp values not labelled represent medial MACOps (1M, 2M, 3M, or 4M)

IV.4.2.3.2. Anteromedial and posterior condylar corner osteophytes in X-ray studies

Anteroposterior and lateral radiographs were observed to assess relative tubercle height (Fig. 210, Fig. 212).

Radiographic density in the inferosuperior view did not show a significant correlation between the anteromedial aspect of the intercondylar area (including the AM corner and Parsons' knob) and knee OA (Fig. 213), $r_s(98)=0.108$, $p=0.316$.

In the lateral radiograph, the relative size of Parsons' knob, PM, and PL corners with respect to the main intercondylar tubercles showed a non-significant association with knee OA (Fig. 214): $\chi^2(36)=47.199$, $p=0.100$ (Phi=0.655; Cramer's $V=0.328$). Analysis of frequency distribution showed that Parsons' knob, PM, and PL corner osteophytes grew to the same height or higher than the main tubercles with higher OA grades.

There was only one case of Parsons' knob deeper than both tubercles in the lateral radiograph, and it corresponded to a knee OA grade 3 (Fig. 211).

The position of the Parsons' osteophyte with respect to the tubercles in the AP radiographic view showed no significant association with knee OA (Fig. 215), $\chi^2(4)=4.785$, $p=0.310$ (Phi=0.209; Cramer's $V=0.209$). A weak trend towards a central position of the Parsons' knob is seen in higher OA grades graphically.

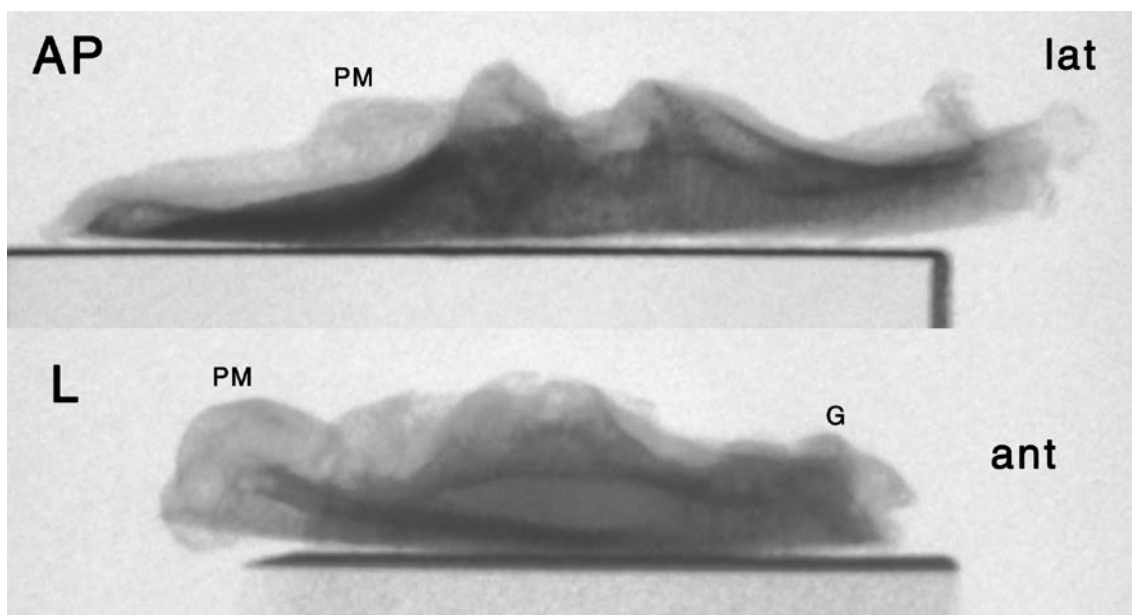


Figure 210. AP and lateral (L) fluoroscopic views of tibia 31 (see corresponding knee radiographs in Figure 143, and 3D model in Figure 144). PM: posteromedial corner osteophyte. G: Parson's knob.

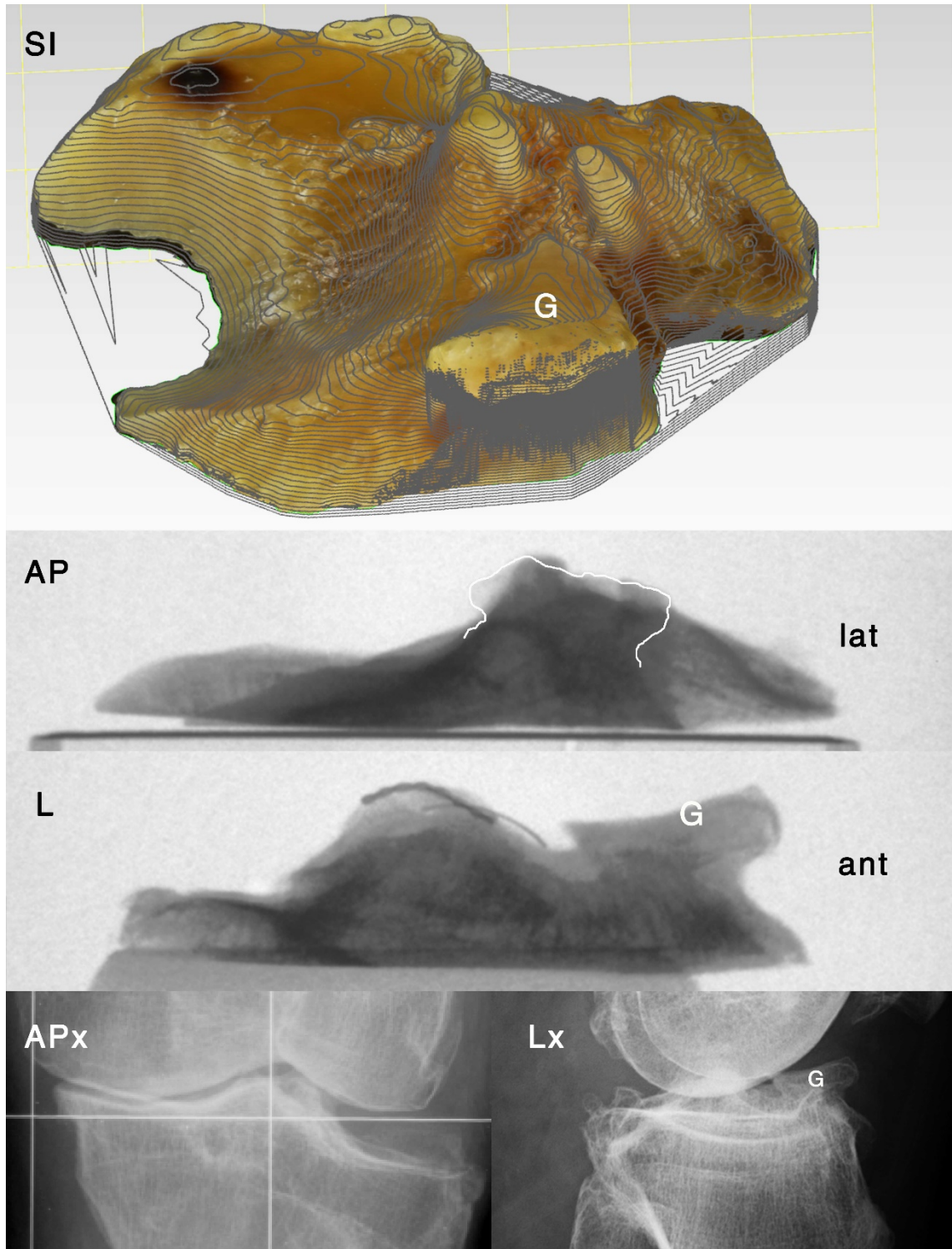


Figure 211. Tibia 70. 3D model with contour lines (SI), AP and lateral (L) fluoroscopic views, standing AP radiograph (APx) and lateral knee radiograph (Lx). Observe Parsons' tubercle (G), located between MT and LT in the AP views (white line surrounding it in the AP fluoroscopic view), deeper than MT and LT in the lateral views. It seems to have been formed over the AFIR. In the lateral fluoroscopic view, metal wires are attached to both tubercles, with the thicker one over the MT.

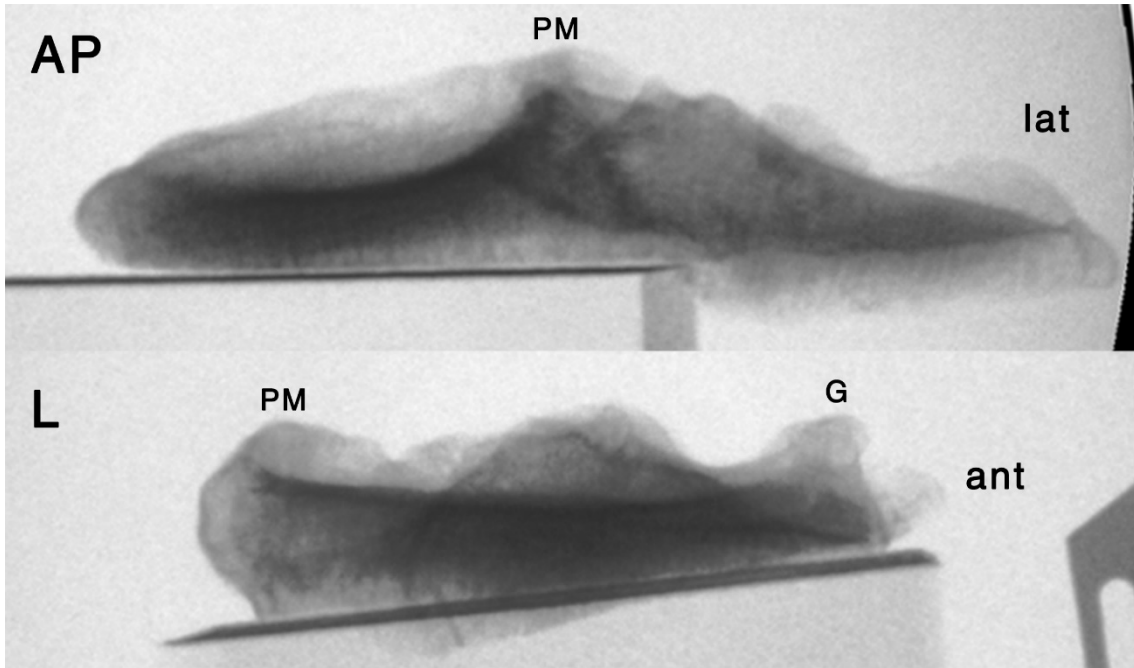


Figure 212. AP and lateral (L) fluoroscopic views of tibia H (see corresponding 3D model in Figure 141). Because of the posteriorly oriented cut, the AP view shows a more elevated medial rim and posteromedial corner (PM). The lateral view has been corrected by taking the condylar axis as the approximate horizontal axis of the image. G: Parsons' tubercle.

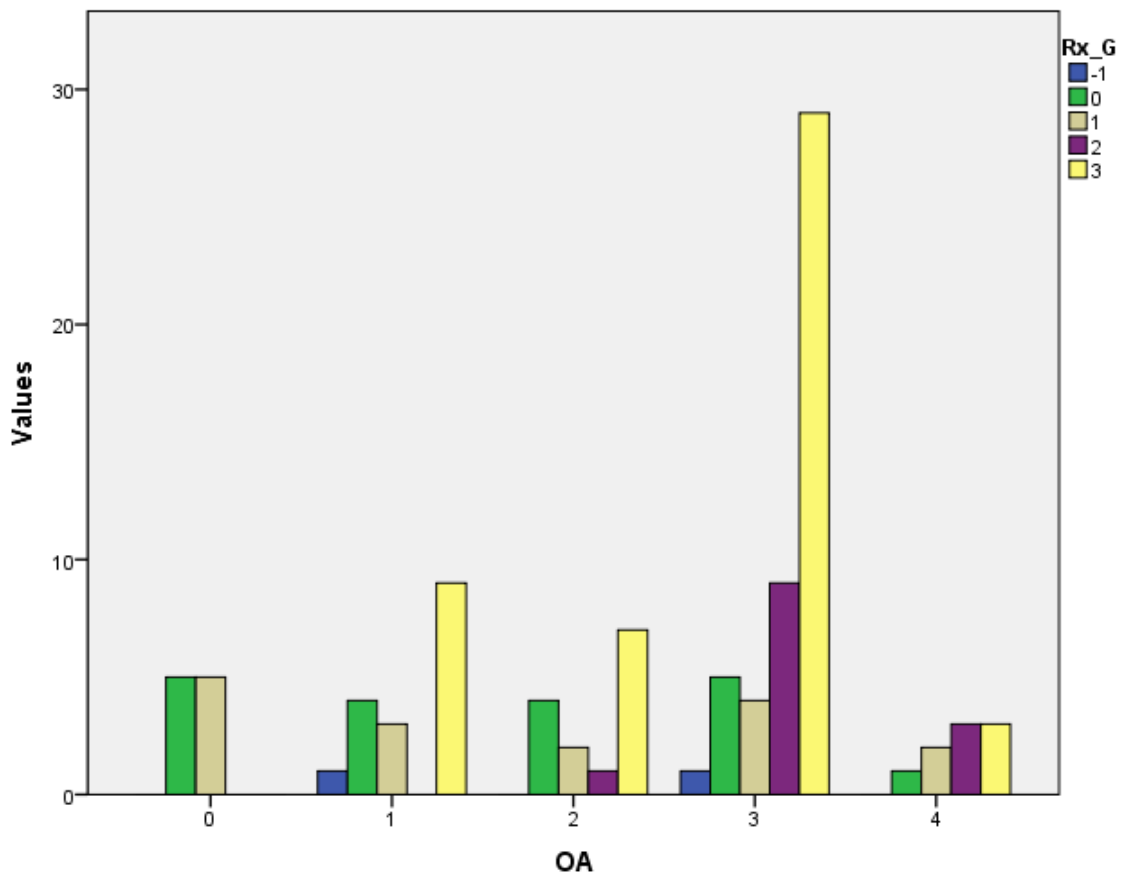


Figure 213. Study II. Histogram of the radiographic density of the Parsons' knob in inferosuperior radiograph (Rx_G): number of tibias in each category, grouped by Ahlbäck OA.

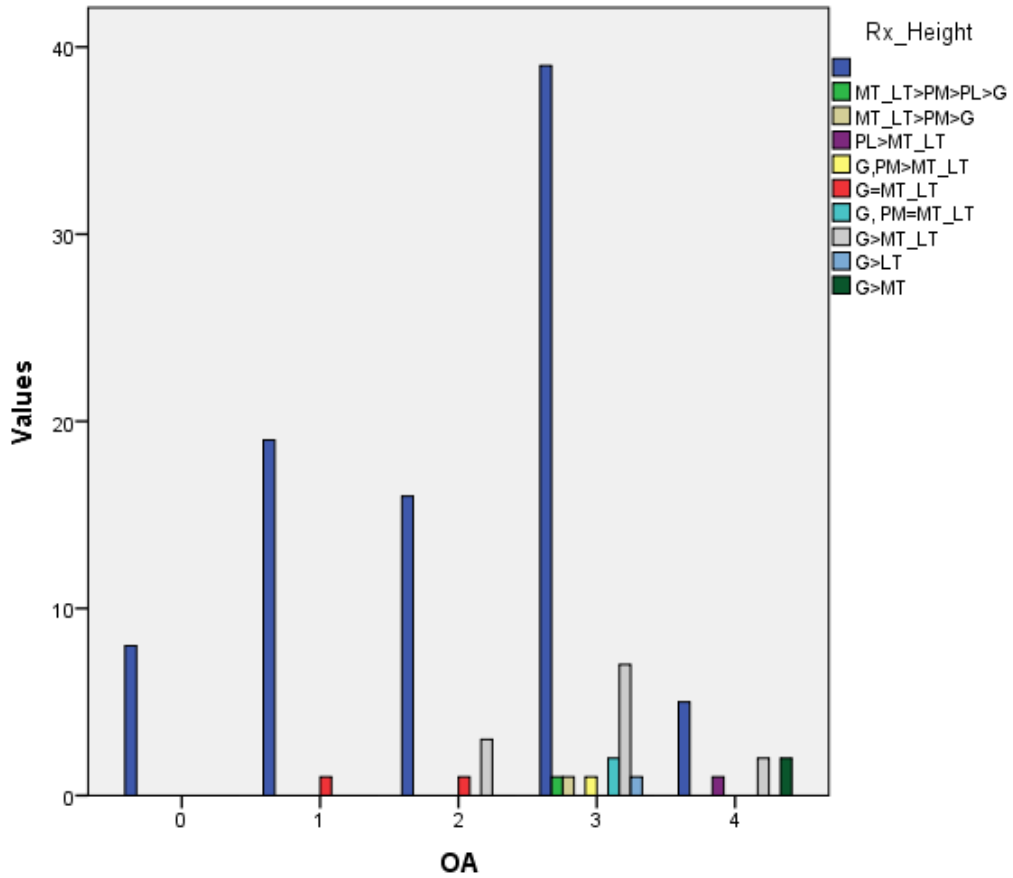


Figure 214. Study II. Histogram of the relative height of the Parsons' tubercle with respect to MT, LT, AM, and AL corner osteophytes in the lateral radiograph (Rx_Height): number of tibias in each category, grouped by Ahlbäck OA. TM

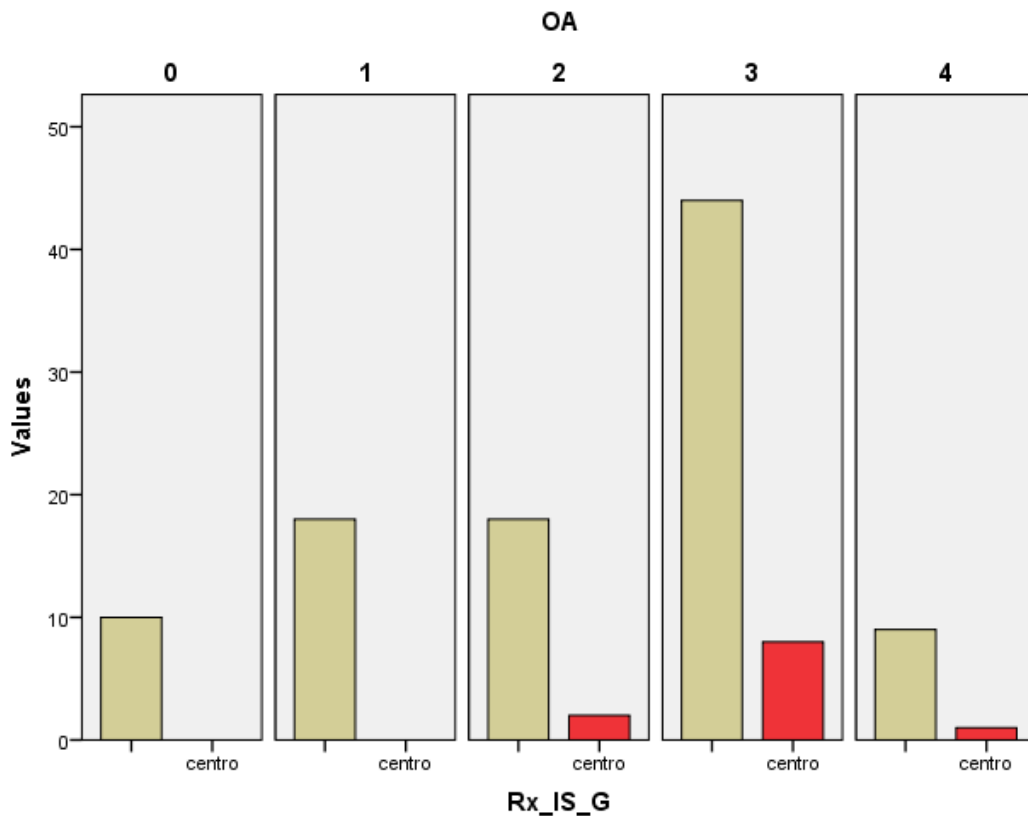


Figure 215. Study II. Histogram of the position of the Parsons' tubercle in AP radiograph, with respect to the anterior intercondylar staircase (Rx_IS_G): number of tibias in in center vs. medial categories, grouped by Ahlbäck OA.

IV.4.3. Parsons' knob in imaging studies of the knee

IV.4.3.1. Parson's knob: comparison of MRI and X-ray studies

Results for Study X, of 158 knees, showed that the mean age of selected patients was 42.4 years (range, 10 to 76 years), at the time of the last imaging study, 52% were males, and 56% were left knees.

48% had a distinguishable Parsons' knob; 85% had MT>LT, 14% had LT>MT, and 1% had MT=LT; 77% were classified as Ahlbäck OA grade 0, 17% OA grade 1, 5% OA grade 2, and 1% was OA grade 3. Diagnosis in MRI studies was classified in simplified pathology groups, with percentages shown in Fig. 216. A case of congenital absence of ACL was found in the sample (Fig. 224).

Percentage of the ML proximal tibial width (measured in the AP radiograph) showed a mean height for the MT of $12.1 \pm 0.3\%$ of the ML width (range, 6.4% to 17.9%), and a LT mean height of $10.7 \pm 0.3\%$ of the ML width (range, 7.0% to 16.1%). Their difference had an average of $1.4 \pm 0.2\%$ (range -3% to 5.7%, where positive value indicates MT > LT) of the radiographic ML width.

No significant association was found between pathology groups and the relative MT–LT size (Fig. 217): $\chi^2(18)=23.079$, $p=0.188$.

A Kruskal-Wallis H test showed that there was a statistically significant difference between Ahlbäck OA grade groups in terms of Parsons' knob size measured on MRI (Fig. 218): knob base, $\chi^2(3)=10.563$, $p=0.014$; height, $\chi^2(3)=10.862$, $p=0.012$; and area, $\chi^2(3)=9.802$, $p=0.020$. It showed means of Parsons' knob size (base x height = area) distributed by knee OA grade groups as follows:

- 2.9 mm x 1.5 mm = 10.2 mm² for OA grade 0,
- 3.1 mm x 1.6 mm = 12.1 mm² for OA grade 1,
- 6.7 mm x 3.5 mm = 23.9 mm² for OA grade 2,
- 6.5 mm x 5.5 mm = 41 mm² for OA grade 3.

A Kruskal-Wallis H test also showed a statistically significant difference between Ahlbäck OA grade groups in terms of radiographic MT–LT height (Fig. 219), as proportion of the tibial plateau's ML width in the AP radiograph: $\chi^2(3)=11.135$, $p=0.011$. The means obtained by groups were as follows: 1.68% for OA grade 0, 0.76% for OA grade 1, 0.62% for OA grade 2, -0.31% for OA grade 3.

Knee OA showed a significant, weak association with a distinguishable Parsons' knob in MRI and radiograph (Fig. 220), $\chi^2(3)=11.519$, $p=0.009$ (Phi=0.270,

Cramer's $V=0.270$), $r_s(158)=0.153$, $p=0.055$; with proportionally more Parsons' knobs with higher OA grades.

Also significant was the association between a distinguishable knob in imaging and the diagnosis (Fig. 221), $\chi^2(9)=19.151$, $p=0.024$ (Phi=0.348, Cramer's $V=0.348$), with frequency analysis showing proportionally more Parsons' knobs in patients with OA, meniscal, and ACL pathology, and less in those with normal knees, fractures and contusions, and with patellofemoral syndrome or instability.

In terms of the Pećina classification of the Parsons' knob, there was a strong association with knee OA in type (Fig. 222), $\chi^2(9)=42.416$, $p<0.001$ (Phi=0.576, Cramer's $V=0.333$); in size, $\chi^2(9)=28.222$, $p=0.001$ (Phi=0.423, Cramer's $V=0.244$), $r_s(158)=0.202$, $p=0.011$; and in the combination of both, type and size (Fig. 223), $\chi^2(9)=86.576$, $p<0.001$ (Phi=0.740, Cramer's $V=0.427$). Frequency distribution analysis showed that C-type (plateau-shaped) knobs were associated with higher OA grades than B-type (dome-shaped) knobs, and the latter with higher OA grades than A-type (cone-shaped) knobs. Higher OA grades also showed proportionally higher knobs. In combination, their association is stronger, and frequency distribution showed the same results.

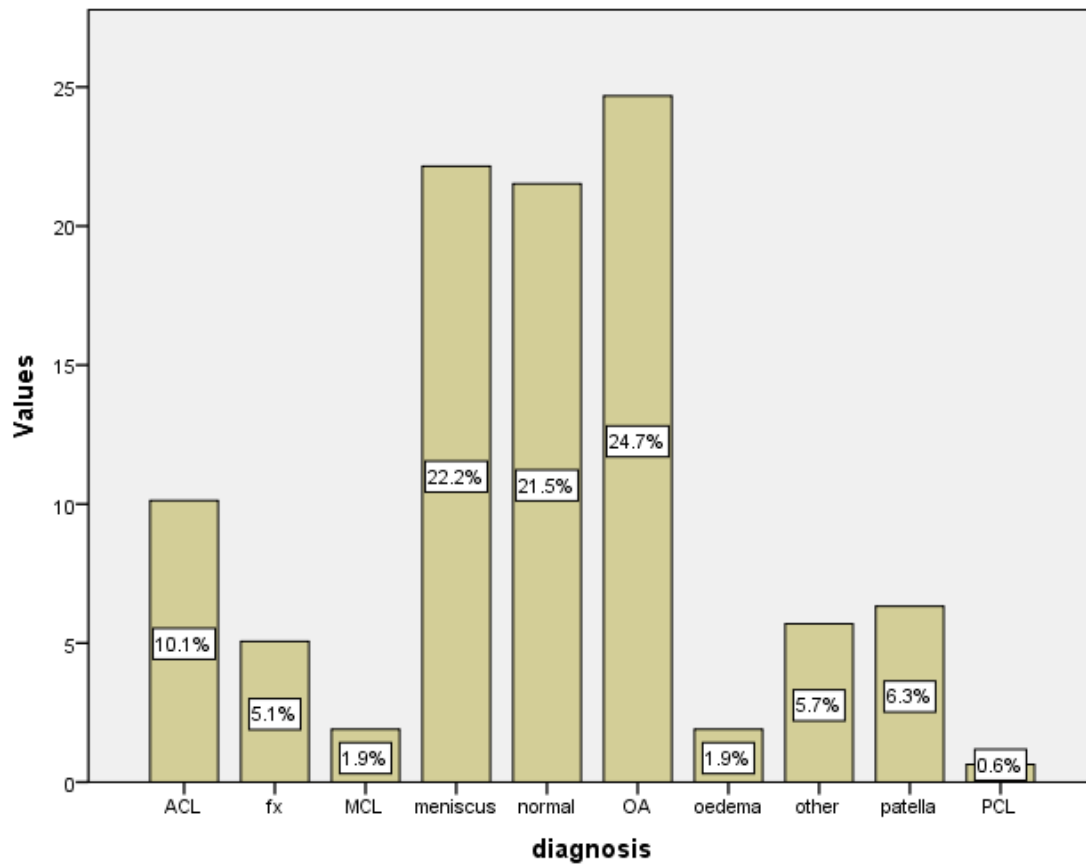


Figure 216. Study X. Histogram of tibias classified into simple diagnostic groups, in percentage. ACL pathology, fracture (fx), medial collateral ligament pathology (MCL), meniscal pathology, normal knees, osteoarthritis, bone edema, other pathologies, femoropatellar pathologies, and PCL pathology.

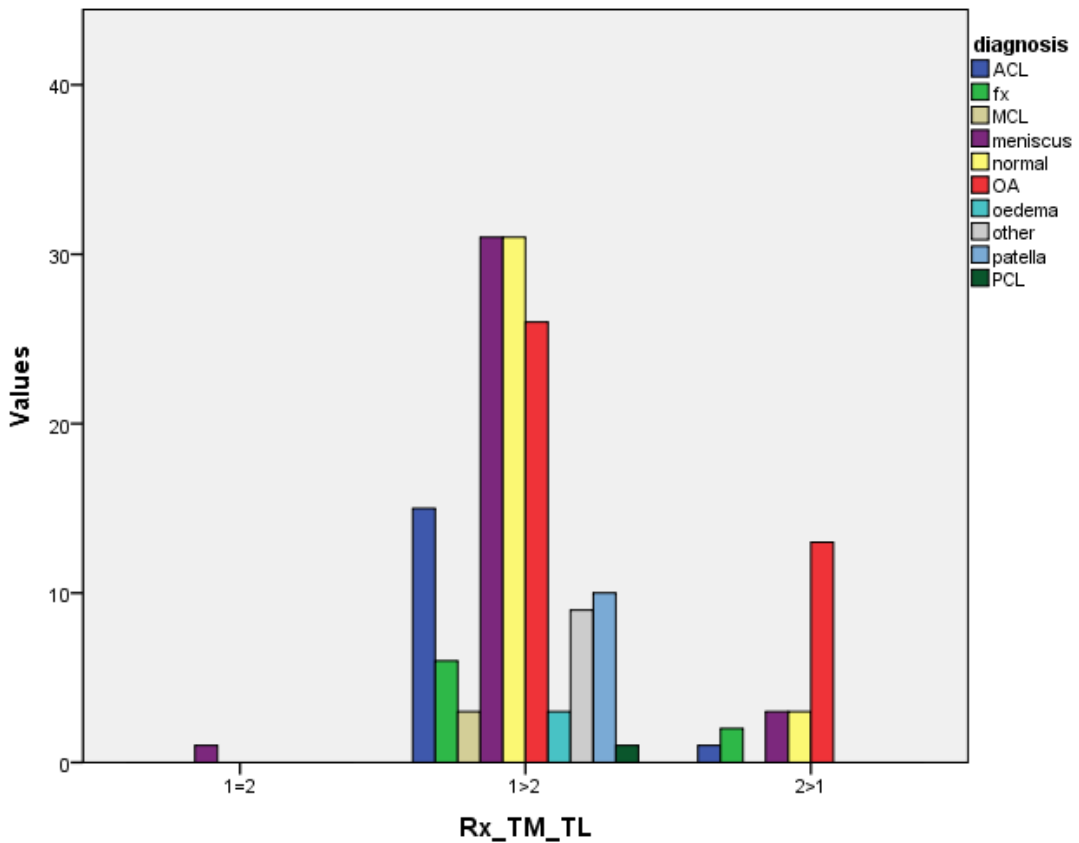


Figure 217. Study X. Histogram of simple diagnostic classes: number of tibias in each category, grouped by relative tubercle size (Rx_TM_TL). 1=MT, 2=LT. See Figure 216. Diagnoses include ACL pathology, fracture (fx), medial collateral ligament pathology (MCL), meniscal pathology, normal knees, osteoarthritis, bone edema, other pathologies, femoropatellar pathologies, and PCL pathology.

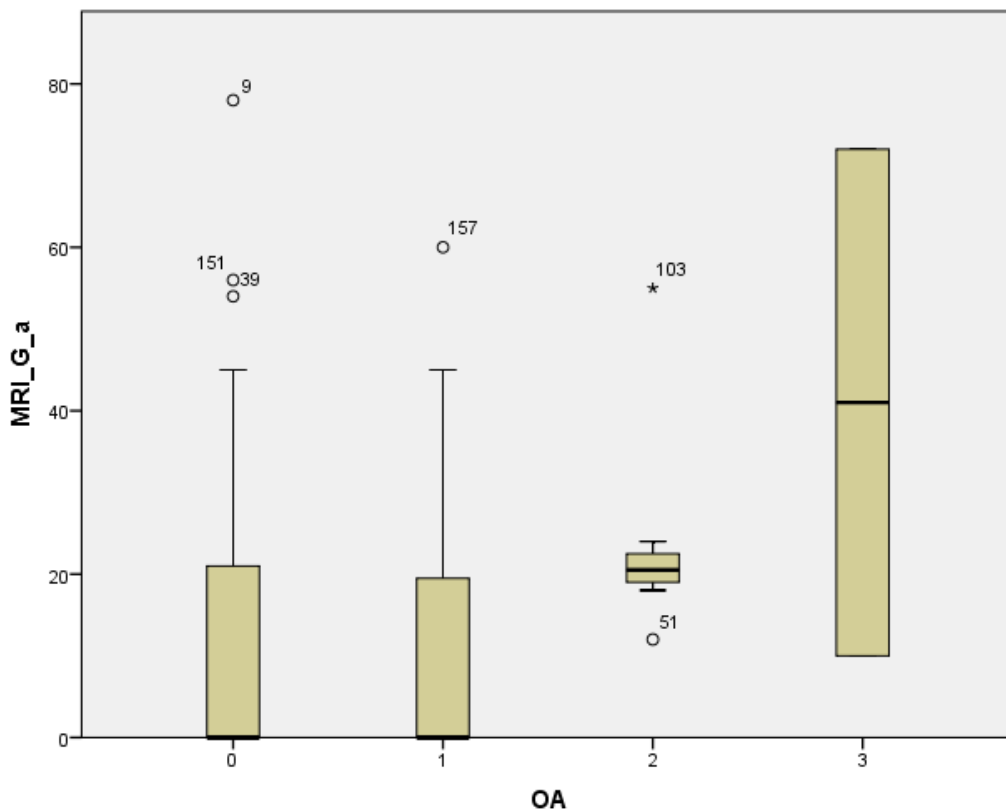


Figure 218. Study X. Box-and-whisker plot of distribution of Parsons' osteophyte area in MRI (MRI_G_a), grouped into Ahlbäck OA grade.

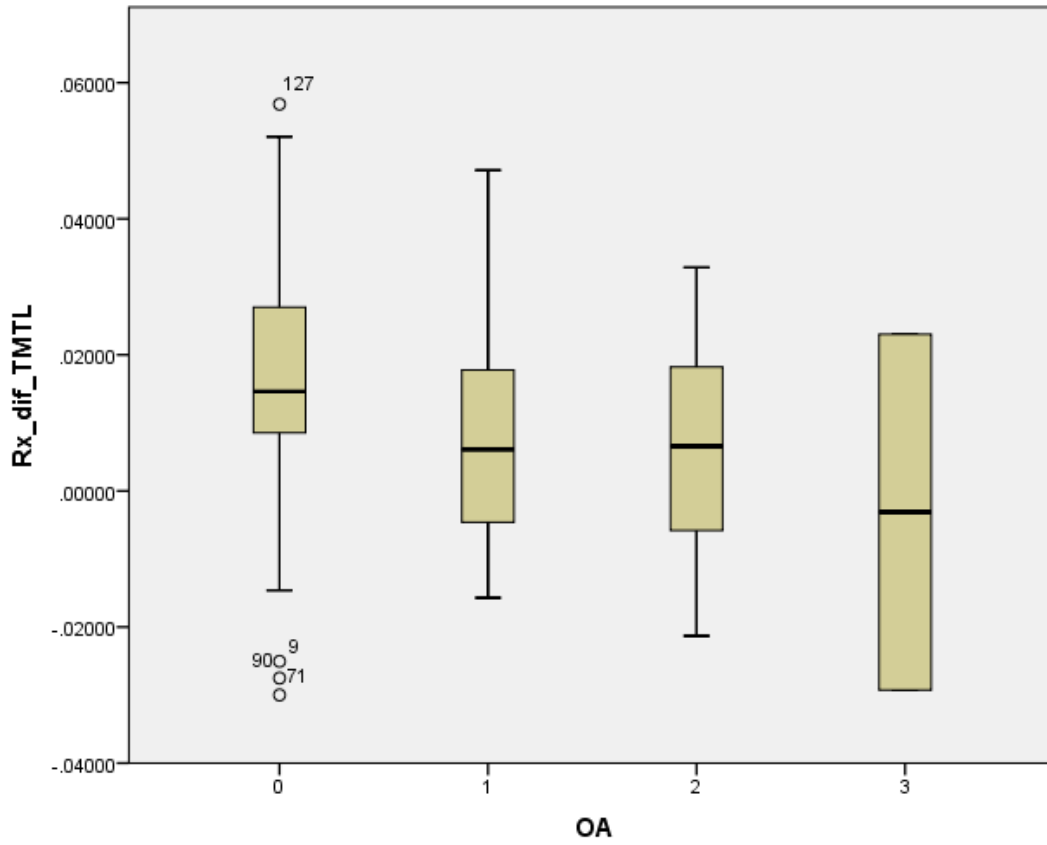


Figure 219. Study X. Box-and-whisker plot of distribution of tubercle height difference in radiograph (Rx_dif_TMTL), grouped into Ahlbäck OA grade.

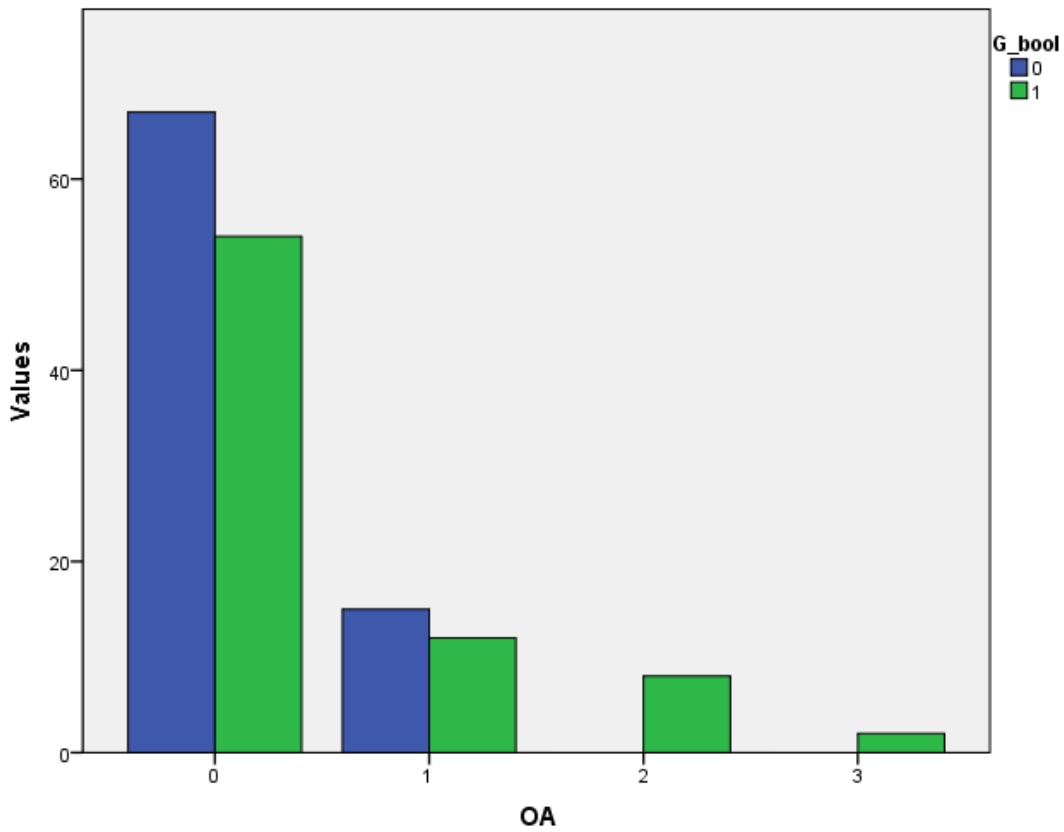


Figure 220. Study X. Histogram of Parsons' osteophyte presence (G_bool): number of tibias in each category, grouped by Ahlbäck OA grade.

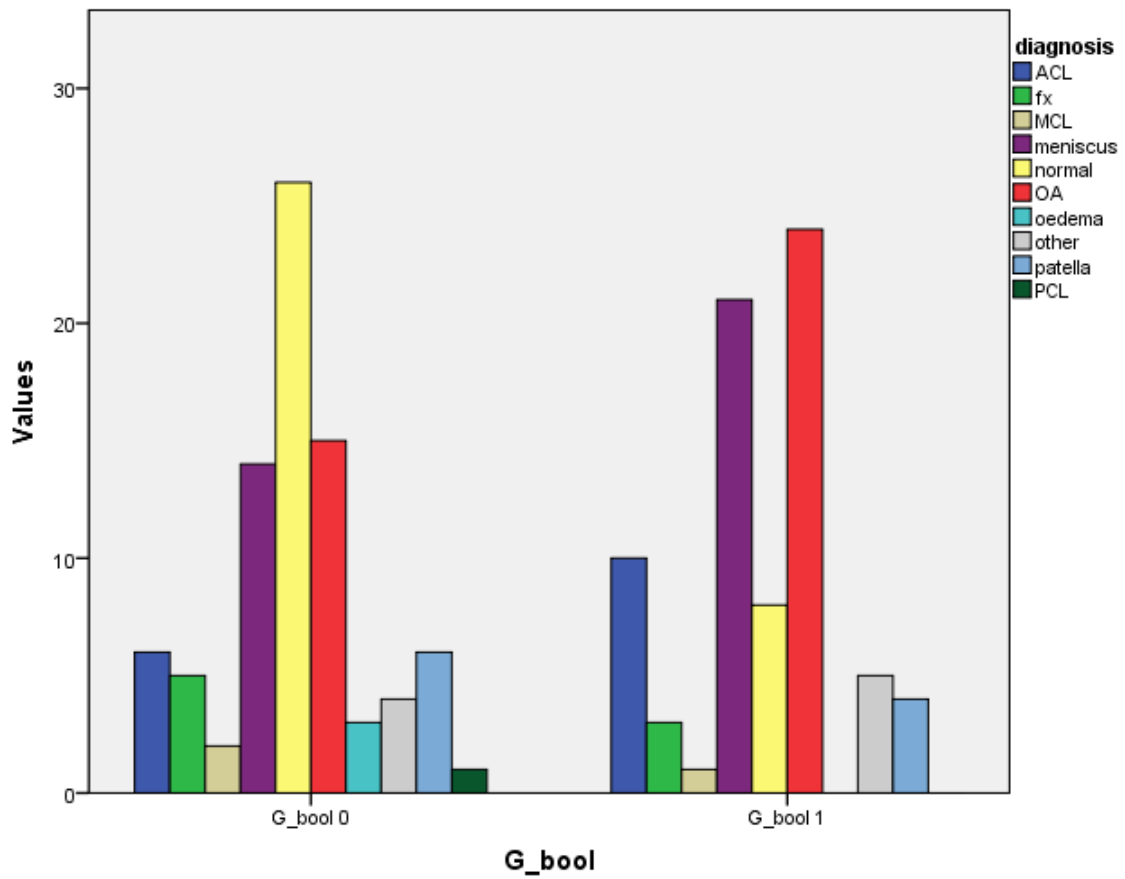


Figure 221. Study X. Histogram of Parsons' osteophyte presence (*G_bool*): number of tibias in each diagnostic category, grouped by the presence or absence of a Parsons' osteophyte. *G_bool* 0: no osteophyte, *G_bool* 1: osteophyte present. See Figure 216.

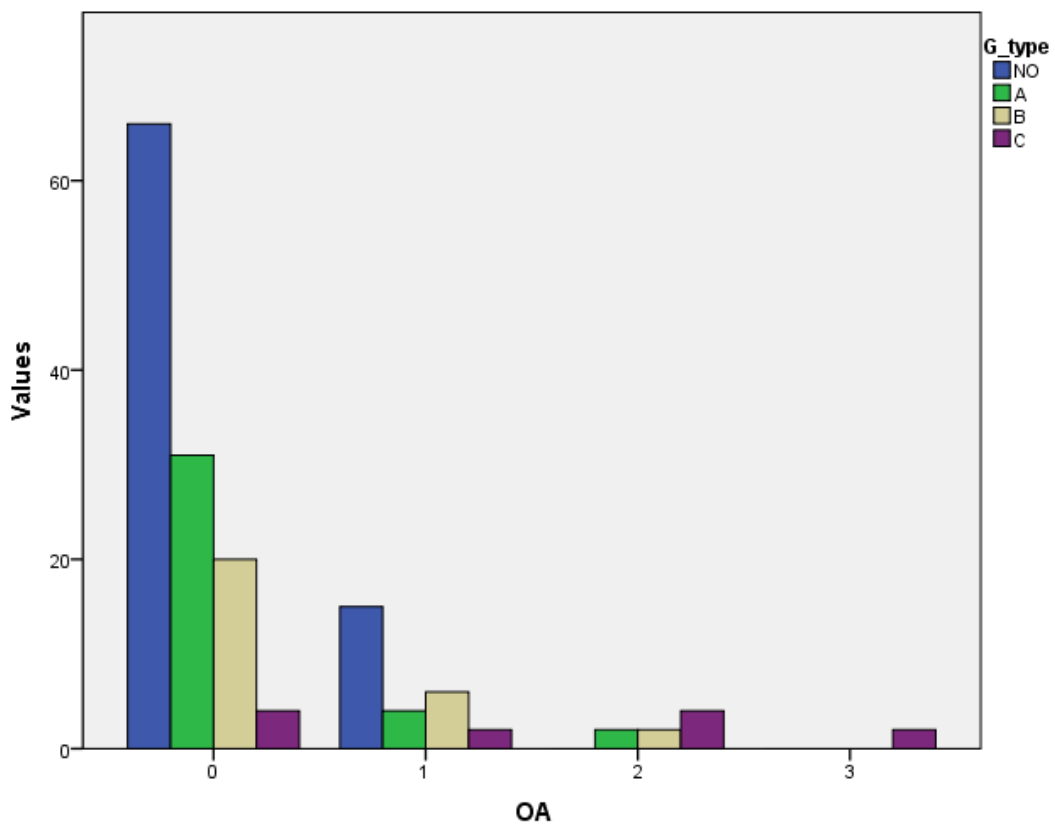


Figure 222. Study X. Histogram of Parsons' osteophyte type (*G_type*): number of tibias in each category, grouped by Ahlbäck OA grade. A=cone-shaped, B= dome-shaped, C= plateau-shaped.

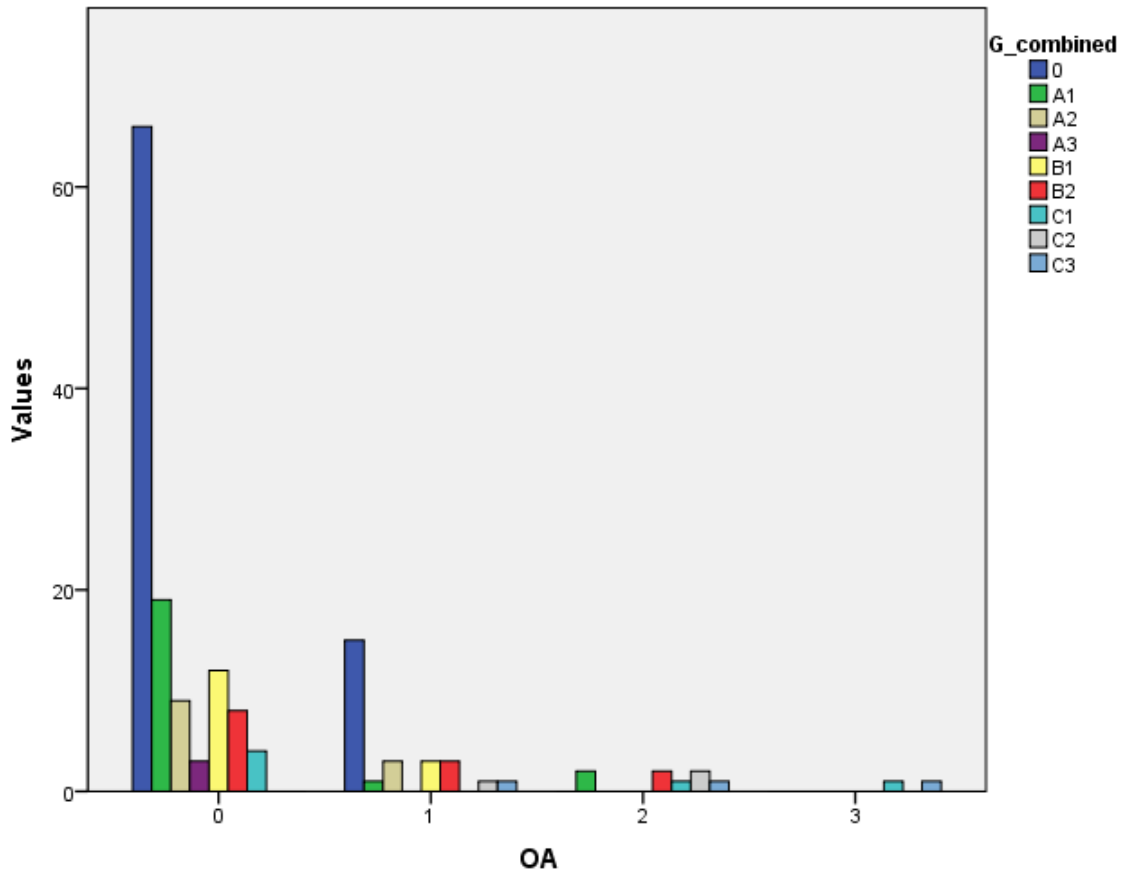


Figure 223. Study X. Histogram of Parsons' osteophyte overall type (G_combined): number of tibias in each category, grouped by Ahlbäck OA grade.

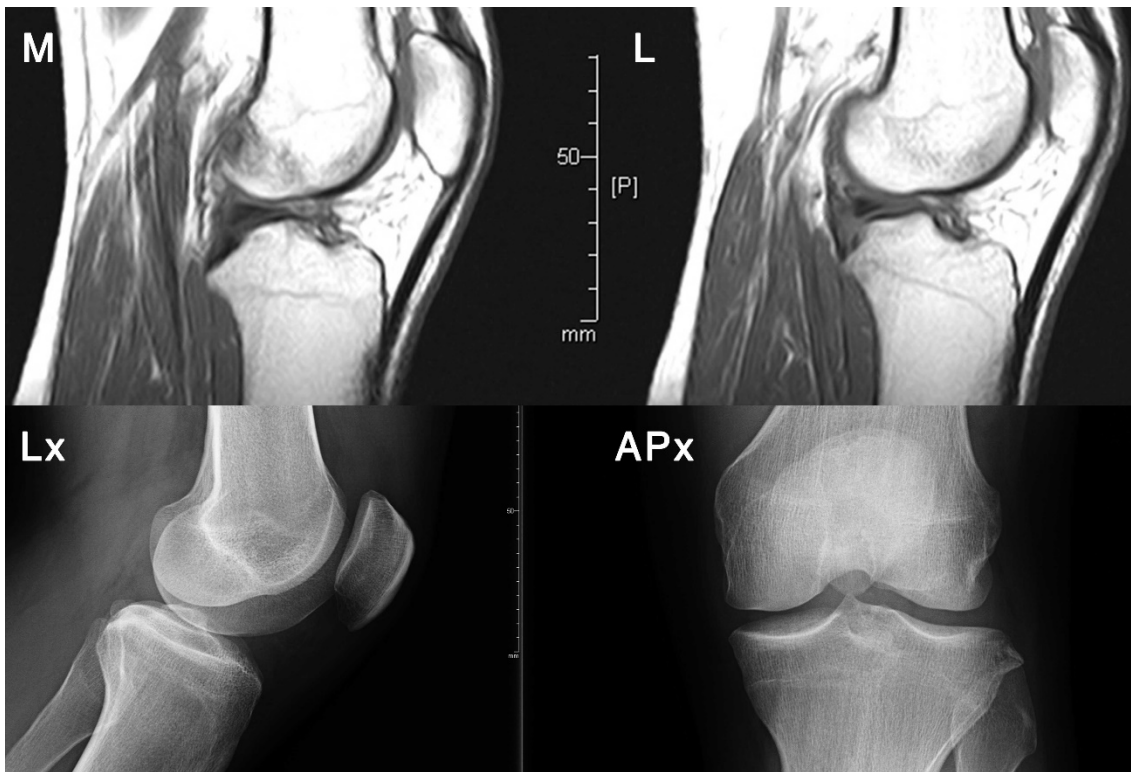


Figure 224. Study X. Case of ACL congenital absence. Sagittal MRI slices through medial (M) and lateral (L) tubercles. Observe the posterior aspects of the tubercles reaching deeper back than usual, and the anterior peak of the lateral tubercle with a small height difference relative to the posterior peak. Lateral (L) and standing AP (AP) knee radiographs. The medial tubercle is clearly seen in both views higher than the lateral tubercle. Observe the lateral tibial osteophyte in the AP view.

IV.4.3.2. Parsons' knob in valgus osteotomy

Results for Study XI for 42 nonpaired knees and 18 paired knees showed a mean age of 65.25 years (range, 50 to 81 years), 78% were females, 52% were right knees. 73% had a varus alignment, and the rest were in valgus. The Ahlbäck classification of knee OA applied to the sample showed the following distribution: 33% OA grade 2, 45% OA grade 3, and 22% OA grade 4.

A Kruskal-Wallis H test showed that there was a statistically significant difference in tibiofemoral angle between the different OA grade groups (Fig. 226), $\chi^2(2)=7.186$, $p=0.028$, with a mean rank tibiofemoral angle of 22.6° for OA grade 2, 32.6° for grade 3, 38.3° for grade 4.

MT and LT classification according to Moon showed no statistically significant association with knee OA: MT (Fig. 227), $\chi^2(12)=16.650$, $p=0.164$ (Phi=0.527, Cramer's V=0.372); LT (Fig. 228), $\chi^2(6)=7.065$, $p=0.315$ (Phi=0.343, Cramer's V=0.243).

No significant association was found between Pećina classification of Parsons' knob and knee OA: knob shape (Fig. 229) $\chi^2(6)=9.917$, $p=0.128$ (Phi=0.407, Cramer's V=0.287); knob type (Fig. 230), $\chi^2(6)=5.914$, $p=0.433$ (Phi=0.314, Cramer's V=0.222), $r_s(60)=0.172$, $p=0.189$; knob combined shape plus type (Fig. 231), $\chi^2(18)=18.734$, $p=0.408$ (Phi=0.559, Cramer's V=0.395).

No significant association was found between simplified knee alignment (varus vs. valgus) and Pećina classification of the Parsons' knob, either: knob shape (Fig. 232), $\chi^2(3)=7.220$, $p=0.065$ (Phi=0.347, Cramer's V=0.347); knob type, $\chi^2(3)=4.374$, $p=0.224$; or combined knob type and shape (Fig. 233), $\chi^2(9)=11.602$, $p=0.237$ (Phi=0.440, Cramer's V=0.440).

A Kruskal-Wallis H test showed no significant difference in tibiofemoral angle among Parsons' knob size groups according to Pećina, $\chi^2(3)=3.804$, $p=0.283$.

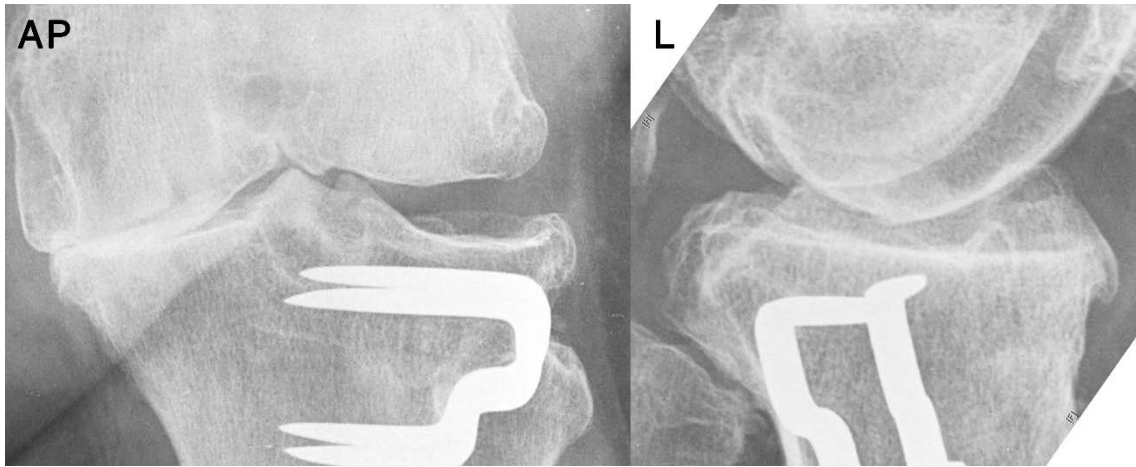


Figure 225. Study XI. Tibia 13, AP standing and lateral (L) knee radiographs. Classified as Ahlbäck OA grade 3, Moon grade 3 for both tubercles, Pécina type 3C for Parsons' tubercle.

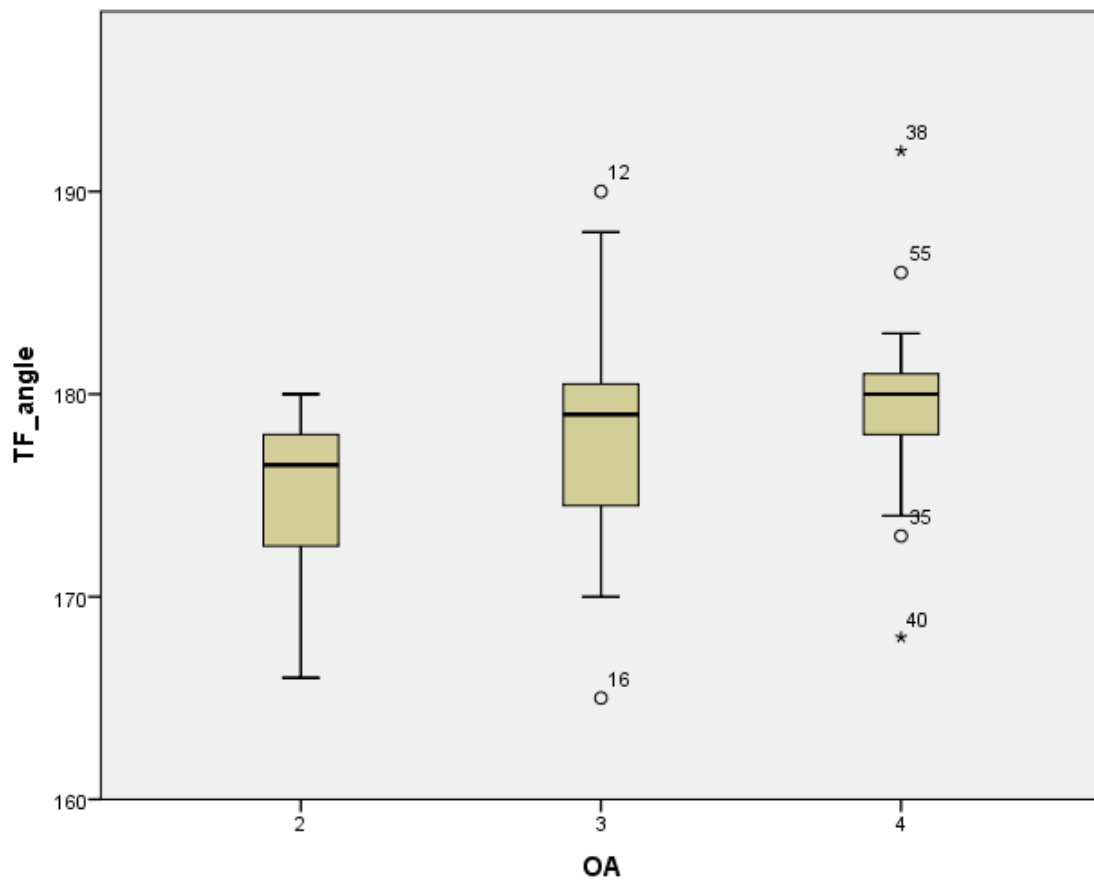


Figure 226. Study XI. Box-and-whisker plot of tibiofemoral angle (TF_angle) distribution grouped in Ahlbäck OA grades.

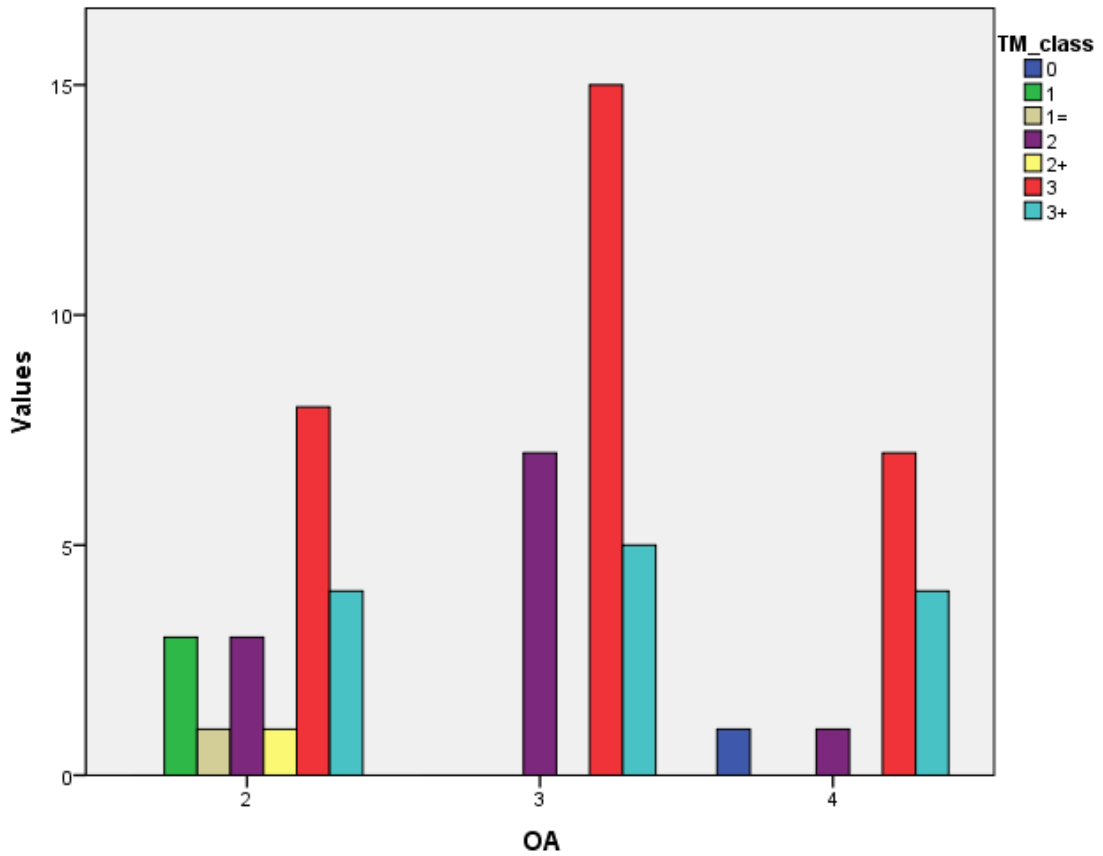


Figure 227. Study XI. Histogram of Woo classification of MT (TM_class): number of tibias in each category, grouped by Ahlbäck OA grade.

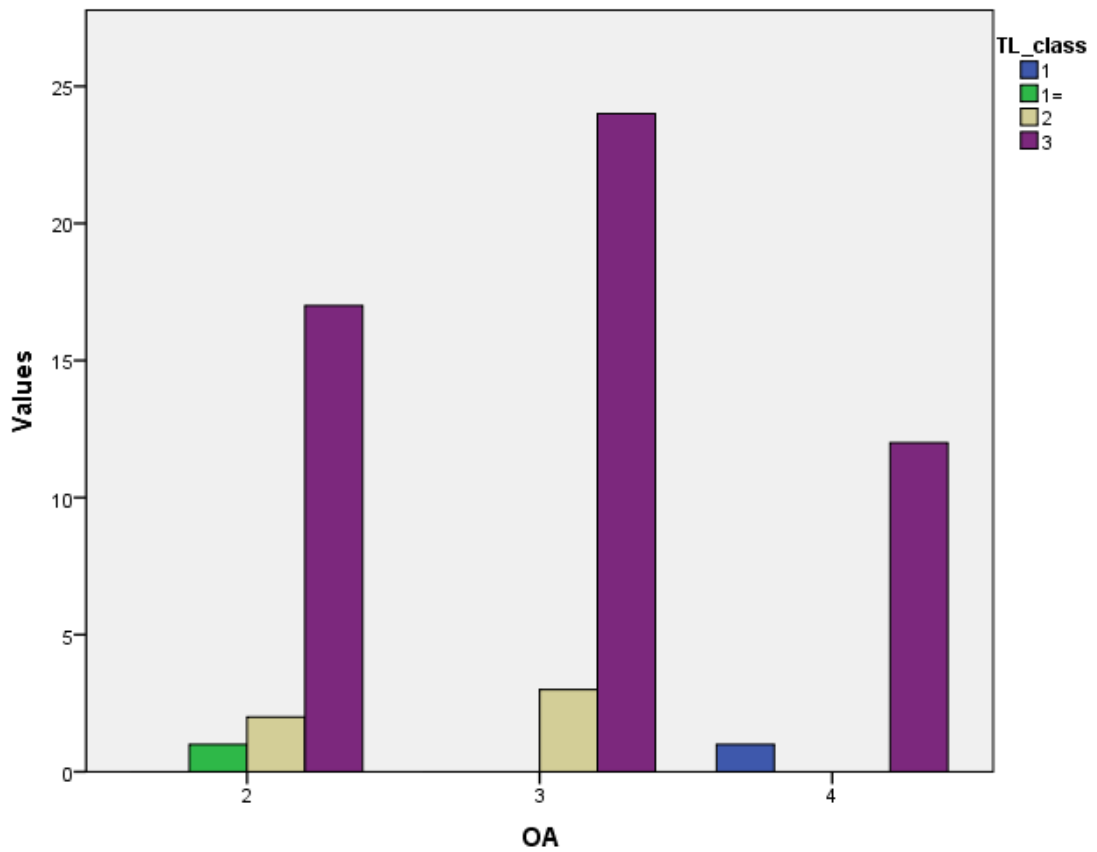


Figure 228. Study XI. Histogram of Woo classification of LT (TL_class): number of tibias in each category, grouped by Ahlbäck OA grade.

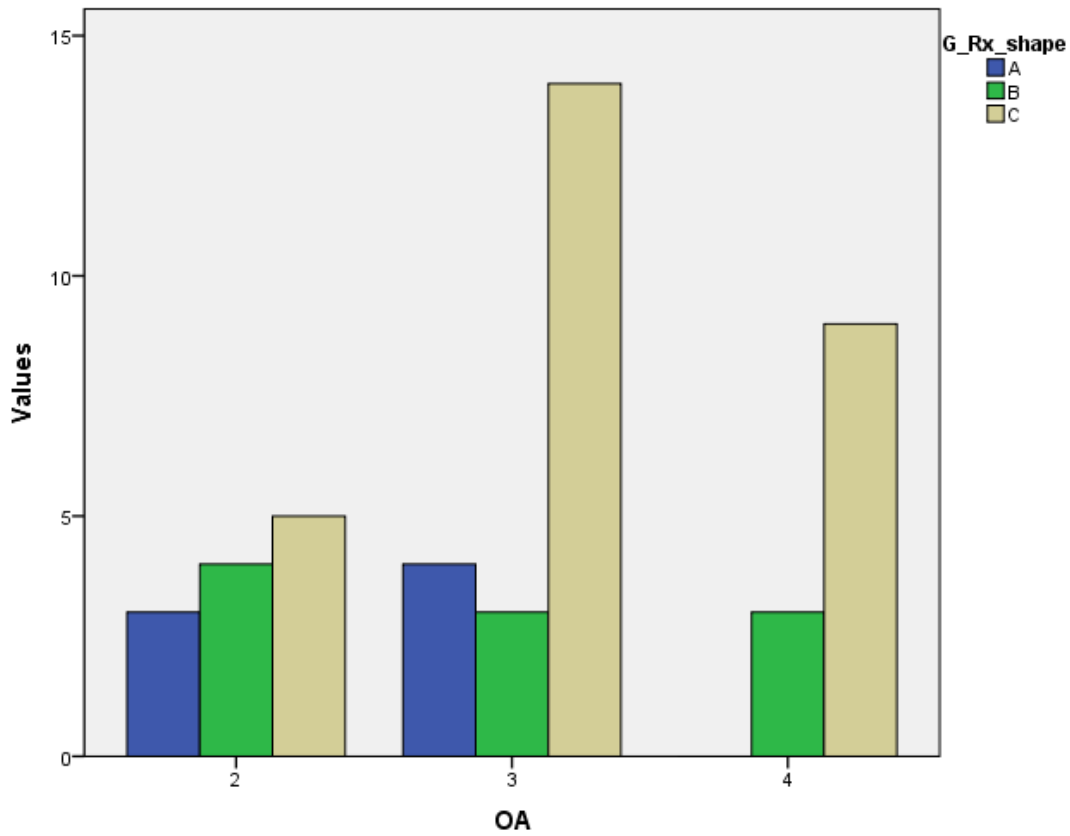


Figure 229. Study XI. Histogram of Parsons' osteophyte shape (*G_Rx_shape*): number of tibias in each category, grouped by Ahlbäck OA grade. A=cone-shaped, B= dome-shaped, C= plateau-shaped.

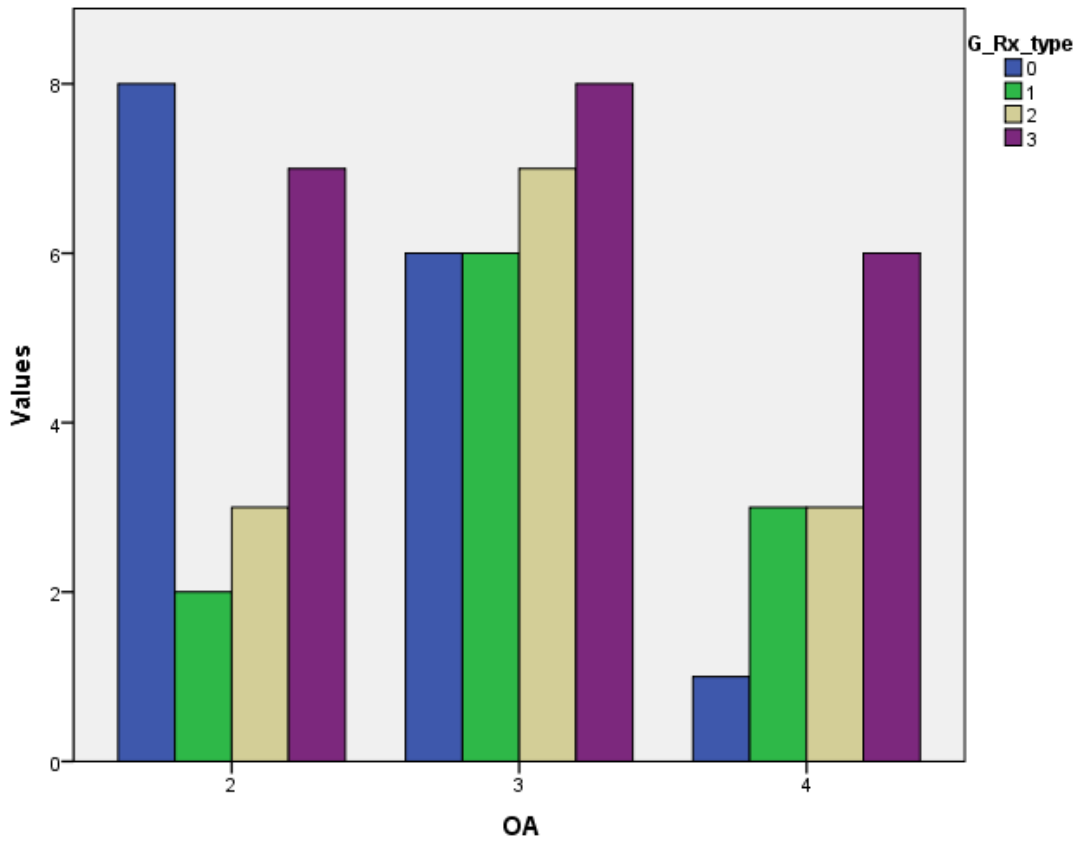


Figure 230. Study XI. Histogram of Parsons' osteophyte type (*G_Rx_type*): number of tibias in each category, grouped by Ahlbäck OA grade.

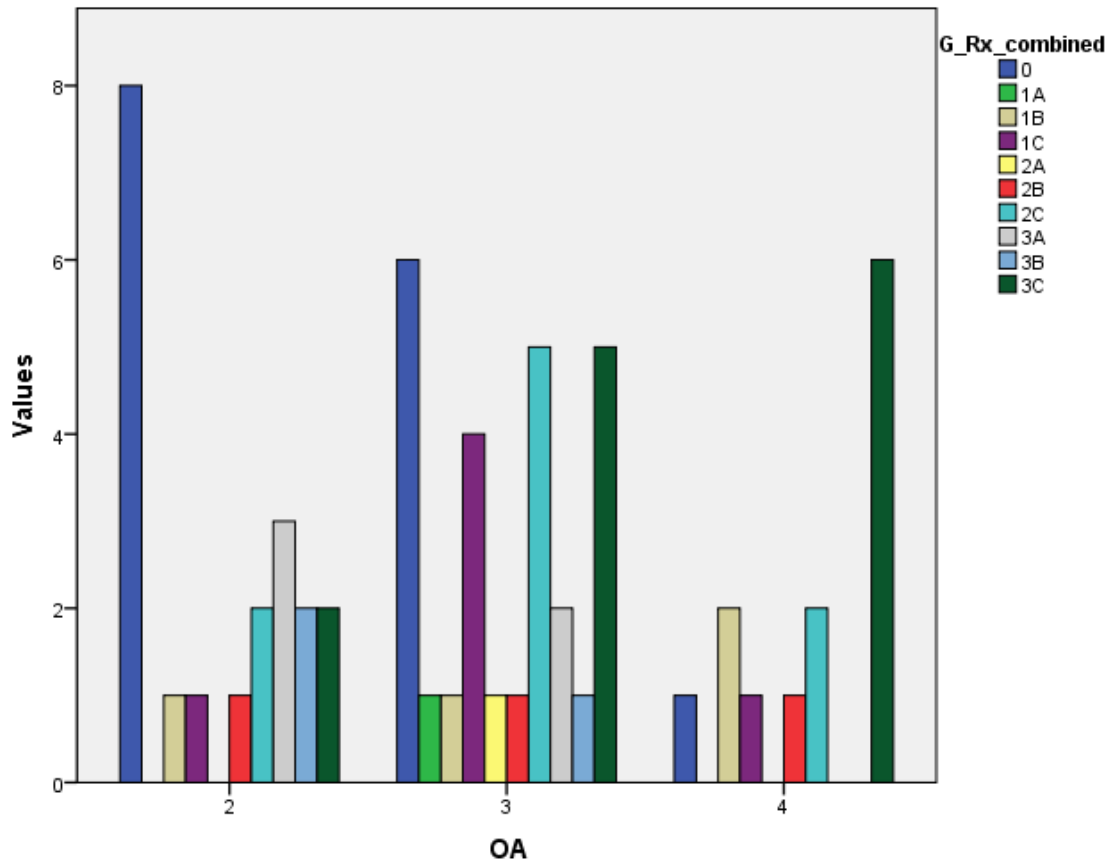


Figure 231. Study XI. Histogram of Parsons' osteophyte combined shape and type (G_Rx_combined): number of tibias in each category, grouped by Ahlbäck OA grade.

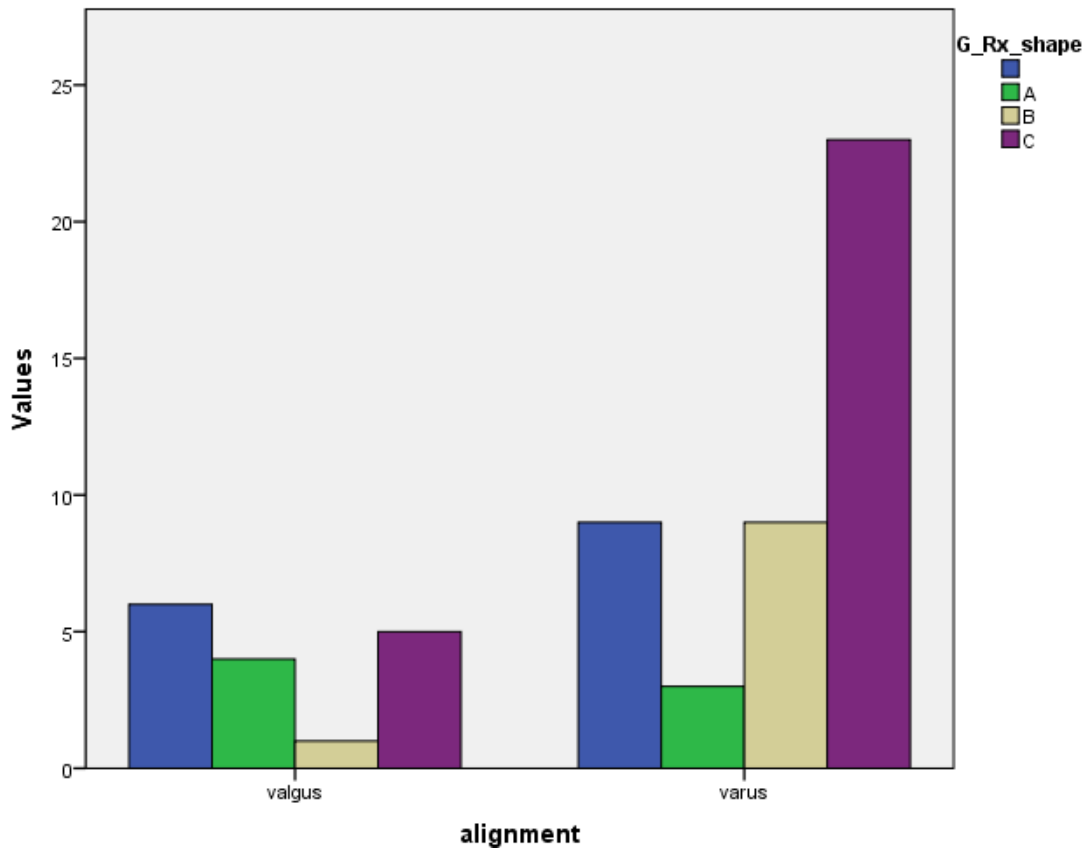


Figure 232. Study XI. Histogram of Parsons' osteophyte shape (G_Rx_shape): number of tibias in each category, grouped by alignment into valgus or varus.

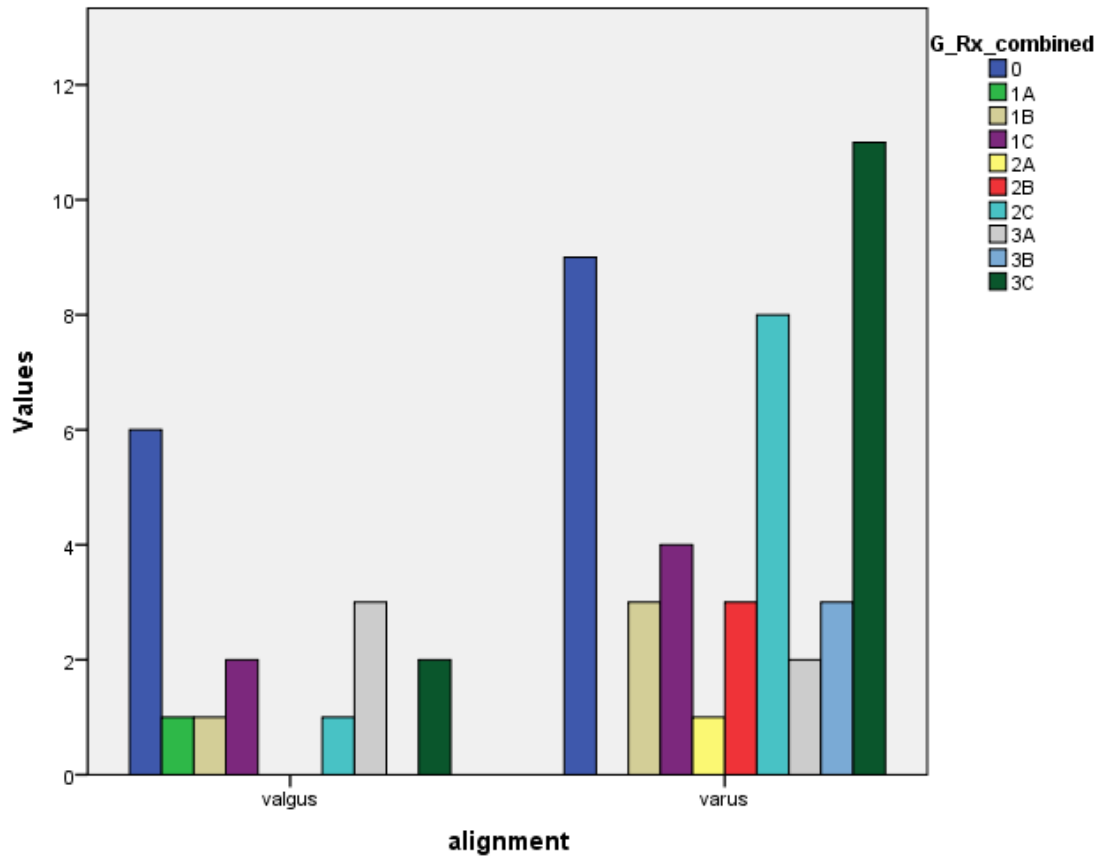


Figure 233. Study XI. Histogram of Parsons' osteophyte combined shape and type (G_Rx_combined): number of tibias in each category, grouped by alignment into valgus or varus.

IV.5. Anteromedial part of the anterior intercondylar area

IV.5.1. Fingerprint, anterior sagittal ridge, and anterior knob

The anterior part of the MAIA, **5**, was found elevated over the LAIA. It was dominated by the anterior fingerprint, **5a**, a flat, round facet surrounded by elevations posteriorly, medially and laterally, and in contact with the anterior wall of the proximal tibia (Fig. 234, Fig. 235).

The fingerprint was found to be delimited by three constant elevations: posteriorly by the anterior AFIR process, medially by the anteromedial corner, and laterally by the anterior intercondylar sagittal ridge (ASIR), **J**. This ridge formed a medially concave curve, from the AFIR posteriorly to the anterior aspect of the proximal tibia. It was in close contact with the anterior AIAR, an approximately straight elevation located slightly lateral to it. When both processes were present in the same specimen (and not united in a common ridge), a recess was present between them (see Fig. 179 above).

A protuberance, the anterior intercondylar knob (AIK), **N**, was found in the anterior border of the proximal tibia, in line with the ASIR or the anterior AIAR (see above Fig. 50 and below Fig. 239).

Anterior to the flat fingerprint was an anterior coronal line, a curved elevation surrounding the fingerprint anteriorly, and marking its border with the anterior wall of the proximal tibia. Unlike the lateral aspect of the AIA, which showed a smoothly sloped transition with the anterior wall, the margin of the medial aspect was thus normally well delimited.

The anterior coronal line connected the sagittal ridge laterally with the anteromedial corner medially. A rough zone of the anterior wall could be distinguished at the medial border of the coronal line – in contact with the anteromedial corner's anterior wall–, the accessory imprint, **5b**, with a gentler downward slope than the surrounding areas.

The medial wall of the fingerprint and lateral wall of the anteromedial corner formed a continuous rectangular shape with a gentler downward slope in a lateral direction, connecting the medial condyle with the MAIA. The wall was divided between both areas by dividing the rectangle in two triangles, with the dividing line connecting the geniculum posteromedially and the anteromedial border of the fingerprint anterolaterally.

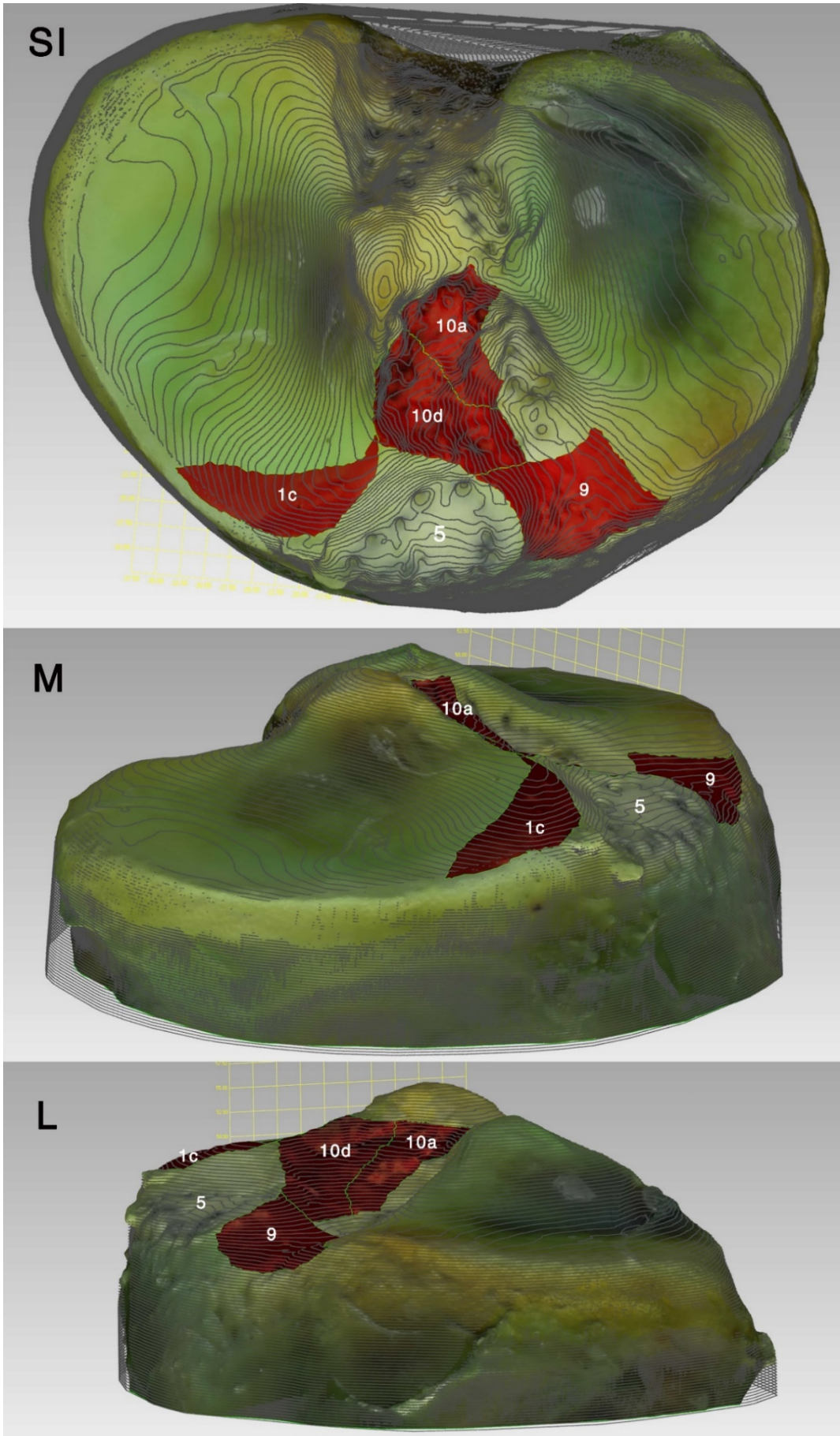


Figure 234. 3D model of Tibia L with contour lines superimposed. Superoinferior (SI), anteromedial (M) and anterolateral (L) views with selected areas of the anterior intercondylar area surrounding area 5, in red.

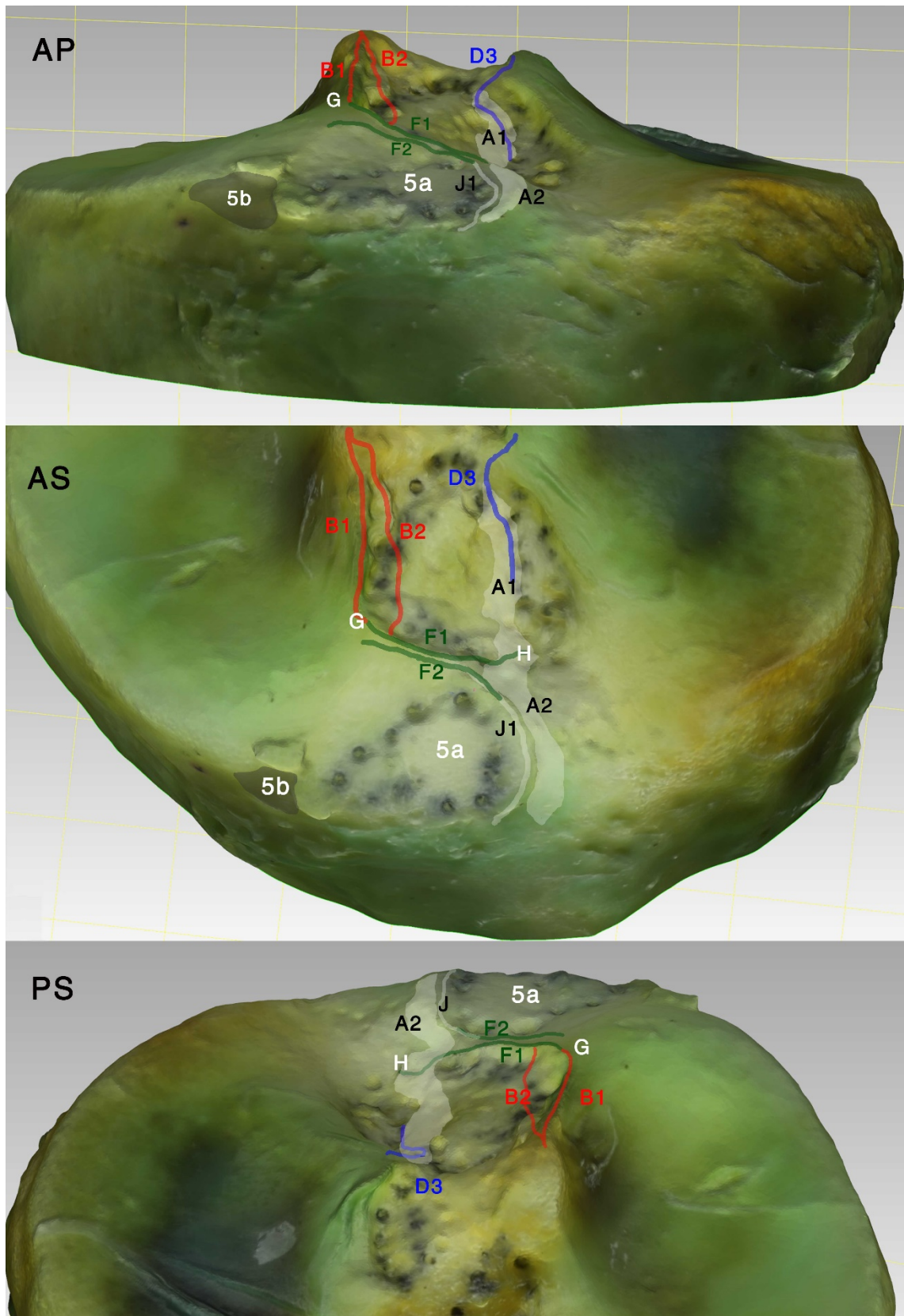


Figure 235. 3D model of Tibia L. Anteroposterior (AP), anterosuperior (AS) and posterosuperior (PS) view of anterior intercondylar area with painted lines over the main processes (AMIR in red, ALIR in blue, AFIR in green, AIAR and ASIR in white). The geniculum (G), lateral-most border of F1 (H), and areas 5a and 5b (gray shading) are also labelled.

IV.5.2. Attachment of the anterior root of the medial meniscus

The attachment of the central, dense ARMM lied in all cases within the margins of the selected area 5 (Fig. 236), with a mean attachment area of 78.5 mm² (95% CI, 64.9 – 92.1 mm²; range, 49 mm² to 128.7 mm²), representing a mean of 38.3% of area 5 (95% CI, 33.6 – 43%; range, 30% to 57%; N=14).

Classified according to Berlet & Fowler, it was found that ten specimens (72%) had a type I attachment; a type II attachment was found in one specimen (7%), which showed a higher wall between areas 1c and 5 (only part of the ARMM was attached to it); and a type III attachment was found in three specimens (21%), two of them showing a higher and deeper AFIR, and the other showing an elevated fingerprint.

Qualitatively, the attachment area showed mainly an oval, kidney-like shape. An anterior intermeniscal ligament was visible in 6 cases attached to the posteromedial corner of the ARMM, near its attachment.

The ARMM attachment was measured in reference to arthroscopically pertinent landmarks. Qualitatively, the center of the ARMM was found to be anterior to the anterior intercondylar ridge (F), the ACL attachment center, ACL attachment anterior border, and the anterior peak of the MT (3a₁, or 3a); anterolateral to the geniculum (G); anteromedial to the anterocentral intercondylar knob (H), and to the ARLM center; lateral to the AM corner (1c, measured with a straight M-L line to its lateral edge); and medial to the anterior sagittal ridge (J).

The center of the ARMM attachment was 33.4 mm (range, 27.3 mm to 38.5 mm) from the center of the PRMM attachment (measured in a straight line, over the surface). With a coefficient of variation (CV) of 10.2%, it is the only measurement that had a significant correlation with AP depth ($r=0.76$, $p=0.003$), and ML width of the tibial plateau ($r=0.85$, $p<0.001$). Proportionally, it represented 46% of the ML width. See Table 12 for all distances obtained from the center of the ARMM attachment to selected anatomic landmarks.

Table 12. Distances in mm, 95% CI, Coefficient of variation (CV), Pearson correlation values for AP and ML, with their corresponding p-values.

ARMM	MM	95% CI	CV	AP	AP P	ML	ML P
MT (3a)	28.1	26.8 – 29.5	7.84	0.414	0.159	0.396	0.181
ACIK (H)	12.6	11.1 – 14.0	19.39	-0.098	0.749	-0.071	0.818
AMIK (G)	12.1	10.5 – 13.6	21.51	0.360	0.227	0.448	0.124
AFIR (F)	10.2	8.5 – 12.0	27.74	-0.138	0.654	-0.122	0.692
ASIR (J)	8.3	7.3 – 9.3	19.56	-0.051	0.869	-0.156	0.610
ACL	15.6	13.5 – 17.6	21.49	-0.140	0.648	0.055	0.859
A ACL	10.5	8.8 – 12.2	27.00	0.032	0.918	0.023	0.941
PRMM	33.4	31.3 – 35.5	10.23	0.760**	.003	0.846**	0.000
1c EDGE	8.8	7.6 – 10.1	23.23	0.461	0.113	0.586*	0.035
ARLM	21.6	19.4 – 23.9	17.43	0.577*	0.039	0.588*	0.035

* Correlation is significant at the 0.01 level (2-tailed).

** Correlation is significant at the 0.05 level (2-tailed). In green, measurements taken in straight line, over the surface. In blue, measurements taken in the shortest straight (roughly ML) line.

NOTE. A ACL: Anterior aspect of ACL attachment. 1c edge: lateral edge of anteromedial corner (border with area 5).

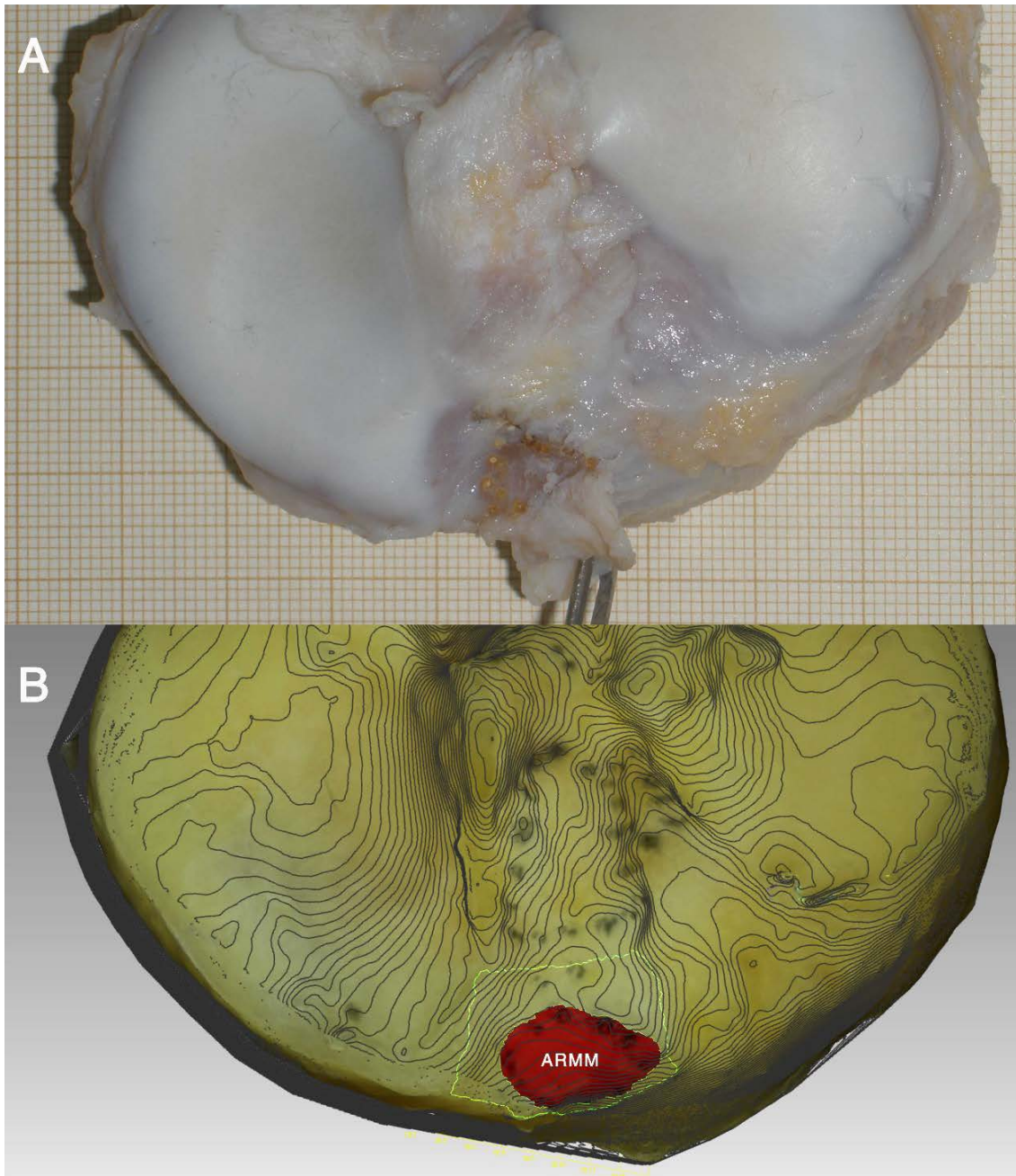


Figure 236. Tibia M. During dissection (A), ARMM dense fibers are detached and marked with pyrography. 3D model (B) shows ARMM footprint highlighted in red, within area 5 (outlined with light green lines).

IV.5.3. Degenerative changes of the anteromedial intercondylar area

The fingerprint itself could be found elevated in pathological tibias. It often seemed more excavated, though, surrounded by osteophytic elevations of the anteromedial corner, Parsons' knob, AFIR, ASIR, ACIK, and the anterior intercondylar knob.

The ASIR and the AIAR were not found more frequently joint or separated in pathological than in normal specimens, with the joint variation being less frequent in general. When elevated, both could be found elevated equally or differently, and when separated an incisure could be present between them (Fig. 237, Fig. 238).

The ASIR showed no correlation with knee OA (Fig. 240), $r_s(94)=0.149$, $p=0.153$.

The anterior intercondylar knob, N, was found in line with the sagittal ridge, near the anterior margin of the MAIA. A bigger osteophyte than the one found in the 3D models could be observed in certain radiographs of the same specimens, oriented anteriorly, superior to the anterior tibial tuberosity (Fig. 239).

The only sizeable anterior protuberance found in normal specimens (Ahlbäck OA grade 3) showed a volume of 50 mm³.

A weak correlation was found between the anterior intercondylar osteophyte and Ahlbäck OA classification (Fig. 241), $r_s(90)=0.262$, $p=0.013$.

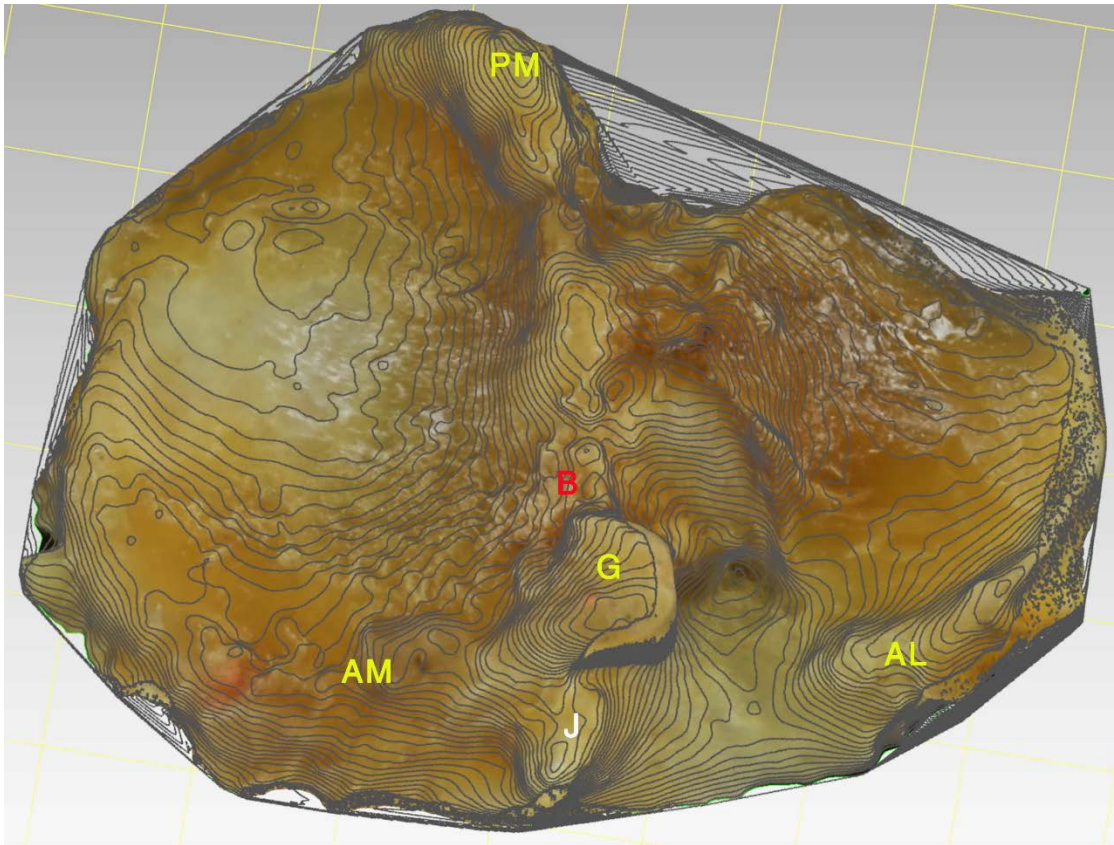


Figure 237. 3D model of tibia 65, with contour lines superimposed (left-mirrored). ASIR (J) elevated, osteophyte grade 3. Also labelled are the Parsons' tubercle (G), AMIR (B), and elevations in the AM, AL and PM corners.

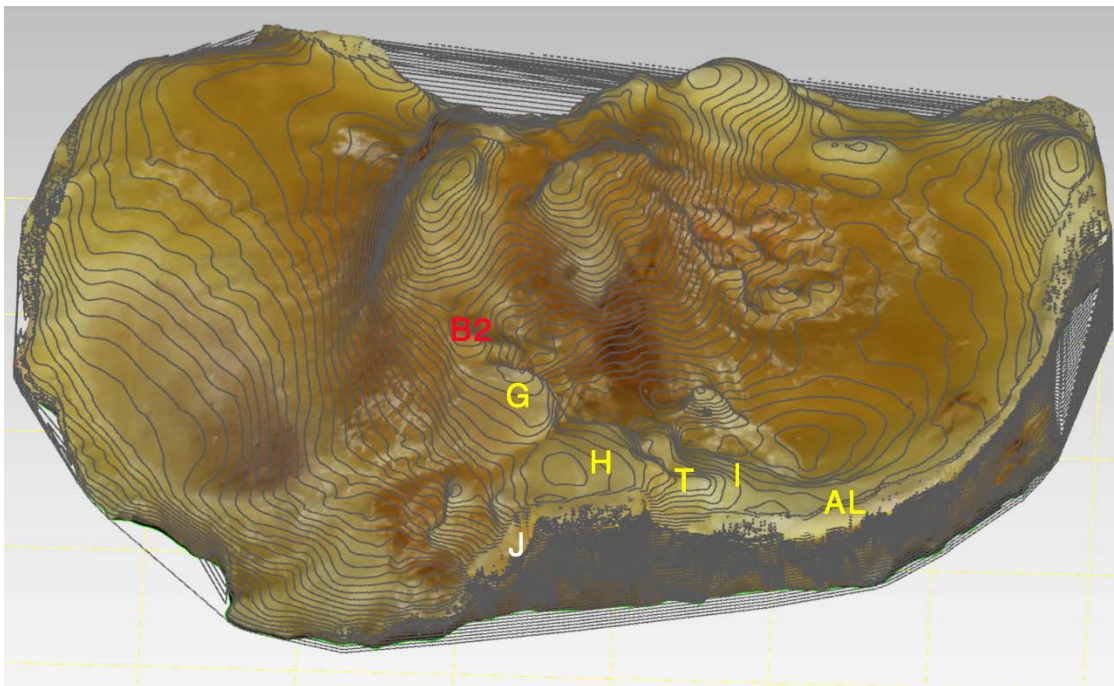


Figure 238. 3D model of tibia 28, with contour lines superimposed. ASIR (J) elevated, osteophyte grade 3, connected with anterocentral intercondylar tubercle (H), in turn connected medially to a tongue-shaped Parsons' tubercle (G) – formed by the connection of B2 with the AFIR (i.e. more posterolateral than the usual position of the Parsons' tubercle) and laterally to the elevated anterior intercondylar saddle, anterolateral knob (I), and anterolateral corner (AL).



Figure 239. Lateral knee radiograph corresponding to tibia 25 showing an anterior intercondylar tubercle (N), osteophyte grade 5. Also labelled is the Parsons' knob (G). Cut specimens usually lacked information on the AIK, and radiographs were used to complement that information.

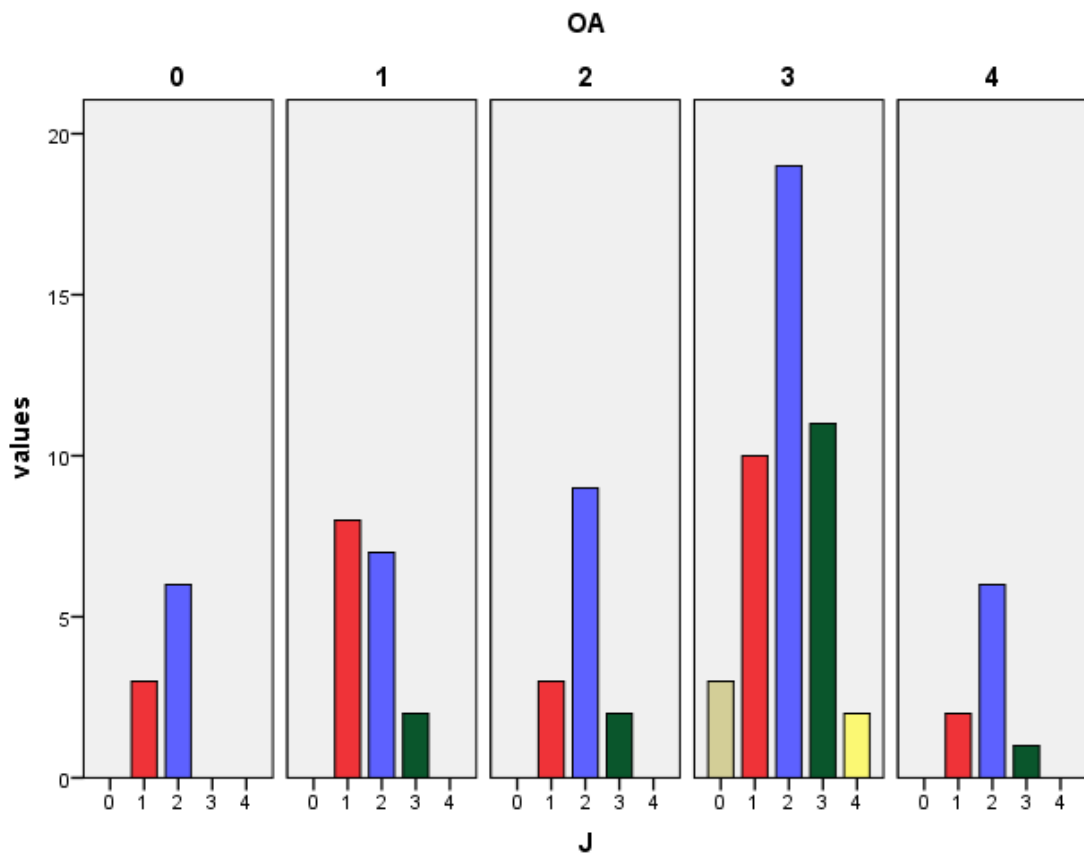


Figure 240. Study II. Histogram of ASIR (J) osteophyte grade: number of tibias in each category, grouped by Ahlbäck OA grade.

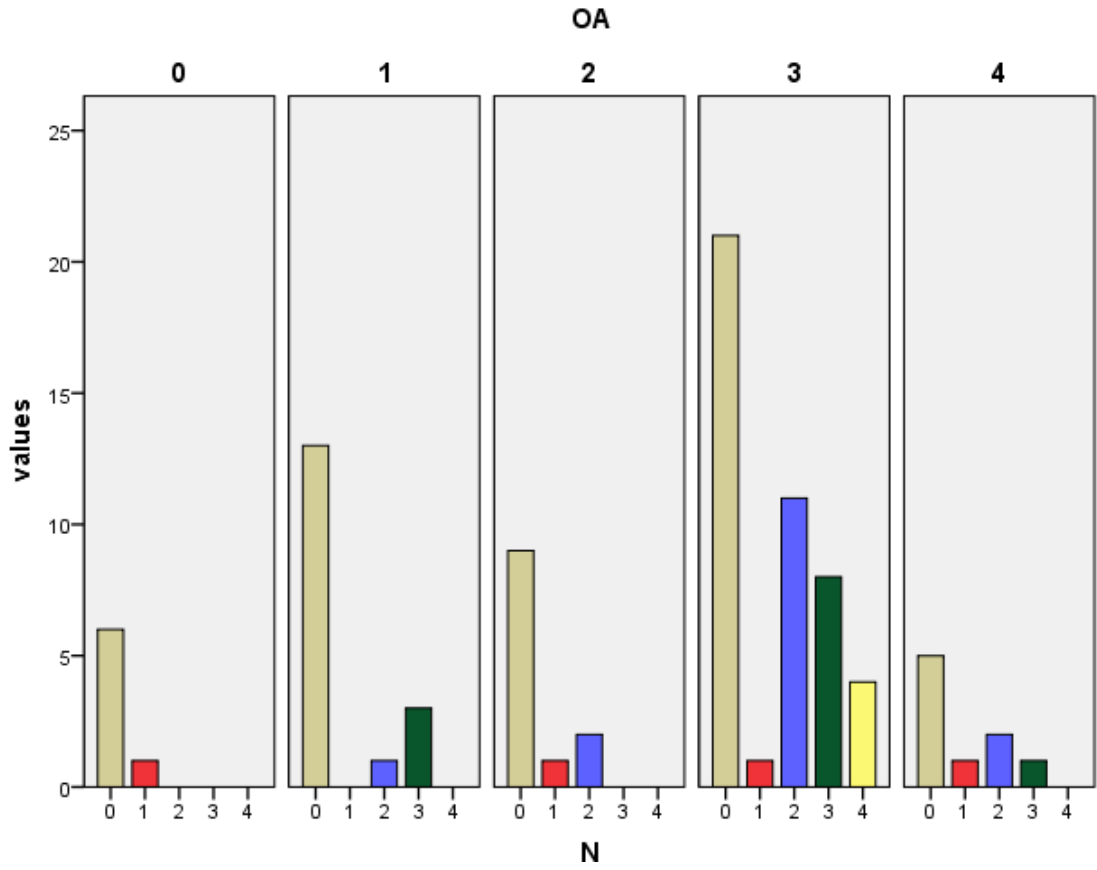


Figure 241. Study II. Histogram of anterior intercondylar knob (N) osteophyte grade: number of tibias in each category, grouped by Ahlbäck OA grade.

IV.6. Lateral part of the anterior intercondylar area

IV.6.1. Anterolateral recess, fossa, and vallecule

The lateral aspect of the anterior intercondylar area was found as a deeper anterolateral groove, which formed the bottom of the bowl where Hoffa's infrapatellar fat pad rested (Fig. 243, Fig. 244). Foramina nutricia were also found in this area, especially in its anterior zone.

A wide, slightly elevated line was observed in the anterolateral groove, dividing areas 7 and 9, the anterior intercondylar saddle, **T**, following the direction of the posterior AFIR. At its intersection with the wall of the lateral condyle, a slight protuberance could be seen in certain specimens, the anterolateral intercondylar knob (ALIK), **I**.

The anterolateral fossa, **7**, was defined as the posterior part of the anterolateral groove, showing a very gentle upwards slope from posterior to anterior, towards **T**. Its posterior aspect was found dominated by foramina nutricia, among them a constant one forming the anterolateral fovea. The fossa was surrounded laterally by a low but steep wall from the lateral condyle, and medially from area 10 by the step corresponding to the inferior aspect of the AIAR laterally, which continued into the fossa's posterior wall, separating it from area 8.

The anterolateral vallecule, **9**, was defined as the anterior part of the anterolateral groove: delimited posteriorly by **T** from area 7, it showed a very gentle downward slope anteriorly until the steeper anterior tibial margin of the lateral AIA. The area widened anteriorly because of the diverging obliquity of its delimiting structures with respect to each other: the anterior AIAR medially (separating it from area 5) and the lateral AIA wall (separating it from the anterolateral corner).

A constant vertical indentation on the anterior aspect of the lateral tubercle, the anterolateral recess, **8**, was delimited superiorly by the anterior peak of the lateral tubercle (4a), medially by the internal ALIR process (D3), and laterally by the central ALIR process (D2). Anteriorly it was delimited by a small step, the posterior wall of the AL fossa.

When different anterior (D3_a) and posterior (D3_b) internal ALIR processes were found, the latter enclosed the vertical fossa proper, **8a**, the deeper aspect of the recess, embedded in the anterior wall of the lateral tubercle. The area between both processes corresponded to the posterior AIAR, with D3_b marking the border between areas 8 and 10 (see below Fig. 245).

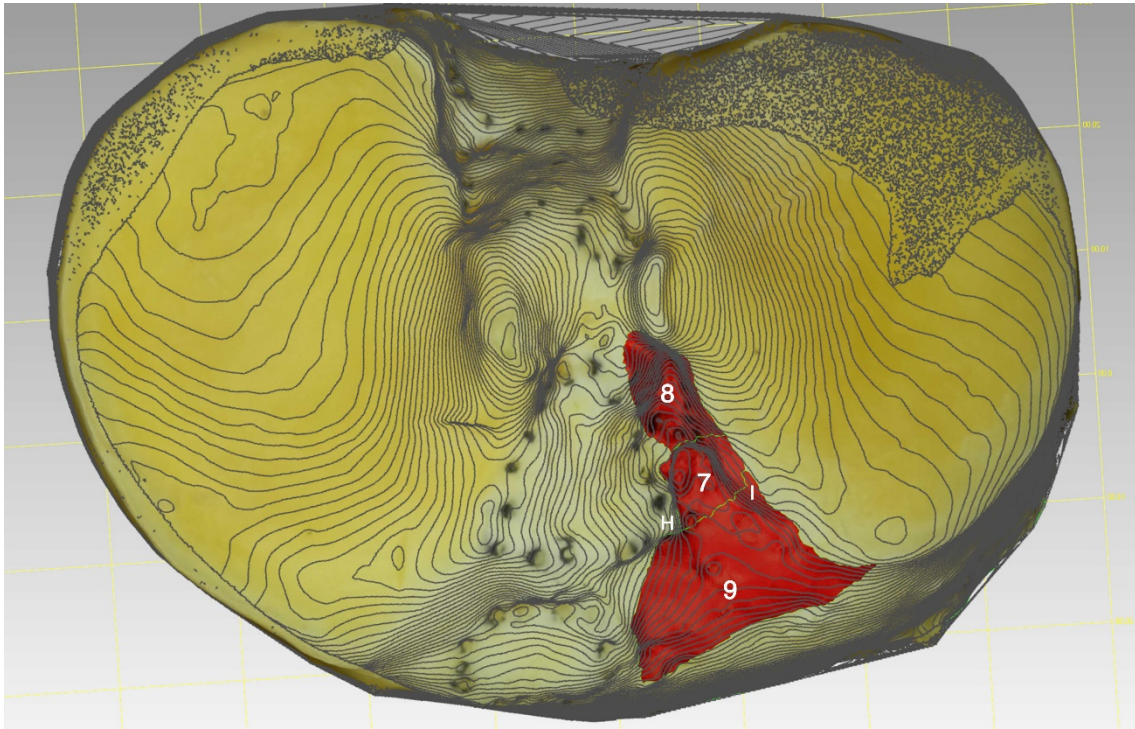


Figure 242. 3D model of Tibia A. Superoinferior view with contour lines superimposed and anterolateral groove areas selected and highlighted in red. Lateral border of F1 (H) and AL knob (I) labelled.

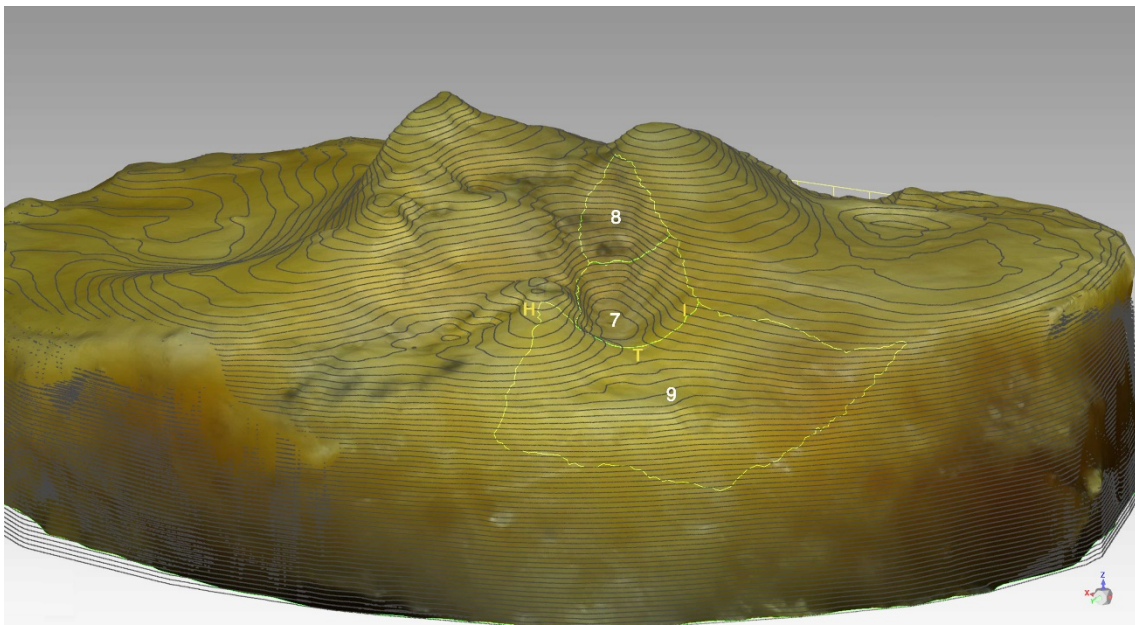


Figure 243. 3D model of Tibia G. Anteroposterior view with contour lines superimposed and anterolateral groove areas selected. Anterocentral knob (H), anterior saddle (T), and anterolateral knob (I) labelled. Notice the absence of an elevated ASIR.

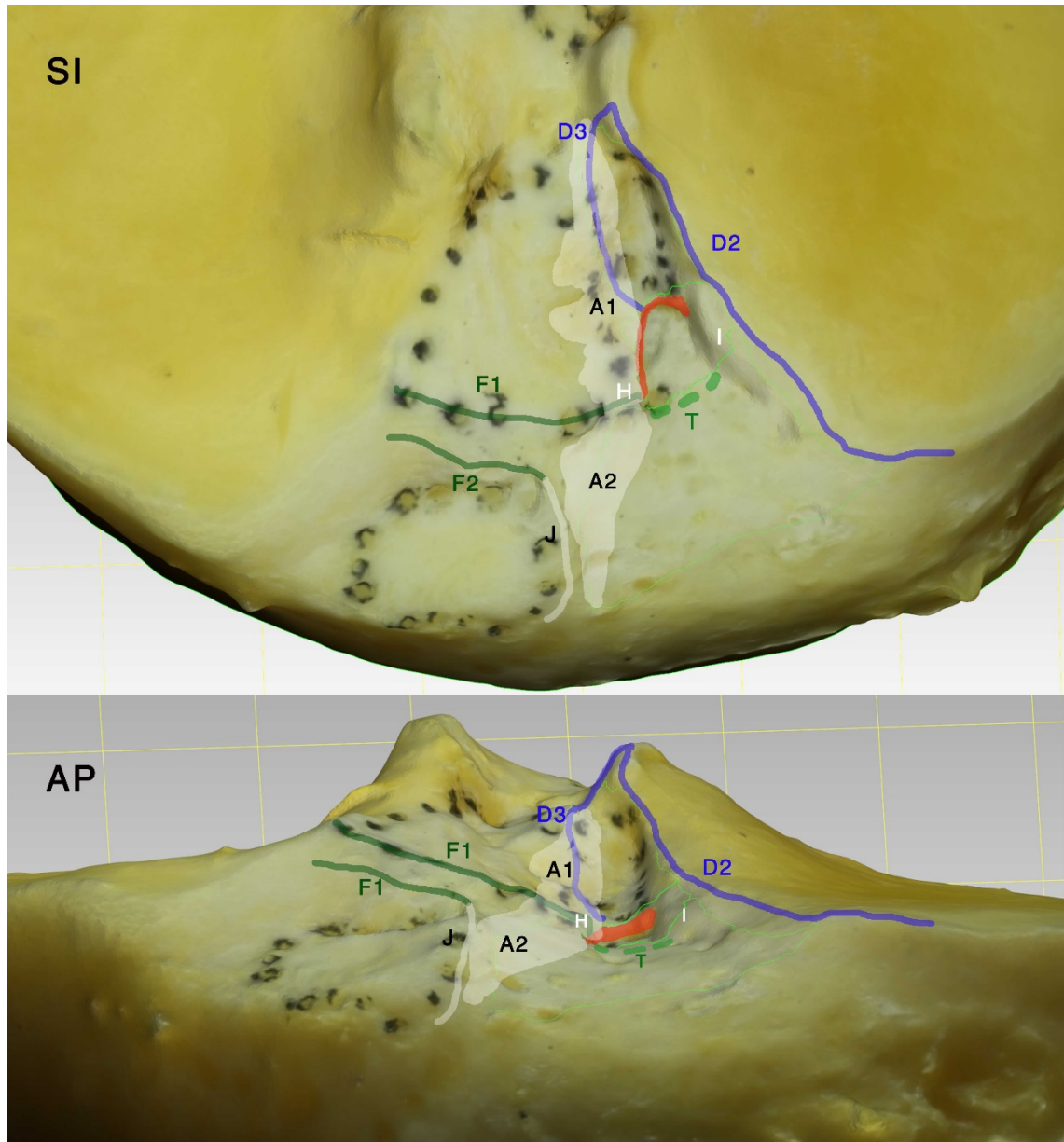


Figure 244. 3D model of Tibia A. Superoinferior (SI) and anteroposterior (AP) views of anterior intercondylar area with painted lines over the main processes (ALIR in blue, AFIR in green, anterior saddle in light green, AIAR and ASIR in white, anterolateral fossa's medial and posterior wall in red). The lateral-most border of F1 (H), and the anterolateral knob (I) are also labelled.

IV.6.2. Attachment of the anterior root of the lateral meniscus

Unlike the fibers of the other meniscal roots, there were no distinct density in the fibers of the anterior root of the lateral meniscus.

A part of lateral meniscal fibers blended with ACL fibers on the same surface. In this study, independent or “main” fibers were cut from the intermingled ones.

The attachment area of the main ARLM had a mean area of 38.8 mm² (95% CI 33.3 – 44.3 mm²; range, 20.6 mm² to 56.8 mm²), and it filled a great part of area 8 in most cases. Compared to area 8, it covered a mean of 78.2% (95% CI 61.5 – 94.9%; range, 46% to 141%; N=14).

The main ARLM attachment area was qualitatively found to fill the central and medial areas of the AL recess. Some fibers commonly inserted inferiorly into the posterior wall of the anterolateral fossa, down to the anterolateral fovea.

Main fibers were also commonly found inserted into the posterolateral aspect of area 10, up to the anterior aspect of the intertubercular ridge, and laterally into the posterior aspect of area 10.

In certain cases, a rough anterolateral meniscal footprint could be drawn with the internal PLIR process (D3) as its lateral border (Fig. 245).

In two specimens, the attachment of main ARLM fibers was observed up to the inner slope of the lateral tubercle, near the posterior root of the lateral meniscus, displaying an almost round lateral meniscus (Fig. 246).

The border between ARLM and ACL attachments was clear in 1 specimen; in 5 specimens there was some overlap between both areas; and in 6 specimens there was no clear distinction between the main fibers in their common border, with 2 specimens showing steadily intertwined fibers along the whole border.

The ARLM attachment was measured in reference to arthroscopically relevant landmarks, and it was found to be anterior to the LT anterior peak (4a); posterior to the AL fossa; lateral to the ACL border; medial to the ALIR; posterolateral to the anterocondylar knob, and to the PRLM center.

The center of the ARLM attachment was 2.7 ± 0.4 mm (range, 2.1 mm to 5 mm), from the most lateral aspect of the ACL attachment (in the shortest lateromedial line), a measurement that had a significant but low correlation with ML width ($r=0.57$, $p=0.003$), CV 27.86%. Proportionally, it represented 4 ± 0.5 % of the ML width of the proximal tibia.

The center of the ARLM attachment was also 3.8 mm (range, 2 mm to 4.8 mm), CV 19.48%, from the ALIR laterally (in the shortest mediolateral line), with a significant but low correlation with AP depth ($r=0.57$, $p=0.003$). Proportionally, it represented 7.5% of the AP measure of the proximal tibia. See Table 13 for all distances obtained from the center of the ARLM attachment to selected anatomic landmarks.

Table 13. Distances in mm, 95% CI, Coefficient of variation (CV), Pearson correlation values for AP and ML, with their corresponding p-values.

ARLM	MM	95% CI	CV	AP	AP P	ML	ML P
LT (4a)	12.0	10.8 – 13.3	17.98	0.129	0.661	0.182	0.534
ALF	5.3	4.3 – 6.3	33.31	0.219	0.453	0.230	0.430
ACL	2.7	2.3 – 3.2	27.86	0.376	0.185	0.575*	0.031
ALIR (D)	3.8	3.4 – 4.2	19.48	0.575*	0.031	0.518	0.058
ACIK (H)	10.0	8.2 – 11.8	29.86	0.495	0.086	0.472	0.103
PRLM	14.1	12.6 – 15.6	18.52	0.321	0.264	0.380	0.180

* Correlation is significant at the 0.01 level (2-tailed).

** Correlation is significant at the 0.05 level (2-tailed).

NOTE. In green, measurements taken in straight line, over the surface. In blue, measurements taken in the shortest straight (roughly ML) line.

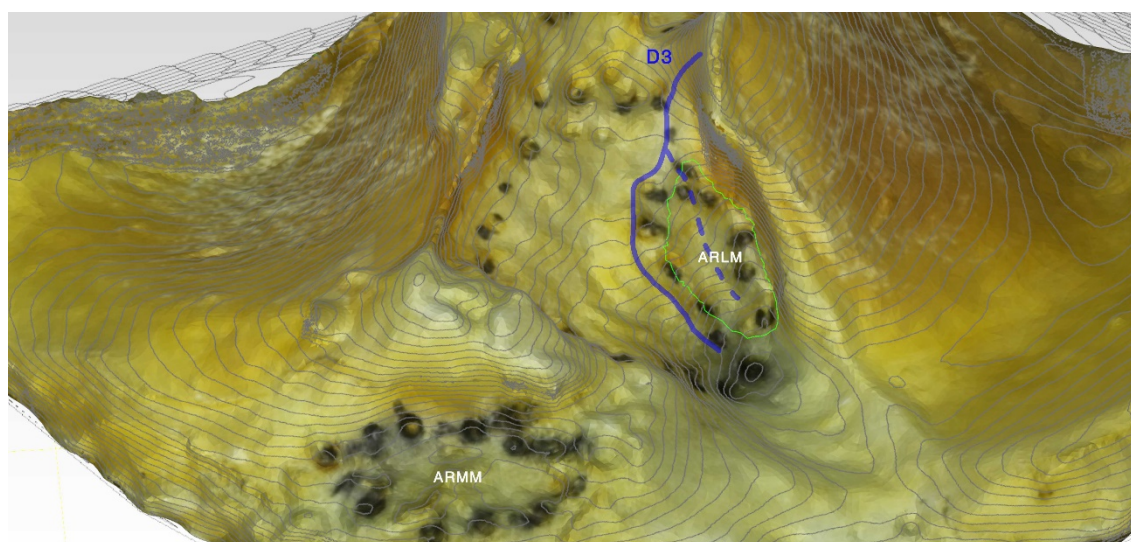


Figure 245.3D model of tibia N, with contour lines superimposed (left-mirrored). The internal ALIR process (D3, drawn in blue, with dotted line marking D3_b) is the osseous limit of a distinct ARLM footprint (delimited by a green line). The specimen shows degenerative changes: elevations of AMIR, AFIR, ASIR. Notice the horseshoe-like shape of area 10.

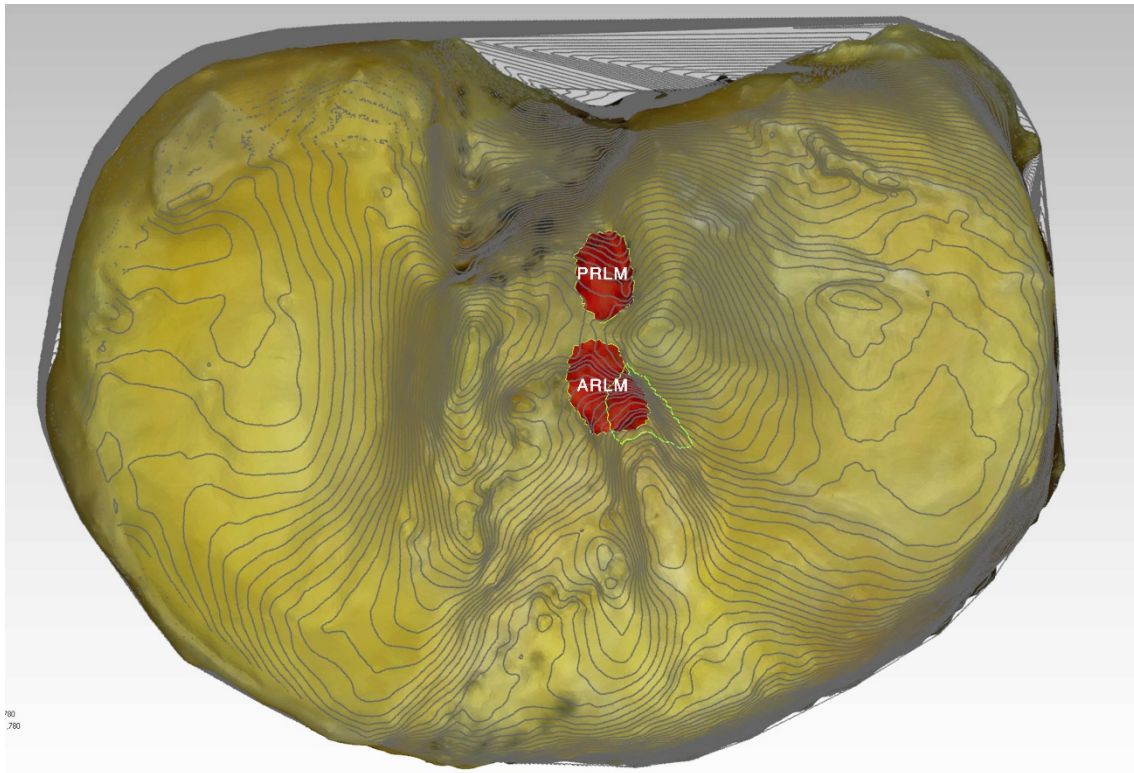


Figure 246. 3D model of tibia G, with contour lines superimposed. Attachments of the ARLM and PRLM are highlighted in red and labelled. The anterolateral fossa is selected (fluorescent green line).

IV.6.3. Degenerative changes of the anterolateral intercondylar area

IV.6.3.1. Qualitative assessment

The anterior intercondylar saddle, T, appeared usually elevated into a ridge connecting the antero-central intercondylar knob, H, with the medial wall of the lateral condyle, at or near the anterolateral intercondylar knob, I (Fig. 247).

The elevation of the ALIK could appear connected as an anterolateral tubercle to the ACIK (through the anterior saddle), to the AL corner, and also to an elevated area 9 (Fig. 248).

Degenerative changes seemed to affect more the areas surrounding the anterolateral fossa: its lateral and medial walls were often found more elevated, as were the anterior saddle and the anterior vallecule, leaving area 7 as a fossa surrounded by elevations, only connecting smoothly with the incisures found in area 10. When degenerative changes affected the bottom of the fossa, the posterior wall (and thus its differentiation with area 8) could become blurred, but this seemed to happen only with high degenerative changes.

The AL vallecule was often found slightly elevated, still forming an anterolateral groove together with the AL fossa, but it could also be found quite elevated, even to a maximum grade-5 osteophyte, usually together with the surrounding elevated areas, like the ACIK, ALIK, or AL corner. In such cases, the AL fossa remained as the only depressed area, surrounded by elevations.

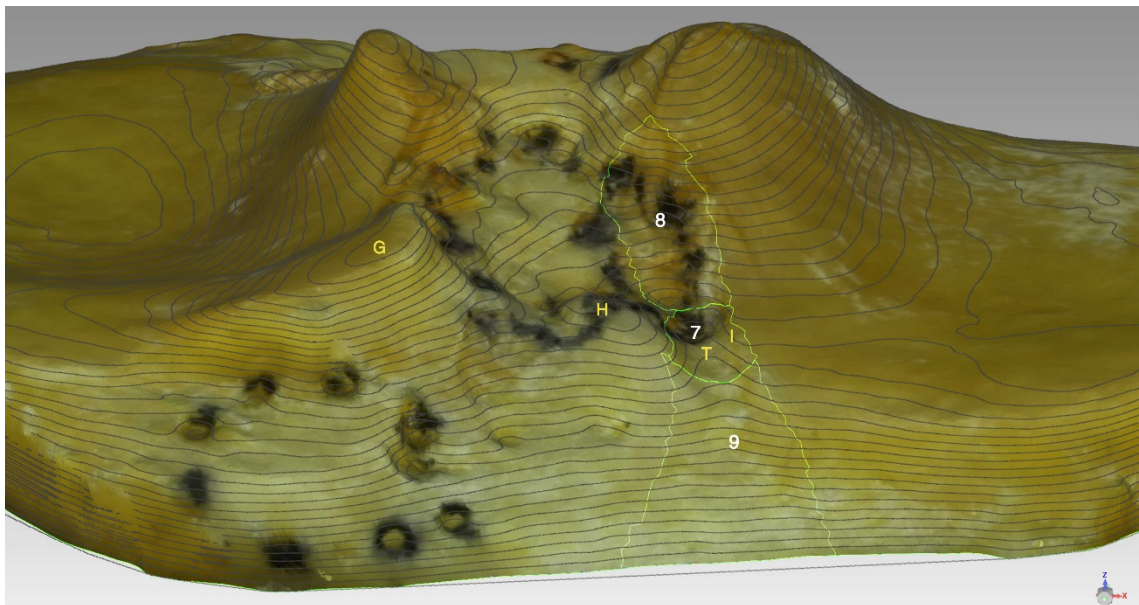


Figure 247. 3D model of tibia E with contour lines superimposed. Areas of the anterolateral groove are selected and labelled (in white). Some degenerative changes can be observed: notice how the slight elevations of the anterocentral knob (H), saddle (T), and anterolateral knob (I) close the space of areas 7 and 9. Parsons' knob (G) has also been labelled.

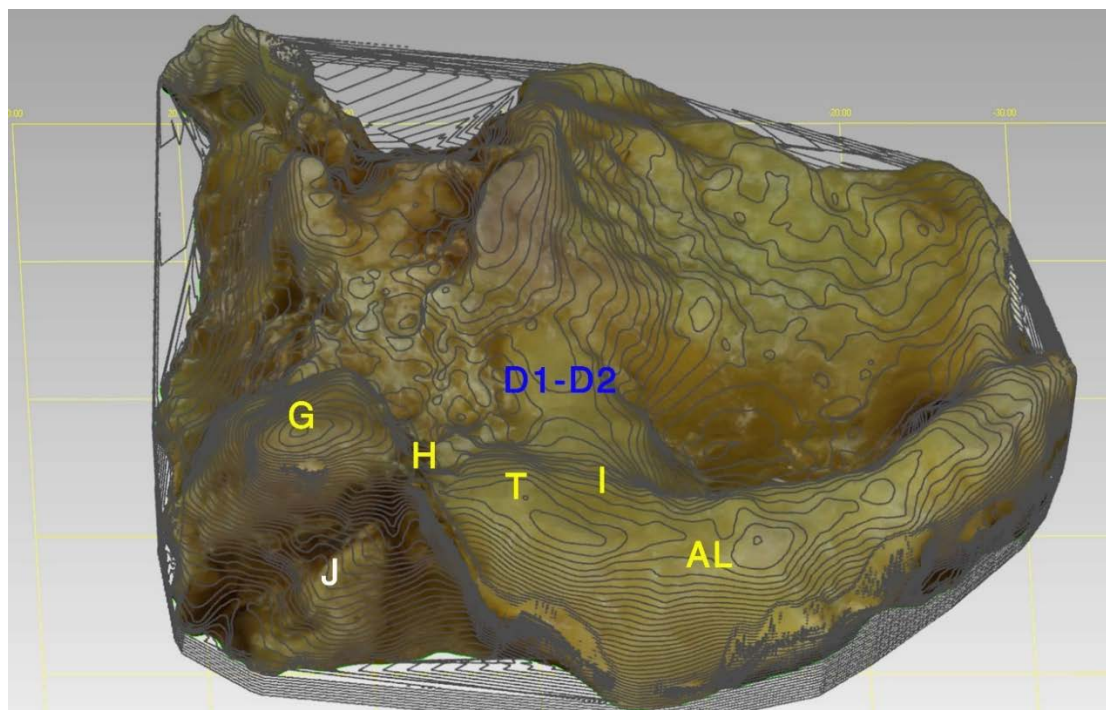


Figure 248. 3D model of tibia 85 with contour lines superimposed. Observe the elevations of D1-D2, Parsons' tubercle (G), ACIK (H), ASIR (J), anterior saddle (T), ALIK (I), and AL corner (continuous with the lateral rim). Elevations cover area 9, leaving just a narrow non-elevated aspect lateral to the ASIR. Notice the marked osseous attrition in the medial condyle (absent in the 3D model) and in the posterior aspect of the lateral condyle.

IV.6.3.2. Quantitative assessment

The anterolateral fossa elevation showed no significant correlation with knee OA (Fig. 249): $r_s(98)=0.142$, $p=0.162$.

The anterior saddle ridge elevation, T, showed a weak correlation with knee OA (Fig. 250): $r_s(95)=0.275$, $p=0.007$.

The AL vallecule elevation also showed a weak correlation with knee OA (Fig. 251): $r_s(93)=0.246$, $p=0.018$. The relation of its osteophytic changes with nearby structures did not show an association with knee OA (Fig. 252): $\chi^2(24)=32.468$, $p=0.116$.

Osteophyte/depression grades of the AL recess showed no significant correlation with knee OA (Fig. 253): $r_s(98)=0.098$, $p=0.337$.

The osteophyte grade of the anterolateral intercondylar knob showed a significant, moderate correlation with knee OA (Fig. 254), $r_s(93)=0.439$, $p<0.001$. Its shape was also strongly associated with OA (Fig. 255), $\chi^2(36)=59.564$, $p=0.008$ ($\Phi=0.736$, Cramer's $V=0.368$). Frequency distribution analysis showed a bigger size more commonly found with higher OA grades; tongue-shaped more frequent than cone-shaped osteophytes in higher OA grades; and ridge-shaped more common than cone-shaped knobs in lower OA grades.

There was no significant association between knee OA and the union of the anterolateral knob with the anterolateral corner into a common osteophyte (Fig. 256), $\chi^2(4)=2,483$, $p=0.648$.

The AL vallecule showed a strong positive association with the shape of the anterolateral intercondylar knob (Fig. 257): $\chi^2(72)=108.082$, $p=0.004$ ($\Phi=1.078$, Cramer's $V=0.381$). Frequency distribution analysis showed a similar relation to the one found in the comparison between the anterolateral knob and knee OA: ridge-type shapes with less elevation, and proportionally more cone-type, and especially tongue-type shapes with more elevation.

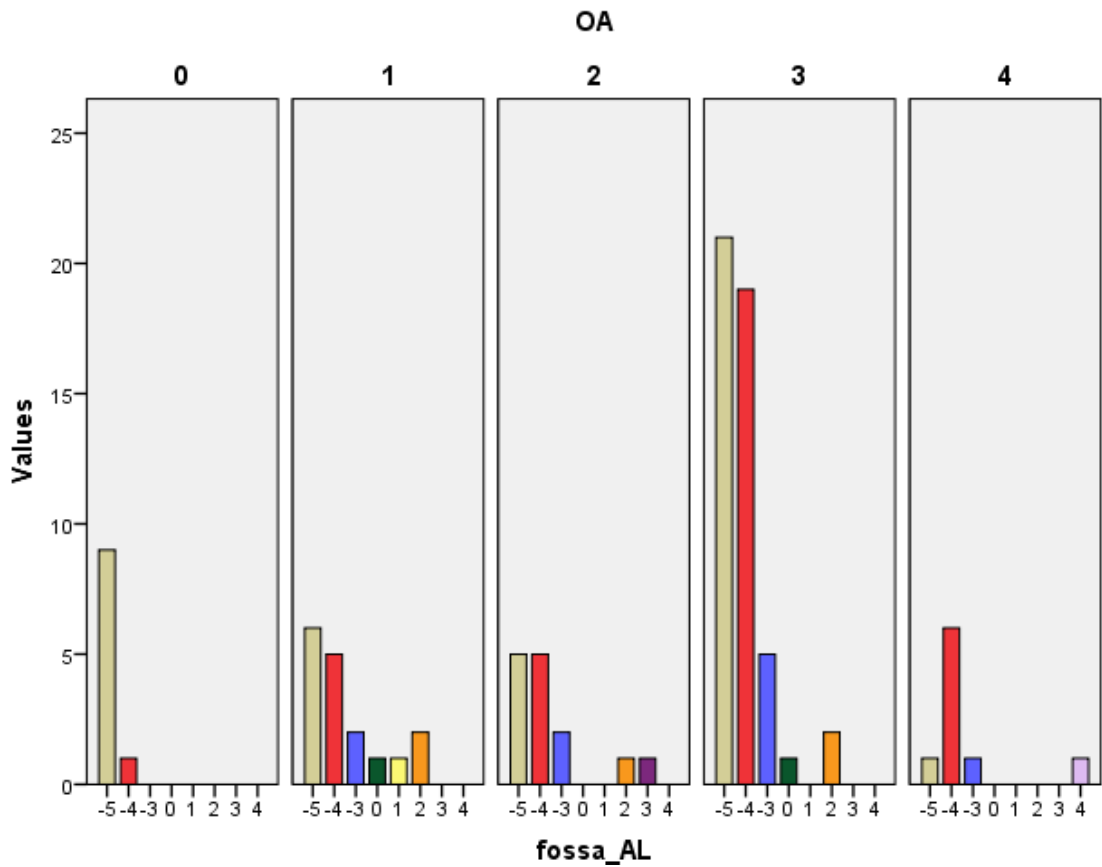


Figure 249. Study II. Histogram of AL fossa osteophyte grade: number of tibias in each category, grouped by Ahlbäck OA grade.

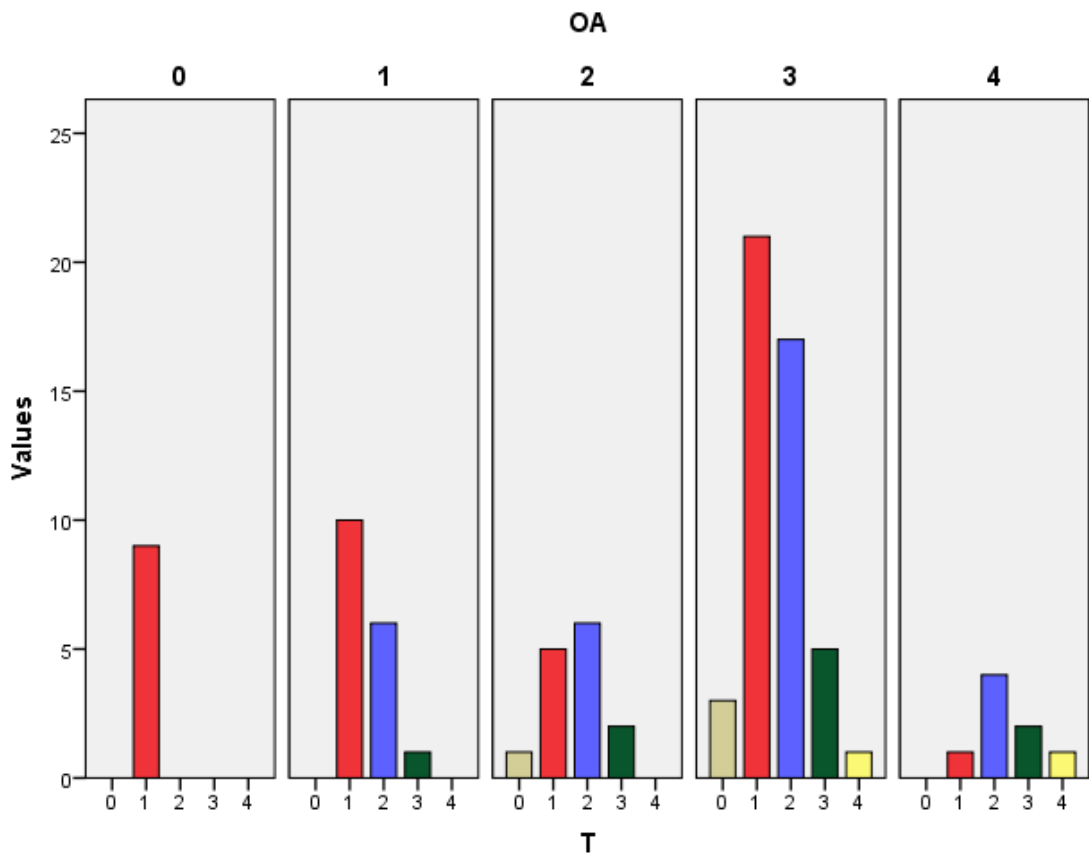


Figure 250. Study II. Histogram of anterior saddle (T) osteophyte grade: number of tibias in each category, grouped by Ahlbäck OA grade.

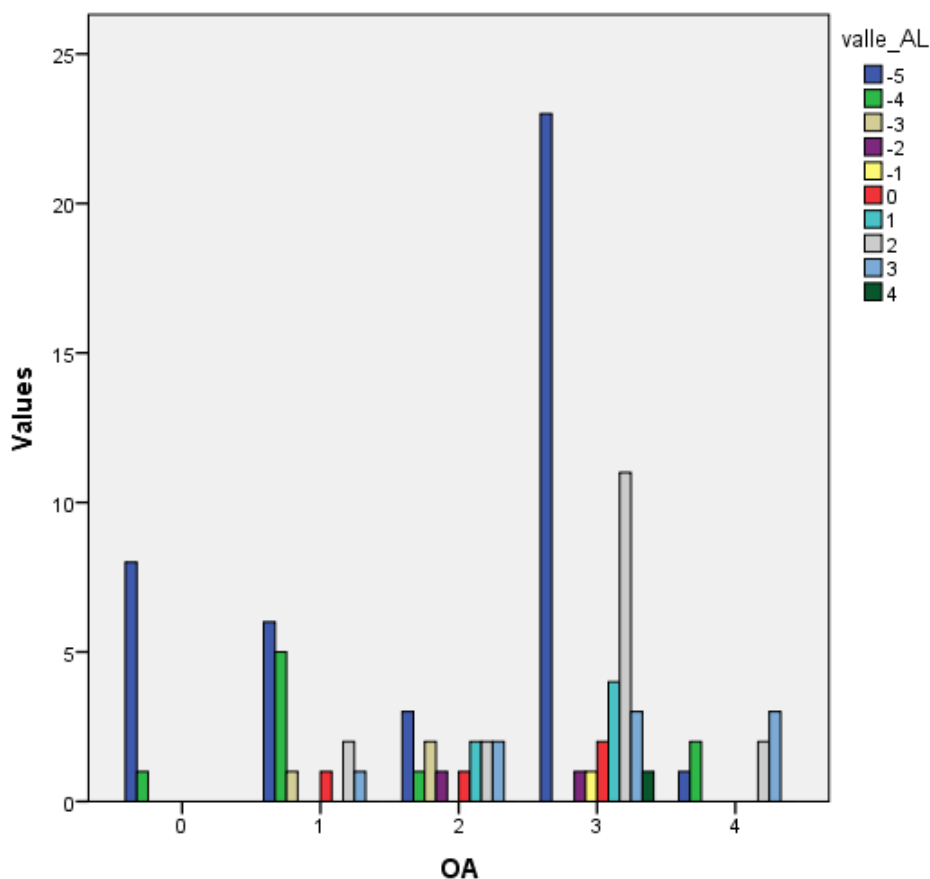


Figure 251. Study II. Histogram of anterolateral vallecule (valle_AL) osteophyte grade: number of tibias in each category, grouped by Ahlbäck OA grade.

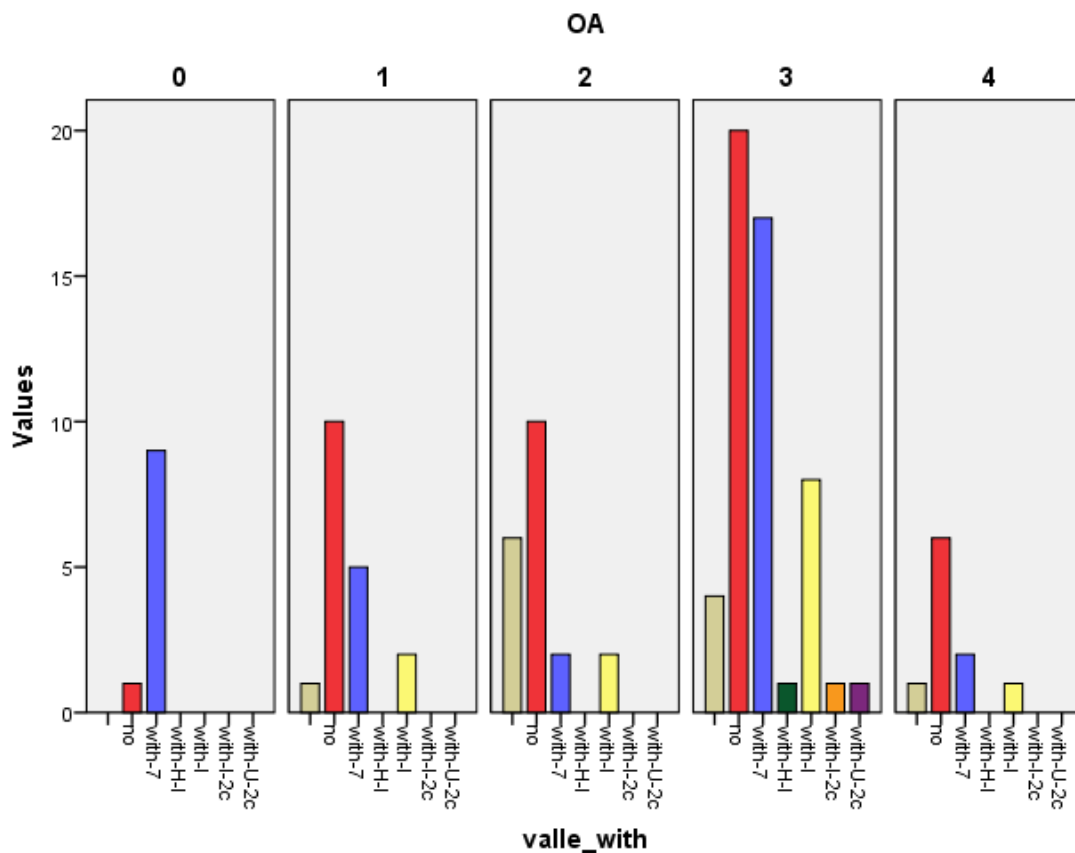


Figure 252. Study II. Histogram of relationship of anterior vallecule elevation with neighboring structures (valle_with): number of tibias in each category, grouped by Ahlbäck OA grade. U: ASIR. "with-" means "area 9 elevated together with".

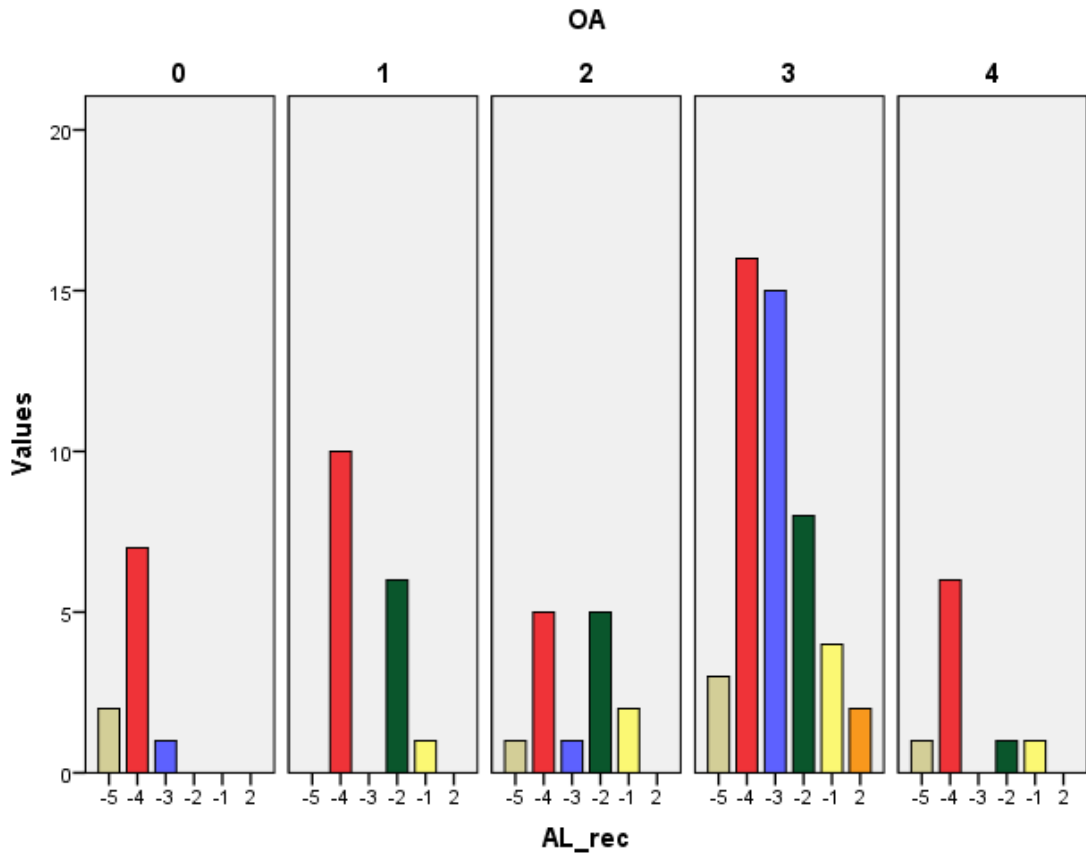


Figure 253. Study II. Histogram of anterolateral recess (AL_rec) depression grade: number of tibias in each category, grouped by Ahlbäck OA grade.

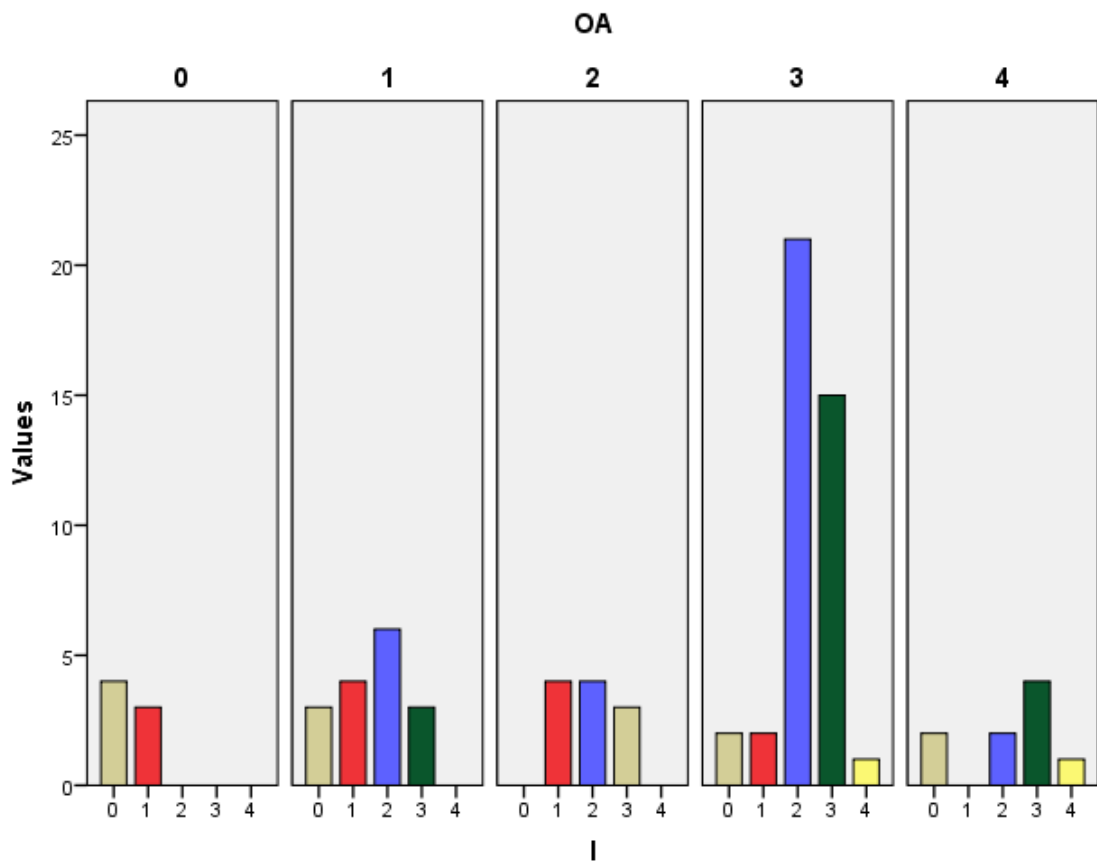


Figure 254. Study II. Histogram of anterolateral intercondylar knob (I) osteophyte grade: number of tibias in each category, grouped by Ahlbäck OA grade.

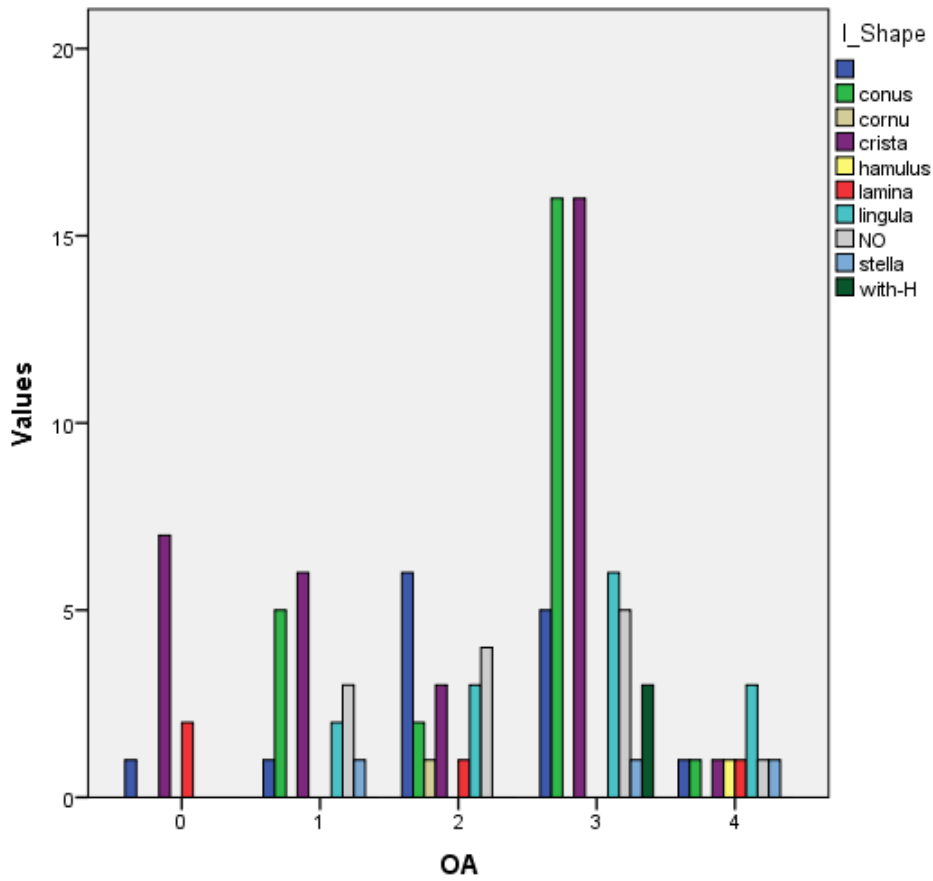


Figure 255. Study II. Histogram of anterolateral intercondylar osteophyte shape (I_Shape): number of tibias in each category, grouped by Ahlbäck OA grade. with-H: elevated together with ACIK.

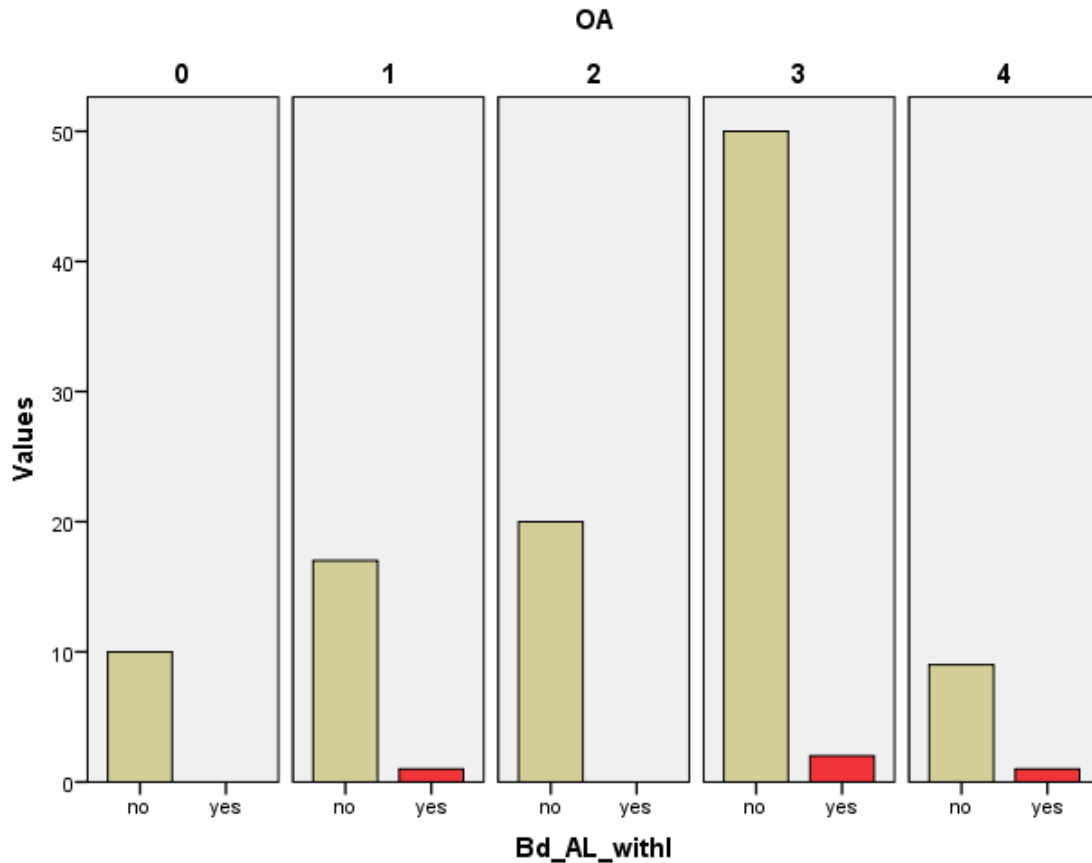


Figure 256. Study II. Histogram of anterolateral intercondylar osteophyte union with the AL corner (Bd_AL_withI): number of tibias showing a connected osteophyte.

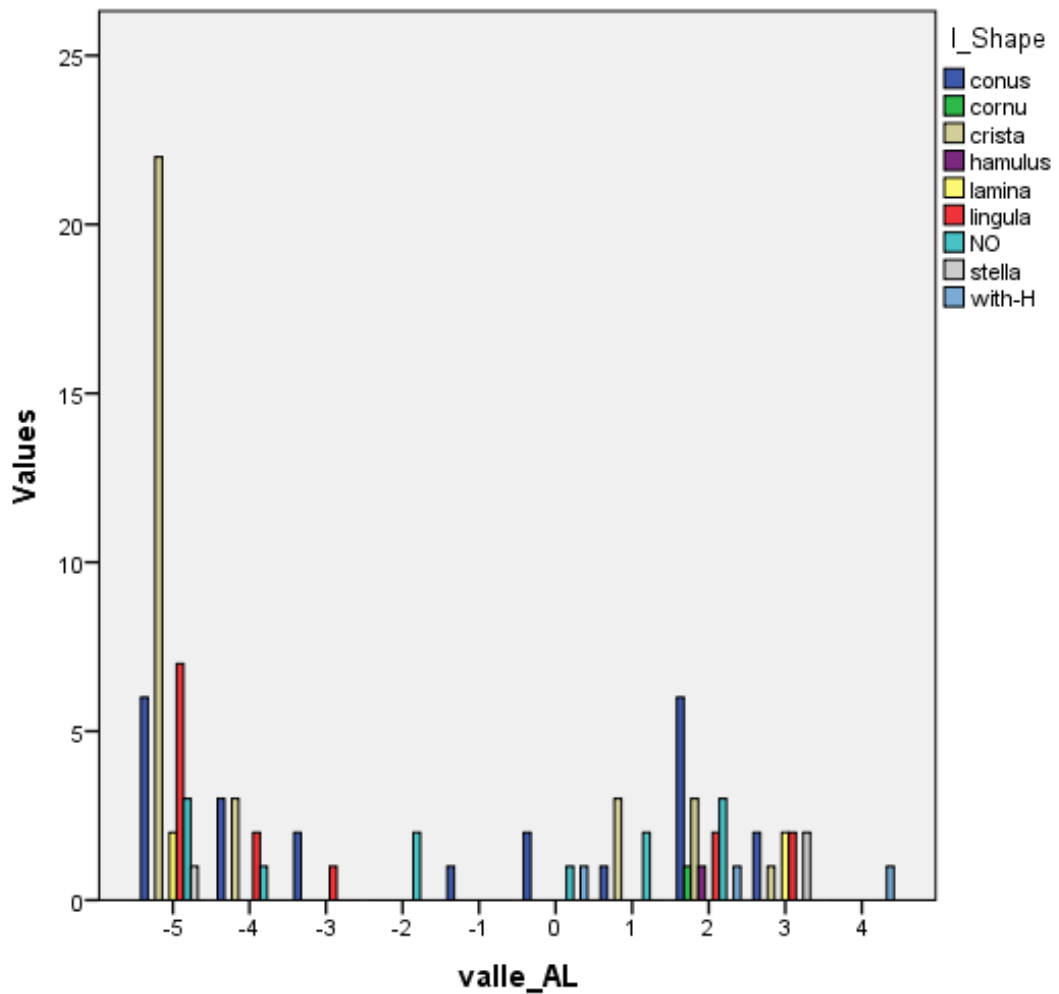


Figure 257. Study II. Histogram of anterolateral intercondylar osteophyte shape (I_Shape): number of tibias in each category, grouped by anterolateral vallecule osteophyte grade. with-H: elevated together with ACIK.

IV.7. Posteromedial part of the anterior intercondylar area

IV.7.1. Anterior intercondylar staircase

The posterior part of the domed medial aspect of the AIA was found as a quarter-turn-staircase-shaped ridge, the anterior intercondylar staircase (AIS), **10**. It connected the higher intertubercular ridge posteriorly with the lower anterolateral fossa laterally, and it was delimited medially by the external AMIR process (B1), anteriorly by the posterior AFIR process (F1), laterally by the posterior AIAR process (A1), and posteriorly by the anterior wall of the intertubercular ridge (area 15).

Viewed from above, area 10 had an irregular, polygon-like shape with rounded borders (Fig. 258), ranging from an acute isosceles triangle – with two similar medial and lateral longer sides – (5 specimens), to a general irregular quadrilateral – with a smaller, arch-like posterior side (4 specimens), with intermediate shapes showing a more triangular shape, but with a wider posterior side (5 specimens).

Given the complexity of the three-dimensional anatomical landmarks of the staircase – with structures crossing it in different directions (such as slopes and ridges, and lines and indentations) –, it will be described in two different ways.

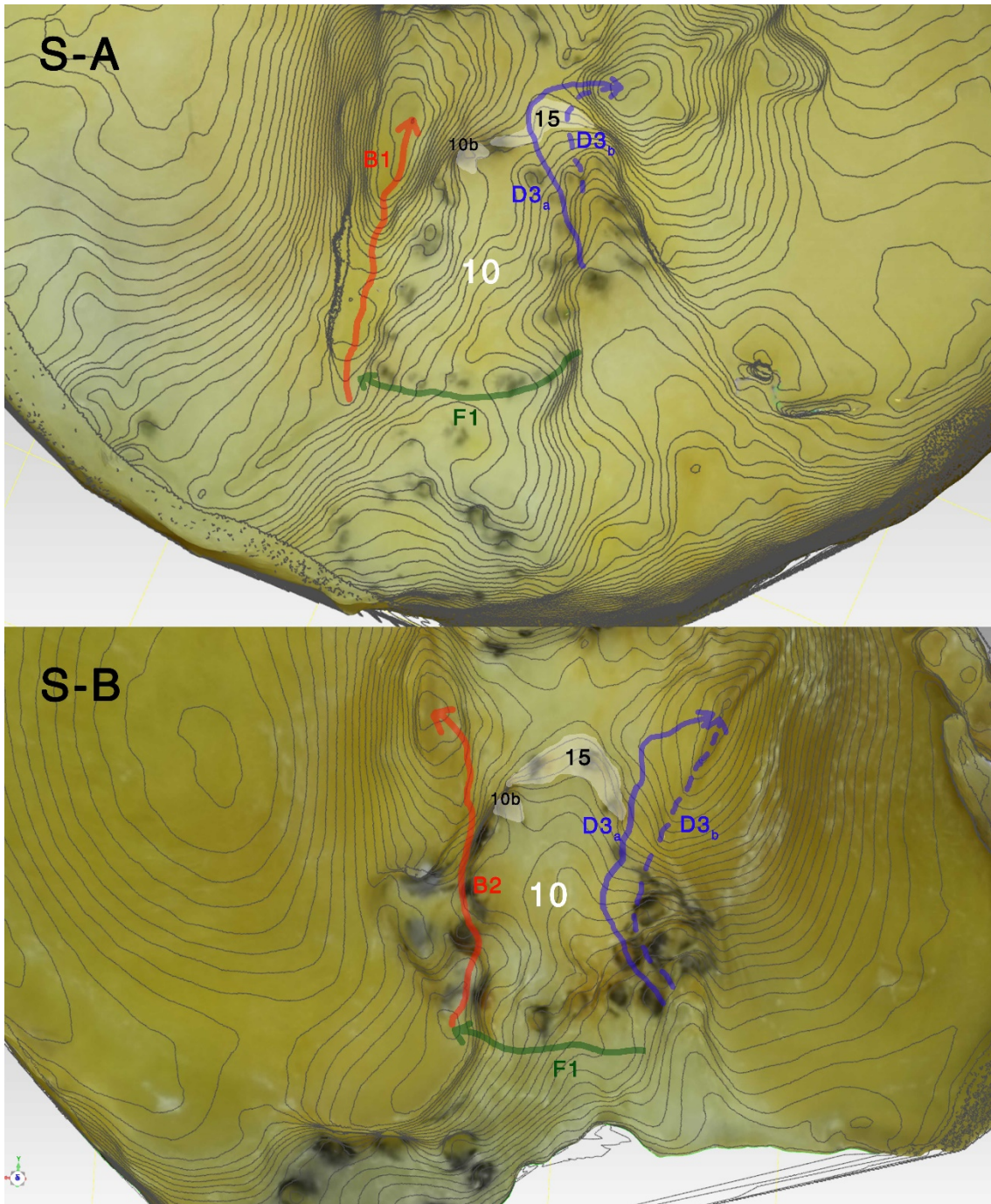


Figure 258. Superoinferior view of the anterior intercondylar area of 3D models of tibias M (S-A) and J (S-B), with contour lines superimposed, with painted lines over the main processes (AMIR in red, ALIR in blue, AFIR in green, posterior wall of area 10 (area 15) and anteromedial fovea in white. Observe in tibia J, with slight degenerative changes, the more rectangular shape of area 10, the elevated central AMIR process (B2), elevated Parsons' knob, and how D3 processes form macroscopically a single D3 line (see below).

IV.7.1.1. Lines and indentations of the anterior intercondylar staircase

Observed in a mediolateral direction, the staircase showed a domed medial aspect, and a steep downward slope laterally (the posterior AIAR, A1) leading to the anterolateral recess and fossa.

The anterolateral fossa gives way in most tibias to a laterally concave indentation in the AIAR, the AIS concavity, **A1b**.

With more detail, different constant lines and indentations could be seen crossing the area (Fig. 259, Fig. 260):

- The posterolateral aspect of area 10 was a medially convex curve, the internal PLIR process (D3), separating the posterolateral aspect of the staircase from area 8. When viewed from anterior, this structure looked like a very steep, almost vertical structure, a sort of AIS “ladder”.
 - A constant incisure was found anterior to D3, **10j**.
- A constant AIS sagittal incisure, **10g**, was found anterior to D3. Its lateral origin was the concavity, and it followed a laterally concave curve. Up to three branches could be distinguished in the posteromedial aspect of the incisure: the main, sagittal branch, **10g₁**, which followed the main indentation into the center of area 15; the oblique branch, **10g₂**, leading directly to area 10b; and the most medial, coronal branch, **10g₃**, which showed an inflection point at or near its crossing with the AIAR, and turned to an anteriorly concave curve.
- A constant AIS coronal incisure, **10h**, was found anterior to the sagittal incisure. It had the same lateral origin as the sagittal incisure (the concavity), showed also a mediolateral orientation, but it separated obliquely in its medial aspect with a milder curve similar to the posterior AFIR.
- The posterior AFIR, F1, was the ridge found anterior to the coronal incisure. In tibias without degenerative changes, an incisure, **10i**, could be described just posterior to F1, different from 10h.
- The anterior border between the stairs and the AIAR (between 10g and 10h or 10i) showed frequently a slight elevation, the sagittal line, **10k**.

Area 10 of all specimens studied are shown with main incisures found in Fig. 261 – Fig. 274.

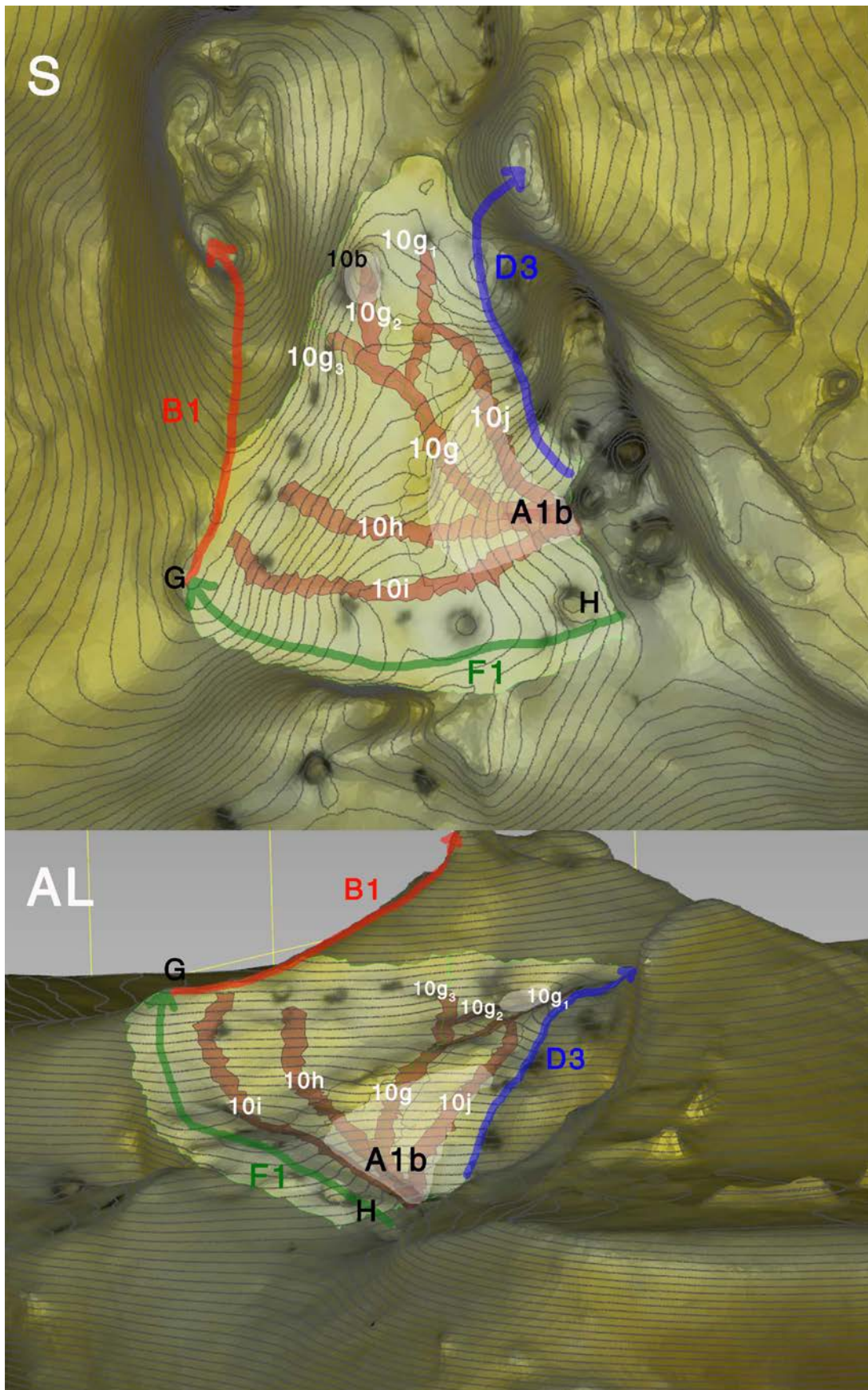


Figure 259. 3D model of Tibia A with contour lines superimposed and area 10 surface highlighted. Superoinferior (S) and anterolateral (AL) views. Common incisures highlighted in red and labelled in white. Also labelled are the ALIR in blue, the AMIR in red, the AFIR in green, and the geniculum (G), the anteromedial fovea (10b), the ACIK (H), and the AIAR (A1b) in black (with the concavity in transparent white). Selected but not labelled are the sagittal line (between 10i, 10h, and 10g), and the posterior line (between 10g, 10j).

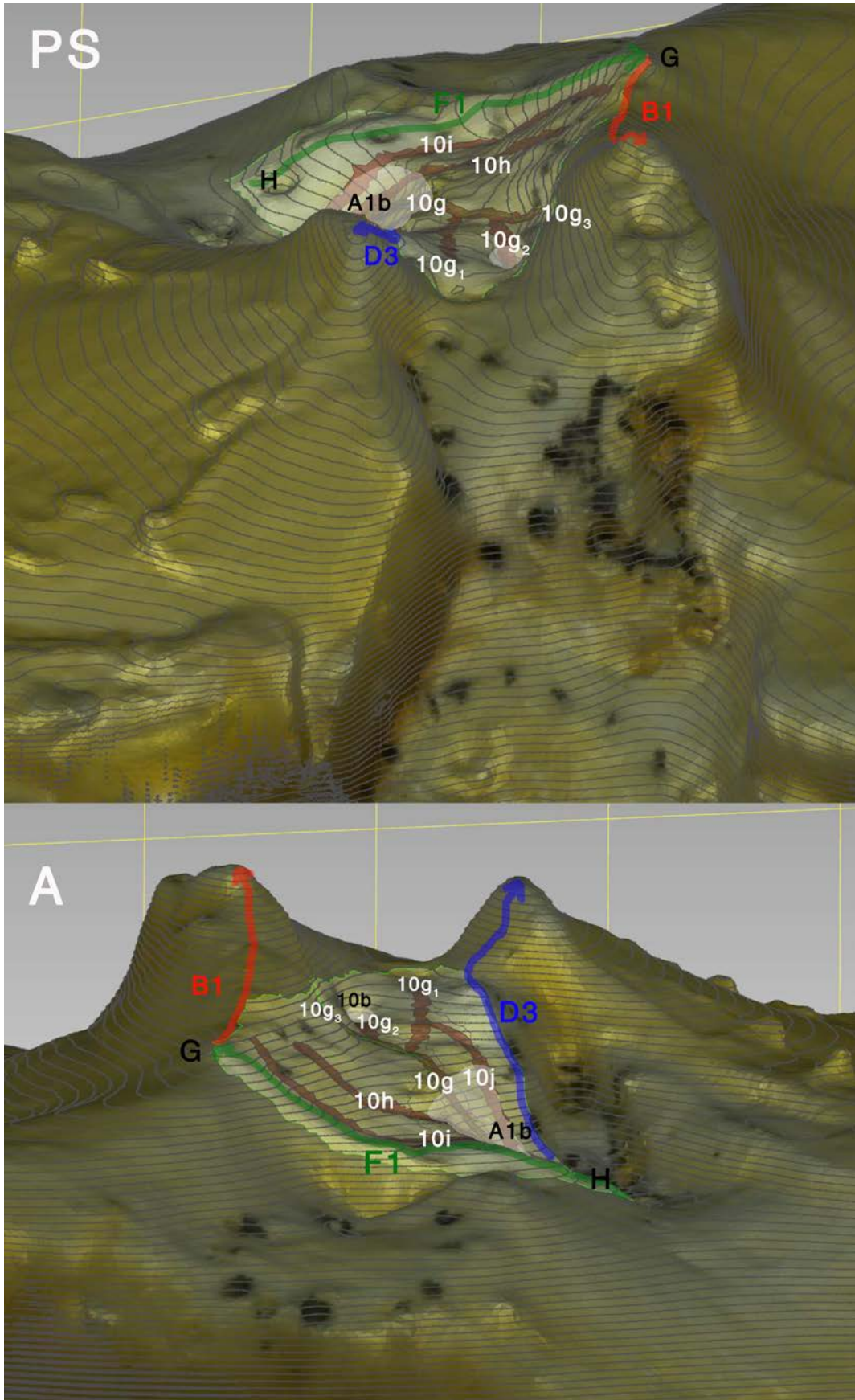


Figure 260. 3D model of Tibia A with contour lines superimposed and area 10 surface highlighted. Posterosuperior (PS) and anteroposterior (A) views. Common incisures highlighted in red and labelled in white. Also labelled are the ALIR in blue, the AMIR in red, the AFIR in green, and the geniculum (G), the anteromedial fovea (10b), the ACIK (H), and the AIAR (A1b) in black (with the concavity in transparent white). Selected but not labelled are the sagittal line (between 10i, 10h, and 10g), and the posterior line (between 10g, 10j).

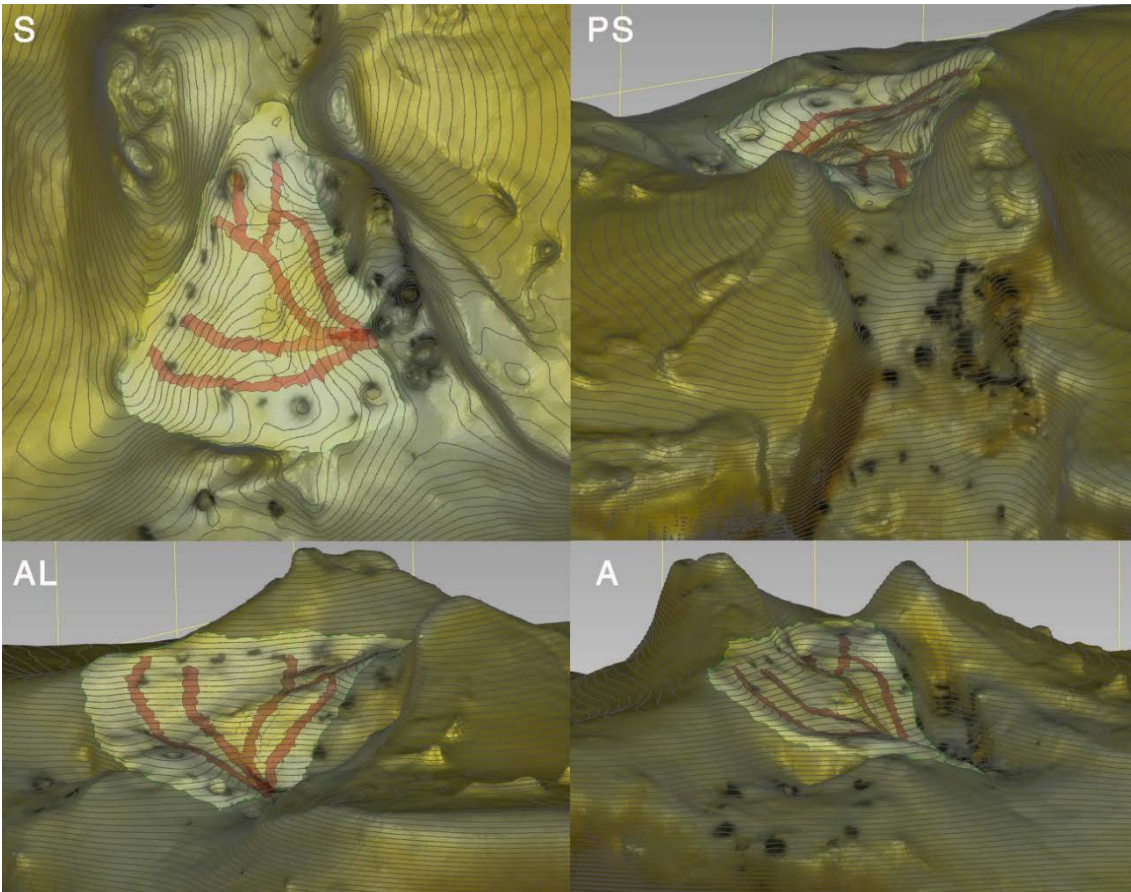


Figure 261. 3D model of tibia A with contour lines. Area 10 highlighted. Incisures selected in red.

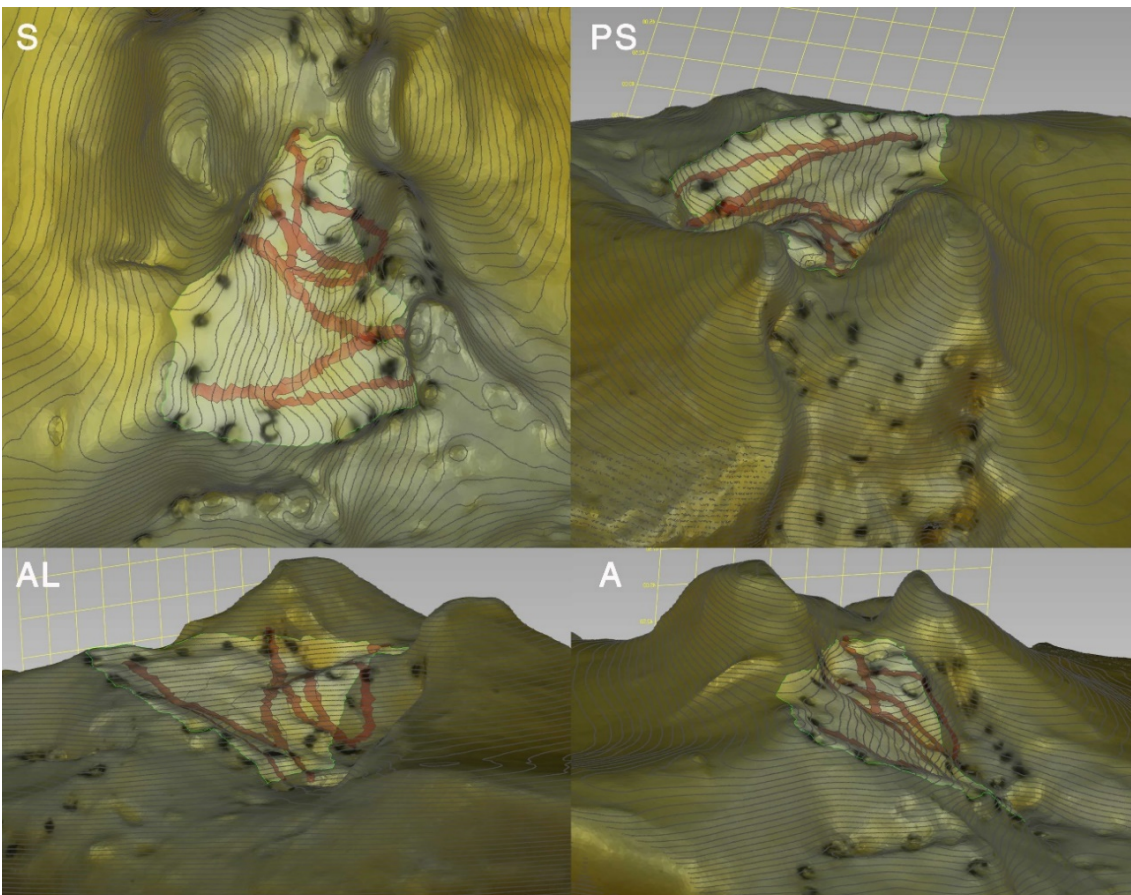


Figure 262. 3D model of tibia B with contour lines. Area 10 highlighted. Incisures selected in red.

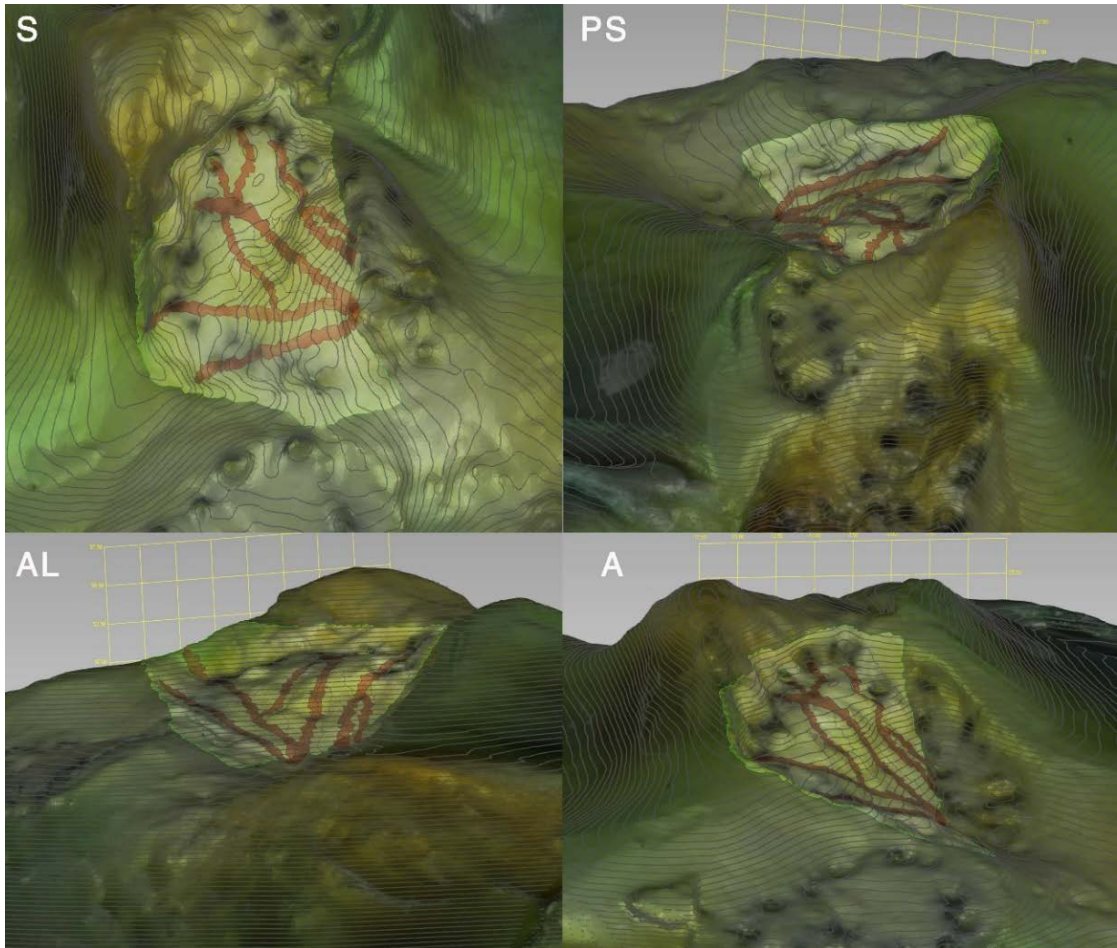


Figure 263. 3D model of tibia C with contour lines. Area 10 highlighted. Incisures selected in red.

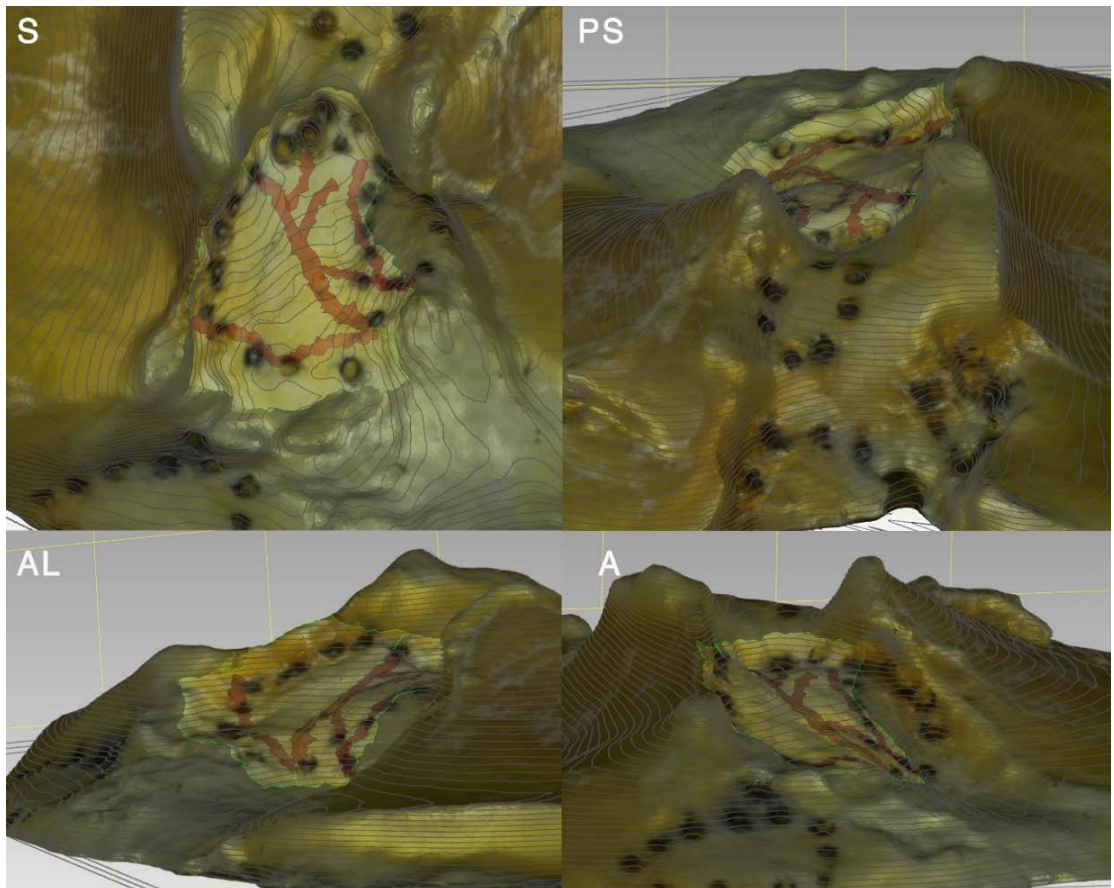


Figure 264. 3D model of tibia D with contour lines. Area 10 highlighted. Incisures selected in red.

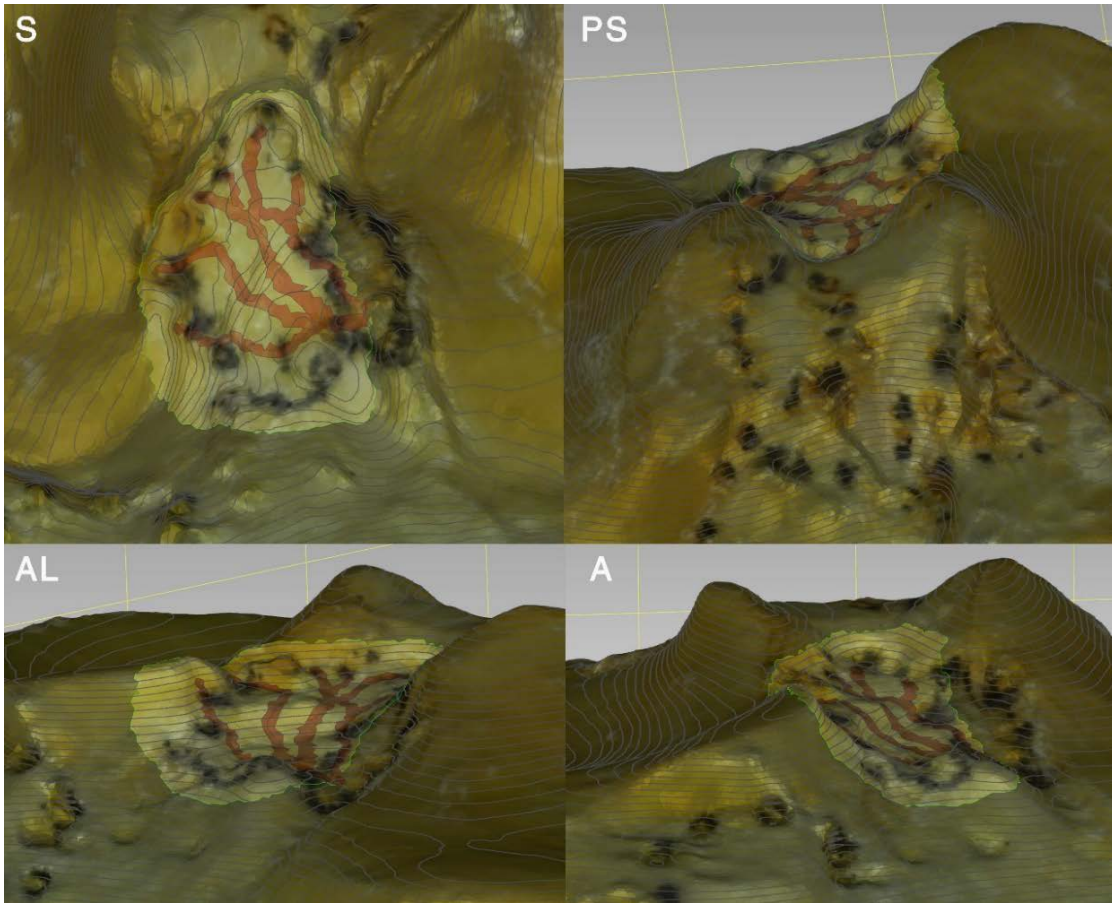


Figure 265. 3D model of tibia E with contour lines. Area 10 highlighted. Incisures selected in red.

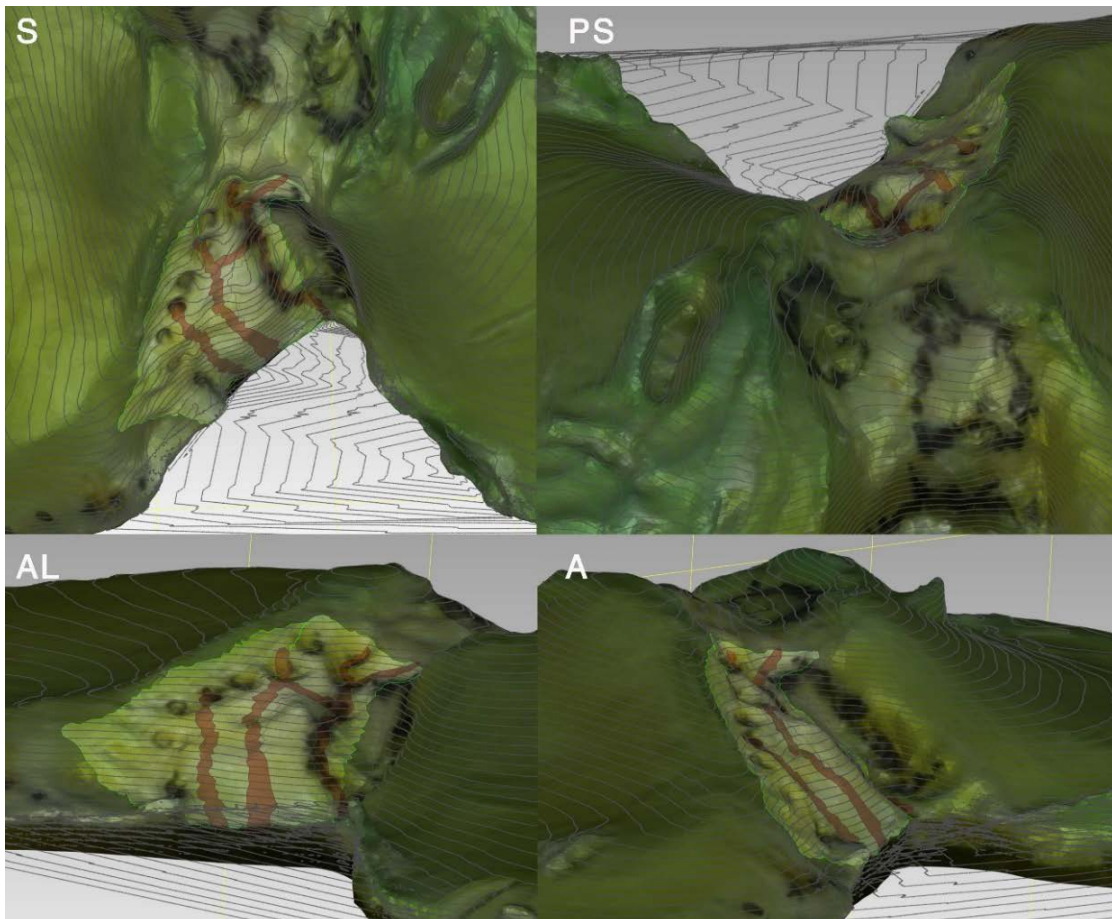


Figure 266. 3D model of tibia F with contour lines. Area 10 highlighted. Incisures selected in red.

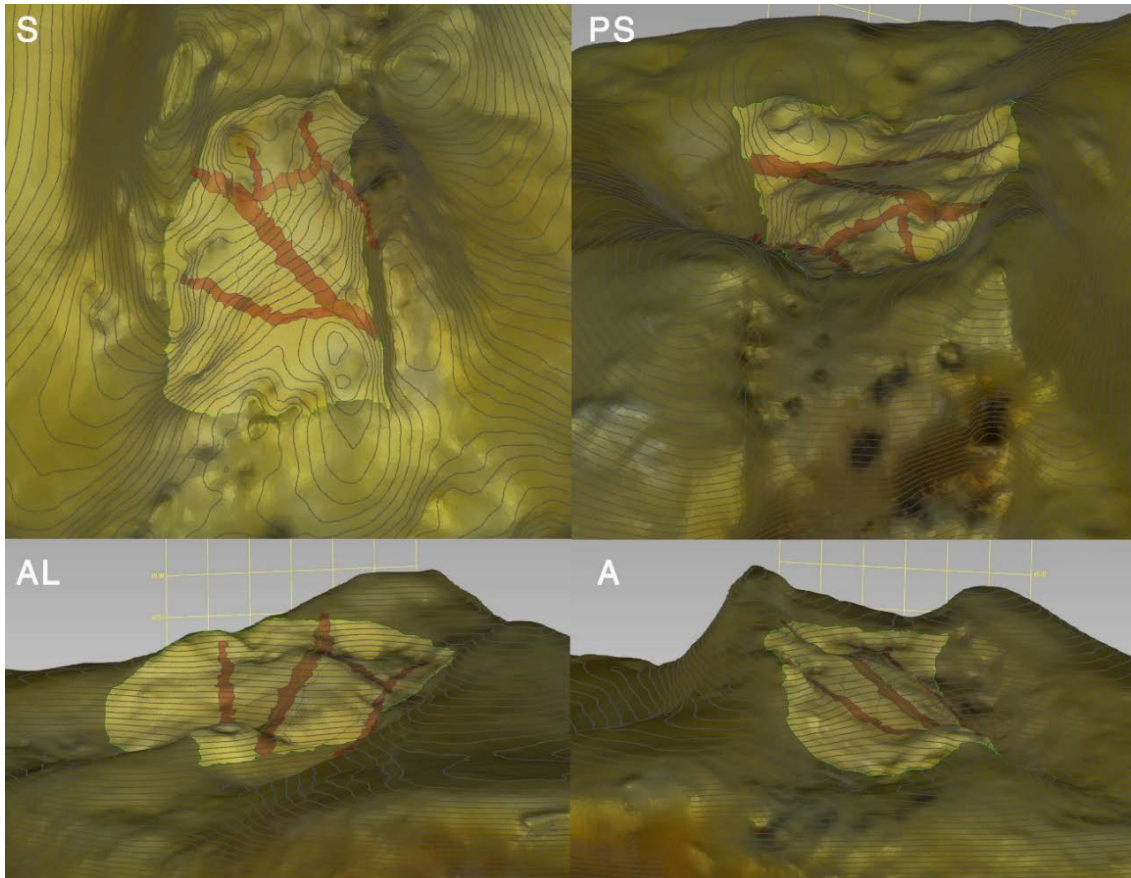


Figure 267. 3D model of tibia G with contour lines. Area 10 highlighted. Incisures selected in red.

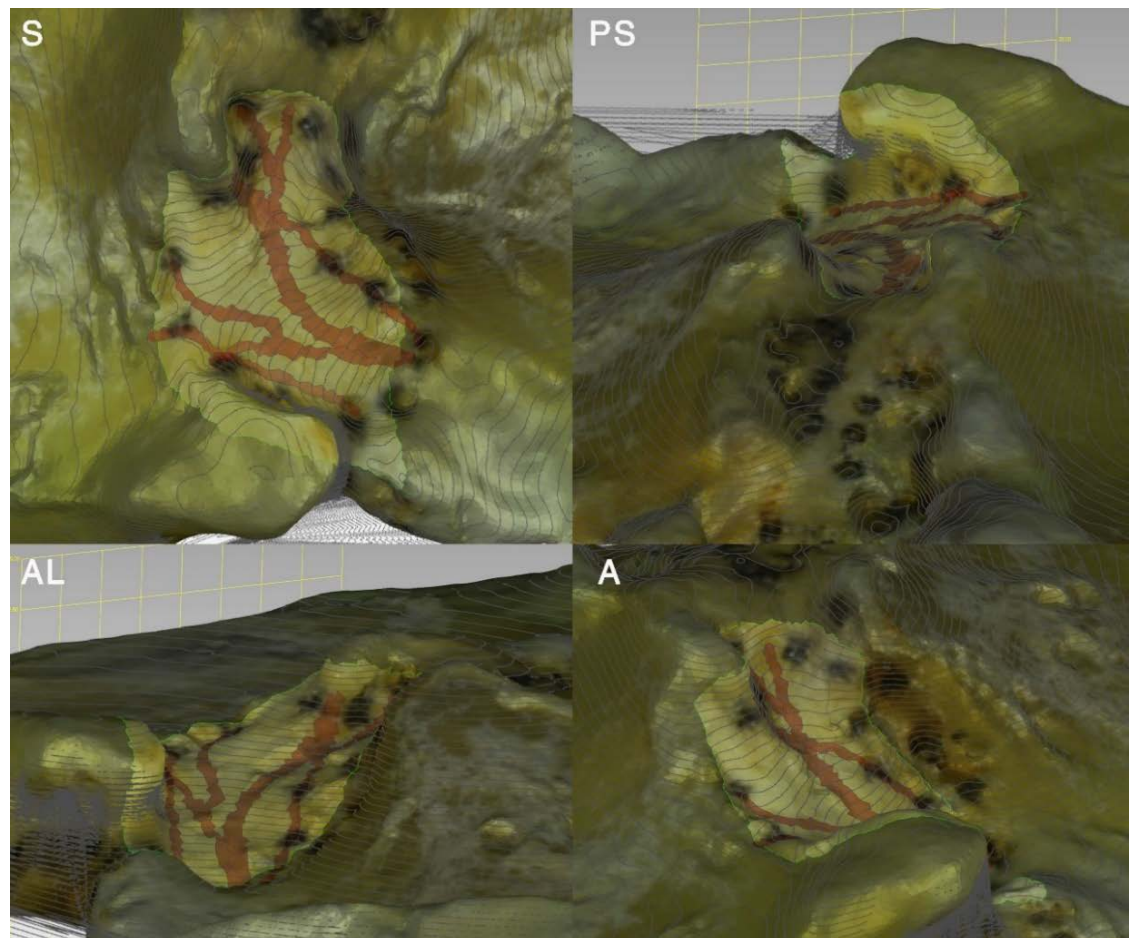


Figure 268. 3D model of tibia H with contour lines. Area 10 highlighted. Incisures selected in red.

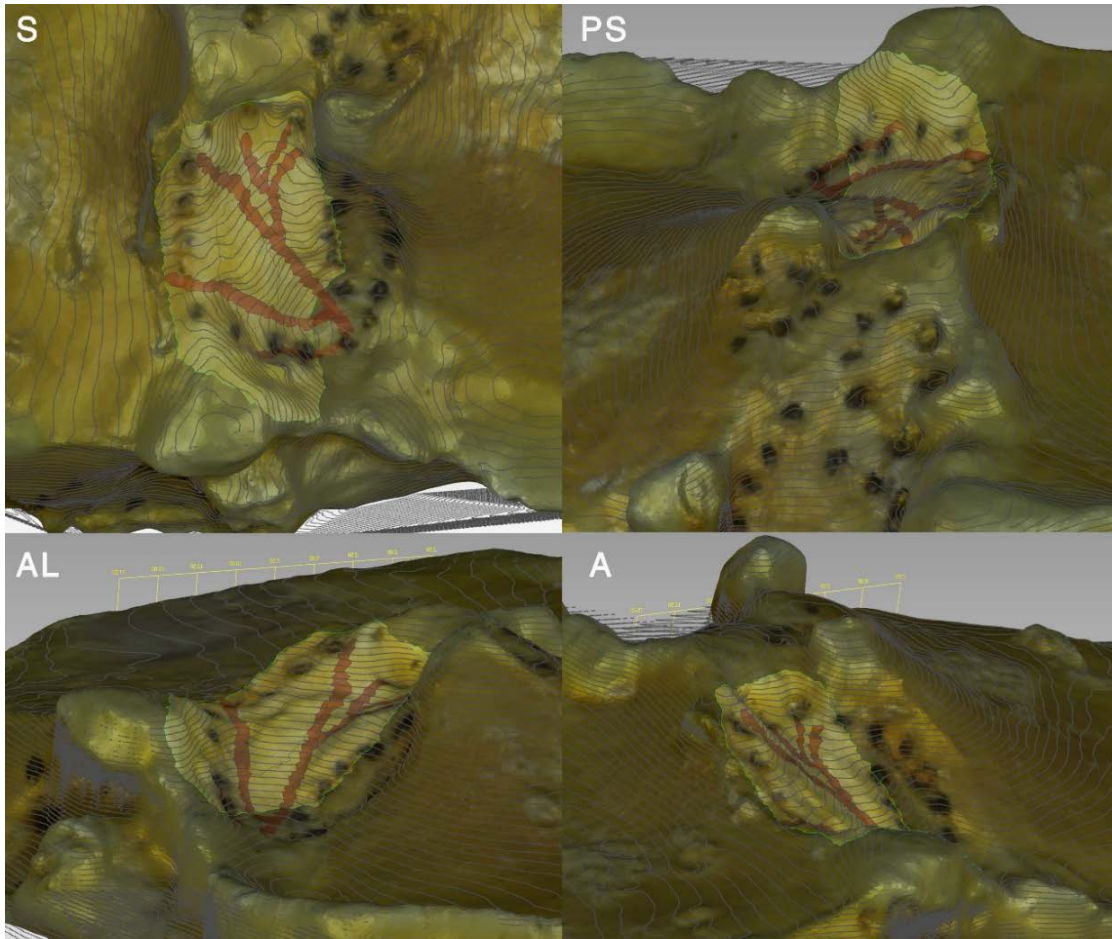


Figure 269. 3D model of tibia I with contour lines. Area 10 highlighted. Incisures selected in red.

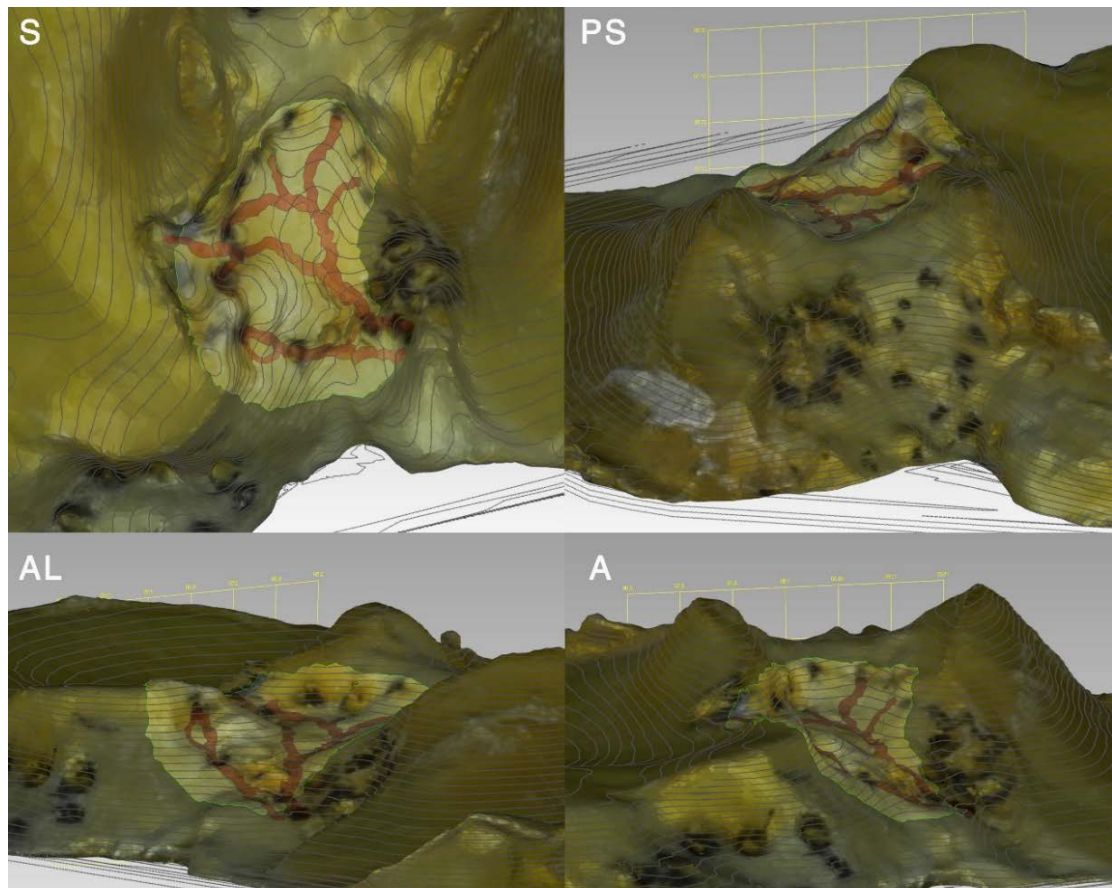


Figure 270. 3D model of tibia J with contour lines. Area 10 highlighted. Incisures selected in red.

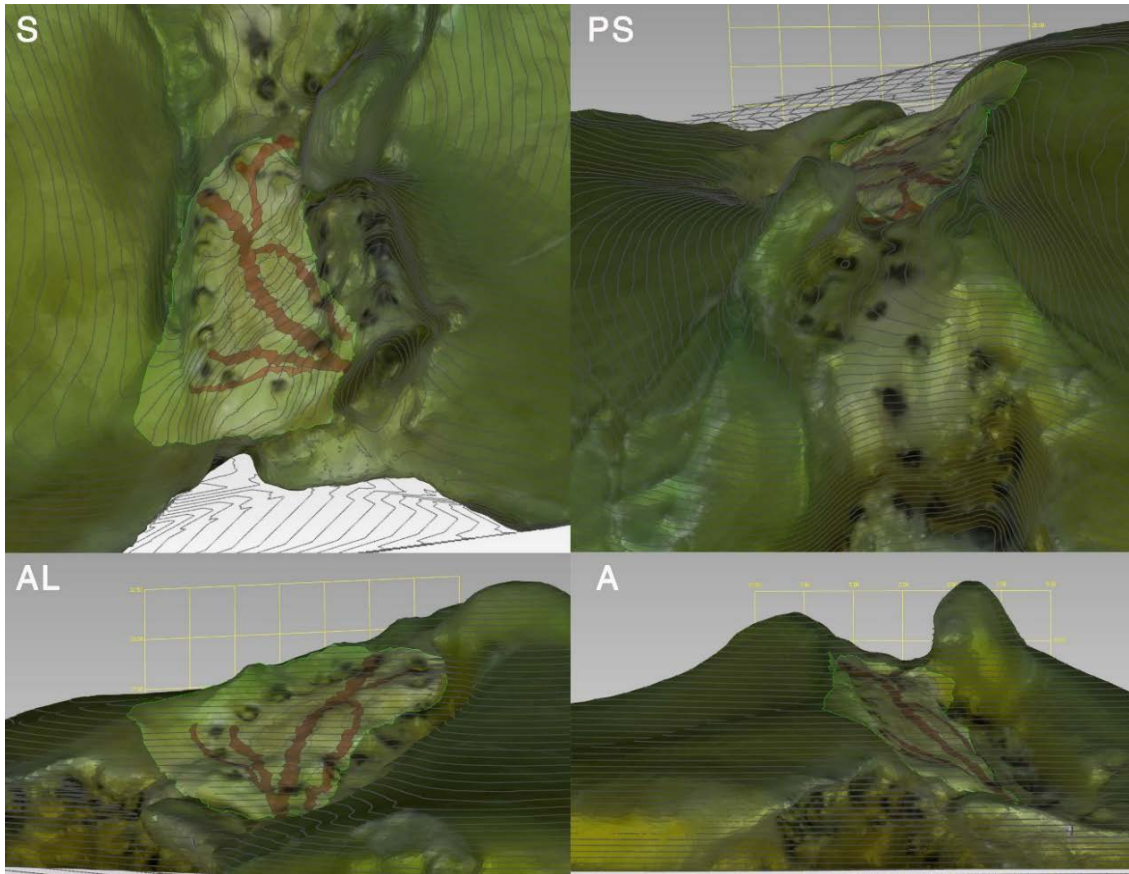


Figure 271. 3D model of tibia K with contour lines. Area 10 highlighted. Incisures selected in red.

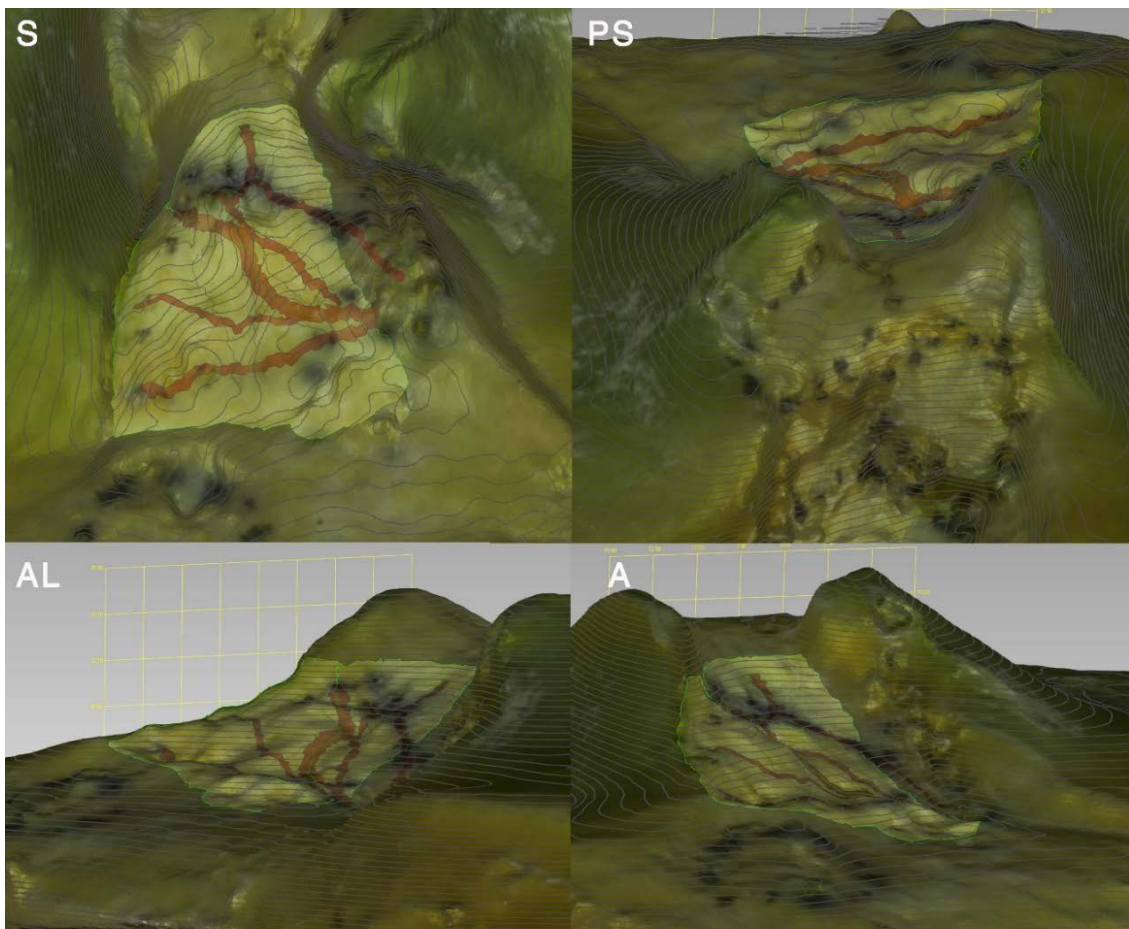


Figure 272. 3D model of tibia L with contour lines. Area 10 highlighted. Incisures selected in red.

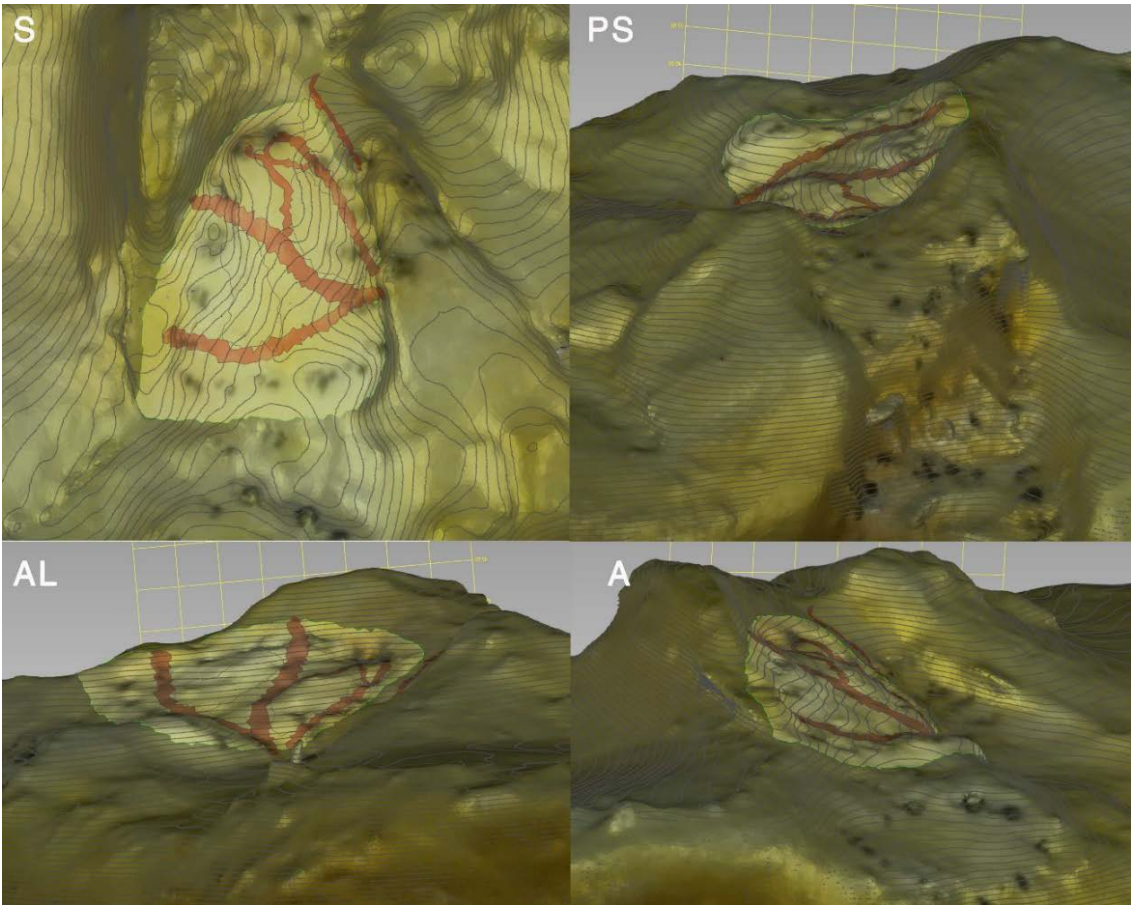


Figure 273. 3D model of tibia M with contour lines. Area 10 highlighted. Incisures selected in red.

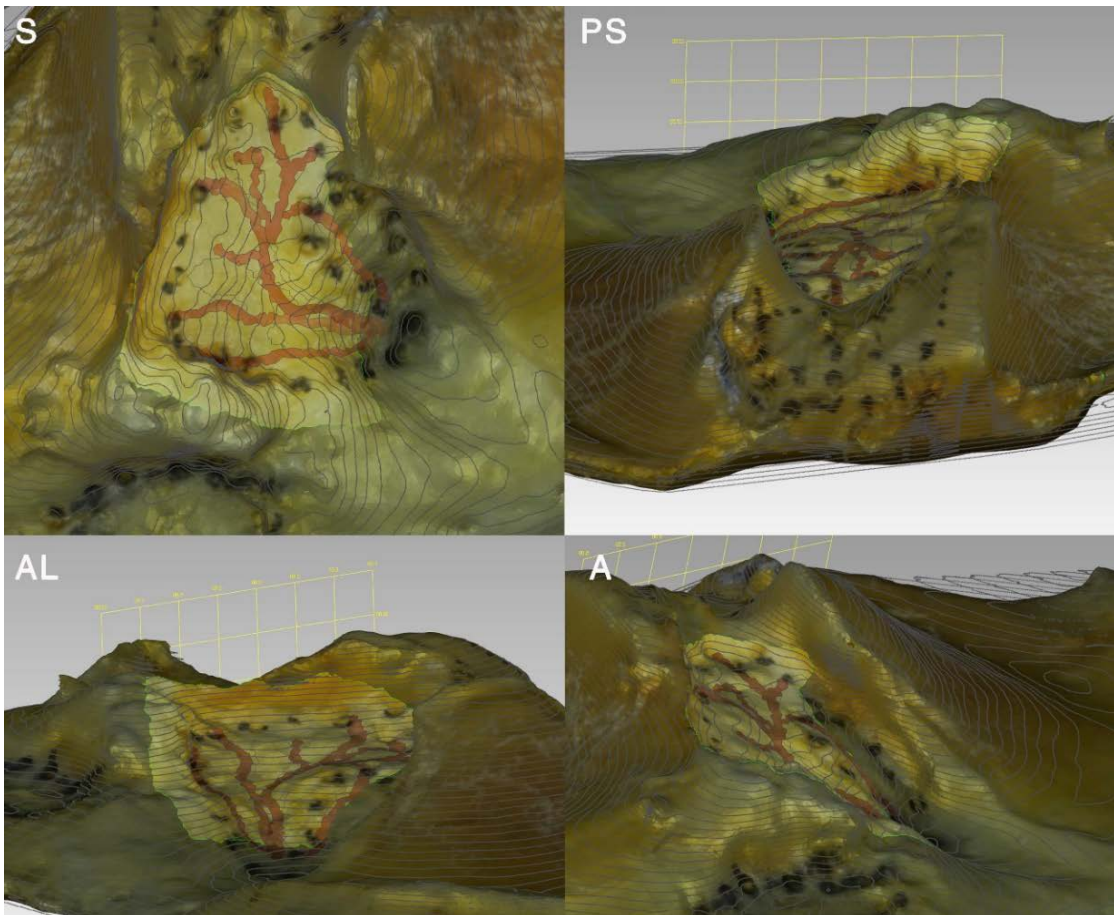


Figure 274. 3D model of tibia N with contour lines. Area 10 highlighted. Incisures selected in red.

IV.7.1.2. Stairs and landings of the anterior intercondylar staircase

Observed as a whole, the AIS showed a moderate downward slope anteriorly, with two constant “stairs”, and two corresponding more horizontal – arthroscopically relevant – areas or “landings”, readily distinguished at a glance in most tibias.

The posterior aspect of the staircase, the superior intercondylar stair, **10a**, led from area 15 posteriorly downwards anteriorly to the posterior AFIR process, F1. It contained:

- The anteromedial fovea, **10b**, a constant, sizeable foramen nutricium in the posteromedial aspect of the staircase, usually lying against its posteromedial wall (beneath the MT anterior peak). Other inconstant, lesser foramina nutricia might appear in this zone near the posterior wall of the AIS.
- The upper landing, **10c**, the most constant horizontal area found in the staircase, was located near 10b. It was distinguished by a much gentler downwards slope than the rest of the superior stair. In some specimens, an even higher horizontal area was found connecting area 10 with area 15.

The anterior aspect of the staircase, the inferior intercondylar stair, **10d**, was found leading downward in a medial to lateral direction, with a slightly posteriorly concave curve similar to the one formed by the posterior AFIR process, F2 (which bordered the stair anteriorly).

- The lower landing, **10f**, located near the center of F1, was usually smaller than the upper landing, but showed a gentler slope.

Two shapes were commonly found in the area between both stairs: (1) a narrow strip of bone with a steep slope, sharply dividing both stairs in a posterolateral to anteromedial direction; and (2) a wider area connecting both stairs through a mild, more horizontal slope, a sort of middle landing, **10e**.

See Fig. 275 for a common example of an AIS with two landings, and Fig. 276 for a common example of an AIS with three landings.

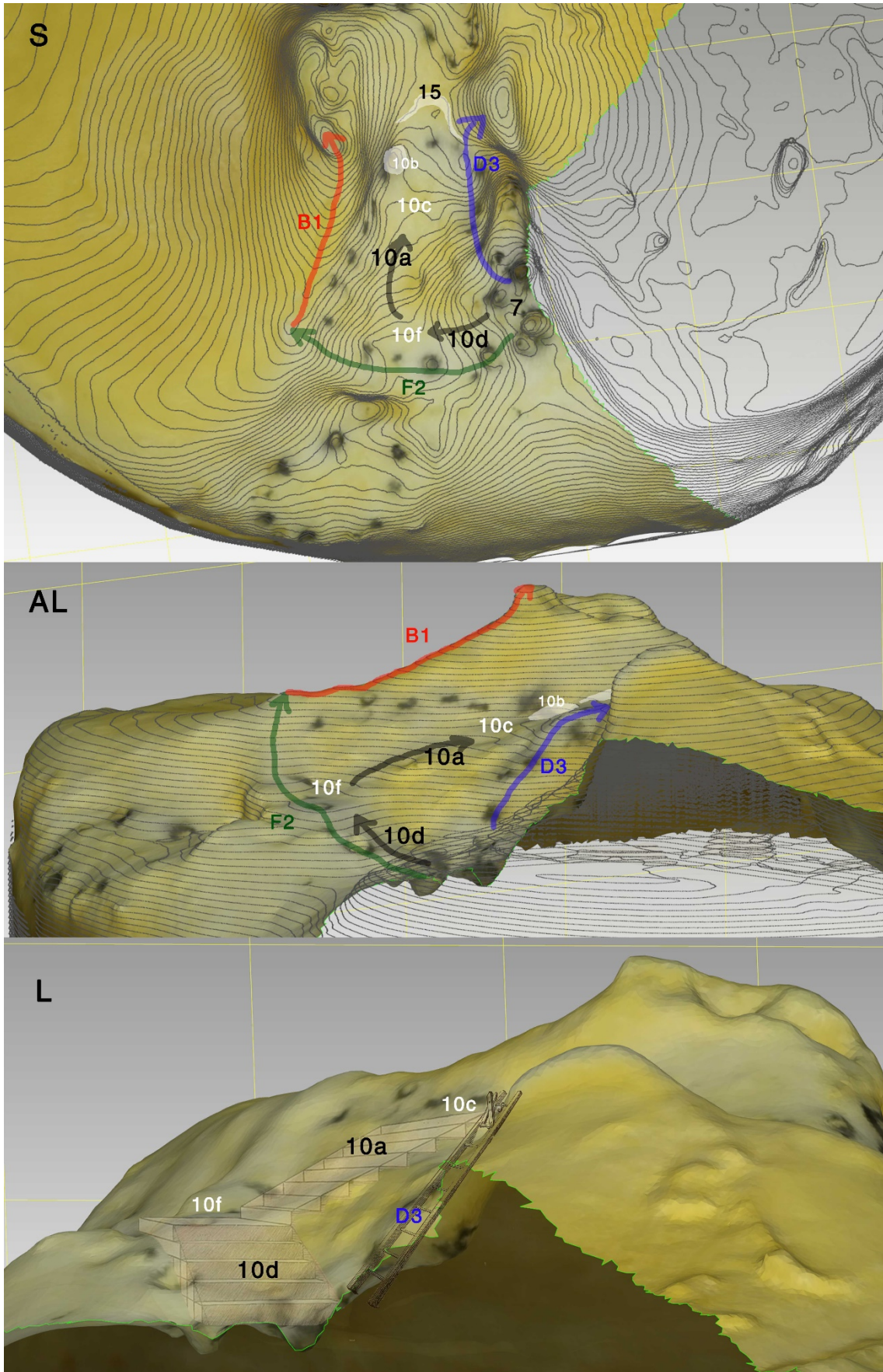


Figure 275. 3D model of tibia A, superior (S) and anterolateral (AL) views of the intercondylar staircase with contour lines superimposed. The directions of the stairs are painted and labelled in black; the landings labelled in white. Also labelled are the ALIR in blue, the AMIR in red, the AFIR in green. Areas 10b, 15, and 7 are also labelled. Lateral view (L) with a quarter-turn staircase and ladder superimposed.

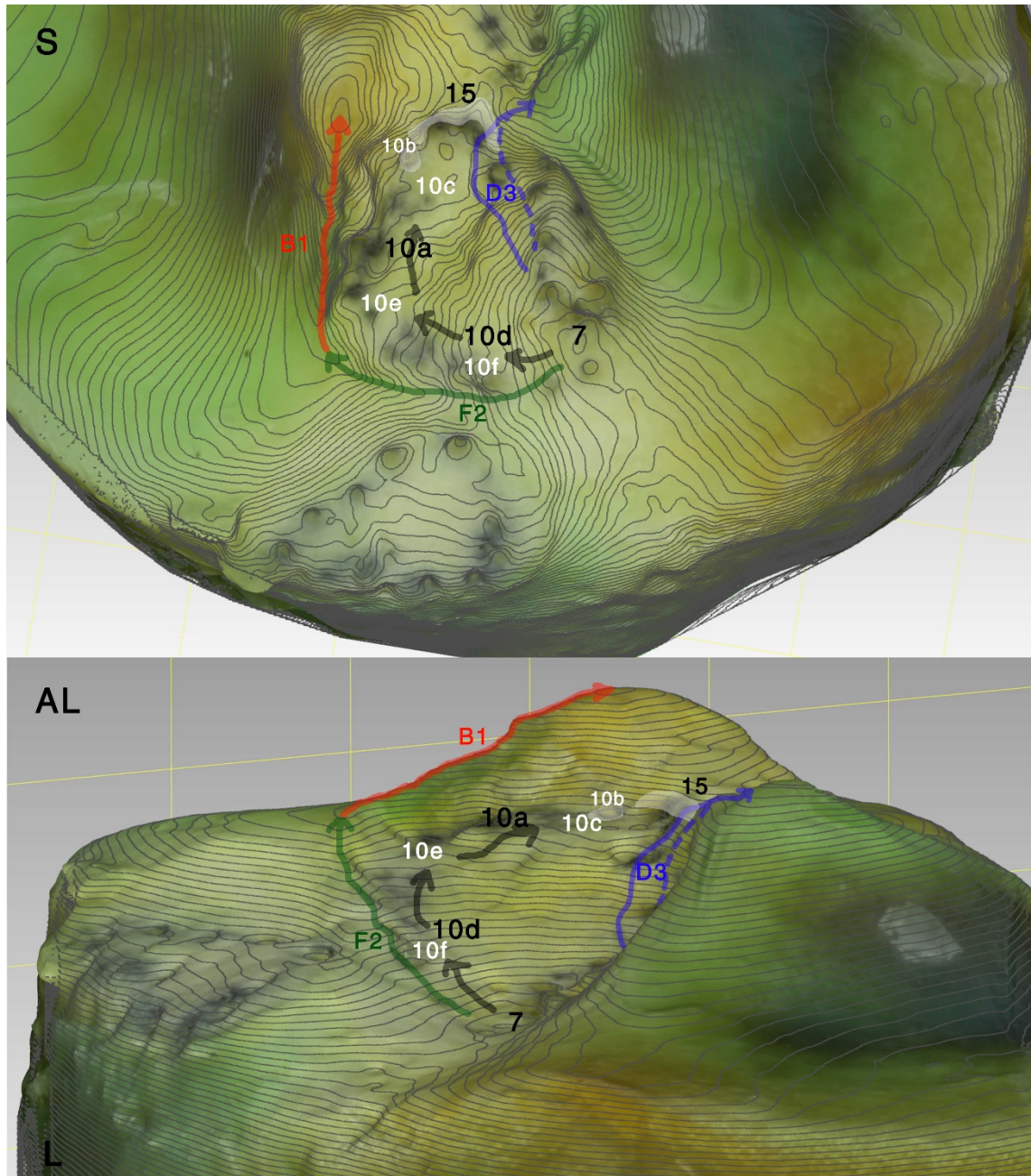


Figure 276. 3D model of tibia C, superior (S) and anterolateral (AL) views of the intercondylar staircase with contour lines superimposed. The directions of the stairs are painted and labelled in black; the landings labelled in white. Also labelled are the ALIR in blue, the AMIR in red, the AFIR in green. Areas 10b, 15, and 7 are also labelled.

IV.7.2. Attachment of the anterior cruciate ligament

IV.7.2.1. Shape of the ACL footprint

The general ACL footprint consistently showed a duck-foot shape, wider anteriorly (delimited by the posterior AFIR), narrowing posteriorly – with a straight line medially (the AMIR), and with a concave curve laterally (following A1b) –, reaching the posterior aspect of area 10.

Two common footprint shapes were found: triangular (eight specimens) and oval (five specimens), with one specimen showing a triangular-like insertion, but with a more open posterior arch.

The divided distal ACL stump showed three distinct fiber groups:

- The direct fibers: rich in ACL fibers, with a long and flat, ribbon-like shape medially.
- The indirect fibers: fan-like expansion of the direct fibers, mainly anteriorly and anteromedially.
- The intermingled fibers: a scarcely populated area laterally, shared with ARLM fibers.

The osseous footprints of the ACL showed a layered Helvetica-type C structure when viewed in a superoinferior direction. The C-shaped layers ranged from a sharp-angled, delta(Δ)-like shape (Fig. 278, Fig. 279) to a more rounded, horseshoe-like shape (Fig. 277), with the latter more commonly found in specimens with degenerative changes.

- The outer C was a steeply sloped zone receiving mainly indirect fibers, formed medially by B2, anteriorly by the inner aspect of F1, and posterolaterally by D3. D3 was the most frequent site of a common intermingled ACL-ARLM attachment in donor specimens.
- The central C formed the more gently sloped aspect of the staircase, where main fibers were found attached. Main fibers also inserted here without intermingled fibers. The outer C and the central C together formed the footprint of the C-shaped ACL attachment area, or ACL fornix.
- The inner C showed a steeper slope, corresponding mainly to the concavity of the AIAR (A1b). Synovial tissue, fat, and intermingled fibers of scarcely populated ACL and ARLM were found in this area.

- The counter of the inner C showed a fan-like flat facet, only rarely receiving ACL fiber insertions.

The external AMIR (B1), the posterior arch (posterior aspect of area 10, in front of area 15), and the anterolateral fossa did not receive ACL fiber attachments.

ACL bundle footprints and C-layers of all specimens studied are shown in Fig. 280 – Fig. 293.

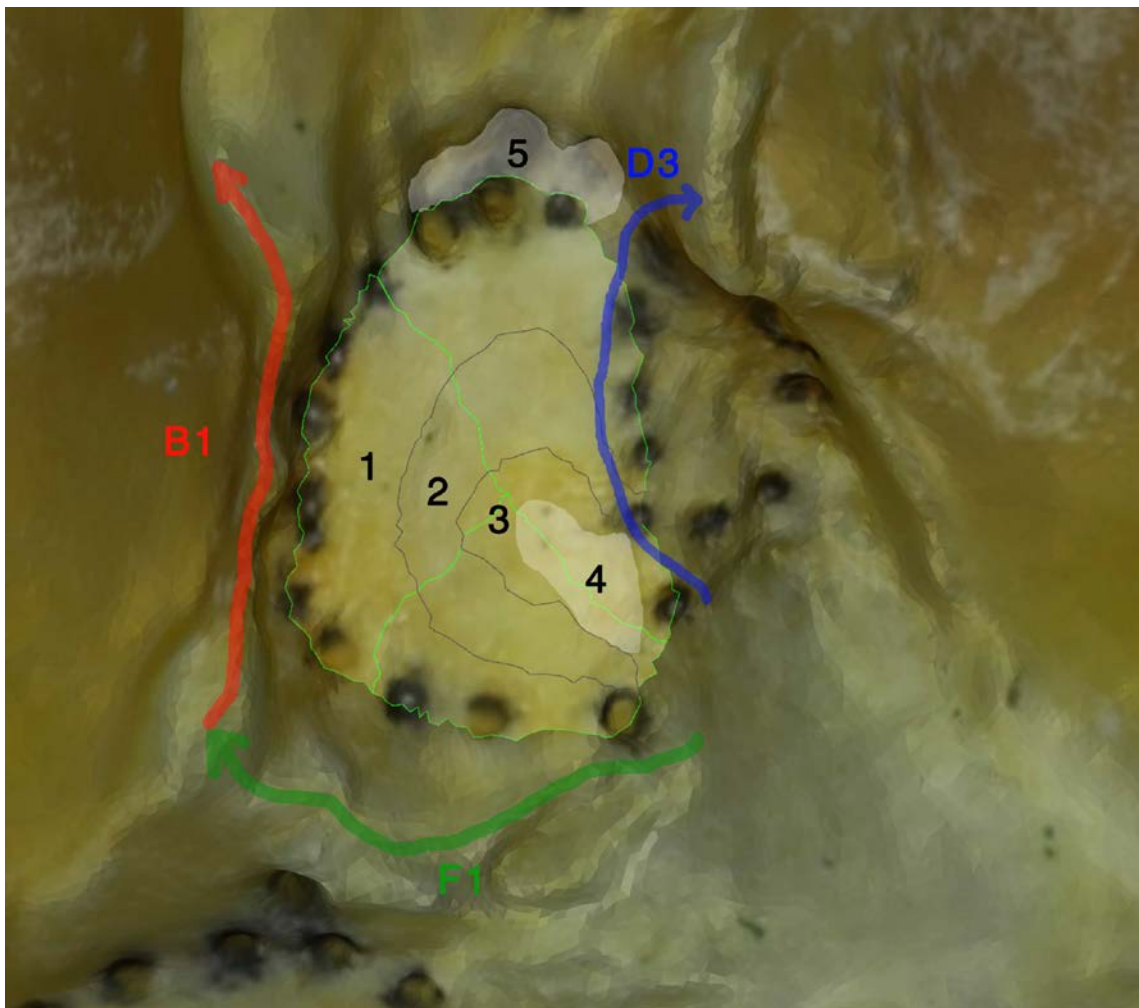


Figure 277. 3D model of Tibia D with ACL footprint highlighted. Superoinferior view. Main C-shaped layers selected (borders in black lines); notice the horseshoe-like shape of the layers, and the degenerative elevations surrounding area 10. ACL bundles selected (borders in light fluorescent green lines). Main zones labelled in black: outer C (1), central C (2), inner C (3), fan-like facet (4), and posterior arch (5). Also painted and labelled are the AMIR in red, the ALIR in blue, and the AFIR in green.

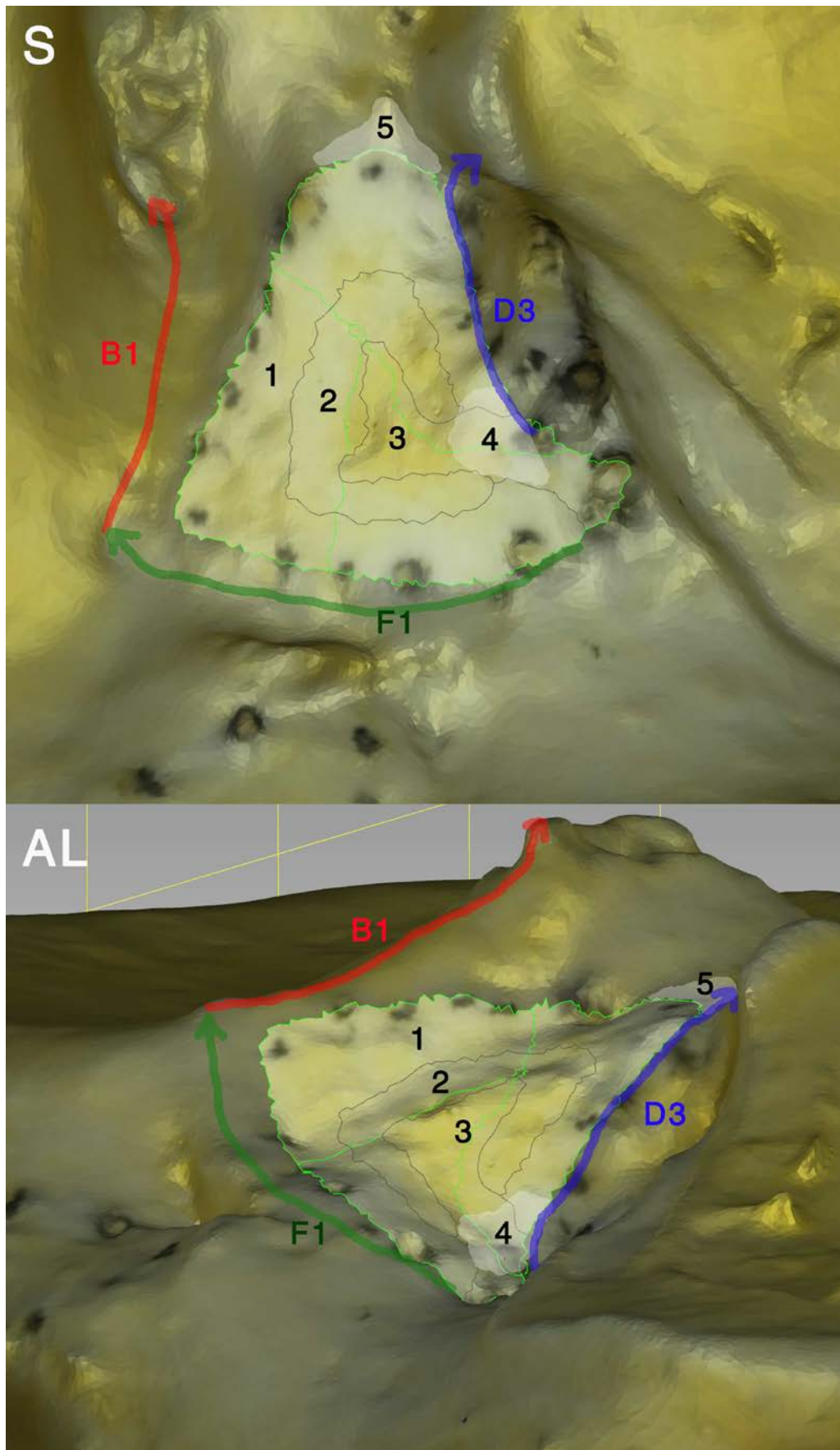


Figure 278. 3D model of Tibia A with ACL footprint highlighted. Superoinferior (S) and anterolateral (AL) views. Main C-shaped layers selected (borders in black lines); notice the Δ -like shape. ACL bundles selected (borders in light fluorescent green lines). Main zones labelled in black: outer C (1), central C (2), inner C (3), fan-like facet (4), and posterior arch (5). Also painted and labelled are the ALIR in blue, the AMIR in red, the AFIR in green.

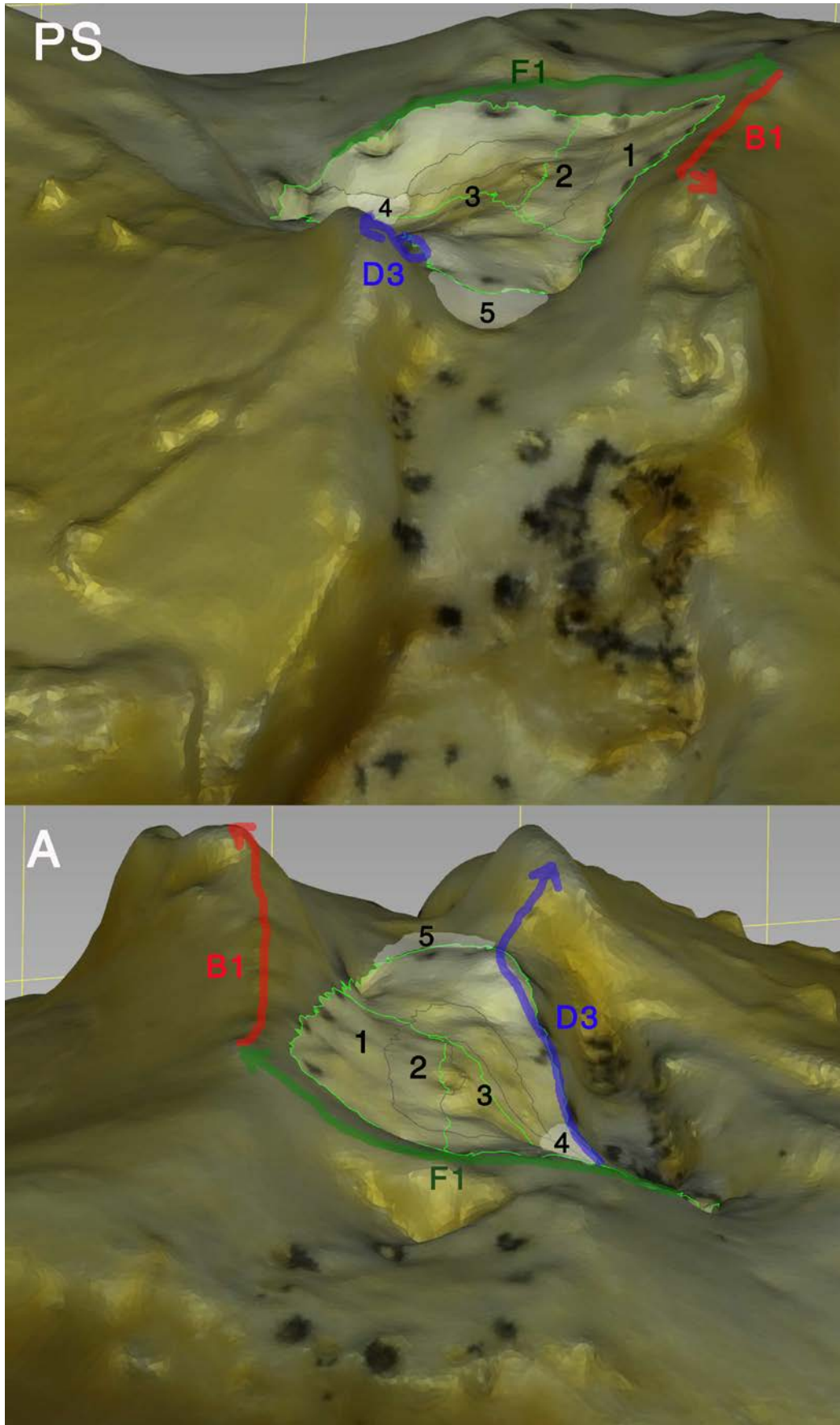


Figure 279. 3D model of Tibia A with ACL footprint highlighted. Posterosuperior (PS) and anteroposterior (A) views. Main C-shaped layers selected (borders in black lines); ACL bundles selected (borders in light fluorescent green lines). Main zones labelled in black: outer C (1), central C (2), inner C (3), fan-like facet (4), and posterior arch (5). Also painted and labelled are the ALIR in blue, the AMIR in red, the AFIR in green.

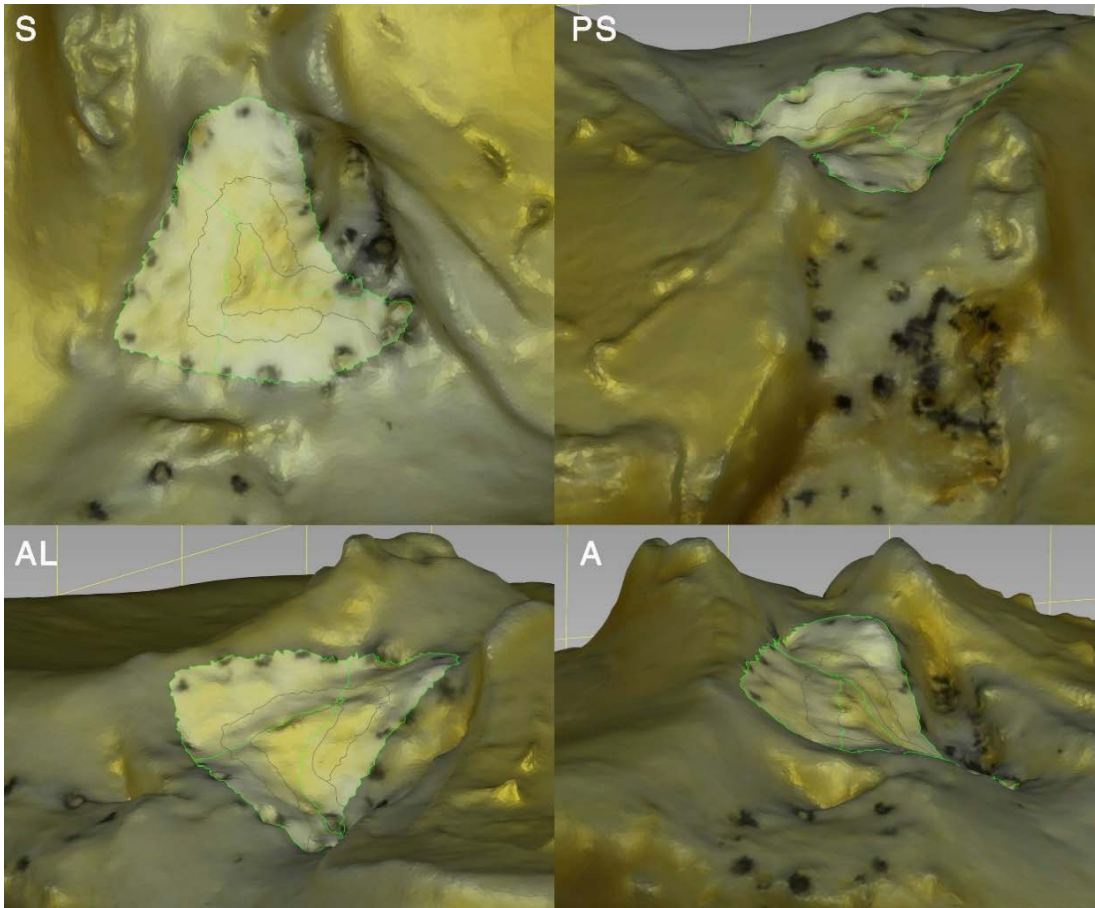


Figure 280. 3D model of Tibia A. ACL bundle footprint highlighted, and C-layers selected.

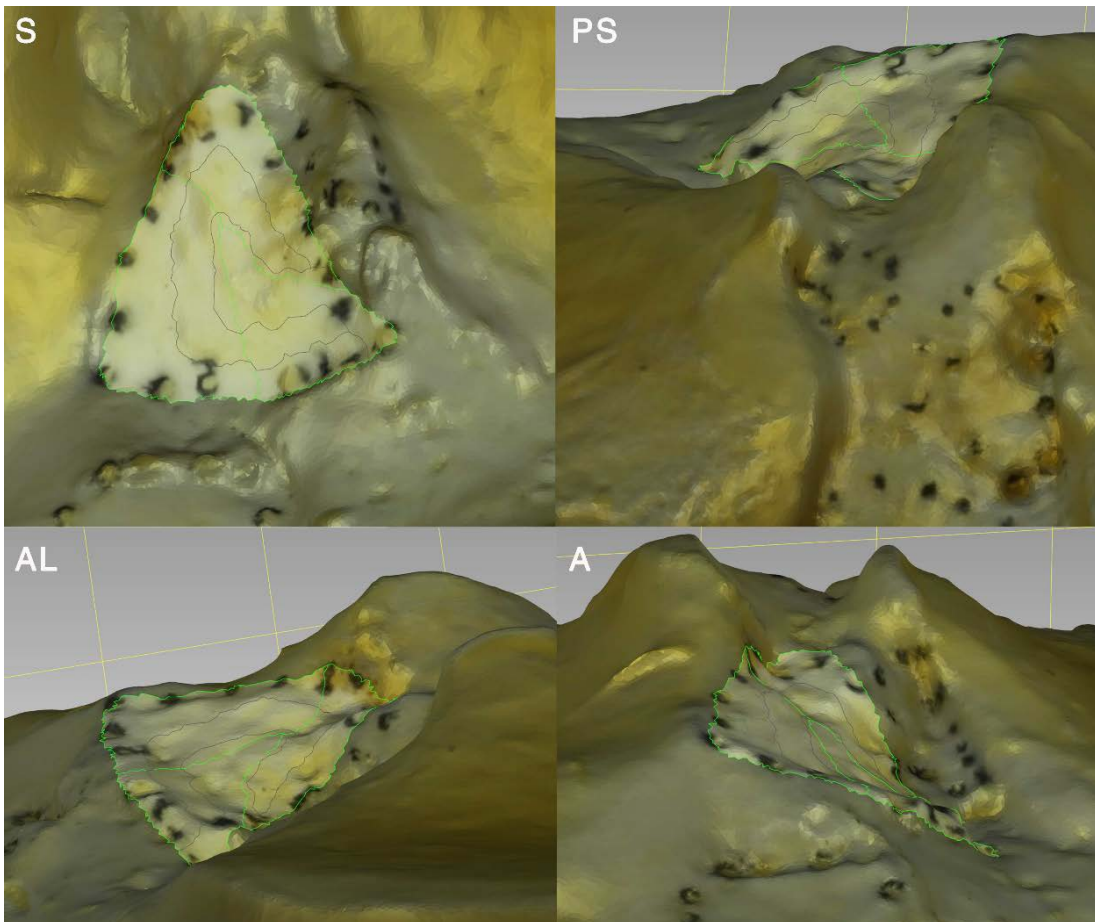


Figure 281. 3D model of Tibia B. ACL bundle footprint highlighted, and C-layers selected.

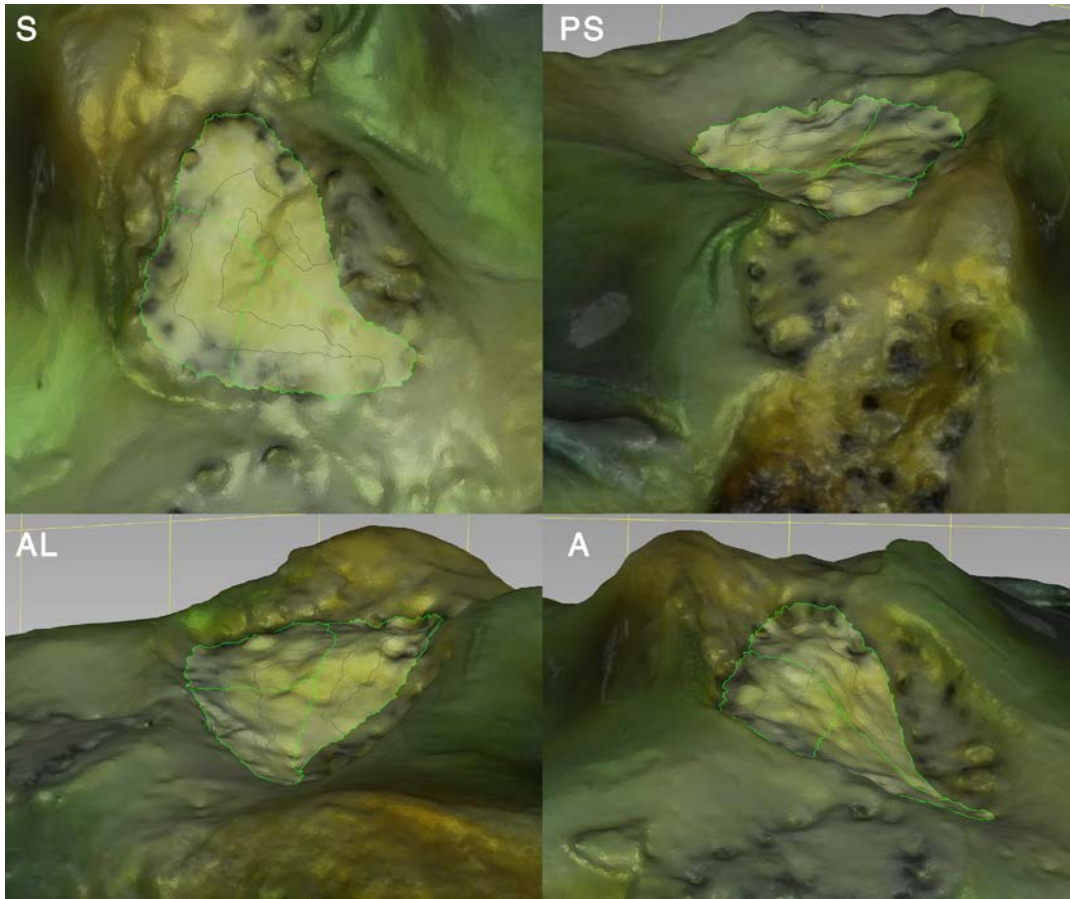


Figure 282. 3D model of Tibia C. ACL bundle footprint highlighted, and C-layers selected.

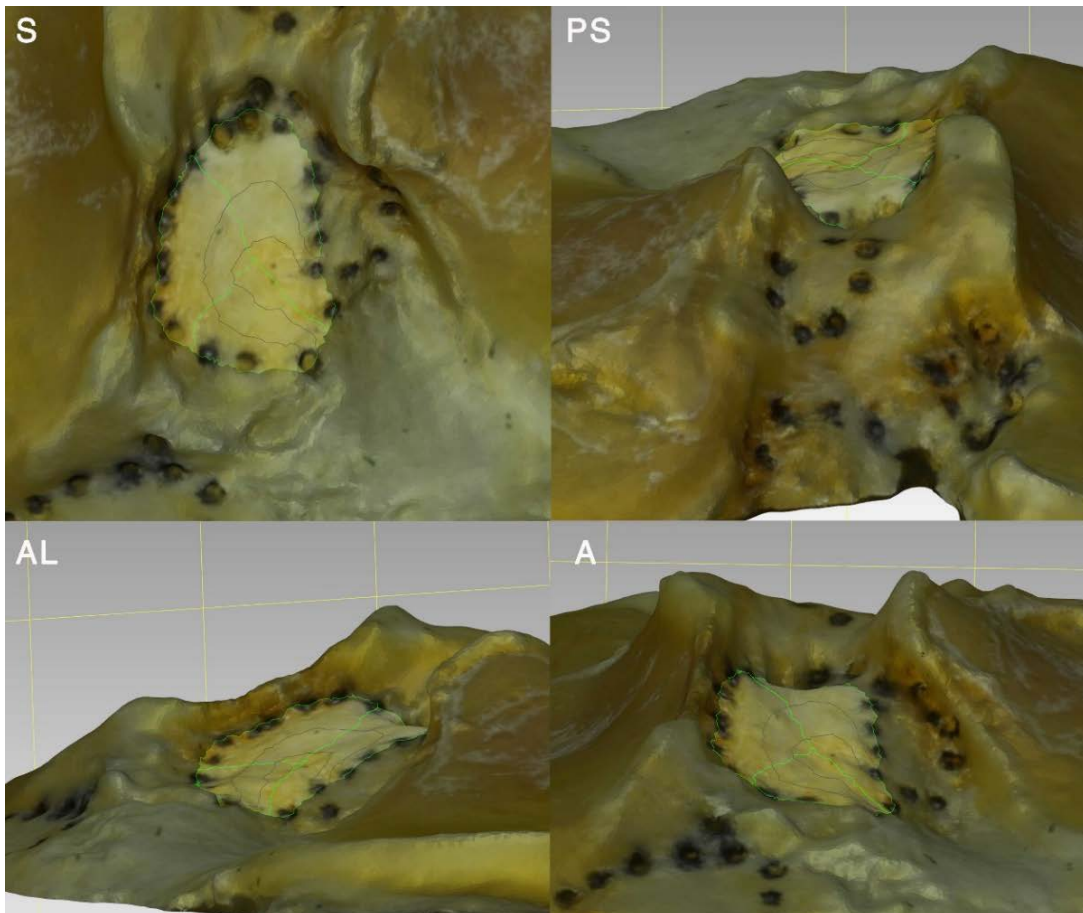


Figure 283. 3D model of Tibia D. ACL bundle footprint highlighted, and C-layers selected.

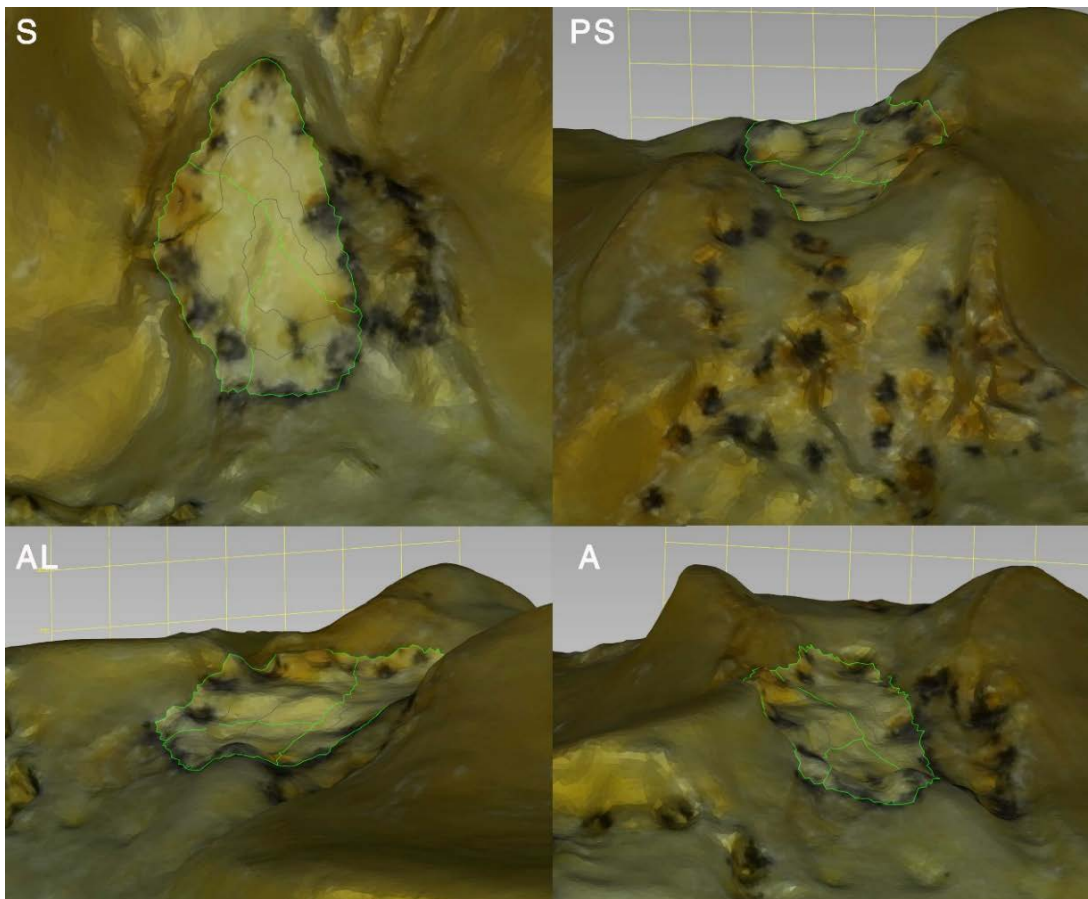


Figure 284. 3D model of Tibia E. ACL bundle footprint highlighted, and C-layers selected.

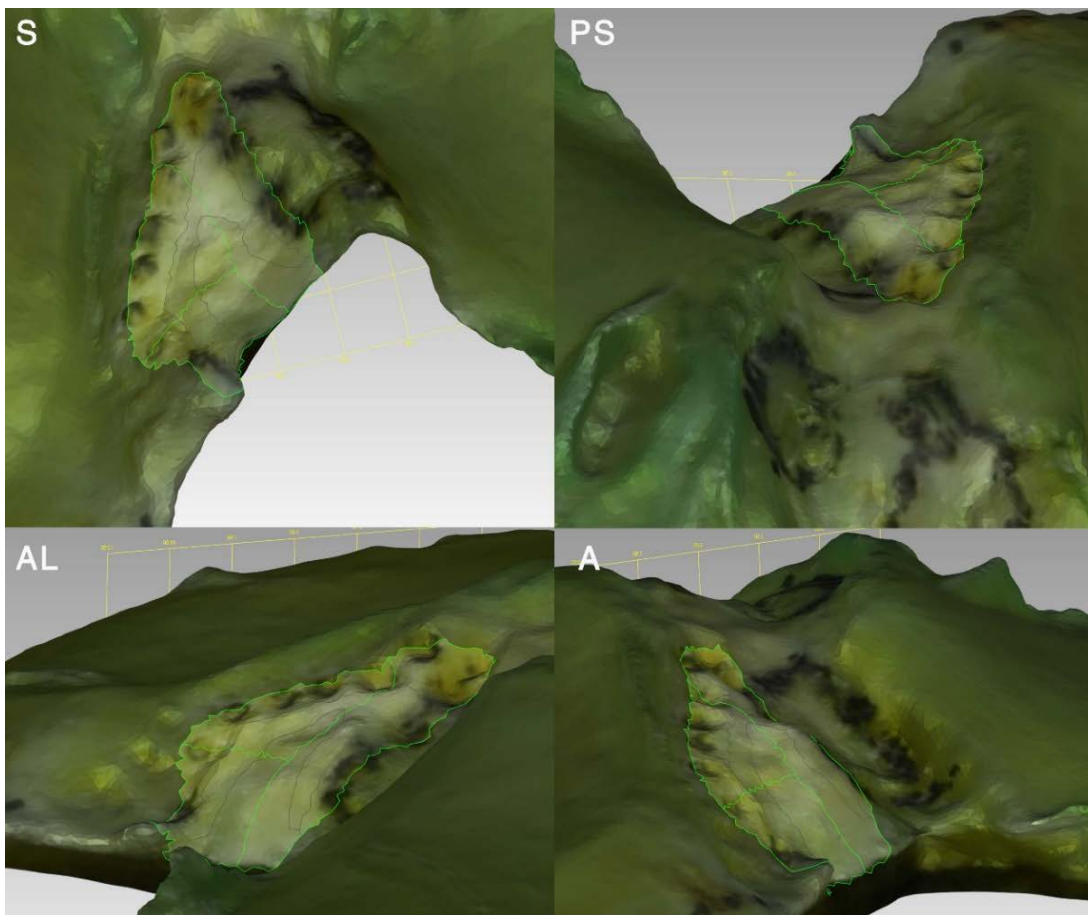


Figure 285. 3D model of Tibia F. ACL bundle footprint highlighted, and C-layers selected.

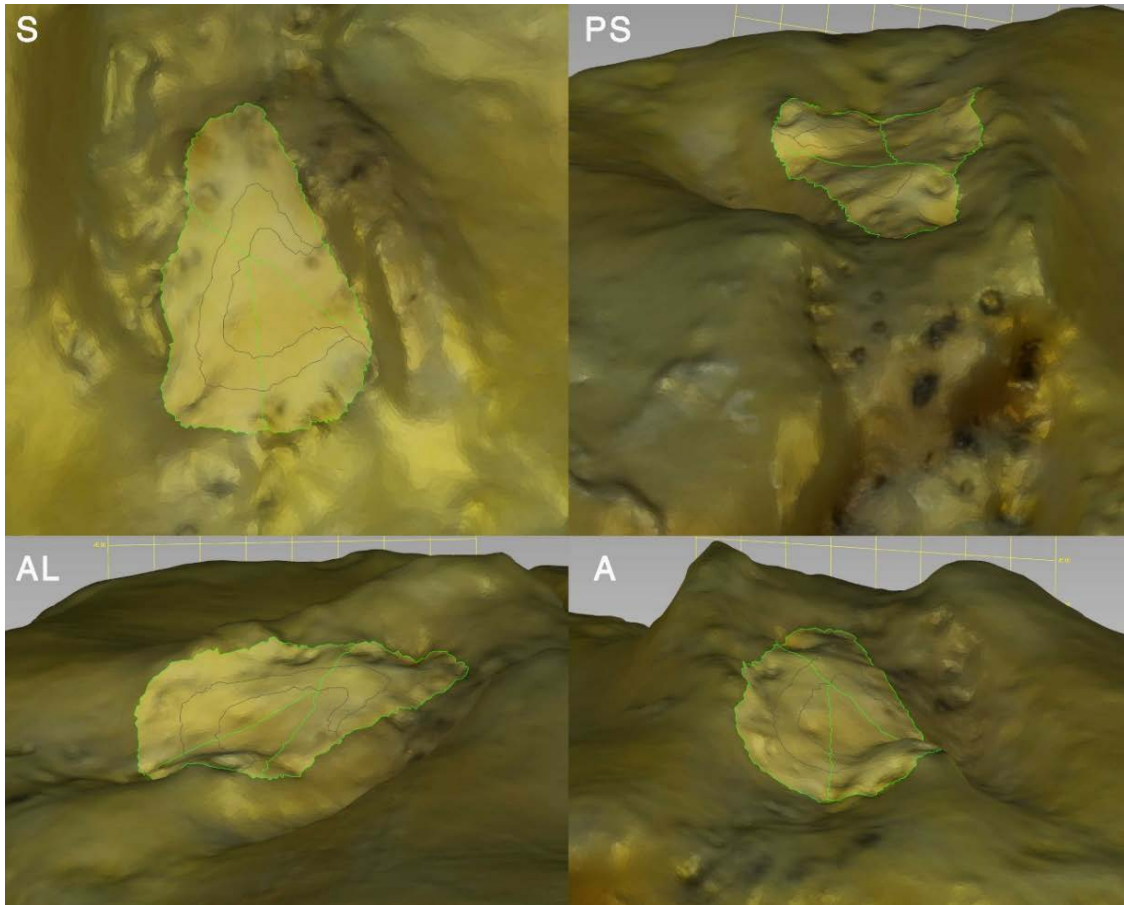


Figure 286. 3D model of Tibia G. ACL bundle footprint highlighted, and C-layers selected.

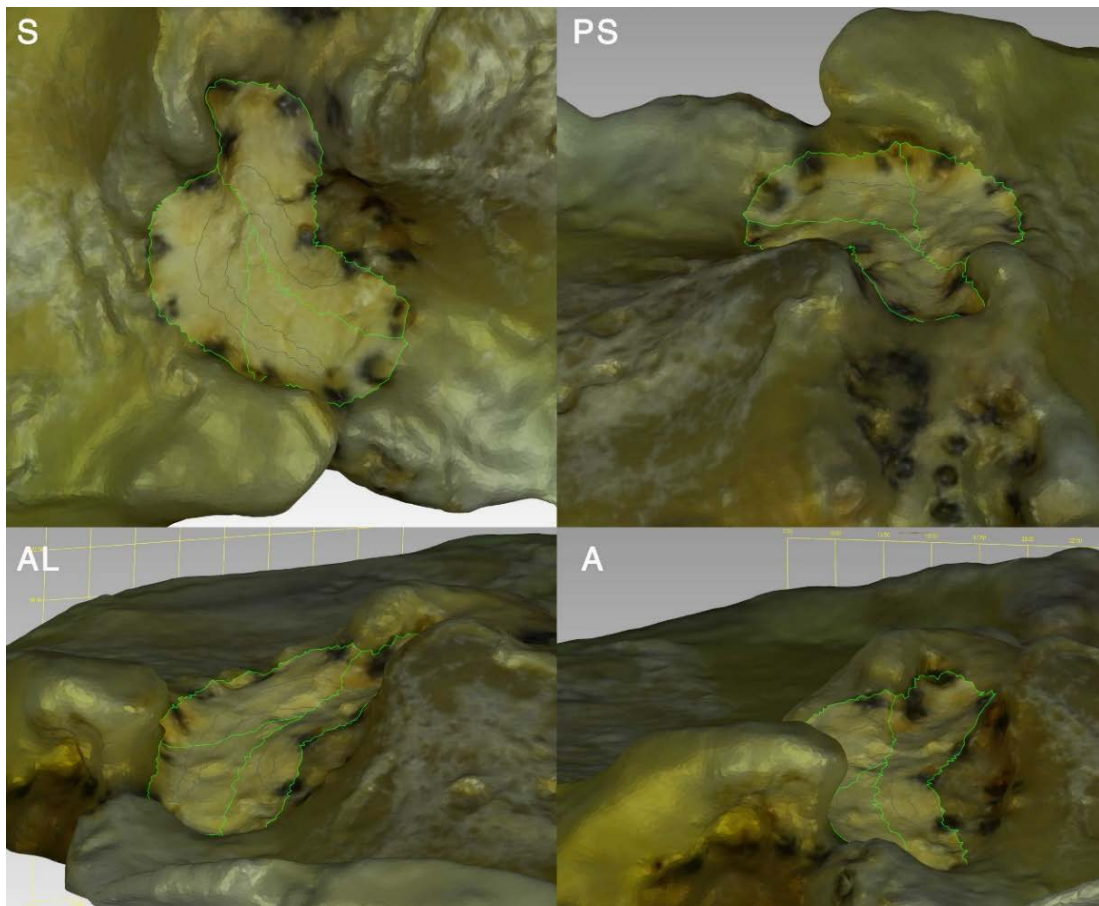


Figure 287. 3D model of Tibia H. ACL bundle footprint highlighted, and C-layers selected.

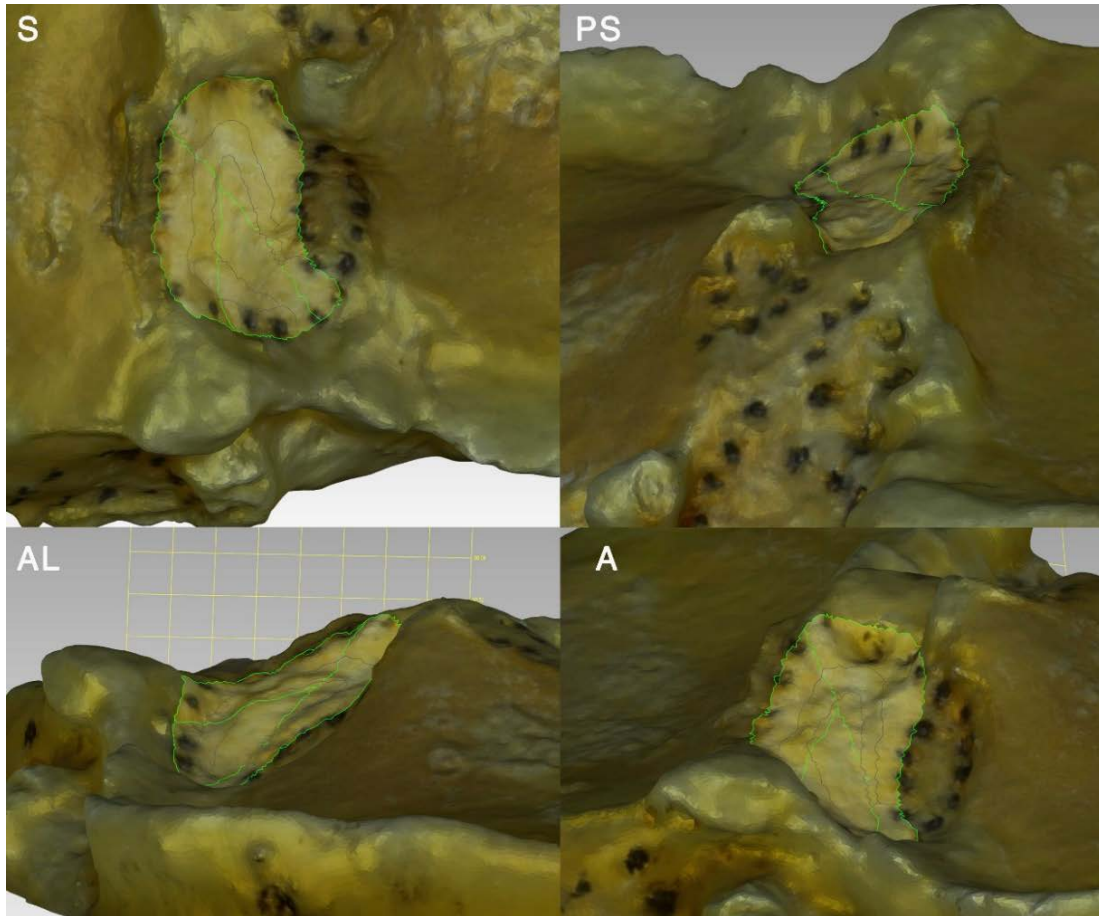


Figure 288. 3D model of Tibia I. ACL bundle footprint highlighted, and C-layers selected.

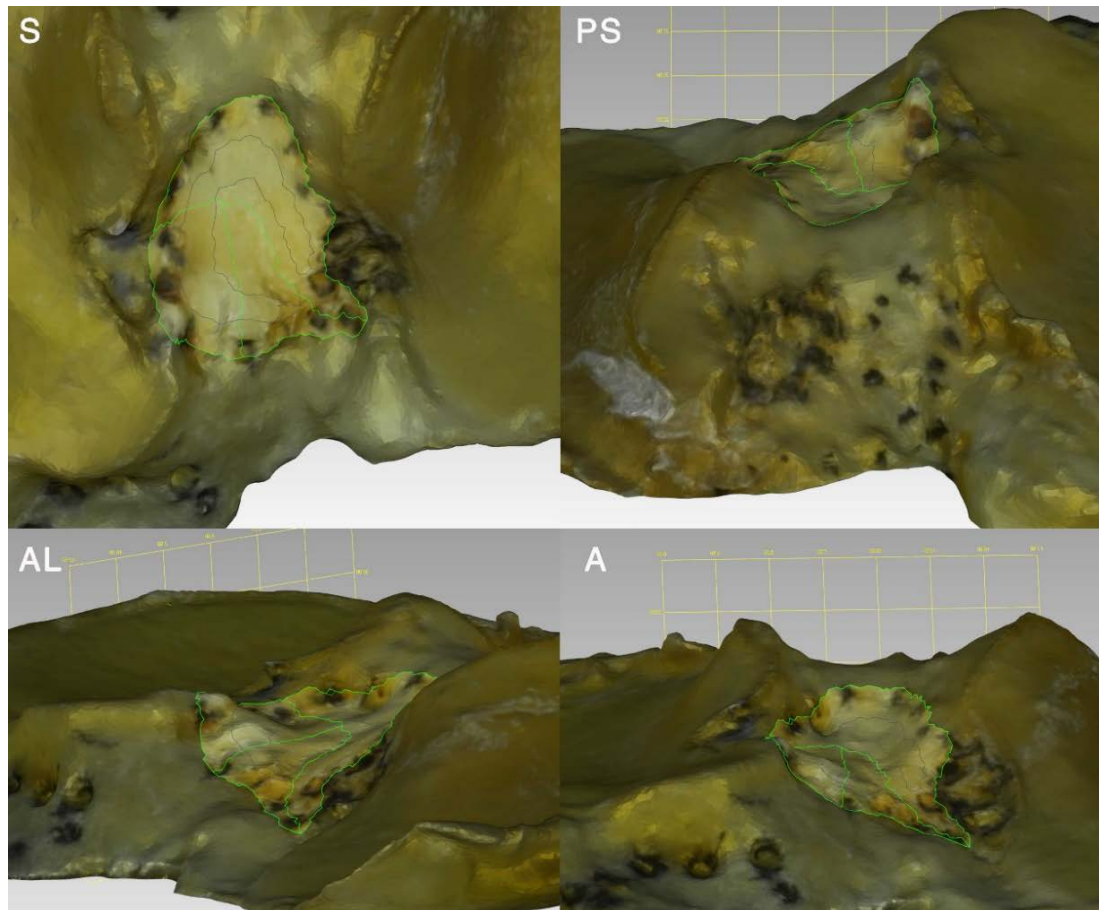


Figure 289. 3D model of Tibia J. ACL bundle footprint highlighted, C-layers selected.

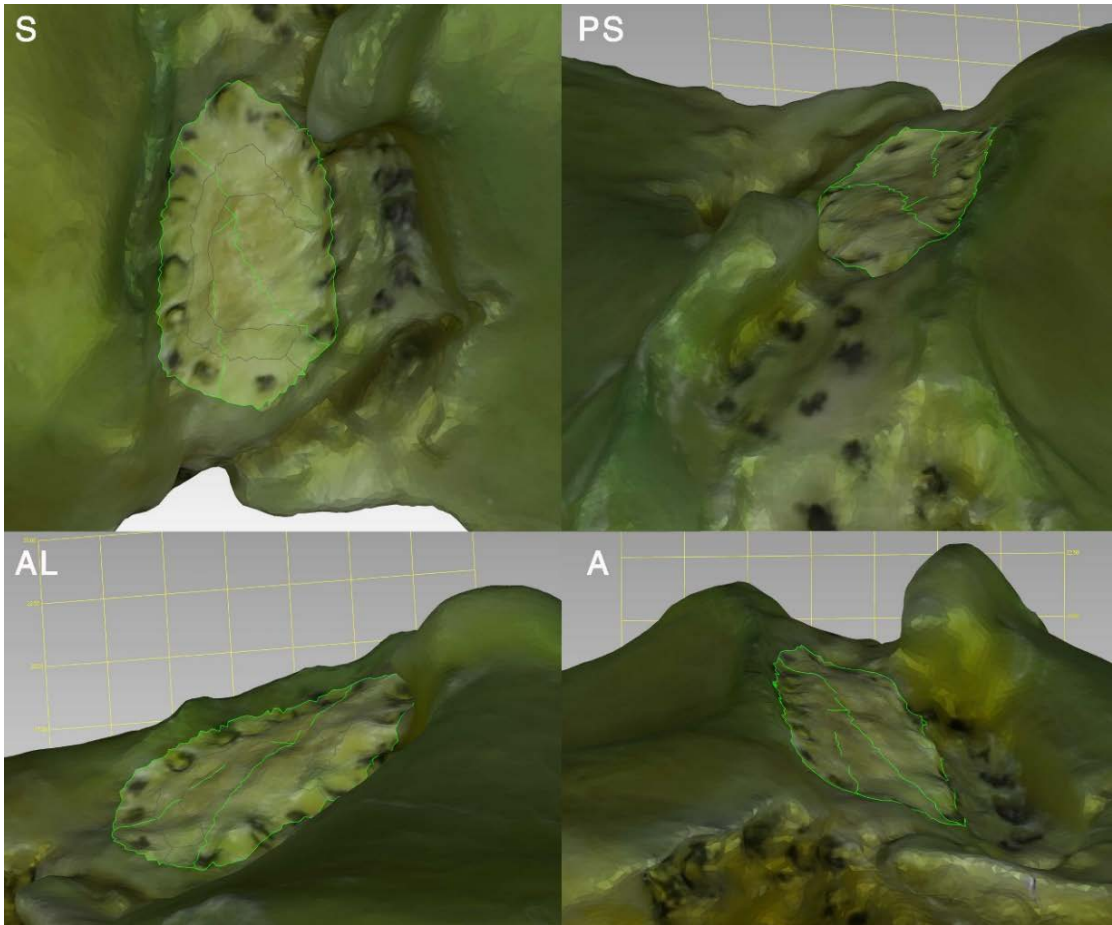


Figure 290. 3D model of Tibia K. ACL bundle footprint highlighted, and C-layers selected.

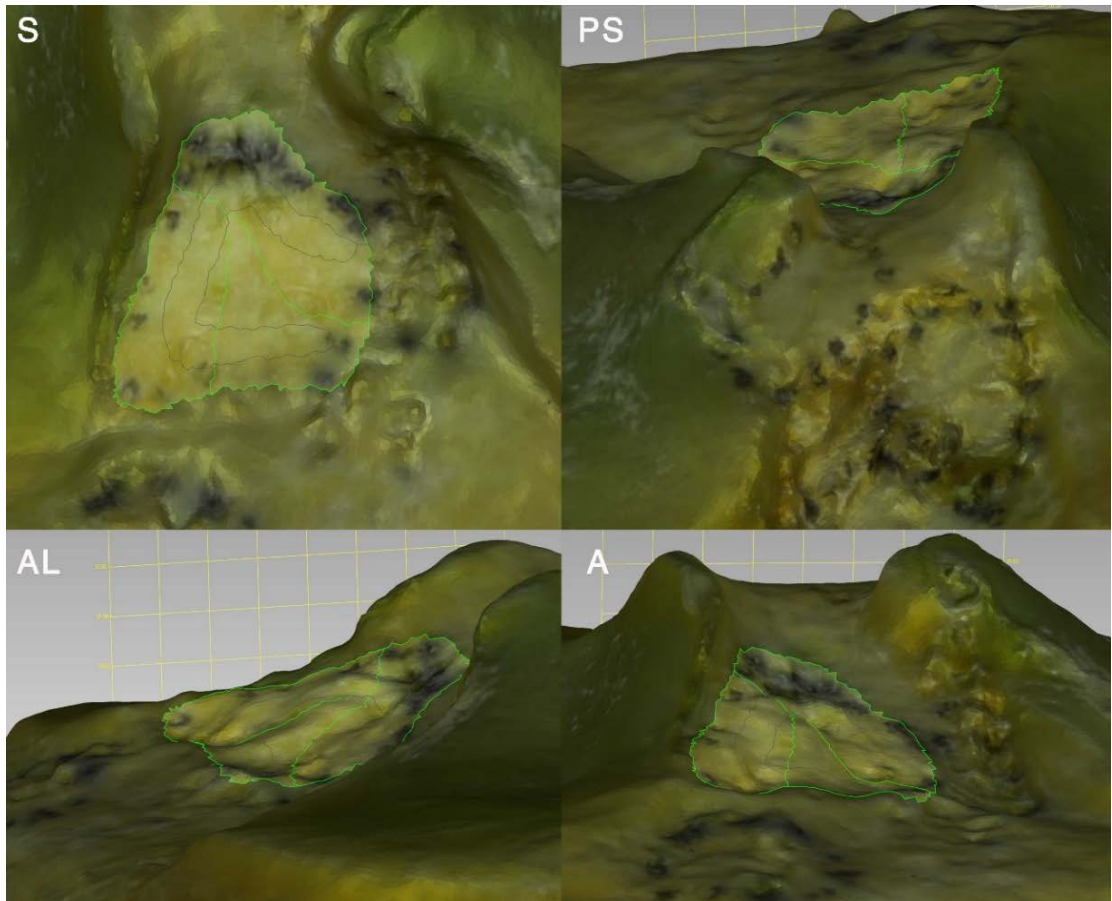


Figure 291. 3D model of Tibia L. ACL bundle footprint highlighted, and C-layers selected.

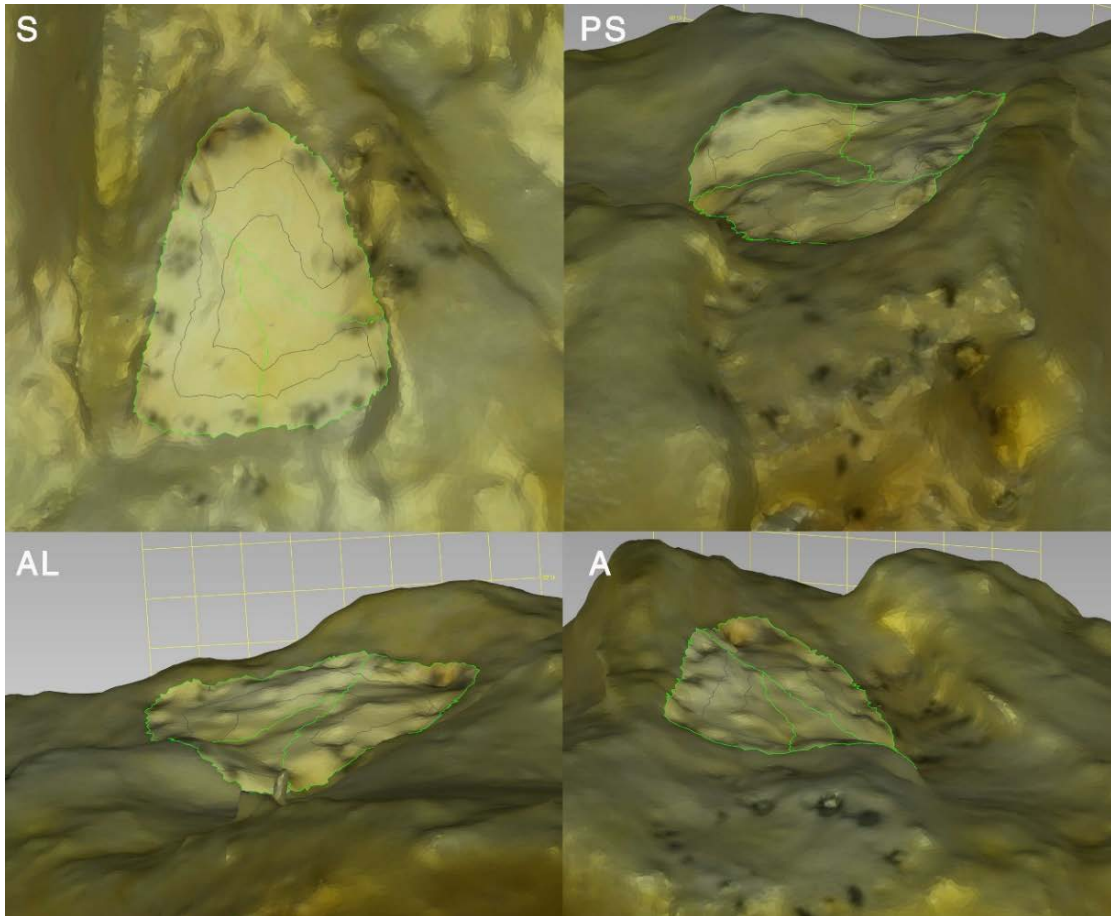


Figure 292. 3D model of Tibia M. ACL bundle footprint highlighted, and C-layers selected.

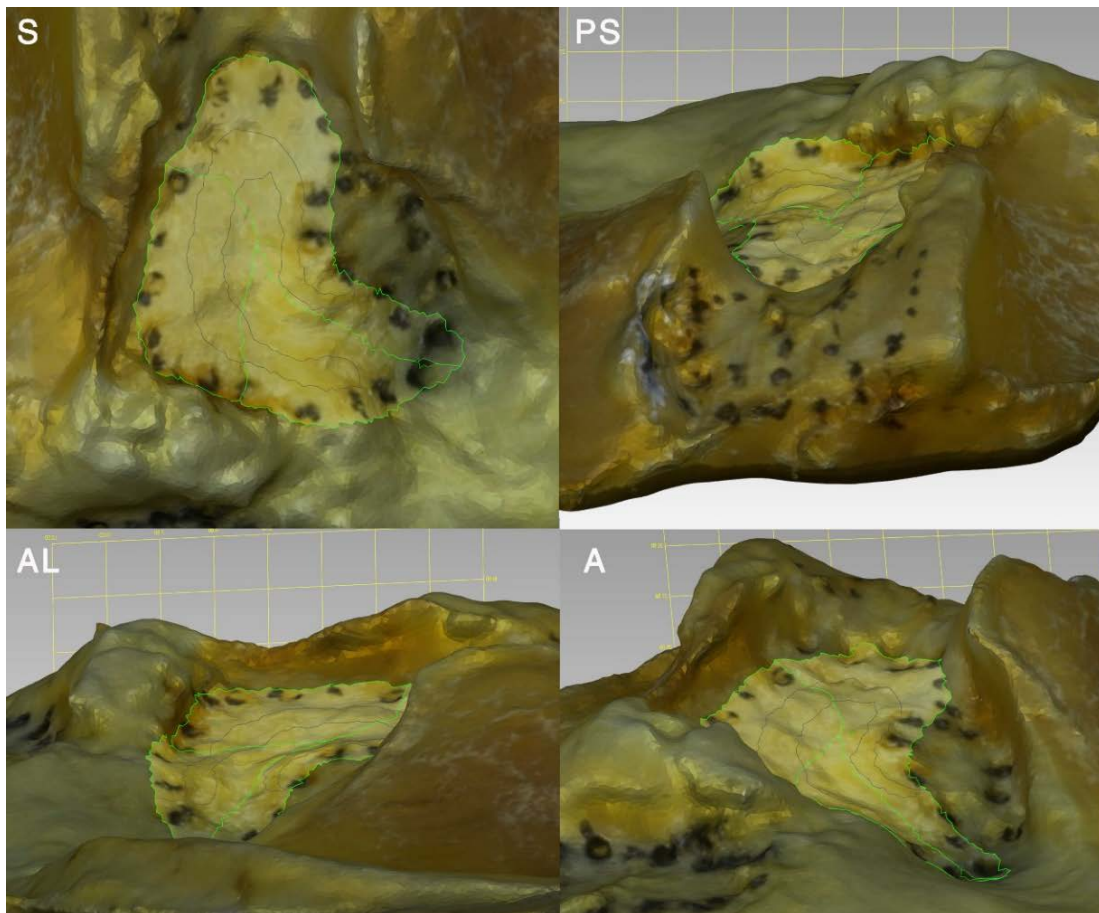


Figure 293. 3D model of Tibia N. ACL bundle footprint highlighted, and C-layers selected.

IV.7.2.2. Area of the ACL footprint

No association was found between the shape of area 10 and condyle attrition, $\chi^2(6)=8.517$, $p=0.203$; between ACL shape and the shape of area 10, $\chi^2(2)=1.750$, $p=0.417$ (Phi=0.354, Cramer's V=0.354); or between ACL shape and condyle attrition, $\chi^2(3)=5.736$, $p=0.125$ (Phi=0.640, Cramer's V=0.640). Frequency distribution analysis showed that oval types were associated with more degenerative changes, so a binary value was assigned to each type (0=triangle, 1=oval), and a Spearman's rank-order correlation was run to determine the relationship between condyle attrition grade and area 10 type: $r_s(14)=0.636$, $p=0.015$.

The size of area 10 was not correlated with age, $r_s(14)=0.173$, $p=0.555$; and no differences were found between males and females, $t(12)=-0.291$, $p=0.785$. No correlation was found between ACL footprint and age, either, $r_s(14)=0.201$, $p=0.490$; nor between males and females, $t(12)=-0.350$, $p=0.733$.

Quantitatively, the ACL area had 145.2 mm² (95% CI 120.4 – 169.9 mm²; range, 81 mm² to 207.1 mm²), and it covered 74.6% of area 10 (95% CI 68.5 – 80.6%; range, 60% to 91%; N=14).

The anteromedial fovea depression (n=14, Ahlbäck OA grades 0–3) showed a mean area of 11.2 mm² (range, 4.4 mm² to 31.2 mm²), and a mean volume of -1.8 mm³ (range, -9.8 mm³ to -0.1 mm³), where negative means volume beneath the surrounding surface.

IV.7.2.3. Distances from ACL footprint center to anatomic landmarks

Qualitatively, the ACL attachment center was measured in reference to arthroscopically identifiable landmarks, being posterior to the AFIR (F1); posterolateral to the geniculum (G); posteromedial to the ACIK (H), to the anteromedial corner of the ARLM attachment, and to the anterolateral fossa; lateral to the AMIR (B1); medial to the ALIR (D2), and to the ARLM center; anterolateral to the anteromedial fovea (10b); anterior to the preeminence ridge (PRE), the posteminence ridge (POE), and the anteriormost (usually anterolateral) border of the PCL; anteromedial to the posteromedial corner of the ARLM, and to the anteromedial corner of the PRMM.

The center of the ACL attachment was 10.9 mm (range, 8 mm to 13.2 mm) from the center of the preeminence ridge, a measurement that had a significant

correlation with AP depth ($r=0.820$, $p<0.001$), ML width ($r=0.852$, $p<0.001$), CV 15.94%. Proportionally, it represented 34% of the AP depth, and 23.5% of the ML width of the proximal tibia. See Table 14 and Table 15 for all distances obtained from the center of the ACL attachment to selected anatomic landmarks.

Table 14. Distances from the ACL center to the selected points, in mm, on the surface, with 95% confidence interval (CI) and coefficient of variation (CV). Pearson correlation with AP depth (AP), and significance (AP p), and ML width (ML) and significance (ML p).

ACL	MM	95% CI	CV	AP	AP P	ML	ML P
ACIK (H)	8.5	7.5 – 9.5	19.03	0.107	0.729	0.063	0.838
AMIK (G)	8.8	7.7 – 9.8	21.41	0.555*	0.039	0.650*	0.012
AFIR (F)	7.6	6.8 – 8.4	18.24	0.350	0.221	0.349	0.221
AISX	1.2	0.8 – 1.6	55.38	0.188	0.519	0.264	0.362
AMIR (B)	7.6	6.6 – 8.6	22.60	0.656*	0.011	0.781**	0.001
ALIR (D)	10.7	9.8 – 11.7	15.33	0.148	0.613	0.158	0.591
ARLM	7.0	6.0 – 8.0	23.94	0.582*	0.029	0.576*	0.031
AM ARLM	6.5	5.8 – 7.2	19.02	0.280	0.332	0.172	0.556
PM ARLM	7.4	6.1 – 8.7	31.06	0.677**	0.008	0.682**	0.007
AM PRLM	13.3	12.1 – 14.5	15.78	0.733**	0.003	0.818**	0.000
AMF (10b)	7.6	6.7 – 8.4	20.47	0.569*	0.034	0.638*	0.014
ALF	9.1	8.3 – 9.9	15.01	0.240	0.409	0.149	0.611
LT (4a)	14.5	13.5 – 15.6	12.68	0.599*	0.024	0.649*	0.012
MT (3a)	13.3	12.2 – 14.4	14.42	0.676**	0.008	0.729**	0.003
PRE (15)	10.9	9.9 – 11.9	15.94	0.820**	0.000	0.852**	0.000
POE (14a)	17.2	15.6 – 18.8	16.41	0.709**	0.004	0.824**	0.000
AL PCL	25.4	22.8 – 28.0	16.89	0.721**	0.005	0.852**	0.000

* Correlation is significant at the 0.05 level (2-tailed).

** Correlation is significant at the 0.01 level (2-tailed).

In green, measurements taken in a straight line over the surface. AL PCL: anterior aspect of PCL attachment.

Table 15. Distances from the ACL center to the selected points, on the surface: range, percentage of the AP depth (AP%) and ML width (ML%), and their 95% confidence interval (CI).

ACL	Range mm	AP%	AP% 95% CI	AP%	ML% 95% CI
ACIK (H)	7.1 – 11.1	17.0	15 – 19.1	11.79	10.4 – 13.2
AMIK (G)	6.5 – 11.8	17.5	15.7 – 19.2	12.09	10.9 – 13.3
AFIR (F)	4.2 – 9.4	15.2	13.7 – 16.7	10.51	9.5 – 11.5
AISX	0.3 – 2.4	2.4	1.7 – 3.2	1.69	1.2 – 2.2
AMIR (B)	5.2 – 11.0	15.1	13.6 – 16.6	10.44	9.4 – 11.5
ALIR (D)	7.7 – 13.9	21.6	19.2 – 23.9	14.92	13.4 – 16.4
ARLM	5.0 – 10.0	13.9	12.4 – 15.5	9.68	8.6 – 10.8
AM ARLM	4.4 – 9.1	13.1	11.7 – 14.5	9.06	8.1 – 10.1
PM ARLM	4.92 – 12.1	14.6	12.5 – 16.7	10.15	8.6 – 11.7
AM PRLM	9.6 – 17.2	26.5	24.9 – 28.2	18.40	17.3 – 19.5
AMF (10b)	4.8 – 9.4	15.0	13.6 – 16.5	10.43	9.4 – 11.4
ALF	7.2 – 11.5	18.2	16.6 – 19.8	12.61	11.5 – 13.7
LT (4a)	11.9 – 17.1	29.1	27.4 – 30.8	20.15	19 – 21.3
MT (3a)	8.4 – 15.8	26.6	24.8 – 28.3	18.41	17.3 – 19.6
PRE (15)	8.0 – 13.2	21.6	20.4 – 22.9	14.99	14.1 – 15.9
POE (14a)	11.8 – 21.8	34.2	31.9 – 36.6	23.72	22.2 – 25.2
AL PCL	19.2 – 31.8	50.4	46.9 – 53.9	34.96	32.7 – 37.2

NOTE. In green, measurements taken in a straight line over the surface. AL PCL: anterior aspect of PCL attachment.

IV.7.2.3.1. Anterior intercondylar staircase X

The measurement points included one identifiable osseous structure near to the ACL center, termed the anterior intercondylar staircase X (AISX), **10X**, the crossing between the sagittal incisure and the inner border of the central C – where the lateral slope becomes steeper (Fig. 294). The ACL center was anterior to it in the same direction as the AMIR, perpendicular to the posterior axis, in 72% of cases (anteromedial to it in 36%, and anterior in 36%), posterior in 14%, anterolateral in 7%, and posterolateral in 7%.

The distance between the AISX and the same sixteen points selected as reference for the ACL center were measured. A Spearman's rank-order correlation was run to determine the relationship between the measurements taken from the AISX and those taken from the ACL center. There was a strong, positive correlation with some of the reference points (see Table 16).

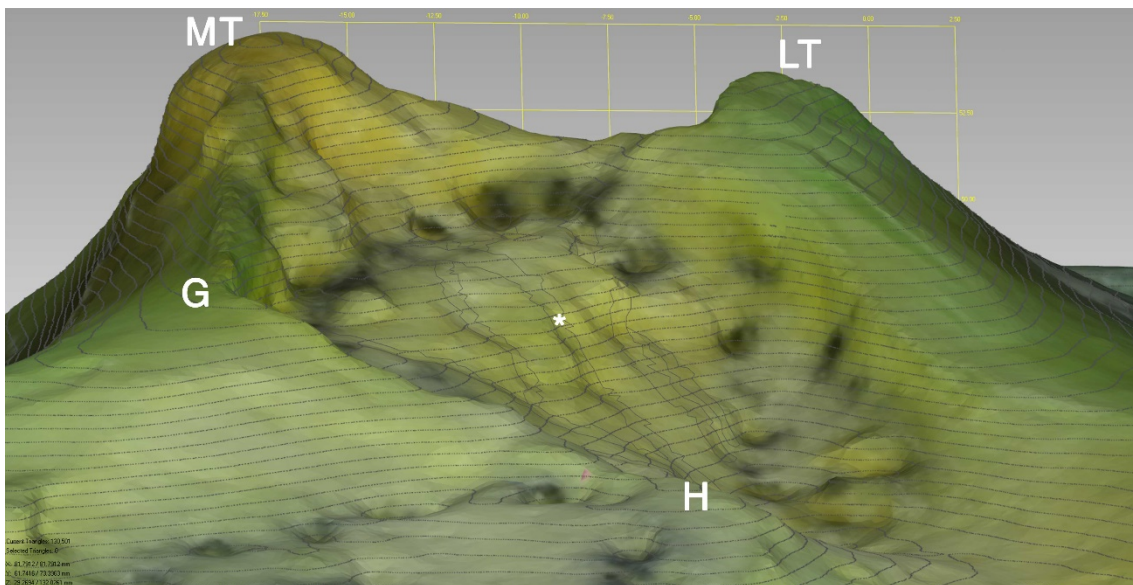


Figure 294. 3D model of tibia C, with contour lines superimposed. Anteroposterior view of the anterior intercondylar staircase. Main incisures in black lines. * AISX: intersection between the main sagittal incisure, and the medial border of the AIAR (notice the mediolateral change in slope). G: geniculum. H: anterocentral intercondylar knob. MT: medial tubercle. LT: lateral tubercle.

Table 16. Spearman's rank-order correlation between distances: ACL center to reference points and AISX to the same reference points; with p-values, and number of specimens for each distance.

ACL CENTER – AISX	SPEARMAN'S RHO	SIG. (2-TAIL)	N
C_H – X_H	.335	.263	13
C_G – X_G	.644*	.013	14
C_AFIR – X_AFIR	.327	.253	14
C_AMIR – X_AMIR	.930**	.000	14
C_ALIR – X_ALIR	.793**	.001	14
C_ARLM – X_ARLM	.771**	.001	14
C_AM-ARLM – X_AM-ARLM	.837**	.000	14
C_PM-ARLM – X_PM-ARLM	.881**	.000	14
C_AM-PRLM – X_AM-PRLM	.846**	.000	14
C_AMF – X_AMF	.574*	.032	14
C_ALF – X_ALF	.925**	.000	14
C_LT – X_LT	.754**	.002	14
C_MT – X_MT	.705**	.005	14
C_PRE – X_PRE	.727**	.003	14
C_POE – X_POE	.873**	.000	14
C_AL-PCL – X_AL-PCL	.956**	.000	13

* Correlation is significant at the 0.05 level (2-tailed).

** Correlation is significant at the 0.01 level (2-tailed).

IV.7.2.4. ACL bundles

IV.7.2.2.1. Qualitative and quantitative description

The sagittal incisure with the coronal branch, 10g₃, marked the footprint of the coronal septum (devoid of ACL fibers) and represented thus the ACL bundle incisure that separated the anteromedial bundle from the posterolateral bundle.

The boundary between the AM and AL bundles was approximately located at the inner border of the central C, approximately corresponding to the sagittal line.

For comparison purposes, area 10 was divided by 10g₃ into a posterolateral (**10_{PL}**) and an anteromedial (**10_{AM}**) aspect (Fig. 295). The anteromedial aspect was in turn divided by the sagittal line into a medial (**10_{AMM}**) and a lateral (**10_{AML}**) part. These areas were selected to compare them to the actual attachment areas of their corresponding bundles, to get an estimation of their non-insertional areas.

The ACL AM bundle attachment area had 84.3 mm² (95% CI, 66.8 – 101.7 mm², range, 43.5 mm² to 142.1 mm²), and it covered 74.2% of area 10_{AM} (95% CI 67.5 – 80.9%; range, 58% to 93%). The ACL PL bundle attachment area had 60.9 mm² (95% CI 51.6 – 70.1 mm²; range, 32.7 mm² to 94.7 mm²), covering 75% of area 10_{PL} (95% CI 67.2 – 82.8%; range, 56% to 100%).

The attachment of the medial portion of the ACL AM bundle attachment had 45.6 mm² (95% CI 36.7 – 56.5 mm², range 22.3 mm² to 84 mm²), representing 71.4% of area 10_{AMM} (95% CI 63.9 – 78.8%; range, 53% to 90%). The ACL AM bundle, lateral part, had 37.7 mm² (95% CI 29.6 – 45.7 mm², range 20.5 mm² to 61.2 mm²), covering 80.9% of area 10_{AML} (95% CI 70.4 – 91.4%; range, 50% to 105%).

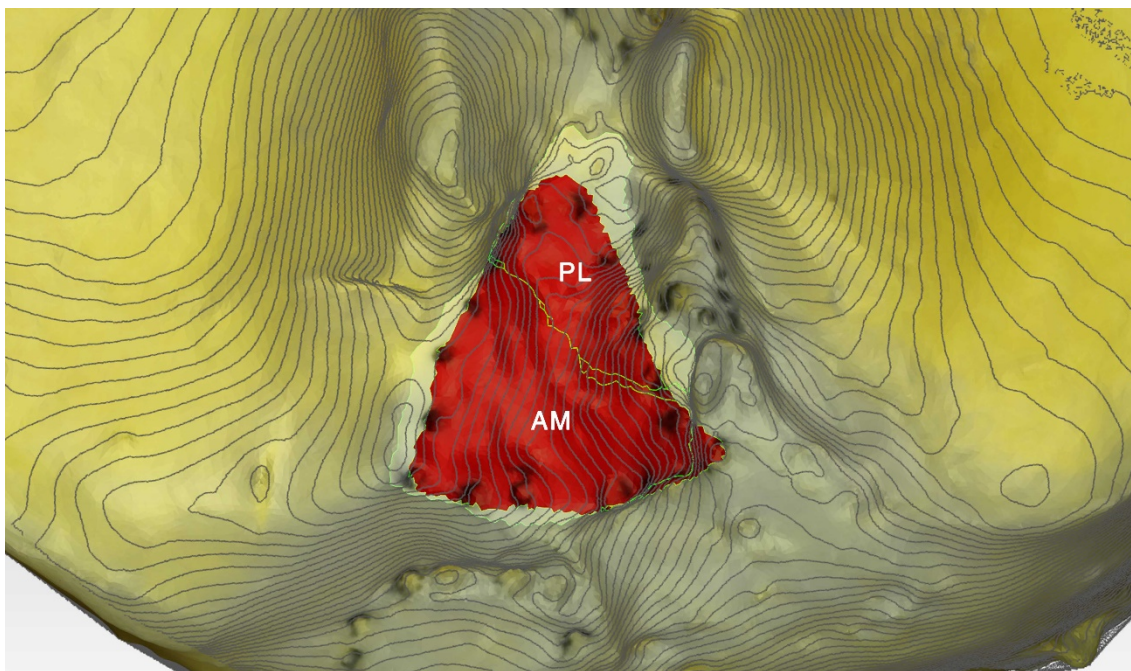


Figure 295. 3D model of tibia B, with contour lines superimposed (left-mirrored). ACL AM and PL bundle footprints highlighted in red. Areas 10_{AM} and 10_{PL} highlighted over the rest of the specimen (surrounding their respective bundle areas). The four areas are surrounded by light fluorescent green lines.

IV.7.2.2.3. Distances from ACL anteromedial and posterolateral bundles

The center of the ACL AM bundle attachment was 13.5 mm (range, 10.5 mm to 15.7 mm) from the center of the preeminence ridge, a measurement that had a significant correlation with AP depth ($r=0.831$, $p<0.001$), ML width ($r=0.859$, $p<0.001$), CV 14.44%. Proportionally, it represented 26.8% of the AP depth, and 18.6% of the ML width of the proximal tibia. See Table 17 and Table 18 for all distances obtained from the center of the ACL AM bundle attachment to selected anatomic landmarks.

Table 17. Distances from the center of the AM bundle of the ACL to the selected points, in mm, on the surface, with 95% confidence interval (CI) and coefficient of variation (CV). Pearson correlation with AP depth (AP), and significance (AP p), and ML width (ML) and significance (ML p).

ACL-AM	MM	95% CI	CV	AP	AP P	ML	ML P
ACIK (H)	7.2	6.0 – 8.4	27.26	0.038	0.901	-0.121	0.694
AMIK (G)	7.4	6.3 – 8.5	26.16	0.558*	0.038	0.703**	0.005
AFIR (F)	5.2	4.2 – 6.1	30.06	0.249	0.392	0.222	0.446
AISX	3.6	3.0 – 4.2	29.53	0.348	0.222	0.368	0.196
AMIR (B)	8.1	6.9 – 9.3	25.49	0.619*	0.018	0.738**	0.003
ALIR (D)	11.3	10.3 – 12.4	16.26	0.703**	0.005	0.630*	0.016
ARLM	8.7	7.5 – 10.0	24.48	0.632*	0.015	0.600*	0.023
AM ARLM	7.2	6.3 – 8.1	21.70	0.475	0.086	0.377	0.184
PM ARLM	10.0	8.4 – 11.6	27.45	0.685**	0.007	0.674**	0.008
AM PRLM	15.9	14.5 – 17.3	14.90	0.745**	0.002	0.817**	0.000
AMF (10b)	9.9	8.9 – 10.9	17.36	0.632*	0.015	0.679**	0.008
ALF	9.6	8.6 – 10.5	16.63	0.349	0.222	0.239	0.410
LT (4a)	17.2	16.0 – 18.4	12.12	0.573*	0.032	0.599*	0.024
MT (3a)	15.3	14.4 – 16.2	10.14	0.627*	0.016	0.664**	0.010
PRE (15)	13.5	12.4 – 14.6	14.44	0.831**	0.000	0.859**	0.000
POE (14a)	18.5	15.2 – 21.7	30.25	0.470	0.090	0.488	0.077
AL PCL	28.3	25.5 – 31.0	16.11	0.774**	0.002	0.874**	0.000
ACL-PL	6.2	5.5 – 6.9	19.08	0.695**	0.006	0.736**	0.003

* Correlation is significant at the 0.05 level (2-tailed).

** Correlation is significant at the 0.01 level (2-tailed).

In green, measurements taken in a straight line over the surface.

Table 18. Distances from the center of the AM bundle of the ACL to the selected points, on the surface: range, percentage of the AP depth (AP%) and ML width (ML%), and their 95% confidence interval (CI).

ACL-AM	Range mm	AP%	AP% 95% CI	AP%	ML% 95% CI
ACIK (H)	5.5 – 11.6	14.4	12 – 16.8	10.0	8.3 – 11.7
AMIK (G)	4.6 – 10.6	14.7	12.9 – 16.6	10.2	8.9 – 11.5
AFIR (F)	1.3 – 7.1	10.3	8.6 – 12	7.2	6 – 8.4
AISX	1.9 – 5.4	7.1	6 – 8.3	4.9	4.2 – 5.7
AMIR (B)	4.7 – 12.3	16.1	14.2 – 18	11.1	9.8 – 12.4
ALIR (D)	8.5 – 14.5	22.6	21.1 – 24.1	15.7	14.5 – 16.8
ARLM	6.3 – 13.2	17.3	15.4 – 19.3	12.0	10.6 – 13.5
AM ARLM	5.1 – 9.8	14.3	12.8 – 15.9	10.0	8.8 – 11.1
PM ARLM	6.8 – 16.3	19.7	17.3 – 22.2	13.7	11.9 – 15.6
AM PRLM	11.6 – 19.8	31.7	29.8 – 33.5	21.9	20.7 – 23.2
AMF (10b)	6.9 – 12.2	19.8	18.3 – 21.4	13.7	12.6 – 14.8
ALF	7.4 – 12.9	19.1	17.5 – 20.8	13.3	12 – 14.5
LT (4a)	14.4 – 20.4	34.4	32.5 – 36.4	23.9	22.6 – 25.2
MT (3a)	13.3 – 18.1	30.6	29.1 – 32.1	21.2	20.3 – 22.1
PRE (15)	10.5 – 15.7	26.8	25.5 – 28.2	18.6	17.7 – 19.6
POE (14a)	2.1 – 24.4	36.7	30.9 – 42.6	25.5	21.4 – 29.5
AL PCL	21.2 – 35.4	56.2	52.8 – 59.6	39.0	36.7 – 41.3
ACL-PL	4.4 – 8.5	12.4	11.4 – 13.4	8.6	7.9 – 9.3

NOTE. In green, measurements taken in a straight line over the surface.

The center of the ACL PL bundle attachment was 11 mm (range, 8.8 mm to 13.6 mm) from the center of the anterior intercondylar ridge, a measurement that had a significant correlation with AP depth ($r=0.803$, $p=0.001$), ML width ($r=0.851$, $p<0.001$), CV 13.08%. Proportionally, it represented 22% of the AP depth, and 15.3% of the ML width of the proximal tibia. See Table 19 and Table 20 for all distances obtained from the center of the ACL PL bundle attachment to selected anatomic landmarks.

Table 19. Distances from the center of the PL bundle of the ACL to the selected points, in mm, on the surface, with 95% confidence interval (CI) and coefficient of variation (CV). Pearson correlation with AP depth (AP), and significance (AP p), and ML width (ML) and significance (ML p).

ACL-PL	MM	95% CI	CV	AP	AP P	ML	ML P
ACIK (H)	11.7	10.3 – 13.0	18.80	0.501	0.081	0.497	0.084
AMIK (G)	12.3	11.1 – 13.5	16.91	0.610*	0.021	0.657*	0.011
AFIR (F)	11.0	10.2 – 11.9	13.08	0.803**	0.001	0.851**	0.000
AISX	2.7	2.2 – 3.1	29.17	0.491	0.074	0.549*	0.042
AMIR (B)	8.3	7.3 – 9.2	20.30	0.647*	0.012	0.732**	0.003
ALIR (D)	10.4	9.2 – 11.6	20.18	0.415	0.140	0.299	0.300
ARLM	5.6	4.8 – 6.5	25.13	0.373	0.189	0.412	0.143
AM ARLM	6.7	5.5 – 7.9	31.23	-0.033	0.911	-0.003	0.992
PM ARLM	4.5	3.6 – 5.4	34.16	0.689**	0.006	0.583*	0.029
AM PRLM	9.9	9.1 – 10.7	14.06	0.688**	0.006	0.764**	0.001
AMF (10b)	5.0	4.2 – 5.8	26.37	0.378	0.183	0.379	0.182
ALF	9.5	8.4 – 10.7	20.95	0.127	0.665	0.019	0.948
LT (4a)	11.2	10.5 – 12.0	11.15	0.349	0.221	0.371	0.191
MT (3a)	11.9	11.2 – 12.6	10.19	0.550*	0.042	0.626*	0.017
PRE (15)	7.5	6.9 – 8.1	14.34	0.768**	0.001	0.768**	0.001
POE (14a)	14.1	12.7 – 15.4	16.29	0.632*	0.015	0.746**	0.002
AL PCL	22.3	20.1 – 24.6	16.59	0.717**	0.006	0.812**	0.001

* Correlation is significant at the 0.05 level (2-tailed).

** Correlation is significant at the 0.01 level (2-tailed).

In green, measurements taken in a straight line over the surface.

Table 20. Distances from the center of the PL bundle of the ACL to the selected points, on the surface: range, percentage of the AP depth (AP%) and ML width (ML%), and their 95% confidence interval (CI).

ACL-PL	Range mm	AP%	AP% 95% CI	AP%	ML% 95% CI
ACIK (H)	9.0 – 16.1	23.1	21 – 25.3	16.1	14.5 – 17.6
AMIK (G)	8.9 – 14.9	24.4	22.6 – 26.3	16.9	15.6 – 18.3
AFIR (F)	8.8 – 13.6	22.0	21.1 – 23	15.3	14.6 – 15.9
AISX	1.5 – 4.2	5.3	4.5 – 6.1	3.7	3.1 – 4.2
AMIR (B)	5.8 – 11.2	16.5	15 – 18	11.4	10.4 – 12.4
ALIR (D)	6.5 – 15.9	20.7	18.5 – 22.9	14.4	12.8 – 16
ARLM	3.3 – 8.0	11.3	9.8 – 12.8	7.8	6.8 – 8.9
AM ARLM	2.5 – 9.5	13.5	11 – 16.1	9.3	7.6 – 11.1
PM ARLM	2.4 – 7.8	8.9	7.4 – 10.3	6.2	5.1 – 7.3
AM PRLM	6.8 – 12.1	19.8	18.6 – 21.1	13.7	12.9 – 14.5
AMF (10b)	2.9 – 7.5	10.0	8.6 – 11.4	6.9	6 – 7.9
ALF	5.8 – 13.8	19.1	16.8 – 21.5	13.3	11.6 – 14.9
LT (4a)	8.9 – 12.9	22.5	21 – 24.1	15.6	14.6 – 16.6
MT (3a)	10.0 – 13.9	23.8	22.5 – 25.1	16.5	15.7 – 17.3
PRE (15)	5.7 – 9.0	15.0	14.2 – 15.8	10.4	9.8 – 11
POE (14a)	9.5 – 17.0	28.0	25.9 – 30.1	19.4	18 – 20.8
AL PCL	15.9 – 27.6	44.4	41.3 – 47.5	30.8	28.7 – 32.8

NOTE. In green, measurements taken in a straight line over the surface.

IV.7.2.2.4. Distances from ACL anteromedial bundle, medial and lateral parts

Mean measures obtained from the AMM bundle center to reference landmarks are included in Table 21 and Table 22, and those obtained from the AML bundle center in Table 23 and Table 24.

Table 21. Distances from the center of the AMM bundle of the ACL to the selected points, in mm, on the surface, with 95% confidence interval (CI) and coefficient of variation (CV). Pearson correlation with AP depth (AP), and significance (AP p), and ML width (ML) and significance (ML p).

ACL-AMM	MM	95% CI	CV	AP	AP P	ML	ML P
ACIK (H)	9.5	8.4 – 10.7	20.10	0.178	0.560	0.079	0.798
AMIK (G)	6.3	5.4 – 7.1	23.19	0.235	0.418	0.284	0.324
AFIR (F)	6.6	5.6 – 7.6	26.13	0.070	0.813	0.064	0.827
AISX	4.1	3.5 – 4.6	25.26	0.407	0.149	0.499	0.070
AMIR (B)	5.7	4.8 – 6.6	27.47	0.562*	0.036	0.564*	0.036
ALIR (D)	13.6	12.2 – 15.0	18.04	0.764**	0.001	0.721**	0.004
ARLM	10.3	8.9 – 11.6	22.70	0.747**	0.002	0.759**	0.002
AM ARLM	9.4	8.4 – 10.4	18.32	0.702**	0.005	0.686**	0.007
PM ARLM	10.1	8.4 – 11.9	30.29	0.735**	0.003	0.721**	0.004
AM PRLM	15.1	13.6 – 16.6	17.15	0.705**	0.005	0.745**	0.002
AMF (10b)	8.6	7.8 – 9.5	17.06	0.608*	0.021	0.623*	0.017
ALF	12.0	10.9 – 13.0	14.85	0.650*	0.012	0.624*	0.017
LT (4a)	17.1	15.7 – 18.5	13.88	0.588*	0.027	0.604*	0.022
MT (3a)	13.0	12.1 – 14.0	12.33	0.371	0.192	0.310	0.281
PRE (15)	12.5	11.1 – 14.0	19.90	0.714**	0.004	0.711**	0.004
POE (14a)	18.6	16.8 – 20.4	16.61	0.693**	0.006	0.771**	0.001
AL PCL	26.9	23.6 – 30.2	20.37	0.695**	0.008	0.779**	0.002
ACL-AML	6.1	5.2 – 7.0	25.34	0.811**	0.000	0.917**	0.000
ACL-PL	6.2	5.4 – 7.0	23.16	0.690**	0.006	0.700**	0.005

* Correlation is significant at the 0.05 level (2-tailed).

** Correlation is significant at the 0.01 level (2-tailed).

NOTE. In green, measurements taken in a straight line over the surface.

Table 22. Distances from the center of the AMM bundle of the ACL to the selected points, on the surface: range, percentage of the AP depth (AP%) and ML width (ML%), and their 95% confidence interval (CI).

ACL-AMM	Range mm	AP%	AP% 95% CI	AP%	ML% 95% CI
ACIK (H)	7.2 – 13.9	19.0	16.7 – 21.3	13.2	11.6 – 14.8
AMIK (G)	3.4 – 8.7	12.6	10.9 – 14.3	8.7	7.6 – 9.9
AFIR (F)	2.4 – 9.1	13.2	11.2 – 15.2	9.1	7.8 – 10.5
AISX	2.4 – 5.9	8.1	7 – 9.2	5.6	4.9 – 6.3
AMIR (B)	3.1 – 8.5	11.3	9.8 – 12.9	7.8	6.8 – 9
ALIR (D)	9.4 – 17.9	27.0	25.1 – 29	18.8	17.3 – 20.3
ARLM	7.1 – 13.9	20.4	18.5 – 22.3	14.2	12.7 – 15.6
AM ARLM	6.2 – 11.8	18.8	17.3 – 20.2	13.0	11.9 – 14.1
PM ARLM	6.6 – 16.0	20.0	17.2 – 22.8	13.9	11.8 – 15.9
AM PRLM	10.9 – 19.7	30.0	27.9 – 32.2	20.8	19.3 – 22.3
AMF (10b)	6.3 – 11	17.2	15.8 – 18.5	11.9	11 – 12.9
ALF	9.1 – 14.8	23.9	22.3 – 25.4	16.5	15.4 – 17.7
LT (4a)	13.7 – 20.6	34.2	32 – 36.3	23.7	22.2 – 25.2
MT (3a)	10.8 – 16.0	26.1	24.3 – 28	18.1	16.8 – 19.4
PRE (15)	6.9 – 15.8	24.9	22.7 – 27	17.3	15.7 – 18.8
POE (14a)	14.1 – 23.7	37.1	34.5 – 39.6	25.7	24 – 27.4
AL PCL	15.5 – 34.2	53.3	48.3 – 58.3	37.0	33.6 – 40.4
ACL-AML	4.1 – 9.3	12.1	10.9 – 13.4	8.4	7.5 – 9.3
ACL-PL	3.7 – 8.4	12.3	11 – 13.6	8.5	7.6 – 9.5

NOTE. In green, measurements taken in a straight line over the surface.

Table 23. Distances from the center of the AML bundle of the ACL to the selected points, in mm, on the surface, with 95% confidence interval (CI) and coefficient of variation (CV). Pearson correlation with AP depth (AP), and significance (AP p), and ML width (ML) and significance (ML p).

ACL-AML	MM	95% CI	CV	AP	AP P	ML	ML P
ACIK (H)	4.4	3.4 – 5.4	37.96	-0.050	0.872	-0.163	0.594
AMIK (G)	9.6	7.9 – 11.3	29.78	0.637*	0.014	0.796**	0.001
AFIR (F)	4.9	3.9 – 5.9	34.73	0.668**	0.009	0.791**	0.001
AISX	5.4	4.7 – 6.1	22.74	0.705**	0.005	0.786**	0.001
AMIR (B)	11.2	9.9 – 12.5	19.74	0.686**	0.007	0.785**	0.001
ALIR (D)	9.2	8.2 – 10.2	19.19	0.527	0.053	0.453	0.104
ARLM	8.1	6.7 – 9.4	28.15	0.583*	0.029	0.576*	0.031
AM ARLM	5.3	4.3 – 6.3	32.61	0.430	0.125	0.378	0.182
PM ARLM	10.8	9.1 – 12.5	27.01	0.688**	0.007	0.708**	0.005
AM PRLM	17.5	16.1 – 19	14.40	0.799**	0.001	0.901**	0.000
AMF (10b)	12.3	10.9 – 13.6	19.19	0.639*	0.014	0.705**	0.005
ALF	7.1	6.3 – 7.9	20.32	0.171	0.560	0.060	0.840
LT (4a)	18.4	17.2 – 19.6	11.48	0.671**	0.009	0.744**	0.002
MT (3a)	18.3	17.2 – 19.5	10.89	0.741**	0.002	0.827**	0.000
PRE (15)	15.2	13.9 – 16.5	14.46	0.853**	0.000	0.927**	0.000
POE (14a)	21.8	19.9 – 23.8	15.57	0.755**	0.002	0.885**	0.000
AL PCL	30.0	27.1 – 32.8	15.95	0.801**	0.001	0.913**	0.000
ACL-PL	8.1	6.7 – 9.6	30.52	0.510	0.062	0.510	0.063

* Correlation is significant at the 0.05 level (2-tailed).

** Correlation is significant at the 0.01 level (2-tailed).

NOTE. In green, measurements taken in a straight line over the surface.

Table 24. Distances from the center of the AML bundle of the ACL to the selected points, on the surface: range, percentage of the AP depth (AP%) and ML width (ML%), and their 95% confidence interval (CI).

ACL-AML	Range mm	AP%	AP% 95% CI	AP%	ML% 95% CI
ACIK (H)	2.7 – 8.2	8.8	6.7 – 10.9	6.1	4.6 – 7.6
AMIK (G)	5.3 – 13.8	19.0	16.3 – 21.7	13.1	11.3 – 15
AFIR (F)	2.2 – 8.0	9.7	8 – 11.3	6.7	5.6 – 7.8
AISX	3.6 – 7.3	10.6	9.6 – 11.8	7.4	6.6 – 8.1
AMIR (B)	7.2 – 14.7	22.2	20.3 – 24.2	15.4	14.1 – 16.7
ALIR (D)	6.4 – 12.6	18.3	16.6 – 20	12.7	11.5 – 14
ARLM	4.8 – 13.8	16.0	13.8 – 18.2	11.1	9.5 – 12.7
AM ARLM	2.7 – 10.1	10.6	8.8 – 12.4	7.4	6.1 – 8.7
PM ARLM	5.6 – 17.5	21.3	18.7 – 24	14.8	12.9 – 16.8
AM PRLM	13.5 – 21.7	34.9	33.2 – 36.7	24.2	23.1 – 25.3
AMF (10b)	7.9 – 15.8	24.4	22.3 – 26.5	16.9	15.5 – 18.4
ALF	5.0 – 9.4	14.2	12.6 – 15.9	9.9	8.7 – 11.1
LT (4a)	14.4 – 22.3	36.7	34.9 – 38.6	25.4	24.3 – 26.6
MT (3a)	15 – 22.4	36.6	35.1 – 38.2	25.4	24.5 – 26.3
PRE (15)	10.7 – 18.6	30.2	28.8 – 31.7	20.9	20 – 21.9
POE (14a)	14.6 – 26.8	43.4	40.8 – 46.1	30.1	28.4 – 31.8
AL PCL	22.7 – 38.7	59.4	56 – 62.9	41.2	39 – 43.5
ACL-PL	5.1 – 15.2	16.1	13.7 – 18.6	11.2	9.4 – 13

NOTE. In green, measurements taken in a straight line over the surface.

IV.7.2.3. Anterior intercondylar staircase in 3D model from arthroscopic video

Study III included 19 patients with a mean age of 26.3 years (range, 17 to 43 years), 83% were males, and 61% were left knees.

In 3D models from arthroscopy, the osseous surface of the ACL attachment was qualitatively found more difficult to ascertain than in 3D models of specimens, due mainly to soft tissue remains and less image quality (Fig. 298). The duck's foot shape of the footprint seemed to be narrower on video than it actually is (Fig. 296). The C-shaped structures of the ACL attachment area were less readily recognizable at a glance than the staircase. The AIAR could always be located, as a steep wall dividing the staircase from the anterolateral fossa (Fig. 299).

Commonly available areas for measuring in the 3D models were the AMIR (100%), the geniculum (94%), the AFIR (94%), as well the posterior arch (89%) and preeminence (94%), and the anteromedial fossa (79%). Other reference structures were generally seen: the concavity within the AIAR (63%), the coronal incisure (63%), and often also the full sagittal incisure (42%).

Commonly covered aspects included the anteromedial fovea (visible in 31%) and the anterocentral intercondylar knob, covered by Hoffa's fat (visible in 42%); and the medial border of the ARLM, including the posterolateral ACL attachment, the posterior AIAR, and the posterior part of the sagittal incisure.

A part of the AIAR could be identified in all cases. The sagittal incisure was not always readily identifiable, and proper soft tissue cleaning was found necessary to locate the AISX.

Identification of the coronal incisure, the AFIR, the posterior arch, and the AL fossa, as well as any osseous landmark, helped to more confidently identify the sagittal ridge, and its crossing with the AIAR.

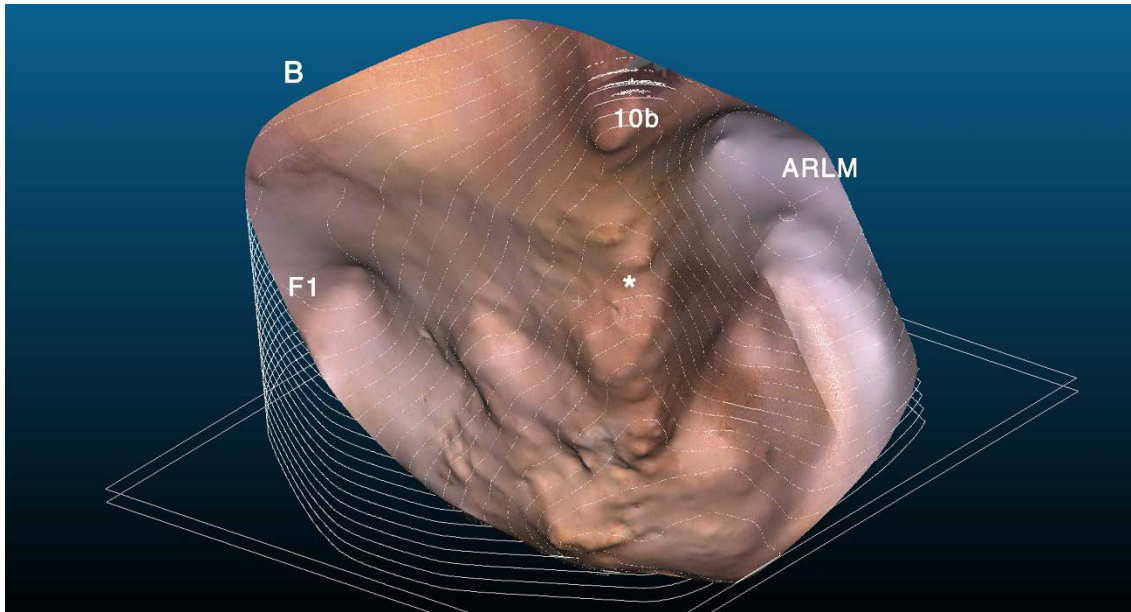


*Figure 296. Study III. Patient 1. 3D model of ACL footprint, based on 18 arthroscopic images taken after cleaning of soft tissues, with contour lines superimposed. Notice from the situation of the contour lines that, because of the superolateral position of the arthroscope (through an anterolateral portal), the horizontal plane (as interpreted by the software) has been placed more inferiorly in its anterior aspect than the actual horizontal plane, hence the apparent upward slope from posterior to anterior. ARLM: lateral soft tissue remains (including ARLM attachment and ARLM – ACL intermingled fibers). B: medial wall of the AMIR. F1: elevation corresponding to a medial or central aspect of the posterior AFIR process. *: AISX.*

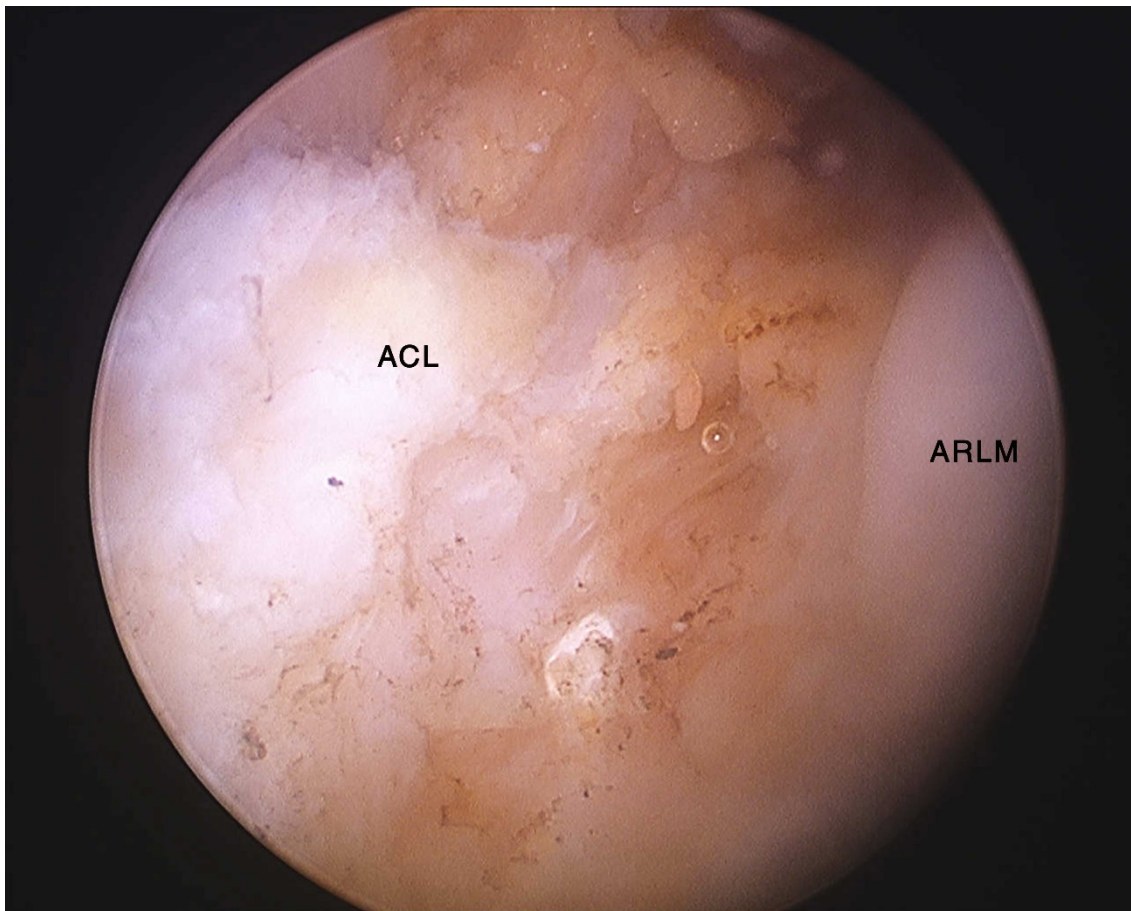


Figure 297. Study III. Patient 1. Intraoperative arthroscopic image of ACL footprint, used for 3D model creation. Observe ACL soft tissue remains over area recognized as part of the AMIR in the 3D model (see Figure 296), and ARLM attachment.

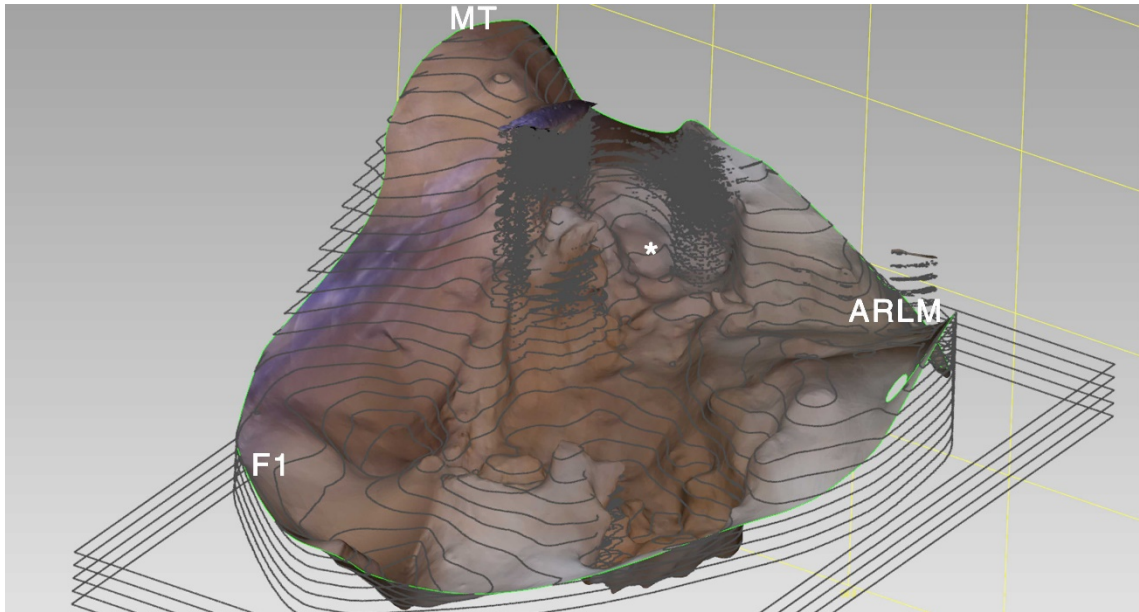


Figure 298. Study III. Patient 7. 3D model of ACL footprint, based on 93 still images of arthroscopic video made from anterolateral and anteromedial portals, after cleaning of soft tissues and passing of suture loop through the ACL femoral tunnel. Contour lines superimposed. Notice remains of soft tissues on area 10, and correct 3D obtained from suture loop posteriorly (over the area), but merged with medial wall anteriorly. ARLM: lateral soft tissue remains (including ARLM attachment and ARLM – ACL intermingled fibers). MT: medial tubercle. F1: elevation corresponding to a medial or central aspect of the posterior AFIR process. *: AISX.

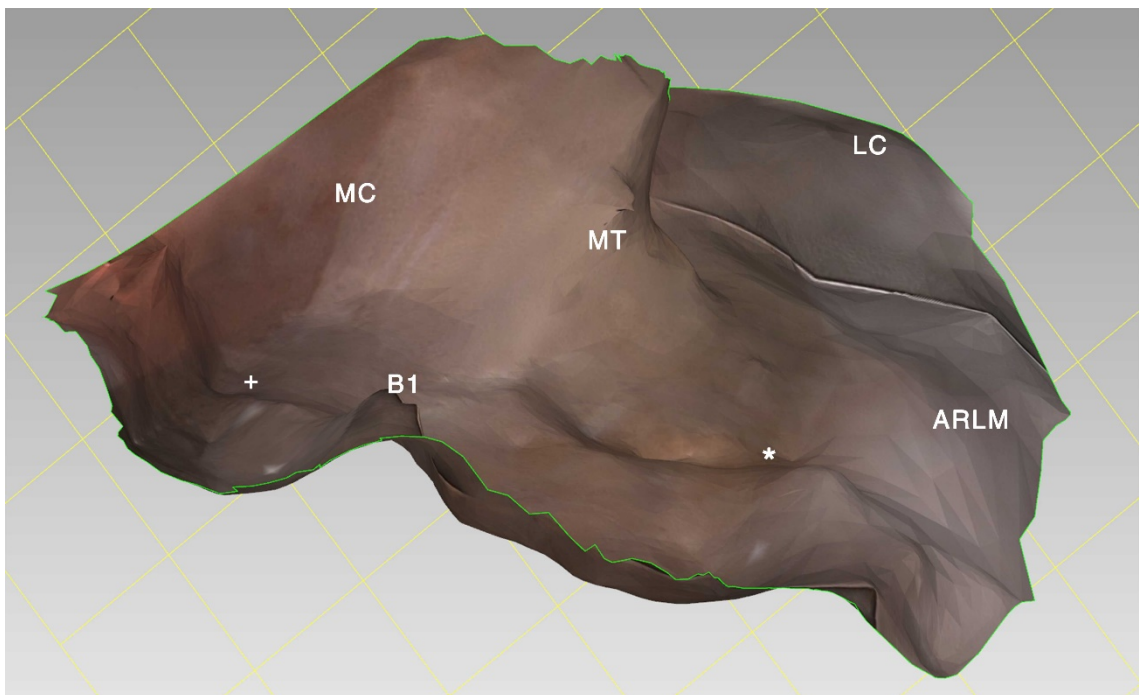


Figure 299. Study III. Patient 18. 3D model of ACL footprint, based on 68 still images of arthroscopic video made from the anterolateral portal, after cleaning of soft tissues. A measuring probe (+) is inserted between B1 and the medial condyle, but no 3D model was obtained of it, its image being merged with the condylar area. Medial (MC) and lateral (LC) femoral condyles also merged into the ACL footprint (notice how part of the medial femoral condyle has a more reddish color, because of the notchplasty performed). ARLM: lateral soft tissue remains (including ARLM attachment and ARLM – ACL intermingled fibers). MT: medial tubercle. B1: central AMIR process. *: AISX.

IV.7.2.4. Anterior intercondylar staircase in tibial spine fractures

The 22 patients included in Study IV had a mean age of 23.7 years (range, 11 to 57 years), 18 (82%) were males, 13 (59%) were left knees. 9% were type I fractures, 14% were type II, 72% were type III, and 5% were type IV fractures of the Meyers & McKeever classification (Fig. 300). 72% were clearly comminuted fractures (Fig. 301). 32% had meniscal lesions associated: the ARLM was affected in 27% (one in a type II fracture, the rest in type III fractures), the ARMM in 9% (all in type III fractures).

In CT sagittal cuts, the anterior aspect of the LT (corresponding approximately to areas 7 and 9) was identified as affected in 77% of cases; the 6 cases of affected ARLM belonged to this group. Area 8 and the anterior peak (4a or at least 4c depending on the available slices) were affected in 23%, all 5 cases with ARLM affected. The internal ALIR process, D3, appeared affected in 81%, and the central process, D2, (at least a part of it) in 50% of cases.

The internal AMIR process, B2, was affected in 100%, and the central process, B1, was clearly identified as affected in 95% of cases (all but for one, with wider sagittal cuts). In all 95%, a part of the medial condyle adjacent to B1 was avulsed as well. The anterior aspect of the MT was affected in at least 91%, with the avulsed bone reaching the anterior (or overall peak) in 86%.

In CT coronal cuts, the anterior part of the central ALIR process (anterior aspect of area 2c) appeared intact in all cases, with the central part affected in 32%.

The AMIR central process seemed to be affected in its medial and anterior aspects in 95%, with the posterior aspect affected in 82%, and area 1c affected in 5% (a case with a lesion of the ARMM).

A part or all the posterior MT tubercle was affected in 41%, while the intertubercular ridge was affected in 27%. The tibial spine – including both tubercles and the intertubercular ridge – was affected in 14%. These were all in the group of more comminuted fractures, and two of them were the only ones associated with tibial plateau fractures.

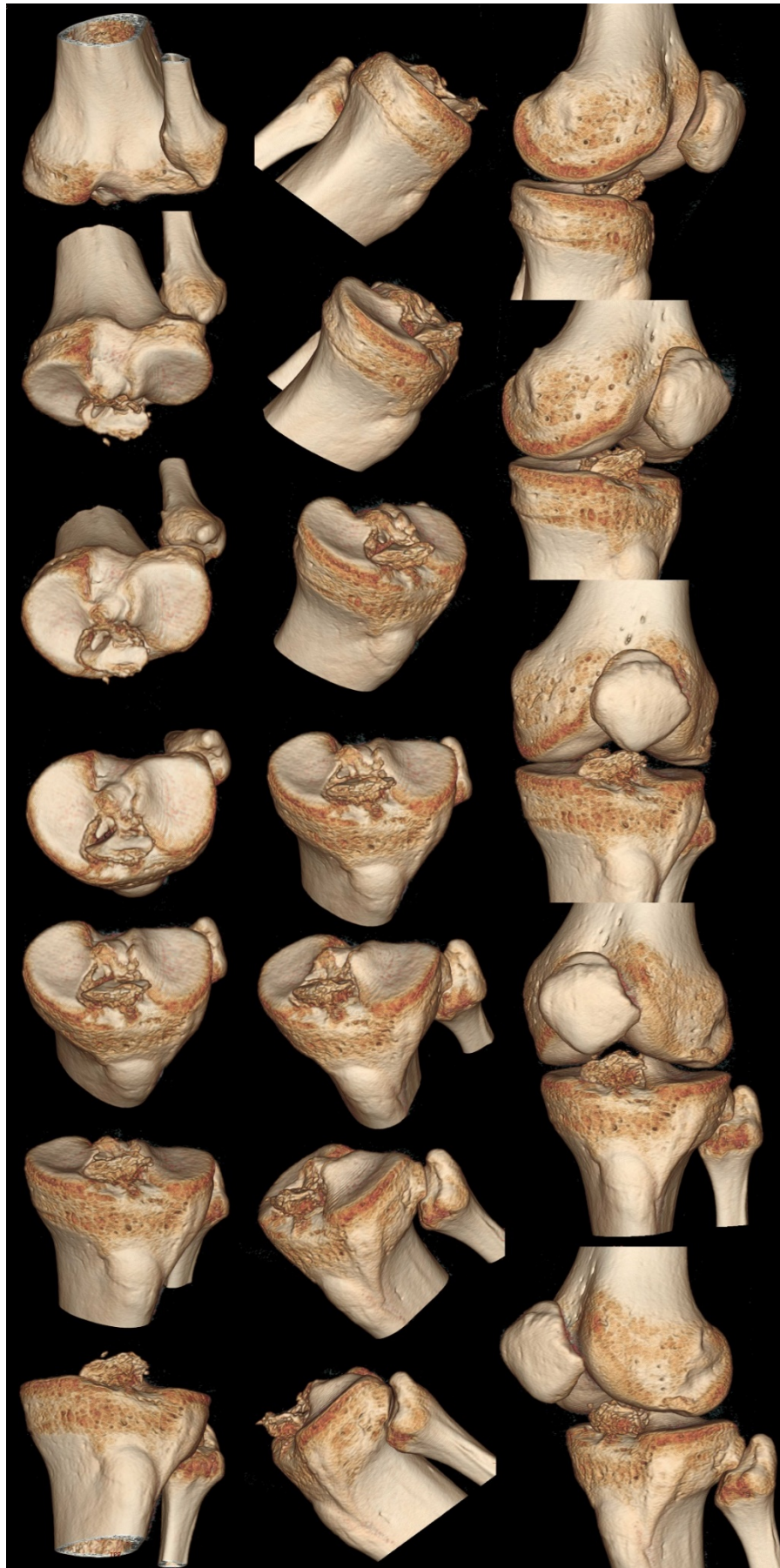


Figure 300. Study IV. 3D volume rendering of the CT of one patient. Left column, sagittal rotation of the 3D model of the tibia. Middle column, axial rotation from medial (top) to lateral (bottom) view of the 3D model of the tibia. Right column, axial rotation of the 3D model of the knee.

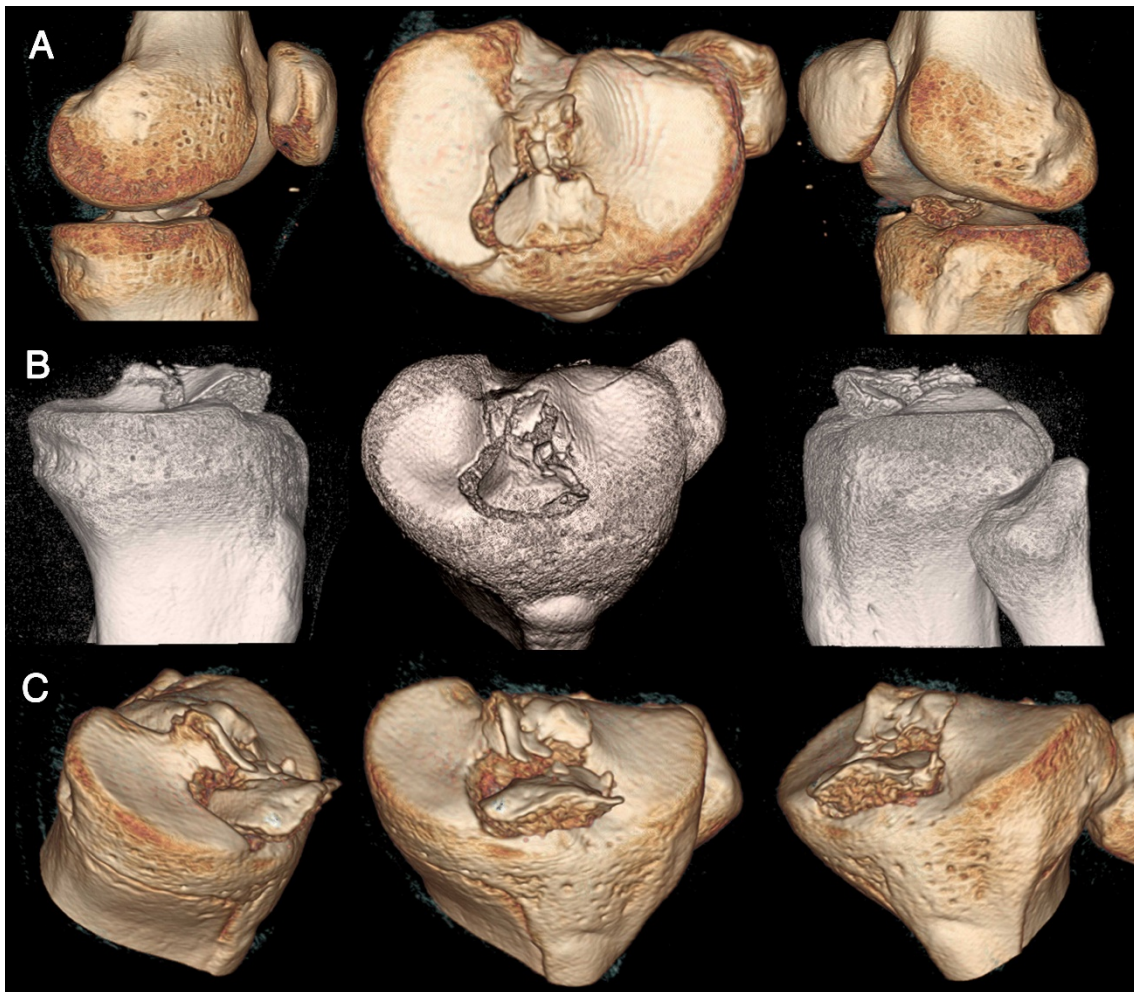


Figure 301. Study IV. Left column, medial view of the 3D model. Middle column, superior view. Right column, lateral view. Each row corresponds to one patient, identified with a letter (A, B, and C).

IV.7.3. Degenerative changes of the anterior intercondylar staircase

IV.7.3.1. Qualitative assessment

The AIAR concavity, A1b, had a bigger radius of curvature in normal tibias than in those with degenerative changes.

In most tibias with degenerative changes, the posterior line, D3_b, appeared elevated together with the main D3_a process, but both could also appear elevated separately, with D3_b appearing as the medial border of a deep and narrow AL recess.

A big, central intertubercular fossa could be observed as the main depression in the posterior aspect of area 10, with the anteromedial fovea, 10b, usually merging with it.

Stairs and landings showed a trend to a higher position in tibias with degenerative changes, but they were not always found equally elevated relative to each other. The lower landing appeared less frequently than in normal tibias, and it was much less commonly found than the upper landing in pathological specimens.

The C-shaped layers were often found elevated independently, with lines and incisures appearing more marked (Fig. 302). The C-shaped layers could be found more selectively elevated medially (Fig. 303), anteromedially (Fig. 180), or posterolaterally (Fig. 184). In some cases the central C was found elevated into a more homogeneous and wider fornix, together with the inner C (Fig. 304).

Even in cases with an elevated AIAR, the fan-like facet usually remained as a smaller, non-elevated concavity.

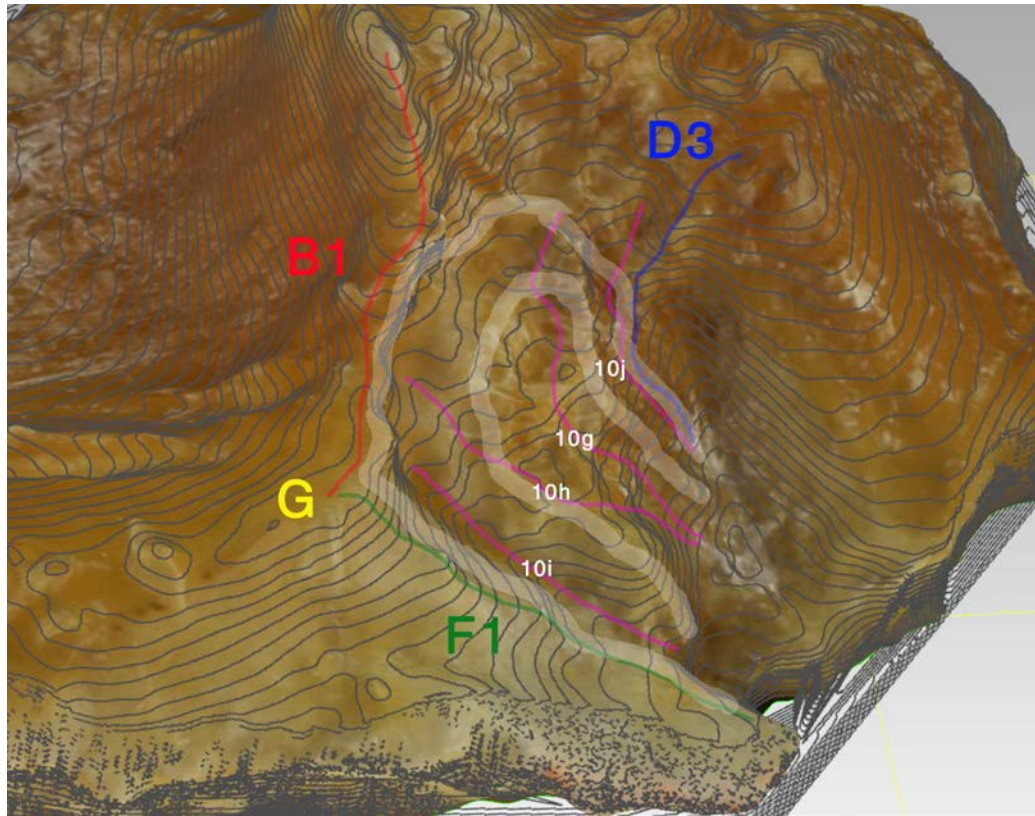


Figure 302. 3D model of tibia 64 with contour lines superimposed. Main AIS incisures (10g, 10h, 10i, 10j) markedly depressed, with elevated horseshoe-shaped C-layers (painted over in white). Also labelled are the external AMIR process (B1), posterior AFIR process (F1), Parson's knob (G), internal ALIR process (D3).

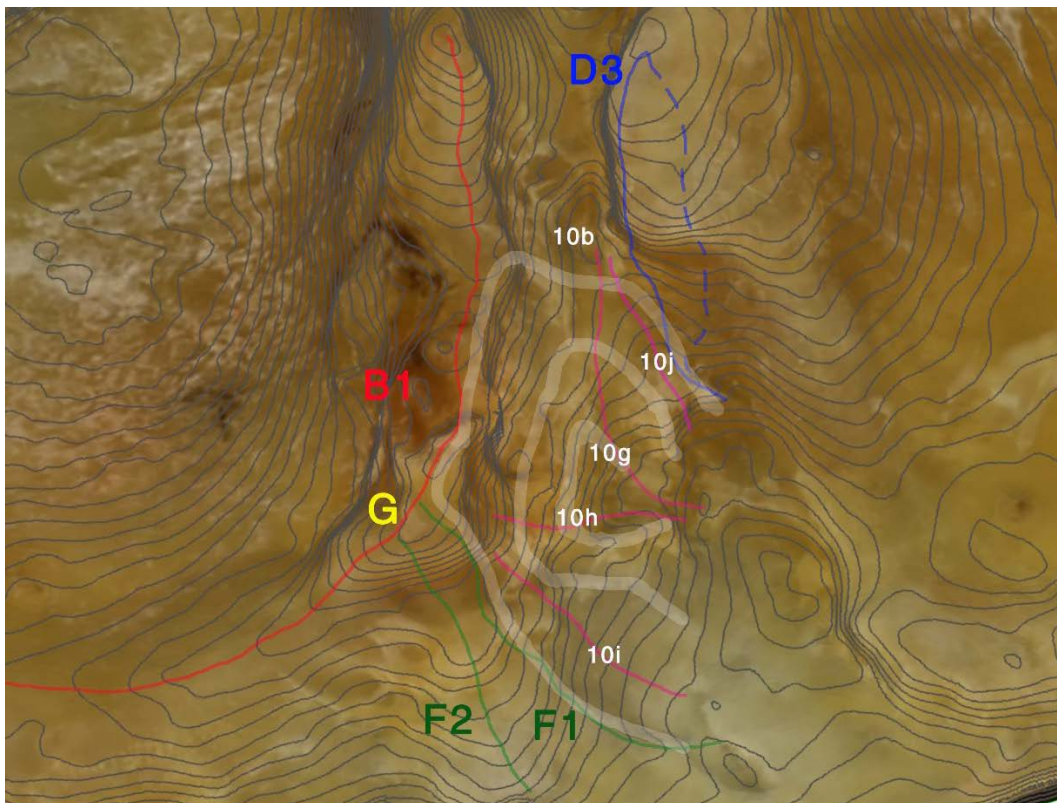


Figure 303. 3D model of tibia 45 with contour lines superimposed. Observe the stepped elevations (white lines) roughly corresponding to the intercondylar C-shaped layers. Notice the intertubercular fossa (10b) in the posterior arch. Also labelled are the Parson's knob (G), the main incisures (10g, 10h, 10i, 10j), external AMIR process (B1), AFIR processes (F1, F2), and internal ALIR processes (D3).

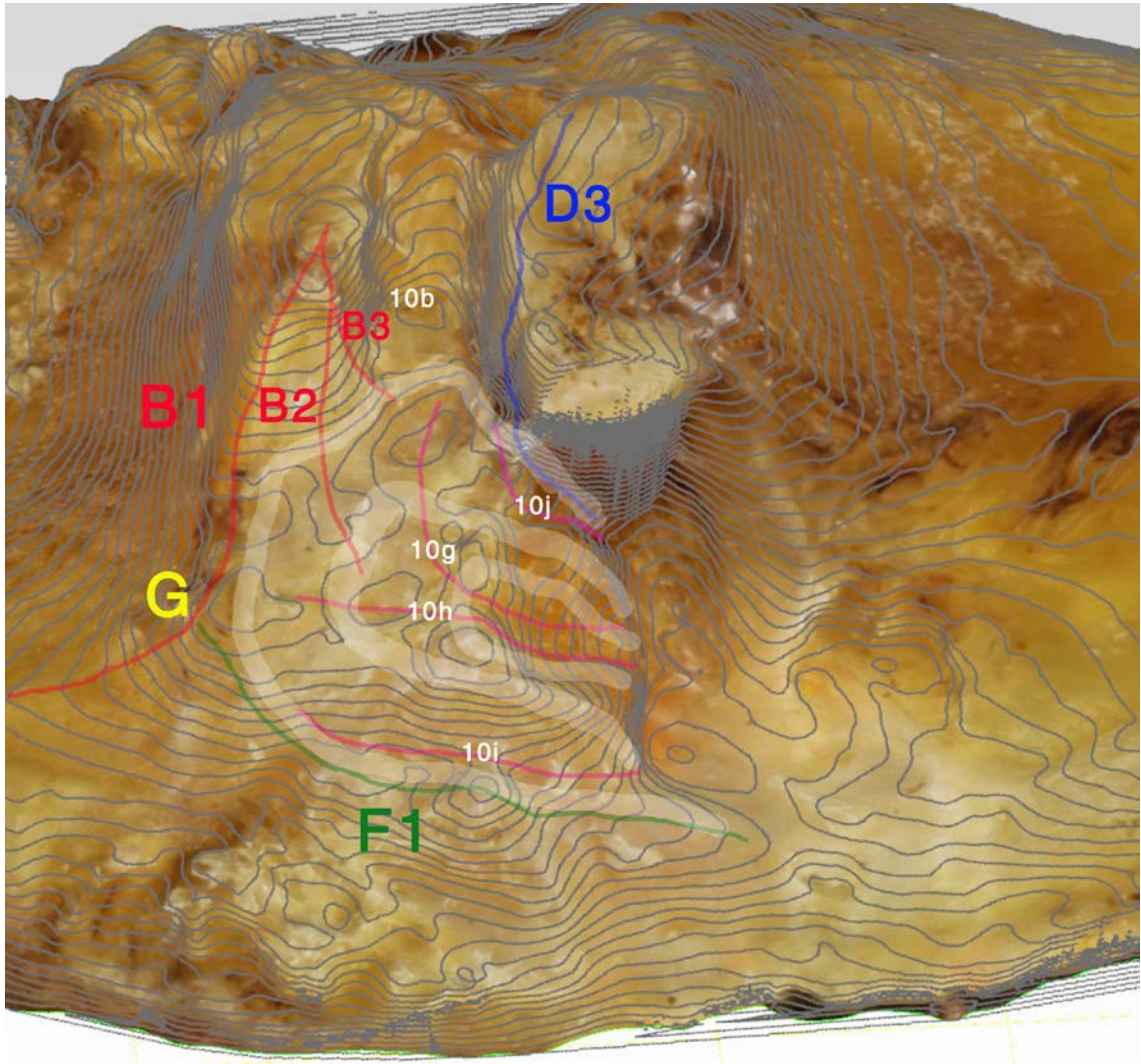


Figure 304. 3D model of tibia 14 with contour lines superimposed. Observe the homogeneous elevation of the fornix and internal C (painted over with white lines), which respects a minor concavity (including the fan-like facet), where 10g and 10h begin together laterally. Also labelled are the geniculum (G), main incisures (10i, 10j), the intertubercular fossa (10b), the AMIR processes (B1, B2, B3), posterior AFIR process (F1), and internal ALIR process (D3).

IV.7.3.2. Quantitative assessment

The upper and lower stair height showed no significant association with knee OA: 10a (Fig. 305), $\chi^2(2)=2.789$, $p=0.947$; 10d (Fig. 306), $\chi^2(12)=15.610$, $p=0.210$.

The upper and lower landing horizontality did not show a significant association with knee OA: 10c (Fig. 307), $\chi^2(4)=9.005$, $p=0.061$; 10f (Fig. 308), $\chi^2(4)=7.656$, $p=0.105$. The horizontal portion of both landings compared to their corresponding stairs did not show an association with knee OA, either: 10c/10a (Fig. 309), $\chi^2(8)=7.743$, $p=0.459$; 10f/10d (Fig. 310), $\chi^2(8)=10.309$, $p=0.244$. Frequency analysis of all values in the staircase showed a trend to more elevation and less horizontality with higher OA grades.

The middle landing shape – mild incisure over surrounding area, horizontal area, or steeper ridge –, showed no significant association with knee OA (Fig. 311): $\chi^2(12)=17.367$, $p=0.136$.

The anteromedial fovea (10b) or intertubercular fossa depression showed no significant association with knee OA (Fig. 312): $\chi^2(16)=11.032$, $p=0.807$.

The depression of the main incisures of area 10, which were easily seen at a glance in many specimens, showed no significant association knee OA, either: 10g (Fig. 313), $\chi^2(24)=35.028$, $p=0.068$; 10h (Fig. 314), $\chi^2(20)=20.287$, $p=0.440$. However, 10g showed a trend towards deeper incisures with higher OA grades in frequency distribution analysis.

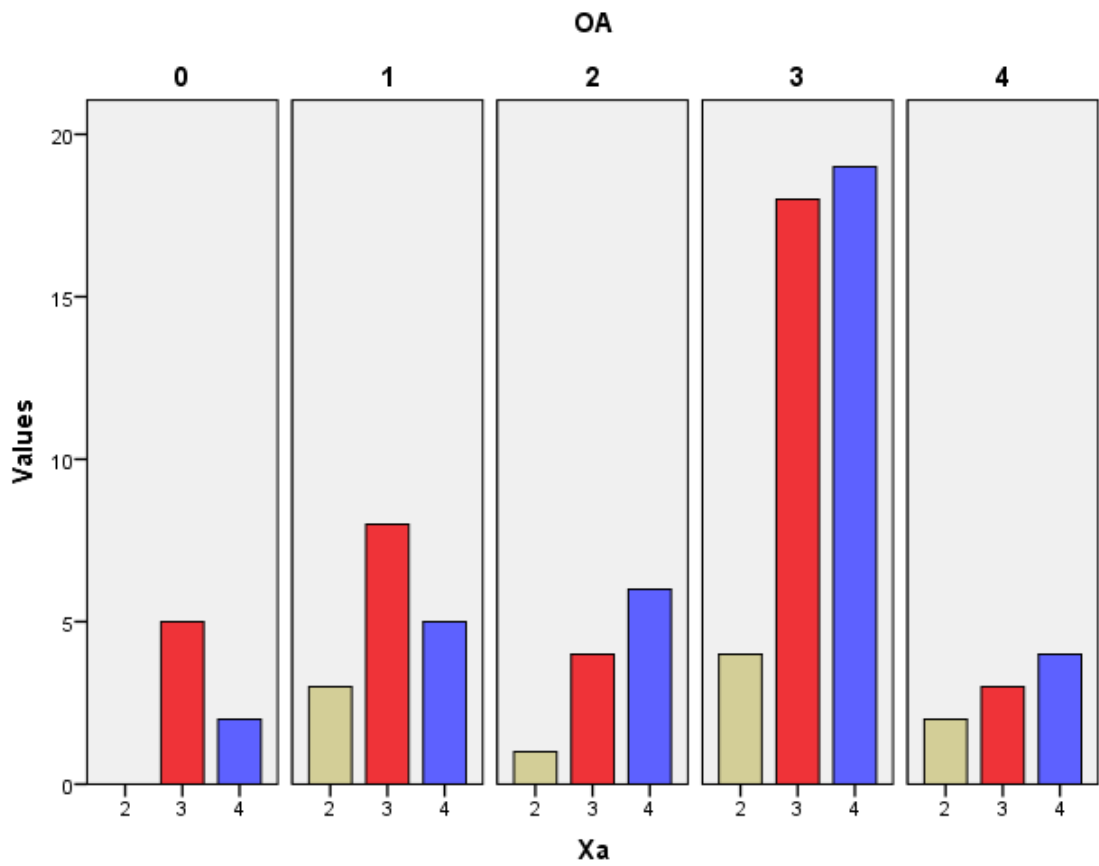


Figure 305. Study II. Histogram of the AIS superior stair (Xa) height grade: number of tibias in each category (0-4), grouped by Ahlbäck OA grade.

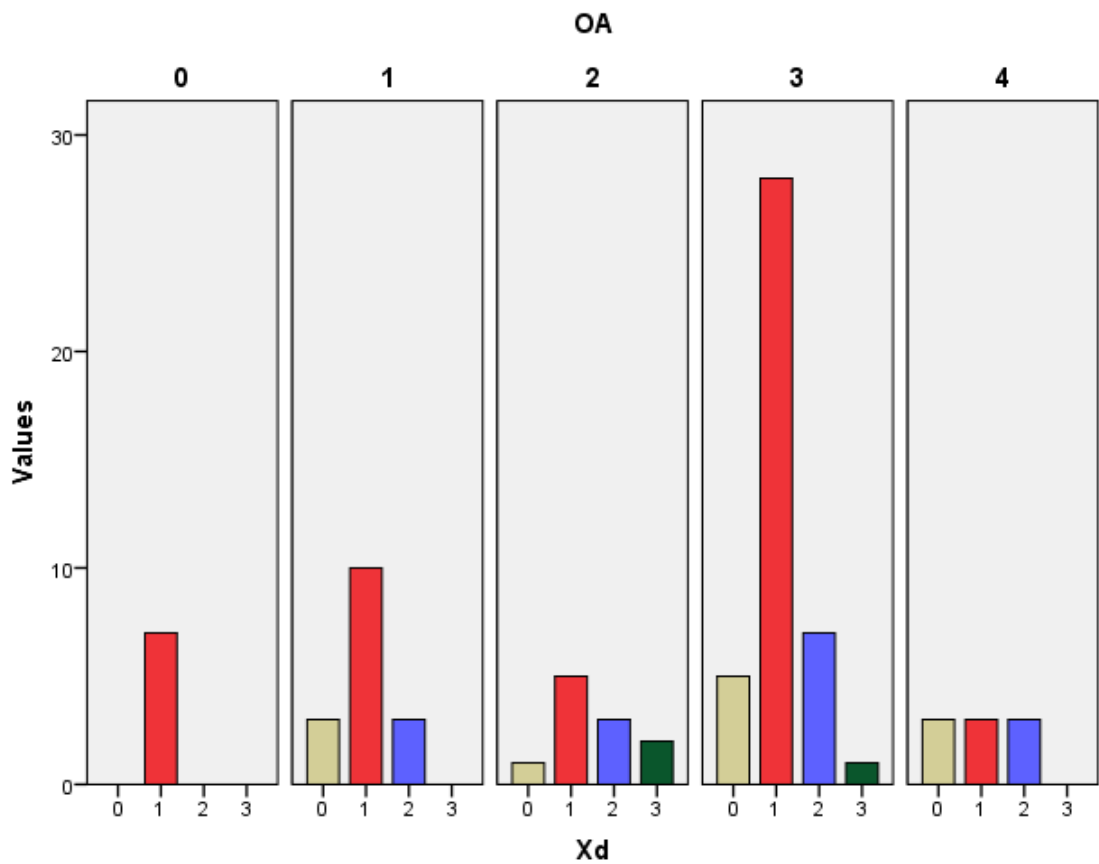


Figure 306. Study II. Histogram of the AIS inferior stair (Xd) height grade: number of tibias in each category (0-4), grouped by Ahlbäck OA grade.

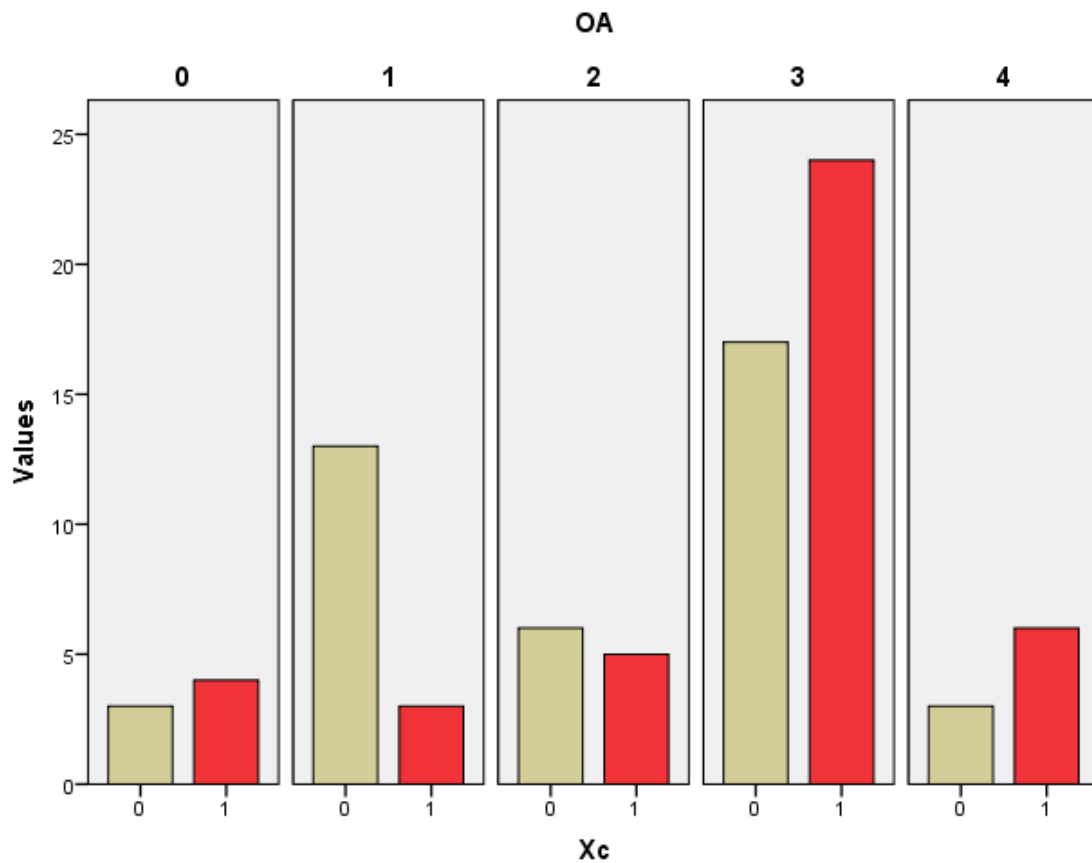


Figure 307. Study II. Histogram of AIS superior landing (X_c) horizontality: number of tibias in each category, grouped by Ahlbäck OA grade. 0=more lamina-shaped; 1=more crest-shaped.

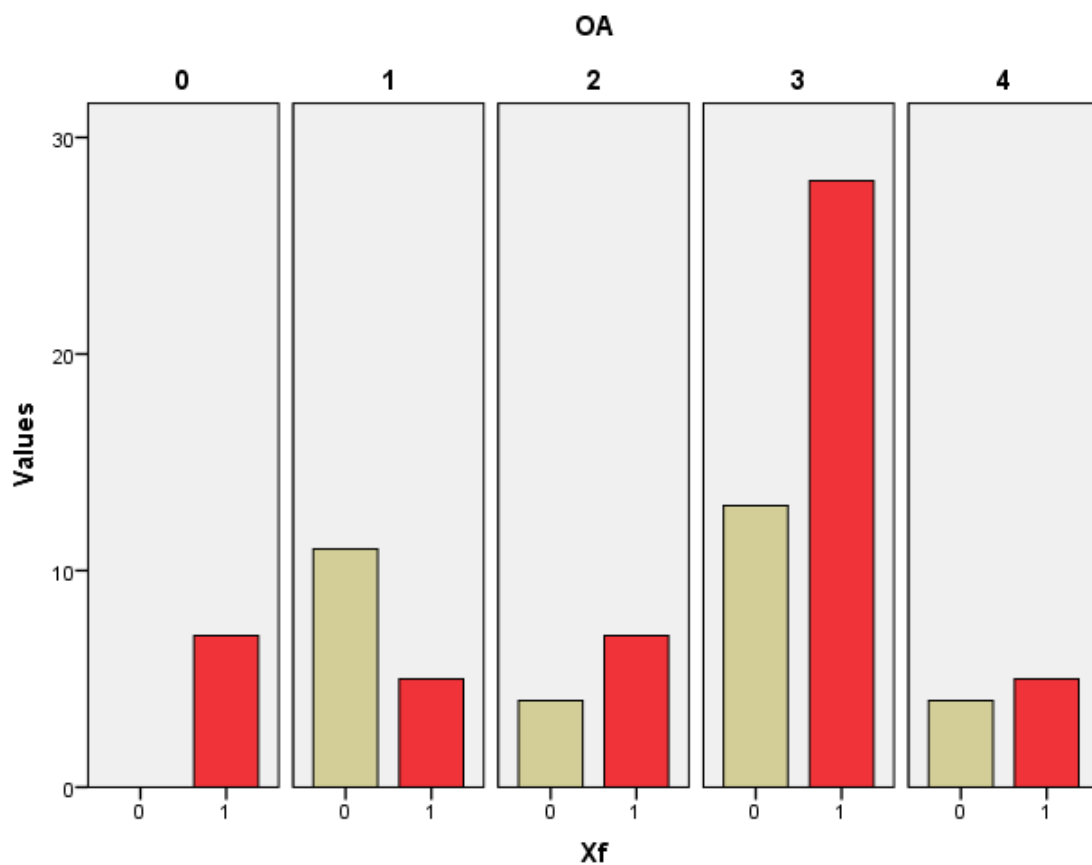


Figure 308. Study II. Histogram of the AIS inferior landing (X_f) horizontality: number of tibias in each category, grouped by Ahlbäck OA grade. 0=more lamina-shaped; 1=more crest-shaped.

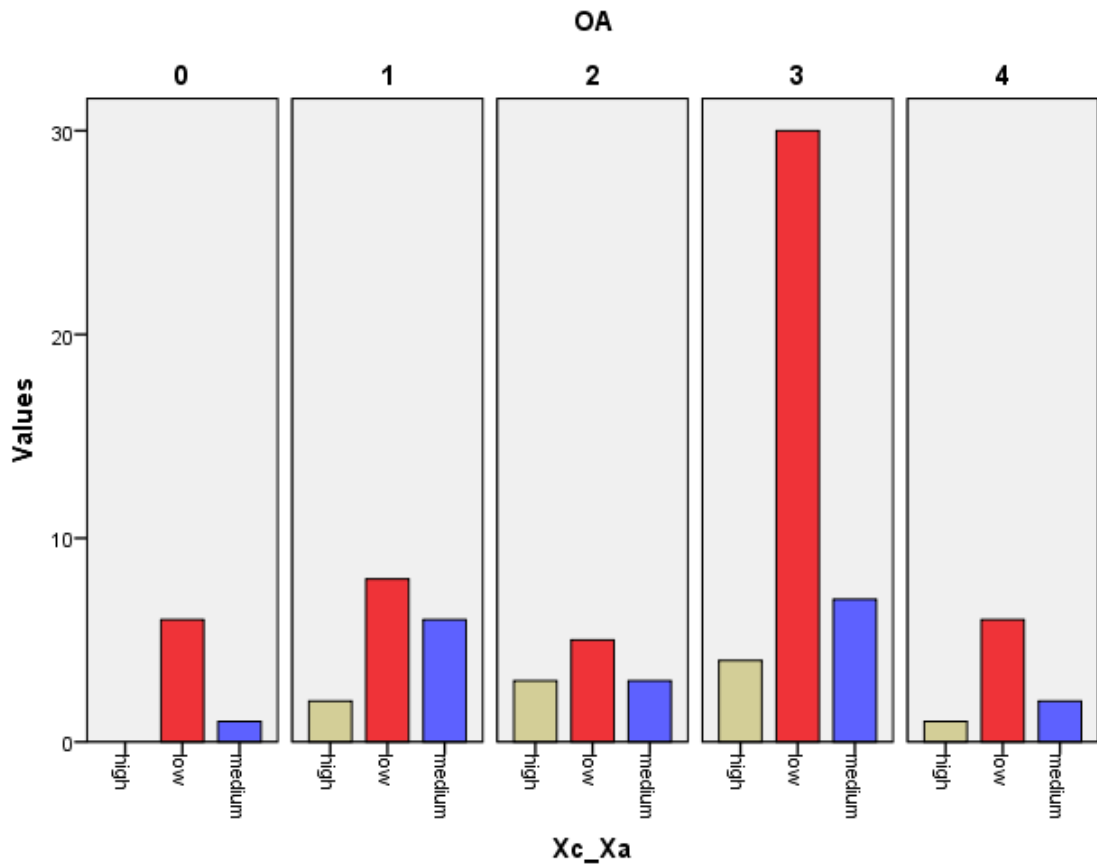


Figure 309. Study II. Histogram of AIS superior landing horizontality as proportion of area 10a (Xc_Xa): number of tibias in each category, grouped by Ahlbäck OA grade.

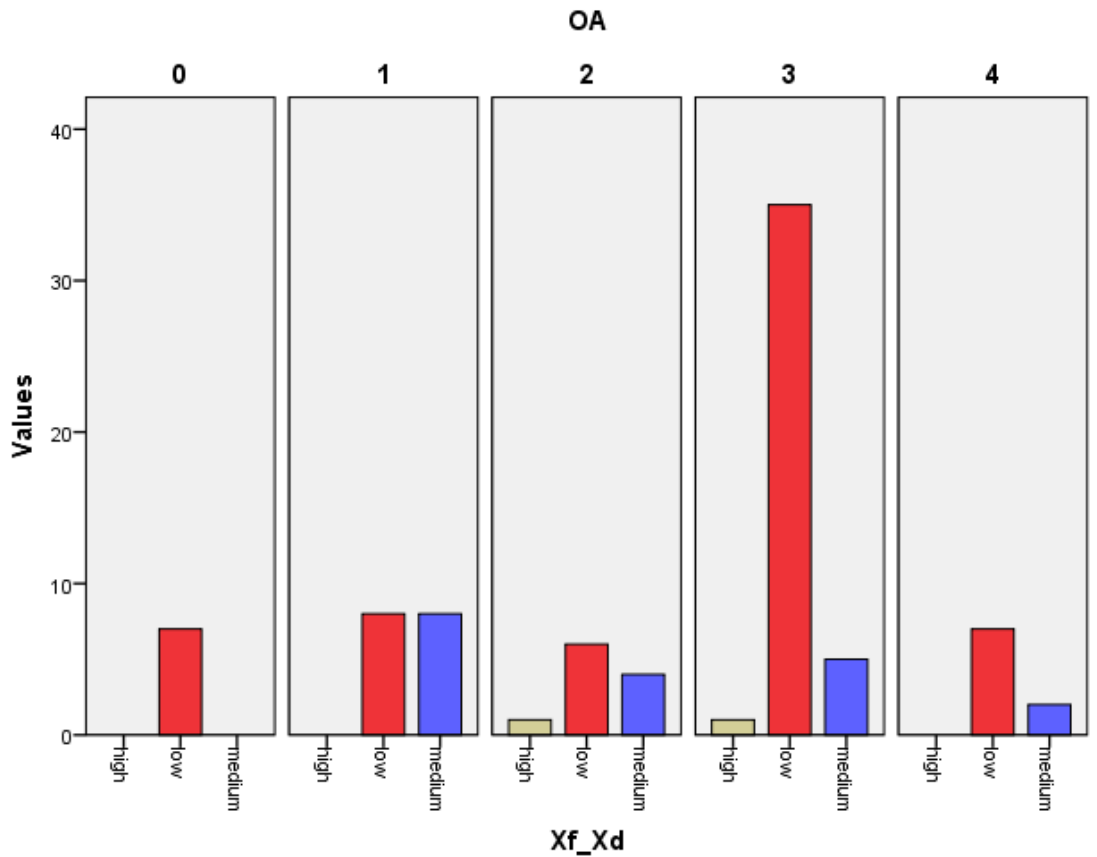


Figure 310. Study II. Histogram of AIS inferior landing horizontality as proportion of area 10d (Xf_Xd): number of tibias in each category, grouped by Ahlbäck OA grade.

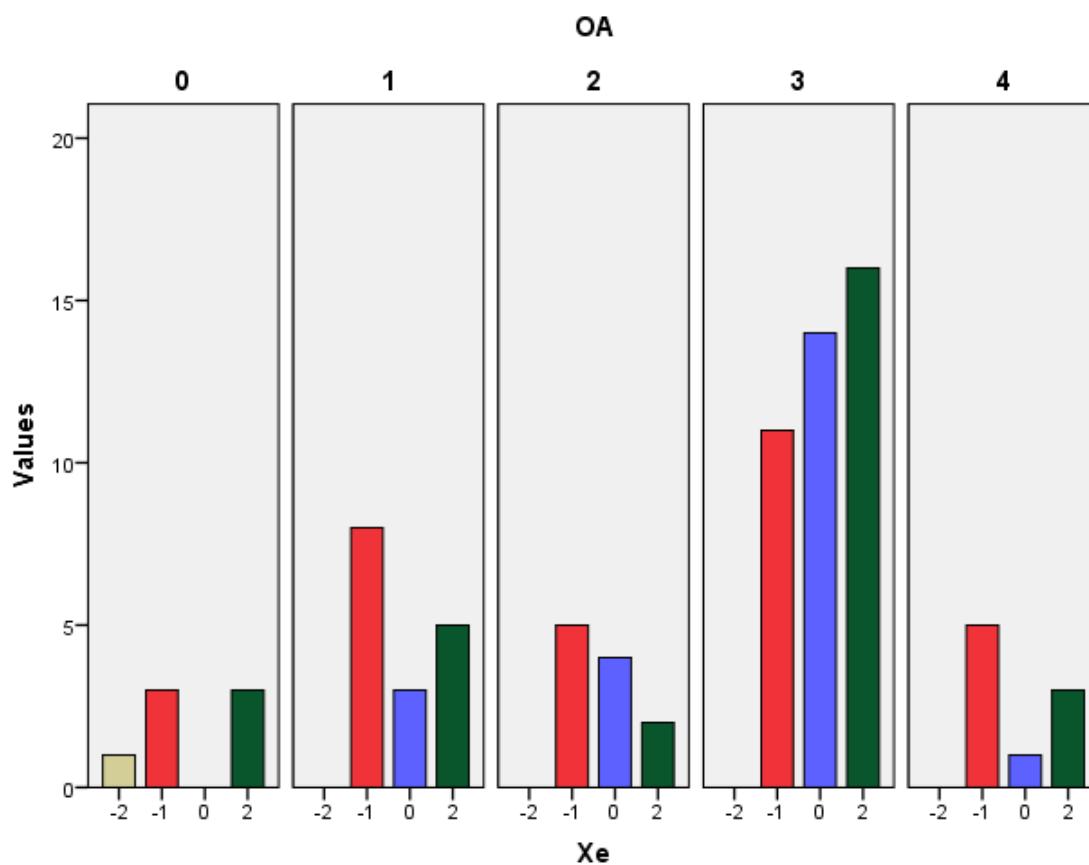


Figure 311. Study II. Histogram of the AIS middle landing (X_e) slope type: number of tibias in each category, grouped by Ahlbäck OA grade. Where 2=crest-type (higher slope), 0=lamina-type, -1=incisure-like (i.e. more horizontal).

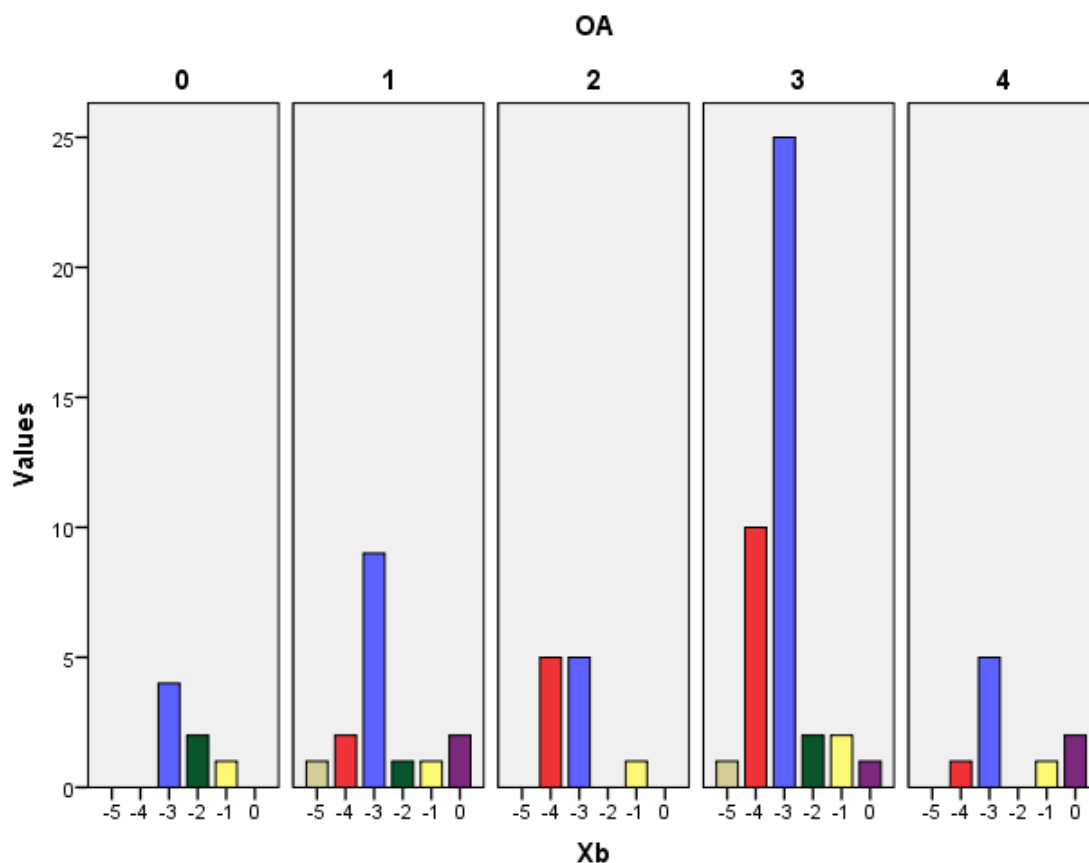


Figure 312. Study II. Histogram of the AIS anteromedial fovea / fossa (X_b) depression grade: number of tibias in each category, grouped by Ahlbäck OA grade.

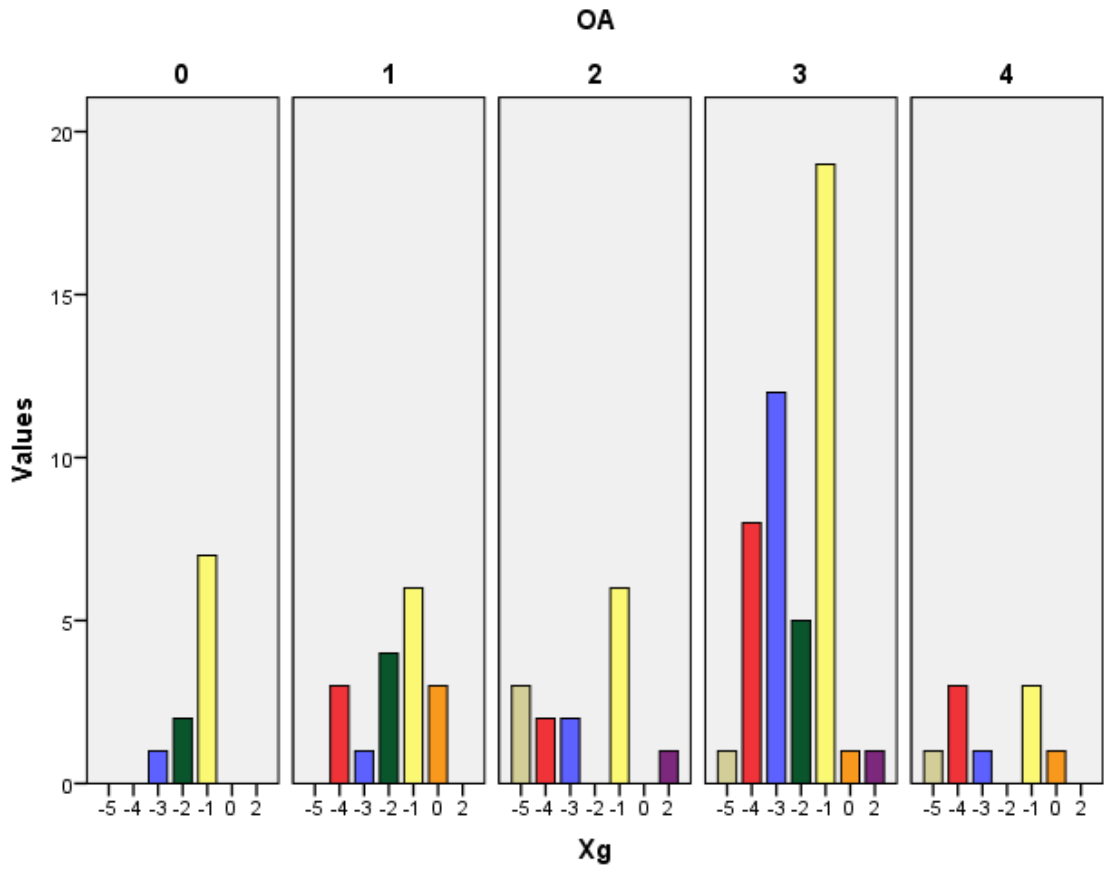


Figure 313. Study II. Histogram of the AIS sagittal incisure (X_g) depression: number of tibias in each category, grouped by Ahlbäck OA grade.

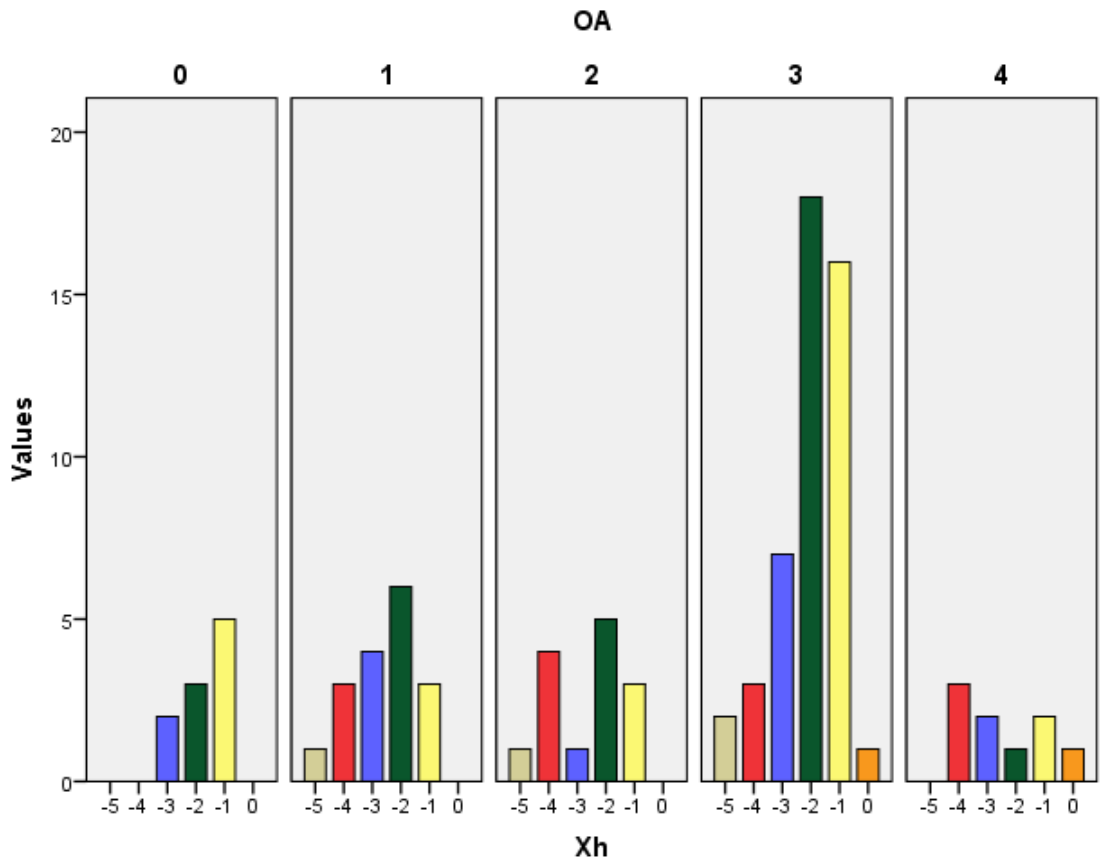


Figure 314. Study II. Histogram of the AIS coronal incisure (X_h) depression: number of tibias in each category, grouped by Ahlbäck OA grade.

IV.8. Intertubercular ridge

IV.8.1. Intertubercular area, and its anterior and posterior walls

The intertubercular ridge was defined as comprising areas 12, 15, and 14a.

The intertubercular area, **12**, was defined as the more horizontal area dominating the ITR, sloping gently downwards in an anteromedial to posterolateral direction, between the intercondylar tubercles. It included the inner slopes of the tubercles, and three well-differentiated, constant zones (Fig. 315, Fig. 316):

- The intertubercular saddle, **12a**, located anterior to the posterolateral recess and just posterior to area 15, found between the inner slope of both intercondylar tubercles, but nearer to the lateral one.
- The posterolateral recess, **12b**, located posterolaterally, was a shallow depression found directly behind the posterior aspect of the LT anterior peak, delimited medially by the internal PLIR process, **E3**, and laterally by a secondary internal PLIR process, **E3b**. Unlike the anterolateral and posteromedial recesses, this area showed a gentle downward slope in a posterior direction, almost horizontal.
- The posterolateral fossa, **12c**, was an anteroposteriorly oriented depression found between **E3b** medially and the lateral tubercle laterally.

The anterior wall of the ITR, **15**, formed the posterior wall of the AIS, and had a variable, arch-like shape when viewed from an anterior to posterior direction: most often round, it ranged from a pointed arch to a wide elliptical arch. It showed usually a steeper slope relative to the adjoining anterior (posterior arch) and posterior (intertubercular saddle) surfaces. Laterally and medially it was enclosed between the anterior aspects of the main tubercles' inner slope. The central, straighter aspect of area 15, just anterior to the intertubercular saddle, was defined as the preeminence (PRE), **V**.

The superior face of the posterior wall of the ITR, **14a**, was a strip of bone with a gentler slope compared to the rest of the posterior wall, located just posterior to area 12. Its central aspect, between both meniscal insertions, was defined as the posteminence (POE), **W**.

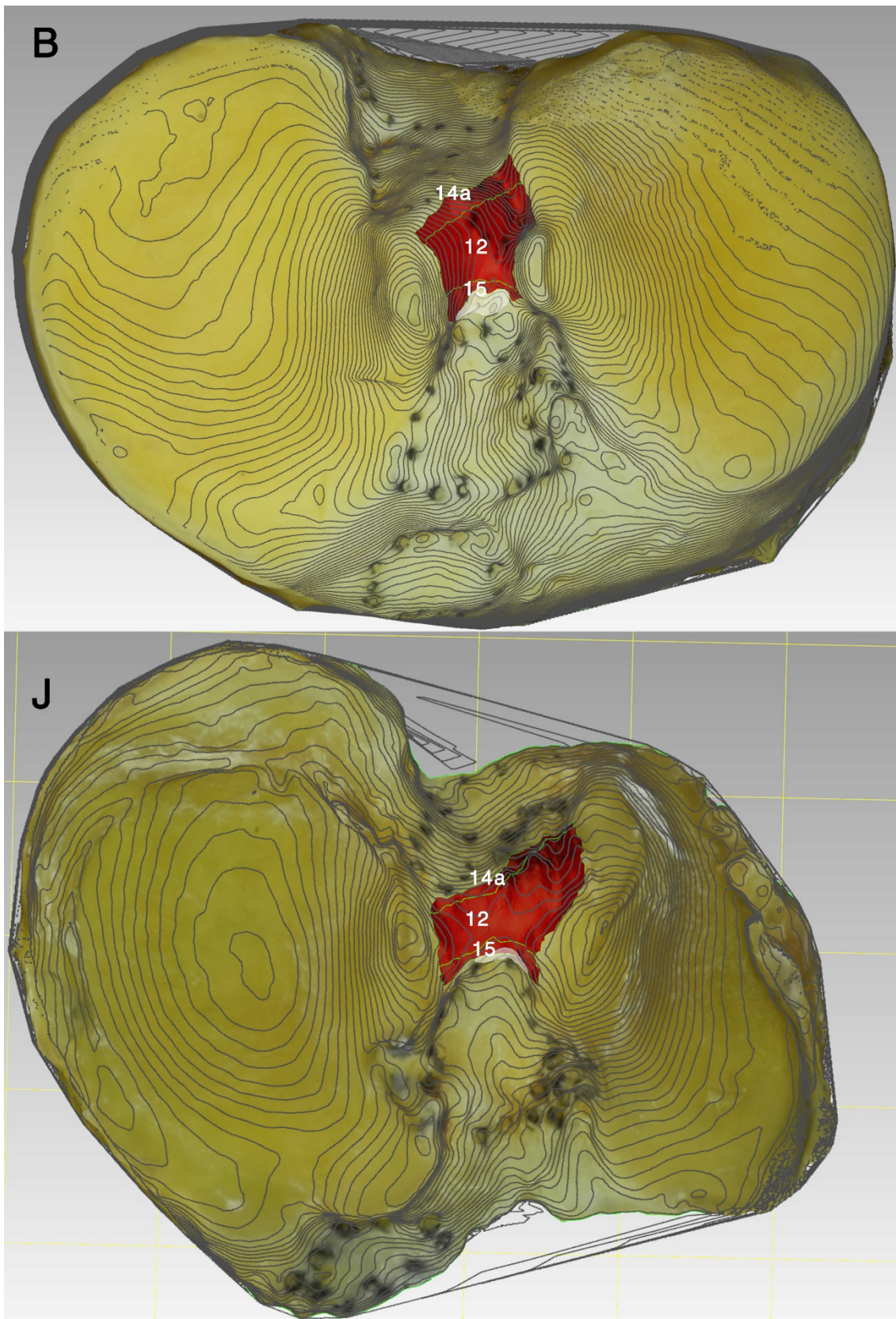


Figure 315. 3D models of tibiae B and J, with contour lines superimposed. Areas 12, 15, and 14a selected (fluorescent green borders), highlighted in red, and labelled. The AIS posterior arch has been painted in white. Notice how tibia J, with degenerative changes, shows steeper anterior and posterior walls of the ITR; a sharper transition between areas 15 and 10, and between 14a and the posterior intercondylar wall; a wider posterolateral recess and a flattened posterolateral fossa (with a wide and flattened LT vallecule and posterior summit); and an elevated (ridge-like) C4 process near 14a.

IV.8.2. Attachment of the posterior root of the lateral meniscus

The footprint of the central, dense fibers of the posterior root of the lateral meniscus was qualitatively found to be most often laterally in the intertubercular ridge, within areas 12 and 14a, and more precisely occupying the posterolateral recess (Fig. 317, Fig. 318).

Two non-paired specimens showed half of the PRLM attachment posterior to posterolateral recess, in area 14b, with an attachment reminiscent of a Dalí's soft melting pocket watch (see tibia J in Fig. 315 above, and tibia A in Fig. 376 below).

The medial aspect of area 12 was the site of attachment of the supplemental fibers of the PRLM, reaching the inner slope of the medial tubercle, as far as its cartilaginous aspect. The anterior wall of the ITR was, however, void of ACL or PRLM fiber insertions.

Quantitatively, the PRLM central fibers had a mean attachment area of 36.1 mm² (95% CI 30.5 – 41.7 mm²; range, 24.7 mm² to 57.7 mm²), representing a mean of 57.9% of area 12 (95% CI 47 – 68.6%; range, 38% to 107%, N=14).

The PRLM attachment center was measured in reference to arthroscopically pertinent landmarks, being posteromedial to the LT anterior peak (4a); posterolateral to the preeminence (PRE), and to the posterior border of the ACL attachment; medial to the LT posterior peak / vallecule (in a straight horizontal line); anterior to the anteriormost (usually anterolateral) border of the PCL, and to the posterolateral wall (14b, at a central point of its lowest area, just behind the tent-shaped ridge); lateral to the posteminence (POE), and to the anterolateral corner of the PRMM attachment.

The center of the PRLM attachment was 9.4 mm (range, 5.1 mm to 13 mm), from the most anterior aspect of the ACL attachment, a measurement that had a significant but low correlation with ML width ($r=0.61$, $p=0.025$), CV 25.29%, and whose correlation with AP depth did not reach statistical significance. Proportionally, it represented 13% of the ML width of the proximal tibia. See Table 25 for all distances obtained from the center of the PRLM attachment to selected anatomic landmarks.

Table 25. Distances in mm, 95% CI, Coefficient of variation (CV), Pearson correlation values for AP and ML, with their corresponding p-values.

PRLM	MM	95% CI	CV	AP	AP P	ML	ML P
LT (4a)	7.4	6.4 – 8.4	22.78	0.209	0.474	0.314	0.274
LT P (4b)	6.5	5.8 – 7.3	19.70	-0.047	0.872	0.030	0.919
AL PCL	9.4	7.9 – 10.8	25.29	0.552	0.050	0.615*	0.025
PLW (14b)	7.8	6.7 – 9.0	25.49	0.308	0.284	0.292	0.311
POE (14a)	4.0	3.4 – 4.6	27.54	0.311	0.278	0.292	0.311
PRE (15)	6.1	5.5 – 6.8	17.98	0.472	0.088	0.509	0.063
AL PRMM	6.2	5.5 – 7.0	20.47	0.042	0.886	0.182	0.533
P ACL	8.8	7.7 – 9.8	20.57	0.427	0.128	0.400	0.157

* Correlation is significant at the 0.01 level (2-tailed).

NOTE. In red, the highest CV value of all data processed for attachment distances. In blue, measurements taken in the shortest straight (roughly ML) line. LT P: posterior peak of the LT. AL PCL: Anterior border of PCL. AL PRMM: anterolateral corner of PRMM. P ACL: posterior aspect of ACL attachment.

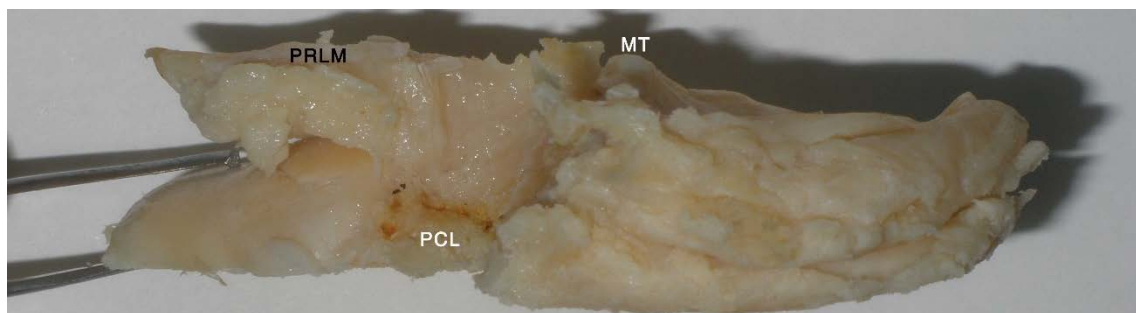


Figure 317. Tibia D. Photograph of its posterior aspect during dissection (forceps is grasping the lateral condyle). The PCL has already been detached (its footprint, surrounding by pyrography marks, is labelled). MT: medial tubercle. PRLM: posterior root of the lateral meniscus.

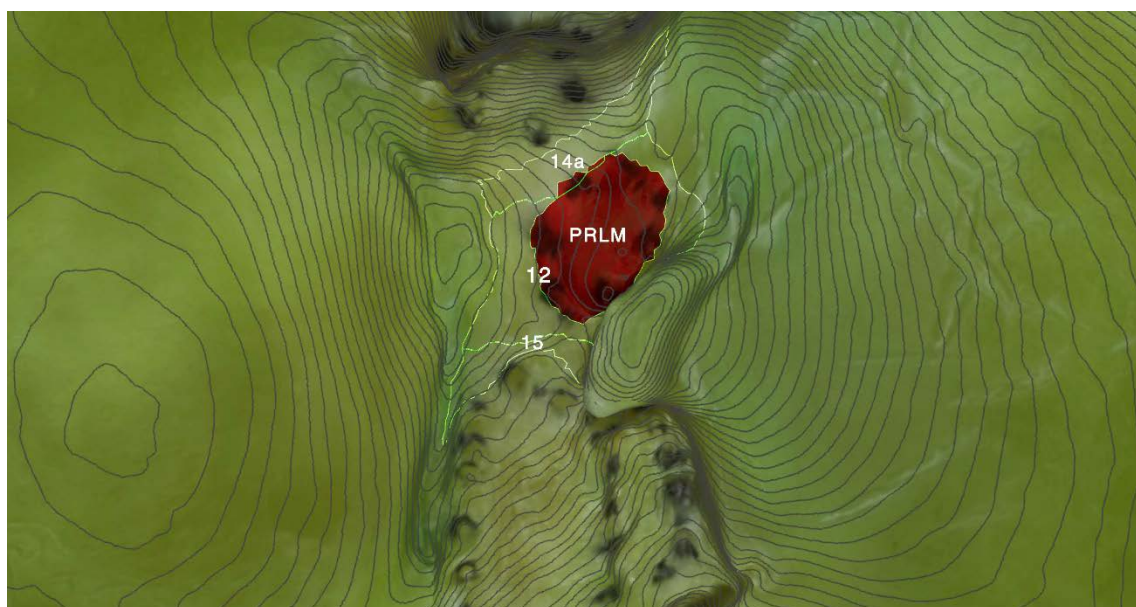


Figure 318. 3D model of tibia K, with contour lines superimposed. Superoinferior view. Intertubercular areas selected (light fluorescent green), with PRLM footprint highlighted in red and labelled.

IV.8.3. Degenerative changes affecting the intertubercular ridge

In specimens with degenerative changes, the posterolateral fossa, 12c, was commonly found as a shallower depression, usually associated with a wider and flattened vallecule and posterior summit.

The elevation of the posterolateral recess and fossa together showed a weak but significant correlation with knee OA (Fig. 323): $r_s(95)=0.278$, $p=0.006$.

The anterior ITR wall (area 15) was usually distinguished by a steeper slope than areas 10 and 12. However, a higher superior stair in the AIS – because of degenerative changes in area 10 – or a smooth transition to the intertubercular saddle – common in specimens without degenerative changes – could make it appear as a smoothly sloped transition between both areas.

The posteminence was defined as the central aspect of area 14a. In tibias with degenerative changes, a line or ridge was observed near this area, the more internal PMIR process, **C4** (Fig. 319, Fig. 320), whose origins were anteromedially the summit of the medial tubercle, and posterolaterally the lateral tubercle's posterior summit. The more internal PMIR process showed a weak but significant correlation with knee OA (Fig. 324): $r_s(95)=0.251$, $p=0.014$.

The intertubercular space showed changes in the AP and lateral radiographic views (Fig. 321): Height changes did not achieve a statistically significant association with Ahlbäck OA classification (Fig. 325), $\chi^2(8)=13.288$, $p=0.102$; but width changes did show a significant association (Fig. 326), $\chi^2(8)=20.533$, $p=0.008$ (Phi=0.432, Cramer's V=0.306). A higher and narrower staircase was found to be associated with higher OA grades.

Radiographic changes in the axial view near the intertubercular area included tiny round osteolysis, related to the anterior fossa (Fig. 322). They showed no significant association with knee OA (Fig. 327): $\chi^2(20)=18.855$, $p=0.531$.

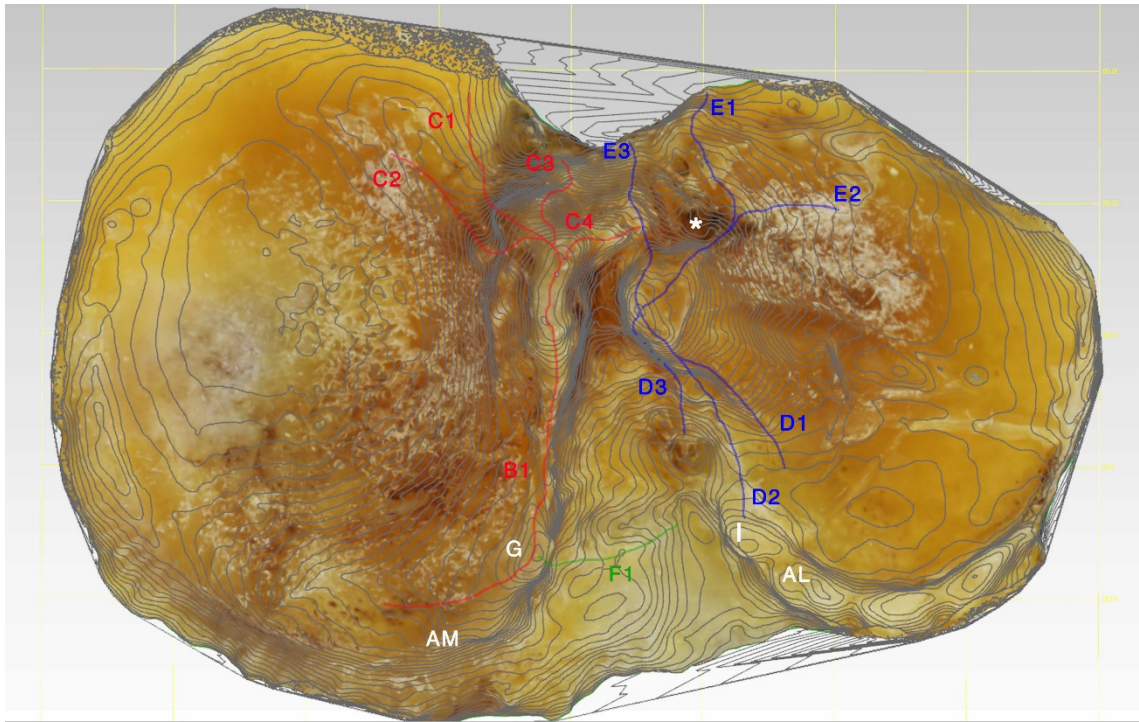


Figure 319. 3D model of tibia 95 with contour lines superimposed. More internal PMIR process (C4) elevated (osteophyte grade 3), with flat-like LT vallicula (). Also labelled are processes of the AMIR (B1), PMIR (C1, C2, C3), ALIR (D1, D2, D3) and PLIR (E1, E2, E3), AFIR (F1), and elevations of Parson's knob (G), ALIK (I), AM and AL corners.*

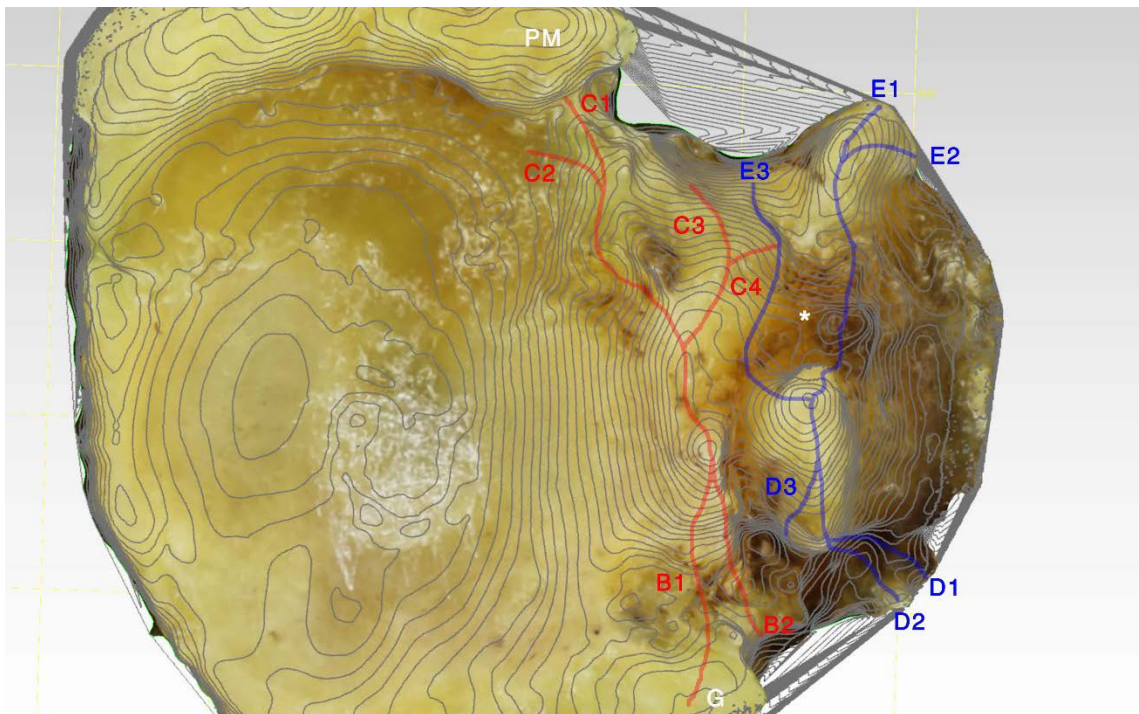


Figure 320. 3D model of tibia 86, with contour lines superimposed. More internal PMIR process (C4) elevated (osteophyte grade 2) and widened, and flattened LT vallicula (). Also labelled are processes of the AMIR (B1, B2), PMIR (C1, C2, C3), ALIR (D1, D2, D3) and PLIR (E1, E2, E3), and elevations of Parson's knob (G) and PM corner.*

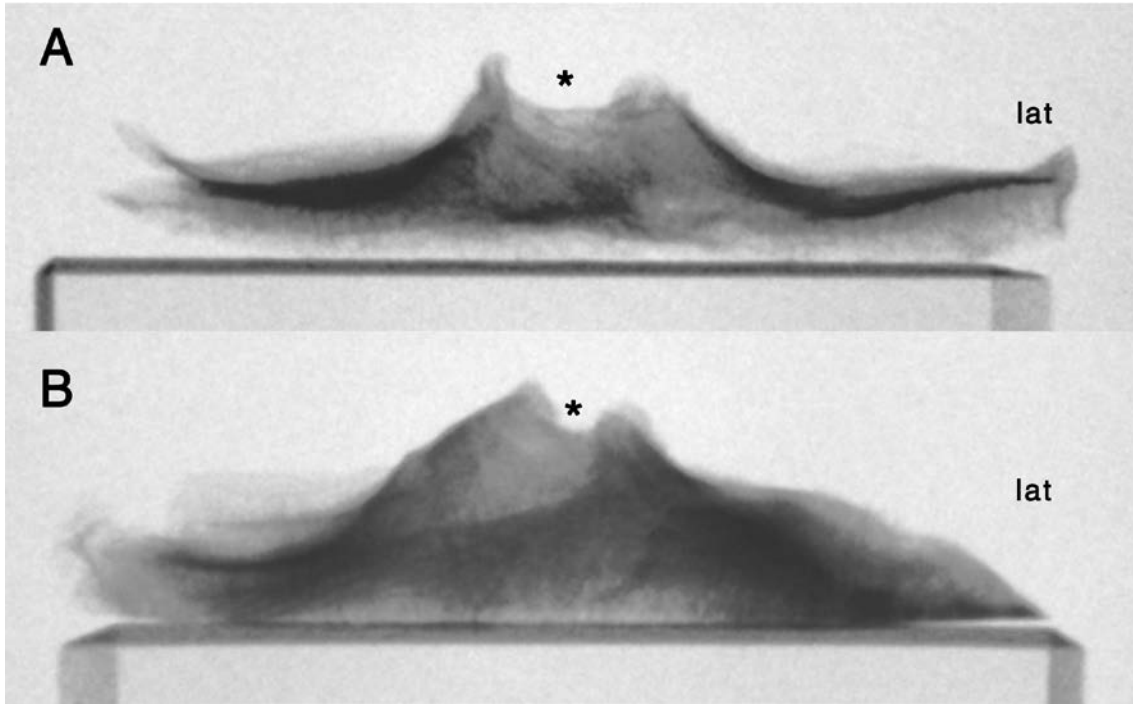


Figure 321. Anteroposterior fluoroscopic images. Tibia 63 (A) shows a widened intertubercular area (*). Tibia 84 (B) shows a narrower and higher intertubercular area (*).

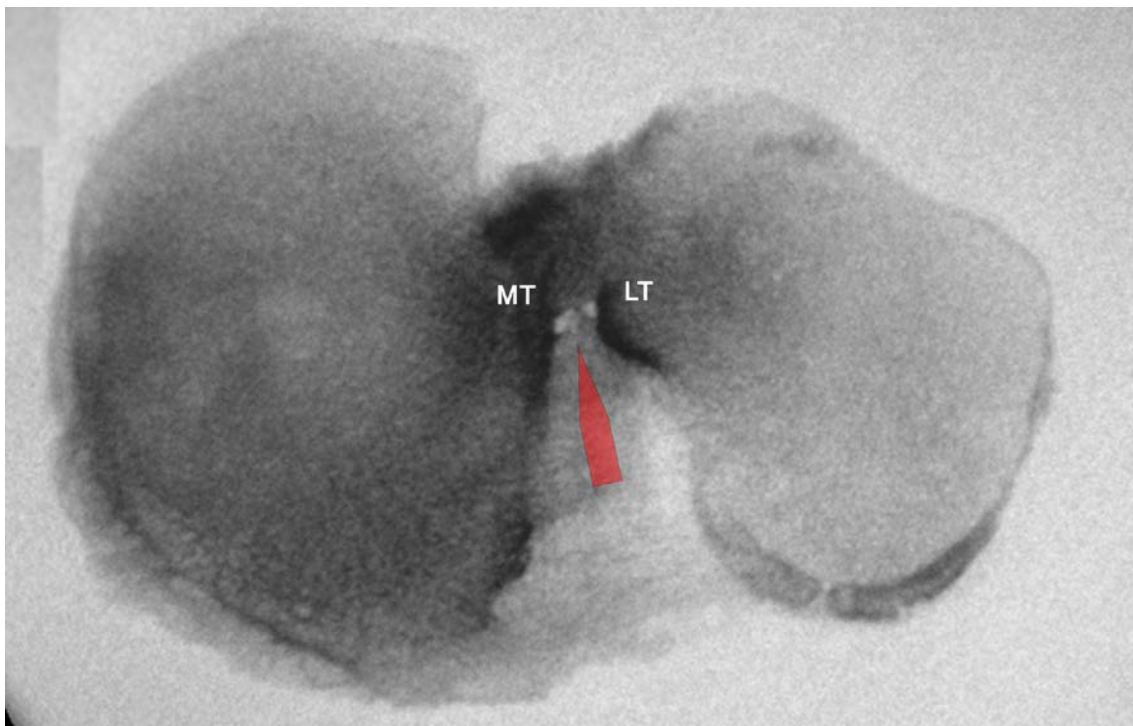


Figure 322. Inferosuperior fluoroscopic image of tibia 95. Red arrowhead over area 10, pointing at osteolyses in the anterior aspect of the intertubercular area, most likely corresponding to foramina nutricia in the posterior arch of area 10. Also labelled are the intercondylar medial (MT) and lateral (LT) tubercles.

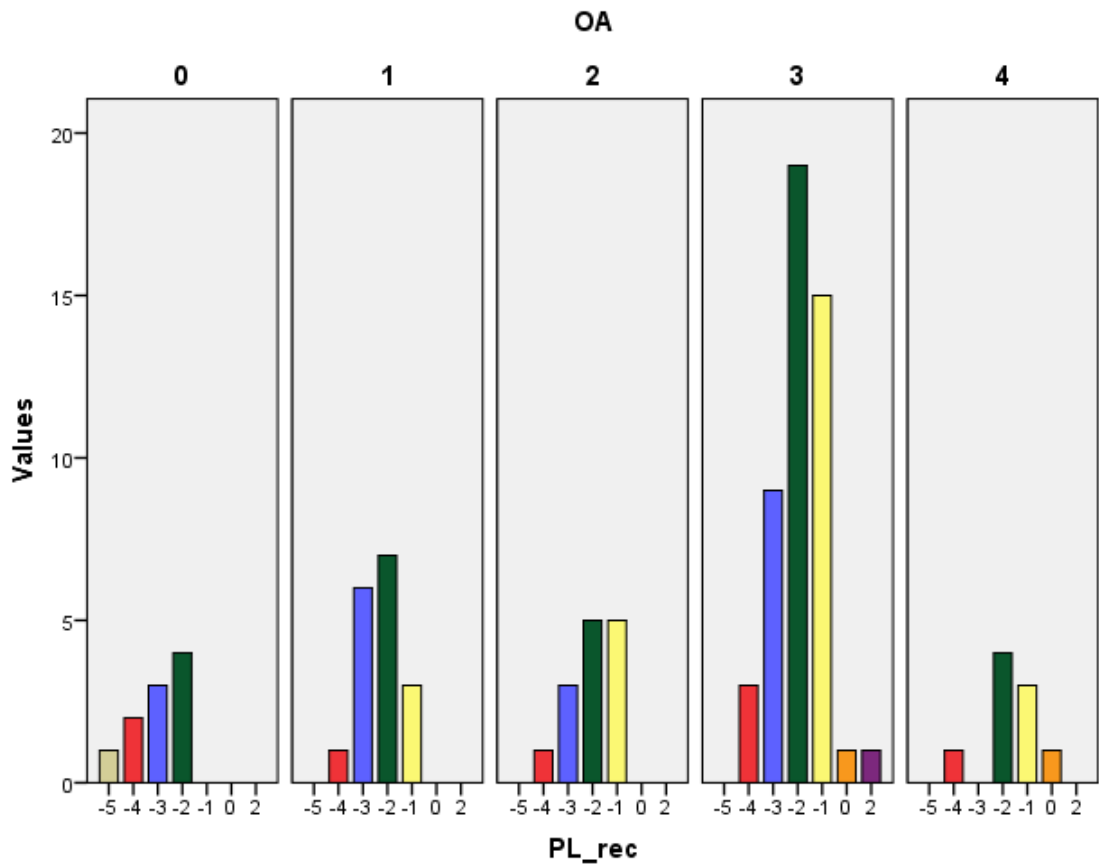


Figure 323. Study II. Histogram of the PL recess (PL_rec) osteophyte grade: number of tibias in each category, grouped by Ahlbäck OA grade.

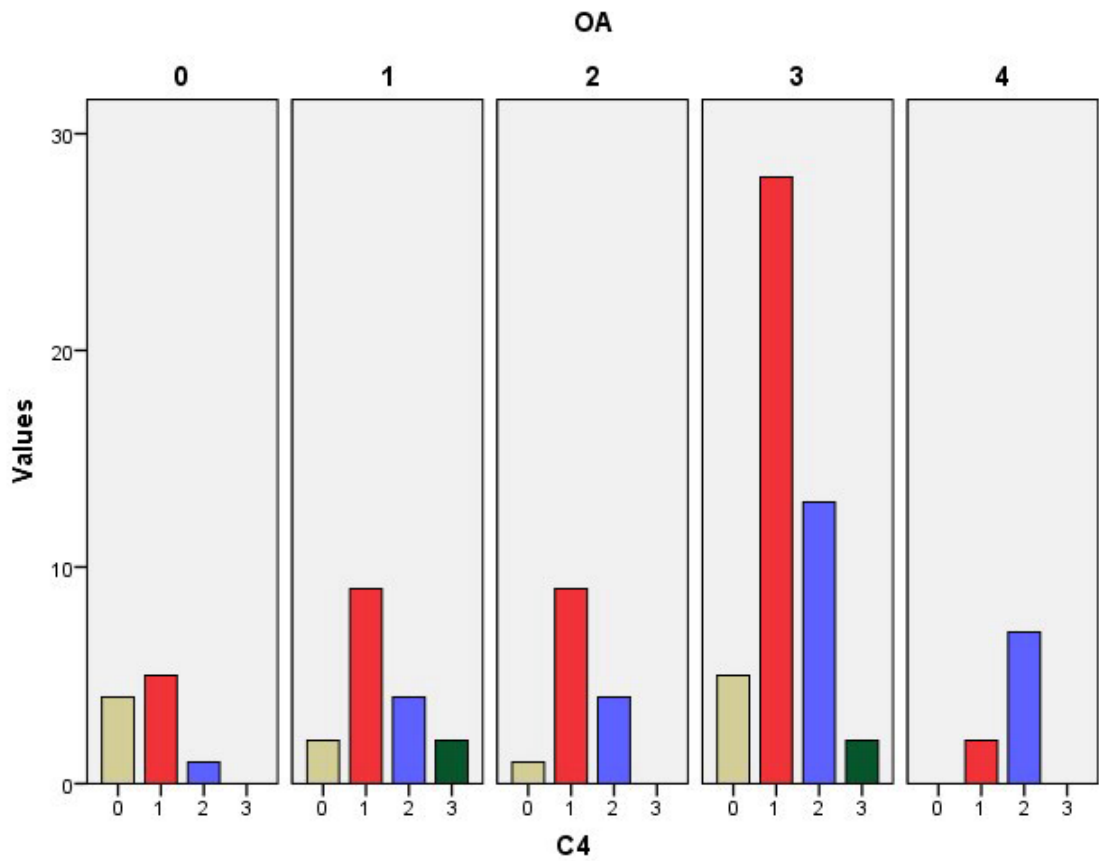


Figure 324. Study II. Histogram of the more internal PMIR process (C4) elevation in area 14a: number of tibias in each category, grouped by Ahlbäck OA grade.

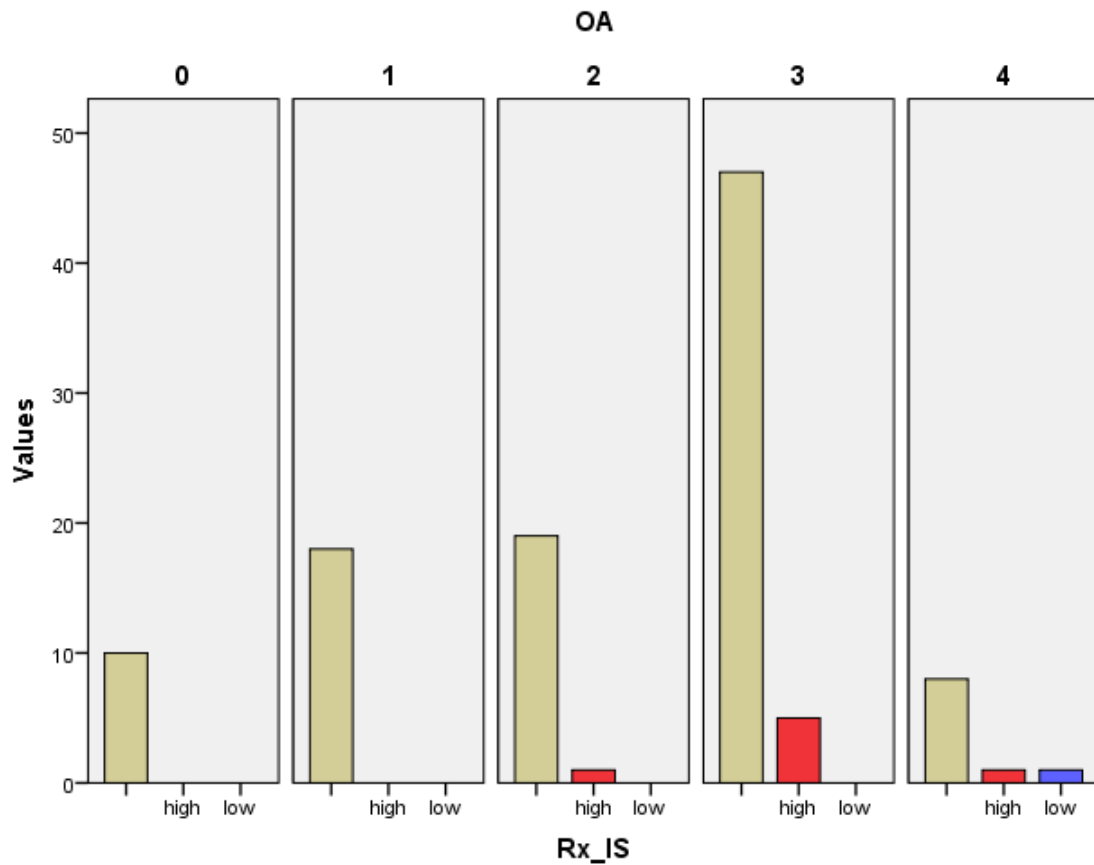


Figure 325. Study II. Histogram of the ITR / AIS height position in AP radiograph (Rx_IS): number of tibias with a normal, high, or low position, grouped by Ahlbäck OA grade.

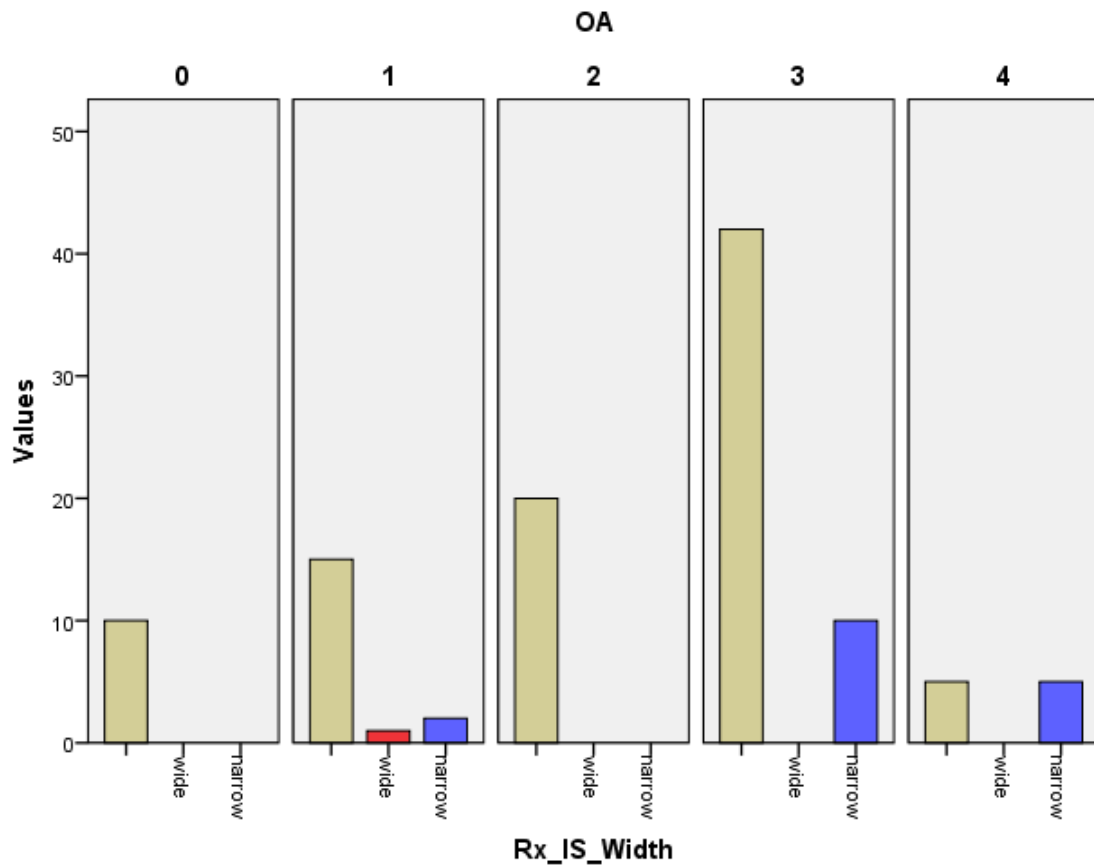


Figure 326. Study II. Histogram of the intertubercular space width in AP radiograph (Rx_IS_Width): number of tibias with a normal, wide, or narrow space, grouped by Ahlbäck OA grade.

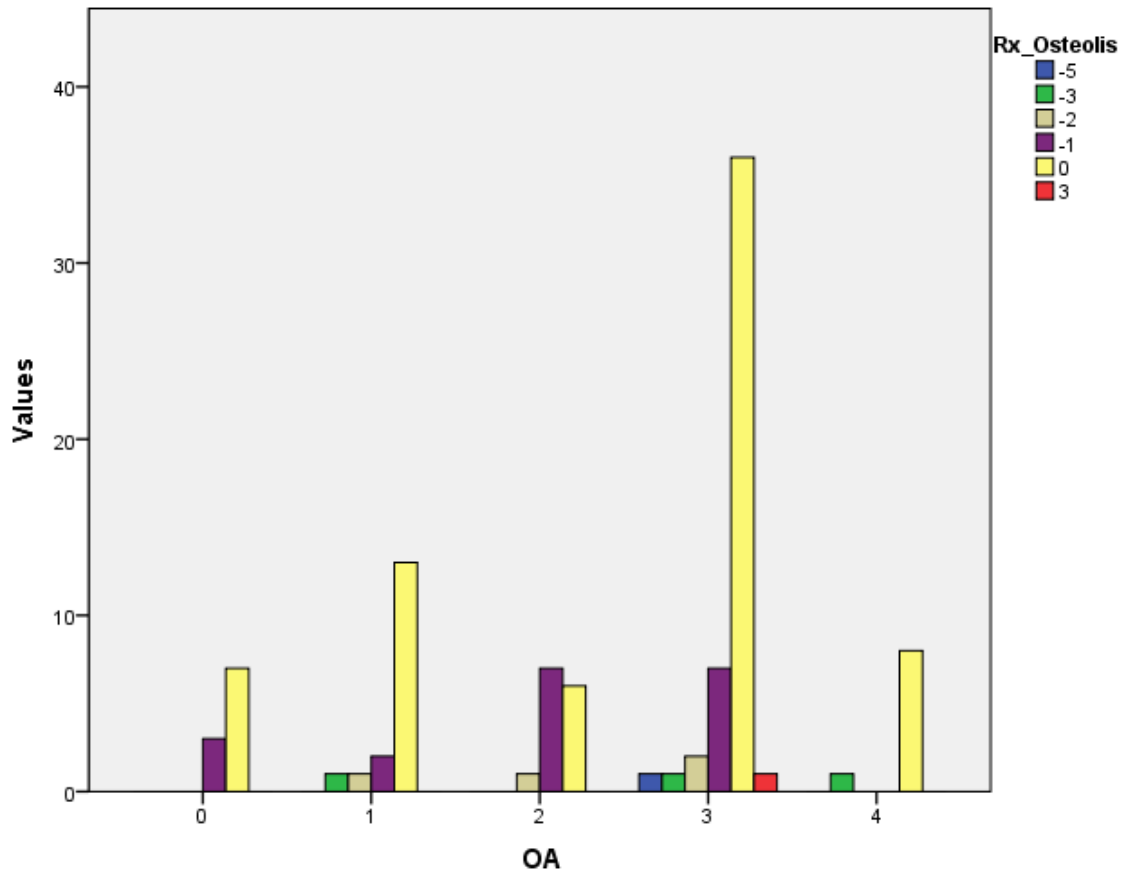


Figure 327. Study II. Histogram of the number of osteolytic circles found in the ITR in radiographs (Rx_Osteolis): number of tibias with the same number, grouped by Ahlbäck OA grade. One tibia showed radiographic density in this area (+3).

IV.9. Posterior intercondylar area

IV.9.1. Posterior intercondylar area and posterior wall

The posterior intercondylar area showed two differently sloping facets: the steeper posterior wall, and the gently sloped posterior facet (area 13).

A coronal, tent-shaped ridge, **M**, separated both facets. It showed a longer medial than lateral side. Its posterolateral origin was in the lateral wall of area 13, coursing anteromedially up until about its peak, from where it coursed posteromedially and inferiorly until it reached C3 (Fig. 329). Immediately posterior and anterior to M, two tent-shaped incisures were found.

The posterior wall was formed by two faces with anteriorly converging mediolateral walls: a lateral face, **14b**, and a medial face, **11**. A sagittal incisure, **K**, was usually formed where they converged, slightly medial to the internal PLIR process, E3, and it ended inferiorly in the peak of the tent-shaped ridge.

The lateral face of the posterior wall, **14b**, showed an obtuse scalene triangular shape, with a longer upper side bordering area 14a, and a shorter side delimited by the tent-shaped ridge.

The medial face of the posterior wall, **11**, bigger than the lateral face, had also a triangular shape, with a shorter inferior side, and the medial side slightly larger than the lateral one. It could be divided into different zones:

- The lateral area, **11a**: a strip of bone demarcated by K laterally and the secondary internal PMIR process, **C3b**, medially.
- The posteromedial recess, **11b**: an almost vertical notch immediately posterior to the medial tubercle, delimited laterally by C3b, and medially by the medial wall of the PIA.
- The posteromedial fossa, **11c**: a small, horizontal (or gently upward sloping) opening of the posterior wall, located lateral to C3 and inferior to the posteromedial recess. A constant sizeable foramen nutricium, the posteromedial fovea, was found in front of the steep posterior wall that separated the fossa from the posteromedial recess. Other inconstant foramina could also appear in the fossa.

See Fig. 328 for a detailed depiction of the posterior wall areas and structures.

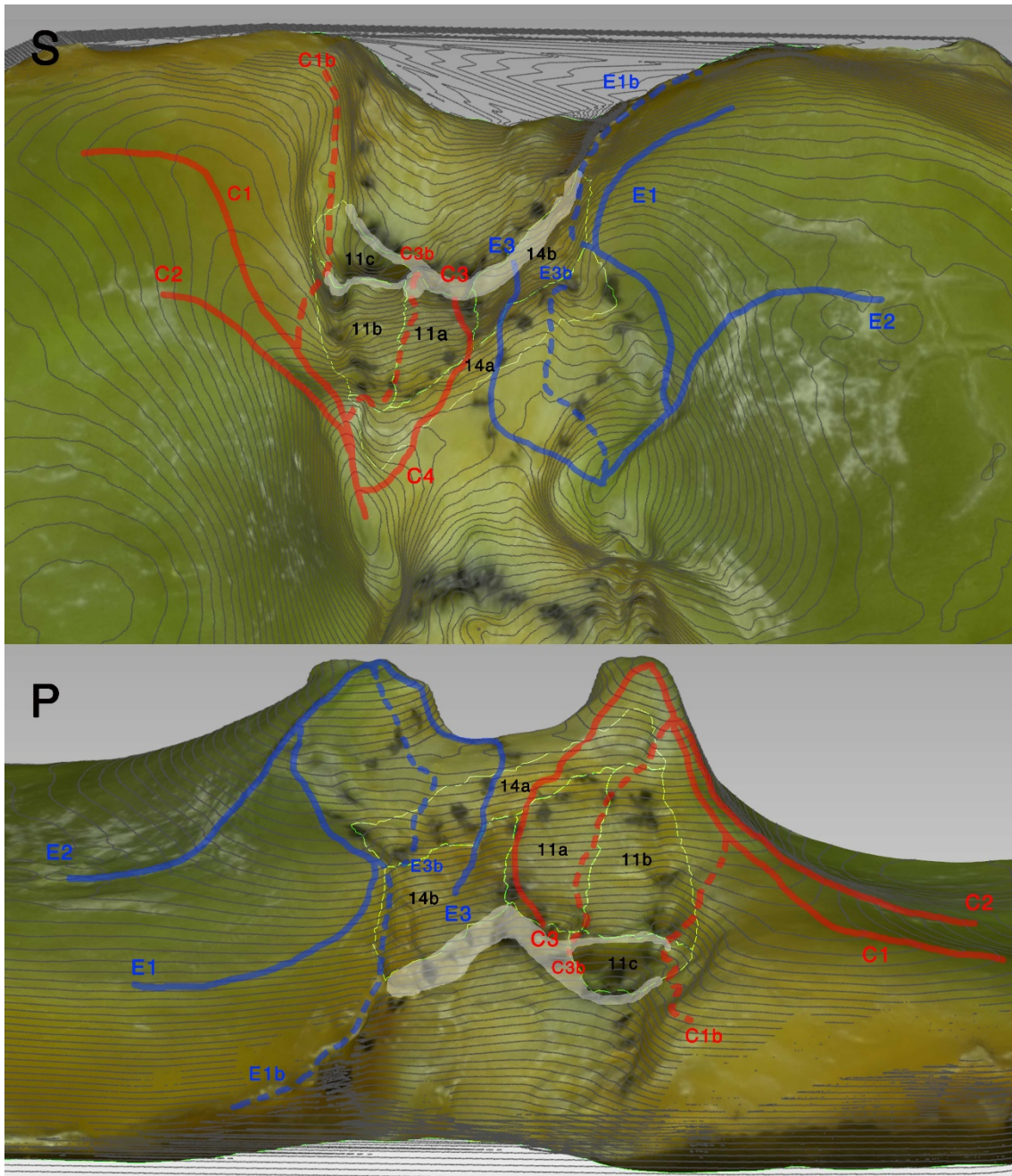


Figure 328. 3D model of tibia L, with contour lines superimposed. Superior (S), and posterior (P) views, with areas of the posterior wall selected (borders in fluorescent green) and labelled in black; tent-shaped ridge in white; painted lines over the main processes (AMIR in red, ALIR in blue); and secondary processes with dashed lines.

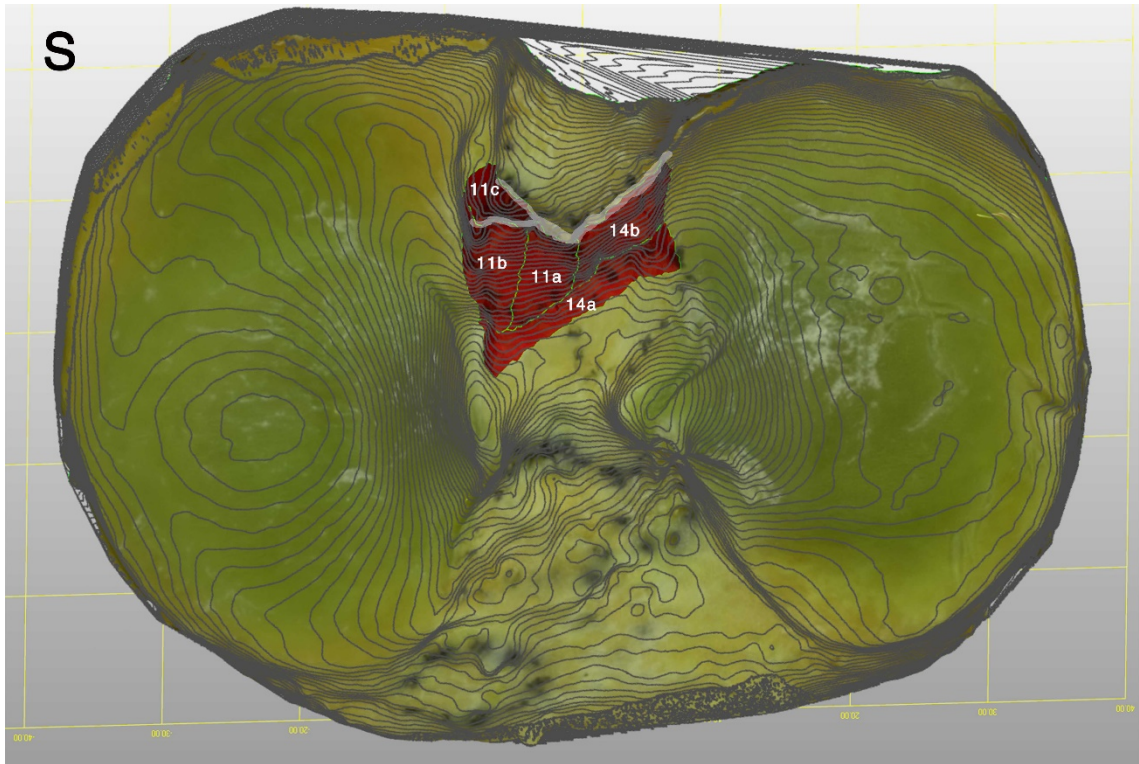


Figure 329. 3D model of tibia L, superior view with contour lines superimposed. Areas of the posterior wall selected (fluorescent green border) and highlighted in red. Tent-shaped ridge painted over in white color.

IV.9.2. Attachment of the posterior root of the medial meniscus

The posteromedial recess (11b) was qualitatively found to be the main attachment area of the posterior root of the medial meniscus, which filled its central and lateral aspects (Fig. 330, Fig. 331). Lateral to it, the medial aspect of area 11a also received some fiber attachments, while the common medial limit was found at the change of slope with the medial wall of the PIA – marked by the central PMIR process, C1. Area 11c did not receive fiber insertions in any of the investigated specimens.

In one specimen, the superior half of the PRMM footprint was found more superiorly and anteriorly, with fibers attached to the medial aspect of the intertubercular ridge (including areas 14a, 12).

Area 11a was the main attachment site for the supplementary fibers of the PRMM, the transverse shiny white fibers (Fig. 330), with some fibers found attached to the medial aspect of area 14b.

Quantitatively, the central fibers of the PRMM had a mean attachment area of 51.3 mm² (95% CI 30.3 – 80.3 mm²; range, 41.7 mm² to 61 mm²), representing a mean of 48.2% of area 11 (95% CI 41.3 – 55.1%; range, 27% to 74%; N=14).

The PRMM attachment center was measured in reference to arthroscopically pertinent landmarks, being posterior to the medial tubercle’s main peak (3a); lateral to the PMIR (in a straight horizontal line); medial to the PM corner of the PRLM; anterior to the PM fovea; anteromedial to the anteriormost (usually anterolateral) border of the PCL; posteromedial to the posteminence (POE); and posterior to the preeminence (PRE), and to the posterior border of the ACL attachment.

The center of the PRMM attachment was 11.9 mm (range, 6.5 mm to 17.7 mm), from the anterior peak of the MT, with a significant correlation with ML width ($r=0.75$, $p=0.002$) and AP depth ($r=0.58$, $p=0.029$), CV 33.19%, representing 16.5% of the ML width of the proximal tibia.

The center of the PRMM attachment was also 12.5 mm (range, 5.4 mm to 18.6 mm) from the posterior aspect of the ACL, with a significant but low correlation with ML width ($r=0.69$, $p=0.006$) and AP depth ($r=0.59$, $p=0.026$), CV 31.02%. It represented 17.5% of the ML width of the proximal tibia. See Table 26 for all distances obtained from the center of the PRMM attachment to selected anatomic landmarks.

Table 26. Distances in mm, 95% CI, Coefficient of variation (CV), Pearson correlation values for AP and ML, with their corresponding p-values.

PRMM	MM	95% CI	CV	AP	AP P	ML	ML P
MT (3a)	11.9	9.6 – 14.2	33.19	0.583*	0.029	0.748**	0.002
PMIR (C)	5.1	4.5 – 5.6	19.11	0.244	0.401	0.001	0.997
PMF (11c)	6.0	5.3 – 6.8	21.08	0.094	0.749	0.170	0.561
AL PCL	7.9	6.6 – 9.2	27.35	-0.125	0.685	0.116	0.706
POE (14a)	5.8	4.8 – 6.8	29.55	0.044	0.883	0.194	0.506
PRE (15)	11.4	9.3 – 13.4	31.35	0.246	0.397	0.454	0.103
PM PRLM	6.8	6.0 – 7.6	20.56	0.123	0.676	0.207	0.478
P ACL	12.5	10.3 – 14.8	31.02	0.593*	0.026	0.695**	0.006

* Correlation is significant at the 0.01 level (2-tailed).

NOTE. In red, the highest CV value of all data processed for attachment distances. In blue, measurements taken in the shortest straight (roughly ML) line.

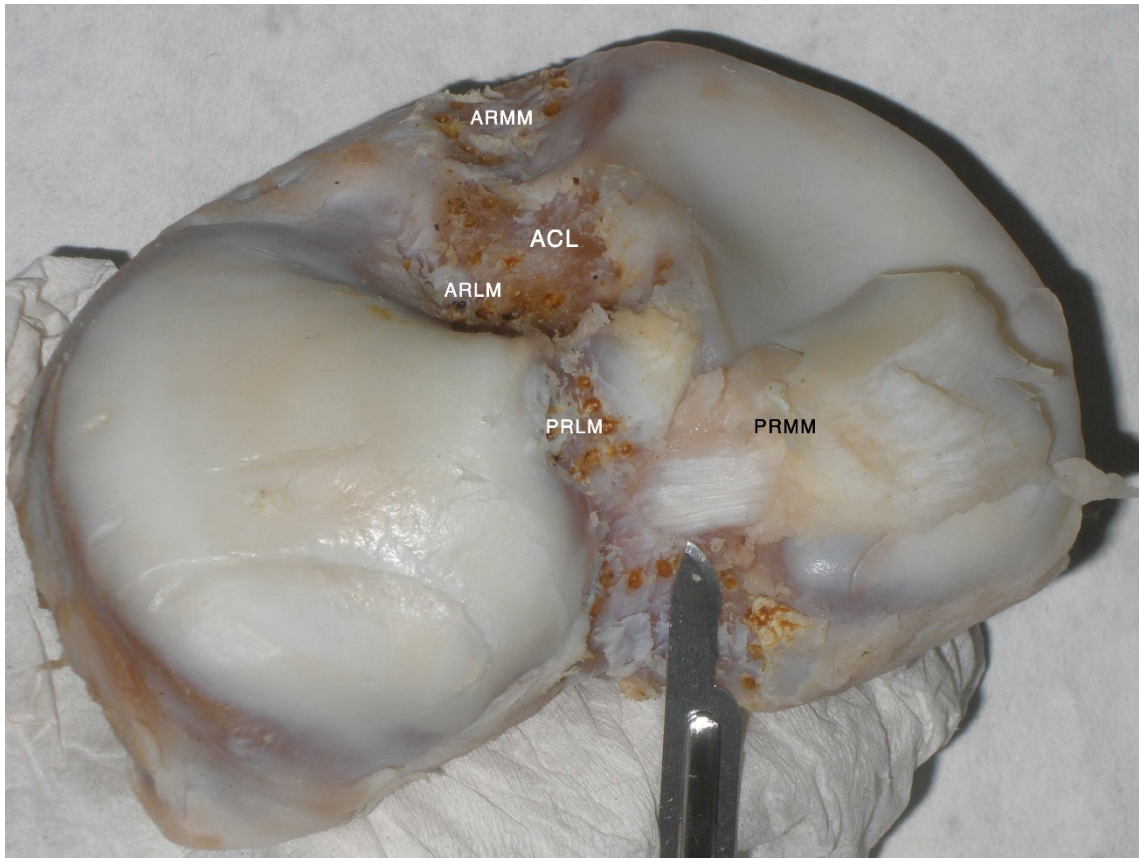


Figure 330. Tibia G. Photograph during dissection (posterior view). Soft tissue has been removed, only the PRMM remains attached, with shiny white fibers (pointed to with a scalpel) almost intact.

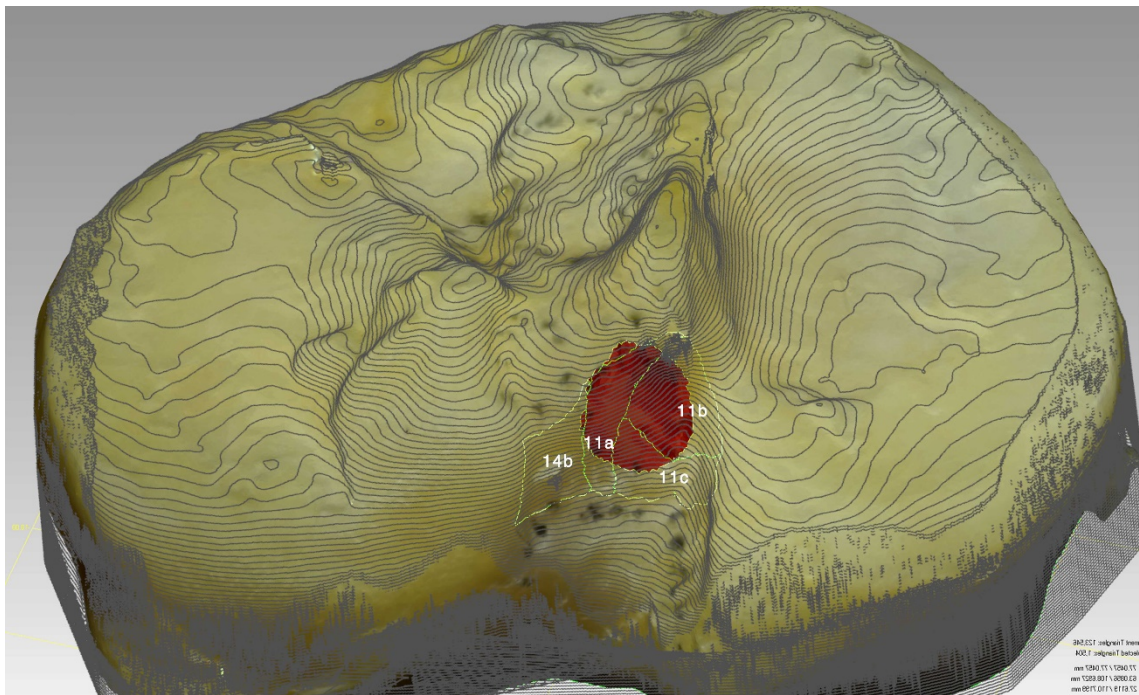


Figure 331. 3D model of tibia M, with contour lines superimposed (let mirrored). Posterior view. Areas of the posterior intercondylar wall selected (light fluorescent green lines) and labelled. PRMM attachment highlighted in red.

IV.9.3. Degenerative changes affecting the posterior wall

The elevation of the posteromedial recess showed a significant but weak correlation with knee OA (Fig. 335): $r_s(98)=0.317$, $p=0.001$.

The sagittal incisure, K, where both faces (14b, 11) of the posterior wall converged anteriorly, was found in some specimens substituted by a line or ridge. Often, this line or ridge was identified with the elevated internal PMIR process (C3), while in some cases it was the internal PLIR process (E3).

Both internal processes of the PMIR (C3) and PLIR (E3) were seen especially developed in arthritic knees (Fig. 332, Fig. 333). Their elevation showed a significant weak correlation with knee OA: C3 (Fig. 336), $r_s(98)=0.315$, $p=0.002$; E3 (Fig. 337), $r_s(96)=0.242$, $p=0.017$.

The posterior wall showed high density in certain axial radiographs (Fig. 334), and a non-significant, negative correlation was found between that density and knee OA (Fig. 338): $r_s(110)=-0.185$, $p=0.052$.

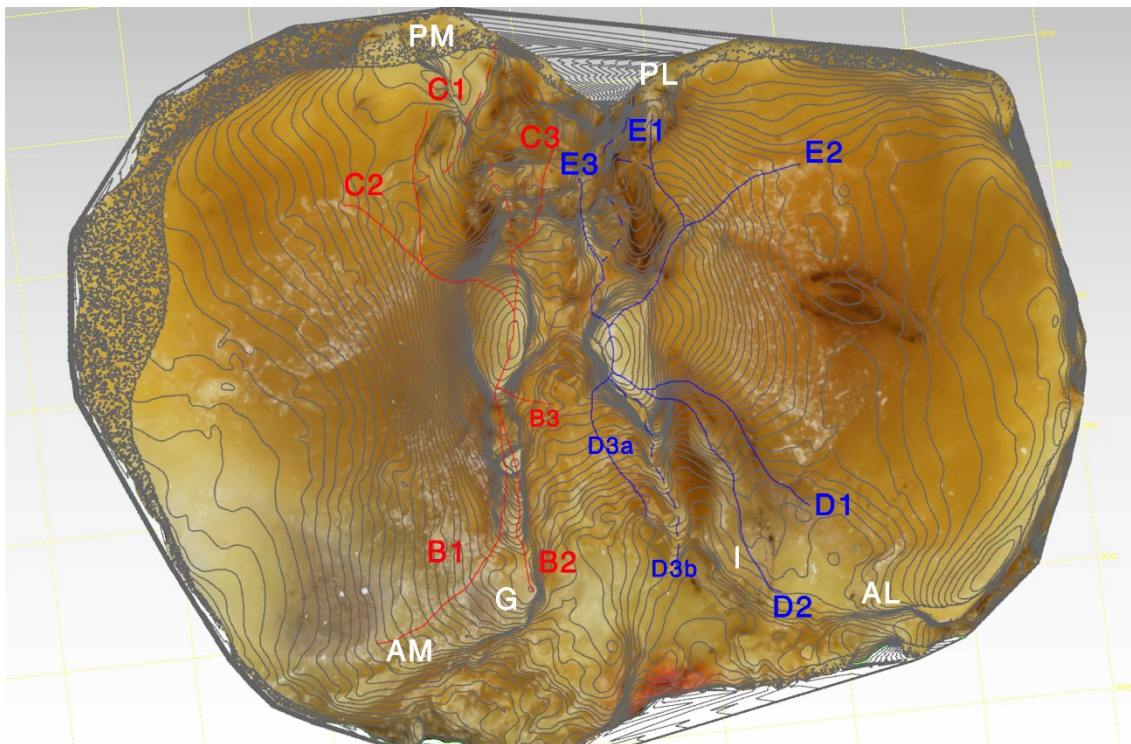


Figure 332. 3D model of tibia 98, with contour lines superimposed (left-mirrored). Elevated processes C3 (osteophyte grade 2) and E3 (grade 3), both delimiting the posteromedial fossa and posterolateral fossa, respectively. Notice also elevated D3b processes delimiting a narrow anterolateral fossa. Also labelled are processes of the AMIR (B1, B2, B3), PMIR (C1, C2), ALIR (D1, D2, D3a) and PLIR (E1, E2), and elevations of Parson's knob (G), ALIK (I), AM, AL, PM, and PL corners in white.

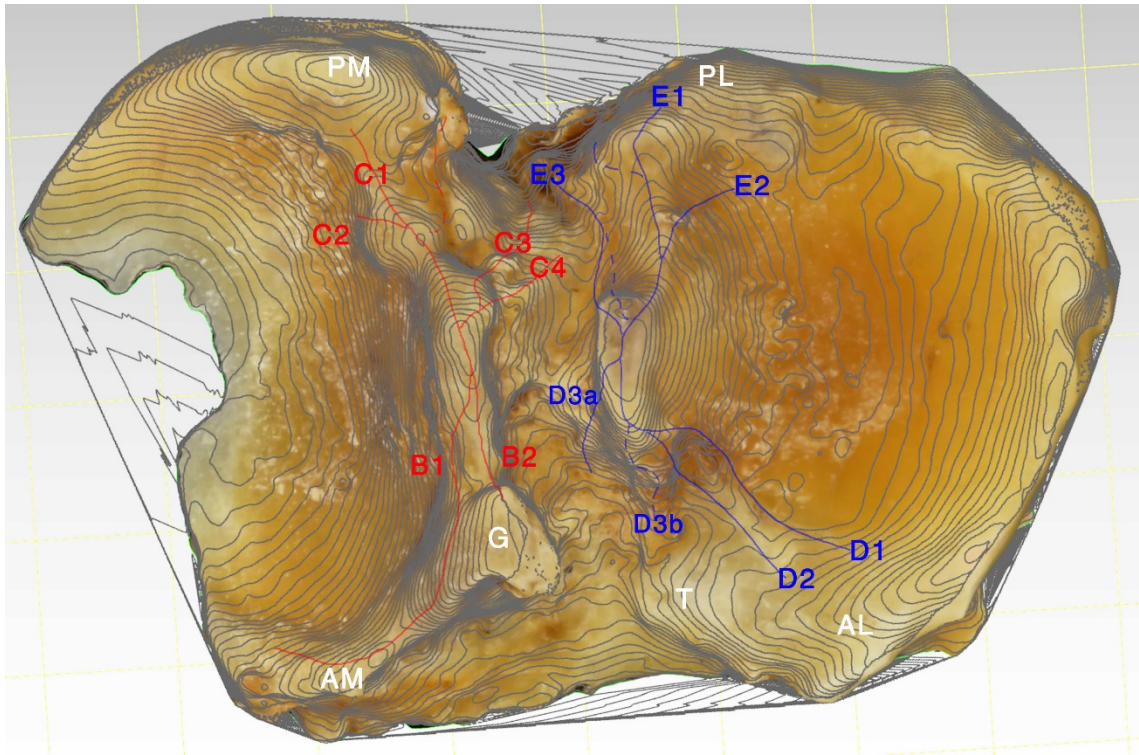


Figure 333. 3D model of tibia 30, with contour lines superimposed (left-mirrored). Elevated processes C3 (osteophyte grade 2) and E3 (grade 3). Also labelled are processes of the AMIR (B1, B2), PMIR (C1, C2, C4), ALIR (D1, D2, D3a, D3b) and PLIR (E1, E2), and elevations of Parson's knob (G), anterior saddle (T) together with AL corner, as well as AM, PM, and PL corners in white.

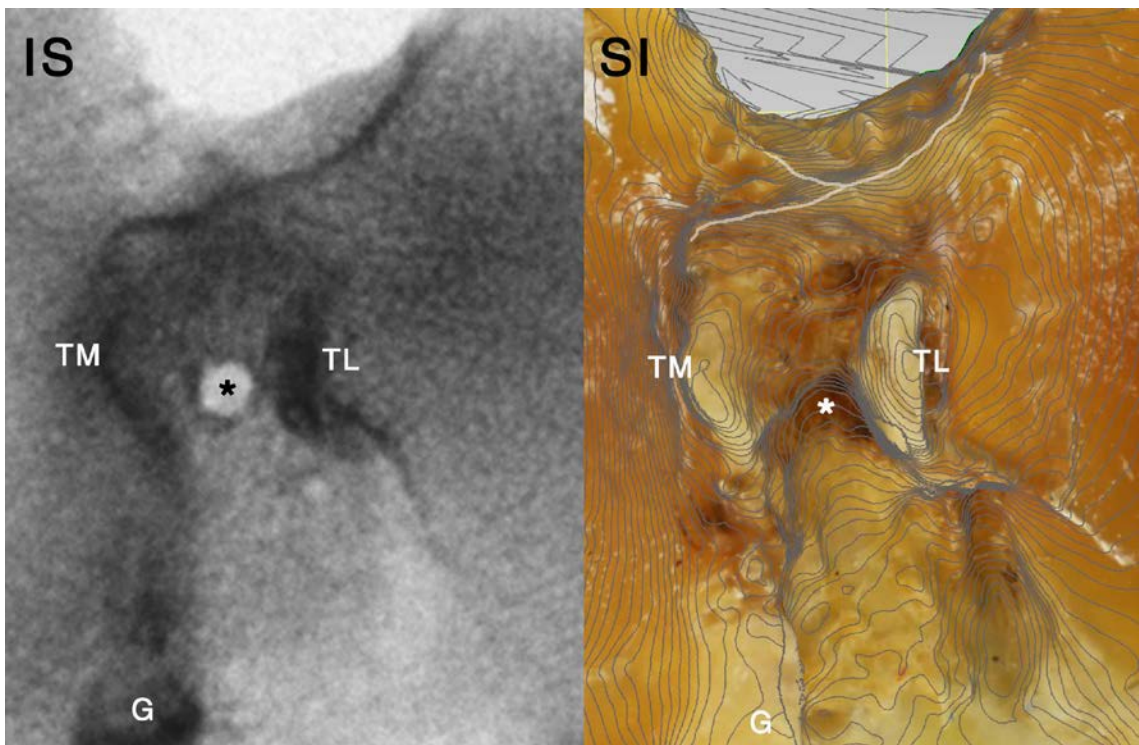


Figure 334. Tibia 15. Inferosuperior fluoroscopic image (IS) and superoinferior view (SI) of the 3D model, with contour lines superimposed. Observe higher radiographic density of the posterior wall, similar to the intercondylar tubercles (TM and TL) and Parson's knob (G), higher in the area corresponding to the tent-shaped ridge and lateral wall of the posterior facet (in white lines over 3D model). Notice also the big round central osteolysis (*) corresponding to the intertubercular fossa.

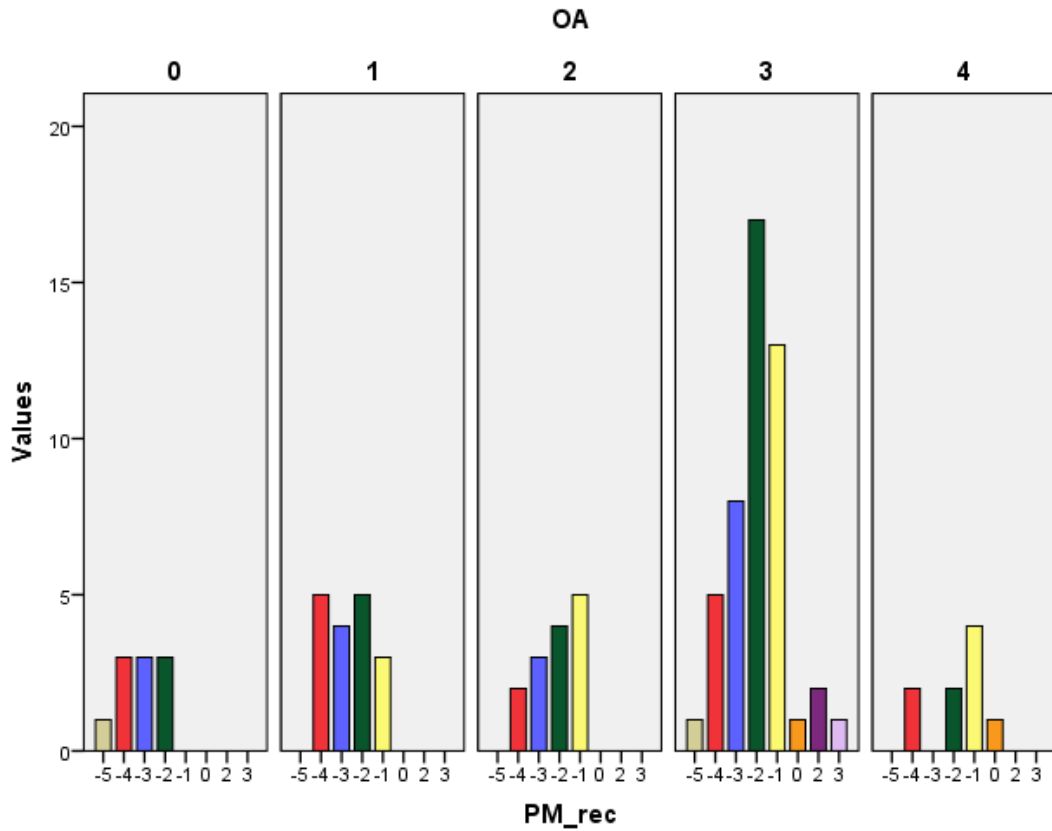


Figure 335. Study II. Histogram of the PM recess depression grade (PM_rec): number of tibias in each category, grouped by Ahlbäck OA grade.

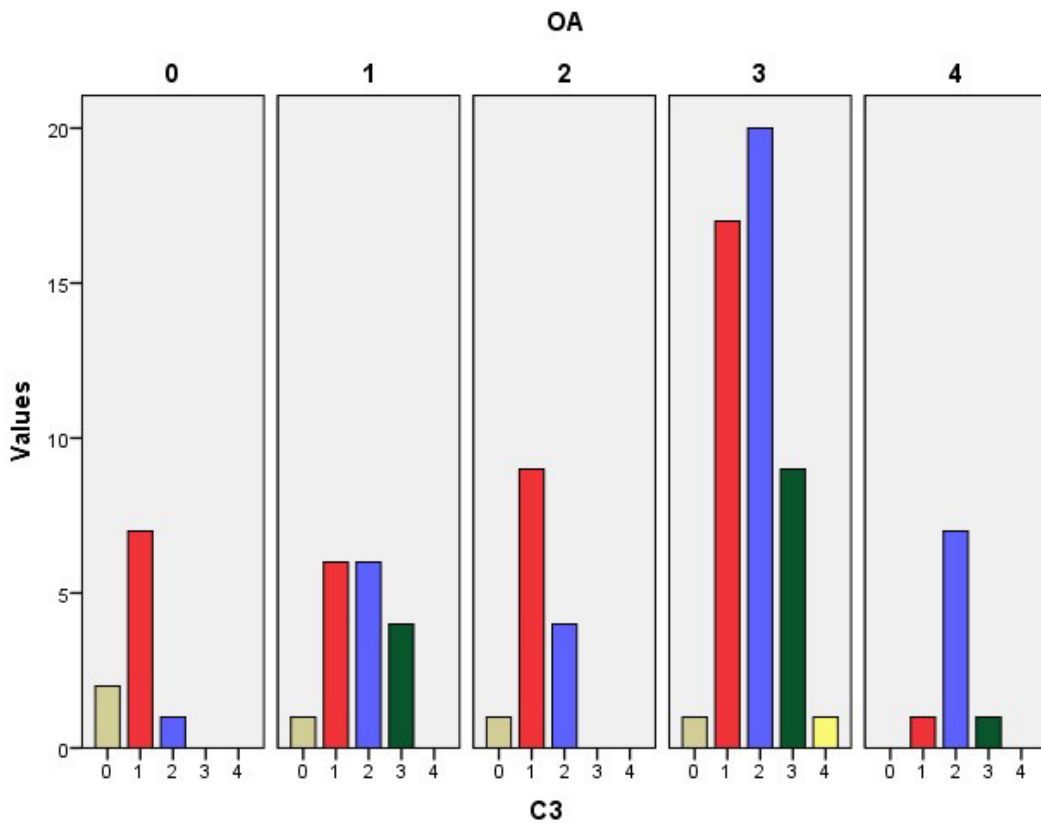


Figure 336. Study II. Histogram of the internal PMIR process (C3) elevation: number of tibias in each category, grouped by Ahlbäck OA grade.

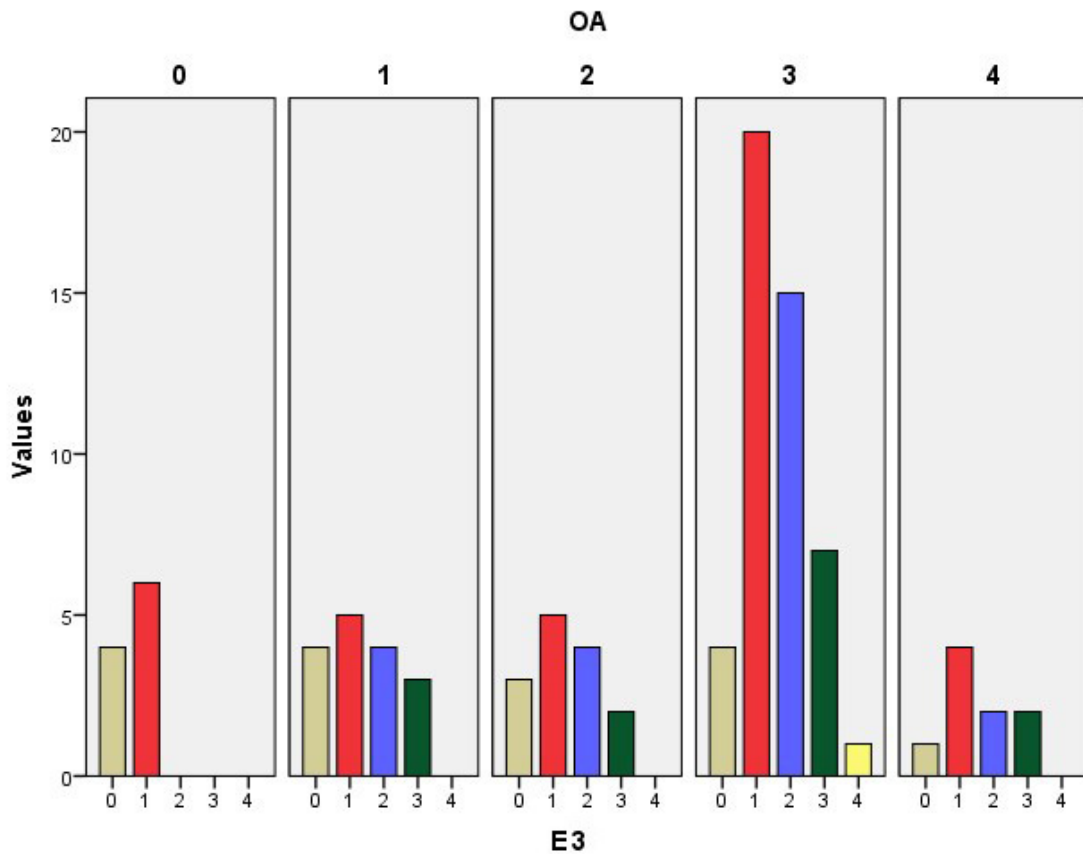


Figure 337. Study II. Histogram of the internal PLIR process (E3) elevation: number of tibias in each category, grouped by Ahlbäck OA grade.

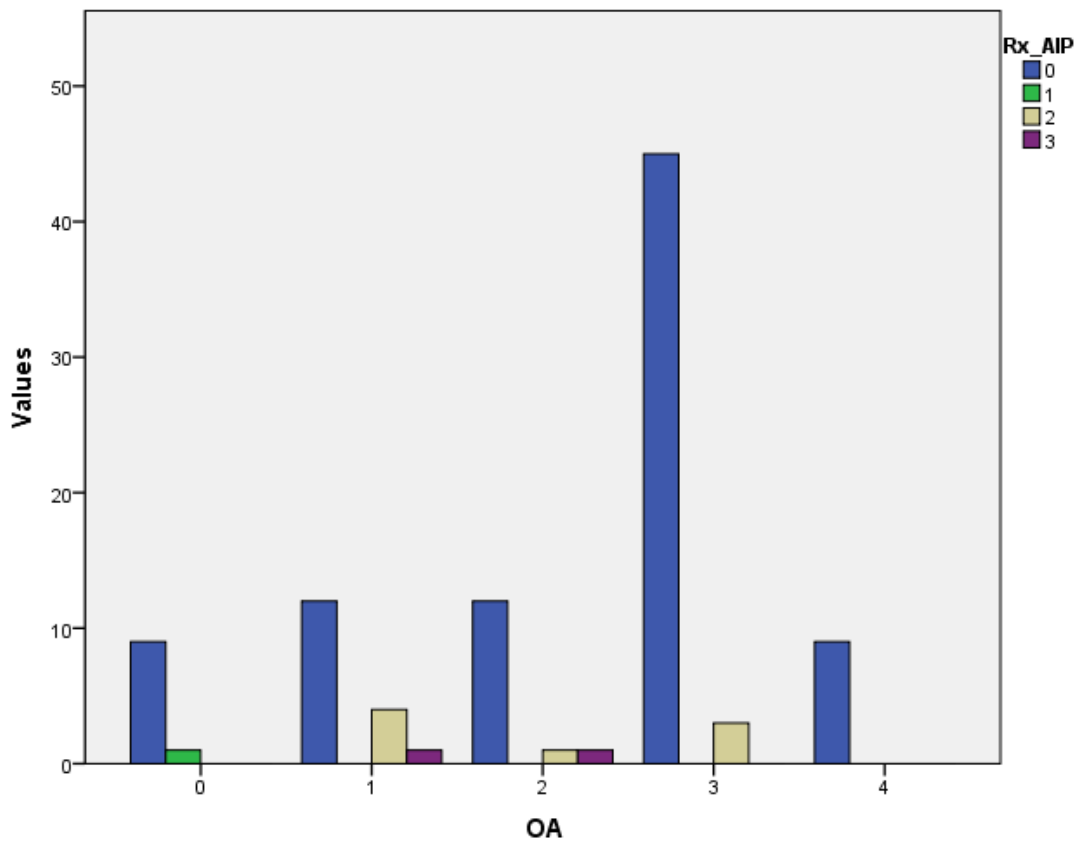


Figure 338. Study II. Histogram of radiographic density of the posterior intercondylar area in inferosuperior radiographs (Rx_AIP): number of tibias in each category, grouped by Ahlbäck OA grade.

IV.10. Posterior facet

IV.10.1. Intercondylar triangle and posterior rim

The posterior facet of the PIA, **13**, had a gentler slope than the posterior wall of the PIA, and was enclosed by steep medial and lateral walls, beneath secondary processes C1_b and E1_b respectively.

IV.10.1.1. Lines and indentations of the posterior facet

The posterior facet showed some constant structures (Fig. 339, Fig. 340):

- The ICT medial sagittal line, **13g**, a wide, slight elevation that divided area 13 in a wider medial and a narrower lateral part. Its anterior origin was the peak of the tent-shaped ridge, and followed a posteromedial direction with a gentle, medially convex curve.
- The ICT lateral sagittal line, **13i**, a slight elevation just medial to the lateral wall, shared a common origin with 13g, and followed a posterior direction with a gentle, laterally convex curve.
- The ICT coronal line, **13h**, a mediolateral line which connected the posterior aspect of the medial and lateral walls. At its union with the upper limits of the medial and lateral walls, the secondary central PMIR (C1_b) and PLIR (E1_b) processes, abrupt posterior corners are formed.
- The posterior intercondylar ridge (PIR), **Q**, appeared as a zig-zagging ridge (as a capital M without its right stroke), with superior peaks at the posteroinferior edges of the lateral and medial walls, and a middle (inferior) peak at the posterior end of 13g.

The union of the ICT sagittal line and the lateral aspect of the coronal line formed the posterior geniculate ridge, which showed usually a right or slight acute angle. Its peak formed the posterior geniculum, **P**.

The incisures formed lateral to 13g and medial to 13i were connected, forming a gothic arch-like incisure, **13j**, between them.

Area 13 of all specimens studied are shown (with main incisures) in Fig. 341 – Fig. 350.

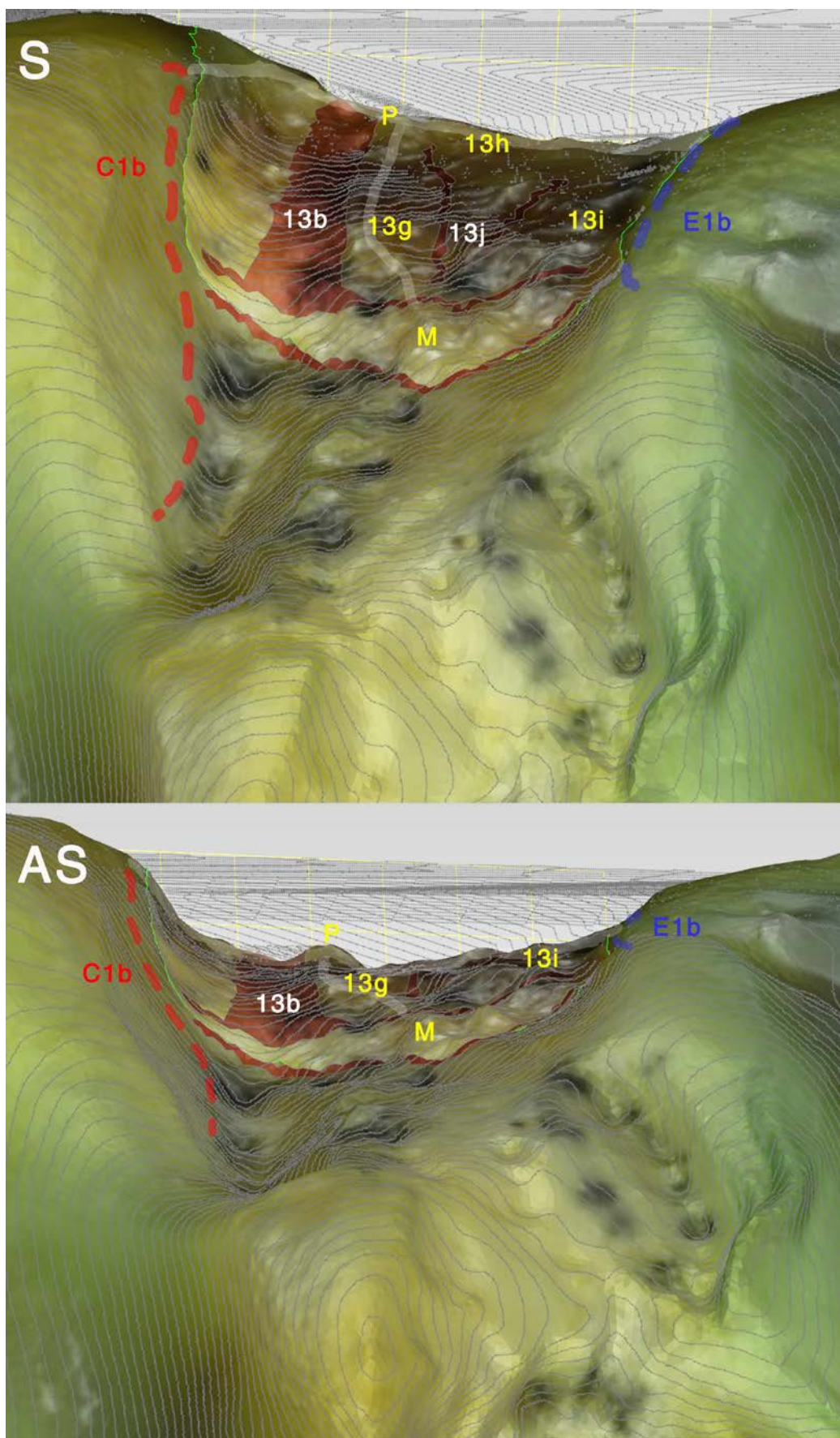


Figure 339. 3D model of Tibia C with contour lines superimposed and area 13 selected (fluorescent green borders). Superior (S) and anterosuperior (AS) views. Main incisures highlighted in red and labelled in white. Main lines and ridges labelled in yellow, with geniculate ridge painted in white. Also painted and labelled are the secondary central PLIR in blue, secondary central PMIR in red.

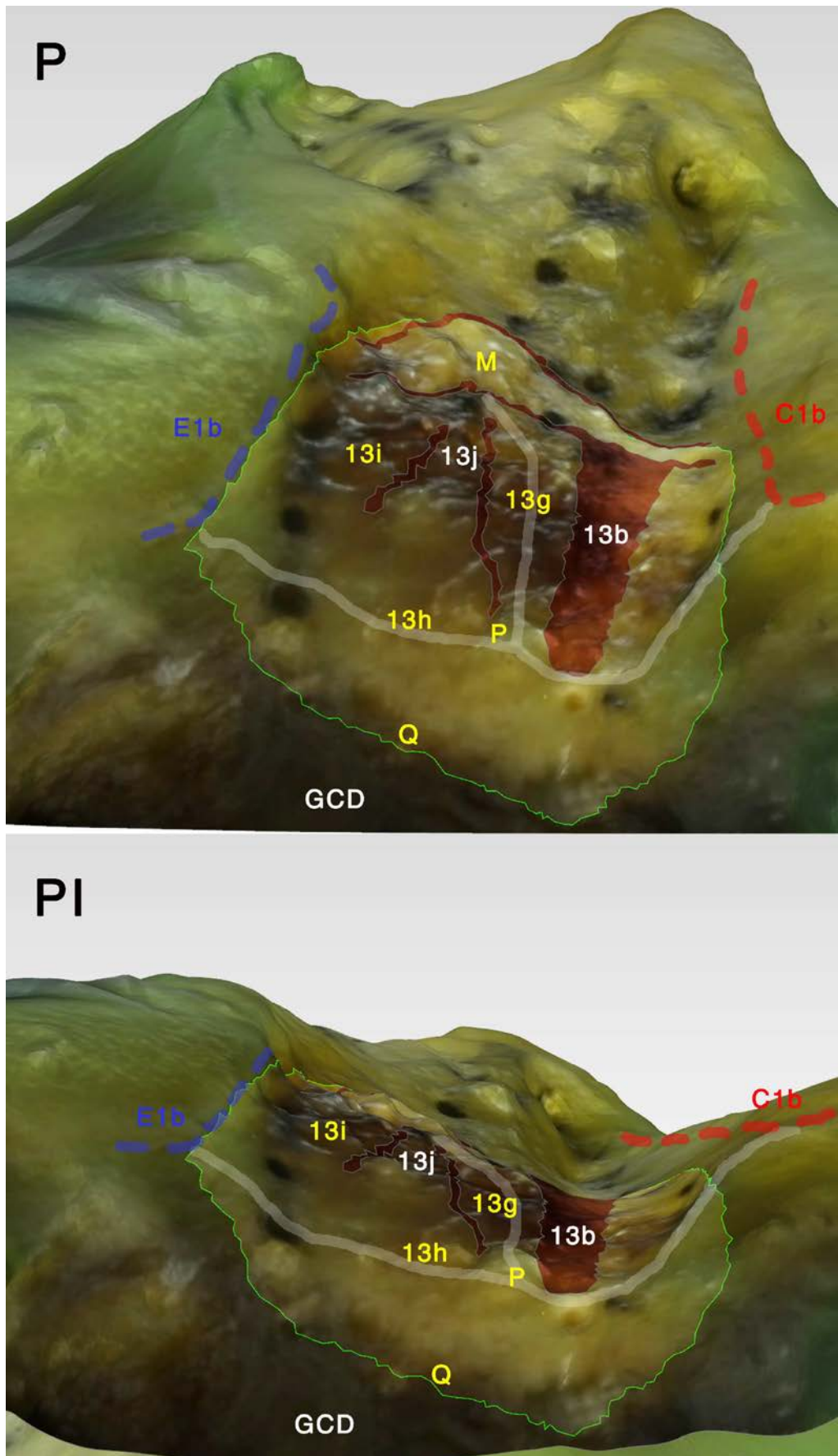


Figure 340. 3D model of Tibia C with area 13 selected (fluorescent green borders). Posterior (P) and posteroinferior (PI) views. Main incisures highlighted in red and labelled in white. Main lines and ridges labelled in yellow, with geniculate ridge painted in white. Also painted and labelled are the secondary central PLIR in blue, secondary central PMIR in red.

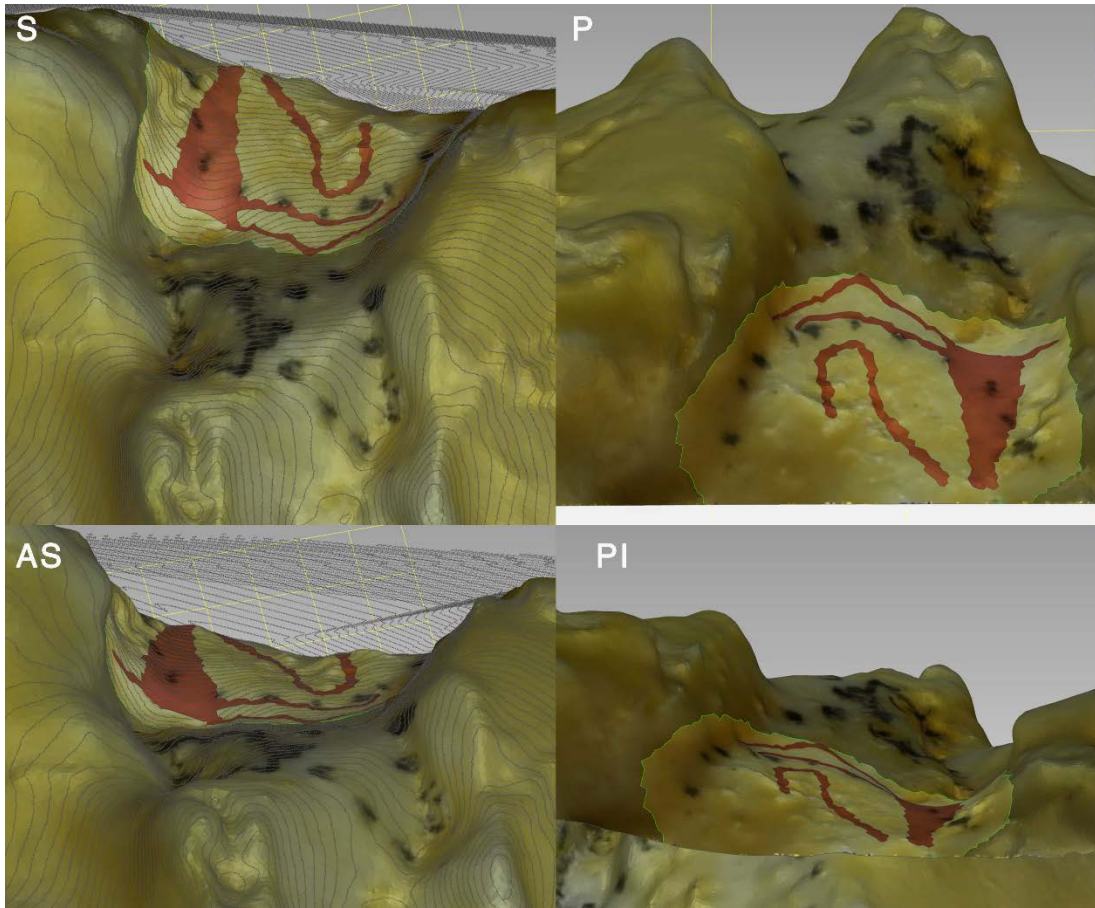


Figure 341. 3D model of Tibia A with area 13 selected, incisures selected and highlighted in red.

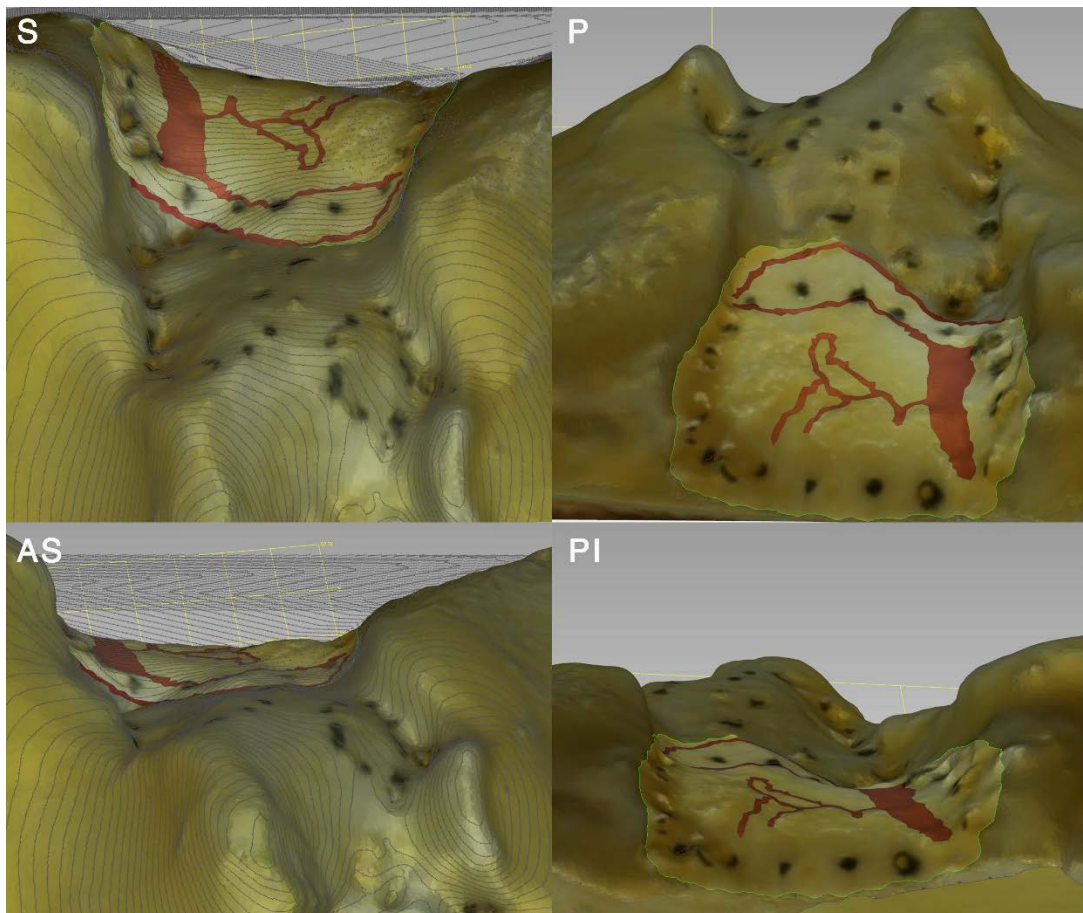


Figure 342. 3D model of Tibia B with area 13 selected, incisures selected and highlighted in red.

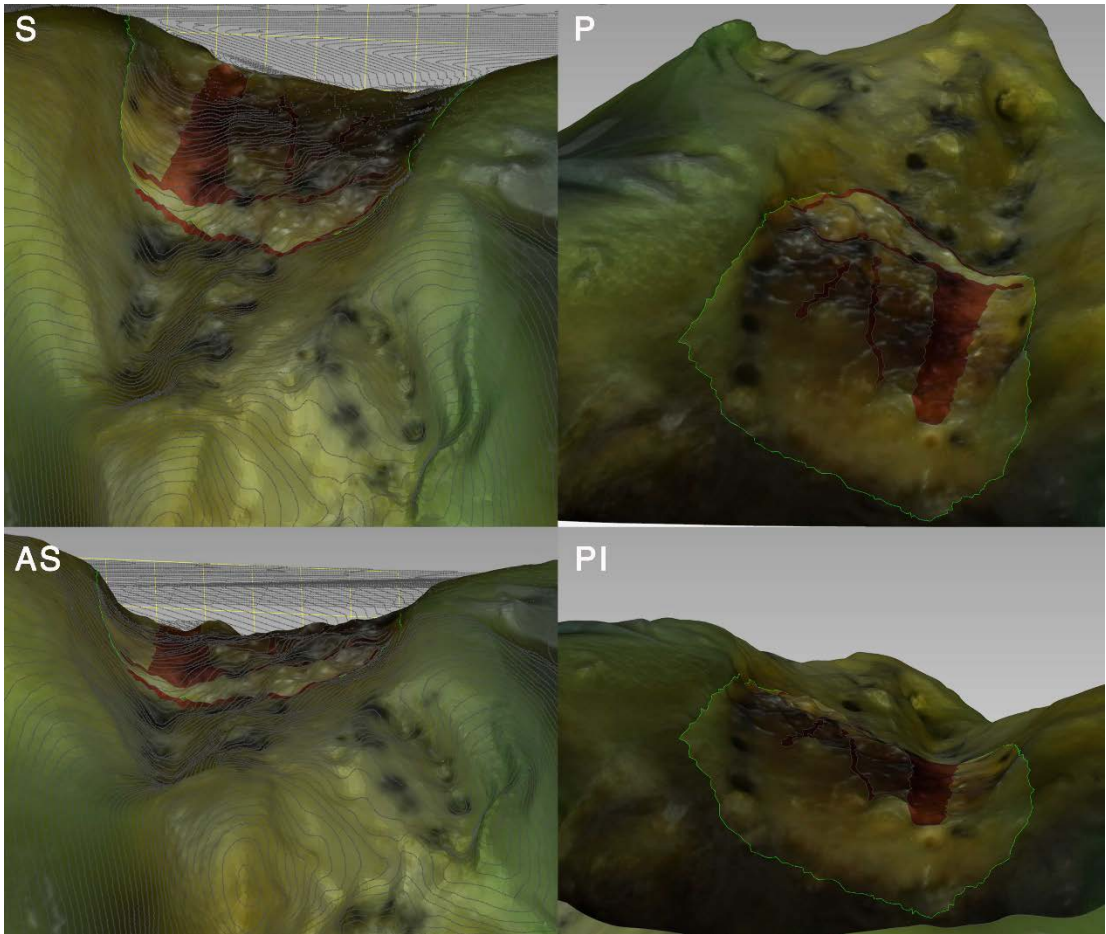


Figure 343. 3D model of Tibia C with area 13 selected, incisures selected and highlighted in red.

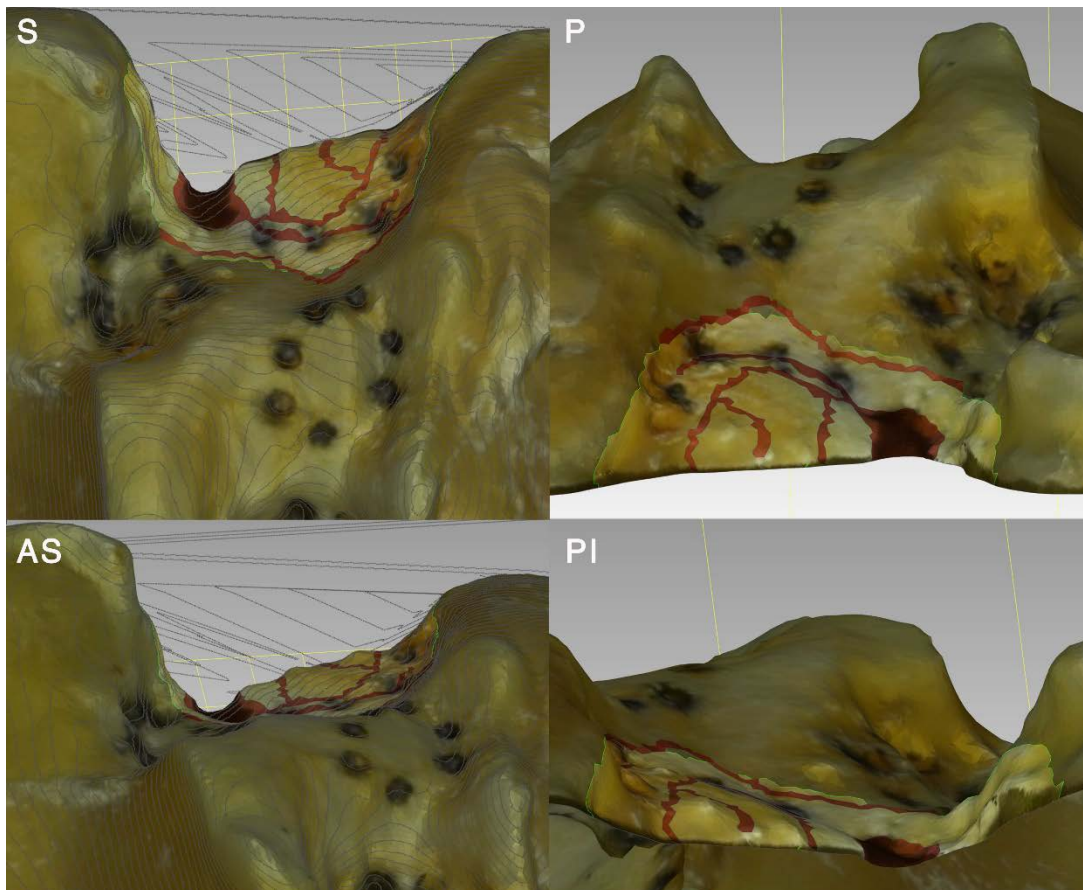


Figure 344. 3D model of Tibia D with area 13 selected, incisures selected and highlighted in red.

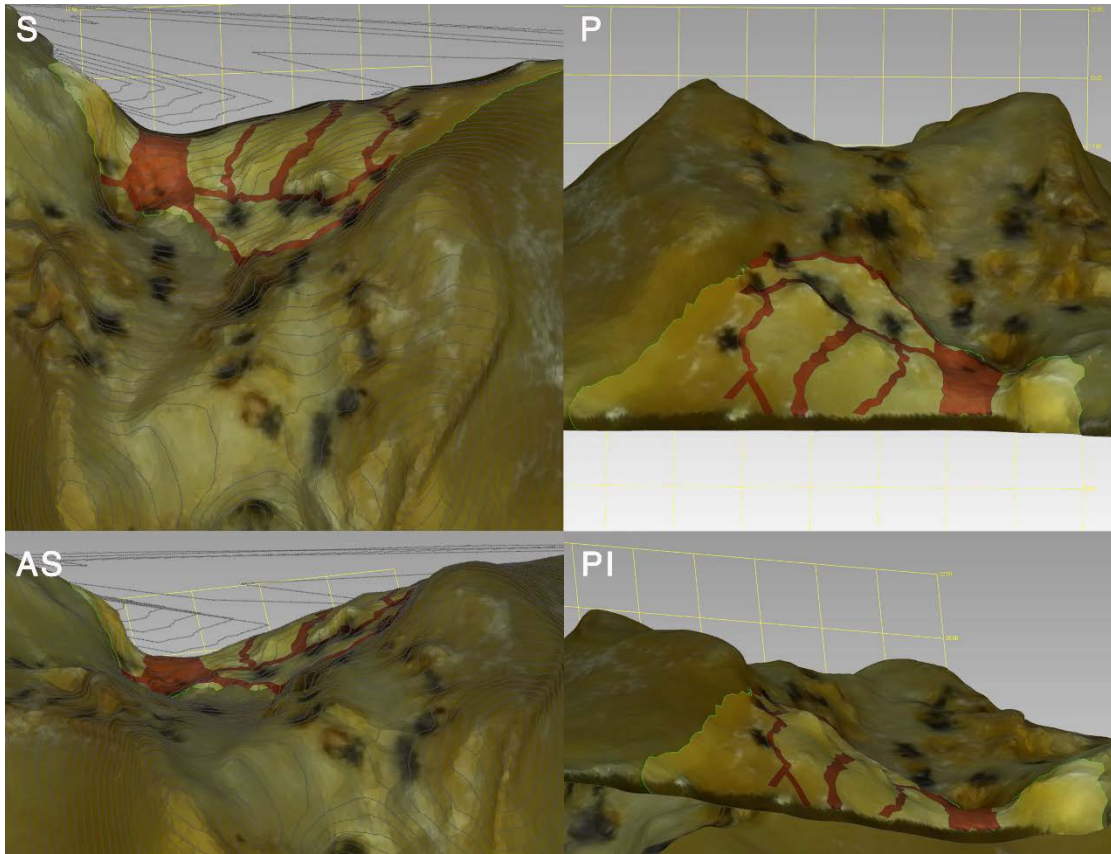


Figure 345. 3D model of Tibia E with area 13 selected, incisures selected and highlighted in red.

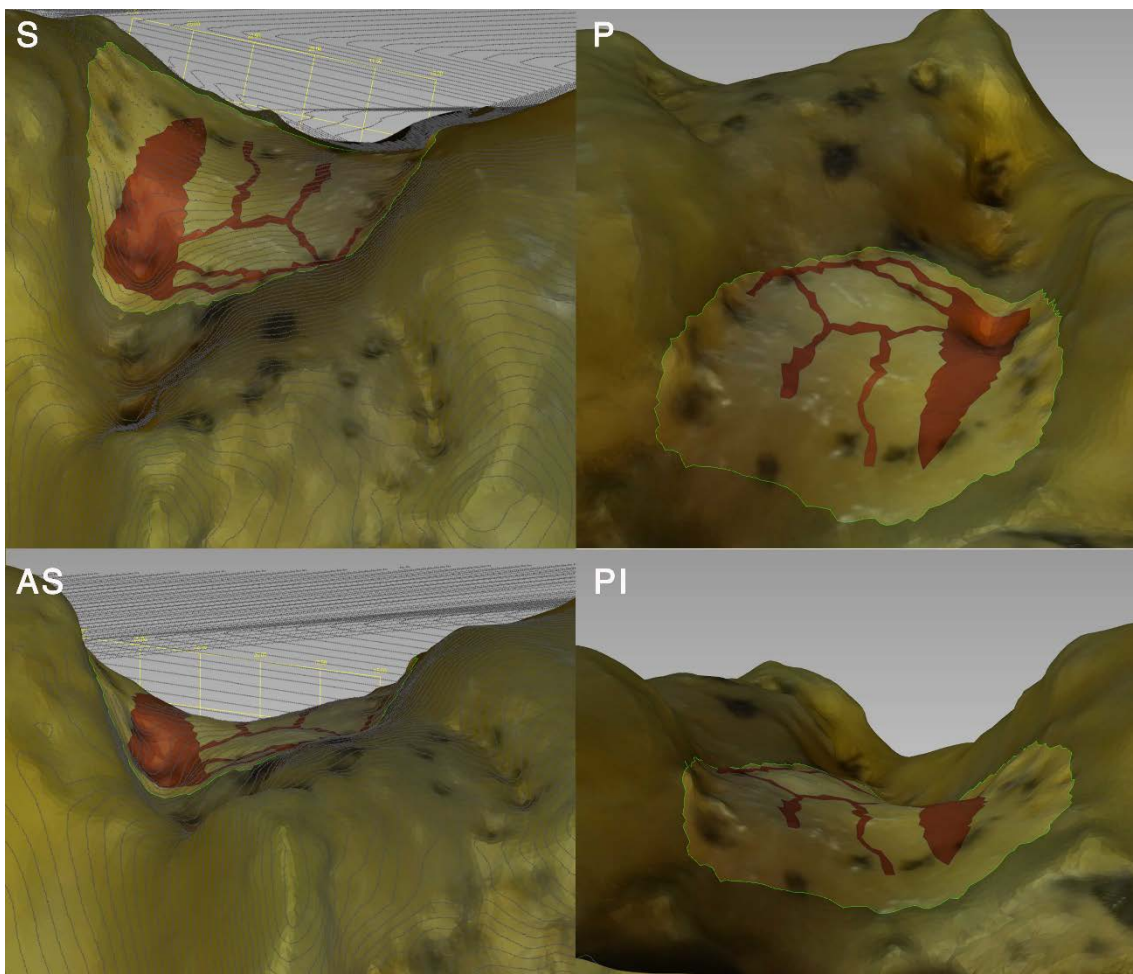


Figure 346. 3D model of Tibia G with area 13 selected, incisures selected and highlighted in red.

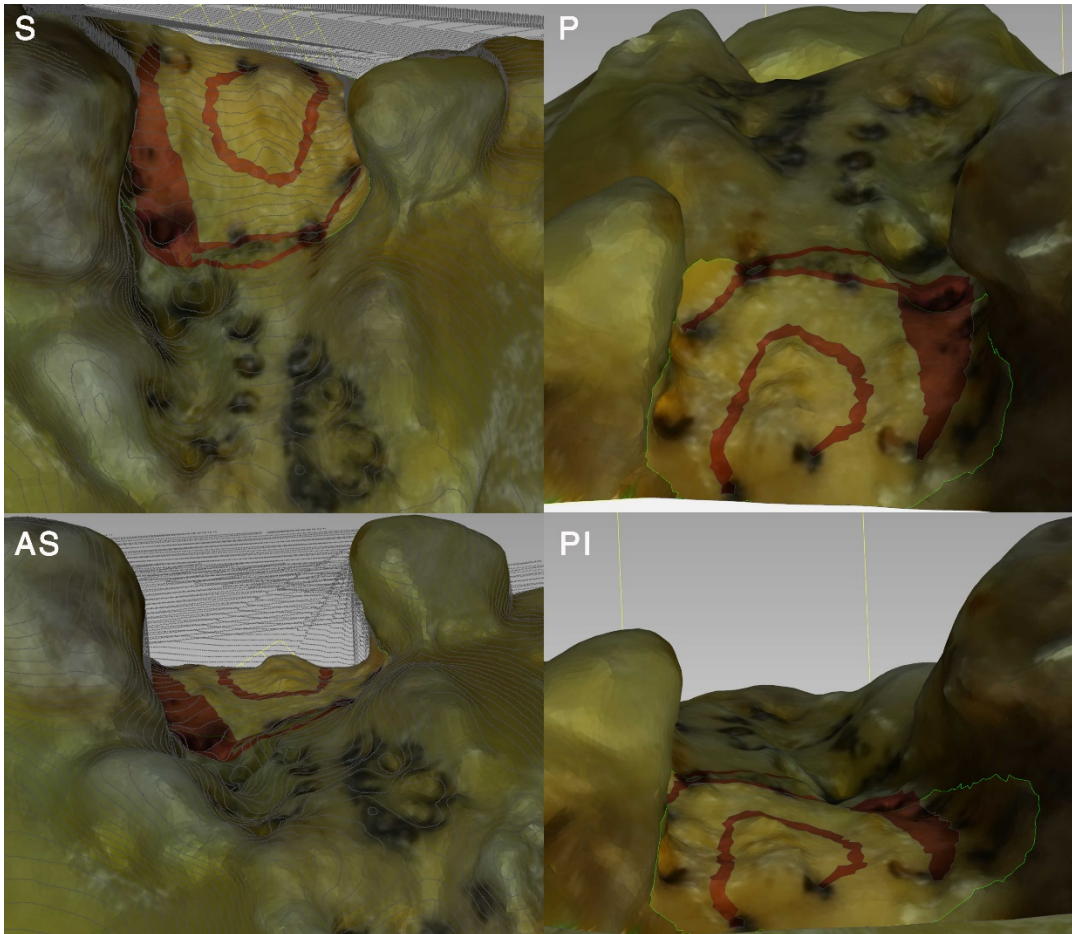


Figure 347. 3D model of Tibia H with area 13 selected, incisures selected and highlighted in red.

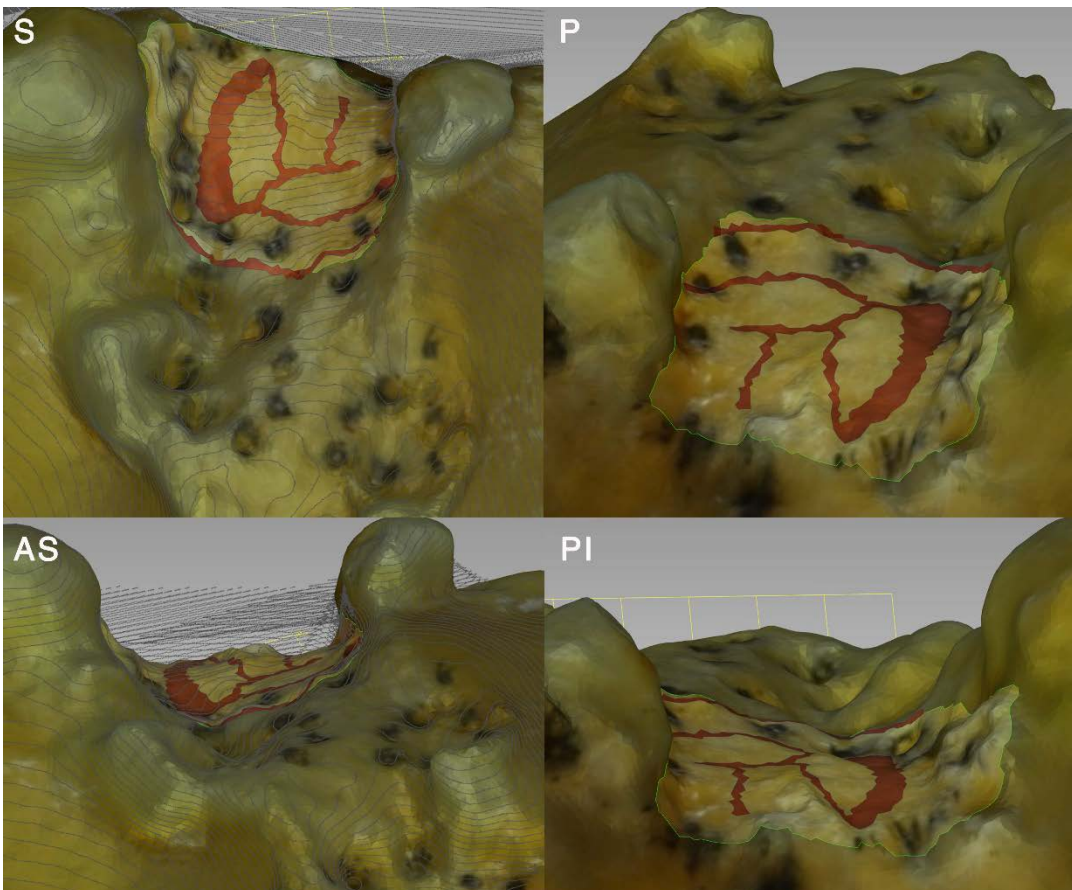


Figure 348. 3D model of Tibia I with area 13 selected, incisures selected and highlighted in red.

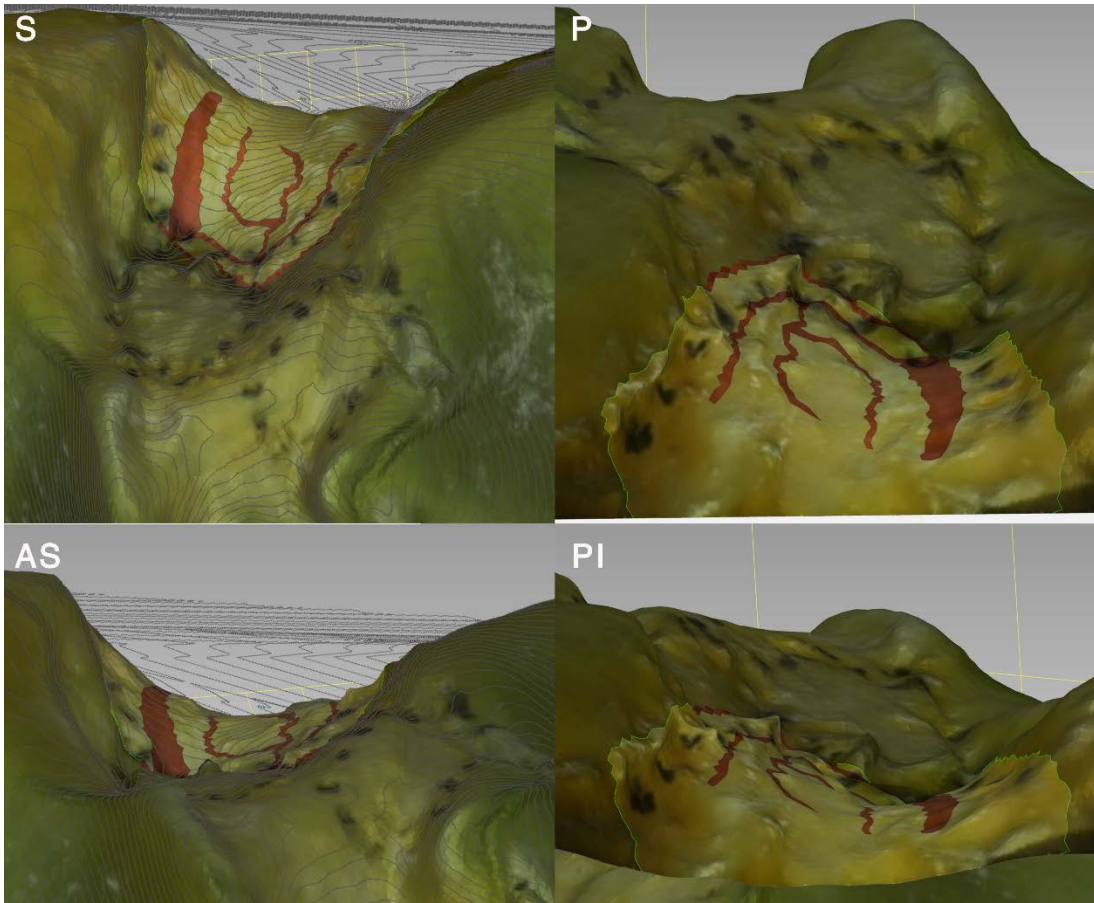


Figure 349. 3D model of Tibia L with area 13 selected, incisures selected and highlighted in red.

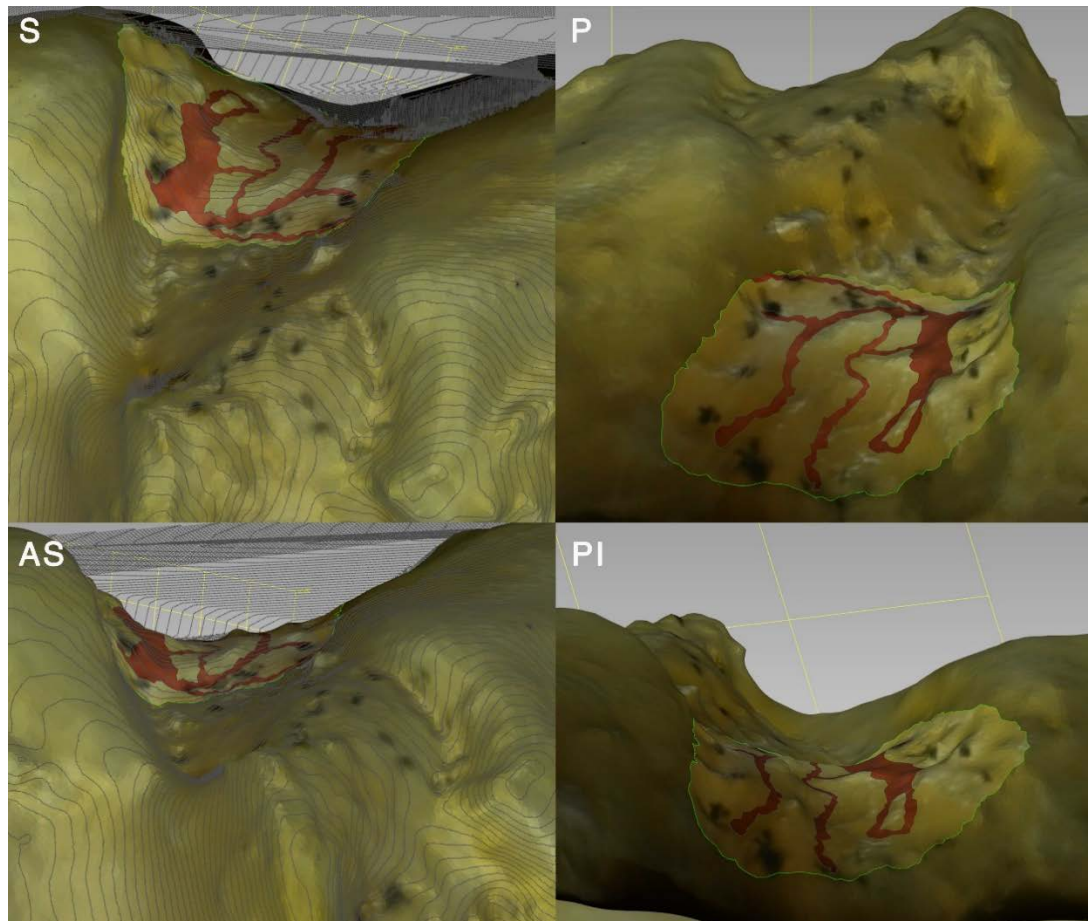


Figure 350. 3D model of Tibia M with area 13 selected, incisures selected and highlighted in red.

IV.10.1.2. Common areas of the posterior facet

Constant structures divided the osseous surface of the posterior facet into different zones (Fig. 352, Fig. 353):

The intercondylar circular triangle (ICT), anterior to the coronal line, had a general Releaux triangle shape, and showed a gentle downward slope in a posterior direction. Anteriorly, its boundary was the tent-shaped ridge.

The ICT widened from anterior to posterior, because of the posteriorly diverging medial and lateral walls. However, both walls showed a trend to bend posterolaterally, hence the posteromedial corner seemed to enclose the facet, while the posterolateral corner seemed to open it laterally.

The ICT was in turn divided in a lateral and a medial part:

- The lateral part of the triangle, the posterior intercondylar stair (PIS), **13a**, had a shape similar to a curved stair, convex laterally. It led from the posterior geniculum upwards to the peak of the tent-shaped ridge. It was demarcated medially and inferiorly by the posterior geniculate ridge.
- The medial part of the triangle, the posteromedial groove, **13b**, was a narrow zone bordered laterally by the ICT sagittal line. It appeared as a constant notch with a continuous downwards slope posteriorly, narrowing in an anterior to posterior direction.

The posterior intercondylar rim (PIR), **13c**, was a moderately sloped strip of bone, located between the coronal line and the posterior intercondylar ridge. It represented a transition zone between the gently sloped ICT and the steeply sloped posterior wall of the proximal tibia.

Behind the PIR was the champagne-glass drop-off (CGD), **16**, with its superior peak at the posteroinferior aspect of the lateral wall, hence located slightly lateral relative to the PIA.

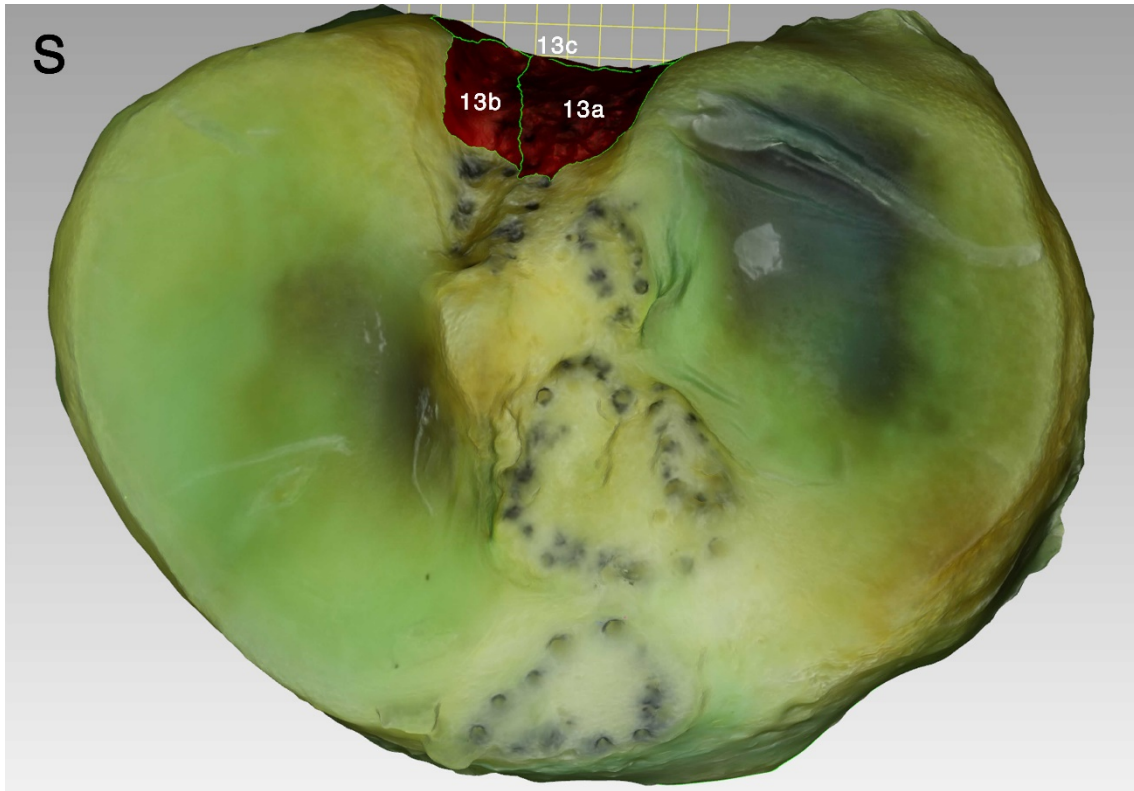


Figure 351. 3D model of tibia C, superior view (S). Posterior facet areas selected, highlighted in red, and labelled.

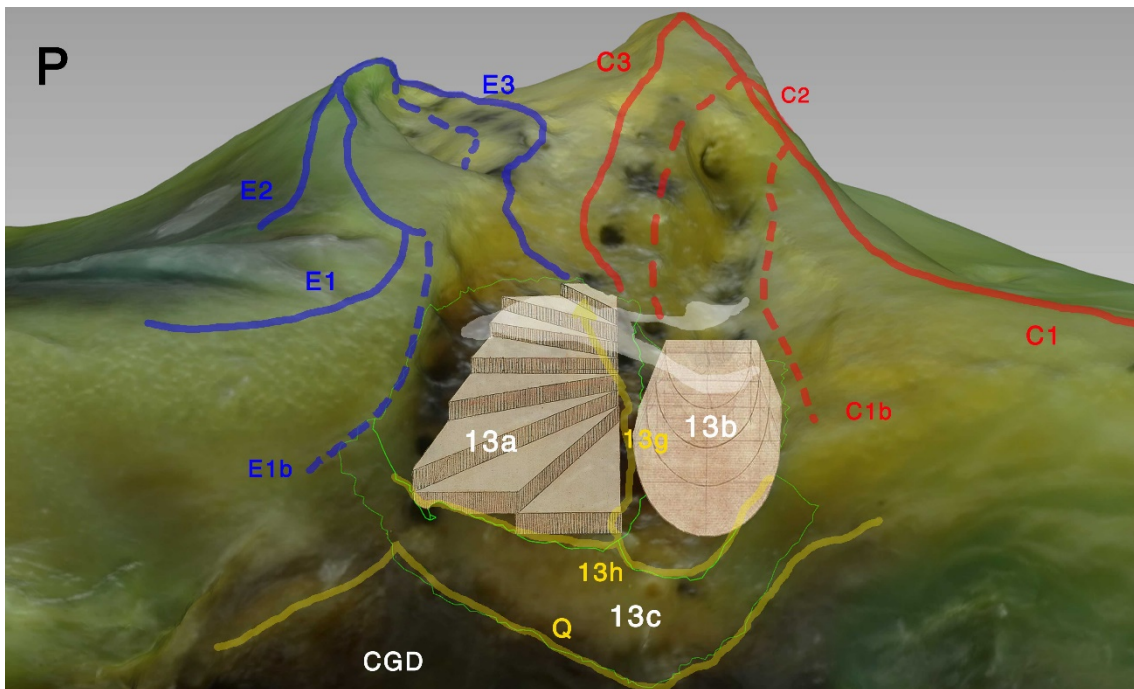


Figure 352. 3D model of Tibia C, posterior view (P). Posterior facet areas selected (fluorescent green borders) and labelled in white, with a curved stair superimposed to area 13a, and a canal superimposed to area 13b. Main lines and ridges in yellow, with tent-shaped ridge painted in white. Also painted and labelled are the PLIR processes in blue, PMIR processes in red.

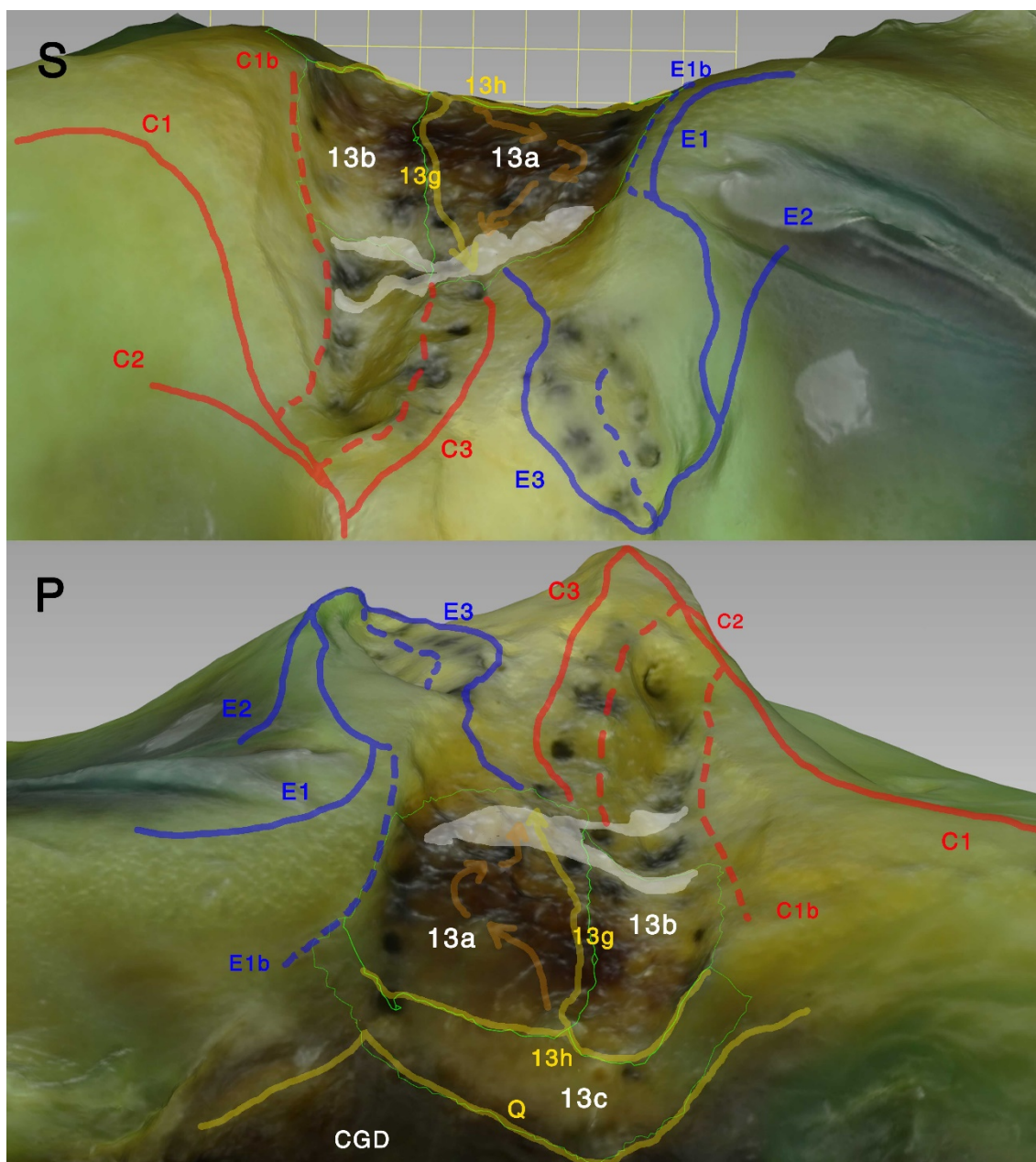


Figure 353. 3D model of Tibia C, superior (S) and posterior (P) views. Posterior facet areas selected (fluorescent green borders) and labelled in white. Main lines and ridges in yellow, with tent-shaped ridge painted over in white. The posterior intercondylar staircase main direction (upwards) is painted in light brown. Also painted and labelled are the PLIR processes in blue, PMIR processes in red.

IV.10.2. Attachment of the posterior cruciate ligament

IV.10.2.1. Shape and area of the PCL footprint

The posterior cruciate ligament footprint was qualitatively found to be located almost exclusively in the posterior facet.

The attachment area showed a variable shape, usually an irregular quadrilateral with a longer side posteriorly, long medial and lateral sides (the lateral side longer than the medial one), and a smaller side anteriorly. In some cases a pentagon-like shape was found, with its anterior vertex at the peak of the tent-shaped ridge. The

anteriormost insertion fibers of the PCL were often found forming an anterolateral peak.

Some fibers were occasionally found attached anterior to the tent-shaped ridge: in the posterolateral facet, 14b, near the lateral wall (3 specimens), or in area 11b (2 specimens). The posteromedial fossa, 11c, was a constant anteromedial boundary for the PCL footprint, bare of fiber insertions.

Posteriorly, the PIR was found to coincide with the inferior attachment of the joint capsule, and below it coursed the popliteus muscle fibers. It was therefore a constant posterior limit of the PCL footprint.

Quantitatively, the PCL area had 144.6 mm² (95% CI 115.2 – 173.9 mm²; range, 102.2 mm² to 210.2 mm²), and it covered 70.4% of area 13 (95% CI 62.9 – 78%; range, 53% to 86%).

PCL bundle footprints of all specimens studied are shown in Fig. 354 – Fig. 364.

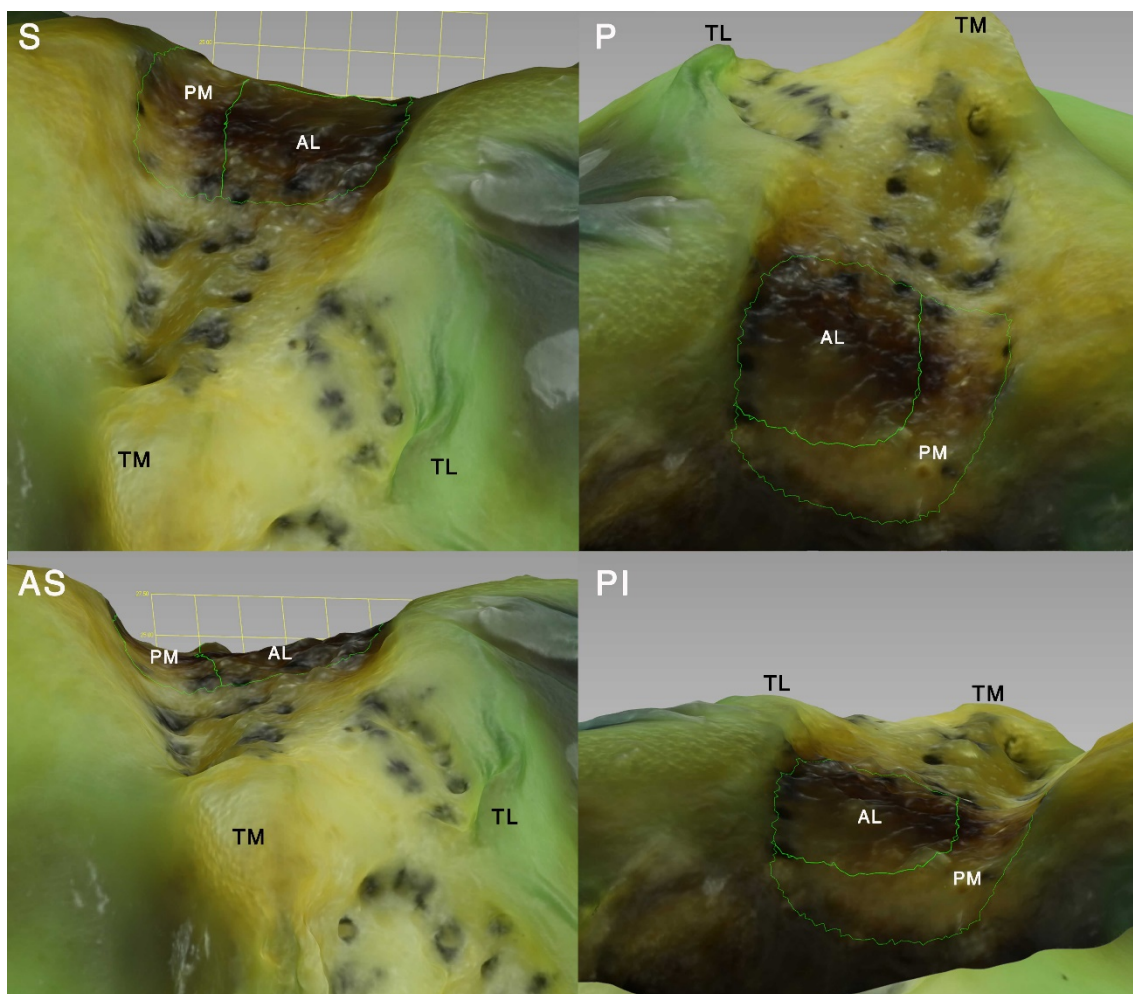


Figure 354. 3D model of tibia C. Superior (S), anterosuperior (AS), posterior (P) and posteroinferior (PI) views. Footprint of PCL bundles selected (fluorescent green lines). AL: anterolateral bundle of the PCL. PM: posteromedial bundle of the PCL.

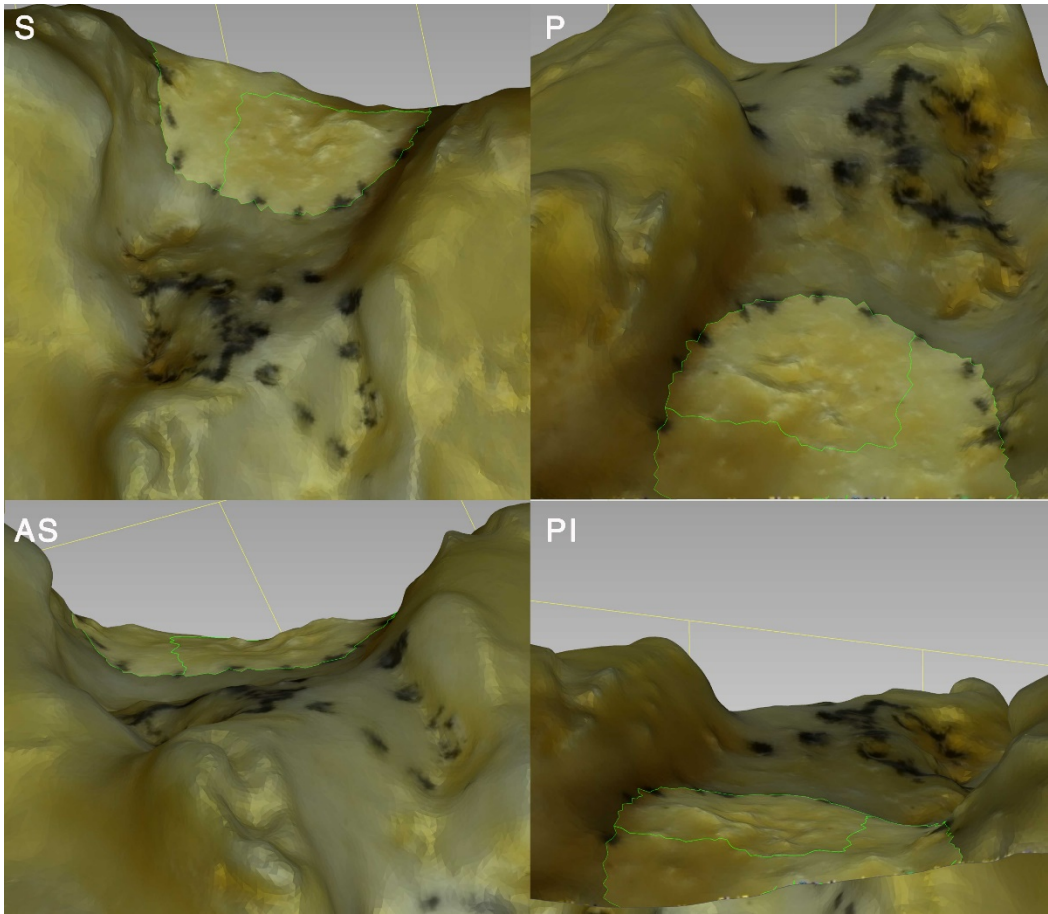


Figure 355. 3D model of tibia A. Footprint of PCL bundles selected and highlighted.

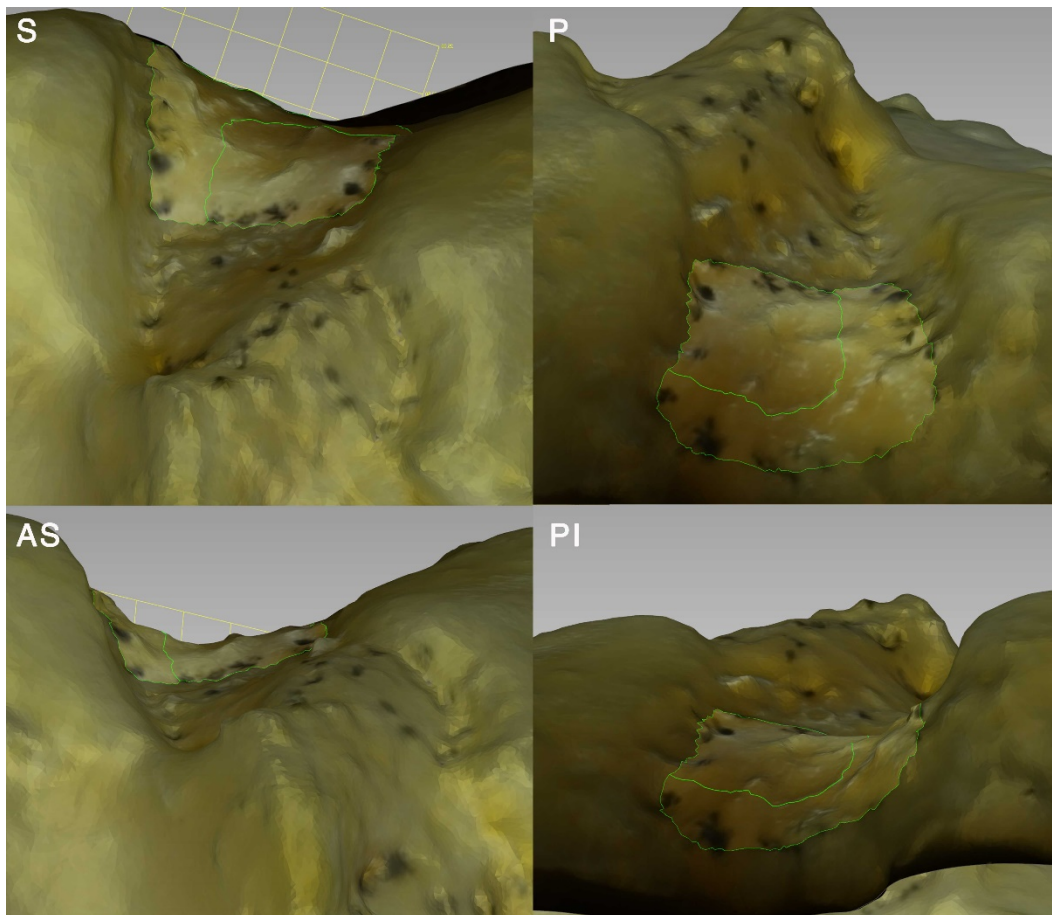


Figure 356. 3D model of tibia B. Footprint of PCL bundles selected and highlighted.

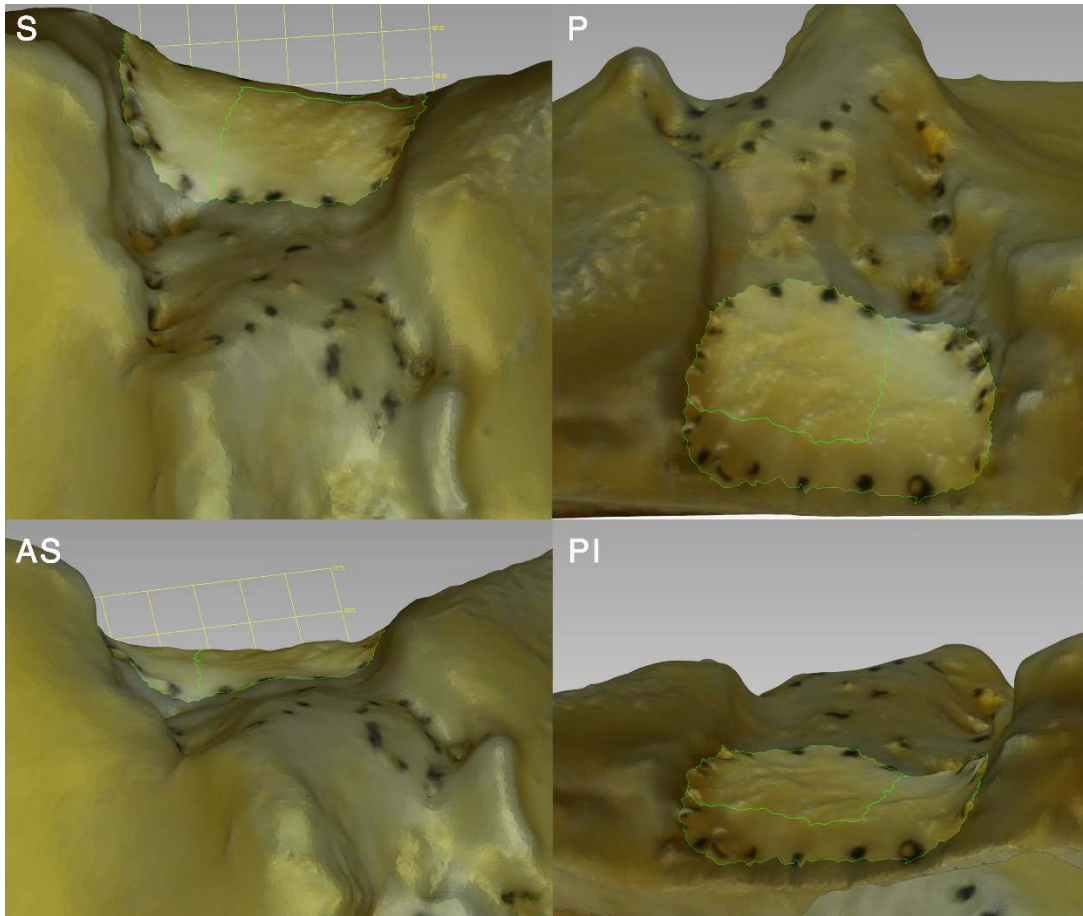


Figure 357. 3D model of tibia D. Footprint of PCL bundles selected and highlighted.

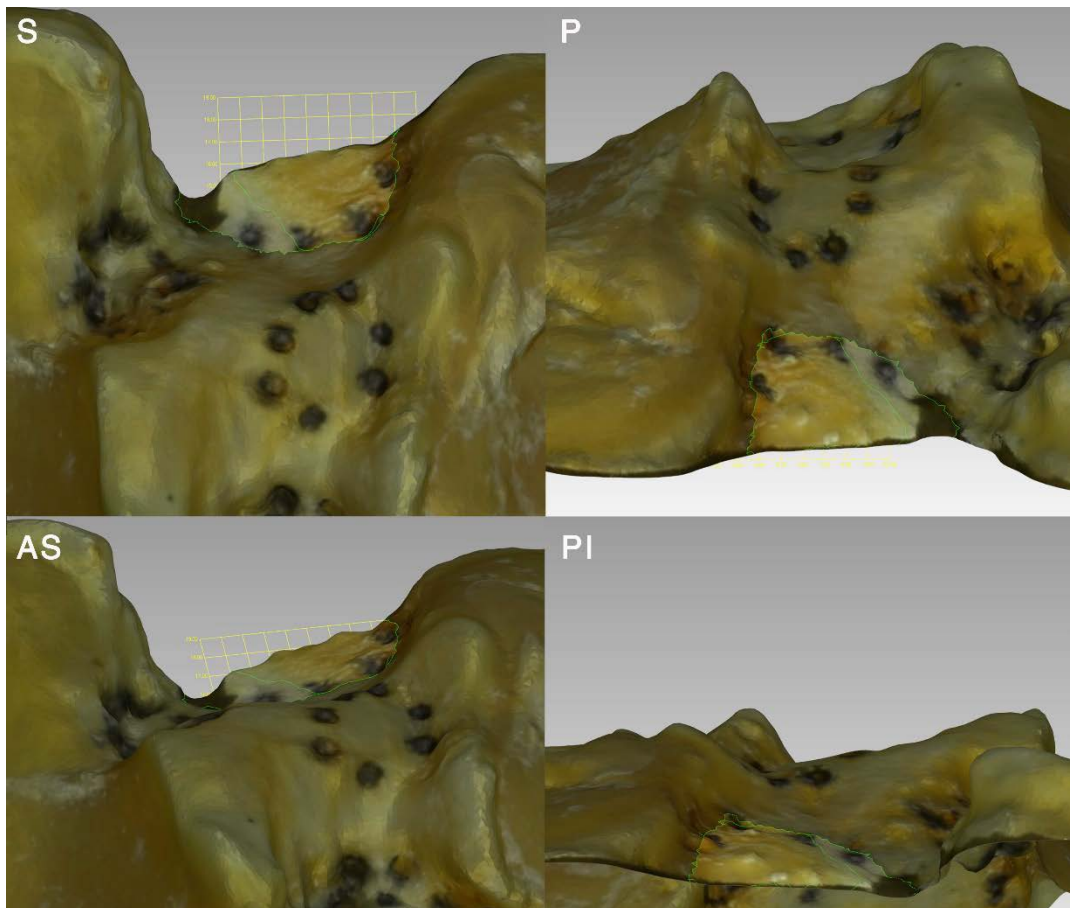


Figure 358. 3D model of tibia E. Footprint of PCL bundles selected and highlighted.

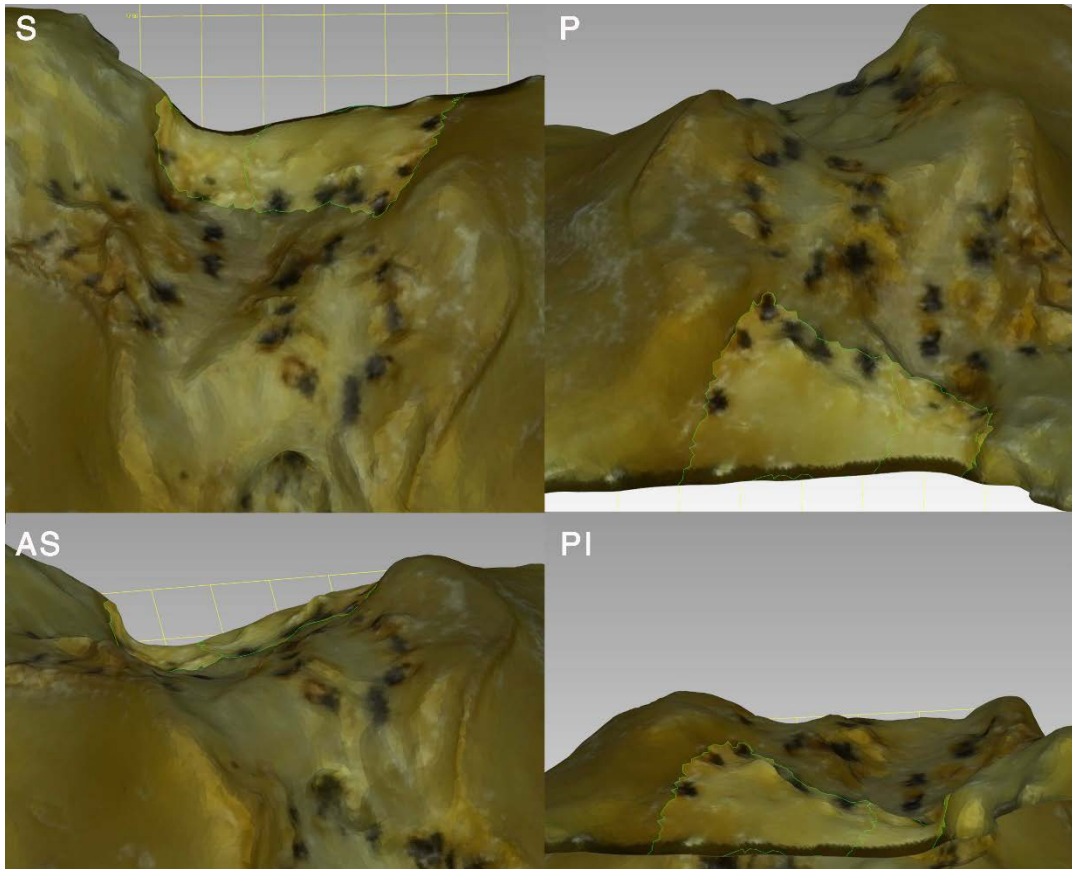


Figure 359. 3D model of tibia F. Footprint of PCL bundles selected and highlighted.

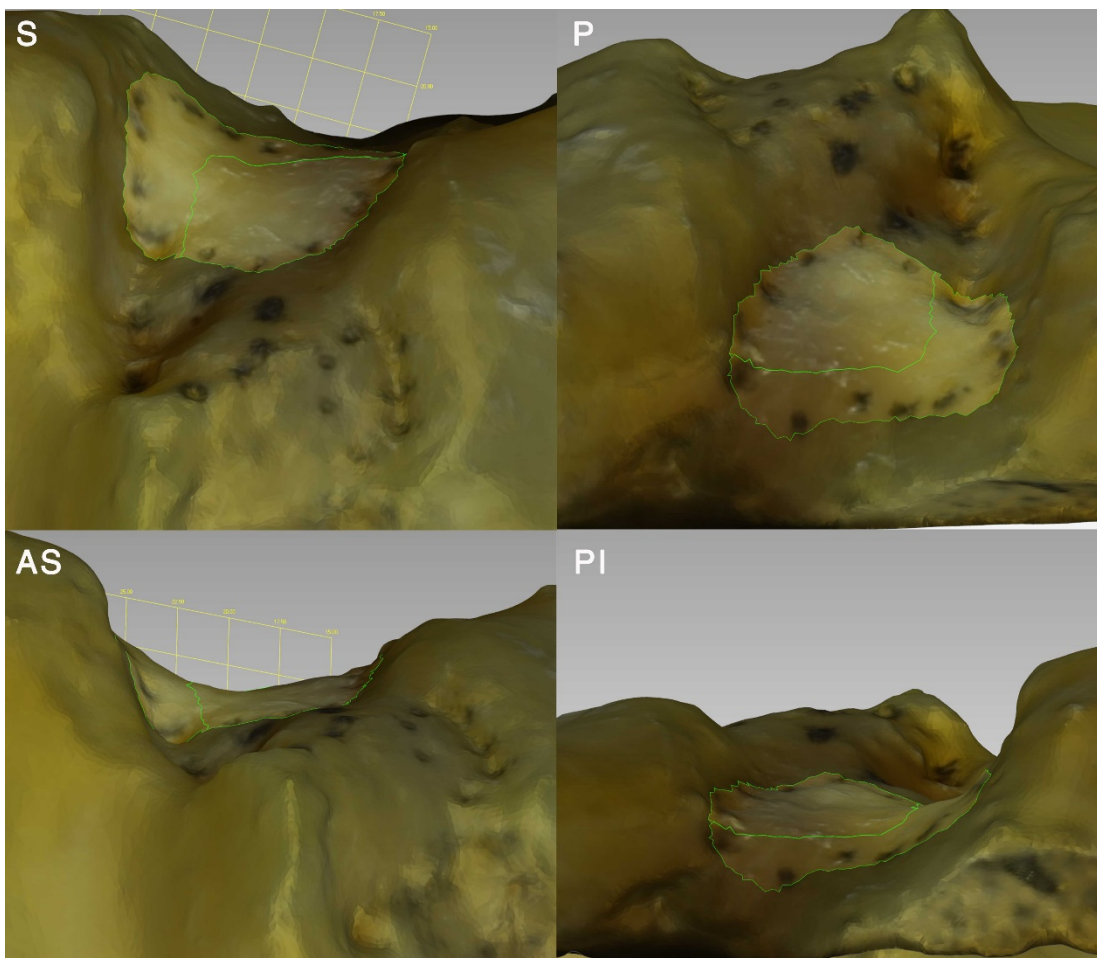


Figure 360. 3D model of tibia G. Footprint of PCL bundles selected and highlighted.

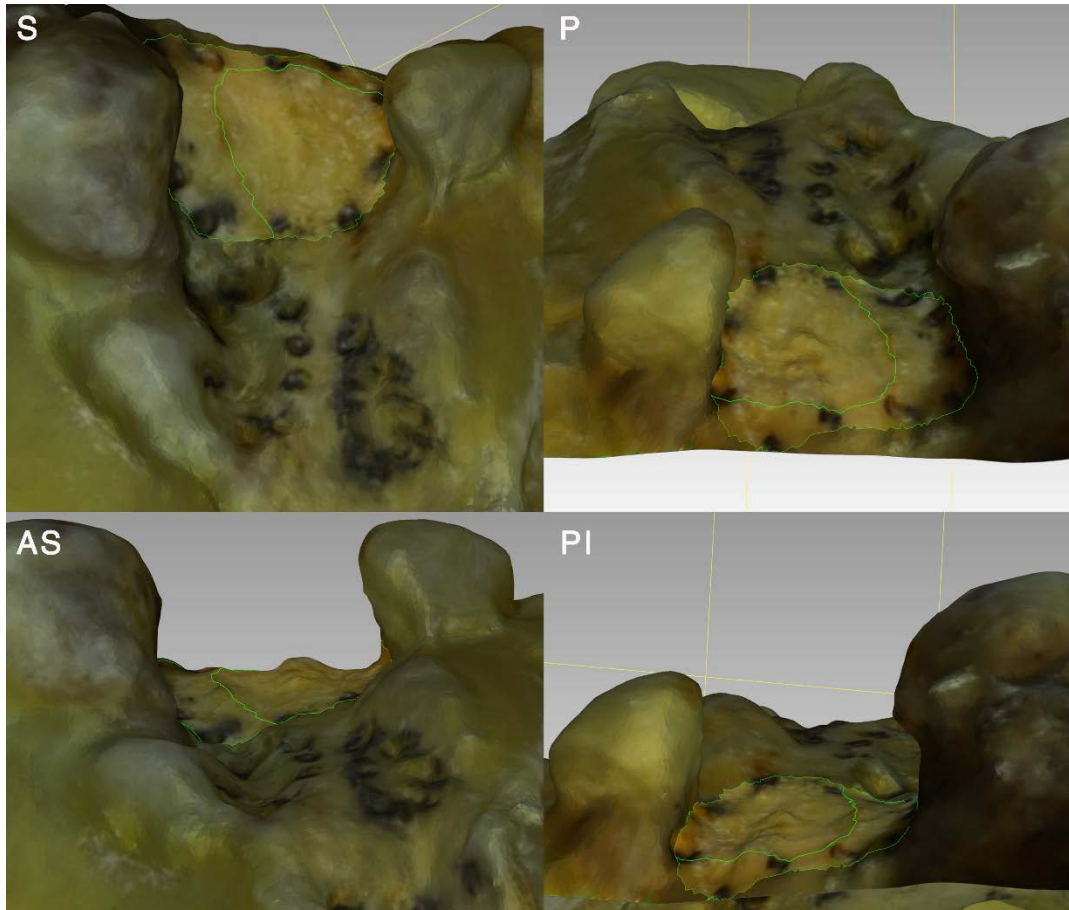


Figure 361. 3D model of tibia H. Footprint of PCL bundles selected and highlighted.

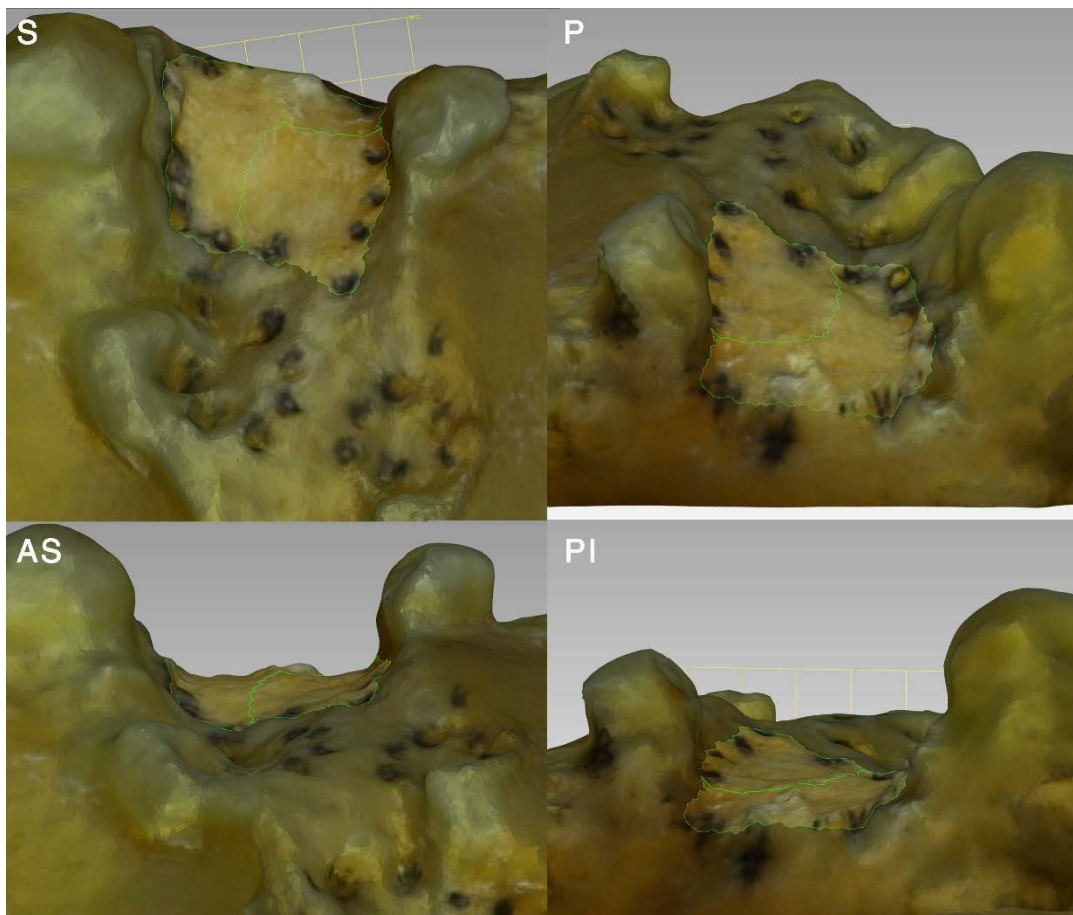


Figure 362. 3D model of tibia I. Footprint of PCL bundles selected and highlighted.

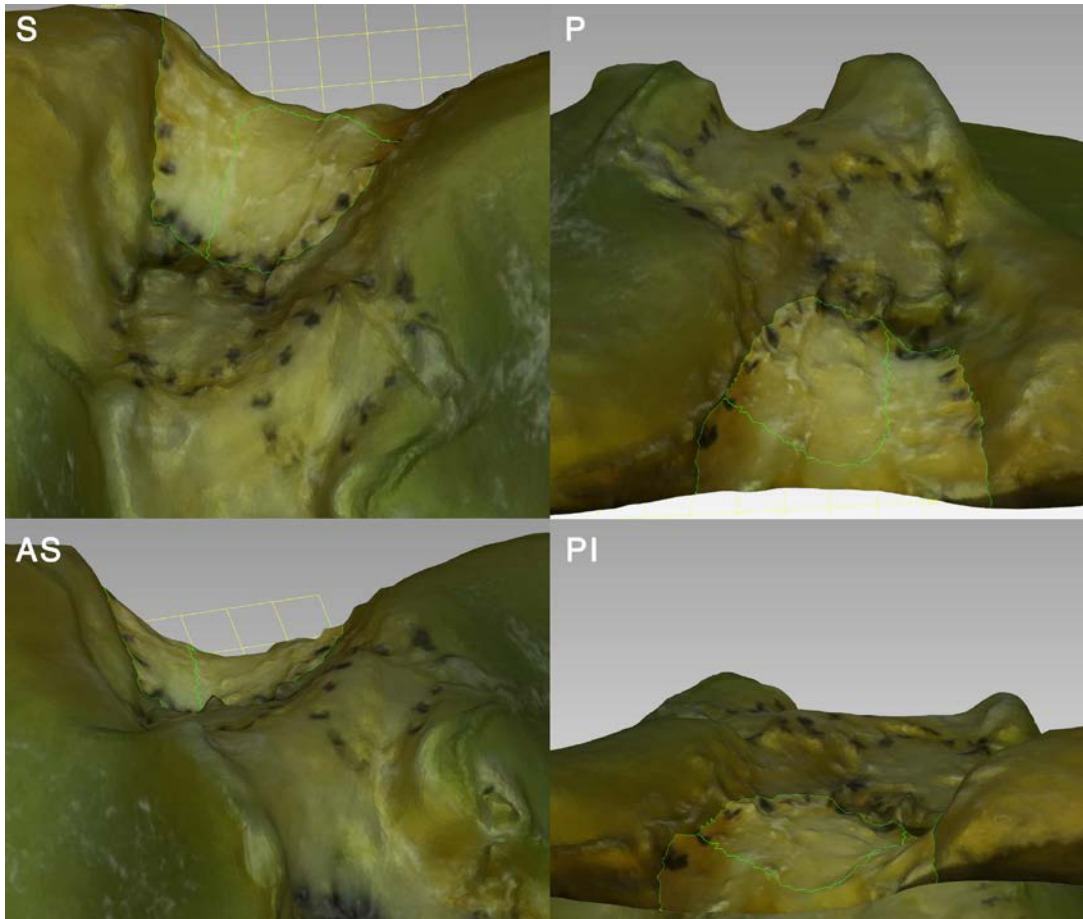


Figure 363. 3D model of tibia L. Footprint of PCL bundles selected and highlighted.

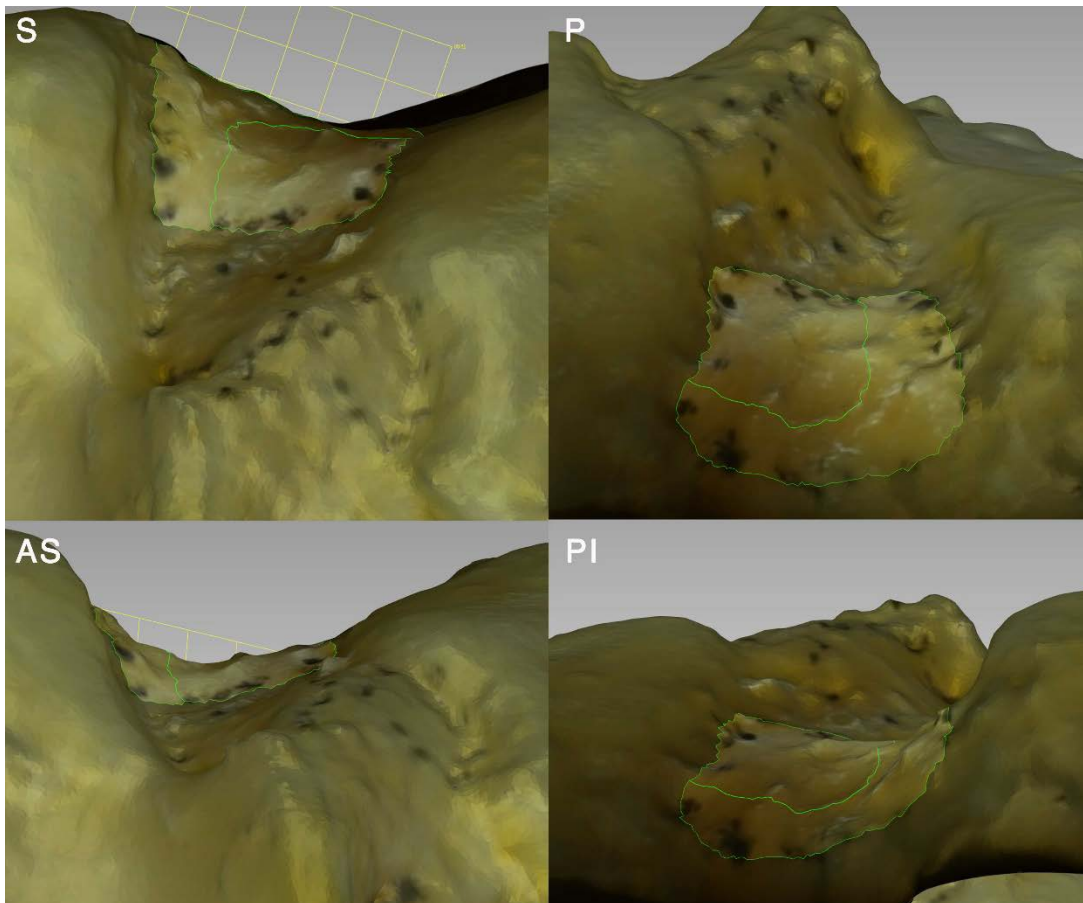


Figure 364. 3D model of tibia M. Footprint of PCL bundles selected and highlighted.

IV.10.2.2. Distances from PCL footprint center to anatomic landmarks

The PCL attachment center was measured in reference to arthroscopically identifiable landmarks, being lateral to the secondary central PMIR process, C1_b (selected in a straight mediolateral line) and ICT sagittal line center (in anteroposterior and mediolateral directions); medial to the secondary central PLIR process, E1_b (selected in a straight mediolateral line); posterolateral to the PM fossa and PL corner of the PRMM; posteromedial to the posterolateral wall's (14b) inferior border, and to the PM corner of the PRLM; anterolateral to the posterior geniculum (P); anteromedial to the anterior border of the CGD.

The center of the PCL attachment was 2.8 mm (range, 1.6 – 4 mm) from the posterior geniculum, with a significant correlation with ML width ($r=0.901$, $p=0.002$) and AP depth ($r=0.851$, $p=0.007$), CV 33.68%, representing 3.7% of the ML width, and 5.3% of the AP depth. The anteriormost border of the PCL was 2.7 mm from its center, with slightly worse p-values for ML width and AP depth correlation, but with a better CV at 25.04% (PBR has a value beyond the 75 percentile). See Table 27 and Table 28 for all distances obtained from the center of the PCL attachment to selected anatomic landmarks.

*Table 27. Distances from the center of the PCL footprint to the selected points, in mm, on the surface, with 95% confidence interval (CI) and coefficient of variation (CV). Pearson correlation with AP depth (AP), and significance (AP p), and ML width (ML) and significance (ML p). * Correlation is significant at the 0.05 level (2-tailed). ** Correlation is significant at the 0.01 level (2-tailed). P: posterior geniculum.*

PCL	MM	95% CI	CV	AP	AP P	ML	ML P
PMIR	9.4	8.5 – 10.3	11.76	0.563	0.146	0.824*	0.012
PLIR	8.6	7.3 – 9.9	18.10	0.529	0.177	0.601	0.115
PMF	8.4	6.8 – 10.0	22.36	0.847**	0.008	0.796*	0.018
PLW	8.6	7.1 – 10.0	20.19	0.703	0.052	0.770*	0.025
A PCL	2.7	2.1 – 3.3	25.04	0.710*	0.049	0.724*	0.042
P	2.8	2.0 – 3.6	33.68	0.851**	0.007	0.901**	0.002
CGD	7.2	6.6 – 7.7	9.05	0.547	0.161	0.159	0.707
PM PRLM	12.9	11.3 – 14.5	14.99	0.420	0.300	0.677	0.065
PL PRMM	8.5	7.0 – 9.9	20.29	0.681	0.063	0.643	0.086

* Correlation is significant at the 0.05 level (2-tailed).

** Correlation is significant at the 0.01 level (2-tailed).

NOTE. P: posterior geniculum.

Table 28. Distances from the PCL center to the selected points, on the surface: range, percentage of the AP depth (AP%) and ML width (ML%), and their 95% confidence interval (CI).

PCL	Range mm	%AP	95% CI	%ML	95% CI
PMIR	7.7 – 11.0	17.5	16 – 19.1	12.4	11.6 – 13.2
PLIR	6.6 – 10.5	16.0	13.8 – 18.3	11.3	9.8 – 12.8
PMF	5.8 – 11.4	15.6	13 – 18.2	11.0	9.4 – 12.7
PLW	5.8 – 10.9	15.9	13.5 – 18.4	11.3	9.7 – 12.8
A PCL	1.4 – 3.6	5.0	4 – 6	3.5	2.9 – 4.2
P	1.6 – 4.0	5.3	3.9 – 6.6	3.7	2.8 – 4.6
CGD	6.5 – 8.2	13.4	12.5 – 14.3	9.5	8.7 – 10.3
PM PRLM	10.7 – 16.4	23.9	21.2 – 26.7	16.9	15.3 – 18.6
PL PRMM	5.7 – 11.6	15.7	13.3 – 18.1	11.1	9.5 – 12.7

NOTE. P: posterior geniculum.

IV.10.2.3. PCL bundles

IV.10.2.3.1. Qualitative and quantitative description

Qualitatively, the geniculate ridge was found to mark the division between PCL bundles, with an anterolateral bundle footprint located in the PIS (13a), and the posterolateral bundle attached to the posteromedial groove (13b) and the posterior rim (13c).

For comparison purposes, area 13 was divided by the geniculate ridge into an anterolateral (**13_{AL}**) and a posteromedial (**13_{PM}**) aspect. Both areas were selected to compare them to the actual attachment areas of their corresponding bundles.

The PCL AL bundle attachment area had 64.9 mm² (95% CI, 51.3 – 78.5 mm²; range, 37.8 mm² to 106.1 mm²), and it covered 85.5% of area 13_{AL} (95% CI 73.6 – 97.4%; range, 61% to 107%). The PCL PM bundle attachment area had 74.8 mm² (95% CI 59.2 – 90.5 mm²; range, 45.8 mm² to 104.1 mm²), covering 61% of area 13_{PM} (95% CI 52.7 – 69.4%; range, 47% to 80%).

IV.10.2.3.2. Distances from PCL anterolateral and posteromedial bundles

The footprint center of both PCL bundles were measured in reference to the same arthroscopically identifiable landmarks as the PCL footprint center, and the results obtained are shown in Table 29 and Table 30 for the AL bundle, and in Table 31 and Table 32 for the PM bundle.

Table 29. Distances from the center of the AL bundle of the PCL to the selected points, in mm, on the surface, with 95% confidence interval (CI) and coefficient of variation (CV). Pearson correlation with AP depth (AP), and significance (AP p), and ML width (ML) and significance (ML p).

PCL-AL	MM	95% CI	CV	AP	AP P	ML	ML P
PMIR	10.0	8.5 – 11.5	20.83	-0.007	0.985	-0.236	0.512
PLIR	7.5	4.6 – 10.3	52.94	0.246	0.494	0.608	0.062
PMF	8.3	7.1 – 9.4	19.93	0.443	0.200	0.705*	0.023
PLW	5.9	4.8 – 7.0	26.19	0.648*	0.043	0.818**	0.004
A PCL	5.3	4.6 – 6.0	14.90	0.760*	0.029	0.887**	0.003
P	3.9	3.5 – 4.3	13.21	-0.198	0.584	0.195	0.589
CGD	7.8	6.8 – 8.8	15.85	0.037	0.930	-0.022	0.959
PM PRLM	10.0	8.4 – 11.6	22.35	0.776**	0.008	0.855**	0.002
PL PRMM	7.7	6.6 – 8.9	20.50	0.284	0.426	0.409	0.240
PCL-PM	5.5	4.4 – 6.5	25.48	-0.551	0.124	0.027	0.945

* Correlation is significant at the 0.05 level (2-tailed).

** Correlation is significant at the 0.01 level (2-tailed).

NOTE. P: posterior geniculum.

Table 30. Distances from the center of the AL bundle of the PCL to the selected points, on the surface: range, percentage of the AP depth (AP%) and ML width (ML%), and their 95% confidence interval (CI).

PCL-AL	Range mm	%AP	95% CI	%ML	95% CI
PMIR	4.6 – 12.3	19.4	16.3 – 22.5	13.6	11.5 – 15.7
PLIR	4.0 – 17.5	14.3	9.1 – 19.5	9.9	6.6 – 13.2
PMF	6.9 – 11.4	15.9	13.9 – 17.9	11.1	9.9 – 12.3
PLW	3.8 – 8.4	11.2	9.5 – 12.9	7.8	6.7 – 9
A PCL	4.1 – 6.5	9.9	8.8 – 10.9	7.0	6.4 – 7.6
P	3.2 – 4.7	7.6	6.5 – 8.6	5.3	4.7 – 5.8
CGD	5.8 – 9.3	14.5	12.6 – 16.5	10.3	8.9 – 11.8
PM PRLM	6.2 – 14.0	19.0	16.8 – 21.4	13.3	11.7 – 14.9
PL PRMM	5.4 – 10.3	14.9	12.8 – 17	10.4	9 – 11.8
PCL-PM	3.9 – 8.7	10.4	8 – 12.8	7.3	5.8 – 8.8

NOTE. P: posterior geniculum.

Table 31. Distances from the center of the PM bundle of the PCL to the selected points, in mm, on the surface, with 95% confidence interval (CI) and coefficient of variation (CV). Pearson correlation with AP depth (AP), and significance (AP p), and ML width (ML) and significance (ML p).

PCL-PM	MM	95% CI	CV	AP	AP P	ML	ML P
PMIR	8.7	7.7 – 9.8	14.13	0.472	0.238	0.675	0.066
PLIR	10.8	9.3 – 12.4	17.38	0.593	0.122	0.717*	0.045
PMF	9.0	7.4 – 10.6	21.68	0.791*	0.019	0.703	0.052
PLW	9.6	6.8 – 12.4	35.06	0.756*	0.030	0.779*	0.023
A PCL	1.3	0.8 – 1.7	42.44	-0.377	0.358	-0.107	0.802
P	3.7	2.5 – 4.9	38.85	0.694	0.056	0.775*	0.024
CGD	7.7	6.7 – 8.6	14.83	0.621	0.100	0.393	0.335
PM PRLM	14.1	11.7 – 16.5	20.45	0.568	0.142	0.736*	0.037
PL PRMM	10.5	8.4 – 12.6	23.64	0.208	0.621	0.164	0.697

* Correlation is significant at the 0.05 level (2-tailed).

** Correlation is significant at the 0.01 level (2-tailed).

NOTE. P: posterior geniculum.

Table 32. Distances from the center of the PM bundle of the PCL to the selected points, on the surface: range, percentage of the AP depth (AP%) and ML width (ML%), and their 95% confidence interval (CI).

PCL-PM	Range mm	%AP	95% CI	%ML	95% CI
PMIR	6.4 – 10.1	16.2	14.5 – 18	11.5	10.4 – 12.6
PLIR	8.5 – 13.7	20.1	17.5 – 22.8	14.2	12.6 – 15.9
PMF	5.7 – 11.7	16.7	14 – 19.4	11.8	10 – 13.6
PLW	2.8 – 13.7	17.8	12.8 – 22.8	12.5	9.2 – 15.9
A PCL	0.5 – 2.0	2.4	1.5 – 3.3	1.7	1.1 – 2.3
P	1.4 – 5.6	6.8	4.7 – 8.9	4.8	3.4 – 6.2
CGD	5.1 – 8.7	14.3	12.6 – 15.9	10.1	8.9 – 11.3
PM PRLM	9.4 – 18.8	26.2	22 – 30.4	18.5	15.9 – 21.1
PL PRMM	7.0 – 14.7	19.6	15.7 – 23.5	13.9	11.1 – 16.7

NOTE. P: posterior geniculum.

IV.10.3. Degenerative changes of the posterior facet

In some tibias with degenerative changes, the intercondylar circular triangle showed a more quadrilateral shape, or even a pentagon, because the curves formed by the lateral and medial walls with the posterior wall of the PIA (leading to the anterior peak) took sharper turns, instead of the smoothly curved convergence found in normal specimens.

Area 13 overall horizontality, divided into a binary model of vertical crest-like type vs. more horizontal facet-like type (Fig. 365) showed an association with knee OA that did not reach significance (Fig. 368): $\chi^2(4)=9.403$, $p=0.052$. Frequency distribution analysis showed that a more horizontal area 13 was more commonly seen in the lowest and highest OA grades.

The elevation of the ICT sagittal line (Fig. 366, Fig. 367) showed a weak positive correlation with knee OA that did not reach significance (Fig. 369): $r_s(86)=0.211$, $p=0.051$.

The posterior intercondylar geniculum was qualitatively not found to become markedly elevated over osteophytic ICT lines.

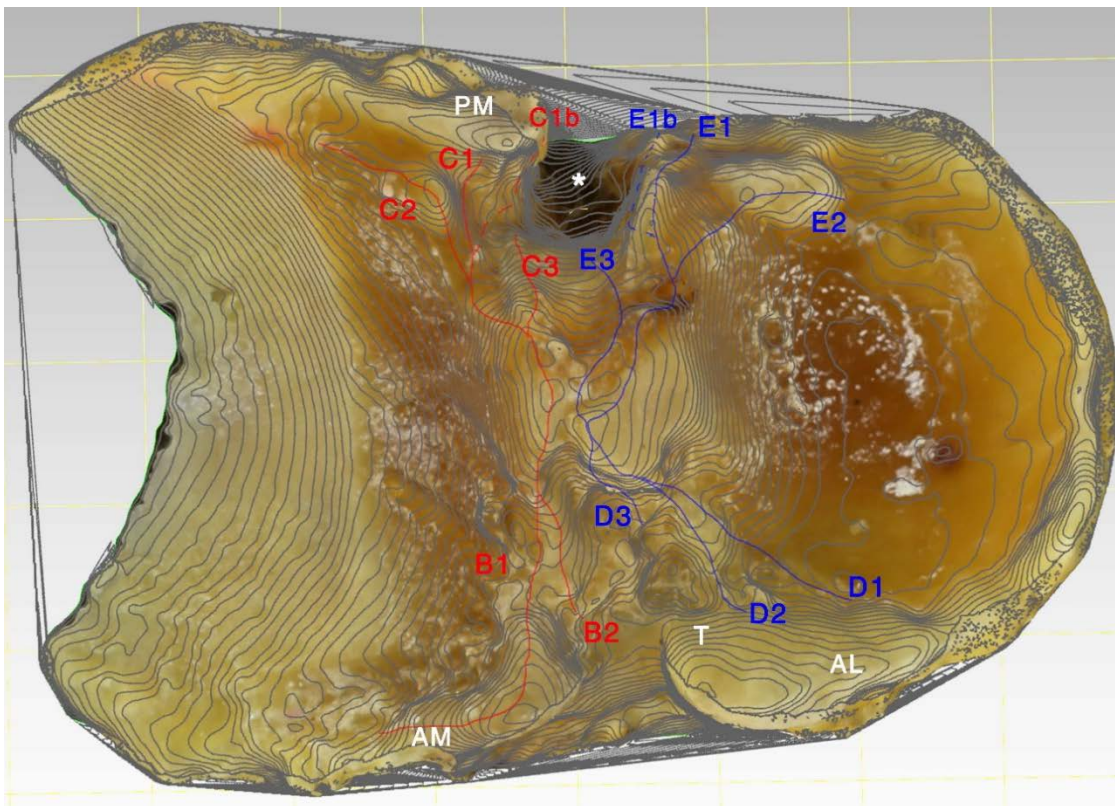


Figure 365. 3D model of tibia 77, with contour lines superimposed. Elevated processes C3 (grade 2) and E3 (grade 3), and elevations of the medial (C1_b) and lateral (E1_b) walls enclosing a more horizontal posterior facet (*), with no elevation of the ICT sagittal line. Also labelled are processes of the AMIR (B1, B2), PMIR (C1, C2), ALIR (D1, D2, D3_a) and PLIR (E1, E2), and elevations of Parson's knob (G), AM, AL, and PM, corners in white. Observe how AL and the saddle elevation (T) form together a common osteophyte covering area 9.

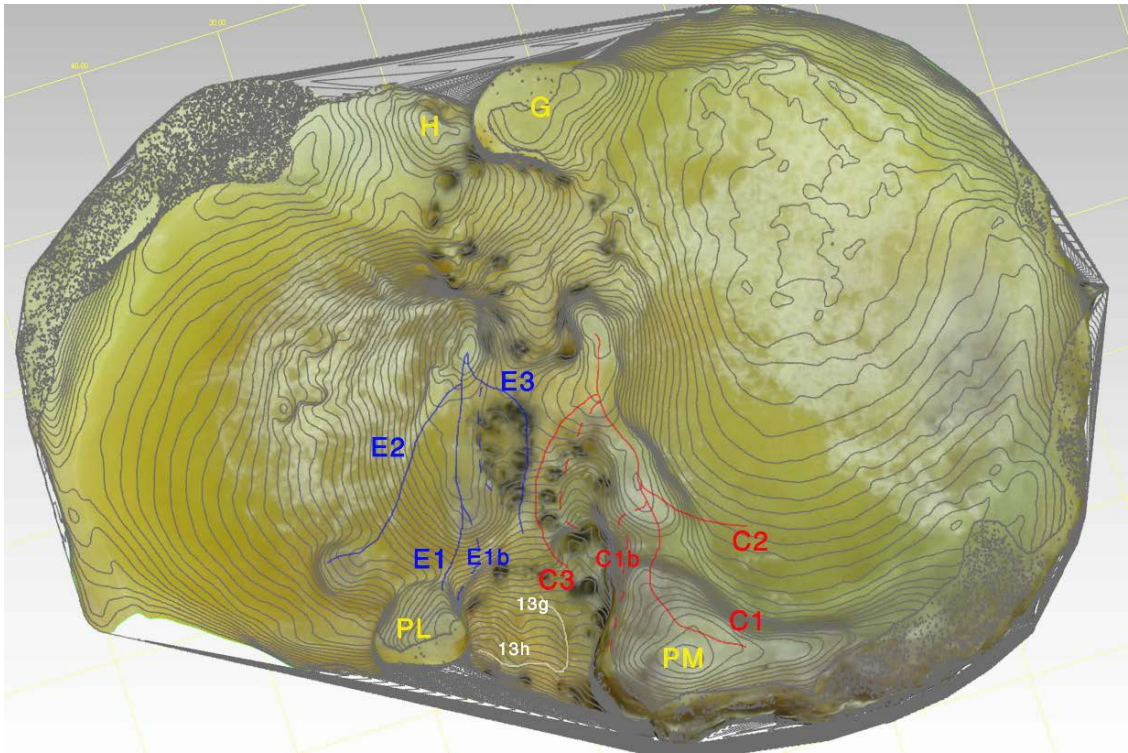


Figure 366. 3D model of tibia H, with contour lines superimposed; posterior view (posterior is at the bottom, medial is on the right side). Observe the more vertical (ridge-like) slope of the facet, and its enclosing by PM (grade 4) and PL (grade 3) corner osteophytes. The ICT line (13g) is not found particularly elevated (grade 1) over the surrounding areas. Notice also the ridge formed by C3 and E3 (grade 3) dividing the posterior wall in its two main faces (14b, 11), instead of the common incisure where both faces converge in normal tibias. Also labelled are the Parsons' knob (G), ACIK (H), and processes of the PMIR (C1, C1b, C2) and PLIR (E1, E1b, E2), as well as the ICT coronal line (10h).

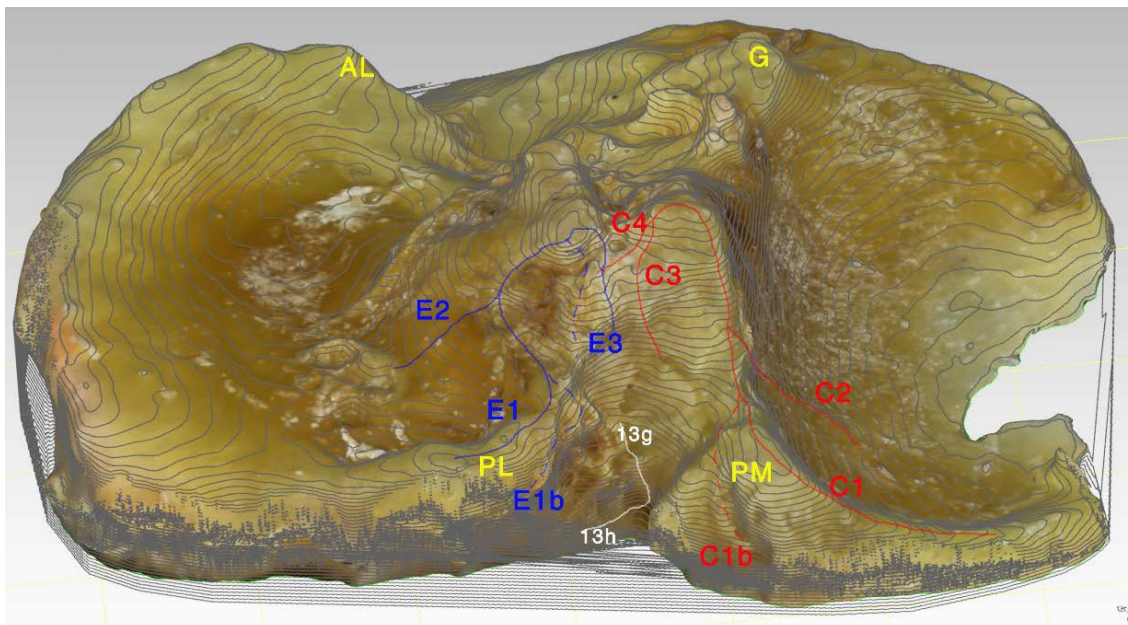


Figure 367. 3D model of tibia 42, with contour lines superimposed (left-mirrored); posterior view (posterior is at the bottom, medial is on the right side). Elevated ICT sagittal line (13g, osteophyte grade 2) and vertical (i.e. ridge-like) area 13. Notice also elevated ICT coronal line (13h), lateral growth of PM corner osteophyte (enclosing area 13 from the medial wall, C1b), medial growth of PL corner osteophyte (enclosing area 13 from the lateral wall, E1b), and elevated E3 process (grade 3). Also labelled are the Parsons' knob (G), processes of the PMIR (C1, C2, C3, C4) and PLIR (E1, E2), as well as AL corner elevation.

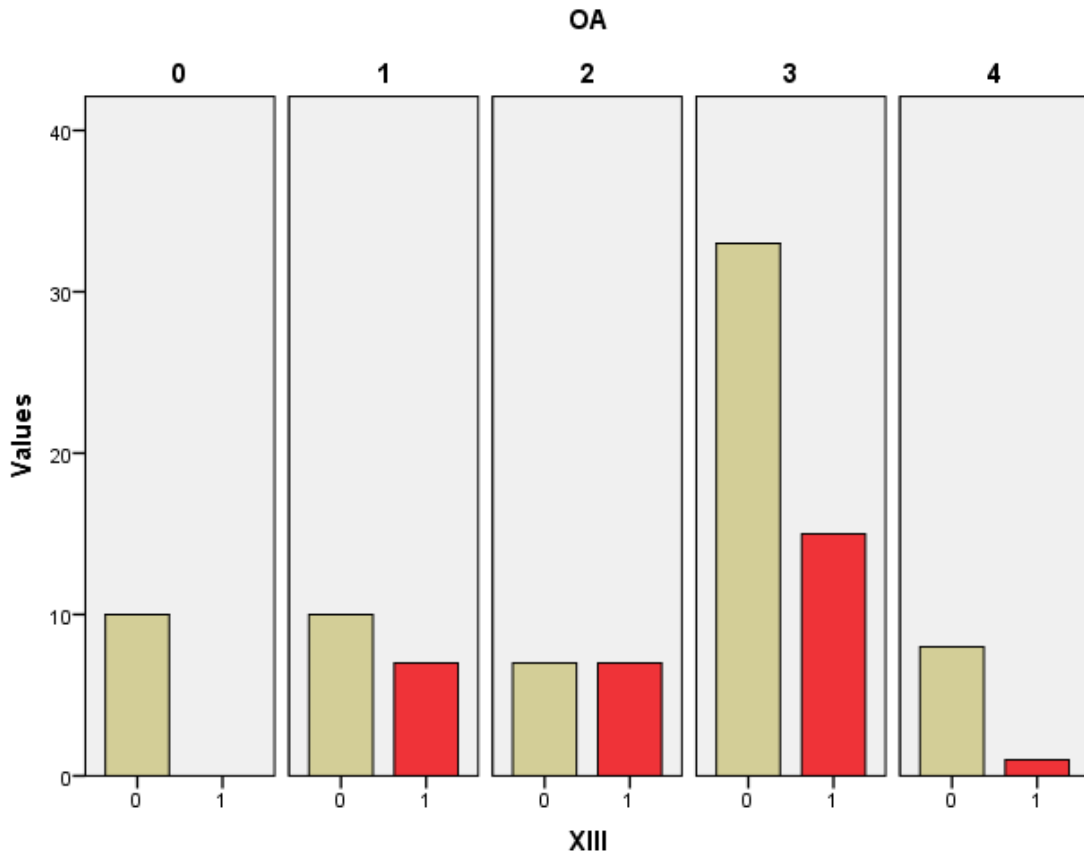


Figure 368. Study II. Histogram of area 13 (XIII) classification: number of tibias in each category, grouped by Ahlbäck OA grade. 0=facet-like (more horizontal); 1=ridge-like (more vertical)

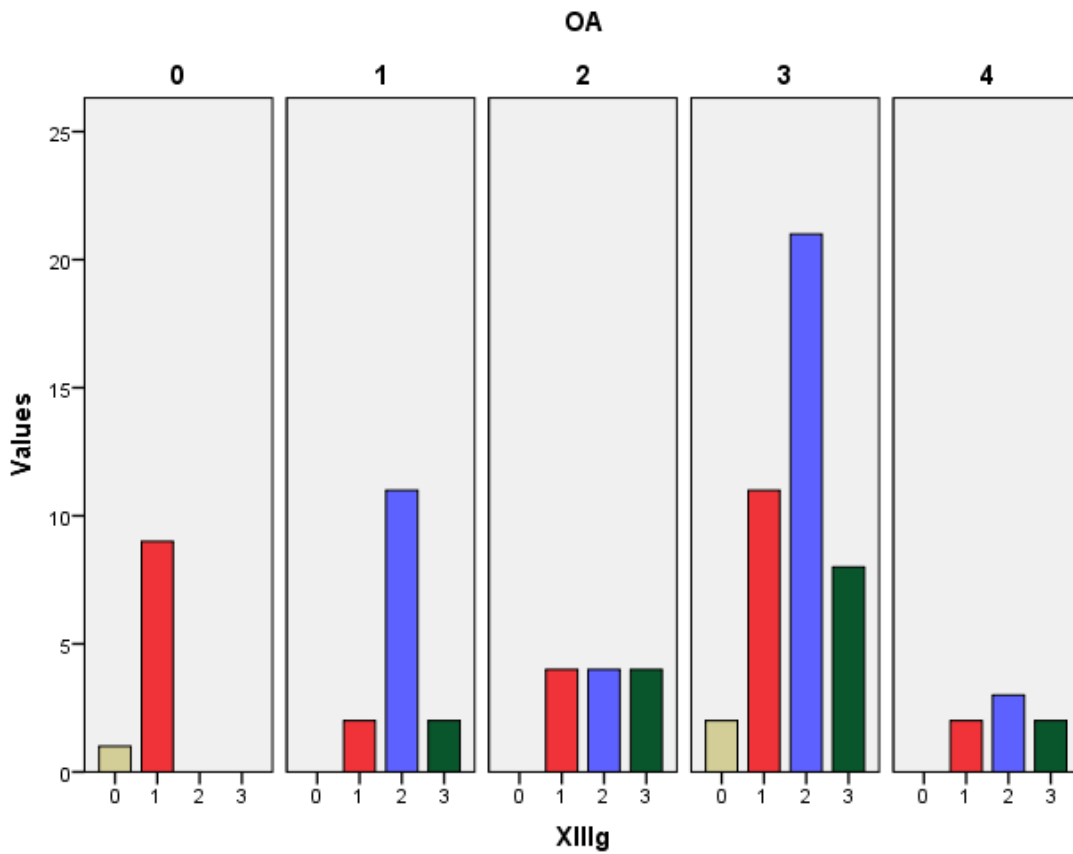


Figure 369. Study II. Histogram of ICT sagittal line (XIIIg) osteophyte grade: number of tibias in each category, grouped by Ahlbäck OA grade.

IV.11. General anatomic overview: imaging and histology studies

IV.11.1. Identification of structures in plain radiography

IV.11.1.1. Inferosuperior (axial) fluoroscopic images

In the inferosuperior radiographs the anterior intercondylar area showed lesser density compared to surrounding areas. That contrasted with the higher density found in the posterior intercondylar area. The main intercondylar tubercles and the intertubercular ridge were usually the densest zones radiographically, especially in pathological tibias (Fig. 370).

Predominant trabeculae in the AIA were concentric, parallel to the anterior border of the tibia in the thinnest specimens (Fig. 371, Fig. 372). Pyrography marks were not visible.

Attachment areas of menisci and ligaments could be observed marked with pyrography and painted with barium sulfate in new radiographs (see Fig. 373, Fig. 374, and Fig. 375).

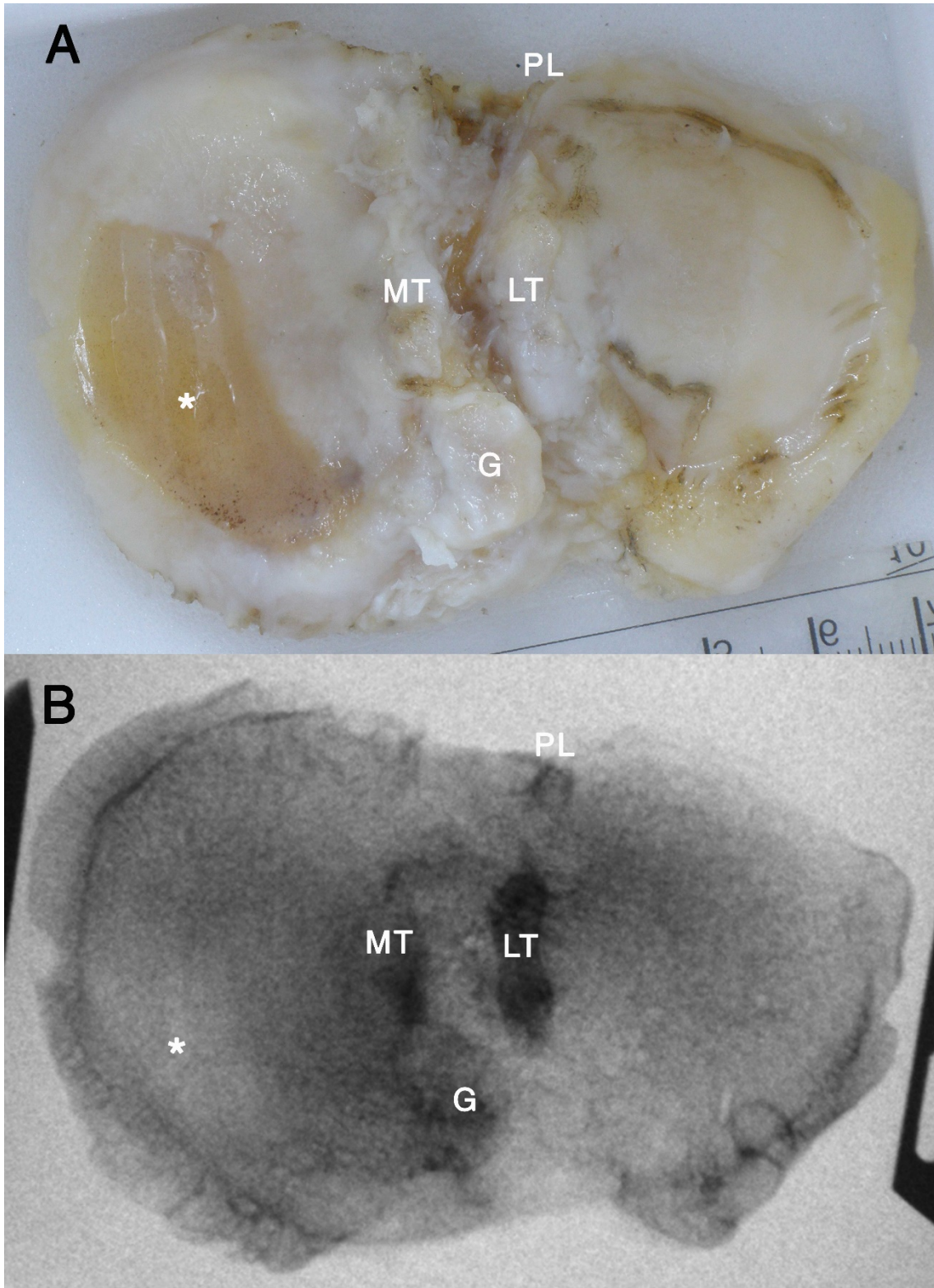


Figure 370. Pathological Tibia E. Superoinferior photograph of specimen (A) and inferosuperior fluoroscopic view (B). Observe the long-type attrition of areas 3-4 (). Note the higher density on the long LT osteophyte, with a lesser density on the MT, Parsons' (G), and PL corner osteophytes.*

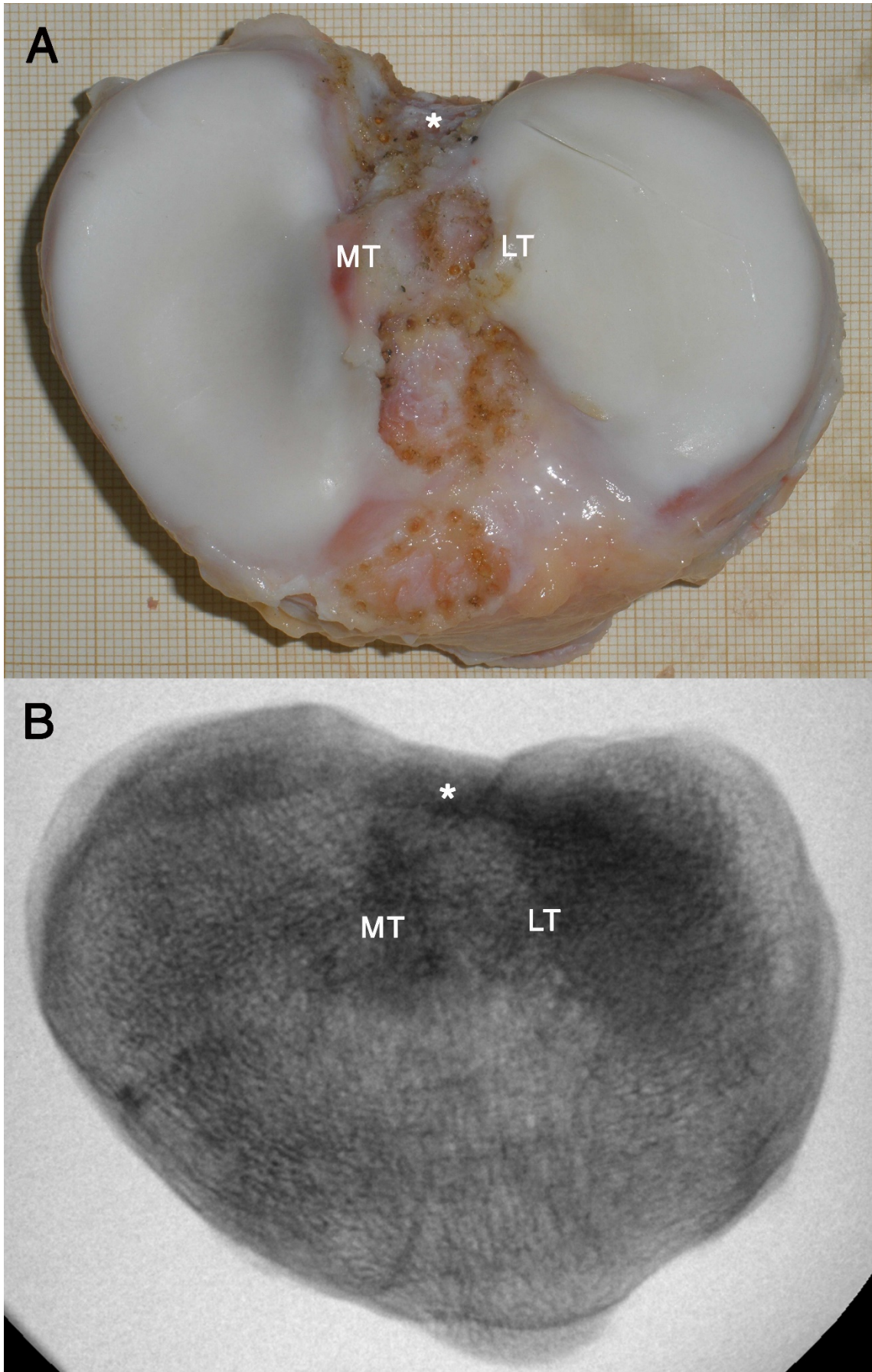


Figure 371. Donor Tibia C. Superoinferior photograph of specimen (A). Inferosuperior fluoroscopic view (B). Observe a higher density on the MT, posterior facet (), and LT tubercle and its external slope.*

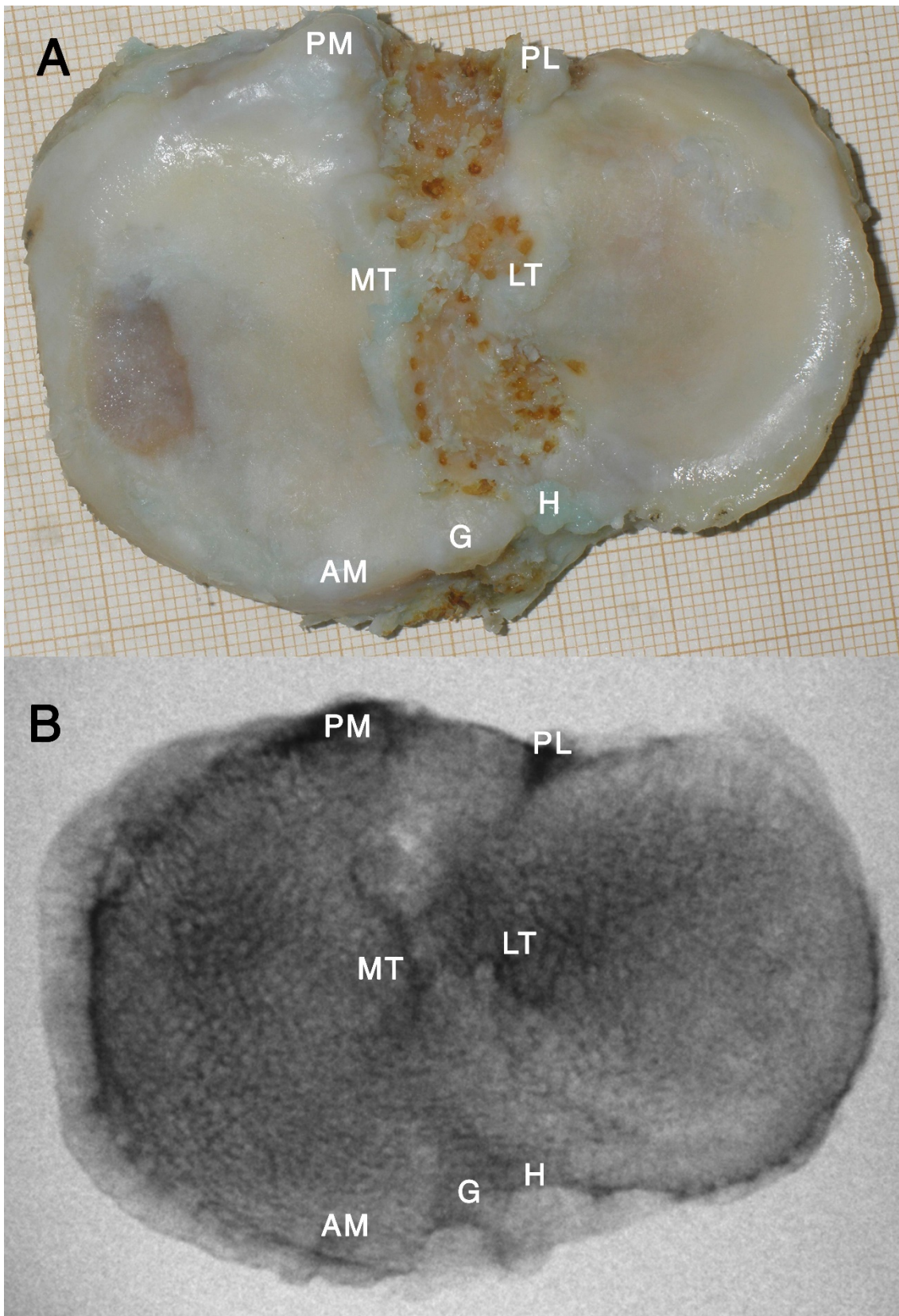


Figure 372. Donor Tibia I. Superoinferior photograph of specimen (A). Inferosuperior radiograph (B). Observe a higher density on posterior corner osteophytes (PM, PL), LT (and its external slope), MT, Parsons' knob (G), ACIK (H), and AM corner.

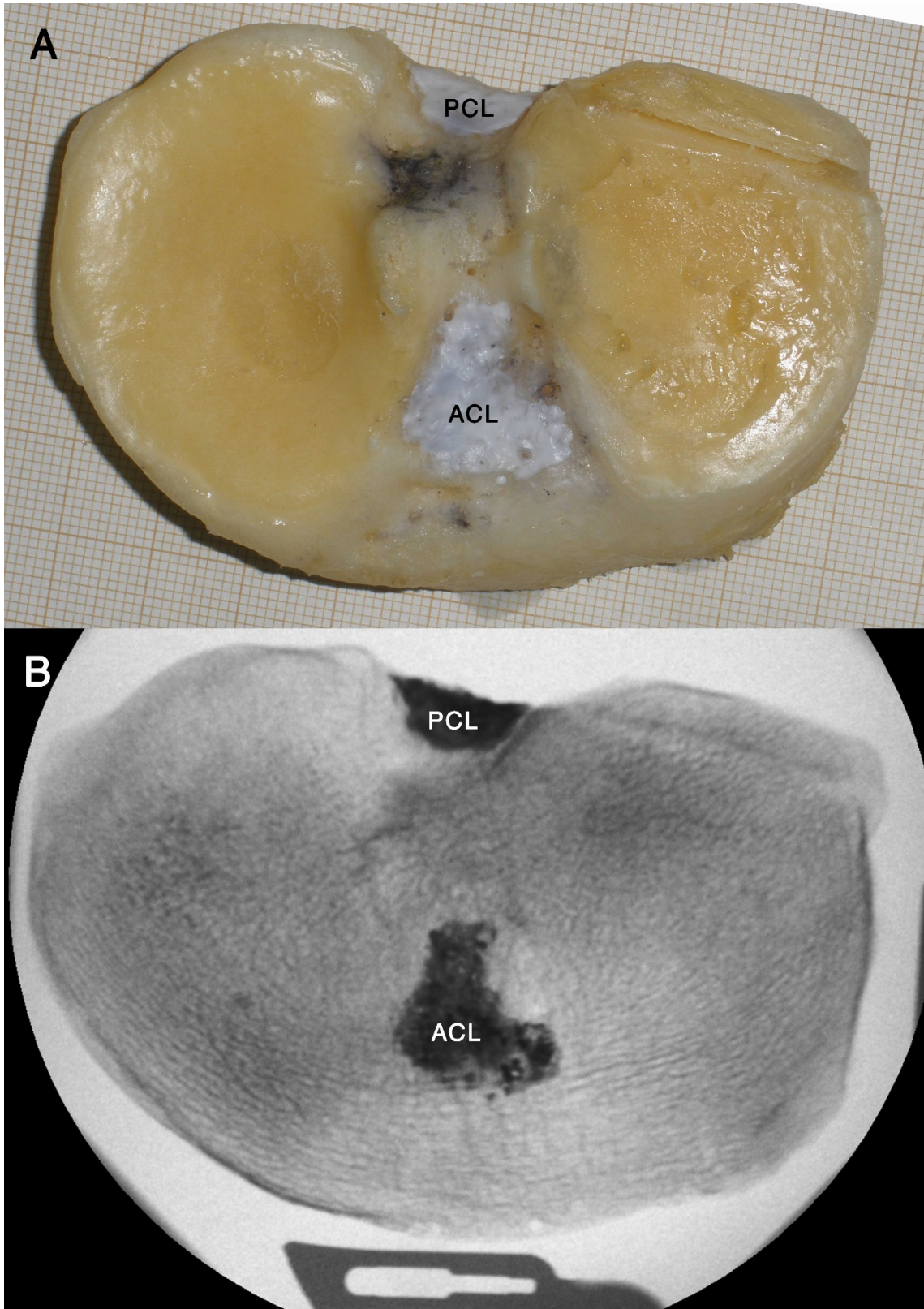


Figure 373. Donor Tibia A. Superoinferior photograph of specimen with ACL and PCL painted with barium sulfate (A). Inferosuperior radiograph (B).

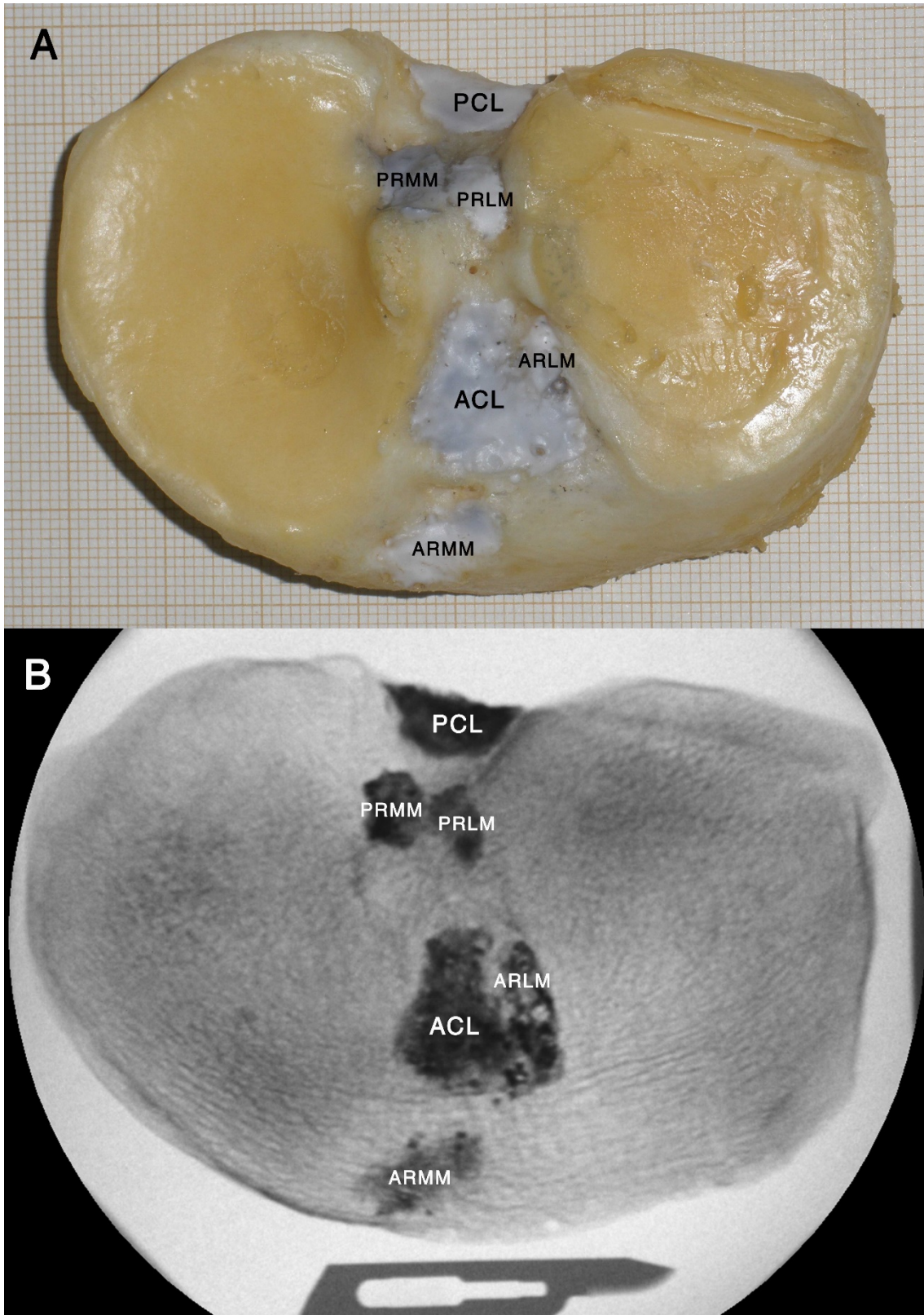


Figure 374. Donor Tibia A. Superoinferior photograph of specimen with attachments of ligaments and menisci painted with barium sulfate (A). Inferosuperior fluoroscopic view (B).

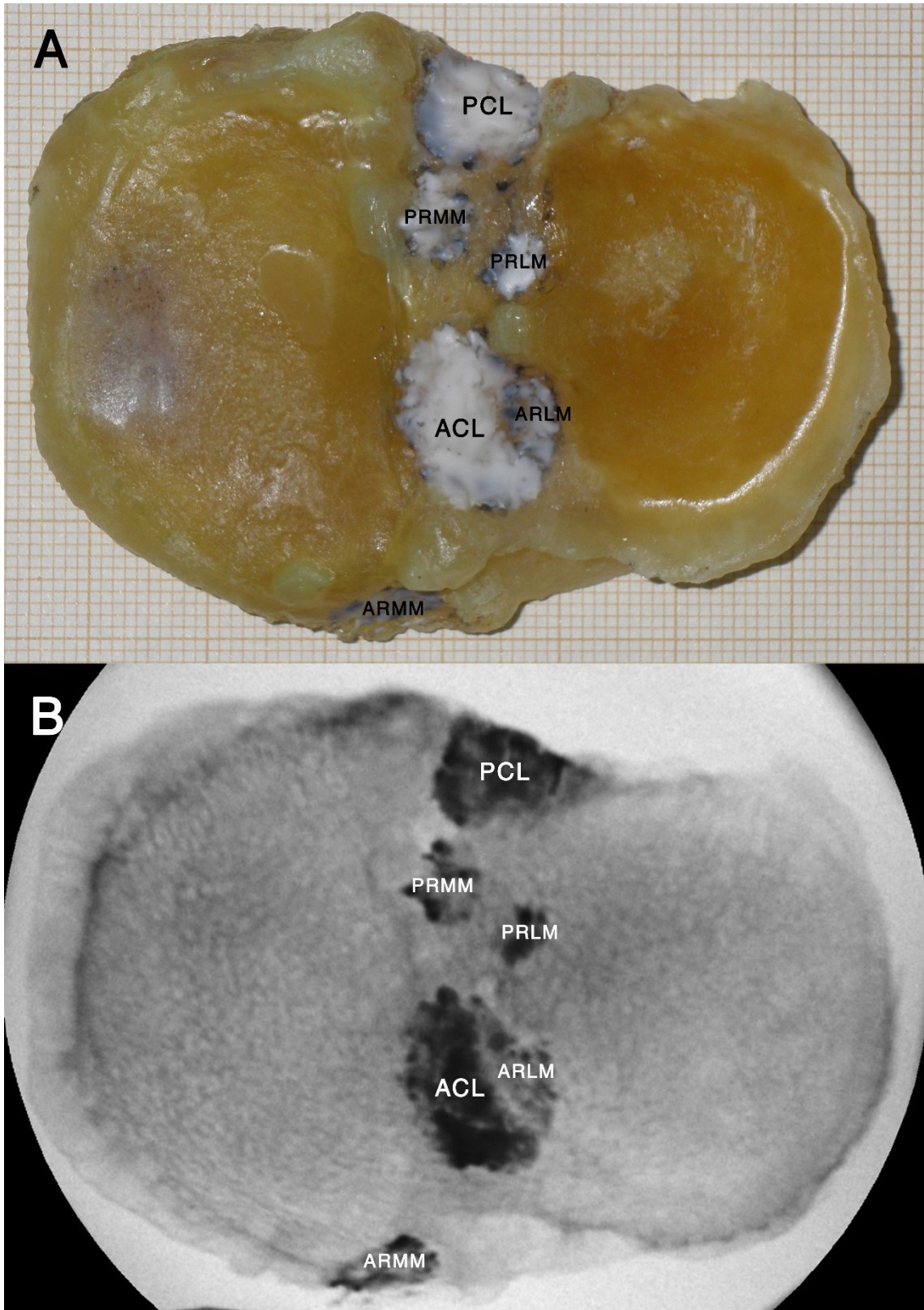


Figure 375. Donor Tibia I with ligamentous and meniscal attachment areas painted with barium sulfate. Superoinferior photograph of specimen (A). Inferosuperior fluoroscopic view (B).

IV.11.1.2. Anteroposterior fluoroscopic images

Tubercle shape was variable depending on the X-ray beam's incident angle. The external slope of the LT was often convex or approached a straight line, while the external slope of the MT was concave. The intertubercular ridge showed a variable height, and there was a common, gentler slope downward from the internal slope of the MT to the internal slope of the LT. See Fig. 376 – Fig. 379.

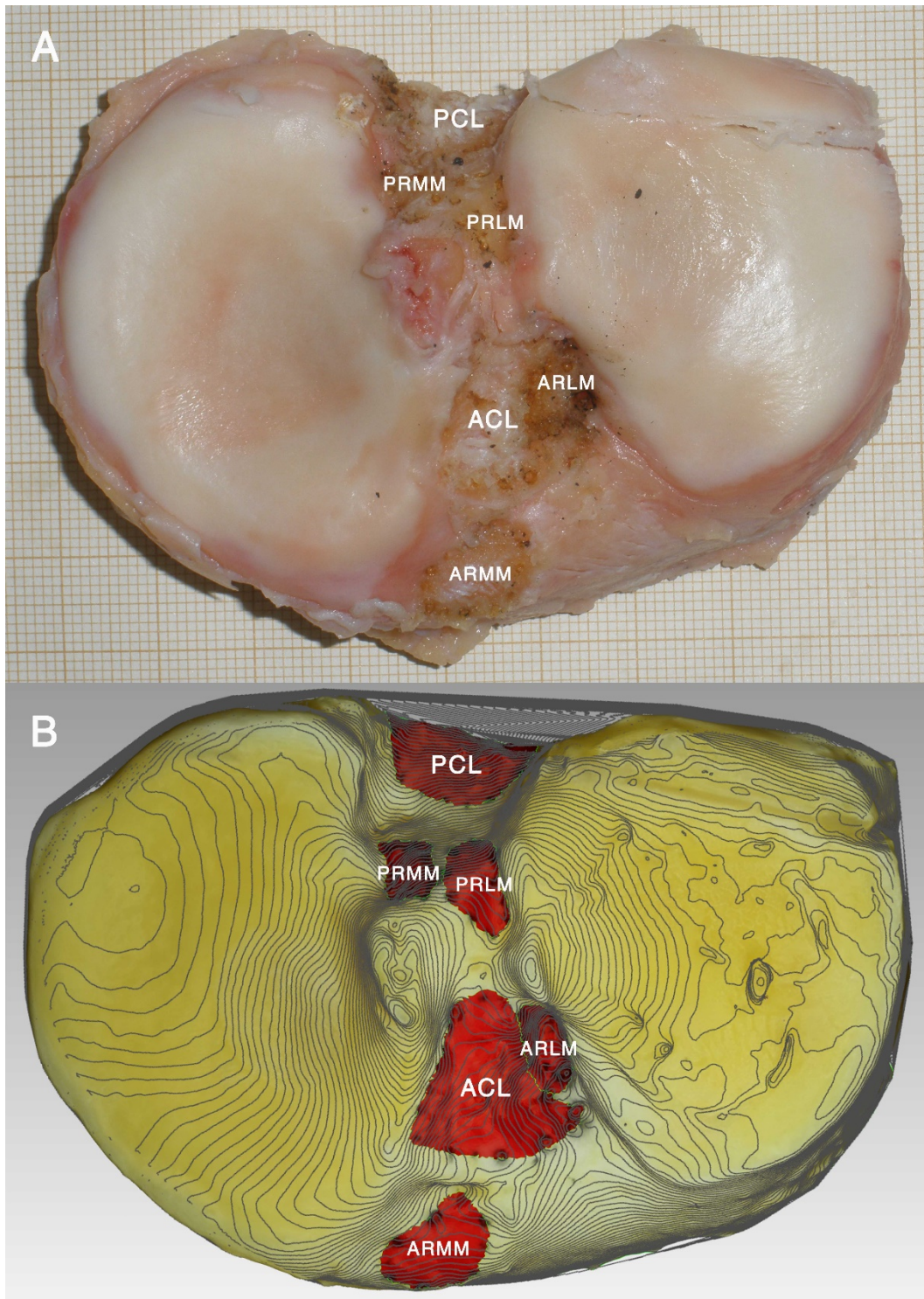


Figure 376. Tibia A. Superoinferior radiograph (A). 3D model, superoinferior view, with attachments selected.

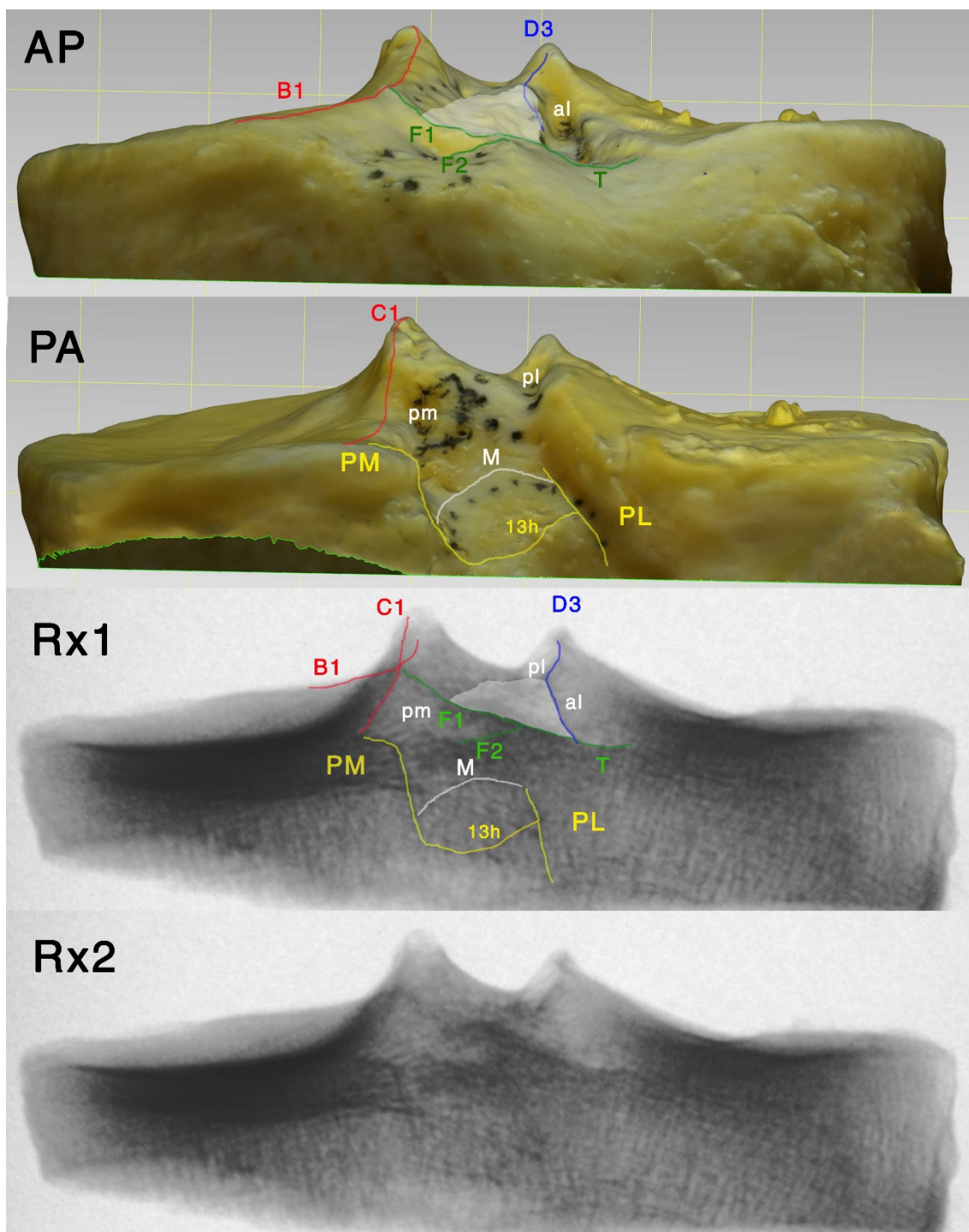


Figure 377. 3D model of tibia A: AP and PA views. Marked are AMIR (B1), PMIR (C1), ALIR (D3), AFIR (F1, F2) processes, anterior saddle (T), tent-shaped ridge (M), and ICT coronal line (13h). Medial aspect of the posterior corner (PM) and inferior aspect of lateral wall of PIA (PL) are also marked. The anterior intercondylar staircase is painted over in white, and visible recesses (with less dense radiographic areas) are labelled in white (al: anterolateral recess; pl: posterolateral recess; pm: posteromedial recess). AP fluoroscopic view with (Rx1) and without (Rx2) corresponding marks over the same recognizable structures. Notice that the processes marked as F1 and T includes the ACIK (H) in the middle, not recognizable in the fluoroscopic view. The more radiographic dense area between F2 and M corresponds probably to the MAIA (fingerprint and anterior AIAR).

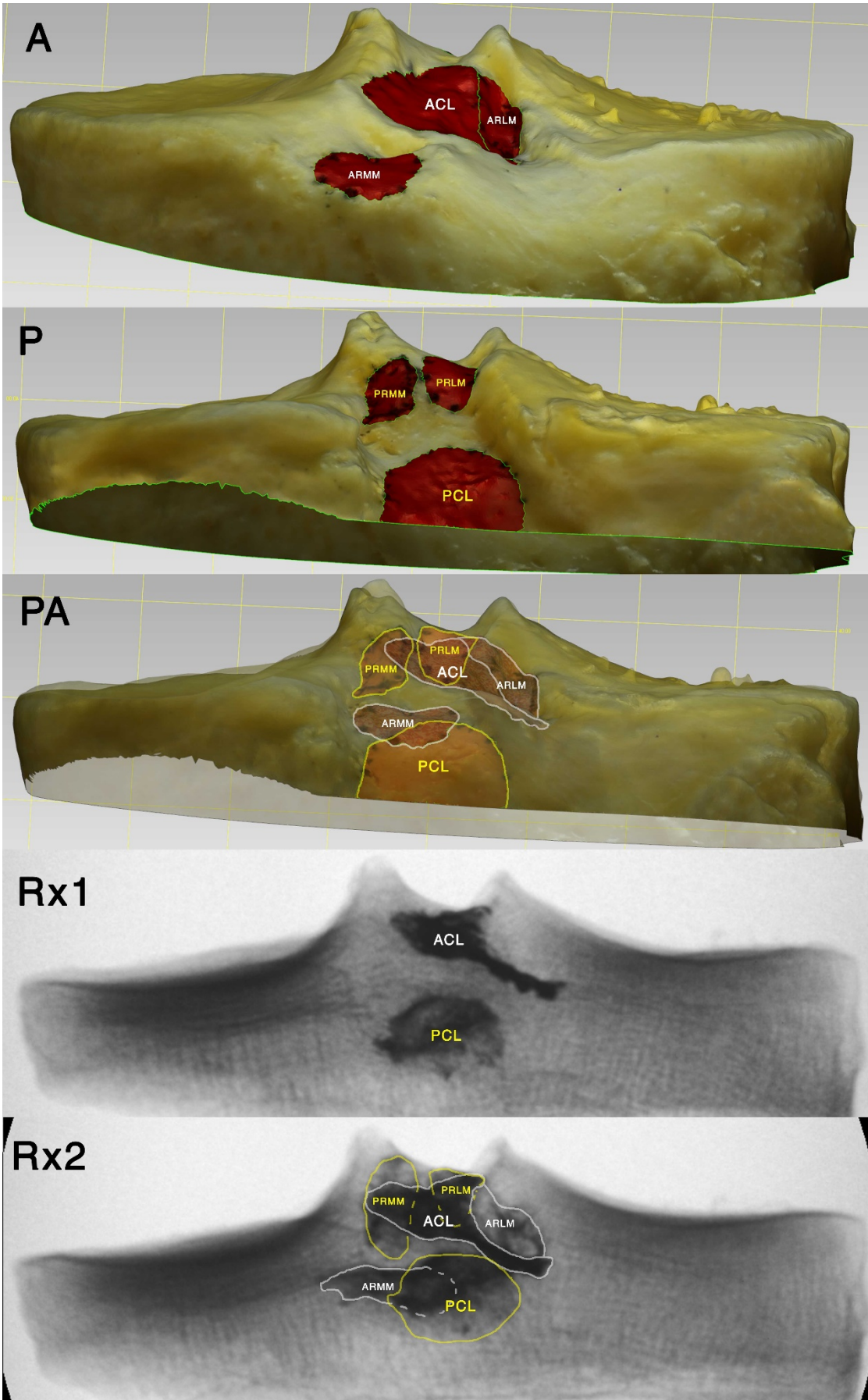


Figure 378. 3D model of tibia A. Anterior (A), posterior (P) and posterior view with posterior aspect transparent (PA). AP fluoroscopic view with ACL and PCL painted with barium sulfate (Rx1). AP fluoroscopic view with all attachments painted (Rx2). Attachment areas labelled and marked (in white, anterior attachments; in yellow, posterior attachments).

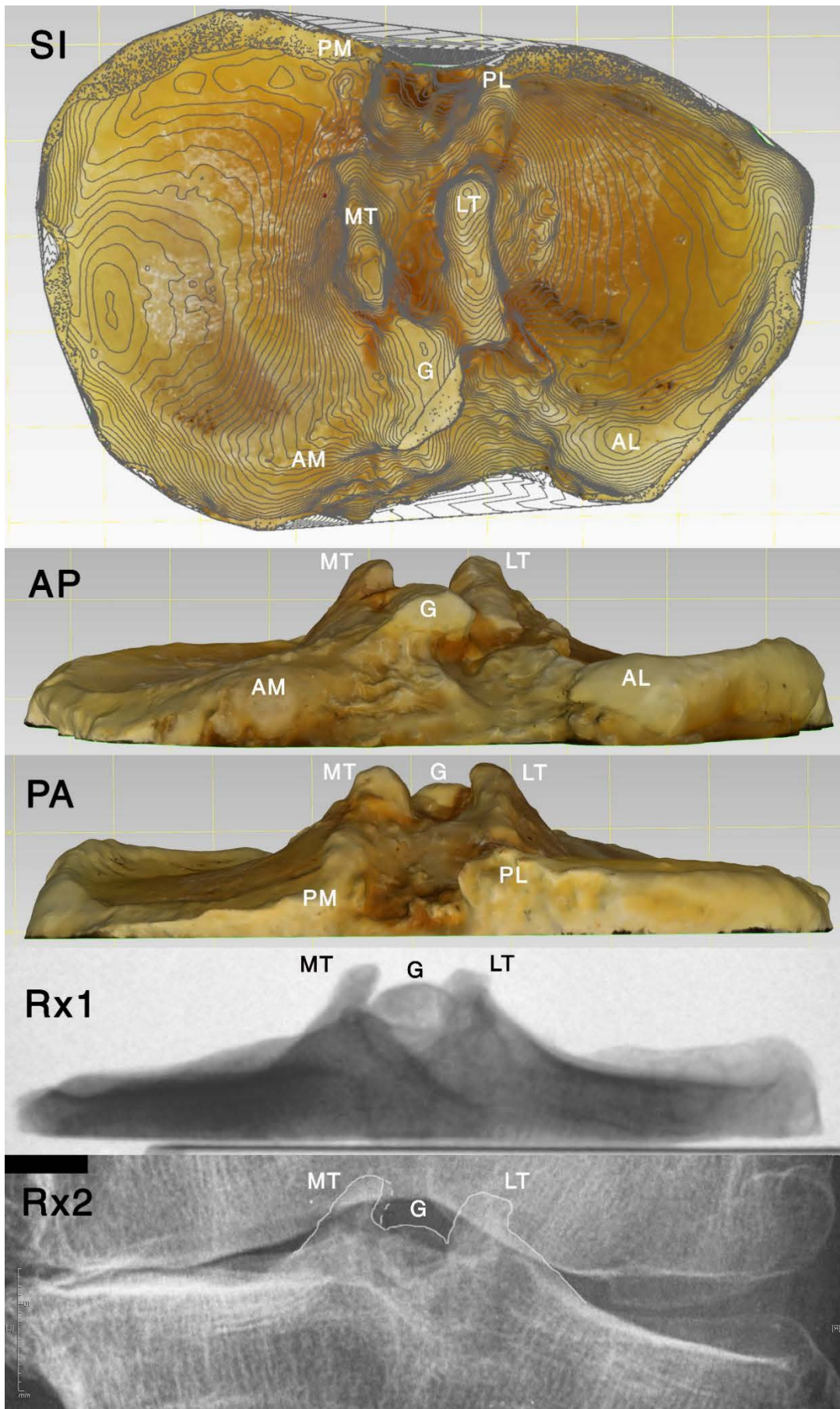


Figure 379. 3D model of pathological tibia E. Superoinferior view (SI). AP view (AP). PA view (PA). PA radiograph of specimen (Rx1). AP standing knee radiograph before TKA surgery (Rx2), with contour of intercondylar tubercles (MT, LT) and Parsons' knob (G) in white. Also labelled are AM, AL, PM, and PL corner elevations

IV.11.1.3. Lateral fluoroscopic images

The main intercondylar tubercles were superimposed on the lateral view, and they were difficult to distinguish in most cases. Metallic marks (metal wires) on their peaks made their identification easier.

The main guides to distinguish them were their anterior and posterior processes in tibias without degenerative changes:

- The medial tubercle showed a high anterior process, AMIR, making its anterior aspect slightly convex. Its posterior process, PMIR, had a steep downward slope, which made its lateral shape concave in non-pathological tibias.
- The lateral tubercle showed a convex posterior aspect, which was formed by its high posterior process, PLIR. Its anterior aspect was almost invariably concave, even in pathological tibias, because the anterior process, ALIR, only rarely developed a deep, high osteophyte that could be confused with the AMIR.

See Fig. 380 – Fig. 382.

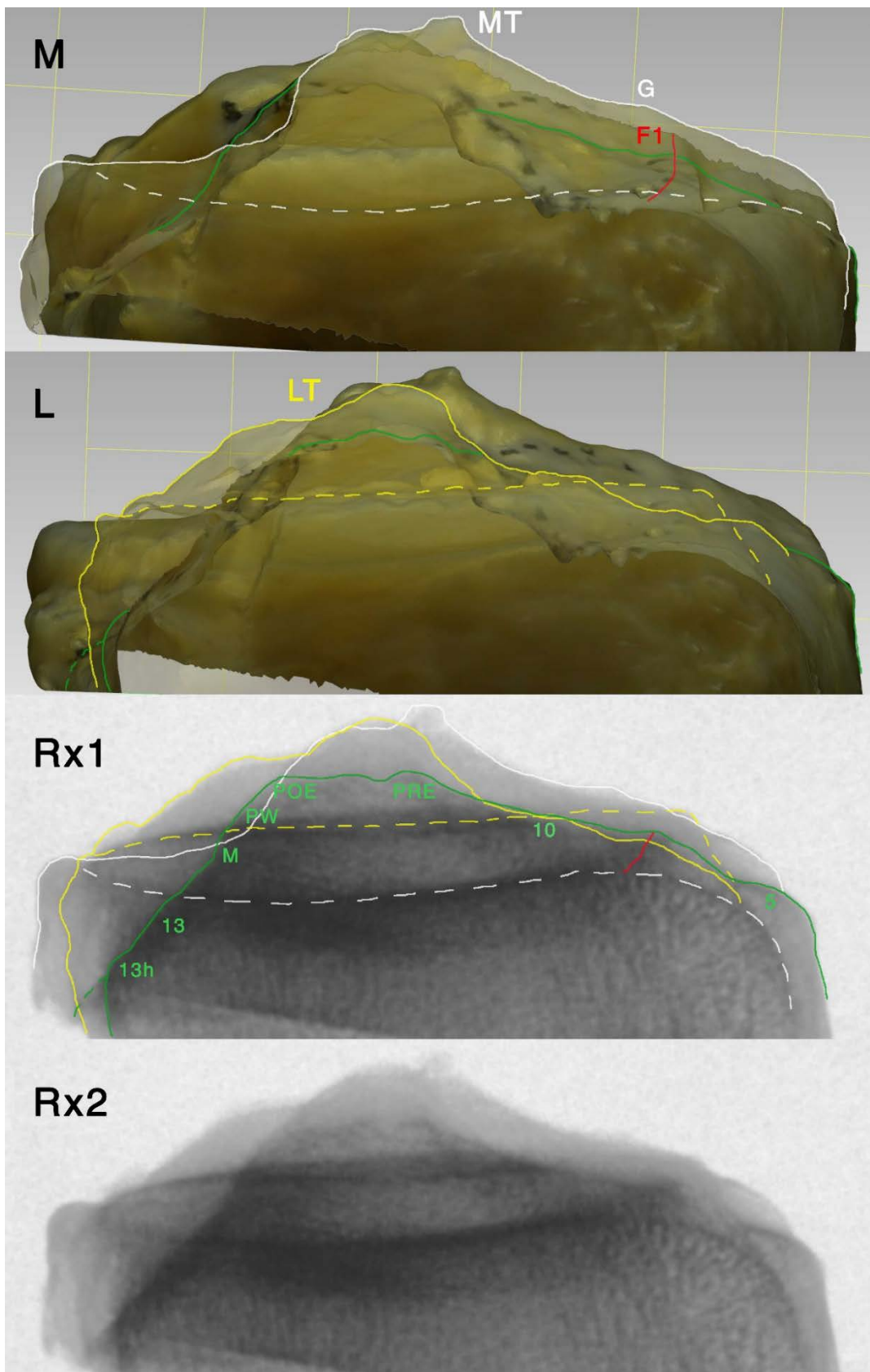


Figure 380. 3D model of tibia A. Medial view with medial side transparent (M), lateral view with lateral side transparent (L). Lateral fluoroscopic view with (Rx1) and without (Rx2) corresponding marks over recognizable structures. White line over MT (AMIR, PMIR), yellow line over LT (ALIR, PLIR). Dashed lines over condyle surfaces (white over medial, yellow over lateral one). Green line over highest (and densest) intercondylar area, including the fingerprint (5), anterior AFIR process (F2), AIS (10, following border between outer and central C-layers), posterior wall (PW) and facet (13), with changes of slope at 13h, POE, PRE. Red line over posterior AFIR process (F1).

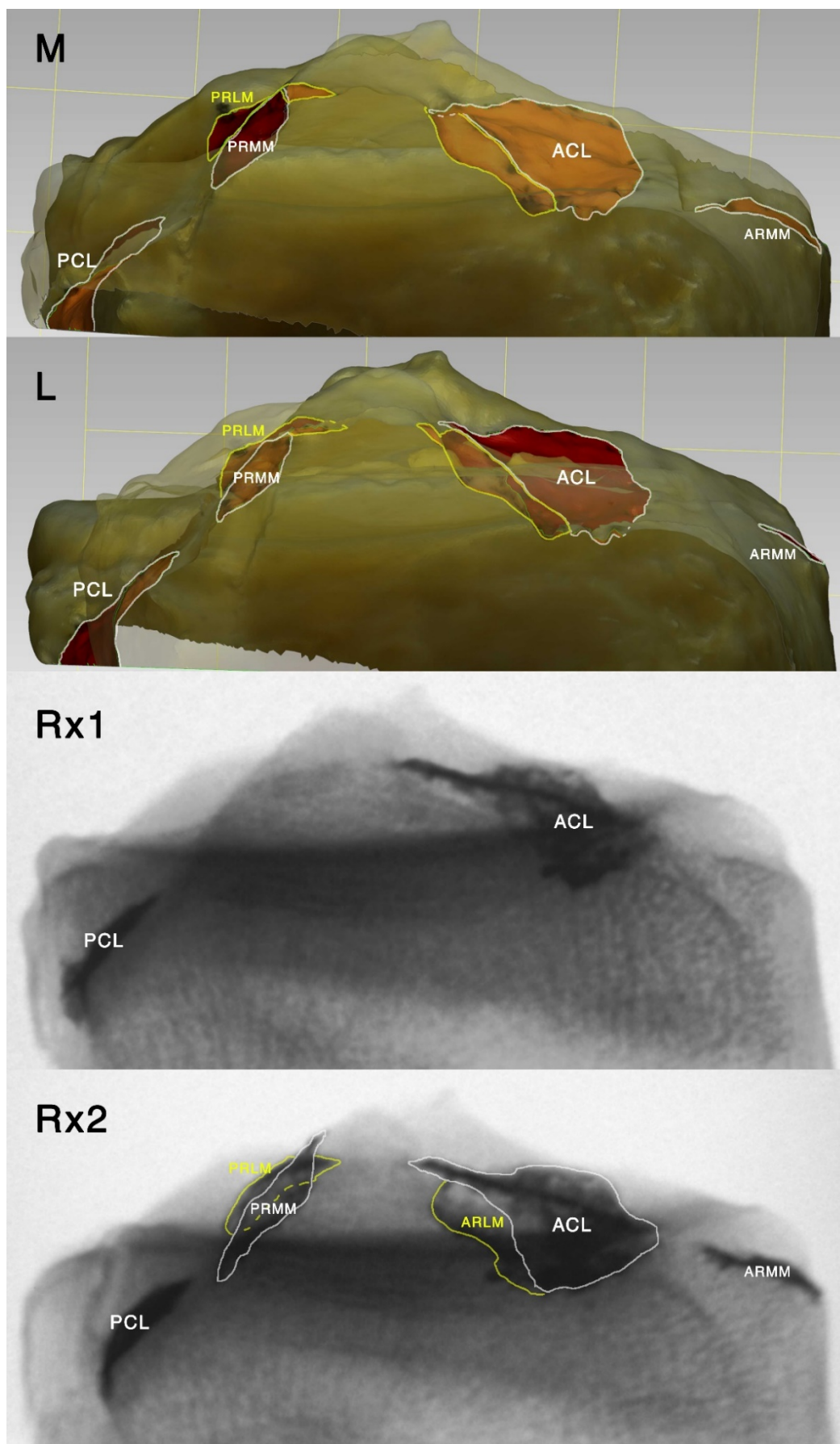


Figure 381. 3D model of tibia A. Medial view with medial side transparent (M). Lateral view with lateral side transparent (L). Lateral fluoroscopic view with ACL and PCL painted with barium sulfate (Rx1). Lateral fluoroscopic view with all attachments painted (Rx2). Attachment areas labelled and marked.

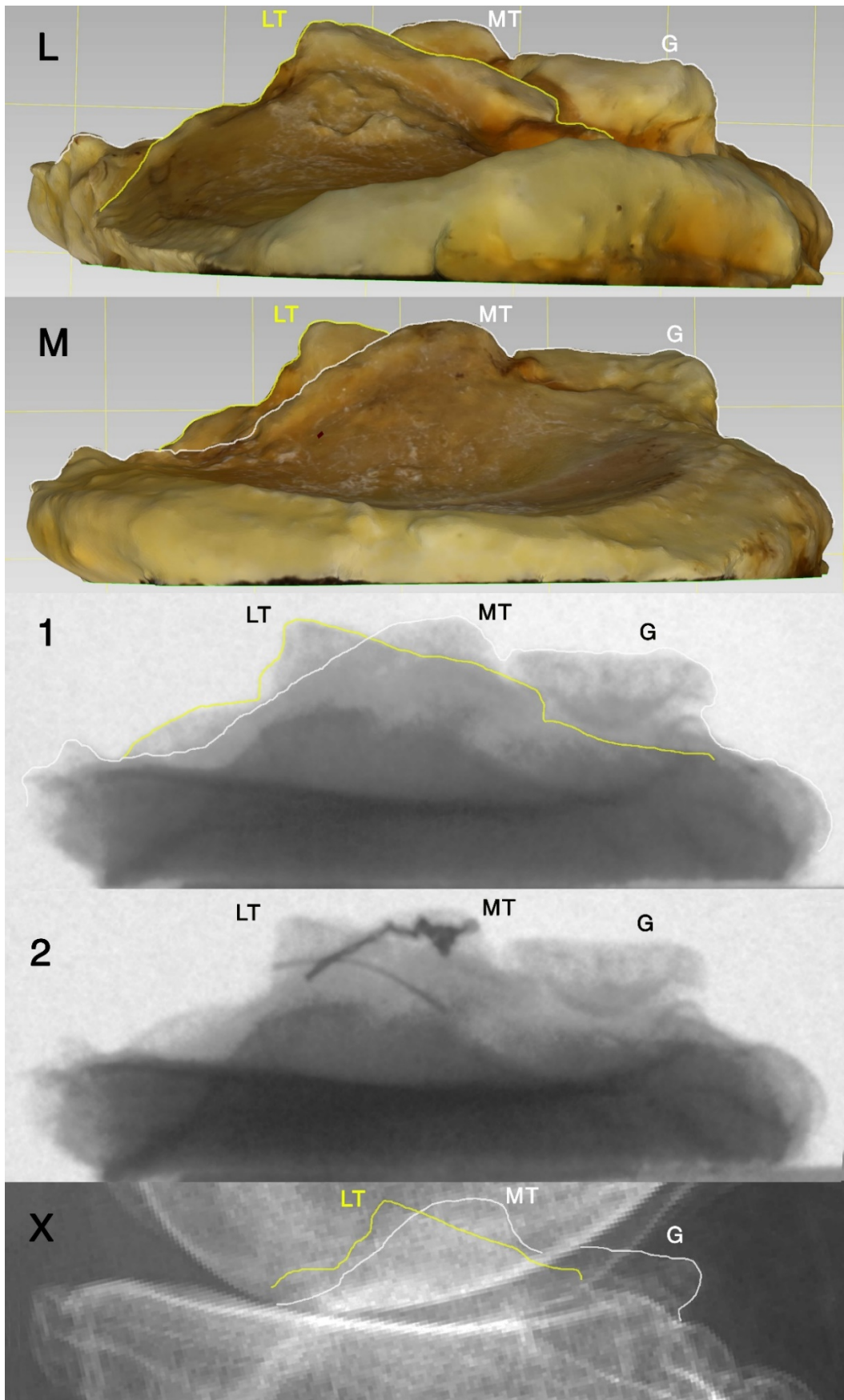


Figure 382. 3D model of pathological tibia E. Lateral view (M). Medial view (L). Lateral fluoroscopic view (1). Lateral fluoroscopic view with metal bands glued to the intercondylar tubercles (2). MT has a thicker metal band attached to it. Lateral knee radiograph prior to TKA surgery (X). Anterior is to the right of the image. Contour of MT (in white) and LT (in yellow), including their anterior and posterior processes, have been drawn over images. Also labelled is the Parsons' tubercle (G).

IV.11.2. Sectional anatomy and histology of normal specimens

IV.11.2.1. Anteroposterior (sagittal) cuts and radiographs

Through the lateral tubercle: cortical bone was thicker in the ALIR (D1-D2), and very thin in the anterior peak (4a). Compression trabeculae (perpendicular to the cortical) predominated over tension trabeculae, but farther from the articular surface there were more trabeculae parallel to the bone axis. Compression trabeculae predominated in the ALIR.

Through the intertubercular area: there was thin cortical overall. Compression trabeculae perpendicular to the cortex predominated in the anterior aspect (AIAR, AFIR); in the posterior area (ITR, posterior wall) there was a mix of compression and tension trabeculae.

Through the medial tubercle: there was thin cortical bone, thicker in the AMIR and PMIR, with very thin cortical bone in the MT apex (3a). Compression trabeculae were found in the anterior AMIR, Parsons, and anteromedial area; and compression and tension trabeculae in the posterior AMIR, MT.

See Fig. 383, Fig. 384.

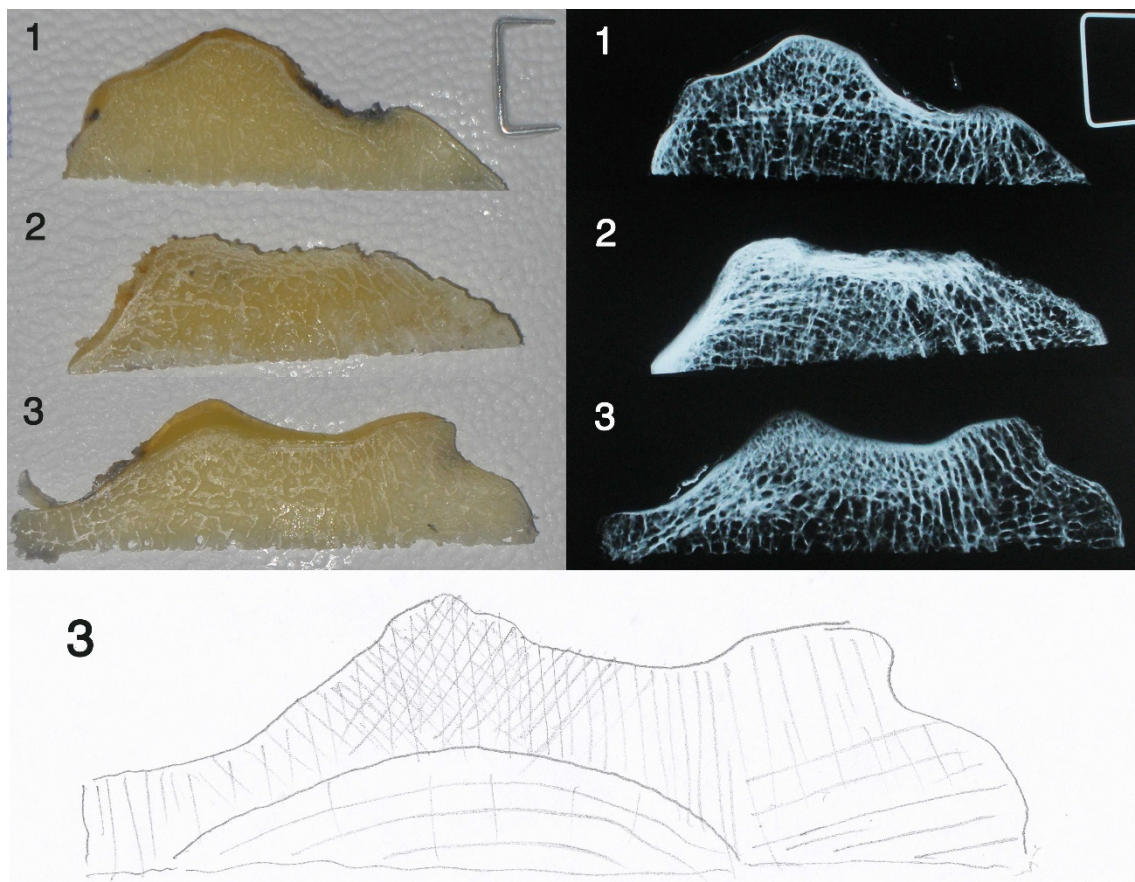


Figure 383. Tibia D. Sagittal cuts (upper left side) with corresponding radiographs (upper right side). 1=cut through lateral tubercle. 2=cut through intertubercular area. 3= cut through medial tubercle. Drawing of trabeculae of cut through medial tubercle at the bottom.

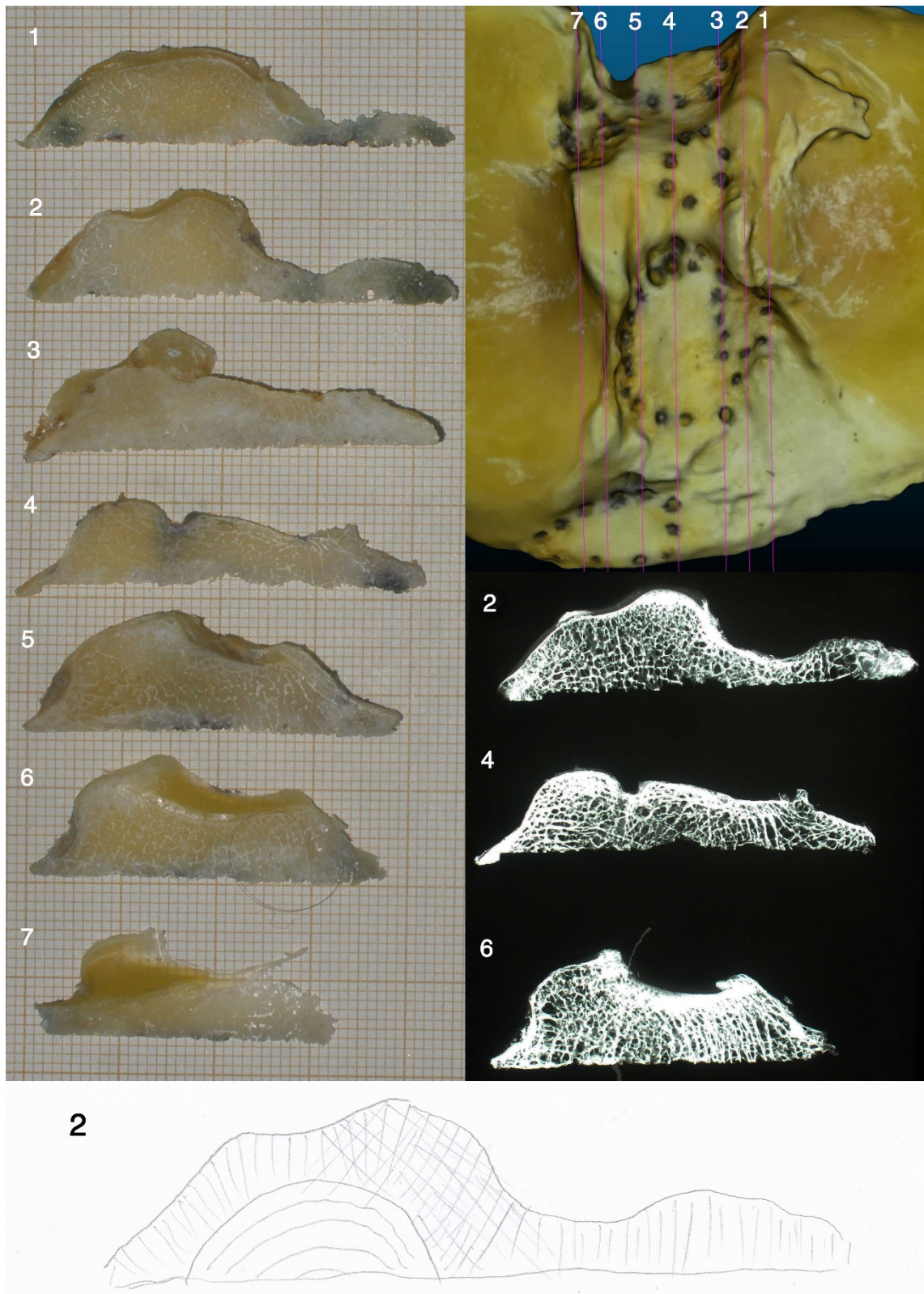


Figure 384. Tibia E. 3D model with drawing of approximate location of cuts over it, with cuts numbered (in the top right corner). Photographs of sagittal cuts (left side) with corresponding radiographs (middle right side), and drawing of trabeculae of cut through lateral tubercle (at the bottom).

IV.11.2.2. Mediolateral (coronal) cuts and radiographs

Through the attachment of the ARMM: There was thin cortical bone and compression and tension trabeculae (none predominated).

Through the AFIR: There was thicker cortical bone in the ridge. Compression and tension trabeculae were found immediately under the cortical bone, below it compression trabeculae predominated.

Through the attachment of the ACL and ARLM: There was thin cortex, and dense compression and tension trabeculae.

Through the tubercles: Dense cortical bone in their articular aspect, becoming thinner upwards internally towards their peaks, and growing thicker again downwards internally from their peaks to the intertubercular ridge. Dense trabeculae were found perpendicular to the cortical bone of the main intercondylar tubercles, and less trabeculae with other directions. As the distance from the surface grew, trabeculae showed a more parallel disposition, in line with compression forces of the tibial axis.

Through the PRLM attachment: There was thin cortical bone in the PRLM attachment area, thick in the rest of the intertubercular ridge. Tension trabeculae were the most common, with some trabeculae showing compression.

Through the attachment area of the PRMM: Thick cortical bone. Tension trabeculae predominated, although perpendicular trabeculae were observed near the surface. Far below the surface they became vertical, parallel to the tibial axis.

Through the PCL attachment area: There was thick cortical bone at the attachment. Tension trabeculae were found in the surface, below it they turned to compression trabeculae.

See Fig. 385 (with Fig. 387 and Fig. 388) and Fig. 386 (with Fig. 389).

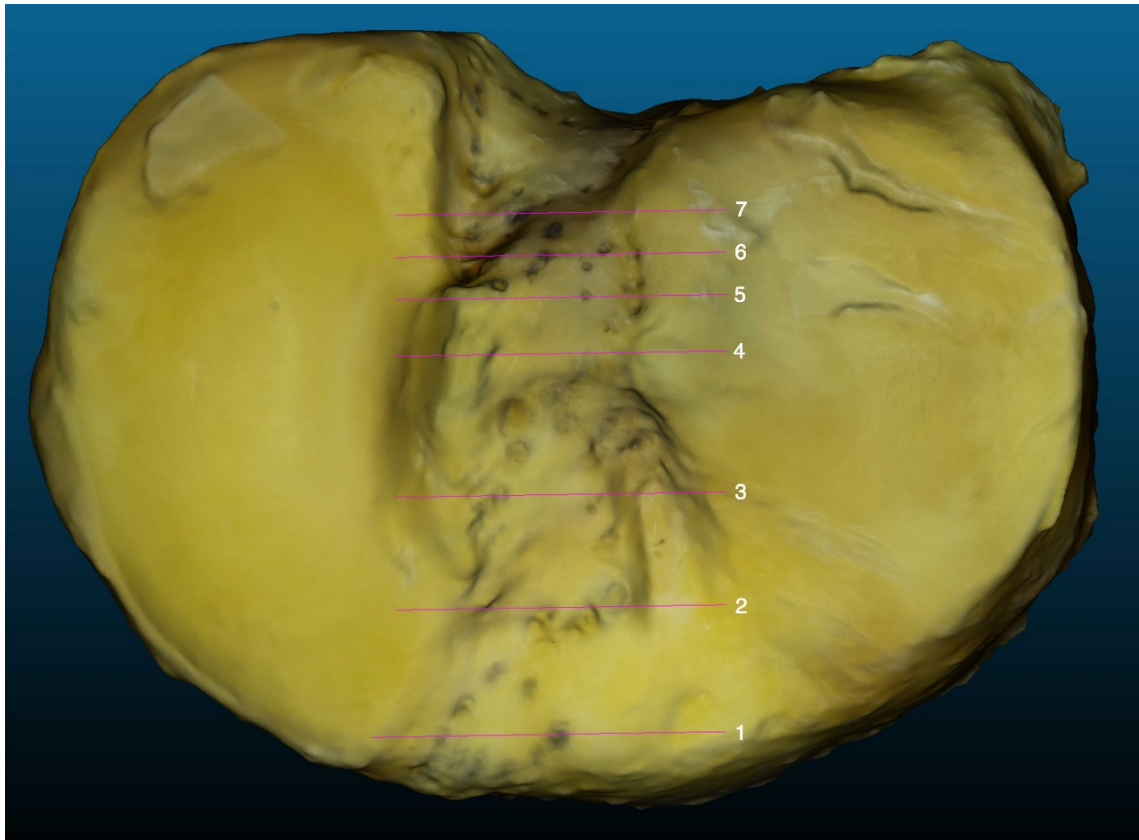


Figure 385. 3D model of tibia G with drawing of approximate location of cuts over it, with cuts numbered corresponding to the numbers in Figure 387, Figure 388.

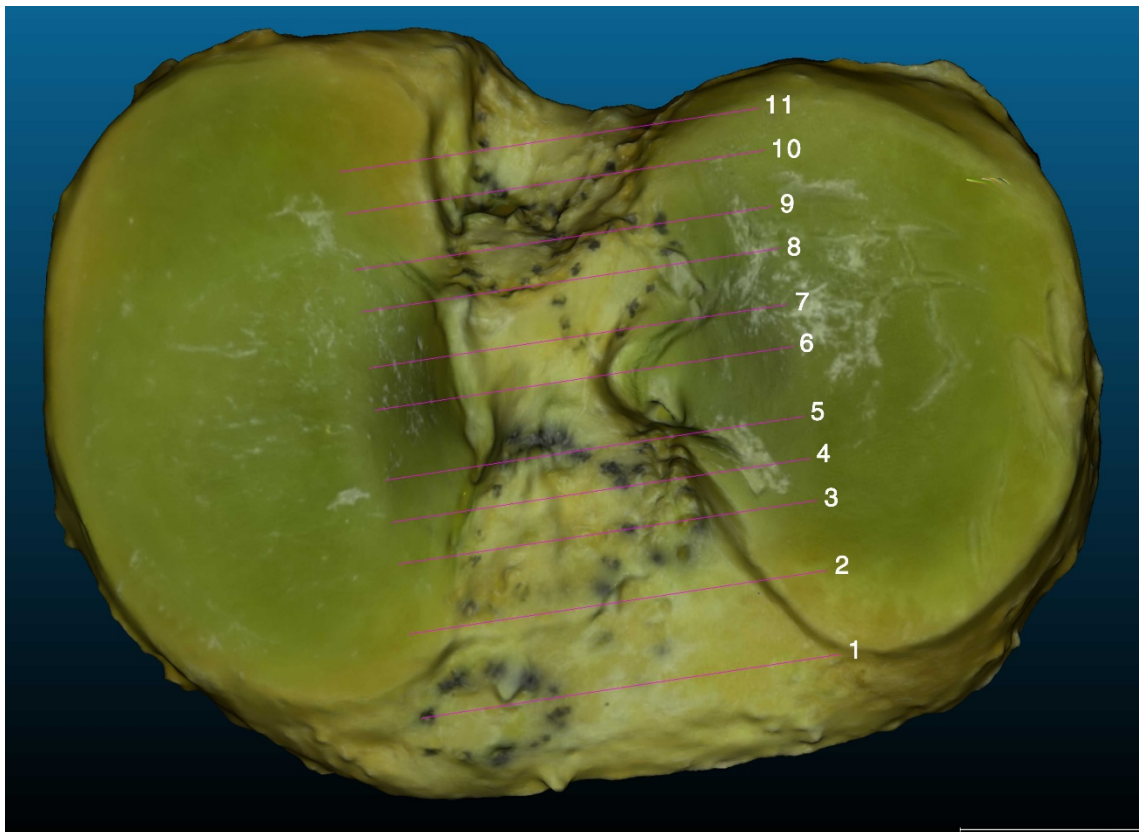


Figure 386. 3D model of tibia L with drawing of approximate location of cuts over it, with cuts numbered corresponding to the numbers in Figure 389.

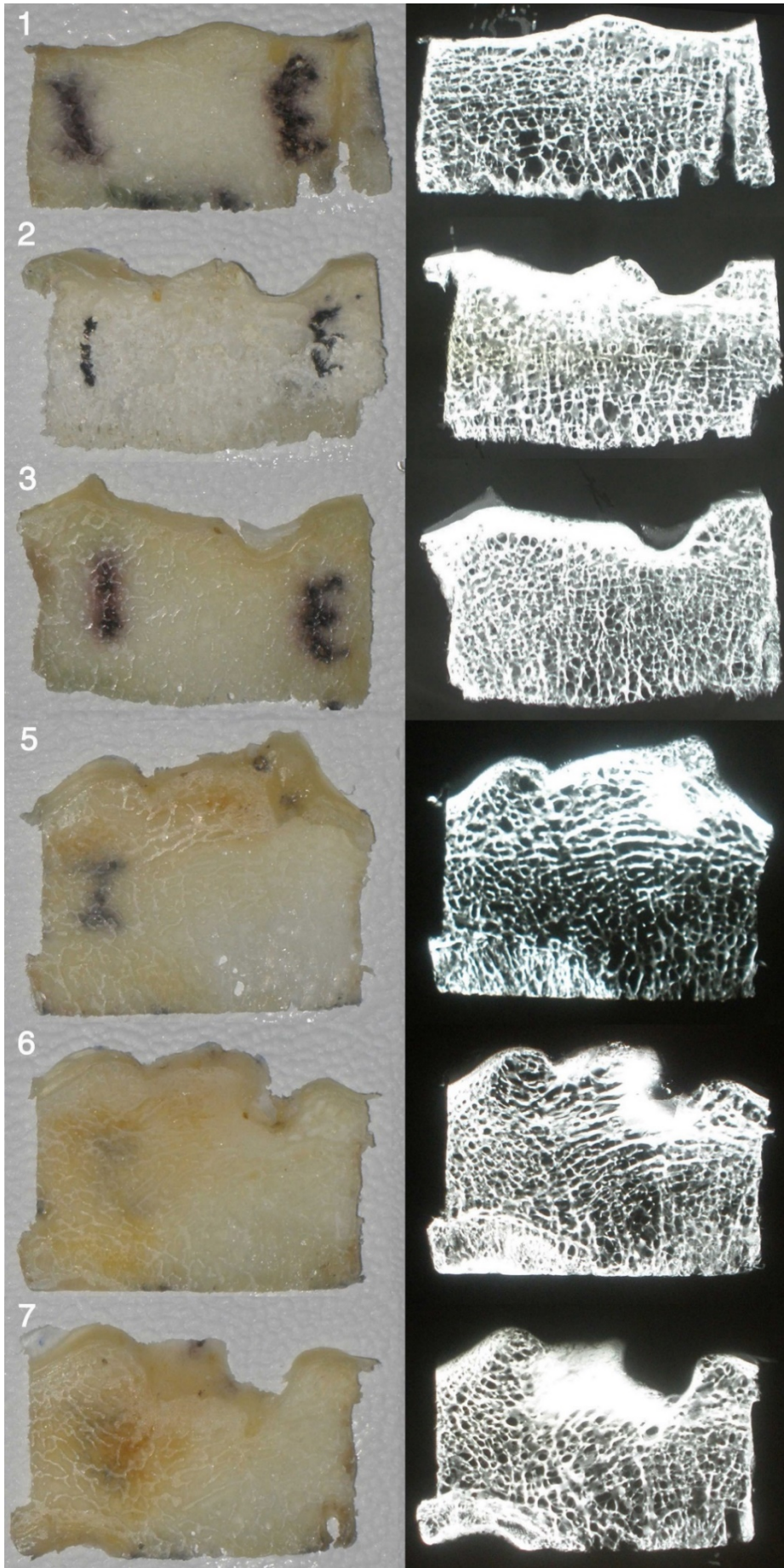


Figure 387. Tibia G. Photographs of coronal cuts (left side) with corresponding radiographs (right side), numbered according to Figure 385.

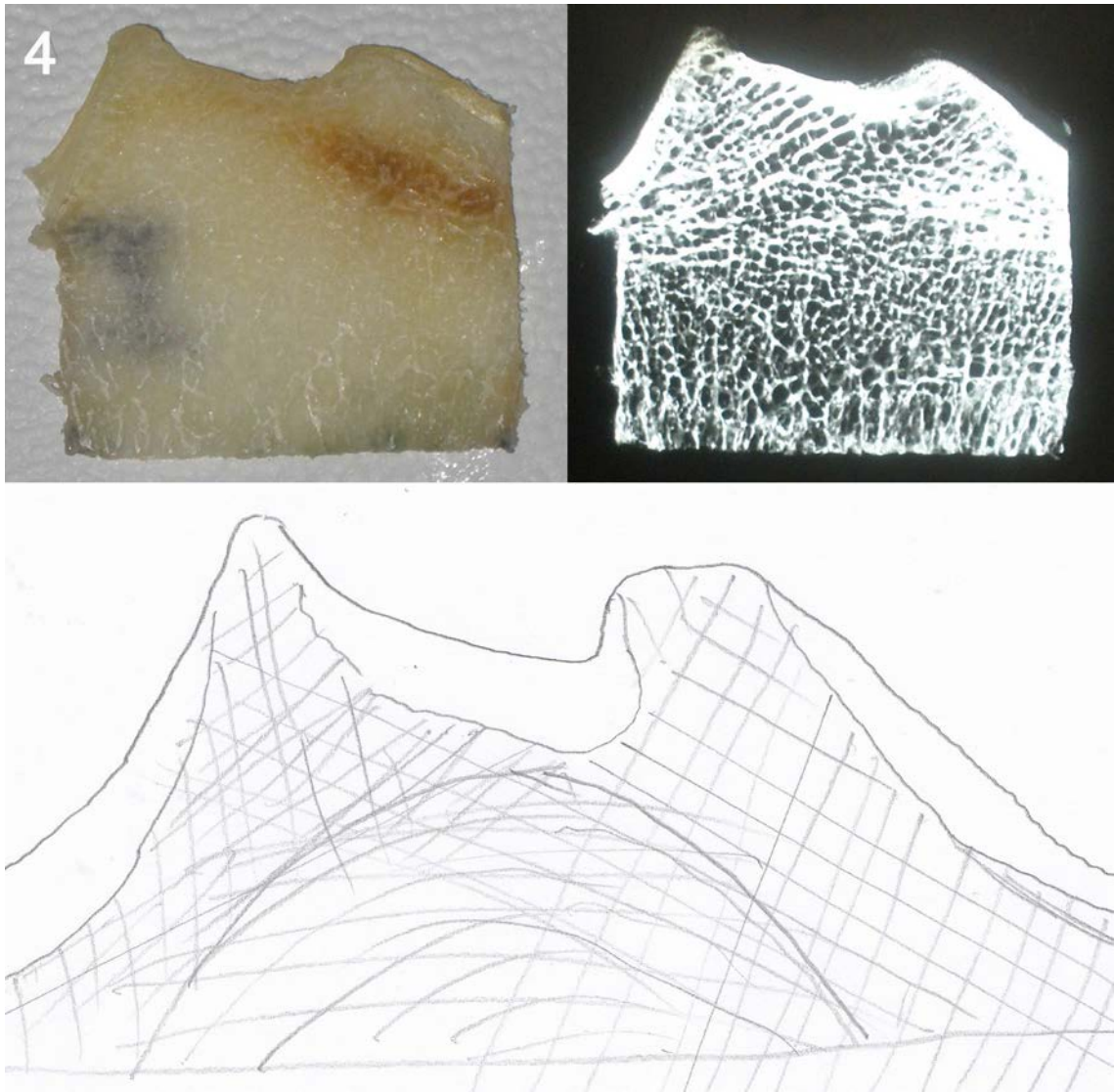


Figure 388. Tibia G. Coronal cut (top left image) with corresponding radiograph (top right image), and drawing of trabeculae (bottom image). Numbered according to Figure 385.

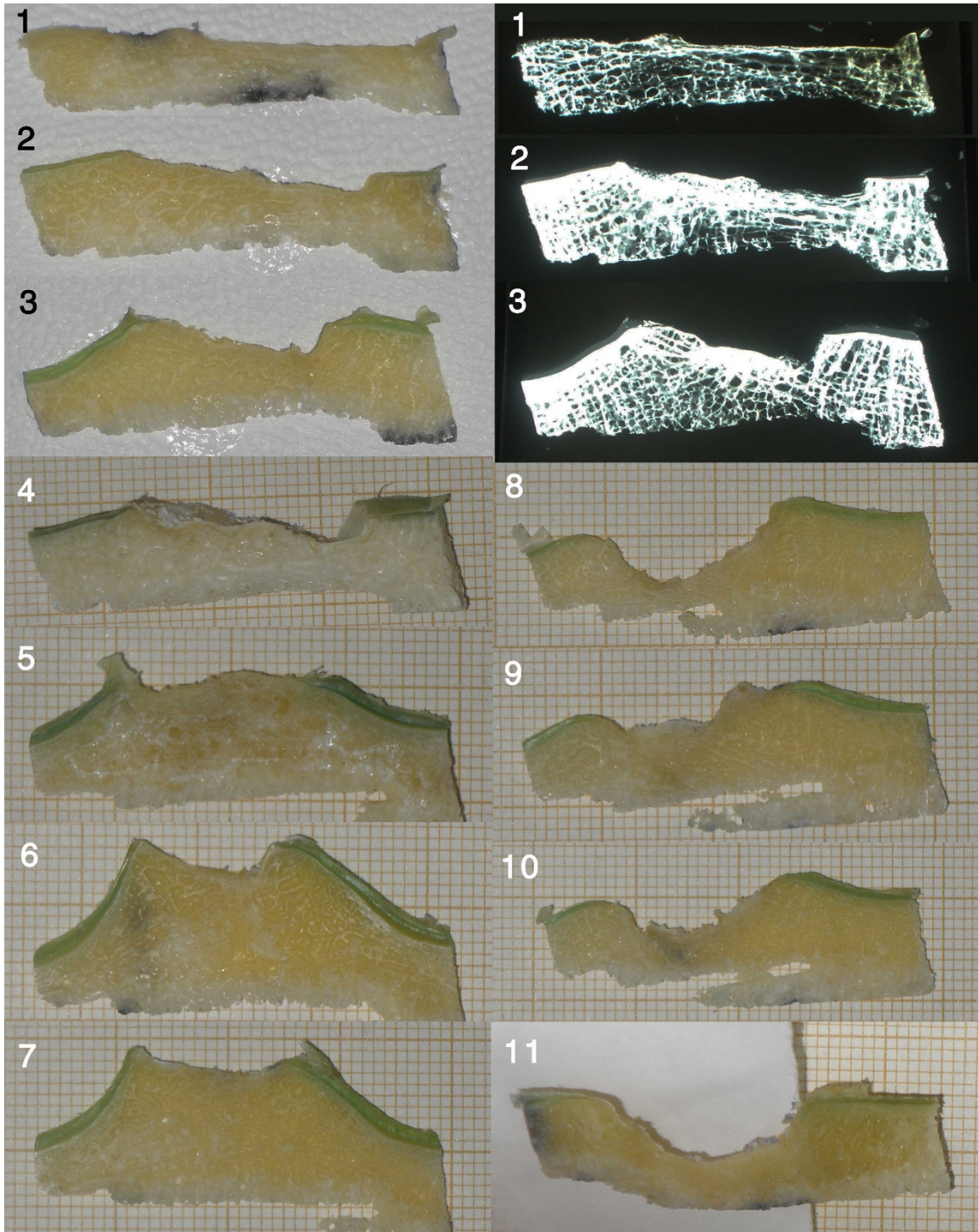


Figure 389 Tibia L. Photographs of coronal cuts (left side and lower right side), with corresponding radiographs (upper right side), numbered according to Figure 386.

IV.11.3. Sectional anatomy and histology of pathological specimens

IV.11.3.1. Anteroposterior (sagittal) cuts and radiographs

Findings are described dividing the tibias into three coronal aspects.

Anterior intercondylar area: Compression trabeculae predominated. In the center of the AIA there were almost no tension trabeculae, and compression trabeculae were thicker and scarcer.

Intertubercular area: Most trabeculae were perpendicular to the anterior and posterior processes of the intercondylar tubercles. A lesser proportion of tension trabeculae was found in this area.

Posterior intercondylar area: Most trabeculae were perpendicular to the posterior aspect, crossing trabeculae with origin in the anterior aspect of the corresponding tubercle. Some tension trabeculae were observed.

The cortical bone in the three areas was thin, except for the anterior area of both tubercles.

Osteophytes and subchondral cysts were also seen (Fig. 391).

Parsons: In one case the Parsons' tubercle was cut without cleaning the soft tissue first, and its relationship with the ACL insertion could be observed directly (Fig. 390).

See Fig. 392 – Fig. 396.

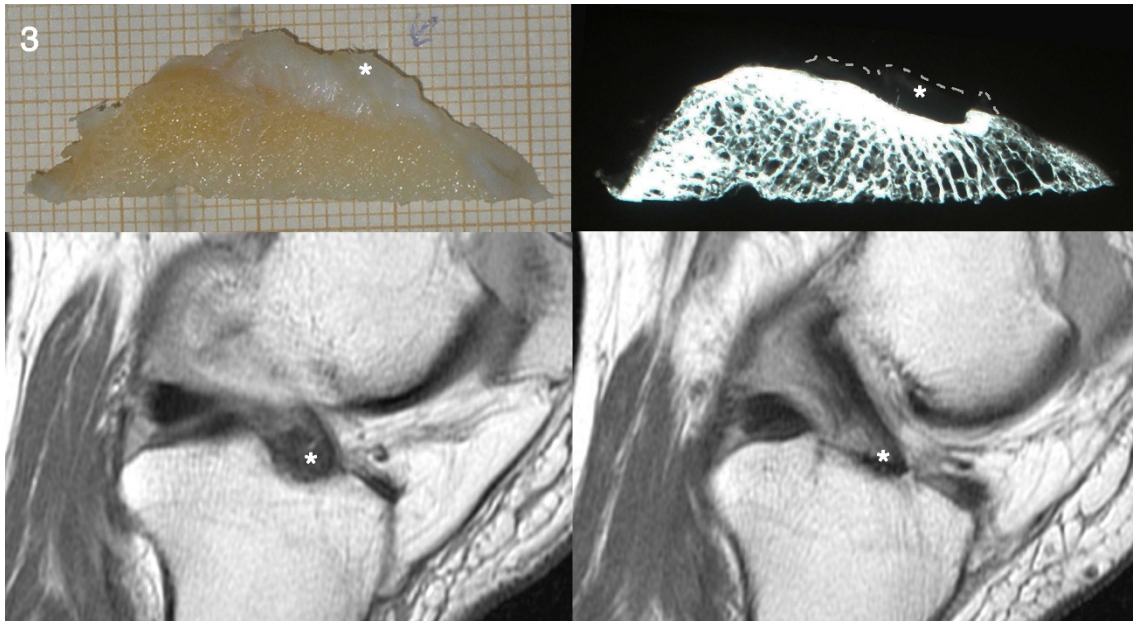


Figure 390. Pathological tibia Ro. Fresh, unfixed specimen. Sagittal cut (top left) through ACL insertion (*). Radiograph (top right), with soft tissue surrounded by white dashed line. T1W MRI cuts through the same area (bottom images), with marked ACL attachment (*).

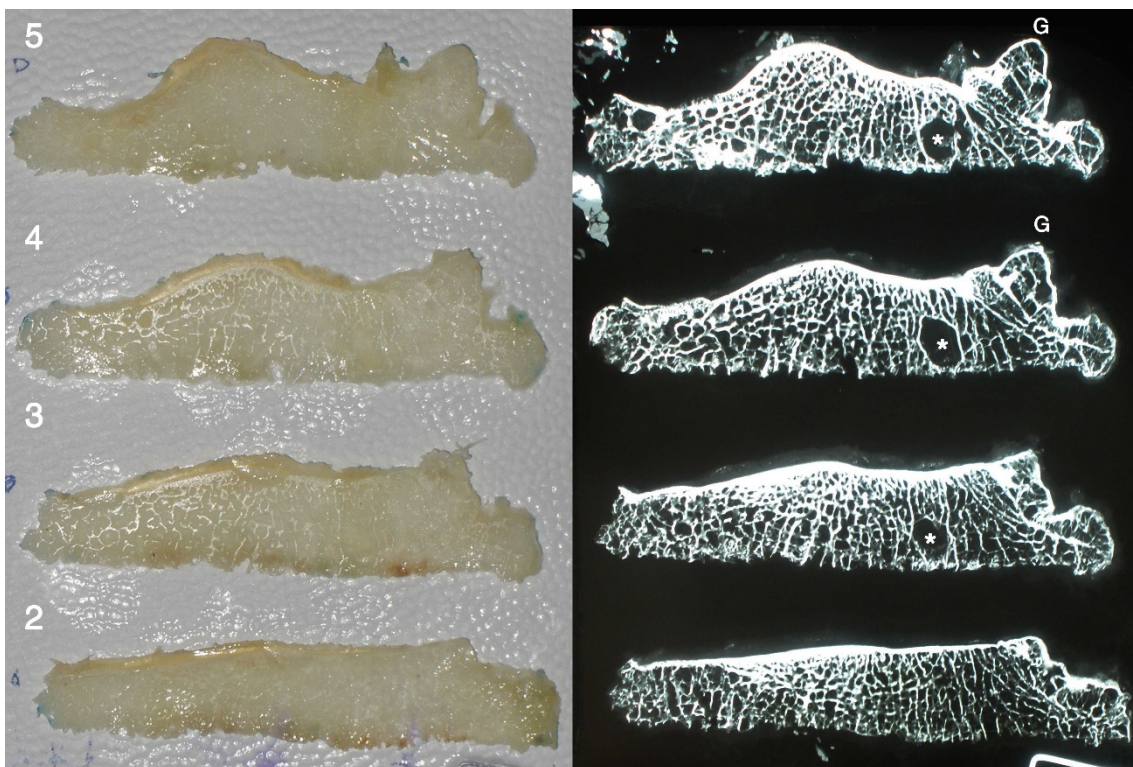


Figure 391. Pathological tibia 21. Sagittal cuts (left side) numbered sequentially from medial condyle (2) to medial tubercle (5), with corresponding radiographs (right side). Observe the Parsons' tubercle (G) anteriorly, and a subchondral cyst (*) beneath the AMIR.

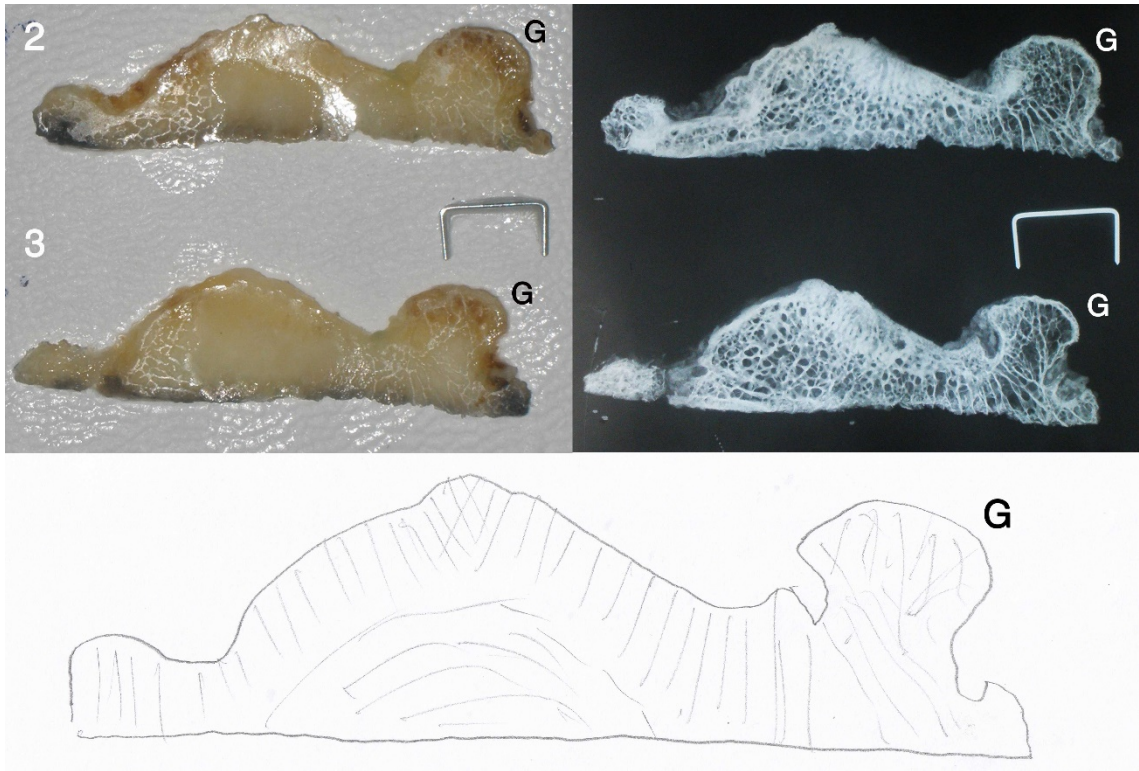


Figure 392. Pathological tibia F. Fixed specimen sagittal cuts (top left) through the Parsons' tubercle. Corresponding radiographs (top right). Drawing of trabeculae (bottom image).

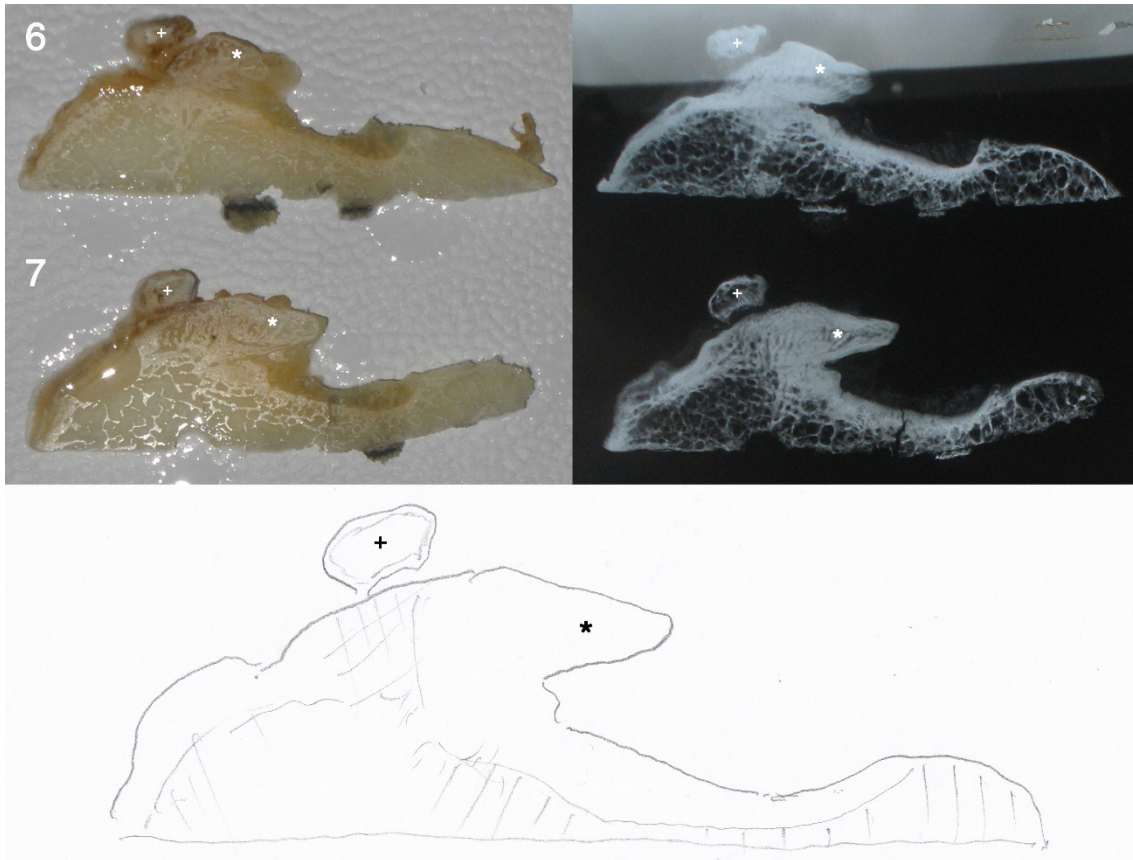


Figure 393. Pathological tibia Mu. Sagittal cut through LT (top left). Corresponding radiographs (top right). Drawing of trabeculae (bottom image). Osteophyte affecting the anterior (*) and posterior peak (+).

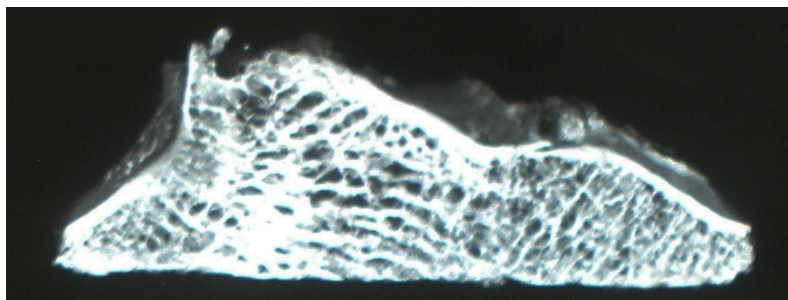


Figure 394. Pathological tibia 64. Radiograph of sagittal cut, through B2 (anterior, to the left) and C1 (posterior, with osteophyte)

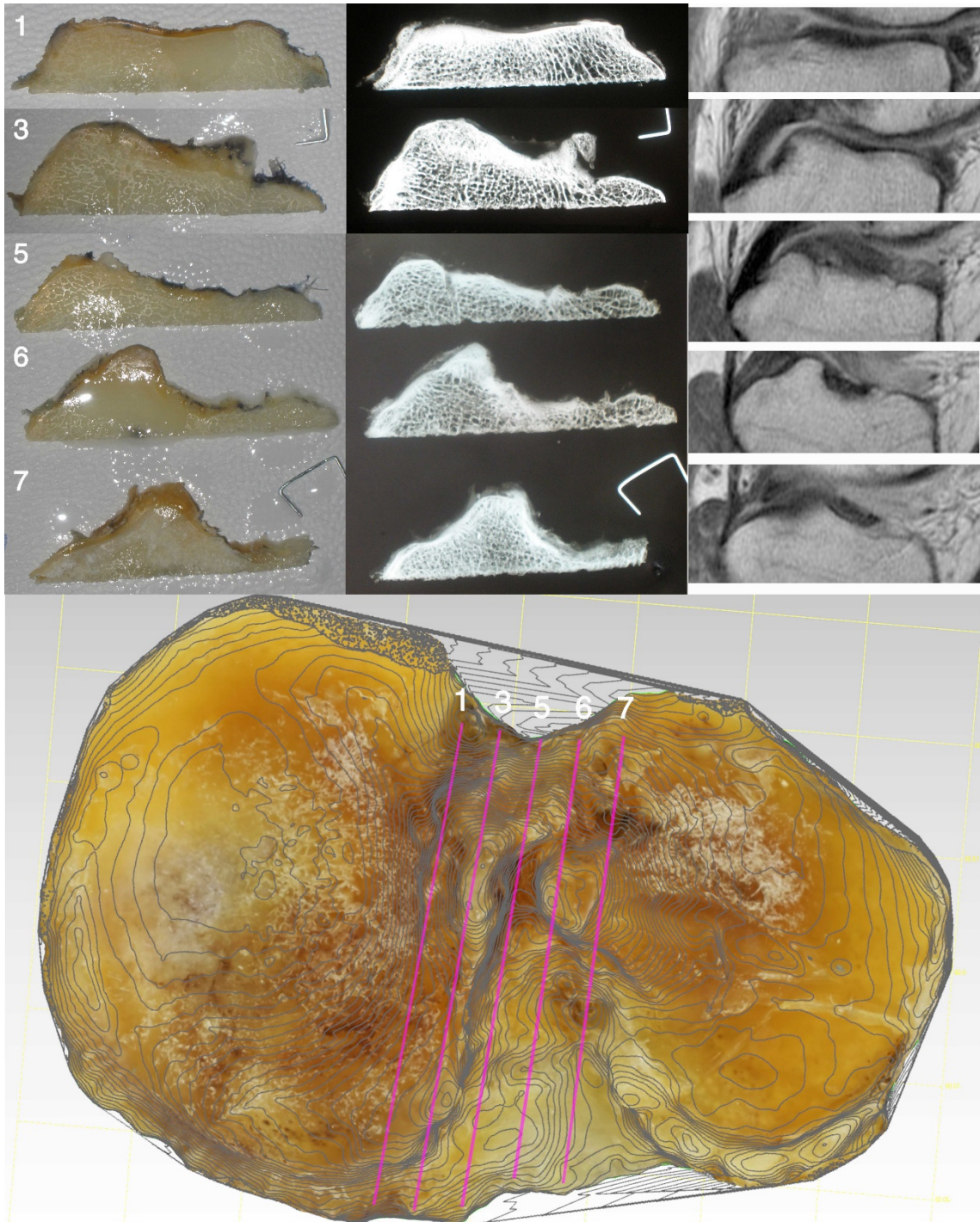


Figure 395. 3D model of pathological tibia 95 with drawing of approximate location of cuts over it, with cuts numbered from medial to lateral. Sagittal cuts (top left images), corresponding radiographs (top middle images), and approximate corresponding knee MRI slices before TKA surgery (top right images).

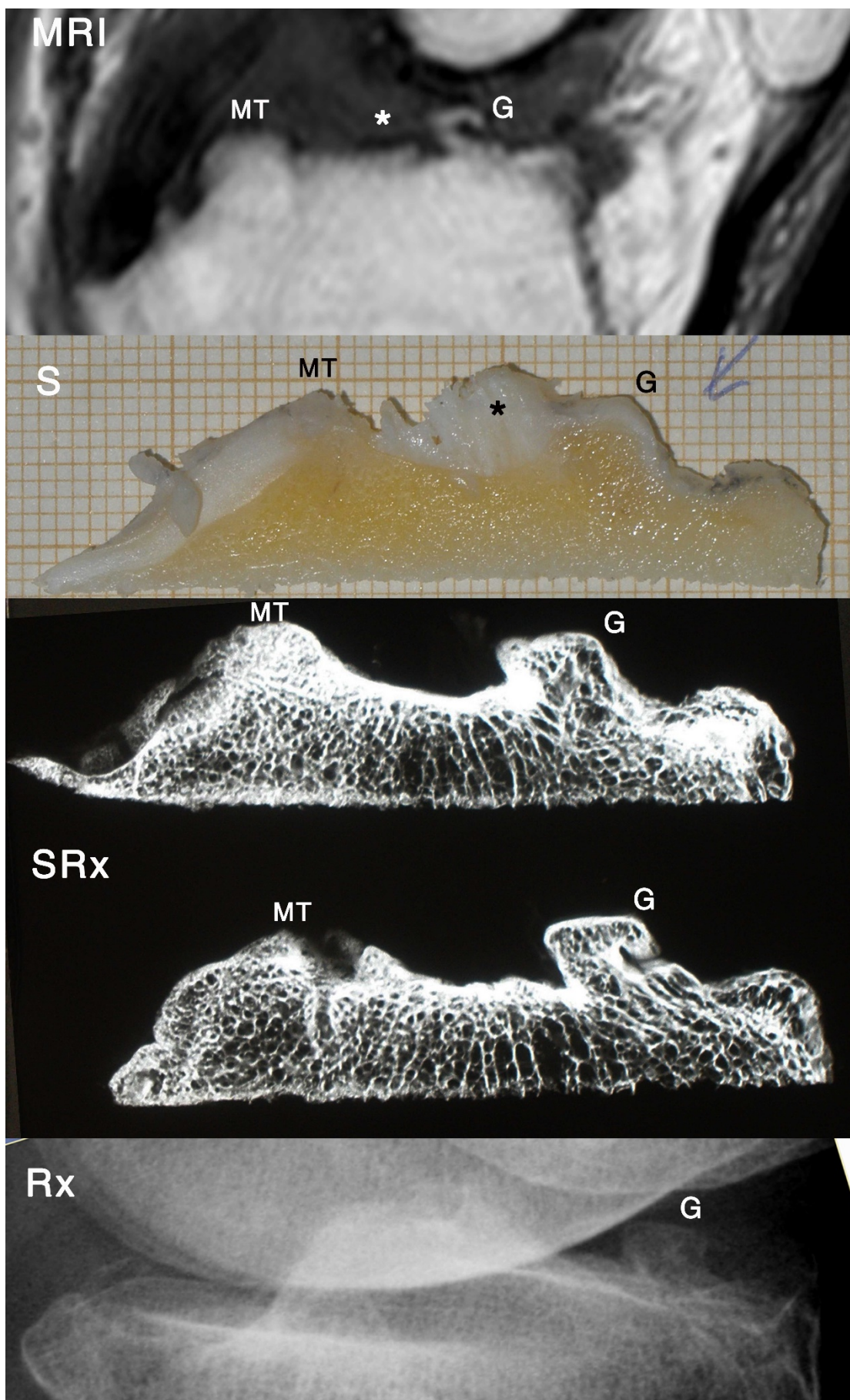


Figure 396. Pathological tibia Ri. MRI sagittal slice through Parsons (MRI), fresh cut (S); radiographs of cuts (SRx); lateral knee radiograph, previous to surgery (Rx). Parsons' knob (G), ACL attachment (*), and lateral aspect of MT labelled.

IV.11.3.2. Mediolateral (coronal) cuts and radiographs

Dense cortical bone was found between the main intercondylar tubercles, and in the posterior intercondylar area.

Anterior intercondylar area: Compression and tension trabeculae were found mixed. The Parsons' tubercle could be observed in transverse cuts (Fig. 398).

Through the tubercles: Compression trabeculae predominated beneath the condyles, and they were perpendicular to the external slope of the medial tubercle, and to the external slope of the lateral tubercle (Fig. 399, Fig. 397)

Posterior intercondylar area: Tension trabeculae predominated (Fig. 400).

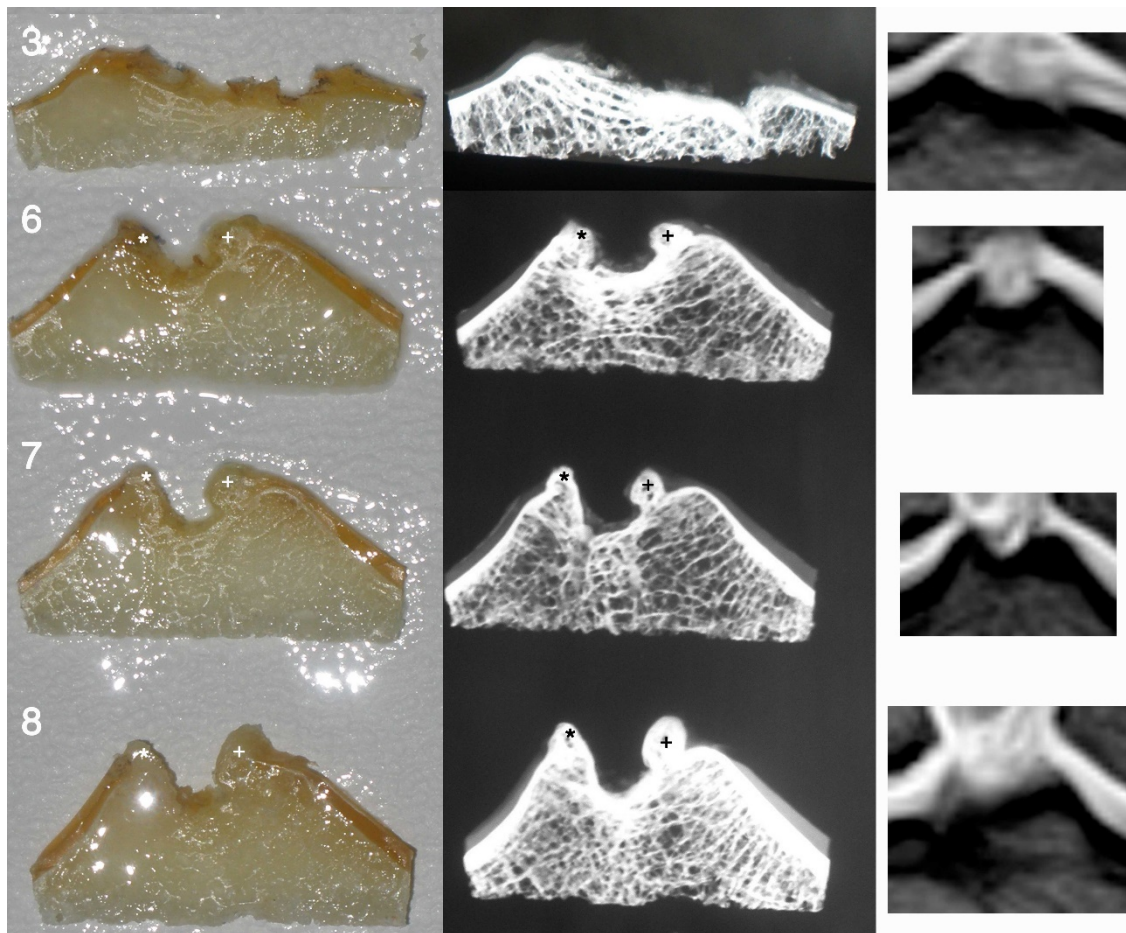


Figure 397. Pathological tibia 79. Coronal cuts through eminence (left side images), numbered from anterior aspect to posterior ITR (upper to lower images). Corresponding radiographs (middle images) and approximate knee MRI slices (right side images). Labeled are osteophytes of MT () and LT (+).*

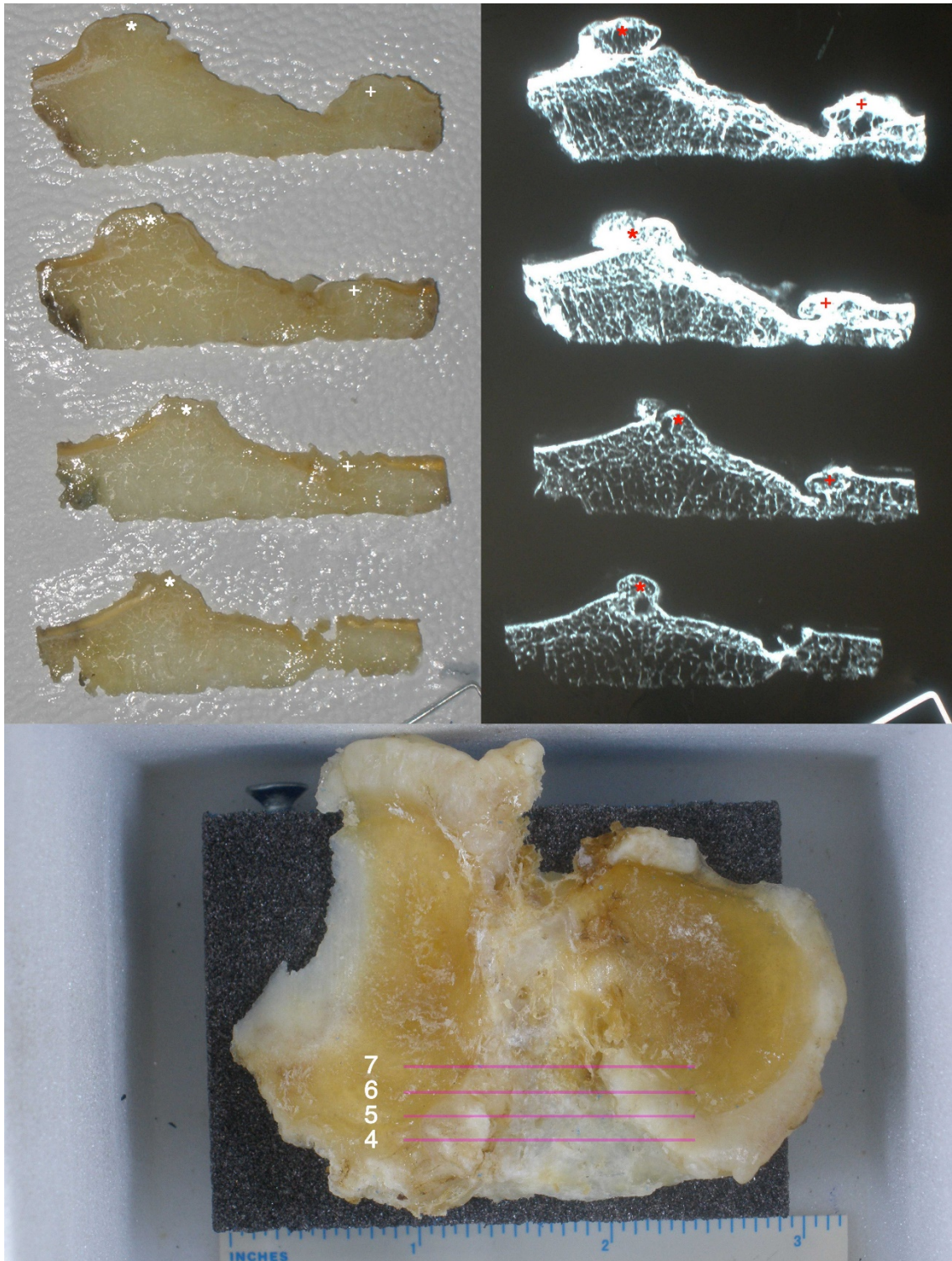


Figure 398. Pathological tibia 22. Coronal cuts through anterior aspect. Photograph with drawing of approximate location of cuts over it, with cuts numbered from anterior to posterior (inferior image), coronal cuts fixed (top left), and corresponding radiographs (top right). Labelled are the medial osteophyte (*), corresponding to the Parsons' knob and AMIR, and the lateral osteophyte (*), corresponding to the elevation of the AL corner and of D1-D2.

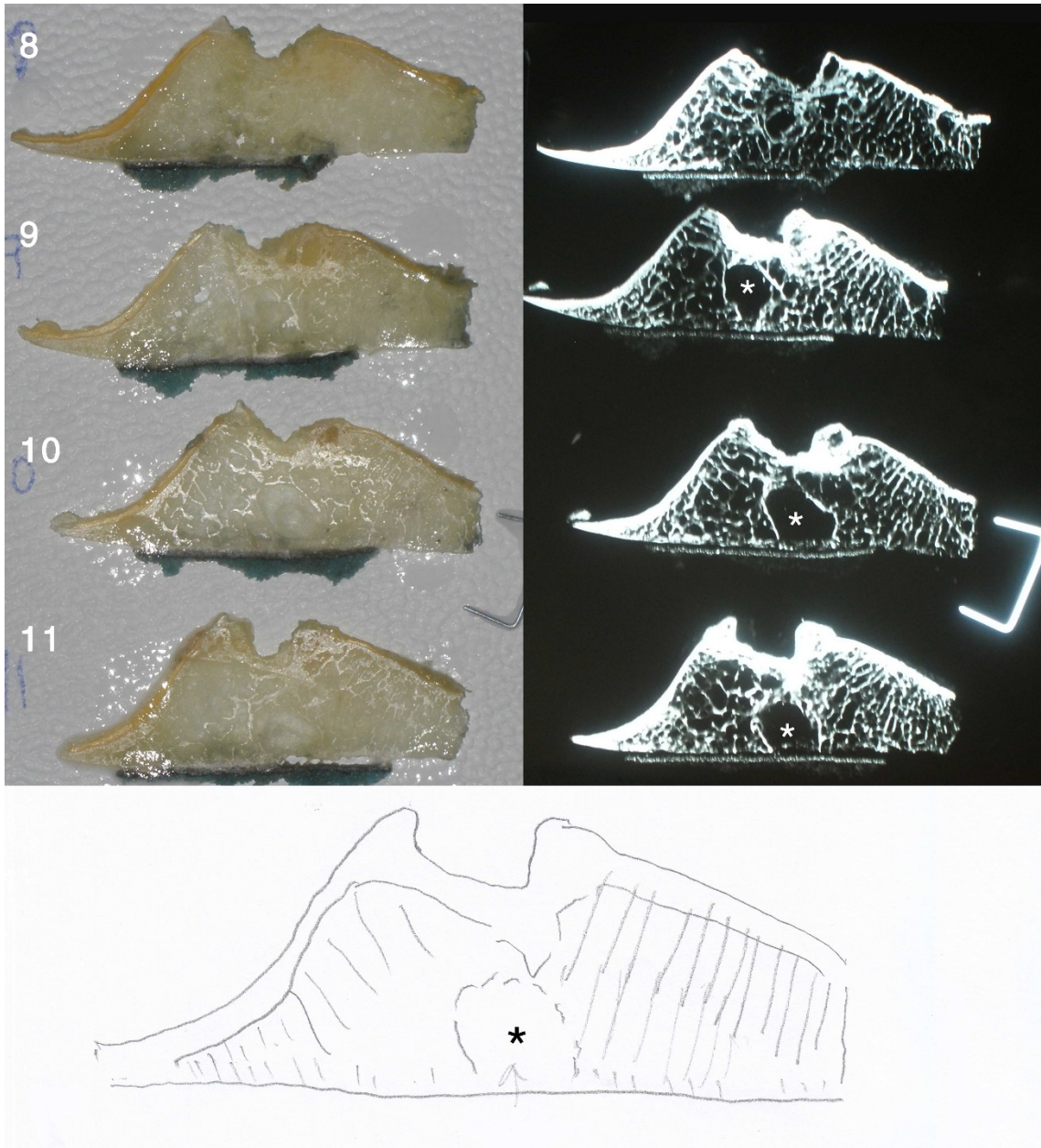


Figure 399. Pathological tibia 14. Coronal cuts through the eminence (top left images). Corresponding radiographs (top right). Drawing of trabeculae (bottom image) with cyst (*).

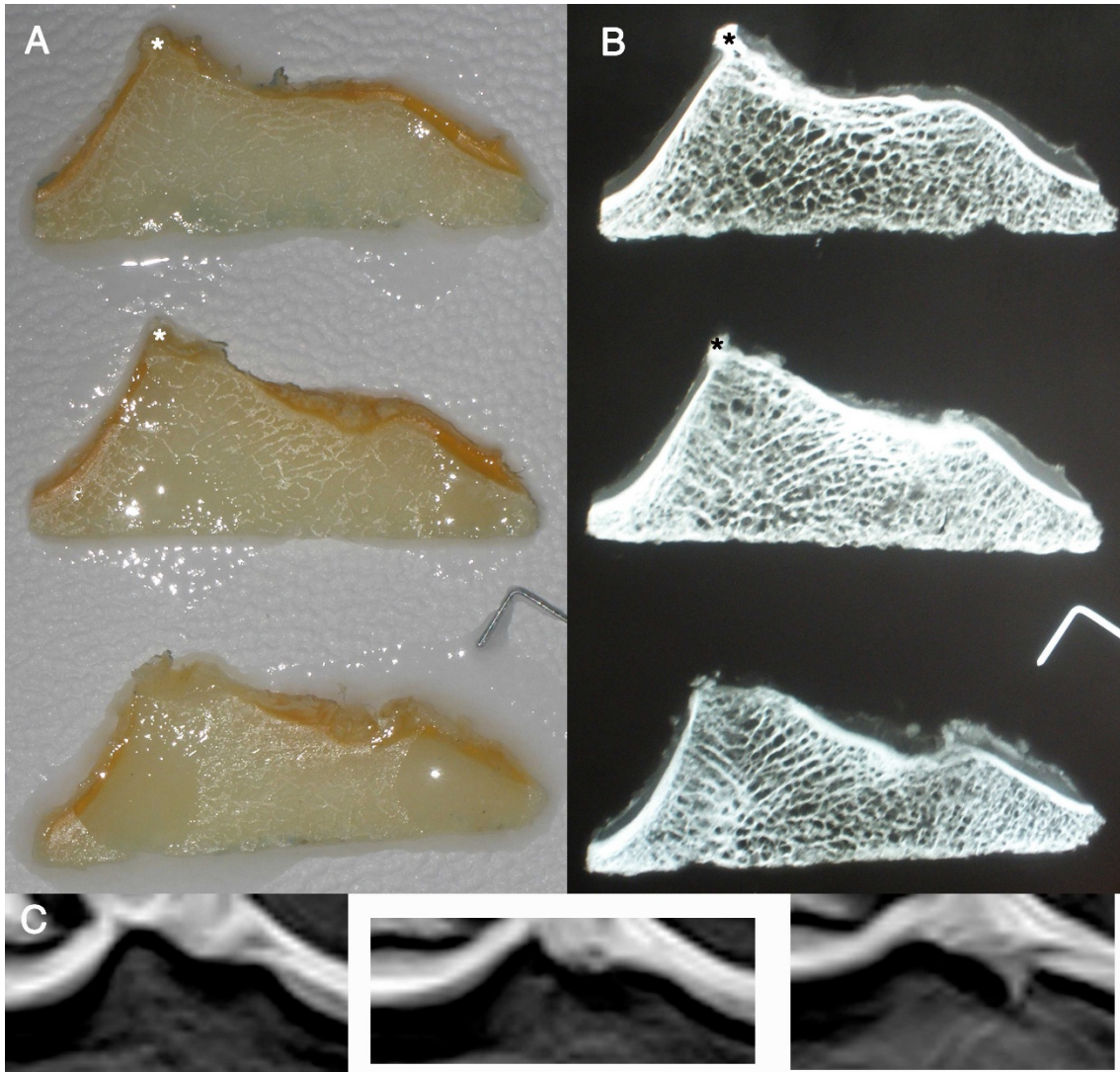


Figure 400. Pathological tibia 64. Coronal cuts through eminence (left side images), anterior to posterior (upper to lower images). Corresponding radiographs (right side images). Knee MRI slices through similar areas (bottom images, left to right). MT osteophyte (*).

IV.11.3.3. Horizontal (axial) cut of the tubercles

The peak of the intercondylar tubercles showed a very thick bone. Beneath the tubercles' peaks, near the cortical bone, many thick trabeculae were found, which diminished in an inferior and external direction (Fig. 401).

Compression and tension trabeculae seemed to cross at an approximately 90° angle.

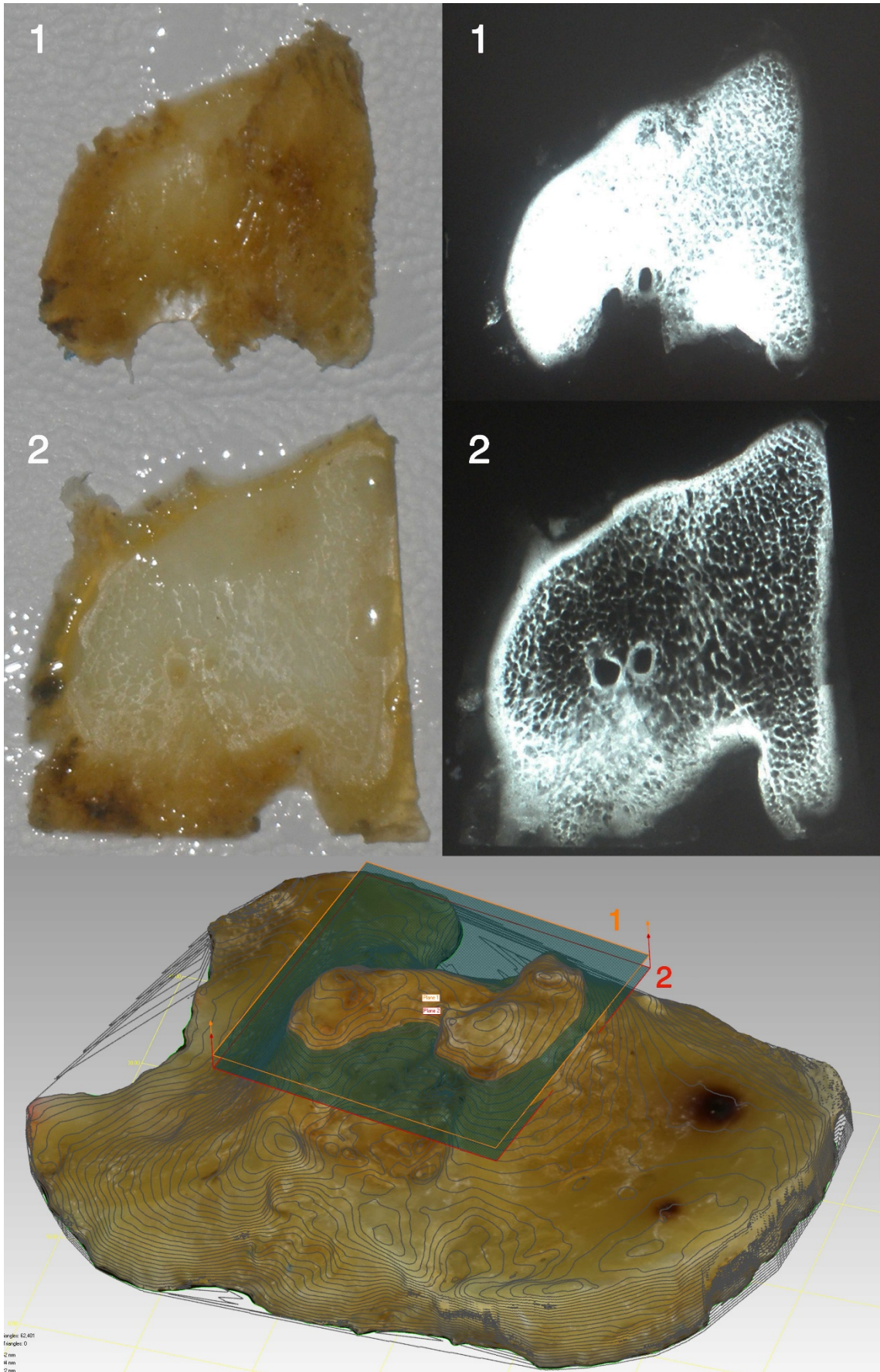


Figure 401. 3D model of pathological tibia 80 with approximate planes of axial cuts over it (bottom image). Axial cuts (top left images), corresponding radiographs (top right images). Observe the presence of foramina nutricia in the anterior aspect of the ITR, corresponding to the posterior arch of the AIS.

IV.11.4. Histology of the Parsons' knob

To differentiate between the different tissue compartments of the Parson's knob, images from staining, polarized light and scanning electronic microscopy were compared.

The more superficial zone was found to be composed of connective tissue, thicker on its base and thinner on the top. Under it a zone of fibrocartilage was found, with its base formed by trabecular bone.

Stained collagen of ACL fibers were observed attached to the Parson's knob in anteroposterior slices. Under polarized light collagen fibers could be observed in their different arrangement. The scanning electronic microscopy showed the light bony structure surrounding fibrocartilage and connective tissue.

See Fig. 402 – Fig. 408.

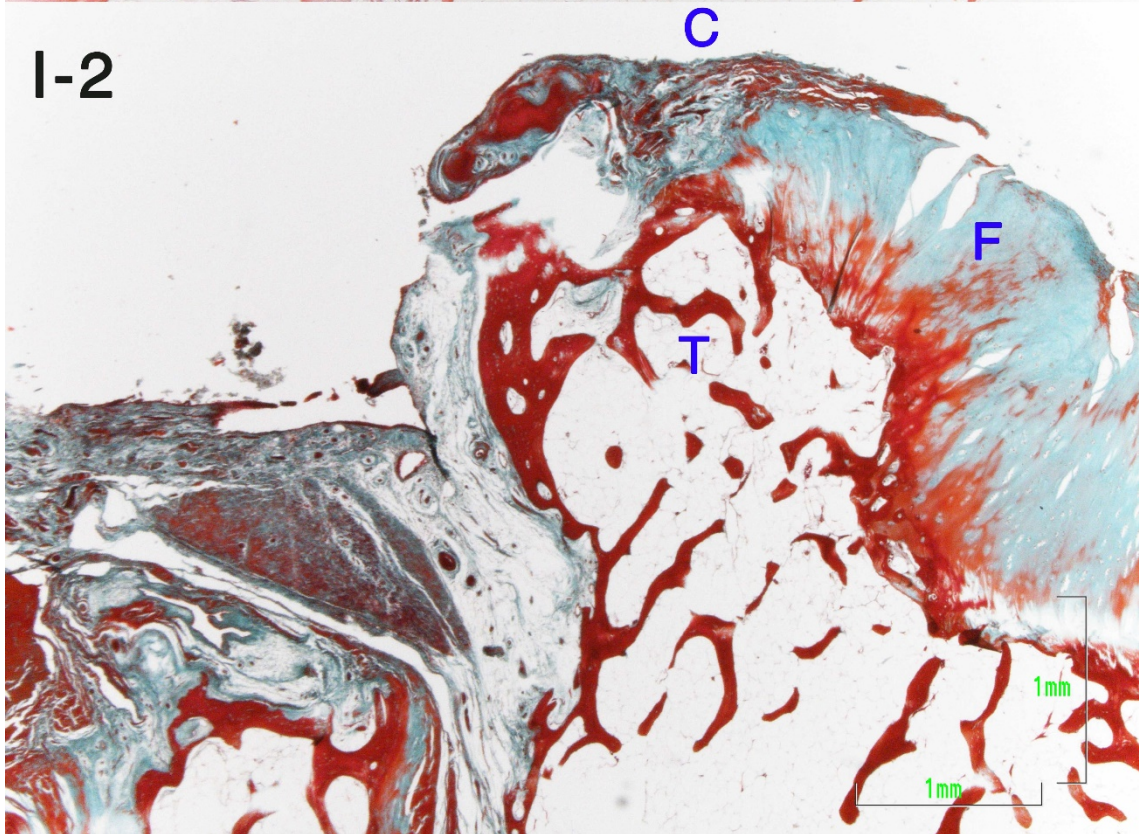
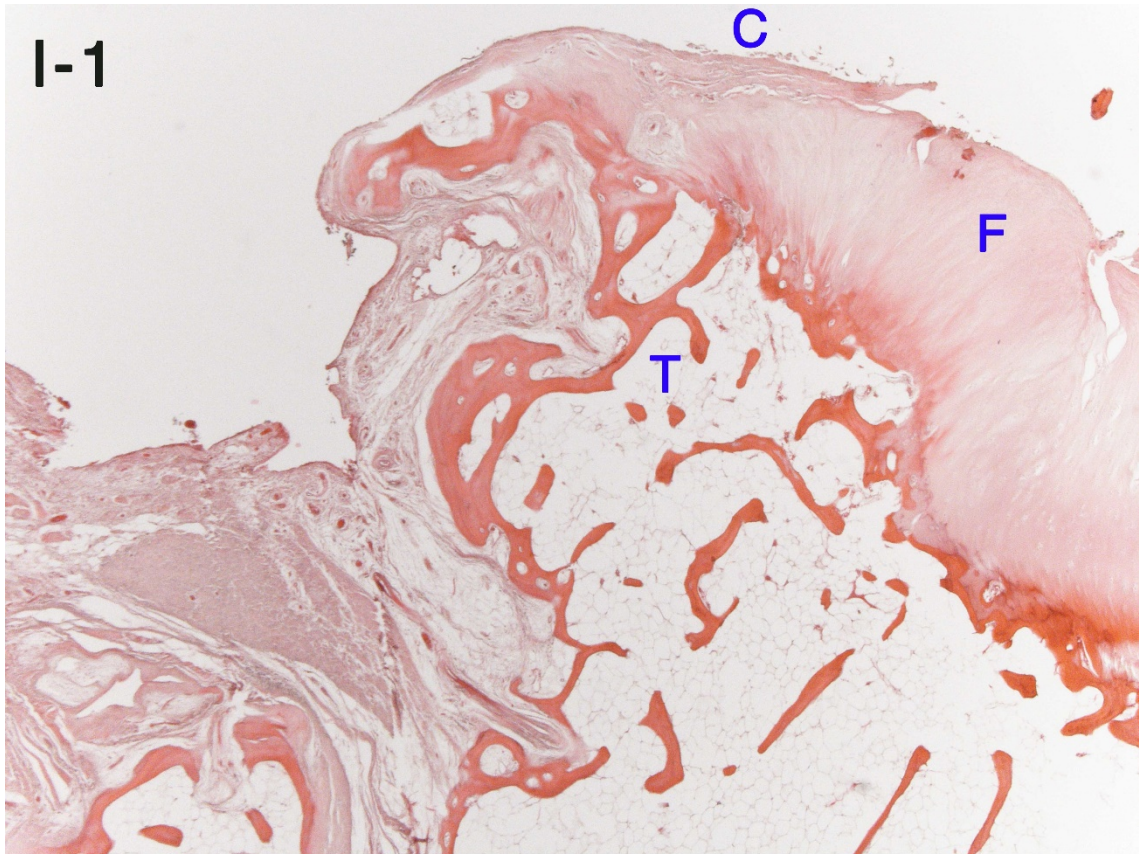


Figure 402. Coronal cut of Parsons' tubercle (lateral aspect to the left, medial to the right of the image). Prico-Sirius red stain, with myocyte nuclei in brown, collagen fibers in bright red, and elastic and muscle fibers with yellowish tones (I-1). Masson's trichrome stain, with muscle fibers in red/pink, collagen in blue/green, and nuclei in brown (I-2). F: fibrocartilage; T: bone trabeculae; C: connective tissue.



Figure 403. Scanning electron microscopy of Parsons' tubercle (coronal cut), corresponding to Figure 402. Lateral aspect to the left, medial to the right of the image. F: fibrocartilage; T: bone trabeculae; C: connective tissue.

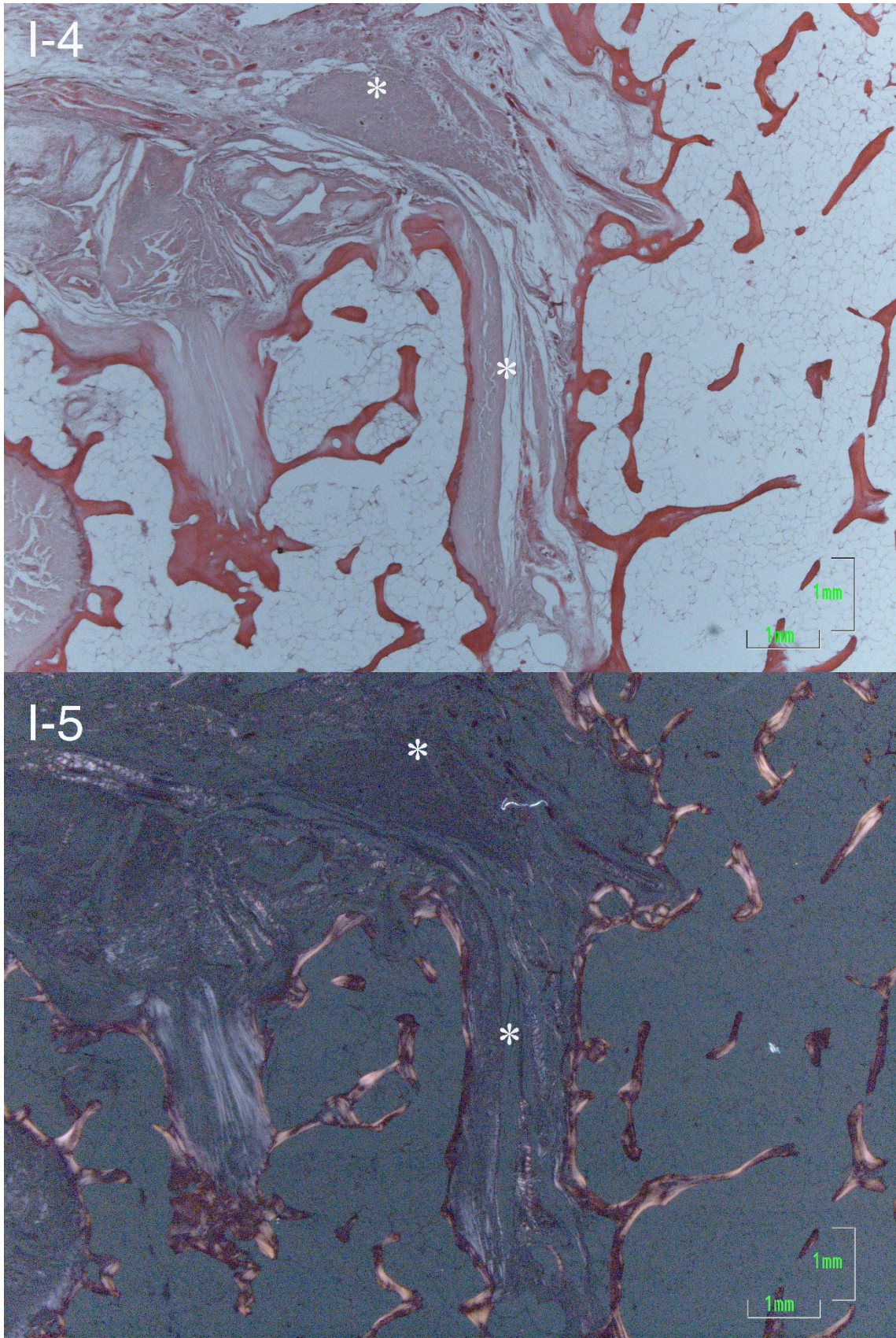


Figure 404. Detail of Figure 402. Prico-Sirius red stain (I-4) and polarized light microscopy (I-5). Fibers of the ACL attachment (*).

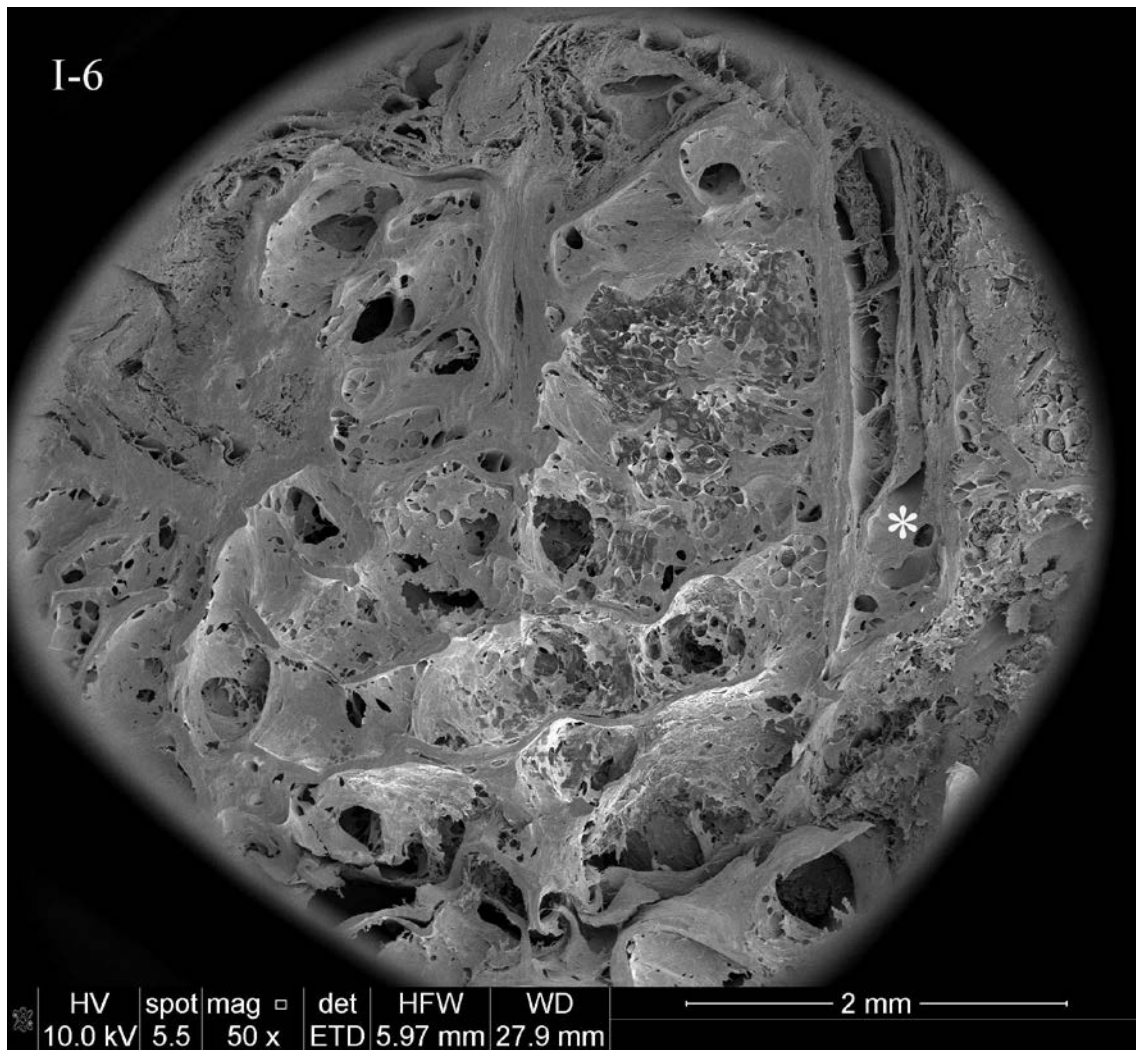


Figure 405. Scanning electron microscopy corresponding to Figure 404. Fibers of the ACL attachment (*).

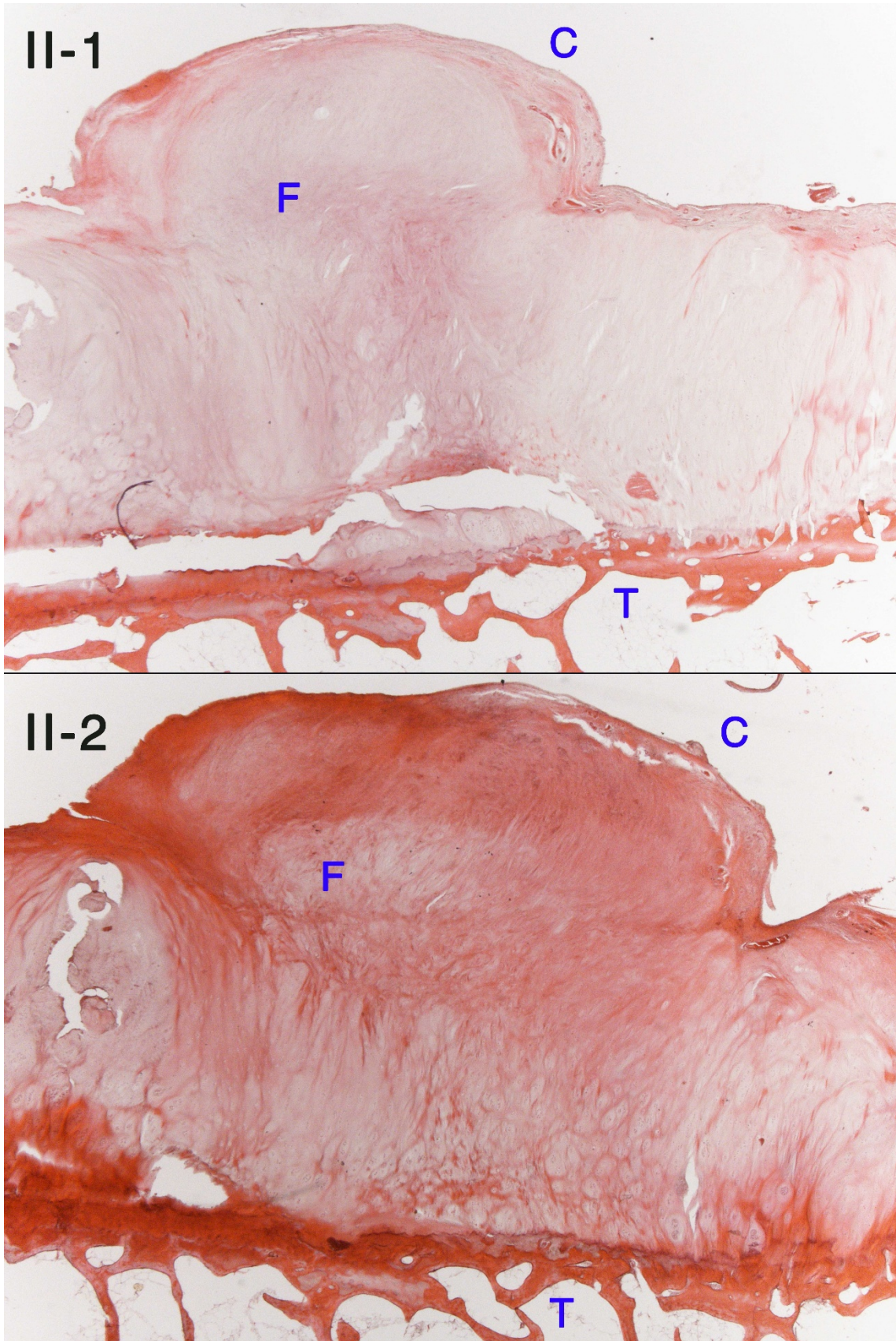


Figure 406. Sagittal cut of Parsons' tubercle (posterior aspect to the left, anterior to the right of the image). Prico-Sirius red stain, with myocyte nuclei in brown, collagen fibers in bright red, and elastic and muscle fibers with yellowish tones (II-1). Hematoxylin and eosin stain, with muscle fibers in dark red, collagen in pale pink, and nuclei in blue/purple (II-2). Image shows fibrocartilage surrounded by connective tissue and resting on bone trabeculae.

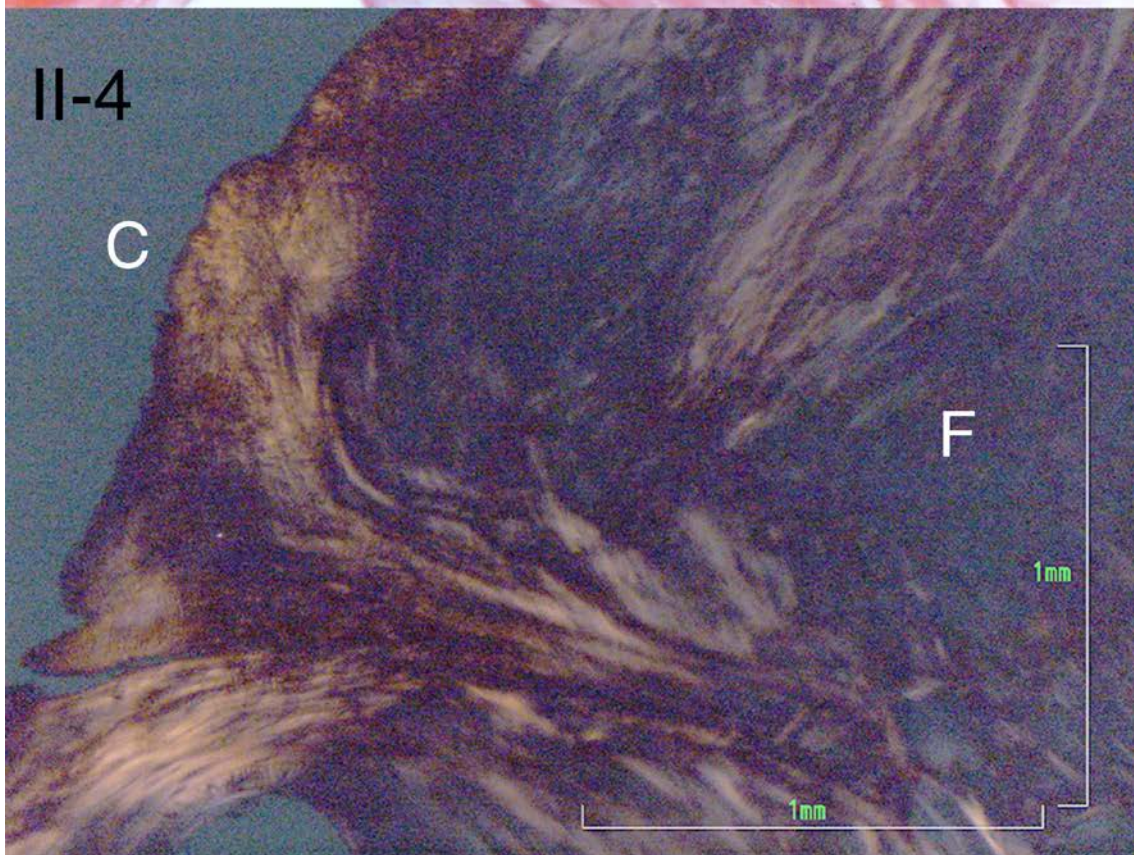
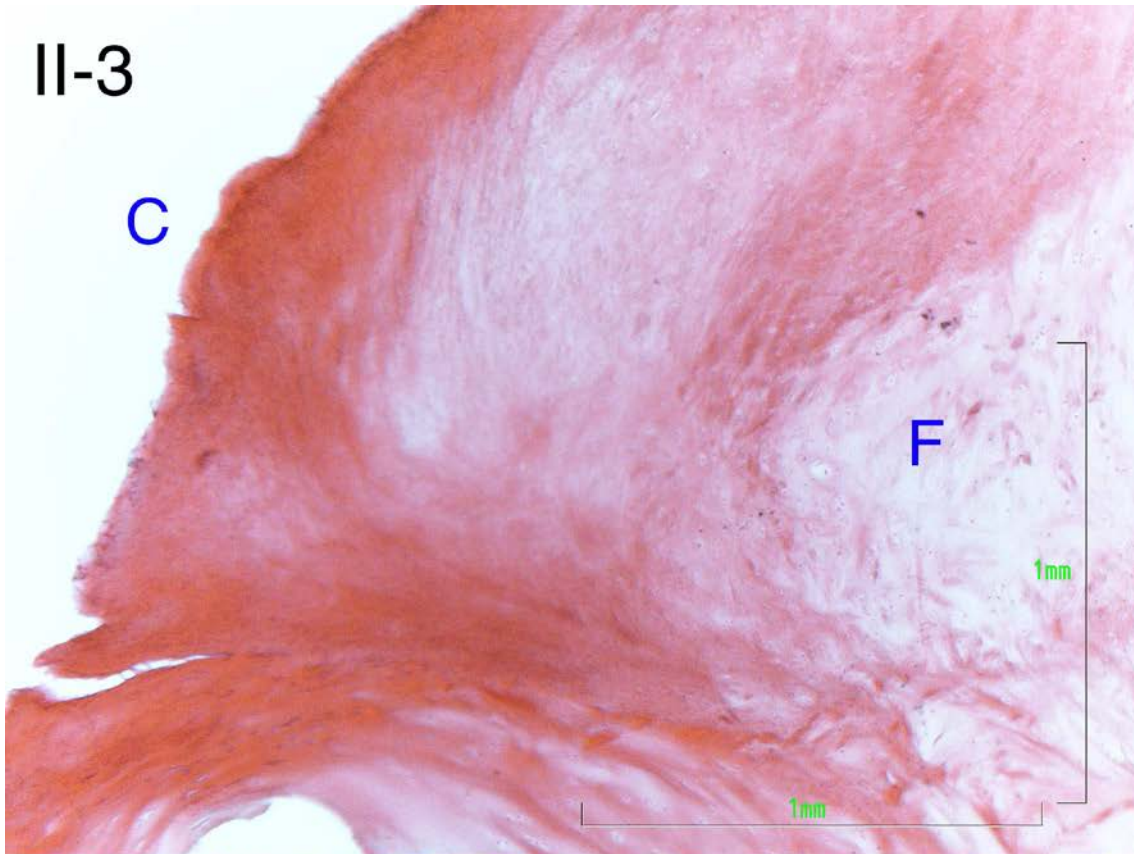


Figure 407. Base of Parsons' tubercle (detail of Figure 406), hematoxylin and eosin stain (II-3) and corresponding polarized light microscopy (II-4).

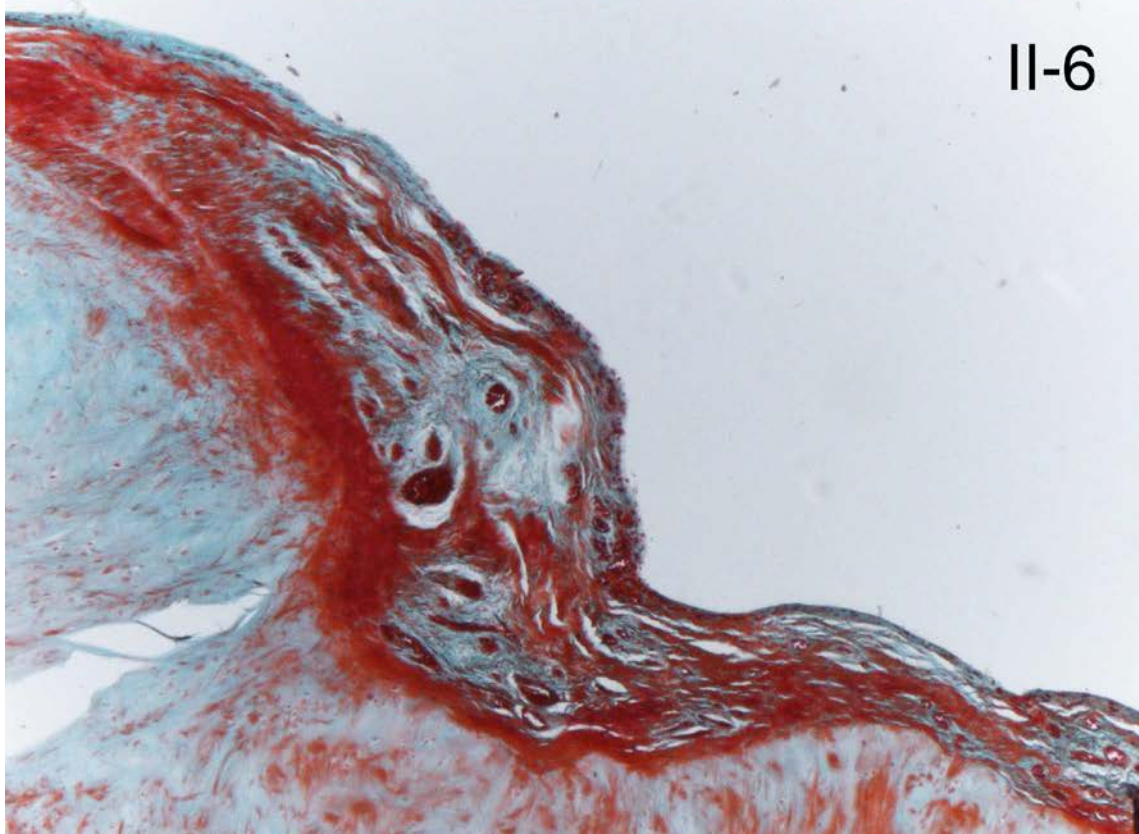
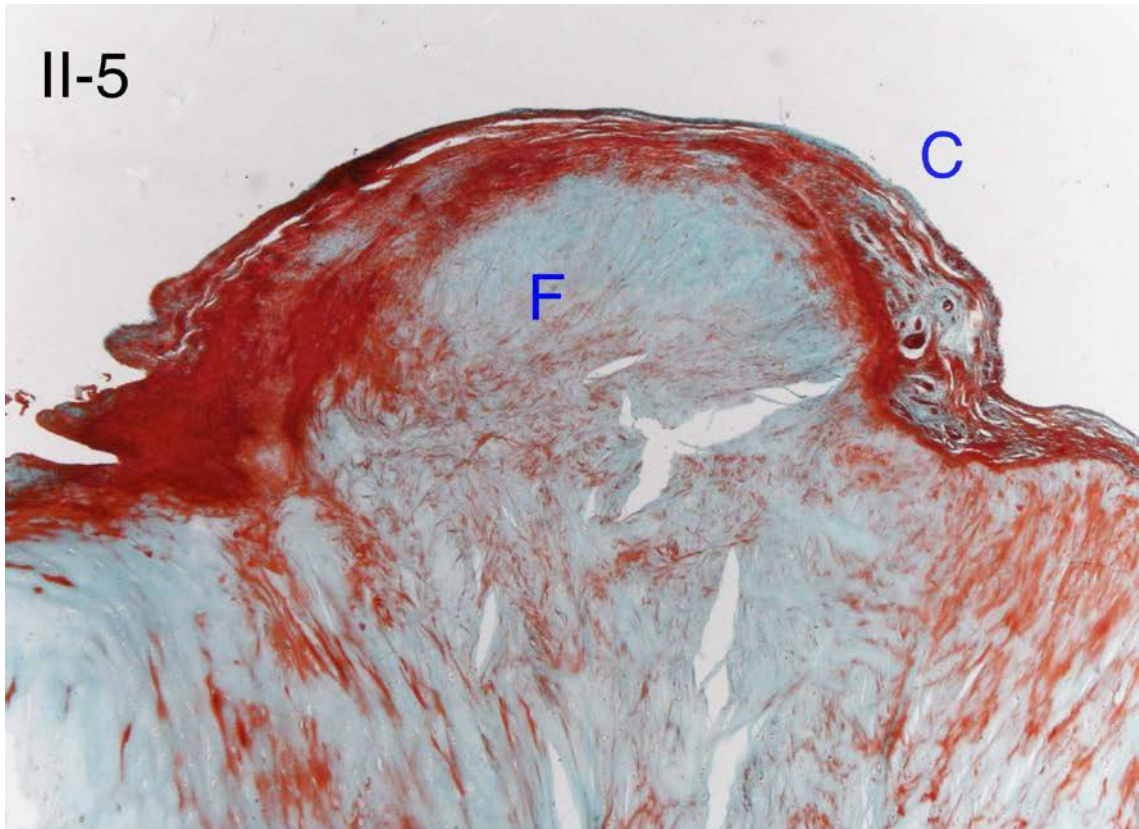


Figure 408. Sagittal cut of Parsons' tubercle (posterior aspect to the left, anterior to the right of the image). Masson's trichrome stain, with muscle fibers in red/pink, collagen in blue/green, and nuclei in brown (II-5). Detail of its anterior base (II-6). F: fibrocartilage; C: connective tissue.

IV.12. Osteophytes and diagnosis of osteoarthritis

IV.12.1. Osteophyte grade and maximum attrition zone of the condyles

Osteophytes were investigated to assess the association of their growth (osteophyte grade) with areas of bone attrition (MAC) in the medial condyle. Results of the comparison (and frequency distribution analysis) were as follows:

- MT (Figure 409), $\chi^2(21)=54.011$, $p<0.001$ (Phi=0.762; Cramer's V=0.440): lower grades with 1M, a constant distribution with 2M, and higher grades found with 3M, 4M.
- MT Width (Figure 410), $\chi^2(21)=54.011$, $p<0.001$ (Phi=0.598; Cramer's V=0.345): lower grades with 1M, a constant distribution with 2M, higher grades with 3M, and highest with 4M.
- LT (Figure 411), $\chi^2(15)=43.114$, $p<0.001$ (Phi=0.681; Cramer's V=0.393): lower grades with 1M, intermediate with 2M, higher grades with 3M, and highest with 4M.
- LT Width (Figure 412), $\chi^2(12)=29.116$, $p=0.004$ (Phi=0.560; Cramer's V=0.323): lower grades with 1M, higher grades with 3M, 4M, and also 2M.
- B1 (Figure 413), $\chi^2(9)=22.634$, $p=0.007$ (Phi=0.493; Cramer's V=0.285): lower grades with 1M and 2M, higher with 3M and 4M.
- B2 (Figure 414), $\chi^2(12)=45.490$, $p<0.001$ (Phi=0.699; Cramer's V=0.404): lower grades with 1M, intermediate grades with 2M, and higher grades with 3M and 4M.
- C1 (Figure 415), $\chi^2(12)=24.351$, $p=0.018$ (Phi=0.512; Cramer's V=0.295): lower grades with 1M, intermediate with 2M, higher with 3M, and highest with 4M.
- C2 (Figure 416), $\chi^2(9)=10.109$, $p=0.342$.
- D1–D2 (Figure 417), $\chi^2(12)=8.174$, $p=0.771$.
- D3 (Figure 418), $\chi^2(12)=19.692$, $p=0.073$ (Phi=0.460; Cramer's V=0.266): lower grades with 1M, intermediate with 2M, higher with 3M, and highest in 4M.
- E1 (Figure 419), $\chi^2(12)=45.706$, $p<0.001$ (Phi=0.701; Cramer's V=0.405): lower grades with 1M, 2M, higher grades with 4M, and highest grades in 3M.
- E2 (Figure 420), $\chi^2(12)=8.325$, $p=0.759$.

- F1 (Figure 421), $\chi^2(12)=10.647$, $p=0.559$.
- F2 (Figure 422), $\chi^2(9)=20.017$, $p=0.018$ (Phi=0.464; Cramer's V=0.268): lower grades with 1M, 2M, higher grades with 4M, and highest with 3M.
- G (Figure 423), $\chi^2(15)=27.548$, $p=0.025$ (Phi=0.544; Cramer's V=0.314): lower grades with 1M, 2M, higher grades with 3M, 4M.
- H (Figure 424), $\chi^2(12)=12.988$, $p=0.370$.
- J (Figure 425), $\chi^2(12)=24.262$, $p=0.019$ (Phi=0.514; Cramer's V=0.296): lower grades with 1M, 2M, higher grades with 3M, 4M.
- N (Figure 426), $\chi^2(12)=15.566$, $p=0.212$.
- I (Figure 427), $\chi^2(12)=15.432$, $p=0.219$.
- AM corner (Figure 428), $\chi^2(12)=21.594$, $p=0.042$ (Phi=0.482; Cramer's V=0.278): lower grades found with 1M, 2M, higher grades with 3M, 4M.
- AL corner (Figure 429), $\chi^2(15)=25.258$, $p=0.047$ (Phi=0.521; Cramer's V=0.301): lower grades with 1M, intermediate with 2M, higher with 4M, and highest with 3M.
- Medial rim, anterior part (Figure 430), $\chi^2(9)=25.902$, $p=0.002$ (Phi=0.528; Cramer's V=0.305): lowest grades with 1M, low grades with 2M, higher with 3M, highest with 4M.
- Medial rim, posterior part (Figure 431), $\chi^2(12)=23.829$, $p=0.021$ (Phi=0.506; Cramer's V=0.292): lower grades with 1M, intermediate with 2M, and higher grades with 3M, 4M.
- Lateral rim, anterior part (Figure 432), $\chi^2(12)=34.702$, $p=0.001$ (Phi=0.611; Cramer's V=0.353): lower grades with 1M, intermediate with 2M, higher with 3M, and highest with 4M.
- Lateral rim, posterior part (Figure 433), $\chi^2(12)=17.999$, $p=0.116$ (Phi=0.440; Cramer's V=0.254): lower grades with 1M, 2M, higher grades with 4M, and highest grades with 3M.
- PM corner (Figure 434), $\chi^2(12)=31.763$, $p=0.007$ (Phi=0.584; Cramer's V=0.337): lower grades with 1M, intermediate with 2M, higher grades with 3M, 4M.
- PL corner (Figure 435), $\chi^2(15)=28.322$, $p=0.020$ (Phi=0.552; Cramer's V=0.319): lower grades with 1M, 2M, intermediate to high grades with 3M, 4M.
- AL fossa (Figure 436), $\chi^2(18)=20.548$, $p=0.303$.
- T (Figure 437), $\chi^2(12)=13.247$, $p=0.351$.

- AL vallecule (Figure 438), $\chi^2(27)=21.759$, $p=0.750$.
- AL recess (Figure 439), $\chi^2(15)=18.460$, $p=0.239$.
- PM recess (Figure 440), $\chi^2(21)=20.898$, $p=0.465$.
- PL recess (Figure 441), $\chi^2(18)=23.100$, $p=0.187$.
- 14a-14b ridge, C4 (Figure 442), $\chi^2(9)=5.563$, $p=0.783$.
- C3 (Figure 443), $\chi^2(12)=15.590$, $p=0.211$.
- E3 (Figure 444), $\chi^2(12)=12.394$, $p=0.415$.
- Area 13 horizontality (Figure 445), $\chi^2(12)=2.764$, $p=0.429$.

No significant association was found between osteophyte grade and maximal attrition in the lateral condyle.

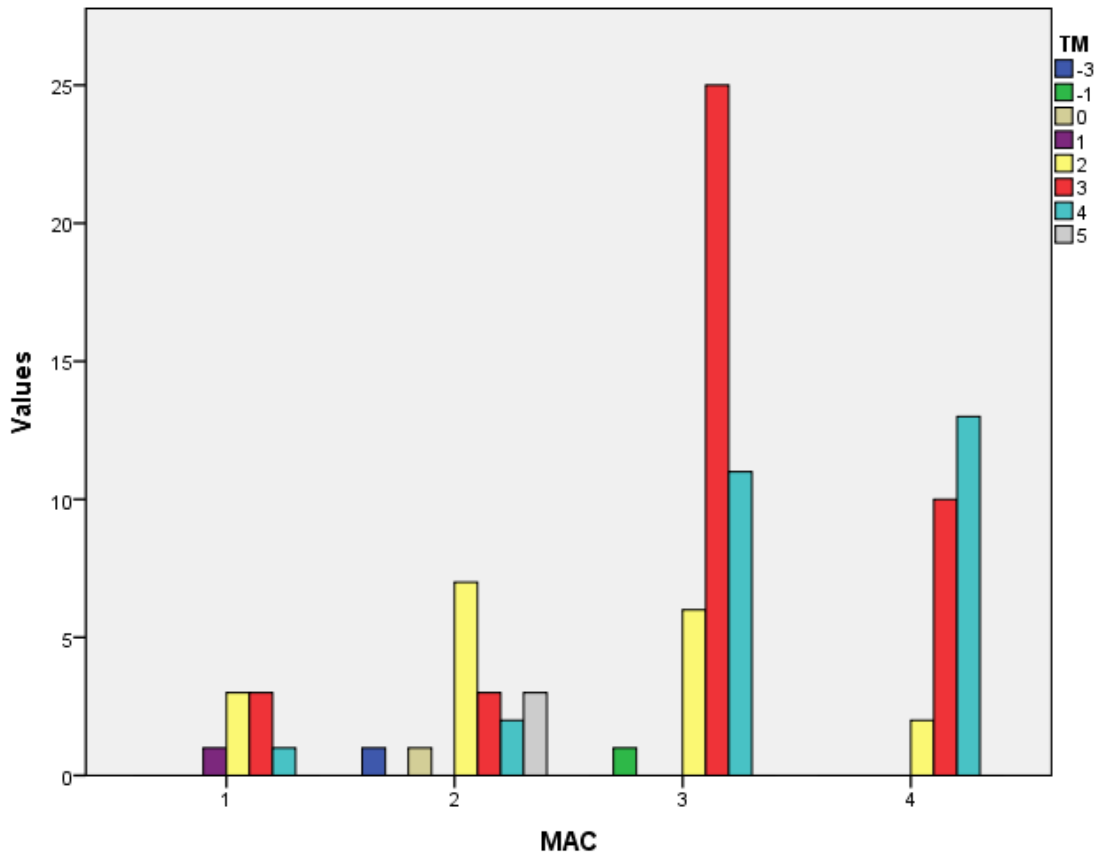


Figure 409. Study II. Histogram of MT osteophyte grade (TM): number of varus knees in each category, grouped by maximum attrition area of the medial condyle of the tibia.

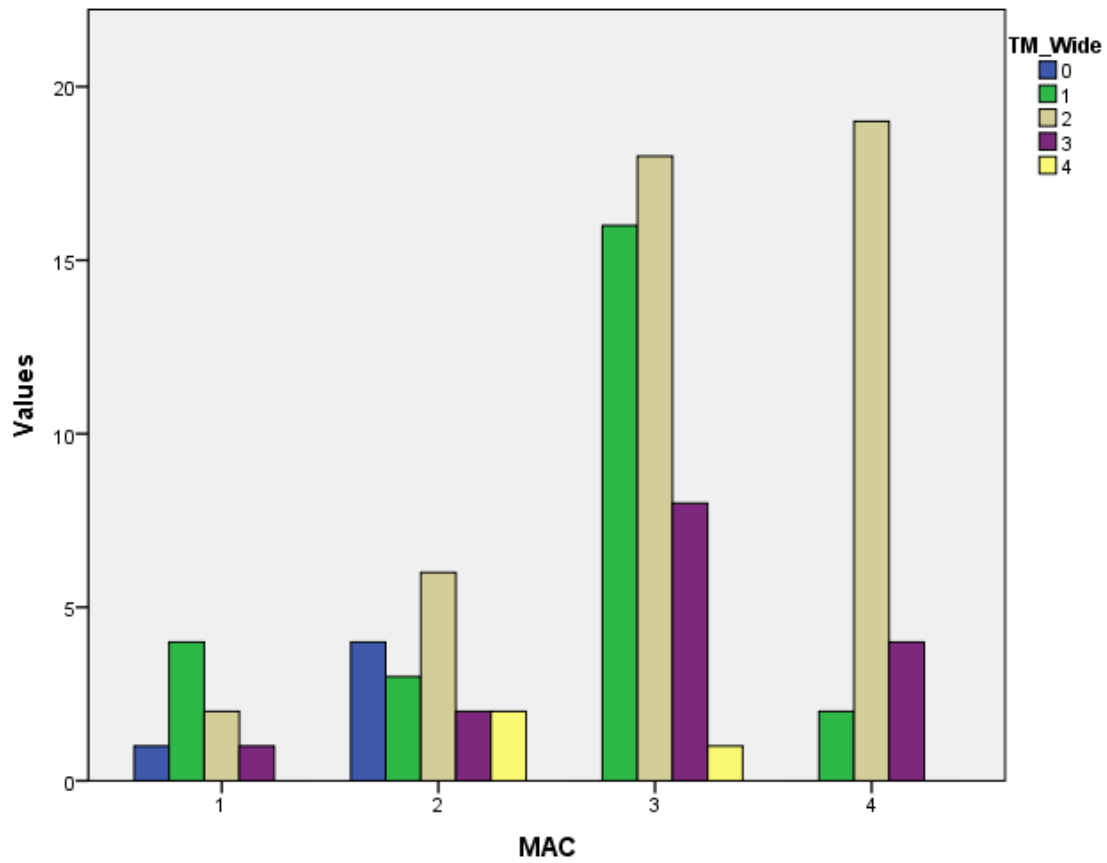


Figure 410. Study II. Histogram of MT width (TM_Wide): number of varus knees in each category, grouped by maximum attrition area of the medial condyle of the tibia.

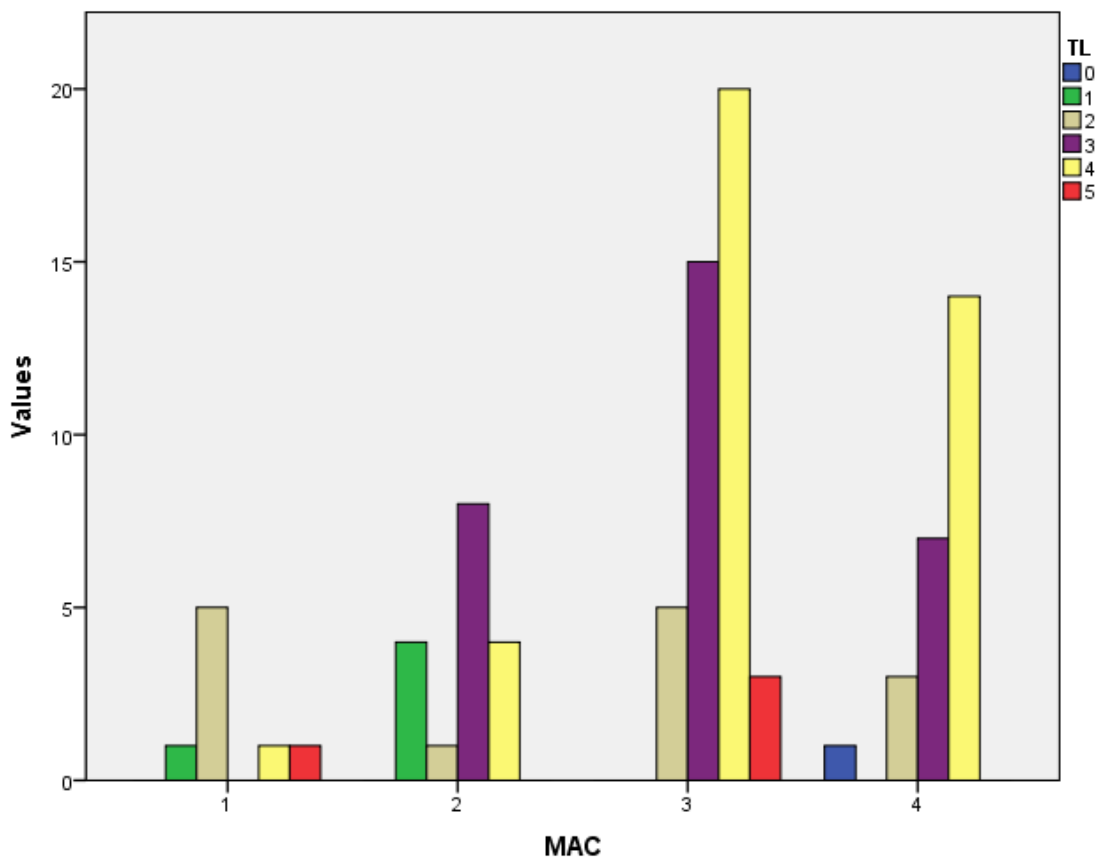


Figure 411. Study II. Histogram of LT osteophyte grade (TL): number of varus knees in each category, grouped by maximum attrition area of the medial condyle of the tibia.

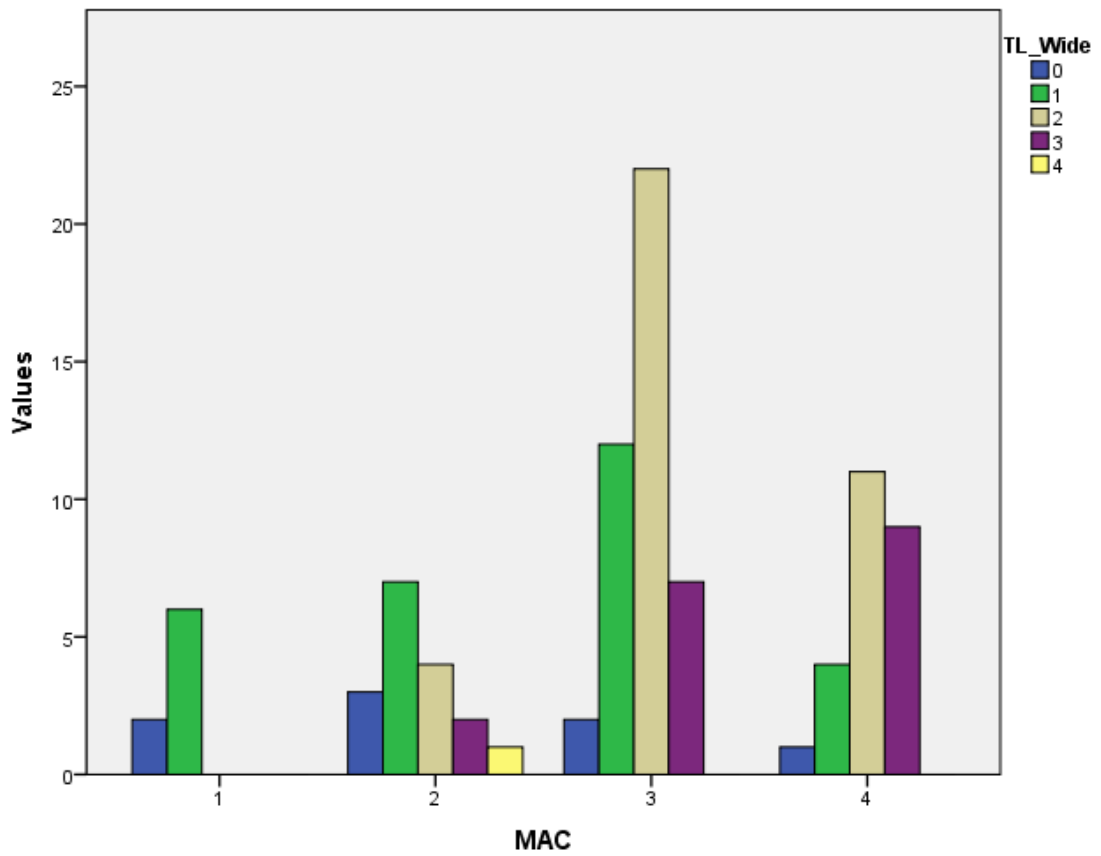


Figure 412. Study II. Histogram of LT width (TL_Wide): number of varus knees in each category, grouped by maximum attrition area of the medial condyle of the tibia.

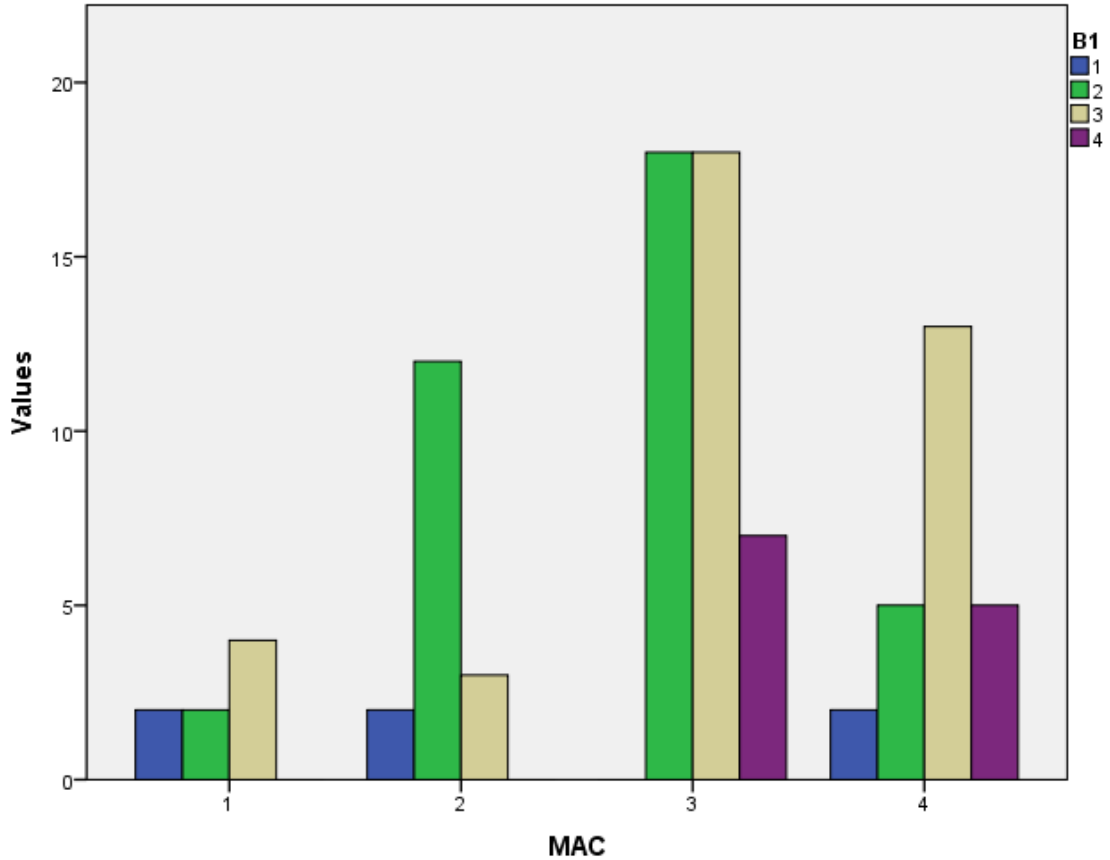


Figure 413. Study II. Histogram of external AMIR process (B1) osteophyte grade: number of varus knees in each category, grouped by maximum attrition area of the medial condyle.

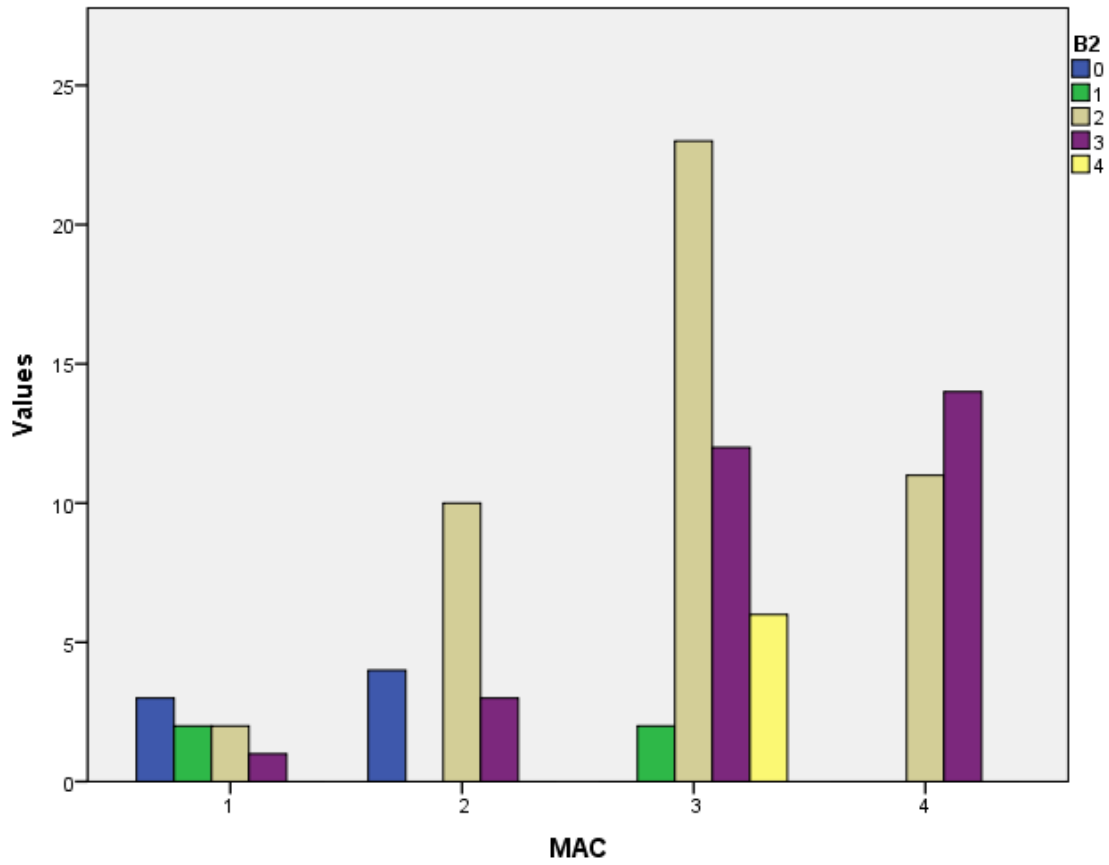


Figure 414. Study II. Histogram of central AMIR process (B2) osteophyte grade: number of varus knees in each category, grouped by maximum attrition area of the medial condyle.

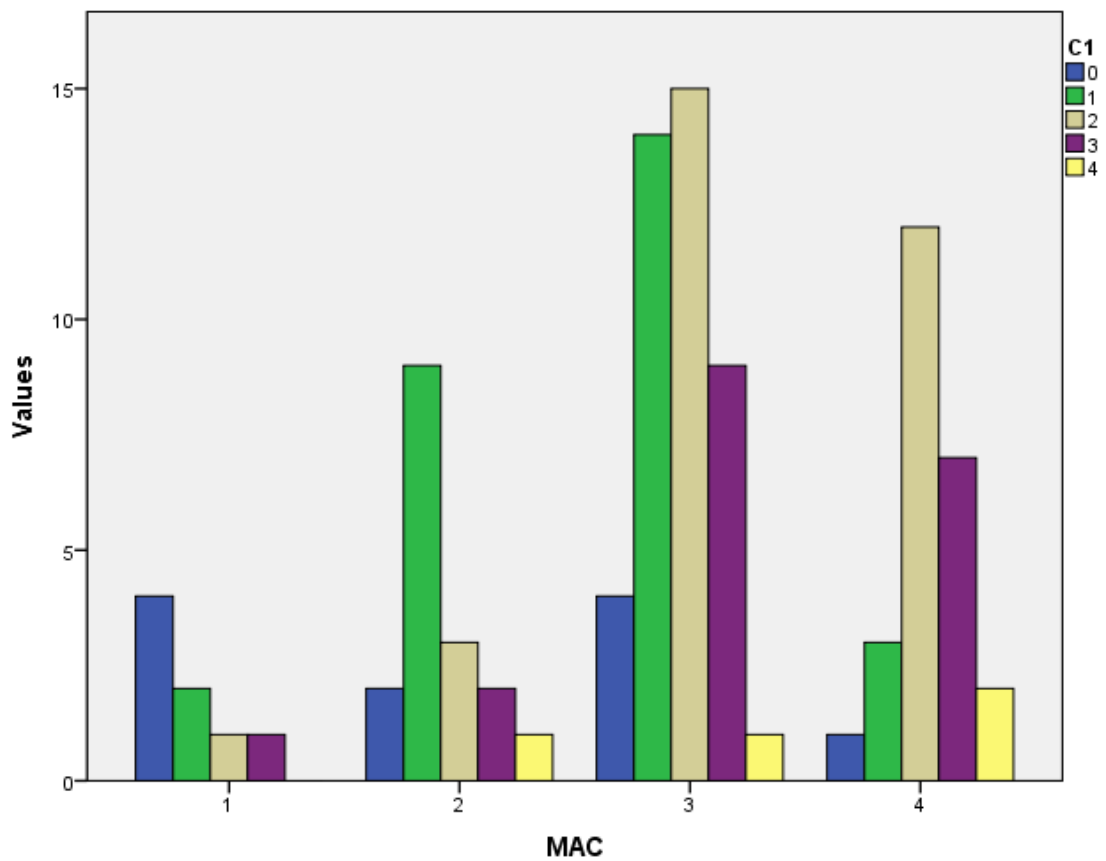


Figure 415. Study II. Histogram of central PMIR process (C1) osteophyte grade: number of varus knees in each category, grouped by maximum attrition area of the medial condyle.

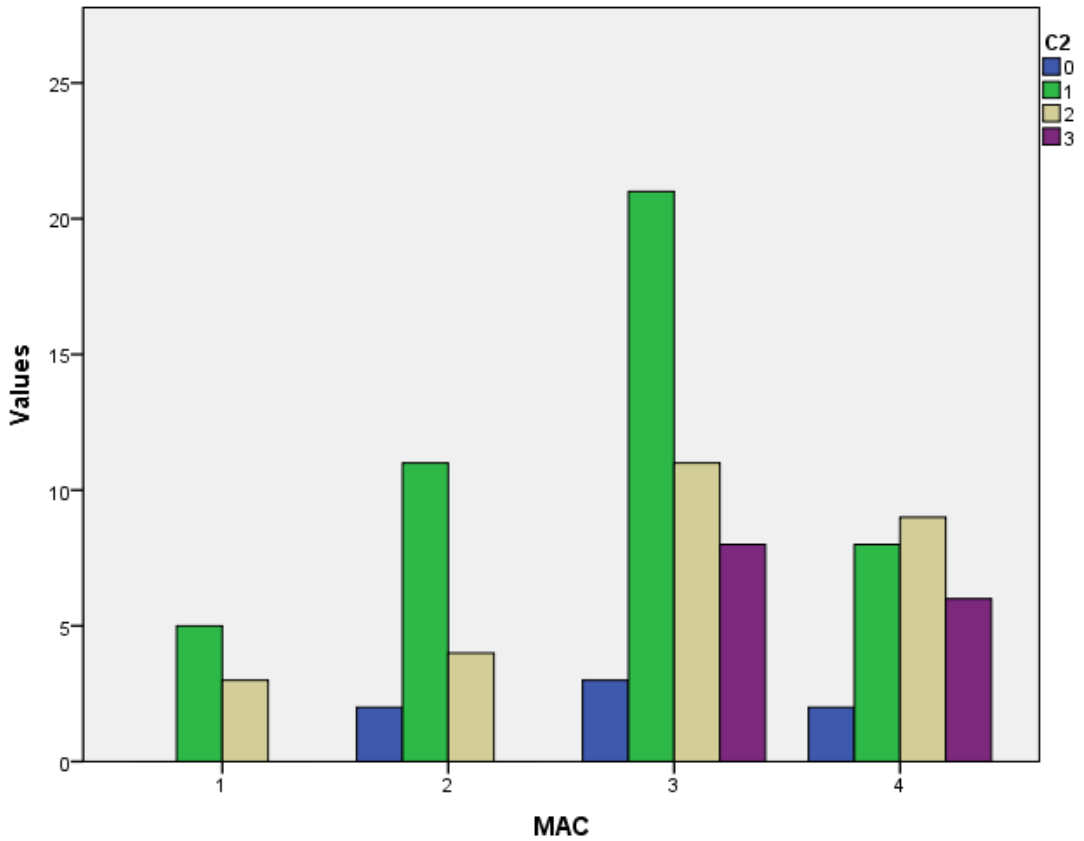


Figure 416. Study II. Histogram of external PMIR process (C2) osteophyte grade: number of varus knees in each category, grouped by maximum attrition area of the medial condyle.

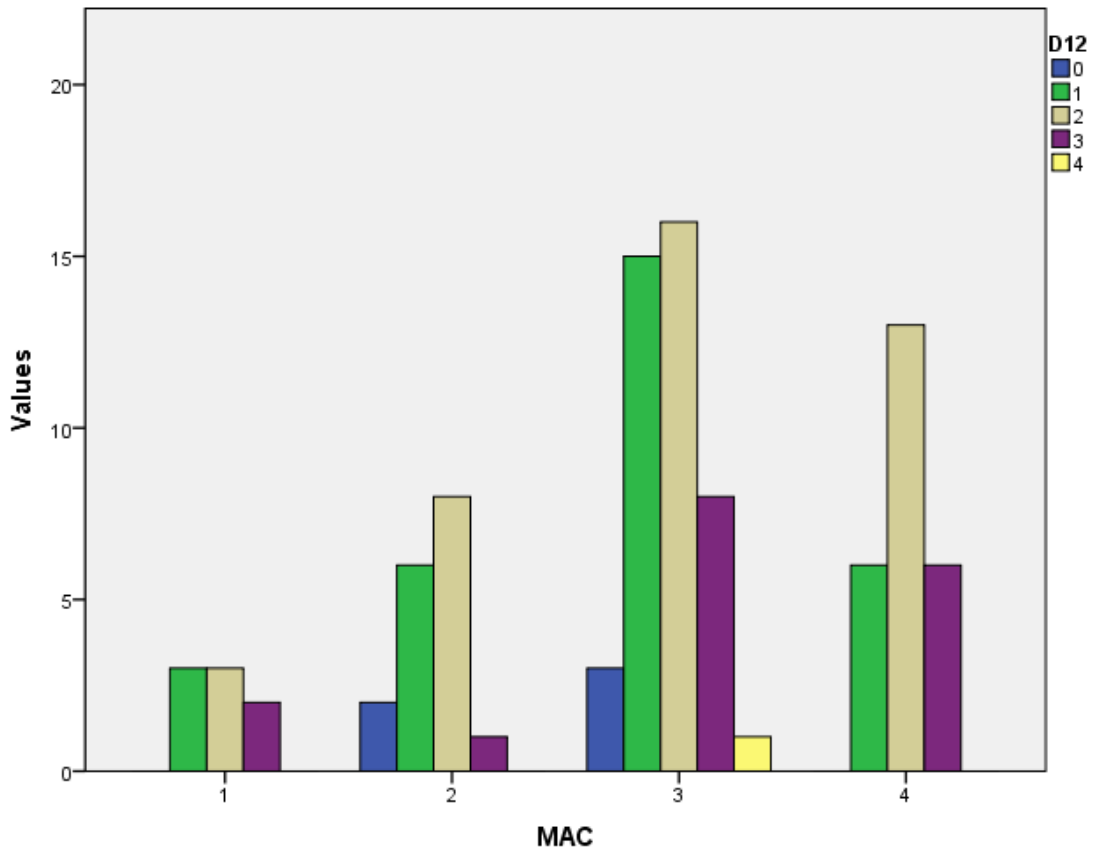


Figure 417. Study II. Histogram of central and external ALIR process (D1-D2) osteophyte grade: number of varus knees in each category, grouped by maximum attrition area of the medial condyle of the tibia.

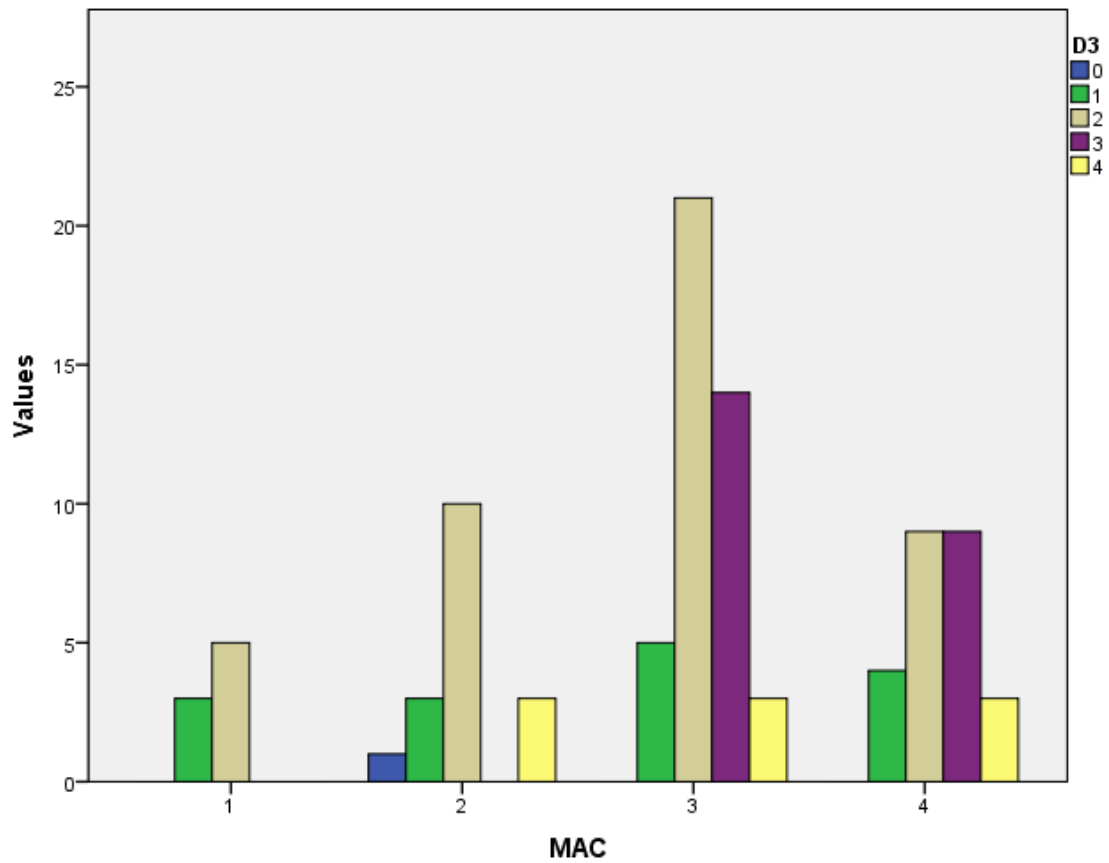


Figure 418. Study II. Histogram of internal ALIR process (D3) osteophyte grade: number of varus knees in each category, grouped by maximum attrition area of the medial condyle.

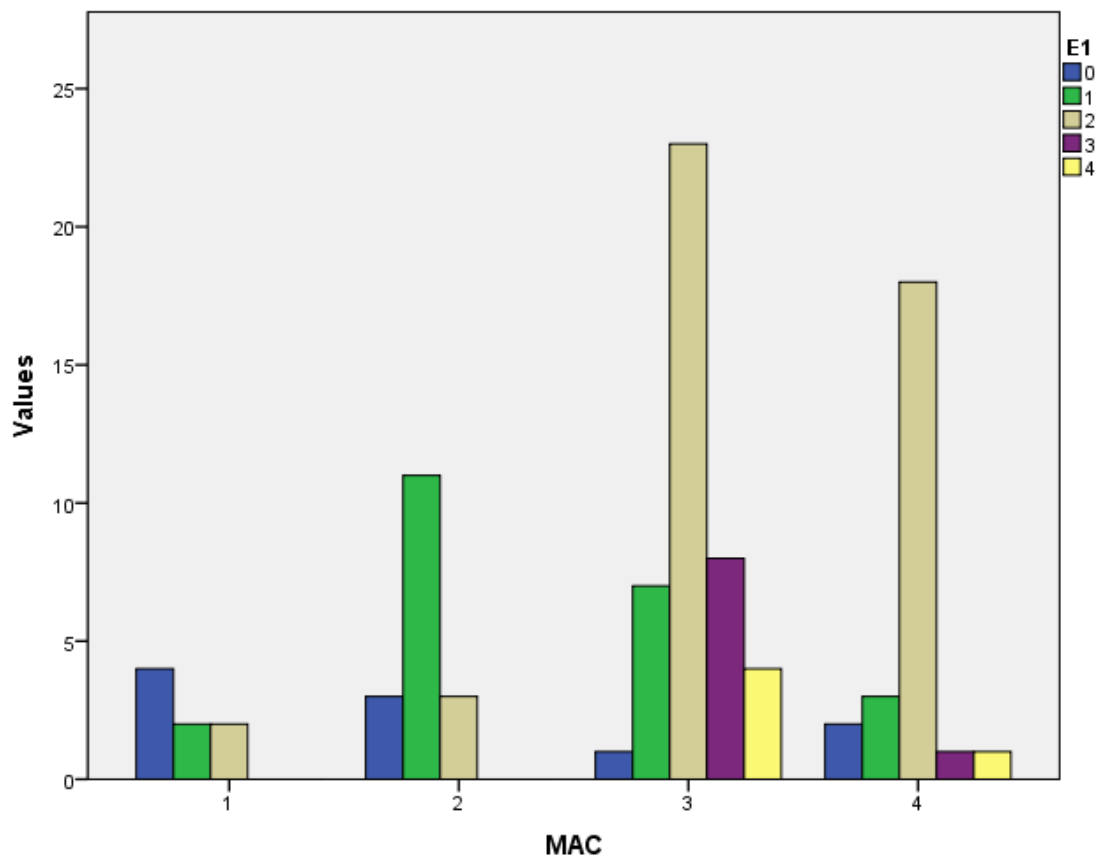


Figure 419. Study II. Histogram of central PLIR process (E1) osteophyte grade: number of varus knees in each category, grouped by maximum attrition area of the medial condyle of the tibia.

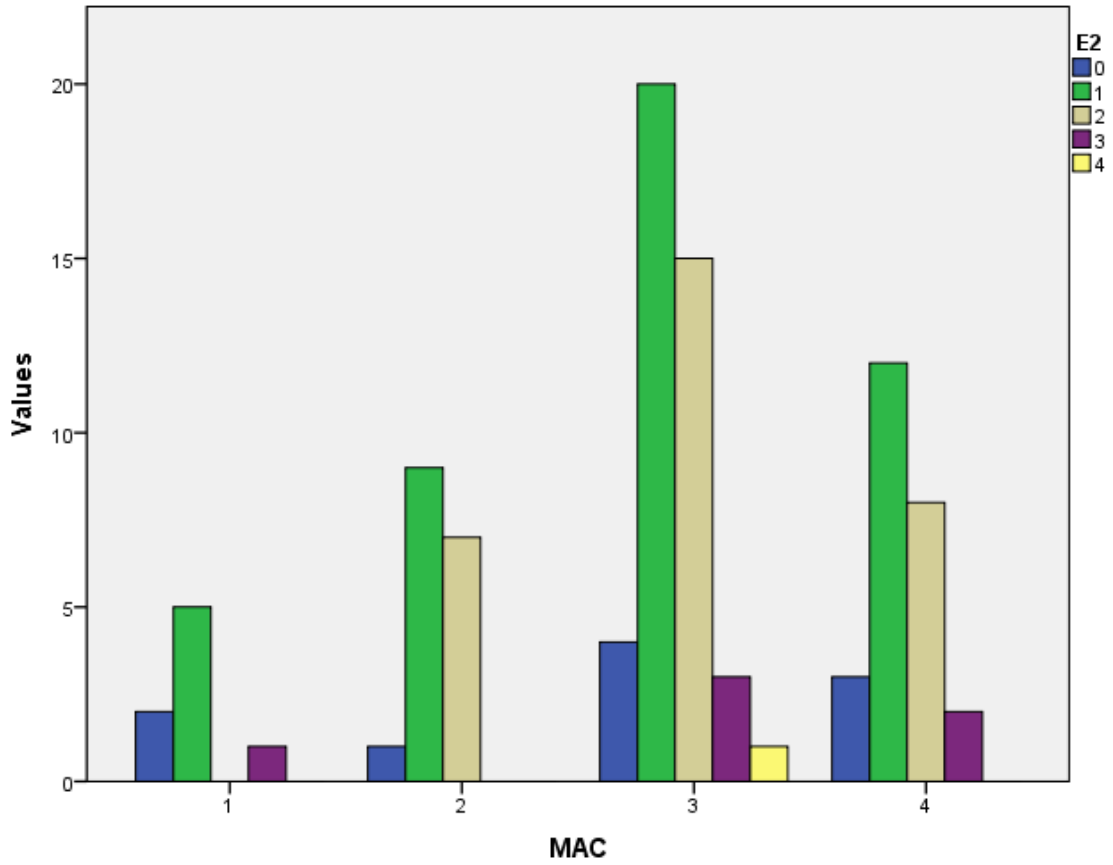


Figure 420. Study II. Histogram of external PLIR process (E2) osteophyte grade: number of varus knees in each category, grouped by maximum attrition area of the medial condyle.

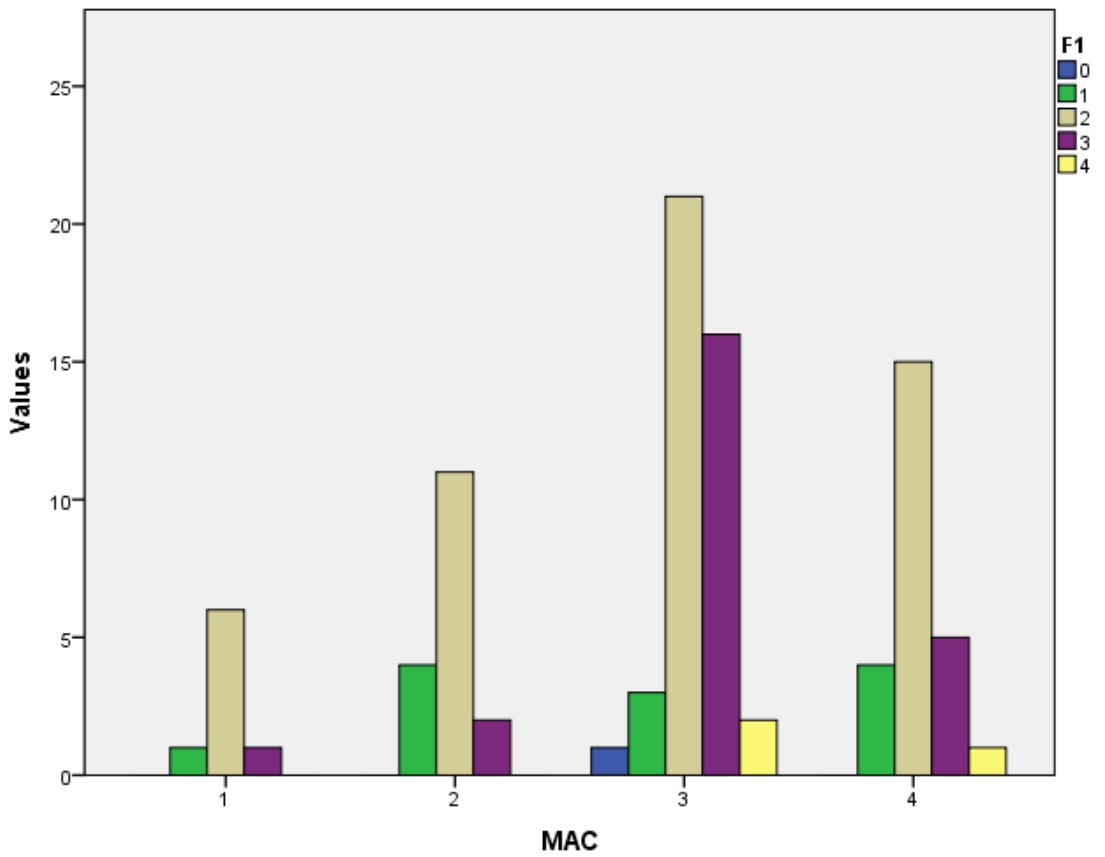


Figure 421. Study II. Histogram of posterior AFIR process (F1) osteophyte grade: number of varus knees in each category, grouped by maximum attrition area of the medial condyle.

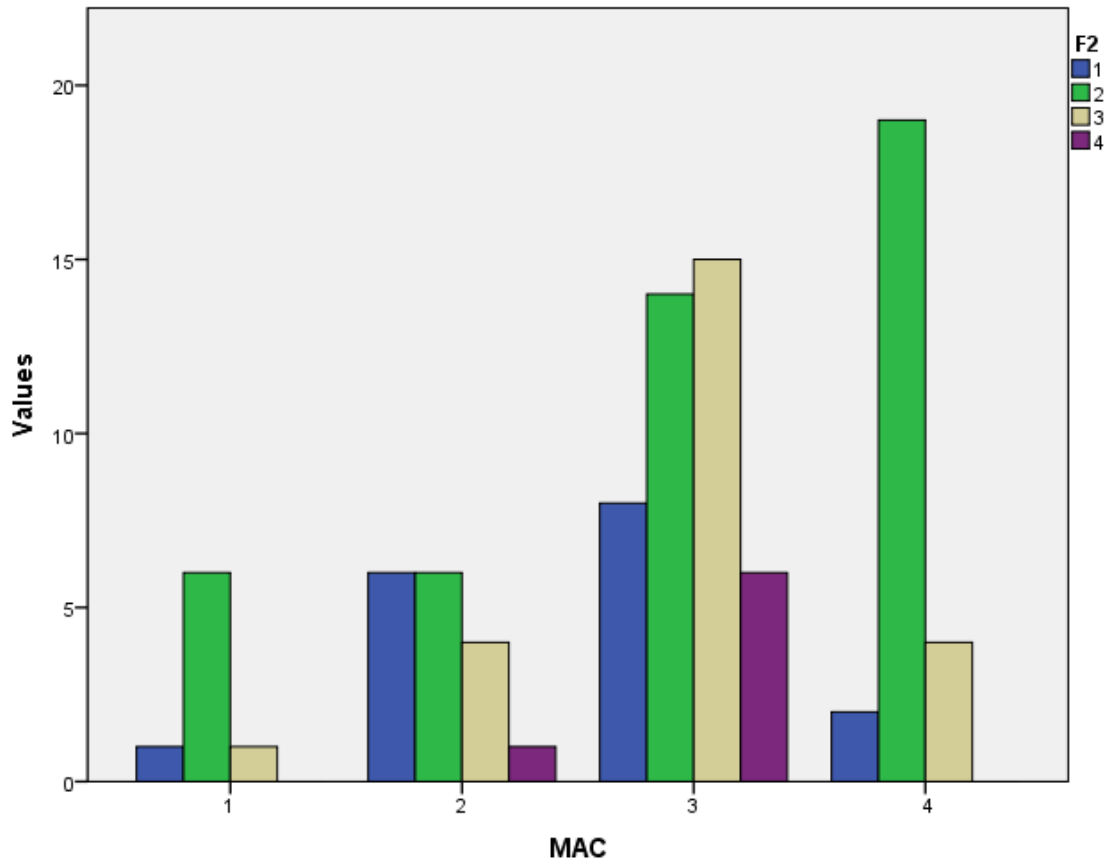


Figure 422. Study II. Histogram of anterior AFIR process (F2) osteophyte grade: number of varus knees in each category, grouped by maximum attrition area of the medial condyle.

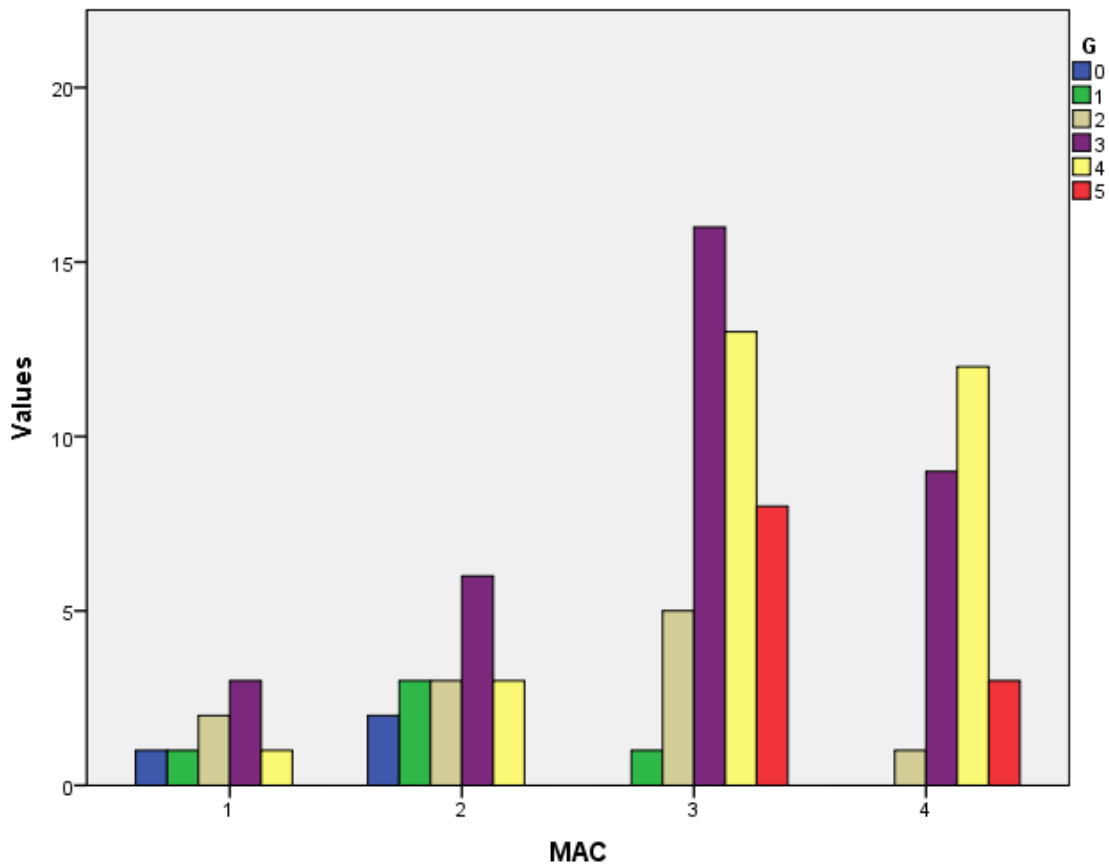


Figure 423. Study II. Histogram of Parsons' knob (G) osteophyte grade: number of varus knees in each category, grouped by maximum attrition area of the medial condyle of the tibia.

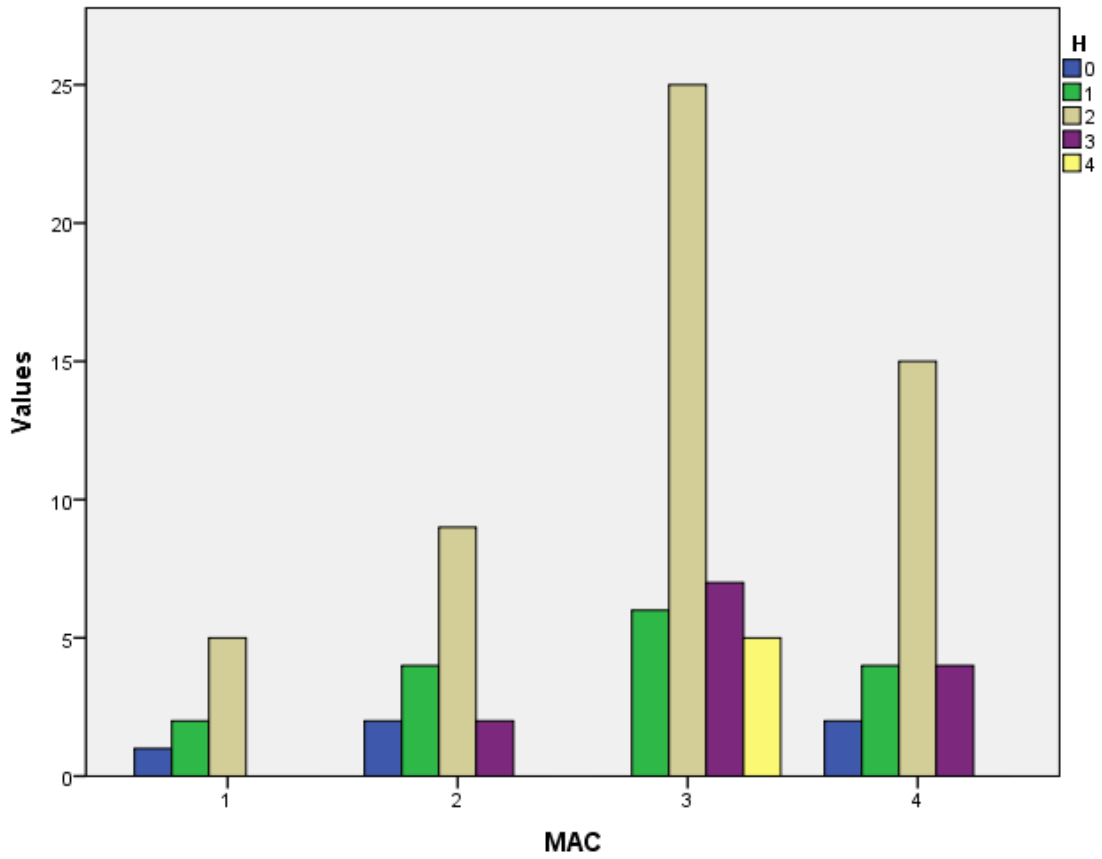


Figure 424. Study II. Histogram of ACIK (H) osteophyte grade: number of varus knees in each category, grouped by maximum attrition area of the medial condyle of the tibia.

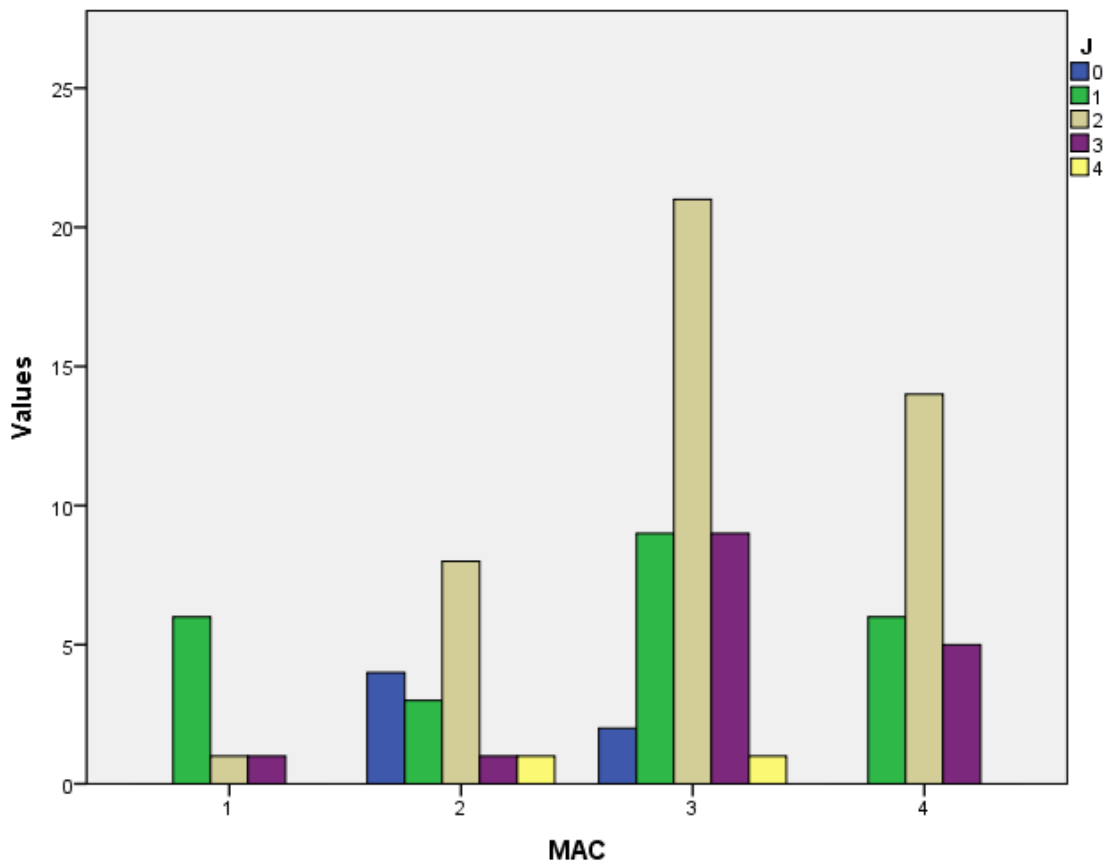


Figure 425. Study II. Histogram of ASIR (J) osteophyte grade: number of varus knees in each category, grouped by maximum attrition area of the medial condyle of the tibia.

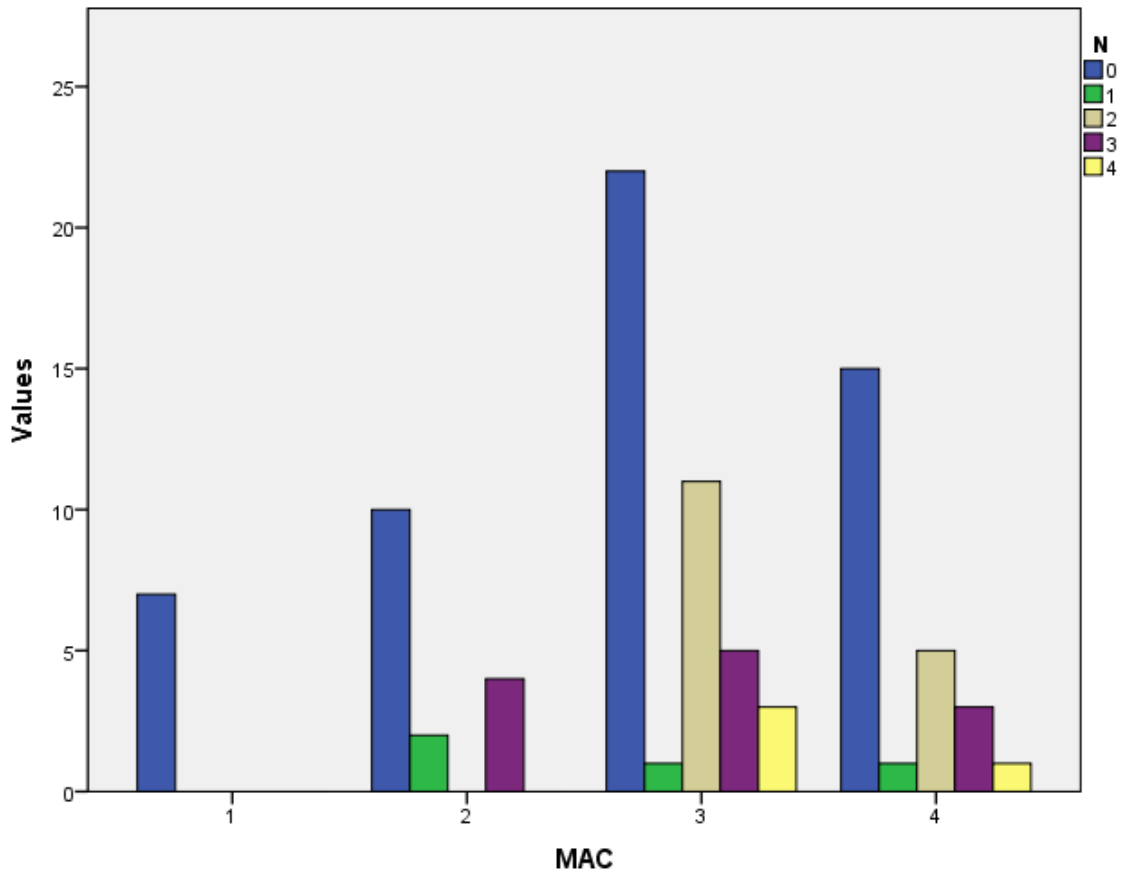


Figure 426. Study II. Histogram of AIK (N) osteophyte grade: number of varus knees in each category, grouped by maximum attrition area of the medial condyle of the tibia.

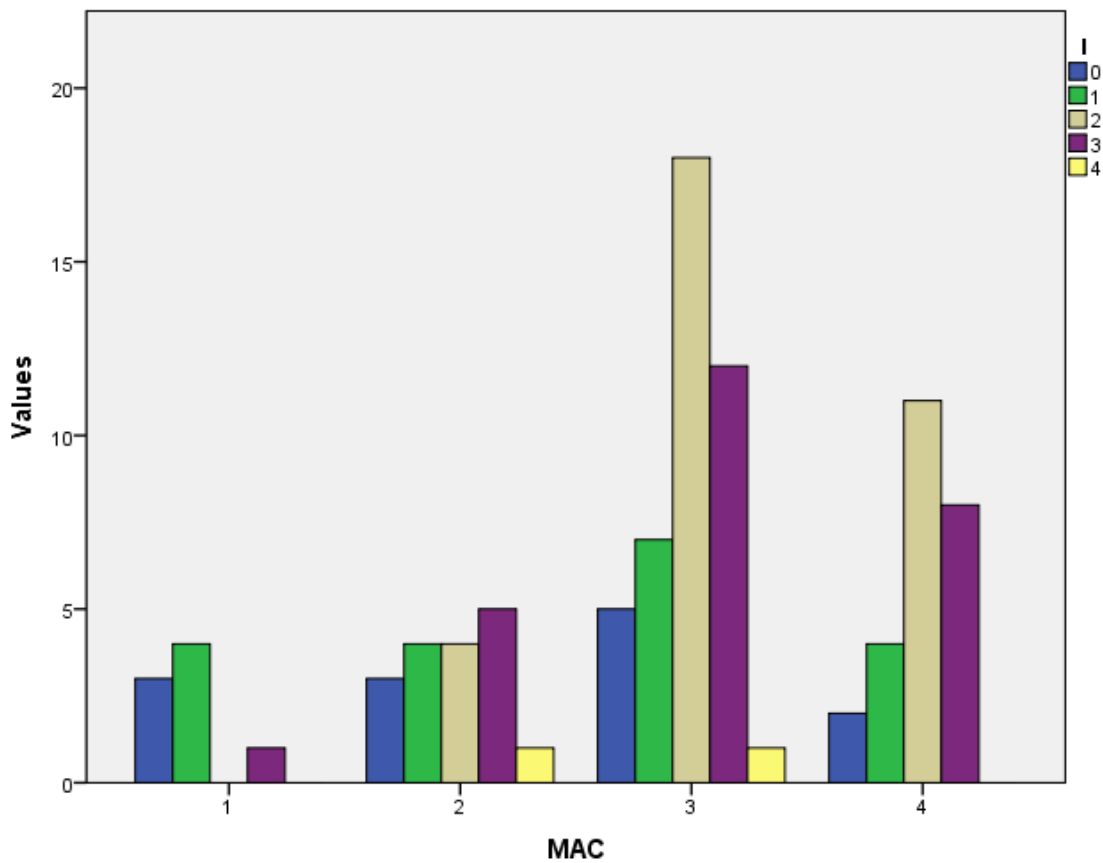


Figure 427. Study II. Histogram of ALIK (I) osteophyte grade: number of varus knees in each category, grouped by maximum attrition area of the medial condyle of the tibia.

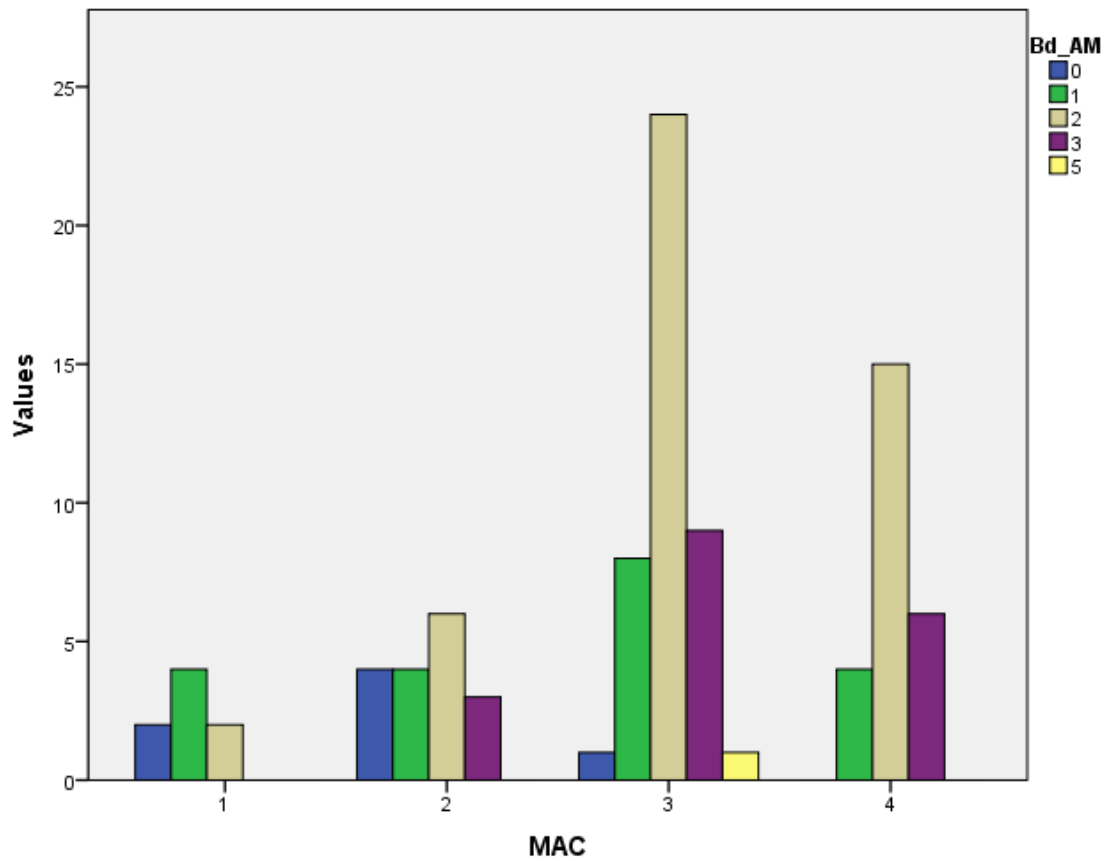


Figure 428. Study II. Histogram of AM corner (Bd_AM) osteophyte grade: number of varus knees in each category, grouped by maximum attrition area of the medial condyle of the tibia.

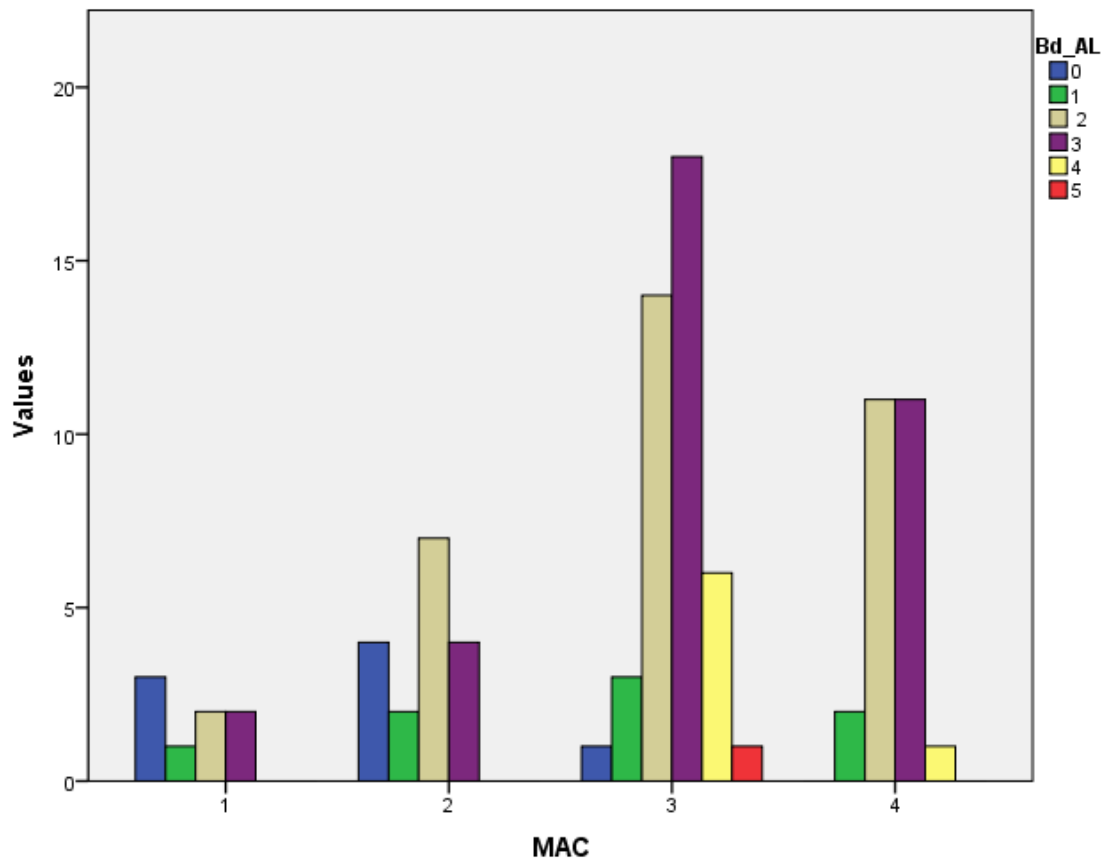


Figure 429. Study II. Histogram of AL corner (Bd_AL) osteophyte grade: number of varus knees in each category, grouped by maximum attrition area of the medial condyle of the tibia.

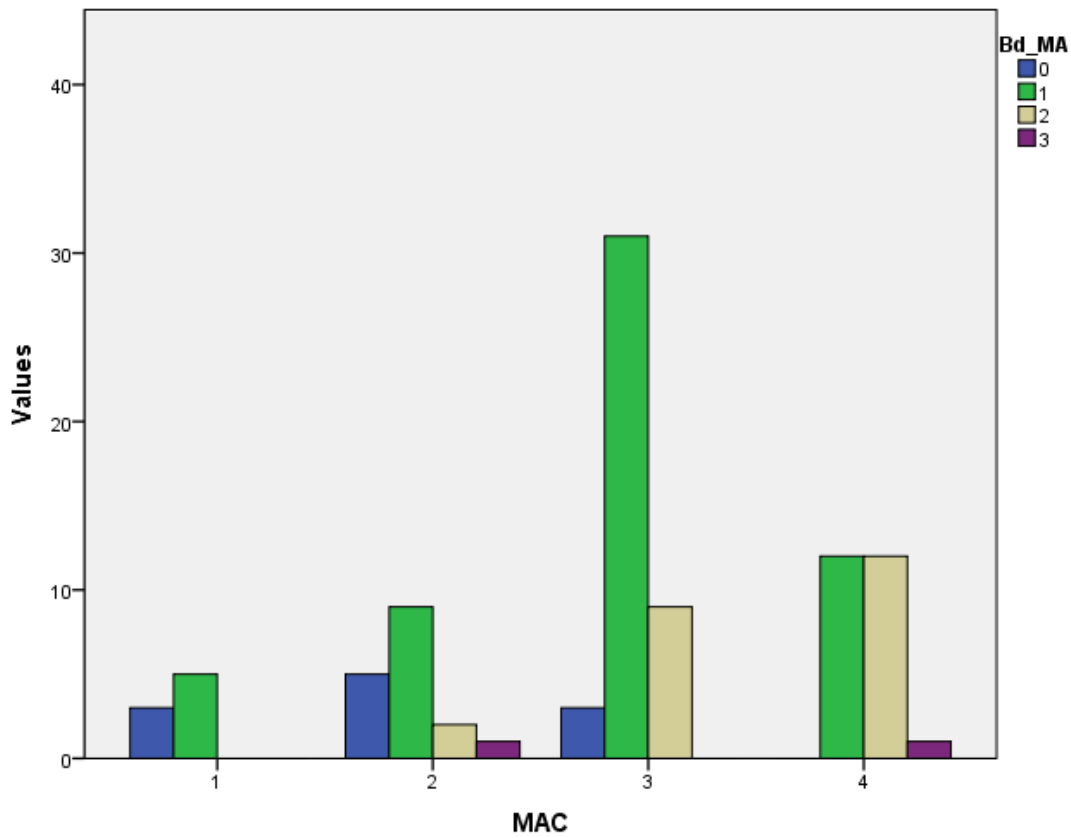


Figure 430. Study II. Histogram of medial rim, anterior part (Bd_MA), osteophyte grade: number of varus knees in each category, grouped by maximum attrition area of the medial condyle of the tibia.

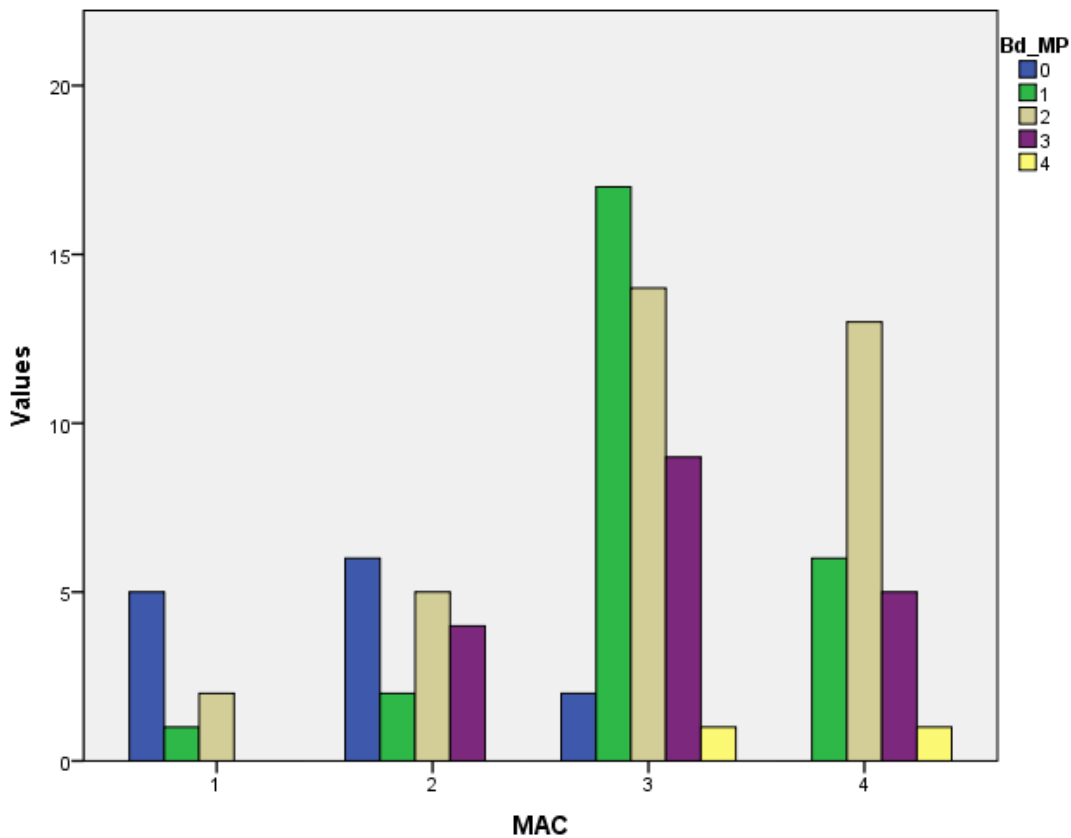


Figure 431. Study II. Histogram of medial rim, posterior part (Bd_MP), osteophyte grade: number of varus knees in each category, grouped by maximum attrition area of the medial condyle of the tibia.

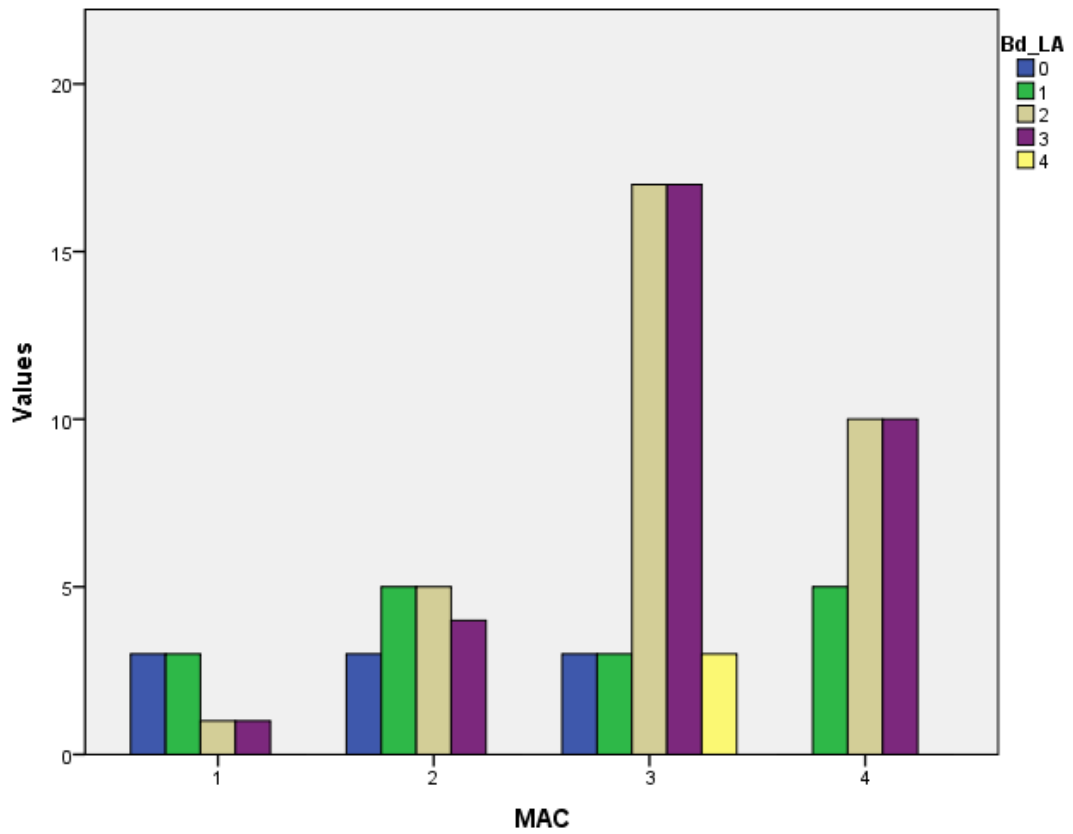


Figure 432. Study II. Histogram of lateral rim, anterior part (Bd_LA), osteophyte grade: number of varus knees in each category, grouped by maximum attrition area of the medial condyle of the tibia.

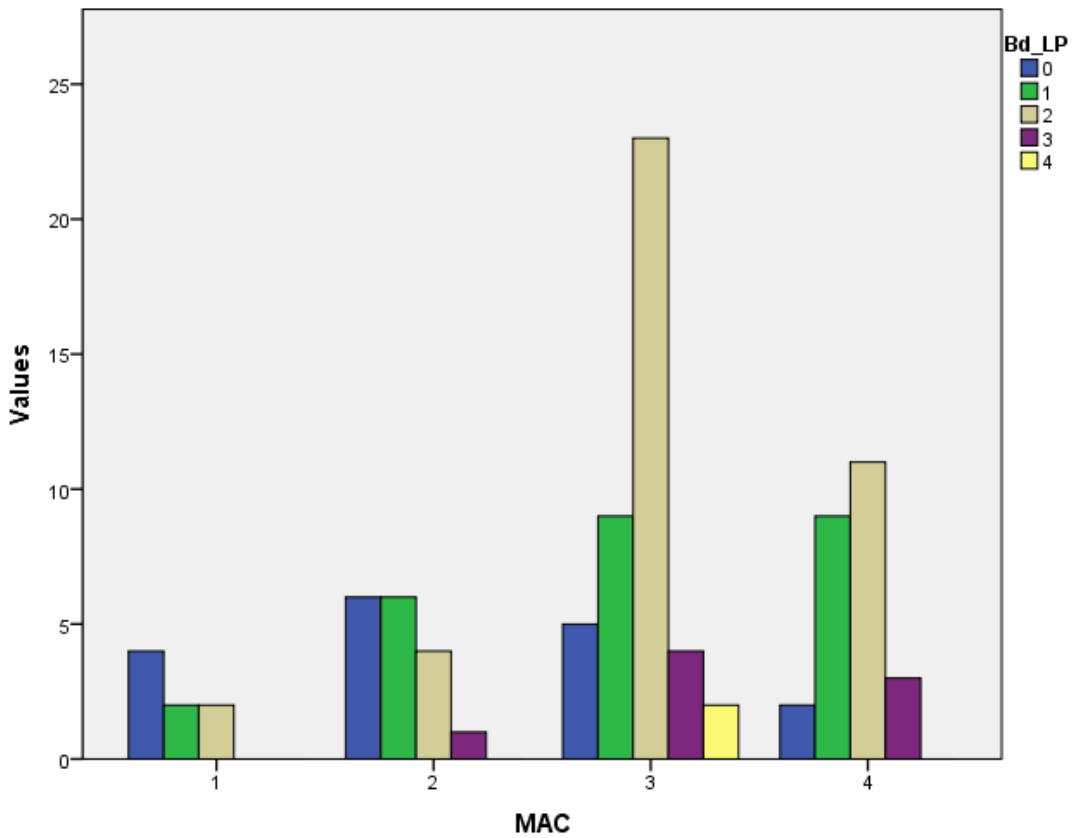


Figure 433. Study II. Histogram of lateral rim, posterior part (Bd_LP), osteophyte grade: number of varus knees in each category, grouped by maximum attrition area of the medial condyle of the tibia.

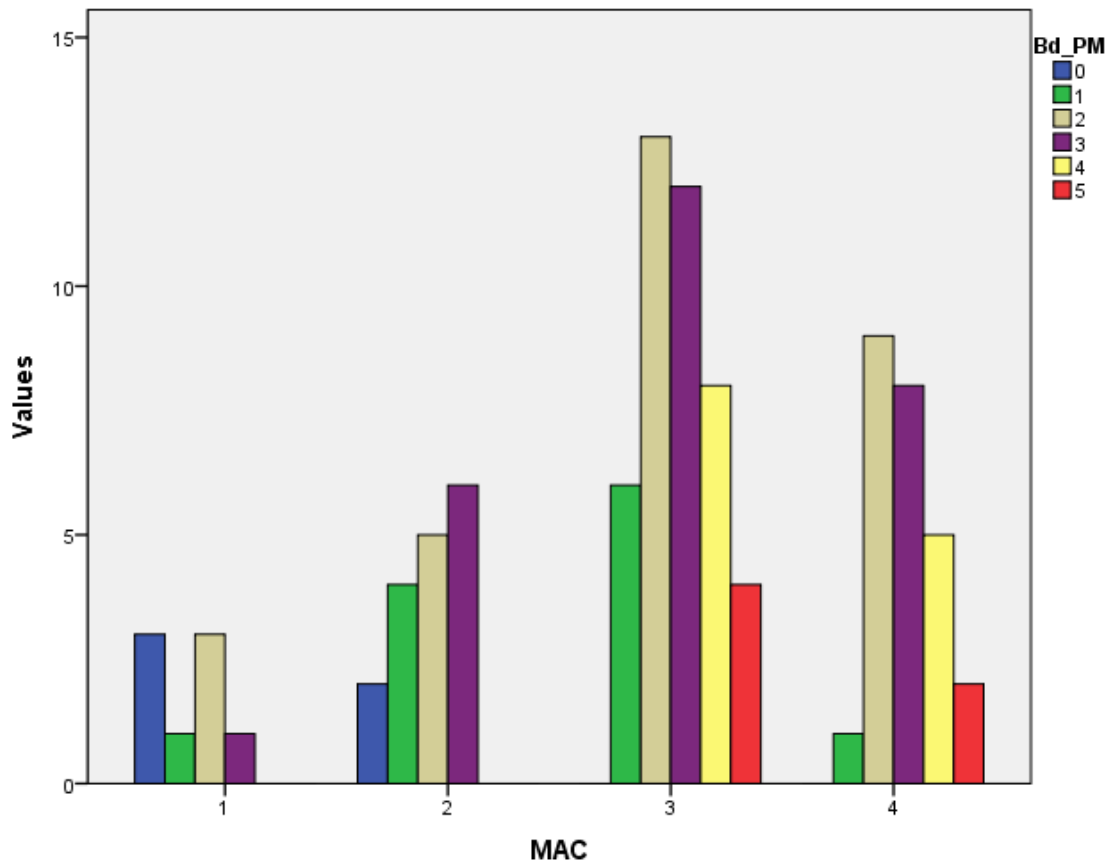


Figure 434. Study II. Histogram of PM corner (Bd_PM) osteophyte grade: number of varus knees in each category, grouped by maximum attrition area of the medial condyle.

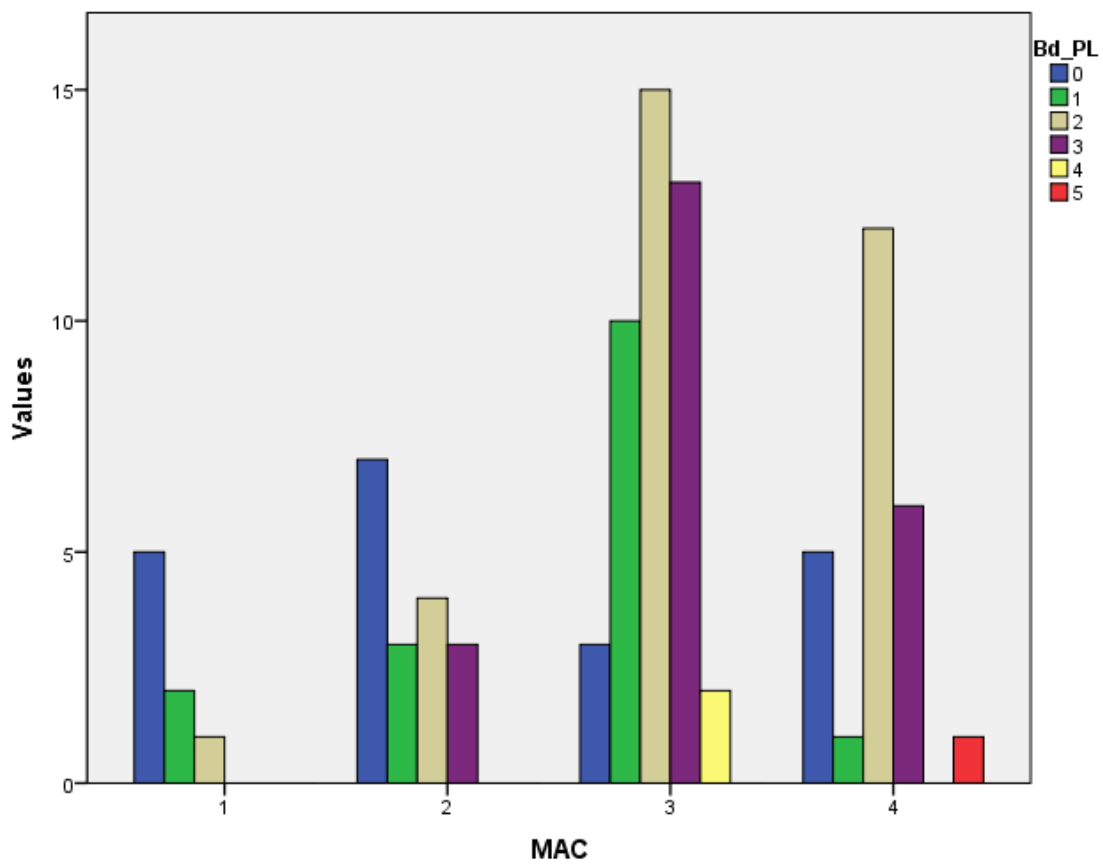


Figure 435. Study II. Histogram of PL corner (Bd_PL) osteophyte grade: number of varus knees in each category, grouped by maximum attrition area of the medial condyle.

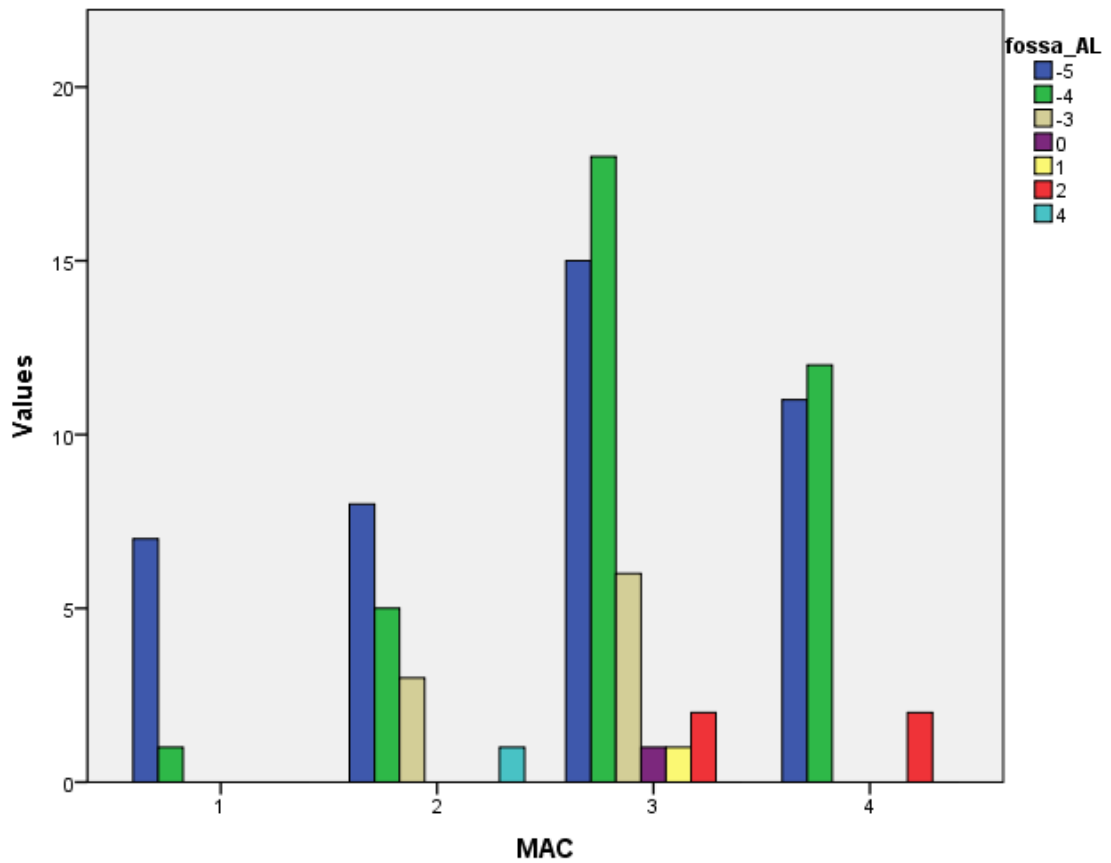


Figure 436. Study II. Histogram of AL fossa osteophyte grade: number of varus knees in each category, grouped by maximum attrition area of the medial condyle of the tibia.

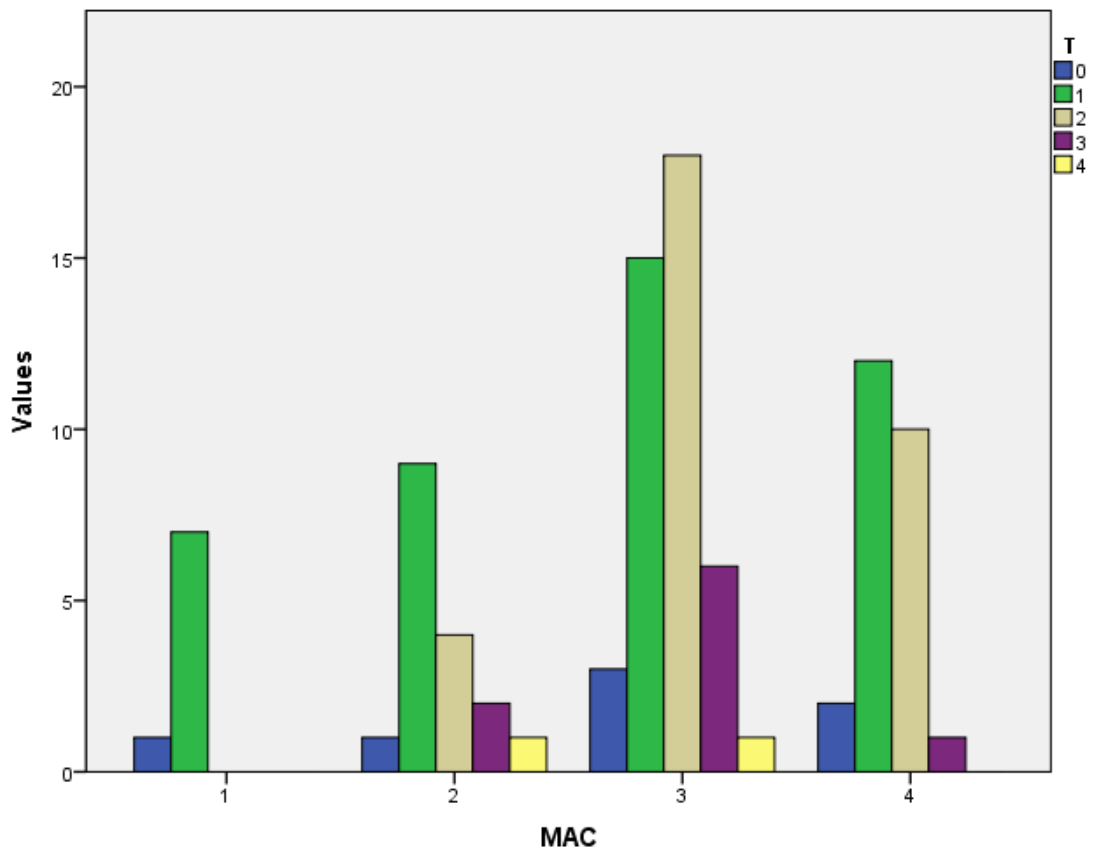


Figure 437. Study II. Histogram of anterior saddle (T) osteophyte grade: number of varus knees in each category, grouped by maximum attrition area of the medial condyle.

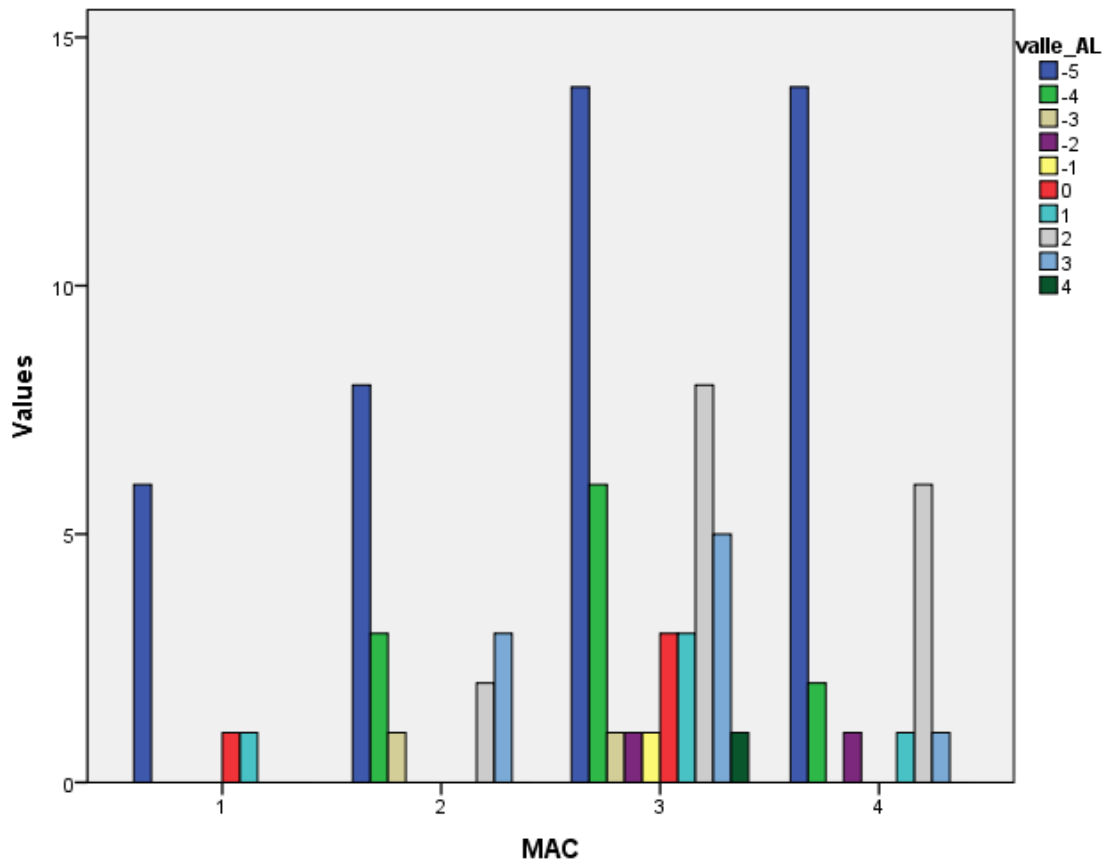


Figure 438. Study II. Histogram of AL vallecula (valle_AL) elevation grade: number of varus knees in each category, grouped by maximum attrition area of the medial condyle.

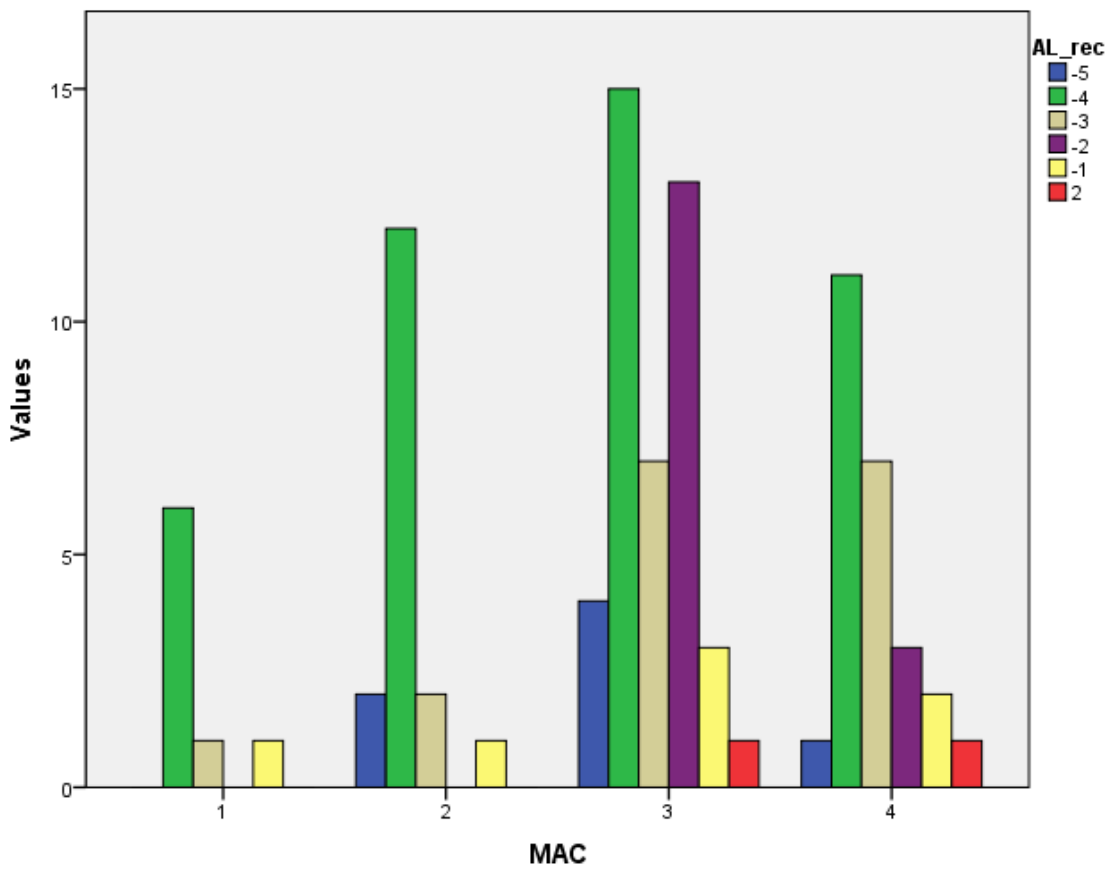


Figure 439. Study II. Histogram of AL recess (AL_rec) osteophyte grade: number of varus knees in each category, grouped by maximum attrition area of the medial condyle.

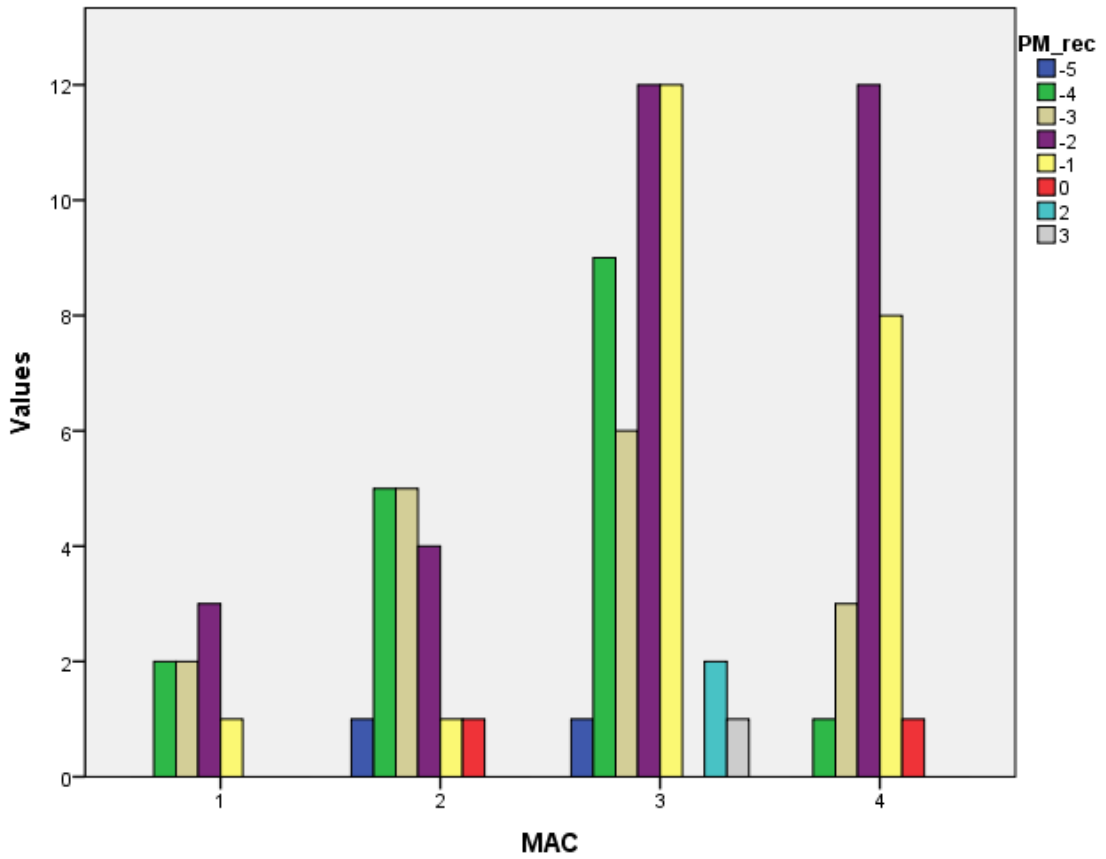


Figure 440. Study II. Histogram of PM recess (PM_rec) osteophyte grade: number of varus knees in each category, grouped by maximum attrition area of the medial condyle.

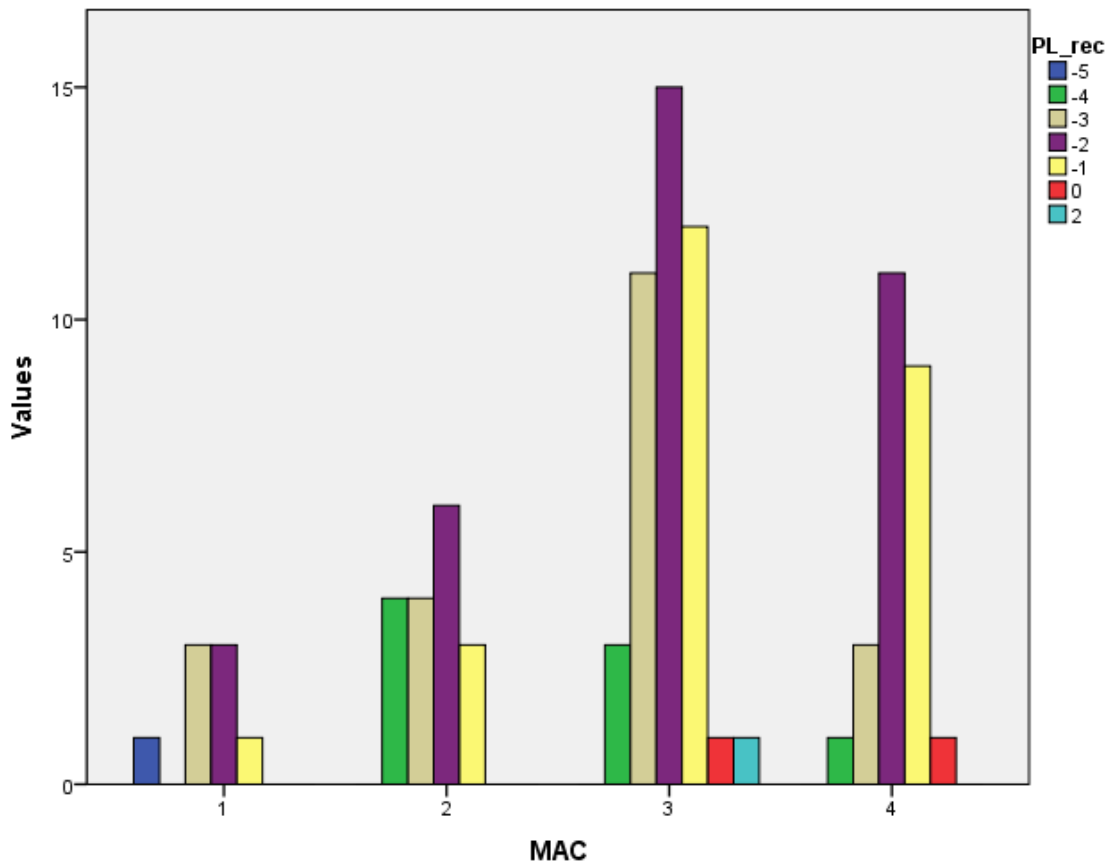


Figure 441. Study II. Histogram of PL recess (PL_rec) osteophyte grade: number of varus knees in each category, grouped by maximum attrition area of the medial condyle.

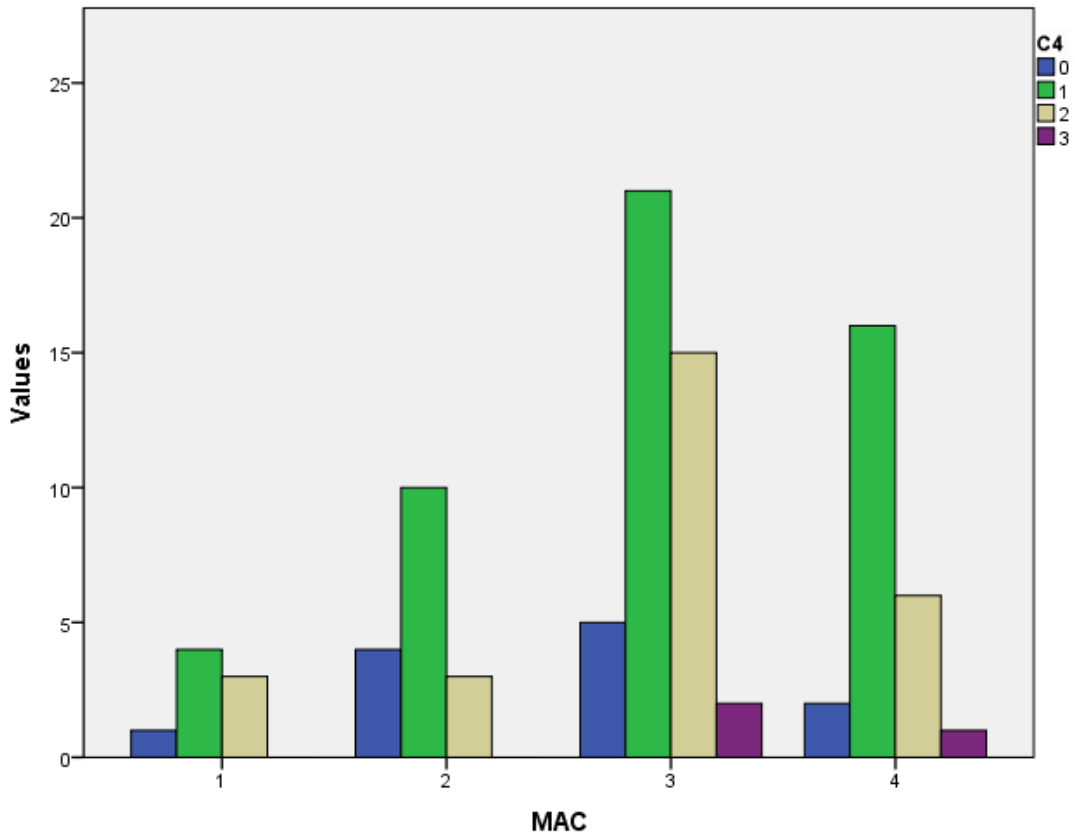


Figure 442. Study II. Histogram of more internal PMIR process (C4) osteophyte grade: number of varus knees in each category, grouped by maximum attrition area of the medial condyle of the tibia.

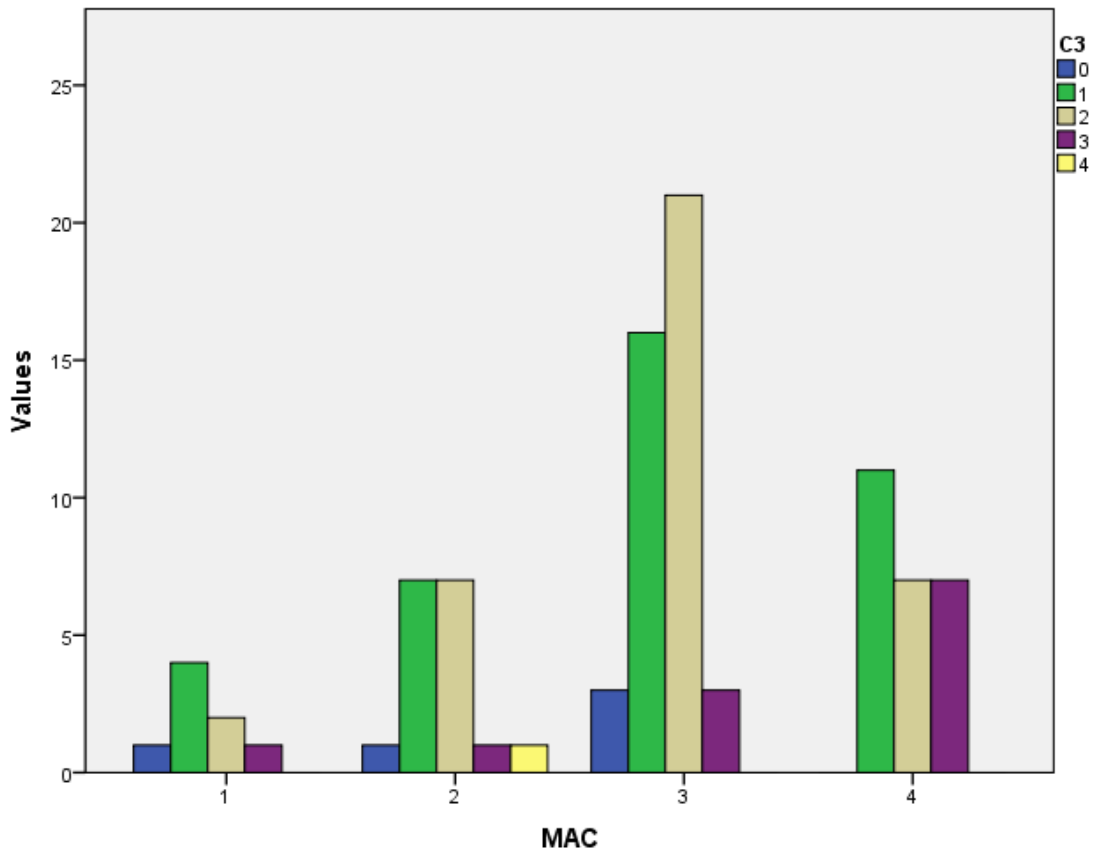


Figure 443. Study II. Histogram of internal PMIR process (C3) osteophyte grade: number of varus knees in each category, grouped by maximum attrition area of the medial condyle.

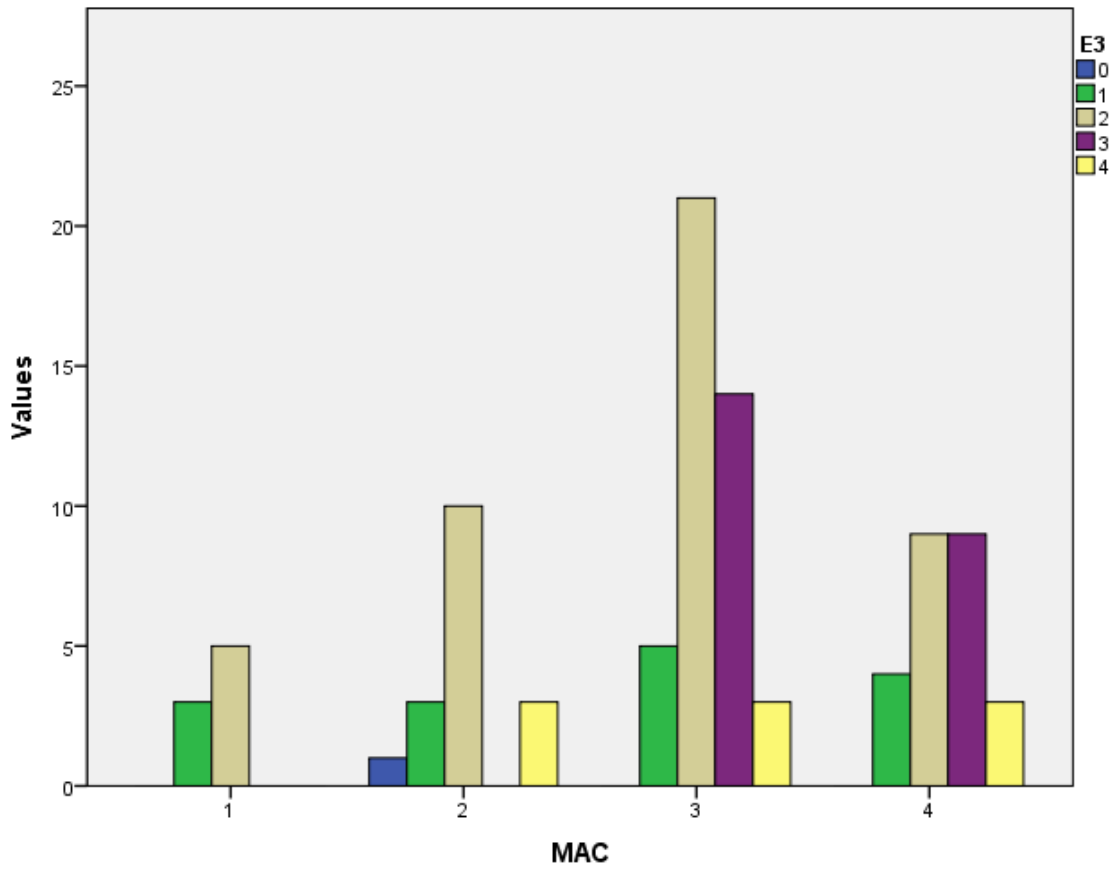


Figure 444. Study II. Histogram of internal PLIR process (E3) osteophyte grade: number of varus knees in each category, grouped by maximum attrition area of the medial condyle.

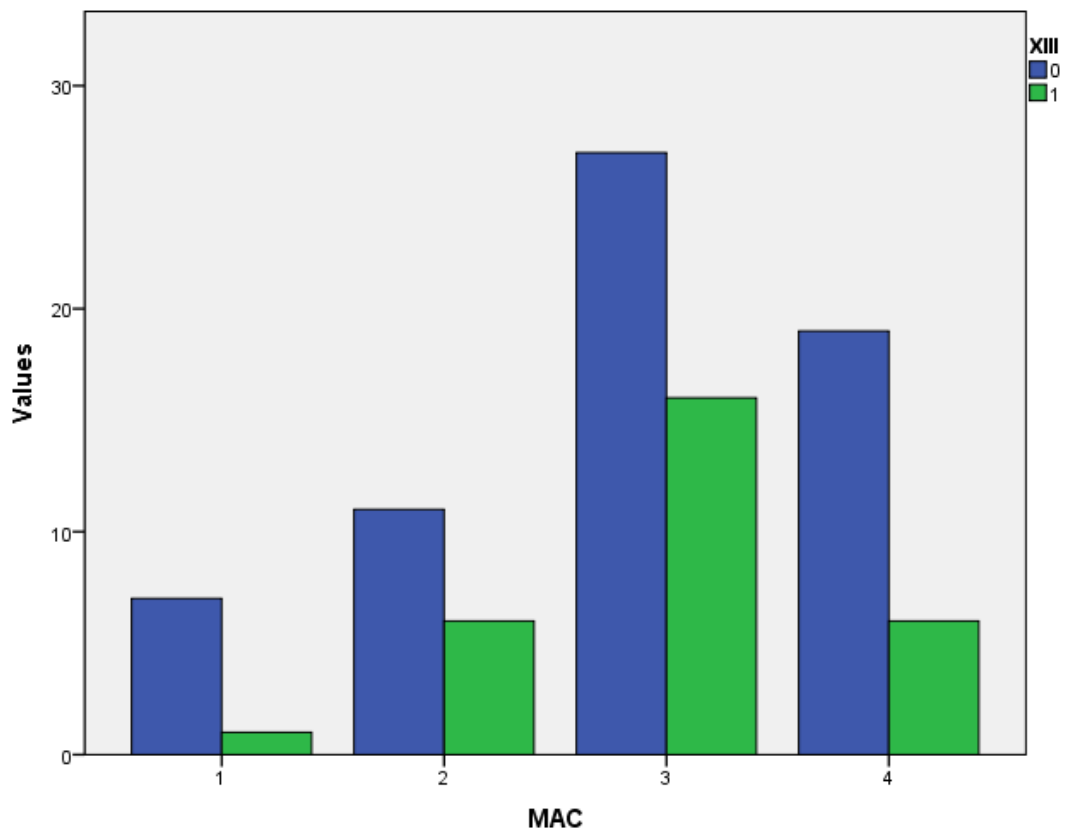


Figure 445. Study II. Histogram of area 13 (XIII) horizontality: number of varus knees, grouped by maximum attrition area of the medial condyle of the tibia. 0=facet-like (more horizontal); 1=ridge-like (more vertical).

IV.12.2. Osteophyte grade and condyle attrition

Osteophyte elevations that could be observed in knee AP and lateral radiographs were summed up for each specimen, and a total osteophyte score was obtained.

A quadratic model was obtained to predict the level of medial attrition from the total osteophyte score (Fig. 446): $F(2, 95) = 122.140$, $p < 0.001$, $R^2 = 0.720$, $b_1 = -0.152$, $b_2 = 0.001$.

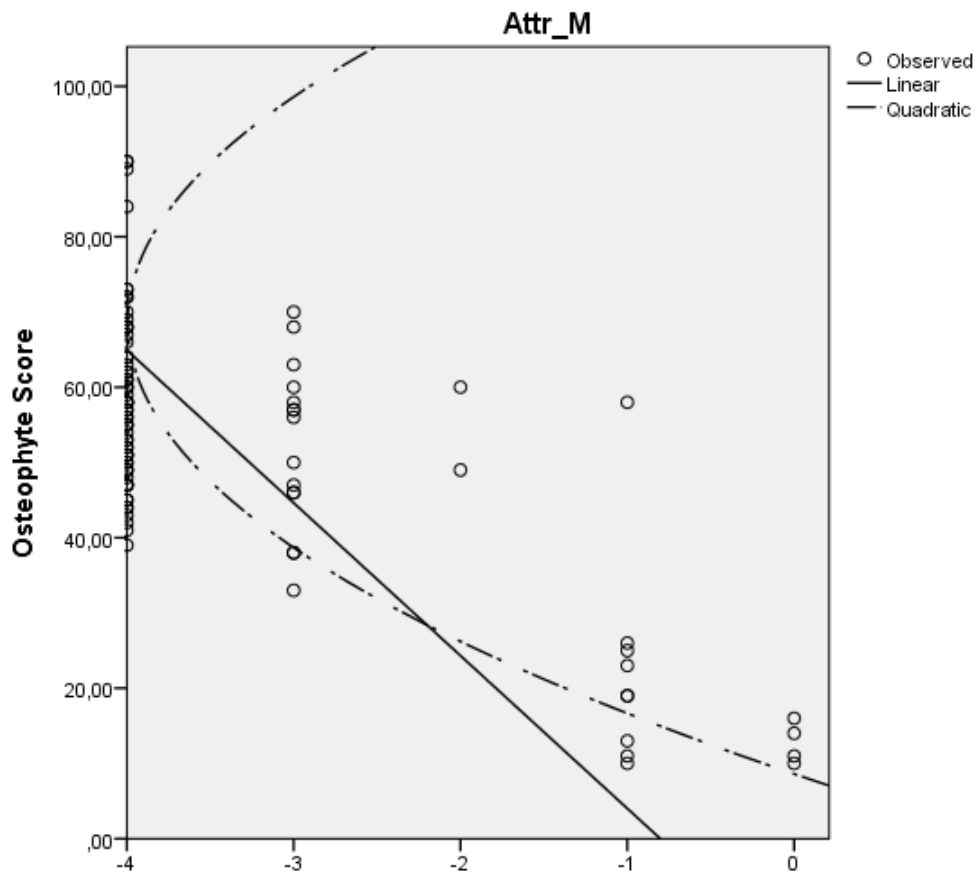


Figure 446. Study II. Best fit regression models obtained to predict attrition of the medial condyle (Attr_M) from total osteophyte growth.

A multiple regression analysis was run to predict attrition level of medial and lateral condyles from all individual osteophytes defined in this study.

The best model obtained for medial condyle attrition level included five variables (see Table 33 and Fig. 447 – Fig. 451): $F(5, 92) = 40.407$, $p < 0.001$, $R^2 = 0.687$. The regression equation obtained was as follows:

$$\text{Attr}_M = -0.284 - 0.352B_1 - 0.305MT - 0.177Bd_{AL} - 0.169G - 0.227Bd_{AM}$$

Table 33. Coefficients table for best model predicting medial condyle attrition.

	B	Std Err	Beta	t	Sig.
(Constant)	-0.284	0.239		-1,187	0.238
B1	-0.352	0.093	-0.280	-3,772	0.000
MT	-0.305	0.072	-0.298	-4,250	0.000
AL corner	-0.177	0.091	-0.159	-1,944	0.055
G	-0.169	0.073	-0.169	-2,309	0.023
AM corner	-0.227	0.099	-0.178	-2,285	0.025

A simpler model, excluding the AM corner – difficult to distinguish in normal knee radiographs from the Parsons' knob –, gave a similar predictive value (Table 34): $F(4, 93)=47.066$, $p<0.001$, $R^2=0.669$. The regression equation obtained was then:

$$\text{Attr}_M = -0.279 - 0.383B_1 - 0.335MT - 0.255Bd_{AL} - 0.192G$$

Table 34. Coefficients table for best model predicting medial condyle attrition, without AM corner.

	B	Std Err	Beta	t	Sig.
(Constant)	-0.279	0.244		-1.143	0.256
B1	-0.383	0.094	-0.305	-4.056	0.000
MT	-0.335	0.072	-0.328	-4.648	0.000
AL corner	-0.255	0.086	-0.230	-2.970	0.004
G	-0.192	0.074	-0.191	-2.586	0.011

When combined with Ahlbäck OA classification, a model with four variables is obtained for medial attrition, with a slight improvement over osteophyte-only models (Table 35): $F(4, 93)=59.560$, $p<0.001$, $R^2=0.714$.

$$\text{Attr}_M = -0.398 - 0.331OA - 0.378B_1 - 0.204MT - 0.163Bd_{MP}$$

Table 35. Coefficients table for best model predicting medial condyle attrition, including Ahlbäck OA grade.

	B	Std Err	Beta	t	Sig.
(Constant)	-0.550	0.203		-2.704	0.008
OA	-0.360	0.067	-0.365	-5.358	0.000
B1	-0.420	0.084	-0.334	-4.985	0.000
MT	-0.240	0.070	-0.235	-3.447	0.001
PM rim	-0.186	0.079	-0.160	-2.362	0.020

The value obtained for a regression model to predict medial condyle attrition from a single variable, Ahlbäck OA grade (Fig. 452), results in $F(1, 96)=88.148$, $p<0.001$, $R^2=0.479$.

The best model obtained for lateral condyle attrition level included seven variables (see Table 36 and Fig. 453 – Fig. 459): $F(7, 90)=22.182$, $p<0.001$, $R^2=0.633$. The regression equation obtained was as follows:

$$\text{Attr}_L = 0.112 - 0.249\text{MT} - 0.477\text{Bd}_{\text{MA}} - 0.145\text{Bd}_{\text{AL}} - 0.199\text{D}_{1-2} - 0.250\text{C}_4 - 0.190\text{Bd}_{\text{PL}} - 0.232\text{C}_3$$

Table 36. Coefficients table for best model predicting lateral condyle attrition.

	B	Std Err	Beta	t	Sig.
(Constant)	0.112	0.262		0.426	0.671
MT	-0.249	0.078	-0.246	-3.195	0.002
AM corner	-0.477	0.123	-0.269	-3.875	0.000
AL corner	-0.145	0.090	-0.132	-1.607	0.112
D1-2	-0.199	0.093	-0.150	-2.141	0.035
C4	-0.250	0.108	-0.158	-2.314	0.023
PL corner	-0.190	0.073	-0.194	-2.600	0.011
C3	-0.232	0.097	-0.168	-2.397	0.019

A simpler model, with structures easily identifiable in a radiographic study, included three variables (Table 37 **Error! Reference source not found.**): $F(3, 94)=33.478$, $p<0.001$, $R^2=0.517$. The regression equation was then:

$$\text{Attr}_L = -0.461 - 0.361\text{MT} - 0.508\text{Bd}_{\text{MA}} - 0.335\text{Bd}_{\text{AL}}$$

Table 37. Coefficients table for best model predicting lateral condyle attrition, excluding variables not commonly seen in radiographs.

	B	Std Err	Beta	t	Sig.
(Constant)	-0.461	0.260		-1.773	0.079
MT	-0.361	0.083	-0.356	-4.342	0.000
AM corner	-0.508	0.136	-0.286	-3.722	0.000
AL corner	-0.335	0.092	-0.304	-3.648	0.000

Adding Ahlbäck OA grade as a variable did not alter the result of the multiple regression obtained to predict the level of lateral condyle attrition.

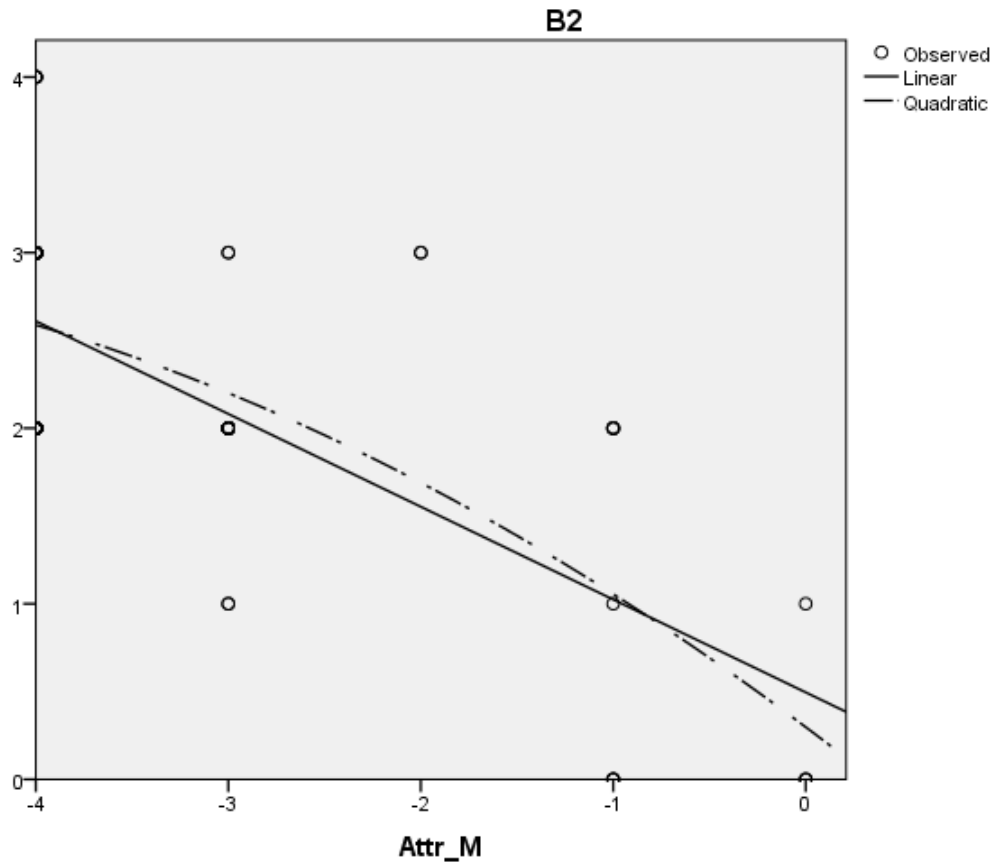


Figure 447. Study II. Best fit regression models obtained to predict attrition of the medial condyle from central AMIR process (B2) osteophyte grade.

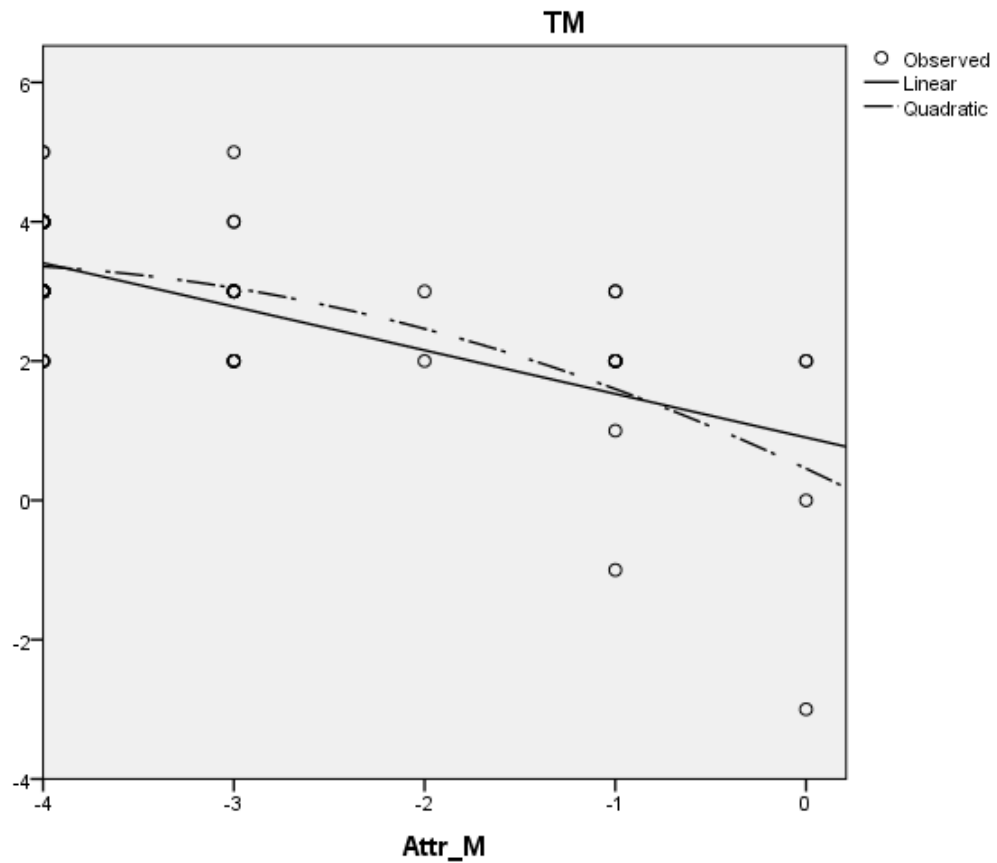


Figure 448. Study II. Best fit regression models obtained to predict attrition of the medial condyle (Attr_M) from MT osteophyte grade (TM).

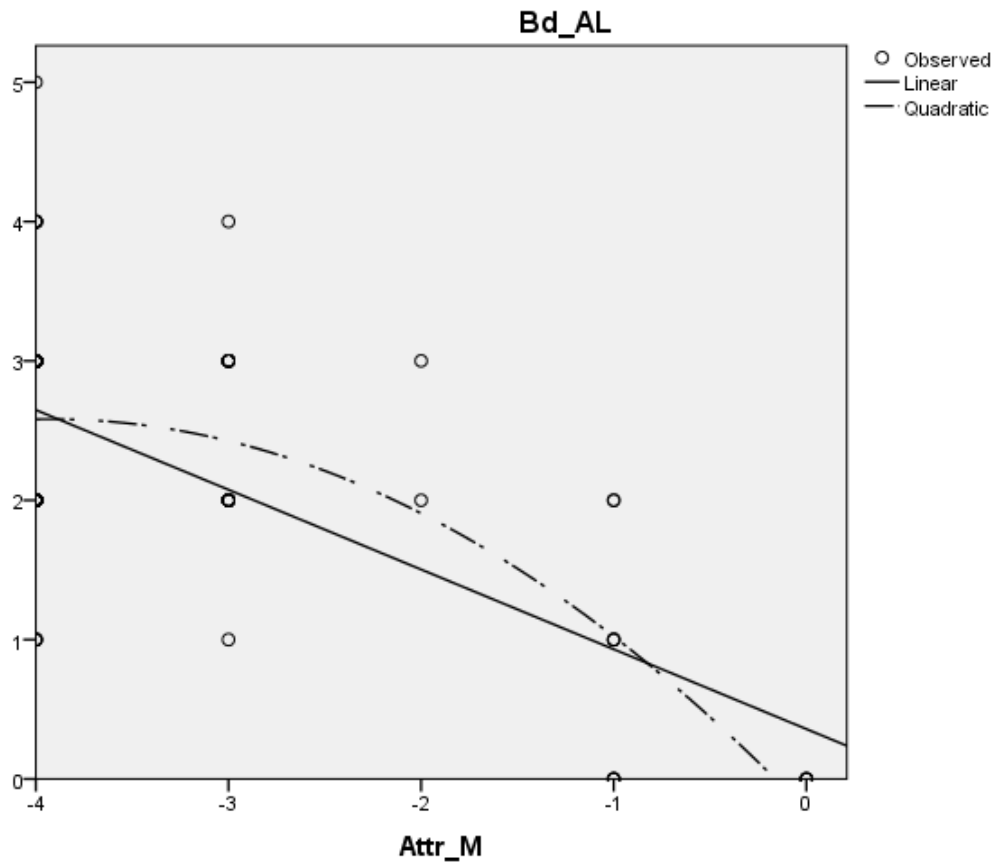


Figure 449. Study II. Best fit regression models obtained to predict attrition of the medial condyle (Attr_M) from the AL corner (Bd_AL) osteophyte grade.

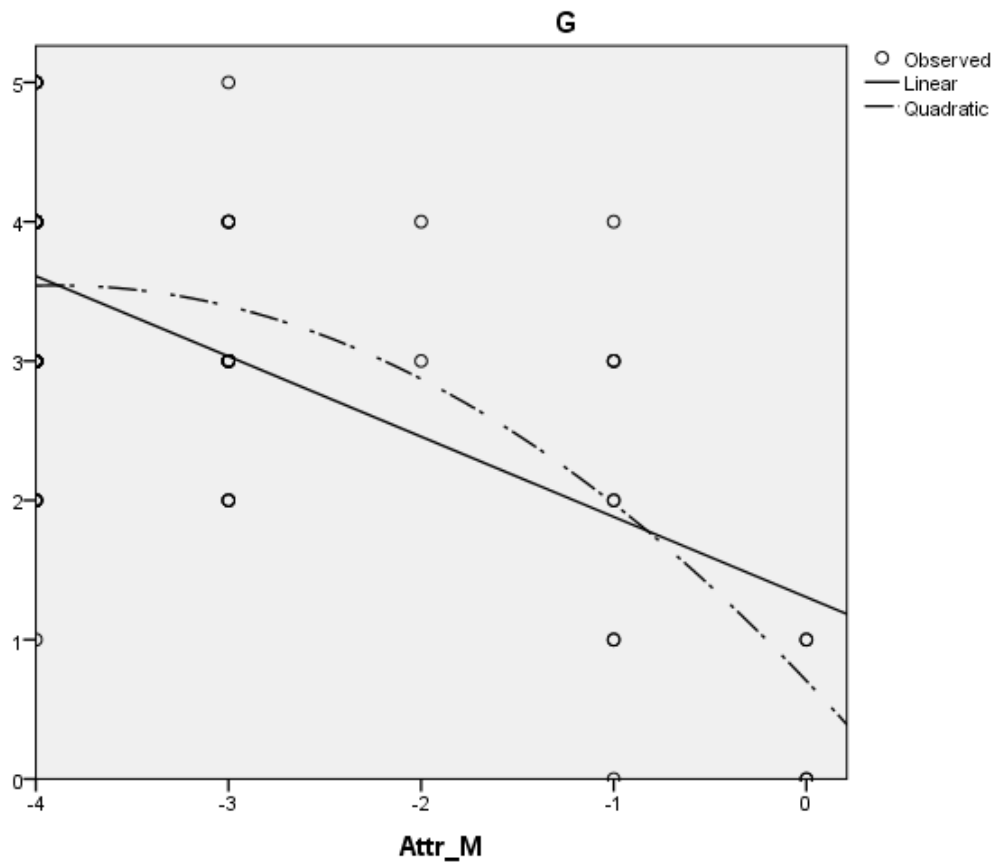


Figure 450. Study II. Best fit regression models obtained to predict attrition of the medial condyle (Attr_M) from Parson's knob (G) osteophyte grade.

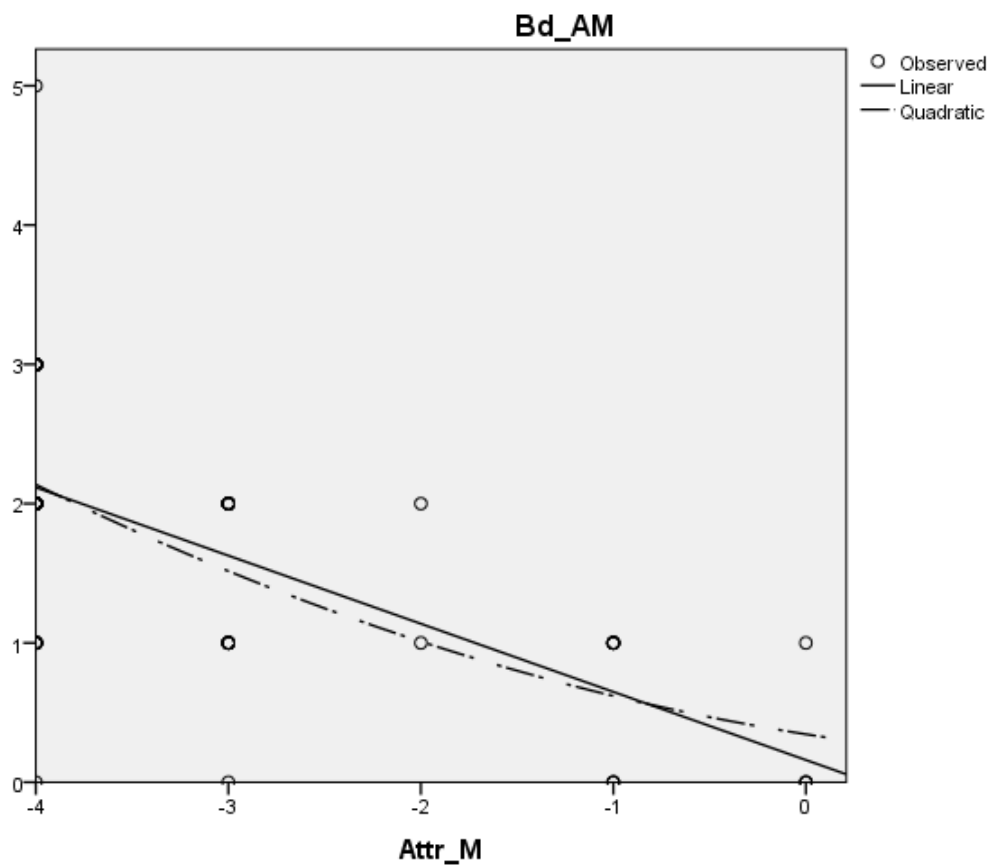


Figure 451. Study II. Best fit regression models obtained to predict attrition of the medial condyle (Attr_M) from AM corner (Bd_AM) osteophyte grade.

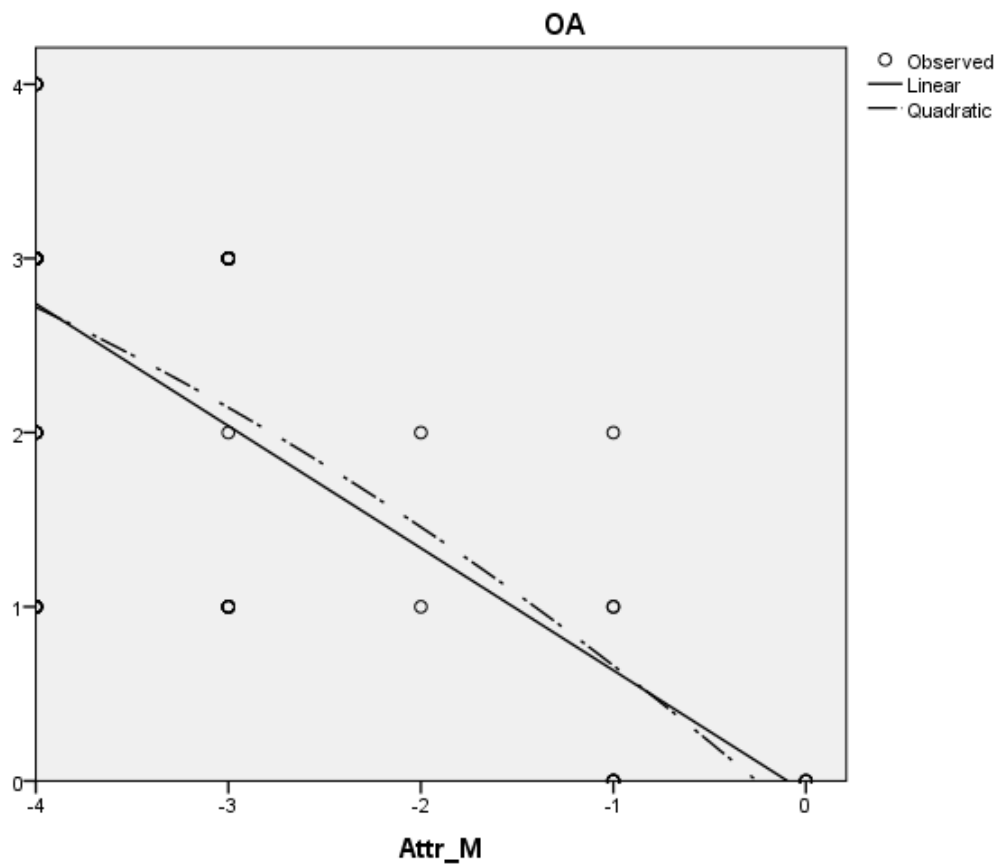


Figure 452. Study II. Best fit regression models obtained to predict attrition of the medial condyle (Attr_M) from Ahlbäck OA grade.

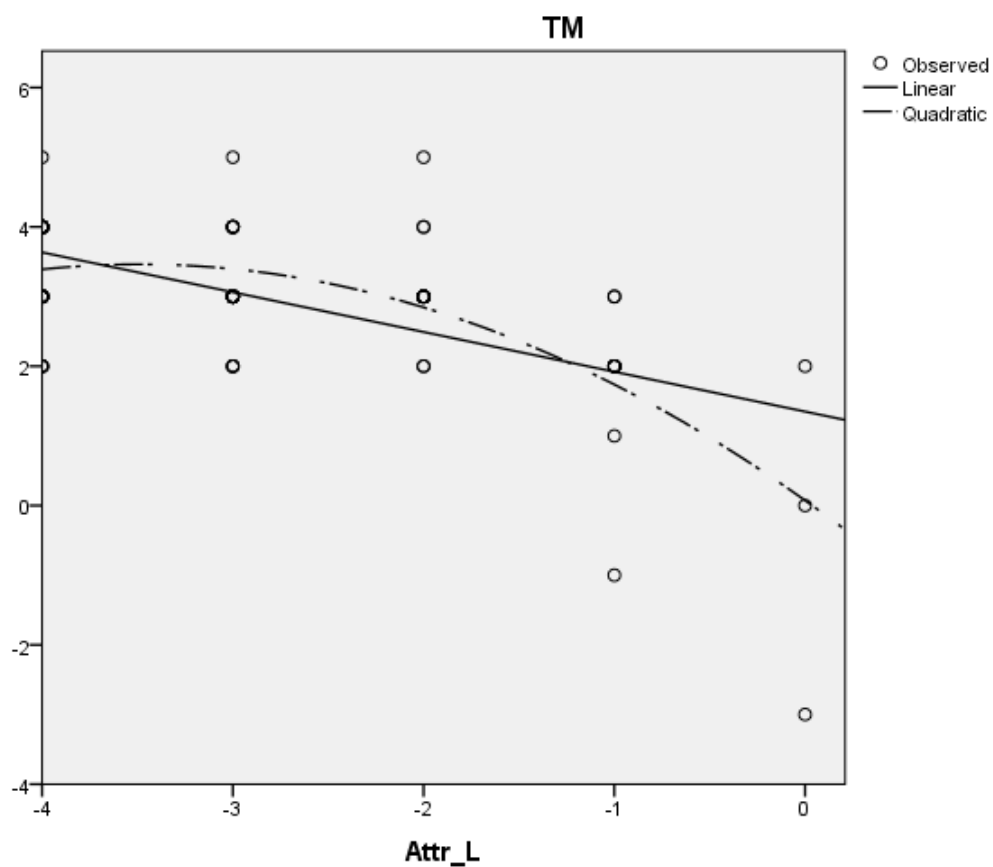


Figure 453. Study II. Best fit regression models obtained to predict attrition of the lateral condyle (Attr_L) from MT osteophyte grade (TM).

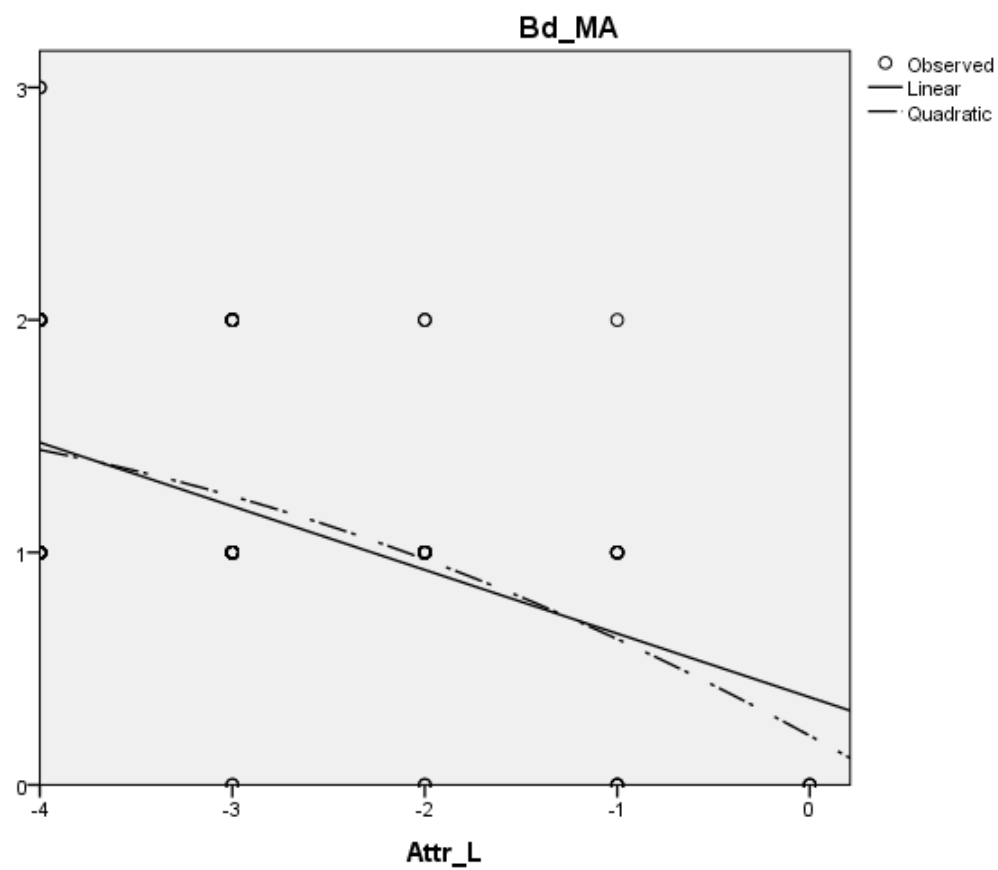


Figure 454. Study II. Best fit regression models obtained to predict attrition of the lateral condyle (Attr_L) from the medial rim, anterior part (Bd_MA), osteophyte grade.

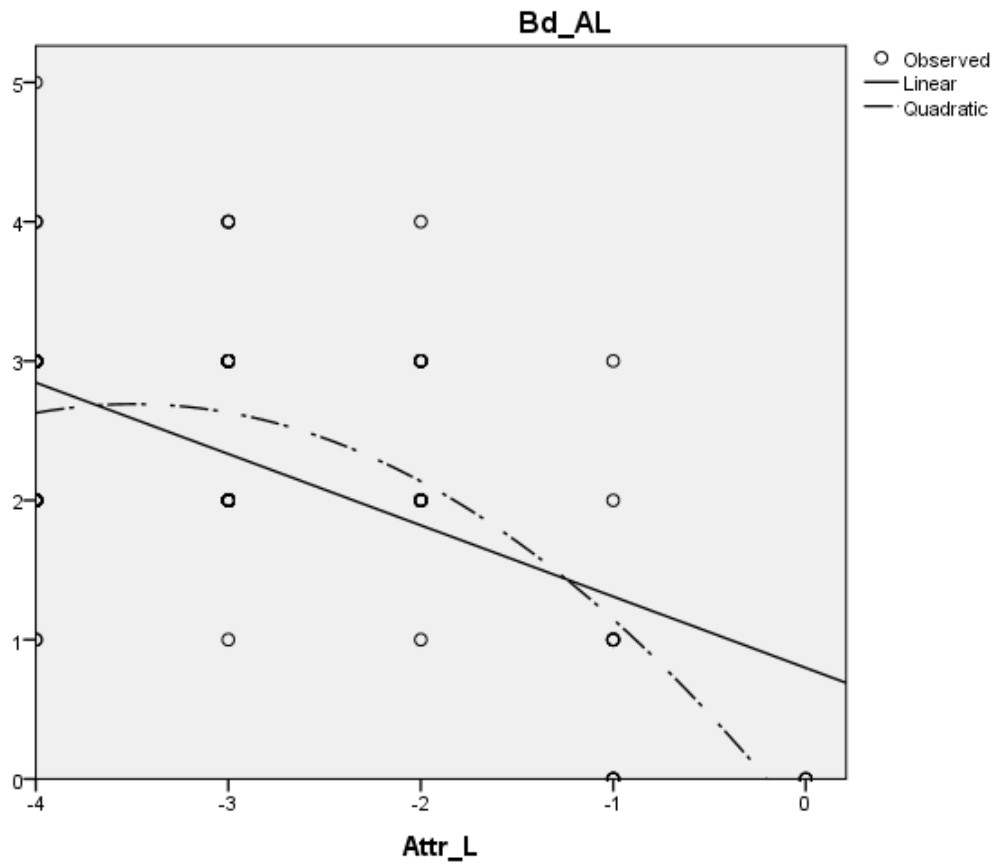


Figure 455. Study II. Best fit regression models obtained to predict attrition of the lateral condyle (Attr_L) from AL corner (Bd_AL) osteophyte grade.

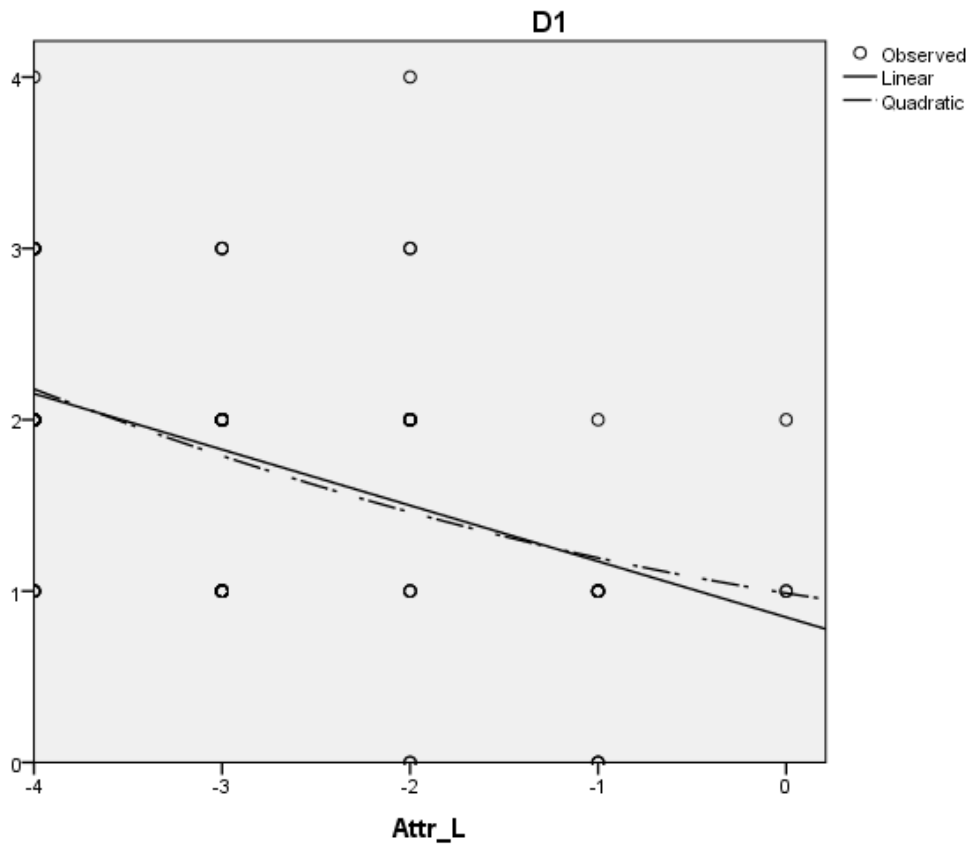


Figure 456. Study II. Best fit regression models obtained to predict attrition of the lateral condyle (Attr_L) from central and external ALIR processes (D1-D2) osteophyte grade.

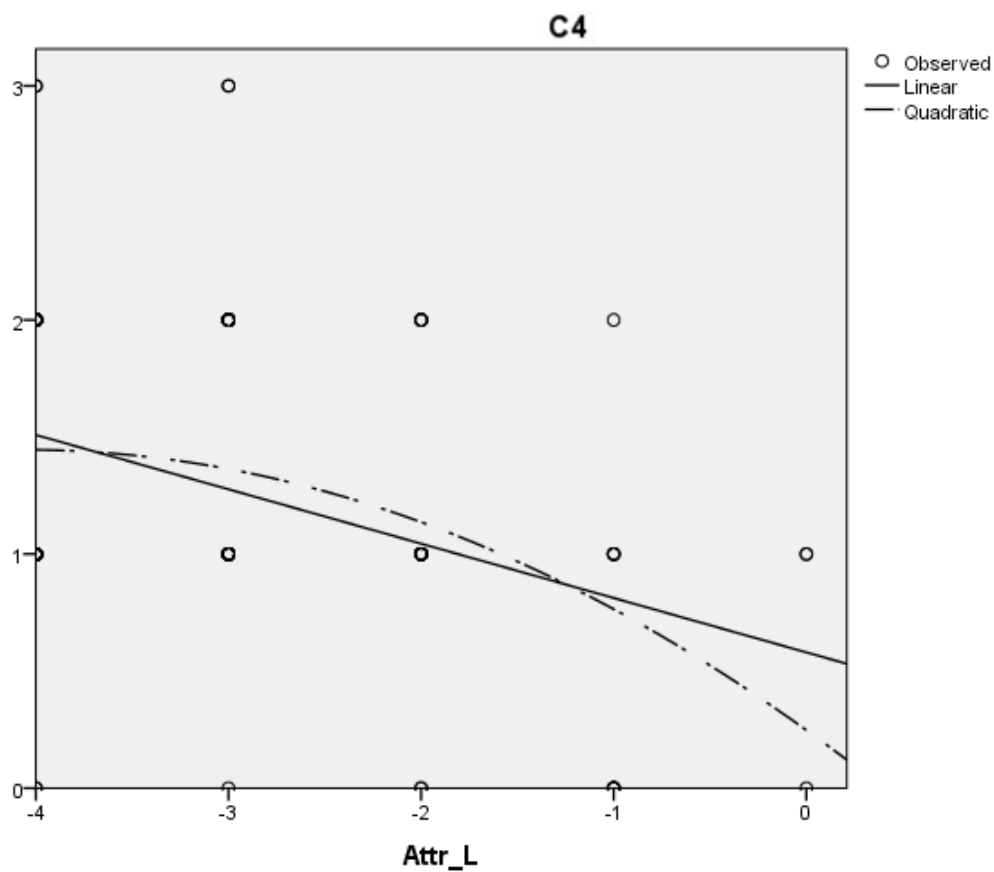


Figure 457. Study II. Best fit regression models obtained to predict attrition of the lateral condyle (Attr_L) from the more internal PMIR process (C4) osteophyte grade.

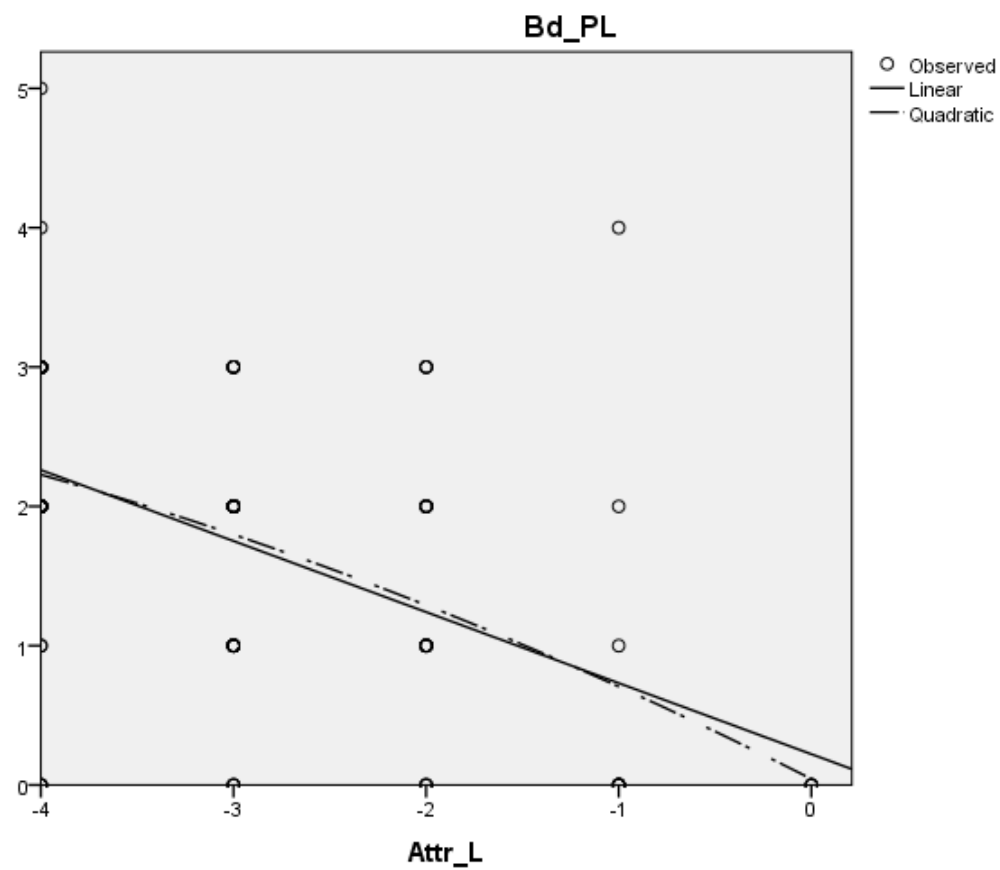


Figure 458. Study II. Best fit regression models obtained to predict attrition of the lateral condyle (Attr_L) from PL corner (Bd_PL) osteophyte grade.

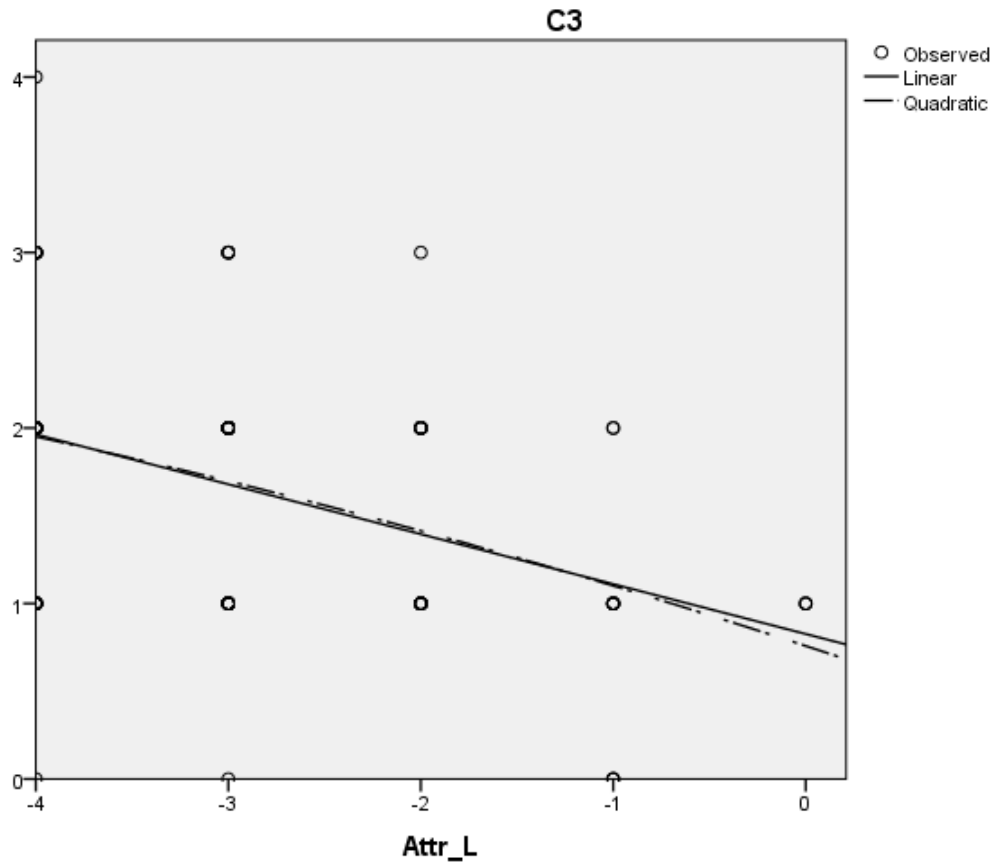


Figure 459. Study II. Best fit regression models obtained to predict attrition of the lateral condyle (Attr_L) from the internal PMIR process (C3) osteophyte grade.

IV.12.3. American Knee Society Clinical Rating System

Combined condyle attrition was obtained by adding the medial and lateral condyle attrition grade.

Results of correlation analysis of the American Knee Society Clinical Rating System (KS) were as follows:

- Ahlbäck OA classification: Knee Score, $r_s=-0.236$, $p=0.030$; Function Score, $r_s=0.119$, $p=0.282$.
- Combined condyle attrition (Attr-M+L): Knee Score, $r_s=0.061$, $p=0.582$; Function Score, $r_s=-0.78$, $p=0.479$.
- Osteophyte score: Knee Score, $r_s=-0.248$, $p<0.001$; Function Score, $r_s=0.038$, $p=0.733$.

Kruskal-Wallis H tests showed that there were no statistically significant differences in any item of the KS between Ahlbäck OA grade groups, but for the Knee Score item: $\chi^2(3)=0.229$, $p=0.973$, with a mean overall KS score of

- 130.77 for Ahlbäck OA grade 1,
- 132.95 for Ahlbäck OA grade 2,
- 127.45 for Ahlbäck OA grade 3,
- 125.59 for Ahlbäck OA grade 4.

Specific scores and confidence intervals are available in Table 38. For comparison of points obtained for each item, grouped in each OA grade, see Fig. 460 – Fig. 473.

A regression analysis was run to estimate the best curve fit for the equation that relates KS with combined condyle attrition, with total osteophyte score, and with Ahlbäck OA classification. In all cases, the best fit curve were cubic:

- KS Knee Score item:
 - Ahlbäck OA grade (Figure 476): $F(3, 81)=212.326$, $p<0.001$, $R^2=0.887$ ($B_1=0.214$, $t=9.321$, $p<0.001$; $B_2=-0.005$, $t=-5.471$, $p<0.001$; $B_3=0.00002886$, $t=3.912$, $p<0.001$).
 - Combined condyle attrition (Figure 474): $F(3, 81)=750.984$, $p<0.001$, $R^2=0.965$ ($B_1=-0.526$, $t=-15.992$, $p<0.001$; $B_2=0.11$, $t=9.372$, $p<0.001$; $B_3=-0.00007367$, $t=-6.959$, $p<0.001$).

- Osteophyte score (Figure 475): $F(3, 81)=305.803$, $p<0.001$, $R^2=0.919$ ($B_1=3.531$, $t=10.759$, $p<0.001$; $B_2=-0.77$, $t=-6.355$, $p<0.001$; $B_3<0.001$, $t=4.661$, $p<0.001$).
- KS Knee Function item :
 - Ahlbäck OA grade (Figure 479): $F(3, 81)=223.367$, $p<0.001$, $R^2=0.892$ ($B_1=0.097$, $t=3.967$, $p<0.001$; $B_2=-0.001$, $t=-1.683$, $p=0.096$; $B_3=0.00004415$, $t=0.992$, $p=0.324$).
 - Combined condyle attrition (Figure 477): $F(3, 81)=1164.147$, $p<0.001$, $R^2=0.977$; $B_1=-0.318$, $t=-11.008$, $p<0.001$; $B_2=0.005$, $t=5.652$, $p<0.001$; $B_3=-0.00002077$, $t=-3.934$, $p<0.001$).
 - Osteophyte score (Figure 478): $F(3, 81)=440.982$, $p<0.001$, $R^2=0.942$ ($B_1=2.297$, $t=7.633$, $p<0.001$; $B_2=-0.037$, $t=-4.386$, $p<0.001$; $B_3<0.001$, $t=3.347$, $p=0.001$).

Table 38. Study II. KS items and knee OA: Item scores (mean and 95% confidence intervals) by Ahlbäck OA grade group.

	OA 1	CI 95%	OA 2	CI 95%	OA 3	CI 95%	OA 4	CI 95%	P-VALUE
EF_SCORE	59.52	48.95–70.08	54.20	44.65–63.75	53.15	46.95–59.35	37.09	24.29–49.88	0.076
EF_Pain_Move	20.63	13.55–27.7	18.00	12.15–23.85	18.90	15.16–22.64	9.00	-0.05–18.05	0.136
EF_Pain_Rest	-1.25	-3.31–0.81	-1.75	-3.32--0.18	-0.90	-1.58--0.22	-2.00	-4.5–0.5	0.483
EF_Pain_Stair	5.31	2.84–7.79	4.75	2.82–6.68	4.70	3.44–5.96	2.00	-0.5–4.5	0.259
EF_Ext	-1.69	-2.94--0.43	-1.45	-2.72--0.18	-3.12	-4.15--2.09	-3.70	-6.54--0.86	0.126
EF_Flexum		–	-0.50	-1.55–0.55	-0.70	-1.23--0.17	-0.80	-2.05–0.45	0.225
EF_ROM	12.89	11.93–13.85	12.50	11.67–13.33	11.61	10.98–12.24	11.19	10.15–12.23	0.052
EF_Varus	-0.75	-1.84–0.34	-1.60	-2.72--0.48	-0.56	-0.92--0.2	-1.60	-3.36–0.16	0.122
EF_Inest_ML	14.38	13.46–15.29	14.25	13.39–15.11	13.40	12.52–14.28	13.00	10.5–15.5	0.527
EF_Inest_AP		–		–	9.74	9.49–9.99		–	0.187
EF_FUNCT	71.25	56.71–85.79	78.75	68.77–88.73	74.30	67.91–80.69	88.50	72.68–104.32	0.208
EF_Pt_Walk	35.63	27.61–43.64	38.00	32–44	36.20	32.02–40.38	46.00	39.09–52.91	0.231
EF_Pt_Help	-6.88	-10.37--3.38	-3.75	-6.77--0.73	-4.30	-6.02--2.58	-2.50	-7.04–2.04	0.102
EF_Pt_Climb	42.50	37.94–47.06	44.50	41.29–47.71	42.40	40.37–44.43	45.00	39.94–50.06	0.562

NOTE. EF_ = Physical examination items (from the American Knee Society Clinical Rating System). Knee Score (SCORE) includes pain with movements (Pain_Move), pain while resting (Pain_Rest), pain with stair climbing (Pain_Stair), extension lag (Ext), flexum, range of motion (ROM), varus, and instability (Inest) in AP and ML planes. Knee function (FUNCT) includes walking distance (Pt_Walk), use of help (Pt_Help), and stair climbing (Pt_Climb).

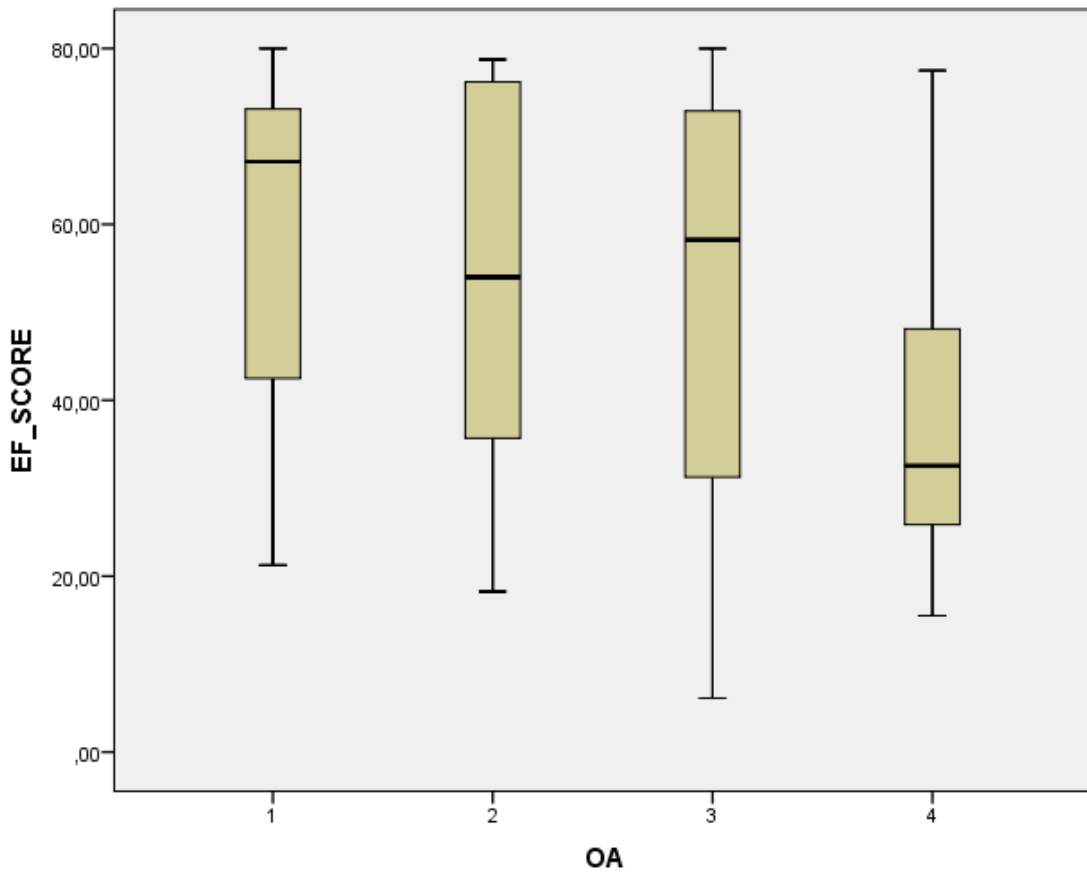


Figure 460. Study II. Box-and-whisker plot of distribution of points obtained for the Knee Score part of KS Knee Score (EF_SCORE), grouped into Ahlbäck OA grade.

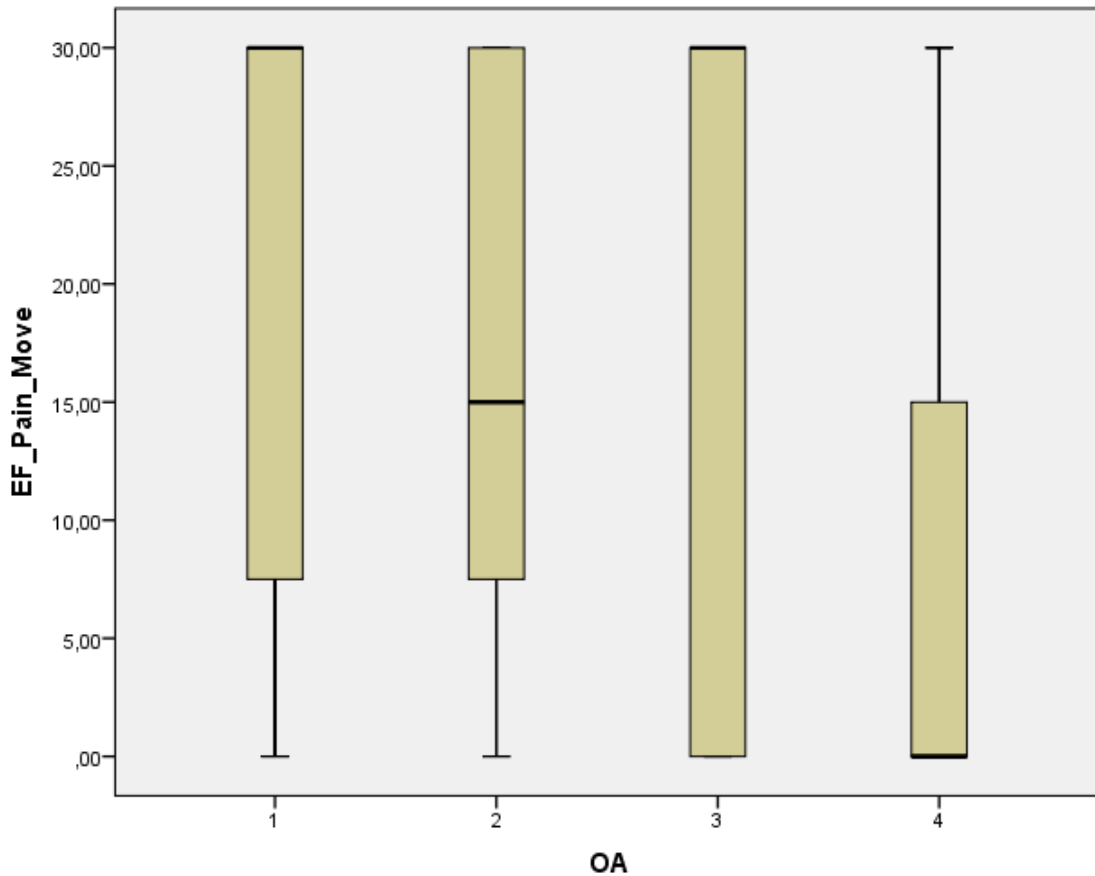


Figure 461. Study II. Box-and-whisker plot of distribution of points for the Pain (Movement) item in KS Knee Score (EF_Pain_Move), grouped into Ahlbäck OA grade.

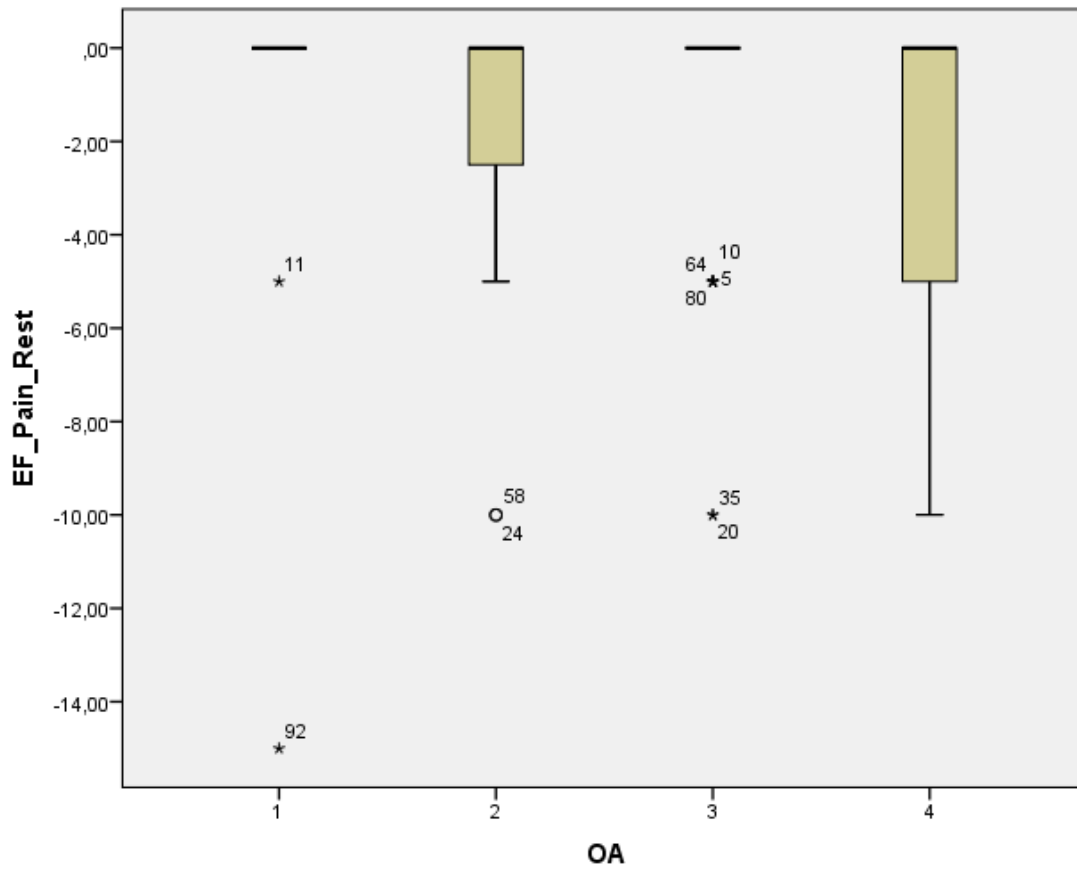


Figure 462. Study II. Box-and-whisker plot of distribution of points for the Pain (Rest) item in KS Knee Score (EF_Pain_Rest), grouped into Ahlbäck OA grade.

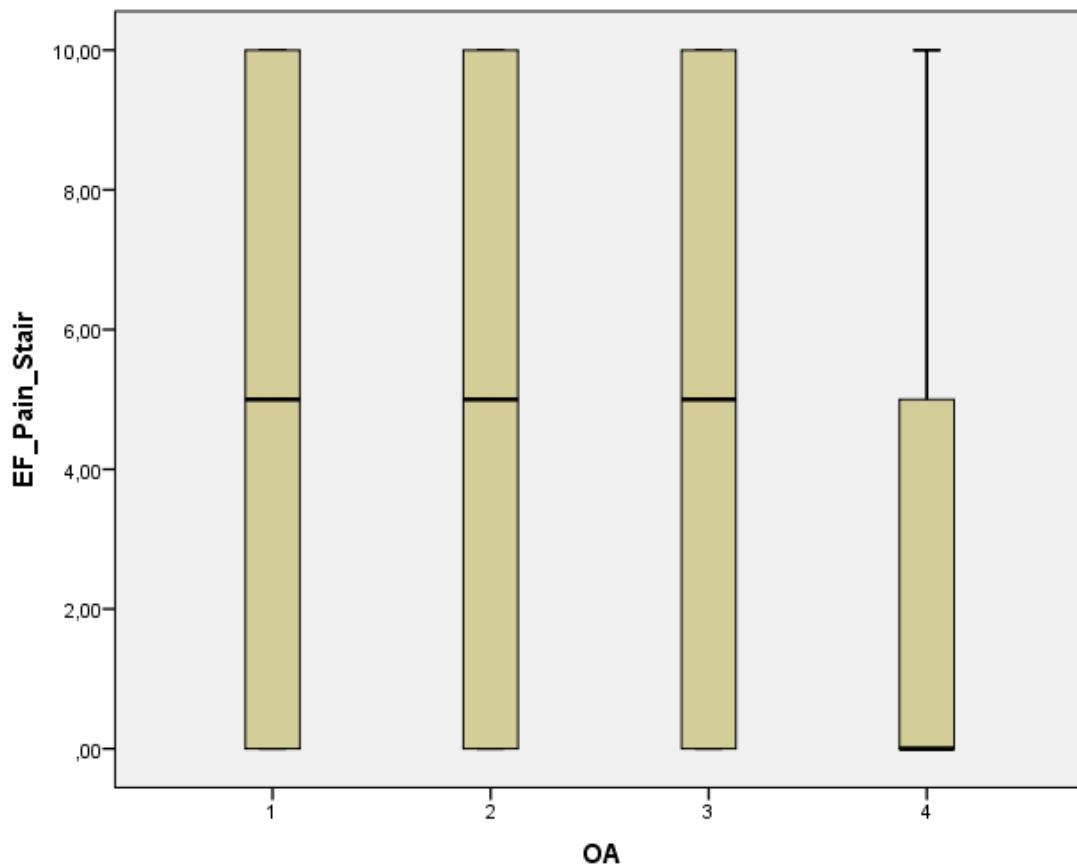


Figure 463. Study II. Box-and-whisker plot of distribution of points for the Pain (Stairs) item in KS Knee Score (EF_Pain_Stair), grouped into Ahlbäck OA grade.

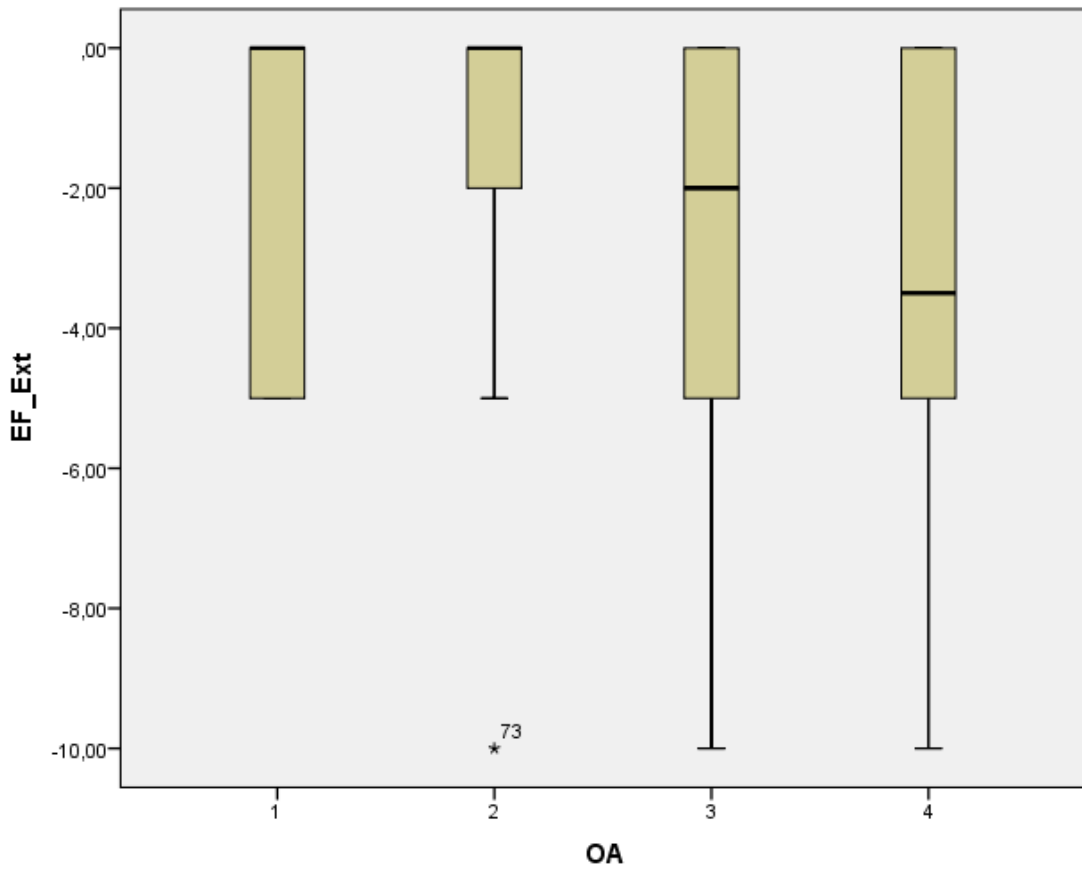


Figure 464. Study II. Box-and-whisker plot of distribution of points for the Extension Lag item in KS Knee Score (EF_Ext), grouped into Ahlbäck OA grade.

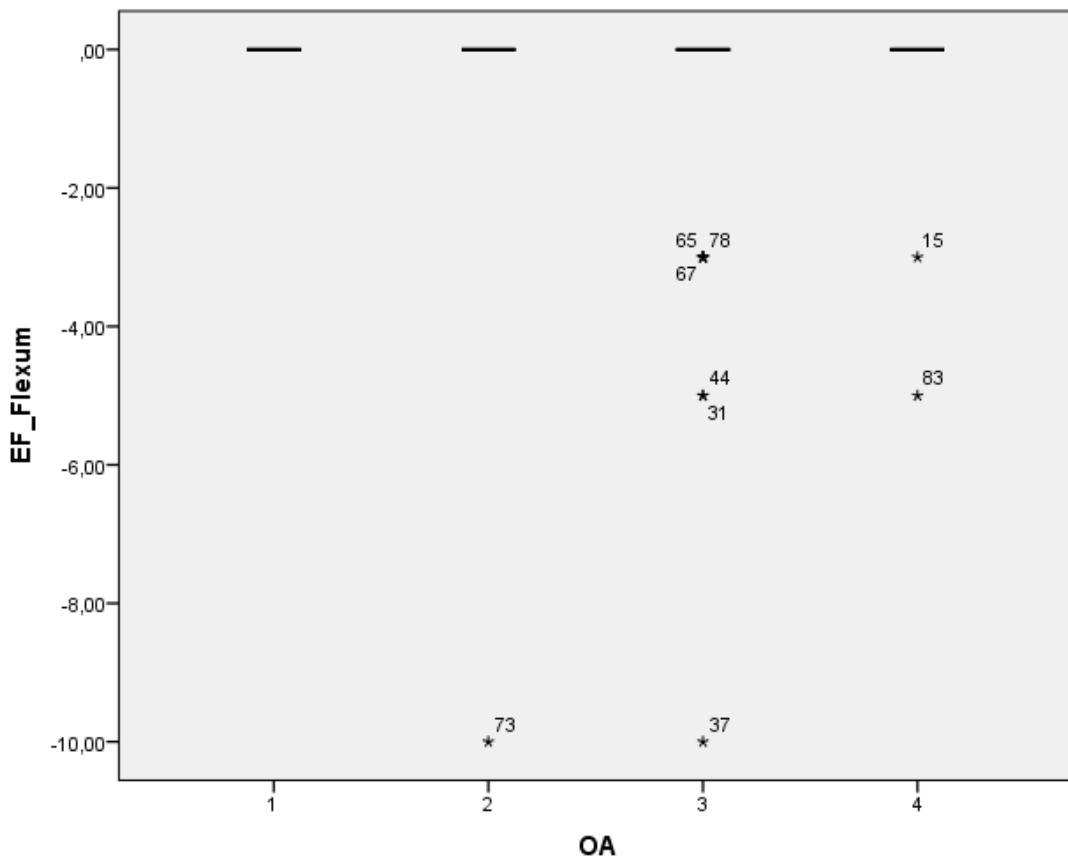


Figure 465. Study II. Box-and-whisker plot of distribution of points for the Flexum item in KS Knee Score (EF_Flexum), grouped into Ahlbäck OA grade.

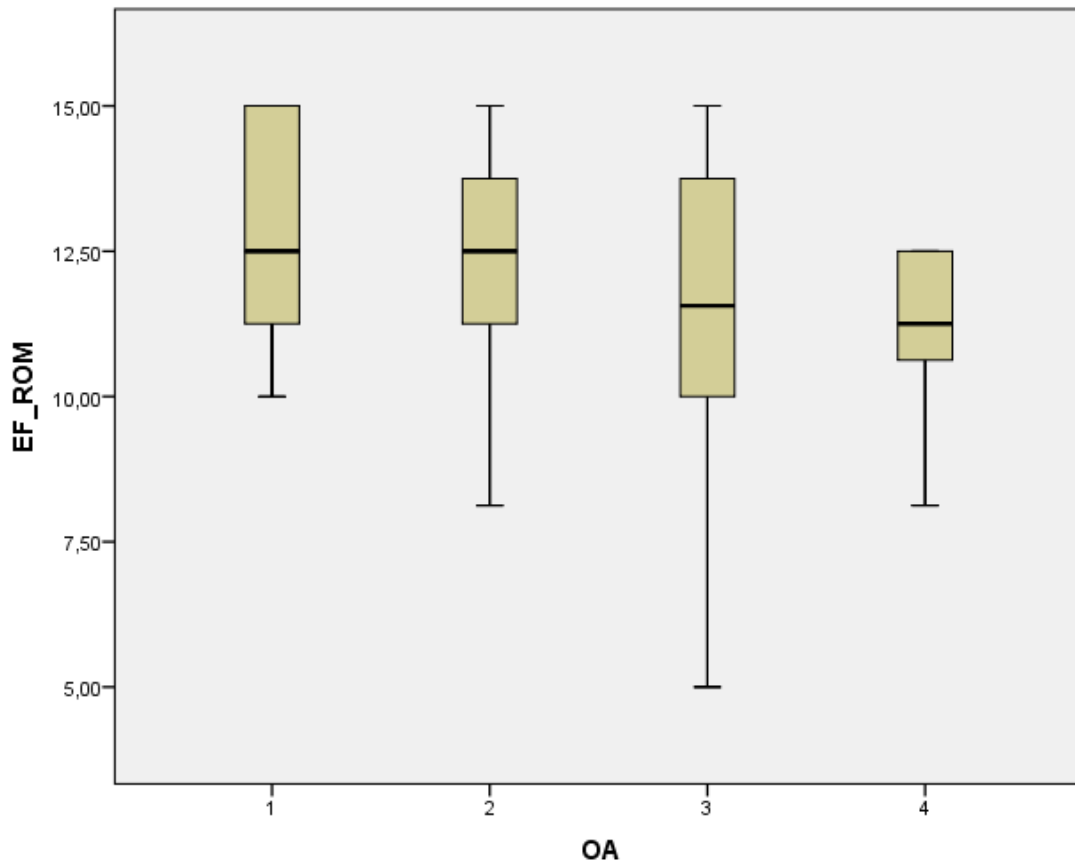


Figure 466. Study II. Box-and-whisker plot of distribution of points for the Range of Motion item in KS Knee Score (EF_ROM), grouped into Ahlbäck OA grade.

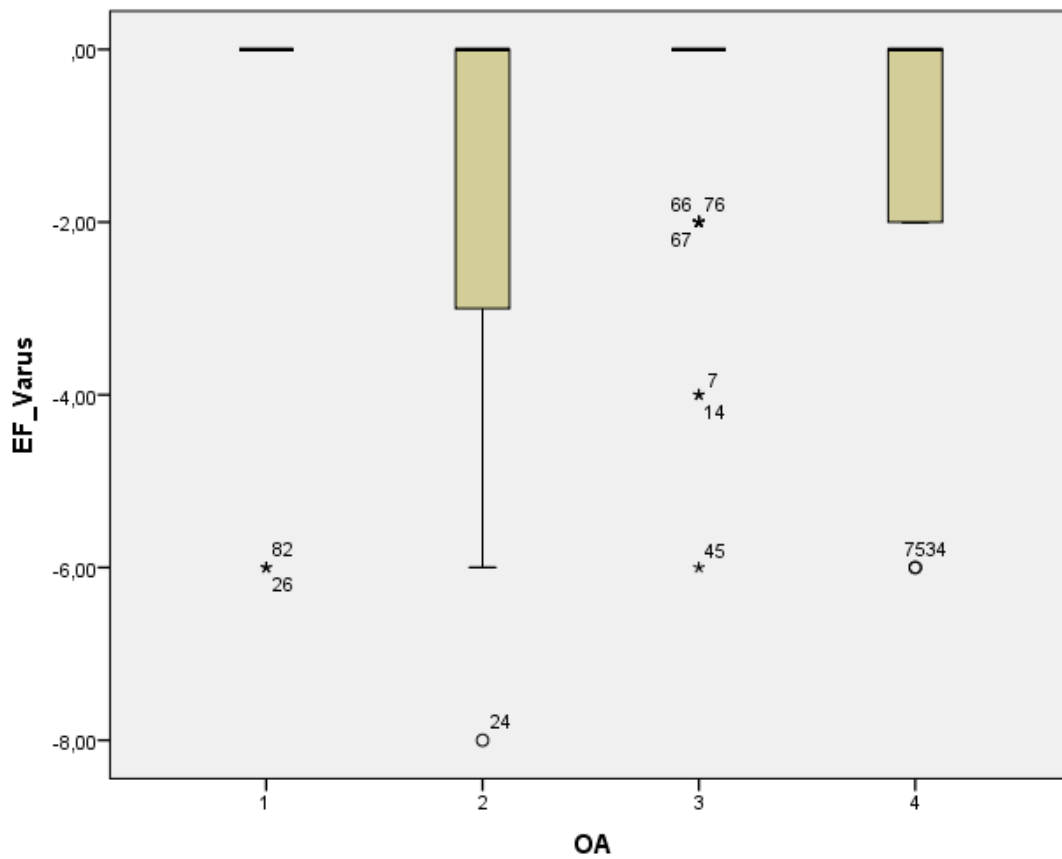


Figure 467. Study II. Box-and-whisker plot of distribution of points for the Alignment item in KS Knee Score (EF_Varus), grouped into Ahlbäck OA grade.

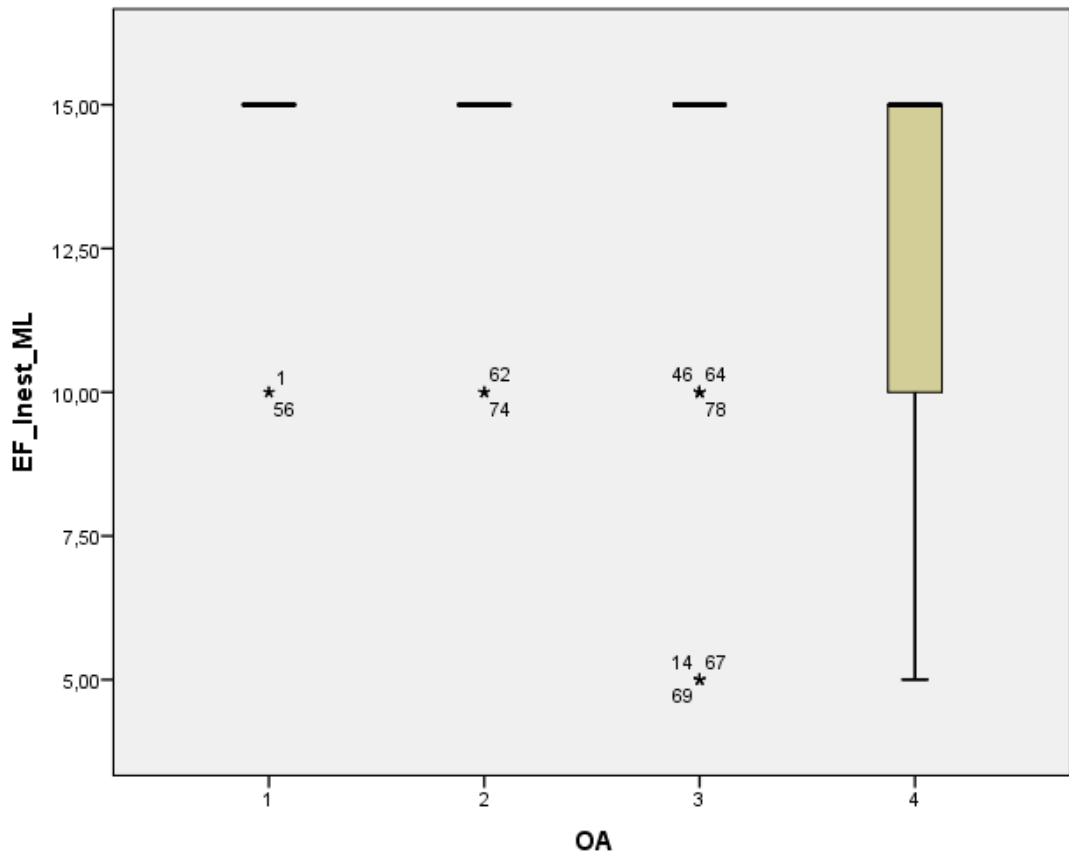


Figure 468. Study II. Box-and-whisker plot of distribution of points for the Mediolateral Instability item in KS Knee Score (EF_Inest_ML), grouped into Ahlbäck OA grade.

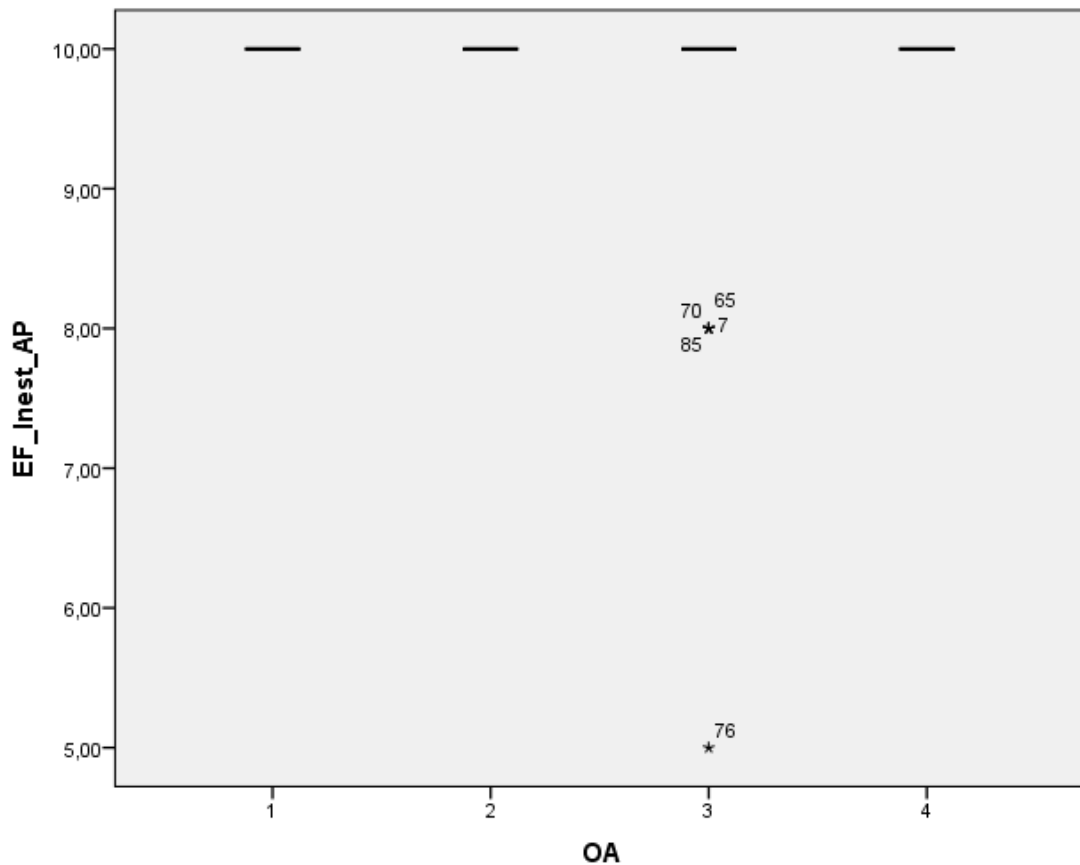


Figure 469. Study II. Box-and-whisker plot of distribution of points for the Anteroposterior Instability item in KS Knee Score (EF_Inest_AP), grouped into Ahlbäck OA grade.

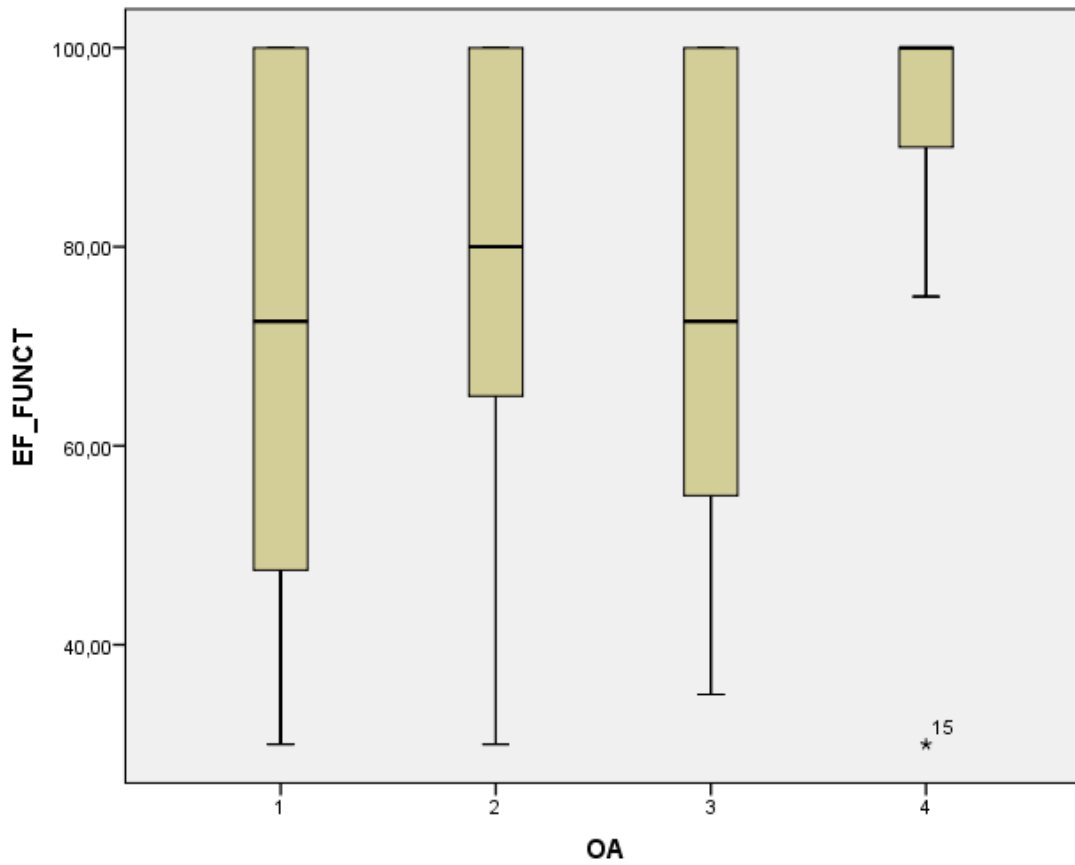


Figure 470. Study II. Box-and-whisker plot of distribution of points obtained for the Function Score part of KS Knee Score (EF_FUNCT), grouped into Ahlbäck OA grade.

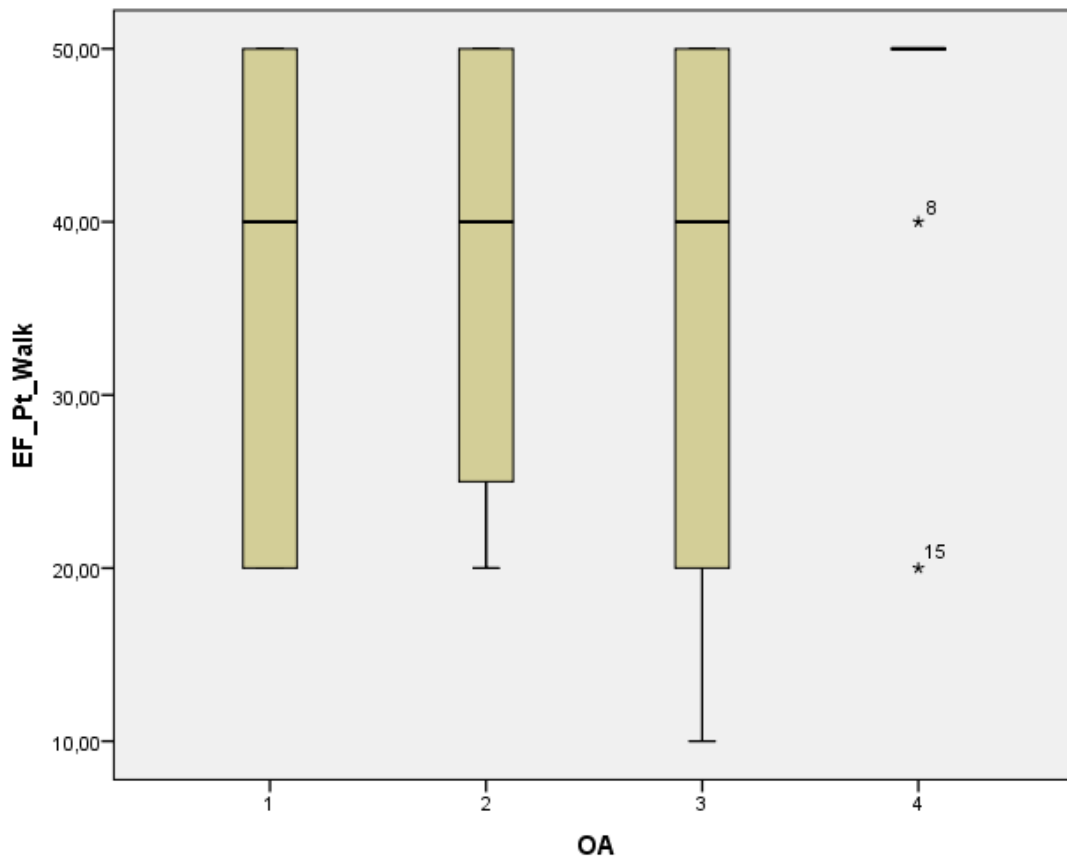


Figure 471. Study II. Box-and-whisker plot of distribution of points for the Walking Distance item in KS Knee Score (EF_Pt_Walk), grouped into Ahlbäck OA grade

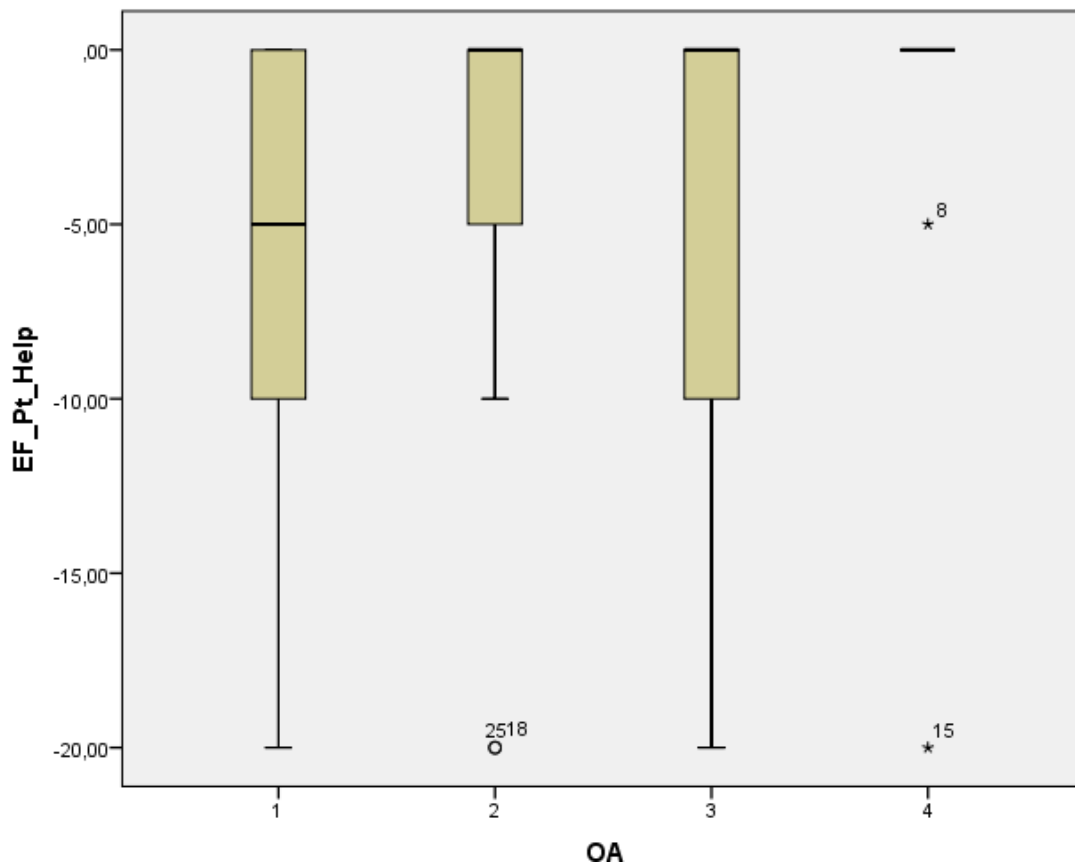


Figure 472. Study II. Box-and-whisker plot of distribution of points for the Help item in KS Knee Score (EF_Pt_Help), grouped into Ahlbäck OA grade.

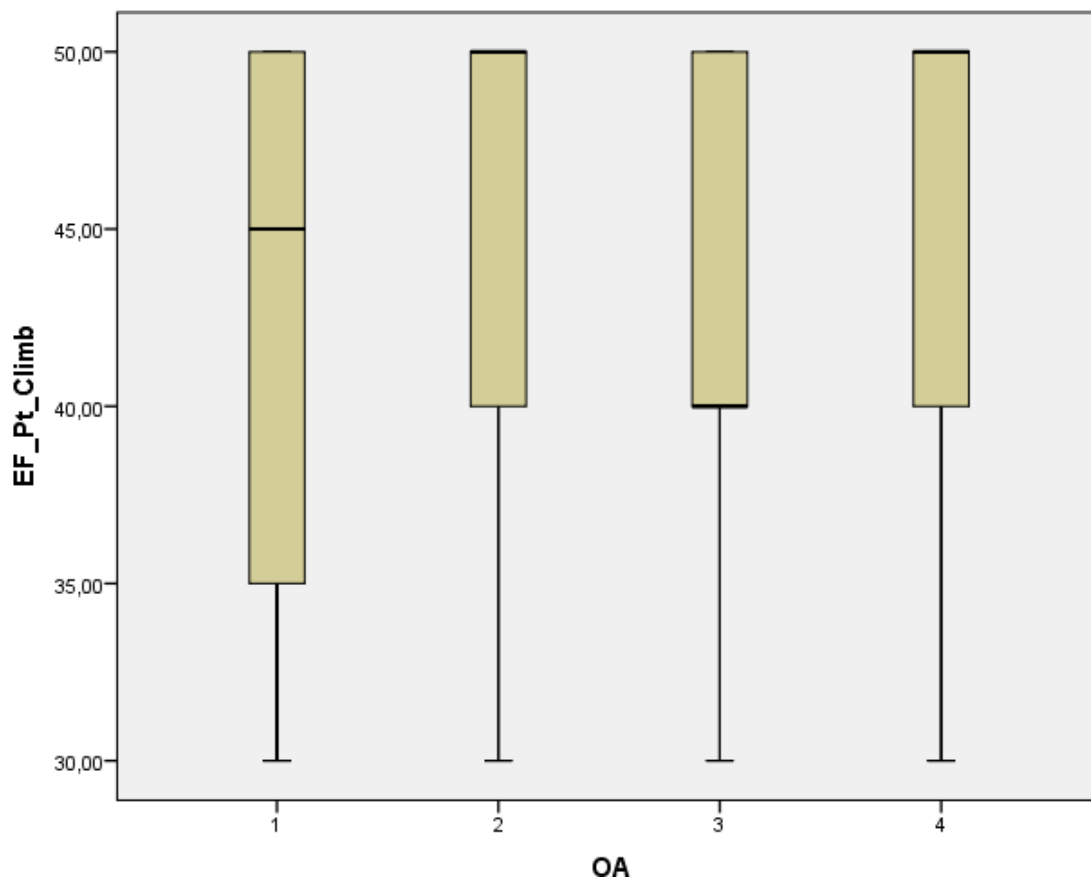


Figure 473. Study II. Box-and-whisker plot of distribution of points for the Climb item in KS Knee Score (EF_Pt_Climb), grouped into Ahlbäck OA grade.

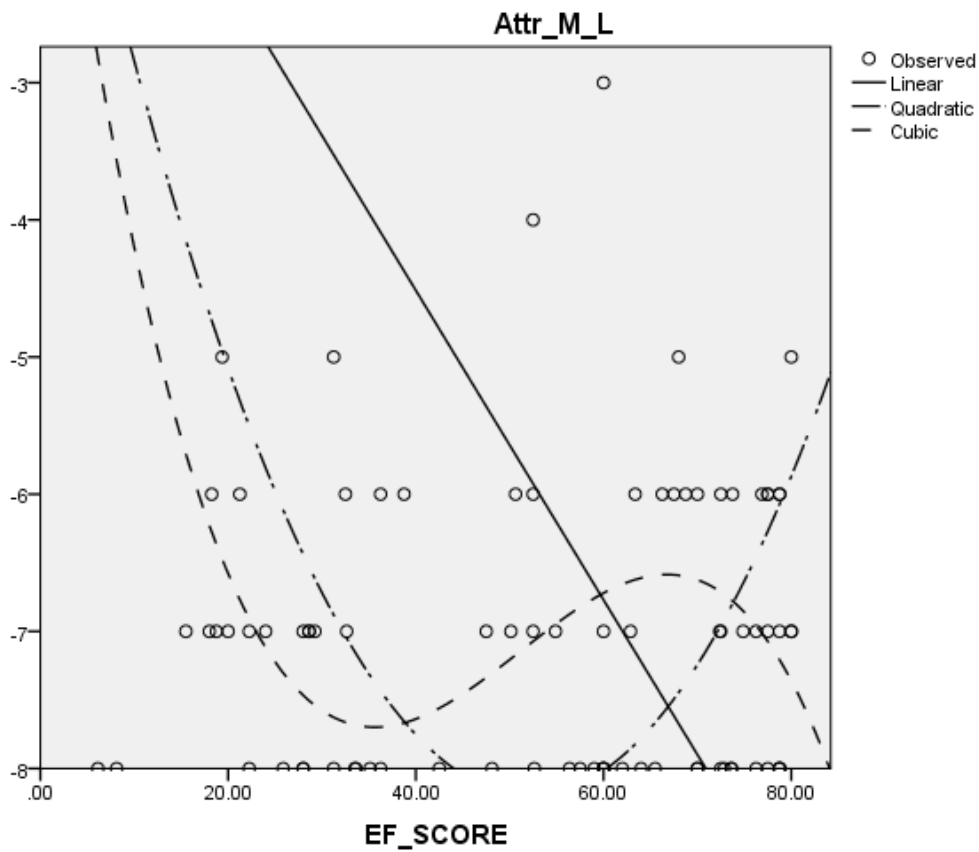


Figure 474. Study II. Best fit regression models obtained to predict KS Knee Score (EF_SCORE) from the combined attrition of the medial and lateral condyles (Attr_M_L).

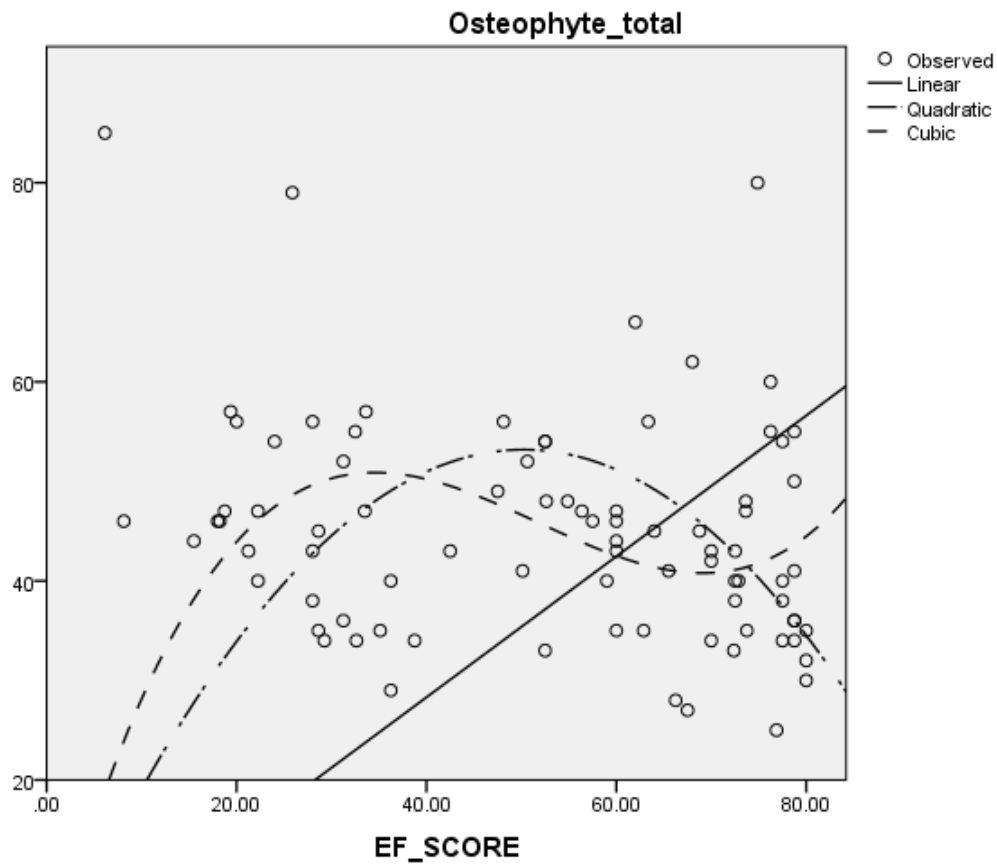


Figure 475. Study II. Best fit regression models obtained to predict KS Knee Score (EF_SCORE) from total osteophyte growth.

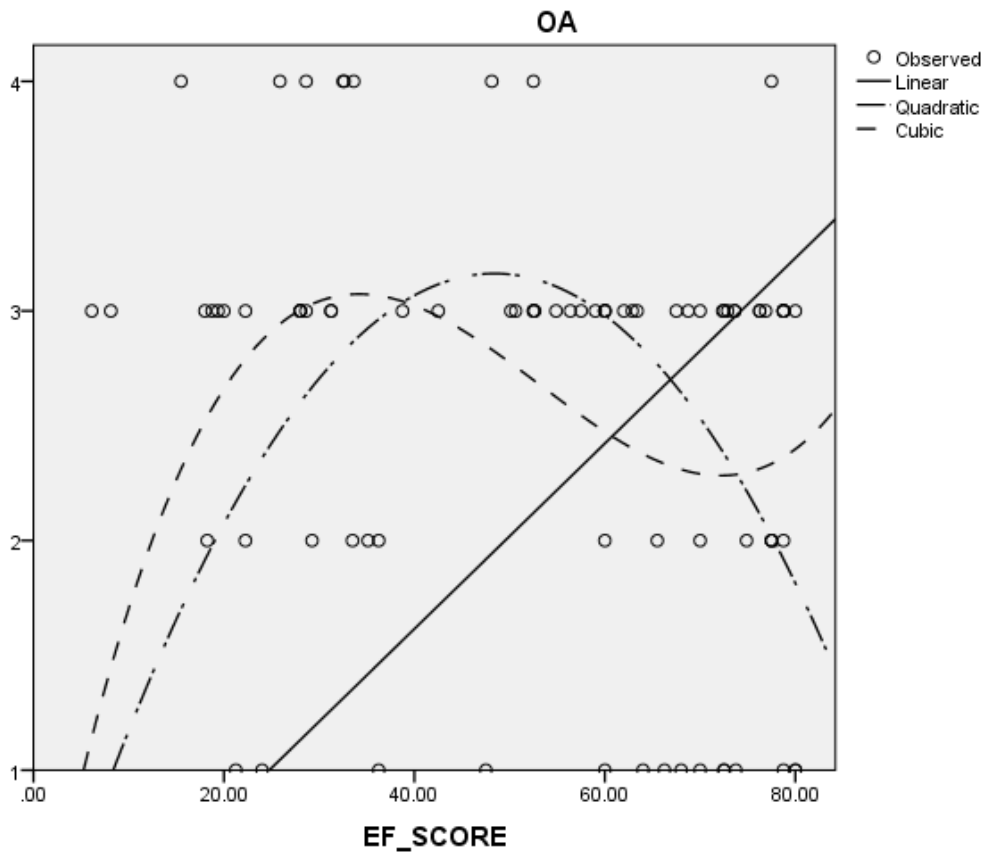


Figure 476. Study II. Best fit regression models obtained to predict KS Knee Score (EF_SCORE) from Ahlbäck OA grades.

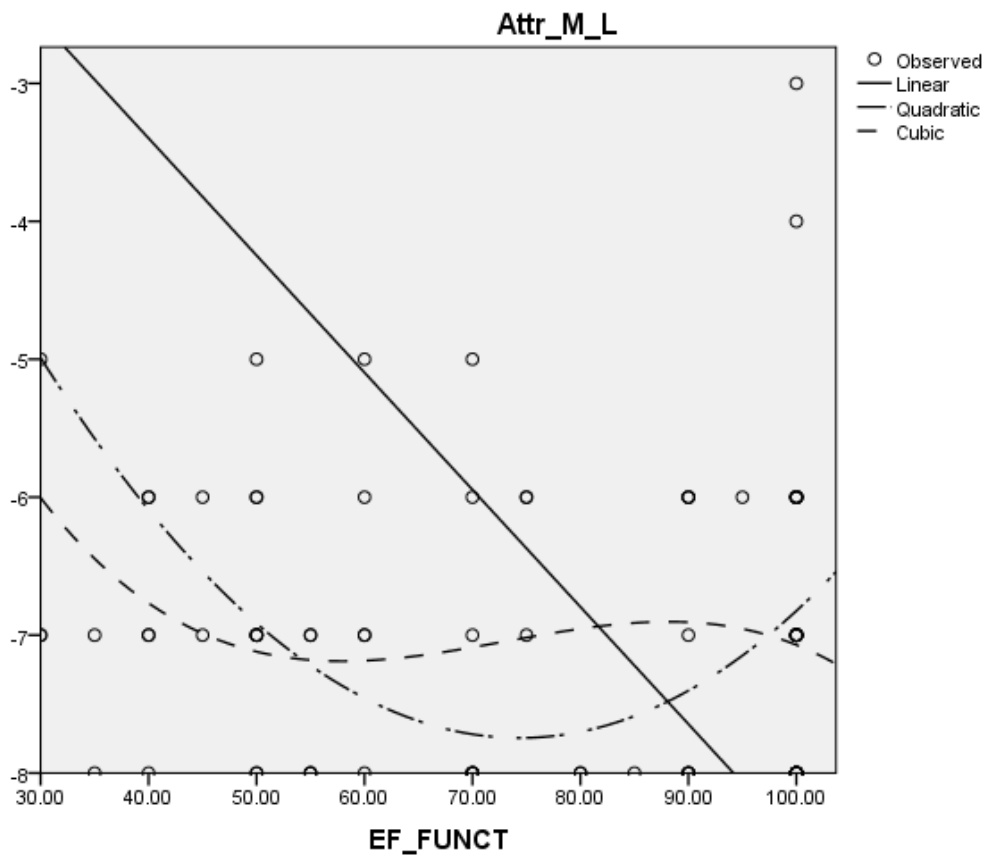


Figure 477. Study II. Best fit regression models obtained to predict KS Function Score (EF_FUNCT) from the combined attrition of the medial and lateral condyles (Attr_M_L)

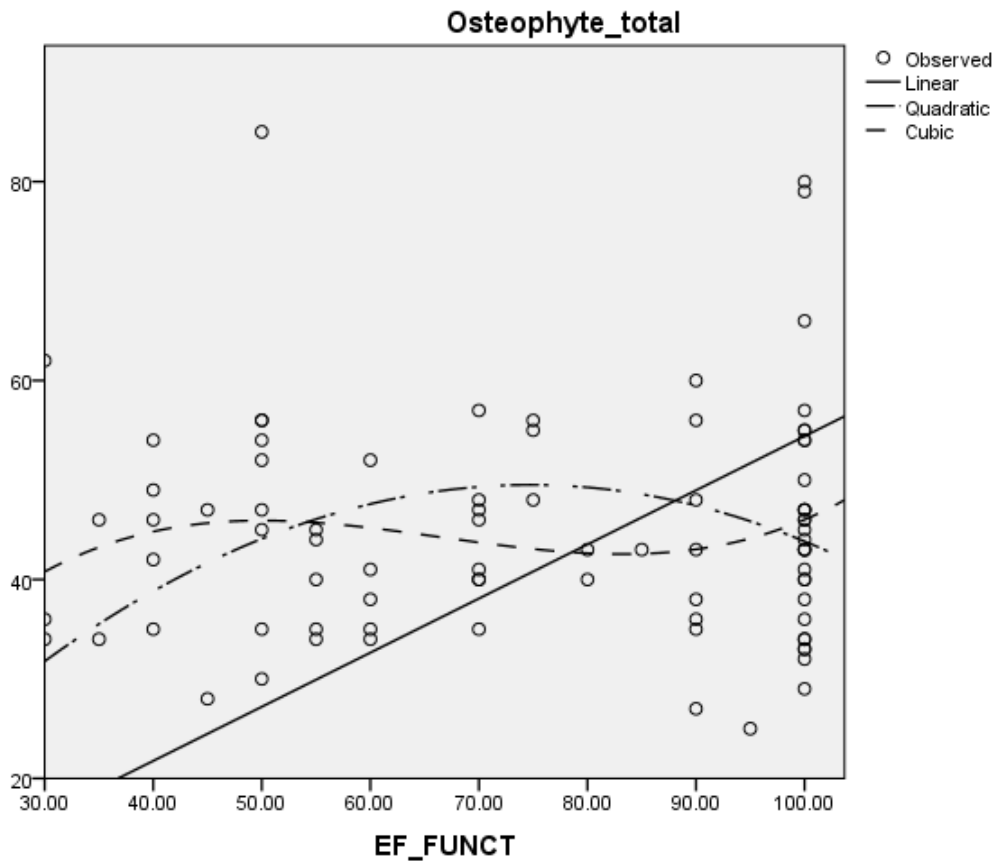


Figure 478. Study II. Best fit regression models obtained to predict KS Function Score (EF_FUNCT) from total osteophyte growth.

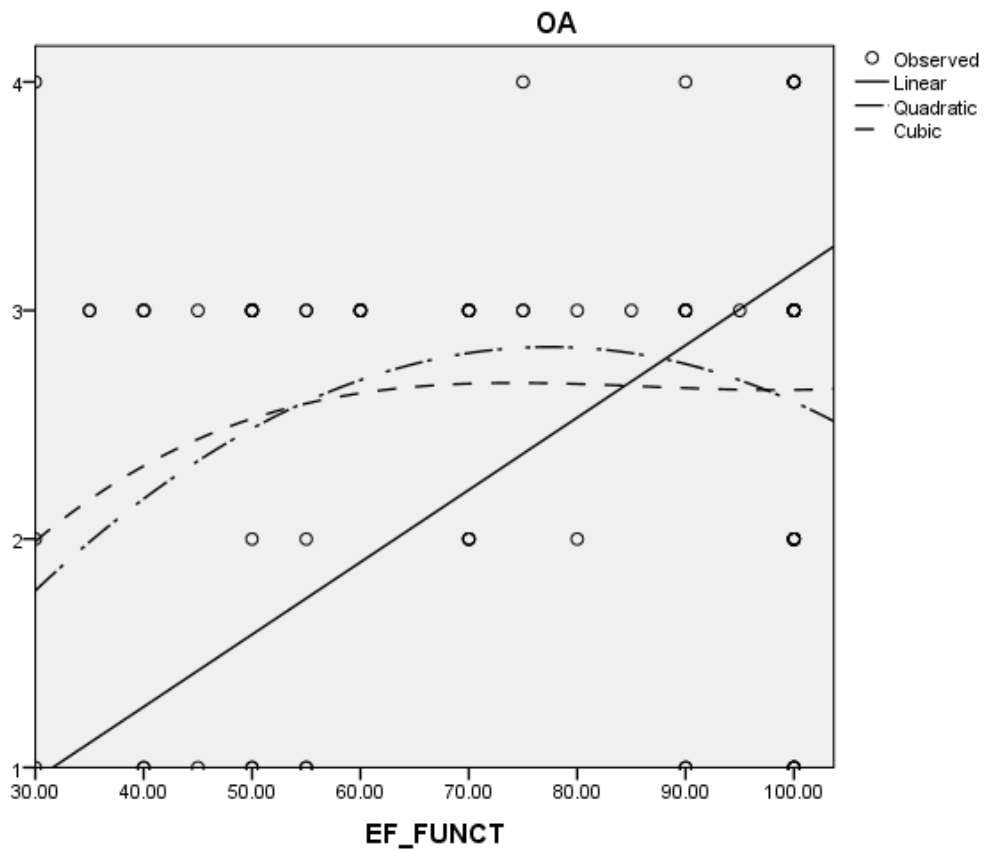


Figure 479. Study II. Best fit regression models obtained to predict KS Function Score (EF_FUNCT) from Ahlbäck OA grades.

V. Discussion

V.0. Method (Study I & Study II)

V.0.1. Specimen preparation

Ligamentous and meniscal attachments were outlined using pyrography marks, a method first described by Sclavunos⁶⁵.

V.0.2. Scan and fluoroscopic image system validation

Previous studies of the osseous surface of the knee have used 3D surface obtained from laser scans⁶⁶⁻⁶⁸, and less accurate 3D volume renderings obtained from CT scans^{69, 70}. No previous study of the knee has investigated its surface anatomy with this work's level of detail, which was obtained by using photogrammetry software with high quality photographs taken from precise distances and angles.

During photography sessions, it was impossible to avoid certain shadows and reflections, depending on the individual specimen's size and location over the sanding sponge, and the exact sunlight intensity at the moment. Photographs relied heavily on natural light, and those obtained in autumn (normal specimens) were darker and had more reflections and shadows than those obtained during the summer (pathological specimens).

V.0.3. Measurement system validation

The estimated measurement error lacks precision, since it does not take into account all the triangles selected from the osseous surface. However, the selection of triangles tested (12 triangles tested of 40 selected in each specimen) is believed to offer a more conservative assumption in terms of potential cumulative error, since the double-triangle centers were only found in soft tissue center areas. Hence, the actual measurement error is expected to be less than the estimated one.

V.0.5. Anatomical measurements

Areas in this work are defined as purely osseous surfaces, with osseous limits, in contrast with Jacobsen's²¹ common selection of soft tissue insertional areas.

Even when areas were selected avoiding textures, pyrography marks were often visible on the surface. Also, the same person did all processing tasks, making it impossible to blindfold the area selection process.

The posterior tibial axis was drawn according to previous studies^{71, 72} by connecting the posterior limits of the medial and lateral condyles, and the anterior tibial axis⁷³ by connecting the anterior limits (as shown in Fig. 30).

Area centers were defined in a vertical plane departing from the calculated three-dimensional centroids, unlike previous works which made use of two-dimensional⁷¹ or simplified three-dimensional calculations⁷⁴. Although this is not the most exact calculation possible, it is difficult to improve precision using the technology available.

The few previous similar works using 3D scanners reported^{68, 75} an accuracy and repeatability of $\pm 50 \mu\text{m}$, citing just the manufacturer's a priori specifications, and using a hard probe of the scanner to select the periphery of attachment areas. The calculated accumulated error of the obtained measurements in this study was $\pm 0.5 \text{ mm}$, and selection of the previously outlined areas was made directly on the 3D design software. Apart from limitations of photogrammetry, no probe was needed, and human error was thus reduced. In contrast with the theoretical accuracy reported in previous studies, in this study an estimated error has been offered for each step of the process. An approximation to the true 3D center of each defined area and their distance is thus improved.

Measurements were taken following the osseous surface, to imitate the arthroscopy probe during surgery. Distances were thus calculated following the surface, as would be done in the operative setting, e.g. during arthroscopy by moving the probe along the most direct path from the selected landmark. Only in certain cases, when the probe would not have been placed over the area (as over the lateral fossa for lateral wall measure) were direct measures used.

As in Edwards et al.⁷¹, correlation of distances obtained with the corresponding specimen's AP and ML size have been obtained, but unlike previous studies using simpler two-dimensional straight AP and ML lines, this work offers a higher complexity with three-dimensional oblique lines. Therefore, correlation values

are expected to also evaluate a relation to a common direction found from the attachment center to the selected osseous landmark, i.e. to a vector perpendicular (for the AP size) or parallel (for the ML size) to the posterior axis. Actual measurements, AP, and ML size being equal, if the direction of measurements to a selected point were nearer to the AP or ML vector, the p-value obtained would be lower. Nevertheless, the combination of p-values and coefficient of variation for each measurement is expected to yield reliable estimates of the precision of the values obtained.

3D models of all tibias will be available for download, so that identification of structures and repeated measurements of areas will be possible. Therefore, the scientific principle of reproducibility is safeguarded.

V.0.6. Osteophyte grades

Elevations and depressions were graded by comparing them to surrounding areas. This process necessarily included a subjective evaluation of both (1) the *original* height of the area, and (2) the *original* height of the surrounding areas. The first exploratory assessment and the next two grading assessments done of all specimens are believed to have limited intraobserver errors.

Microscopic soft tissue remains were often left in attachment areas, and in some cases they were noticed as wrinkles in 3D models in areas 5, 10, 8, 12, 11b, and 13. This might have introduced an overestimation of osteophyte grade in certain specimens.

V.0.7. Correlation between paired specimens

In the study by Kohn & Moreno⁷⁶, a Pearson product-moment correlation was run to determine the relationship between right and left knees studied (42 knees from 21 donors), reporting results as follows: ARMM, $r=0.78$; PRMM, $r=0.88$; ARLM, $r=0.67$; PRLM, $r=0.55$.

The Pearson correlation test does not seem to offer a good assessment of similarity between right and left knees, therefore a multiple regression test was run to predict AP and ML size of the proximal tibia from all attachment areas measured, and a dummy variable for left vs. right knees was included in the model.

Qualitatively, it was observed that, while paired specimens were similar to each other at a glance, they differed in many anatomic details from those described in

this study. Differences in paired specimens have also been found before in similar studies^{77, 78}.

Given the quantitative and qualitative data presented in this study, as well as the common practice in previous similar studies, inclusion of all fourteen knees is justified in this study for the investigation of surface anatomy and attachment areas.

V.1. General anatomy

V.1.1. Normal anatomy

V.1.1.1. Qualitative assessment of areas

V.1.1.1.1. Osseous areas

Special difficulties were found when separating areas 5 from 9, and also 5 from 10, and 13 from 11c, because of the variability in their borders as defined in this work: anterior AIAR between 5 and 9, both AFIR processes between areas 5 and 10, and the low tent-shaped ridge (or the tent-shaped incisure anterior to it) between areas 11c and 13.

Percentages vary considerably because of the total area of the tibial plateau available for calculation. Partially available areas – due to excessive cuts anteriorly (affecting areas 5, 9), posteriorly (area 13), or mediolaterally (affecting the condyles) – were included in calculations of the total area of specimens to obtain percentages, but they were not included in the calculation of the mean size of these areas.

Areas of the posteromedial corner (3 specimens), posterolateral corner (2 specimens), Parsons' knob (7 specimens), and anterocentral intercondylar knob (4 specimens) were also taken into account for the proximal tibial area, but were not divided between neighboring areas, affecting thus mostly the mean size obtained for areas 1d, 2d, 5, 10, 9, which might therefore be slightly underestimated if compared to previous studies, like Jacobsen's.

V.1.1.1.2. Attachment areas

Poirier² described the attachment of cruciate ligaments and menisci as “clearly traced over the surfaces”. Parsons¹² stated similarly that “there is a definite mechanical reason for each one being as it is, and [that] they are good examples of a broad generalization, (...) that bones are moulded by the contiguous soft parts much more than they mould those parts, and that every little elevation and depression has its meaning”. Jacobsen also agrees with Parsons' statement that “throughout the region the fibrous insertions leave facets and that every little elevation and depression has its meaning. On macerated bones the insertion facets are clearly separated from the areas which serve for the attachment of the loose connective tissue between the fibrous structures. These areas are slightly excavated, look more porous, and exhibit foramina nutricia.” This belief is also shared by Berlet and Fowler⁷⁹, who found that “insertion facets were clearly

separated from the areas that serve for the attachment of the loose connective tissue.”

In this study, ligamentous and meniscal insertions have been studied in relation to the detailed osseous elevations and depressions investigated.

V.1.1.2. Quantitative assessment of areas

Mean sizes obtained include a mean ML width of 72.2 mm (90% CI 68.9 – 75.5 mm; range, 63.2 mm to 81.6 mm), with a mean 75.4 mm for males (n=8), 67.9 mm for females (n=6), mean difference, 7.5 ± 5.3 mm; and a mean AP depth of 50.1 (90% CI 47.3 – 52.9 mm; range, 41.1 mm – 56.1 mm), with a mean 52.6 mm for males (n=6), 46.8 mm for females (n=6), mean difference, 5.8 ± 5.4 mm.

These findings correlate well with the 78 mm width, 56 mm depth reported by Robert¹⁰; ML width of 74 mm (range, 58 mm to 87 mm), and AP depth of 47 mm (range, 40 mm to 55 mm) by Morgan et al.⁸⁰; 77.7 ± 5.9 mm width, 50.5 ± 6.2 mm depth by Colombet et al.⁸¹; AP depth of 47.3 ± 3.8 mm for the intercondylar area found in Kwak et al.⁸²; ML width of 79.2 ± 4.6 mm for males, 68.6 ± 4.8 mm for females, AP depth of 56.8 ± 3.5 mm for males, 50 ± 3.8 mm for females found in Mahfouz et al.⁸³ for Caucasians, with an average 9-mm larger ($p < 0.01$) ML and 5-mm larger ($p < 0.01$) male AP dimensions.

These measures correlate fine with those obtained by Edwards et al.⁷¹, with a mean ML width of 80 ± 6 mm, AP depth of 52 ± 5 mm; with those obtained by Dargel et al.⁸⁴, with a mean ML width of 81.0 ± 3.35 mm for males, 72.2 ± 3.80 mm for females (difference, 10.86%, $p < 0.001$).

These measures are in contrast with measurements found in Yue et al.⁸⁵: ML width of 86.0 ± 5.6 mm for white males (range, 74.9 mm to 100.2 mm), 76.4 ± 4.0 mm for white females (range, 70.3 mm to 82 mm); and AP depth of 67.5 ± 3.6 mm for white males (range, 62.4 mm to 75.3 mm), 59.7 ± 2.6 mm for white females (range, 54.6 mm to 64.1 mm).

There has been much debate recently as to the need for sex-specific total knee arthroplasty. Several studies support the existence of such sex-specific variations⁸⁶⁻⁸⁹ – suggesting that females tend to have smaller mediolateral dimensions for any given anteroposterior femoral dimension than males –, although it remains questionable whether these differences are of clinical relevance^{90, 91}.

Differences have been found in this study between male and female mediolateral and anteroposterior sizes. However, it did not take into account the difference in sizes between the men and women studied, which has been assumed in previous studies to be the main reason for the differences^{89, 91-94}.

No statistically significant differences were found in ML width or AP depth between right and left knees in this study, which is in accordance with data found in Gandhi et al.⁹⁵

There are two main variables affecting measurements: the axis selected, which in this study (as in Edwards et al.) is the posterior tibial axis for the AP depth, and a perpendicular to it for the ML width measurement; and the precise medial and lateral borders selected for the ML width, which in this study were the medial and lateral condylar rims (the most elevated areas), while in other studies – where measurements obtained are greater than in this one – could be further externally, corresponding to the most medial and lateral points taken from a superoinferior view of the tibia.

V.1.2. Pathologic anatomy

Lack of previous radiographic assessment of donor tibias from Study I precluded a proper classification according to Ahlbäck and Rydberg⁵³, but qualitative investigation of degenerative changes in all donor specimens compared to findings of pathological tibias seem to support the initial evaluation made during arthrotomy and physical examination of the knee.

Varus angle in standing short knee radiograph was found in Khan et al.⁹⁶ to be associated with an increased risk of knee-compartment-specific degenerative changes, which agrees with findings of this study. They also agree with results of previous studies using full-length radiographs, like Sharma et al.⁹⁷ Kraus et al.⁹⁸, Hsu et al.⁹⁹, etc.

V.2. Tubercles

V.2.1. Intercondylar area and tubercles

The tibial spine is described by the Weber brothers in relation to the condyles, with its medial aspect sloping sharply towards the medial condyle, the lateral more gently.

The first detailed description of the tibial spine is found in Robert¹⁰, as “a saddle-shaped elevation” lying in the center between the medial and lateral borders of the tibial plateau, but nearer to the posterior margin. The tibial spine “engages the intercondylar fossa as an imperfect pivot”, with the tubercles “sloping downward anteriorly and posteriorly, internally and externally.” The intercondylar area is described as having an “hourglass shape”. Height measurements on specimens were reported as 10 mm for the medial tubercle, 8 mm for the lateral tubercle

Poirier & Charpy² described the tubercles as pyramidal eminences, articular in one of their faces, and delimiting two intercondylar areas anteriorly and posteriorly. In a similar way were described by Testut^{6, 15} the tubercles and the intercondylar areas.

Fick¹¹ described both tubercles as ca. 1 cm high, and inserting between both femoral condyles, not filling the intercondylar fossa. The anterior and posterior intercondylar areas were described as approximately triangular, forming together an hourglass-like shape.

Parsons¹² described the tibial spine as consisting “of two eminences placed side by side (...), and separated by an oblique groove which runs backward and outward. Each of these eminences is the portion of the articular surface which is nearest the centre of the head of the tibia; and each, no doubt, rises up here because it corresponds to the intercondylar notch of the femur, for here the head of the tibia is relieved from pressure.”

Jacobsen²¹ described the slopes of both tubercles as weight-bearing, cartilage-covered areas, articulating directly with the cartilage on the femoral condyles. The cartilage junction is on their summits or slightly internal to it. The MT was reported as 10 mm high (range, 8 mm to 12 mm), and the LT as 7 mm high (range, 3 mm to 10 mm).

As in Jacobsen, areas 3 (medial tubercle) and 4 (lateral tubercle) have been defined independently from the other areas, hence including in them part of the cartilage-covered condylar areas 1b and 2b, their anterior and posterior ridges, and part of their inner (non-cartilage-covered) slopes. This selection was used for tubercle slope calculations.

Tubercles are covered with thick hyaline cartilage and articulate with corresponding surfaces on the femoral condyles, as found in McLeod et al.¹⁰⁰. The medial tubercle is the larger prominence and is located anterior to the lateral tubercle.

Both main intercondylar tubercles represent the pivot of rotation of the femur on the tibia, according to Tardieu¹⁰¹. The close fit of the tibial tubercles in the intercondylar fossa is linked to Man's erect posture and bipedal locomotion, allowing only a small amplitude of independent rotation, and thereby contributing to stability of the joint¹⁰¹. The articular cartilage is thickest over the intercondylar eminence and it has been postulated, therefore, that the majority of the weight transmitted through the femur is carried by the intercondylar eminence¹⁰⁰, although there is little evidence to support this.

Hence, contrary to Parsons belief, the most obvious function of the tibial spine (more precisely, both elevated tubercles and their external slopes), in non-degenerative knees, is to stabilize the tibiofemoral joint by engaging the femoral intercondylar fossa, so that mediolateral and rotational movement is not possible in full extension^{102, 103}. These movements are possible only with the knee flexed. The most comprehensive review of the history of publications on knee function and range of motion to date is found in Wetz & Jacob¹⁰⁴.

Results from this study agree with previous descriptions of the shape of the main intercondylar tubercles. Previous reports of tubercular height show greater measures than those found in this study, although they agree well with Jacobsen's reported measures: MT, 8.41 mm (range, 6.42 mm to 11.06 mm), LT (4a), 7.77 mm (range, 5.75 mm to 9.47 mm). Although only 14 specimens were measured, measurements were done digitally over a 3D model, obtaining the precise highest points of the tubercles studied, and they were measured against the bicondylar tibial plane obtained, hence it is more likely to offer a more exact report than previous studies that relied on caliper measurements over the specimen.

V.2.2. Processes

Robert¹⁰ described the intercondylar area (the “articular part not covered by meniscus”) as lying horizontal to the tibial axis, with its medial aspect elevated against the medial condyle, the lateral aspect elevated against the lateral condyle. He described the intercondylar area as not contacting the distal femur in any case.

Parsons described the external tubercle to be limited anteriorly and posteriorly by the external meniscus, while the internal tubercle is developed anterointernally (in the slight ridge forming the ACL attachment) and posteroexternally (in the intertubercular area, described as a ridge). The little knob is the only elevation reported by Parsons as marking the ACL attachment.

Jacobsen also described the internal aspect of the AIA as formed by the internal aspect of medial tubercle (where the ACL attaches), and area 1c. Only the inconstant Parsons’ knob, an anterior (either medial or lateral) knob is described as an elevated limit.

The anterior aspect of the medial tubercle is the most recognized elevation surrounding the intercondylar area, and it has been called medial intercondylar ridge by Purnell et al.⁶⁹, Nishimori et al.¹⁰⁵, Tensho et al.⁷⁰, Shino et al.¹⁰⁶; or simply considered part of the medial tubercle in Edwards et al.⁷¹. It has been reported in other studies as an anatomic reference point for ACL footprint location, without a mention to its elevation or connection with the MT, described as medial plateau articular cartilage in Heming et al.¹⁰⁷, anteromedial rim by Siebold et al.¹⁰⁸, medial plateau border by Ziegler et al.¹⁰⁹.

The anterolateral intercondylar ridge (ALIR) has also been reported as the anterolateral rim, an anatomic landmark, by Siebold et al.¹⁰⁸.

The vallecule found in this study between the anterior and posterior peaks of the lateral tubercle is described by Jacobsen²¹: “The contour of the tuberculum laterale has a slightly arcuate notch behind the anterior, highest peak (on a level with area 12), at the site of the cornu posterior menisci lateralis. This notch was absent in only 3% of the macerated specimens.” The central PLIR most likely corresponds to what was described as the “tall posterior arch of the tuberculum laterale” by him.

The main intercondylar tubercles have been described in this work as formed by their most obvious elevations, their summits and surrounding areas, but also by anterior and posterior processes that form the border of the intercondylar area

with the condyles. In normal specimens, the medial tubercle shows a high central anterior process and a low central posterior process, whereas the lateral tubercle shows a wide and high central posterior process, and a low central anterior process.

A case report of a unilateral aplasia of both cruciate ligaments in Balke et al.¹¹⁰ showed an abnormally high and deep tibial spine, fully covered in articular cartilage, and a narrow intercondylar notch.

The external aspect of the medial tubercle (including its medial, anteromedial and posteromedial slopes) finds its counterpart in a slim cartilaginous band situated on the part of the femoral condyle that faces the intercondylar fossa. The role of the interaction of these two surfaces in guiding the automatic rotation of the knee have been dealt with repeatedly, e.g. in the textbooks of Gerrish¹¹¹, Langer & Toldt¹¹², Cunningham¹¹³. First described kinematically by Brantigan & Voshell¹¹⁴ as instantaneous centers of transverse axis of rotation of the tibia, Shaw & Murray¹¹⁵ and Trent, Walker & Wolf¹¹⁶ confirmed the axis of voluntary rotation passes through this anatomic structure, and Fuss¹¹⁷ – because of that precise position found in his study – suggested its relevance for guiding that motion (see Fig. 480 and Fig. 481). Yildirim et al.¹¹⁸ found that in all rotations, the medial contact moved inwards to engage the intercondylar eminence, which appeared to act as the pivot area.

The constant shapes found in this study of both intercondylar tubercles and their processes are proposed to represent the best fit for the rotation pivot of the femur on the tibia¹⁰¹ – like the close fit of the tibial tubercles, that interlock with the intercondylar fossa^{102, 103} –, providing thus an osseous restriction to translation with internal rotation of the femur over the tibia, thereby contributing to stabilize the tibiofemoral joint. It is further hypothesized that, because of their different shape, the AMIR is the main anterior stabilizer in conjunction with medial femoral condyle, and the PMIR is the main posterior stabilizer together with the lateral femoral condyle, and that these osseous limits to translation during rotation complement the function of ligaments and menisci in different degrees of flexion^{117, 119}.

The different processes described here (but for the AMIR) and their function have not been described before.



Figure 480. Maximal possible internal rotation of the femur with removal of capsular and collateral ligaments and of the menisci, but with intact cruciate ligaments. Modified from Fuss (1991)¹¹⁷.

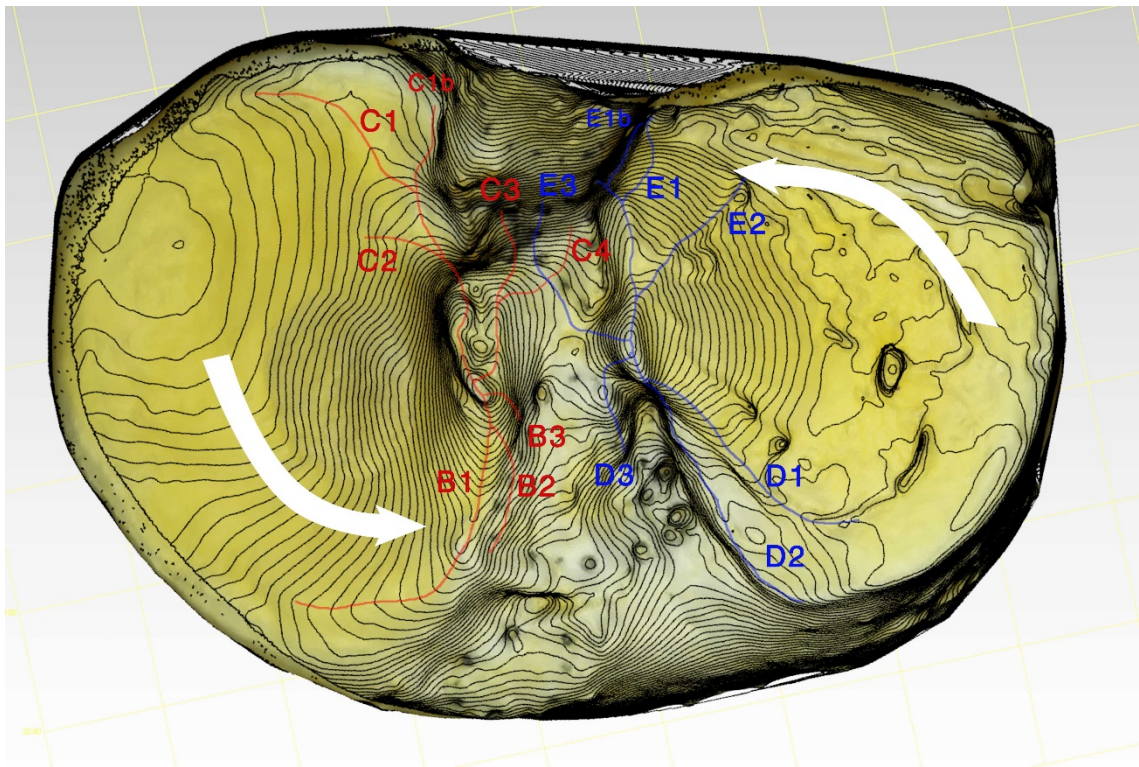


Figure 481. 3D model of tibia A, with contour lines superimposed. Main processes of the medial tubercle (in red) and lateral tubercle (in blue), labelled. In white, curves loosely following each condyle's radius of curvature, representing potential internal rotation of the femoral condyles over their respective tibial condyles. The AMIR and PLIR processes appear as potential osseous limits to translation in the different degrees of rotation. Osteophytic elevations of these processes could therefore constrain tibiofemoral movements in more unstable knees.

V.2.3. Tubercle size in knee radiographs

V.2.3.1. Tubercle size in adults

Results for adults (Study V) agree with previous reports, showing 75% MT>LT, 16% of LT>MT, 4% of MT = LT. In the MRI studies medial and lateral tubercles showed a mean difference in size of $1.7 \pm 0.5\%$ (where positive means MT>LT); range, -8.7% to 14.4%.

Men showed a statistically significant greater AP depth in radiography, and a greater distance to the posterior condylar aspect in MRI. Men also showed a significantly greater MT height than women in radiography, and a greater MT-LT height difference in radiography (relative to ML width), that almost reached statistical significance ($p=0.051$). Therefore, even though no association was found between tubercle size and reported pathology, absolute and relative tubercle size (given their stabilizing function) are proposed as potential risk factors for the known higher risk of ACL lesions in women¹²⁰⁻¹²⁹, apart from the already studied decreased area, stiffness, stress at failure, and modulus of elasticity of the female ACL¹³⁰.

V.2.3.2. Tubercle size in children

Results for children (Study VI) show a higher proportion of MT>LT (86%), and a lesser proportion of LT>MT (9%) than in adults. Even though MT=LT (1%) also shows a lesser proportion, most in the unclassified group (4%) were probably MT=LT. A significant association is found between lateral meniscal pathology and LT>MT, LT=MT groups, and also between patellar pathology and the LT>MT group, although the small numbers do not let derive any hypothesis.

The mean difference in height between tubercles, $1.7 \pm 0.3\%$ (positive value indicates MT>LT), range, -2.1% to 5.9%, was similar to adults. MT height relative to ML width in AP radiograph was found to be greater than women (as in adults), and the difference in LT height relative to ML width was not found significant, as in adults, although the difference found was greater, and the p -value (0.068) much nearer to the significance threshold than in adults ($p=0.944$).

Age was not found to be associated with differences in tubercle height, although it showed a significant, low negative correlation in radiography, which suggests a growth of the proximal tibia not matched by the growth of the tubercles during development, and thus a hypothetically more important stabilizing role of the

tubercles (and potential role in osteochondral lesions) in children compared to adults.

Because all patients selected were investigated due to a preexisting pathology, no extrapolation of the data to the general population is possible.

V.2.3.3. Tubercle size in adults with osteochondritis

Even though the study design did not include patients without osteochondritis, in adults with osteochondritis (Study VII) the relative height of the tubercles (80% MT>LT, 12% LT>MT, 8% MT=LT), and the proportional height of the tubercles relative to the ML width in AP radiograph were similar to those found in Study V: mean MT height $12.4 \pm 1.1\%$ (range, 8.5% to 17.9%) vs. MT height in normal adults, $12.1 \pm 0.4\%$ (range, 1% to 16.7%); mean LT height $10.8 \pm 0.9\%$ (range, 7.1% to 16.6%) vs. LT height in normal adults, $10.4 \pm 0.4\%$ (range, 0% to 14.2%). They showed an average difference of $1.6 \pm 0.8\%$, which compares well with the $1.7 \pm 0.5\%$ in normal adults. No differences were found between men and women.

The smaller range of tubercle height (with higher values) in patients with osteochondritis cannot be hypothesized to represent a difference, because of the study design – which did not include a control group –, and also because the number of patients included in Study V was greater.

V.2.3.4. Tubercle size in children with osteochondritis

In children with osteochondritis (Study VIII), even though no comparison was made with patients without osteochondritis, the relative height of the tubercles (only MT>LT), and the proportional height of the tubercles relative to the ML width contrasted to the measures found in children from Study VI: mean MT height $13.4 \pm 1.2\%$ (range, 11% to 20.2%), vs. MT height in children without osteochondritis of $14.2 \pm 0.5\%$ (range, 8.6% to 22%); mean LT height, $11.4 \pm 1\%$ (range, 8.8% to 17%) vs. LT height in children without osteochondritis of $12.5 \pm 0.6\%$ (range, 6.8% to 20.5%); with an average difference of $2 \pm 0.6\%$ (range - 0.7% to 4.1%, where positive value indicates MT>LT) vs. the difference of $1.7 \pm 0.3\%$ (range, -2.1% to 5.9%) in children without osteochondritis.

In contrast with findings in adults (normal and pathologic), and with children without osteochondritis, where the mean difference in size in MRI and radiograph showed a trend to be greater in men, it was found in this study to show

a trend to greater differences in females, although that difference was not statistically significant.

No conclusion can be derived from the comparison of these two descriptive studies, and comparison of age groups is not possible, but – because of the association found between the affected condyle and MT height, relative MT-LT height (higher values were associated with medial condyle lesions), it is suggested that absolute and relative tubercle size might indeed be a risk factor in the development of osteochondritis.

V.2.3.5. Tubercle size in osteonecrosis

Values obtained for patients with osteonecrosis (Study IX) in relative tubercle size (88% MT>LT, 10% LT>MT, 2% MT=LT) and radiographic mean height relative to ML width show similar results to patients with osteochondritis: MT, $13.5 \pm 0.5\%$ (range, 9.3% to 18.2%); LT, $11.5 \pm 0.5\%$ (range, 7.4% to 14.6%); mean difference, $2 \pm 0.5\%$.

Since the design of Study IX did not include a control group of patients without osteonecrosis for comparison, the greater height (and smaller range) found in patients with osteonecrosis cannot be hypothesized to represent a difference. No differences were found between men and women, or between those with and without osteoarthritic changes.

V.2.3.6. Tubercle size in osteochondral fracture

Results for patients with osteochondral fracture (Study X) also showed a different distribution of relative tubercle size (89% MT>LT, 11% LT>MT), and a mean radiographic height relative to the ML width slightly greater than in patients of Study V, especially marked on the lateral tubercle: MT, $12.9 \pm 2.1\%$ (range, 8.3% to 15.2%); LT, $11.2 \pm 2.5\%$ (range, 6.6% to 13.7%); mean difference, $1.7 \pm 1.1\%$.

A statistically significant association was also found between an affected medial condyle and MRI height, with a mean 3.7 mm higher MT. The difference was not significant for radiographic studies (2.8% higher MT), though.

The design of this study did not include tibias without osteochondral fracture for comparison, but based on the findings of this study, it is hypothesized that tubercle height, and more precisely the difference in height between tubercles, might be risk factors for osteochondral fracture.

V.2.4. Degenerative changes

V.2.4.1. General discussion

Chondrogenesis and enchondral ossification in response to abnormal stresses on the articular surface could be responsible⁴⁰⁻⁴² for tubercular osteophytes, as they are areas that still possess some articular cartilage.

Thomas et al.³⁰ considered that sharpening of the tibial tubercles was a type of osteophyte formation similar to marginal osteophytes, but this was assessed subjectively.

Reiff et al.¹³¹ were the first to propose a measure of tibial lengthening as a ratio of tubercle height divided by tibial plateau width. They also measured angulation of the tubercles to evaluate the so-called tibial peaking or spiking. Their study included 55 patients, and they found a significant association of tibial lengthening and spiking with osteoarthritis.

Donnelly et al.⁶², in a study of 1003 women, reported a positive association between medial and lateral tubercle height and medial and lateral osteophytes, but their study did not confirm that isolated tibial spiking was a reliable marker for the presence of osteoarthritis of the knee, and so it could not be reported as a sign of early osteoarthritis. They found that angulation of the tip of the medial and lateral tubercles had a higher association than tubercle height with regard to tibial osteophytes.

The findings in both Reiff et al. and Connelly et al. support Alexander's⁴³ theory that tibial spiking is a form of osteophyte formation.

Boegård et al.¹³² found that the presence of marginal osteophytes had a high positive predictive value for cartilage defect detected in MRI, especially at the medial tibial aspect. Marginal osteophytes were also found to increase in size with decreasing minimal joint space width. No relation was found, however, between central osteophytes and MRI-detected cartilage lesions in the tibiofemoral joint.

Unlu et al.¹³³ found a significant association between medial tubercle height (ratio of more than 0.16) and MRI-detected cartilage defects in the medial tibiofemoral compartment, which could be accepted as a feature of OA in the tibiofemoral joint. A weak association was found between lateral tubercle height and MRI-detected cartilage defects at the lateral femoral condyle. These finds were explained by the higher prevalence of medial tibiofemoral OA, and the more

frequent detection of cartilage defects at the femoral condyles in MRI. Lateral tubercle angulation showed a correlation with osteophytes at the medial tibial condyle, but not at the lateral tibiofemoral joint. As in Reiff et al., the association of medial tubercle height and osteophytes was weak.

Hayeri et al.⁴² did find an association with their lateral intercondylar spine height index and the global grading of osteoarthritis, but not with the medial intercondylar spine index.

Apart from the suggested cause of femoral compression on the tibia for osteophyte formation in adjacent or opposite areas of the tibial plateaus (possibly due to more preserved cartilage), it has also been suggested that osteophyte formation contributes to stability. The association found in this study between tubercle osteophyte formation and Ahlbäck OA classification strengthens this hypothesis.

It is hypothesized further that tubercle spiking and slope show a trend towards diminishing size because of erosion of the femoral condyles on the intercondylar area and on the nude areas (possibly because of mediolateral and rotatory instability), which further confounds any attempt to classify osteoarthritis grades based only on tubercle size, width, or slope.

In tibias with degenerative changes, the AMIR and the PLIR show osteophytic growths – as do the medial and lateral intercondylar tubercles – which seem to represent osseous limits for translational movements during external knee rotation, as well as for high external rotation degrees. These findings strengthen the hypothetical stabilizing role of the main tubercular processes, as secondary stabilizers of the tibiofemoral joint in the different degrees of flexion.

Whereas the – usually non-elevated – PMIR has been qualitatively found to be elevated in osteoarthritic tibias, reaching in some cases a height similar or even higher than the PLIR (or the main intercondylar tubercles), the ALIR – especially its anterior aspect – was only rarely found to reach the elevation of the AMIR, and never of tubercles. The elevation of both of these processes would suggest a stabilizing role of the osteophytes as osseous limits for internal knee rotation in degenerative (hence more unstable) knees.

It is possible that the anterolateral secondary osseous limit to internal knee rotation, which would theoretically correspond to the ALIR, is formed by a combination of the D1-D2 elevation, the anterolateral corner, and the

anterolateral knob – apart from other periarticular osseous, ligamentous and tendinous limits outside the scope of this work. Or these findings could mean that the main role of the osteophytic elevation of the PMIR is an osseous limit to mediolateral translation in a more posteriorly located femoral compression on the tibia during the range of motion, like the posteromedial corner and posterior rim limit the posterior translation of the tibia during flexion, supplementing the deteriorated function of soft tissue restrains.

More detailed biomechanical and functional studies are needed to assess the precise role of the tubercles and their processes in stabilizing the tibiofemoral joint in its full range of motion, in normal and pathological tibias.

V.2.4.2. Tubercle size

Results for the relative height of the tubercles in the sample studied (most of them with degenerative changes) showed a distribution similar to that described in Bauer, with a lesser proportion of MT>LT (61.6%) vs. LT>MT (33%) than that found in posterior studies, including this work (Study V, see above). This distribution did not show an association with knee OA, though, so Ahlbäck OA grade (especially among the greater grades seen in this study) is not demonstrated to be related to the relative size of the main tubercles.

A weak, statistically significant correlation was found between osteophyte grade of both MT and LT, and knee OA, and so was radiographic density of the MT, which suggest an increase in height and density with degenerative changes that support the nature of the osteophytic growth in the tubercles as marginal osteophytes. That relation was not found with measurements made by hand over the specimens.

V.2.4.3. Tubercle width and attrition

Tubercle width was found to be weakly correlated to knee OA, and so was attrition of the LT, which would suggest they are also part of the degenerative changes affecting the tibial spine in the development of osteoarthritis.

Attrition direction of the MT was found to be mainly in an AM direction in varus knees, which would suggest erosion from the lateral aspect of the intercondylar fossa in the anterior aspect of the MT (downwards in a medial direction). Among the few valgus knees, the AL direction was found in most cases, which would suggest erosion from the medial aspect of the intercondylar fossa in the anterior aspect of the MT (downwards in a lateral direction).

Attrition direction of the LT showed more AL (and AM-PL, L) involvement in higher OA grades, while more AM (and AL-PM) in lesser OA grades, which would suggest erosion from the lateral aspect of the intercondylar fossa in lesser grades, and from the medial aspect of the intercondylar fossa in higher grades. Varus knees were found associated with the AL group, which also supports the medial and anterior femoral translation with respect to the tibia in varus knees.

Examination of attrition direction in radiography also showed an association with knee OA, which reached statistical significance only for the LT, which suggests its utility as an approximation to the underlying pathology. The precise direction was often not clear from plain radiographs, though, and many were left as inconclusive: only 41% of radiographs were classified for MT attrition direction, and 53% for LT attrition direction.

V.2.4.4. Tubercle slope

Tubercle slope showed a weak correlation with knee OA, and with tibiofemoral angle, but no differences were found between groups based on Ahlbäck OA grade. Graphically, a trend is seen towards a greater MT slope for grades 1 and 2, but lesser slopes for grades 3 and 4, while for LT slope it seems greater in grades 1 and 4. The combined MT-LT slope shows a marked increase in grade 1, then decreasing in grades 2 and 3, and increasing in grade 4 (although with greater variation). Slope angle variation in higher OA grades is believed to be related to attrition of the nude area, hence the best fit demonstrated for a cubic regression model (MT, $p=0.063$, LT, $p=0.311$).

Previous studies have shown that sagittal tibial slope was associated with an increased risk of ACL injury: Vyas et al.¹³⁴ found an increased medial tibial slope in the teenage population with open physes and ACL injuries; Alentorn-Geli et al.¹³⁵ noted an increased posterior tibial slope of the lateral compartment in patients with ACL injury (which can be explained as increased anterior tibial translation^{136, 137}, and therefore strain on the ACL); Simon et al.¹³⁸ found that the lateral tibial plateau in the uninjured contralateral knees had a significantly steeper posterior slope; Sturnick et al.¹³⁹ found the lateral tibial slope as a risk factor in female athletes only; and Rahnemai-Azar et al.¹⁴⁰ found that every degree increase in lateral tibial slope was associated with a 32% increase in the risk of an ACL injury.

A narrower lateral femoral condyle has also been associated with ACL injuries^{140, 141}, and tentatively explained as the rotation that the knee allows during a pivoting movement¹⁴⁰. A narrower intercondylar notch has also been found as an independent risk factor with ACL injury^{135, 138, 139, 142, 143}, which may be more relevant in the female population¹⁴².

Various authors have shown differences in osseous morphology between the female population and the male population, as osseous morphology relates to the risk of an ACL injury^{141, 144, 145}.

This study has selected the whole three-dimensional tubercular slope – including the tubercle peaks and their interior borders, as well as the anterior and posterior slopes of their respective processes –, which adds complexity and anatomic variation to the measure obtained, later simplified by obtaining a two-dimensional slope with the plane formed by the tibial condyles. This study also included a small sample, with an unequal distribution of degenerative changes (more specimens with high Ahlbäck OA grades). Further studies are needed to investigate the three-dimensional tubercle slope changes, and to evaluate a simpler, two-dimensional coronal slope measured from imaging studies (like AP knee radiograph, or coronal MRI slices), to assess its value as an early sign of degenerative changes, and as a potential risk factor for knee instability (and its role in potential injuries).

V.2.4.4. Tubercle processes

All main processes were found to correlate weakly with knee OA, but for the central PMIR process, which showed a weak, non-significant correlation with OA. That complicates further the potential role of the elevations of the ALIR and PMIR in tibias with degenerative changes. Radiographically, no increase in density was observed in the processes in higher OA grades.

V.3. Condyles

V.3.1. Condyles and condylar rims

The Weber brothers⁹ assigned a main function for the knee range of motion to both “asymmetrical shapes” of the femoral condyles over their respective tibial flat areas, namely “rolling” (rotation) for the lateral condyle, “sliding” (bending) for the medial condyle – forward in extension, backward in flexion.

The anatomy of both tibial condyles were long ago described by Robert¹⁰ with precision. Research has historically shown the geometry of both condyles to have a main role in tibiofemoral joint biomechanics¹⁰⁴, regardless of the subject-to-subject differences in terms of slopes and concavity or convexity of the condyles¹⁴⁶.

In this study, division and description of the tibial condylar areas was made following Jacobsen²¹, to make areas comparable with his study. Therefore, the limits of areas 1a-1b, 2a-2b were selected by the presence of thin cartilage in fresh specimens. This selection was found to be subjective and therefore unreliable for precise measurements.

Two constant anatomic landmarks have been described: the elevated condylar curvatures. Visible not only in fresh specimens, but also by observing the osseous surface, the selection of these osseous structures as a limit between inner condylar areas seems a better alternative for future works. They are hypothesized to represent the change from regions of cartilage-to-meniscus contact to cartilage-to-cartilage contact, where cartilage is up to 50% thicker¹⁴⁷, which may result in reduced contact stress¹⁴⁸.

External condylar rims have also been found difficult to select as external borders, since their slight elevation is internal to the true outer margin of the tibia, from where it begins sloping sharply downwards. In pathological tibias, the rim is even less reliable as an objective limit, since they appear variably wider and more elevated, with osteophytes growing either vertically or outwards, or in any oblique combination of both¹⁴⁹. Therefore, a poor intra-observer and inter-observer reliability is expected for measurements of areas 1a, 1b, and 2a, 2b. The best way to assess condylar and proximal tibial width is probably from a superoinferior view of the specimen, taken exactly from the tibial axis.

When dividing the corners, Jacobsen’s description has also been followed, and their osseous limits have been described with further detail. An additional

posterolateral corner (area 2d) has been proposed, that was not defined by Jacobsen²¹, since it is not distinguished by thinner cartilage. However, the need was found in the study of degenerative changes to distinguish the (frequently elevated) posteromedial aspect of the lateral condyle from other condylar zones.

A round elevation was found at the base of the medial tubercle slope on the inner aspect of the nude, weight-bearing area. It was found in two paired tibias of a 17-year-old patient: a round button-like ridge in one, and a corresponding button-like line in the other. Of unknown clinical meaning, it is proposed that this area is elevated by the same mechanisms responsible for osteophyte formation in arthritic tibias, namely pressure on adjacent (weight-bearing) areas.

V.3.2. Degenerative changes

V.3.2.1. Condylar margins

V.3.2.1.1. Rims

The condylar rims have been proposed to be divided in two parts, anterior and posterior, roughly delimited by an imaginary line dividing the condyle in two equal anterior and posterior parts. This is a conventional division to facilitate classification and grading, and in fact the external aspect of the rim (divided between the anterior and posterior parts) is in some cases more elevated than the more anterior and posterior aspects, which would warrant a division into three areas. A division of the condylar rims into more parts was deemed impractical from the point of view of potential radiographic classification of osteophytes, though.

The specimens available in this study did not allow, in certain cases, for an assessment of the full size and location of marginal osteophytes from the 3D models alone. These were complemented (when margins were found cut) by comparing the 3D models with the corresponding knee AP and lateral radiographs, observing the relative height of cut margins compared to elevated margins available on the 3D models. In this regard, the division of medial and lateral rims in anterior and posterior aspects seemed to offer the more complete and precise information, because it was still possible to classify rims with radiographs alone. The *main direction* of osteophytes, as it is found in Nagaosa, Lanyon, & Doherty¹⁴⁹, was not recorded.

Chondrogenesis and enchondral ossification in response to abnormal stresses on the articular surface^{40, 41} could be responsible for the frequent osteophyte

formation in the tibial plateau borders⁴², which still possess some articular cartilage, including the rims and the corners. This would be indicated by cartilage loss, and subsequent sclerosis and eburnation in certain regions of the tibial plateaus, indicating a shift in the areas of femoral compression on the tibial cartilage. Border osteophytes would then grow in the direction of least resistance^{35, 43}.

Contrary to the definition in Thomas et al.³⁰ and in the definition and images of Resnick's encyclopedic work on musculoskeletal imaging²³, no intra-articular osteophytes were found in the tibial plateau. Osteophytes that seemed intra-articular were found in this work to be in all cases posterior or anterior marginal osteophytes, or intercondylar osteophytes. No intra-articular osteophytic growth – different from cartilage-covered tubercles, condylar rims and corners – has been attested in the tibial condyles in the course of this study.

V.3.2.1.2. Corners

All corners showed a statistically significant correlation with knee OA, with the AM, AL, PM corner osteophytes showing a moderate correlation, and the PL corner osteophyte's correlation being weak. Neither the AP measurement of the corner osteophytes directly from the specimens, nor radiographic density in axial radiographs showed an association with knee OA, though.

The PM corner was qualitatively found to be greater (wider and higher) than the PL corner in pathological tibias, and measurements from donor tibias seem to confirm that, even though the sample studied is small.

Wichtl¹⁵⁰ described a bone spur on lateral radiographs, located posteriorly over the posterior intercondylar area, apparently at the edge of the lateral tibial condyle, which he called *tuberculum intercondylare quartum*. Drawing an analogy from Politzer & Pick's³¹ findings, Wichtl deduced that it was situated at the insertion of the PCL, and considered that it was associated with the Parsons' tubercle. This was not found by Ravelli¹⁵¹, where only 11 tubercles were found out of 1000 knee radiographs, and only in 4 of them was also a Parsons' tubercle identified.

Jacobsen²¹ did not identify such an osseous knob in any of his fresh specimens, but in one patient he observed a knob on the lateral tubercle, outside the PCL. "Among the macerated bones, two had osseous knobs on the posterior, curved part of the tuberculum laterale". It was never found at the PCL footprint,

therefore Jacobsen interpreted that the spur actually represented a knob formation on the posterior part of the LT.

Observations from this study support a bigger osteophyte arising from the posteromedial corner, clearly visible on lateral radiographs, and – if big enough – also on anteroposterior views, either between the tubercles, medial or even slightly lateral to the tibial spine, depending on knee rotation. Images shown in Wichtl¹⁵⁰ and Wagner¹⁵² as examples of a posterolateral osteophyte are believed to be, as a matter of fact, examples of posteromedial corner osteophytes.

Results show – as in Jacobsen – the presence of a posterolateral corner osteophyte in many specimens, but it does not correspond to the radiologic description made in previous studies. These findings suggest – agreeing with Jacobsen's description – that the osteophyte is unrelated to PCL traction, and represents a marginal osteophyte.

Since the *tuberculum intercondylare quartum* has been recognized and measured because of its size in radiographic studies, it seems right to keep calling the bigger posterior corner osteophyte with that name, but taking into account that in most cases it represents a posteromedial corner osteophyte, that in certain cases both posterior corner osteophytes might be present – and it is important to recognize the presence of a distinct (generally smaller) posterolateral tubercle –, and that in some cases both might be confounded and have a similar size.

V.3.2.1. Condyle wear

V.3.2.1.2. General discussion

In osteoarthritis of the knee, the medial condyle is ten times more frequently involved than the lateral condyle, leading to varus deformity^{35, 153}.

Loss of cartilage and bone at the tibiofemoral joint produces instability, present also with fully extended knee, according to Hallén & Lindahl¹⁵⁴.

Outerbridge¹⁵⁵ proposed a classification for chondromalacia of the patella, which is today popular to grade osteoarthritic changes during arthroscopy. Nevertheless, degenerative changes have been classified in this study according to the 5-grade system described in Weidow et al.¹⁵⁶, also used by Rajgopal et al.¹⁵⁷, because it seems more appropriate for the evaluation of chondral surfaces in osteoarthritic knees. Because of the surgical technique used for tibial cuts in TKA – where cuts need not be made inferior to major bone loss –, the actual tibial articular damage could not be assessed in some specimens. All specimens with

cut condylar surfaces have been compared with previous corresponding knee AP and lateral radiographs, to more precisely account for osseous defects, but the defect may have been underestimated in some specimens.

Ahlbäck's radiological study of 370 knees with clinical osteoarthritis found that in 85% of the knees only one compartment was affected, and that the medial joint space was affected 10 times more often than the lateral. Hernborg & Nilsson²⁹ studied 94 symptomatic joints, and found that in 90% the radiographic lesions were exclusively medial and rarely progressed to involve the lateral compartment when followed over many years.

The so-called "anteromedial osteoarthritis of the knee" was identified in a study of articular wear patterns by White et al.¹⁵⁸ as a distinct clinicopathological entity occurring in association with a varus deformity and increased prominence of the extension facet of the medial plateau, typically in knees with an intact ACL. It was shown in White et al. that in a patient with Ahlbäck grade 4 osteoarthritis, when seating and knees flexed at 90°, the femur would roll backwards and lie on to the intact posterior parts of the tibial plateaus.

Harman et al.¹⁵⁹ analyzed the size and wear of tibial plateaus resected during TKA in osteoarthritic knees, to assess the effect of a deficient ACL. In varus knees, the articular wear area was larger and more posterior on the medial plateau in ACL-deficient knees, which is consistent with the posterior femoral subluxation and posterior tibiofemoral contact observed after acute ACL rupture. Conversely, wear patterns were more prominent in the anterior and middle zones of the medial plateau in ACL-intact knees. No change was found laterally in the plateau. They found more varus angulation and wear in cases of ACL rupture.

This is consistent with what was found arthroscopically by Vasara et al.¹⁶⁰, that ACL rupture can cause abnormal knee kinematics determining the progressive worsening of the cartilage wear.

In Weidow et al.¹⁵⁶ ACL rupture was not considered the primary etiology of the degenerative changes of the knee in patients affected by late arthritis. It seems possible that late degenerative changes might be the cause of the ACL rupture (and not the consequence), due mainly to femoral intercondylar fossa abrasion^{161, 162}, and to the increased joint shear force caused by the absence of the physiological cartilage layer¹⁶³. They studied whether bone attrition was present or not, and where, and found that medial wear was greater in the anterior regions

and lateral wear more in the posterior regions, and hypothesized that this wear pattern was due to the differential condylar motions of the femur as put forward by Brandsson et al.¹⁶⁴, and by radio-stereometric studies by Kärrholm et al.¹⁶⁵ and Jonsson and Kärrholm¹⁶⁶. They showed that the internal rotation of the tibia on increasing flexion corresponded to posterior translation of the lateral and anterior displacement of the medial femoral condyle as confirmed by Hill et al.¹⁶⁷ and Kärrholm et al.¹⁶⁸ with weight-bearing.

A retrospective, MRI-based study by Biswall et al.¹⁶⁹ related rapid cartilage degeneration to meniscal injuries and ACL tears, observing that cartilage lesions in the central region of the medial compartment were prone to more rapid progression of cartilage loss when compared with those in the anterior and posterior regions of the medial and lateral tibiofemoral compartments.

Moschella et al.¹⁷⁰ found that 75.9% of men studied had ACL-deficient knees with severe cartilage wear of the medial plateau. In ACL-intact knees, the damage was mainly centromedial, whereas in ACL-deficient knees, the damage to the medial condyle was anteromedial, posteromedial, and centrolateral, which support the hypothesis that abnormal knee kinematics determine anteroposterior displacement of the tibiofemoral contact area^{164, 171, 172}. Their results also support the conclusions by Weidow et al., proposing the damage or absence of the medial meniscus as increasing the potential for ACL abrasion against the tibial spine and femoral intercondylar notch, and the torsional deformity of the proximal tibia (or distal femur) damaging the ligament synovial sheath and increasing joint shear force due to thickening of the cartilage layer (centrolateral cartilage wear was found in a median of 10.5%). They also found an increasing narrowing of the joint space in the medial compartment according to the Ahlbäck classification was associated with worsening of the cartilage wear pattern.

Hodge et al.¹⁷³ studied the pattern of knee osteoarthritis in Saudi Arabian and American knees, to assess the damage of joint hypermobility associated with habitual squatting, kneeling, and other deep flexion postures. Extreme anterior wear patterns were found in the Saudi Arabian population compared to Americans, and it was assumed that hypermobility lead to anteromedial and posterolateral condylar contact positions, as has been shown in more dynamic flexion activities like stair climbing^{174, 175}.

Van de Velde, Gill & Li¹⁷⁶ found in an in vivo dual fluoroscopic analysis an increased medial translation of the tibia (ca. 1 mm between 15° and 90° of flexion), anterior translation (ca. 3 mm), and internal rotation (ca. 2 mm) in ACL-deficient knees at low flexion angles, and cartilage contact points were found shifted posteriorly and laterally. In Van de Velde et al.¹⁷⁷ it was found that cartilage deformation increased gradually in the medial compartment of PCL-deficient knees in flexion of more than 75°, with contact in the medial compartment shifting anteriorly and medially, when compared to intact knees. No significant differences were found between both groups in the lateral compartment.

Rajgopal et al.¹⁵⁷ found that progression of arthritic changes in varus knees – in the medial and lateral compartments – was directly related to the degree of varus deformity when the deformity exceeded 15 degrees. Articular wear was more prevalent in the anterior zones of the tibia, with most patients studied having an intact ACL (86.7%), in contrast with the antero-medial involvement described by White et al. Increasing age was also found to be significantly associated with increased varus deformity, while BMI, posterior tibial slope, gender, and ROM did not have any significant role in that progression, which confirmed results of epidemiological studies by Sharma et al.¹⁷⁸, Brouwer et al.¹⁷⁹

V.3.2.2.2. Condylar wear patterns and grades

The most common location of medial articular wear in medial OA was found anteromedially (47%), followed by posteromedial (26%) and anterolateral (18%) areas. When compared with Ahlbäck OA classification and attrition grades, a strong association was found, with higher grades of OA/attrition associated with anterior bone attrition, and lower grades of OA/attrition associated with attrition of posterior areas.

The lateral articular wear in medial OA was concentrated internally, posteriorly (1L, 24%; 1L-2L, 23%; 2L-1L, 19%; 1L-4L, 13%), and also anteriorly (2L-1L, 19%, 2L, 11%). These zones were strongly associated with the medial articular wear: zone 3M with 1L, 4M with 2L, 2M with 1L, and 1M with 2L.

These findings agree with the study by Weidow et al.¹⁵⁶, and their interpretation of the different femoral condylar motion in osteoarthritis¹⁶⁴⁻¹⁶⁶: In normal knees, the femur rotates externally with flexion provided that the foot is in neutral rotation. Up to 40 degrees of flexion, the flexion facet centers displace about 4–5

mm anteroposteriorly (Kärrholm et al. 2000). There is anterior translation on the medial and posterior translation on the lateral side. This pattern of motion implies that the maximum load during gait will be somewhat differently transferred to the tibia in the 2 compartments.

Internal rotation of the tibia with increasing flexion corresponds to posterior translation of the lateral and anterior translation of the medial femoral condyle with weight bearing^{167, 168}, and attrition of medial areas (including 4M) is consistent with a higher instability found in knees with a higher tibiofemoral angle, which is associated with higher OA grades.

The findings of a more posterior wear pattern for lesser grades of OA are in contrast with the interpretation of Weidow et al. that “in early stages of the disease, the degenerative changes might have been located mainly in the anterior part of the tibial joint area”, after Cooke et al.^{180, 181}, Keyes et al.¹⁸²

In lateral OA, it was found that the posterolateral area (60%) was the most frequently affected. No association was found between affected areas and knee OA, nor with the medial articular wear. A sample with more valgus knees is needed to be able to derive a meaningful hypothesis.

Articular wear patterns were identified by direct observation by one observer, and not by other more objective techniques. However, this observation was made relying on 3D models with superimposed contour lines and a depth grid, auxiliary tools that are believed to improve intra-observer and inter-observer reliability, which has been shown to be good in similar studies that relied on observation alone^{156, 157}.

Lateral bone attrition grade was difficult to assess objectively, because of the gentle, almost convex lateral tubercle slope in some areas. Further studies are needed to assess intra-observer and inter-observer reliability of attrition grade estimation.

V.3.2.2.3. Condyle wear and ACL absence

V.3.2.2.3.1. Study II

Only in 3.06% of the knees studied was the ACL absent, and in 2.04% there was a clear anteroposterior instability present during physical examination, which correlates fine with recent findings in Rajgopal et al., with 86.7% of patients with an “intact ACL”. This is in contrast with the study by Moschella et al., with 75.9% of ACL-deficient knees, but in their study the ACL was considered ruptured when

fibers were “visibly attenuated, stretched or absent”, and when physical examination demonstrated soft end point.

The most common location of articular wear in knees with an absent ACL and clear AP instability was associated with bone attrition in posterior areas (1M and 4M), while instability only in history taking (“giving way”) was associated with medial areas, 3M and 4M. This suggests that the feeling of “giving way” of the knee is related to the varus alignment and instability caused by osteoarthritic pathology, while AP instability found during examination might be a good predictor of pathology related to ACL-deficient knees.

A trend toward a lesser MT slope and a greater LT slope was also observed graphically with worsening ACL pathology, although this difference between groups did not reach significance.

Harman et al.¹⁵⁹ found that absence of the ACL resulted in a more posterior location of maximum wear in the medial compartment of the knee, which agrees with results in this study. They also found a more varus angulation and wear in cases with ACL rupture, a correlation which in this study was very weak.

Brandsson et al.¹⁶⁴ reported that patients with rupture of the anterior cruciate ligament maintained a more externally rotated tibial position on the injured side during extension from 55 degrees. This loss of internal rotation was mainly due to a more anterior position of the lateral condyles and only to a small and insignificant increase in the posterior femoral condylar location medially. Because of that, Weidow et al. considered it likely that the findings in Harman et al. were an effect of late degenerative rupture of the ligament not being the primary etiology of the arthrosis.

A deficient ACL shows unstable translations of the tibia^{166, 183, 184}. ACL instability has thus been previously correlated to arthritic wear patterns of the articular surface of the tibia – especially of the medial plateau – and more varus deformity, more specifically in North American, European, Middle Eastern, and Indian populations^{96, 156, 158, 159, 185-187}. There seems to be a connection between the integrity of the ACL, varus deformity, and osteoarthritis, through compartmental overload and abnormal articular motion. Instability secondary to ligament injury, repetitive impingement between the ACL and a narrow intercondylar notch (particularly in the presence of intercondylar osteophytes)^{188, 189}, and a lateral thrust during the stance phase of gait in patients with varus deformity may lead

to attenuation and stretching of the lateral stabilizing structures, causing ACL deficiency^{161, 190, 191}.

This study is mainly descriptive in nature, and cannot answer to such biomechanical questions. Like many of those mentioned, it can merely suggest a relationship between ACL injury and condylar wear pattern, but the low number of knees affected by ACL pathology further prevents the proposal of new hypotheses.

Douglas et al.¹⁹² did not find a relationship between ACL status and knee instability. Furthermore, they found that degenerative changes were present in every ACL obtained during TKA surgery, corroborating earlier findings by Lee et al.¹⁶¹. Rajgopal et al. concluded that no meaningful classification of the functional status of the ACL was possible without mechanical testing or advanced imaging studies, and consequently they simply noted whether an ACL was present or absent upon inspection of each knee intraoperatively.

The classification of the integrity of the ACL was based mainly on the visual assessment with classification of the ACL as either “intact” or “absent”. Two other categories were also used, to assess their relevance as predictors of condylar wear: one subjective, during history taking (“giving way” of the knee), and one objective, during physical examination (anteroposterior instability or Lachman test positive). This would mean that attenuated ligaments, apart from completely normal ligaments, were pooled in the “intact” group. Other classification systems, with thinned or attenuated ligaments as a separate group, have been proposed before¹⁹³⁻¹⁹⁶, but MRI studies have been shown to be necessary to adequately and reliably characterize the integrity of the ACL^{197, 198}.

V.3.2.2.3.2. Study XIII

A tibiofemoral angle of 178.3° was found for Study XIII, in contrast with the mean 171.9° found for all knees in Study II (and 169.3° found for ACL-absent knees). This is probably a consequence of the presence of more valgus (25%) and neuter (8%) knees in Study XIII, compared to Study II, where all ACL-absent knees were in varus.

In contrast with finds in relative tubercle size for non-degenerative knees, only 50% were MT>LT, while LT>MT (33%) and MT=LT (17%) showed a greater proportion than usual.

Differences were also found in the mean MT height $13.3 \pm 1.4\%$ (range, 10.3% to 16.8%) vs. MT height in normal adults, $12 \pm 0.4\%$ (range, 1% to 16.7%); mean LT height $12.1 \pm 1.3\%$ (range, 7.9% to 15%) vs. LT height in normal adults, $10.4 \pm 0.4\%$ (range, 0% to 14.2%). They showed an average difference of $1.1 \pm 1.7\%$, also in contrast with the $1.7 \pm 0.5\%$ in normal adults.

Although these finds suggest a different morphology in osteoarthritic knees with absent ACL, no firm hypothesis can be derived, because the design of the study did not include a control group of degenerative tibias without ACL pathology.

V.4. Anterior intercondylar area

V.4.1. Anterior intercondylar area's ridge

The anterior intercondylar area's ridge (AIAR) was first described by Parsons¹² as a “slight oblique ridge (...) which runs forward and inward from the outer tubercle, and forms the anterior boundary of the oblique groove”.

Negru¹⁹⁹ was the first to name it *crista area intercondylaris anterior*, and described it as dividing the AIA into “a lateral deeply excavated half” and “a medial taller, domed half”. This was confirmed by Jacobsen²¹, who described it as a ridge running approximately in an anteroposterior direction, dividing the AIA into a lateral, deeper part, and a medial plateau. It was the only numerical reference, 6, given to a non-areal structure, since the area defined by the ridge (the downward slope of the medial AIA into the lateral AIA) was given the numbers 8 for its posterior aspect, and 7 for its anterior one.

Observations from this work confirm the existence of this elevation of the medial aspect of the AIA over the lateral one. The ridge has been included as part of the medial AIA area in this study, since it was deemed to form part of the posteromedial (area 10) and anteromedial (area 5) elevations over the lateral aspect. The term AIAR has been reserved for the laterally downward sloping wall of the medial area into the lateral one, and the letter A was reserved for it – leaving Jacobsen's number 6 as an obsolete reference to that oblique wall area.

The AIAR has also been proposed in this work to be divided in two distinct parts: the posterior aspect, dividing area 10 from areas 8, 7, described by Siebold et al.¹⁰⁸ as the medial upslope of the anterolateral fossa; and the anterior aspect, separating area 5 from area 9.

V.4.2. Parsons' knob

Parsons¹² referred to the tibial attachment of the ACL as indicated by “a little knob on the outer margin of the internal articular facet. From this the attachment runs transversely outward to about the mid-sagittal line of the tibial head. (...) this tubercle rises up just where it is relieved from the pressure of the anterior crucial ligament posteriorly, and the anterior cornu of the internal semi-lunar cartilage anteriorly.” Even though it seems quite clear that he referred only to the little anteromedial knob, Jacobsen found (when reporting area 10) that “commonly there is anteriorly a Parsons' knob or even a crest towards area 5”. He also described an anterolateral knob as a Parsons' knob: “In a few cases (among the

macerated bones) the knob was found at the antero-lateral corner of area 10 rather than at the cartilaginous border.”

More recent studies have also described an elevation in this position, which has been named “ACL ridge” by Ziegler et al.¹⁰⁹, “anterior ridge” by Tensho et al.⁷⁰, or “anterior intercondylar ridge” by Shino et al.¹⁰⁶. Tensho et al. already suspected that this ridge might have already been identified before as the Parsons’ knob – so for example as the anterior bone bulge of the ACL attachment in Berg et al.²⁰⁰, and more recently Nishimori et al.¹⁰⁵ clearly referred to the whole ridge as the “Parsons’ knob”.

Our finding supports a constant ridge dividing areas 10 and 5, medially ending at the junction with the central AMIR process, with which it forms a common geniculate ridge, called “L-shaped ridge” by Tensho et al.⁷⁰. Its curved junction, proposed to be called the geniculum due to its curved nature, was not found elevated over both ridges in normal tibias, but has been associated with the inconstant elevation called Parsons’ knob or tubercle.

This description of ridge forming the anterior border of the ACL attachment (and transverse limb of the geniculate ridge) fits better with what has been described in this study as the posterior AFIR process. The anterior AFIR process has been described in studies assessing the ARMM insertion, or maybe some of those studies referred to both as the same ridge. No studies to date had described both as distinct structures, and in fact both processes have been found in this study to be often united in a common ridge.

An inconstant AFIR recess was found between both processes, which may correspond to what Jacobsen²¹ described as a “wedge-shaped part of area 7 forcing its way in between areas 5 and 10”. Supporting this is his description of the notch as accommodating the anterior intermeniscal ligament, and serving as attachment to synovial membrane and lesser foramina nutricia.

The lateral corner of the AFIR, at its junction with the AIAR, was found elevated over both ridges in some specimens, forming an elevation or knob, which agrees with the description by Jacobsen of a lateral Parsons’ knob. This has been described more recently and named “ACL tubercle” in Ziegler et al.¹⁰⁹

V.4.3. Degenerative changes to the AIA

V.4.3.1. Anterior intercondylar ridge and anterior knob

The anterior AFIR elevation showed a weak positive correlation with knee OA, but the weak association of posterior AFIR and AFIR recess did not reach significance. Results are similar to nearby process elevations, and suggest the involvement of multiple factors in their osteophyte formation. Possible alternative mechanisms involve traction of the ACL, ARMM, or anterior intermeniscal ligament, and the same mechanisms affecting marginal osteophytes.

The name antero-central intercondylar knob was applied to the highest elevation on the lateral-most edge of the F1 ridge, at or near its intersection with the AIAR. Described as the anterolateral corner of the ACL, it has also been called “ACL tubercle”¹⁰⁹.

The ACIK was hypothesized to correspond to the anterolateral corner of area 10, and to become elevated due to ACL traction – similar to the mechanism attributed in the literature to the Parsons’ tubercle elevation –, but the higher osteophytic elevation in this area was often found more medial to the anterolateral corner of area 10, and could also be found slightly more anterior or posterior to it, and it was often joined to other adjacent elevations.

In some cases, a slight depression appeared in the middle of converging ridges – i.e. at the confluence of anterior and posterior AFIR processes, the anterior AIAR, and the anterior sagittal ridge –, as a sort of anterior intercondylar fovea or fossa, attracting attention over any elevation. The selection of this whole elevation, including the fovea, is the reason for the negative volume obtained for the knob in one of the specimens.

Neither the osteophyte grade nor its shape were found to be related to knee OA. The Parsons’ osteophyte was always higher than the ACIK in all pathological specimens studied (and also wider and deeper in most cases) – although no comparative study was done regarding precise volume or area.

The observed variability of the ACIK – as “the highest lateral point of the AFIR” – because of the different osteophyte development, makes it unreliable as an anatomic landmark.

V.4.3.2. Parsons' knob

V.4.3.2.1. General discussion

Parsons¹² described how the “tibial attachment of the anterior cruciate ligament is indicated by a little knob on the outer margin of the internal articular facet”, and how “this tubercle rises up just where it is relieved from the pressure of the anterior crucial ligament posteriorly, and the anterior cornu of the internal semi-lunar cartilage anteriorly.”

Danzig et al.²⁰¹, in a description of normal, osseous, intraarticular proximal tibia radiographic landmarks reported that “in some patients, a bony spicule, Parsons' knob, can be identified just anterior to the medial tibial spine. This spicula identifies the precise insertion of the anterior part of the anterior cruciate.”

Politzer and Pick³¹ described and depicted the *tuberculum intercondylare tertium*, a prominence 2 cm anterior to the intercondylar eminence on the lateral radiograph of the knee, and visible between the MT and LT in the AP view. According to the authors it is situated in the anteromedial corner of the ACL attachment, and also suggested traction on the ACL as the cause, and more specifically by the anterior bundle²⁰².

Jacobsen²¹ noted this bony elevation, a broad based cone, in four of the thirteen fresh specimens studied, and among the seventy-five macerated specimens studied that prominence was noted in 45%, with 11% of specimens being so large that he preferred to class them as “tubercle”. That tubercle was also observed by him during arthrotomy of patients where a *tuberculum tertium* had been seen on knee radiograph.

Ravelli¹⁵¹ found the tubercule in just 3% of 1000 knee radiographs, and just once it appeared between both intercondylar tubercles; in all other cases it was found medial to the medial tubercle. A *tuberculum intercondylicum quartum* was found in 11 cases (1%), and in 4 of them together with a Parsons' tubercle.

Schlüter & Becker²⁰² found the tubercule in ca. 8% of 1115 knees, and the *tuberculum quartum* in 20 cases (1.9%), 7 of which in common with a Parsons' tubercle.

Jonasch⁴⁹ found a Parsons' tubercle in 6.2% of 906 knees, and a *tuberculum intercondylicum quartum* in 0.9%, and no cases where both appeared in the same knee.

Radiographic studies by Oeser²⁰³, Berg²⁰⁰, Brossman et al.²⁰⁴, Pećina et al.⁶³ have yielded a prevalence of 10% to 61% in the population studied. The extent to which this variation represents genuine inter-population differences in frequency rather than methodological differences between studies is unclear²⁰⁵.

Parsons suggested that the knob was an osseous response of the tibia to traction from ACL fibers, and so did Politzer and Prick³¹, while Schlüter & Becker²⁰² found the tubercle in patients in their twenties (17 cases) without degenerative changes, but with sports activities, hence supporting the hypothesis of ACL traction. The experimental work of Noyes et al.³² demonstrated that such a bony response would be seen with repeated, slow strain-rate tensile loading.

Felsenreich²⁰⁶ noted its appearance in cases of previous ACL injury. Pećina et al.⁶³ showed that it appears more frequently in patients with previous ACL injury.

Oeser²⁰³ found it more frequent in patients over 50 and in conjunction with knee osteoarthritis, interpreting it as the declining muscle function placing more strain on the ACL.

Data from Brossman et al.²⁰⁴ showed a significant association between the presence of Parsons' tubercle and increasing age and presence of tibiofemoral osteoarthritis, which the authors attributed to chronic stress of the ACL in degenerative knees.

Yian et al.²⁰⁷ found an association between the Parsons' tubercle and the location of the ARMM attachment, with a more inferior location associated with a more prominent tubercle.

Mays and Cooper²⁰⁵ used the same 4-point scale as Brossman et al.²⁰⁴ to classify osteophyte size, and they found no association with osteoarthritis, age, or "any general bone-forming tendency".

It has been also suggested by Jones²⁰⁸ in a study of 120 consecutive patients that this osteophyte impinges on the intercondylar notch, which causes a loss of terminal extension of 5° to 10°, with chronic anterior knee pain with forced extension being the clinical sign. Six months after arthroscopic resection 14 of 15 patients regained full extension, although the authors did not recommend the procedure for an extension lag of more than 15°, because of secondary capsular contracture limiting the benefits of surgery.

V.4.3.2.2. Parsons' osteophyte size, shape, forming structures

The term Parsons' knob (and anteromedial intercondylar knob or AMIK) has been used in this study generally for the osteophyte growing anteromedially between the anterior articular surface of the internal condyle, the attachment of the anterior cruciate ligament, and the attachment of the anterior root of the medial meniscus – i.e. between areas 1, 10, and 5. The term Parsons' tubercle has been reserved for elevations of greater size (approaching the size of the main intercondylar tubercles). For a smooth, curved continuation of the geniculate ridge, the word geniculum was preferred. Because of its assumed nature as an osteophyte, the terms Parsons' elevation or Parsons' osteophyte have also been used.

Even though measurement from donors show a greater PM corner than Parsons' knob, qualitative assessment of pathological tibias and graphic comparison of histograms for both osteophytes (relating osteophyte grade and Ahlbäck OA grade) suggest that, while the PM corner is wider and higher in lesser knee OA grades (when it appears), (1) a sizeable Parsons' knob appears more frequently than a sizeable PM corner osteophyte in lesser OA grades, and (2) the Parsons' knob develops into a tubercle generally higher and deeper than the PM corner osteophyte in higher OA grades. Also, although the PM corner osteophyte can be seen as very wide by following medially its connection with an elevated posterior rim of the medial condyle, the Parsons' knob has also been observed to join often the elevated AFIR and ACIK, forming together a much wider osteophytic structure.

Measures of the Parsons' knob taken by hand over the specimen were found to be associated with knee OA, tibiofemoral angle, and varus – with higher values showing greater AP depth and ML width –, but not with age. Osteophyte grade showed also a moderate correlation with knee OA, and a weak correlation with age. This further strengthens the explanation of the Parsons' knob as a sign of degenerative disease, and not only related to age or tibiofemoral angle.

Differences in results of this study compared with paleoanthropological research, regarding the relationship of the Parsons' knob with OA disease, are believed to lie on the standard criteria used for diagnosing osteoarthritis in paleoanthropological remains²⁰⁹, which offer insufficient detail for a clinical study, and do not warrant detection of degenerative changes in detail.

Osteophyte shape was also found associated with knee OA: While a simple conic elevation appears in all grades, the more frequent star-shaped osteophyte – explained as a combination of simple ridges (frequent in lower grades) or cones from different surrounding elevations –, appears more frequently in higher OA grades; this suggests the involvement of multiple structures in the formation of the tubercle in higher grades. Little hook- and hook-shaped osteophytes, also frequent in higher OA grades, seem to be vertical elevations of lip- or tongue-shaped osteophytes, the last one more frequently found in lower grades.

The participation of different structures in the formation of the Parsons' knob was found to be associated with knee OA: the anteromedial corner was the main formant in higher OA grades, while B and F formed the elevation in lower OA grades. Hence, while the geniculum was the a priori most natural candidate for the origin of the Parsons' osteophyte, findings from arthritic tibias do not confirm a single central origin point or zone, or any constant ridges that form the elevation. In fact, these findings would suggest that while the Parsons' osteophyte is, as a matter of fact, related to the geniculum (and thus to the anteromedial border of the ACL) in lesser OA grades, greater Parsons' tubercles are formed in conjunction with the anteromedial corner osteophyte.

Given the association of the formants of the Parsons' osteophyte with the maximum attrition zone of both condyles, it is proposed that, while the knob in lesser OA grade would most likely represent a traction osteophyte of the ACL attachment (as it was originally described), greater elevations are most likely multi-factorial in nature, probably including the same mechanisms described for the development of marginal osteophytes. This is also supported by the lack of association found between Parsons' osteophyte grade and ACL pathology. More precisely, it is suggested that the Parsons' osteophyte – in conjunction with the anteromedial corner osteophyte – can have a stabilizing function of the knee joint similar to the one proposed for the AMIR process (and its elevation) in this study.

Due to the anatomic variation found in this study, the suggestion in previous studies²⁰⁰ that the Parsons' knob can be used arthroscopically or fluoroscopically as a landmark for ACL reconstruction cannot be supported. Based on results of this study, the internal (posterolateral) aspect of the geniculum (curved ridge formed between B2 and F1) should be used instead, which would often – but not always – correspond to the internal aspect of a Parsons' osteophyte, when one is present.

Attrition direction over the Parsons' osteophyte, which was mainly found in its anterior aspect, showed a strong association with bone attrition, statistically significant only with the lateral condyle wear in medial osteoarthritis. The association found suggests a common anterior attrition with a lateral direction or directly lateral attrition for 1M (2L) and 3M (1L), and a common anterior attrition with medial direction for 2M (1L) and 4M (2L).

These findings would suggest a common "external" knee rotational pattern (1M-2L, 3M-1L) that brings the lateral aspect of the femoral intercondylar notch (i.e. the anteromedial aspect of the lateral femoral condyle) in contact with the Parsons' knob, and a common "internal" knee rotational pattern (2M-1L, 4M-2L), where the medial aspect of the femoral intercondylar fossa (i.e. the anterolateral aspect of the medial condyle) impinges against the anterior aspect of the Parsons knob.

Bone attrition grade and maximal attrition zones were found to be related to the attrition grade of the osteophyte in the same way as they were related knee OA (and attrition of both condyles), showing that 3M and 4M articular wear are related to advanced stages of the disease, while 1M and 2M are related to early stages. This would suggest that attrition patterns, which have been termed of "external" and "internal" knee rotation in this study, show different attrition zones for early (1M, 2M) and late (3M, 4M) stages of the disease.

V.4.3.2.3. Anteromedial and posterior condylar corner osteophytes in X-ray studies

Radiographic density in the axial view did not show a correlation with knee OA for the AM osteophyte (including the anteromedial corner and Parsons' osteophytes), hence bone density of osteophytes has not been found to increase with higher stages of the disease.

Lateral views showed that the AM corner osteophyte, as well as the posterior corner osteophytes (especially the posteromedial one) could reach a height equal or greater than the main intercondylar tubercles. Their height showed an association with knee OA, but this was not significant ($p=0.100$). Only one Parsons' osteophyte was noted to be deeper than both tubercles in the lateral view.

AP views showed no association between knee OA and the position of the Parsons' osteophyte, but a trend was appreciated with a more central position of the

Parsons' osteophyte between the tubercles. That would suggest that bigger osteophytes appear more centrally, and is possibly related to the shape of the osteophyte growing in a lateral direction (see above for tongue-, little hook- and hook-shaped osteophytes' association with knee OA).

V.4.4. Parsons' knob in imaging studies of the knee

V.4.4.1. Parson's osteophyte: comparison of MRI and X-ray studies

The sample studied showed a distribution of relative tubercle size similar to studies of the general population. Almost half of patients showed a Parsons' knob, even though the majority (77%) were classified as Ahlbäck OA grade 0.

MT height and LT height showed similar values to Study V, but the mean difference between tubercles was $1.44 \pm 0.25\%$ of the ML width (in AP radiograph), compared to the $1.67 \pm 0.5\%$ found in normal adults, and to the $1.69 \pm 0.35\%$ in normal children. A statistically significant difference was found between OA grade groups, with decreasing MT–LT difference for higher OA grades. Grade 2 had few knees (5%), and only two knees were included in grade 3, and one was LT>MT and the other MT>LT, so no conclusion can be drawn for that group.

Nevertheless, a trend was clearly appreciated toward less difference between tubercles, which could suggest (a) that a certain tubercle configuration is more prone to degenerative changes, or (b) that osteoarthritic changes (especially tibiofemoral joint space narrowing) influence tubercle osteophyte growth, affecting both tubercles in a different manner, and altering their relationship. The latter seems the a priori more likely explanation.

The size of the Parsons' knob showed increasing area (height and AP depth) with higher OA grades, and the presence of a Parsons' knob was also linked to certain diagnoses, mainly OA, meniscal and ACL pathologies – but not to instability. The knob appeared less frequently in knees diagnosed as normal, or having contusions, fractures, or patellofemoral pathology.

The classification by Pećina et al.⁶³ showed a strong association with OA, and an association (although weaker) was also found by separating the two main components of the classification: type and size of the osteophyte. Higher osteophytes were found in higher OA grades, and in order of increasing frequency with higher OA grades they were cone-shaped, dome-shaped, and plateau-shaped.

These findings in osteophyte shape in 3D models would suggest that radiographic plateau-shaped knobs include 3D little hook- and hook-shaped osteophytes, while 3D cone-, lip- or tongue-shaped knobs would be included within radiographic cone or dome-shaped, with lesser types (ridge-shaped or little cone-shaped) appearing radiographically mainly as cone-shaped, or maybe not visible at all if they are not high enough. Further studies are needed to compare 3D shapes with radiographic shapes, but the utility of Pećina's simple classification of radiographic shape and size of the Parsons' osteophyte is supported by this study for early OA stages.

A case of congenital ACL absence

Ligament absence was classified into three types by Manner et al.²¹⁰, correlating findings in MRI and tunnel view radiographs: Type I includes hypoplasia or aplasia of the ACL with a normal PCL, and the notch width index and height are found decreased, the lateral tubercle hypoplastic, and the medial tubercle normal. Type II includes aplasia of the ACL and hypoplasia of the PCL, with notch width index decreased (more than in Type I, but with a wide range of measurements), notch height decreased, lateral tibial tubercle aplastic, and medial tibial tubercle hypoplastic. Type III includes aplasia of both ACL and PCL, complete absence of the femoral intercondylar notch (notch width index is zero), with the area covered by hyaline cartilage, both tibial tubercles are aplastic, the distal femoral joint surface is concave, and the proximal tibial joint surface is convex, forming a ball-and-socket knee joint.

Giorgi⁵⁰ suspected that the development of the tibial spine was influenced by tension of the ACL; thus, aplasia of the ACL may lead to a flattened eminence. Manner et al. found only a hypoplastic lateral tubercle – and not the medial tubercle – with ACL absence, with the whole spine being flattened in type-II and III dysplasia. However, recent studies have reported a high, deep tibial spine (combined with a narrow femoral intercondylar notch) in arthroscopic, MRI, and radiographic studies, where the so-called “dromedary-sign” appears: it was found in one case of congenital absence of the ACL and PCL¹¹⁰, and more recently in one case of congenital absence of the ACL, and hypoplasia of the PCL (Manner Type II)²¹¹. It is hypothesized that the difference in tubercle development with ligament absence is dependent on the affected stage of development of the ligaments.

In the case of congenital absence of the ACL found in this study, a deeper (medial and lateral) spine could be seen, with a narrowed femoral intercondylar notch,

and a tubercle relation $MT > LT$, which agrees with the finds of Manner et al.²¹⁰ for a Type I aplasia. No “dromedary-sign” was seen in radiographs.

V.4.4.2. Parson’s osteophyte in valgus osteotomy

Results from Study XI support the known association between tibiofemoral angle (greater varus deformity) and osteoarthritis^{35, 153, 157}.

Neither the Pećina⁶³ classification of the Parsons’ osteophyte, nor its components (size and type) showed an association with knee oA or tibiofemoral angle in the sample studied (Ahlbäck OA grades 2–4). However, this study included a confounding variable for knee OA, in that all knees had undergone surgery to change their tibiofemoral angle, and had thus altered the natural history of the disease. Therefore, no conclusions can be drawn about the utility of the Pećina classification for higher OA grades.

The classification of tubercle size proposed by Moon⁶⁴ was found to be exposed to subjective evaluation. The lack of proper anatomic description of the suggested normal medial tubercle height in radiography leaves the classification – otherwise described with objective references – prone to poor intra-observer and inter-observer reliability. No other studies to date have tested the classification system proposed by Moon.

V.5. Anteromedial part of the anterior intercondylar area

V.5.1. Fingerprint, anterior sagittal ridge, and anterior knob

The tibial fingerprint was first described and named *impressio digitalis* by Negru¹⁹⁹, also described as a slight groove or impression by Jacobsen²¹, as a flat intercondylar area in Berlet & Fowler⁷⁹.

Parsons¹² describes the insertion area of the ARMM as “the inner side of a slight ridge”. Jacobsen describes area 5, the anteromedial part of the AIA, as an elevation forming a ridge continuous with the anterior aspect of the AIAR, while in some cases it appears as a deep impression with a ridge (most likely the AFIR) dividing it from area 10. In Kohn and Moreno⁷⁶ the elevated area 5 with surrounding ridges is described as a “distinct tubercle”.

In Berlet & Fowler⁷⁹, the sharp slope described lateral to the most common meniscal attachment corresponds to the slope between areas 5 and 1c, while the most common attachment area is referenced as the “flat area between the articular surfaces that Jacobsen called the *crista areae intercondylaris anterior*”. In Johnson et al.²¹², the landmarks demarcating the ARMM attachment site are “the anterior border of the ACL tibial insertion, the articular margin of the anteromedial tibial plateau and the anterior intercondylar fossa”.

In this study, a more precise description has been given of the elevated limits of area 5 in general, and the flat fingerprint in particular: the slope dividing area 5 from 1c medially; the anterior AIAR and – when differentiated – the ASIR, delimiting area 5 laterally from area 9; and the anterior AFIR process, F2, delimiting area 5 posteriorly from area 10.

The anterior AFIR process was found to be highly variable in its medial (near the geniculum) and lateral (near the union of F1 and the ASIR) origin, precise shape (straight or with an anteriorly concave curve), and direction (anteriorly or posteriorly oriented in a mediolateral direction).

Area 5 measured a mean 226 mm² (range, 97 mm² to 362 mm²), representing 7% (range, 0.6% to 21%) of the tibial plateau area. In Jacobsen, it measured 116 mm² (range, 68 mm² to 174 mm²), representing a mean 11% (range, 8% to 18%) of the intercondylar area.

It is hypothesized that a part of the different measurements between the tibias was due to the division between areas 5 and 9 – the inconstant elevated division

by the anterior AIAR, the ASIR, or both –, difficult to standardize. In this study the most obvious visible process of the anterior sagittal ridge was used as a limit between both areas, thus usually leaving the common inter-ridge space within area 9, but leaving it within area 5 when only the (lateral) AIAR was available.

Also, the cut limited the availability of the full area in two specimens, and degenerative changes affected the anterior intercondylar area in four specimens.

V.5.2. Attachment of the anterior root of the medial meniscus

Three main fibrous components are therefore attached anteriorly: the main, dense fibers; the indirect fibers; and the transverse meniscal ligament¹⁰.

The central, most prominent portions of the native attachment of the meniscal roots were identified according to a previously described technique^{74, 213, 214}, by varying the tension on each root to define the area of the attachment site with the densest tissue concentration.

The insertion the dense ARMM fibers showed a general oval and frequently smooth kidney-like shape⁷⁹.

The ARMM central, higher density fiber attachment area measured 78.5 mm² (95% CI, 64.9 – 92.1 mm²; range, 49 mm² to 129.7 mm²), which supports the 101.7 mm² (95% CI, 82.4 – 120.9 mm²) of Ellman et al.²¹⁴, and the 56.3 mm² (95% CI, 46.9 – 65.8 mm²) of LaPrade et al.²¹³. For comparison purposes, an area of 139 ± 43 mm² (range, 39 mm² to 244 mm²) was described by Kohn & Moreno⁷⁶, and a mean 99.3 mm² (range, 64.9 mm² to 156.2 mm²) by Berlet & Fowler⁷⁹, although no distinction was made in those studies between the main and supplemental fiber insertion areas. LaPrade et al. found a mean (main + supplemental) fiber attachment area of 110.4 mm² (95% CI 92.2 – 128.5 mm²).

The accessory imprint was included in the selected area 5 in four specimens, while it was left partly or fully outside area 5 in eight specimens. While the anterior fingerprint was the most common site of attachment for the ARMM, and the elevations delimiting area 5 were also the absolute limit to ARMM attachment in all cases, attachment of dense fibers showed a certain degree of anatomical variation. At this level of macroscopic detail, the statement in Berlet & Fowler (citing Jacobsen) that “insertion facets were clearly separated from the areas that serve for the attachment of the loose connective tissue” cannot be withheld.

The Berlet and Fowler classification⁷⁹ applied to this study showed a distribution comparable to the one described by their authors, but with less type II attachments: 72% type I (vs. 59% in the original study), 7% type II (vs. 24%), and 21% type III (vs. 15%). Contrary to the findings of this study, more type II tibias were found according to the classification modified by De Coninck et al.²¹⁵ for MR imaging.

Another classification had been previously proposed by Ohkoshi et al.²¹⁶, with rare variants (11% of cases) named according to the attachment site, which included the ACL type, the transverse ligament type, the coronary ligament type, and the infrapatellar fold type (to the infrapatellar synovial fold). These have been found in the literature, with the ACL type being reported the most common variant²¹⁷⁻²²¹, except in neonates where the attachment seems to be more variable^{222, 223}. Other reported variants include attachment to the femoral condyle²²⁴, or the posterior horn of the medial meniscus floating free²²⁵. None of these anatomic variations were found in this study.

In this study, a strong association was found between degenerative changes and Berlet & Fowler types II and III: All tibias without degenerative changes were type I. Specimens classified as type II and III showed degenerative changes, and no clear case of ARMM fully attached to areas 1c or to the anterior wall of the tibia were found, which would support the hypothesis that some types from the Berlet & Fowler classification are in fact related to degenerative changes of area 5 and surrounding structures.

The anterior intermeniscal ligament was first described by Winslow in 1732^{10, 226}, and is described by the Weber brothers⁹ as absent in most cases. Such a connection between the ARMM and the ARLM was found in this study in 43% of donor tibias (4 paired and 2 non-paired specimens), which correlates well with the 69% found in Kohn et al.⁷⁶, with the 70% found in Berlet and Fowler⁷⁹, and with the 50% found in LaPrade et al.²¹³, but contrasts to the 94% found in Nelson and LaPrade²²⁷. The precise insertion area in the lateral meniscus was not noted, and a classification into types^{227, 228} was not done.

A connection between the ARMM and the ACL as intermingled fibers⁷⁶, or as a meniscocruciate ligament⁷⁹, was not found in this study.

The measures taken from the ARMM center to selected points correlated well with measures obtained by LaPrade et al.²¹³ in a straight line, and similar

measures were obtained by Wang et al.²²⁹ for the distance to the lateral border of area 1c.

A slightly lesser distance was obtained in Johnson et al.²¹² between the ARMM and the anterior ACL, but this is compatible with the selection of the posterior border of the ARMM instead of the center: mean, 7 mm (range, 6 mm to 8 mm) from the anterior border of the ACL, vs. 10.5 mm (95% CI 8.8 mm – 12.2 mm; range, 6 mm to 18.5 mm) in this study, comparable to the 9.2 mm (95% CI, 7.5 – 11 mm) described in LaPrade et al.

V.5.3. Degenerative changes of the anteromedial AIA

The anterior sagittal intercondylar ridge, J, was in some cases clearly separated from the anterior AIAR, in some cases it was the only ridge present of the two, but often the AIAR and ASIR were coincident, and in some cases they were separated just by a narrow incisure. In some cases, only the anterior AIAR was clearly elevated, while the medial border of the anterior fingerprint faded without a clear elevated line. When evaluating the ASIR elevation in pathological tibias, the most prominent sagittal ridge elevation was selected, without taking into account these differences.

The ASIR showed no correlation with knee OA, but because it lies between the fingerprint and area 9 – and both can become elevated with degenerative changes –, a precise assessment of the elevation of the ridge (in relation with surrounding areas) is more difficult.

The anterior intercondylar knob, N, did show a correlation with knee OA, which – together with the fact that it can be easily seen in lateral knee radiographs – might make it useful to evaluate degenerative changes.

The potential impingement of a big AIK tubercle with the patellar tendon, and consequently its hypothetical involvement in knee pain, warrants further studies of this osteophyte.

V.6. Lateral part of the anterior intercondylar area

V.6.1. Anterolateral intercondylar recess, fossa, and vallecula

In this study, Jacobsen's²¹ nomenclature has been followed by referring to the more likely area of main ARLM attachment as area 8. Without the intermingled fibers of the ARLM, that area corresponded to the anterolateral recess, located centrally beneath the lateral tubercle. This is supported by Robert's²³⁰ description of the ARLM attachment as "a lasso-like shape, on a rhombus-shaped fossa", located in front of the LT peak, in the anterior intercondylar area; by Fick's¹¹ description of the attachment area as a "triangular rough facet in front of the [lateral] tubercle, and widens outward over the anterior curve of the plateau in a facet-forming way over the anterior facet of the bone (...)"; and by Paturet's¹⁹ description of a tiny canal-shaped or cup-shaped depression in front of the lateral tubercle.

Parsons found that the ARLM attached "just in front of a slight oblique ridge", making reference possibly to the internal ALIR process, D3, or to the posteriormost aspect of the AIAR. Jacobsen referred only indirectly to the anterolateral recess when describing the ARLM attachment: "the most posterior fibres may insert on the central, vertical wall of the tuberculum laterale", which in Jacobsen seems to be described (at least partially) as part of area 9.

It is also found in Johnson et al.²¹² that the ARLM attachment "is directly anterior to the lateral tibial spine and adjacent to the tibial insertion of the ACL". In their work, the intermingled fibers of the ARLM were not studied, since the ARLM and ACL were studied separately as a basis for arthroscopically assisted meniscal transplantation, with an aim to avoid damaging the ACL (in ACL-intact knees), or to avoid causing "blowout" in bone tunnel placement for simultaneous reconstruction of ACL and ARLM.

Jacobsen's reference to areas 8 and 7 as posterior and anterior parts of the lateral slope of the AIAR, respectively, seemed too difficult to be delimited exactly from area 10, as Jacobsen himself admitted: "on macerated bones it may be difficult to determine the boundary between areas 8 and 10". The limit between areas 8 and 7 seemed to be the ARLM attachment area, which was therefore not defined by an osseous structure, and the only clue to the location of area 7 seemed to be a reference to the AFIR as "an extension" that might be sent from area 7 "up between areas 5 and 10".

The anterolateral groove, so named in this work to distinguish it from the posteromedial groove (located in the posterior facet), corresponds to Negru's¹⁹⁹ "deeply excavated half", to Jacobsen's²¹ "deep valley", and to Johnson's²¹² "anterior intercondylar fossa".

In Ziegler et al.¹⁰⁹, as in Jacobsen, the term "anterolateral fossa" seems to be applied to the whole anterolateral recess and groove: "A bony depression immediately medial to the lateral tibial plateau articular cartilage border and anterior to the lateral tibial eminence", which "corresponded to the attachment of the anterior horn of the lateral meniscus, which inserted along the medial upslope of this bony depression. The posterior-most aspect of the anterolateral fossa was located just posterior to the posterior aspect of the anterior horn of the lateral meniscus attachment."

In Tensho et al.⁷⁰ the "lateral groove" seems to be applied more specifically – according to the images, where the groove lies behind the AFIR – to what has been described in this study as the anterolateral fossa.

It is proposed in this study that the term anterolateral groove should exclude the anterolateral recess (the anterior wall of the lateral tubercle) and the lateral wall of area 10 (the AIAR), both of which begin at a slight elevation over the anterolateral groove proper. It is also proposed that the anterolateral groove be divided in two constant zones: the anterolateral fossa, area 7, posteriorly, and the anterolateral vallecule, area 9, anteriorly.

The anterolateral fossa is probably the area described by Paturet¹⁹ as a "small canal-shaped or cup-shaped depression" in front of the lateral tubercle. This area contains a constant pit, the anterolateral fovea, immediately anterior to the slight elevation separating it posteriorly from the anterolateral recess. This was already described by Jacobsen as one of the foramina nutricia in the posterior aspect of the anterolateral groove: "The most constant of the foramina is a large one at the posterior tip of [area 9], between area 8 and the anterior edge of the tuberculum laterale".

Area 8 measured a mean 55 mm² (range, 26 mm² to 85 mm²), representing 1.7% (range, 1% to 3%) of the tibial plateau area. In Jacobsen, it measured 42 mm² (range, 24 mm² to 57 mm²), representing a mean 4% (range, 2% to 6%) of the intercondylar area.

Area 7 measured a mean 48 mm² (range, 15 mm² to 97 mm²), representing a mean 1.5% (range, 0.7% to 3%), and area 9 measured a mean 155 mm² (range, 84 mm² to 265 mm²), representing a mean 4.5% (range, 3% to 7.5%). In Jacobsen, area 9 (corresponding loosely to areas 7 and 9 in this study) measured 144 mm² (range, 57 mm² to 269 mm²), representing a mean 13% (range, 6% to 21%) of the intercondylar area.

As already discussed above (see §V.5.1. Fingerprint, anterior sagittal ridge, and anterior knob), the anatomic variation of the AFIR accounts for the differences in the selected area 5 vs. area 9.

Precise osseous landmarks have been described in this work that might help to precisely delimit anatomic areas, without making reference to soft tissue insertions. Also, a clear nomenclature, compatible with the rest of the names used for the proximal tibia, has been proposed to define each anatomic aspect.

V.6.2. Attachment of the anterior root of the lateral meniscus

No difference in density was found between fibers of the ARLM attachment. It is a well-known fact^{11, 12, 76, 109, 212, 213, 231-233} that a part of lateral meniscal fibers blend with ACL fibers on the same surface. In this study, where the ARLM was cut first (before the ACL investigation), main fibers were cut from the ARLM intermingled fibers, and these were left inside the area investigated during dissection of the ACL attachment.

The attachment area of the main ARLM had a mean area of 38.8 mm² (95% CI 33.3 – 44.3 mm²; range, 20.6 mm² to 56.8 mm²), which supports the mean of ca. 51.8 mm² of non-overlapped area of ARLM attachment found by LaPrade et al.²¹³, from a mean ARLM attachment area of 140.7 (95% CI 121.6 – 159.8 mm²), with an ACL-ARLM overlap of 88.9 ± 40.8 mm², or 63.2% of the ARLM. It also supports the mean of ca. 44.7 mm² of non-overlapped area of ARLM attachment found by Ellman et al.²¹⁴, from a mean ARLM attachment area of 101.7 mm² (range, 82.4 mm² to 120.9 mm²), with a 44% of fibers overlaid by ACL fibers. A mean area of 93 mm² (range, 47 mm² to 137 mm²) was found by Kohn and Moreno⁷⁶, without distinction of main and intermingled fibers.

The attachment area was found to be oval or triangular in shape, and due to the concavity of area 8 a half cylinder or cone better described most cases (Kohn & Moreno described it as cylindrical).

LaPrade et al.²¹³ accounted for as much as 63% of the ARLM attachment in common with the ACL, and Ellman et al.²¹⁴ found that 44% of the ARLM attachment was overlapped by ACL fibers. In their study, the ACL was first delimited, then transected and carefully dissected off of the underlying ARLM fibers. In this study, the ARLM was cut first at its border with the ACL, leaving the intermingled fibers of the ARLM within the ACL stump, mainly in area 10. Because of the different method used, it can be assumed that this work offers a minimum area for the main ARLM attachment, trying to offer the most precise description of the ACL attachment, while in studies like those by LaPrade et al. and Ellman et al., for example, the ACL attachment area might have not been described as precisely.

Qualitatively, it was found that most ARLM attachments studied lied immediately adjacent to the ACL attachment area; this was in accordance with Johnson et al.²¹², that the ARLM attached “directly adjacent and parallel to the anterior half of the ACL footprint”.

It was also found that that the lateral wall of the anterolateral recess, the medial border of the lateral condyle, was devoid of fibers, as it was clear from different previous studies^{21, 109, 212, 213}. The superior aspect of the anterolateral recess (the anterior aspect of the lateral tubercle peak) was also found free of fiber attachments, and this bare area could therefore correspond to that described by Ziegler et al.¹⁰⁹: “the posterior-most aspect of the anterolateral fossa was located just posterior to the posterior aspect of the anterior horn of the lateral meniscus attachment”.

It was found that the ARLM attachment filled a great part of the anterolateral recess in most cases, more precisely its central and medial aspects, and the rest of the insertion corresponded mainly to the AIAR within area 10. The variation found in the area filled by the attachment was due to degenerative changes of the zone in some specimens (making area 8 usually narrower), and to the anatomic variation of the ACL insertion, which left more or less ARLM to be selected lateral to it. Some fibers seemed to attach marginally to the posterior wall of the anterolateral fossa, but no microscopic study was carried out.

The measures taken from the ARLM center correlated well with measures obtained by LaPrade et al.²¹³ in a straight line, but differences were found in distances to the ACL center, 2.7 mm (95% CI 2.3 mm – 3.2 mm) in this study vs.

5 mm (3.8 – 6.1 mm) in LaPrade et al.; and to the nearest edge of the lateral articular cartilage, both measures in straight line, 3.8 mm (95% CI 3.4 mm – 4.2 mm) in this study vs. 7.1 mm (6.3 – 8.0 mm) in LaPrade et al. This can be explained by the different area selected for ARLM and ACL, because of the differing detachment method. Contrary to these finds, the distance between the ARLM and ACL attachment centers had a range of 6 to 10 mm in Johnson et al.²¹², which is slightly greater than that found in this study, again probably because of the method used for arthroscopic measurements. Measures similar to these study were obtained by Wang et al.²²⁹ for the distance to the PRLM center, and to the axial line of the lateral tubercle.

V.6.3. Degenerative changes of the lateral AIA

While the anterolateral fossa and anterolateral recess depression grade showed no significant correlation with knee OA, the elevation of the anterior saddle ridge and anterolateral vallecule (from a groove or -5 to a maximum of grade 4) did show a weak correlation with knee OA.

The relationship of the AL vallecule with nearby structures was not found to be related to knee OA: a relationship with the anterolateral fossa (forming the anterolateral groove) was the most common one – and the most likely in lower OA grades –, followed by a joint elevation with the anterolateral knob; in higher grades the most common variations were a common elevation with the anterior sagittal ridge, with the anterolateral corner, or with the anterocondylar knob.

The anterolateral intercondylar osteophyte showed a moderate correlation with knee OA, as did its shape: tongue-shaped osteophytes were more common in higher OA grades, and ridge-type shapes more common in lower OA grades, with cone-shaped osteophytes centrally distributed. That is similar to the findings in this study for the anteromedial (or Parsons') and anterocondylar knobs.

The hypothesis that the ALIK grew internally from the anterolateral corner into the anterolateral groove was tested by comparing their combined osteophyte and knee OA, which showed no association. The association of ALIK osteophyte grade with the AL vallecule osteophyte/depression grade was also tested, with results showing a similar pattern to those found in their individual comparisons with

knee OA, which does not help in assessing their common relation (OA grade being a likely confounding variable).

V.7. Posteromedial part of the anterior intercondylar area

V.7.1. Anterior intercondylar staircase

The depiction of the ACL attachment area in Fick¹¹ (see below Fig. 488) is possibly the first approach to its three-dimensional description: in it, the footprint elevation over the anterolateral groove is clearly seen, as well as its elevated anteromedial limit, the geniculate ridge.

Parsons¹² describes the ACL attachment area as the “oblique groove” delimited anteriorly by the slight oblique ridge (the AIAR) “which runs forward and inward from the outer tubercle”.

This area is delimited anteromedially by a little knob “on the outer margin of the internal articular facet”, the so-called Parsons’ knob, and from there the attachment runs “transversely outward to about the mid-sagittal line of the tibial head”. From the point of view of the anterior intercondylar area, Negru¹⁹⁹ describes the anterior intercondylar area as “a medial taller, domed half” (the medial AIA) contrasting with “a lateral deeply excavated half” (the anterolateral groove).

Jacobsen²¹ describes it as “a prolongation of the medial plateau backwards between the tuberculum laterale and mediale, reaching posteriorly as far as the anterior slope of the eminence.” Anteriorly it is found sharply demarcated from area 5, and medially the area “follows the cartilaginous border of the condylus medialis tibiae right to the peak of the tuberculum mediale, the ligament fibres inserting on the cartilaginous border.”

Arnoczky²³² describes the area as “a fossa in front of and lateral to the anterior tibial spine”, and it has also been described to be “anterior and lateral to the medial tibial spine”²³⁴, and has been called “anterior intercondylar fossa”²³⁵. Girgis et al.²³⁶ describe “a wide depressed area in front of and lateral to the anterior tibial spine (medial intercondylar tubercle)”. It has also recently been called a depression or fovea⁶⁹.

In this study area 10 was found to be of triangular, or of an irregular quadrilateral shape, with intermediate forms showing a wider and more rounded posterior arch. This is supported by Tensho et al.⁷⁰, where the bony prominence described as the site of attachment of the ACL is described as having oval vs. triangular morphologies. The shape of the osseous area was not found to be associated with degenerative changes, or with the ACL attachment shape, but it was qualitatively

found that osteophytic elevations were associated with a narrower anterior side and a wider posterior side, i.e. with a more quadrilateral shape.

The ridge dominating area 10 was found to have a constant quarter-turn, staircase-like shape, with the lower stair anteriorly – leading upwards from lateral to medial –, and the upper stair posteriorly – leading straight posteriorly to the intertubercular ridge, in the medial aspect of area 10. The geniculate ridge can therefore be thought of as a balustrade-like anterior and medial border to the anterior intercondylar staircase, and the quite vertical posterior line can be seen as a sort of ladder connecting the anterolateral fossa directly with the intertubercular ridge.

Area 10 measured a mean 196.7 mm² (range, 107.4 mm² to 283 mm²), representing 6% (range, 5.2% to 6.7%) of the tibial plateau area. In Jacobsen²¹, it measured 182 mm² (range, 132 mm² to 278 mm²), representing a mean 17% (range, 13% to 24%) of the intercondylar area. In Duthon et al.²³⁴, the fossa measured approximately 11 mm wide (range, 8 mm to 12 mm) and 17 mm deep (range, 14 mm to 21 mm), which would account for a total area of ca. 187 mm².

In this study, area 5 can be delimited taking a part of area 10 because of the variable structure of the AFIR. Also, the Parsons' tubercle was selected separately, and it included a greater area in specimens with degenerative changes.

V.7.2. Attachment of the anterior cruciate ligament

V.7.2.1. Quantitative and qualitative determination of attachment

V.7.2.1.1. ACL footprint shape

The ACL attachment area was long ago described¹⁰ as having a long axis oriented in the anteroposterior direction, with a variable, oval or triangular shape^{70, 237-240}, the latter with the base opened anteriorly.

In this study, 64% of the footprints (nine specimens) were triangular, and the rest oval. This supports its description as triangular by Norwood and Cross²⁴¹, and Petersen et al.²³⁸, and recent finds in Ferretti et al.⁶⁶, in which 50% were triangular, and in Tensho et al.⁷⁰, where 41.6% were described as triangular. It is in contrast with Tállay et al.²³⁹, with 77.8% oval and 22.2% triangular, with Abreu-e-Silva et al.²⁴² where oval-shaped pattern was found in 87.5%, and with Odensten & Gillquist²⁴⁰, Harner et al.²³⁷, Luites et al.²⁴³, where the ACL footprint was described as being oval.

The oval shape was found to be strongly associated with degenerative changes of the proximal tibia, but not specifically with osseous changes to the shape of area 10. A study with more specimens is probably necessary for a correct assessment of these findings. Further studies are needed to assess the intra-observer and inter-observer reliability of the classification into oval vs. triangular shape, since intermediate, “more oval” and “more triangular” shapes can also be described, as well as irregular patterns (like Fig.-eight-like shapes) defined by the osseous elevations of the borders of area 10.

V.7.2.1.2. Anteromedial and anterior border of the ACL footprint

A fan-like expansion of the ACL, with fibers arranged in an orderly manner (in contrast with the unordered location of the main central fibers), is found anteromedially and anteriorly^{10, 230, 236, 244-247}, forming a sharp anteromedial angle in what has been described as the “duck’s foot” by Amis and Jakob²⁴⁸, and also thereafter^{66, 231, 234, 249}. In this study the most recent convention^{231, 248} has been followed, by naming the dense, central fibers the direct fibers, and the anterior and anteromedial fan-like expansion fibers the indirect fibers of the ACL.

The ACL footprint has also been described as the foot-like region²³², and “duck-foot-like”²⁵⁰. Observations showed that the shape of the ACL attachment area, with its laterally (and slightly posteriorly) concave curve and wider anterior area, more closely resembles a duck’s foot, and because of that this name is proposed to be applied to the whole footprint area, reserving the name “duck’s foot proper”, or anterior arch, for the fan-like expansion of indirect fibers.

The ACL attaches medially to the central AMIR process, B2, lateral to the cartilaginous boundary B1 (the external AMIR process), which is usually more elevated than B2 up to the medial tubercle peak. This is supported by previous studies^{10, 250}, but is in contrast with the statement in Tensho et al.⁷⁰ that “ligament fiber attached to the tip of the medial intercondylar tubercle”; and with Jacobsen’s one, that “the insertion covers the steep, central side of the tuberculum mediale”. Jacobsen’s description could refer to the lower aspect of the medial tubercle’s internal slope (i.e. to the B2 process), in which case it would agree with findings of this study.

The anterior border of the ACL attachment is the duck’s foot proper, a flattened-out fiber area²⁵¹ attaching to the anterior intercondylar ridge^{105, 109, 250}, giving it a curved concave shape when viewed in a posteromedial to anterolateral direction.

When no anterior insertion ridge was described, the anterior limit of the ACL attachment has been usually referred to as the transverse intermeniscal ligament^{10, 69}.

In this study, the posterior AFIR process, F1, has been described as the anterior site of attachment of the ACL. This is supported by the observations in Tensho et al.⁷⁰, where an anterior ridge was found in all cases, and histological evaluation confirmed that “the ACL was attached posterior to the border of this protrusion” in all cases. It has also been supported by the more recent histological work in Oka et al.²⁵⁰. Kongcharoensombat et al.²⁵² reported that the transverse ligament was positioned at the anterior margin of the ACL tibial footprint. The transverse ligament has been found at the AFIR recess (when both were present), located slightly anterior to the posterior AFIR process.

The anteromedial border of the attachment is marked by the geniculum, described by Parsons¹² as a “little knob (...) on the outer margin of the internal articular facet”, a “tubercle [which] rises up just where it is relieved from the pressure of the anterior crucial ligament posteriorly, and the anterior cornu of the internal semi-lunar cartilage anteriorly”.

A microscopic and histologic study is needed to confirm the hypothesis that – as it is assumed for the Parsons’ knob anteromedially – the AFIR and the ACIK represent anterior and anterolateral structures elevated by traction of the ACL.

Regarding the lateral border of the ACL footprint, the presence of fibers of the ARLM and ACL in the anterolateral fossa is not demonstrated in this study. Referenced with gross pyrography marks, ACL fibers seem to reach the anterolateral fossa in two specimens of the youngest patients, and one with important degenerative changes, all with mildly elevated staircases. In specimens with more elevated (adult or degenerative) staircases, the division between the anterolateral fossa and the insertion of the ACL lied clearly within the staircase. Hence, microscopic and histologic studies are needed to confirm the suspicion that no fibers insert laterally beyond the elevated AIS ridge, which would then be considered an elevation of the AIA most likely caused by traction of the ACL.

V.7.2.1.3. The C-shaped ACL and its lateral overlap with the ARLM attachment

An almost semicircular-like ACL attachment was described by Robert¹⁰ more than a hundred years ago.

The concept of an osseous structure corresponding to the main ACL attachment is found in the “oblique groove” described by Parsons¹² as running forward and inward from the lateral tubercle (and including a transverse aspect from the anteromedial knob “outward to about the mid-sagittal line of the tibial head”).

A similar attachment pattern is found Paturet’s¹⁹ description of an oblique posterior aspect of the anterior intercondylar area bordering the medial condyle (see below Fig. 503).

In line with a recent description of the ACL midsubstance as flat and ribbon-like^{244-246, 253}, a more lineal, C-like tibial attachment area has been recently described by the ACL Study Group in Siebold et al.²³¹, with their histological finds published in Oka et al.²⁵⁰. A reference is found in Śmigielski et al.²⁵⁴ to a previous report of 67% C-shaped, 24% J-shaped, and 9% Cc-shaped attachments among 111 specimens, referring to the ARLM as attached within the “concavity” created by the C-shape. Their findings agree with this study in that ACL fibers insert in a medially convex C-shaped attachment area, especially on what has been called in this study the outer and central C, forming together the ACL *fornix* – corresponding to the more elevated osseous structure of the anterior intercondylar staircase.

However, scattered ACL fibers were also clearly found in this study attached to the inner C – corresponding to the AIAR. The AIAR and the fan-like facet could correspond to the “special facet” for the conjoined insertion – of the ACL with the ARLM – found by Jacobsen in two specimens²¹. That intermingled fibers of the ACL and ARLM insert near each other is well known from previous publications^{10, 12, 70, 76, 109, 212, 213, 231-233, 236, 248}. This is in contrast with the statement in Siebold et al. that “the centre of the “C” is the place of the wide bony insertion of the anterior root of the lateral meniscus (...). It is covered by fat tissue and overpassed by the flat ACL ligament from anterior.” It is also in contrast with the observations by Śmigielski et al., where “no fibres were inserted centrally, and none attached in the area ascribed by proponents of a double-bundle nature of the ACL as the attachment of the posterolateral bundle.”

The most common attachment shape of direct fibers found in this study, a Helvetica C, is also in contrast with the mainly comma- or J-shaped attachment described and illustrated in Siebold et al., where the superior arch of the C (corresponding to the border between the ACL and ARLM, i.e. the footprint of the PL bundle) is absent. Horseshoe-shaped osseous C-layers were more commonly found in tibias with degenerative changes to the anterior intercondylar staircase and surrounding structures.

In this study, dissection of soft tissues was carried out with the fat tissue and ARLM first, leaving the ACL stump surrounded by synovial tissue untouched. Dissection was then done from the inside out, and the scarcely populated lateral area of the ACL footprint was found to have remains of fibers not continuous with the fibers of the ACL stump, which were supposed to represent the cut transverse ARLM fibers. In Siebold et al., firstly “the overlaying fat pat [sic] between the insertion of the lateral meniscus and the crossing ACL was carefully removed”. As an example for comparison, in Hara et al.²⁵⁵ soft tissues were removed leaving the ACL stump intact, then small fibrous ACL bundles were separated and followed to their bony attachment sites, which were marked.

It is hypothesized that because of the dissection type (the ARLM was cut first), and inside-out fiber identification in this study, the ACL border is recorded as the traditional duck’s foot shape, which is the most common shape reported to date, and which shows the maximum area of ACL attachment. A minimalist C- or comma-shaped ACL insertion, posited mainly by ACL Study Group, does not seem to contradict previous works in light of the different method used, but concentrates during ACL dissection on the attachment of the main fibers, leaving probably some scattered and intermingled fibers cut out on the area classified in their study as of ARLM attachment.

As already stated, it is believed^{12, 21, 79} that every little elevation and depression has its meaning, with insertion facets clearly separated from areas where loose connective tissue is inserted between the fibrous structures (areas slightly excavated, more porous, and with foramina nutricia). The anterior intercondylar staircase elevation is hypothesized in this study to be caused by traction of the ACL fibers attached to it. This elevation is greater in the external, C-shaped aspect (the fornix), but is also seen concentrically – although lower – in the inner C, where ACL fibers have also macroscopically been found attached to in this study.

Since the counter of the inner C, the fan-like facet, shows a conspicuous lack of elevation accompanying ACL footprint degenerative changes, and it remains at the same elevation level as the inferior aspect of the ARLM attachment (over the anterolateral fossa), it is probably safe to assume that this facet receives more ARLM fiber insertions, and only marginally (if any) ACL fibers.

More studies are necessary to clearly delimit the common area of ACL – ARLM attachment overlap, and to evaluate its importance in force and tension resistance for both tissues²¹⁴, assessing the relevance of this area regarding surgical repair. The lateral end of the AIAR should probably be considered the natural lateral boundary when reconstructing the ACL, until a carefully designed study of the overlap between ACL and ARLM attachments – with alternating dissection methods, precise marking of the attachment areas, and microscopic and histologic assessment – brings more insight in the matter.

V.7.2.1.4. Posterior Arch

A strip of bone of area 10 was observed surrounding the anterior wall of the intertubercular fossa, behind the ACL attachment area, free of fiber insertions.

Jacobsen²¹ refers to this area as area 15, a strip of bone behind area 10, devoid of ACL fibers, along the anterior wall of the ITR: “a narrow area which, like area 14, serves as attachment for the loose connective tissue which ensheathes the cruciate ligaments and, like them, is extrasynovial. This area constantly houses one or more small arterial and venous branches from the vasa genus media which run downwards along the posterior aspect of the ligamentum cruciatum anterius, penetrating the bone through a foramen nutricium.”

The location and number of foramina nutricia varies in this area, but a common bigger anteromedial fovea was found in most specimens. A bigger fossa developed in certain specimens just in front of the anterior wall of the ITR.

Foramina nutricia were already noted in this area by Humphry²⁵⁶, and Jacobsen²¹ noted a constant finding of one or more foramina, although some authors have not described them^{257, 258}. The vessels of these foramina form probably part of the branches of the middle genicular vessels, which run downwards along the posterior aspect of the ACL, penetrating the bone through the foramina, to the proximal tibial epiphysis^{232, 259}.

This area bare of ACL fiber attachment was also found in Girgis et al.²³⁶ in “the tip and upper part of the anterior surface of the anterior tibial spine”; by Hara et

al.²⁵⁵, and Tensho et al.⁷⁰, where histologic studies demonstrated fat tissue and vascular bundles, but no ACL fiber insertion. It was given the name “ACL fovea” by Purnell et al.⁶⁹, “bare area” by Hara et al., and “intertubercular fossa” by Tensho et al.⁷⁰. Results from this study do not support the findings by Tensho et al. that there is an almost constant central fossa (96.6% of cases) in the posterior intercondylar staircase, although their illustrations of CT volume renderings seem to show the central, more rounded aspect of the anterior wall of the ITR, in contact with the intertubercular saddle posteriorly, which is indeed an almost constant finding in this work, too. A similar reference anatomic landmark to this area would be the preeminence in this study.

The lack of ACL fiber attachment in the cartilaginous area of the lateral tubercle is supported by previous macroscopic and histologic studies^{21, 70}.

In this study, no contact zone was found between the PRLM attachment and the ACL attachment areas. No such contact zone is mentioned in Kohn and Moreno⁷⁶, nor in Johnson²¹² (where fibers are said to be adjacent). The lack of such a contact zone is supported by the finding of an area bare of fiber insertions posterior to the ACL, the posterior arch.

In contrast with this, Girgis et al.²³⁶ found in 9 of the 44 specimens studied that “the tibial attachment extended posteriorly around the anterior tibial spine until it reached the posterior horn of the lateral meniscus with which this posterior extension blended”. In Ziegler et al.¹⁰⁹, a “fibrous attachment” was found connecting the posterolateral ACL bundle and the PRLM in 11 out of 12 cases. Lahlaïdi²⁶⁰ studied this fibrous-like structure as a meniscoligamentous band connecting the ACL with the PRLM, classifying it into five types, a study that has been later complemented histologically by Zemirline et al.²⁶¹

In this study, macroscopic assessment of the posterior area of the ACL attachment yielded a constant border bare of fiber insertions, the posterior arch. Only synovial tissue and other soft tissues were extirpated in the transition between intrasynovial and extrasynovial zones, although no microscopic or histologic study of fiber attachments was done anterior or posterior to this area.

V.7.2.1.5. Quantitative assessment of the ACL footprint area

Area 10 contained most of the attachment area of the ACL, and it covered 74.6% of area 10 (95% CI 68.5 – 80.6%; range, 60% to 91%).

Quantitatively, the ACL area had 145.2 mm² (95% CI 120.4 – 169.9 mm²; range, 81 mm² to 207.1 mm²). This correlated well with the areas and approximate oval-shaped areas (πab , where a and b are the semi-major and semi-minor axes, respectively) obtained in previous studies: with the ca. 147 mm² (17 ± 3 mm length, 11 ± 2 mm width) found in Odensten & Gillquist²⁴⁰; with the ca. 141 mm² (18 mm, range 14 mm to 21 mm length; 10 mm, range 8 mm to 12 mm width) found in Morgan et al.⁸⁰; with the 143.4 ± 31.6 mm found in Muneta et al.²⁶²; with the 136 ± 33 mm found in Harner et al.²³⁷; with the ca. 140 mm² (18.5 ± 1.5 mm length, 8.8 ± 1.1 mm posterior width, 10.3 ± 1.5 mm middle width, 9.0 ± 2.2 mm anterior width) found in Heming et al.¹⁰⁷; with the ca. 157.75 mm² (19.5 ± 2.6 mm length, 10.3 ± 1.9 mm width) found in Tállay et al.²³⁹; with the ca. 132 mm² (17.2 ± 1.2 mm length, 9.9 ± 0.8 mm width) found in Hara et al.²⁵⁵

These measures compared fine with the ca. 174.55 mm² (17.5 ± 2.6 mm length, 12.7 ± 2.7 mm width) found in Colombet et al.⁸¹; with the 114.6 mm² for the right knee, 121.6 mm² for the left knee found in Dargel et al.⁷⁷; with the ca. 120 mm² (17 ± 2 mm length, 9 ± 2 mm width) found in Cuomo et al.²⁶³, and in Giron et al.²⁶⁴; with the 114 mm² ± 36 mm² (range, 67 mm² to 259 mm²) found in Siebold et al.¹⁰⁸; with the 206 ± 10.3 mm² of cross-section area found in Ferretti et al.⁶⁶ (in their photographs the selected ACL area seem to stretch too far posteriorly, including the posterior arch, which would account for a slightly greater measure); with the 119.1 mm² found in Otsubo et al.²⁶⁵

These measures contrasted to the ca. 388 mm² (38 mm length, 13 mm width) in Girgis et al.²³⁶ due to the measured AP depth, so large probably because of the fibers identified by them as forming the ACL in the posterior arch and ITR (see also their illustration of the ACL footprint). It also contrasted to the 229 ± 53 mm² found in Luites et al.²⁴³; to the ca. 61.35 mm² (10.7 ± 1.3 length, 7.3 ± 1.1 mm posterior width, 7.4 ± 1.3 anterior width) obtained in CT studies by Purnell et al.⁶⁹; to the ca. 225 mm² (18.5 ± 1.9 mm length, 15.5 ± 1.0 mm width) found in Abreu-e-Silva et al.²⁴² (where images point to a selection of the posterior arch and ARLM area, too).

No differences were found in this study between male and females in the size of area 10 or ACL footprint, in support of previous research^{266, 267}.

No investigation was made of segmental width and length in this study. The selection of pairs of ML or AP points to represent the whole ACL attachment area

was deemed an oversimplification of the real measure, incompatible with a precise study of the complex three-dimensional structure of the footprint.

No precise study of ACL fiber insertion was done, therefore areas bare of ACL fiber attachments – corresponding to fat or synovial tissue, or ARLM intermingled fiber insertions – were accounted for as part of the ACL footprint. This simplified assessment of the ACL footprint is comparable to previous studies.

V.7.2.1.6. Distances from ACL footprint center to anatomic landmarks

Measures taken from the ACL center correlated well^a with measures obtained in a straight line by Odensten & Gillquist²⁴⁰ for the border of the articular surface of the medial tibial condyle (compared with the distance to the AMIR in this study); with measures taken by Hutchinson & Bae²⁶⁸ (but for the ACL sagittal center to the PCL, which is significantly less than the mean value obtained in this study); by Purnell et al.⁶⁹ for the distance between the posterior border of the ACL and the anterior border of the PCL; by Edwards et al.⁷¹ for the AMIR and the posteminence (with slightly lesser values in their study); by Ziegler et al.¹⁰⁹ for anterior, medial, and lateral structures (differences are found with distances to the ARLM, PRLM, and the posteminence).

These measures also compare fine with the finds in Tensho et al.⁷⁰, although there are no identical landmarks selected in this study, and theirs were taken over 3D volume rendering of specimens – see Lee et al.²⁶⁹ for support of comparatively lesser measures obtained in 3D CT.

Measures from this study contrasted^b with the values obtained in Ferretti et al.⁶⁶, showing a posterior location of the ACL center, which is compatible with the interpretation that the posterior arch was also selected to obtain their greater mean ACL area.

The measurement from the posterior border of the ACL to the “PCL notch” in Heming et al.¹⁰⁷ contrasted to the distance found in this study to the anterior border of the PCL, but compared well with the distance to the medial plateau cartilage and to the MT, which could mean that the selected “PCL notch”

^a As an approximation to the posterior ACL border, the preeminence was taken as a reference, by subtracting the ACL – PRE distance from the distance of the ACL to the target anatomic landmark (for comparison with Hutchinson & Bae, Purnell et al.).

^b The ASIR was taken as reference for measures of distances to the anterior intermeniscal ligament.

corresponded to the posteminence or posterior wall, in which case measurements would correlate well with this study. The measurement from the center of the ACL to the anterior border of the PCL was also greater than the one found in Morgan et al.⁸⁰ (with also a greater ACL footprint AP depth, probably including the posterior arch), and in Edwards et al.⁷¹

These findings contradict the interpretation by Hwang et al.²⁷⁰ (based mainly on works by Heming et al. and Edwards et al.), where the center of the ACL is placed approximately 15 mm in front of the anterior border of the PCL footprint. In this study, this distance from ACL center to the anterior border of the PCL is approximately 25 mm, and this difference is not justified by the selection of distances over the surface in this study: mean distance to anterior border of the PCL in straight line, 23.1 mm (95% CI 21.0 – 25.5 mm). The old assessment by the Weber brothers⁹ of a distance of 15 – 20 mm between (the borders of) both cruciate ligaments is then supported by findings in this study.

This study supports the conclusions in Edwards et al. (also in Ferretti et al.), in recommending the use of the MT / AMIR as a reliable reference anatomic landmark during the ACL reconstruction procedure. It also supports the use of the over-the-back ridge (in contrast with Ferretti et al.), as well the anterior border of the PCL as stable landmarks. More studies are needed, however, to ascertain the precise distance, which in this study has been shown to be greater (in straight line and over the surface) than previously assessed.

According to the results obtained in this study, the best anatomic landmarks to be taken as reference for the location of the ACL center would be the anterior-most border of the PCL, the preeminence, the posteminence, the AMIR, the anteromedial border of the PRLM, the MT peak, the posteromedial border of the ARLM, the anteromedial fossa, the LT peak, the anteromedial angle of the anterior intercondylar staircase, and the ARLM center. Taking into account data from other studies combined with these, the most reliable landmarks – supported by more than one study – would be the anterior-most border of the PCL (with more studies needed to clarify the real distance between it and the ACL center), the posteminence, the MT peak, and the AMIR.

Special consideration merits the antero-central intercondylar knob, H, as a reference point. When locating the lateral border of the AFIR, the highest elevation lateral to its center was selected, when in fact a more stable position –

in normal tibias – would have probably been the lateral-most aspect of the AFIR (i.e. the most likely anterolateral border of the staircase). A similar problem is seen in selecting the Parsons' elevation instead of the internal anteromedial angle of the AIS.

Further studies are needed to clarify the reliability of the anteromedial and anterolateral angles of area 10 as anatomic landmarks for reference. An intraclass correlation coefficient should be obtained of the different landmarks with arthroscopic views (preferably in vivo), to clarify their potential for identification during surgery.

V.7.2.1.7. Anterior intercondylar staircase X

The AISX did not demonstrate good correlation or CV with the ACL center probably because of its diverging directions, hence the different distances and low correlation with the center. Nevertheless, it was the nearest identifiable osseous structure for reference of the ACL center during arthroscopy.

Distances from ACL center to anatomic landmarks correlated strongly with distances from AISX to the same anatomic landmarks, which suggest that the easiest, most precise way to locate the center of the ACL when performing arthroscopic surgery is first to locate the osseous AISX, and secondly, from the selected reference points, obtain the distances in relation to the AISX – positioning the reconstructed ACL center slightly anteromedial to the AISX. In order of preference, these would be the best points to set the reconstructed ACL center: the anterior-most border of the PCL, the preeminence, the posteminence, the AMIR, the anteromedial border of the PRLM, the posteromedial border of the ARLM, the MT peak, the LT peak, the anteromedial fossa, and the ARLM center.

The AISX is then proposed as a placeholder of the ACL center, the closest approximation known to it, and it could be used to orient measures from reference landmarks towards it. Taking into account data from the ACL center measurements, the best reference landmarks would remain the anterior-most border of the PCL (with more studies needed to clarify the real distance between it and the ACL center), the posteminence, the MT peak, and the AMIR. The use of multiple reference points could potentially improve the location of the ACL center.

Assessment of the axis of relative direction of the AISX and the true center of the ACL footprint showed that the posterior axis – and therefore the AMIR as an

arthroscopically pertinent perpendicular vector of it – is the standard anterior / anteromedial line to take as reference to place the ACL center slightly in front of the AISX.

V.7.2.2. ACL fiber bundles

V.7.2.2.1. ACL division into bundles

The ACL has long been described as a group of fascicles that change in tension and length through the range of motion. Almost as old as the division of the ACL into discrete parts or bundles of fibers that change together with knee movements by the Weber brothers⁹ is the discussion of their precise function and insertion areas, with precise functional measurements offered first by Robert¹⁰.

Welsh²⁴⁷ and Odensten & Gillquist²⁴⁰ found no histological evidence of separation into bundles. Arnoczky²³² described the ACL as a single broad continuum of fascicles, but with different portions taut through the range of motion. This has been supported recently by proponents of the C-shaped tibial insertion²³¹. The oldest technique for surgical repair of the torn ACL by Hey Grooves treated it as a single bundle²⁷¹.

A division in two main parts was proposed in Abbot et al.²⁷², with an anteromedial part that tightens with knee flexion, and a posterolateral part that tightens with knee extension. This was followed by the surgical technique in Lam²⁷³, and a similar division has been since described by Girgis et al.²³⁶, later supported by Reiman & Jackson²⁷⁴, Arnoczky & Warren²⁷⁵. Opponents consider this an oversimplification of the complex function of the ACL fibers²⁴⁷, and supporters cite the consensus of the ACL description as a “two-bundle concept”²³⁸, and the growing paradigm that “anatomic” reconstruction of the cruciate ligaments achieves improved function, and can control not only anterior tibial translation^{171, 276-278}, but also tibial rotation^{279, 280}.

Norwood & Cross²⁴¹ divided the ACL into three functional bundles, mapped their attachments, and described their different actions in resisting rotatory instabilities. This was supported by Amis & Dawkins²⁸¹ – albeit with a rather different method and division –, by Butler et al.²⁸², and by Friedrich & O’Brien²⁸³, and later applied to surgical repair by Shino et al.²⁸⁴. The function and footprint of the three bundles have since been further investigated following the original description by Norwood & Cross, mainly by Japanese researchers^{245, 265, 285, 286}, who have applied it to surgical repair^{106, 285, 287, 288}. These findings have since been

supported in many mammal species²⁸⁹⁻²⁹¹. From 6 to 10 fiber bundles were individualized in the three ACL studied by Mommersteeg et al.²⁹². Support for a three-bundle reconstruction is also given for more “anatomic” and functional restoration ACL^{285, 286, 293}.

As previous studies that used cadaver knees^{66, 71, 81, 237, 246, 294}, in this study the ACL could be divided in two distinct components, an anteromedial and a posterolateral bundle^{66, 71, 81, 237, 246, 294}. In some of these studies^{66, 69, 72, 73, 81, 237, 243}, their differentiation was made clear when the ACL was in tension with the knee in flexion of 90°. Using the described technique in Edwards et al.⁷¹, the ACL stump was held with forceps and tension was applied proximally, perpendicular to the tibial plateau, applying also rotational and translational movements. A mediolateral inter-space was identified as the division between bundles, and this in turn was hypothesized to correspond to the coronal septum that divides both bundles, as described in previous investigations of fetuses^{75, 295}.

A similar technique was applied in this study to all specimens, but the ACL stump was first separated in a medial and lateral aspect, and then cut through the coronal septum. A main ACL sagittal inter-space could be identified by visual inspection alone from its anterior aspect, dividing the anteromedial bundle in a medial and a lateral part, changing with traction and rotation, fitting the description made by Norwood & Cross²⁴¹, and Otsubo et al.²⁶⁵. A division based on fiber orientation, gap and/or fat (“based on anatomy, not dependent on function”) has been recently supported by Tantisricharoenkul et al.²⁹⁶

The main fat inter-spaces were then delimited by knowing their location from previous works. Other inter-spaces were noted to leave fibers commonly grouped together, to form smaller “bundles”; coronal inter-spaces were later noted to correspond roughly to incisures observed over the osseous surface.

The main anteroposterior inter-space was identified at a glance on the anterior ACL through the synovial tissue in all 14 specimens, although this was found not to correspond to the real inter-space interiorly in 4 of the 10 cases. Once the first attempt at cutting the fat-filled zones to their origin was made, if it did not correspond to the expected inter-spaces, dissection continued following the encountered spaces from the inside out.

During dissection of the specimens, it was noticed that blunt division of fibers or fiber bundles could not be carried out with precision to their tibial origin, and the

blade had to be used in all cases to finish dissection to bone, consistent with the synovial fibrous tissue and inter-fibril adhesions described in the literature^{265, 297} in a segment about 5 mm proximal to the tibial insertion.

Main inter-spaces were marked with pyrography in one specimen, but in thirteen only the ACL footprint borders were marked. Main and secondary inter-spaces were recorded in photographs and in schematic drawings. Then they were transposed to the 3D model, where they were noted to correspond to changes in osseous structures (incisures and slopes). No microscope or microsurgical instruments were used for bundle differentiation, which limit the precise identification of such correspondances.

V.7.2.2.2. Qualitative assessment of AM and PL footprints

Notwithstanding the lack of precise markings, the description of main and secondary inter-spaces correlates well with the potential bundle divisions of the ACL as described by Zhao and Huangfu²⁹⁷, but contrasts with their work in the common origin found in this study for lines 2 and 3 as illustrated by them, which seem to correspond in this investigation with the division of the sagittal incisure into the oblique branch (10g₁) and coronal branch (10g₃), respectively. This study offers greater detail regarding the osseous surface and the three-dimensional structure of the inter-spaces.

Although all of the reports in the literature describe techniques for “double bundle ACL reconstruction,” major differences between these techniques are found, most of them disagreeing on the PL bundle location (and thus PL tunnel drilling site).

The oldest description of the double bundle insertion was also made by the Weber brothers⁹, where the ACL attachment in the proximal tibia is described as an angled line: the posterior bundle attached in a narrow, posterior to anterior line; and the anterior bundle attached in a wide, medial to lateral line.

Results from this study support the classical description of the AM and PL bundle footprints^{67, 71, 73, 109, 236-238, 269, 298, 299}, with a posteromedial to anterolateral dividing line between the AM and PL bundle, the PL bundle located posteriorly with a lateral extension anteriorly, and the AM bundle located anteriorly with a posterior extension medially.

Similar distributions are also found (but with anatomic variations) in Colombet et al.⁸¹, Giron et al.²⁶⁴, Tállay et al.²³⁹ (27.3% with AM/PL orientation, 22.7% with

anteroposterior orientation, 40.9% with AL/PM orientation and 9.1% with lateromedial orientation), Hara et al.²⁵⁵ (60% oblique or classical type, 40% transverse or anterior vs. posterior orientation).

This is in contrast with the mainly lateral position of the PL and mainly medial position of the AM bundle described in Luites et al.²⁴³, and in Siebold et al.¹⁰⁸ (before his correction to a posterior vs. anterior position²⁴⁹ in light of his newer C-shape description²³¹), Dargel et al.³⁰⁰; with the anterior position of the AM and posterior position of the PL bundle described by Petersen et al.²³⁸, Zantop et al.²⁸⁰, Ferretti et al.⁶⁶.

Gross anatomic variations have not been found in this study. Gross anatomic variations found in previous cadaveric studies should be revised in light of the study by Zhao and Huangfu²⁹⁷ and the osseous references described in this study.

Because the bundle division was observed at the coronal branch of the sagittal incisure, 10g₃, this is hypothesized to mark the site of least traction between the marginal fibers of each bundle. However, degenerative changes were noticed especially in the main sagittal branch, 10g₁ (making it seem more depressed in relation with surrounding areas), which may indicate that the real division between the two main bundles courses farther posteriorly into the posterior arch, giving a more medial vs. lateral position of the bundle centers than reported here.

More precise functional studies are necessary to clearly define the function and insertion of individual fibers, especially regarding the fibers attached to the AIAR, which might change the definition of an oblique type to a transverse type of attachment as seen in Hara et al. Nevertheless, a medial vs. lateral bundle attachment is not justified anatomically (based on the medial C-shaped attachment of the main ACL fibers), and it could represent a confusion with the sagittal inter-space that divides the AM bundle in two parts.

The posterior arch was thus found in this study to be posterior to the PL bundle, supporting the finds in Hara et al.²⁵⁵. No investigation was made during this study to assess the relationship of the ARLM attachment to the footprint of the ACL bundles. By observation alone, the position of the ARLM attachment recorded in this study showed it was adjacent to the ACL footprint, but its center was slightly posterior to the ACL center. This does not support the finds of Ziegler et al.¹⁰⁹, where the AM bundle is in contact with the ARLM attachment in all cases.

Regarding the distribution of the AMM and AML bundles, it would have been logically expected that the main incisures noticed in pathological tibias, 10h and 10g, divided the ACL into the three (posterior, intermediate, and anterior) main bundles, in a distribution similar to what was found by Amis and Dawkins²⁸¹, with a theoretically proportional division of the main and indirect fiber attachment areas of the layered-C for PL, AMM, and AML bundles (see Fig. 482). The footprints found in this work, however, support the classical division of the ACL^{106, 241, 265, 286, 301}: an almost straight anteroposterior line (coincident with the AIS sagittal line) that divides the AM bundle in a higher medial part (almost without ACL fibers attached to the AIAR) and a lower lateral part, which contain almost all the central AIAR fibers of the AM bundle.

Similar to the double bundle division, it is hypothesized that incisures mark the site of least traction (between the marginal fibers of each bundle), and lines and ridges the site of more traction of the marginal fibers. Degenerative changes were noticed especially in the main coronal branch, 10h (making it seem more depressed in relation with surrounding areas), which may indicate that the real division between the two main anterior bundles courses farther through it. No study was made regarding elevations in the sagittal line, though.

A study should be done to more precisely locate the borders of the three bundles (especially the AMM and AML division), that include physiological stress of individual fibers during traction, compression, and rotation of the knee, in line with the works by Mommersteeg et al.²⁹² and Hara et al.²⁵⁵, with careful and microscopic marking, and histological studies of the areas of traction.

These findings support a posterior and central position of the PL bundle within the superior stair, and an anterior and central position of the AM bundle in the inferior stair for an “anatomic” reconstruction of the ACL, almost in line with each other and with the center of the ACL, as has been favored recently^{106, 249, 285, 288, 302, 303} – as opposed to a medial vs. lateral position of both tunnels.

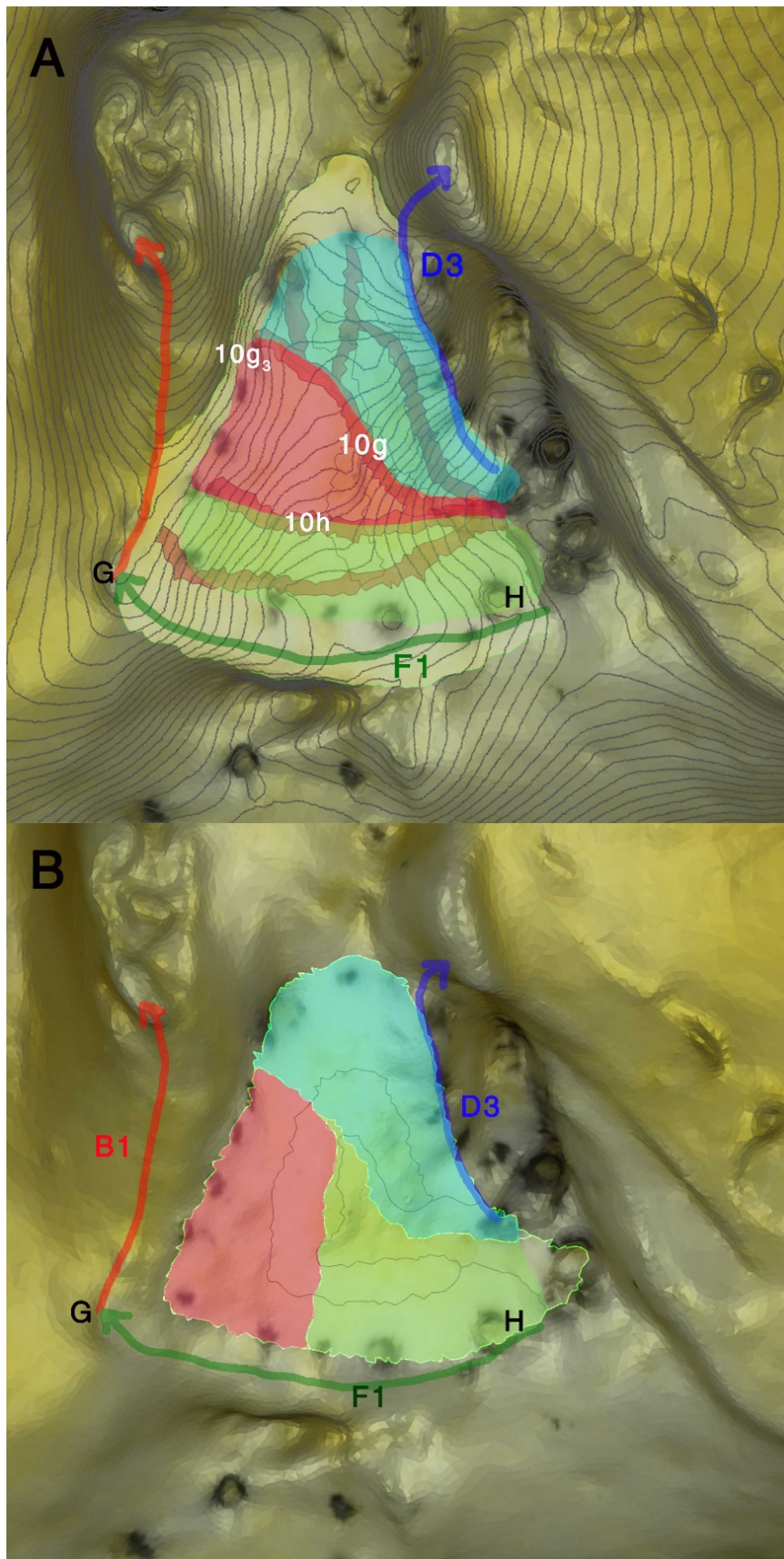


Figure 482. 3D model of tibia A. Superoinferior view of anterior intercondylar staircase. A (with contour lines superimposed): hypothetical location of the three bundles over the marked ACL footprint, following incisures 10g and 10h for their division. B: The real footprint of the three bundles as obtained in this study. PL bundle (in cyan), AMM bundle (in magenta), and AML bundle (in bright green). Labelled are the ALIR in blue, the AMIR in red, the AFIR in green, the geniculum (G), and the ACIK (H). See also Figure 259 and Figure 278 for the corresponding images.

A bony ridge has been recently reported to exist between the two femoral ACL attachment bundles, the lateral bifurcate ridge^{75, 304}, which together with the lateral intercondylar ridge described by William Clancy Jr³⁰⁵ help delimit the femoral ACL reconstruction. Unlike the lateral intercondylar ridge, the bifurcate ridge – which separates the AM and PL bundle attachments – is more subtle, harder to locate, and may not always be apparent during arthroscopic surgery. A distinct change of slope resembling a ledge more than a convex bifurcate ridge has been observed between both bundles, a subtler structure more difficult to identify arthroscopically¹⁰⁹. According to Noyes and Barber-Westin³⁰⁶, “because of the lack of a clear anatomic division of the ACL into two bundles, there is discrepancy among authors on anatomic descriptions of the ACL bundles and recommendations for the surgical technique on tibial and femoral tunnels for two bundle graft recommendations.”

No study to date had reported such detailed anatomic landmarks for the division of the ACL into tibial bundles, which – if supported by future works with more specimens, and with functional and histologic studies – shall give a more convincing argument to adopt a general two-bundle ACL tibial reconstruction.

V.7.2.2.3. Quantitative assessment of AM and PL footprint areas

The ACL AM bundle attachment area had 84.3 mm² (95% CI, 66.8 – 101.7 mm², range, 43.5 mm² to 142.1 mm²), and the PL bundle attachment area had 60.9 mm² (95% CI 51.6 – 70.1 mm²; range, 32.7 mm² to 94.7 mm²), or 58% AM vs. 42 % PL.

This compared well (but mostly in the lower limit for both bundles) with the 67 ± 18 mm² for the AM bundle, 52.4 ± 17.6 mm² for the PL bundle or ca. 57% AM vs. 43% PL in Takahashi et al.⁷³; 67 ± 31 mm² (range, 32 mm² to 152 mm²) for the AM bundle, 52 ± 20 mm² (range, 22 mm² to 90 mm²) for the PL bundle, or ca. 65% AM vs. 35% PL in Siebold et al.¹⁰⁸; with the 67 ± 18.4 mm² for the AM bundle, 52.4 ± 17.6 mm² for the PM bundle, or ca. 56% AM vs. 44 % PL, in Takahashi et al.⁷³; with the 75.9 ± 22.4 mm² for the AM bundle, 73.3 ± 22.9 mm² for the PL bundle (an almost equal distribution of both bundles) in Lee et al.²⁶⁹

It compared fine with the 56 ± 21 mm² for the AM bundle, 53 ± 21 mm² for the PL bundle (or ca. 51% AM vs. 49% PL) in Harner et al.²³⁷

It also compared well with the bundle areas calculated as oval-shaped areas (πab , where a and b are the semi-major and semi-minor axes, respectively): with the ca. 67.93 mm² (9.3 ± 1.2 mm length, 9.3 ± 1 mm width) for the AM bundle, ca.

43.73 mm² (8.0 ± 1.1 mm length, 6.8 ± 1.1 mm width) for the PL bundle, or 61% AM vs. 39% PL found in Kasten et al.³⁰⁷; with the ca. 85 mm² (9.8 ± 1.8 mm length, 11.1 ± 2.1 mm width) for the AM bundle, ca. 47.5 mm² (8.7 ± 2.3 mm length, 7.9 ± 2.0 mm width) for the PL bundle, or ca. 64% AM vs. 36% PL bundle found in Ferretti et al.⁶⁶; with the ca. 85 mm² (9.8 ± 1.8 mm length, 11.1 ± 2.1 mm width) for the AM bundle, ca. 47.5 mm² (8.7 ± 2.3 mm length, 7.9 ± 2.0 mm width) for the PL bundle, or ca. 64% AM vs. 36% PL found in Ferretti et al.⁶⁶

It contrasted with the 136 ± 37 mm² for the AM bundle, 93 ± 33 mm² for the PL bundle (but correlated well with the 59% surface area for AM, 41% for PL bundle) in Luites et al.²⁴³

Bundle areas are usually not oval-shaped, but triangular or irregular quadrilateral. Oval calculations were thus obtained as rough approximations between both: triangular areas (as was frequently the PL bundle footprint) would be lesser than presented here, and irregular quadrilateral areas (as was often the AM bundle footprint) would be greater.

By selecting the bundles exactly as half the ACL footprint, the coronal inter-space was consciously divided between them. In a more precise study of their limit, both bundles would have shown a slightly lesser area, since incisures were found to represent the inter-spaces which (by definition) are devoid of ACL fibers.

V.7.2.2.4. Distances from AM and PL footprint centers to anatomic landmarks

Measures taken from the ACL center correlated well with measures obtained in a straight line by Colombet et al.⁸¹ for the distance of the AM bundle to the POE (and percentage of the ML width), and to the PL bundle; by Iriuchishima et al.³⁰⁸ for the distance of the AM bundle from the anterior margin of the PCL (but a lesser distance from the PL bundle to the PCL was observed in their study); by Ziegler et al.¹⁰⁹ for anterior, posterior, and mediolateral distances to the AM bundle, but only for mediolateral distances to the PL bundle (a greater distance is found in their work between the bundle centers, and differences with PL measures point to a more posterior absolute location of the PL bundle in the AIA than in this study); by Lee et al.²⁶⁹ for the distance between AL and PM bundle centers.

These measures contrasted with those found in Ferretti et al.⁶⁶, which show a more posterior (and slightly more medial) location^c of the AM and PL bundle centers, especially with the latter. This is compatible with the interpretation that the posterior arch was also included in their greater mean ACL area.

These measures also contrasted with measures taken by Siebold et al.¹⁰⁸ for the AMIR and ALIR, which (since both measures were lesser) derived probably from the two-dimensional selection of measure points, and possibly a selection of the B2 process medially instead of the superior point of B1, and of the ALIR near the lateral tubercle instead of a central point more anteriorly, as it was done in this study. There was a similar distance found in this study from the AM bundle center to the anterior border of the AM (compared with the distance to the AFIR in this study), but a greater one from the center of the PL bundle to the anterior border of the PRLM.

These measures also contrasted with those by Zantop et al.²⁸⁰, both bundles being more anterior in this study with respect to the ARLM center; with measures from both bundle centers to the anterior border of the PCL in Edwards et al.⁷¹ (greater in this study).

These findings contradict the interpretation by Hwang et al.²⁷⁰ (based mainly on Edwards et al.), where the center of the AM bundle is placed approximately 20 mm, and the center of the PL bundle 11 mm in front of the anterior border of the PCL footprint.

V.7.2.2.5. Quantitative assessment of AMM and AML footprints, and distances to anatomic landmarks

The attachment area of the medial portion of the ACL AM bundle measured 45.6 mm² (95% CI 36.7 – 56.5 mm², range 22.3 mm² to 84 mm²); the lateral portion of the ACL AM bundle measured 37.7 mm² (95% CI 29.6 – 45.7 mm², range 20.5 mm² to 61.2 mm²), or 31% AMM, 27% AML, 42 % PL.

This compared well with the 34.5 mm² for the AMM bundle, 31.0 mm² for the AML bundle (or ca. 29% AM, 26% AML, 45% PL) obtained by Otsubo et al.²⁶⁵

No study had been done before this study to assess the distance of the AM bundle parts to the different anatomic landmarks defined for the proximal tibia.

^c The ASIR was taken as reference for measures of distances to the anterior intermeniscal ligament.

V.7.2.3. Anterior intercondylar staircase in 3D model from arthroscopic video

The value of 3D vision has been described³⁰⁹⁻³¹² for different surgical procedures, with the addition of the third dimension in endoscopy entailing a natural view on the operating field, which facilitates orientation in space and identification of dissection planes. However, 3D systems fail to overcome the visual side effects of stereopsis (each eye receiving different projections), namely eye strain, blurry sight, headache, and fatigue; projecting a good-quality stereoscopic image onto screen is a challenge^{310, 312-314} with known difficulties arising from the extreme fragility of the systems; and they represent high costs^{315, 316}.

A previous study using 3D schematic intra-operative visualization of ACL attachments on a 3D model based on MRI slices found that attachment locations were not identified more reliably than using common 2D MR sequences³¹⁷.

The system proposed in this study is a new, simple surgical navigation system that could potentially offer a more precise location of the ACL center in real time, by using the appropriate photogrammetry software during arthroscopic surgery.

3D models obtained from commonly used instruments during arthroscopy helped identify anatomic structures, from those previously found in the osseous 3D surface of the tibia during the course of this study. This identification was qualitatively easier by studying 3D models compared to the original two-dimensional video images alone. A study is needed to more precisely assess the advantage (if any) of using 3D models to assess the defined structures, e.g. by comparing the usual arthroscopic technique (2D video and palpation) with the enhanced technique adding intraoperative 3D models obtained during surgery.

The staircase seemed narrower in the 3D models obtained, possibly because of the caution that is exercised during radio frequency ablation of the ACL stump, to avoid damaging the ARLM, but maybe also because of the special optics used in arthroscopy.

Video quality, inexperience with the 3D modeling process, lack of knowledge by the main surgeons of the 3D structures involved, as well as the lack of proper soft tissue cleaning are the main reasons proposed as explanation for the identification of less structures than expected over the osseous 3D surface – compared to the detailed anatomy described in this work.

No previous study has evaluated the use of photogrammetry to obtain 3D models and precise measurements from arthroscopic or endoscopic video.

V.7.2.4. Anterior intercondylar staircase in tibial spine fractures

Tibial spine fractures were first classified by Meyers & McKeever³¹⁸ into three types: Type I, nondisplaced; Type II, partially displaced or hinged; and Type III, completely displaced. Zaricznyj³¹⁹ extended the classification to Type IV, which includes those cases with comminution of the tibial spine fracture. Different studies have attested combinations with proximal tibia fractures³²⁰; so e.g. Wiley & Baxter³²¹ showed a photograph and illustration of a Type II eminence fracture with extensive involvement of the medial articular surface.

All studies published to date include case reports or series of patients. The distribution of Meyers & McKeever types compares well with the distribution found in the series by Di Caprio et al.³²⁰. More type I and type II (and much less type III) fractures were found in a series of children in Casalonga et al.³²²

From the series of 12 patients with a Type III fracture in Lowe et al.³²³, no meniscal tissue interposition was found intraoperatively in the fracture site, with the attachment of the medial meniscus anterior to the fracture fragment, and the lateral meniscal attachment more posterior, attached to the anterior cruciate ligament, displaced together with the avulsed fragment. Findings were consistent in all age-groups (range, 9 to 63 years old).

This study only found a reported avulsion of the ARLM in less than half of type III fractures. In all cases, the anterior peak and the anterolateral recess were affected on CT images. Because of the retrospective nature of this study – with arthroscopic finds available from the operative report, and reports by the (usually on-call) radiologist from the CT –, it is logical to assume that only the clearest meniscal avulsions were reported, while some partial avulsions of the ARLM would have been left unreported. That assumption is based on the common attachment of the ARLM and ACL, and the fact that in 81% of fractures studied (and in 100% of Type III fractures) the internal ALIR process appeared affected, and in up to 50% of all cases the fracture reached the medial border of the lateral condyle.

Due to the distance between slices in the CT images available for study, it was difficult to clearly delimit the affected area. Nevertheless, the lateral aspect was often found affected. This supports the presence of intermingled ACL–ARLM

fibers, while the almost uniform involvement of the AIAR and central AMIR process supports the presence of strong ACL fibers attached to (or quite near to) them.

V.7.3. Degenerative changes of the anterior intercondylar staircase

Height of the stairs, horizontality of the upper and lower landings (and presence of a more or less horizontal middle landing), and size of the landings compared to the stairs: all these variables were assessed subjectively – comparing them to surrounding areas when necessary –, and none showed a significant association with knee OA.

The presence of a more depressed fossa at or near the posterior arch – instead of the common anteromedial fovea – was not found to be related to knee OA, either.

Depression of the main incisures was not significantly related to knee OA, but the main sagittal incisure (10g₁) – which showed a wider grade range than 10h, from -5 to a +2 elevation – showed an almost significant association ($p=0.068$) with the knee OA, with frequency analysis showing a trend towards deeper incisures with higher OA grades. All cases of a sagittal elevation in this area (predominating over any depression) appeared also in higher OA grades.

In tibias with degenerative changes, both lines behind and in front of 10g could therefore appear fused together with it in a sort of ACL bundle ridge. These finds support the hypothesis of the nature of the incisure (and surrounding areas) as an approximate macroscopic limit between main ACL bundles, where traction is exerted in different directions.

V.8. Intertubercular ridge

V.8.1. Intertubercular area

The intertubercular area was described in Parsons¹² as an “oblique groove” which separates the two tubercles; also, “the internal tubercle is prolonged (...) backward and outward by a marked, oblique, rounded ridge, which I do not remember seeing described, but which, nevertheless, I believe is always present. (...) Along the summit of this ridge, as far as the internal tubercle, the posterior fibres of the posterior cornu of the external semi-lunar cartilage are attached.”

The anterior wall of the ITR was described as “a small ridge which runs across the long axis of the anterior crucial groove, dividing it into an anterior part for the anterior crucial ligament, and a posterior part, in which the anterior fibers of the [PRLM] lie”; this ridge forms “the summit of the anterior crucial groove which slopes downward from it both anteriorly and posteriorly”.

As the site of attachment for the PRLM, it was similarly described by Johnson²¹² as the “intertubercular notch”. Jacobsen described the intertubercular ridge as including all the eminence, “a concave ridge” that connects the two summits of the medial and lateral tubercles “which passes from the central side of the tuberculum mediale obliquely backwards and laterally to meet the tuberculum laterale. (...) this ridge comprises large areas (11 and 12) and smaller areas (14 and 15). Anteriorly the ridge first slopes rather steeply down (cf. the small area 15) but thereafter the inclination continues evenly into area 10. Posteriorly, it drops rather abruptly down towards area 14. Even on macerated bone the junction between areas 13 and 14 is always distinct.” The intertubercular area proper is described as a more (or even completely) horizontal area between both tubercles.

The ITR has been recently described and named “intertubercle ridge” and tibial ACL ridge by Purnell et al.⁶⁹, this last term also used by Tensho et al.⁷⁰

To avoid a reference to osseous areas by the insertion of soft tissues, area 12 was assigned in this study to the intertubercular area, while area 15 was assigned to the anterior wall of the ITR, and area 14 was divided in its superior, gentle slope, 14a, as the posterior wall of the ITR, and the inferior, sharp slope, 14b, as the lateral aspect of the posterior wall.

The oblique line or ridge found near area 14a, the more internal PMIR process, C4, has been referred to as the interspinous over-the-back ridge first by McGuire et al.³²⁴ and then others^{71, 263, 268}, or retro-eminence ridge^{81, 109}. Initially, this

anatomic landmark was described by Hutchinson and Bae²⁶⁸ as a slope whose front edge “is intimately associated with the anterior border of the PCL when the knee is flexed”, but it was described in Edwards et al.⁷¹ as the “transverse interspinous ridge on the apex of the posterior slope”, accompanied by an accurate illustration of a ridge on top of the posterior wall of the PIA.

In this work, the central aspect of the gently sloping posterior wall of the ITR has been proposed as the constant anatomic landmark for reference, because of the inconstant presence of the previously described line or ridge. Because of the circumlocutionary nature of the “over-the-back” description, related to arthroscopic surgical vision (and confusing from a general anatomic perspective), and the etymologically unsound use of Latin *retro-*, the name *posteminence* is proposed in this study to refer to that central zone within area 14a, whether an elevated line or ridge is found on it or not.

Also, a corresponding anterior gently sloping area of the ITR, the central aspect of area 15, is proposed to be called the preeminence.

Area 12 is also described in Jacobsen as “more horizontal than area 11, in certain cases completely horizontal, and is on a higher level, the medial process of the facet being on top of the [crista intertubercularis] above the level of area 11.”

V.8.2. Attachment of the posterior root of the lateral meniscus

The site of attachment of the main PRLM fibers lies on the lateral aspect of the ITR. Robert¹⁰ described the PRLM attachment as “immediately behind the LT peak (...) higher than the PRMM”. Frazer³²⁵ also described only a small insertion facet behind the lateral tubercle. In Poirier² the attachment is depicted as wide, reaching the MT, and it is described by Fick¹¹ in the same way referencing Poirier’s depiction, which is repeated in Paturet¹⁹.

Parsons¹² described the intertubercular area: “(...) the internal tubercle is prolonged backward and outward by an oblique ridge, to which part of the posterior cornu of the external semi-lunar cartilage is attached.” The lateral aspect of area 12 (corresponding to areas 12b and 12c in this work) is described by Jacobsen²¹ as “a slightly sloping segment of the posterior aspect of the [crista intertubercularis] and tuberculum laterale”. In accordance with Parsons (and in contrast with Robert and Frazer), Jacobsen described “a lateral as well as a medial insertion” of the PRLM, with the latter attaching on the inner slope of the medial tubercle, not reaching the cartilaginous area. Johannsen et al.⁷⁴ also found that

“in addition to its main root fiber attachment, there was a continuation of the posterior fibers that coursed to the posterior aspect of the lateral margin of the medial tibial eminence.”

Johnson et al.²¹² described the PRLM attachment area as “directly posterior to the lateral tibial spine, adjacent and anterior to the insertion of the posterior horn of the medial meniscus”, and three-dimensionally it is described as “directed posteromedially”. In Johannsen et al.⁷⁴, the attachment was described as “posteromedial from the lateral tibial eminence apex”, and there was also found “a continuation of the posterior fibers that coursed to the posterior aspect of the lateral margin of the medial tibial eminence.”

No fibers were found attached to the cartilaginous boundary of the lateral tubercle, in line with the aforementioned studies. The PRLM attachment area was found in this study to reach in some cases the posterior vertical aspect of the lateral tubercle behind the posterolateral recess, which was also described in Jacobsen: “some fibres of the lateral insertion may arise from the cartilaginous border where area 12 adjoins the anterior peak of the tuberculum laterale.”

The PRLM central fibers had a mean attachment area of 36.1 mm² (95% CI 30.5 – 41.7 mm²; range, 24.7 mm² to 57.7 mm²), which supported the 28.5 mm² (range, 21.3 mm² to 38.4 mm²) found by Johnson et al.²¹², and the 39.2 ± 2.9 mm² found by Johannsen et al.⁷⁴. A mean area of 93 mm² (range, 47 mm² to 137 mm²) was found by Kohn and Moreno⁷⁶, and of 83.1 mm² (range, 63.6 mm² to 102.7 mm²) by Ellman et al.²¹⁴, without distinction of main and indirect fibers.

It was found that the attachment of main fibers usually filled half or more of area 12. In one case it filled more than 100% of the area, where degenerative changes to the posterior and anterior wall together with a narrow intertubercular space left a comparatively long ARLM insertion. A more precise study is needed, by selecting the posterolateral recess (the area lateral to the internal PLIR) and comparing the attachment area to it.

Measures taken from the PRLM center are comparable with measures obtained by Johannsen et al.⁷⁴ in a straight line, but in their work slightly greater mean distances were found from the PRLM center to posterior and medial structures (PCL, PRMM) and slightly lesser mean distances to lateral (PLIR) and anterior structures (LT, ARLM), which is compatible with a rather more anterolateral location of the PRLM center in their work. A similar value to the one found in this

study is given in Wang et al.²²⁹ for the distance between the PRLM and the PLIR in a straight mediolateral line.

V.8. Degenerative changes of the intertubercular ridge

As assessed qualitatively in normal and pathological tibias, the posterolateral recess seems to be wider and shallower with degenerative changes – in some cases showing an elevated area over the intertubercular area –, with a significant weak correlation with knee OA. Wider recesses are in turn qualitatively seen to be related with a wider and flattened LT vallecule and posterior summit (see above §IV.2.5.1. Qualitative assessment of degenerative changes).

The more internal PMIR process, C4, corresponding to the oblique ridge described by Parsons, and to the *retro-eminence ridge* described in the literature, was found as a slight line or ridge (osteophyte grade range 0 – 3), usually located in the change of slope between areas 12 and 14a, or within the slope of area 14a. It had a significant weak correlation with Ahlbäck OA classification.

In radiographic views, staircase width was found significantly associated with knee OA, but staircase height changes did not achieve significance. A narrower and higher staircase was found with higher OA grades. However, whereas narrowing of the staircase is most likely related to an internal widening of both tubercles (and less likely to staircase degenerative changes), staircase height is judged compared to tubercle height (in turn related to knee OA), hence the presence of that confounding variable supports that the high p-value ($p=0.102$) is in fact lower. More studies are needed to assess this aspect.

The characteristic single or multiple tiny round osteolyses found in axial radiographic views at or near the anterior intertubercular area are supposed to represent foramina nutricia of the posterior arch. The number of osteolyses per specimen was not found to be associated with knee OA.

V.9. Posterior intercondylar area

V.9.1. Posterior intercondylar area and posterior wall

The posterior intercondylar area has also been called “posterior intercondylar fossa”³²⁶.

Jacobsen described area 14 as an irregular area, “slightly depressed in relation to the insertion facets” that “serves as attachment for the loose connective tissue between the structures”. This description and the illustration on the article fits the description for the area which has been named 14a in this study, but also the area around the tent-shaped ridge and especially the posteromedial fossa, since the area also “[shows] foramina nutricia in varying numbers, size, and site”. A constant foramen nutricium was found in this study, the posteromedial fovea, which was not described by Jacobsen.

Area 11, on the other hand, was described as “an almost vertically oriented facet on the posterior, sloping side of the tuberculum mediale”.

Fick¹¹ described the attachment area of the PRMM as a “steep triangular facet behind the medial tubercle”.

Parsons¹² described a “small eminence” sometimes present in “the floor of the posterior crucial groove”, where the PRMM is said to be attached, and Jacobsen also describes one case of an osseous knob in this area. This inconstant knob or tubercle could correspond to the elevation of C3 (giving the impression of an ‘eminence’ created between C3 and C1), less likely to the elevation of C1, or to the tent-shaped ridge. No distinct protuberance (apart from these elevations) has been found during the course of this study that fit the descriptions made by Parsons and Jacobsen.

Jacobsen’s description of areas 14 and 11 has been refined in this work, adapting them to include all the osseous surface of the posterior wall, by selecting differing slopes, and observed elevations or depressions. Thus, area 14b has been defined as the lateral face of the posterior wall, and area 11 as the medial face. A differentiation was also apparent between the superior aspect of the posterior wall, area 14a, which shows a gentle slope, and the rest of the posterior wall.

In specimens without degenerative changes, area 11a was difficult to delimit exactly, due to the minimal depression of K and/or minimal elevation of C3 over

the surrounding areas. Lacking surrounding landmarks, it might be defined laterally by a straight superior line from the peak of the tent-shaped ridge.

V.9.2. Attachment of the posterior root of the medial meniscus

Qualitatively, the attachment area of the central PRMM fibers comprised mainly areas 11a and 11b, and only marginally were fibers found on areas 14b, 11c, and 13. Shiny white fibers were found attached mainly on area 11b, but also on areas 11a, 14b, 13. The medial wall (beneath the C1 process) was free of fiber attachments.

Robert¹⁰ and Fick¹¹ described the PRMM attachment as located directly behind the medial tubercle. In Jacobsen, the PRMM attachment area (Jacobsen's area 11) corresponds to areas 11a and 11b in this study, and it is also found "nowhere in direct continuity with the articular cartilage on the medial condyle". In Kohn and Moreno⁷⁶, the posteromedial recess is described as "a distinct bony depression on the tibial plateau", with the PRMM attached to it, "located directly behind the medial intercondylar tubercle next to the posterior cruciate ligament".

In Johnson et al.²¹² the attachment of the PRMM is on the "downslope of the posterior intercondylar fossa", behind the PRLM attachment. Both attachments are adjacent to one another, with the PRMM "slightly more medial and directly posterior", attached "directly in line with a posteromedial arthroscopic portal", and "directly anterior to the tibial insertion of the PCL". Three-dimensionally it is described as being vertical and facing "predominantly posterior".

The transverse shiny white fibers of the posterior root of the medial meniscus were neither marked nor measured with the center of the medial meniscal root attachment (Fig. 22), because the surgical techniques have focused on root fixation of the main medial meniscal fiber bundle³²⁷⁻³³¹.

The PRMM central fibers showed a mean attachment area of 51.3 mm² (95% CI 30.3 – 80.3 mm²; range, 41.7 to 61 mm²), which correlated fine with the 47.3 mm² (range, 41.2 mm² to 53.6 mm²) found by Johnson et al.²¹², with the 68.0 mm² (95% CI 59.1 – 76.9 mm²) found by Ellman et al.²¹⁴, and with the 30.4 ± 2.9 mm² found by Johannsen et al.⁷⁴. A mean area of 80 mm² (range, 38 mm² to 147 mm²) was found by Kohn and Moreno⁷⁶, without distinction of central and shiny white fibers, which should be compared with the mean 47.3 ± 4.4 mm² of the shiny white fibers found in Johannsen et al., representing ca. 60% of the main plus indirect PRMM attachment.

Measures taken from the PRLM center compare well with measures obtained by Johannsen et al.⁷⁴ in a straight line. Distances found in this study are greater than those found in Wang et al.²²⁹ to the PCL border (posterior) and the MT (anterior), although the distance to the “anterior border of tibial posterior intercondylar fossa” – which can be understood as the posteminence, or the PM fossa – had a similar distance in this study. The only explanations for both measurements in opposing directions being different are that either the specimens in this study had a deeper AP mean distance, or that the precise points selected as PCL border and MT were somehow nearer to the PRMM center in their study.

It was found that the attachment of main fibers usually filled half of area 11. Without area 11c, main fibers covered approximately three quarters of the area, which left shiny white fibers inserted onto parts of area 11a-b, and marginally on 14b and 11c. Some fibers seemed to attach marginally to the posterior wall of the posteromedial fossa, but no microscopic study was carried out.

V.9.3. Degenerative changes of the posterior intercondylar area

The posteromedial recess elevation showed a significant weak correlation with knee OA. The osteophyte grade ranged from a -5 depression to a +3 elevation, a maximum height that seems compatible with the potential existence of higher elevations, like the cases of “small eminence” reported in Parsons, or the case of an osseous knob reported in Jacobsen. No sizeable knob or tubercle was found in this area, though.

The internal PLIR process, E3, showed higher elevation changes marking the border between areas 11 and 14b in the posterior wall, and it was therefore included with the study of the posterior wall. Its elevation showed a significant but weak correlation with knee OA, as did the internal PMIR process, C3.

Axial radiographs showed a frequent higher density in the area of the wall, most likely due to a higher slope of the wall than to a higher density of the area. The density grade showed an almost significant, very weak ($p=0.052$) negative correlation with knee OA, which would suggest a slightly gentler slope in the posterior wall with higher OA grades, which would counteract the effects of a hypothetical denser bone of higher OA grades in the area. This gentler slope is hypothesized to be caused to a small extent by degenerative elevations in the area, from the posteminence superiorly to the tent-shaped ridge inferiorly.

V.10. Posterior facet

V.10.1. Posterior intercondylar triangle and posterior rim

The attachment site for the PCL was described as a “discrete, well-defined, flat facet” with a “gently descending surface” by Poirier², a description supported by Jacobsen²¹, who found it a flat facet without protuberances.

Anderson et al.³³² described the facet as “located below the articular surface of the tibia in a sulcus between two osseous prominences, which were the posterior aspects of the medial and lateral tibial plateaus”.

In contrast with the previous flat description of the facet, recent studies have found recognizable osseous landmarks. Amis et al.³²⁶ described a posterior tibial “shelf”, with the PCL attaching anterior and posterior to it. This shelf is probably to be identified with the posterior rim (the moderately sloped strip of bone posterior to the facet), while Anderson et al.³³² have more precisely described a transverse elevation, the “bundle ridge” which “did not extend through the attachment of the medial fibers of the posteromedial bundle”.

Observations from this study support the presence of a constant – albeit irregular – coronal elevation (the ICT coronal line) that marks a change to a slightly sharper slope posteriorly, the posterior rim, within the intercondylar triangle.

Another constant anatomic landmark is the “small transverse ridge” described by Amis et al.³²⁶ as marking the posterior limit of the PCL footprint, and the attachment of the knee joint capsule. This ridge has been recently described by Spiridonov et al.³³³ at its limit with the “champagne-glass drop-off”, so named on the basis of its lateral radiographic and anatomic appearance.

The PCL footprint was studied with three-dimensional laser photography by Tajima et al.⁶⁸, and they described an “anterolateral slope” in the superolateral aspect of the facet (where the AL bundle attaches), and a “posteromedial slope” in its inferomedial aspect (where the PM bundle attaches). They also described the facet as trapezoid-shaped. Anderson et al. considered the posteromedial slope to be comparable to the posterior aspect of the “medial groove” described by them as located at the distal base of the medial tibial wall, oriented anteroposteriorly. The study by Van Hoof et al.³³⁴ found qualitative results similar to Tajima et al., with an anterolateral slope (at the superolateral aspect of the posterior intercondylar area), the attachment area of the AL bundle; and a posteromedial slope in the inferomedial aspect of the fossa, the insertion area of the PM bundle.

Observations in this study also support the existence of an anterolateral sloping ridge, the posterior intercondylar stair, which was also found to form the footprint of the AM bundle. Medially, however, a clear osseous medial groove has been observed (which can also be observed in the 3D surfaces illustrated in Tajima et al.), but have been overlooked by Tajima et al. in describing a part of it together with the posterior rim as the “posteromedial slope” where the PM bundle attaches. The posteromedial groove described in this study seems to be wider and reach thus farther laterally than the one illustrated in Anderson et al., since it was found to form the central aspect of the medial insertion of the PM bundle, but the description of its location is similar to theirs.

The posterior facet was described by Jacobsen as located “at the foot of the eminence massif, deeply depressed between the two condylar joint surfaces. (...) It does not reach the cartilage edges on either side, as the ligament fibres do not insert on to the cartilage.” While the facet is described from the point of view of the PCL attachment, the internal branches of the posterior central processes of the PMIR and PLIR were found to define an osseous upper limit for the insertion facet, well below their cartilaginous boundary with the posterior condyles.

Results from this study also support the “lateral cartilage point” of the lateral wall at its junction with the ICT coronal ridge, described in Anderson et al.³³². However, the described “abrupt distolateral turn” of the articular cartilage in the lateral condyle – which has been described in this work to make a smooth posterior curve – is in fact the union of the central ALIR process (secondary branch, E1b, i.e. the upper limit of the lateral wall) and the ICT coronal ridge.

Anteriorly the facet is delimited by the tent-shaped ridge, where the sharper slope of the posterior wall joins the gentler slope of the posterior facet. Anteromedially, though, its boundary with area 11c – with which it is connected by a gentle upslope continuous with the posteromedial groove – is difficult to delimit.

V.10.2. Attachment of the posterior cruciate ligament

V.10.2.1. Qualitative assessment and borders

The PCL attachment was described by Robert¹⁰ as having a triangular shape, “almost quadrilateral”, broader and leaning to the lateral aspect in its posterior border, with an anterior peak located slightly medial, and connected to both the PRMM and PRLM attachments through fibrous fibers. A triangular shape is also

described by Paturet¹⁹. The shape has also been described as trapezoidal, with a posterior base^{326, 335-339}.

This study supports a circular triangular shape of the anterior aspect of the posterior facet, leaning laterally at its posterior base. Depending on the roughness of curvature changes of the sides distally, the circular triangle can appear as a quadrilateral, or even a pentagon. In contrast with Robert's description of a medial peak of the PCL attachment, observations made in this study support the more recent description of the peak being located either centrally or slightly lateral^{332, 336}.

Medial and lateral limits of the PCL attachment have been found beneath the secondary medial (C1_b) and lateral (E1_b) processes, which agrees with the described limits in Anderson et al.³³², as the inferior aspect of the posterior medial and lateral intercondylar walls, and in Jacobsen²¹, with PCL fibers attaching "well below the edge of the lateral condyle".

The distal border of the PCL was marked by the champagne-glass drop-off ridge, as found in previous studies^{326, 333, 335}.

No investigation was done in this study of the attachment or course of the anterior and posterior meniscomfemoral ligaments of Humphrey and Wrisberg^{76, 236, 332, 340}, first reported by Josias Weitbrecht in 1742³⁴⁰, and described in detail by the Weber brothers⁹ and Robert¹⁰. They are suggested to contribute to make the cross-sectional area of the PCL complex larger²³⁷.

A case like those described by Cunningham³⁴¹ and Jacobsen²¹, where the PCL inserted directly into the posterior aspect of the MT and its peak, was not found in this study.

V.10.2.2. PCL footprint area and distances from its center to anatomic landmarks

Quantitatively, the PCL area had 144.6 mm² (95% CI 115.2 – 173.9 mm²; range, 102.2 mm² to 210.2 mm²). This compared well with the ca. 139 mm² (70 ± 26 mm² for the AL bundle, 69 ± 17 mm² for the PM bundle) by Harner et al.²³⁷; with the ca. 162 mm² (46.7 ± 15.6 mm² for the AL bundle, 115.8 ± 54.6 mm² for the PL bundle) by Takahashi et al.³⁴²

It correlated fine with the 192 mm² (range, 80 mm² to 302 mm²) by Anderson et al.³³², and with the 189.1 ± 63 mm² (range, 68.6 mm² to 263.4 mm²) by Van Hoof et al.³³⁴

Results of this study contrasted with the 243.9 ± 38.2 mm² (range, 193.3 mm² to 330.5 mm²) by Tajima et al.⁶⁸. It also contrasted with the bundle areas calculated as oval-shaped areas (πab , where a and b are the semi-major and semi-minor axes, respectively), with the ca. 388 mm² (38 mm length, 13 mm width) in Girgis et al.²³⁶

Measures from the center of the PCL to anatomic landmarks compared well to measures by Anderson et al.³³². The measure from the center to the posterior coronal ridge compared fine with Ramos et al.³³⁷

V.10.2.3. PCL bundles

V.10.2.3.1. Bundle division and qualitative assessment

Just as old as the division of the ACL is the division of the PCL into discrete bundles, first by the Weber brothers⁹, followed by a detailed discussion of their function and insertion by Robert¹⁰.

On the other hand Welsh²⁴⁷, who considered the division of the ACL in two discrete parts an oversimplification, did not even mention any division of the PCL. As “inseparable” were the PCL bundles defined in Girgis et al.²³⁶. The oldest technique for surgical repair of the torn PCL by Hey Grooves treated it as a single bundle²⁷¹.

A division in two main bundles that become taut in the range of motion – anatomically and biomechanically distinct – is as popular today as the ACL “double bundle” concept^{236, 241, 339, 343-348}, albeit with far less research papers comparatively. Six to ten fiber bundles were individualized by Mommersteeg et al.²⁹² in the three PCL studied. Four main parts and their insertions were reported by Makris et al.³⁴⁹, and eight fiber bundles were described by Petersen & Tillmann³⁵⁰.

Double bundle PCL reconstructions that restore the posteromedial bundle in addition to the main anterolateral bundle seem to improve knee stability over single bundle reconstructions in vitro^{351, 352}, but clinical studies have not demonstrated improved subjective or objective outcomes³⁵³⁻³⁵⁶. Nevertheless, there is growing evidence in favor of a more “anatomic” reconstruction of the cruciate ligaments improving results³⁵⁷⁻³⁶¹. This is supported in the literature for

the ACL, whose injuries are more frequent and thus facilitate more research^{279, 280}.

It is well-known^{332, 335} that PCL bundles are compact and difficult to separate at the tibial attachment. No anatomic separation of the attachments of the bundles were found on the tibial plateau, but were found in this study by holding the PCL stump with forceps and applying tension proximally and then applying rotational and translational movements. An anteroposterior inter-space between fibers was found, and (medial and lateral) bundles were separated mid-substance dissecting them bluntly, then finishing dissection with a blade. A constant mediolateral inter-space was found during dissection, leaving a squared anterolateral, and a right-angled posteromedial bundle footprints. No study has assessed the variable outcomes of this previously described technique, as is available for the ACL²⁹⁷.

The oldest description of the double bundle insertion was made by the Weber brothers⁹, where the posterior bundle attachment is described as narrow, and the anterior bundle attachment as wide. Fick¹¹ also reported two different areas of PCL attachment when the capsule is detached: an anterior and a posterior aspect.

The PCL footprint has since been classically described as similar to the ACL bundle attachment, with an oblique and curved dividing line coursing posterolaterally to anteromedially, the AL bundle located mainly anteriorly, and the PM bundle mainly posteriorly^{68, 237, 326, 335, 338, 339, 344, 351, 362}. It has also been described as a central AL bundle, and two posterior footprints for the PM bundle³⁴⁵.

More recent studies have modified the description of the PM footprint as enveloping the AL bundle, giving the appearance of having two arms^{332, 363-365}, forming approximately a right angle with each other, the thickest portion being the medial and posteromedial aspect, the posterolateral fibers being markedly thinner than the rest of the bundle, described as the “posterior oblique” PCL fibers^{332, 349}.

Results from this study support the latter, with clear footprints and anatomic landmarks as osseous boundaries between the bundles. The ICT coronal line divides (in its lateral aspect) the anteromedial and posterolateral bundles frontally as anterior and posterior parts of the PCL³³². Results also agree with the description of Amis et al.³²⁶, Edwards et al.³³⁵, and Petersen et al.³³⁸, that the

lateral aspect of the “posterior arm” of the PM bundle (attached to the posterior rim) has a greater attachment area than the medial aspect.

The ICT coronal line curves anteriorly in its medial aspect with a right to acute angle, to form the posterior geniculate ridge together with the ICT sagittal line which mark the border of the sagittal division of the bundles. The footprint of the PL bundle, the anterolateral part of the ICT, was also found in this study to be dominated by the posteromedial groove. The geniculate ridge is therefore proposed to be described as the *PCL bundle ridge*.

Only limited, marginal osseous landmarks have been described in previous studies to guide tibial tunnel placement^{332, 333, 364}. With this study new key anatomic landmarks have been recognized that could more accurately guide the localization of PCL attachment centers on the proximal tibia.

Osseous limits were selected instead of soft tissue or cartilage limits, to avoid inter-observer variability. The AL-PM bundle division was defined as the geniculate ridge in this work. It is hypothesized that the main elevations described are the main traction zones of the posterior cruciate ligament, hence the actual sagittal border corresponds probably to a site slightly medial to the ICT sagittal line, at its border with the posteromedial groove. Given the findings from the anterior cruciate ligament, it is hypothesized that this area immediately lateral to the ICT sagittal line and near the posteromedial groove represents the true limit between bundles. This should be studied in future research.

Degenerative changes point to a slight elevation of the wide 13g line, hypothesized to represent most likely the traction of the marginal (medial) fibers of the AL bundle.

V.10.2.3.2. Area of AL and PM footprints and distances to anatomic landmarks

The AL bundle attachment area had 64.9 mm² (95% CI, 51.3 – 78.5 mm²; range, 37.8 mm² to 106.1 mm²), and the PM bundle attachment area had 74.8 mm² (95% CI 59.2 – 90.5 mm²; range, 45.8 mm² to 104.1 mm²), or 46% AL vs. 54% PM.

These measures compared well with the 70 ± 26 mm² for the AL bundle, 69 ± 17 mm² for the PM bundle (or an approximately equal distribution) by Harner et al.²³⁷, where no significant differences between areas were found.

It also compared well with the bundle areas calculated as oval-shaped areas (πab , where a and b are the semi-major and semi-minor axes, respectively): with the ca. 56.5 mm^2 ($8 \pm 2 \text{ mm}$ length, $9 \pm 2 \text{ mm}$ width) for the AM bundle, ca. 47.1 mm^2 ($6 \pm 1 \text{ mm}$ length, $10 \pm 2 \text{ mm}$ width) for the PL bundle, or ca. 54% AM vs. 46% PL bundle found in Edwards et al.³³⁵

It compared fine with the $46.7 \pm 15.6 \text{ mm}^2$ (range, 24.3 mm^2 to 82.9 mm^2) for the AL bundle, but contrasted with the high variability of the $115.8 \pm 54.6 \text{ mm}^2$ (range, 38.7 mm^2 to 241.8 mm^2) for the PM bundle (or ca. 29% AL vs. 71% PM) by Takahashi et al.³⁴²

It contrasted with the $93.1 \pm 16.6 \text{ mm}^2$ (range, 68.0 mm^2 to 128.1 mm^2) for the AL bundle, $150.8 \pm 31.0 \text{ mm}^2$ (range, 109.4 mm^2 to 227.8 mm^2) for the PM bundle (or ca. 38% AL vs. 62% PM) by Tajima et al.⁶⁸

It also contrasted with the 112 mm^2 (range, 55 mm^2 to 151 mm^2) for the AL bundle, 60 mm^2 (range, 55 mm^2 to 151 mm^2) for the PM bundle (or 65% AL vs. 35% PM) by Anderson et al.³³²

A greater distance between bundle centers was found in Tajima et al.⁶⁸. A similar distance to the posterior axis was found for the AL bundle center in Edwards et al.³³⁵. Distances compared well with those by Anderson et al.³³² for the AL center anteriorly (to the posterior wall^d), and laterally (to the lateral wall^e); slightly greater distances from the PM center to the AL center, and from the PM center to the posterior wall shows that the PM bundle center was estimated as slightly posterior to the position obtained in this study.

It is difficult to obtain reliable and precise measurements of the PM bundle: The lack of a precise fiber boundary present a limitation hard to overcome with plain anatomic studies. The variable PM footprint area is hypothesized to correspond to the previously described blending of the posterior fibers with the capsule and periosteum around the posterior coronal ridge³²⁶. That, together with the variable definition of the PM bundle border with the AL bundle in previous works makes it very difficult to compare measures obtained in this study with those of others.

^d Measures to the shiny white fibers were approximated from measures to posterolateral wall and posteromedial fossa.

^e Measures to the lateral cartilage point are approximated from measures to the PLIR.

V.10.3. Degenerative changes of the posterior facet

The posterior facet was classified subjectively into either a more vertical, ridge-like, or a more horizontal, facet-like area, and this showed an almost significant ($p=0.052$) association with knee OA, with a horizontal area more frequent in lowest and highest OA grades, and vertical ridge more frequent in intermediate grades. These findings could be interpreted as an inclination of the area caused by degenerative changes around the area, which would be compensated in the highest OA grades by more degenerative changes.

The osteophyte grade of the ICT sagittal line showed a weak positive correlation with knee OA, which – relating it to the degenerative changes of the anterior intercondylar staircase – would suggest traction of marginal PCL (AL bundle) fibers located in this area, and thus the border between the main PCL bundles should be located adjacent to it, most likely lateral to it.

V.11. Imaging and histology studies

V.11.1. Identification of structures in plain radiography

The study by Ravelli¹⁵¹ was the first to try to systematically identify anatomic bone contour from plain knee radiographs.

Jacobsen described²¹ the proximal tibia's normal anatomy and gave important hints to identify the most common structures in the lateral radiographic view. A more exact depiction of radiographic landmarks of the proximal tibia's profile was given in a later work²², where pins and lead marks were attached to the specimens studied, and lateral radiographs done in different degrees of rotation. There, the posterior arch of the lateral tubercle is described as the most characteristic landmark to distinguish both tubercles, with a description of its changing shape and position depending on rotation of the specimen. The AIAR and posterior borders of both condyles are also described with detail.

The different comparisons of similar radiographic and 3D model views of each specimen have shown that many anatomic details could be identified in the most common AP standing and lateral knee radiographs.

Danzig et al.²⁰¹ studied AP and lateral radiographic views of cadaveric specimens, to identify the tubercles and other structures of the tibial plateau, using metallic markers to improve identification.

The method described by Jacobsen and Danzig et al. has been reproduced in this study by using metal wires attached to the tubercles, but they have not been found to be qualitatively more helpful in identifying the tubercle shape in the lateral view than an identification based solely on their anatomic description in normal specimens.

The lateral radiographic view was shown by White et al.¹⁵⁸ to be useful in accurately determining the site and extent of tibial plateau erosions, contrary to the opinion of Altman et al.³⁶⁶ that they had little significance. Results from observing osteophytic elevations in this study suggest that lateral radiographic views might offer indirect clues as to the site and extent of tibial plateau erosions.

V.11.2. Sectional anatomy and histology

Poirier² described the trabecular architecture of the proximal tibia in the coronal plane as forming two main systems (see below Fig. 502): a system of vertical trabeculae connecting the diaphysis to the condyles, and a system of arcuate fibers converging from the diaphysis into the articular facets of the tibial tubercles.

In his study of knee trabeculae, Takechi³⁶⁷ found two main types of trabecular arrangements in sagittal cuts of the proximal tibia: one type from the tibial tuberosity to the posterior articular surface, and another from the posterior cortex to the posterior articular surface and eminentia. In coronal cuts, trabeculae are perpendicular to the articular surface and parallel to the bone axis.

Other detailed trabecular architectures studied include the study of the pars interarticularis of the lower lumbar vertebrae by Krenz & Troup³⁶⁸, and the study of the tarsal bones by Sinha et al³⁶⁹.

In his book on knee biomechanics, Maquet³⁷⁰ showed that resorption and apposition are balanced, within certain limits of force. An increase in force causes an increase in bone formation; bone resorption follows a decrease in forces. Bone tissue quantity is therefore proportional to the force magnitude. Using photoelastic models, he demonstrated the direction of significant loads – and thus stress distribution – in the frontal plane.

Trabecular architecture is therefore directly influenced by mechanical needs of the bone. Trabeculae beneath cortical bone were found perpendicular to it, and their crossing over each other is suggested to be caused by the irregularity of the osseous surface of the eminence and its posterior aspect.

In its anterior aspect, fewer trabeculae are seen, and they are parallel to the mechanical axis of the tibia. As they move away from the osseous surface, trabeculae are found to be more vertically oriented.

Tension trabeculae are also found, but are fewer than compression ones, and decrease in inferior levels.

When observed in tibias with advanced degenerative changes, there is some vanishing of trabeculae, producing cysts within the spongy bone, changes in the cortical thickness in some areas, and osteophytic elevations.

V.11.3. Histology

Histologic investigation showed that ligament fibers were attached to the posterolateral aspect of the Parsons' tubercle, while the medial aspect was covered by cartilage.

The Parsons's knob in degenerative tibias was found to be similar to an osteophytic structure, with a superficial connective tissue, fibrocartilage and trabecular bone, as shown in Junker et al³⁷¹.

Because it is found in certain knees without other signs of osteoarthritis, a possible explanation is suggested by its presence in cases of traction injuries of the ACL³⁷², a mechanism that was suggested early in the description of the knob¹²,
31.

V.12. Osteophytes and diagnosis of osteoarthritis

V.12.1. Osteophyte grade and maximum attrition zone of the condyle

The growth of marginal osteophytes has been proposed to be determined by pressure upon the articular surface. Van Osch et al.²⁶ showed that, in animal models, osteophytes develop at sites of adjacent cartilage loss, therefore large osteophytes may serve as a marker for nearby cartilage loss. This could explain the findings in the longitudinal radiographic study by Wolfe & Lane³⁷³, where an association was noted between osteophytes and disease progression only in knees where the joint space was minimally narrowed or normal, since osteophytes may have served as evidence for nearby cartilage loss not yet detectable as joint space narrowing on the radiograph³⁷⁴.

In this study, in order to test the hypothesis that osteophyte growth was different depending on the zone of femoral pressure on the tibia, the association of osteophyte grade with the zone of maximum attrition of the tibial condyle was studied. A general overview of the results shows that higher osteophyte grades are associated with MAC areas 3M, 4M, and lower osteophyte grades with MAC areas 1M, 2M. This agrees with the association of areas 3M, 4M with higher OA grades, and 1M, 2M with lower OA grades, supporting the hypothesis that osteophyte growth is associated with narrowing of the tibiofemoral joint space.

More specifically, slight differences are found in higher osteophyte grades in certain osteophytes. The highest osteophyte grades of MT, LT, C1, D3 (not statistically significant), AM rim, and AL rim are associated with a posteromedial attrition; whereas the highest osteophyte grades of E1, F2, AL corner, and PL rim are associated with an anteromedial attrition.

The association of MAC with corresponding lateral condyle attrition zones has already been described: posteromedial attrition in the medial condyle associated with anteromedial attrition in the lateral condyle, or 4M-2L; anteromedial attrition in the medial condyle with posteromedial attrition in the lateral condyle, or 3M-1L. This together with the findings related to the aforementioned osteophytes would suggest that osteophytes grow at a certain distance from the most common tibiofemoral pressure zones. It is not possible to derive any hypothesis from these findings because of the small sample size, and because a more complex study design is needed to assess other factors that might influence

osteophyte growth, such as tibiofemoral angle, instability, insertional pathology of ligaments or menisci, or attrition grade.

V.12.2. Osteophyte grade and condyle attrition

V.12.2.1. Ahlbäck classification system of osteoarthritis

Studies by DeHaven & Collins³⁷⁵, Lysholm, Hamberg, & Gillquist³⁷⁶, and Brandt et al.³⁷⁷ have shown that radiographic observations do not correlate well with arthroscopic findings, suggesting insensitivity of the radiographs for detecting early articular cartilage loss. In Boegård et al.³⁷⁸, however, it was shown that joint space width less than 3 mm reflects cartilage defects on MRI.

Weidow et al.⁵⁴ investigated the reproducibility of the Ahlbäck classification based on routine weight-bearing radiographs, and its validity in the classification of bone attrition by comparison with specimens removed during total knee replacement, hence studying patients with a more advanced disease. They found poor interobserver error values and specificity, and concluded that the Ahlbäck classification has variable reproducibility and validity. This agreed with a previously reported low agreement of intraobserver reliability and interobserver reproducibility of the Ahlbäck classification³⁷⁹. They tried to define radiographic changes that indicated the presence of bone destruction, but failed, concluding that the information available on conventional radiographs is insufficient.

They also reported that determining femoral attrition in lateral OA was less reliable than in medial OA, as the only difference between these two variations of the disease. They thought that this could be explained by the more posterior location of the wear on the lateral condyle (as posited by Boegård et al.³⁷⁸), a part that would not articulate against the tibia in the common position for weight-bearing radiographs, but would require exposure at further flexion of the knee joint, i.e. the tunnel view (Resnick & Vint³⁸⁰).

The Multicenter ACL Revision Study (MARS) group conducted a multicenter prospective longitudinal cohort study³⁸¹ of 632 patients undergoing revision surgery after ACL reconstruction, to investigate articular cartilage changes radiographically and arthroscopically. They found that all radiographic classification systems studied (Kellgren-Lawrence^{382, 383}, International Knee Documentation Committee^{384, 385}, Fairbank ^{386, 387}, Brandt et al.³⁷⁷, and Jäger-Wirth^{388, 389}) had small to medium correlations with arthroscopic findings classified by the modified Outerbridge classification³⁹⁰.

Previous studies with weight-bearing radiographs and joint space narrowing had similar findings, but without assigning classification scales^{377, 391-394}. Contrary to previous studies, the MARS group concluded that Ahlbäck classification system showed good reliability for classifying tibiofemoral osteoarthritis of the knee.

They also found that the Ahlbäck classification shows a better reliability as applied to the Rosenberg view³⁹⁵ than to the anteroposterior radiographic view³⁵, relying on the ability of the Rosenberg view to visualize the mid-flexion surface of the femoral condyles, which is a common site of degenerative wear^{377, 396}. However, previous studies found a better reliability of the Ahlbäck classification as applied to the anteroposterior view, even when arthroscopically the disease was classified in most patients as stage 1 or 2³⁹⁷.

The MARS group also found that unilateral Rosenberg knee radiographs showed less reliability than bilateral images did, but this improvement in reliability was not noted with anteroposterior weight-bearing radiographs.

V.12.2.2. Classifications including osteophytes

Osteophytes and cartilage loss are central radiographic features of osteoarthritis^{398, 399}, and osteophytes have been considered the most specific signs of knee osteoarthritis⁴⁰⁰, although osteophytes can occur as an apparently isolated feature associated with age²⁹.

Radiographs are relatively insensitive and cannot exclude minor, especially focal, lesions in cartilage and bone¹⁴⁹. However, sensitive imaging techniques have shown a stronger association between osteophyte and cartilage lesions¹³². Osteophytes have also been shown to be related to two risk factors for disease progression³⁷⁴: limb malalignment (related to tibiofemoral compression), and pre-existing cartilage loss.

Osteophytes are known to occur tardily, reducing thus its sensitivity compared to tibiofemoral joint space narrowing. Some radiographic classifications of osteoarthritis take into account osteophytes, though. So for example Kellgren & Lawrence^{382, 383} describe four pathological grades, a mix of joint space narrowing and osteophytes.

Originally, Ahlbäck also described in his thesis³⁵, apart from joint space narrowing, subchondral bone reactions (considered as appearing late in the development of the disease) for an osteoarthritis classification. Osteophytes were not included in his later classification⁵³, though. The association of decreasing

joint space width and increasing marginal osteophytes has also been found by others^{58, 132}.

More recent classifications include those by Menkes⁴⁰¹, who describes six pathological grades, and adds +1 if osteophytes are marked; and the one by Piperno⁴⁰², where two categories are individualized: joint space narrowing, divided into five pathological grades, and osteophytes, divided into three different pathological categories, making the classification less uniform and not completely progressive.

The Osteoarthritis Research Society International (OARSI) developed a classification based on an atlas⁴⁰³ that takes into account joint space narrowing, osteophytes, subchondral bone sclerosis, erosion, and desaxation. The atlas has been revised by Altman and Gold⁴⁰⁴. Use of the OARSI atlas to define radiographic tibiofemoral OA has been shown in Culvenor et al.⁴⁰⁵ to result in rates almost double than that observed with the Kellgren & Lawrence system.

An ultrasonographic atlas has also been proposed to assess osteophyte size in Koski et al.⁴⁰⁶, finding a reliability and reproducibility similar to radiographic examination, and a significant correlation between osteophyte size (as a summed ultrasonographic grade) and the arthroscopic grade of degenerative changes of the articular cartilage at the medial compartment. In the same study, a slight, not statistically significant correlation was found between a summed radiographic osteophyte grade and arthroscopy.

Donnelly et al.⁶² did not find an association with pain for medial osteophytosis, nor with joint space narrowing, but they did find a weak association between knee pain and lateral tubercle spiking. They concluded that “isolated tibial spiking is therefore not a reliable marker for the presence of knee OA and should not routinely be reported.”

In Nagaosa, Lanyon, & Doherty¹⁴⁹, osteophytes were studied in size and direction in radiographs. They found a correlation between lateral tibial osteophyte size and narrowing of the medial tibiofemoral compartment; medial tibiofemoral joint osteophyte size and varus malalignment. Attrition of the tibiofemoral joint was found to be associated with grade 2 or 3 osteophytes (from 0–3 grading) in both lateral and medial tibiofemoral joint compartments. It was noted that osteophyte shapes may differ and the curvature of an osteophyte or its placement near the joint capsule may stabilize the joint. They also noted that the association

at several sites between osteophyte grades and summated osteophyte scores supports the concept of a constitutional tendency toward osteophytosis and a “hypertrophic” bone response in some subjects.

Marshall & Olson⁴⁰⁷ proposed that local instability is an important biomechanical trigger to osteophyte formation. Williams & Brandt⁴⁰⁸ showed that osteophyte formation in an unstable joint is promoted by joint movement, while Palmoski & Brandt⁴⁰⁹ showed that it was inhibited by immobilization. Also, removal of osteophytes during total knee arthroplasty is known to increase instability⁴¹⁰, which is an indirect proof of the splinting function of osteophytes. This stabilizing role is better achieved when growing outwards to widen the articular surface^{407, 408}, but at the lateral plateau vertical osteophytes – growing upwards – can also stabilize the joint according to Pottenger et al⁴¹⁰, presumably by creating a newly raised tibial surface and reducing excessive valgus motion. It was shown in Nagaosa, Lanyon, & Doherty¹⁴⁹ that – in contrast with small osteophytes – larger osteophytes extend predominantly upwards or downwards, which may reflect an anatomical limitation to lateral growth (imposed by the restraints of adjacent fibrous structures), or the need to widen and strengthen the osteophyte base to protect against fracture.

This study showed that the sum of all osteophytic elevations visible on a precise 3D surface of the tibia is capable of predicting 72% of the attrition of the medial condyle.

Studied individually, more precise regression equations were obtained – with osteophytes visible on common knee radiographs –, that could predict the medial condyle attrition (66.9%) and lateral condyle attrition (51.7%)

Combined with Ahlbäck OA grade – as a proxy for tibiofemoral joint narrowing –, the selected variables could explain 71.4% of the medial condyle attrition, but the lateral condyle attrition did not improve.

After evaluating each variable separately, tibiofemoral joint space narrowing – graded according to the Ahlbäck classification – offered the best predictive value (47.9%) for medial tibial condyle attrition.

The Ahlbäck classification system primarily focuses on narrowing of the joint space, both as an indirect sign of cartilage loss and as the best variable in assessing radiographic progression of knee OA^{366, 411}. It is proposed that the addition of a certain score to the Ahlbäck classification, based on the selected

osteophytes found in this study, could substantially improve the assessment of articular wear assessed from AP and lateral knee radiographs. Such a system should be compared with existing classifications, such as the Kellgren-Lawrence classification, the most widely used classification in epidemiological studies. For its application to clinical practice, though, the proposed osteophyte grading – which has been investigated on precise 3D surfaces and complemented with knee radiographs – should first be assessed for intra- and interobserver reliability based on radiographic studies alone.

V.12.3. American Knee Society Clinical Rating System

In 1989, Insall et al.⁴¹² published the American Knee Society Clinical Rating System (KS), considered a concise, user friendly scoring method that has been widely adopted and supported⁴¹³. The KS system is divided into a Knee Score and a Functional Score, each consisting of 100-point scales.

As described in Scott and Insall Surgery of the Knee, 5th ed⁴¹³, the KS Clinical Rating System avoids the arbitrary classification of composite scores into categorical ratings such as “Excellent,” “Good,” etc.^{412, 414, 415}; the KS Knee Score has shown poor reliability with acceptable responsiveness according to psychometric testing, while the KS Function Score has demonstrated good reliability with questionable responsiveness^{414, 416-418}; and their combined use as an assessment instrument has been supported by validation tests^{416, 418}.

While it is acknowledged that knee pain does not always correlate well with radiographic disease severity, it is important to investigate whether one radiographic classification system is able to differentiate symptomatic and asymptomatic knees better than others⁴¹⁹, something that the Kellgren-Lawrence⁴²⁰ and the Ahlbäck⁴²¹ classification systems have been able to do, especially with higher grades of radiographic osteoarthritis.

Some defend the former³⁹¹, arguing that marginal osteophytes are the most sensitive radiographic feature for the detection of osteoarthritis, more than joint space narrowing, subchondral sclerosis, and subchondral cysts. Both classifications show a good correlation⁴²², though, and Ahlbäck seems easier to apply and suitable for the assessment of medial compartment OA of the knee (the most frequently affected compartment in knee OA), and it appears to be especially useful for surgical treatment.

Osteophytes have been found to correlate with knee pain in studies by Cicuttini et al.⁴²³, and Lanyon et al.⁴²⁴, and pain may be the driver for functional impairment. Dowsey et al.⁴²⁵ found a meaningful association between osteophytes in the lateral compartment and pre-operative function in patients with advanced OA presenting for knee replacement; however, the mechanism by which these osteophytes affected function was not evident from the study. They found it plausible that lateral osteophytes are an indication of severity and chronicity of disease, and are in this way a correlate of functional loss, rather than a cause of the loss per se. It is known that in classic varus knee osteoarthritis, medial compartment disease is eventually followed by lateral compartment disease; hence, by the time this is established (with the presence of lateral osteophytes), the severity of symptoms and functional loss would be likely worse than for pure medial disease alone.

This study showed a statistically significant, weak negative correlation of the Knee Score item with the Ahlbäck classification, and with total osteophyte score, but not with combined condyle attrition. Function Score was not found to be correlated with any of the variables studied. These finds suggest that the worsening of knee pain and function during the development of osteoarthritis is multi-factorial, depending partly on tibiofemoral joint narrowing and osteophyte growth, but not directly on articular wear.

This is in contrast with the high coefficients of determination found in the regression models obtained to predict Knee Score and Knee Function for all three variables, with combined condyle attrition as the most predictive model (96.5% Knee Score, 97.7% Knee Function), followed by total osteophyte score (91.9% Knee Score, 94.2% Knee Function) and Ahlbäck classification (88.7% Knee Score, 89.2% Knee Function). Because of the cubic nature of the models obtained, it is proposed that a kind “functional plateau” exists in this study’s sample of patients with a late stage of the disease, whereby function and pain not only do not worsen, but in fact improve. This would suggest that growth of marginal osteophytes could indeed stabilize the tibiofemoral knee joint at a certain stage of the disease, enough to slow down knee pain and function impairment, and even improve the signs and symptoms of osteoarthritis, before being destabilized again in later stages of the disease.

A study with an appropriate design should be done to ascertain whether this finds can be extrapolated to the general population.

VI. Conclusion

VI.1. Anatomy

VI.1.1. Osseous surface

Areas and structures of the proximal tibia described previously in the literature have been redefined, their limits have been refined by using only osseous elevations or depressions – instead of soft tissue attachments –, and new areas, subareas, structures, and substructures have also been reported. This study has thus created a more straightforward, complete, and reproducible system for the description of the anatomy of the proximal tibia, useful for future anatomic studies, for reference in imaging studies, or for reports of arthroscopic or open surgery.

These newly described osseous anatomic landmarks have been used to more accurately describe the location of ligamentous and meniscal attachments, obtaining precise distances from the center of each attachment to arthroscopically relevant structures.

They have also been used to define the most common osteophytic growths.

VI.1.2. Attachment areas and osseous elevations

This study has shown that osseous elevations and depressions are indeed linked to soft tissue insertions – and more specifically elevations were noticed beneath and/or surrounding ligamentous and meniscal attachments. However, when observed in detail over surface anatomy, this historical tenet cannot be withheld: Osseous elevations and depressions cannot be simply relied upon as constant, immediate borders of ligamentous and meniscal attachments.

VI.1.3. Cruciate ligament detachment: bundle distinction and references.

This study has found that fibrous, synovial, and fat tissues surround the surface of both cruciate ligaments, which could explain why results vary widely,

depending on how these tissues are treated and how the examiner defines the essential components of the ligament.

Important anatomic structures have been defined on the ACL and PCL footprints and surrounding areas. While exact differentiation of fiber bundles is impossible without including biomechanical and histological observations, and it is likely that ligaments form a continuum of fibers, this study has offered a detailed three-dimensional depiction of the corresponding position of the two main inter-spaces that cross both ligaments in their osseous footprints: a sagittal incisure dividing the ACL, and a geniculate ridge dividing the PCL.

VI.2. Tubercle height and pathology

The findings of this study for patients with osteochondritis, osteonecrosis, and osteochondral fracture suggest that the difference in height between tubercles – and not only the size of the medial tubercle – might be associated with the development of these pathologies.

VI.3. Degenerative changes

VI.3.1. Corner osteophytes

No intra-articular osteophytes were found in the sample studied, even when apparent in radiographs, which suggests that no intra-articular osteophytes appear in the knee joint.

The *tuberculum intercondylare quartum* – a big posterior osteophyte visible on radiographs – has been found mainly posteromedially, instead of posterolaterally as it was commonly believed.

VI.3.2. Parsons' knob and histology

The knob described by Parsons as appearing in the anteromedial aspect of the ACL attachment has been shown in this study to more likely correspond to the geniculum, the knee-like turn of the geniculate ridge.

The structure described radiographically in posterior publications and named Parsons' knob or tubercle has been shown to correspond to an elevation appearing near to the geniculum, but also lateral to it along the anterior frontal ridge, involving different structures of the anterior intercondylar area that are very difficult to distinguish in common knee radiographs.

Histologically it is similar to an osteophyte, and an association has been found with osteoarthritis. Nevertheless, traction of the ACL – as traditionally held – can

also be supported as cause for the appearance of the knob. The nature of the Parsons' knob, therefore, is believed to be of either a capsular or marginal osteophyte, or more likely a combination of both.

VI.3.3. Degenerative changes

Osteophytes evaluated have been found to be related to tibiofemoral joint space narrowing (evaluated using the Ahlbäck classification), and to more knee pain and worse knee function (graded by the American Knee Society Clinical Rating System). Osteophytes have also been found to be related to bone erosion in both condyles:

- Certain osteophytic growths have been found to be related to the pattern of articular wear.
- The grade of certain osteophytes has been shown to be related to the degree of bone erosion.

The pattern of articular wear – as an indication of knee biomechanics – and degree of bone erosion are in turn relevant for preoperative planning.

VI.4. Surface anatomy

This work has established a new, accessible form of investigation of detailed anatomic structures, by using three-dimensional surface reconstruction and geographic information system tools.

References

1. Gray H. *Anatomy of the Human Body*. 20 ed. Philadelphia: Lea & Febiger; 1918.
2. Charpy A, Nicolas A, Prenant A, Porier P, Jacques P. *Ostéologie. Squelette de la jambe. Tibia*. In: Poirier P, Charpy A, editors. *Traité d'Anatomie Humaine* Paris: L. Battaille et Cie, Éditeurs; 1892.
3. Putz R, Pabst R, Taylor AN. *Sobotta Atlas of Human Anatomy*. Baltimore, MD: Williams & Wilkins; 1997.
4. Gray G, Mayo G. *Gray's Anatomy*. 27 ed. Philadelphia, Pa: Lea & Febiger; 1965.
5. Pernkopf E. *Atlas of Topographical and Applied Human Anatomy*. 2 ed. Baltimore, MD: Urban & Schwarzenberg-Munich; 1980.
6. Testut L, Jacob O. *Traité d'anatomie topographique avec applications médico-chirurgicales*. 4 ed. Paris: Gaston Doin; 1922.
7. Grant JCB. *Grant's Atlas of Anatomy*. 5th ed. Baltimore, MD: Williams & Wilkins Co; 1962.
8. FIPAT. *Terminologia Anatomica*. Stuttgart: Thieme; 1998.
9. Weber W, Weber E. *Mechanik der menschlichen Gehwerkzeuge: Eine anatomisch-physiologische Untersuchung*. Göttingen: Dieterische Buchhandlung; 1836.
10. Robert HLF. *Untersuchungen über die Anatomie und Mechanik des Kniegelenkes*. Giessen: Rickersche Buchhandlung; 1855.
11. Fick R. *Handbuch der Anatomie und Mechanik der Gelenke unter Berücksichtigung der bewegenden Muskeln*. Jena: Gustav Fischer; 1904.
12. Parsons FG. *Observations of the Head of the Tibia*. *J Anat Physiol*. 1906;41:83-7.
13. Pirogoff N. *Anatome Topographica Sectionibus per Corpus Humanum Congelatum Triplici Directione Ductis Illustrata*. Petropoli: Typis Jacobi Trey; 1855.
14. Spalteholz W. *Knochen, Gelenke, Bänder*. Leipzig: Verlag von S. Hirzel; 1896.
15. Testut L. *Traité d'Anatomie Humaine*. 4th ed: Octave Doin; 1899.
16. Sobotta J. *Atlas der deskriptiven Anatomie des Menschen*. München: J. F. Lehmann; 1904.
17. Orts Llorca F. *Anatomía Humana*. 2 ed. Barcelona: Editorial Científico Médica; 1959.
18. Szentágothai J, Kiss F. *Az ember anatómiájának atlasza*. Budapest: Posner Grafikai Műintézet; 1946.

19. Paturet G. *Traité d'anatomie humaine*. Paris: Masson & Cie Editeurs; 1951.
20. Smillie IS. *Injuries of the Knee Joint*. 4 ed. Edinburgh: Churchill Livingstone; 1975.
21. Jacobsen K. Area intercondylaris tibiae: Osseous surface structure and relation to soft tissue structures and applications to radiography. *J Anat*. 1974;117(Pt 3):605-18.
22. Jacobsen K. Landmarks of the knee joint of the lateral radiograph during rotation. *RöFO*. 1976;125(5):399-404.
23. Resnick DL. *Diagnosis of Bone and Joint Disorders*. 4th ed. Philadelphia: Saunders; 2002.
24. Thompson RC, Basset CA. Histological observations on experimentally induced degeneration of articular cartilage. *J Bone Joint Surg Am*. 1970;52(3):435-43.
25. Gilbertson EM. Development of periarticular osteophytes in experimentally induced osteoarthritis in the dog. A study using microradiographic, microangiographic, and fluorescent bone-labelling techniques. *Ann Rheum Dis*. 1975;34(1):12-25.
26. van Osch GJ, van der Kraan PM, van Valburg AA, van den Berg WB. The relation between cartilage damage and osteophyte size in a murine model for osteoarthritis in the knee. *Rheumatol Int*. 1996;16(3):115-9.
27. Heine J. Über die Arthritis deformans. *Virchows Arch path Anat*. 1926;260:521.
28. Danielsson L, Hernborg J. Clinical and roentgenologic study of knee joints with osteophytes. *Clin Orthop Relat Res*. 1970;69:302-12.
29. Hernborg J, Nilsson BE. The relationship between osteophytes in the knee joint, OA and aging. *Acta Orthop Scand*. 1973;44(1):69-74.
30. Thomas RH, Resnick D, Alazraki NP, Daniel D, Greenfield R. Compartmental evaluation of osteoarthritis of the knee. A comparative study of available diagnostic modalities. *Radiology*. 1975;116(3):585-94.
31. Politzer G, Pick J. Über einen röntgenologisch wichtigen Knochenbefund am medialen Kondylus der Tibia. *Fortschr Geb Rontgenstr*. 1937;56:649-52.
32. Noyes FR, DeLucas JL, Torvik PJ. Biomechanics of anterior cruciate ligament failure: an analysis of strain-rate sensitivity and mechanisms of failure in primates. *J Bone Joint Surg Am*. 1974;56(2):236-53.
33. Pommer G. Zur Kenntnis der Ausheilungsbefunde bei Arthritis deformans, besonders im Bereiche ihrer Knorpelursen, nebst einem Beitrag zur Kenntnis der lakunären Knorpelresorption. *Virchows Arch path Anat*. 1915;219:261-78.
34. Lang FJ. Osteo-arthritis deformans contrasted with osteo-arthritis deformans juvenilis. *J Bone Joint Surg Am*. 1932;14(3):563 -73.
35. Ahlbäck S. Osteoarthrosis of the knee. A radiographic investigation. *Acta Radiol Diagn (Stockh)*. 1968;Suppl 277:7-72.
36. Jaffe HL. *Metabolic, degenerative and inflammatory diseases of bone and joints*. Philadelphia: Lea & Febiger; 1972.
37. Keefer CS, Parker F, Myers WK, Irwin RL. Relationship between anatomic changes in knee joint with advancing age and degenerative arthritis. *Arch Intern Med*. 1934;53(3):325-44.

38. Nichols EH, Richardson FL. Arthritis deformans. *J Med Res.* 1909;21(2):149-222.
39. Auxhausen G. Neue Untersuchungen über die Rolle der Knorpelnekrose in der Pathogenese der Arthritis deformans. *Arch f klin.* 1914;104:301-46.
40. Moskowitz RW, Goldberg VM. Studies of osteophyte pathogenesis in experimentally induced osteoarthritis. *J Rheumatol.* 1987;14(2):311-20.
41. van der Kraan PM, van den Berg WB. Osteophytes: relevance and biology. *Osteoarthritis Cartilage.* 2007;15(3):237-44.
42. Hayeri MR, Shiehorteza M, Trudell DJ, Heflin T, Resnick D. Proximal tibial osteophytes and their relationship with the height of the tibial spines of the intercondylar eminence: paleopathological study. *Skeletal Radiol.* 2010;39(9):877-81.
43. Alexander CJ. Osteoarthritis: a review of old myths and current concepts. *Skeletal Radiol.* 1990;19(5):327-33.
44. Lloyd-Roberts GC. The role of capsular changes in osteoarthritis of the hip joint. *J Bone Joint Surg Br.* 1953;35(4):627-42.
45. Martel W, Braunstein EM. The diagnostic value of buttressing of the femoral neck. *Arthritis Rheum.* 1978;21(1):161-4.
46. Mouchet A, Noureddine A. Note sur l'épine du tibia. *Bull mem soc ant Paris.* 1925;95:58-61.
47. Bauer C. Die Beziehung der Weite der Kniegelenkspalte zueinander und zur Form der Eminentia intercondyloidea. *Zentralbl Chir.* 1931;58:1317-9.
48. Schlüter K, Becker R. Die Form der Eminentia intercondylica tibiae. *Arch Orthop Unfallchir.* 1955;47(6):703-19.
49. Jonasch E. Untersuchungen über die Form der Eminentia intercondyloidea tibiae im Röntgenbild. *Fortschr Geb Rontgenstr Nuklearmed.* 1958;89(7):81-5.
50. Giorgi B. Morphologic variation of the intercondylar eminence of the knee. *Clin Orthop.* 1956;8:209-17.
51. Fairbank HAT. Osteo-chondritis dissecans. *Br J Surg.* 1933;21(81):67-82.
52. Freiberg AH. Osteochondritis dissecans. *J Bone Joint Surg Am.* 1923;5(1):3-17.
53. Ahlbäck S, Rydberg J. Röntgenologisk klassifikation och undersökningsteknik vid gonartros. *Läkartidningen.* 1980;77(22):2091-6.
54. Weidow J, Cederlund CG, Ranstam J, Karrholm J, Ahlbäck grading of osteoarthritis of the knee: poor reproducibility and validity based on visual inspection of the joint. *Acta Orthop.* 2006;77(2):262-6.
55. Leach RE, Gregg T, Siber FJ. Weight-bearing radiography in osteoarthritis of the knee. *Radiology.* 1970;97(2):265-8.
56. Siu D, Cooke TD, Broekhoven LD, Lam M, Fisher B, Saunders G, et al. A standardized technique for lower limb radiography. Practice, applications, and error analysis. *Invest Radiol.* 1991;26(1):71-7.
57. Buckland-Wright JC, Macfarlane DG, Lynch JA, Jasani MK, Bradshaw CR. Joint space width measures cartilage thickness in osteoarthritis of the knee: high

- resolution plain film and double contrast macroradiographic investigation. *Ann Rheum Dis*. 1995;54(4):263-8.
58. Buckland-Wright JC, MacFarlane DG, Lynch JA, Jasani MK. Quantitative microfocal radiographic assessment of osteoarthritis of the knee from weight bearing tunnel and semiflexed standing views. *J Rheumatol*. 1994;21:1734–41.
 59. Ravaud P, Auleley GR, Chastang C, Rousselin B, Paolozzi L, Amor B, et al. Knee joint space width measurement: an experimental study of the influence of radiographic procedure and joint positioning. *Br J Rheumatol*. 1996;35(8):761-6.
 60. McDaniel G, Mitchell KL, Charles C, Kraus VB. A comparison of five approaches to measurement of anatomic knee alignment from radiographs. *Osteoarthritis Cartilage*. 2010;18(2):273-7.
 61. Weidow J. Lateral osteoarthritis of the knee. *Acta Orthop Suppl*. 2010;77(sup322):2-44.
 62. Donnelly S, Hart DJ, Doyle DV, Spector TD. Spiking of the tibial tubercles -- a radiological feature of osteoarthritis? *Ann Rheum Dis*. 1996;55(2):105-8.
 63. Pećina M, Bajok I, Pećina HI. Tuberculum intercondylare tibiae tertium as a predictive factor for anterior cruciate ligament injury. *Am J Sports Med*. 2001;29(6):709-11.
 64. Moon KH. New view on the initial development site and radiographic classification system of osteoarthritis of the knee based on radiographic analysis. *Int J Biomed Sci*. 2012;8(4):233-43.
 65. Slavunos G. Über eine einfache Methode zur Feststellung und Abbildung der Umriss der Muskelansätze. *Anat Anz*. 1907;30:64-9.
 66. Ferretti M, Doca D, Ingham SM, Cohen M, Fu FH. Bony and soft tissue landmarks of the ACL tibial insertion site: an anatomical study. *Knee Surg Sports Traumatol Arthrosc*. 2012;20(1):62-8.
 67. van Eck CF, Lesniak BP, Schreiber VM, Fu FH. Anatomic single- and double-bundle anterior cruciate ligament reconstruction flowchart. *Arthroscopy*. 2010;26(2):258-68.
 68. Tajima G, Nozaki M, Iriuchishima T, Ingham SJ, Shen W, Smolinski P, et al. Morphology of the tibial insertion of the posterior cruciate ligament. *J Bone Joint Surg Am*. 2009;91(4):859-66.
 69. Purnell ML, Larson AI, Clancy W. Anterior cruciate ligament insertions on the tibia and femur and their relationships to critical bony landmarks using high-resolution volume-rendering computed tomography. *Am J Sports Med*. 2008;36(11):2083-90.
 70. Tensho K, Shimodaira H, Aoki T, Narita N, Kato H, Kakegawa A, et al. Bony landmarks of the anterior cruciate ligament tibial footprint: A detailed analysis comparing 3-dimensional computed tomography images to visual and histological evaluations. *Am J Sports Med*. 2014;42(6):1433-40.
 71. Edwards A, Bull AM, Amis AA. The attachments of the anteromedial and posterolateral fibre bundles of the anterior cruciate ligament: Part 1: tibial attachment. *Knee Surg Sports Traumatol Arthrosc*. 2007;15(12):1414-21.

72. Tsukada H, Ishibashi Y, Tsuda E, Fukuda A, Toh S. Anatomical analysis of the anterior cruciate ligament femoral and tibial footprints. *J Orthop Sci.* 2008;13(2):122-9.
73. Takahashi M, Doi M, Abe M, Suzuki D, Nagano A. Anatomical study of the femoral and tibial insertions of the anteromedial and posterolateral bundles of human anterior cruciate ligament. *Am J Sports Med.* 2006;34(5):787-92.
74. Johannsen AM, Civitarese DM, Padalecki JR, Goldsmith MT, Wijdicks CA, LaPrade RF. Qualitative and quantitative anatomic analysis of the posterior root attachments of the medial and lateral menisci. *Am J Sports Med.* 2012;40(10):2342-7.
75. Ferretti M, Levicoff EA, Macpherson TA, Moreland MS, Cohen M, Fu FH. The fetal anterior cruciate ligament: an anatomic and histologic study. *Arthroscopy.* 2007;23(3):278-83.
76. Kohn D, B. M. Meniscus insertion anatomy as a basis for meniscus replacement: a morphological cadaveric study. *Arthroscopy.* 1995;11(1):96-103.
77. Dargel J, Pohl P, Tzikaras P, Koebke J. Morphometric side-to-side differences in human cruciate ligament insertions. *Surg Radiol Anat.* 2006;28(4):398-402.
78. Edwards A, Bull AM, Amis AA. The attachments of the anteromedial and posterolateral fibre bundles of the anterior cruciate ligament. Part 2: femoral attachment. *Knee Surg Sports Traumatol Arthrosc.* 2008;16(1):29-36.
79. Berlet GC, Fowler PJ. The anterior horn of the medial meniscus. An anatomic study of its insertion. *Am J Sports Med.* 1998;26(4):540-3.
80. Morgan CD, Kalman VR, Grawl DM. Definitive landmarks for reproducible tibial tunnel placement in anterior cruciate ligament reconstruction. *Arthroscopy.* 1995;11(3):275-88.
81. Colombet P, Robinson J, Christel P, Franceschi JP, Djian P, Bellier G, et al. Morphology of anterior cruciate ligament attachments for anatomic reconstruction: a cadaveric dissection and radiographic study. *Arthroscopy.* 2006;22(9):984-92.
82. Kwak DS, Surendran S, Pengatteeeri YH, Park SE, Choi KN, Gopinathan P, et al. Morphometry of the proximal tibia to design the tibial component of total knee arthroplasty for the Korean population. *Knee.* 2007;14(4):295-300.
83. Mahfouz M, Abdel Fatah EE, Bowers LS, Scuderi G. Three-dimensional morphology of the knee reveals ethnic differences. *Clin Orthop Relat Res.* 2012;470(1):172-85.
84. Dargel J, Michael JW, Feiser J, Ivo R, Koebke J. Human knee joint anatomy revisited: morphometry in the light of sex-specific total knee arthroplasty. *J Arthroplasty.* 2011;26(3):346-53.
85. Yue B, Varadarajan KM, Ai S, Tang T, Rubash HE, Li G. Gender differences in the knees of Chinese population. *Knee Surg Sports Traumatol Arthrosc.* 2011;19(1):80-8.
86. Booth REJ. The gender-specific (female) knee. *Orthopedics.* 2006;29(9):768-9.
87. Conley S, Rosenberg A, Crowninshield R. The female knee: anatomic variations. *J Am Acad Orthop Surg.* 2007;15(Suppl 1):31-6.
88. Hitt K, Shurman JRn, Greene K, McCarthy J, Moskal J, Hoeman T, et al. Anthropometric measurements of the human knee: correlation to the sizing of

- current knee arthroplasty systems. *J Bone Joint Surg Am.* 2003;85-A(Suppl 4):115-22.
89. Poilvache PL, Insall JN, Scuderi GR, Font-Rodriguez DE. Rotational landmarks and sizing of the distal femur in total knee arthroplasty. *Clin Orthop Relat Res.* 1996;331:35-46.
 90. Barrett WP. The need for gender-specific prostheses in TKA: does size make a difference? *Orthopedics.* 2006;29(9 Suppl):53-5.
 91. Merchant AC, Arendt EA, Dye SF, Fredericson M, Grelsamer RP, Leadbetter WB, et al. The female knee: anatomic variations and the female-specific total knee design. *Clin Orthop Relat Res.* 2008;466(12):3059-65.
 92. Mensch JS, Amstutz HC. Knee morphology as a guide to knee replacement. *Clin Orthop Relat Res.* 1975;112:231-41.
 93. Seedhom BB, Longton EB, Wright V, Dowson D. Dimensions of the knee. Radiographic and autopsy study of sizes required by a knee prosthesis. *Ann Rheum Dis.* 1972;31(1):54-8.
 94. Yoshioka Y, Siu D, Cooke TD. The anatomy and functional axes of the femur. *J Bone Joint Surg Am.* 1987;69(6):873-80.
 95. Gandhi S, Singla RK, Kullar JS, Suri RK, Mehta V. Morphometric analysis of upper end of tibia. *J Clin Diagn Res.* 2014;8(8):AC10-3.
 96. Khan FA, Koff MF, Noiseux NO, Bernhardt KA, O'Byrne MM, Larson DR, et al. Effect of local alignment on compartmental patterns of knee osteoarthritis. *J Bone Joint Surg Am.* 2008;90(9):1961-9.
 97. Sharma L, Song J, Felson DT, Cahue S, Shamiyeh E, Dunlop DD. The role of knee alignment in disease progression and functional decline in knee osteoarthritis. *JAMA.* 2001;286(2):188-95.
 98. Kraus VB, Vail TP, Worrell T, McDaniel G. A comparative assessment of alignment angle of the knee by radiographic and physical examination method. *Arthritis Rheum.* 2005;52(17):1730-5.
 99. Hsu RW, Himeno S, Coventry MB, Chao EY. Normal axial alignment of the lower extremity and load-bearing distribution at the knee. *Clin Orthop Relat Res.* 1990;255:215-27.
 100. McLeod WD, Moschi A, Andrews JR, Hughston JC. Tibial plateau topography. *Am J Sports Med.* 1977;5(1):13-8.
 101. Tardieu C. Morpho-functional analysis of the articular surfaces of the knee joint in primates. In: Chiarelli AB, Corruccini RS, editors. *Evolutionary Biology.* Berlin: Springer-Verlag; 1981. p. 68-80.
 102. Prescher S. Anatomie des Kniegelenks (Articulatio genus). In: Wirtz DC, editor. *AE-Manual der Endoprothetik.* Berlin: Arbeitsgemeinschaft Endoprothetik; 2011.
 103. Noyes FR, Grood ES. Scientific basis for examination and classification of knee ligament injuries. In: Noyes FR, editor. *Noyes' Knee Disorders Surgery, Rehabilitation, Clinical Outcomes.* Second ed. Philadelphia: Elsevier; 2017.

104. Wetz HH, Jacob HAC. Zur funktionellen Anatomie und Kinematik des Femurotibialgelenks: Forschungsergebnisse von 1836–1950. *Orthopäde*. 2001;30:135-44.
105. Nishimori M, Furuta T, Deie M. Parsons' knob, the bony landmark of the tibial insertion of the anterior cruciate ligament, evaluated by three-dimensional computed tomography. *AP-SMART*. 2014;1(4):126-31.
106. Shino K, Mae T, Tachibana Y. Anatomic ACL reconstruction: rectangular tunnel/bone-patellar tendon-bone or triple-bundle/semitendinosus tendon grafting. *J Orthop Sci*. 2015;20(3):457-68.
107. Heming JF, Rand J, Steiner ME. Anatomical limitations of transtibial drilling in anterior cruciate ligament reconstruction. *Am J Sports Med*. 2007;35(10):1708-15.
108. Siebold R, Ellert T, Metz S, Metz J. Tibial insertions of the anteromedial and posterolateral bundles of the anterior cruciate ligament: morphometry, arthroscopic landmarks, and orientation model for bone tunnel placement. *Arthroscopy*. 2008;24(2):154-61.
109. Ziegler CG, Pietrini SD, Westerhaus BD, Anderson CJ, Wijdicks CA, Johansen S, et al. Arthroscopically pertinent landmarks for tunnel positioning in single-bundle and double-bundle anterior cruciate ligament reconstructions. *Am J Sports Med*. 2011;39(4):743-52.
110. Balke M, Mueller-Huebenthal J, Shafizadeh S, Liem D, Hoeher J. Unilateral aplasia of both cruciate ligaments. *J Orthop Surg Res*. 2010;5:11.
111. Gerrish FH. *Text-Book of Anatomy*. Philadelphia: Lea Brothers; 1899.
112. Langer Cv, Toldt C. *Lehrbuch der systematischen und topographischen Anatomie*. 7 ed. Vienna: Braumüller; 1902.
113. Cunningham DJ. *Manual of Practical Anatomy*. 9 ed. London: Oxford University Press; 1939.
114. Brantigan OC, Voshell AF. The mechanism of the ligament and menisci of the knee joint. *J Bone Joint Surg Am*. 1941;23:44-66.
115. Shaw JA, Murray DG. The longitudinal axis of the knee and the role of the cruciate ligaments in controlling transverse rotation. *J Bone Joint Surg Am*. 1974;56A:1603-9.
116. Trent PS, Walker PS, Wolf B. Ligament length patterns, strength, and rotational axes of the knee joint. *Clin Orthop Relat Res*. 1976;117:263-70.
117. Fuss FK. Voluntary rotation in the human knee joint. *J Anat*. 1991;179:115-25.
118. Yildirim G, Walker PS, Sussman-Fort J, Aggarwal G, White B, Klein GR. The contact locations in the knee during high flexion. *Knee*. 2007;14(5):379-84.
119. Grood ES, Stowers SF, Noyes FR. Limits of movement in the human knee. Effect of sectioning the posterior cruciate ligament and posterolateral structures. *J Bone Joint Surg Am*. 1988;70(1):88-97.
120. Agel J, Arendt EA, Bershadsky B. Anterior cruciate ligament injury in national collegiate athletic association basketball and soccer: a 13-year review. *Am J Sports Med*. 2005;33(4):524-30.

121. Lindenfeld TN, Schmitt DJ, Hendy MP, Mangine RE, Noyes FR. Incidence of injury in indoor soccer. *Am J Sports Med.* 1994 22(3):364-71.
122. Kim S, Bosque J, Meehan JP, Jamali A, Marder R. Increase in outpatient knee arthroscopy in the United States: a comparison of National Surveys of Ambulatory Surgery, 1996 and 2006. *J Bone Joint Surg Am.* 2011;93(11):994-1000.
123. Gwinn DE, Wilckens JH, McDevitt ER, Ross G, Kao TC. The relative incidence of anterior cruciate ligament injury in men and women at the United States Naval Academy. *Am J Sports Med.* 2000;28(1):98-102.
124. Elliot DL, Goldberg L, Kuehl KS. Young women's anterior cruciate ligament injuries: an expanded model and prevention paradigm. *Sports Med.* 2010;40(5):367-76.
125. Messina DF, Farney WC, DeLee JC. The incidence of injury in Texas high school basketball. A prospective study among male and female athletes. *Am J Sports Med.* 1999;27(3):294-9.
126. Mountcastle SB, Posner M, Kragh JFJ, Taylor DC. Gender differences in anterior cruciate ligament injury vary with activity: epidemiology of anterior cruciate ligament injuries in a young, athletic population. *Am J Sports Med.* 2007;35(10):1635-42.
127. Hootman JM, Dick R, Agel J. Epidemiology of collegiate injuries for 15 sports: summary and recommendations for injury prevention initiatives. *J Athl Train.* 2007;42(2):311-9.
128. Prodromos CC, Han Y, Rogowski J, Joyce B, Shi K. A meta-analysis of the incidence of anterior cruciate ligament tears as a function of gender, sport, and a knee injury-reduction regimen. *Arthroscopy.* 2007;23(12):1320-5.
129. Trojian TH, Collins S. The anterior cruciate ligament tear rate varies by race in professional Women's basketball. *Am J Sports Med.* 2006;34(6):895-8.
130. Chandrashekar N, Slauterbeck J, Hashemi J. Sex-based differences in the anthropometric characteristics of the anterior cruciate ligament and its relation to intercondylar notch geometry: a cadaveric study. *Am J Sports Med.* 2005;33(10):1492-8.
131. Reiff DB, Heron CW, Stoker DJ. Spiking of the tubercles of the intercondylar eminence of the tibial plateau in osteoarthritis. *Br J Radiol.* 1991;64(766):915-7.
132. Boegård T, Rudling O, Petersson IF, Jonsson K. Correlation between radiographically diagnosed osteophytes and magnetic resonance detected cartilage defects in the patellofemoral joint. *Ann Rheum Dis.* 1998;57(7):395-400.
133. Unlu Z, Tarhan S, Goktan C, Tuzun C. The correlation between magnetic resonance detected cartilage defects and spiking of tibial tubercles in osteoarthritis of the knee joint. *Acta Med Okayama.* 2006;60(4):207-14.
134. Vyas S, van Eck CF, Vyas N, Fu FH, Otsuka NY. Increased medial tibial slope in teenage pediatric population with open physes and anterior cruciate ligament injuries. *Knee Surg Sports Traumatol Arthrosc.* 2011;19(3):372-7.
135. Alentorn-Geli E, Mendiguchía J, Samuelsson K, Musahl V, Karlsson J, Cugat R, et al. Prevention of anterior cruciate ligament injuries in sports. Part I: systematic review of risk factors in male athletes. *Knee Surg Sports Traumatol Arthrosc.* 2014;22(1):3-15.

136. Lipps DB, Oh YK, Ashton-Miller JA, Wojtys EM. Morphologic characteristics help explain the gender difference in peak anterior cruciate ligament strain during a simulated pivot landing. *Am J Sports Med.* 2012;40(1):32-40.
137. Sutton KM, Bullock JM. Anterior cruciate ligament rupture: differences between males and females. *J Am Acad Orthop Surg.* 2013;21(1):41-50.
138. Simon RA, Everhart JS, Nagaraja HN, Chaudhari AM. A case-control study of anterior cruciate ligament volume, tibial plateau slopes and intercondylar notch dimensions in ACL-injured knees. *J Biomech.* 2010;43(9):1702-7.
139. Sturnick DR, Vacek PM, DeSarno MJ, Gardner-Morse MG, Tourville TW, Slauterbeck JR, et al. Combined anatomic factors predicting risk of anterior cruciate ligament injury for males and females. *Am J Sports Med.* 2015;43(4):839-47.
140. Rahnemai-Azar AA, Yaseen Z, van Eck CF, Irrgang JJ, Fu FH, Musahl V. Increased lateral tibial plateau slope predisposes male college football players to anterior cruciate ligament injury. *J Bone Joint Surg Am.* 2016;98(12):1001-6.
141. van Diek FM, Wolf MR, Murawski CD, van Eck CF, Fu FH. Knee morphology and risk factors for developing an anterior cruciate ligament rupture: an MRI comparison between ACL-ruptured and non-injured knees. *Knee Surg Sports Traumatol Arthrosc.* 2014;22(5):987-94.
142. Souryal TO, Freeman TR. Intercondylar notch size and anterior cruciate ligament injuries in athletes. A prospective study. *Am J Sports Med.* 1993;21(4):535-9.
143. Houseworth SW, Mauro VJ, Mellon BA, Kieffer DA. The intercondylar notch in acute tears of the anterior cruciate ligament: a computer graphics study. *Am J Sports Med.* 1987;15(3):221-4.
144. Anderson AF, Dome DC, Gautam S, Awh MH, Rennirt GW. Correlation of anthropometric measurements, strength, anterior cruciate ligament size, and intercondylar notch characteristics to sex differences in anterior cruciate ligament tear rates. *Am J Sports Med.* 2001;29(1):58-66.
145. Tillman MD, Smith KR, Bauer JA, Cauraugh JH, Falsetti AB, Pattishall JL. Differences in three intercondylar notch geometry indices between males and females: a cadaver study. *Knee.* 2002;9(1):41-6.
146. Hashemi J, Chandrashekar N, Gill B, Beynon BD, Slauterbeck JR, Schutt RC, Jr., et al. The geometry of the tibial plateau and its influence on the biomechanics of the tibiofemoral joint. *J Bone Joint Surg Am.* 2008;90(12):2724-34.
147. Li G, Park SE, DeFrate LE, Schutzer ME, Ji L, Gill TJ, et al. The cartilage thickness distribution in the tibiofemoral joint and its correlation with cartilage-to-cartilage contact. *Clin Biomech (Bristol, Avon).* 2005;20(7):736-44.
148. Li G, Lopez O, Rubash H. Variability of a three-dimensional finite element model constructed using magnetic resonance images of a knee for joint contact stress analysis. *J Biomech Eng.* 2001;123(4):341-6.
149. Nagaosa Y, Lanyon P, Doherty M. Characterisation of size and direction of osteophyte in knee osteoarthritis: a radiographic study. *Ann Rheum Dis.* 2002;61(4):319-24.
150. Wicthl O. Tuberculum intercondylicum quartum tibiae. *Röntgenpraxis.* 1941;13:397-9.

151. Ravelli A. Zum Röntgenbild des menschlichen Kniegelenkes. *RöFO*. 1949;71:614-9.
152. Wagner A. Über ein grosses Tuberculum intercondylicum quartum tibiae. *Z Orthop Ihre Grenzgeb*. 1962;95:368-9.
153. Cerejo R, Dunlop DD, Cahue S, Channin D, Song J, Sharma L. The influence of alignment on risk of knee osteoarthritis progression according to baseline stage of disease. *Arthritis Rheum*. 2002;46(10):2632-6.
154. Hallén LG, Lindahl O. The lateral stability of the knee-joint. *Acta Orthop Scand*. 1965;36(2):179-91.
155. Outerbridge RE. The etiology of chondromalacia patellae. *J Bone Joint Surg Br*. 1961;43(4):752-7.
156. Weidow J, Pak J, Karrholm J. Different patterns of cartilage wear in medial and lateral gonarthrosis. *Acta Orthop Scand*. 2002;73(3):326-9.
157. Rajgopal A, Noble PC, Vasdev A, Ismaily SK, Sawant A, Dahiya V. Wear Patterns in Knee Articular Surfaces in Varus Deformity. *J Arthroplasty*. 2015;30(11):2012-6.
158. White SH, Ludkowsky PF, Goodfellow JW. Anteromedial osteoarthritis of the knee. *J Bone Joint Surg Br*. 1991;73(4):582-6.
159. Harman MK, Markovich GD, Banks SA, Hodge WA. Wear patterns on tibial plateaus from varus and valgus osteoarthritic knees. *Clin Orthop Relat Res*. 1998;352:149-58.
160. Vasara AI. Arthroscopic cartilage indentation and cartilage lesions of anterior cruciate ligament-deficient knees. *Am J Sports Med*. 2005;33(3):408-14.
161. Lee GC, Cushner FD, Vigorita V, Scuderi GR, Insall JN, Scott WN. Evaluation of the anterior cruciate ligament integrity and degenerative arthritic patterns in patients undergoing total knee arthroplasty. *J Arthroplasty*. 2005;20(1):59-65.
162. Stein V, Li L, Guermazi A, Zhang Y, Kent Kwok C, Eaton CB, et al. The relation of femoral notch stenosis to ACL tears in persons with knee osteoarthritis. *Osteoarthritis Cartilage*. 2010;18(2):192-9.
163. Huss RA, Holstein H, O'Connor JJ. The effect of cartilage deformation on the laxity of the knee joint. *Proc Inst Mech Eng H*. 1999;213(1):19-32.
164. Brandsson S, Karlsson J, Eriksson BI, Kärrholm J. Kinematics after tear in the anterior cruciate ligament: dynamic bilateral radiostereometric studies in 11 patients. *Acta Orthop Scand*. 2001;72(4):372-8.
165. Kärrholm J, Selvik G, Elmqvist LG, Hansson LI. Active knee motion after cruciate ligament rupture. *Stereoradiography. Acta Orthop Scand*. 1988;59(2):158-64.
166. Jonsson H, Kärrholm J. Three-dimensional knee joint movements during a step-up: evaluation after anterior cruciate ligament rupture. *J Orthop Res*. 1994;12(6):769-79.
167. Hill PF, Vedi V, Williams A, Iwaki H, Pinskerova V, Freeman MA. Tibiofemoral movement 2: the loaded and unloaded living knee studied by MRI. *J Bone Joint Surg Br*. 2000;82(8):1196-8.
168. Kärrholm J, Brandsson S, Freeman MA. Tibiofemoral movement 4: changes of axial tibial rotation caused by forced rotation at the weight-bearing knee studied by RSA. *J Bone Joint Surg Br*. 2000;82(8):1201-3.

169. Biswal S, Hastie T, Andriacchi TP, Bergman GA, Dillingham MF, Lang P. Risk factors for progressive cartilage loss in the knee: a longitudinal magnetic resonance imaging study in forty-three patients. *Arthritis Rheum.* 2002;46(11):2884-92.
170. Moschella D, Blasi A, Leardini A, Ensini A, Catani F. Wear patterns on tibial plateau from varus osteoarthritic knees. *Clin Biomech (Bristol, Avon).* 2006;21(2):152-8.
171. Georgoulis AD, Papadonikolakis A, Papageorgiou CD, Mitsou A, Stergiou N. Three-dimensional tibiofemoral kinematics of the anterior cruciate ligament-deficient and reconstructed knee during walking. *Am J Sports Med.* 2003;31(1):75-9.
172. Vergis A, Hammarby S, Gillquist J. Fluoroscopic validation of electrogoniometrically measured femorotibial translation in healthy and ACL deficient subjects. *Scand J Med Sci Sports.* 2002;12(4):223-9.
173. Hodge WA, Harman MK, Banks SA. Patterns of knee osteoarthritis in Arabian and American knees. *J Arthroplasty.* 2009;24(3):448-53.
174. Nagura T, Dyrby CO, Alexander EJ, Andriacchi TP. Mechanical loads at the knee joint during deep flexion. *J Orthop Res.* 2002;20(4):881-6.
175. Nagura T, Otani T, Suda Y, Matsumoto H, Toyama Y. Is high flexion following total knee arthroplasty safe?: evaluation of knee joint loads in the patients during maximal flexion. *J Arthroplasty.* 2005;20(5):647-51.
176. Van de Velde SK, Gill TJ, Li G. Evaluation of kinematics of anterior cruciate ligament-deficient knees with use of advanced imaging techniques, three-dimensional modeling techniques, and robotics. *J Bone Joint Surg Am.* 2009;91 Suppl 1:108-14.
177. Van de Velde SK, Bingham JT, Gill TJ, Li G. Analysis of tibiofemoral cartilage deformation in the posterior cruciate ligament-deficient knee. *J Bone Joint Surg Am.* 2009;91(1):167-75.
178. Sharma L, Lou C, Cahue S, Dunlop DD. The mechanism of the effect of obesity in knee osteoarthritis: the mediating role of malalignment. *Arthritis Rheum.* 2000;43(3):568-75.
179. Brouwer GM, van Tol AW, Bergink AP, Belo JN, Bernsen RM, Reijman M, et al. Association between valgus and varus alignment and the development and progression of radiographic osteoarthritis of the knee. *Arthritis Rheum.* 2007;56(4):1204-11.
180. Cooke TD, Pichora D, Siu D, Scudamore RA, Bryant JT. Surgical implications of varus deformity of the knee with obliquity of joint surfaces. *J Bone Joint Surg Br.* 1989;71(4):560-5.
181. Cooke D, Scudamore A, Li J, Wyss U, Bryant T, Costigan P. Axial lower-limb alignment: comparison of knee geometry in normal volunteers and osteoarthritis patients. *Osteoarthritis Cartilage.* 1997;5(1):39-47.
182. Keyes GW, Carr AJ, Miller RK, Goodfellow JW. The radiographic classification of medial gonarthrosis. Correlation with operation methods in 200 knees. *Acta Orthop Scand.* 1992;63(5):497-501.
183. Li G, Moses JM, Papannagari R, Pathare NP, DeFrate LE, Gill TJ. Anterior cruciate ligament deficiency alters the in vivo motion of the tibiofemoral cartilage contact

- points in both the anteroposterior and mediolateral directions. *J Bone Joint Surg Am.* 2006;88(8):1826-34.
184. Dennis DA, Mahfouz MR, Komistek RD, Hoff W. In vivo determination of normal and anterior cruciate ligament-deficient knee kinematics. *J Biomech.* 2005;38(2):241-53.
 185. Mullaji AB, Marawar SV, Luthra M. Tibial articular cartilage wear in varus osteoarthritic knees: correlation with anterior cruciate ligament integrity and severity of deformity. *J Arthroplasty.* 2008;23(1):128-35.
 186. Bennett LD, Buckland-Wright JC. Meniscal and articular cartilage changes in knee osteoarthritis: a cross-sectional double-contrast macroradiographic study. *Rheumatology (Oxford).* 2002;41(8):917-23.
 187. Casscells SW. Gross pathological changes in the knee joint of the aged individual: a study of 300 cases. *Clin Orthop Relat Res.* 1978;132:225-32.
 188. Ireland ML, Ballantyne BT, Little K, McClay IS. A radiographic analysis of the relationship between the size and shape of the intercondylar notch and anterior cruciate ligament injury. *Knee Surg Sports Traumatol Arthrosc.* 2001;9(4):200-5.
 189. Kennedy JC, Weinberg HW, Wilson AS. The anatomy and function of the anterior cruciate ligament. As determined by clinical and morphological studies. *J Bone Joint Surg Am.* 1974;56(2):223-35.
 190. Pap G, Machner A, Nebelung W, Awiszus F. Detailed analysis of proprioception in normal and ACL-deficient knees. *J Bone Joint Surg Br.* 1999;81(5):764-8.
 191. Noyes FR, Schipplein OD, Andriacchi TP, Saddemi SR, Weise M. The anterior cruciate ligament-deficient knee with varus alignment. An analysis of gait adaptations and dynamic joint loadings. *Am J Sports Med.* 1992;20(6):707-16.
 192. Douglas MJ, Hutchison JD, Sutherland AG. Anterior cruciate ligament integrity in osteoarthritis of the knee in patients undergoing total knee replacement. *J Orthop Traumatol.* 2010;11(3):149-54.
 193. Fruensgaard S, Johannsen HV. Incomplete ruptures of the anterior cruciate ligament. *J Bone Joint Surg Br.* 1989;71(3):526-30.
 194. Bak K, Scavenius M, Hansen S, Nørring K, Jensen KH, Jørgensen U. Isolated partial rupture of the anterior cruciate ligament. Long-term follow-up of 56 cases. *Knee Surg Sports Traumatol Arthrosc.* 1997;5(2):66-71.
 195. Noyes FR, Mooar LA, Moorman CTr, McGinniss GH. Partial tears of the anterior cruciate ligament. Progression to complete ligament deficiency. *J Bone Joint Surg Br.* 1989;71(5):825-33.
 196. Kocher MS, Micheli LJ, Zurakowski D, Luke A. Partial tears of the anterior cruciate ligament in children and adolescents. *Am J Sports Med.* 2002;30(5):697-703.
 197. Waldstein W, Merle C, Bou Monsef J, Boettner F. Varus knee osteoarthritis: how can we identify ACL insufficiency? *Knee Surg Sports Traumatol Arthrosc.* 2015;23(8):2178-84.
 198. Johnson AJ, Howell SM, Costa CR, Mont MA. The ACL in the arthritic knee: how often is it present and can preoperative tests predict its presence? *Clin Orthop Relat Res.* 2013;471(1):181-8.

199. Negru D. Beitrag zum Studium der normalen Anatomie des Kniegelenkes im Röntgenbilde. *Fortschr Geb Rontgenstr Nuklearmed.* 1943;68:194-201.
200. Berg EE. Parsons' knob (tuberculum intercondylare tertium). A guide to tibial anterior cruciate ligament insertion. *Clin Orthop Relat Res.* 1993;292:229-31.
201. Danzig LA, Newell JD, Guerra JJ, Resnick D. Osseous landmarks of the normal knee. *Clin Orthop Relat Res.* 1981;156:201-6.
202. Schlüter K, Becker R. Die Form der Eminentia intercondylica tibiae. *Arch Orthop Unfallchir.* 1955 47(6):703-19.
203. Oeser H. Der mediale Tibiacondylensporn. *Röntgenpraxis.* 1938;10:416-8.
204. Brossmann J, White LM, Stäbler A, Preidler KW, Andresen R, Haghghi P, et al. Enlargement of the third intercondylar tubercle of Parsons as a sign of osteoarthritis of the knee: a paleopathologic and radiographic study. *Radiology.* 1996;198(3):845-9.
205. Mays S, Cooper L. A palaeopathological investigation of the third intercondylar tubercle of Parsons. *Int J Osteoarchaeol.* 2009;19(6):735-41.
206. Felsenreich F. Die Röntgendiagnose der veralteten Kreuzbandläsion des Kniegelenks. *Fortschr Geb Rontgenstr.* 1934(49):341-6.
207. Yian EH, Gallo L, Hughes RE, Kuhn JE. The relationship between Parson's tubercle and the insertion of the anterior horn of the medial meniscus. *Arthroscopy.* 2001;17(7):737-40.
208. Jones RE. The role of arthroscopic debridement: Is there one? 9th Annual Current Concepts in Joint Replacement Spring Meeting; May 18-21; Las Vegas 2008.
209. Rogers J, Waldron T. A field guide to joint disease in archaeology. New York: John Wiley & Sons; 1995.
210. Manner HM, Radler C, Ganger R, Grill F. Dysplasia of the cruciate ligaments: radiographic assessment and classification. *J Bone Joint Surg Am.* 2006;88(1):130-7.
211. Vanden Bossche S, Vanzieleghem B, Declercq H, Verstraete K. Absent anterior cruciate ligament. *JBR-BTR.* 2015;99(1):31-3.
212. Johnson DL, Swenson TM, Livesay GA, Aizawa H, Fu FH, Harner CD. Insertion-site anatomy of the human menisci: gross, arthroscopic, and topographical anatomy as a basis for meniscal transplantation. *Arthroscopy.* 1995;11(4):386-94.
213. LaPrade CM, Ellman MB, Rasmussen MT, James EW, Wijdicks CA, Engebretsen L, et al. Anatomy of the anterior root attachments of the medial and lateral menisci: a quantitative analysis. *Am J Sports Med.* 2014;42(10):2386-92.
214. Ellman MB, LaPrade CM, Smith SD, Rasmussen MT, Engebretsen L, Wijdicks CA, et al. Structural Properties of the Meniscal Roots. *Am J Sports Med.* 2014;42(8):1881-7.
215. De Coninck T, Vanrietvelde F, Seynaeve P, Verdonk P, Verstraete K. MR imaging of the anatomy of the anterior horn of the medial meniscus. *Acta Radiol.* 2016.
216. Ohkoshi Y, Takeuchi T, Inoue C, Hashimoto T, Shigenobu K, Yamane S. Arthroscopic studies of variants of the anterior horn of the medial meniscus. *Arthroscopy.* 1997;13(6):725-30.

217. Bhargava A, Ferrari DA. Posterior medial meniscus-femoral insertion into the anterior cruciate ligament. A case report. *Clin Orthop Relat Res.* 1998;348:176-9.
218. Kim SJ, Choi CH. Bilateral complete discoid medial menisci combined with anomalous insertion and cyst formation. *Arthroscopy.* 1996;12(1):112-5.
219. Kim S, Lee Y, Kim D. Intraarticular anatomic variants associated with discoid meniscus in Koreans. *Clin Orthop Relat Res.* 1998;356:202-7.
220. Pinar H, Akseki D, Karaođlan O, Ozkan M, Uluç E. Bilateral discoid medial menisci. *Arthroscopy.* 2000;16(1):96-101.
221. Rainio P, Sarimo J, Rantanen J, Alanen J, Orava S. Observation of anomalous insertion of the medial meniscus on the anterior cruciate ligament. *Arthroscopy.* 2002;18(2):E9.
222. Kale A, Kopuz C, Edýzer M, Aydin ME, Demýr M, Ynce Y. Anatomic variations of the shape of the menisci: a neonatal cadaver study. *Knee Surg Sports Traumatol Arthrosc.* 2006;14(10):975-81.
223. Kale A, Kopuz C, Dikici F, Demir MT, Corumlu U, Ince Y. Anatomic and arthroscopic study of the medial meniscal horns' insertions. *Knee Surg Sports Traumatol Arthrosc.* 2010;18(6):754-9.
224. Jung YB, Yum JK, Bae YJ, Song KS. Anomalous insertion of the medial menisci. *Arthroscopy.* 1998;14(5):505-7.
225. Aranha A, Nor M. Congenital rudimentary medial meniscus--report of a case of development arrest of medial meniscus. *Singapore Med J.* 1990;31(2):189-90.
226. Winslow J. *Exposition anatomique de la structure du corps humain.* Paris: G. Desprez; 1732.
227. Nelson EW, LaPrade RF. The anterior intermeniscal ligament of the knee. An anatomic study. *Am J Sports Med.* 2000;28(1):74-6.
228. Aydingöz U, Kaya A, Atay OA, Oztürk MH, Doral MN. MR imaging of the anterior intermeniscal ligament: classification according to insertion sites. *Eur Radiol.* 2002;12(4):824-9.
229. Wang YJ, Yu JK, Luo H, Yu CL, Ao YF, Xie X, et al. An anatomical and histological study of human meniscal horn bony insertions and peri-meniscal attachments as a basis for meniscal transplantation. *Clin Med J (Engl).* 2009;122(5):536-40.
230. Robert HE, Bouguennec N, Vogeli D, Berton E, Bowen M. Coverage of the anterior cruciate ligament femoral footprint using 3 different approaches in single-bundle reconstruction: a cadaveric study analyzed by 3-dimensional computed tomography. *Am J Sports Med.* 2013;41(10):2375-83.
231. Siebold R, Schuhmacher P, Fernandez F, Smigielski R, Fink C, Brehmer A, et al. Flat midsubstance of the anterior cruciate ligament with tibial "C"-shaped insertion site. *Knee Surg Sports Traumatol Arthrosc.* 2015;23(11):3136-42.
232. Arnoczky SP. Anatomy of the Anterior Cruciate Ligament. *Clin Orthop Relat Res.* 1983;172:19-25.
233. Brody JM, Hulstyn MJ, Fleming BC, Tung GA. The meniscal roots: gross anatomic correlation with 3-T MRI findings. *AJR Am J Roentgenol.* 2007;188(5):W446-50.

234. Duthon VB, Barea C, Abrassart S, Fasel JH, Fritschy D, Menetrey J. Anatomy of the anterior cruciate ligament. *Knee Surg Sports Traumatol Arthrosc.* 2006;14(3):204-13.
235. Bicer EK, Lustig S, Servien E, Selmi TA, Neyret P. Current knowledge in the anatomy of the human anterior cruciate ligament. *Knee Surg Sports Traumatol Arthrosc.* 2010;18(8):1075-84.
236. Girgis FG, Marshall JL, Monajem A. The cruciate ligaments of the knee joint. Anatomical, functional and experimental analysis. *Clin Orthop Relat Res.* 1975;106:216-31.
237. Harner CD, Baek GH, Vogrin TM, Carlin GJ, Kashiwaguchi S, Woo SL. Quantitative analysis of human cruciate ligament insertions. *Arthroscopy.* 1999;15(7):741-9.
238. Petersen W, Zantop T. Anatomy of the anterior cruciate ligament with regard to its two bundles. *Clin Orthop Relat Res.* 2007;454:35-47.
239. Tallay A, Lim MH, Bartlett J. Anatomical study of the human anterior cruciate ligament stump's tibial insertion footprint. *Knee Surg Sports Traumatol Arthrosc.* 2008;16(8):741-6.
240. Odensten M, Gillquist J. Functional anatomy of the anterior cruciate ligament and a rationale for reconstruction. *J Bone Joint Surg Am.* 1985;67(2):257-62.
241. Norwood LA, Cross MJ. Anterior cruciate ligament: functional anatomy of its bundles in rotatory instabilities. *Am J Sports Med.* 1979;7(1):23-6.
242. Abreu-e-Silva GM, Oliveira MH, Maranhao GS, Deligne LM, Pfeilsticker RM, Novais EN, et al. Three-dimensional computed tomography evaluation of anterior cruciate ligament footprint for anatomic single-bundle reconstruction. *Knee Surg Sports Traumatol Arthrosc.* 2015;23(3):770-6.
243. Luites JW, Wymenga AB, Blankevoort L, Kooloos JG. Description of the attachment geometry of the anteromedial and posterolateral bundles of the ACL from arthroscopic perspective for anatomical tunnel placement. *Knee Surg Sports Traumatol Arthrosc.* 2007;15(12):1422-31.
244. Sasaki N, Ishibashi Y, Tsuda E, Yamamoto Y, Maeda S, Mizukami H, et al. The femoral insertion of the anterior cruciate ligament: discrepancy between macroscopic and histological observations. *Arthroscopy.* 2012;28(8):1135-46.
245. Iwahashi T, Shino K, Nakata K, Otsubo H, Suzuki T, Amano H, et al. Direct anterior cruciate ligament insertion to the femur assessed by histology and 3-dimensional volume-rendered computed tomography. *Arthroscopy.* 2010;26(9 Suppl):S13-20.
246. Mochizuki T, Fujishiro H, Nimura A, Mahakkanukrauh P, Yasuda K, Muneta T, et al. Anatomic and histologic analysis of the mid-substance and fan-like extension fibres of the anterior cruciate ligament during knee motion, with special reference to the femoral attachment. *Knee Surg Sports Traumatol Arthrosc.* 2014;22(2):336-44.
247. Welsh RP. Knee joint structure and function. *Clin Orthop Relat Res.* 1980;147:7-14.
248. Amis AA, Jakob RP. Anterior cruciate ligament graft positioning, tensioning and twisting. *Knee Surg Sports Traumatol Arthrosc.* 1998;6(Suppl 1):S2-12.

249. Siebold R, Takada T, Feil S, Dietrich C, Stinton SK, Branch TP. Anatomical "C"-shaped double-bundle versus single-bundle anterior cruciate ligament reconstruction in pre-adolescent children with open growth plates. *Knee Surg Sports Traumatol Arthrosc.* 2016;24(3):796-806.
250. Oka S, Schuhmacher P, Brehmer A, Traut U, Kirsch J, Siebold R. Histological analysis of the tibial anterior cruciate ligament insertion. *Knee Surg Sports Traumatol Arthrosc.* 2016;24(3):747-53.
251. Amis AA, Jakob, Roland P. Anterior cruciate ligament graft positioning, tensioning and twisting. *Knee Surg, Sports Traumatol, Arthrosc.* 1998;6([Suppl 1]):S2-S12.
252. Kongcharoensombat W, Ochi M, Abouheif M, Adachi N, Ohkawa S, Kamei G, et al. The transverse ligament as a landmark for tibial sagittal insertions of the anterior cruciate ligament: a cadaveric study. *Arthroscopy.* 2011;27(10):1395-9.
253. Smigielski R, Zdanowicz U, Drwiega M, Ciszek B, Ciszewska-Lyson B, Siebold R. Ribbon like appearance of the midsubstance fibres of the anterior cruciate ligament close to its femoral insertion site: a cadaveric study including 111 knees. *Knee Surg Sports Traumatol Arthrosc.* 2015;23(11):3143-50.
254. Śmigielski R, Zdanowicz U, Drwiega M, Ciszek B, Williams A. The anatomy of the anterior cruciate ligament and its relevance to the technique of reconstruction. *Bone Joint J.* 2016;98(8):1020-6.
255. Hara K, Mochizuki T, Sekiya I, Yamaguchi K, Akita K, Muneta T. Anatomy of normal human anterior cruciate ligament attachments evaluated by divided small bundles. *Am J Sports Med.* 2009;37(12):2386-91.
256. Humphry GM. *A treatise on the human skeleton (including the joints).* Cambridge: McMillan and Co.; 1858.
257. Pfab B. Zur Blutgefäßversorgung der Menisci und Kreuzbänder. *Dtsch Z Chir.* 1927(205):258-64.
258. Crock HV. The arterial supply and venous drainage of the bones of the human knee joint. *Anatomical Record.* 1962(144):199-217.
259. Toy BJ, Yeasting RA, Morse DE, McCann P. Arterial supply to the human anterior cruciate ligament. *J Athl Train.* 1995;30(2):149-52.
260. Lahlaïdi A. Valeur morphologique des insertions postérieures du ménisque externe dans le genou humain. *Rev Chir Orthop Reparatrice Appar Mot.* 1971;57(8):593-600.
261. Zemirline A, Gerard R, Uguen A, Stindel E, Dubrana F. Meniscoligamentous band between the posterior horn of the lateral meniscus and the anterior cruciate ligament: arthroscopic, anatomical and histological observations. *Surg Radiol Anat.* 2010;32(2):129-33.
262. Muneta T, Takakuda K, Yamamoto H. Intercondylar notch width and its relation to the configuration and cross-sectional area of the anterior cruciate ligament. A cadaveric knee study. *Am J Sports Med.* 1997;25(1):69-72.
263. Cuomo P, Edwards A, Giron F, Bull AM, Amis AA, Aglietti P. Validation of the 65 degrees Howell guide for anterior cruciate ligament reconstruction. *Arthroscopy.* 2006;22(1):70-5.

264. Giron F, Cuomo P, Edwards A, Bull AM, Amis AA, Aglietti P. Double-bundle "anatomic" anterior cruciate ligament reconstruction: a cadaveric study of tunnel positioning with a transtibial technique. *Arthroscopy*. 2007;23(1):7-13.
265. Otsubo H, Shino K, Suzuki D, Kamiya T, Suzuki T, Watanabe K, et al. The arrangement and the attachment areas of three ACL bundles. *Knee Surg Sports Traumatol Arthrosc*. 2012;20(1):127-34.
266. Stijak L, Radonjic V, Nikolic V, Blagojevic Z, Aksic M, Filipovic B. Correlation between the morphometric parameters of the anterior cruciate ligament and the intercondylar width: gender and age differences. *Knee Surg Sports Traumatol Arthrosc*. 2009;17(7):812-7.
267. Papachristou G, Sourlas J, Magnissalis E, Plessas S, Papachristou K. ACL reconstruction and the implication of its tibial attachment for stability of the joint: anthropometric and biomechanical study. *Int Orthop*. 2007;31(4):465-70.
268. Hutchinson MR, Bae TS. Reproducibility of anatomic tibial landmarks for anterior cruciate ligament reconstructions. *Am J Sports Med*. 2001;29(6):777-80.
269. Lee JK, Lee S, Seong SC, Lee MC. Anatomy of the anterior cruciate ligament insertion sites: comparison of plain radiography and three-dimensional computed tomographic imaging to anatomic dissection. *Knee Surg Sports Traumatol Arthrosc*. 2015;23(8):2297-305.
270. Hwang MD, Piefer JW, Lubowitz JH. Anterior cruciate ligament tibial footprint anatomy: systematic review of the 21st century literature. *Arthroscopy*. 2012;28(5):728-34.
271. Groves EW. The crucial ligaments of the knee-joint: Their function, rupture, and the operative treatment of the same. *Br J Surg*. 1919;7(28):505-15.
272. Abbott LC, John B, Saunders M, Bost FC, Anderson CE. Injuries to the ligaments of the knee joint. *J Bone Joint Surg Am*. 1944;26(3):503-21.
273. Lam SJ. Reconstruction of the anterior cruciate ligament using the Jones procedure and its Guy's Hospital modification. *J Bone Joint Surg Am*. 1968;50(6):1213-24.
274. Reiman PR, Jackson DW. Anatomy of the anterior cruciate ligament. In: Jackson DW DD, editor. *The anterior cruciate deficient knee*. St Louis: CV Mosby Co; 1987. p. 17-26.
275. Arnoczky SP, Warren RF. Anatomy of the cruciate ligaments. In: Feagin JA, editor. *The crucial ligaments*. New York: Churchill Livingstone; 1988. p. 179-95.
276. Yagi M, Wong EK, Kanamori A, Debski RE, Fu FH, Woo SL. Biomechanical analysis of an anatomic anterior cruciate ligament reconstruction. *Am J Sports Med*. 2002;30(5):660-6.
277. Zaffagnini S, Martelli S, Acquaroli F. Computer investigation of ACL orientation during passive range of motion. *Comput Biol Med*. 2004;34(2):153-63.
278. Woo SL, Kanamori A, Zeminski J, Yagi M, Papageorgiou C, Fu FH. The effectiveness of reconstruction of the anterior cruciate ligament with hamstrings and patellar tendon . A cadaveric study comparing anterior tibial and rotational loads. *J Bone Joint Surg Am*. 2002;84(6):907-14.

279. Petersen W, Tretow H, Weimann A, Herbort M, Fu FH, Raschke M, et al. Biomechanical evaluation of two techniques for double-bundle anterior cruciate ligament reconstruction: one tibial tunnel versus two tibial tunnels. *Am J Sports Med.* 2007;35(2):228-34.
280. Zantop T, Wellmann M, Fu FH, Petersen W. Tunnel positioning of anteromedial and posterolateral bundles in anatomic anterior cruciate ligament reconstruction: anatomic and radiographic findings. *Am J Sports Med.* 2008;36(1):65-72.
281. Amis AA, Dawkins GP. Functional anatomy of the anterior cruciate ligament. Fibre bundle actions related to ligament replacements and injuries. *J Bone Joint Surg Br.* 1991;73(2):260-7.
282. Butler DL, Guan Y, Kay MD, Cummings JF, Feder SM, Levy MS. Location-dependent variations in the material properties of the anterior cruciate ligament. *J Biomech.* 1992;25(5):511-8.
283. Friedrich NF, O'Brien WR. Functional anatomy of the cruciate ligaments. In: Jakob RP, Stäubli HU, editors. *The Knee and the Cruciate Ligaments.* Berlin: Springer-Verlag; 1992. p. 78-91.
284. Shino K, Nakata K, Nakamura N, Mae T, Ohtsubo H, Iwahashi T, et al. Anatomic anterior cruciate ligament reconstruction using two double-looped hamstring tendon grafts via twin femoral and triple tibial tunnels. *Oper Tech Orthop.* 2005;15(2):130-4.
285. Tanaka Y, Shino K, Horibe S, Nakamura N, Nakagawa S, Mae T, et al. Triple-bundle ACL grafts evaluated by second-look arthroscopy. *Knee Surg Sports Traumatol Arthrosc.* 2012;20(1):95-101.
286. Fujie H, Ohtsubo H, Fukano S, Suzuki T, Suzuki D, Mae T, et al. Mechanical functions of the three bundles consisting of the human anterior cruciate ligament. *Knee Surg Sports Traumatol Arthrosc.* 2011;19 Suppl 1:S47-53.
287. Kinugasa K, Hamada M, Yoneda K, Matsuo T, Mae T, Shino K. Cross-sectional area of hamstring tendon autograft after anatomic triple-bundle ACL reconstruction. *Knee Surg Sports Traumatol Arthrosc.* 2015:1-8.
288. Tanaka Y, Yonetani Y, Shiozaki Y, Kanamoto T, Kita K, Amano H, et al. MRI analysis of single-, double-, and triple-bundle anterior cruciate ligament grafts. *Knee Surg Sports Traumatol Arthrosc.* 2014;22(7):1541-8.
289. Tischer T, Ronga M, Tsai A, Ingham SJ, Ekdahl M, Smolinski P, et al. Biomechanics of the goat three bundle anterior cruciate ligament. *Knee Surg Sports Traumatol Arthrosc.* 2009;17(8):935-40.
290. Kato Y, Ingham SJ, Linde-Rosen M, Smolinski P, Horaguchi T, Fu FH. Biomechanics of the porcine triple bundle anterior cruciate ligament. *Knee Surg Sports Traumatol Arthrosc.* 2010;18(1):20-5.
291. Proffen BL, McElfresh M, Fleming BC, Murray MM. A comparative anatomical study of the human knee and six animal species. *Knee.* 2012;19(4):493-9.
292. Mommersteeg TJ, Kooloos JG, Blankevoort L, Kauer JM, Huiskes R, Roeling FQ. The fibre bundle anatomy of human cruciate ligaments. *J Anat.* 1995;187(Pt 2):461-71.

293. Matsuo T, Mae T, Shino K, Kita K, Tachibana Y, Sugamoto K, et al. Tibiofemoral relationship following anatomic triple-bundle anterior cruciate ligament reconstruction. *Knee Surg Sports Traumatol Arthrosc.* 2014;22(9):2128-35.
294. Sakane M, Fox RJ, Woo SL, Livesay GA, Li G, Fu FH. In situ forces in the anterior cruciate ligament and its bundles in response to anterior tibial loads. *J Orthop Res.* 1987;15(2):285-93.
295. Fu FH, van Eck CF, Tashman S, Irrgang JJ, Moreland MS. Anatomic anterior cruciate ligament reconstruction: a changing paradigm. *Knee Surg Sports Traumatol Arthrosc.* 2015;23(3):640-8.
296. Tantisrichaenkul G, Linde-Rosen M, Araujo P, Zhou J, Smolinski P, Fu FH. Anterior cruciate ligament: an anatomical exploration in humans and in a selection of animal species. *Knee Surg Sports Traumatol Arthrosc.* 2014;22(5):961-71.
297. Zhao J, Huangfu X. Arbitrary starting point of separation affects morphology of the 2 bundles of anterior cruciate ligament at insertion sites. *Arthroscopy.* 2010;26(2):184-91.
298. Zantop T, Petersen W, Sekiya JK, Musahl V, Fu FH. Anterior cruciate ligament anatomy and function relating to anatomical reconstruction. *Knee Surg Sports Traumatol Arthrosc.* 2006;14(10):982-92.
299. Doi M, Takahashi M, Abe M, Suzuki D, Nagano A. Lateral radiographic study of the tibial sagittal insertions of the anteromedial and posterolateral bundles of human anterior cruciate ligament. *Knee Surg Sports Traumatol Arthrosc.* 2009;17(4):347-51.
300. Dargel J, Schmidt-Wiethoff R, Feiser J, Koebke J, Schluter-Brust K, Eysel P, et al. Relationship between human femorotibial joint configuration and the morphometry of the anterior cruciate ligament. *Arch Orthop Trauma Surg.* 2011;131(8):1095-105.
301. Iwahashi T, Shino K, Nakata K, Nakamura N, Yamada Y, Yoshikawa H, et al. Assessment of the "functional length" of the three bundles of the anterior cruciate ligament. *Knee Surg Sports Traumatol Arthrosc.* 2008;16(2):167-74.
302. Forsythe B, Kopf S, Wong AK, Martins CA, Anderst W, Tashman S, et al. The location of femoral and tibial tunnels in anatomic double-bundle anterior cruciate ligament reconstruction analyzed by three-dimensional computed tomography models. *J Bone Joint Surg Am.* 2010;92(6):1418-26.
303. Lorenz S, Elser F, Mitterer M, Obst T, Imhoff AB. Radiologic evaluation of the insertion sites of the 2 functional bundles of the anterior cruciate ligament using 3-dimensional computed tomography. *Am J Sports Med.* 2009;37(12):2368-76.
304. Fu FH, Jordan SS. The lateral intercondylar ridge--a key to anatomic anterior cruciate ligament reconstruction. *J Bone Joint Surg Am.* 2007;89(10):2103-4.
305. Hutchinson MR, Ash SA. Resident's ridge: assessing the cortical thickness of the lateral wall and roof of the intercondylar notch. *Arthroscopy.* 2003;19(9):931-5.
306. Noyes FR, Barber-Westin SD. Anterior cruciate ligament primary reconstruction: Diagnosis, operative techniques, and clinical outcomes. In: R. NF, editor. *Noyes' knee disorders Surgery, rehabilitation, clinical outcomes.* Second ed. Philadelphia, PA: Elsevier; 2017. p. 137-220.

307. Kasten P, Szczodry M, Irrgang J, Kropf E, Costello J, Fu FH. What is the role of intra-operative fluoroscopic measurements to determine tibial tunnel placement in anatomical anterior cruciate ligament reconstruction? *Knee Surg Sports Traumatol Arthrosc.* 2010;18(9):1169-75.
308. Iriuchishima T, Ingham SJ, Tajima G, Horaguchi T, Saito A, Tokuhashi Y, et al. Evaluation of the tunnel placement in the anatomical double-bundle ACL reconstruction: a cadaver study. *Knee Surg Sports Traumatol Arthrosc.* 2010;18(9):1226-31.
309. Storz P, Buess GF, Kunert W, Kirschniak A. 3D HD versus 2D HD: Surgical task efficiency in standardised phantom tasks. *Surg Endosc.* 2012;26(5):1454-60.
310. Wilhelm D, Reiser S, Kohn N, Witte M, Leiner U, Mühlbach L, et al. Comparative evaluation of HD 2D/3D laparoscopic monitors and benchmarking to a theoretically ideal 3D pseudodisplay: even well-experienced laparoscopists perform better with 3D. *Surg Endosc.* 2014;28(8):2387-97.
311. Aykan S, Singhal P, Nguyen DP, Yigit A, Tuken M, Yakut E, et al. Perioperative, pathologic, and early continence outcomes comparing three-dimensional and two-dimensional display systems for laparoscopic radical prostatectomy--a retrospective, single-surgeon study. *J Endourol.* 2014;28(5):539-43.
312. Tanagho YS, Andriole GL, Paradis AG, Madison KM, Sandhu GS, Varela JE, et al. 2D versus 3D visualization: impact on laparoscopic proficiency using the fundamentals of laparoscopic surgery skill set. *J Laparoendosc Adv Surg Tech A.* 2012;22(9):865-70.
313. Hofmeister J, Frank TG, Cuschieri A, Wade NJ. Perceptual aspects of two-dimensional and stereoscopic display techniques in endoscopic surgery: review and current problems. *Semin Laparosc Surg.* 2001;8(1):12-24.
314. McLachlan G. From 2D to 3D: the future of surgery? *Lancet.* 2011;378(9800):1368.
315. Bolenz C, Gupta A, Hotze T, Ho R, Cadeddu JA, Roehrborn CG, et al. Cost comparison of robotic, laparoscopic, and open radical prostatectomy for prostate cancer. *Eur Urol.* 2010;57(3):453-8.
316. Broeders IA. Robotics: The next step? *Best Pract Res Clin Gastroenterol.* 2014;28(1):225-32.
317. Swami VG, Cheng-Baron J, Hui C, Thompson RB, Jaremko JL. Reliability of 3D localisation of ACL attachments on MRI: comparison using multi-planar 2D versus high-resolution 3D base sequences. *Knee Surg Sports Traumatol Arthrosc.* 2015;23(4):1206-14.
318. Meyers MH, McKeever FM. Fracture of the intercondylar eminence of the tibia. *J Bone Joint Surg Am.* 1970;52(8):1677-84.
319. Zaricznyj B. Avulsion fracture of the tibial eminence: Treatment by open reduction and pinning. *J Bone Joint Surg Am.* 1977;59(8):1111-4.
320. Di Caprio F, Buda R, Ghermandi R, Ferruzzi A, Timoncini A, Parma A, et al. Combined arthroscopic treatment of tibial plateau and intercondylar eminence avulsion fractures. *J Bone Joint Surg Am.* 2010;92 Suppl 2:161-9.
321. Wiley JJ, Baxter MP. Tibial spine fractures in children. *Clin Orthop Relat Res.* 1990;255:54-60.

322. Casalonga A, Bourelle S, Chalencon F, De Oliviera L, Gautheron V, Cottalorda J. Tibial intercondylar eminence fractures in children: The long-term perspective. *Orthop Traumatol Surg Res.* 2010;96(5):525-30.
323. Lowe J, Chaimsky G, Freedman A, Zion I, Howard C. The anatomy of tibial eminence fractures: arthroscopic observations following failed closed reduction. *J Bone Joint Surg Am.* 2002;84(11):1933-8.
324. McGuire DA, Hendricks SD, Sanders HM. The relationship between anterior cruciate ligament reconstruction tibial tunnel location and the anterior aspect of the posterior cruciate ligament insertion. *Arthroscopy.* 1997;13(4):465-73.
325. Frazer JES. *The anatomy of the human skeleton.* Second ed. London: J. & A. Churchill; 1920.
326. Amis AA, Gupte CM, Bull AM, Edwards A. Anatomy of the posterior cruciate ligament and the meniscofemoral ligaments. *Knee Surg Sports Traumatol Arthrosc.* 2006;14(3):257-63.
327. Marzo JM, Kumar BA. Primary repair of medial meniscal avulsions: 2 case studies. *Am J Sports Med.* 2007;35(8):1380-3.
328. Griffith CJ, LaPrade RF, Fritts HM, Morgan PM. Posterior root avulsion fracture of the medial meniscus in an adolescent female patient with surgical reattachment. *Am J Sports Med.* 2008;36(4):789-92.
329. Harner CD, Mauro CS, Lesniak BP, Romanowski JR. Biomechanical consequences of a tear of the posterior root of the medial meniscus. Surgical technique. *J Bone Joint Surg Am.* 2009;91(Suppl 2):257-70.
330. Koenig JH, Ranawat AS, Umans HR, Difelice GS. Meniscal root tears: diagnosis and treatment. *Arthroscopy.* 2009;25(9):1025-32.
331. LaPrade RF, Wills NJ, Spiridonov SI, Perkinson S. A prospective outcomes study of meniscal allograft transplantation. *Am J Sports Med.* 2010;38(9):1804-12.
332. Anderson CJ, Ziegler CG, Wijdicks CA, Engebretsen L, LaPrade RF. Arthroscopically pertinent anatomy of the anterolateral and posteromedial bundles of the posterior cruciate ligament. *J Bone Joint Surg Am.* 2012;94(21):1936-45.
333. Spiridonov SI, Slinkard NJ, LaPrade RF. Isolated and combined grade-III posterior cruciate ligament tears treated with double-bundle reconstruction with use of endoscopically placed femoral tunnels and grafts: operative technique and clinical outcomes. *J Bone Joint Surg Am.* 2011;93(19):1773-80.
334. Van Hoof T, Cromheecke M, Tampere T, D'Herde K, Victor J, Verdonk PC. The posterior cruciate ligament: a study on its bony and soft tissue anatomy using novel 3D CT technology. *Knee Surg Sports Traumatol Arthrosc.* 2013;21(5):1005-10.
335. Edwards A, Bull AM, Amis AA. The attachments of the fiber bundles of the posterior cruciate ligament: an anatomic study. *Arthroscopy.* 2007;23(3):284-90.
336. Sheps DM, Otto D, Fernhout M. The anatomic characteristics of the tibial insertion of the posterior cruciate ligament. *Arthroscopy.* 2005;21(7):820-5.
337. Ramos LA, de Carvalho RT, Cohen M, Abdalla RJ. Anatomic relation between the posterior cruciate ligament and the joint capsule. *Arthroscopy.* 2008;24(12):1367-72.

338. Petersen W, Zantop T, Tillmann B. Anatomie des hinteren Kreuzbandes sowie der posterolateralen und posteromedialen Strukturen. *Arthroskopie*. 2006;19(3):198-206.
339. Harner CD, Xerogeanes JW, Livesay GA, Carlin GJ, Smith BA, Kusayama T, et al. The human posterior cruciate ligament complex: an interdisciplinary study. Ligament morphology and biomechanical evaluation. *Am J Sports Med*. 1995;23(6):736-45.
340. Niess C, Stumpf U, Petermann J. Anatomie, Häufigkeit und Verteilung der meniskofemorale Ligamente. *Arthroskopie*. 2000;13(1-2):11-6.
341. Cunningham DJ. *Textbook of Anatomy*. 11th ed. London: Oxford University Press; 1972.
342. Takahashi M, Matsubara T, Doi M, Suzuki D, Nagano A. Anatomical study of the femoral and tibial insertions of the anterolateral and posteromedial bundles of human posterior cruciate ligament. *Knee Surg Sports Traumatol Arthrosc*. 2006;14(11):1055-9.
343. Morgan CD, Kalman VR, Grawl DM. The anatomic origin of the posterior cruciate ligament: where is it? Reference landmarks for PCL reconstruction. *Arthroscopy*. 1997;13(3):325-31.
344. Race A, Amis AA. The mechanical properties of the two bundles of the human posterior cruciate ligament. *J Biomech*. 1994;27(1):13-24.
345. Covey DC, Sapega AA, Sherman GM. Testing for isometry during reconstruction of the posterior cruciate ligament. Anatomic and biomechanical considerations. *Am J Sports Med*. 1996;24(6):740-6.
346. Sidles JA, Larson RV, Garbini JL, Downey DJ, Matsen FAR. Ligament length relationships in the moving knee. *J Orthop Res*. 1988;6(4):593-610.
347. Harner CD, Livesay GA, Kashiwaguchi S, Fujie H, Choi NY, Woo SL. Comparative study of the size and shape of human anterior and posterior cruciate ligaments. *J Orthop Res*. 1995;13(3):429-34.
348. Arnoczky SP, Warren RF, Ashlock MA. Replacement of the anterior cruciate ligament using a patellar tendon allograft. An experimental study. *J Bone Joint Surg Am*. 1986;68(3):376-85.
349. Makris CA, Georgoulis AD, Papageorgiou CD, Moebius UG, Soucacos PN. Posterior cruciate ligament architecture: evaluation under microsurgical dissection. *Arthroscopy*. 2000;16(6):627-32.
350. Petersen W, Tillmann B. Anatomie des hinteren Kreuzbandes. *Arthroskopie*. 2000;13:3-10.
351. Harner CD, Janaushek MA, Kanamori A, Yagi M, Vogrin TM, Woo SL. Biomechanical analysis of a double-bundle posterior cruciate ligament reconstruction. *Am J Sports Med*. 2000;28(2):144-51.
352. Race A, Amis AA. PCL reconstruction. In vitro biomechanical comparison of 'isometric' versus single and double-bundled 'anatomic' grafts. *J Bone Joint Surg Br*. 1998;80(1):173-9.

353. Wang CJ, Weng LH, Hsu CC, Chan YS. Arthroscopic single- versus double-bundle posterior cruciate ligament reconstructions using hamstring autograft. *Injury*. 2004;35(12):1293-9.
354. Houe T, Jørgensen U. Arthroscopic posterior cruciate ligament reconstruction: one- vs. two-tunnel technique. *Scand J Med Sci Sports*. 2004;14(2):107-11.
355. Kohen RB, Sekiya JK. Single-bundle versus double-bundle posterior cruciate ligament reconstruction. *Arthroscopy*. 2009;25(12):1470-7.
356. Kim YM, Lee CA, Matava MJ. Clinical results of arthroscopic single-bundle transtibial posterior cruciate ligament reconstruction: a systematic review. *Am J Sports Med*. 2011;39(2):425-34.
357. Greiner P, Magnussen RA, Lustig S, Demey G, Neyret P, Servien E. Computed tomography evaluation of the femoral and tibial attachments of the posterior cruciate ligament in vitro. *Knee Surg Sports Traumatol Arthrosc*. 2011;19(11):1876-83.
358. Galloway MT, Grood ES, Mehalik JN, Levy M, Saddler SC, R. NF. Posterior cruciate ligament reconstruction. An in vitro study of femoral and tibial graft placement. *Am J Sports Med*. 1996;24(4):437-45.
359. Mannor DA, Shearn JT, Grood ES, Noyes FR, Levy MS. Two-bundle posterior cruciate ligament reconstruction. An in vitro analysis of graft placement and tension. *Am J Sports Med*. 2000;28(6):833-45.
360. McGuire DA, Hendricks SD. Comparison of anatomic versus nonanatomic placement of femoral tunnels in Achilles double-bundle posterior cruciate ligament reconstruction. *Arthroscopy*. 2010;26(5):658-66.
361. Apsingi S, Bull AM, Deehan DJ, Amis AA. Review: femoral tunnel placement for PCL reconstruction in relation to the PCL fibre bundle attachments. *Knee Surg Sports Traumatol Arthrosc*. 2009;17(6):652-9.
362. Osti M, Tschann P, Kunzel KH, Benedetto KP. Anatomic characteristics and radiographic references of the anterolateral and posteromedial bundles of the posterior cruciate ligament. *Am J Sports Med*. 2012;40(7):1558-63.
363. Kennedy NI, Wijdicks CA, Goldsmith MT, Michalski MP, Devitt BM, Aroen A, et al. Kinematic analysis of the posterior cruciate ligament, part 1: the individual and collective function of the anterolateral and posteromedial bundles. *Am J Sports Med*. 2013;41(12):2828-38.
364. Kennedy NI, LaPrade RF, Goldsmith MT, Faucett SC, Rasmussen MT, Coatney GA, et al. Posterior cruciate ligament graft fixation angles, part 1: biomechanical evaluation for anatomic single-bundle reconstruction. *Am J Sports Med*. 2014;42(10):2338-45.
365. Kennedy NI, LaPrade RF, Goldsmith MT, Faucett SC, Rasmussen MT, Coatney GA, et al. Posterior cruciate ligament graft fixation angles, part 2: biomechanical evaluation for anatomic double-bundle reconstruction. *Am J Sports Med*. 2014;42(10):2346-55.
366. Altman RD, Fries JF, Bloch DA, MD JC, Derek TC, Genant H, et al. Radiographic assessment of progression in osteoarthritis. *Arthritis Rheum*. 1987;30(11):1214-25.

367. Takechi H. Trabecular architecture of the knee joint. *Acta Orthop Scand.* 1977;48(6):673-81.
368. Krenz J, Troup JDG. The structure of the pars interarticularis of the lower lumbar vertebrae and its relation to the etiology of spondylolysis. *J Bone Joint Surg Br.* 1973;55:753-41.
369. Sinha DN. Cancellous structure of tarsal bones. *J Anat.* 1985;140(Pt 1):111-7.
370. Maquet PGJ. *Biomechanics of the Knee - With Application to the Pathogenesis and the Surgical Treatment of Osteoarthritis.* Berlin: Springer-Verlag; 1976.
371. Junker S, Krumbholz G, Frommer KW, Rehart S, Steinmeyer J, Rickert M, et al. Differentiation of osteophyte types in osteoarthritis - proposal of a histological classification. *Joint Bone Spine.* 2016;83(1):63-7.
372. Bullough PG. *Orthopaedic pathology.* Missouri: Mosby Elsevier; 2010.
373. Wolfe F, Lane NE. The longterm outcome of osteoarthritis: rates and predictors of joint space narrowing in symptomatic patients with knee osteoarthritis. *J Rheumatol.* 2002;29(1):139-46.
374. Felson DT, Gale DR, Elon Gale M, Niu J, Hunter DJ, Goggins J, et al. Osteophytes and progression of knee osteoarthritis. *Rheumatology (Oxford).* 2005;44(1):100-4.
375. DeHaven KE, Collins HR. Diagnosis of internal derangements of the knee. The role of arthroscopy. *J Bone Joint Surg Am.* 1975;57(6):802-10.
376. Lysholm J, Hamberg P, Gillquist J. The correlation between osteoarthrosis as seen on radiographs and on arthroscopy. *Arthroscopy.* 1987;3(3):161-5.
377. Brandt KD, Fife RS, Braunstein EM, Katz B. Radiographic grading of the severity of knee osteoarthritis: relation of the Kellgren and Lawrence grade to a grade based on joint space narrowing, and correlation with arthroscopic evidence of articular cartilage degeneration. *Arthritis Rheum.* 1991;34(11):1381-6.
378. Boegård T, Rudling O, Petersson IF, Sanfridsson J, Saxne T, Svensson B, et al. Postero-anterior radiogram of the knee in weight-bearing and semiflexion. Comparison with MR imaging. *Acta Radiol.* 1997;38(6):1063-70.
379. Galli M, De Santis V, Tafuro L. Reliability of the Ahlbäck classification of knee osteoarthritis. *Osteoarthritis Cartilage.* 2003;11(8):580-4.
380. Resnick D, Vint V. The "Tunnel" view in assessment of cartilage loss in osteoarthritis of the knee. *Radiology.* 1980;137(2):547-8.
381. Wright RW. Osteoarthritis classification scales: Interobserver reliability and arthroscopic correlation. *J Bone Joint Surg Am.* 2014;96(14):1145-51.
382. Kellgren JH, Lawrence JS. Radiological assessment of osteo-arthrosis. *Ann Rheum Dis.* 1957;16(4):494-502.
383. Schiphof D, Boers M, Bierma-Zeinstra SM. Differences in descriptions of Kellgren and Lawrence grades of knee osteoarthritis. *Ann Rheum Dis.* 2008;67(7):1034-6.
384. Irrgang JJ, Anderson AF, Boland AL, Harner CD, Neyret P, Richmond JC, et al. Responsiveness of the International Knee Documentation Committee Subjective Knee Form. *Am J Sports Med.* 2006;34(10):1567-73.

385. Hefti F, Müller W, Jakob RP, Stäubli HU. Evaluation of knee ligament injuries with the IKDC form. *Knee Surg Sports Traumatol Arthrosc.* 1993;1(3-4):226-34.
386. Fairbank TJ. Knee joint changes after meniscectomy. *J Bone Joint Surg Br.* 1948;30(4):664-70.
387. Tapper EM, Hoover NW. Late results after meniscectomy. *J Bone Joint Surg Am.* 1969;51(3):517-26.
388. Scheller G, Sobau C, Bulow JU. Arthroscopic partial lateral meniscectomy in an otherwise normal knee: Clinical, functional, and radiographic results of a long-term follow-up study. *Arthroscopy.* 2001;17(9):946-52.
389. Schroeder-Boersch H, Toews P, Jani L. Reproduzierbarkeit von radiologischen Arthrosemerkmalen. *Zeit Orth.* 1998;136(4):293-7.
390. Curl WW, Krome J, Gordon ES, Rushing J, Smith BP, Poehling GG. Cartilage injuries: a review of 31,516 knee arthroscopies. *Arthroscopy.* 1997;13(4):456-60.
391. Kijowski R, Blankenbaker D, Stanton P, Fine J, De Smet A. Arthroscopic validation of radiographic grading scales of osteoarthritis of the tibiofemoral joint. *AJR Am J Roentgenol.* 2006;187(3):794-9.
392. Blackburn WDJ, Bernreuter WK, Rominger M, Loose LL. Arthroscopic evaluation of knee articular cartilage: a comparison with plain radiographs and magnetic resonance imaging. *J Rheumatol.* 1994;21(4):675-9.
393. Fife RS, Brandt KD, Braunstein EM, Katz BP, Shelbourne KD, Kalasinski LA, et al. Relationship between arthroscopic evidence of cartilage damage and radiographic evidence of joint space narrowing in early osteoarthritis of the knee. *Arthritis Rheum.* 1991;34(4):377-82.
394. Wright RW, Boyce RH, Michener T, Shyr Y, McCarty EC, Spindler KP. Radiographs are not useful in detecting arthroscopically confirmed mild chondral damage. *Clin Orthop Relat Res.* 2006;442:245-51.
395. Rosenberg TD, Paulos LE, Parker RD, Coward DB, Scott SM. The forty-five-degree posteroanterior flexion weight-bearing radiograph of the knee. *J Bone Joint Surg Am.* 1988;70(10):1479-83.
396. Dervin GF, Feibel RJ, Rody K, Grabowski J. 3-Foot standing AP versus 45 degrees PA radiograph for osteoarthritis of the knee. *Clin J Sport Med.* 2001;11(1):10-6.
397. Pires R, Pires AC, Giordano V, Djahjah MC, Pecegueiro N. Estudo comparativo entre incidências radiográficas para a osteoartrose do joelho. *Acta Reumatol Port.* 2009;34(2B):380-7.
398. van Saase JL, van Romunde LK, Cats A, Vandenbroucke JP, Valkenburg HA. Epidemiology of osteoarthritis: Zoetermeer survey. Comparison of radiological osteoarthritis in a Dutch population with that in 10 other populations. *Ann Rheum Dis.* 1989;48(4):271-80.
399. Lawrence JS, Bremner JM, Bier F. Osteo-arthrosis. Prevalence in the population and relationship between symptoms and x-ray changes. *Ann Rheum Dis.* 1966;25(1):1-24.
400. Carrillon Y. Imaging knee osteoarthritis. In: Bonnin M, Chambat P, editors. *Osteoarthritis of the Knee.* Paris: Springer-Verlag; 2008.

401. Menkes CJ. Radiographic criteria for classification of osteoarthritis. *J Rheumatol.* 1991;Suppl 27(28):13-5.
402. Piperno M, Hellio Le Graverand MP, Conrozier T, Bochu M, Mathieu P, Vignon E. Quantitative evaluation of joint space width in femorotibial osteoarthritis: comparison of three radiographic views. *Osteoarthritis Cartilage.* 1998;6(4):252-9.
403. Altman RD, Hochberg M, Murphy WAJ, Wolfe F, Lequesne M. Atlas of individual radiographic features in osteoarthritis. *Osteoarthritis Cartilage.* 1995;3(Suppl A):3-70.
404. Altman RD, Gold GE. Atlas of individual radiographic features in osteoarthritis, revised. *Osteoarthritis Cartilage.* 2007;15 Suppl A:A1-56.
405. Culvenor AG, Engen CN, Oiestad BE, Engebretsen L, Risberg MA. Defining the presence of radiographic knee osteoarthritis: a comparison between the Kellgren and Lawrence system and OARSI atlas criteria. *Knee Surg Sports Traumatol Arthrosc.* 2015;23(12):3532-9.
406. Koski JM, Kamel A, Waris P, Waris V, Tarkiainen I, Karvanen E, et al. Atlas-based knee osteophyte assessment with ultrasonography and radiography: relationship to arthroscopic degeneration of articular cartilage. *Scand J Rheumatol.* 2016;45(2):158-64.
407. Marshall JL, Olsson SE. Instability of the knee. A long-term experimental study in dogs. *J Bone Joint Surg Am.* 1971;53(8):1561-70.
408. Williams JM, Brandt KD. Exercise increases osteophyte formation and diminishes fibrillation following chemically induced articular cartilage injury. *J Anat.* 1984;139(Pt 4):599-611.
409. Palmoski MJ, Brandt KD. Immobilization of the knee prevents osteoarthritis after anterior cruciate ligament transection. *Arthritis Rheum.* 1982;25(10):1201-8.
410. Pottenger LA, Phillips FM, Draganich LF. The effect of marginal osteophytes on reduction of varus-valgus instability in osteoarthritic knees. *Arthritis Rheum.* 1990;33(6):853-8.
411. Hart DJ, Spector TD. The classification and assessment of osteoarthritis. *Baillieres Clin Rheumatol.* 1995;9(2):407-32.
412. Insall JN, Dorr LD, Scott RD, Scott WN. Rationale of the Knee Society clinical rating system. *Clin Orthop Relat Res.* 1989 248(13-4).
413. Brekke AC, Noble PC, Parsley BS, Mathis KB. Scoring Systems and Their Validation for the Arthritic Knee. In: Scott WN, editor. *Insall & Scott Surgery of the Knee.* Philadelphia: Churchill Livingstone; 2012.
414. Davies AP. Rating systems for total knee replacement. *Knee.* 2002;9:261-2
415. Drake BG, Callahan CM, Dittus RS, Wright JG. Global rating systems used in assessing knee arthroplasty outcomes. *J Arthroplasty.* 1994;9:409-17.
416. Bach CM, Nogler M, Steingruber IE, Ogon M, Wimmer C, Göbel G, et al. Scoring systems in total knee arthroplasty. *Clin Orthop Relat Res.* 2002;399:184-96.
417. Kreibich DN, Vaz M, Bourne RB, Rorabeck CH, Kim P, Hardie R, et al. What is the best way of assessing outcome after total knee replacement? *Clin Orthop Relat Res.* 1996;331:221-5.

418. A. LE, N. KJ, J. WR, A. WE, B. SC, Group' KO. Validity and responsiveness of the Knee Society Clinical Rating System in comparison with the SF-36 and WOMAC. *J Bone Joint Surg Am.* 2001;83:1856-64.
419. Hannan MT, Felson DT, Pincus T. Analysis of the discordance between radiographic changes and knee pain in osteoarthritis of the knee. *J Rheumatol.* 2000;27(6):1513-7.
420. Neogi T, Felson D, Niu J, Nevitt M, Lewis CE, Aliabadi P, et al. Association between radiographic features of knee osteoarthritis and pain: results from two cohort studies. *BMJ.* 2009;339:b2844.
421. Hernández-Vaquero D, Fernández-Carreira JM. Relationship between radiological grading and clinical status in knee osteoarthritis. A multicentric study. *BMC Musculoskelet Disord.* 2012;13:194.
422. Petersson IF, Boegård T, Saxne T, Silman AJ, Svensson B. Radiographic osteoarthritis of the knee classified by the Ahlbäck and Kellgren & Lawrence systems for the tibiofemoral joint in people aged 35-54 years with chronic knee pain. *Ann Rheum Dis.* 1997;56(8):493-6.
423. Cicuttini FM, Baker J, Hart DJ, Spector TD. Association of pain with radiological changes in different compartments and views of the knee joint. *Osteoarthritis Cartilage.* 1996;4(2):143-7.
424. Lanyon P, O'Reilly S, Jones A, Doherty M. Radiographic assessment of symptomatic knee osteoarthritis in the community: definitions and normal joint space. *Ann Rheum Dis.* 1998;57(10):595-601.
425. Dowsey MM, Dieppe P, Lohmander S, Castle D, Liew D, Choong PF. The association between radiographic severity and pre-operative function in patients undergoing primary knee replacement for osteoarthritis. *Knee.* 2012;19(6):860-5.

Appendix I. German literature

Mechanik der menschlichen Gehwerkzeuge: Eine anatomisch-physiologische Untersuchung (1836)

The following are passages extracted from the book *Mechanik der menschlichen Gehwerkzeuge: Eine anatomisch-physiologische Untersuchung* (1836), by brothers Wilhelm & Eduard Weber:

[Intercondylar area:] Das obere Ende der Tibia, auf welchem das Oberschenkelbein steht, ist durch eine mittlere Erhabenheit in zwei seitliche Hälften getheilt, die man auch die Condylen der Tibia nennt, und welche zwei sehr flache Gelenkflächen tragen (...). Beide sind von einander durch jene Erhabenheit, eminentia intermedia, getrennt, welche zum inneren Condylus hin steiler, zum äusseren flacher abfällt.

[Condyle function:] (...) bei der Bewegung des Knies beide Condylen des Oberschenkels sich nicht gleich verhalten, sondern, dass sich bei der Beugung und Streckung der äussere Condylus auf der Fläche der Tibia mehr rolle, der innere Condylus auf ihr mehr schleife, dass ferner bei der Pronation und Supination die senkrechte Drehungsaxe ungefähr mit dem inneren Condylus zusammen falle, und der äussere Condylus daher um ihn herumgehe.

[ACL bundles (see Fig. 437)] Fig.1 zeigt das vordere Kreuzband, ligamentum cruciatum anticum des rechten Kniegelenks. Der innere Condylus des Oberschenkelbeins ist weggenommen, so dass man den äusseren Condylus von seiner inneren, der Kniekehle zugekehrten Seite sieht, und erkennen kann, wie an ihr das vordere Kreuzband c a befestigt ist. Man sieht daselbst, dass es bei gestreckter aufrechter Lage in einer senkrechten Line c' a' am äusseren Condylus fest sitzt. Zwei Reihen von Puncten deuten an, welche Lage das äussere Seitenband an der äusseren Seite des Knies hat, und wo seine obere Befestigung ist. Denkt man sich nun, dass das so gestreckte Bein um 90° gebogen würde, so

wird sich zwar das von a' entspringende Bündel nach hinten, das von c' entspringende aber in gleichem Maasse nach vorn drehen, und folglich in dem Grade als ersteres erschlafft, letzteres sich spannen müssen. Fig.2. zieht diese veränderte Lage des Bandes.

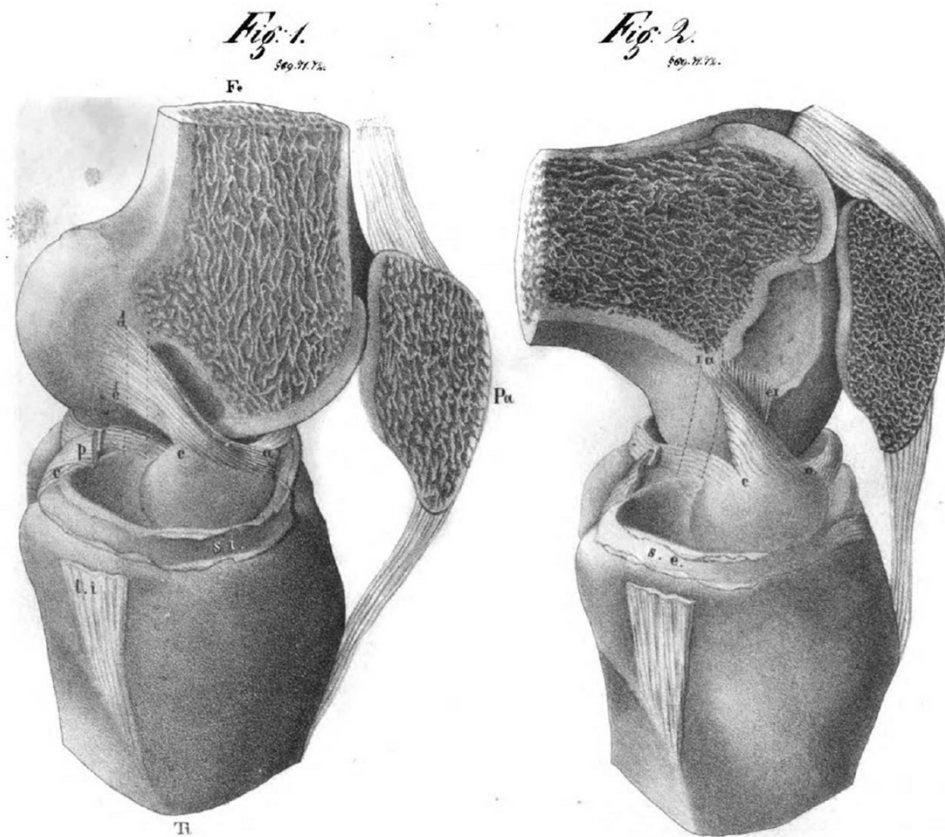


Figure 483. ACL bundles. Image modified from Weber & Weber (1836)⁹, originally labelled Taf. V. (from digitalized copy at Europeana collections; condition: out of copyright – noncommercial re-use).

[ACL:] Das vordere Kreuzband, welches vom äusseren Condylus des Oberschenkelbeins kommt, geht nach vorn zur Fläche der Tibia herab und befestigt sich daselbst in der Grube vor den Hügeln der eminentia intermedia, und zwischen beiden Spitzen derselben in einer winkelförmig gebrochenen Linie, deren einer Schenkel von hinten nach vorn, deren anderer Schenkel von rechts nach links geht. Hierdurch zerfällt das Band in zwei Theile, in einen hinteren und vorderen. Der hintere Theil, welcher sich in dem von hinten nach vorn gehenden Schenkel befestigt, ist unten schmal, und wird an seinem oberen Ansatzpunkte am condylus externus femoris breit; der andere vordere Theil, welcher sich an dem queren, von rechts nach links gehenden Schenkel befestigt, ist unten breit und oben, wo er über dem andern liegt, schmal. Wenn das Knie gebogen wird, so winden sich beide Theile um einander.

[PCL bundles (see Fig. 443):] Fig.1. zeigt das hintere Kreuzband, ligamentum cruciatum posticum, des linken Kniegelenks. Der äussere Condylus des Oberschenkelbeins ist weggenommen, so dass man den inneren Condylus von seiner der Kniekehle zugekehrten Seite sieht, und erkennt, auf welche Weise das hintere Kreuzband c p an ihm befestigt ist. Die Linie nämlich c' p', in der es am inneren Condylus festsetzt, liegt am gestreckten aufrechten Knie horizontal. Wird daher das Bein um 90° gebogen, so muss der Punct c' herab, p' aber in gleichem Maasse heraufsteigen, und folglich das in c' befestigte Bündel, welches gespannt war, erschlaffen, das in p' befestigte Bündel aber, welches schlaff war, allmählig sich spannen, wie es Fig.2. wirklich darstellt.

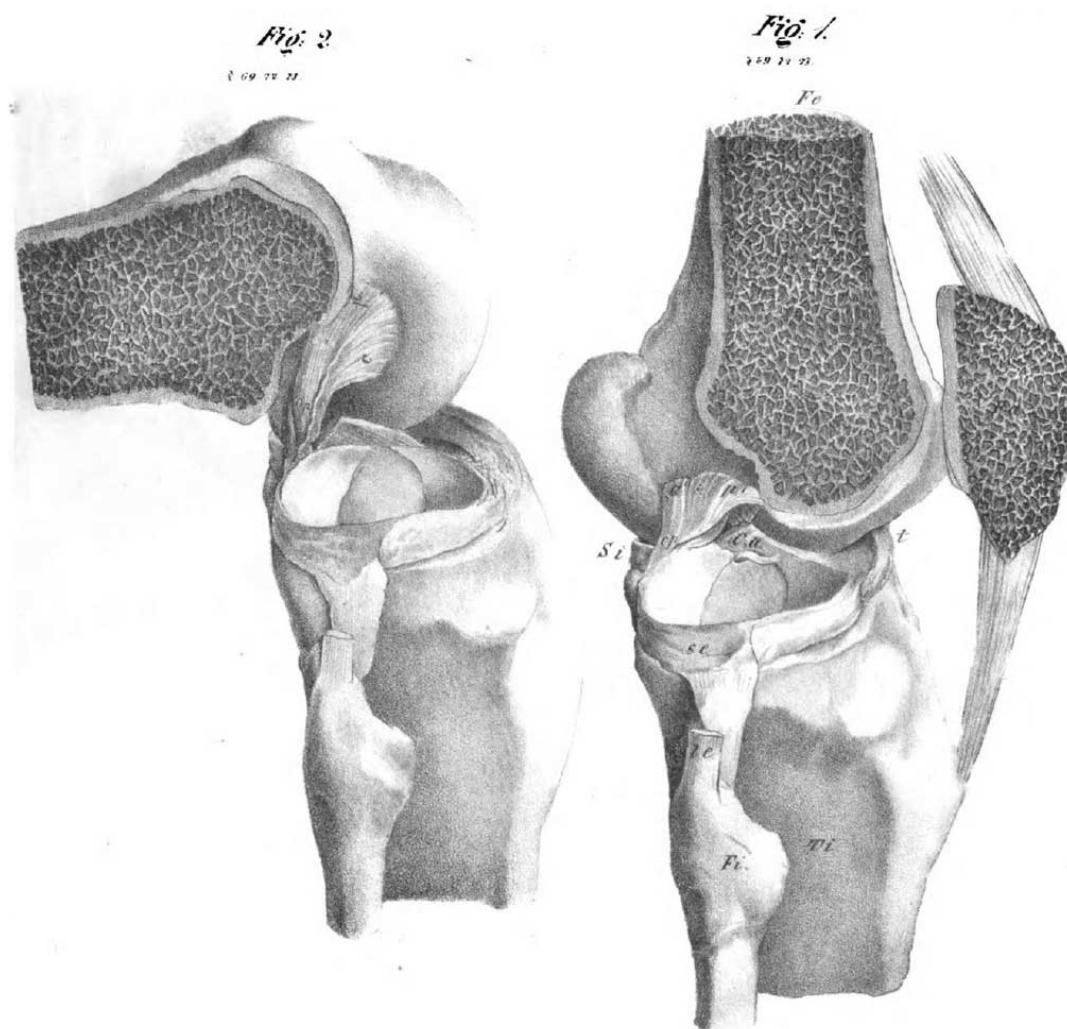


Figure 484. PCL bundles. Image modified from Weber & Weber (1836)⁹, originally labelled Taf. VI. (from digitalized copy at Europeana collections; condition: out of copyright – noncommercial re-use).

[PCL attachment:] Das hintere Kreuzband, welches vom inneren Condylus des Oberschenkelbeins kommt, geht nach hinten zur Fläche der Tibia herab, und befestigt sich am Rande derselben in der Vertiefung zwischen beiden Condylen

der Tibia. Seine Ursprungsstelle liegt daher 15-20 Millimeter hinter der des vorderen Kreuzbandes, und näher, als dieses, an der Linie, welche die Gelenkfläche in zwei seitliche Hälften theilt. Auch an diesem Bande kann man zwei Theile unterscheiden, von welchen der hintere oben breit und unten schmal, der vordere oben schmal und unten breit ist. Der erstere setzt sich am Oberschenkel weiter nach vorn, am vorderen bogenförmigen Rande des die Condylen von einander trennenden Sinus, an, der andere ist weiter nach hinten, am Condylus, angewachsen, und seine Fasern haben daher fast eine senkrechte Lage. Dieses letztere Bündel ist es, welches bei beträchtlicher Streckung von neuem stark gespannt wird.

Untersuchungen über die Anatomie und Mechanik des Kniegelenkes (1855)

The following are passages extracted from the book *Untersuchungen über die Anatomie und Mechanik des Kniegelenkes (1855)*, by Heinrich Ludwig Ferdinand Robert:

[Intercondylar area:] Fast in der Mittle erhebt sich eine sattelförmige Erhabenheit (*Eminentia intermedia*), welche nach vorn und hinten, so wie zu beiden Seiten, abfällt und als unvollkommener Zapfen in die *Fossa intercondyloidea* des Oberschenkels eingreift. Dieser Zapfen liegt von dem äussern und innern Rande fast gleich weit entfernt, dem intern Rande dagegen bedeutend näher als dem vordern. Von diesem Zapfen aus theilt sich die Fläche in vier Theile, von denen die beiden seitlichen überknorpelt, die vor und hinten derselben gelegenen nicht überknorpelt sind. (...)

Die überknorpelten Theile, welche von beiden Seiten der *Eminentia intermedia* absteigen, (...) stehen nirgends mit einander in Berührung, indem der sehr höckerige nicht überknorpelte Theil dieser Fläche in Form einer Sanduhr zwischen ihnen gelagert ist. Auf der *Eminentia intermedia* liegen sie am nächsten 10 Mm. von einander, mit ihrem hintern Rande 15 Mm.; mit ihrem vordern 68 Mm. entfernt. Die *eminetia intermedia* selbst liegt 36 Mm. von dem vordern und 17 Mm. von dem hintern Rande. (...)

[Das nicht überknorpelte Theil der Gelenkfläche] liegt daher ein weit grösserer nicht überknorpelter Theil vorn zwischen den Gelenkflächen als hinten. Ersterer liegt horizontal zu der *Axe* des Knochens und erhebt sich mit seinem innern Theil gegen die innere Knorpelfläche; letzterer fällt nach hinten gegen die vordere

Fläche unter einem Winkel von 140° ab. Er ist der einzige Theil der obern Fläche, welcher bei keiner Stellung in unmittelbarer oder mittelbarer Berührung mit dem Oberschenkel kommt. Sein äusserer Theil erhebt sich gegen die äussere Knorpelfläche.

[Condyle function:] Die beide überknorpelten Flächen, welche (..) nicht horizontal, sondern unter $8-10^\circ$ gegen die Knochenaxe geneigt sind, unterscheiden sich in Lage, Grösse, Form und Oberfläche.

Beide liegen zwar in ihrer Mitte in einem Horizont, allein nach dem oben angegebenen ihrer Durchmesser liegt die äussere mehr nach vorn, die innere mehr nach hinten von der Eminentia intermedia. Erstere ist breiter und kürzer (44 Mm. lang, 36 Mm. breit) und ähnelt mehr der Form einer Rhombe, letztere ist länger und schmaler (47 Mm. lang, 31 Mm. breit) und hat mehr eine Eiform. – Die wesentlichste Differenz zeigt sich an frisch geöffneten Gelenken in den Curven ihrer Oberfläche. Die innere zeigt eine in der Mitte, jedoch mehr nach vorn gelegene Concavität, welche fast in der ganzen Peripherie von einem planen, hinten breiter und vorn schmaler werdenden Theil umgeben ist. Nach innen wird dieselbe von der nach dieser Knorpelfläche steil abfallenden Eminentia intermedia begrenzt, welche sich über die tiefste Stelle derselben, 10 Mm., erhebt, von dem vordern Theil des innern Randes der Knorpelfläche allmählig aufsteigt und nach hinten rasch abfällt. Ihre vorn höhere Spitze ist 7 Mm. breit. Sie fällt gegen die Grube der Gelenkfläche unter einem Winkel von 125° ab. Diese nimmt von der ganzen Gelenkfläche 27 Mm. der Länge und 26 Mm. der Breite nach ein. Ihre Concavität von vorn nach hinten beträgt 2 Mm. Tiefe. Der Halbmesser der Curve misst daher in dieser Richtung 36 Mm. Die quere Concavität von dem äussern planen Theil bis zur Basis der am hintern Rande 8 Mm. hohen Eminentia beträgt 4 Mm. Bei der Breite in dieser Richtung misst der Krümmungshalbmesser der Curve 26 Mm. Der plane Rand ist hinten 11, seitlich 5 und vorn 3 Mm. breit. – Die Oberfläche der äussern Knorpelfläche hat eine von hinten nach vorn um ihre Eminentia intermedia herumlaufende Wellenform. Die Eminentia intermedia ist nicht so hoch an dieser Seite, indem sie sich über die Mitte dieser Fläche nur 8 Mm. erhebt und 2 Mm. niedriger ist, als die der andern Seite. Sie ist 6 Mm. von ihrer Basis aus hoch, ihre nach hinten gelegene höhere Spitze 5 Mm. breit. Sie liegt etwas weiter nach vorn als die der andern Seite, so dass die Knorpelflächen beider Gelenkspitzen sich gerade gegenüber liegen. Im Gegensatz zu der der innern Knorpelfläche fällt ihr vorderer Rand steil ab,

während ihr hinterer sich allmählig senkt. Auch ihr Abfallen gegen die Gelenkfläche ist viel allmählicher. Der Winkel gegen die Fläche beträgt 150° . Der innere, hinter der Eminentia liegende Rand dieser Knorpelfläche liegt am höchsten, sie vertieft sich im hintern Drittheil am weitesten, erhebt sich wieder und senkt sich am vordern Rande so bedeutend, dass derselbe die tiefste Stelle der Gelenkfläche darstellt. Der Durchschnitt dieser Fläche von vorn nach hinten bildet eine Wellenlinie, deren hintere Erhebung 8 Mm., deren vordere 3 Mm. beträgt. Von innen nach aussen ist diese Fläche concav, und zwar in den Senkungen der Wellenfläche am tiefsten, auf den Erhebungen am flachsten, jene Tiefe beträgt 4 Mm., diese nur 2 Mm. An der hintern Seite dieser Fläche steigt der Knorpelüberzug in Form einer dreieckigen Fläche an der hintern Seite des Knochens herab, auf welcher die Sehne des M. popliteus verläuft.

[ARMM:] Noch weiter nach vorn wird er immer dünner und spaltet sich in drei bandartige Streifen, welche anfangs zwar noch in die Gelenkhöhle vorspringen, bei Erschlaffung der Capsel (im Streckzustande) sich dicht aneinander legen, bei der Spannung derselben (im Beugezustand) sich von einander entfernen und endlich nicht mehr vorspringend sich zwar nicht constant, jedoch in mehreren Fällen als bandartige Faserzüge verfolgen liessen. Der stärkste bildet das oben erwähnte Verbindungsband zwischen beiden halbmondförmigen Knorpeln und läuft unter dem Fettpolster der flügelförmigen Bänder nach dem vordern Theile des äussern Randes des äussern halbmondförmigen Knorpels; der zweite bildet das feste Substrat des s. g. Schleimbandes und geht zu dessen Insertion an den Oberschenkelkopf; der dritte endlich weniger constante zieht sich längs des vordern innern Randes der Knorpelfläche fort und inserirt sich vor der Eminentia intermedia.

[ARLM:] [Es] inserirt sich nach Bildung der Schlinge in einer rautenförmigen Grube vor [der Spitze] am nicht überknorpelten Theil.

[ACL:] Seine Insertion auf der oberen Fläche der Tibia liegt in der Axe des Körpers dieses Knochens. Sie beginnt mit kurzen Faserbündeln auf dem Sattel der Eminentia media etwas der äussern Gelenkfläche näher, dicht vor der hintern Insertion des äussern halbmondförmigen Knorpels und erstreckt sich mit längern Faserzügen bis zum vordern Ende der Capsel, dem Anfange der Fettpolster, 12 Mm. von der vordern Kante der Tibia entfernt. Der innere Rand der Insertion liegt dem vor der Eminentia liegenden Knorpelrande unmittelbar an, der äussere deckt die mit ihr durch dichtes Bindegewebe und einzelne

Faserzüge innig verwebte vordere Insertion des äussern halbmondförmigen Knorpels, von dem Knorpelrande 6 Mm. entfernt. Diese von vorn nach hinten und etwas von innen nach aussen gestellte Ursprungsstelle ist 20Mm. lang, vorn 10, und hinten 5 Mm. breit und hat demnach eine unregelmässige Form, deren Faserzüge an der vordern und innern Seite in einem festen rechten Winkel zu einander gestellt sind, während die hintern sich mehr unregelmässig inseriren. Während diese letzteren Faserzüge direct von dem Knochen in das Band eintreten, liegen die ersten eine Zeitlang noch dem Knochen an, und gehen erst, nachdem sie sich radienartig vereinigt und etwas nach aussen spiralig an einander gelegt haben, in das Band über.

[ACL attachment:] Eben so gestattet die fast in einem Halbkreis gestellte Insertion des Bandes auf der Tibia zwar die Rotation, allein ohne eine Bedingung derselben abzugeben.

[ACL bundles:] Bei Beugung unter einem rechten Winkel wird die bei Streckung senkrechte Insertionsstelle horizontal gestellt, und die hintern Fasern legen sich daher kreuzend an die vordern, was zu einer spiraligen Umwicklung bei der Beugung unter einem spitzen Winkel führt. Eine verschiedene Spannung des Bandes bei Beugung und Streckung habe ich nicht beobachtet. Weber behauptet zwar, das es bei gebogener Lage fast ganz schlaff sei, bei der Streckung sich spanne. (Ich habe an frischen Präparaten dieses nicht beobachten können, glaubte indess bei der Streckung einen grössern Widerstand der hintern, bei der Beugung der vordern zu bemerken.) Indessen ist eine solche Beurtheilung einer verschiedenen Spannung durch Anschauung an Präparaten mannigfaltigen Fehlerquellen unterworfen, da durch die Präparation selbst der Zusammenhang zu sehr gestört wird. Genauern Aufschluss geben daher Messungen der Entfernungen der einzelnen Punkte der Insertionsstellen von einander. (...) Es folgt hieraus, dass, wenn die Drehung der äussern Gelenkfläche auf einer und derselben Ebene oder seiner Stelle der Tibia erfolgte, die Spannung der vordern Fasern des Bandes, welche sich oben inseriren, bei der Beugung allmählig abnimmt, während die Spannung der sich unten inserirenden Faserzüge bei einem gewissen Grade der Beugung zwar abnimmt, sich sodann aber wieder steigert. Zur Abnahme der Spannung der Fasern trägt jedoch noch bei der Beugung bei, dass bei derselben der Drehkopf eine andere tiefere Stelle der Gelenkfläche der Tibia berührt, als dieses bei der Streckung der Fall ist. Verringert aber wird die Erschlaffung der vordern Faserbündel durch die Torsion

während der Beugung, während die gespannten hintern Faserbündel gegen die vordern um so mehr andrängen und dieselben in die Höhe heben, je mehr der obere Insertionspunkt unter den untern herabtritt, wie dieses bei der Beugung um so mehr stattfindet, je spitzer der Winkel derselben wird. (...)

[PRLM:] Sie entsteht nämlich dicht hinter der Spitze derselben vom Knorpelrande selbst, höher als der innere halbmondförmige Knorbel (...).

[PRMM:] Der halbmondförmige Knorpel der inner Knorpelfläche entspringt mit einem sehr spitzen Ende dicht hinter der Eminentia mammillaris, nahe dem Rande der Knorpelfläche und verbreitet sich rasch, indem er sich unmittelbar auf denselben auflegt.

[PCL footprint:] [Hat eine] fast viereckige Form, die vorn etwas ausgezogen ist und nach hinten breiter wird, so dass sie einem Dreieck nähert, dessem Basis 14 Mm. breit, dessen Höhe 17 Mm. beträgt, und dessen Basis nach hinten und etwas nach aussen, dessen Spitze nach vorn und etwas nach innen gestellt is.

[relationship with the PRMM:] Die Faserbündel treten jedoch nicht von ihrer Insertionsstelle sogleich ab, sondern sind durch dichtes Bindegewebe und selbst durch kurze fibröse Faserbündel mit den vor ihnen liegenden hintern Insertionen beider halbmondförmiger Knorpel verbunden.

[PCL bundles:] Bei gestreckter Lage des Unterschenkels hat das Band einen nur etwas von senkrechter Richtung abweichenden Verlauf, indem es von unten nach oben aufsteigend etwas nach vorn und innen von dieser Richtung abweicht. Sein über der Eminentia der Tibia liegender Theil hat die vordere Fläche etwas nach innen und unten, die hintere etwas nach aussen und oben gerichtet, der dicke Rand sieht nach vorn und aussen, der scharfe nach hinten und innen.

Handatlas der Anatomie des Menschen (1896) by Spalteholz

The following passage is extracted from the book Handatlas der Anatomie des Menschen (1896), by Werner Spalteholz:

Das obere Endstück der tibia verbreitet sich stark zu den zwei seitlich ausladenden Schienbeinknorren, condylus medialis und condylus lateralis. Jeder derselben besitzt eine proximal gerichtete, dreieckig-ovale, etwas vertiefte, überknorpelte facies articularis superior; zwischen den beiden liegt eiene vorn und hinten breitere, rauhe Fläche, die sich in der Mitte zu der eminentia

intercondyloidea erhebt und dort in zwei kleinen Zacken endet, dem tuberculum intercondyloideum mediale und tuberculum intercondyloideum laterale. Das Feld vor der eminentia heisst fossa intercondyloidea anterior, das hinter derselben fossa intercondyloidea posterior. Die überknorpelte Fläche setzt sich jederseits ein Stück auf die eminentia fort. An dem äusseren Umfang der facies articul. Sup. fällt der Knochen scharf ab als margo infraglenoidalis.

Fig. 485 was the illustration accompanying this section in the first edition of the book.

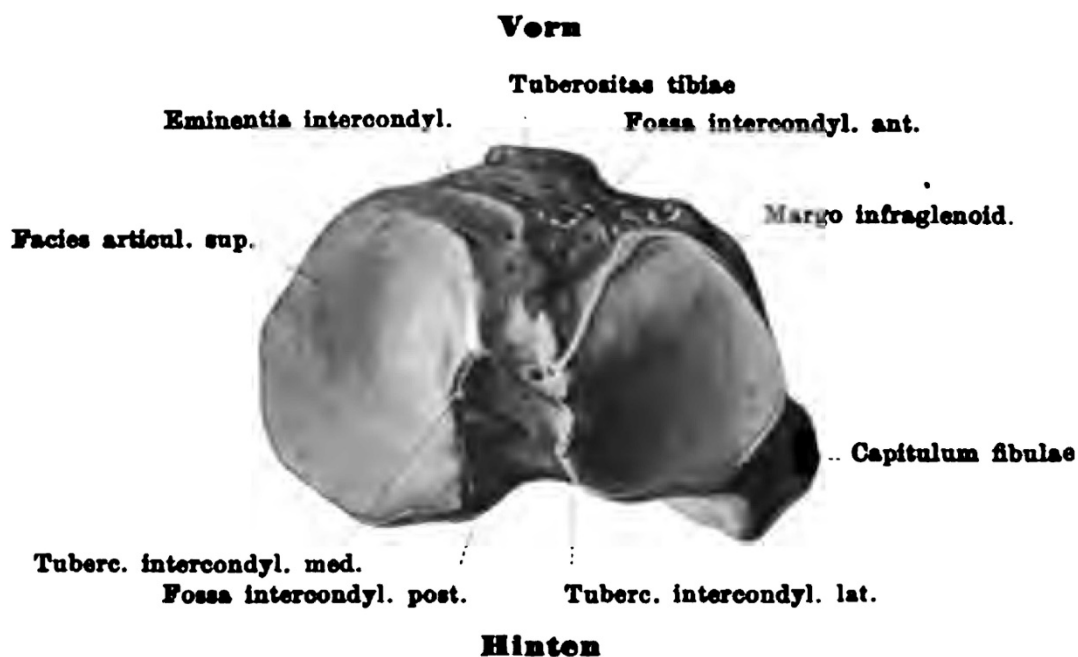


Figure 485. Superoinferior view of a right tibia (anterior is above). Modified from Spalteholz (1896)¹⁴.

Handbuch der Anatomie und Mechanik der Gelenke unter Berücksichtigung der bewegenden Muskeln (1904)

The following are passages extracted from the book Handbuch der Anatomie und Mechanik der Gelenke unter Berücksichtigung der bewegenden Muskeln (1904), by Rudolf Fick:

[Intercondylar area:] Beide [Schienbein]flächen erheben sich gegen die Mitte (der ganzen proximalen Schienbeinepiphyse) und bilden dort die beiden Zwischenknorrenhöcker [Eminentiae intercondyleae]. Durch diese Erhebung werden sie von lateral nach medial deutlich konkav, wie man am besten auf „Frontal“ – schnitten erkennt [Fig. 486]. Der Zwischenhöcker fällt übrigens zur medialen Fläche hin steiler ab als zur lateralen. Der Zwischenhöcker liegt nicht

genau „central“ (auf der proximalen Schienbeinfläche), sondern dem hinteren Rand (derselben) erheblich (um fast 2 cm) näher als dem vorderen. Er stellt einen etwa 1 cm hohen Zapfen dar, der in die Hohlkehle zwischen die beiden Femurrollen hineinragt, dieselbe aber nicht ganz ausfüllt. Vor und hinter dem Zwischenhöcker liegen knorpelfreie, rauhe, etwa dreieckige Felder, die zusammen eine sanduhrähnliche Figur bilden.

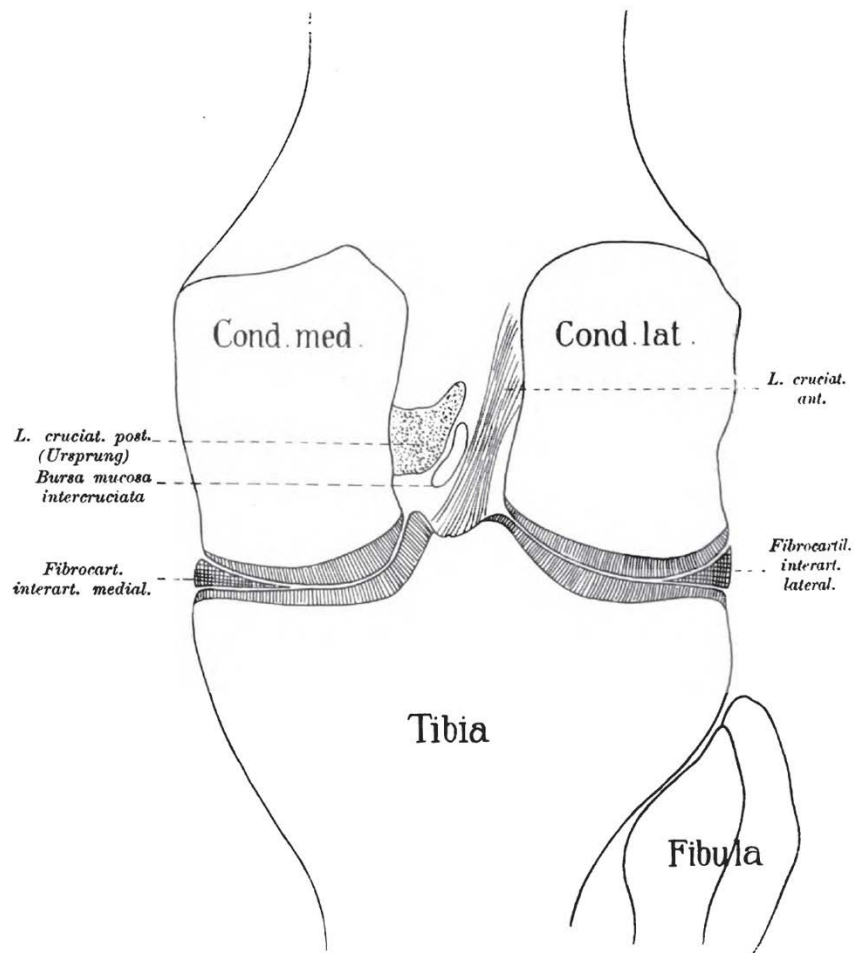


Figure 486. Schematic coronal cut of a right knee, viewed from behind. Modified from Fick (1904)¹¹.

[ARLM (see Fig. 487):] Die vordere Spitze befestigt sich an der dreieckigen rauhen Fläche vor dem medialen Zwischenhöcker und breitet sich noch über den vorderen Rand der Schienbeinendfläche hinaus fächerförmig auf die Vorderfläche des Knochens an den Untergelenkrand hin aus (...)

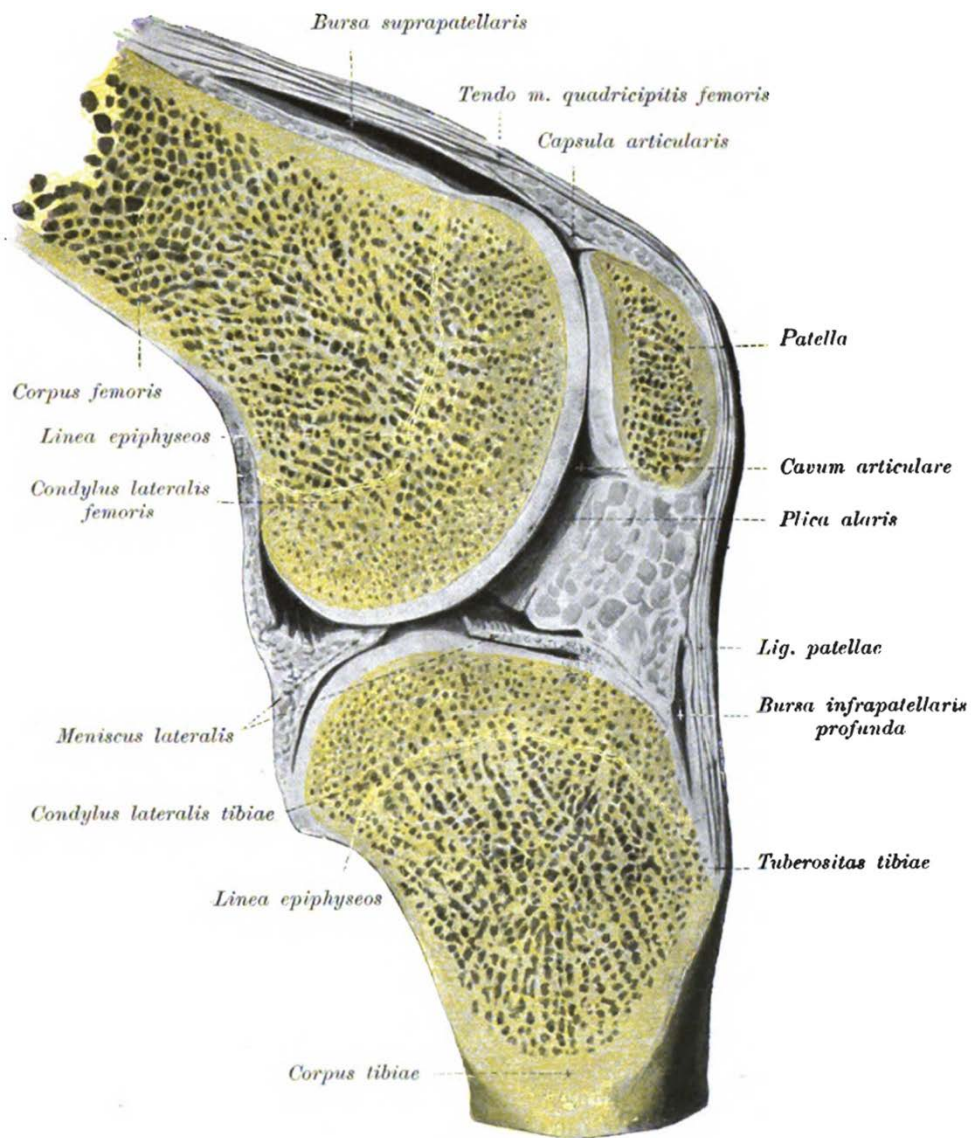


Figure 487. Depiction of a sagittal cut of a right, slightly flexed knee showing the lateral meniscus. Modified from Fick (1904)¹¹.

[ACL (see Fig. 488):] Das am Schienbein vorne, d. h. Vor dem medialen Zwischenhöcker [Eminentia intercondylea tibiae] (...) ansetzende und deshalb als „vorderes“, von den B. N. A. Bezeichnete Kreuzband entspringt an der lateralen Wand der Zwischenrollengrube [Foss. Intercond. Femoris, facies lateralis], also an der lateralen Femurrollee. Die Ursprungsstelle ist etwa 2 cm hoch und nimmt den hintersten Teil der Rolleninnenseite ein, entlang dem medialen Knorpelrand der lateralen Rolle (...). Das Band verläuft von da als platt-rundlicher Strang nach ab-, vor-, und etwas medialwärts zu dem dreieckigen Feld an der oberen Schienbeinfläche vor dem Zwickenhöcker (...). Der Ansatz des Bandes am Schienbein (...) liegt zwischen dem vordersten Ausläufer des Hinterhornes des lateralen C-Knorpels und dem Ansatz des Vorderhornes des medialen C-Knorpels und kann direkt in den Knorpelüberzug des medialen Schienbeintellers verfolgt werden. Sein Ansatz liegt gerade in der Längsachse des Schienbeinschaftes (...).

Meist verbinden sich einige Bündel des vorderen Kreuzbandansatzes mit dem Vorderende des lateralen C-Knorpels (...).

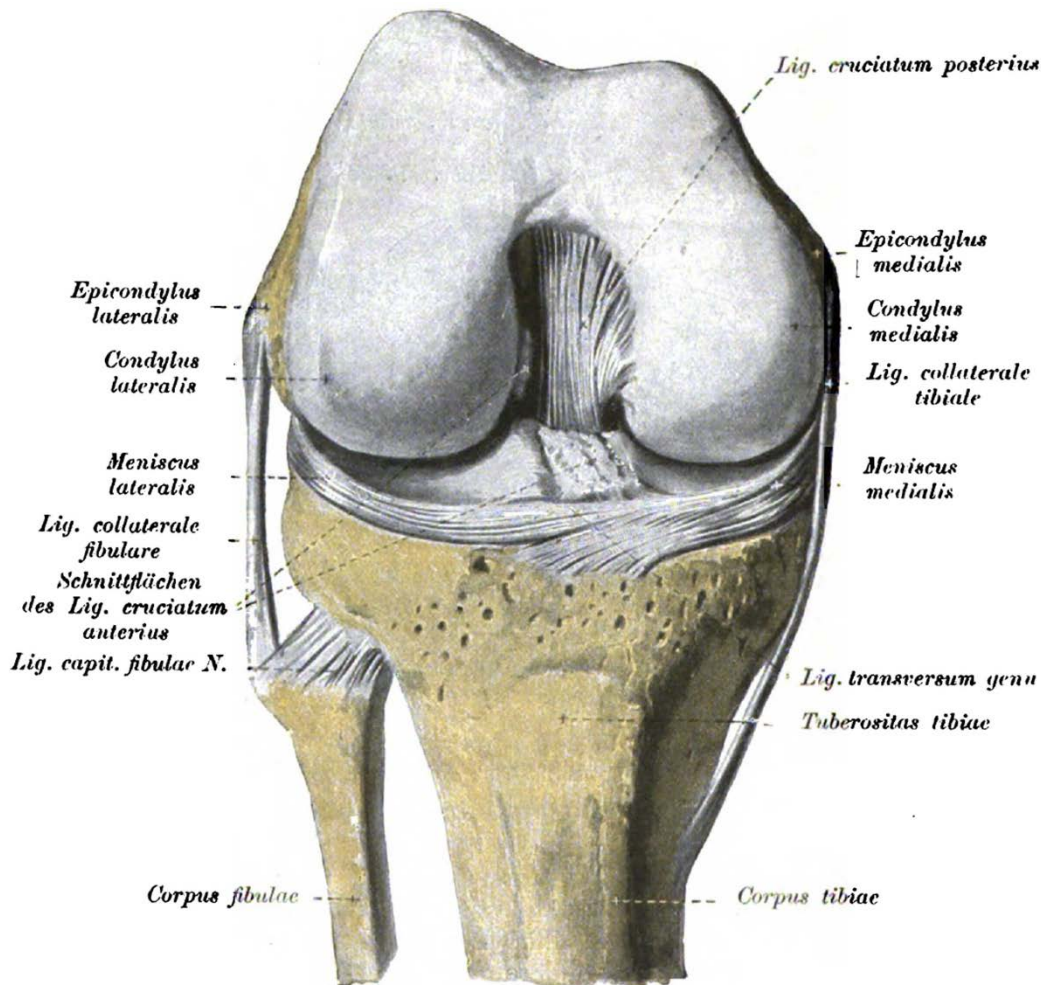


Figure 488. Anterior view of right knee, bent, with ACL detached. Modified from Fick (1904)¹¹.

[PRLM:] Ja, man kann sagen, der laterale C-Knorpel ist ein Stück weit in den medialen hineingeschoben, denn die Enden des medialen umfassen die des lateralen C, wie aus [Fig. 501] (nach Poirier) hervorgeht.

[PRMM:] Die hintere Spitze des medialen C-Knorpels setzt sich als deutlich quergebänderte Haut an der dreieckigen abschüssigen Fläche hinter dem medialen Zwischenhöcker an.

[PCL attachment:] Das am Schienbein hinten ansetzende Kreuzband ist etwas stärker als das vordere. Es entspringt auch in der Zwischenrollengruppe [F. Intercondylea fem.], aber von der medialen Wand derselben, also von der lateralen Fläche der medialen Rolle und angrenzenden Teilen des vorderen und unteren Randes der Fossa intercondylea. (...) Vom Ursprung aus verläuft das Band nach ab-, rück- und etwas lateralwärts zum Ausschnitt des hinteren Schienbeinrandes. Das hintere Kreuzband verläuft steiler, weniger schräg als das

vordere. Der Bandansatz liegt etwa 2 cm hinter der Mitte der oberen Schienbeinfläche, hinter den Ansatzstellen des Hinterhornes beider C-Knorpel (...), mit denen es durch ziemlich derbe Bündel verbunden ist. Der Bandansatz greift etwa 1/2 cm auf dem hinteren Schienbeinrand über. Auch dieses Band läuft beim Aufrechtstehenden nicht in „einer Ebene“, sondern so, daß man an den unteren Teilen des Bandes von einer Vorder- und einer Hinterseite (wenn die Kapsel abpräpariert ist) sprechen kann [see Fig. 489] an den oberen Teilen aber besser von einer lateralen und einer medialen; und zwar wird die oben „laterale“ Seite unten zur „Hinterseite“ (...).

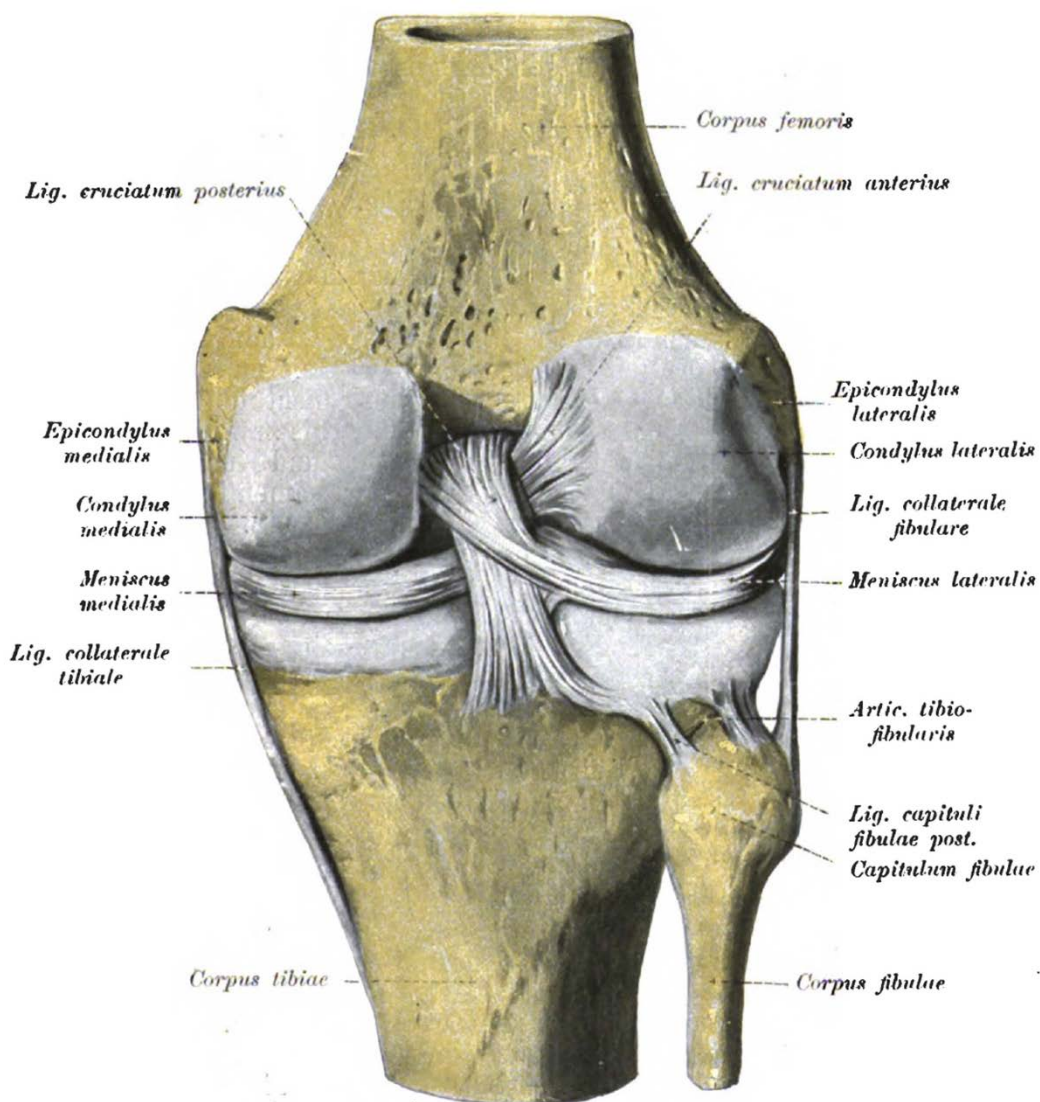


Figure 489. Right knee, extended, with capsule detached (posterior view). Modified from Fick (1904)¹¹.

Atlas der deskriptiven Anatomie des Menschen (1904) by Sobotta

The following are passages extracted from the English translation Atlas and Text-Book of Human Anatomy (1906), volume I, Bones, ligaments, joints, and muscles, by Sobotta:

[The tibia:] The *superior extremity* is the thickest portion of the bone. It presents two condyles, which articulate with the lower end of the femur, and are known as the *internal* and *external condyles*. They exhibit upon their upper surfaces two rounded, triangular, slightly concave areas, the *internal* and *external articular surfaces*, for the femoral condyles, whose concavities (especially that of the external one) are considerably less than the convexities of the femoral condyles. These areas are separated by a median elevation, the *intercondyloid eminence* or *spinous process*, which presents two small tubercles, the *internal* and *external intercondyloid tubercles*, and in front and behind the eminence are small shallow depressions which are known respectively as the *anterior* and *posterior intercondyloid fossae* [Fig. 490]. The articular surfaces are bounded by the almost vertical bony margins of the upper end of the tibia, the *infraglenoid margin* (...).

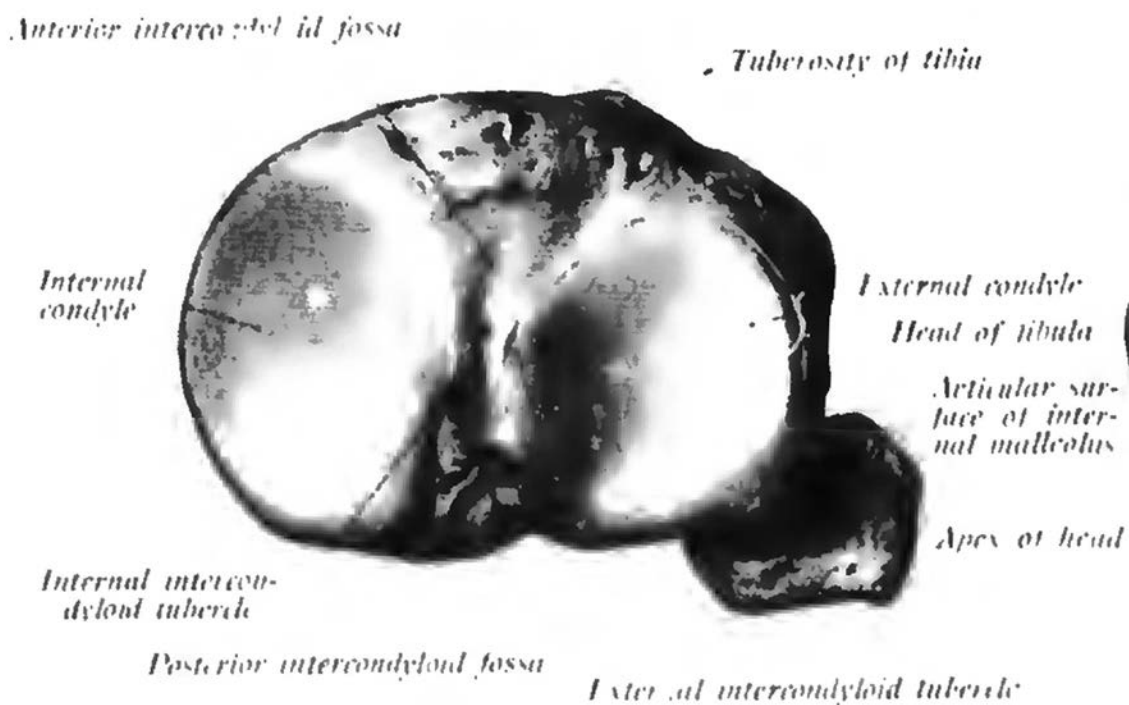


Figure 490. Superoinferior view of a right knee (anterior is above). Modified from Sobotta (1906)¹⁶.

Appendix II. Russian and Eastern literature

Anatome Topographica Sectionibus per Corpus Humanum Congelatum Triplici Directione Ductis Illustrata (1855)

The following illustrations (Fig. 491 – Fig. 496) were extracted from *Anatome Topographica Sectionibus per Corpus Humanum Congelatum Triplici Directione Ductis illustrata* (1855) by Nikoláj Ivánovich Pirogón (under the Latinized name Nicolau Pirogoff), originally published in Russian as *Топографическая анатомия по распилам через замороженные трупы. Т. 4. — СПб., 1853.*

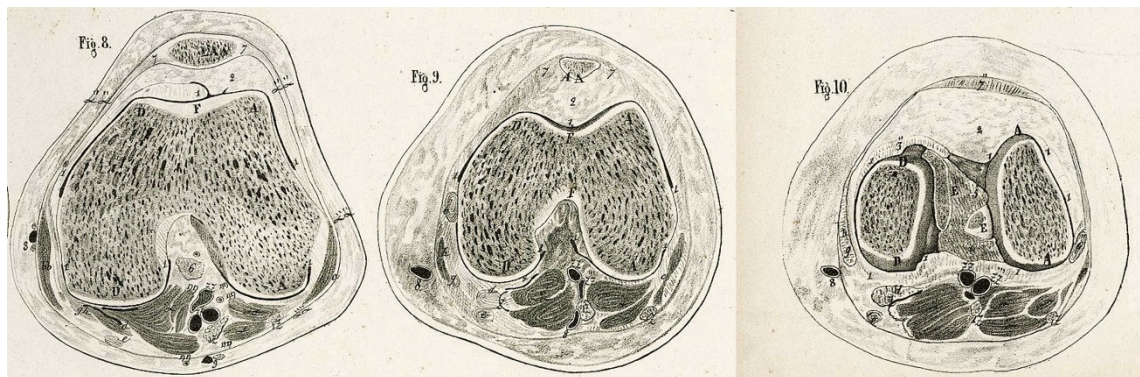


Figure 491. Axial cuts of the knee, modified from “ice anatomy” by Pirogón (1855)¹³.

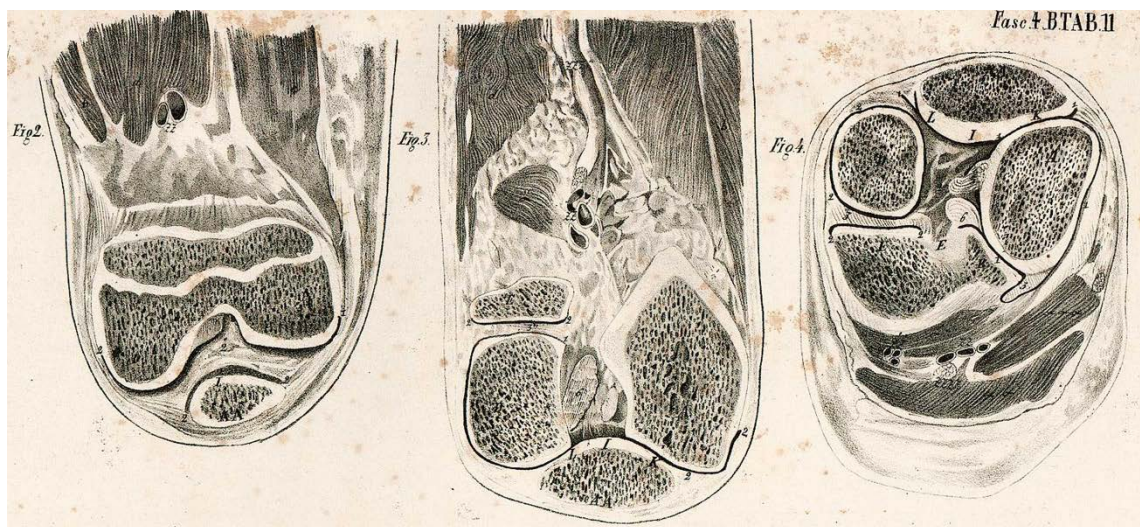


Figure 492. Axial oblique cuts of the knee, modified from “ice anatomy” by Pirogón (1855)¹³.

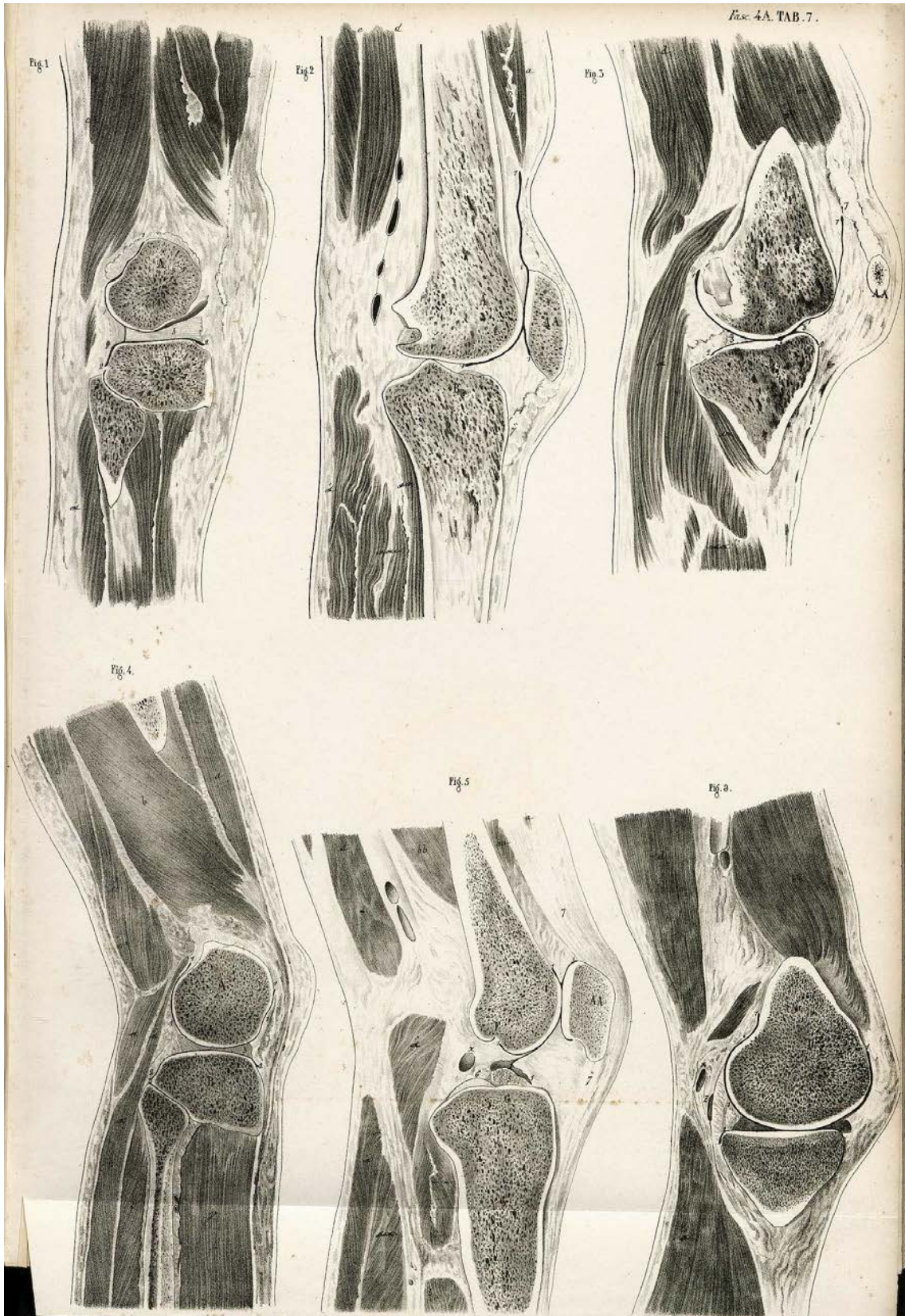


Figure 493. Sagittal cuts of the knee in extension, modified from "ice anatomy" by Pirog6v (1855)¹³.

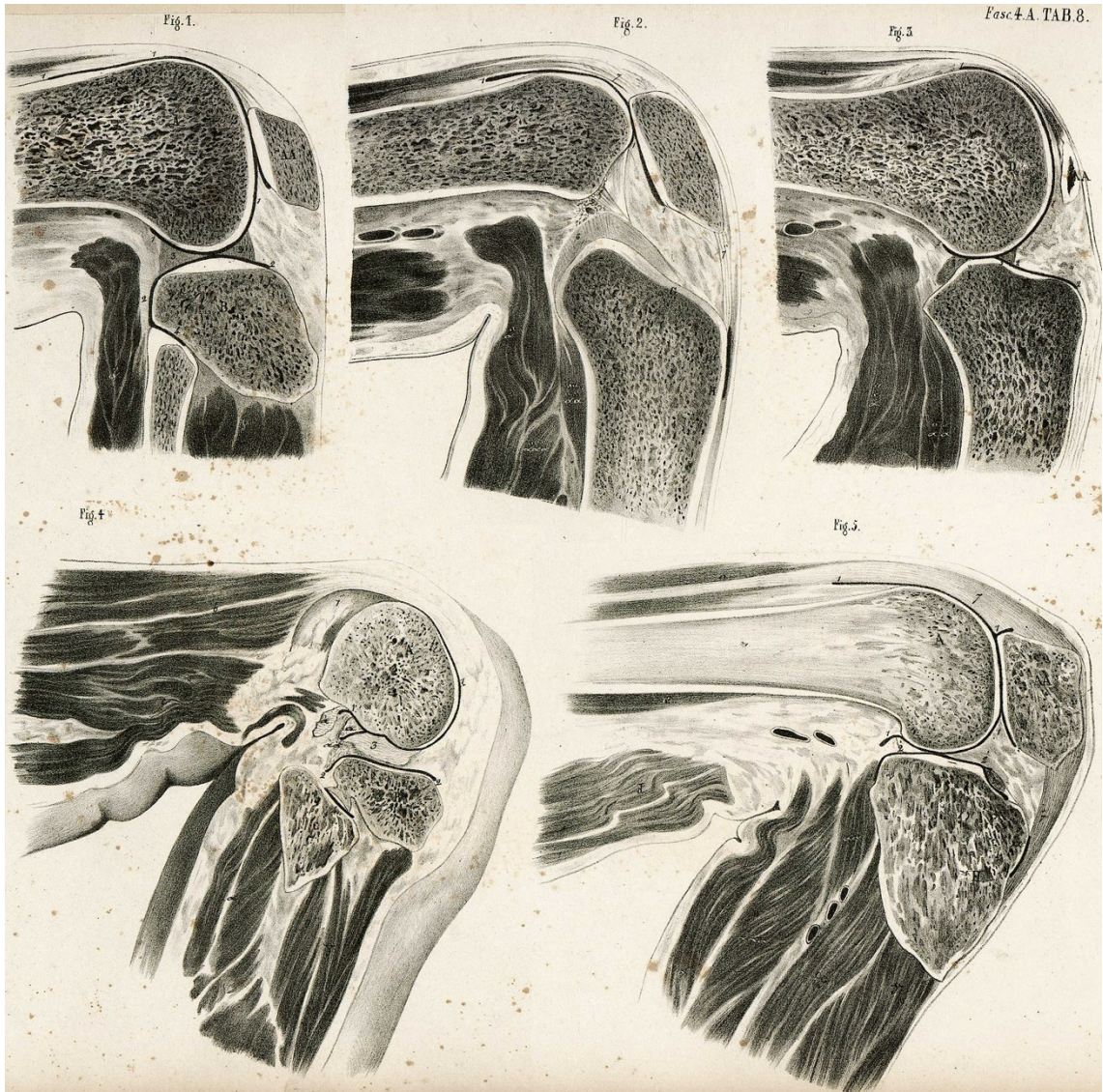


Figure 494. Sagittal cuts of the knee in approximately 90° of flexion, modified from “ice anatomy” by Pirogón¹³.

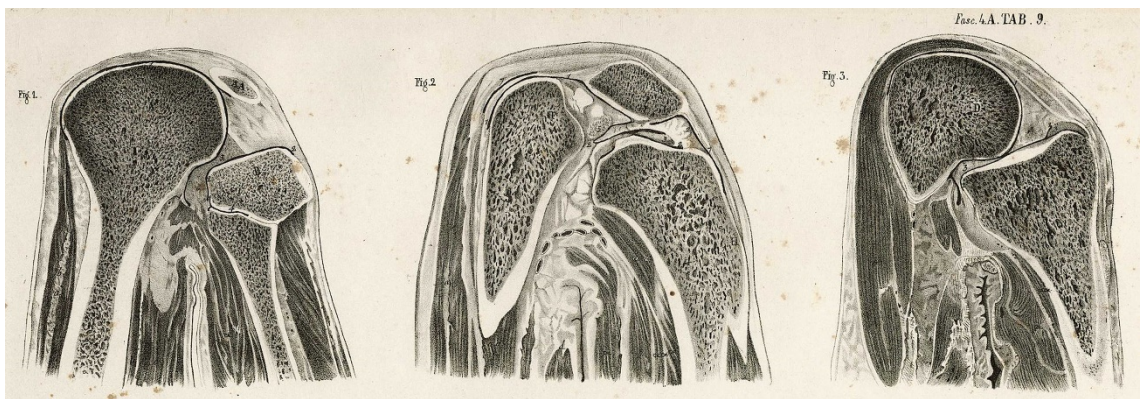


Figure 495. Sagittal cuts of the knee in high flexion degrees, modified from “ice anatomy” by Pirogón (1855)¹³.

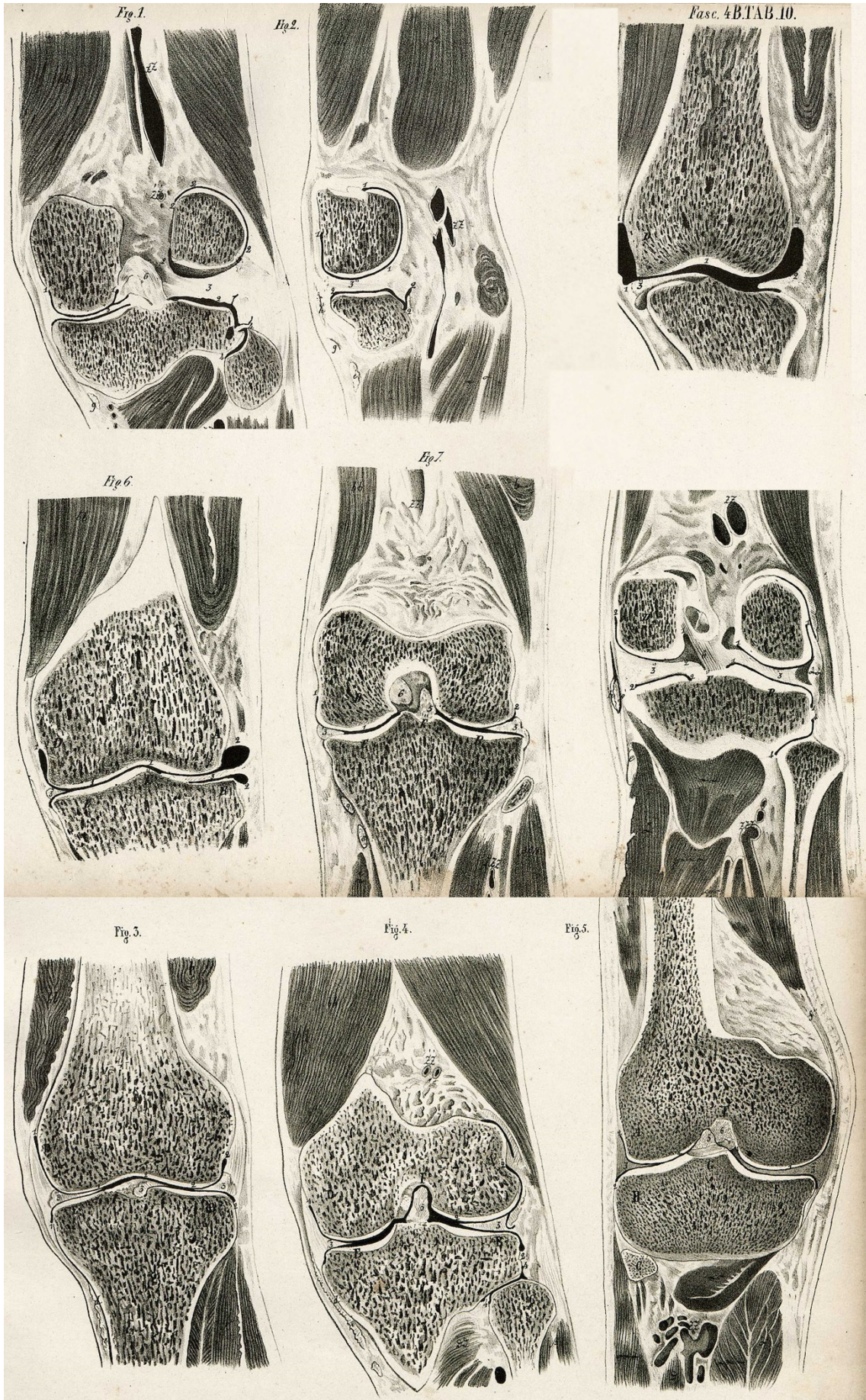


Figure 496. Coronal cuts of the left knee in extension, modified from "ice anatomy" by Pirog6v (1855)¹³.

Az ember anatómiájának atlasza (1962) by Kiss and Szentágothai

Fig. 497 is an illustration extracted from the book *Atlas of Human Anatomy*, 48th edition (1962), by Ferenc Kiss and János Szentágothai. Images taken from the Russian translation *Анатомический атлас человеческого тела. В 3-х томах. (1973 г.)*. The other illustrations including the proximal tibia – not shown – are quite similar to Fick's original images.

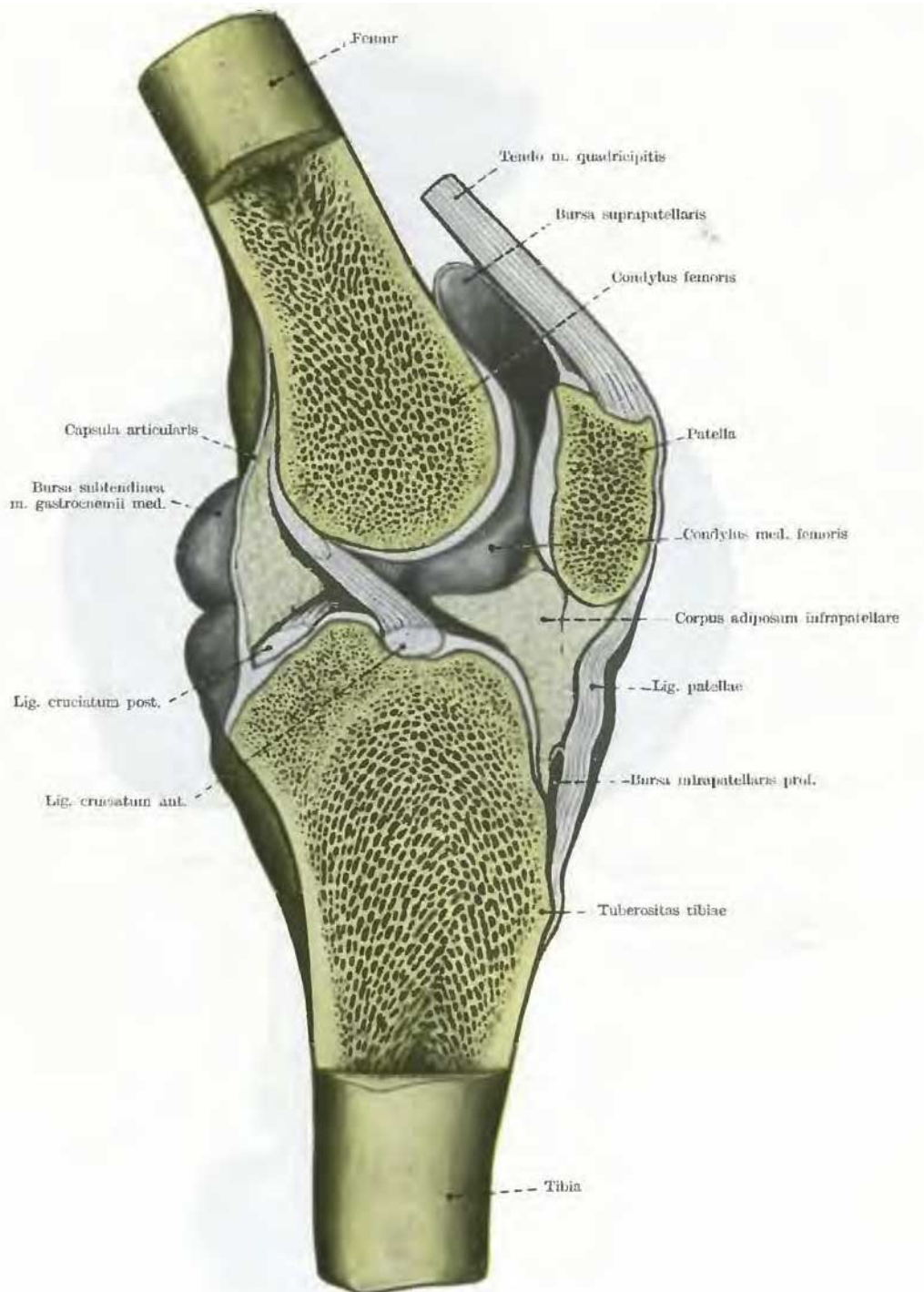


Figure 497. Depiction of sagittal cut of the knee through lateral tubercle, with ACL attachment shown. Modified from Kiss & Szentágothai (1973)¹⁸.

Appendix III. English literature

Observations of the Head of the Tibia (1904)

The following text is a summary of the article Observations of the Head of the Tibia (1904), by Frederick Gymer Parsons:

The spine of the tibia consists always of two eminences placed side by side, separated by an oblique groove which runs backward and outward. Each of these eminences is the portion of the articular surface which is nearest the centre of the head of the tibia; the external tubercle is limited anteriorly and posteriorly by the two horns of the external semilunar cartilage, while internally the anterior crucial ligament bounds it and lies in the oblique groove separating the two tubercles.

The internal tubercle is not bounded anteriorly and posteriorly by the semilunar cartilage, as the outer one is, but by the anterior and posterior crucial ligaments. It is prolonged forward and inward by a slight ridge, and backward and outward by a marked, oblique, rounded ridge (see Fig. 498). In front and behind this oblique ridge lie the anterior and posterior crucial ligaments. Along the summit of this ridge, as far as the internal tubercle, the posterior fibres of the posterior cornu of the external semilunar cartilage are attached.

The anterior cornu of the external semilunar cartilage is attached just in front of a slight oblique ridge which runs forward and inward from the outer tubercle, and forms the anterior boundary of the oblique groove which may be spoken of as the anterior crucial groove. Some of the anterior fibres of this cornu are continued into the outer part of the anterior crucial ligament. The main part of the posterior cornu of the external semilunar cartilage is attached just behind a small ridge which runs across the long axis of the anterior crucial groove, dividing it into an anterior part for the anterior crucial ligament, and a posterior part, in which the anterior fibres of the posterior cornu of the external semi-lunar cartilage lie (see Fig. 499).

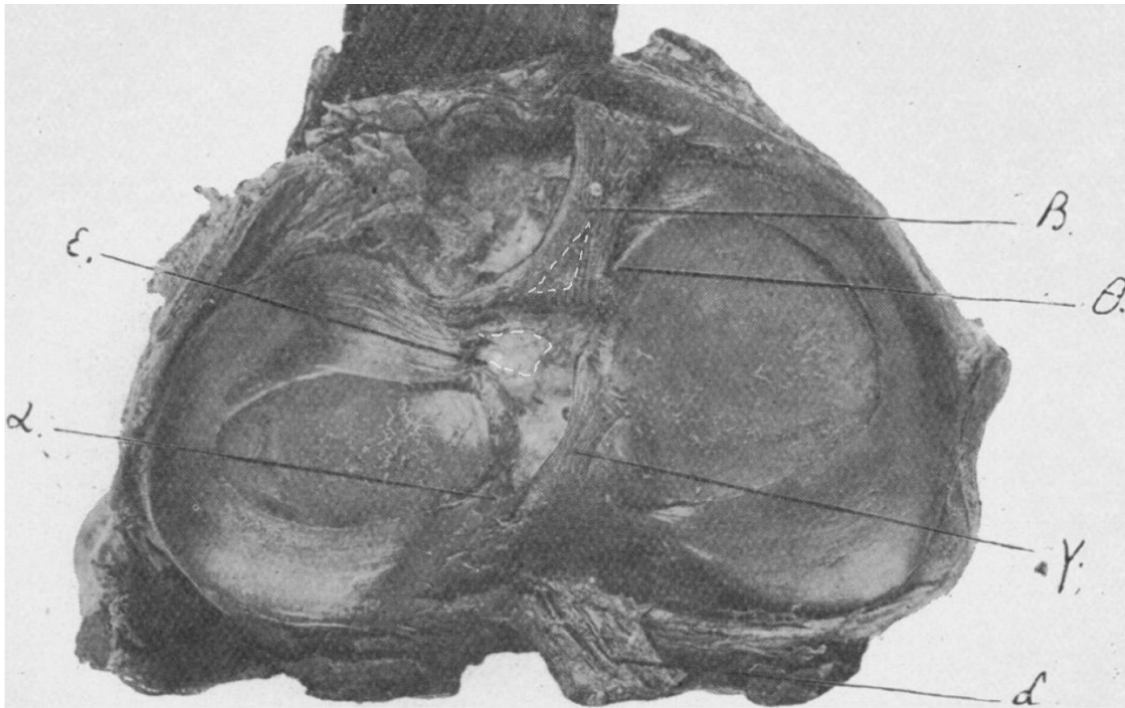


Figure 498. Proximal tibia with cruciate ligaments turned back (anterior is up). Image modified from Parsons (1906)¹². β : ACL reflected; ϵ : ARLM attachment; θ : AMIK (Parsons' knob). White dashed lines (added to the original image) separate the AIAR from the main C-shaped attachment of the ACL, and also delineate the thinner central aspect of the reflected ACL stump – as the hypothesized mirror image of the AIAR. Notice the delta-like appearance of the area drawn in the ACL stump (and also of the surrounding detached fibers) corresponding to a more closed C-shaped attachment.

The anterior attachment of the internal semilunar cartilage is to the inner side of a slight ridge which is usually present in the midline of the head of the tibia, at the junction of its anterior and second quarters. The posterior cornu of the internal semilunar cartilage is attached to the floor of the posterior crucial groove, where a small eminence is sometimes present.

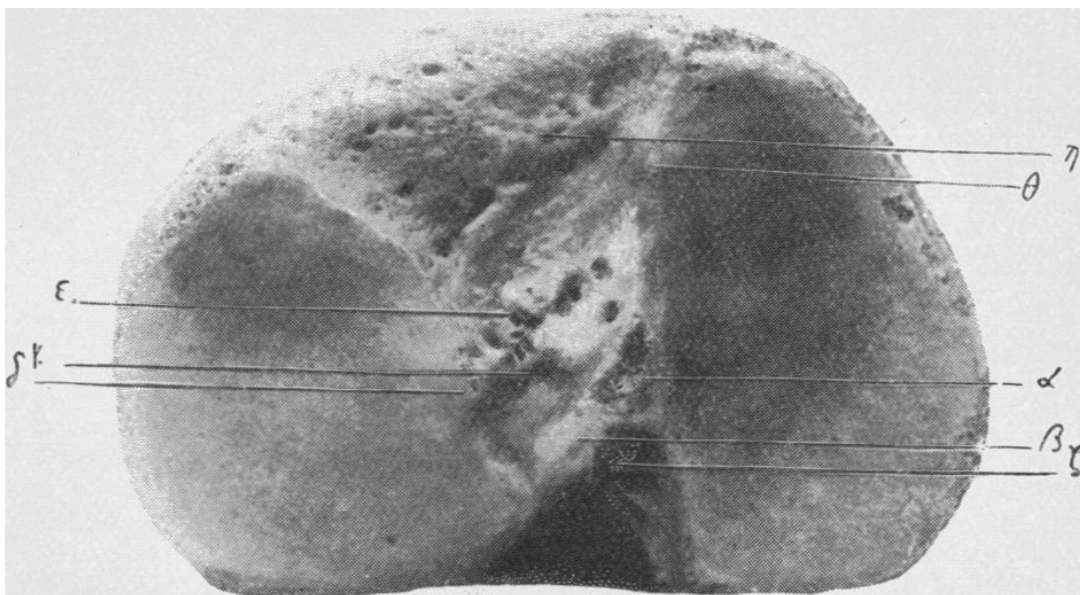


Figure 499. Proximal tibia. Image modified from Parsons (1906)¹². β : Intertubercular ridge.

The tibial attachment of the anterior crucial ligament is indicated by a little knob on the outer margin of the internal articular facet. From this the attachment runs transversely outward to about the midsagittal line of the tibial head. This tubercle rises up just where it is relieved from the pressure of the anterior crucial ligament posteriorly, and the anterior horn of the internal semilunar cartilage anteriorly.

The attachment of the posterior crucial ligament is in the junction of the superior and posterior surfaces of the head.

Anatomy of the Human Body (1918) by Gray

The following is a passage extracted from the book *Anatomy of the Human Body*, 20th edition (1918), by Henry Gray (see Fig. 500):

Between the articular facets, but nearer the posterior than the anterior aspect of the bone, is the intercondyloid eminence (*spine of tibia*), surmounted on either side by a prominent tubercle, on to the sides of which the articular facets are prolonged; in front of and behind the intercondyloid eminence are rough depressions for the attachment of the anterior and posterior cruciate ligaments

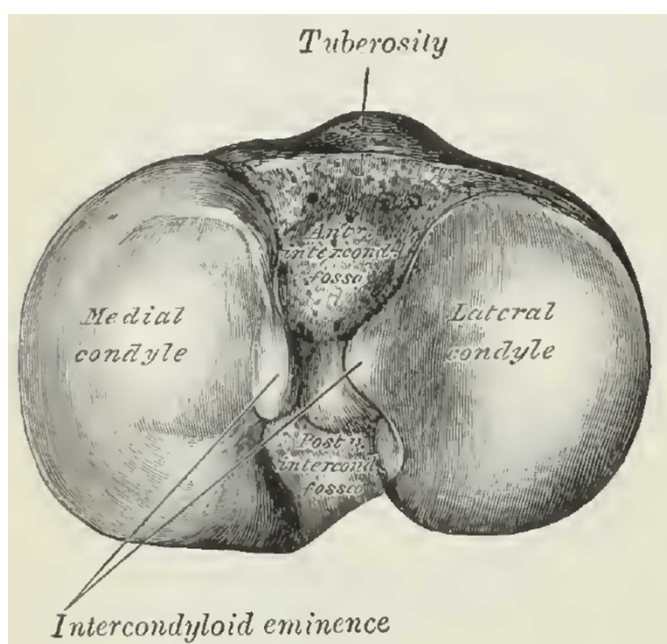


Figure 500. Upper surface of right tibia. Modified from Gray (1918)¹.

and the menisci. The anterior surfaces of the condyles are continuous with one another, forming a large somewhat flattened area; this area is triangular, broad above, and perforated by large vascular foramina; narrow below where it ends in a large oblong elevation, the tuberosity of the tibia, which gives attachment to the ligamentum patellæ; a bursa intervenes between the deep surface of the ligament and the part of the bone immediately above the tuberosity. *Posteriorly*, the condyles are separated from each other by a shallow depression, the posterior intercondyloid fossa, which gives attachment to part of the posterior cruciate ligament of the knee-joint.

Appendix IV. French and Romance literature

Traité d'Anatomie Humaine (1892) by Poirier & Charpy

The following are passages extracted from the series *Traité d'Anatomie Humaine*, first volume, *Ostéologie. Squelette de la jambe. Tibia* (1892), by Paul-Julien Poirier & Adrien Charpy:

[Intercondylar area (see Fig. 501):] La base ou plateau tibial, de contour irrégulièrement ovalaire, présente deux surfaces articulaires, séparées par une bande rugueuse antéro-postérieure. Les facettes articulaires, horizontales, très légèrement concaves, sont dites cavités glénoïdes du tibia. L'interne, ovalaire, est plus longue et plus concave que l'externe qui présente souvent une convexité antéro-postérieure. Ces deux surfaces articulaires se relèvent en pointe vers la partie moyenne du plateau tibial et forment ainsi ce qu'on appelle les épines du tibia. Celles-ci, éminences pyramidales, articulaires par une de leurs faces, appartiennent bien à la Surface articulaire; ce ne sont point du tout, comme on le dit à tort, des tubercules d'insertion. Ce relèvement des cavités glénoïdes augmente la concavité transversale des surfaces articulaires et par suite agrandit la Surface de contact avec les condyles fémoraux convexes transversalement.

En avant et en arrière des épines, les cavités glénoïdes sont séparées par deux surfaces triangulaires, rugueuses; l'antérieure est large et horizontale; la postérieure, plus petite, descend très obliquement vers la face postérieure de l'os entre les tubérosités tibiales qu'elle sépare par une large échancrure.

[Ligament and meniscal attachment:] (...) Les empreintes d'attache des ligaments croisés sont nettement dessinées sur ces surfaces qui donnent également insertion aux ligaments ou freins des ménisques articulaires.

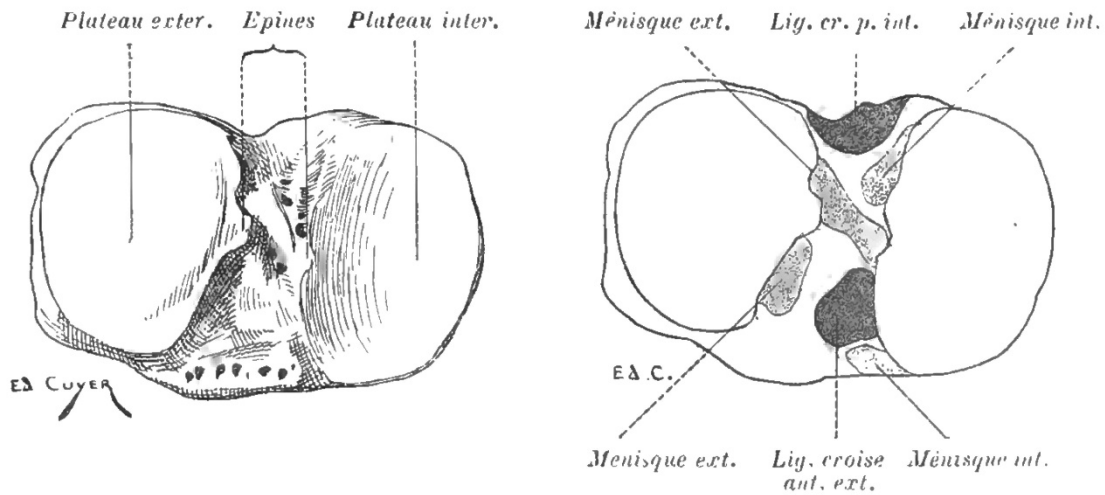


Figure 501. Depiction of osseous surface (left image) and attachment areas (right image). Ligamentous attachments in black, meniscal attachments in grey. Modified from Poirier (1892)².

[Bone trabeculae (see Fig. 502):] Les lamelles principales du tissu spongieux de l'extrémité supérieure forment deux systèmes: un système de travées verticales qui se détachent de la diaphyse et montent verticalement dans les condyles tibiaux, vers les cavités glénoïdes dont ils constituent les piliers; et un système de fibres arquées qui, s'appuyant sur le cylindre diaphysaire, convergent vers l'axe du cylindre en se superposant : quelques-unes de ces travées vont aboutir à cette partie verticale des cavités glénoïdes sur l'existence et le rôle de laquelle j'ai appelé l'attention : leur présence témoigne de l'importance des pressions que subissent les facettes articulaires des épines tibiales.

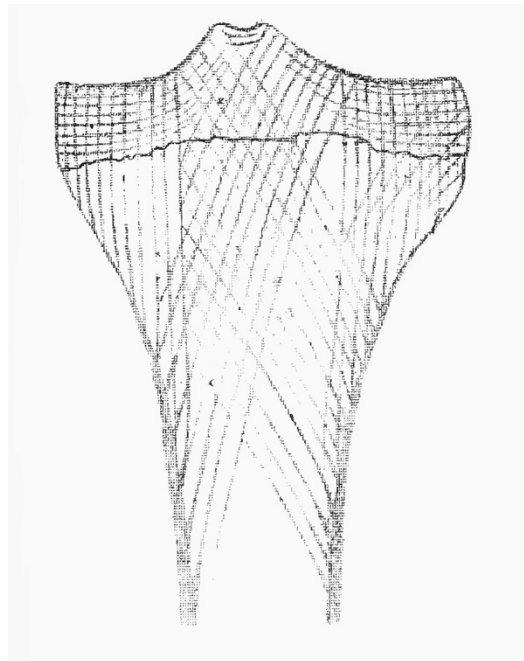


Figure 502. Architecture of the proximal extremity of the tibia. Modified from Poirier (1892)².

Traité d'Anatomie Humaine (1899) by Testut

The following is a passage extracted from the series *Traité d'Anatomie Humaine*, 4th edition, volume 1 (1899) by Léo Testut:

L'extrémité supérieure est très volumineuse, quadrangulaire, allongée dans le sens transversal. Destinée à s'articuler avec les condyles fémoraux, elle présente, à cet effet, deux surfaces articulaires horizontales, légèrement excavées à leur centre et connues sous le nom de cavités glénoïdes du tibia. On les distingue en

externe et interne : la cavité glénoïde interne est un peu plus longue que la cavité glénoïde externe ; mais, en revanche, celle-ci est un peu plus large. Entre les deux cavités s'élève une forte saillie, l'épine du tibia, plus rapprochée du plan postérieur de l'os que du plan antérieur. Cette épine se résout en haut en deux tubercules plus ou moins saillants, sur lesquels vient s'implanter le ligament postérieur du fibro-cartilage semi-lunaire externe. En avant comme en arrière de l'épine, s'étalent deux surfaces triangulaires, rugueuses et fort irrégulières [les surfaces pré- et rétro-spinales]: elles séparent l'une de l'autre les parties correspondantes des deux cavités glénoïdes et donnent insertion à des ligaments.

Traité d'anatomie humaine (1951) by Paturet

The following are passages extracted from the series *Traité d'Anatomie Humaine*, first volume (1951), by George Paturet (see Fig. 503):

Surface interglénoïdienne. – La surface interglénoïdienne est divisée en trois parties : a) l'une, moyenne, est constituée par un massif osseux, irrégulier, quadrangulaire : c'est l'*éminence intercondylienne du tibia*, elle-même surmontée de deux saillies pyramidales plus ou moins proéminentes appelées *épines du tibia* ou *épines tibiales* ; b) les deux autres placées respectivement en avant et en arrière des épines constituent les surfaces *préspinale* et *rétrospinale* du tibia (...).

a) Les épines du tibia sont situées à l'union du tiers antérieur et des deux tiers postérieurs de la surface interglénoïdienne. Elles sont l'une *interne*, l'autre *externe* ; l'interne est généralement plus saillante et un peu plus antérieure que l'externe ; elles sont séparées l'une de l'autre par une échancrure, l'*échancrure interépineuse* ; celle-ci est rugueuse dans sa moitié antérieure, régulière, lisse et unie dans sa moitié postérieure, et sur l'os sec elle semble se continuer en arrière de l'épine tibiale externe avec la cavité glénoïde externe. Les deux épines tibiales déterminent par leur surélévation un relèvement des cavités glénoïdes et une augmentation de l'étendue des surfaces articulaires glénoïdiennes ; elles représentent en quelque sorte le mur de soutènement de la partie centrale, infléchie en haut, de la cavité glénoïde correspondante (Rouvière).

En avant et en arrière des épines tibiales, la surface interglénoïdienne présente deux champs triangulaires, en partie hérissés de rugosités, qui vont en s'élargissant à mesure qu'on s'éloigne du massif épineux : ce sont les *surfaces*

pré- et rétrospinale, au niveau desquelles s'insèrent les ligaments croisés du genou et les freins méniscaux.

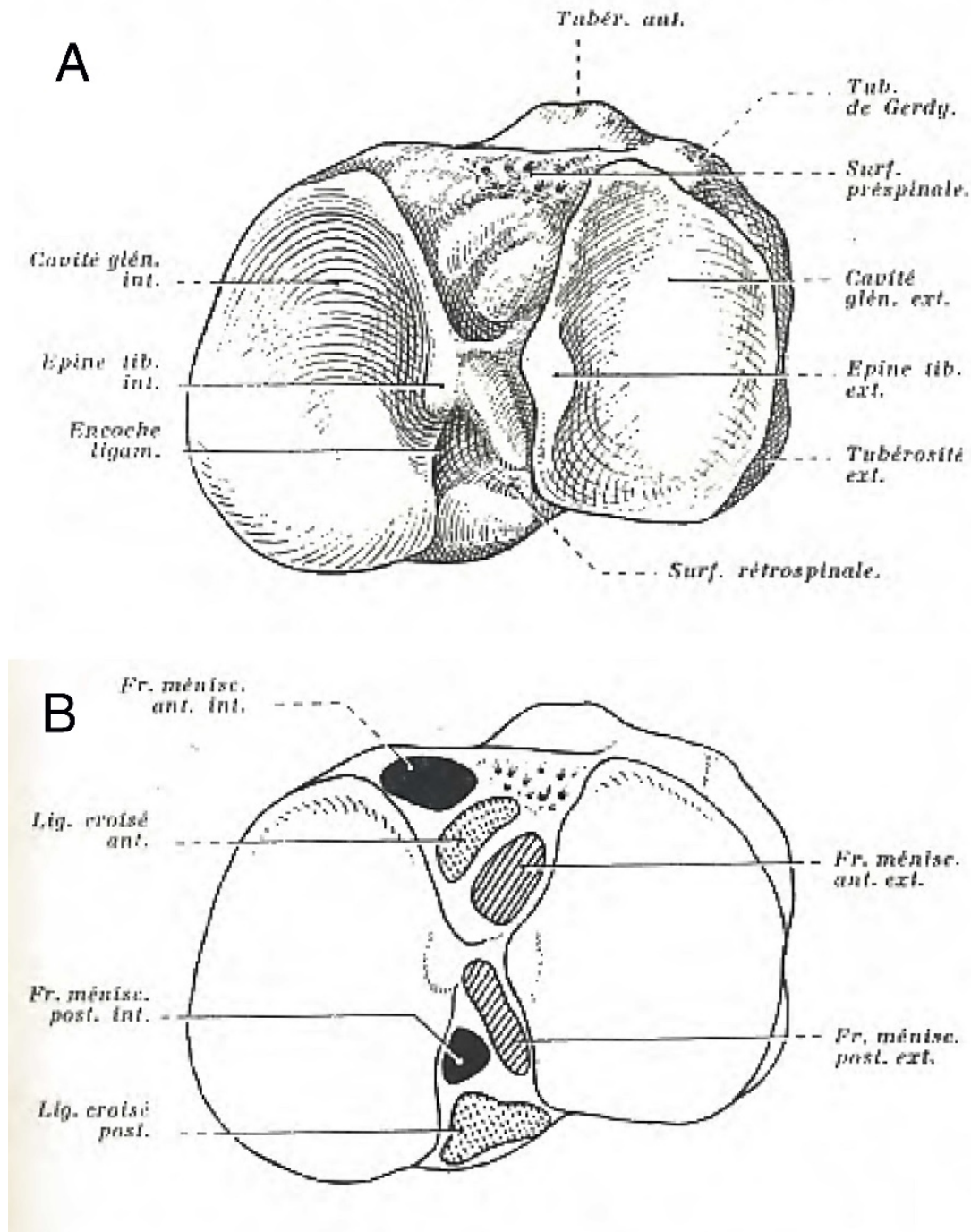


Figure 503. Image modified from Paturet (1951)¹⁹ (anterior is up, medial is left) Observe the ACL attachment – dotted surface – in the inferior image (B) corresponding to the comma-like elevation depicted in the osseous surface (A).

b) La surface préspinale est la plus étendue ; elle occupe les deux tiers de la surface interglénoïdienne ; de forme triangulaire à base antérieure, elle atteint par l'intermédiaire de celle dernière la face antérieure des plateaux tibiaux dont elle est séparée par un bord mousse à contour polycyclique ; elle est légèrement inclinée de dedans en dehors et d'arrière en avant. Elle présente *deux facettes*

ovales qui bordent le versant axial de la cavité glénoïde interne : α) l'une, *antérieure*, à grand axe presque transversal, représente l'empreinte d'insertion du frein méniscal antéro-interne ; cette empreinte affleure le rebord antérieur du plateau tibial interne ; β) l'autre, *postérieure*, à grand axe oblique en avant et en dehors, représente l'empreinte d'insertion du ligament croisé antéro-externe ; en dehors de cette dernière empreinte, et en avant de l'épine tibiale externe, on remarque l'existence d'une petite dépression, tantôt disposée en gouttière, tantôt cupuliforme, correspondant à l'insertion du frein méniscal antéro-externe.

La capsule de l'articulation du genou s'insère sur la partie la plus antérieure de la surface préspinale, suivant une ligne courbe à concavité antérieure située à 3 ou 4 millimètres en arrière du bord antérieur.

c) La surface rétrospinale, plus petite que la précédente, est inclinée obliquement de haut en bas, d'avant en arrière et de dehors en dedans, de telle sorte qu'en dedans elle est bordée et surplombée par le segment rétrospinal du bord axial de la cavité glénoïde interne.

Beaucoup plus régulière que la surface préspinale, elle présente d'avant en arrière *trois empreintes* d'insertion qui sont : α) l'empreinte du frein méniscal postéro-externe, qui atteint le versant postérieur de l'épine tibiale externe ; et dont le grand axe est oblique d'avant en arrière et de dedans en dehors ; β) l'empreinte d'insertion du frein méniscal postéro-interne, beaucoup moins étendue que la précédente, et de forme triangulaire ; elle borde le versant axial de la cavité glénoïde interne en arrière de l'encoche ligamentaire ; γ) et l'empreinte d'insertion du ligament croisé postéro-interne, également de forme triangulaire, qui s'étend même quelque peu sur le rebord postérieur du plateau tibial externe.

La capsule articulaire du genou s'insère sur la surface rétrospinale en marge du bord axial des cavités glénoïdes, laissant la plus grande partie de cette surface en dehors de l'articulation ; d'autre part, elle atteint le champ d'insertion du ligament croisé postérieur.

Anatomía Humana (1959) by Orts Llorca

The following is a passage extracted from the book *Anatomía Humana*, 2^a edición (1959) by Francisco Orts Llorca:

Ambas superficies articulares están separadas entre sí, en su parte media, por un relieve óseo bien aparente: la espina de la tibia (*eminencia intercondylica*), en la cual se pueden distinguir dos tubérculos separados por una depresión. El

tubérculo interno (*tuberculum intercondylicum tibiale*) se eleva más y es más vertical que el externo (*tuberculum intercondylicum fibulare*). Por delante y detrás de la espina de la tibia las cavidades articulares están separadas por dos superficies rugosas, llamadas prespinal y retroespinal. La superficie retroespinal (*fossa intercondylica posterior*) es un canal que contribuye a separar ambos cóndilos tibiales; la prespinal (*fossa intercondylica anterior*) es más extensa y rugosa, pero no excavada. Veremos que en estas superficies se insertan los ligamentos cruzados. A la espina de la tibia y a las superficies pre y retroespinal, desprovistas de revestimiento cartilaginoso y que separan ambas cavidades glenoideas, se las llama, en conjunto, área intercondylica. La superficie prespinal se continúa hacia abajo por una porción rugosa, que termina en la tuberosidad anterior de la tibia.

